

パイスター分子制御による未来型物質変換研究

平成27年度～平成31年度私立大学戦略的研究基盤形成支援事業

研 究 成 果 報 告 書

令和2年5月

学校法人名：関西学院

大 学 名：関西学院大学

研究組織名：パイスター分子制御研究センター

研究代表者：羽村 季之（関西学院大学 理工学研究科 教授）

## 目次

研究発表主要論文.....	1
(雑誌論文・学会発表要旨)	
雑誌論文表紙等.....	420
公開シンポジウム 講演プログラム.....	432



Cite this: *Chem. Commun.*, 2019, 55, 11021

Received 17th July 2019,  
Accepted 23rd August 2019

DOI: 10.1039/c9cc05500b

rsc.li/chemcomm

# Intramolecular benzoallene–alkyne cycloaddition initiated by site-selective $S_N2'$ reaction of epoxytetracene en route to $\pi$ -extended pyracylene†

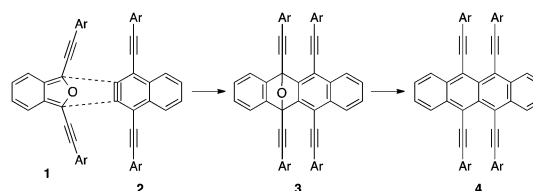
Kei Kitamura,‡ Kenta Asahina, Kazuhiko Adachi and Toshiyuki Hamura \*

A hydrogen halide promoted cascade reaction of epoxytetracene to afford halo-benzoindenotetracene including a benzoallene intermediate was developed. The remaining two alkynyl groups in benzoindenotetracene were further reacted with norbornadiene or arylamine through transition metal-catalyzed cyclization to give  $\pi$ -extended pyracylene derivatives.

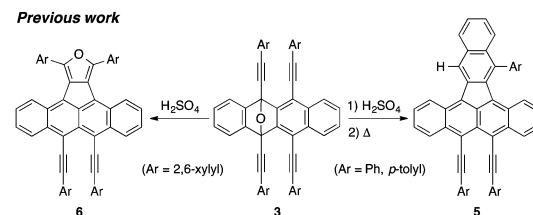
Introduction of  $\pi$ -conjugated substituents at the *peri* position onto the polyacene core would induce a distortion, which leads to unique physical properties due to the positive or negative  $\pi$ - $\pi$  interaction.<sup>1,2</sup> Another interesting feature of this distorted  $\pi$ -conjugated structure is its potentially high reactivities caused by the closely located multiple bonds at the *peri* position.<sup>3</sup> In this context, we previously reported efficient synthetic access to 5,6,11,12-tetrakis(phenylethynyl)tetracenes (**4**), a new class of  $\pi$ -extended tetracenes, *via* the [4+2] cycloaddition of dialkynylisobenzofuran **1** and dialkynyl-naphthalene **2** (Scheme 1).<sup>4,5</sup>

An initial study on the reactivities inherent in the *peri*-ethynyl-substituted tetracene derivatives **3** and **4** led to the development of the following two reactions: (1) thermal isomerization of  $\pi$ -extended rubrene **4** to benzoindenotetracene **5** (**3**  $\rightarrow$  **4**  $\rightarrow$  **5**) and (2) acid promoted cyclization of epoxytetracene **3** to furan **6** (**3**  $\rightarrow$  **6**) (Scheme 2).<sup>6</sup>

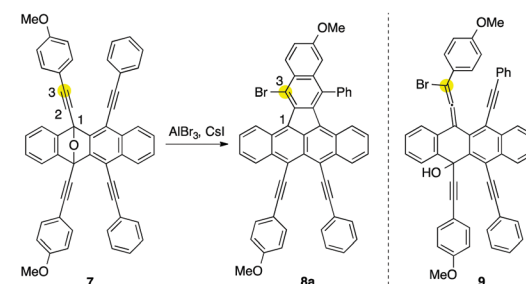
Upon further investigation along these lines, we accidentally found that epoxytetracene **7** underwent cascade reaction upon treatment with  $AlBr_3$  and  $CsI$ , affording bromo-benzoindenotetracene **8a** in low yield (Scheme 3).<sup>7</sup> Product **8a** might be formed by site-selective  $S_N2'$  attack by bromide ions at the  $C_3$  position in epoxytetracene **7** and subsequent intramolecular [4+2] cycloaddition of benzoallene intermediate **9**.



Scheme 1 A synthetic route to  $\pi$ -extended rubrene **4**.



Scheme 2 Two reaction modes of *peri*-ethynyl-substituted epoxytetracene **3**.



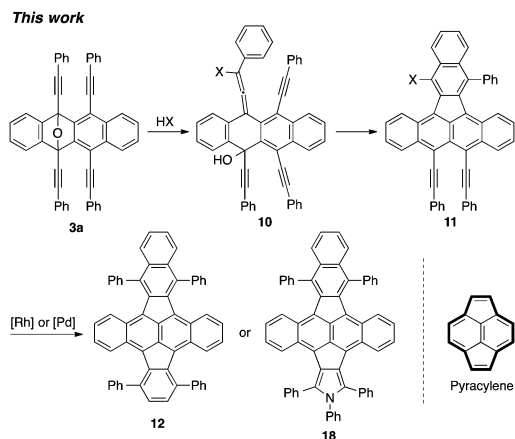
Scheme 3 Lewis acid promoted cascade reaction of epoxytetracene **7** to afford benzoindenotetracene **8**.

Department of Applied Chemistry for Environment, School of Science and Technology, Kwansei Gakuin University, 2-1 Gakuen, Sanda, Hyogo 669-1337, Japan. E-mail: thamura@kwansei.ac.jp

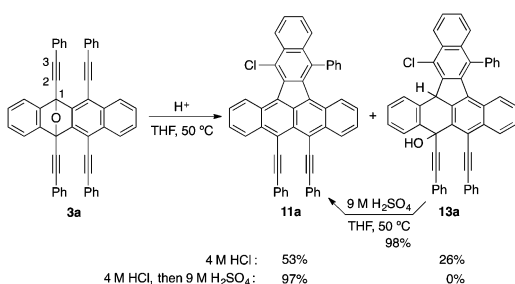
† Electronic supplementary information (ESI) available. CCDC 1871070 and 1871071. For ESI and crystallographic data in CIF or other electronic format see DOI: 10.1039/c9cc05500b

‡ Present address: Faculty of Pharmaceutical Sciences, Tokushima Bunri University, 180 Yamashiro-cho, Tokushima 770-8514, Japan.

Based on this knowledge, we developed an acid-promoted cascade reaction of epoxytetracene **3a** to afford halo-benzoindenotetracene **11**. In this successive process, hydrogen halide served as an initiator for site-selective  $S_N2'$  reaction of epoxytetracene **3a**, thus generating benzoallene intermediate **10**, which, in turn, underwent intramolecular [4+2] cycloaddition



**Scheme 4** Intramolecular benzoallene-alkyne cycloaddition of **3a** and transition metal-catalyzed coupling reaction and cyclization of **11**.



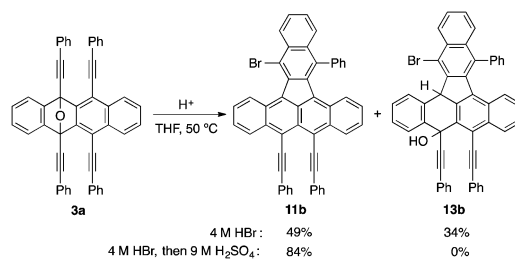
**Scheme 5** Acid promoted cascade reaction of epoxytetracene **3a** to afford benzoindenotetracene **11a**.

to give halo-benzoindenotetracene **11**. Further transformation through transition metal-catalyzed coupling reaction, followed by cyclization of **11**, produced novel  $\pi$ -extended pyracylene derivatives **12** and **18** with potentially unique properties based on the  $12\pi$ -antiaromatic pyracylene framework (Scheme 4).<sup>8</sup>

Scheme 5 shows the cascade reaction of epoxytetracene **3a**. Upon treatment of **3a** with 4 M HCl (THF, 50 °C, 10 h),  $S_N2'$  attack by chloride ions occurred site-selectively at the C<sub>3</sub> position, and subsequent intramolecular cyclization of the resulting benzoallene intermediate **10a** (X = Cl, see Scheme 4) gave chloro-benzoindenotetracene **11a** and dihydrobenzoindenotetracene **13a**<sup>9</sup> in 53% and 26% yields, respectively.

In this successive process, prolonged reaction and/or higher reaction temperature under similar conditions did not promote the formation of indenotetracene **11a**. On the other hand, use of a stronger acid (9 M H<sub>2</sub>SO<sub>4</sub>) was effective for dehydration of **13a** to **11a** (98% yield). Based on this result, epoxytetracene **3a** was sequentially treated with 4 M HCl and 9 M H<sub>2</sub>SO<sub>4</sub> (THF, 50 °C) to give **11a** in 97% yield. These results indicated two possible routes for the formation of **11a** from epoxytetracene **3a** (*vide infra*).

The structure of **11a** was elucidated by X-ray crystal structure analysis after recrystallization from chloroform/hexane (Fig. S4, ESI†).<sup>10</sup> There are two independent half molecules in the unit cell, and each molecule adopts a different conformation. The common feature of these molecules is a twist conformation in

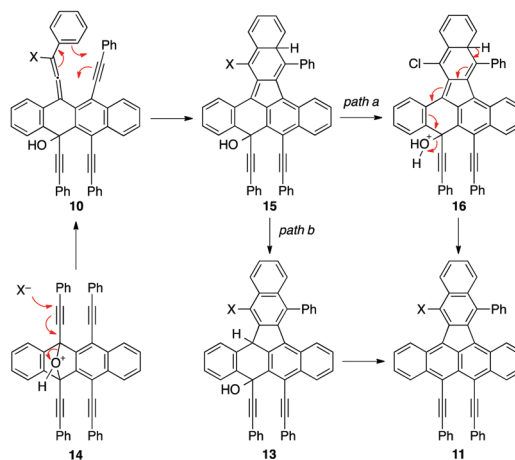


**Scheme 6** HBr promoted cascade reaction of epoxytetracene **3a** to give bromo-benzoindenotetracene **11b**.

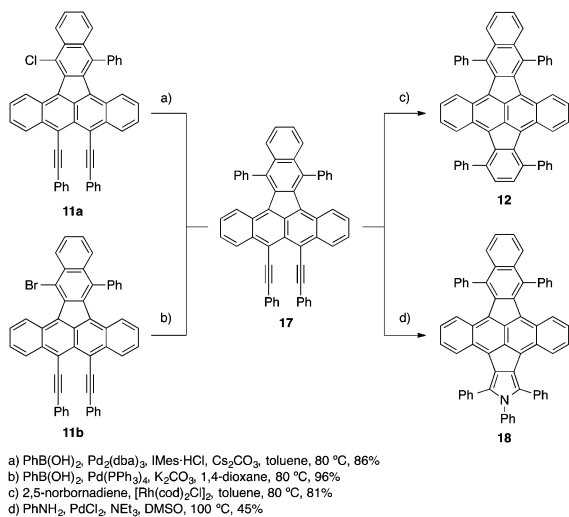
the tetracene and naphthalene moieties. The end-to-end twist angles of the tetracene and naphthalene planes are 16.4° and 10.8° for Mol-A, and 4.1° and 14.4° for Mol-B. In addition, the two ethynyl units are oriented aside from each other due to the steric  $\pi$ -congestion. The C<sub>29</sub>··C<sub>32</sub> and C<sub>30</sub>··C<sub>33</sub> distances are 2.84 Å and 3.31 Å in Mol-A, and 2.87 Å and 3.43 Å in Mol-B. The steric repulsion of the two alkynyl groups was also evaluated by the torsion angle (C<sub>29</sub>-C<sub>15</sub>-C<sub>17</sub>-C<sub>32</sub> = 12.1° for Mol-A and C<sub>29</sub>-C<sub>15</sub>-C<sub>17</sub>-C<sub>32</sub> = 2.9° for Mol-B). Moreover, the sp carbon atoms of the acetylene units were deformed from linearity (*e.g.* C<sub>15</sub>-C<sub>29</sub>-C<sub>30</sub> = 172.2° for Mol-A and C<sub>17</sub>-C<sub>32</sub>-C<sub>33</sub> = 171.1° for Mol-B).

Further examination of the reactivity of **3a** with Brønsted acids revealed that 4 M HBr also promoted the cascade reaction, affording the cyclized product **11b** in 49% yield, accompanied by a sizable amount of dihydrobenzoindenotetracene **13b** (Scheme 6). Again, sequential treatment of **3a** with 4 M HBr and 9 M H<sub>2</sub>SO<sub>4</sub> cleanly gave the aromatized product **11b** in 84% yield without producing the dihydro-derivative **13b**.<sup>11</sup>

The plausible mechanism for the formation of halo-benzoindenotetracene **11** is depicted in Scheme 7. In the first step, site-selective  $S_N2'$  attack of halide ions on protonated epoxytetracene **14** gave halo-allene intermediate **10**, which underwent an intramolecular Diels-Alder reaction, affording the heptacyclic alcohol **15**. Subsequent aromatization of **15** to the final product **11** has two routes. The first is the direct pathway by the dehydrative aromatization of the protonated intermediate **16** (path a).



**Scheme 7** Plausible reaction mechanism for the formation of halo-benzoindenotetracene **11**.



Scheme 8 Suzuki–Miyaura cross coupling of **11** and transition metal catalyzed cyclization of **17**.

The second is a stepwise process *via* 1,5-hydrogen shift of polycycle **15** to dihydrotetracene **13**, followed by its dehydrative aromatization (path b). As evidenced by the acid-promoted aromatization of **3a** (*vide supra*), the dehydration from **13** to **11** was much slower than that from **16**.

The halo-benzoindenotetracene **11**, thus obtained, is synthetically attractive since both the halogen atom introduced in the naphthalene moiety and proximal alkynyl groups at the *peri*-position can be used for further functionalization by transition metal catalysed coupling reaction and annulation, leading to the selective synthesis of highly condensed aromatic compounds (Scheme 8). Indeed, Suzuki–Miyaura coupling of **11a** with  $\text{Pd}_2(\text{dba})_3$  in the presence of IMes-HCl gave diphenyl-benzoindenotetracene **17** in 86% yield. Bromide **11b** also served as a good substrate in the coupling reaction to give **17** in high yield. Further  $\pi$ -extension by ring-construction using the proximal alkynyl groups in **17** was realized by the Rh catalyzed [2+2+2] cycloaddition with norbornadiene to give pyracylene **12** in 81% yield.<sup>12–14</sup> Pyrrole-containing  $\pi$ -extended pyracylene **18** was also prepared by treatment of **17** with aniline in the presence of  $\text{PdCl}_2$  and  $\text{NEt}_3$ .<sup>15</sup> These cyclopenta-fused polycyclic aromatics, thus obtained, have attracted substantial attention since pyracylene exhibits a considerable antiaromatic contribution to its electronic structure as well as a high electron affinity derived from its 12 $\pi$ -electron framework.<sup>8</sup>

To evaluate their electronic properties, the UV-visible absorption spectra and the cyclic voltammograms of **17**, **12**, and **18** were measured (Fig. 1 and 2). The absorption spectrum of compound **12** showed the longest wavelength absorption at  $\lambda_{\text{max}} = 710$  nm, which is red-shifted by 31 nm and 70 nm in comparison with those of **17** and  $\pi$ -extended tetracene **4** (Ar = Ph), respectively. Moreover, it is remarkably red-shifted by nearly 100 nm with respect to that of tetrabenzo-fused pyracylene,<sup>8c</sup> indicating effective  $\pi$ -extension by the peripheral substituents. Pyrrole-fused derivative **18** exhibited a similar absorption band ranging from 550 nm to 750 nm and had its absorption maximum at 707 nm. Time-dependent DFT calculations suggested that the longest

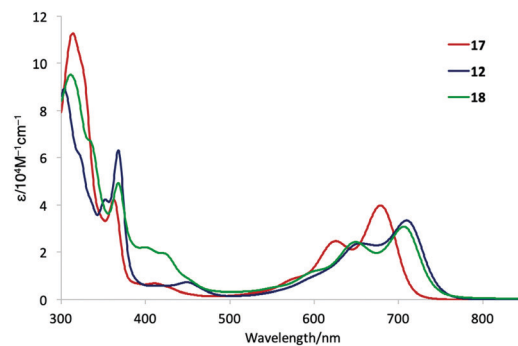


Fig. 1 UV–Vis absorbance spectra of **12**, **17**, and **18** in toluene.

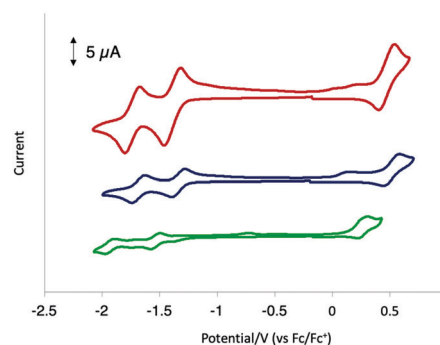


Fig. 2 Cyclic voltammograms of **17**, **12**, and **18** in THF.

wavelength of **12** is predominantly contributed by the HOMO  $\rightarrow$  LUMO transition at 711 nm with oscillator strength  $f = 0.40$ , which is consistent with experimental data. The cyclic voltammograms of **12**, **17**, and **18** were recorded in degassed THF (1.0 mM) using  $n\text{-Bu}_4\text{NPF}_6$  as a supporting electrolyte. In the reduction process, compounds **12** and **17** exhibited two reversible waves ( $E_{1/2} = -1.34$  V and  $-1.68$  V for **12**;  $E_{1/2} = -1.39$  V and  $-1.74$  V for **17**), reflecting their low-lying LUMO energy levels derived from their high electron affinities. In the oxidation process, irreversible waves were observed ( $E_{\text{onset}} = +0.31$  V for **12**;  $E_{\text{onset}} = +0.34$  V for **17**). The electrochemical gaps for **12** and **17** are 1.65 eV and 1.73 eV, respectively, which are in excellent agreement with the HOMO–LUMO energy gaps obtained from the onsets of their absorption spectra (748 nm, 1.66 eV for **12**; 715 nm, 1.73 eV for **17**). Pyrrole-containing derivative **18** showed two major reduction waves ( $E_{1/2} = -1.54$  V and  $-1.93$  V) and an irreversible oxidation wave ( $E_{\text{onset}} = +0.15$  V), which are negatively shifted compared to those of **12**. This difference was due to the existence of the electron donating pyrrole moiety in **18**. The energy gap is in good agreement with the onsets of the absorption spectra (744 nm, 1.67 eV).

To gain insight into their aromatic character, the nucleus-independent chemical shift (NICS) values were calculated for compounds **17**, **12**, and **18** (B3LYP/6-31G\*). The values of the two pentagonal rings in **12** are more positive (+8.4, +8.5) than that of **17** (+3.7), showing enhanced antiaromatic character after ring formation (Fig. 3). A similar tendency was observed for the pentagonal ring in **18**, although the value of the pentagonal ring (+5.8) fused to the naphthalene ring decreased.

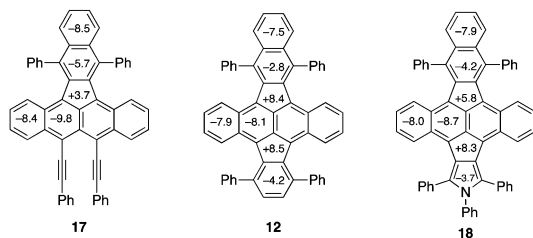


Fig. 3 NICS(0) values for compounds **17**, **12**, and **18** calculated at the GIAO-B3LYP/6-31G\* level.

A Brønsted acid promoted cascade reaction of epoxytetracene to afford halo-benzoindenetetracene was developed. The key process was initial site-selective  $S_N2'$  reaction of epoxytetracene, which selectively generated a benzoallene-alkyne intermediate. Further transformations including ruthenium-catalyzed [2+2+2] cycloaddition with norbornadiene or arylamine produced  $\pi$ -extended pyracylene. Further studies on developing the unique reactivities inherent in the *peri*-ethynyl-substituted polyacene derivatives are currently underway in our laboratory.

This work was supported by JSPS KAKENHI Grant Number JP15H05840 in the Middle Molecular Strategy and JST ACT-C Grant Number JPMJCR12YY, Japan.

## Conflicts of interest

There are no conflicts to declare.

## Notes and references

- For related reviews, see: (a) M. M. Richter, *Chem. Rev.*, 2004, **104**, 3003–3036; (b) M. Bendikov, F. Wudl and D. F. Perepichka, *Chem. Rev.*, 2004, **104**, 4891–4946; (c) J. E. Anthony, *Angew. Chem.*, 2008, **120**, 460–492 (*Angew. Chem., Int. Ed.*, 2008, **47**, 452–483); (d) S. Toyota, *Chem. Rev.*, 2010, **110**, 5398–5424.
- (a) B. Bossenbroek, D. C. Sanders, H. M. Curry and H. Shechter, *J. Am. Chem. Soc.*, 1969, **91**, 371–379; (b) H. A. Staab and J. Ipaktschi, *Chem. Ber.*, 1971, **104**, 1170–1181; (c) A. E. Jungk and G. M. J. Schmidt, *Chem. Ber.*, 1971, **104**, 3272–3288 see also: (d) R. A. Pascal, Jr., *Chem. Rev.*, 2006, **106**, 4809–4819.
- (a) B. Bossenbroek, D. C. Sanders, H. M. Curry and H. Shechter, *J. Am. Chem. Soc.*, 1969, **91**, 371–379; (b) H. A. Staab and J. Ipaktschi, *Chem. Ber.*, 1971, **104**, 1170–1181; (c) J. Blum, W. Baidossi, Y. Badrieh, R. E. Hoffman and H. Schumann, *J. Org. Chem.*, 1995, **60**, 4738–4742; (d) Y.-H. Kung, Y.-S. Cheng, C.-C. Tai, W.-S. Liu, C.-C. Shin, C.-C. Ma, Y.-C. Tsai, T.-C. Wu, M.-Y. Kuo and Y.-T. Wu, *Chem. – Eur. J.*, 2010, **16**, 5909–5919; (e) Y.-T. Wu, T. Hayama, K. K. Baldrige, A. Linden and J. S. Siegel, *J. Am. Chem. Soc.*, 2006, **128**, 6870–6884; (f) X. Chen, P. Lu and Y. Wang, *Chem. – Eur. J.*, 2011, **17**, 8105–8114.
- For our recently developed synthetic method of isobenzofurans, see: (a) T. Hamura and R. Nakayama, *Chem. Lett.*, 2013, **42**, 1013–1015; (b) K. Asahina, S. Matsuoka, R. Nakayama and T. Hamura, *Org. Biomol. Chem.*, 2014, **12**, 9773–9776; (c) R. Kudo, K. Kitamura and T. Hamura, *Chem. Lett.*, 2017, **46**, 25–28.
- For our synthetic application of isobenzofurans to polyacene derivatives, see: (a) K. Kitamura, K. Asahina, Y. Nagai, K. Zhang, S. Nomura, K. Tanaka and T. Hamura, *Org. Biomol. Chem.*, 2018, **16**, 9143–9146; (b) S. Eda and T. Hamura, *Molecules*, 2015, **20**, 19449–19462; (c) R. Akita, K. Kawanishi and T. Hamura, *Org. Lett.*, 2015, **17**, 3094–3097; (d) S. Eda, F. Eguchi, H. Haneda and T. Hamura, *Chem. Commun.*, 2015, **51**, 5963–5966; (e) H. Haneda, S. Eda, M. Aratani and T. Hamura, *Org. Lett.*, 2014, **16**, 286–289.
- K. Kitamura, K. Asahina, Y. Nagai, H. Sugiyama, H. Uekusa and T. Hamura, *Chem. – Eur. J.*, 2018, **24**, 14034–14038.
- Iodo-benzoindenetetracene **8b** was also included in the products. The structure of **8a** was determined by X-ray analysis after recrystallization. For details, see the ESI†.
- (a) K. F. Lang and E.-A. Theiling, *Chem. Ber.*, 1956, **89**, 2734–2737; (b) X. Gu, W. A. Luhman, E. Yagodkin, R. J. Holmes and C. J. Douglas, *Org. Lett.*, 2012, **14**, 1390–1393; (c) Chaolumen, M. Murata, Y. Sugano, A. Wakamiya and Y. Murata, *Angew. Chem., Int. Ed.*, 2015, **54**, 9308–9312; (d) Chaolumen, M. Murata, A. Wakamiya and Y. Murata, *Org. Lett.*, 2017, **19**, 826–829; (e) T. Wombacher, S. Foro and J. J. Schneider, *Eur. J. Org. Chem.*, 2016, 569–578; (f) T. Wombacher, A. Gassmann, S. Foro, H. Seggern and J. J. Schneider, *Angew. Chem., Int. Ed.*, 2016, **55**, 6041.
- The structure was determined by 2D-NMR spectroscopy (HMBC, HMQC). For details, see the ESI†.
- $C_{50}H_{27}Cl$ ,  $M_w = 663.16$ ,  $0.55 \text{ mm} \times 0.10 \text{ mm} \times 0.08 \text{ mm}$ , triclinic, space group  $P\bar{1}$ ,  $Z = 4$ ,  $T = 200(2) \text{ K}$ ,  $a = 10.264(5) \text{ \AA}$ ,  $b = 14.861(8) \text{ \AA}$ ,  $c = 24.721(11) \text{ \AA}$ ,  $\alpha = 92.409(6)^\circ$ ,  $\beta = 91.727(7)^\circ$ ,  $\gamma = 104.223(7)^\circ$ ,  $V = 3649(3) \text{ \AA}^3$ ,  $\lambda(\text{Mo K}\alpha) = 0.71075 \text{ \AA}$ ,  $\mu = 0.139 \text{ mm}^{-1}$ . A total of 42 434 reflections were measured and 16 719 were independent. Final  $R1 = 0.0666$ ,  $wR2 = 0.2024$  (11 364 refs;  $I > 2\sigma(I)$ ), and GOF = 1.070 (for all data,  $R1 = 0.0945$ ,  $wR2 = 0.2493$ ).
- 11 Treatment of epoxytetracene **3a** with aq. HI gave iodo-benzoindenetetracene **11c** in low yield accompanied by benzoindenetetracene **5**.
- (a) C. Zhang, J. Huang, M. L. Trudell and S. P. Nolan, *J. Org. Chem.*, 1999, **64**, 3804–3805; (b) G. A. Grasa, M. S. Viciu, J. Huang, C. Zhang, M. L. Trudell and S. P. Nolan, *Organometallics*, 2002, **21**, 2866–2873.
- (a) A. K. Dutta, A. Linden, L. Zoppi, K. K. Baldrige and J. S. Siegel, *Angew. Chem., Int. Ed.*, 2015, **54**, 10792–10796; (b) I. R. Márquez, N. Fuentes, C. M. Cruz, V. Puente-Muñoz, L. Sotorrios, M. L. Marcos, D. Choquesillo-Lazarte, B. Biel, L. Crovotto, E. Gómez-Bengoá, M. T. González, R. Martín, J. M. Cuerva and A. G. Campaña, *Chem. Sci.*, 2017, **8**, 1068–1074.
- The  $\pi$ -extended pyraclenes **12** and **18** show poor solubility in common organic solvents. For that reason,  $^{13}\text{C}$  NMR spectra of **12** could not be obtained.
- X. Chen, J. Jin, Y. Wang and P. Lu, *Chem. – Eur. J.*, 2011, **17**, 9920–9923.

## PAPER



Cite this: *J. Mater. Chem. C*, 2019,  
7, 3294

Received 29th December 2018,  
Accepted 13th February 2019

DOI: 10.1039/c8tc06603e

rsc.li/materials-c

## Ambipolar transistors based on chloro-substituted tetraphenylpentacene†

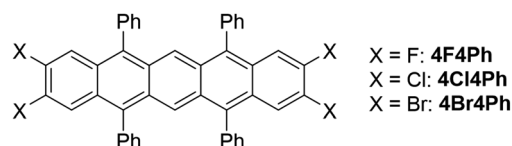
Ryonosuke Sato,<sup>†</sup> Shohei Eda,<sup>‡</sup> Haruki Sugiyama,<sup>§</sup> Hidehiro Uekusa,<sup>‡</sup>  
Toshiyuki Hamura<sup>‡</sup> and Takehiko Mori<sup>†</sup>

Thin-film transistors of halogen-substituted tetraphenylpentacenes are investigated. These compounds exhibit mainly hole transport, but the chlorine compound shows considerably higher performance than the fluorine and bromine compounds. In addition, the chlorine compound shows ambipolar properties, though the hole mobility is four times larger than the electron mobility. These compounds have basically the same crystal structures, but the remarkable halogen dependence is explained by the critical location of the LUMO levels, as well as intermolecular transfers, which sensitively change depending on the stacking geometry. In particular, hole and electron transfer exhibit different periodicity depending on the slip distance along the molecular long axis, and this is related to the appearance of the electron transport properties.

### Introduction

Transistors of rubrene have been extensively studied owing to the highest performance in single-crystal organic transistors.<sup>1–5</sup> Rubrene has a uniform stacking structure,<sup>6</sup> and it is comparatively difficult to make rubrene thin-film transistors. On the other hand, pentacene is a representative transistor material,<sup>7,8</sup> and its thin-film transistors have been investigated for a long time. A variety of related compounds have been investigated as transistor materials,<sup>9–11</sup> among which tetramethyl and dibromo derivatives have been reported to show hole-transporting properties with mobilities of 0.2–0.3 cm<sup>2</sup> V<sup>-1</sup> s<sup>-1</sup>,<sup>12,13</sup> and perfluoropentacene is known to show electron-transporting properties.<sup>14</sup> In this connection, tetraphenylpentacene is interesting (X = H in Scheme 1), which has been reported to show a hole mobility of 10<sup>-3</sup> cm<sup>2</sup> V<sup>-1</sup> s<sup>-1</sup> in thin-film transistors.<sup>15</sup>

Usually pentacene shows only hole transport, and electron transport is observed only when calcium is used as the electrode



Scheme 1 Molecular structures of 4X4Ph.

material.<sup>16</sup> However, ambipolar transport is observed using Ag electrodes on poly(methyl methacrylate) (PMMA),<sup>17</sup> and Ag/Al electrodes on tetratetracontane (TTC).<sup>18</sup> TTC is an excellent passivation layer even when a gold electrode is used, and enables the observation of ambipolar transistor properties in copper phthalocyanine,<sup>18–20</sup> indigos,<sup>21–24</sup> quinoidal oligothiophene,<sup>25</sup> semiquinones,<sup>26</sup> diketopyrrolopyrroles,<sup>27,28</sup> and isoindigos.<sup>29,30</sup>

We have recently developed a versatile synthetic route to prepare substituted acenes using cycloaddition reactions.<sup>31–33</sup> Using this route, we can directly obtain acenes where the terminal hydrogens are substituted by halogens. The carrier polarity is sensitive to the terminal halogens because of the induced polarization.<sup>9</sup> In the present paper, thin-film transistors of halogen-substituted tetraphenylpentacenes (4X4Ph, where X = F, Cl, and Br in Scheme 1) are investigated.

### Experimental

#### Synthesis

The halogen-substituted tetraphenylpentacenes 4X4Ph were prepared in two ways by using dibromodiphenylisobenzofuran **2c** as a synthetic building block (Scheme 2). Thus, the one-pot successive [4+2] cycloadditions of dihaloarynes and isobenzofurans

<sup>a</sup> Department of Materials Science and Engineering, Tokyo Institute of Technology, O-okayama, Meguro-ku, Tokyo 152-8552, Japan. E-mail: sato.r.ah@m.titech.ac.jp, mori.t.ae@m.titech.ac.jp

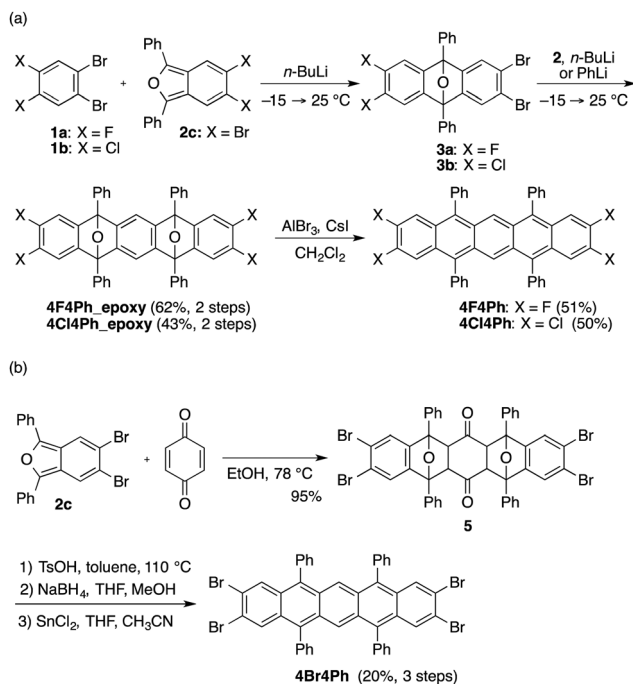
<sup>b</sup> Department of Applied Chemistry and Environment, Kwansai Gakuin University, 2-1 Gakuen, Sanda, Hyogo 669-1337, Japan. E-mail: thamura@kwansai.ac.jp

<sup>c</sup> Department of Chemistry, Tokyo Institute of Technology, O-okayama, Meguro-ku, Tokyo 152-8551, Japan

† Electronic supplementary information (ESI) available: Additional information for preparative details, structure analysis, and transfer integrals. CCDC 1887275–1887277. For ESI and crystallographic data in CIF or other electronic format see DOI: 10.1039/c8tc06603e

‡ Present address: RIKEN, 2-1, Hirosawa, Wako, Saitama 351-0198, Japan.

§ Present address: Research and Education Center for Natural Sciences, Keio University, 4-1-1 Hiyoshi, Kohoku-ku, Yokohama, Kanagawa 223-8521, Japan.

Scheme 2 Syntheses of pentacenes **4X4Ph**.

efficiently gave diepoxypentacenes **4X4Ph\_epoxy** (X = F, Cl),<sup>31</sup> which were converted to pentacenes **4F4Ph** and **4Cl4Ph** by reductive aromatization (Scheme 2a). On the other hand, due to the poor site-selectivity in the bromine–lithium exchange of tetrabromoepoxyanthracene **3c** for generation of aryne, pentacene **4Br4Ph** was alternatively prepared in four-steps including double Diels–Alder reactions of isobenzofuran **2c** and 1,4-benzoquinone as a key reaction (Scheme 2b).

### Device fabrication

Thin-film transistors were fabricated onto an n-doped Si substrate with a thermally grown SiO<sub>2</sub> dielectric layer (300 nm,  $C = 11.5 \text{ nF cm}^{-2}$ ). The passivation layer tetratetracontane (C<sub>44</sub>H<sub>90</sub>, TTC,  $\epsilon = 2.5$ ) with a thickness of 20 nm was evaporated under a vacuum of  $10^{-4}$  Pa on the substrates,<sup>19,20</sup> where the calculated overall capacitance of the gate dielectrics was  $10.4 \text{ nF cm}^{-2}$ .<sup>34</sup> Then **4X4Ph** with a thickness of 50 nm was evaporated. The top-contact electrodes were patterned by Au thermal deposition through a metal mask; the channel length ( $L$ ) and width ( $W$ ) were 100  $\mu\text{m}$  and 1000  $\mu\text{m}$ , respectively. The measurements were conducted under a vacuum of  $10^{-3}$  Pa by using a Keithley 4200 semiconductor parameter analyzer. The mobilities were estimated from the saturated-region transfer characteristics.

## Results and discussion

### Energy levels

The highest occupied molecular orbital (HOMO) levels and the lowest unoccupied molecular orbital (LUMO) levels together with the energy gaps are summarized in Table 1. The HOMO

Table 1 Energy levels and gaps of **4X4Ph**

X	$E_{\text{HOMO}}$ (eV)	$E_{\text{LUMO}}$ (eV)	Absorption edge (nm)	$E_g$ (eV)
H	−5.01	−3.07	638	1.94
F	−5.17	−3.18	622	1.99
Cl	−5.19	−3.29	651	1.90
Br	−5.20	−3.31	656	1.89

levels are estimated from the oxidation potentials of the cyclic voltammograms, and the energy gaps are obtained from the absorption edges (Fig. S2 and S3, ESI†). Accordingly, the LUMO levels are evaluated by adding the energy gaps to the HOMO levels. The energy levels of the halogen substituted compounds are lower than those of the unsubstituted pentacene (HOMO/LUMO =  $-5.0/-3.2 \text{ eV}$ )<sup>35</sup> and the tetraphenylpentacene (X = H,  $-4.95/-3.07 \text{ eV}$ ).<sup>36</sup> In general, a F substituted compound is a stronger acceptor than the corresponding Cl and Br compounds. In the present series, however, the LUMO levels indicate that **4F4Ph** is a weaker acceptor than **4Cl4Ph** and **4Br4Ph**. The HOMO levels are not significantly different, but the optical gaps of **4Cl4Ph** and **4Br4Ph** are obviously smaller than that of **4F4Ph**. The difference of the LUMO levels may be attributed to the spread of the molecular orbitals to the halogen atoms. It has been reported that hole-transporting properties appear when the HOMO level is higher than  $-5.6 \text{ eV}$ , whereas electron-transporting properties appear when the LUMO level is lower than  $-3.2 \text{ eV}$ .<sup>37</sup> The HOMO levels of these compounds are within the threshold. The LUMO levels of **4Cl4Ph** and **4Br4Ph** are certainly within the electron transporting limit, but **4F4Ph** and **4H4Ph** are critically out of the limit. Therefore, the energy levels indicate hole dominant ambipolar transport, but the electron transport may potentially depend on the substituents.

### Transistor properties

Thin-film transistors with bottom-gate top-contact geometry were fabricated onto a TTC-treated SiO<sub>2</sub> layer, where **4X4Ph** was thermally evaporated. The transfer and output characteristics are shown in Fig. 1. From these characteristics, the transistor parameters are extracted as summarized in Table 2. All compounds show hole transport, whereas only **4Cl4Ph** shows ambipolar transport. The hole mobility of **4Cl4Ph** ( $0.016 \text{ cm}^2 \text{ V}^{-1} \text{ s}^{-1}$ ) is much higher than those of **4F4Ph** and **4Br4Ph**. This mobility is also much larger than the reported value ( $10^{-3} \text{ cm}^2 \text{ V}^{-1} \text{ s}^{-1}$ ) of **4H4Ph**.<sup>15</sup> The hole mobility of **4Cl4Ph** is four times larger than the electron mobility. The electron threshold voltage is also considerably larger than the hole threshold voltage. Then, the hole transport is obviously dominant. This is also evident in the output characteristics (Fig. 1d), where the inverse current due to the electron transport is comparatively small, whereas large inverse current due to the hole transport is observed even from a positive  $V_D = 20 \text{ V}$  in Fig. 1e.

### Crystal structures

The crystal data are listed in Table 3. These compounds are approximately isostructural, where the stacking structure has a close resemblance to rubrene (Fig. 2).<sup>6</sup> The torsion angles of

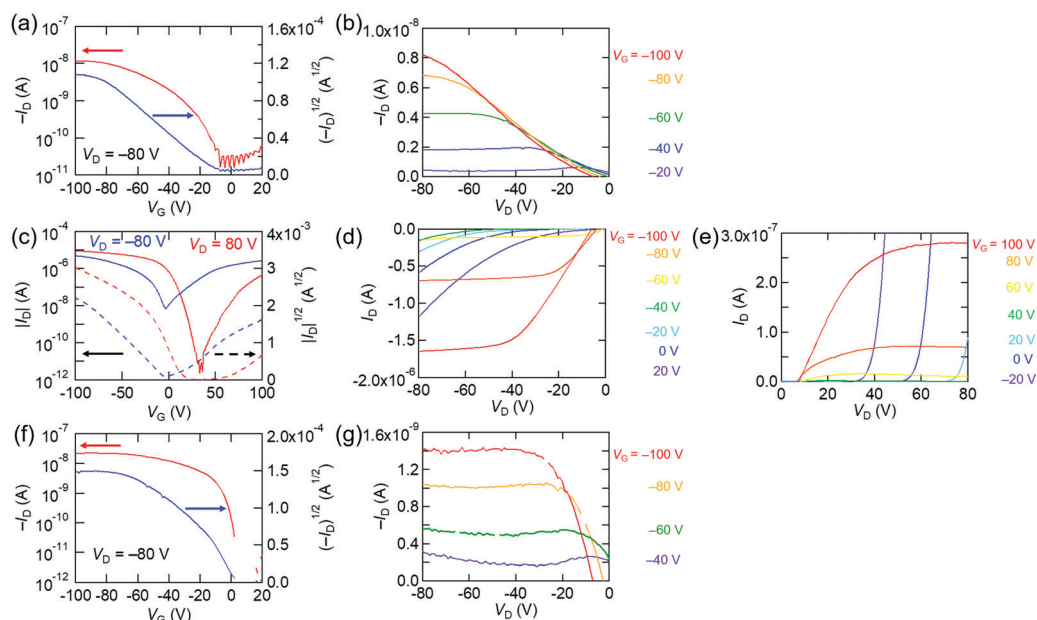


Fig. 1 (a) Transfer and (b) output characteristics of **4F4Ph**. (c) Transfer and (d and e) output characteristics of **4Cl4Ph**. (f) Transfer and (g) output characteristics of **4Br4Ph**.

Table 2 Transistor properties of **4X4Ph**

Compounds		$\mu_{\text{ave}} [\mu_{\text{max}}]$ ( $\text{cm}^2 \text{V}^{-1} \text{s}^{-1}$ )	$V_{\text{th}}$ (V)	$I_{\text{on}}/I_{\text{off}}$
<b>4F4Ph</b>	p	$4.4 \times 10^{-5}$ [ $6.0 \times 10^{-5}$ ]	-9	$5 \times 10^2$
<b>4Cl4Ph</b>	p	0.013 [0.016]	-5	$3 \times 10^3$
	n	$3.3 \times 10^{-3}$ [ $6.4 \times 10^{-3}$ ]	58	$2 \times 10^5$
<b>4Br4Ph</b>	p	$2.3 \times 10^{-4}$ [ $2.9 \times 10^{-4}$ ]	3	$3 \times 10^4$

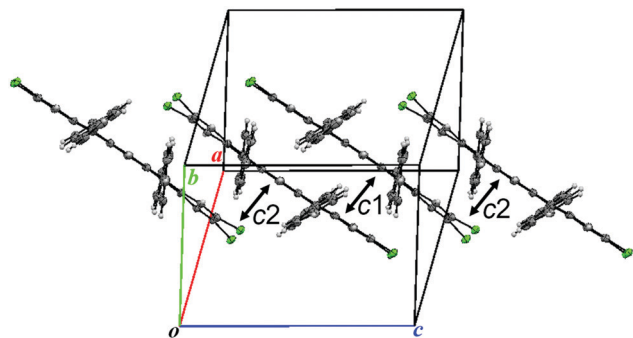
phenyl groups from the pentacene skeleton are  $58.7$ – $66.0^\circ$  in **4F4Ph**,  $62.0$ – $72.9^\circ$  in **4Cl4Ph**, and  $67.6$ – $86.7^\circ$  in **4Br4Ph**, which tend to be smaller than  $80.8^\circ$  in rubrene (Table S1, ESI†).<sup>6</sup> In addition, the rubrene molecule is located on an inversion

center, whereas the present molecules are located on a general position. In contrast to rubrene with uniform stacks, the present compounds have dimerized stacks similar to tetrafluorotetra-phenylanthracene.<sup>38</sup> Here,  $c1$  with the distance between the molecular centers  $R \sim 4.9 \text{ \AA}$  makes a dimer (Table 4), and  $c2$  ( $R > 8.7 \text{ \AA}$ ) corresponds to the interdimer interaction.

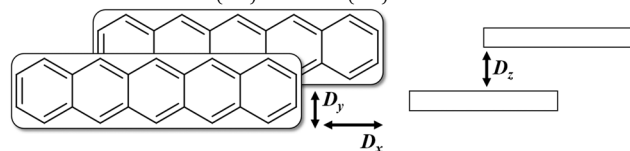
In order to analyze the intermolecular interactions, the transfer integrals  $t$  are calculated for the HOMO ( $t_h$ ) and the LUMO ( $t_e$ ) as listed in Table 4.<sup>39</sup> Interstack transfers are negligibly small, and not shown in Table 4. The transfers are estimated from the HOMO and LUMO overlaps. As another method, the transfers are evaluated from the level splitting of

Table 3 Crystallographic data of **4X4Ph** (X = F, Cl, and Br)

Crystal	<b>4F4Ph</b>	<b>4Cl4Ph</b>	<b>4Br4Ph</b>
Formula	$\text{C}_{46}\text{H}_{26}\text{F}_4$	$\text{C}_{46}\text{H}_{26}\text{Cl}_4$	$\text{C}_{46}\text{H}_{26}\text{Br}_4$
Formula weight	654.67	720.47	898.31
Crystal size ( $\text{mm}^3$ )	$0.07 \times 0.06 \times 0.02$	$0.122 \times 0.071 \times 0.031$	$0.099 \times 0.048 \times 0.033$
$\mu$ ( $\text{mm}^{-1}$ )	0.789	0.388	5.826
Crystal system	Triclinic	Triclinic	Triclinic
Space group	$P\bar{1}$	$P\bar{1}$	$P\bar{1}$
Z	2	2	2
$a$ ( $\text{\AA}$ )	10.0390(2)	10.3770(13)	10.3811(3)
$b$ ( $\text{\AA}$ )	13.0700(2)	12.874(2)	13.2135(4)
$c$ ( $\text{\AA}$ )	13.4090(2)	13.3509(17)	13.8306(4)
$\alpha$ (deg.)	112.658(1)	86.033(6)	81.924(2)
$\beta$ (deg.)	103.943(1)	77.911(4)	77.158(2)
$\gamma$ (deg.)	92.256(1)	74.579(5)	72.986(2)
$V$ ( $\text{\AA}^3$ )	1558.15(5)	1681.1(4)	1762.94(9)
$\rho$ ( $\text{g cm}^{-3}$ )	1.395	1.423	1.692
Total reflns.	18 385	16 286	20 752
Unique reflns. ( $R_{\text{int}}$ )	5593 (0.0399)	7546 (0.0693)	6332 (0.1139)
$R_1$ ( $F^2 > 2\sigma(F^2)$ )	0.0677	0.0694	0.0685
$wR_2$ (All reflections)	0.2312	0.2303	0.1983
GOF	0.968	1.029	1.013
Temperature (K)	173(2)	93(2)	123(2)

Fig. 2 Crystal structure of **4Cl4Ph**.Table 4 Intermolecular transfer integrals and slip distances in **4X4Ph**

Compounds	Transfer integrals <sup>a</sup> (meV)		Slip distances <sup>b</sup> (Å)				
	$t_h$	$t_e$	$D_x$	$D_y$	$D_z$	$R$	
<b>4F4Ph</b>	$c1$	-58.1 (48.2)	4.4 (0.8)	3.32	0.05	3.66	4.94
	$c2$	-19.4 (16.8)	-5.9 (9.0)	7.95	0.46	3.60	8.74
<b>4Cl4Ph</b>	$c1$	-51.1 (43.2)	15.9 (9.4)	3.09	0.32	3.68	4.82
	$c2$	-8.2 (8.8)	-6.6 (8.4)	7.92	1.11	3.74	8.82
<b>4Br4Ph</b>	$c1$	-39.6 (34.6)	8.8 (5.2)	3.08	0.43	3.85	4.96
	$c2$	4.8 (3.2)	-1.9 (2.9)	7.85	2.09	4.23	9.16



<sup>a</sup> From orbital overlaps. Values in parentheses are from level splittings.

<sup>b</sup> Slip distances in a diad from the definitions indicated in the scheme.  $R$  is the distance between the molecular centers.

the diads. Although the signs of transfers are not determined in the latter method, both of these two calculation methods show the same tendency:  $|t_h| > |t_e|$ , indicating hole dominant transport. The comparatively high LUMO levels are the principal reason for the hole dominant transport, but the small electron bandwidth is also responsible.

The bandwidth is determined by  $c2$ , and the interdimer  $|t_e|$  ( $c2$ ) of **4Br4Ph** (1.9 meV) is particularly small; this may be related to the absence of electron transport in **4Br4Ph**. It is a characteristic of **4Cl4Ph** that the intradimer  $|t_e|$  ( $c1$ ) is larger than those of **4F4Ph** and **4Br4Ph**. In particular, the intradimer  $|t_e|$  ( $c1$ ) of **4F4Ph** is even smaller than  $c2$ , and the bandwidth is limited by  $c1$ . This is a reason that the electron transport in **4F4Ph** is hampered rather than would be naively expected from the geometry.

Since transfer integrals are sensitive to the geometry of the diads,<sup>40</sup> slip distances along the molecular long axis ( $D_x$ ) and along the molecular short axis ( $D_y$ ) are evaluated as well as the interplanar distances ( $D_z$ ) (Table 4). It is reasonable that the  $c2$  interaction with large  $D_x \sim 7.9$  Å affords a smaller transfer than the  $c1$  interaction with small  $D_x \sim 3.1$  Å. Since the HOMO and LUMO have nodes on each benzene ring,<sup>40</sup> the transfer is a periodical function of  $D_x$  (Fig. 3). The previous calculation indicates that the HOMO transfer has peaks at  $D_x = 0, 2.8, 5.6,$  and  $8.5$  Å, in which  $2.8$  Å corresponds to the size of a

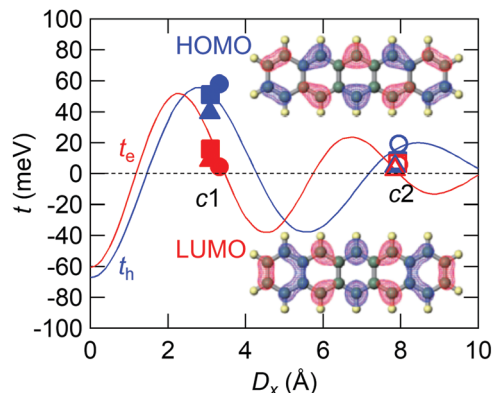


Fig. 3 Intermolecular transfers as a function of  $D_x$  at  $D_y = 0$  Å and  $D_z = 3.4$  Å, together with the HOMO and LUMO of pentacene.<sup>40</sup> Circles are for **4F4Ph**, squares for **4Cl4Ph**, and triangles for **4Br4Ph**.

benzene ring.<sup>40</sup> The  $c1$  and  $c2$  overlaps are not far from the second and fourth peaks, leading to a comparatively large  $|t_h|$ . The LUMO transfer periodicity is slightly smaller than this, which makes peaks at  $D_x = 0, 2.3, 4.5, 6.7,$  and  $8.9$  Å. This is because the HOMO spreads to the outer rings, but the LUMO spreads to the inner rings (Fig. 3).<sup>40</sup> Accordingly, the LUMO transfer has nodes at  $D_x = 1.2, 3.5, 5.8,$  and  $8.0$  Å. The actual  $D_x$  values of the present crystals are not definitely on the LUMO peaks, and particularly that of  $c2$  ( $D_x \sim 7.9$  Å) is close to the node.  $D_x$  values of **4Cl4Ph** and **4Br4Ph** for  $c1$  are  $3.1$  Å, but that of **4F4Ph**  $c1$  is  $3.3$  Å (Table 4), which is around the node of the LUMO transfer ( $D_x = 3.5$  Å).<sup>40</sup> This is the reason for significantly small  $c1$  in **4F4Ph**. Similar  $D_x$  sensitivity has been recently reported in halogenated tetraazapentacenes as well.<sup>41</sup>

In addition, we could not neglect the influence of the nonzero  $D_y$  (Fig. S4–S9, ESI†). The  $c2$  interaction of **4Br4Ph** has exceptionally large  $D_y = 2.09$  Å and  $D_z = 4.23$  Å, which is related to the poor transistor performance. Accordingly, the absence of electron transport in **4F4Ph** is probably related to the small  $c1$  value for electrons together with the high LUMO level, whereas the difference of **4Cl4Ph** and **4Br4Ph** is derived from the magnitude of the  $c2$  values.

### Thin-film properties

X-ray diffraction (XRD) patterns and atomic force microscopy (AFM) images of the thin films deposited on the tetratetracontane (TTC)-modified Si/SiO<sub>2</sub> substrates were observed. As shown in Fig. 4a, the XRD patterns show diffraction peaks around  $2\theta = 7.1$ – $7.4^\circ$ . The  $d$ -spacings,  $11.9$ – $12.5$  Å, correspond to  $b \sin \alpha \sin \gamma$  of the crystal lattice, indicating that the crystallographic  $ac$  plane is aligned parallel to the substrate (Fig. 4b). Not only the (010) peaks but also the (020) peaks are observed in the three films, and the (040) peaks are observed in the **4Cl4Ph** and **4Br4Ph** films. The pentacene core has the side-on arrangement rather than the end-on arrangement. Then, the terminal halogen atoms do not contribute to the polarization at the gate interface. This is a reason that charge polarity does not depend on the halogen electronegativity. The molecular planes are tilted by  $65.4^\circ$  (**4F4Ph**),  $70.2^\circ$  (**4Cl4Ph**), and  $74.6^\circ$  (**4Br4Ph**) with respect to the substrates.

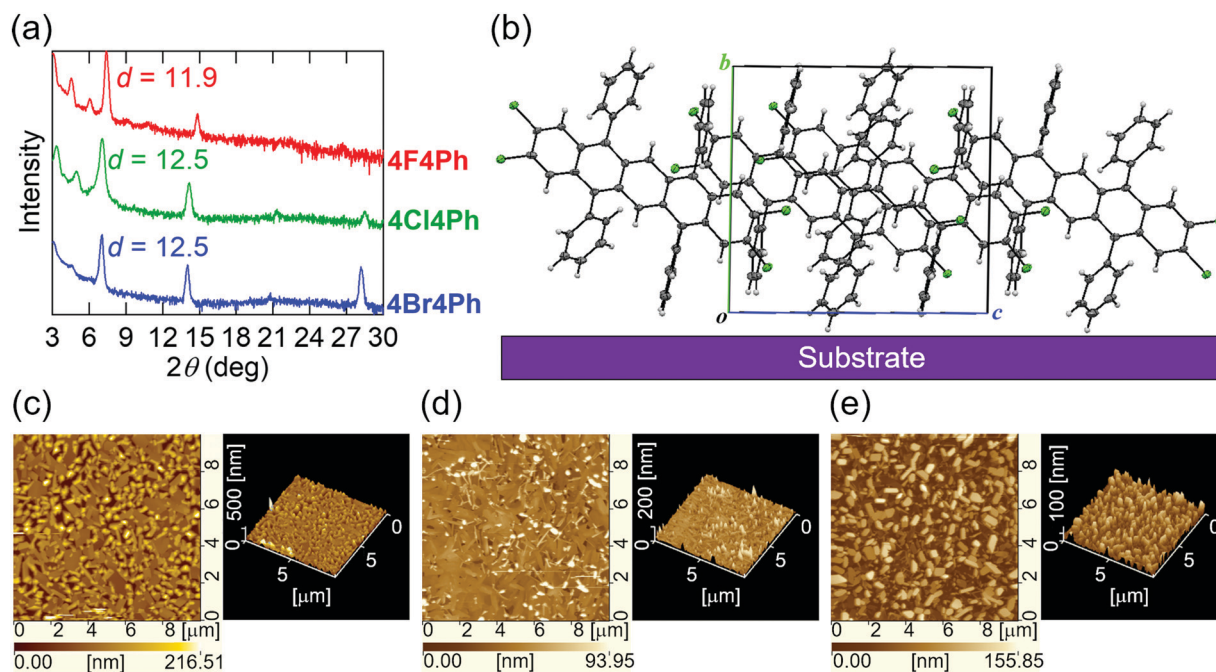


Fig. 4 Thin-film properties of **4X4Ph**. (a) XRD patterns and (b) molecular orientation in the thin-film **4Cl4Ph**. AFM images of (c) **4F4Ph**, (d) **4Cl4Ph**, and (e) **4Br4Ph**.

The **4Br4Ph** molecules are standing most close to the perpendicular direction to the substrate. It is generally known that the mobility attains a maximum at a perpendicular molecular arrangement.<sup>24</sup> This may be the reason that the mobility of **4Br4Ph** is five times larger than that of **4F4Ph**.

Atomic force microscopy (AFM) images of the thin films are shown in Fig. 4c–e. The grains of the three films have the same size of about 1  $\mu\text{m}$ . However, in the **4F4Ph** and **4Br4Ph** films, rod-like microcrystals cover the substrate, but in the **4Cl4Ph** film, plate-like microcrystals densely cover the substrate. The **4F4Ph** and **4Br4Ph** films show relatively sparse coverage in comparison with the **4Cl4Ph** film. The **4F4Ph** film shows larger roughness than the **4Cl4Ph** and **4Br4Ph** films, and this may be related to the absence of the (040) XRD peak in the **4F4Ph** film. The thin-film quality is to some extent responsible for the significantly different mobilities of these materials.

## Conclusions

Thin-film transistors of **4X4Ph** show mainly hole transport. **4Cl4Ph** exhibits higher performance than **4F4Ph** and **4Br4Ph**. In addition, **4Cl4Ph** shows electron transport as well. These compounds have basically the same crystal structures, but the remarkable halogen dependence, as well as the hole dominant transport, is explained by the critical location of the LUMO levels, as well as intermolecular transfers, which sensitively change depending on the stacking geometry. In particular, the periodicity of the LUMO transfer is different from that of the HOMO transfer, and sensitively influences the appearance of electron transport.

## Conflicts of interest

There are no conflicts to declare.

## Acknowledgements

We thank Dr H. Kojima (Nara Institute of Science and Technology) for the results in Fig. 3, which are taken from ref. 40. This work was partly supported by ACT-C Grant Number JPMJCR12YY and JPMJCR12ZB from JST, Japan, a Grant-in Aid for Scientific Research (No. 16K13974, 18H02044, 15H05840, 17K05745, and 18H04504) from the Ministry of Education, Culture, Sports, Science, and Technology of Japan, and Takahashi Industrial and Economic Research Foundation. The authors are grateful to the Tokyo Institute of Technology Center for Advanced Materials Analysis for XRD measurements and Prof. Kakimoto for AFM measurements.

## Notes and references

- 1 V. Podzorov, V. M. Pudalov and M. E. Gershenson, *Appl. Phys. Lett.*, 2003, **82**, 1739.
- 2 V. C. Sundar, J. Zaumseil, V. Podzorov, E. Menard, R. L. Willett, T. Someya, M. E. Gershenson and J. A. Rogers, *Science*, 2004, **303**, 1644.
- 3 V. Podzorov, E. Menard, A. Borissov, V. Kiryukhin, J. A. Rogers and M. E. Gershenson, *Phys. Rev. Lett.*, 2004, **93**, 086602.
- 4 R. W. I. de Boer, M. E. Gershenson, A. F. Morpurgo and V. Podzorov, *Phys. Status Solidi*, 2004, **201**, 1302.
- 5 J. Takeya, M. Yamagishi, Y. Tominari, R. Hirahara, Y. Nakazawa, T. Nishikawa, T. Kawase, T. Shimoda and S. Ogawa, *Appl. Phys. Lett.*, 2007, **90**, 102120.

- 6 O. D. Jurchescu, A. Meetsma and T. T. M. Palstra, *Acta Crystallogr., Sect. B: Struct. Sci.*, 2006, **62**, 330.
- 7 C. D. Dimitrakopoulos and P. R. L. Malenfant, *Adv. Mater.*, 2002, **14**, 99.
- 8 H. Klauk, M. Halik, U. Zschieschang, G. Schmid, W. Radlik and W. Weber, *J. Appl. Phys.*, 2002, **92**, 5259.
- 9 A. R. Murphy and J. M. J. Fréchet, *Chem. Rev.*, 2007, **107**, 1066.
- 10 J. E. Anthony, *Angew. Chem., Int. Ed.*, 2008, **47**, 452.
- 11 K. Takimiya, S. Shinamura, I. Osaka and E. Miyazaki, *Adv. Mater.*, 2011, **23**, 4347.
- 12 H. Meng, M. Bendikov, G. Mitchell, R. Helgeson, F. Wudl, Z. Bao, T. Siegrist, C. Kloc and C.-H. Chen, *Adv. Mater.*, 2003, **15**, 1090.
- 13 T. Okamoto, M. L. Senatore, M.-M. Ling, A. B. Mallik, M. L. Tang and Z. Bao, *Adv. Mater.*, 2007, **19**, 3381.
- 14 Y. Sakamoto, T. Suzuki, M. Kobayashi, Y. Gao, Y. Fukai, Y. Inoue, F. Sato and S. Tokito, *J. Am. Chem. Soc.*, 2004, **126**, 8138.
- 15 Q. Miao, X. Chi, S. Xiao, R. Zeis, M. Lefenfeld, T. Siegrist, M. L. Steigerwald and C. Nuckolls, *J. Am. Chem. Soc.*, 2006, **128**, 1340.
- 16 T. Yasuda, T. Goto, K. Fujita and T. Tsutsui, *Appl. Phys. Lett.*, 2004, **85**, 2098.
- 17 L.-Y. Chiu, H.-L. Cheng, H.-Y. Wang, W.-Y. Chou and F.-C. Tang, *J. Mater. Chem. C*, 2014, **2**, 1823.
- 18 A. Opitz, M. Horlet, M. Kiwull, J. Wagner, M. Kraus and W. Brütting, *Org. Electron.*, 2012, **13**, 1614.
- 19 M. Kraus, S. Richler, A. Opitz, W. Brütting, S. Haas, T. Hasegawa, A. Hinderhofer and F. Schreiber, *J. Appl. Phys.*, 2010, **107**, 094503.
- 20 M. Kraus, S. Haug, W. Brütting and A. Opitz, *Org. Electron.*, 2011, **12**, 731.
- 21 M. Irimia-Vladu, E. D. Glowacki, P. A. Troshin, G. Schwabegger, L. Leonat, D. K. Susarova, O. Krystal, M. Ullah, Y. Kanbur, M. A. Bodea, V. F. Razumov, H. Sitter, S. Bauer and N. S. Sariciftci, *Adv. Mater.*, 2012, **24**, 375.
- 22 E. D. Glowacki, G. Voss and N. S. Sariciftci, *Adv. Mater.*, 2013, **25**, 6783.
- 23 O. Pitayatanakul, T. Higashino, T. Kadoya, M. Tanaka, H. Kojima, M. Ashizawa, T. Kawamoto, H. Matsumoto, K. Ishikawa and T. Mori, *J. Mater. Chem. C*, 2014, **2**, 9311.
- 24 O. Pitayatanakul, K. Iijima, M. Ashizawa, T. Kawamoto, H. Matsumoto and T. Mori, *J. Mater. Chem. C*, 2015, **3**, 8612.
- 25 T. Higashino, J. Cho and T. Mori, *Appl. Phys. Express*, 2014, **7**, 121602.
- 26 T. Higashino, S. Kumeta, S. Tamura, Y. Ando, K. Ohmori, K. Suzuki and T. Mori, *J. Mater. Chem. C*, 2015, **3**, 1588.
- 27 E. D. Glowacki, H. Coskun, M. A. Blood-Forsythe, U. Monkowius, L. Leonat, M. Grzybowski, D. Gryko, M. S. White, A. Aspuru-Guzik and N. S. Sariciftci, *Org. Electron.*, 2014, **15**, 3521.
- 28 K. Iijima and T. Mori, *Chem. Lett.*, 2017, **46**, 357.
- 29 M. Ashizawa, N. Masuda, T. Higashino, T. Kadoya, T. Kawamoto, H. Matsumoto and T. Mori, *Org. Electron.*, 2016, **35**, 95.
- 30 D. Yoo, T. Hasegawa, M. Ashizawa, T. Kawamoto, H. Masunaga, T. Hikima, H. Matsumoto and T. Mori, *J. Mater. Chem. C*, 2017, **5**, 2509.
- 31 H. Haneda, S. Eda, M. Aratani and T. Hamura, *Org. Lett.*, 2014, **16**, 286.
- 32 S. Eda, F. Eguchi, H. Haneda and T. Hamura, *Chem. Commun.*, 2015, **51**, 5963.
- 33 S. Eda and T. Hamura, *Molecules*, 2015, **20**, 19449.
- 34 K.-J. Baeg, Y.-Y. Noh, J. Ghim, B. Lim and D.-Y. Kim, *Adv. Funct. Mater.*, 2008, **18**, 3678.
- 35 T. Yasuda, T. Goto, K. Fujita and T. Tsutsui, *Appl. Phys. Lett.*, 2004, **85**, 2098.
- 36 I. Kaur, W. Jia, R. P. Kopreski, S. Selvarasah, M. R. Dokmeci, C. Pramanik, N. E. McGruer and G. P. Miller, *J. Am. Chem. Soc.*, 2008, **130**, 16274.
- 37 M. L. Tang, A. D. Reichardt, P. Wei and Z. Bao, *J. Am. Chem. Soc.*, 2009, **131**, 5264.
- 38 A. Izumoto, H. Kondo, T. Kochi and F. Kakiuchi, *Synlett*, 2017, 2609.
- 39 T. Mori, A. Kobayashi, Y. Sasaki, H. Kobayashi, G. Saito and H. Inokuchi, *Bull. Chem. Soc. Jpn.*, 1984, **57**, 627.
- 40 H. Kojima and T. Mori, *Bull. Chem. Soc. Jpn.*, 2011, **84**, 1049.
- 41 M. Chu, J.-X. Fan, S. Yang, D. Liu, C. F. Ng, H. Dong, A.-M. Ren and Q. Miao, *Adv. Mater.*, 2018, **30**, 1803467.

## Reactive Intermediates

## Didehydroisobenzofuran: A New Reactive Intermediate for Construction of Isoacenofuran

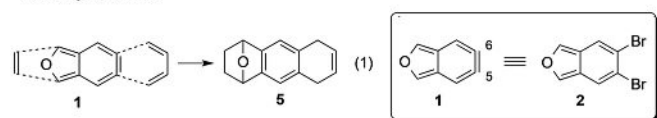
Suguru Matsuoka, Sunna Jung, Kaoru Miyakawa, Yu Chuda, Ryo Sugimoto, and Toshiyuki Hamura\*<sup>[a]</sup>

**Abstract:** An efficient generation method of didehydroisobenzofuran, a new heteroaryne species, was developed by bromine/lithium exchange of the dibromoisobenzofuran. The reactive intermediate, thus generated, was trapped by appropriate arynophile to give the [2+2], [2+3], and [2+4] cycloadducts, respectively. Moreover, the reaction could be applied to the syntheses of isoanthracenofurans (anthra[2,3-*c*]furans), a new class of heteroacenes, with isoelectronic structure to the corresponding acenoheteroles (anthra[2,3-*b*]furans).

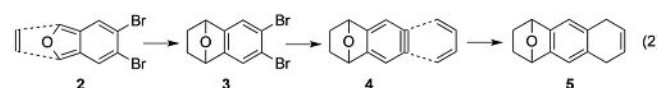
Design and generation of a reactive intermediate is an important subject in organic chemistry, because discovery of a new reactivity inherent in its unique structure would lead to develop a new reaction, which opens a way to access to various functionalized organic molecules (Scheme 1).<sup>[1]</sup>

In this context, we previously reported a formal synthetic use of didehydroisobenzofuran **1**, possessing a highly strained

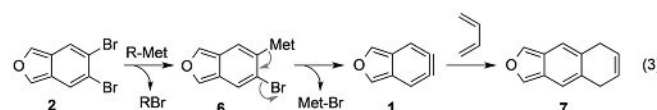
## • Direct synthetic use



## • Formal synthetic use (previous work)



## • Two-step generation of didehydroisobenzofuran and its trapping (this work)



**Scheme 1.** Didehydroisobenzofuran, a new reactive intermediate for construction of polycyclic structure.

[a] S. Matsuoka, Dr. S. Jung, K. Miyakawa, Y. Chuda, R. Sugimoto, Prof. Dr. T. Hamura  
Department of Applied Chemistry for Environment  
Kwansei Gakuin University, 2-1 Gakuen, Sanda 669-1337 (Japan)  
E-mail: thamura@kwansei.ac.jp

Supporting information and the ORCID identification number(s) for the author(s) of this article can be found under:  
<https://doi.org/10.1002/chem.201804655>.

1,2-didehydroarene structure at the C<sub>5</sub>/C<sub>6</sub> position, enabling rapid construction of polycyclic structures through the successive cycloadditions [Eqs. (1) and (2)].<sup>[2]</sup> In this process, dibromoisobenzofuran **2** served as a synthetic equivalent to **1**, allowing expeditious assembly of polycycle **5** by two directional [2+4] cycloadditions.<sup>[3–5]</sup> Further study on developing the synthetic utility of dibromoisobenzofuran **2** revealed that the direct generation of didehydroisobenzofuran **1** was feasible by two-step protocol including the bromine/lithium exchange of dibromoisobenzofuran **2** [Eq. (3)]. This new heteroaryne, thus generated, was trapped with arynophile to give functionalized isobenzofuran with various synthetic potential.<sup>[6,7]</sup> Moreover, the [2+4] cycloadduct was converted to isoanthracenofuran, a new class of heteroacenes with isoelectronic structure to the corresponding anthra[2,3-*b*]furans, which is described in this communication.

Table 1 shows the initial study for the generation of didehydroisobenzofuran, which was trapped with arynophile.<sup>[8,9]</sup> Upon treatment of dibromodiphenylisobenzofuran **8**, a model substrate, with *n*BuLi (2.0 equiv) in the presence of diphenylisobenzofuran **9** (1.5 equiv, THF, 0 °C → RT, 3 h), [2+4] cycloaddition occurred to give the cycloadduct **10** in 40% yield (entry 1). The structure of **10** was determined by NMR analysis. Screening of the reaction conditions revealed that toluene was a choice of solvent to produce the desired product in better yield (entry 3). Moreover, *s*BuLi and PhLi were also available for

**Table 1.** Generation and trapping of didehydroisobenzofuran.

Entry	R-Met	Solvent	Yield [%]
1	<i>n</i> -BuLi	THF	40
2	<i>n</i> -BuLi	Et <sub>2</sub> O	42
3	<i>n</i> -BuLi	toluene	57
4	<i>s</i> -BuLi	THF	38
5	PhLi	THF	41
6	<i>t</i> -BuLi	THF	— <sup>[2]</sup>
7	<i>i</i> -PrMgBr	THF	— <sup>[3]</sup>
8	<i>i</i> -PrMgBr-LiCl	THF	19

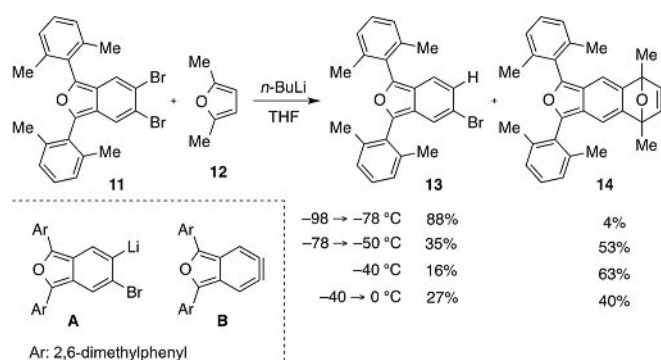
[1] R-Met (2.0 equiv) and diphenylisobenzofuran **9** (1.5 equiv) were used.  
[2] Reduced 5-bromo-1,3-diphenylisobenzofuran was produced in 14% yield. [3] Starting materials were recovered.

the generation of didehydroisobenzofuran, giving the cycloadduct **10** in moderate yield (entries 4 and 5). These results were in contrast to the poor results using *t*BuLi, *i*PrMgBr, and *i*PrMgCl-LiCl (entries 6–8).

In these reactions, one plausible structure of by-products was the dual cycloadduct (structure not shown) by further reaction with the initially formed cycloadduct **10**, which was detected by MALDI-TOF mass spectrometry (Figure S1 in the Supporting Information).<sup>[10]</sup> This competing reaction with didehydroisobenzofuran was due to the similar reactivity of the furan moiety in **10** compared with that of diphenylisobenzofuran **9**.

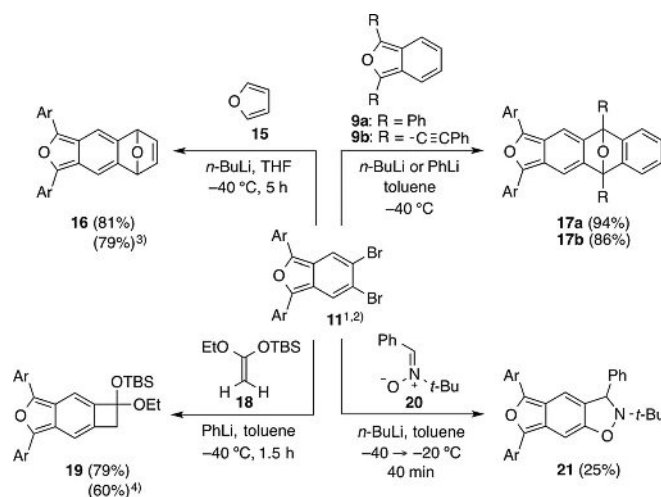
To suppress the formation of the above-mentioned multiple cycloadducts, dibromoisobenzofuran **11**<sup>[11]</sup> possessing sterically crowded 2,6-xylyl groups in the furan moiety was tested as another precursor of didehydroisobenzofuran. In addition, to gain the precise behavior regarding the two-step generation of didehydroisobenzofuran, the reaction was conducted at lower temperature: upon treatment of **11** with 1.2 equivalents of *n*BuLi (1.60 M in hexane) in the presence of dimethyl furan **12** (6.0 equiv, THF,  $-95 \rightarrow -78^\circ\text{C}$ , 5 min), the [2+4] cycloadduct **14** was obtained only in 4% yield, and the major product was bromoisobenzofuran **13** lacking one bromine atom (88%). This result implies that aryllithium species **A** generated by the Br/Li exchange of **11** has a finite lifetime at  $-78^\circ\text{C}$ .<sup>[12,13]</sup>

On the other hand, if the same reaction was performed initially at  $-78^\circ\text{C}$  followed by warming to  $-50^\circ\text{C}$ , [2+4] cycloadduct **14** was obtained as a major product in 53% yield. At  $-50^\circ\text{C}$ , lithio species **A** underwent 1,2-elimination of LiBr to generate the didehydroisobenzofuran **B**. This behavior made it possible for us to control generation of the two reactive species **A** and **B** (Scheme 2).



**Scheme 2.** [2+4] Cycloaddition of sterically congested didehydroisobenzofuran.

By using various arynophiles, functionalized isobenzofuranes were accessible by the [2+4], [2+3], and [2+2] cycloadditions (Scheme 3). Typical experimental procedure is represented by furan cycloaddition: To a mixture of dibromide **11** and furan **15** (5.0 equiv) in THF was slowly added *n*BuLi (1.5 equiv in hexane) at  $-40^\circ\text{C}$ . After five hours, the reaction was stopped by adding water. Extractive workup followed by purification by silica-gel column chromatography gave the cycloadduct **16** in 81% yield. Similarly, diphenylisobenzofuran **9a** and dialkynyl-

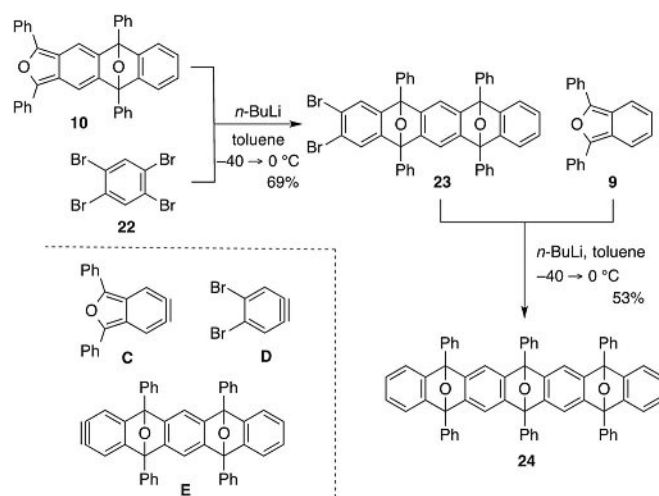


**Scheme 3.** [2+4], [2+3], and [2+2] Cycloadditions of didehydroisobenzofuran. 1) Ar: 2,6-dimethylphenyl. 2) Arynophile (1.2–5.0 equiv) and R-Li (1.5–2.5 equiv) were used. 3) *n*BuLi, toluene,  $-78^\circ\text{C} \rightarrow \text{rt}$ . 4) *n*BuLi, toluene,  $-40^\circ\text{C}$ .

isobenzofuran **9b** proved to be applicable for the [2+4] cycloaddition, affording pentacycles **17a** and **b** in 94 and 86% yield, respectively. Moreover, ketene silyl acetal **18** worked well as a trapping agent to give the [2+2] cycloadduct **19** in 79% yield. In addition, the [2+3] cycloaddition was realized by reaction of didehydroisobenzofuran **B** and nitron **20** to produce the cycloadduct **21**, albeit in low yield.<sup>[14]</sup>

As one of the synthetic application, the high-ordered polycene framework could be efficiently synthesized by two-directional annulation of didehydroisobenzofuran (Scheme 4).<sup>[15]</sup>

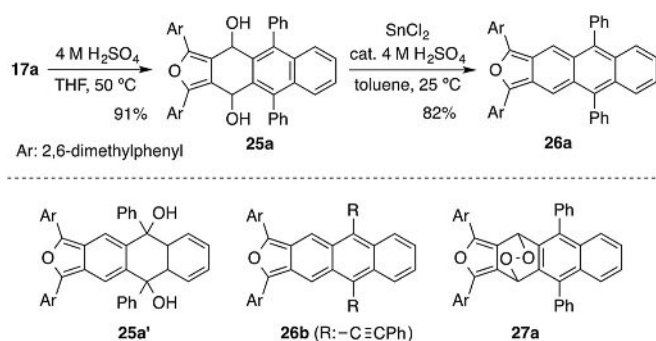
In the first step, the [2+4] cycloaddition of didehydroisobenzofuran **C** and diphenylisobenzofuran **9** described in Table 1 (entry 3) was conducted to give the mono-cycloadduct **10**, which was directly used as an arynophile by reaction with dibromobenzene **22**<sup>[16]</sup> (*n*BuLi, toluene,  $-40 \rightarrow 0^\circ\text{C}$ ), giving the diepoxypentacene **23**. Subsequent third cycloaddition of heptacyclic



**Scheme 4.** Efficient synthetic access to high-ordered polycene framework via two-directional annulations of didehydroisobenzofuran **C**.

aryne **E**, generated from **23**, and isobenzofuran **9** occurred cleanly to produce the highly condensed polycycle **24** as a mixture of stereoisomers.

Scheme 5 shows the conversion of the [2+4] cycloadduct **17a** to the isoanthracenofuran **26a** by two-step sequences including the reductive aromatization of the ring opened diol derivative. Interestingly, the first ring opening of the substrate **17a** with 4 M H<sub>2</sub>SO<sub>4</sub> (THF, 50 °C) proceeded in S<sub>N</sub>2' manner



Scheme 5. Syntheses of isoanthracenofurans **26a** and **b**.

to give the diol **25a** in high yield without producing the isomeric diol **25a'**. Subsequent reductive aromatization of **25a** occurred cleanly by treatment with three equivalents of SnCl<sub>2</sub> (toluene, 25 °C). Evaporation of the solvent, followed by washing the crude product with MeOH gave essentially pure isoanthracenofuran **26a** as a blue solid. Importantly, the product **26a** is a new class of heteroacene in that an *o*-quinoidal structure is only drawn in the closed-shell resonance form, and therefore, it would show unique physical properties, as well as high reactivities compared to the corresponding isoelectronic acene analogues (e.g., diphenyltetracene).<sup>[17]</sup> Indeed, NMR analysis showed that isoanthracenofuran **26a** dissolved in CDCl<sub>3</sub> was readily oxidized to the endoperoxide **27a** (Figure S2 in the Supporting Information), although **26a** was relatively stable in the solid-state and could be stored under Ar atmosphere for several months.

In a similar two-step sequence, the isobenzofuran **17b** could also be converted to the dialkynylated isoanthracenofuran **26b**, which was more stable than diaryl derivative **26a**. In this case, the formation of endoperoxide **27b** occurred gradually after 1 h (Figure S4 in the Supporting Information).

The absorption spectra of **26a** and **b** in CH<sub>2</sub>Cl<sub>2</sub> are shown in Figure 1, together with that of 1,3-diarylisobenzofuran **17a** for comparison. Isoanthracenofuran **26a** has its absorption maximum at 647 nm, which is largely redshifted compared to isobenzofuran **17a** ( $\lambda_{\text{abs}} = 358$  nm). This result clearly shows the significant effect by introducing butadiene units on to the isobenzofuran core, which makes the structure more quinoidal. In addition, the introduction of phenylethynyl groups into the acene core significantly affects the photophysical property: the alkynyl derivative **26b** exhibits an absorption in the near-infrared (NIR) region with the maximum at 720 nm, which is redshifted about 73 nm in comparison with that of **26a**, revealing its quite narrow band gap electronic structure.

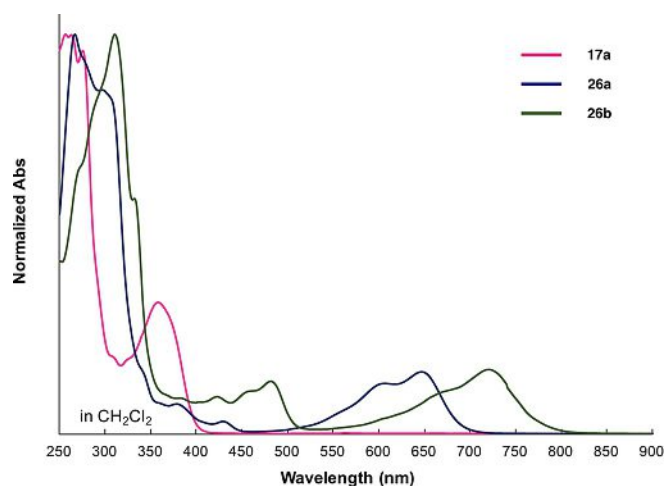


Figure 1. UV/Vis absorption spectra of isobenzofuran **17a**, and isoanthracenofurans **26a** and **b** (in CH<sub>2</sub>Cl<sub>2</sub>).

In summary, an efficient generation method of didehydroisobenzofuranes, a new heteroaryne species, was developed by bromine-metal exchange of the dibromoisobenzofuranes. The reactive intermediates, thus generated, were efficiently trapped by appropriate arynophiles to give the various cycloadducts, and some of them could be converted to anthra[2,3-*c*]furans, a novel class of heteroacenes, with isoelectronic structure to the corresponding (anthra[2,3-*b*]furans). Further synthetic applications are under active investigation in our laboratory.

## Acknowledgements

This work was supported by JSPS KAKENHI Grant Number JP15H05840 in Middle Molecular Strategy and JST ACT-C Grant Number JPMJCR12YY, Japan.

## Conflict of interest

The authors declare no conflict of interest.

**Keywords:** conjugated molecules • didehydroisobenzofuranes • isoacenofuranes • polycycles • reactive intermediates

- [1] a) R. A. Moss, M. S. Platz, M. Jones, Jr., *Reactive Intermediate Chemistry*, Wiley, Hoboken, **2004**; b) M. S. Singh, *Reactive Intermediates in Organic Chemistry*, Wiley-VCH, Weinheim, **2014**.
- [2] a) S. Eda, T. Hamura, *Molecules* **2015**, *20*, 19449–19462; b) H. Haneda, S. Eda, M. Aratani, T. Hamura, *Org. Lett.* **2014**, *16*, 286–289.
- [3] For selected reviews on isobenzofuranes, see: a) W. Friedrichsen, *Adv. Heterocycl. Chem.* **1980**, *26*, 135–241; b) W. Friedrichsen, *Adv. Heterocycl. Chem.* **1999**, *73*, 1–96.
- [4] For selective synthetic examples of isobenzofuranes, see: a) P. Binger, P. Wedemann, R. Goddard, U. H. Brinker, *J. Org. Chem.* **1996**, *61*, 6462–6464; b) R. Rodrigo, *Tetrahedron* **1988**, *44*, 2093–2135; c) H. N. C. Wong, *Acc. Chem. Res.* **1989**, *22*, 145–152; d) Y.-M. Man, T. C. W. Mak, H. N. C. Wong, *J. Org. Chem.* **1990**, *55*, 3214–3221; e) S.-H. Chan, C.-Y. Yick, H. N. C. Wong, *Tetrahedron* **2002**, *58*, 9413–9422; f) J. E. Rainbolt, G. P. Miller, *J. Org. Chem.* **2007**, *72*, 3020–3030.

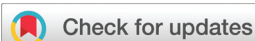
- [5] For preparation of isobenzofuranes, see: a) R. N. Warrener, *J. Am. Chem. Soc.* **1971**, *93*, 2346–2348; b) R. N. Warrener, M. Shang, D. N. Butler, *Chem. Commun.* **2001**, 1550–1551; c) A. Sygula, R. Sygula, P. W. Rabideau, *Org. Lett.* **2006**, *8*, 5909–5911; d) B. J. Pei, W. H. Chan, A. W. M. Lee, *Org. Lett.* **2011**, *13*, 1774–1777.
- [6] Recently, we developed one-pot synthetic method of 1,3-diarylisobenzofurans by sequential reaction of methyl 2-formylbenzoate with two identical or different aryl metal species: T. Hamura, R. Nakayama, *Chem. Lett.* **2013**, *42*, 1013–1015. See also: K. Asahina, S. Matsuoka, R. Nakayama, T. Hamura, *Org. Biomol. Chem.* **2014**, *12*, 9773–9776.
- [7] For our synthetic application of isobenzofuranes to polyacene derivatives, see: a) R. Akita, K. Kawanishi, T. Hamura, *Org. Lett.* **2015**, *17*, 3094–3097; b) S. Eda, F. Eguchi, H. Haneda, T. Hamura, *Chem. Commun.* **2015**, *51*, 5963–5966. See also Ref. [2].
- [8] For selected reviews on arynes, see: a) R. W. Hoffmann, *Dehydrobenzene and Cycloalkynes*, Academic Press, New York, **1967**; b) S. V. Kessar in *Comprehensive Organic Synthesis, Vol. 4* (Ed.: B. M. Trost), Pergamon Press, Oxford, **1991**, pp. 483–515; c) H. Pellissier, M. Santelli, *Tetrahedron* **2003**, *59*, 701–730; d) H. H. Wenk, M. Winkler, W. Sander, *Angew. Chem. Int. Ed.* **2003**, *42*, 502–528; *Angew. Chem.* **2003**, *115*, 518–546; e) H. Yoshida, K. Takaki, *Synlett* **2012**, *23*, 1725–1732; f) A. Bhunia, S. R. Yetra, A. T. Biju, *Chem. Soc. Rev.* **2012**, *41*, 3140–3152; g) A. V. Dubrovskiy, N. A. Markina, R. C. Larock, *Org. Biomol. Chem.* **2013**, *11*, 191–218.
- [9] For our recent report on benzyne chemistry, see: T. Hamura, Y. Chuda, Y. Nakatsuji, K. Suzuki, *Angew. Chem. Int. Ed.* **2012**, *51*, 3368–3372; *Angew. Chem.* **2012**, *124*, 3424–3428. See also Ref. [2].
- [10] For details, see the Supporting Information.
- [11] Dibromoisobenzofuran **11** was efficiently prepared in four steps including the sequential reactions of methyl 2-formylbenzoate with two identical aryl Grignard reagent. For details, see the Supporting Information.
- [12] For selected examples of halogen/lithium exchange of functionalized arenes, see: a) J. Clayden, *Organolithiums: Selectivity for Synthesis in Tetrahedron Organic Chemistry Series, Vol. 23*, Pergamon Press, Oxford, **2002**, pp. 111–147; b) P. Beak, D. J. Allen, *J. Am. Chem. Soc.* **1992**, *114*, 3420–3425; c) C. Nájera, J. M. Sansano, M. Yus, *Tetrahedron* **2003**, *59*, 9255–9303; d) M. Dabrowski, J. Kubicka, S. Lulinski, J. Serwatowski, *Tetrahedron* **2005**, *61*, 6590–6595.
- [13] For selected reactions of *o*-dihalobenzenes with *n*BuLi, see: a) H. Gilman, R. D. Gorsich, *J. Am. Chem. Soc.* **1956**, *78*, 2217–2222; b) L. S. Chen, G. J. Chen, C. Tamborski, *J. Organomet. Chem.* **1980**, *193*, 283–292; c) K. C. Caster, C. G. Keck, R. D. Walls, *J. Org. Chem.* **2001**, *66*, 2932–2936; d) J. W. Coe, M. C. Wirtz, C. G. Bashore, J. Candler, *Org. Lett.* **2004**, *6*, 1589–1592.
- [14] Regarding the solvent choice used in these cycloadditions, the suitable conditions are dependent on the substrate combination and organolithium reagents.
- [15] For selected reviews on polyacenes, see: a) M. Bendikov, F. Wudl, D. F. Perepichka, *Chem. Rev.* **2004**, *104*, 4891–4946; b) J. E. Anthony, *Chem. Rev.* **2006**, *106*, 5028–5048; c) J. E. Anthony, *Angew. Chem. Int. Ed.* **2008**, *47*, 452–483; *Angew. Chem.* **2008**, *120*, 460–492; d) H. F. Bettinger, *Pure Appl. Chem.* **2010**, *82*, 905–915.
- [16] Tetrabromobenzene (**22**) can serve as a 1,4-benzdiyne equivalent. For pioneering studies by Hart on the generation and trapping of 1,4-benzdiyne equivalents, see: a) H. Hart, D. Ok, *J. Org. Chem.* **1986**, *51*, 979–986; b) H. Hart, C.-Y. Lai, G. Nwokogu, S. Shamouilian, A. Teuerstein, C. Zlotogorski, *J. Am. Chem. Soc.* **1980**, *102*, 6649–6651. Other examples, see: c) Y.-L. Chen, J.-Q. Sun, X. Wei, W.-W. Wong, A. W. M. Lee, *J. Org. Chem.* **2004**, *69*, 7190–7197; d) G. E. Morton, A. G. M. Barrett, *J. Org. Chem.* **2005**, *70*, 3525–3529; e) I. I. Schuster, L. Cracium, D. M. Ho, R. A. Pascal, Jr., *Tetrahedron* **2002**, *58*, 8875–8882; f) H. M. Duong, M. Bendikov, D. Steiger, Q. Zhang, G. Sonmez, J. Yamada, F. Wudl, *Org. Lett.* **2003**, *5*, 4433–4436.
- [17] Recently, a synthetic method of isoacenothiophenes, non-classical 5-heteroacenes, was developed, see: X. Shi, T. Y. Gopalakrishna, Q. Wang, C. Chi, *Chem. Eur. J.* **2017**, *23*, 8525–8531.

Manuscript received: September 12, 2018

Accepted manuscript online: October 17, 2018

Version of record online: November 14, 2018

## COMMUNICATION

View Article Online  
View Journal | View Issue

## A new synthetic route to 5,6,11,12-tetraarylethynyltetracenes†

 Kei Kitamura,<sup>a</sup> Kenta Asahina,<sup>a</sup> Yusaku Nagai,<sup>a</sup> Keshu Zhang,<sup>a</sup> Shogo Nomura,<sup>b</sup> Katsunori Tanaka<sup>id</sup> <sup>b,c</sup> and Toshiyuki Hamura<sup>id</sup> <sup>\*a</sup>

 Cite this: *Org. Biomol. Chem.*, 2018, **16**, 9143

 Received 1st October 2018,  
Accepted 8th November 2018

DOI: 10.1039/c8ob02450b

rsc.li/obc

A new synthetic route to 5,6,11,12-tetrakis(arylethynyl)tetracenes,  $\pi$ -extended rubrenes, was developed via [4 + 2] cycloadditions of dialkynylisobenzofuran and 1,4-naphthoquinone. Introduction of arylethynyl groups by double nucleophilic additions to tetracenequinone gave sterically congested (arylethynyl)tetracenes after reductive aromatization. The photophysical properties of the newly prepared  $\pi$ -conjugated molecules are also evaluated.

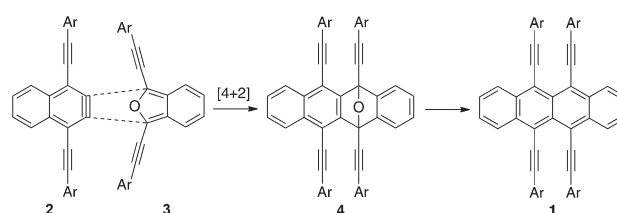
We previously reported a preparation of 5,6,11,12-tetraarylethynyltetracene **1**, a new class of  $\pi$ -extended rubrenes, via [4 + 2] cycloaddition of dialkynylisobenzofuran **2** and dialkynylisobenzofuran **3** (Scheme 1).<sup>1,2</sup> In this reaction, two alkynyl groups on the naphthalene **2** can lower the LUMO energy, allowing the practical construction of the sterically overcrowded structure through their efficient HOMO–LUMO interaction.

This approach, however, has a problem in that the yield of the aromatization (**4**  $\rightarrow$  **1**) is low or moderate owing to the unexpected reactivities derived from the closely located *peri*-ethynyl groups in epoxytetracene **4** under the acidic conditions.<sup>3</sup>

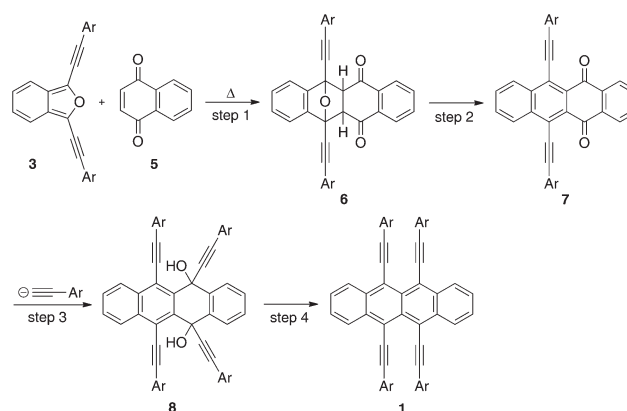
To solve this problem, we focused on developing a new synthetic route to  $\pi$ -extended rubrene **1** using dialkynylisobenzofuran **3** as a reactive platform.<sup>4,5</sup> Our second approach consists of four-step syntheses, which is depicted in Scheme 2.<sup>6</sup> In the first step, the [4 + 2] cycloaddition of dialkynylisobenzofuran **3** and 1,4-naphthoquinone (**5**) gives the cycloadduct **6**, which is converted to the tetracenequinone **7** by aromatization (step 2). Subsequent introduction of two alkynyl groups by double nucleophilic additions of alkynyl anions (step 3), and reductive aromatization of the resulting diol **8** would produce the target

compound **1** (step 4). Along these lines, we now report an efficient synthetic access to  $\pi$ -extended rubrenes possessing various arylethynyl groups at the *peri*-positions. Moreover, photophysical properties of the newly prepared poly-ethynylated tetracenes are evaluated. Also described is the application of the parent compound **1a** to a cellular imaging agent.

Scheme 3 shows the [4 + 2] cycloaddition of dialkynylisobenzofuran. Upon mixing of isobenzofuran **3a** and naphthoquinone **5** (CH<sub>2</sub>Cl<sub>2</sub>, r.t.), a new spot corresponding to the cycloadduct **6a** was observed by TLC. Further reaction at the same temperature, however, did not completely consume the start-



**Scheme 1** The first syntheses of  $\pi$ -extended rubrenes **1** via [4 + 2] cycloaddition of naphthalene and isobenzofuran.



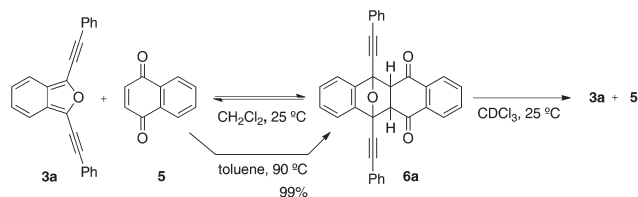
**Scheme 2** New synthetic route to  $\pi$ -extended rubrenes **1**.

<sup>a</sup>Department of Applied Chemistry for Environment, School of Science and Technology, Kwansai Gakuin University, 2-1 Gakuen, Sanda, Hyogo 669-1337, Japan. E-mail: thamura@kwansai.ac.jp

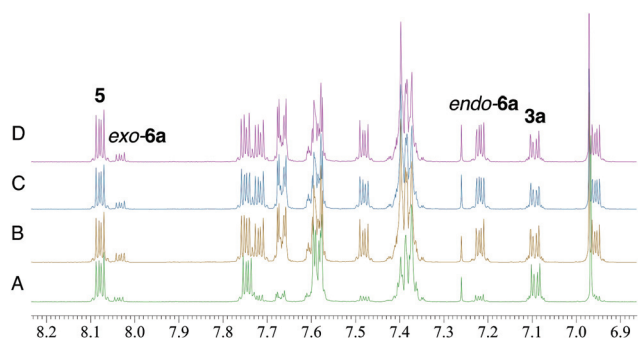
<sup>b</sup>Biofunctional Synthetic Chemistry Laboratory, RIKEN Cluster for Pioneering Research, 2-1 Hirosawa, Wako-shi, Saitama 351-0198, Japan

<sup>c</sup>Biofunctional Chemistry Laboratory, Kazan Federal University, 18 Kremlyovskaya street, Kazan 420008, Russia

†Electronic supplementary information (ESI) available. See DOI: 10.1039/c8ob02450b



**Scheme 3** [4 + 2] cycloaddition between isobenzofuran **3a** and 1,4-naphthoquinone (**5**).

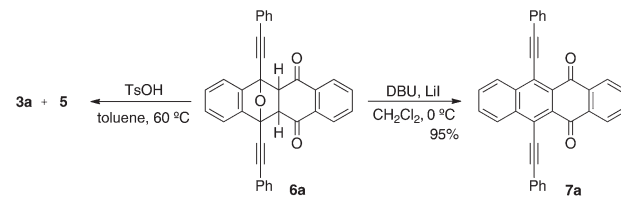


**Fig. 1** [4 + 2] cycloaddition between isobenzofuran **3a** and 1,4-naphthoquinone (**5**) monitored by NMR. (a) A: 5 min, B: 2 h, C: 7 h, D: 15 h.

ing materials **3a** and **5**, indicating their equilibrium with the cycloadduct **6a**. Indeed,  $^1\text{H}$  NMR analysis revealed that the cycloadduct **6a** including *endo*- and *exo*-isomers was readily formed after dissolving the isobenzofuran **3a** and naphthoquinone **5** in  $\text{CDCl}_3$  at room temperature (see A in Fig. 1). After 7 h, the ratio of **3a**, **5**, *exo-6a*, and *endo-6a* almost became constant (see D in Fig. 1). The stereochemistry of the *exo-6a* and *endo-6a* was tentatively assigned by consideration of the chemical shift of each methine proton.<sup>7</sup>

After further study of this [4 + 2] cycloaddition, we were pleased to find that the solvent choice is crucial to produce the high yield of the cycloadduct **6a**: when the above-mentioned reaction was performed in toluene at 90 °C, the [4 + 2] cycloadduct **6a** gradually precipitated from the solution due to its low solubility in toluene, affording the essentially pure product **6a** almost in quantitative yield (Scheme 3). Interestingly, the *endo* isomer **6a** was solely produced under these conditions. By dissolving in  $\text{CDCl}_3$  (25 °C, 26 h), the cycloadduct **6a** again underwent cycloreversion to give the dialkynylisobenzofuran **3a** and 1,4-naphthoquinone (**5**).<sup>8</sup>

Scheme 4 shows the conversion of the [4 + 2] cycloadduct **6a** to tetracenequinone **7a**. Upon heating of cycloadduct **6a** in the presence of TsOH at 60 °C, the cycloreversion occurred quickly, and the aromatized product **7a** was not obtained at all.<sup>9,10</sup> On the other hand, treatment of the cycloadduct **6a** with LiI and DBU at low temperature ( $\text{CH}_2\text{Cl}_2$ , 0 °C)<sup>11</sup> underwent the clean aromatization without invoking the cycloreversion to give the tetracenequinone **7a** in 95% yield.

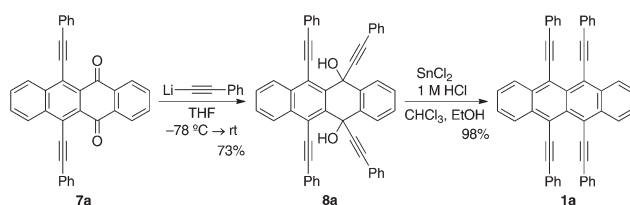


**Scheme 4** Aromatization of cycloadduct **6a** to tetracenequinone **7a**.

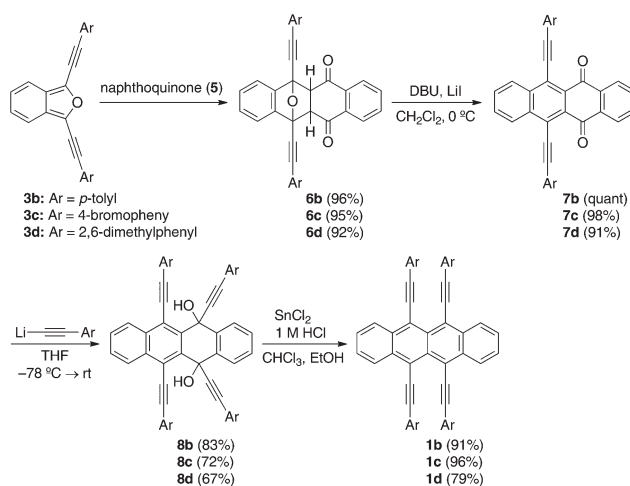
Further transformation of the tetracenequinone **7a** to  $\pi$ -extended rubrene **1a** was achieved through double nucleophilic additions of phenylethynyllithium, followed by  $\text{Sn}^{\text{II}}$ -mediated reductive aromatization (Scheme 5). Importantly, the nucleophilic addition of alkynyllithium to **7a** occurred cleanly by warming the reaction mixture to room temperature, in spite of the high steric hindrance between incoming nucleophile and proximal alkynyl groups.

In a similar manner, the substituted derivatives **1b** and **1c**, having four *p*-tolylethynyl or (4-bromophenyl)ethynyl groups at both *peri*-positions, were efficiently synthesized by this four-step sequence including the tetracenequinones **7b** and **7c** as key intermediates (Scheme 6).

It should be noted that the developed method has high synthetic potential in that the sterically congested derivative **1d**



**Scheme 5** Transformation of tetracenequinone **7a** to  $\pi$ -extended rubrene **1a**.



**Scheme 6** Preparation of  $\pi$ -extended rubrenes **1b**–**1d**.

possessing four 2,6-xylylethynyl groups on the tetracene core was easily accessible in good yield. This is a sharp contrast from our previous method by acid-promoted aromatization of the epoxy tetracene **4d** (Ar: 2,6-xylyl), where the product **1d** was obtained in poor yield, and a sizable amount of furan (structure not shown) was produced.<sup>1</sup>

To evaluate the photophysical properties, UV-Vis spectra of  $\pi$ -extended rubrenes **1a–1d** were measured in chloroform (Fig. 2). The  $\pi$ -extended rubrene **1a** has its absorption maximum at 640 nm, which was greatly red-shifted over 100 nm from that of the parent rubrene, indicating effective  $\pi$ -extension by the existence of four phenylethynyl groups on the tetracene core. The  $\pi$ -extended rubrenes **1b** and **1c** with *para*-substitution denoted the similar tendency of **1a**, whereas the absorption maximum of the sterically congested derivative **1d** was slightly blue-shifted (623 nm).

Fluorescence spectra were also measured in chloroform (Fig. 3). The  $\pi$ -extended rubrenes **1a–1d** showed a fluorescent maximum peaking at around 690 nm, which were excited at their absorption maximum. A larger Stokes shift was observed in **1d** (1620  $\text{cm}^{-1}$ ) compared to that of **1a** (1200  $\text{cm}^{-1}$ ). The absolute fluorescent quantum yields of these  $\pi$ -extended derivatives were nearly 10%, which were lower than that of the parent rubrene.

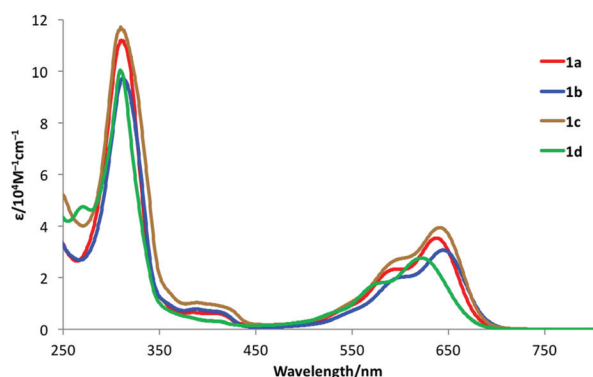


Fig. 2 UV-Vis absorption spectra of  $\pi$ -extended rubrenes **1a–1d**.

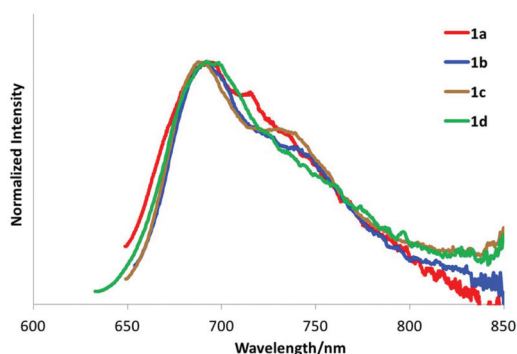


Fig. 3 Fluorescence spectra of  $\pi$ -extended rubrenes **1a–1d**.

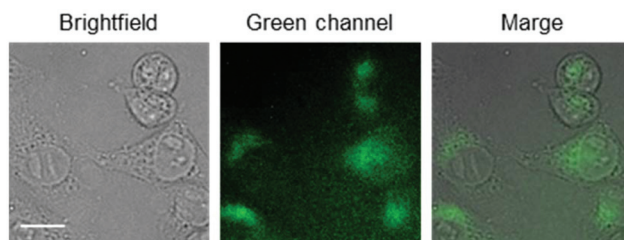


Fig. 4 Fluorescence imaging of HeLaS3 cells by  $\pi$ -extended rubrene. The cells were treated with 100  $\mu\text{M}$  of **1a** for 30 min at 37  $^{\circ}\text{C}$  and analyzed by fluorescence microscopy. Green channel:  $\lambda_{\text{em}} = 620 \text{ nm}$ ,  $\lambda_{\text{ex}} = 700 \text{ nm}$ . Scale bar: 20  $\mu\text{m}$ .

Finally, preliminary investigation of cellular imaging using  $\pi$ -extended rubrene was performed by treating the HeLa cells with **1a** for 30 min at 37  $^{\circ}\text{C}$ . Fluorescence signals from cells upon excitation at 620 nm indicate a future applicability of  $\pi$ -extended rubrene as a bioimaging probe (Fig. 4).

## Conclusions

In conclusion, [4 + 2] cycloaddition of dialkynylisobenzofuran and 1,4-naphthoquinone allowed rapid construction of alkynylated tetracenequinones, which were amenable to transformation *en route* to tetrakis(arylethynyl)tetracenes. Further studies on the application of these attractive  $\pi$ -conjugated molecules to organic electronics materials and fluorescent probes are underway in our laboratories.

## Conflicts of interest

There are no conflicts to declare.

## Acknowledgements

This work was supported by JSPS KAKENHI Grant Number JP15H05840 in Middle Molecular Strategy and JST ACT-C Grant Number JPMJCR12YY, Japan.

## Notes and references

- (a) K. Kitamura, K. Asahina, Y. Nagai, H. Sugiyama, H. Uekusa and T. Hamura, *Chem. – Eur. J.*, 2018, **24**, 14034–14038; (b) T. Hamura, *Patent JP 2016169213*, 2016.
- For related reviews, see: (a) M. M. Richter, *Chem. Rev.*, 2004, **104**, 3003–3036; (b) M. Bendikov, F. Wudl and D. F. Perepichka, *Chem. Rev.*, 2004, **104**, 4891–4946; (c) J. E. Anthony, *Angew. Chem.*, 2008, **120**, 460–492, (*Angew. Chem., Int. Ed.*, 2008, **47**, 452–483).
- For related distorted  $\pi$ -crowded ethynyl naphthalene derivatives, see: (a) B. Bossenbroek, D. C. Sanders, H. M. Curry and H. Shechter, *J. Am. Chem. Soc.*, 1969, **91**, 371–379;

- (b) H. A. Staab and J. Ipaktschi, *Chem. Ber.*, 1971, **104**, 1170–1181; (c) A. E. Jungk and G. M. J. Schmidt, *Chem. Ber.*, 1971, **104**, 3272–3288. See also: (d) R. A. Pascal, Jr., *Chem. Rev.*, 2006, **106**, 4809–4819.
- 4 (a) T. Hamura and R. Nakayama, *Chem. Lett.*, 2013, **42**, 1013–1015; (b) K. Asahina, S. Matsuoka, R. Nakayama and T. Hamura, *Org. Biomol. Chem.*, 2014, **12**, 9773–9776; (c) R. Kudo, K. Kitamura and T. Hamura, *Chem. Lett.*, 2017, **46**, 25–28.
- 5 For our synthetic application of isobenzofurans to polycene derivatives, see: (a) S. Eda and T. Hamura, *Molecules*, 2015, **20**, 19449–19462; (b) R. Akita, K. Kawanishi and T. Hamura, *Org. Lett.*, 2015, **17**, 3094–3097; (c) S. Eda, F. Eguchi, H. Haneda and T. Hamura, *Chem. Commun.*, 2015, **51**, 5963–5966; (d) H. Haneda, S. Eda, M. Aratani and T. Hamura, *Org. Lett.*, 2014, **16**, 286–289.
- 6 For syntheses of substituted rubrene derivatives, see: (a) A. S. Paraskar, A. R. Reddy, A. Patra, Y. H. Wijsboom, O. Gidron, L. J. W. Shimon, G. Leitun and M. Bendikov, *Chem. – Eur. J.*, 2008, **14**, 10639–10647; (b) J. Zhang, S. Sarrafpour, T. E. Haas, P. Müller and S. W. Thomas, *J. Mater. Chem.*, 2012, **22**, 6182–6189.
- 7 For a related [4 + 2] cycloaddition of diphenylisobenzofuran with 1,4-naphthoquinone, and structural characterization of the *endo/exo*-cycloadducts, see: T. Wombacher, S. Foro and J. J. Schneider, *Eur. J. Org. Chem.*, 2016, 569–578. See also ref. 5b and 6.
- 8 The perfect *endo* selectivity observed in the [4 + 2] cycloaddition of isobenzofuran **3a** and naphthoquinone **5** is presumably due to the lower solubility of the *endo* cycloadduct **6a** in toluene than that of the *exo* cycloadduct **6a**. Therefore, the *endo* cycloadduct **6a** was selectively precipitated from the solution under the equilibrium between the starting materials and the cycloadducts. In a similar manner, the *endo* cycloadducts **6b–6d** were obtained as a single stereoisomer by precipitation owing to their poor solubility with EtOH or heptane. For details, see ESI.†
- 9 A similar approach for preparation of substituted rubrenes by using [4 + 2] cycloaddition of diarylisobenzofuran and naphthoquinone was developed, see: J. A. Dodge, J. D. Bain and A. R. Chamberlin, *J. Org. Chem.*, 1990, **55**, 4190–4198.
- 10 Under the acidic conditions, dialkynylisobenzofuran **3a** was gradually decomposed, which promoted the cycloreversion of the cycloadduct **6a**.
- 11 For related base-induced aromatization, see: (a) R. Polley and M. Hanack, *J. Org. Chem.*, 1995, **60**, 8278–8282; (b) S.-H. Chan, C.-Y. Yick and H. N. C. Wong, *Tetrahedron*, 2002, **58**, 9413–9422.

## Polycycles | Very Important Paper |

VIP Tetrakis(phenylethynyl)tetracene: A New  $\pi$ -Extended Rubrene DerivativeKei Kitamura,<sup>[a]</sup> Kenta Asahina,<sup>[a]</sup> Yusaku Nagai,<sup>[a]</sup> Haruki Sugiyama,<sup>[b]</sup> Hidehiro Uekusa,<sup>[b]</sup> and Toshiyuki Hamura\*<sup>[a]</sup>

**Abstract:** An efficient synthetic route to 5,6,11,12-tetrakis(arylethynyl)tetracenes, new  $\pi$ -extended rubrene derivatives, was developed by means of [2+4] cycloaddition of dialkynynaphthalene and dialkynylisobenzofuran. Importantly, two alkynyl groups introduced into the aryne exerts a significant effect in lowering the LUMO energy, allowing practical access to sterically overcrowded polycyclic structures through an efficient HOMO–LUMO interaction. Study on the potential reactivity inherent in the *peri*-ethynyl-substituted tetracenes revealed several interesting reactivities. X-ray analysis of these new  $\pi$ -extended derivatives showed distorted structures to reduce steric repulsion due to the existence of the substituents at the *peri*-positions.

Rubrene (**1**), 5,6,11,12-tetraphenyltetracene (Figure 1), is of interest as it has various interesting properties, including electrochemiluminescence,<sup>[1]</sup> photooxidation,<sup>[2]</sup> and high carrier mobility.<sup>[3]</sup> Recently, syntheses of substituted derivatives have been studied not only to develop the new properties inherent in the unique  $\pi$ -conjugated structure, but also to improve the performance.<sup>[4]</sup>

In this context,  $\pi$ -extended rubrene **2**, possessing four ethynyl groups incorporated into the aryl–aryl bonds of **1**, has attractive physical properties in view of the distorted  $\pi$ -conjugated structure with positive or negative  $\pi$ – $\pi$  interaction between the pairs of substituents at the 5,12- and 6,11-positions.<sup>[5,6]</sup> Several interesting reactivities are expected based on the closely located triple bonds at the both *peri*-positions.<sup>[7]</sup> In spite of these attractive features, there has been no report on the synthesis of highly alkynylated derivatives like **2**, probably due to the limited availability of the appropriate  $\pi$ -conjugated building blocks, and/or the lack of practical methods to introduce

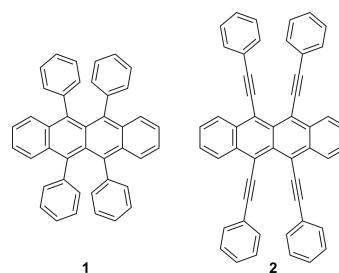
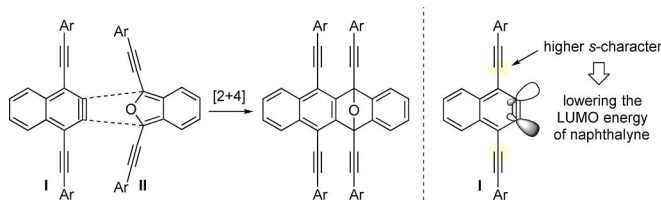


Figure 1. Rubrene (**1**) and  $\pi$ -extended rubrene **2**.

multiple functionalities at the sterically crowded 5,6,11,12-positions in the tetracene core.

To address these synthetic problems, we were intrigued by the use of the two reactive molecules, aryne and isobenzofuran, for the construction of sterically overcrowded structure as following three reasons: 1) the aryne precursor, 1,2-dibromoaryne, is easily prepared starting from dibrominated quinone derivatives (*vide infra*); 2) substituted isobenzofurans, including novel  $\pi$ -extended arylethynyl derivatives **II**, became accessible by our recently developed synthetic method;<sup>[8,9]</sup> and most importantly 3) the combination of a pair of two highly reactive species allows cyclization despite the severe steric repulsion between the incoming bulky arynophile **II** and the substituted aryne species **I**. In this strategy, two alkynyl groups within an aryne species **I** would exert a significant effect in lowering the LUMO energy of **I** by the inductive electron withdrawal of the *sp* carbon with higher *s* character, which leads to the efficient HOMO–LUMO interaction of **I** and **II**, allowing practical access to sterically overcrowded structure (Scheme 1).

Herein, we disclose the success of this scenario: tetraaryl-ethynyltetracenes, viewed as novel  $\pi$ -extended rubrene derivatives, can be synthesized by aryne cycloaddition using isobenzofuran as a trapping agent.<sup>[10]</sup> X-ray analysis of the new  $\pi$ -ex-



Scheme 1. Synthetic strategy for sterically overcrowded tetracene derivatives.

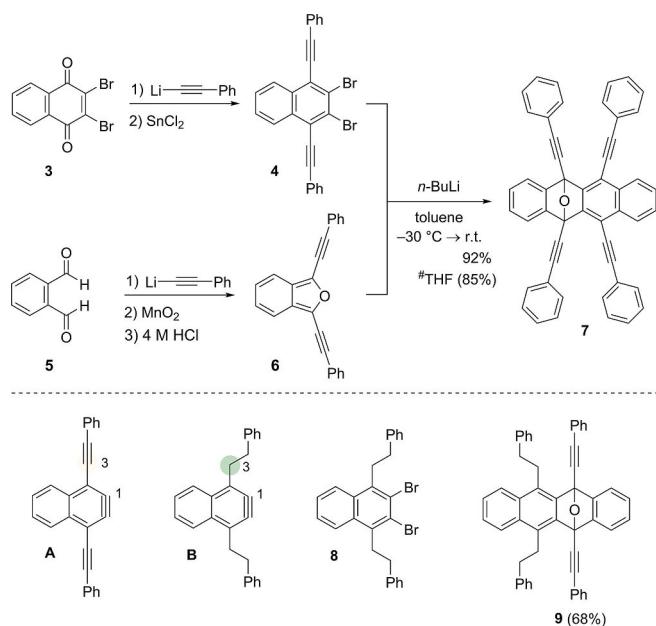
[a] Dr. K. Kitamura, Dr. K. Asahina, Y. Nagai, Prof. Dr. T. Hamura  
Department of Applied Chemistry for Environment  
Kwansei Gakuin University, 2-1 Gakuen, Sanda 669-1337 (Japan)  
E-mail: thamura@kwansei.ac.jp

[b] H. Sugiyama, Prof. Dr. H. Uekusa  
Department of Chemistry, School of Science, Tokyo Institute of Technology  
Ookayama 2, Meguro-ku, Tokyo 152-8551 (Japan)

Supporting information and the ORCID identification number(s) for the author(s) of this article can be found under:  
<https://doi.org/10.1002/chem.201803294>.

tended derivatives show the distorted structure to reduce steric repulsion due to the existence of the substituents at the *peri*-positions. Unexpected reactivities of epoxytetracene and its aromatized product inherent in these sterically crowded structures were also revealed, which are described in this Communication.

Scheme 2 shows the preparation of the epoxytetracene **7**. Starting from dibromonaphthoquinone **3**, dibromodialkynyl-naphthalene **4** (the precursor of dialkynyl-naphthalene) was prepared by double nucleophilic additions of phenylethyne-



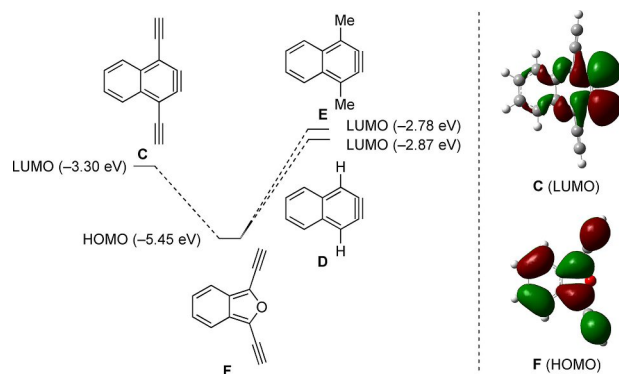
**Scheme 2.** [2+4] Cycloaddition of naphthalene and isobenzofuran.

lithium to the naphthoquinone **3** followed by reductive aromatization ( $\text{SnCl}_2$ , 50% AcOH aq., EtOH,  $50^\circ\text{C}$ ). Bis(phenylethynyl)isobenzofuran **6**, another reactive precursor for dialkynyl-naphthalene, was synthesized by the successive nucleophilic additions of phenylethyneyllithium to *o*-phthalaldehyde (**5**), selective oxidation, and subsequent acid-promoted cyclization of the resulting keto-alcohol.<sup>[8c]</sup> With these two molecules in hand, we examined the key aryne cycloaddition. Upon treatment of dibromonaphthalene **4** with *n*BuLi in the presence of dialkynylisobenzofuran **6** (THF,  $-30^\circ\text{C} \rightarrow \text{r.t.}$ ), dialkynyl-naphthalene **A**, was cleanly generated and trapped by isobenzofuran to give the cycloadduct **7** in 85% yield. Experimentally, toluene was the solvent of choice for the reaction, giving **7** in excellent yield.

Further study on this aryne cycloaddition revealed that the existence of the two alkynyl units at  $\text{C}_1$ - and  $\text{C}_4$ -positions of the naphthalene core in **4** was effective to obtain the high yield of the cycloadduct, since the corresponding [2+4] cycloaddition of the dialkynyl-naphthalene **B**, generated from the dibromide **8** under similar reaction conditions, gave the moderate yield of the cycloadduct **9** (68% yield).

These results are ascribed to the difference in the *s* character of the  $\text{C}_3$  carbon in naphthalenes **A** and **B**, which affects the

LUMO energy of the arynes. Indeed, calculations showed that LUMO energy of the diethynyl-naphthalene **C**, model substrate of **A**, is  $-3.30$  eV, which is lower than that of the parent aryne **D** (Figure 2). This increased electrophilicity of **C** allows an



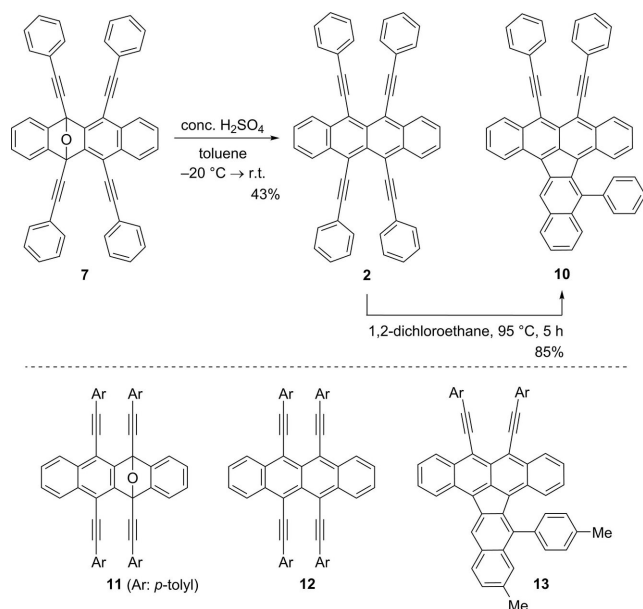
**Figure 2.** HOMO–LUMO gap between the substituted naphthalenes **C–E** and diethynylisobenzofuran **F** obtained by DFT calculations (B3LYP/6–311G (d,p)).

effective interaction with diethynylisobenzofuran **F** (HOMO–LUMO gap: 2.15 eV). By contrast, the difference in this value between dimethylnaphthalene **E** (model substrate of **B**) and isobenzofuran **F** was larger (HOMO–LUMO gap: 2.67 eV), due to the electron-donating nature (lower *s* character) of the methyl group ( $\text{sp}_3$ ) in **E**. By taking advantage of this strategy, sterically congested cycloadduct **15**, with bulkier aryethynyl groups on the tetracene core, was also accessible in good yield (Scheme S6 in the Supporting Information).

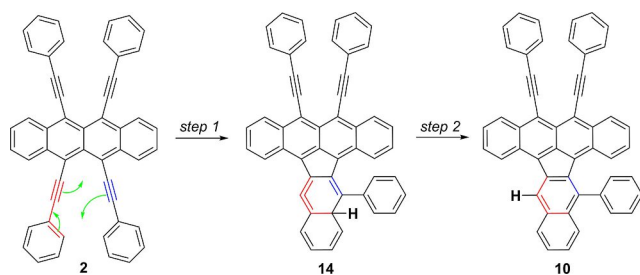
Aromatization of the cycloadduct **7** was performed by treatment with catalytic amount of  $\text{H}_2\text{SO}_4$  in toluene ( $-20^\circ\text{C} \rightarrow \text{r.t.}$ ) to give the  $\pi$ -extended rubrene **2** in 43% yield.<sup>[11]</sup> It should be noted that this multi-alkynylated product **2** was easily isomerized to benzoindenotetracene **10** under thermal conditions (dichloroethane,  $95^\circ\text{C}$ ; Scheme 3).

The substituted derivative **12**, with four *p*-tolylethynyl groups at both *peri*-positions, was also efficiently synthesized by this two-step sequence including the [2+4] cycloadduct **11** as a key intermediate (Schemes S3 and S4 in the Supporting Information). Thermal isomerization of **12** also occurred cleanly by heating at  $80^\circ\text{C}$  for 5 h to give benzoindenotetracene **13** in 95% yield. The formation of benzoindenotetracenes **10** and **13** was formally explained by successive pericyclic reactions (Scheme 4).<sup>[12]</sup> In the first step, the intramolecular Diels–Alder reaction between the arenene and yne moiety of the proximal aryethynyl groups in **2** produced heptacycle **14** with a highly strained isoaromatic cyclic allene structure.<sup>[13]</sup> Subsequent hydrogen atom transfer of **14** gave benzoindenotetracene **10** (step 2).<sup>[14]</sup>

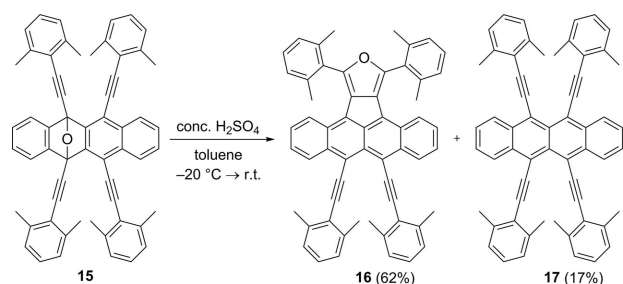
Moreover, unexpected reactivity inherent in the sterically congested structure with *peri*-alkynyl groups was observed when the epoxytetracene **15**,<sup>[15]</sup> possessing four bulky 2,6-xylylethynyl groups, was treated with concentrated  $\text{H}_2\text{SO}_4$  (toluene,  $-20^\circ\text{C} \rightarrow \text{r.t.}$ ), affording furan **16** in 62% yield as a major product, along with the  $\pi$ -extended rubrene **17** (17%; Scheme 5).<sup>[16]</sup> This result is in contrast to the corresponding reaction of



Scheme 3.  $\pi$ -Extended rubrene and its thermal reactivity.



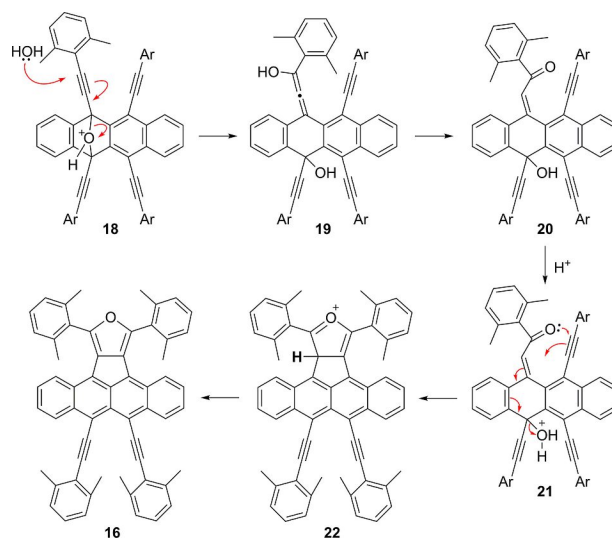
Scheme 4. Thermal isomerization of  $\pi$ -extended rubrene 2 into benzoindeno[1,2-*b*]tetracene 10.



Scheme 5. Unexpected formation of furan 16 from epoxytetracene 15.

epoxytetracenes 7 and 11, which produced aromatized products 2 and 12 as a major product, respectively (vide supra).

Scheme 6 shows the proposed reaction mechanism for the formation of furan 16. In the first step, the epoxy ring in epoxytetracene 15 was cleaved with water in a  $S_N2'$  fashion from the protonated intermediate 18 to give the enol 19, which underwent keto–enol tautomerization, affording the enone 20. In the next step, dehydrative intramolecular cyclization of the protonated intermediate 21 followed by aromatization of the resulting hexacycle 22 gave furan 16. To clarify the origin of the oxygen incorporated into the furan 16 by water



Scheme 6. Proposed reaction mechanism for the formation of furan 16.

or molecular oxygen, the above-mentioned aromatization was conducted in the presence of 20 equivalents of  $\text{H}_2^{18}\text{O}$  (conc.  $\text{H}_2\text{SO}_4$ , toluene,  $-20 \rightarrow 50\text{ }^\circ\text{C}$ ), affording  $^{18}\text{O}$ -labeled furan 16- $^{18}\text{O}$  with 34% incorporation.<sup>[17]</sup> This result clearly indicates that the residual water in the solvent and concentrated  $\text{H}_2\text{SO}_4$  worked as a nucleophile to cleave the epoxy ring in 15, leading to the formation of furan 16 (vide supra).

The structures of  $\pi$ -extended rubrenes 2, 12, and 17 were elucidated by X-ray crystal structure analysis (Figures 3–5).<sup>[18–21]</sup> The common feature of these products is that they adopt a planar conformation in the tetracene core. The end-to-end twist of the tetracene core is  $0^\circ$  for 2 and 12, and  $1.0^\circ$  for 17.<sup>[4a]</sup> In addition, they are highly distorted to avoid the intramolecular steric repulsion at the *peri*-position. In the case of the parent compound 2, three modes of distortion are observed to relieve the steric congestion of the *peri*-phenylethynyl groups. The first is extending the distance between the substituents at the *peri*-position of the tetracene plain by ex-

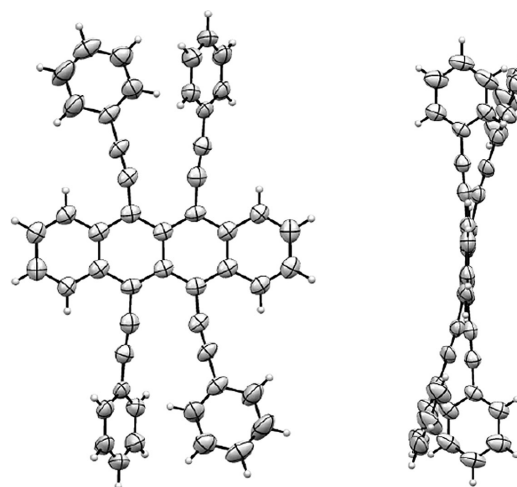
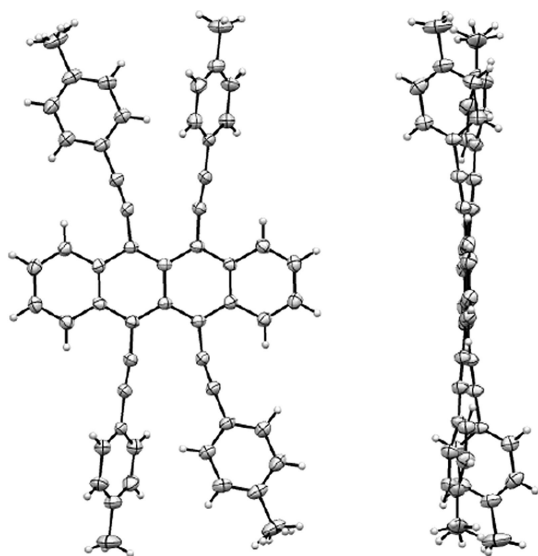
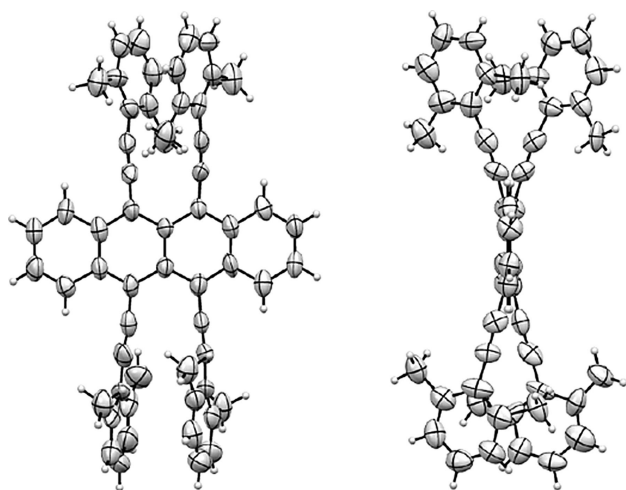


Figure 3. X-ray crystal structure of 2 (left: top view, right: side view). Displacement ellipsoids are drawn at the 50% probability level.



**Figure 4.** X-ray crystal structure of **12** (left: top view, right: side view). Displacement ellipsoids are drawn at the 50% probability level.



**Figure 5.** X-ray crystal structure of **17** (left: top view, right: side view). Displacement ellipsoids are drawn at the 50% probability level.

panding the relevant bond angles of the tetracene ( $C_{11}-C_{15}-C_{12}=122.2^\circ$ ) as shown in Table 1. The second is the shifting the phenylethynyl groups up and down the tetracene plane forming a dihedral angle  $15.2^\circ$ . The third is deforming the sp carbon atoms of the acetylene units from linearity (e.g.  $C_{11}-C_{19}-C_{20}=172.7^\circ$ ,  $C_{19}-C_{20}-C_{21}=173.5^\circ$ ). Similarly, the *p*-Me derivative **12** has three modes of distortion to reduce steric repulsion of the *peri*-phenylethynyl groups. In this case, twisting of the two substituents out of the tetracene plane is small (dihedral angle:  $9.2^\circ$ ) in comparison to that found in **2**. Moreover, the bulkier *m*-dimethylphenyl groups in **17** force even greater distortions with the two phenylethynyl groups out of the tetracene plane (dihedral angle:  $30.8^\circ$ ). In this case, the arylethynyl groups of **17** are rotated out of the tetracene plane, in which the proximal aromatic groups bound to the sp-hybridized

**Table 1.** Structural parameters of **2**, **12**, and **17** obtained by X-ray analyses; bond lengths in Å and angles in  $^\circ$ .

	<b>2</b> <sup>[a]</sup>	<b>12</b> <sup>[a]</sup>	<b>17</b>
$C_{19}\cdots C_{22}$	2.740(7)	2.728(2)	2.73(1)
$[C_{25}\cdots C_{28}]$			[2.78(1)]
$C_{20}\cdots C_{23}$	3.388(7)	3.368(2)	3.12(1)
$[C_{26}\cdots C_{29}]$			[3.27(1)]
$C_{11}-C_{15}-C_{12}$	122.2(4)	121.9(1)	122.6(8)
$[C_5-C_{16}-C_6]$			[123.7(8)]
$C_{11}-C_{19}-C_{20}$	172.7(6)	171.7(1)	176(1)
$[C_6-C_{25}-C_{26}]$			[177(1)]
$C_{19}-C_{20}-C_{21}$	173.5(6)	175.5(1)	172(1)
$[C_{25}-C_{26}-C_{27}]$			[171(1)]
$C_{12}-C_{22}-C_{23}$	166.7(5)	166.7(1)	177(1)
$[C_5-C_{28}-C_{29}]$			[173(1)]
$C_{22}-C_{23}-C_{24}$	179.5(6)	176.5(1)	169(1)
$[C_{28}-C_{29}-C_{30}]$			[174(1)]
$C_{19}-C_{11}-C_{12}-C_{22}$	15.2(4)	9.2(1)	30.8(6)
$[C_{25}-C_6-C_5-C_{28}]$			[28.3(6)]

[a] Because of the presence of symmetry, the top half of the structure is identical to the bottom half.

carbon atoms are parallel each other to avoid their steric repulsion.

In summary, [2+4] cycloaddition of dialkynyl naphthalene and dialkynylisobenzofuran allowed rapid construction of *peri*-alkynylated epoxytetracenes, which could be further transformed into tetrakis(arylethynyl)tetracenes. Further study on application of these attractive  $\pi$ -conjugated molecules to organic electronics materials are under active investigation in our laboratories.

## Acknowledgements

This work was supported by JSPS KAKENHI Grant Number JP15H05840 in Middle Molecular Strategy and JST ACT-C Grant Number JPMJCR12YY, Japan.

## Conflict of interest

The authors declare no conflict of interest.

**Keywords:** crowded tetracene • cycloaddition • dialkynylisobenzofuran • naphthalene • polycycles • rubrene

[1] a) E. A. Chandross, J. W. Longworth, R. E. Visco, *J. Am. Chem. Soc.* **1965**, *87*, 3259–3260; b) D. M. Hercules, *Acc. Chem. Res.* **1969**, *2*, 301–307;

- c) M. M. Richter, *Chem. Rev.* **2004**, *104*, 3003–3036, and references therein.
- [2] a) M. Yamada, I. Isao, H. Kurado, *Bull. Chem. Soc. Jpn.* **1988**, *61*, 1057; b) H. E. Gspöner, C. M. Previtali, N. A. Garcia, *J. Photochem.* **1987**, *36*, 247; c) A. M. Caminade, F. E. Khatib, M. Koenig, J. M. Aubry, *Can. J. Chem.* **1985**, *63*, 3203; d) J. M. Aubry, J. Rigaudy, N. K. Cuong, *Photochem. Photobiol.* **1981**, *33*, 149–155; e) W. G. Herkstroeter, P. B. Merkel, *J. Photochem.* **1981**, *16*, 331; f) N. J. Turro, M.-F. Chow, S. Kanfer, M. Jacobs, *Tetrahedron Lett.* **1981**, *22*, 3–6; g) Y. Harada, T. Takahashi, S. Fujisawa, T. Kajiwara, *Chem. Phys. Lett.* **1979**, *62*, 283.
- [3] a) H. E. Katz, Z. Bao, *J. Phys. Chem. B* **2000**, *104*, 671–678; b) C. D. Dimitrakopoulos, P. R. L. Malenfant, *Adv. Mater.* **2002**, *14*, 99; c) V. C. Sundar, J. Zaumseil, V. Podzorov, E. Menard, R. L. Willett, T. Someya, M. E. Gershenson, J. A. Rogers, *Science* **2004**, *303*, 1644; d) J. Takeya, M. Yamagishi, Y. Tominari, R. Hirahara, Y. Nakazawa, T. Nishikawa, T. Kawase, T. Shimoda, S. Ogawa, *Appl. Phys. Lett.* **2007**, *90*, 102120; e) M. Bendikov, F. Wudl, D. F. Perepichka, *Chem. Rev.* **2004**, *104*, 4891; f) J. E. Anthony, *Angew. Chem. Int. Ed.* **2008**, *47*, 452–483; *Angew. Chem.* **2008**, *120*, 460–492.
- [4] a) A. S. Paraskar, A. R. Reddy, A. Patra, Y. H. Wijsboom, O. Gidron, L. J. W. Shimon, G. Leitus, M. Bendikov, *Chem. Eur. J.* **2008**, *14*, 10639–10647; b) J. Zhang, S. Sarrafpour, T. E. Haas, P. Müller, S. W. Thomas, *J. Mater. Chem.* **2012**, *22*, 6182–6189.
- [5] For related distorted  $\pi$ -crowded ethynyl naphthalene derivatives, see: a) B. Bossenbroek, D. C. Sanders, H. M. Curry, H. Shechter, *J. Am. Chem. Soc.* **1969**, *91*, 371–379; b) H. A. Staab, J. Ipaktschi, *Chem. Ber.* **1971**, *104*, 1170–1181; c) A. E. Jungk, G. M. J. Schmidt, *Chem. Ber.* **1971**, *104*, 3272–3288; see also: d) R. A. Pascal, Jr., *Chem. Rev.* **2006**, *106*, 4809–4819.
- [6] For preparation of sterically overcrowded molecules with acetylene linkage, see: a) S. Toyota, T. Yamamori, T. Makino, *Tetrahedron* **2001**, *57*, 3521–3528; b) T. Makino, S. Toyota, *Bull. Chem. Soc. Jpn.* **2005**, *78*, 917–928; c) S. Toyota, *Chem. Rev.* **2010**, *110*, 5398–5424.
- [7] a) J. Blum, W. Baidossi, Y. Badrieh, R. E. Hoffman, H. Schumann, *J. Org. Chem.* **1995**, *60*, 4738–4742; b) Y.-H. Kung, Y.-S. Cheng, C.-C. Tai, W.-S. Liu, C.-C. Shin, C.-C. Ma, Y.-C. Tsai, T.-C. Wu, M.-Y. Kuo, Y.-T. Wu, *Chem. Eur. J.* **2010**, *16*, 5909–5919; c) Y.-T. Wu, T. Hayama, K. K. Baldrige, A. Linden, J. S. Siegel, *J. Am. Chem. Soc.* **2006**, *128*, 6870–6884; d) X. Chen, P. Lu, Y. Wang, *Chem. Eur. J.* **2011**, *17*, 8105–8114.
- [8] a) T. Hamura, R. Nakayama, *Chem. Lett.* **2013**, *42*, 1013; b) K. Asahina, S. Matsuoka, R. Nakayama, T. Hamura, *Org. Biomol. Chem.* **2014**, *12*, 9773; c) R. Kudo, K. Kitamura, T. Hamura, *Chem. Lett.* **2017**, *46*, 25.
- [9] For our synthetic application of isobenzofurans to polyacene derivatives, see: a) S. Eda, T. Hamura, *Molecules* **2015**, *20*, 19449; b) R. Akita, K. Kawanishi, T. Hamura, *Org. Lett.* **2015**, *17*, 3094; c) S. Eda, F. Eguchi, H. Haneda, T. Hamura, *Chem. Commun.* **2015**, *51*, 5963; d) H. Haneda, S. Eda, M. Aratani, T. Hamura, *Org. Lett.* **2014**, *16*, 286.
- [10] Similar approach for preparation of substituted rubrenes by using aryne-isobenzofuran cycloaddition was developed, see: J. A. Dodge, J. D. Bain, A. R. Chamberlin, *J. Org. Chem.* **1990**, *55*, 4190–4198.
- [11] Treatment of **7** with TsOH in toluene at 40 °C also gave the desired product **2**, albeit low yield (20%).
- [12] For related intramolecular [4+2] cycloadditions of alkynes with arynes, see: a) D. Rodríguez, A. Navarro, L. Castedo, D. Domínguez, C. Saá, *Org. Lett.* **2000**, *2*, 1497–1500; b) D. Rodríguez, A. N. Vázquez, L. Castedo, D. Domínguez, C. Saá, *J. Org. Chem.* **2003**, *68*, 1938–1946; c) M. E. Hayes, H. Shinokubo, R. L. Danheiser, *Org. Lett.* **2005**, *7*, 3917–3920; d) R. C. Burrell, K. J. Daoust, A. Z. Bradley, K. J. DiRico, R. P. Johnson, *J. Am. Chem. Soc.* **1996**, *118*, 4218–4219; see also references [7a–c].
- [13] Cyclic allene intermediate **14** could also be produced from a 1,4-vinyl biradical intermediate. For related discussions, see references [5a, 12a].
- [14] Further reaction at higher reaction temperature (o-dichlorobenzene, 185 °C) gave no cyclized product by the intramolecular Diels–Alder reaction between aryne and yne moiety in **10**, only giving a complex mixture of products.
- [15] The epoxytetracene **15** was prepared in 76% yield by [2+4] cycloaddition of the corresponding naphthalene. For details, see the Supporting Information.
- [16] The structure of furan **16** was determined by X-ray analysis. For details, see Supporting Information.
- [17] As for the incorporation of <sup>18</sup>O in furan **16**, see Supporting Information.
- [18] Crystal data for **2**: C<sub>50</sub>H<sub>28</sub>·CHCl<sub>3</sub>, M<sub>r</sub> = 748.09, dark blue crystal, 0.160 × 0.080 × 0.010 mm, monoclinic, space group P2<sub>1</sub>/c, Z = 2, T = 123(2) K, a = 5.789(4), b = 19.8929(12), c = 16.4108(11) Å, β = 98.980(14)°, V = 1866.7(13) Å<sup>3</sup>, λ(Cu<sub>Kα</sub>) = 1.54186 Å, μ = 2.499 mm<sup>-1</sup>. Intensity data were collected in the ω-scan mode using an R-Axis RAPID II, Imaging plate camera (Rigaku). The structure was solved by direct methods (SHELXS97) and refined with full-matrix least-squares on F<sup>2</sup> (SHELXL2014/7). A total of 16906 reflections were measured and 3334 were independent. Final R1 = 0.1117, wR2 = 0.2881 [I > 2σ(I)], and GOF = 1.036 (for all data, R1 = 0.1818, wR2 = 0.3409). CCDC 1827084 (**2**) contains the supplementary crystallographic data for this paper. These data can be obtained free of charge from The Cambridge Crystallographic Data Centre.
- [19] Crystal data for **12**: C<sub>54</sub>H<sub>36</sub>, M<sub>r</sub> = 684.83, blue crystal, 0.283 × 0.066 × 0.040 mm, triclinic, space group P1̄, Z = 1, T = 173(2) K, a = 5.9966(3), b = 9.8974(6), c = 16.3668(8) Å, α = 76.792(3), β = 83.345(3), γ = 85.615(3)°, V = 938.06(9) Å<sup>3</sup>, λ(Cu<sub>Kα</sub>) = 1.54186 Å, μ = 0.520 mm<sup>-1</sup>. Intensity data were collected in the ω-scan mode using an R-Axis RAPID II, Imaging plate camera (Rigaku). The structure was solved by dual-space methods (SHELXT2014/7) and refined with full-matrix least-squares on F<sup>2</sup> (SHELXL2014/7). A total of 10977 reflections were measured and 3370 were independent. Final R1 = 0.0384, wR2 = 0.1062 [I > 2σ(I)], and GOF = 1.138 (for all data, R1 = 0.0465, wR2 = 0.1184). One methyl group of C27 has a 60 degree rotation type disorder with occupancy factors of 0.5. CCDC 1827085 (**12**) contains the supplementary crystallographic data for this paper. These data can be obtained free of charge from The Cambridge Crystallographic Data Centre.
- [20] Crystal data for **17**: C<sub>58</sub>H<sub>44</sub>, M<sub>r</sub> = 740.93, dark blue crystal, 0.186 × 0.012 × 0.010 mm, triclinic, space group P1̄, Z = 2, T = 138(2) K, a = 7.360(4), b = 14.300(12), c = 18.969(15) Å, α = 89.14(3), β = 82.40(5), γ = 84.221(19)°, V = 1969(3) Å<sup>3</sup>, λ(Cu<sub>Kα</sub>) = 1.54186 Å, μ = 0.533 mm<sup>-1</sup>. Intensity data were collected in ω-scan mode using an R-Axis RAPID II, Imaging plate camera (Rigaku). The structure was solved by dual-space methods (SHELXT2014/7) and refined with full-matrix least-squares on F<sup>2</sup> (SHELXL2014/7). A total of 22022 reflections were measured and 7017 were independent. Final R1 = 0.2689, wR2 = 0.5214 [I > 2σ(I)], and GOF = 1.461 (for all data, R1 = 0.3693, wR2 = 0.5911). CCDC 1827087 (**17**) contains the supplementary crystallographic data for this paper. These data can be obtained free of charge from The Cambridge Crystallographic Data Centre.
- [21] Due to the disorder of the chloroform crystalline solvent molecule in the crystal, the R factor of **2** is high. The chloroform molecule is located on near the inversion center. Also, the high R factor of **17** is due to the poor crystallinity and unfavored crystalline shape as thin film for the X-ray single crystal structural determination. The observed X-ray diffraction spots are spread and separated by the incomplete molecular order or cracking in the crystal.

Manuscript received: June 28, 2018  
 Revised manuscript received: August 1, 2018  
 Accepted manuscript online: August 2, 2018  
 Version of record online: September 12, 2018

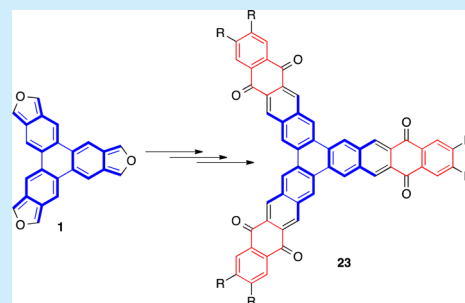
# Star-Shaped Polycyclic Aromatic Ketones via 3-Fold Cycloadditions of Isobenzofuran Trimer Equivalent

Hitoshi Tozawa, Takamasa Kakuda, Kazuhiko Adachi, and Toshiyuki Hamura\*<sup>ID</sup>

Department of Applied Chemistry for Environment, School of Science and Technology, Kwansei Gakuin University, 2-1 Gakuen, Sanda, Hyogo 669-1337, Japan

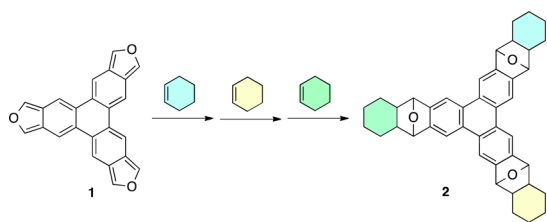
**S** Supporting Information

**ABSTRACT:** Three-directional annulations of isobenzofuran trimer equivalent are developed. Importantly, the successive cycloadditions could be controlled under suitable conditions, selectively affording the dual or triple cycloadduct, which leads to the alternative preparation of the symmetrical and unsymmetrical star-shaped polycyclic aromatic ketones. <sup>1</sup>H NMR analysis of the star-shaped aromatic ketone indicated the  $\pi$ - $\pi$  interactions through the aggregation in solution.



Multidirectional annulations of two or more rings onto a reactive core ring is one of the most efficient ways to highly condensed aromatic compounds.<sup>1,2</sup> In this context, we became interested in the synthetic use of isobenzofuran trimer **1** or its equivalent as a reactive platform<sup>3,4</sup> since, through its successive cycloadditions, it would allow for rapid access to *star-shaped* polycyclic compounds<sup>5</sup> with potentially attractive properties derived from the unique molecular structure (Scheme 1).

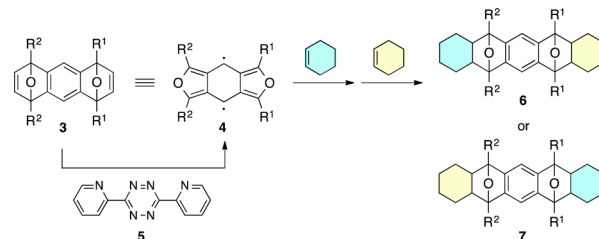
## Scheme 1. Three-Fold Annulations of Isobenzofuran Trimer



In relation to this synthetic strategy, we previously reported an efficient protocol of the ring-selective generation of isobenzofuran for selective construction of *linearly* fused polycycles (Scheme 2).<sup>2</sup> In this process, diepoxyanthracene **3**, the synthetic equivalent to a bisisobenzofuran **4**, was treated with 3,6-di(2-pyridyl)-1,2,4,5-tetrazine (**5**) to successively generate the two isobenzofuran species in a ring-selective manner, allowing the alternative synthesis of polyacene derivatives **6** and/or **7** through the iterative [4 + 2] cycloadditions.

Herein, we disclose 3-fold annulations of isobenzofurans for preparation of *star-shaped* polycyclic aromatic compounds with six electron-withdrawing carbonyl groups onto the aromatic core. The key of this approach is the design and the synthesis of

## Scheme 2. Dual Annulation of Bisobenzofuran



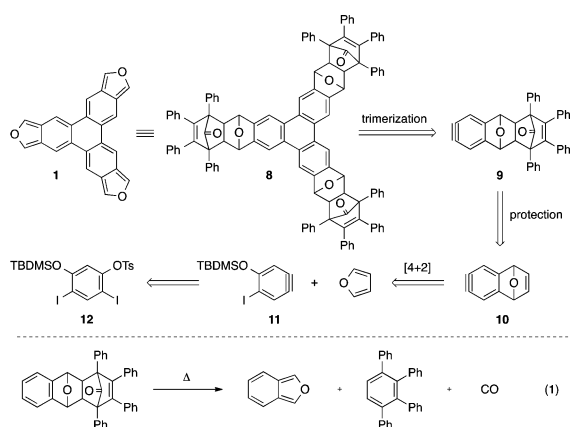
the synthetic equivalent to isobenzofuran trimer **1**. Along these lines, trisepoxytrinaphthylene **8**, prepared by [4 + 2] cycloaddition and trimerization of two aryne species **9** and **11**, turned out to serve as a synthetic equivalent to **1** by thermally induced elimination of carbon monoxide and subsequent retro Diels–Alder reaction (eq 1 in Scheme 3).<sup>6</sup> It is important to note that protection of the double bond in epoxynaphthalene is essential for the aryne cyclotrimerization (vide infra), and the trimer **8** undergoes retro Diels–Alder reaction to generate the three isobenzofurans, which are successively trapped with dienophiles, producing the 3-fold cycloadducts. Moreover, the successive cycloadditions can be controlled under suitable conditions, selectively affording the dual or triple cycloadduct, which leads to the selective preparation of the symmetrical and unsymmetrical star-shaped polycyclic aromatic ketones.

Starting from diiodide **12**,<sup>7</sup> corresponding to a bisbenzyne equivalent,<sup>8</sup> the trimer **8** was efficiently prepared (Scheme 4). Upon heating of epoxynaphthalene **13**<sup>9</sup> with tetraphenylcyclopentadienone, Diels–Alder reaction occurred stereoselectively to give the silyl triflate **14** as a single isomer. The

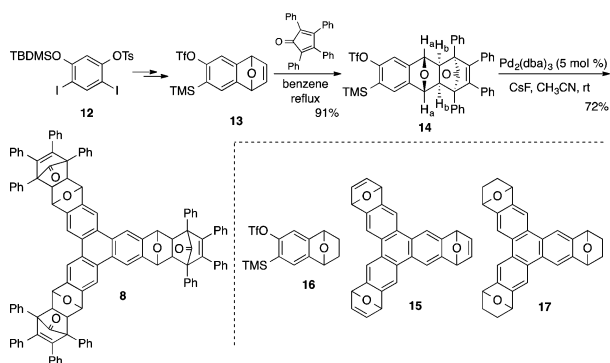
Received: June 24, 2017

Published: July 25, 2017

## Scheme 3. Strategy for Preparation of Isobenzofuran Trimer Equivalent



## Scheme 4. Preparation of Isobenzofuran Trimer Equivalent

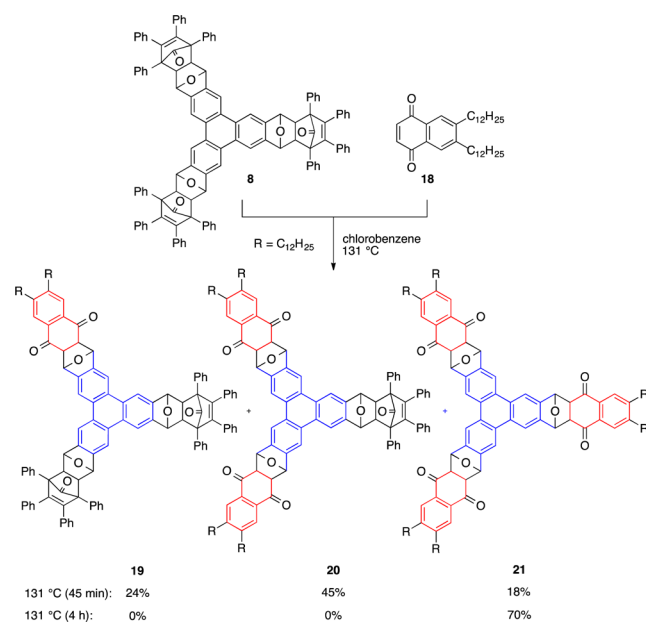


stereochemistry of **14** was determined by X-ray analysis,<sup>10</sup> where the two protons ( $H_b$ ) on the bridge-head carbon and the carbonyl group were antioriented with respect to the epoxy bridge. This is due to the concave topology of the epoxynaphthalene **13**, which forces the tetraphenylcyclopentadienone to approach along the convex side of **13**.<sup>11</sup>  $^1H$  NMR analysis of **14** showed the absence of vicinal coupling between  $H_a$  and  $H_b$ , indicating the dihedral angle approached  $90^\circ$ , which was also confirmed by the X-ray structure.

The silyl triflate **14**, thus obtained, was subjected to Pd-catalyzed aryne cyclotrimerization by treatment with  $CsF$ ,<sup>12</sup> cleanly affording the trimer **8**, which consisted of a mixture of two diastereomers (ds 6:1) with respect to the three epoxy rings. The important point in this reaction is that tetraphenylcyclopentadienone played a key role not only as a protecting group of the double bond in **13** but also as an initiator for the generation of isobenzofuran (vide infra). Indeed, the corresponding reaction of nonprotected substrate **13** gave no trimer **15**, which would be also a suitable precursor of **1** by tetrazine methodology (Scheme 2).<sup>3a</sup> This is due to the existence of the double bond within the rigid oxabicyclic structure in **13**, which may react with Pd catalyst under the reaction conditions to give a complex mixture of products.<sup>13</sup> In this case, however, the cyclotrimerization proceeded cleanly with the saturated aryne precursor **16** under the same reaction conditions, affording triepoxytrinaaphthylene **17** in 64% yield.

Scheme 5 shows the successive generation of isobenzofuran and its trapping with dienophile. Upon heating of **8** in the presence of naphthoquinone **18** ( $131^\circ C$ , 4 h), iterative [4 + 2] cycloadditions occurred cleanly to give the 3-fold cycloadduct

## Scheme 5. Multiple Cycloadditions of Isobenzofuran Trimer Equivalent



**21** in 70% yield as a mixture of stereoisomers. TLC analysis showed that the initially formed monocycloadduct **19** and dicycloadduct **20** were gradually converted to the tricycloadduct **21**. Indeed, the same reaction in a shorter reaction time ( $131^\circ C$ , 45 min) selectively gave the dicycloadduct **20** in 45% yield, accompanied by the mono- and tricycloadducts **19** (24%) and **21** (18%), respectively. As for the solubility of the products, introduction of the long alkyl chains into naphthoquinone is essential since the similar reaction with parent naphthoquinone produced extremely insoluble products in all common organic solvents, which precluded their characterization.

The stereochemistry of the dicycloadduct **20** was determined by NMR analysis, where two sets of the coupled aliphatic methine protons ( $H_c$  and  $H_d$ ,  $H_e$  and  $H_f$ ), characteristic as an *endo* isomer, were observed.<sup>2,4f</sup> Moreover, the two peaks of aliphatic methine protons  $H_b$  and  $H_b'$ , which were noncoupled with  $H_a$  and  $H_a'$  on the right fused ring (vide supra), were independently located at 3.17 and 3.21 ppm as the doublet indicated the structure as the *endo-endo/anti* isomer with  $C_1$  symmetry rather than the symmetrical *endo-endo/syn* isomer (Figure 1). This result showed that the two successive cycloadditions occurred in an *endo* manner, where the two dienophiles approached across opposite faces of the triphenylene core.

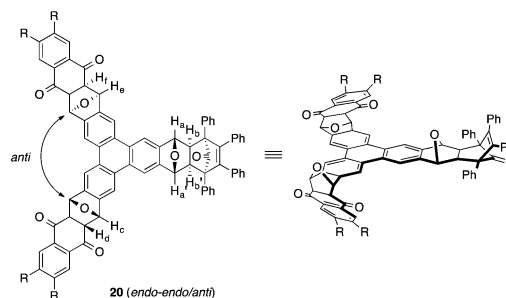


Figure 1. Stereochemistry of the dual cycloadduct **20**.

The 3-fold cycloadduct **21**, initially produced by heating at 131 °C for 45 min (Scheme 5), was composed of two diastereomers (ds 4:1). The major product **21a** has two *endo* and one *exo* stereochemistries on the oxabicyclo moieties, which were determined by the presence of both coupled and noncoupled aliphatic methine signals. Moreover, the six singlets corresponding to the aromatic protons on the triphenylene moiety indicated the product as a nonsymmetric *exo-endo-endo/syn-anti* isomer (Figure 2). On the other hand, the lack of

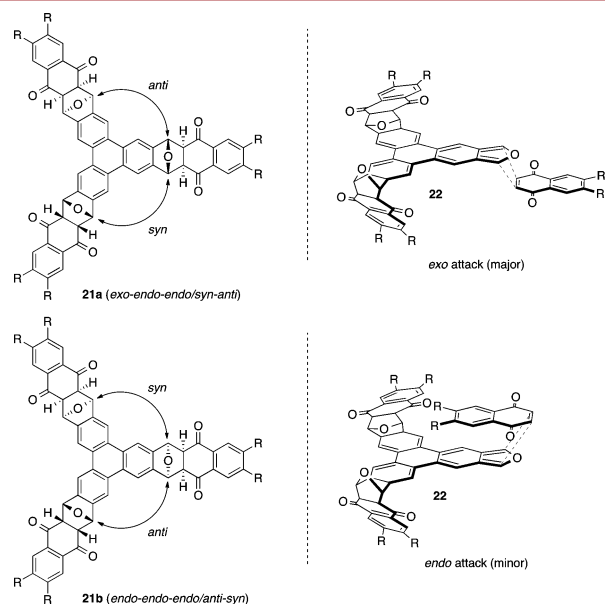


Figure 2. Stereochemistry of the 3-fold cycloadduct **21**.

noncoupling protons on the oxabicyclo moieties and the three singlets on the aromatic protons on the triphenylene moiety established the minor product **21b** as an *endo-endo-endo/anti-syn* isomer. The formation of the major cycloadduct **21a** was explained by the *exo* attack of the dienophile to the isobenzofuran **22** to avoid the steric repulsion by both sides of the polycyclic framework in **22**.

Further study on the stereochemistry of the 3-fold cycloadduct **21** revealed that stereoisomerization was observed by heating the same reaction for a longer reaction time to produce several kinds of diastereomers (*exo-exo-endo* and *exo-exo-exo* isomers) in addition to the above-mentioned major stereoisomer **21a**,<sup>14</sup> which were cleanly converted to the corresponding star-shaped polyketone **23** by acid-promoted aromatization (TsOH in toluene at 50 °C). Purification of the crude product by silica-gel column chromatography gave the poly ketone **23** in high yield (Scheme 6). Owing to the six long alkyl chains introduced to three directions at the end of the aromatic rings, the product **23** was highly soluble in hexane, CH<sub>2</sub>Cl<sub>2</sub>, CHCl<sub>3</sub>, toluene, and Et<sub>2</sub>O.<sup>15</sup>

<sup>1</sup>H NMR analysis of the product **23** showed that all peaks were significantly broadened at room temperature. On the other hand, these broadened signals gradually sharpened at higher temperature (90 °C). Moreover, the aromatic signals were shifted downfield by increasing the temperature (Figure 3) or decreasing concentration (Figure 4), which indicated the aggregation in solution.<sup>16</sup>

Finally, it should be emphasized that the unsymmetrical star-shaped polyketone **28** could be accessed by using the  $\pi$ -extended isobenzofuran **25** as a key intermediate (Scheme 7).

### Scheme 6. Acid-Promoted Aromatization of the Cycloadduct **21** to Star-Shaped Polyketone **23**

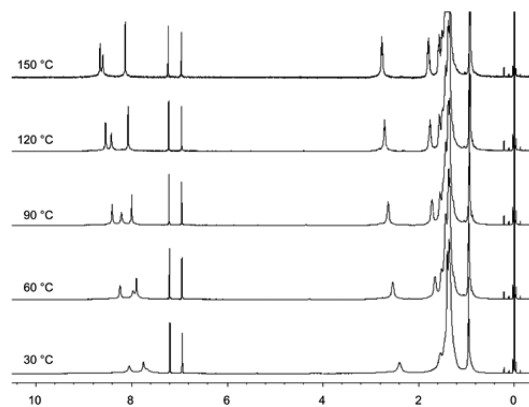
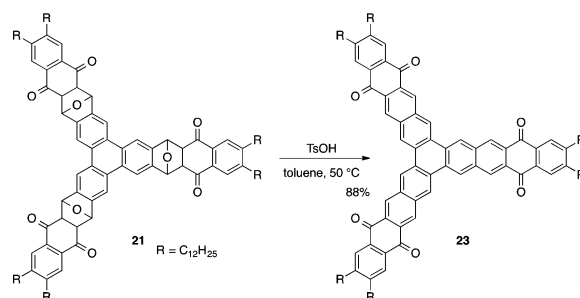


Figure 3. Temperature-dependent <sup>1</sup>H NMR spectra of **23** in *o*-C<sub>6</sub>D<sub>4</sub>Cl<sub>2</sub> (2.97 × 10<sup>-2</sup> M).

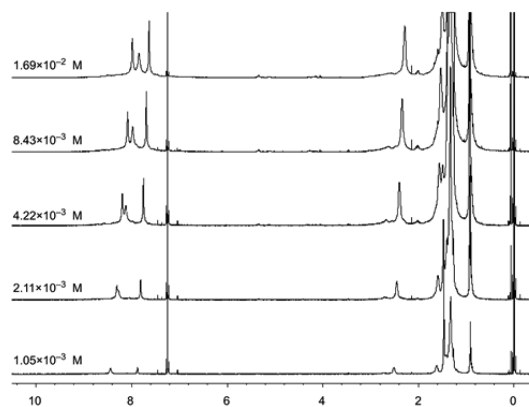


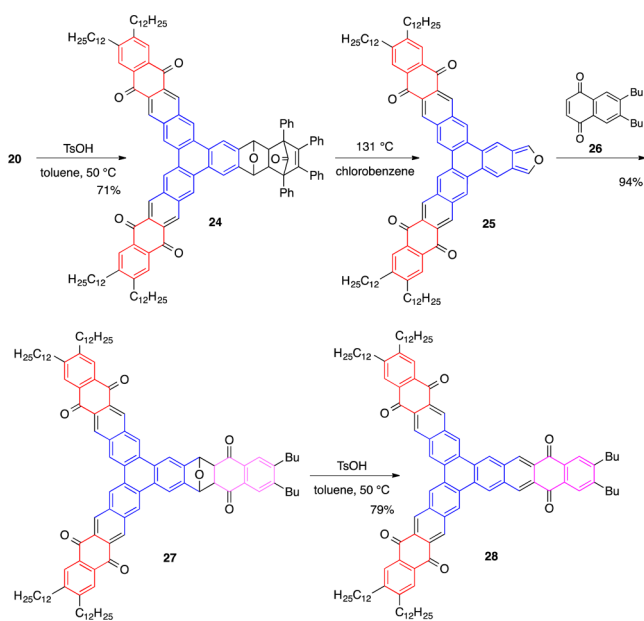
Figure 4. Concentration-dependent <sup>1</sup>H NMR spectra of **23** at 50 °C in CDCl<sub>3</sub>.

When dual-cycloadduct **20** was treated with TsOH in toluene at 50 °C, dehydrative aromatization occurred cleanly to give tetraketone **24** in 71% yield.

$\pi$ -Extended polyketone **24** was then heated in chlorobenzene at 131 °C to generate the highly condensed isobenzofuran **25**,<sup>3c</sup> which was trapped with naphthoquinone **26** to give the unsymmetrical star-shaped polyketone **28** after acid-induced aromatization. As for the third [2 + 4] cycloaddition of the  $\pi$ -extended isobenzofuran **25**, aromatization of dual cycloadduct **20** to tetraketone **24** was indispensable since the corresponding thermal reaction of **20** with naphthoquinone **26** gave the desired cycloadduct in low yield due to the retro Diels–Alder reaction of **20**.

In summary, successive cycloaddition of isobenzofuran trimer equivalent allowed us to construct symmetrical and unsym-

### Scheme 7. Preparation of Unsymmetrical Star-Shaped Polyketone 28



metrical star-shaped polycyclic aromatic ketones with valuable synthetic potential. Further synthetic applications are under active investigation in our laboratory.

#### ■ ASSOCIATED CONTENT

##### Supporting Information

The Supporting Information is available free of charge on the ACS Publications website at DOI: [10.1021/acs.orglett.7b01932](https://doi.org/10.1021/acs.orglett.7b01932).

Experimental procedures and compound characterization data (PDF)

#### ■ AUTHOR INFORMATION

##### Corresponding Author

\*E-mail: [thamura@kwansei.ac.jp](mailto:thamura@kwansei.ac.jp).

##### ORCID

Toshiyuki Hamura: [0000-0003-2857-2273](https://orcid.org/0000-0003-2857-2273)

##### Notes

The authors declare no competing financial interest.

#### ■ ACKNOWLEDGMENTS

This work was supported by JSPS KAKENHI Grant Number JP15H05840 in Middle Molecular Strategy and JST ACT-C Grant Number JPMJCR12YY, Japan.

#### ■ REFERENCES

- (1) For recent reviews, see: (a) Pérez, D.; Peña, D.; Guitián, E. *Eur. J. Org. Chem.* **2013**, 2013, 5981. (b) Scott, L. T. *Polycyclic Aromat. Compd.* **2010**, 30, 247.
- (2) For selective examples, see: (a) Haneda, H.; Eda, S.; Aratani, M.; Hamura, T. *Org. Lett.* **2014**, 16, 286. (b) Akita, R.; Kawanishi, K.; Hamura, T. *Org. Lett.* **2015**, 17, 3094.
- (3) For preparation of isobenzofuran, see: (a) Warrener, R. N. *J. Am. Chem. Soc.* **1971**, 93, 2346. (b) Warrener, R. N.; Shang, M.; Butler, D. N. *Chem. Commun.* **2001**, 1550. (c) Sygula, A.; Sygula, R.; Rabideau, P. W. *Org. Lett.* **2006**, 8, 5909. (d) Pei, B. J.; Chan, W. H.; Lee, A. W. M. *Org. Lett.* **2011**, 13, 1774. (e) Hamura, T.; Nakayama, R. *Chem. Lett.*

**2013**, 42, 1013. (f) Asahina, K.; Matsuoka, S.; Nakayama, R.; Hamura, T. *Org. Biomol. Chem.* **2014**, 12, 9773.

- (4) For selective synthetic applications of isobenzofuran, see: (a) Binger, P.; Wedemann, P.; Goddard, R.; Brinker, U. H. *J. Org. Chem.* **1996**, 61, 6462. (b) Rodrigo, R. *Tetrahedron* **1988**, 44, 2093. (c) Wong, H. N. C. *Acc. Chem. Res.* **1989**, 22, 145. (d) Man, Y.-M.; Mak, T. C. W.; Wong, H. N. C. *J. Org. Chem.* **1990**, 55, 3214. (e) Chan, S.-H.; Yick, C.-Y.; Wong, H. N. C. *Tetrahedron* **2002**, 58, 9413. (f) Rainbolt, J. E.; Miller, G. P. *J. Org. Chem.* **2007**, 72, 3020.
- (5) (a) Kanibolotsky, A. L.; Perepichka, I. F.; Skabara, P. J. *Chem. Soc. Rev.* **2010**, 39, 2695. (b) Zhang, H.; Wu, D.; Liu, S. H.; Yin, J. *Curr. Org. Chem.* **2012**, 16, 2124. (c) Lynett, P. T.; Maly, K. E. *Org. Lett.* **2009**, 11, 3726. (d) Alonso, J. M.; Díaz-Álvarez, A. E.; Criado, A.; Pérez, D.; Peña, D.; Guitián, E. *Angew. Chem., Int. Ed.* **2012**, 51, 173. (e) Rüdiger, E. C.; Porz, M.; Schaffroth, M.; Rominger, F.; Bunz, U. H. F. *Chem. - Eur. J.* **2014**, 20, 12725. (f) Yao, B.; Zhou, Y.; Ye, X.; Wang, R.; Zhang, J.; Wan, X. *Org. Lett.* **2017**, 19, 1990. (g) Tanokashira, N.; Kukita, S.; Kato, H.; Nehira, T.; Angkouw, E. D.; Mangindaan, R. E. P.; de Voogd, N. J.; Tsukamoto, S. *Tetrahedron* **2016**, 72, 5530.

- (6) (a) Fieser, L. F.; Haddadin, M. J. *J. Am. Chem. Soc.* **1964**, 86, 2081. (b) Fieser, L. F.; Haddadin, M. J. *Can. J. Chem.* **1965**, 43, 1599. (c) Luo, J.; Hart, H. *J. Org. Chem.* **1989**, 54, 1762.

(7) The diiodide **12** was prepared from resorcinol in four steps. For details, see [Supporting Information](#).

- (8) For pioneering studies by Hart on the generation and trapping of 1,4-benzdiazine equivalents, see: (a) Hart, H.; Ok, D. *J. Org. Chem.* **1986**, 51, 979. (b) Hart, H.; Lai, C.-Y.; Nwokogu, G.; Shamoulian, S.; Teuerstein, A.; Zlotogorski, C. *J. Am. Chem. Soc.* **1980**, 102, 6649. Other examples, see: (c) Chen, Y.-L.; Sun, J.-Q.; Wei, X.; Wong, W.-Y.; Lee, A. W. M. *J. Org. Chem.* **2004**, 69, 7190. (d) Morton, G. E.; Barrett, A. G. M. *J. Org. Chem.* **2005**, 70, 3525. (e) Schuster, I. I.; Craciun, L.; Ho, D. M.; Pascal, R. A., Jr. *Tetrahedron* **2002**, 58, 8875. (f) Duong, H. M.; Bendikov, M.; Steiger, D.; Zhang, Q.; Sonmez, G.; Yamada, J.; Wudl, F. *Org. Lett.* **2003**, 5, 4433. (g) Hamura, T.; Arisawa, T.; Matsumoto, T.; Suzuki, K. *Angew. Chem., Int. Ed.* **2006**, 45, 6842.

(9) Epoxynaphthalene **13** was prepared by a five-step protocol including the [2 + 4] cycloaddition of benzyne with furan. For details, see [Supporting Information](#).

(10) For details, see [Supporting Information](#).

- (11) By now, there has been no report on the determination of the stereochemistry of the Diels–Alder adduct like **14** by X-ray analysis. Among various possibilities, long-range <sup>13</sup>C–H coupling is a reliable probe to evaluate the stereochemistry of the cycloadduct. See: (a) Tan, R. Y. S.; Russell, R. A.; Warrener, R. N. *Tetrahedron Lett.* **1979**, 20, 5031. (b) Coxon, J. M.; Battiste, M. A. *Tetrahedron* **1976**, 32, 2053. For the X-ray structure of **14**, see [Supporting Information](#).

- (12) (a) Peña, D.; Escudero, S.; Pérez, D.; Guitián, E.; Castedo, L. *Angew. Chem., Int. Ed.* **1998**, 37, 2659. (b) Peña, D.; Pérez, D.; Guitián, E.; Castedo, L. *Org. Lett.* **1999**, 1, 1555. (c) Peña, D.; Cobas, A.; Pérez, D.; Guitián, E.; Castedo, L. *Org. Lett.* **2000**, 2, 1629. (d) Peña, D.; Pérez, D.; Guitián, E.; Castedo, L. *J. Org. Chem.* **2000**, 65, 6944. (e) Romero, C.; Peña, D.; Pérez, D.; Guitián, E. *Chem. - Eur. J.* **2006**, 12, 5677.

- (13) (a) Lautens, M.; Hiebert, S.; Renaud, J.-L. *J. Am. Chem. Soc.* **2001**, 123, 6834. (b) Shih, H.-T.; Shih, H.-H.; Cheng, C.-H. *Org. Lett.* **2001**, 3, 811. (c) Li, Y.; Yang, W.; Cheng, G.; Yang, D. *J. Org. Chem.* **2016**, 81, 4744.

(14) For the stereoisomerization of the cycloadduct **21**, see [Supporting Information](#).

(15) The star-shaped polyketone **23** was insoluble in polar solvents, e.g., EtOAc, acetone, DMF, and DMSO.

- (16) Watson, M. D.; Fechtenkötter, A.; Müllen, K. *Chem. Rev.* **2001**, 101, 1267.

## Water-soluble 1,3-Diarylisobenzoheteroles: Syntheses and Characterization

Hitoshi Tozawa, Kei Kitamura, and Toshiyuki Hamura\*

Department of Applied Chemistry for Environment, School of Science and Technology, Kwansei Gakuin University, 2-1 Gakuen, Sanda, Hyogo 669-1337

(E-mail: thamura@kwansei.ac.jp)

Efficient synthetic route to water-soluble 1,3-diarylisobenzoheteroles, including isobenzofuran, isobenzothiophene, and isobenzoselenophene, was developed. Based on our one-pot synthetic method for diarylisobenzofurans, novel D- $\pi$ -D and A- $\pi$ -A types of diarylisobenzoheteroles became accessible, and they could be smoothly converted to the water-soluble isobenzoheteroles. The photophysical properties of newly prepared isobenzoheteroles are also evaluated.

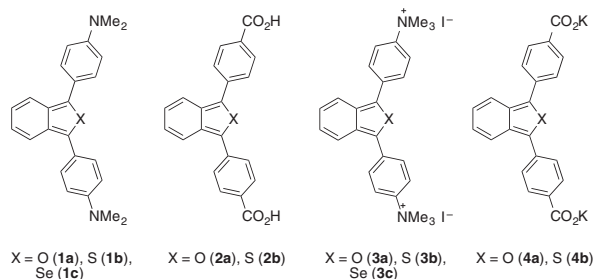
**Keywords:** Isobenzoheteroles | Water-soluble materials | Divergent synthesis

Isobenzoheteroles, such as isobenzofuran, isobenzothiophene, and isobenzoselenophene, have unique  $\pi$ -conjugated systems with a quinoid structure, which can serve as a component in functional materials.<sup>1</sup> However, the chemistry of these molecules is still not fully explored, presumably due to the scarce availability of various substituted derivatives.<sup>2,3</sup>

In this context, we recently reported an efficient synthetic access to 1,3-diarylisobenzofurans by sequential reactions of methyl 2-formylbenzoate with two aryl Grignard reagents.<sup>4</sup> Notably, this process allowed us to prepare various functionalized diarylisobenzofurans, e.g. the D- $\pi$ -D congener possessing two electron-donating dimethylaminophenyl groups onto the isobenzofuran core, which exhibited an interesting electrochromic behavior.<sup>5</sup>

Based on this knowledge, we have now developed facile syntheses of novel D- $\pi$ -D and A- $\pi$ -A types of diarylisobenzoheteroles **1** and **2**. Importantly, these functionally attractive isobenzoheteroles were smoothly converted to water-soluble isobenzoheteroles **3** and **4** containing doubly substituted quaternary ammonium salts or potassium carboxylates, which would have potential utility for *in vivo* fluorescence imaging and singlet oxygen acceptors (Figure 1).<sup>6,7</sup>

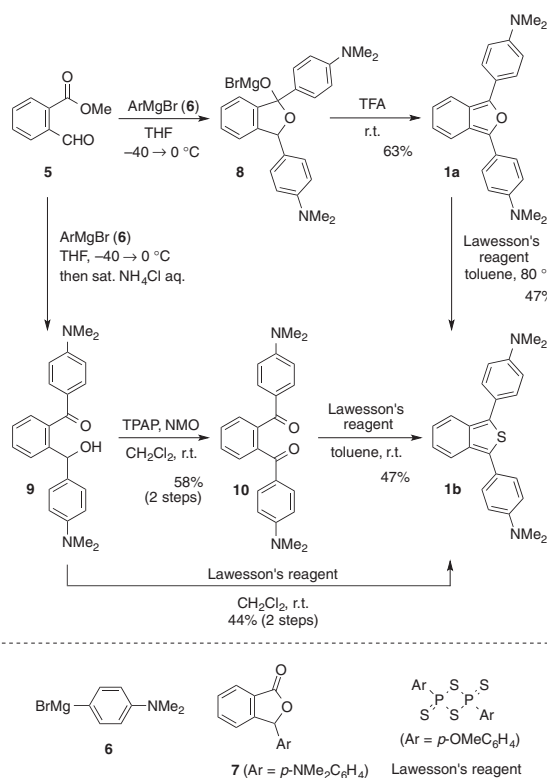
The photophysical properties of these newly prepared diarylisobenzoheteroles are also evaluated, which is described in this communication.



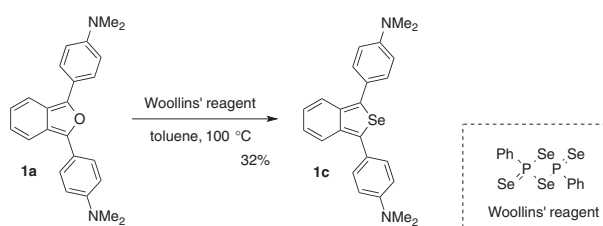
**Figure 1.** D- $\pi$ -D and A- $\pi$ -A types of 1,3-diarylisobenzoheteroles, and water-soluble 1,3-diarylisobenzoheteroles.

On the basis of our previous protocol, the D- $\pi$ -D type of diarylisobenzofuran **1a** was prepared via double nucleophilic additions of (4-dimethylaminophenyl)magnesium bromide (**6**) (3.3 equiv) to *o*-formyl benzoate **5** (Scheme 1). In this reaction, the selective nucleophile attack of the Grignard reagent to the formyl group in **5** and subsequent transesterification of the resulting adduct gave 3-phenylphthalide **7**, which, in turn, accepted a second nucleophile, affording adduct **8**. Final acid-promoted dehydrative aromatization of **8** (CF<sub>3</sub>CO<sub>2</sub>H, r.t.) efficiently produced the diarylisobenzofuran **1a**.

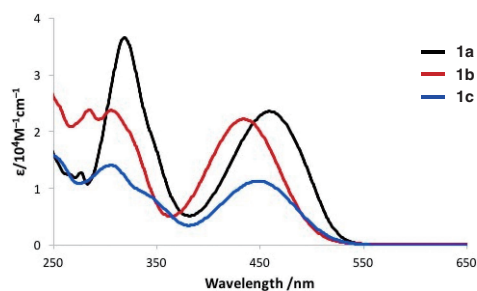
Further study on this successive process revealed that ring-opened keto-alcohol **9** was selectively produced by treatment of adduct **8** under milder acidic conditions (sat. aq. NH<sub>4</sub>Cl).<sup>3f</sup> This finding allowed the divergent syntheses of isobenzoheteroles from a single starting material **5**. Thus, keto-alcohol **9**,<sup>8</sup> obtained by the reaction of **5** with Grignard reagent **6** and sat. aq. NH<sub>4</sub>Cl quench, was oxidized (TPAP, NMO, CH<sub>2</sub>Cl<sub>2</sub>, r.t.)<sup>9</sup> to give diketone **10**, which was treated with Lawesson's reagent (CH<sub>2</sub>Cl<sub>2</sub>, r.t.),<sup>10</sup> affording the D- $\pi$ -D type of isobenzothiophene **1b** in 47% yield as bright orange solids. The formation of **1b**



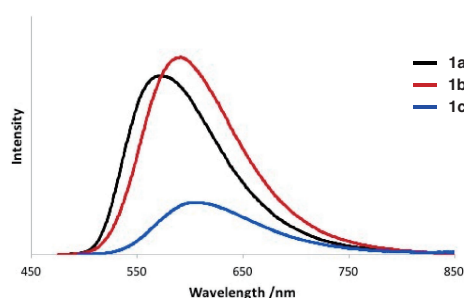
**Scheme 1.** Efficient synthetic route to D- $\pi$ -D type of isobenzofuran **1a** and isobenzothiophene **1b**.



**Scheme 2.** D- $\pi$ -D type of isobenzoselenophene **1c**.



**Figure 2.** UV-vis absorption spectra of isobenzoheteroles **1a-1c** in  $\text{CH}_3\text{CN}$ .



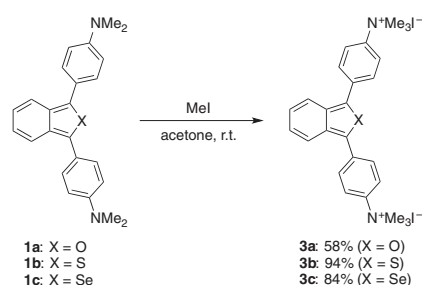
**Figure 3.** Fluorescence spectra of isobenzoheteroles **1a-1c** in  $\text{CH}_3\text{CN}$ .

might be explained by the conversion of diketone to dithio-ketone by reaction with Lawesson's reagent and its cyclization.<sup>1a,11</sup>

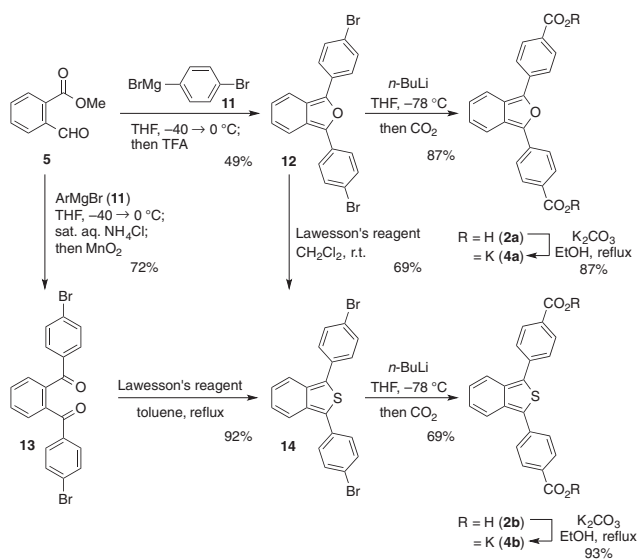
Aside from the reaction mechanism, it is interesting to note that keto-alcohol **9** and isobenzofuran **1a**, which corresponded to the reduced form of the diketone **10**, could also be directly converted to the isobenzothiophene **1b** by using Lawesson's reagent. In these cases, no oxidizing agents were required to obtain the isobenzothiophene **1b**.

Moreover, isobenzoselenophene **1c** with dimethylamino-phenyl groups on each aromatic ring could be accessed from isobenzofuran **1a** by treatment with Woollins' reagent (toluene, 100 °C),<sup>12</sup> where the formal exchange of oxygen to selenium on the central heterocyclic ring in **1a** was observed to give the isobenzoselenophene **1c** in 32% yield as bright orange solids (Scheme 2).<sup>13</sup> In contrast, similar reaction of diketone **10** with Woollins' reagent (toluene, 100 °C) gave the desired product **1c** in quite low yield (3%).

The absorption and fluorescence spectra of D- $\pi$ -D type isobenzoheteroles were measured in acetonitrile (Figures 2 and 3).<sup>14</sup> The isobenzofuran **1a** has its absorption maximum at 459 nm and emission maximum at 573 nm, and it exhibited high fluorescence ( $\Phi_F$  0.76). On the other hand, the absorption



**Scheme 3.** N-Methylation of 1,3-diarylisobenzoheteroles **1** to water-soluble isobenzoheteroles **3**.

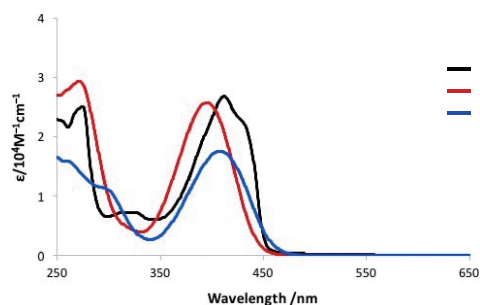


**Scheme 4.** Efficient synthetic route to A- $\pi$ -A type of isobenzoheterole **2** and water-soluble isobenzoheterole **4**.

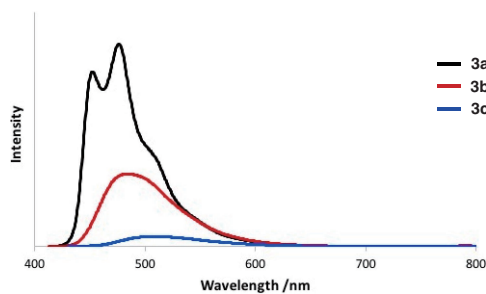
maximum of isobenzothiophene **1b** and isobenzoselenophene **1c** was slightly blue-shifted (**1b**: 434 nm, **1c**: 448 nm). The emission peaks of these dyes were observed at 592 and 605 nm, respectively, which resulted in the larger Stokes shift in comparison with **1a**. Moreover, isobenzothiophene **1b** exhibited high fluorescent quantum yield ( $\Phi_F$  0.88) the same as **1a**, whereas isobenzoselenophene **1c** showed much lower yield ( $\Phi_F$  0.34).

We next examined the conversion of these D- $\pi$ -D types of isobenzoheteroles **1a-1c** to water-soluble  $\pi$ -conjugers by N-methylation (Scheme 3). Upon treatment of **1a** with MeI (acetone, r.t.), double methylation occurred cleanly, and the quaternary ammonium salt **3a** was gradually precipitated from the reaction mixture, affording essentially pure product **3a** after filtration. Similar reactions of isobenzoheteroles **1b** and **1c** also gave quaternary ammonium salts **3b** and **3c** in good yields, respectively. These quaternary ammonium salts, thus obtained, have been extensively characterized by spectroscopic means, and as one of the characteristic features, they were highly soluble in water, MeOH,  $\text{CH}_3\text{CN}$ , and DMSO.

Another water-soluble isobenzoheterole **4** having potassium carboxylates at each aromatic ring could also be synthesized (Scheme 4). When diarylisobenzofuran **12**, prepared by the sequential reactions of methyl 2-formylbenzoate (**5**) with (4-bromophenyl)magnesium bromide, was treated with *n*-BuLi



**Figure 4.** UV-vis absorption spectra of isobenzoheteroles **3a**–**3c** in H<sub>2</sub>O.



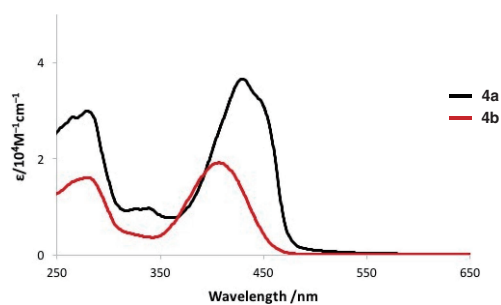
**Figure 5.** Fluorescence spectra of isobenzoheteroles **3a**–**3c** in H<sub>2</sub>O.

(THF,  $-78^{\circ}\text{C}$ ), bromine–lithium exchange occurred quickly, and subsequent trapping of the dilithio-intermediate with CO<sub>2</sub> efficiently gave the A- $\pi$ -A type of diarylisobenzofuran **2a** in 87% yield. Conversion of the dicarboxylic acid **2a** to potassium salt **4a** was realized by treatment with K<sub>2</sub>CO<sub>3</sub> in refluxing EtOH,<sup>15</sup> leading to the water-soluble diarylisobenzofuran **4a** as orange solids.

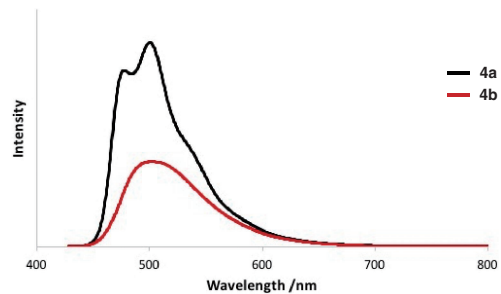
In addition, A- $\pi$ -A type of diarylisobenzothiophene **2b** was prepared from the same starting material **5**. Double nucleophilic additions of Grignard reagent **11** to **5**, and selective oxidation of the resulting diol gave diketone **13**, which was treated with Lawesson's reagent, affording isobenzothiophene **2b** after carboxylation of the dibromide **14**.<sup>16</sup> As for the formation of the diarylisobenzothiophene **14**, isobenzofuran **12** was also a suitable substrate, and the isobenzothiophene **14** was obtained in good yield. As described for the synthesis of **4a**, the A- $\pi$ -A congener **2b** was converted to the potassium carboxylate **4b** by treatment with K<sub>2</sub>CO<sub>3</sub>.<sup>17</sup>

Finally, photophysical properties of water-soluble isobenzoheteroles **3** and **4** were studied, and the absorption and fluorescence spectra in H<sub>2</sub>O are shown in Figures 4–7.<sup>14</sup> Water-soluble isobenzofuran **3a** has its absorption maximum at 412 nm and emission maximum at 476 nm with excellent fluorescence quantum yield ( $\Phi_F$  0.91). Slightly lower absorption maximum was observed for isobenzothiophene **3b**, which also showed excellent fluorescence quantum yield in MeCN ( $\Phi_F$  0.88), albeit moderate in H<sub>2</sub>O ( $\Phi_F$  0.46).<sup>18</sup> In contrast, the fluorescence quantum yield of isobenzoselenophene **3c** was only 0.09, although the absorption maximum of **3c** was similar to **3a**.<sup>19</sup>

Similar trend of the properties was observed for the potassium carboxylates **4** as in the case of quaternary ammonium salts **3**, where isobenzofuran **4a** showed red-shifted absorption



**Figure 6.** UV-vis absorption spectra of isobenzoheteroles **4a** and **4b** in H<sub>2</sub>O.



**Figure 7.** Fluorescence spectra of isobenzoheteroles **4a** and **4b** in H<sub>2</sub>O.

from isobenzothiophene **4b** about 22 nm, thus indicating a more quinoidal structure of **4a**. Moreover, they exhibited moderate to high fluorescence quantum yield in H<sub>2</sub>O (**4a**:  $\Phi_F$  0.83, **4b**: 0.54). In this manner, isobenzoheteroles with acquired water-solubility exhibited typical photophysical properties, and thus they would be a promising component for biological applications and water-soluble  $\pi$ -materials for electronic devices.<sup>15c</sup>

In summary, we developed a divergent process that is capable of converting the same starting material, methyl 2-formylbenzoate, into diarylisobenzofurans, diarylisobenzothiophenes, and diarylisobenzoselenophenes including functionally attractive water-soluble isobenzoheteroles. The application of these novel  $\pi$ -conjugated molecules for singlet oxygen acceptors and fluorescent probes are currently underway in our laboratory.

This work was supported by JSPS KAKENHI Grant Number JP15H05840 in Middle Molecular Strategy and JST ACT-C.

Supporting Information is available on <http://dx.doi.org/10.1246/cl.170137>.

## References and Notes

- a) S. T. Meek, E. E. Nesterov, T. M. Swager, *Org. Lett.* **2008**, *10*, 2991. b) H. Zhang, A. Wakamiya, S. Yamaguchi, *Org. Lett.* **2008**, *10*, 3591.
- For reviews, see: a) W. Friedrichsen, *Adv. Heterocycl. Chem.* **1980**, *26*, 135. b) W. Friedrichsen, *Adv. Heterocycl. Chem.* **1999**, *73*, 1. c) R. Rodrigo, *Tetrahedron* **1988**, *44*, 2093.
- For selected examples of isobenzoheteroles, see: a) M. P. Cava, M. J. Mitchell, A. A. Deana, *J. Org. Chem.* **1960**, *25*, 1481. b) R. N. Warrener, *J. Am. Chem. Soc.* **1971**, *93*, 2346.

- c) Y. Kunitobu, Y. Nishina, C. Nakagawa, K. Takai, *J. Am. Chem. Soc.* **2006**, *128*, 12376. d) J. Jacq, C. Einhorn, J. Einhorn, *Org. Lett.* **2008**, *10*, 3757. e) Y. Nishina, T. Kida, T. Ureshino, *Org. Lett.* **2011**, *13*, 3960. f) R. Sivasakthikumar, S. M. Rafiq, E. Sankar, J. A. Clement, A. K. Mohanakrishnan, *Eur. J. Org. Chem.* **2015**, 7816.
- 4 For our recently developed synthetic method of isobenzofurans, see: a) T. Hamura, R. Nakayama, *Chem. Lett.* **2013**, *42*, 1013. b) K. Asahina, S. Matsuoka, R. Nakayama, T. Hamura, *Org. Biomol. Chem.* **2014**, *12*, 9773. c) R. Kudo, K. Kitamura, T. Hamura, *Chem. Lett.* **2017**, *46*, 25.
- 5 T. Hamura, R. Nakayama, K. Hanada, Y. Sakano, R. Katoono, K. Fujiwara, T. Suzuki, *Chem. Lett.* **2013**, *42*, 1244.
- 6 To the best of our knowledge, only one example of water-soluble isobenzofuran has been reported until now, where the synthesis is far from efficiency and generality in view of the preparation of functionalized derivatives, see: F. Amat-Guerri, E. Lempe, E. A. Lissi, F. J. Rodriguez, F. R. Trull, *J. Photochem. Photobiol., A* **1996**, *93*, 49.
- 7 a) D. Song, S. Cho, Y. Han, Y. You, W. Nam, *Org. Lett.* **2013**, *15*, 3582. b) R. Adams, M. H. Gold, *J. Am. Chem. Soc.* **1940**, *62*, 2038. c) I. B. C. Matheson, J. Lee, B. S. Yamanashi, M. L. Wolbarsht, *J. Am. Chem. Soc.* **1974**, *96*, 3343. d) X.-F. Zhang, X. Li, *J. Lumin.* **2011**, *131*, 2263. For reviews, see: e) Y. You, W. Nam, *Chem. Sci.* **2014**, *5*, 4123. f) X. Chen, F. Wang, J. Y. Hyun, T. Wei, J. Qiang, X. Ren, I. Shin, J. Yoon, *Chem. Soc. Rev.* **2016**, *45*, 2976.
- 8 Keto-alcohol **9** was directly converted to diketone **10** without purification due to its gradual conversion to the corresponding isobenzofuran **1a** during the silica gel column chromatography.
- 9 S. V. Ley, J. Norman, W. P. Griffith, S. P. Marsden, *Synthesis* **1994**, 639.
- 10 For reviews, see: a) M. P. Cava, M. I. Levinson, *Tetrahedron* **1985**, *41*, 5061. b) M. Jesberger, T. P. Davis, L. Barner, *Synthesis* **2003**, 1929.
- 11 a) P. Amaladass, J. A. Clement, A. K. Mohanakrishnan, *Eur. J. Org. Chem.* **2008**, 3798. b) A. K. Mohanakrishnan, P. Amaladass, *Tetrahedron Lett.* **2005**, *46*, 4225. For a mechanistic study, see: c) L. Legnani, L. Toma, P. Caramella, M. A. Chiacchio, S. Giofrè, I. Delso, T. Tejero, P. Merino, *J. Org. Chem.* **2016**, *81*, 7733.
- 12 For a review, see: J. D. Woollins, *Synlett* **2012**, 1154.
- 13 a) A. K. Mohanakrishnan, P. Amaladass, *Tetrahedron Lett.* **2005**, *46*, 7201. b) P. Amaladass, N. S. Kumar, A. K. Mohanakrishnan, *Tetrahedron* **2008**, *64*, 7992.
- 14 For the details of absorption and fluorescence spectra, see the Supporting Information.
- 15 a) J. M. Aubry, J. Rigaudy, N. K. Cuong, *Photochem. Photobiol.* **1981**, *33*, 149. b) J. M. Aubry, J. Rigaudy, N. K. Cuong, *Photochem. Photobiol.* **1981**, *33*, 155. c) C. Pramanik, Y. Li, A. Singh, W. Lin, J. L. Hodgson, J. B. Briggs, S. Ellis, P. Müller, N. E. McGruer, G. P. Miller, *J. Mater. Chem. C* **2013**, *1*, 2193.
- 16 In contrast to the conversion of keto-alcohol **9** to isobenzothiophene **1b** with Lawesson's reagent, the similar reaction of the keto-alcohol, obtained by the reaction of **5** with Grignard reagent **11**, did not give the isobenzothiophene **14**. In this case, isobenzofuran **12** was produced as a major product.
- 17 At present, the synthesis of isobenzoselenophene from the expected precursor **12** and **13** was unsuccessful, although the reason was not clear.
- 18 The absorption and emission spectra of **3a**, **3b**, and **3c** were also measured in acetonitrile, see the Supporting Information.
- 19 M. R. Detty, P. N. Prasad, D. J. Donnelly, T. Ohulchanskyy, S. L. Gibson, R. Hilf, *Bioorg. Med. Chem.* **2004**, *12*, 2537.

## Editor's Choice

# 1,3-Dialkynyl- and 1,3-Dialkenylisobenzofurans: New $\pi$ -Extended Congeners Prepared by Double Nucleophilic Addition of Alkynyllithiums to *o*-Phthalaldehyde



T. Hamura

Ryoji Kudo, Kei Kitamura, and Toshiyuki Hamura\*

Department of Applied Chemistry for Environment, School of Science and Technology,  
Kwansei Gakuin University, 2-1 Gakuen, Sanda, Hyogo 669-1337

(E-mail: thamura@kwansei.ac.jp)

Efficient synthetic route to 1,3-dialkynyl- and 1,3-dialkenylisobenzofurans, new  $\pi$ -extended congeners of isobenzofurans, was reported. A three-step protocol including double nucleophilic additions of alkynyllithiums to *o*-phthalaldehyde and selective oxidation enables us to prepare various functionalized  $\pi$ -extended isobenzofurans. The photophysical properties of these  $\pi$ -extended isobenzofurans are also evaluated.

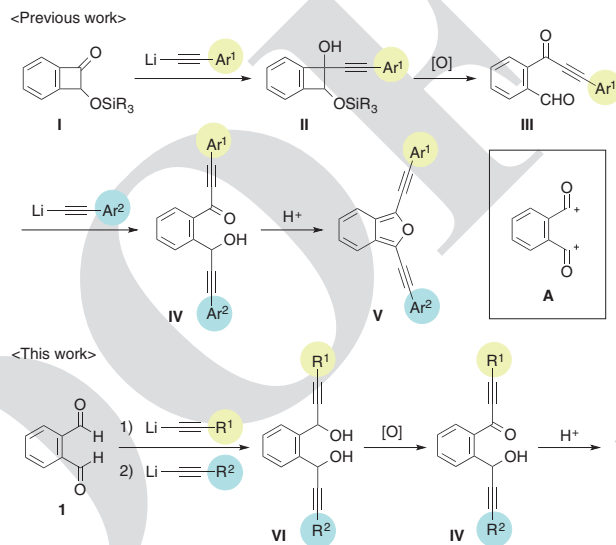
**Keywords:** 1,3-Dialkynylisobenzofuran |  $\pi$ -Extended congener | Three-step synthesis

Isobenzofurans are  $10\pi$  electron systems with a quinoid structure, which can serve as a useful building block for the construction of various natural/unnatural product syntheses.<sup>1–3</sup> In addition, based on their unique physical properties, they have potential utility as a component of functional materials, e.g. fluorophores, OLEDs, and photovoltaics.<sup>4</sup>

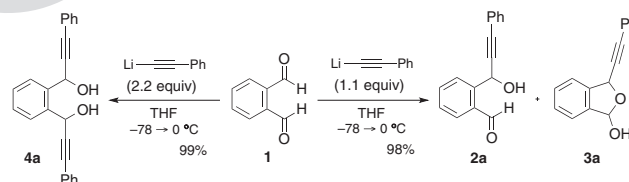
In this context, we previously reported a one-pot synthetic method of 1,3-diarylisobenzofurans by twofold additions of aryl metal species to *o*-formyl benzoate, allowing the rapid preparation of various functionalized derivatives, including an isobenzofuran dimer.<sup>5</sup> Further study, however, revealed that bis(arylethynyl)isobenzofurans **V**, new  $\pi$ -extended derivatives, was not accessible, due to the lower reactivity of the corresponding alkynyl metal species.<sup>6</sup>

Along these lines, an alternative approach to isobenzofurans has been recently developed by using benzocyclobutenones **I** as a masked form of intriguing species **A**, enabling the preparation of various bis(arylethynyl)isobenzofurans **V** (Scheme 1).<sup>6,7</sup> However, it still has a drawback in that multistep syntheses were required to prepare the starting material **I**, which hampered an efficient way to functionalize derivatives of **V**. Herein we wish to describe a new synthetic route to 1,3-dialkynylisobenzofurans **V** by using *o*-phthalaldehyde as a synthetic equivalent of **A**. As shown in Scheme 1, double nucleophilic additions of alkynyllithiums to *o*-phthalaldehyde (**1**), and subsequent selective mono-oxidation of diol **VI** efficiently gives isobenzofuran **V** after acid treatment of the resulting keto-alcohol **IV**. Importantly, stepwise introduction of two alkynyl groups to **1** allows for the selective preparation of symmetrical and unsymmetrical compounds **V**, including novel (alkenyl)ethynyl, (alkyl)ethynyl, and (silyl)ethynyl derivatives. Moreover, dialkenylisobenzofuran, a new  $\pi$ -extended congener, is also accessible by appropriate introduction of two alkenyl groups onto the isobenzofuran core.

Scheme 2 shows the initial model study for successive introduction of two alkynyl groups to *o*-phthalaldehyde (**1**).

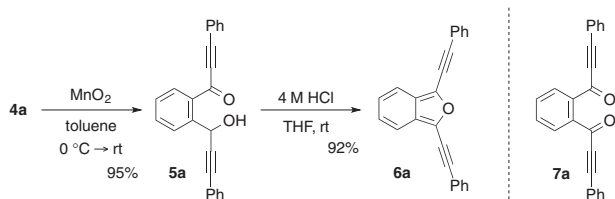


**Scheme 1.** Two synthetic routes to 1,3-dialkynylisobenzofurans.



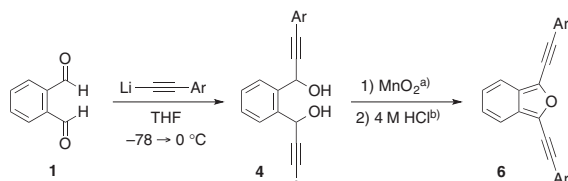
**Scheme 2.** Successive nucleophilic additions of phenylethynyllithium to *o*-phthalaldehyde (**1**).

Upon treatment of **1** with 1.1 equiv of phenylethynyllithium in THF at  $-78^\circ\text{C}$ , nucleophilic addition occurred selectively at one of the formyl groups in **1**, affording keto-alcohol **2a** and lactol **3a** as a mixture of products in 98% combined yield.<sup>8</sup> Importantly, the double additions to **1** did not entirely occur at  $-78^\circ\text{C}$  in spite of the treatment of excess amount of phenylethynyllithium (2.2 equiv). These results indicate that the reactivity of the lithio intermediates of **2a** with phenylethynyllithium is lower than **1** or suppressed by the predominant formation of the lithio intermediates of **3a** in the reaction media. Indeed, TLC analysis showed that second nucleophilic addition occurred gradually by warming the reaction to  $0^\circ\text{C}$ . Quenching the reaction and purification by silica gel column chromatography gave diol **4a** in 99% yield.<sup>9</sup>



**Scheme 3.** Selective oxidation and acid-promoted cyclization to 1,3-bis(phenylethynyl)isobenzofuran (**6a**).

**Table 1.** Symmetrical 1,3-bis(arylethynyl)isobenzofurans



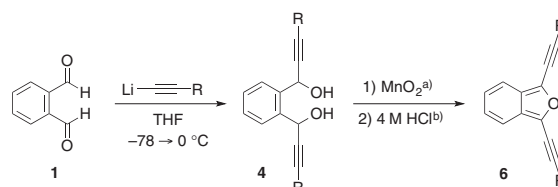
Entry	Ar	Yield of 4/%	Yield of 6/%
1		99 ( <b>4b</b> )	71 ( <b>6b</b> )
2		98 ( <b>4c</b> )	91 ( <b>6c</b> )
3		92 ( <b>4d</b> )	58 ( <b>6d</b> )
4		87 ( <b>4e</b> )	72 ( <b>6e</b> )
5		92 ( <b>4f</b> )	82 ( <b>6f</b> )
6		91 ( <b>4g</b> )	77 ( <b>6g</b> )
7		quant ( <b>4h</b> )	71 ( <b>6h</b> )
8		quant ( <b>4i</b> )	71 ( <b>6i</b> )

<sup>a</sup>1.2 equiv of MnO<sub>2</sub> in toluene at rt. <sup>b</sup>THF, 0 °C.

Selective mono-oxidation of diol **4a** turned out to be possible by using MnO<sub>2</sub> as an oxidant (Scheme 3). Upon treatment of **4a** with MnO<sub>2</sub> (1.2 equiv, MeCN, rt), the oxidation occurred smoothly to give keto-alcohol **5a** in 79% yield, accompanied by a small amount of diketone **7a** (7%). Screening of the reaction conditions revealed that the formation of diketone **7a** was almost completely suppressed by using toluene as a solvent, affording the essentially pure product **5a**. Keto-alcohol **5a**, thus obtained, was directly converted to 1,3-bis(phenylethynyl)isobenzofuran (**6a**) by acid-treatment (4 M HCl, THF, 0 °C → rt).

Various symmetrical (arylethynyl)isobenzofurans **6** were obtained through this three-step sequence (Table 1). Upon treatment of **1** with (4-methylphenyl)ethynyllithium, double nucleophilic additions occurred cleanly to give diol **4b**, which was smoothly converted to isobenzofurans **6b** by selective mono-oxidation and subsequent acid-promoted cyclization (Entry 1). Isobenzofuran **6c** with electron-donating methoxy

**Table 2.** Symmetrical 1,3-dialkynylisobenzofurans



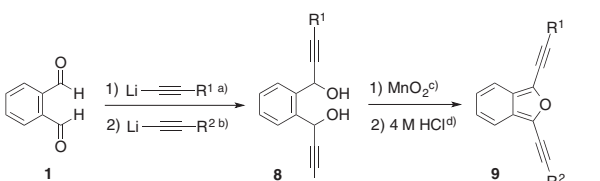
Entry <sup>a</sup>	Ar	Yield of 4/%	Yield of 6/%
1		86 ( <b>4j</b> )	83 ( <b>6j</b> )
2		97 ( <b>4k</b> )	82 ( <b>6k</b> )
3		92 ( <b>4l</b> )	80 ( <b>6l</b> )

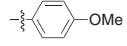
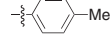
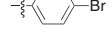
<sup>a</sup>1.2 equiv of MnO<sub>2</sub> in toluene at rt. <sup>b</sup>THF, 0 °C.

group on the aromatic ring was efficiently prepared (Entry 2). It is noted that isobenzofuran **6d**, having an electron-donating dimethylamino group on the aromatic ring, should be purified by silica gel column chromatography *under Ar atmosphere* to avoid gradual oxidation with oxygen, affording **6d** as stable solids.<sup>10</sup> Halogenated derivatives **6e–6g** were also prepared by using (4-halophenyl)ethynyllithium as nucleophiles. Moreover, isomeric pair of alkynylisobenzofurans **6h** and **6i** with respect to the connection of the naphthyl group were selectively synthesized by using the corresponding naphthalenylethynyllithiums (Entries 7 and 8).

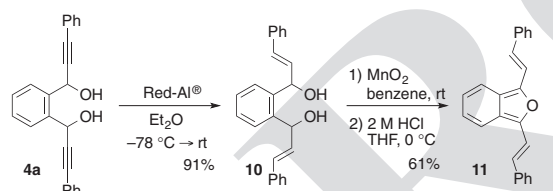
Less  $\pi$ -conjugated (alkenyl)ethynyl-, (alkyl)ethynyl, and (silyl)ethynyl derivatives **6j–6l** were also accessible (Table 2). Due to the potential instability, 1,3-dialkylisobenzofurans have been typically used by in situ generation from appropriate precursors or specially stabilized by steric protection, e.g. incorporating isobenzofuran into an alicyclophane macrocycle.<sup>11</sup> Fortunately, however, isobenzofuran **6k**, *alkynologous* form<sup>12</sup> of the 1,3-dicyclohexylisobenzofuran, which would have an analogous electronic effect as with 1,3-dialkylisobenzofurans, could be carefully purified by silica gel column chromatography under Ar atmosphere.<sup>10</sup>

The unsymmetrical isobenzofurans were also efficiently accessible (Table 3). Taking advantage of the lower reactivity of the formyl group in monoadduct **2a** in comparison with **1** (vide supra), two alkynyl groups were selectively introduced by sequential addition of two kinds of alkynyllithiums to **1**, affording unsymmetrical diols **8a–8e**. Selective mono-oxidation of diols **8a–8e** was again achieved by using MnO<sub>2</sub> (1.2 equiv, toluene, rt), affording keto-alcohols (structure not shown) as a mixture of structural isomers (ca. 1:1), which were smoothly converted to unsymmetrical isobenzofurans **9a–9e** in good yields, respectively. As for the preparation of unsymmetrical isobenzofuran **9b**, this successive protocol including one-pot nucleophilic additions of two kinds of alkynyllithiums to **1** gave the high yield of the desired product **9b** and a very small amount of symmetrical isobenzofuran **6a**. Unfortunately, however, they could not be separated by silica gel column chromatography. In such a case, monoadducts **2a** and **3a** were purified before performing the second nucleophilic addition to avoid the incorporation of the symmetrical product at the final stage.

**Table 3.** Symmetrical 1,3-bis(arylethynyl)isobenzofurans


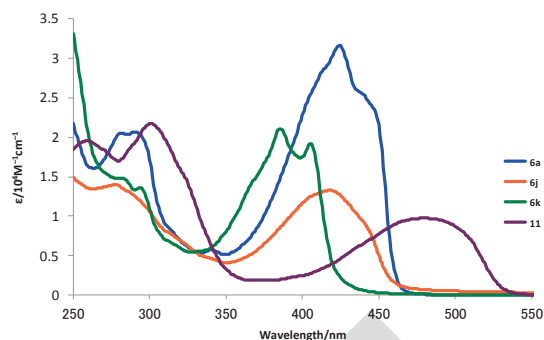
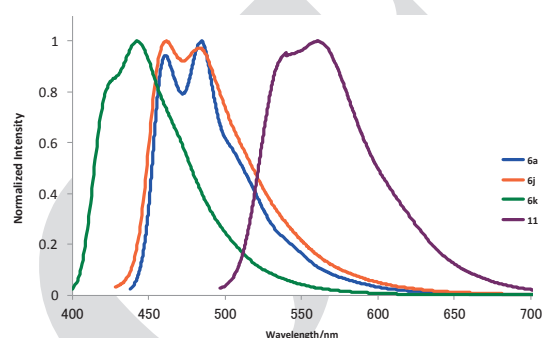
Entry <sup>a</sup>	Ar <sup>1</sup> and Ar <sup>2</sup>	Yield of <b>8</b> /%	Yield of <b>9</b> /%
1	R <sup>1</sup> =  R <sup>2</sup> = 	78 ( <b>8a</b> )	85 ( <b>9a</b> )
2	R <sup>1</sup> =  R <sup>2</sup> = 	78 ( <b>8b</b> )	89 ( <b>9b</b> )
3	R <sup>1</sup> =  R <sup>2</sup> = 	92 ( <b>8c</b> )	58 ( <b>9c</b> )
4	R <sup>1</sup> =  R <sup>2</sup> = 	87 ( <b>8d</b> )	72 ( <b>9d</b> )
5	R <sup>1</sup> =  R <sup>2</sup> = 	92 ( <b>8e</b> )	82 ( <b>9e</b> )

<sup>a</sup>THF, -78 °C. <sup>b</sup>THF, -78 → 0 °C. <sup>c</sup>1.2 equiv of MnO<sub>2</sub> in toluene at rt. <sup>d</sup>THF, 0 °C.

**Scheme 4.** Synthesis of 1,3-dialkenylisobenzofuran.

Moreover, a significant point to be emphasized is that *bis(arylethynyl)isobenzofuran*, a novel  $\pi$ -extended isobenzofuran, was firstly synthesized through the successive processes (Scheme 4). Starting from propargyl alcohol **4a**, double hydro-alumination<sup>13</sup> by treatment with Red-Al<sup>®</sup> (Et<sub>2</sub>O, -78 °C → rt), cleanly gave the high yield of bis-alcohol **10**, which cannot be straightforwardly obtained from our previous method (Scheme 1). Subsequent two-step protocols including the selective mono-oxidation of diol **10** to keto-alcohol gave isobenzofuran **11** in 61% yield. As for the stability, **11** can be stored in the solid state in a refrigerator for a several months, while it is readily decomposed in a no degassed solution.

The absorption and fluorescence spectra of selected isobenzofurans were measured in chloroform (Figures 1 and 2). 1,3-Bis(phenylethynyl)isobenzofuran (**6a**) has its absorption maximum at 424 nm and emission maximum at 484 nm with excellent fluorescence quantum yield ( $\Phi_F$  0.91), which are

**Figure 1.** UV-vis absorption spectra of isobenzofuran.**Figure 2.** Fluorescence spectra of isobenzofuran.

slightly red-shifted in comparison with 1,3-diphenylisobenzofuran ( $\lambda_{\text{abs}}$  415 nm,  $\lambda_{\text{em}}$  482 nm),<sup>14</sup> indicating the small effect on the photophysical properties by insertion of the two alkynyl groups. The absorption and emission spectra of less  $\pi$ -conjugated isobenzofuran **6k** were blue-shifted to 386 and 443 nm, respectively, which exhibited a lower fluorescence quantum yield than that of **6a** ( $\Phi_F$  0.62). Cyclohexenyl-substituted isobenzofuran **6j** showed a similar trend to **6a** in both spectra, although the fluorescence quantum yield was low ( $\Phi_F$  0.32). In sharp contrast, 1,3-bis(phenylethynyl)isobenzofuran **11**, the alkenyl congener of **6a**, showed a broad absorption band ranging from 380 to 530 nm, and peaking at 480 nm. The Stokes shift of **11** was increased to 88 nm and the emission peak was observed at 568 nm with a moderate fluorescence yield ( $\Phi_F$  0.48). In this manner,  $\pi$ -extension by ethenylation significantly affects the photophysical properties, and thus, these newly prepared derivatives would be promising probes for biological applications.<sup>15</sup>

In summary, we developed a new synthetic route to symmetrical and unsymmetrical 1,3-dialkynylisobenzofurans by sequential additions of *o*-phthalaldehyde with two identical or different alkynyllithium. This efficient synthetic method enables us to prepare new  $\pi$ -extended 1,3-dialkenylisobenzofurans. Further studies on synthetic applications and physical properties of these attractive molecules are currently in progress.

This work was supported by JSPS KAKENHI Grant Number JP15H05840 in Middle Molecular Strategy and JST ACT-C.

Supporting Information is available on <http://dx.doi.org/10.1246/cl.160884>.

## References and Notes

- For reviews, see: a) A. O. Patil, A. J. Heeger, F. Wudl, *Chem. Rev.* **1988**, *88*, 183. b) J. Roncali, *Chem. Rev.* **1997**, *97*, 173. c) R. Rodrigo, *Tetrahedron* **1988**, *44*, 2093. d) W. Friedrichsen, *Adv. Heterocycl. Chem.* **1980**, *26*, 135. e) O. Peters, W. Friedrichsen, *Trends Heterocycl. Chem.* **1995**, *4*, 217. f) W. Friedrichsen, *Adv. Heterocycl. Chem.* **1999**, *73*, 1.
- For selective examples of the syntheses of isobenzofuran, see: a) G. Wittig, L. Pohmer, *Chem. Ber.* **1956**, *89*, 1334. b) M. P. Cava, M. J. Mitchell, A. A. Deana, *J. Org. Chem.* **1960**, *25*, 1481. c) R. N. Warrener, *J. Am. Chem. Soc.* **1971**, *93*, 2346. d) J. T. Sharp, C. E. D. Skinner, *Tetrahedron Lett.* **1986**, *27*, 869. e) Y. Kuninobu, Y. Nishina, C. Nakagawa, K. Takai, *J. Am. Chem. Soc.* **2006**, *128*, 12376. f) D.-T. Hsu, C.-H. Lin, *J. Org. Chem.* **2009**, *74*, 9180. g) Y. Nishina, T. Kida, T. Ureshino, *Org. Lett.* **2011**, *13*, 3960.
- For synthetic utility of isobenzofuran, see: a) G. Wittig, A. Krebs, *Chem. Ber.* **1961**, *94*, 3260. b) T. Sasaki, K. Kanematsu, K. Hayakawa, M. Sugiura, *J. Am. Chem. Soc.* **1975**, *97*, 355. c) W. C. Christophel, L. L. Miller, *J. Org. Chem.* **1986**, *51*, 4169. d) H. N. C. Wong, *Acc. Chem. Res.* **1989**, *22*, 145. e) Y.-M. Man, T. C. W. Mak, H. N. C. Wong, *J. Org. Chem.* **1990**, *55*, 3214. f) P. Binger, P. Wedemann, R. Goddard, U. H. Brinker, *J. Org. Chem.* **1996**, *61*, 6462. g) D. Jiang, J. W. Herndon, *Org. Lett.* **2000**, *2*, 1267. h) T. Ernet, A. H. Maulitz, E.-U. Würthwein, G. Haufe, *J. Chem. Soc., Perkin Trans. 1* **2001**, 1929. i) K. Mikami, H. Ohmura, *Org. Lett.* **2002**, *4*, 3355. j) S.-H. Chan, C.-Y. Yick, H. N. C. Wong, *Tetrahedron* **2002**, *58*, 9413. k) Y. Luo, J. W. Herndon, *Organometallics* **2005**, *24*, 3099. l) J. E. Rainbolt, G. P. Miller, *J. Org. Chem.* **2007**, *72*, 3020.
- a) S. T. Meek, E. E. Nesterov, T. M. Swager, *Org. Lett.* **2008**, *10*, 2991. b) H. Zhang, A. Wakamiya, S. Yamaguchi, *Org. Lett.* **2008**, *10*, 3591.
- T. Hamura, R. Nakayama, *Chem. Lett.* **2013**, *42*, 1013.
- K. Asahina, S. Matsuoka, R. Nakayama, T. Hamura, *Org. Biomol. Chem.* **2014**, *12*, 9773.
- For our synthetic application of isobenzofurans to polyacene derivatives, see: a) S. Eda, T. Hamura, *Molecules* **2015**, *20*, 19449. b) R. Akita, K. Kawanishi, T. Hamura, *Org. Lett.* **2015**, *17*, 3094. c) S. Eda, F. Eguchi, H. Haneda, T. Hamura, *Chem. Commun.* **2015**, *51*, 5963. d) H. Haneda, S. Eda, M. Aratani, T. Hamura, *Org. Lett.* **2014**, *16*, 286.
- Product ratio (**2a/3a**) was depending on the conditions of purification. Indeed, keto-alcohol **2a** was partially isomerized to lactol **3a** during the purification by silica gel column chromatography. For details, see Supporting Information.
- For related double nucleophilic additions of alkynyllithiums to phthalaldehyde, see: a) D. Rodríguez, L. Castedo, D. Domínguez, C. Saá, *Org. Lett.* **2003**, *5*, 3119. b) Y.-C. Lin, C.-H. Lin, *Org. Lett.* **2007**, *9*, 2075. c) Y. Liu, S. Zhou, G. Li, B. Yan, S. Guo, Y. Zhou, H. Zhang, P. G. Wang, *Adv. Synth. Catal.* **2008**, *350*, 797.
- For details, see Supporting Information.
- a) S. L. Crump, B. Rickborn, *J. Org. Chem.* **1984**, *49*, 304. b) C. P. Casey, N. A. Strotman, I. A. Guzei, *Beilstein J. Org. Chem.* **2005**, *18*, 1. c) I. Saito, A. Nakata, T. Matsuura, *Tetrahedron Lett.* **1981**, *22*, 1697. d) R. N. Warrener, M. Shang, D. N. Butler, *Chem. Commun.* **2001**, 1550.
- B. Xu, G. B. Hammond, *Synlett* **2010**, 1442.
- a) E. J. Corey, H. A. Kirst, J. A. Katzenellenbogen, *J. Am. Chem. Soc.* **1970**, *92*, 6314. b) K. Ohmori, T. Suzuki, K. Taya, D. Tanabe, T. Ohta, K. Suzuki, *Org. Lett.* **2001**, *3*, 1057.
- a) R. Adams, M. H. Gold, *J. Am. Chem. Soc.* **1940**, *62*, 2038. b) J. Jacq, S. Tsekhanovich, M. Orio, C. Einhorn, J. Einhorn, B. Bessières, J. Chauvin, D. Jouvenot, F. Loiseau, *Photochem. Photobiol.* **2012**, *88*, 633.
- D. Song, S. Cho, Y. Han, Y. You, W. Nam, *Org. Lett.* **2013**, *15*, 3582.

## イソベンゾフランを用いた高次縮環芳香族化合物の合成

羽村 季之\*

*Synthesis of Highly Condensed Aromatic Compounds by Using Isobenzofurans*

Toshiyuki Hamura\*

Isobenzofurans are  $10\pi$  electron systems with a quinoid structure, which make them useful intermediate for natural/unnatural product syntheses. Among various possibilities, [4+2] cycloaddition with dienophiles is a reliable method for the rapid construction of polycyclic structure. In this context, a one-pot synthetic method of 1,3-diarylisobenzofurans has been developed via sequential nucleophilic addition to 2-formylbenzoate. 1,3-Bis(arylethynyl)-isobenzofurans has also been accessible by nucleophilic addition of alkynyllithium to benzocyclobutenone and subsequent oxidative ring cleavage of the four-membered ring.

Based on these new synthetic approaches to various isobenzofurans, successive [4+2] cycloadditions of isobenzofuran with benzyne and/or epoxynaphthalenes were developed, allowing us for rapid construction of various highly condensed aromatic compounds. Moreover, as a potentially versatile method for the rapid, selective assembly of functionalized polycycles, we also exploited the synthetic equivalent of bis-isobenzofuran, *i.e.* diepoxyanthracene, which enabled the iterative generation of isobenzofuran and subsequent functionalization and/or introduction of the fused ring by trapping with dienophile.

The essential point of these integrated syntheses is *isolability of isobenzofuran*, which would provide great opportunities to use this potentially attractive molecules under various reaction conditions.

**Key words:** isobenzofuran, benzyne, epoxynaphthalene, ring selectivity, successive cycloaddition, highly condensed aromatic compounds, integrated syntheses

\*関西学院大学理工学部環境・応用化学科(665-1337 三田市学園 2-1)

\*Department of Applied Chemistry for Environment, Kwansei Gakuin University (Gakuen, Sanda 669-1337, Japan)

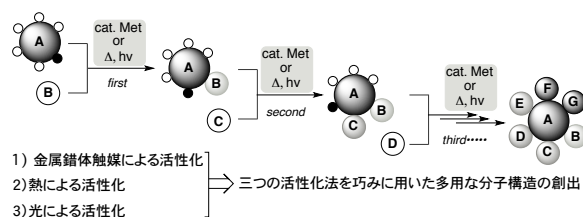
## はじめに

$\pi$  共役系有機化合物は古くより生命科学・材料科学における重要な物質群であるが、これらを構成する芳香環や複素環化合物の合成には制限があり、新物質創製の機会が大きく阻まれている。これは、高度に縮環した芳香族骨格を迅速に構築するための優れた骨格構築法がほとんどないことに加えて、核となる分子の望みの位置に望みの官能基を適切に導入するための一般性の高い合成手法が欠如しているためである。したがって、新しい物性や機能の宝庫である  $\pi$  共役系分子をナノ領域のレベルまで精密に、しかも自在に合成できる新しい合成方法論の開拓が望まれている。

これに対して我々は、反応の情報をプログラム化した“潜在的に高い反応性を内在する分子”をコア分子に選び、これを適切に活性化することにより、これがいわば自発的に反応集積化する合成方法論の開拓を目指して、研究を行っている。すなわち、あらかじめ反応の情報をインプ

ットした高反応性分子 **A** に対して金属錯体触媒、熱あるいは光による活性化の条件下、親反応性分子 **B**, **C**, **D**... を順次作用させ、一連の反応でこれらすべての反応成分を一挙に結合させることによってナノスケールに至る高次構造の選択的構築を図るというものである(スキーム1)。一般的に、高反応性分子はその取り扱いが難しいと見られる傾向にあるが、これをうまく制御することができれば、高反応性分子に内在するエネルギーを化学エネルギーとして巧みに利用する独創的な分子変換反応の開拓が可能になる。この手法では作用させる親反応性分子の種類や反応順序の多様化により、これまで合成が困難であったさまざまな分子構造の創出と新たな物性・機能発現の発見が期待される。本稿では、このような観点から最近我々が高反応性分子として注目しているイソベンゾフランを用いて、特に熱的な活性化による反応集積化を駆使した高次縮環芳香族化合物の効率的合成法の開発について述べる。また、その応用として、近年有機半導体材料と

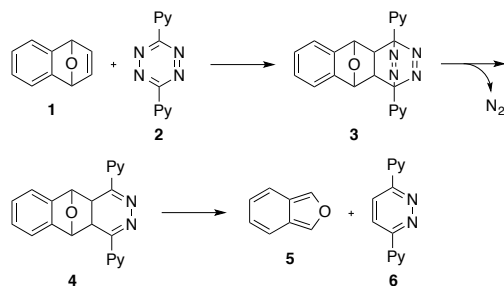
して注目を集めている置換ペンタセンの合成についても紹介する。



Scheme 1 Integrated reaction using reactive molecules.

### 1. 置換イソベンゾフランの効率的合成法の開発

平面  $10\pi$  系のイソベンゾフランは、その独特な  $\pi$  共役構造に由来する興味深い反応性を示す芳香族化合物である<sup>1)</sup>。ナフタレンと等電子構造のこの分子は、オルトキノジメタンのエキソ二重結合部位を酸素で架橋した構造に相当することから、キノイド構造に特徴的な反応性が期待される。実際、フラン環部位をジエン成分とする [4+2] 環付加反応は、その好例である<sup>2)</sup>。しかし、一般的にイソベンゾフランはその高い反応性のため、用事調製によって反応に供するのがほとんどである。特に、1,3-位に置換基を持たないイソベンゾフランの単離に関する報告は極めて限られ、母体化合物であるイソベンゾフラン **5** においては、真空熱分解などの特殊な反応条件が用いられている<sup>3)</sup>。これに関連して、1971年に Warrener らはエポキシナフタレン **1** とジピリジルテトラジン **2** との連続的な Diels-Alder 反応と逆 Diels-Alder 反応によってイソベンゾフラン **5** が合成できることを報告している (スキーム 2)<sup>3a)</sup>。しかし、この反応で得られる反応混合物を常法に従って精製した場合、精製の過程で目的物が直ちにポリマー化してしまう。このため、生成物の確認はこれをジェノフィルで補足することによって行っている<sup>4)</sup>。



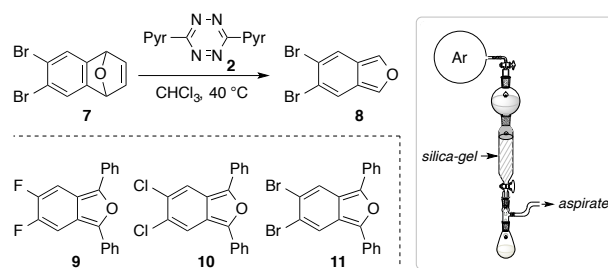
Scheme 2 Preparation of isobenzofuran.

#### 1.1 イソベンゾフランの単離・精製法の開発

イソベンゾフランの単離・精製の問題を踏まえ、既存法でイソベンゾフランを合成した後、どうにかこれを純粋に得る方法を確立できないかと考えた。熱分解による方法では操作法の煩雑さに加えて、置換誘導体への適用は

容易ではない。そこで、一般的な精製法からの工夫を試みたところ、シリカゲルカラムクロマトグラフィーをアルゴンガス雰囲気で行うと、1,3-位に置換基を持たないイソベンゾフランであってもこれを純粋に精製できることを見出した (スキーム 3)<sup>5)</sup>。ジプロモイソベンゾフラン **8** を例にした操作手順は以下の通りである。1) エポキシナフタレン **7** とジピリジルテトラジン **2** のクロロホルム溶液をアルゴンガス雰囲気下で、 $40^\circ\text{C}$  に加熱し、ジプロモイソベンゾフランを含む反応混合物を得る。2) 1) の反応と並行して、シリカゲルをクロマト管に脱気した溶媒で充填する。3) 1) のクロロホルム溶液を減圧留去した後、粗生成物をシリカゲルへチャージする。さらに、上方に不活性ガスを充填したバルーンを取り付け、ダイヤフラムポンプで下方から減圧・吸引し、反応混合物をシリカゲル上に展開させる。4) ナスフラスコに分取した目的化合物を含む溶媒を減圧留去し、生成物 **8** を白色固体として得る。このようにして合成したイソベンゾフランは不活性ガス中で冷凍保存できる<sup>6)</sup>。この単離・精製法で特筆すべきは、この方法を利用すれば、母体化合物 **5** であってもこれを無色油状物質として純粋に入手できる点である。この場合には、生成物をヘキサンの希釈溶液とすることで、これを冷凍庫で1週間程度保存できる。

このように、イソベンゾフランの精製法を工夫することによって、これまで単離が容易ではなかったと考えられていた1,3位に置換基を持たないイソベンゾフランを純粋に入手できるようになった。一方、この方法を用いて置換誘導体 (例えば、**9-11**) を簡便に合成することも明らかにした。これらは、ハロゲン原子を足掛かりとした官能基化や骨格の伸長が可能な汎用性の高い合成ブロックとして期待できる (後述)。



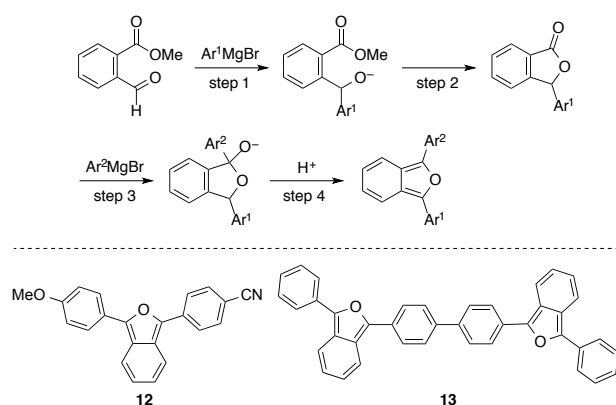
Scheme 3 Preparation of dihaloisobenzofuran.

#### 1.2 置換イソベンゾフランのワンポット合成法の開発

イソベンゾフランの新しい単離・精製法を通じて、母体化合物を含むさまざまなイソベンゾフランを化学的に純粋に取り扱えるようになった。この貴重な発見により、これらを合成ブロックとする合成的利用の機会が飛躍的に増大することが期待される。しかし、上述の合成法では同モル量のテトラジン **2** を必要とすること、また同モル量のジアジン **6** が副生成物として生じることから (スキーム

ム2), 経済性や原子効率の点で満足のものではない。一方, 置換誘導体のその他の代表的な合成法として, 3-アリーールフタリドへの求核付加を利用した 1,3-ジアリーールイソベンゾフランの合成が挙げられる<sup>7)</sup>。しかし, この方法では Friedel-Crafts 反応を利用したフタリドの合成の段階で合成可能な置換様式が芳香環上の置換基の配向性に依存してしまうという欠点がある。

そこで, 多様な芳香環の導入を可能にする 1,3-ジアリーールイソベンゾフランの新たな合成ルートを開拓するため, 塩基性条件での芳香環の導入を検討した。種々の有機金属反応剤を用いて, その可能性を調べたところ, オルトホルミル安息香酸エステルへの Grignard 反応剤の二重求核付加を鍵として, ジアリーールイソベンゾフランがワンポットで合成できることを明らかにした(スキーム 4)<sup>8)</sup>。



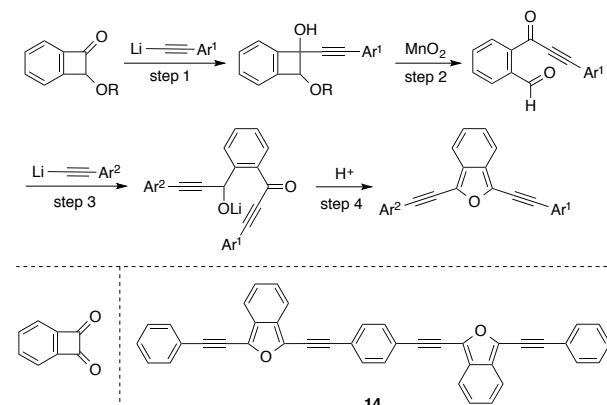
Scheme 4 One-pot preparation of 1,3-diarylisobenzofuran.

この反応では, 1) Grignard 反応剤によるホルミル基への選択的な求核付加 (step 1), 2) ラクトンの形成 (step 2), 2) Grignard 反応剤によるラクトンへの求核付加 (step 3), 3) 酸性条件でのラクトールの脱水・芳香族化 (step 4), が連続的に進行して生成物を与える。一連の反応はワンポットで行えるため操作上簡便であり, 一度の反応で大量のイソベンゾフランの合成が可能である<sup>9)</sup>。また, 出発物質の二つのカルボニル炭素への求核付加が選択的であるという特徴を活かして, 非対称型分子の合成もできる<sup>10)</sup>。芳香環上の置換基の異なる二種類の求核種を順次作用させることによって, 機能性の面から興味を持たれるドナー・アクセプター型分子 **12** やイソベンゾフランダイマー **13** の合成も可能になった。

### 1.3 ベンゾシクロブテンの酸化的開裂を利用したジアリキニルイソベンゾフランの合成

次に, ワンポット合成法のさらなる展開として芳香環とイソベンゾフランをアリキニル基で連結した  $\pi$  拡張型誘導体の合成を目指した。先述の方法に従い, オルトホルミル安息香酸エステルにアリキニルリチウムを作用させたところ, 3-アリキニルフタリドは低収率ながら得られ

るものの, 引き続くラクトンへの求核付加は全くうまくいかなかった。この原因の一つは, アリキニルアニオンの求核性がアリーールアニオンに比べて低いことにあると考え, 新たな合成ルートとして潜在的に高い反応性を持つ小員環化合物<sup>11)</sup>を利用することにした。中でも, 複数の官能基の導入を可能にするアルコキシベンゾシクロブテン<sup>12)</sup>に着目し, その可能性を探ったところ, ベンゾシクロブテンへの求核付加と四員環の酸化的開裂を鍵とする新たな合成法を開発することができた(スキーム 5)<sup>13,14)</sup>。まず, この方法ではシクロブテンへのアリキニルリチウムの求核付加によってベンゾシクロブテノールが得られる(step 1)。次に, これに二酸化マンガンを作用させると, 四員環が酸化的に開裂し<sup>15)</sup>, ケト-アルデヒドへと変換される(step 2)。さらに, これに二度目の求核剤を作用させるとホルミル基への選択的な求核付加, 環化, 酸性での芳香族化が連続的に起こり, ジアリキニルイソベンゾフランを収率良く与える(step 3, 4)<sup>16)</sup>。出発物質であるアルコキシベンゾシクロブテンは, 四員環上の二つのカルボニル基が形式的に区別されたベンゾシクロブテンジオン等価体と見なすことができるため, 2種類の求核剤を順次作用させることにより, 芳香環上に種々の置換基を持つ非対称型のジアリキニルイソベンゾフランの合成が可能である。また, 求核剤を工夫することにより, イソベンゾフランダイマー **14** の合成を行うこともできた。



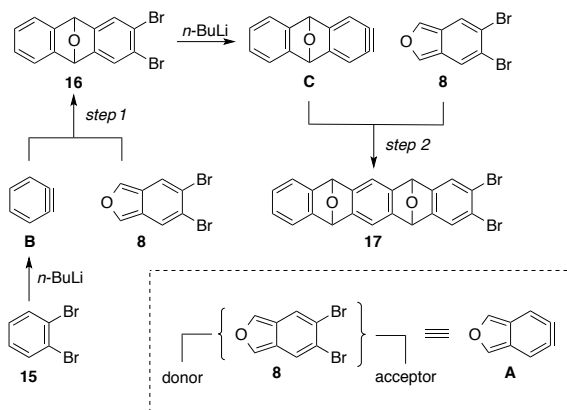
Scheme 5 Preparation of 1,3-bis(arylethynyl)isobenzofuran.

## 2. イソベンゾフランの環付加反応

ベンゼン環が直線状に連なったポリアセンは, その特徴的な  $\pi$  共役構造に基づく興味深い化学的性質を示し, 合成・理論・物性などさまざまな分野から関心を集めている<sup>17)</sup>。近年, こうした  $\pi$  電子系化合物を優れた有機半導体材料として利用するべく, 有機太陽電池, 有機 EL, 有機トランジスタへの応用研究が盛んに行われている。しかし, ポリアセンの一般的な合成法は乏しく, 特に縮環数の大きなポリアセンの合成は限定されている。その主な原因は, 多環式芳香族骨格を

効率良く構築するための優れた合成法が乏しいことにある。加えて、縮環数が増大するにつれて生成物の溶解性や化学的安定性が著しく低下するという合成上の問題もある。

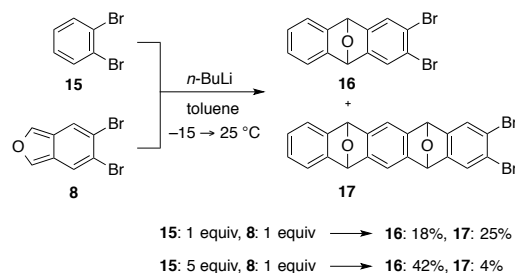
これに対して我々は高次構造の効率的構築のため、イソベンゾフランに電子受容部位を組み込んだジデヒドロイソベンゾフラン **A** に着目した。具体的には、この合成等価体であるジブロモイソベンゾフラン **8** を合成ブロックとして、これとベンザイン<sup>18)</sup>とのドナー・アクセプター型の相互作用を鍵とする連続的な環付加反応によって、多環式芳香族骨格の構築を図るという戦略である(スキーム6)。この方法では、出発物質であるジブロモイソベンゾフランをベンザインのアクセプターとして利用し、ベンザイン **B** との反応を行う(step 1)。次に、得られる環付加体 **16** を今度はベンザインドナーとして利用し、新たに反応系に加えたイソベンゾフラン **8** との反応を行う(step 2)。同様の操作を繰り返し行い、環を自在に伸長させることによって、さまざまな縮環数を持った多環式芳香族ライブラリーの構築が可能となる。



Scheme 6 Formal use of didehydroisobenzofuran by dual [2+4] cycloadditions of benzyne and isobenzofuran.

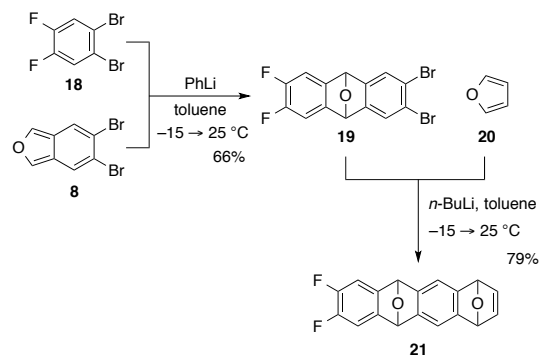
この環付加反応を行う上で想定される問題は、“臭素-リチウム交換の位置選択性”である<sup>19)</sup>。すなわち、ベンザイン前駆体であるジブロモベンゼン **15** と補足剤であるイソベンゾフラン **8** はいずれも臭素原子を有しているため、どちらの側で反応が起こるかは明らかではない。そこで、**15** と **8** を用いて反応を行ったところ、ベンゼン環の側で臭素-リチウム交換が生じた環付加体 **16** が得られた。しかし、その収率は 18%に留まり、むしろ二重環付加体 **17** が多く生じる結果となった(スキーム7)<sup>20)</sup>。これは、出発物質と生成物との臭素-リチウム交換の反応性に有意な差がなく、生成物 **16** から相当量のベンザインが発生したためである。一方、過剰量の出発物質を用いれば二重環付加体 **17** の生成を抑制できることがわかったが、この条件

ではワンポット反応(後述)への適用は難しい。



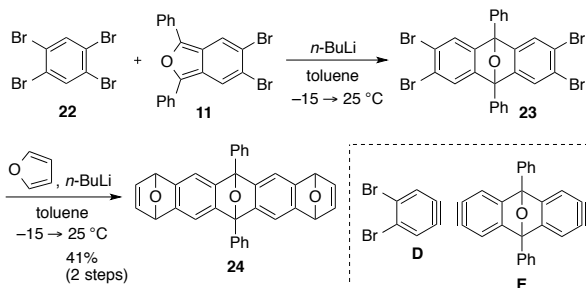
Scheme 7 Initial model study on the selective generation of benzyne.

この問題に対して芳香環に電子求引性置換基を導入し、臭素原子の相対的な電子受容性を上げることによって臭素-リチウム交換を制御できることがわかった。例えば、ジフルオロジブロモベンゼン **18** と **8** の反応では環付加体 **19** を良好な収率で与え、二重環付加体は全く得られなかった(スキーム8)。環付加体 **19** はベンザインドナーとして利用することが可能であり、フランを捕捉剤とする二度目の[4+2]環付加反応によってジエポキシテトラセン **21** が収率良く得られた<sup>6)</sup>。なお、一連の環付加反応は途中で反応を停止することなくワンポットで行うことが可能であり、右方向への環の伸長を逐次的に行えることは合成上、有用である。



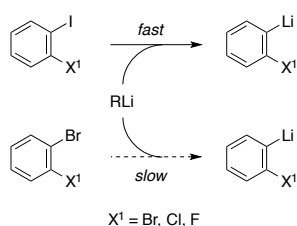
Scheme 8 Successive [2+4] cycloadditions of benzyne and isobenzofuran.

また、テトラブロモベンゼン **22** を出発物質とすると、左右双方向への環の伸長をワンポットで行えた。まず、**22** の選択的な臭素-リチウム交換によってジブロモベンザイン **D** を発生させ、これをイソベンゾフラン **11** で補足すると環付加体 **23** が得られた。この化合物は、左右の芳香環にそれぞれベンザイン発生部位を持つため、反応系内に再度 *n*-BuLi を作用させると、発生するビスアライン **E**<sup>21)</sup> から二重環付加反応がきれいに進行した(スキーム9)。



Scheme 9 Two directional three-fold [4+2] cycloadditions.

1) Type 1: Utilization of more electropositive halogen



2) Type 2: Tuning the reactivity by adjacent halogen

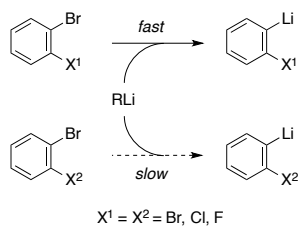
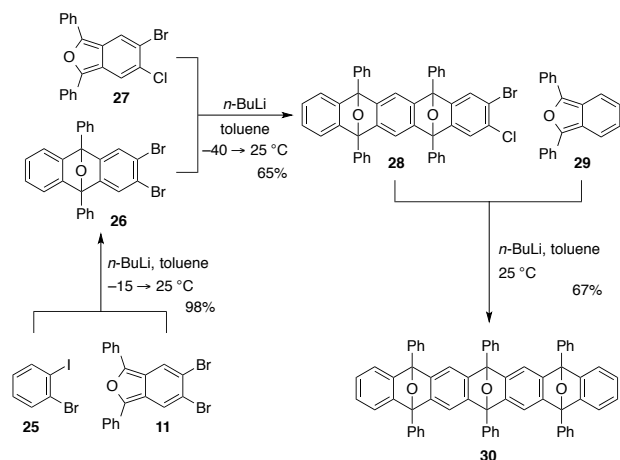


Fig. 1 Two strategies for selective halogen–lithium exchange of 1,2-dihaloarenes.



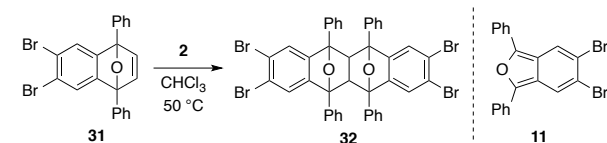
Scheme 10 Mono-directional [2+4] cycloadditions of arynes.

さらに、我々はスキーム 7 で示した置換基を持たない母体ベンザインからの連続的環付加反応を可能にするため、ベンザイン前駆体およびイソベンゾフランを改めて探索した。反応設計の指針は、1) ベンザイン前駆体に電子受容性の高いハロゲン原子を導入する (Type 1), 2) 隣接位のハロゲン原子を利用してハロゲン原子の電子受容性をチューニングする (Type 2), というものである。これにより、ベンザイン前駆体の側での位置選択的なハロゲン–リチウム交換を実現できるものと期待した (図 1)。

検討の結果、2-ブロモオードベンゼンを出発物質として Type 1 を利用した選択的な環付加反応の後、塩素原子を導入したイソベンゾフランを捕捉剤とする二度目の環付加反応を行うことにより (Type 2), スキーム 7 の反応で問題となった多重環付加体の生成を抑えることに成功した。この二つのタイプの位置選択的なハロゲン–リチウム交換を駆使して右方向への環付加反応を 3 回行い、高度に縮環した芳香族骨格 (例えば、トリエポキシヘプタセン 30) の迅速合成を達成した (スキーム 10) <sup>22)</sup>。

### 3. エポキシナフタレンとイソベンゾフランの環付加反応

最近我々は置換イソベンゾフランの合成途上、エポキシナフタレン 31 とイソベンゾフラン 11 とが容易に [4+2]環付加反応を起こし、多環式化合物 32 を与えることを偶然にも見出した (スキーム 11)。これはテトラジン 2 との反応によって生じるイソベンゾフラン 11 が原料であるエポキシナフタレン 31 と環付加反応を起こしたものである。この化合物の生成は、基質 31 の二重結合部位の高い反応性に起因しているが、この形式の熱反応は既に報告例がいくつかあることがわかった <sup>23)</sup>。しかし、これらの報告で驚いたのは環付加反応の立体選択性に関する知見が乏しいこと、さらに強調すべきは環付加体の芳香族化が全くうまくいかないということであった <sup>24)</sup>。得られる環付加体を芳香族化できれば対応するテトラセンへと誘導できるため、この反応は新たなポリアセン合成法として魅力的である。そこで、この熱反応の立体経路と環付加体の芳香族化の可能性について調べた。

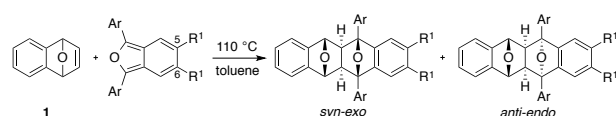


Scheme 11 Unexpected [2+4] cycloaddition of epoxynaphthalene and isobenzofuran.

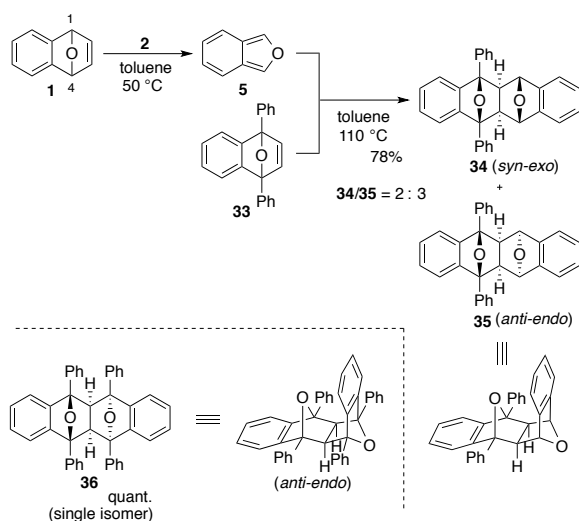
まず、エポキシナフタレン 1 とジフェニルイソベンゾフラン 29 との反応を試みたところ、110 °C で直ちに反応が進行し、syn-exo 体と anti-endo 体がそれぞれ 75:25 の比

で得られた(entry 1)。これらは、いずれもイソベンゾフランがエポキシナフタレンの convex 面から接近することによって生じたものである。同様に芳香環上に電子求引性置換基や電子供与性置換基を持つイソベンゾフランを用いた場合にも syn-exo 体が同程度の選択性で得られた。一方、イソベンゾフラン骨格の5位と6位にハロゲン原子を導入すると選択性は低下し、特にフッ素原子を有する場合、その選択性は1.3 : 1になった(entry 5)。

Table 1. [4+2] cycloaddition of epoxynaphthalene and isobenzofuran.



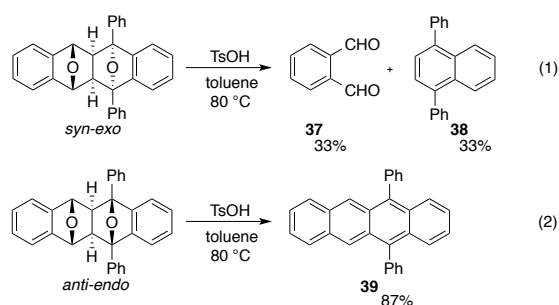
Entry	Ar	R <sup>1</sup>	Time/h	Yield/%	syn-exo : anti-endo
1		H	0.5	96	75 : 25
2		H	0.3	87	77 : 23
3		H	0.3	96	76 : 24
4		H	36	79	80 : 20
5		F	0.3	97	56 : 44
6		Cl	0.3	96	68 : 32
7		Br	0.3	97	67 : 33
8		OMe	0.3	98	76 : 24



Scheme 12 Stereoselective [4+2] cycloaddition of 1,4-disubstituted epoxynaphthalene.

次に、エポキシナフタレンの1位と4位に置換基を持つ基質の反応を試みたところ、**1**の反応とは対照的に endo 選択的に環付加反応が進行した。例えば、ジフェニルエポキシナフタレン **33** とイソベンゾフラン **5** の反応では anti-endo 体が優先的に生じた(anti-endo : syn-exo = 3 : 2)。ジフェニルイソベンゾフラン **29** の場合、syn-exo 体はもはや生成せず、anti-endo 体のみが単一の立体異性体として得られた (スキーム 12)<sup>25)</sup>。

このように、エポキシナフタレンの酸素架橋部位の置換基の有無によって、endo/exo 選択性が逆転することがわかった。そこで次に、それぞれの立体異性体の芳香族化を試みた。まず、anti-endo 体にパラトルエンスルホン酸を作用させたところ、これまでの報告例と同様に Grobe 開裂<sup>26)</sup>が進行し、フタルアルデヒド **37** とナフタレン **38** が得られた (式 1)。酸として硫酸、酢酸、トリフルオロ酢酸、さらには BF<sub>3</sub>·Et<sub>2</sub>O などのルイス酸も試したが、いずれも Grobe 開裂した化合物や複雑な生成物の混合物を与える結果となった。一方、興味深いことに syn-exo 体を同様の条件に付したところ、芳香族化がきれいに進行し、対応する置換テトラセン **39** へと収率良く変換することができた (式 2)<sup>25)</sup>。



このように環付加体の立体化学の違いによって環開裂と芳香族化の二つが生じた。この二つの反応経路について、anti-endo 体ではプロトン化された中間体 **F** の炭素-炭素結合 a と炭素-酸素結合 b がアンチペリプラナーの関係にあるため、左側のエポキシ環からの電子供与による結合開裂が促進されたと理解できる (図 2)。一方、syn-exo 体は炭素-水素結合 c と炭素-酸素結合 d がアンチの関係にあるため、脱水・芳香族化が起こりやすい立体構造を有していると言える。

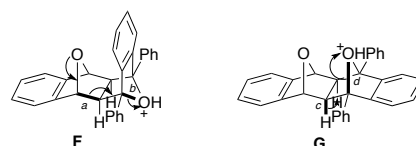
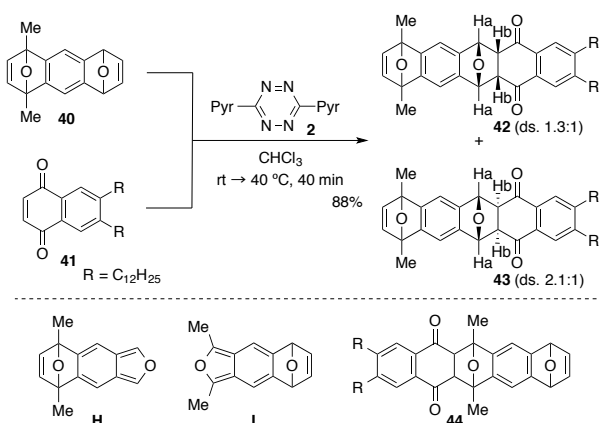


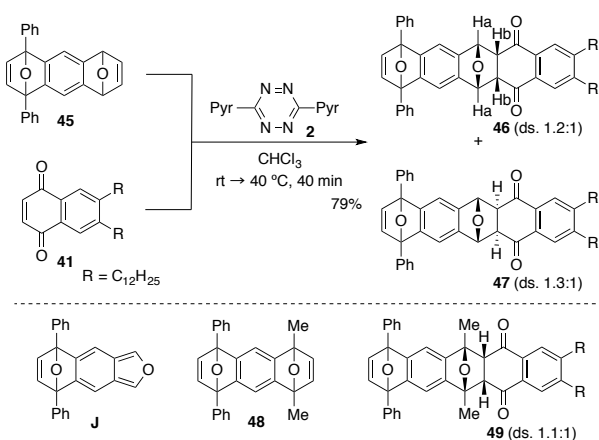
Fig. 2 Ring cleavage or aromatization of the intermediates.

### 2-3. 環選択的なイソベンゾフランの発生

ベンザインの逐次的な発生とイソベンゾフランとの環付加反応によって多環式芳香族化合物を効率良く合成できることを先に述べた。これに対して、イソベンゾフランを逐次的に発生させ、これをジエノフィルで順次補足するという手法によっても多環式構造への迅速なアプローチが可能であることを見出した。この方法では、ジエポキシアントラセンをビス-イソベンゾフラン等価体<sup>27)</sup>として利用し、酸素架橋部位に置換基を適切に導入することにより“環選択的”にイソベンゾフランを発生させることができた。例えば、酸素架橋部位にメチル基を持つジエポキシアントラセン **40** にテトラジンを作用させると、右側の環からイソベンゾフランが選択的に発生し、これがナフトキノンで補足された化合物が高収率で得られた(スキーム 13)<sup>28)</sup>。この際、イソベンゾフラン **I** に由来する化合物は全く得られなかった。これは、立体障害の少ない右側の環の二重結合部分にテトラジンが容易に接近できるためである。なお、この環付加反応は立体選択的であり、endo 体を選択的に与えた (**42** : **43** = 4 : 1)。



Scheme 13 Ring selective generation of isobenzofuran from diepoxyanthracene **40**.



Scheme 14 Ring selective generation of isobenzofurans from diepoxyanthracene **45** and **48**.

同様に、酸素架橋部位にフェニル基を持つ基質 **45** の反応でも立体障害の少ない側から環選択的にイソベンゾフランが発生し、環付加体を与えた(スキーム 14)。さらに、フェニル基およびメチル基を持つ四置換体 **48** からは、メチル基を有する右側の環にナフトキノンが導入された化合物 **49** が単一の位置異性体として収率 43% で得られた。

以上の結果より、イソベンゾフラン発生におけるエポキシナフタレンの反応性は立体障害に基づいて、**K** > **L** > **M** であることが明らかになった(図 3)。

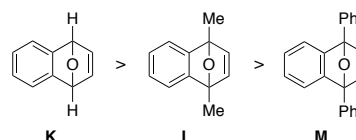
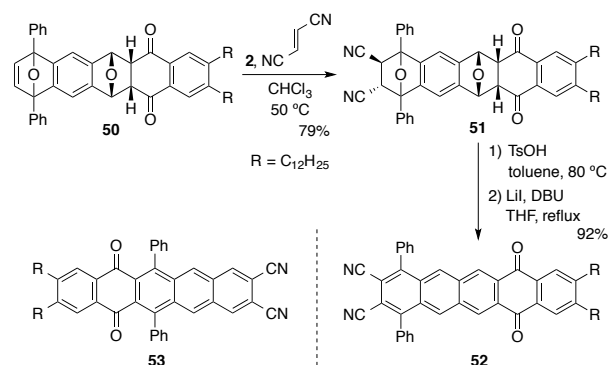


Fig. 3 Order of the reactivity.

さらに、環選択的に合成した環付加体の左側の部位にイソベンゾフランを再度発生させ、二回目の環付加反応を行うことにより、位置選択的に官能基を導入することができた。例えば、環付加体 **50** にフマロニトリルの共存下でテトラジンを作用させるとジシアノ体 **51** が選択的に得られた。これを二段階で芳香族化させることにより、対応するテトラセンキノンへと誘導できた(スキーム 15)。

この一連の変換で重要なことは、作用させる補足剤の順序を変えることによって、**52** とは位置異性体の関係にあるテトラセンキノン **53** の合成が可能なことである。このように、環選択的なイソベンゾフランの発生を鍵として、二方向への環の伸長と官能基化を選択的に行うことにより、多置換芳香族化合物の位置異性体の相補的な変換を達成した。

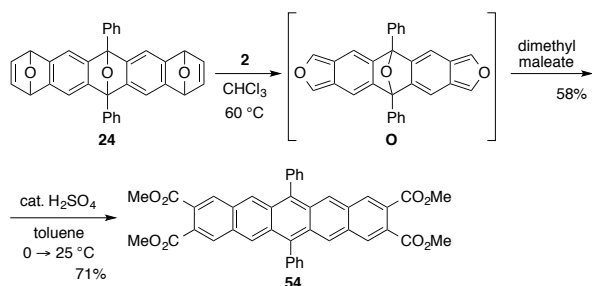


Scheme 15 Second [4+2] cycloaddition.

### 2.4 置換ペンタセンの合成

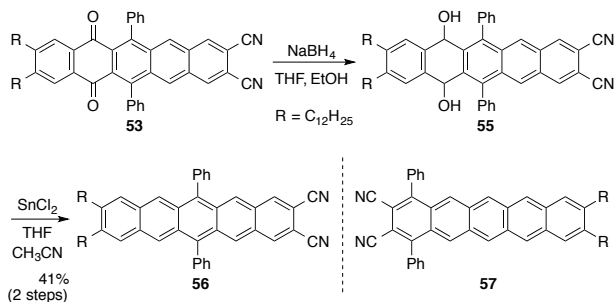
イソベンゾフランを合成ブロックとする多環式芳香族骨格構築のための三つのアプローチを示したが、これらの応用・展開として有機半導体材料として高い関心を集めている置換ペンタセンへの変換を行った。まず、ベンザ

インの多重環付加反応により得られる環付加体 **24** よりビスイソベンゾフラン **O** を発生させ、これをマレイン酸ジメチルで補足した後、酸性で芳香族化すると、4つのエステル基を持つ電子受容型のペンタセン **54** が得られた<sup>6)</sup>。



Scheme 16 Dual [4+2] cycloaddition of bis-isobenzofuran into the substituted pentacene.

また、環選択的なイソベンゾフランの発生を利用して合成した長鎖アルキル基を持つテトラセンキノン **53** を出発物質として、この還元的な芳香族化を含む数工程の変換により、可溶性ペンタセン **56** へと誘導した（スキーム 17）<sup>28)</sup>。この化合物の  $\text{CH}_2\text{Cl}_2$  溶液を空气中・非遮光下で放置し、UV-vis スペクトルより化学的安定性を調べたところ、その半減期は約 288 分であることがわかった<sup>29)</sup>。一方、テトラセンキノン **52** を用いた同様の変換により、**56** の位置異性体に相当するペンタセン **57** を合成することができた。この化合物はペンタセン **56** とは対照的に溶液中で直ちに酸化された。

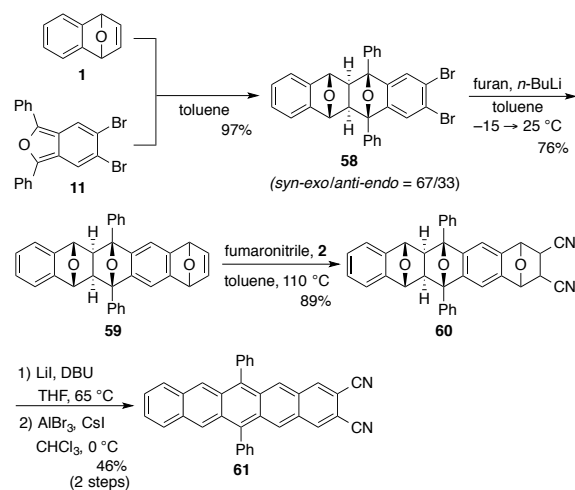


Scheme 17 Selective synthesis of substituted pentacenes.

さらに、イソベンゾフランとエポキシナフタレンの環付加反応とベンザインの環付加反応を組み合わせると多環式骨格を構築した後、適切な条件で芳香族化し、電子受容型ペンタセン **61** を簡便に合成した（スキーム 18）<sup>25,30)</sup>。この合成では、二つの臭素原子を骨格伸長のための足がかりとしてイソベンゾフランに導入し、エポキシナフタレンとの環付加反応を行った後、これをベンザインドナー部位として環付加反応に利用することによってペンタセン骨格の迅速な構築が可能になっている。

このようにイソベンゾフランを合成ブロックとする反

応集積化により、現在までに電子受容型ペンタセン、ドナー・アクセプター型ペンタセン、可溶性ペンタセンの合成に成功しており、置換ペンタセンライブラリーの構築が可能である。これらの手法では、単純な出発物質から鍵中間体（ポリアセン前駆体）を簡便に合成できるため、実用化の観点から重要である。現在、合成した置換ポリアセンの物性研究を行っており、得られる知見を新たな分子設計にフィードバックし、この方法論の完成度を高めていきたいと考えている。



Scheme 18 Synthesis of a substituted pentacene.

## おわりに

芳香族化合物の合成はベンゼンの発見以来、100年以上もの長い歴史を持つが、今なお狙った位置に望みの官能基や環構造を導入できる優れた合成手法が乏しいというのが現状である。そのため、高次構造の構築を目指す場合、その難易度は指数関数的に増大し、必然的に合成できる分子群が限定されてしまっている。このような状況の下、通常取り扱いが難しいとされる高反応性分子を積極的に取り上げ、その性質をうまく引き出すことによって、これらが得意とする自発的な反応性・骨格変換を活用した優れた合成手法が開拓できる（はず）というのが、本研究の骨子である。実際、イソベンゾフランの単離・精製法の発見を契機として、用事調整では難しかったベンザインとの反応が可能になり、反応の連続性と収束性を確保した多環式芳香族骨格構築法の開発に繋がった。また、エポキシナフタレンを反応パートナーとする反応集積化では、立体経路を丁寧に調べることによって、これまで難しいとされていた環付加体の芳香族化が可能であることを明らかにし、これを利用して置換テトラセンや置換ペンタセンの合成を達成した。これらはいずれもイソベンゾフランの合成的有用性の一端を示しているものであるが、今後、

イソベンゾフランを合成ブロックとする反応集積化を駆使して、ナノスケールの領域を視野にいたした多様な高次縮環芳香族化合物の合成と機能性分子創製への展開が可能になるものと期待している。

**謝 辞** 本研究は、筆者が2008年4月に関西学院大学に赴任後、新たな研究テーマとして開始したものである。本研究で得られた成果は、学生諸子の日々の努力と精力的な実験によるものであり、ここに深謝します。特に、本研究で見出した骨格構築法の発展に大きく貢献し、また研究室の立ち上げにも深く関わった羽田大志氏には心から感謝申し上げます。

また、本研究は日本学術振興会科学研究費補助金、文部科学省科学研究費補助金新学術領域研究「反応集積化の合成化学 革新的手法の開拓と有機物質創成への展開」、戦略的創造推進事業さきがけ、戦略的創造推進事業 act-c からの支援により実施したものであり、深く感謝いたします。

## 文 献

- 1) (a) A. O. Patil, A. J. Heeger, F. Wudl, *Chem. Rev.*, **88**, 183 (1988). (b) J. Roncali, *Chem. Rev.*, **97**, 173 (1997). (c) W. Friedrichsen, *Adv. Heterocycl. Chem.*, **26**, 135 (1980). (d) W. Friedrichsen, *Adv. Heterocycl. Chem.*, **1999**, **73**, 1. (e) B. Rickborn, In *Advances in Theoretically Interesting Molecules*; R. P. Thummel, Ed., JAI Press, Greenwich, 1989, Vol. 1, pp. 1–134. (f) D. Wege, In *Advances in Theoretically Interesting Molecules*; R. P. Thummel, Ed., JAI Press, Greenwich, 1998, Vol. 4, pp. 1–52.
- 2) (a) P. Binger, P. Wedemann, R. Goddard, U. H. Brinker, *J. Org. Chem.*, **61**, 6462 (1996). (b) R. Rodrigo, *Tetrahedron*, **44**, 2093 (1988). (c) H. N. C. Wong, *Acc. Chem. Res.*, **22**, 145 (1989). (d) Y.-M. Man, T. C. W. Mak, H. N. C. Wong, *J. Org. Chem.*, **55**, 3214 (1990). (e) S.-H. Chan, C.-Y. Yick, H. N. C. Wong, *Tetrahedron*, **58**, 9413 (2002). (f) J. E. Rainbolt, G. P. Miller, *J. Org. Chem.*, **72**, 3020 (2007).
- 3) (a) R. N. Warrener, *J. Am. Chem. Soc.*, **93**, 2346 (1971). (b) R. N. Warrener, M. Shang, D. N. Butler, *Chem. Commun.*, 1550 (2001). (c) A. Sygula, R. Sygula, P. W. Rabideau, *Org. Lett.*, **8**, 5909 (2006). (d) B. J. Pei, W. H. Chan, A. W. M. Lee, *Org. Lett.*, **13**, 1774 (2011).
- 4) この論文中で、反応の一次生成物であるピリダジン **4** を真空熱分解の条件に付すと(120 °C, 0.1 mm), イソベンゾフラン **5** が純粋に得られることが述べられている。
- 5) 生成物である 5,6-ジブromoイソベンゾフラン **8** のクロロホルム溶液を脱気せずに室温で1日攪拌すると、4,5-ジブromoフタルアルデヒドが収率30%で得られる。
- 6) H. Haneda, S. Eda, M. Aratani, T. Hamura, *Org. Lett.*, **16**, 286 (2014).
- 7) (a) G. Wittig, L. Pohmer, *Chem. Ber.*, **89**, 1334 (1956). (b) M. P. Cava, M. J. Mitchell, A. A. Deana, *J. Org. Chem.*, **25**, 1481 (1960). (d) J. T. Sharp, C. E. D. Skinner, *Tetrahedron Lett.*, **27**, 869 (1986).
- 8) T. Hamura, R. Nakayama, *Chem. Lett.*, **42**, 1013 (2013).
- 9) The successive process is classified as *time integration*, where a sequence of reactions is conducted in one-pot by adding components at intervals. For integration of reactions, see: S. Suga, D. Yamada, J.-i. Yoshida, *Chem. Lett.*, **39**, 404 (2010).
- 10) A convenient single-step synthesis of *symmetrical* 1,3-diarylisobenzofuran was developed. However, *unsymmetrical* derivatives could not be prepared by this method, see: F. Benderradji, M. Nechab, C. Einhorn, J. Einhorn, *Synlett*, 2035 (2006).
- 11) H. Nemoto, *Chem. Pharm. Bull.*, **55**, 961 (2007).
- 12) (a) G. Mehta, S. Kotha, *Tetrahedron*, **57**, 625 (2001). (b) A. K. Sadana, R. K. Saini, W. E. Billups, *Chem. Rev.*, **103**, 1539 (2003).
- 13) For the rearrangement reactions of cyclobutanols, see: (a) M. F. Schlecht, in *Comprehensive Organic Synthesis*, ed. B. M. Trost, I. Fleming and S. V. Ley, Pergamon, Oxford, UK, 1991, vol. 7, pp. 824–826; (b) N. Y. Fu, S. H. Chan, in *The Chemistry of Cyclobutanes*, ed. Z. Rappoport and J. F. Libeman, Wiley, Chichester, 2005, vol. 1, pp. 357–440.
- 14) K. Asahina, S. Matsuoka, R. Nakayama, T. Hamura, *Org. Biomol. Chem.*, **12**, 9773 (2014).
- 15) For a related oxidative ring cleavage of cyclobutanols, see: H. Fujioka, H. Komatsu, A. Miyoshi, K. Murai, Y. Kita, *Tetrahedron Lett.*, **52**, 973 (2011).
- 16) Related conversion of keto-aldehydes to isobenzofurans via nucleophilic addition of an arylmagnesium halide was recently developed, see: J. Jacq, C. Einhorn, J. Einhorn, *Org. Lett.*, **10**, 3757 (2008).
- 17) For selected reviews on polyacenes, see: (a) M. Bendikov, F. Wudl, D. F. Perepichka, *Chem. Rev.*, **104**, 4891 (2004). (b) J. E. Anthony, *Chem. Rev.*, **106**, 5028 (2006). (c) J. E. Anthony, *Angew. Chem.*, **120**, 460 (2008); *Angew. Chem. Int. Ed.*, **47**, 452 (2008). (d) H. F. Bettinger, *Pure Appl. Chem.*, **82**, 905 (2010).
- 18) For selected reviews on arynes: (a) R. W. Hoffmann, *Dehydrobenzene and Cycloalkynes*, Academic, New York, 1967. (b) S. V. Kessar, In *Comprehensive Organic Synthesis*; B. M. Trost, Ed., Pergamon: Oxford, U. K., 1991, Vol. 4, pp. 483–515. (c) H. Pellissier, M. Santelli, *Tetrahedron*, **59**, 701 (2003). (d) H. H. Wenk, M. Winkler, W. Sander, *Angew. Chem. Int. Ed.*, **42**, 502 (2003). (e) H. Yoshida, K. Takaki, *Synlett*, **23**, 1725 (2012). (f) A. Bhunia, S. Yetra, R. A. T. Biju, *Chem. Soc. Rev.*, **41**, 3140

- (2012). (g) A. V. Dubrovskiy, N. A. Markina, R. C. Larock, *Org. Biomol. Chem.*, 11, 191 (2013).
- 19) For selected examples of halogen–lithium exchange of functionalized arenes, see: (a) J. Clayden, *Organolithiums: Selectivity for Synthesis*, Tetrahedron Organic Chemistry Series, Pergamon, Oxford, 2002, Vol. 23, pp. 111–147. (b) P. Beak, D. J. Allen, *J. Am. Chem. Soc.*, 114, 3420 (1992). (c) C. Nájera, J. M. Sansano, M. Yus, *Tetrahedron*, 59, 9255 (2003). (d) M. Dabrowski, J. Kubicka, S. Lulinski, Serwatowski, *J. Tetrahedron*, 61, 6590 (2005).
- 20) For selected reactions of *o*-dihalobenzenes with *n*-BuLi, see: (a) H. Gilman, R. D. Gorsich, *J. Am. Chem. Soc.*, 78, 2217 (1956). (b) L. S. Chen, G. J. Chen, C. Tamborski, *J. Organomet. Chem.*, 193, 283 (1980). (c) K. C. Caster, C. G. Keck, R. D. Walls, *J. Org. Chem.*, 66, 2932 (2001). (d) J. W. Coe, M. C. Wirtz, C. G. Bashore, J. Candler, *Org. Lett.*, 6, 1589 (2004).
- 21) (a) H. Hart, D. Ok, *J. Org. Chem.*, 51, 979 (1986). (b) H. Hart, C.-Y. Lai, G. Nwokogu, S. Shamouilian, A. Teuerstein, C. Zlotogorski, *J. Am. Chem. Soc.*, 102, 6649 (1980). (c) G. E. Morton, A. G. M. Barrett, *J. Org. Chem.*, 70, 3525 (2005). (d) I. I. Schuster, L. Cracium, D. M. Ho, R. A. Pascal, Jr., *Tetrahedron*, 58, 8875 (2002). (e) H. M. Duong, M. Bendikov, D. Steiger, Q. Zhang, G. Sonmez, J. Yamada, F. Wudl, *Org. Lett.*, 5, 4433 (2003). (f) T. Hamura, T. Arisawa, T. Matsumoto, K. Suzuki, *Angew. Chem. Int. Ed.*, 45, 6842 (2006).
- 22) S. Eda, T. Hamura, *Molecules*, 62, 19449 (2015).
- 23) (a) A. Menzek, L. Kelebekli, A. Altumdas, E. Sahin, F. Polat, *Helv. Chim. Acta*, 91, 2367 (2008). (b) D. Margetic, M. E. Maksic, P. Troselj, Z. Marinic, *J. Fluor. Chem.*, 131, 408 (2010).
- 24) (a) T. Sakai, K. Kanematsu, K. Iizuka, *Heterocycles*, 3, 109 (1975). (b) H. Meier, B. Rose, *Liebigs Ann.*, 663 (1997). (c) N. Pichon, A. H. Marchand, P. Mailliet, J. Maddaluno, *J. Org. Chem.*, 69, 7220 (2004). (d) W-X. Niu, E-Q. Yang, Z-F. Shi, X-P. Cao, D. Kuck, *J. Org. Chem.*, 77, 1422 (2012).
- 25) S. Eda, F. Eguchi, H. Haneda, T. Hamura, *Chem. Commun.*, 51, 5963 (2015).
- 26) (a) C. A. Grob, P.W. Schiess, *Angew. Chem., Int. Ed. Engl.*, 6, 1 (1967). (b) C. A. Grob, *Angew. Chem., Int. Ed. Engl.*, 8, 535 (1969). (c) K. Prantz, J. Mulzer, *Chem. Rev.*, 110, 3741 (2010).
- 27) (a) J. Luo, H. Hart, *J. Org. Chem.*, 53, 1341 (1988). (b) H. Qu, W. Cui, J. Li, J. Shao, C. Chi, *Org. Lett.*, 13, 924 (2011).
- 28) R. Akita, K. Kawanishi, T. Hamura, *Org. Lett.*, 17, 3094 (2015).
- 29) (a) I. Kaur, W. Jia, R. P. Kopreski, S. Selvarasah, M. R. Dokmeci, C. Pramanik, N. E. McGruer, G. P. Miller, *J. Am. Chem. Soc.*, 130, 16274 (2008). (b) J. Wang, K. Liu, Y. Y. Liu, C. L. Song, Z. F. Shi, J. B. Peng, H. L. Zhang, X. P. Cao, *Org. Lett.*, 11, 2563 (2009).
- 30) For selected reports on synthesis of 6,13-substituted pentacenes, see: (a) J. E. Anthony, J. S. Brooks, D. L. Eaton, S. R. Parkin, *J. Am. Chem. Soc.*, 123, 9482 (2001). (b) M. M. Payne, J. H. Delcamp, S. R. Parkin, J. E. Anthony, *Org. Lett.*, 6, 1609 (2004). (c) C. R. Swartz, S. R. Parkin, J. E. Bullock, J. E. Anthony, A. C. Mayer, G. G. Malliaras, *Org. Lett.*, 7, 3163 (2005). (d) Q. Miao, X. Chi, S. Xiao, R. Zeis, M. Lefenfeld, T. Siegrist, M. L. Steigerwald, C. Nuckolls, *J. Am. Chem. Soc.*, 128, 1340 (2006). (e) K. Ono, H. Totani, T. Hiei, A. Yoshino, K. Saito, K. Eguchi, M. Tomura, J. Nishida, Y. Yamashita, *Tetrahedron*, 63, 9699 (2007). (f) S. S. Palayangoda, R. Mondal, B. K. Shah, D. C. Neckers, *J. Org. Chem.*, 72, 6584 (2007). (g) Y. Wang, N. Fu, S. Chan, H. Lee, H. N. C. Wong, *Tetrahedron*, 63, 8586 (2007). (h) D. Lehnerr, R. McDonald, R. R. Tykwinski, *Org. Lett.*, 10, 4163 (2008). (i) D. Lehnerr, A. H. Murray, R. McDonald, M. J. Ferguson, R. R. Tykwinski, *Chem. Eur. J.*, 15, 12580 (2009). (j) I. Kaur, W. Jia, R. P. Kopreski, S. Selvarasah, M. R. Dokmeci, C. Pramanik, N. E. McGruer, G. P. Miller, *J. Am. Chem. Soc.*, 130, 16274 (2008). (k) J. Wang, K. Liu, Y. Liu, C. Song, Z. Shi, J. Peng, H. Zhang, X. Cao, *Org. Lett.*, 11, 2563 (2009). (l) M. L. Tang, J. H. Oh, A. D. Reichardt, Z. Bao, *J. Am. Chem. Soc.*, 131, 3733 (2009). (m) S. Li, L. Zhou, K. Nakajima, K. Kanno, T. Takahashi, *Chem. Asian J.*, 5, 1620 (2010).

羽村 季之 関西学院大学工学部・教授 理学博士  
 [経歴] 1998 年慶應義塾大学大学院理工学研究科化学専攻修士課程修了, 2000 年東京工業大学大学院理工学研究科化学専攻博士後期課程中退, 2000 年東京工業大学大学院理工学研究科化学専攻助手, 2007 年同助教, 2007 年科学技術振興機構・さきがけ「構造制御と機能」兼任研究者, 2008 年関西学院大学工学部化学科准教授, 2013 年 4 月より現職。2007 年日本化学会進歩賞, 2008 年 Thieme Chemistry Journal Award, 2012 年文部科学大臣表彰若手科学者賞, 2012 年 Banyu Chemist Award など。[専門] 有機合成化学, 構造有機化学  
 [連絡先] e-mail: thamura@kwansei.ac.jp

*Communication*

## Selective Halogen-Lithium Exchange of 1,2-Dihaloarenes for Successive [2+4] Cycloadditions of Arynes and Isobenzofurans

Shohei Eda and Toshiyuki Hamura \*

Department of Applied Chemistry for Environment, School of Science and Technology,  
Kwansei Gakuin University, 2-1 Gakuen, Sanda, Hyogo 669-1337, Japan;  
E-Mail: shoheie816@gmail.com

\* Author to whom correspondence should be addressed; E-Mail: thamura@kwansei.ac.jp;  
Tel./Fax: +81-79-565-7591.

Academic Editor: Hiroto Yoshida

*Received: 1 October 2015 / Accepted: 20 October 2015 / Published: 23 October 2015*

---

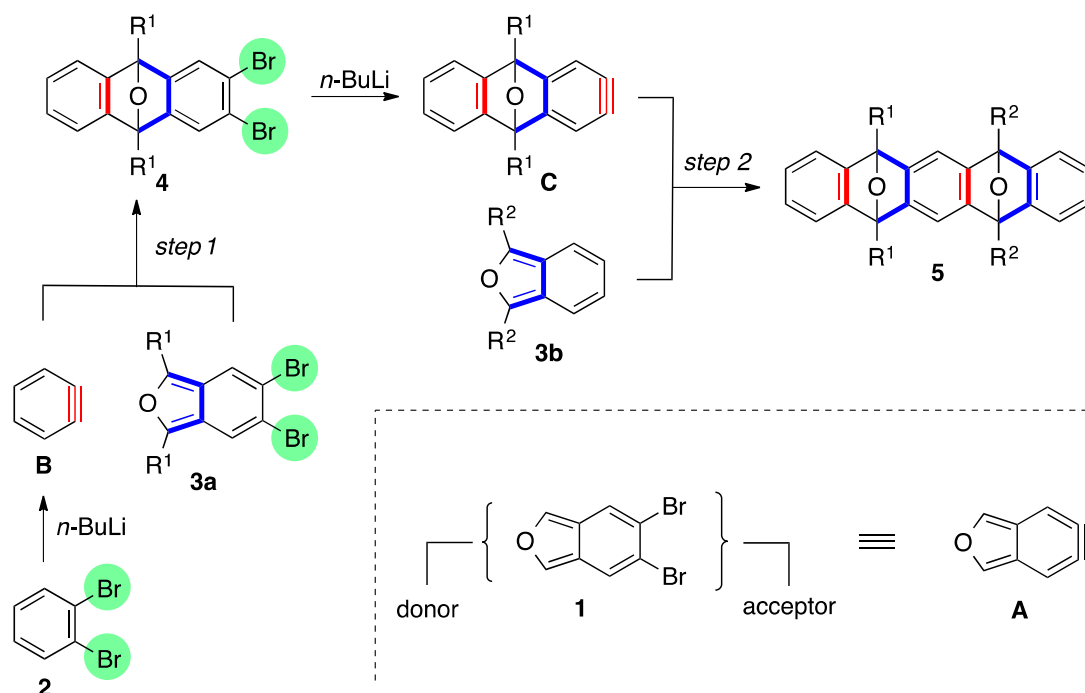
**Abstract:** Successive [2+4] cycloadditions of arynes and isobenzofurans by site-selective halogen-lithium exchange of 1,2-dihaloarenes were developed, allowing the rapid construction of polycyclic compounds which serve as a useful synthetic intermediates for the preparation of various polyacene derivatives.

**Keywords:** aryne; isobenzofuran; [2+4] cycloaddition; 1,2-dihaloarenes; polyacene; halogen-lithium exchange

---

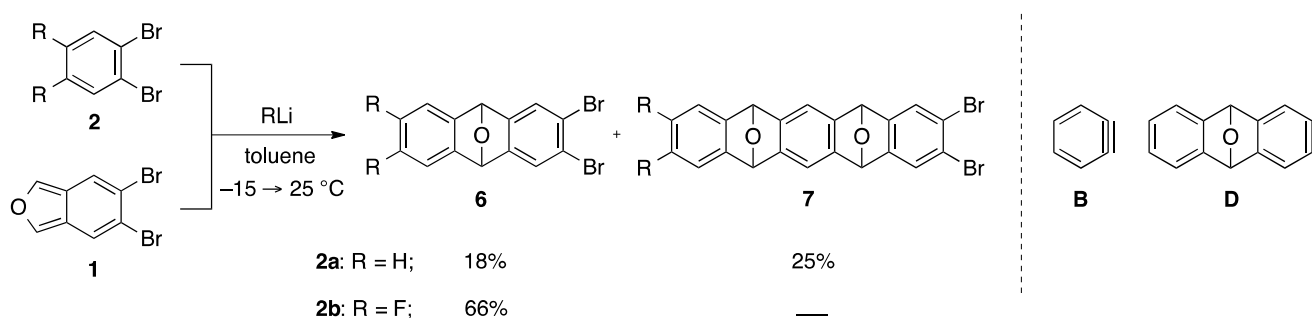
### 1. Introduction

We previously reported dual annulations of dibromoisobenzofuran **1**, a formal equivalent of didehydroisobenzofuran **A**, via [2+4] cycloadditions of aryne [1–9] and isobenzofuran [10–23] (Scheme 1). Selective bromine–lithium exchange from the starting two dibromides **2** and **3** enables the tandem generation of arynes and dual cycloadditions with two different arynophiles (step 1 and step 2). Importantly, successive process can be performed in one-pot by sequential addition of the arynophiles, affording various functionalized polycyclic aromatic compounds [24–26].



**Scheme 1.** Successive [2+4] cycloadditions of arynes and isobenzofurans.

This sequential cycloaddition, however, has a limitation in that the introduction of electron withdrawing groups on the benzene ring in aryne precursor (e.g., **2b**) is required to restrict the competitive formation of the dual cycloadduct (Scheme 2). In fact, treatment of dibromobenzene **2a** with *n*-BuLi in the presence of dibromoisobenzofuran **1** gave cycloadduct **6a** in 18% yield, accompanied by a sizable amount of bis-cycloadduct **7a** (25%). This result indicates that in addition to the generation of benzyne **B**, similar reactivity of two dibromides **2a** and **6a** with *n*-BuLi caused the competitive generation of aryne **D** from the initially formed cycloadduct **6a**. In this case, excess amounts of the starting material **2a** (5.0 equiv.) improved the yields of the mono-cycloadduct **6a** (42%) by selective generation of benzyne **B**. However, it is not an essential solution, since existing of the large amount of the starting material **2a** disturbed the second [2+4] cycloaddition with **6a** in a one-pot process.



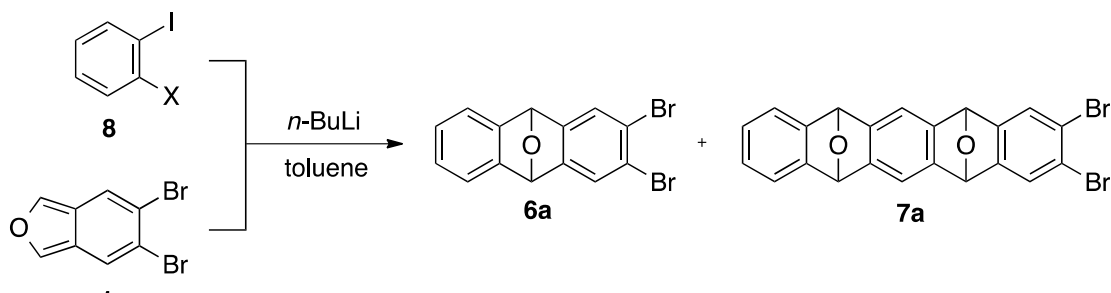
**Scheme 2.** Previous study on the [2+4] cycloaddition of benzyne and dibromoisobenzofuran.

To expand the synthetic utility of this successive processes, we reexamined [2+4] cycloadditions of aryne and isobenzofuran including the parent benzyne species **B** as an initial cycloaddition (*vide supra*). The key to achieve this sequential process is search for a suitable aryne precursor to enable the selective halogen-lithium exchange [27–30]. Along these lines, we select 1,2-dihaloarenes as an aryne precursor



that use of 1,2-dihaloarenes **8a–8c** possessing a more electropositive iodine atom is favored as a benzyne precursor over the bromide **2a** in terms of selectivity and yield.

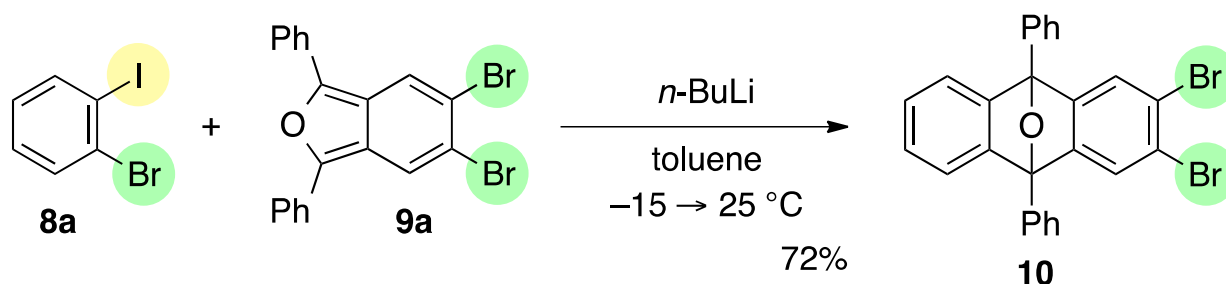
**Table 1.** Initial model study.



Entry	X	Temp. (°C)	Yield of 6a (%)	Yield of 7a (%) <sup>1</sup>
1	<b>8a</b> : Br	−78	60	9
2	<b>8a</b> : Br	−15→25	78	1
3	<b>8b</b> : Cl	−78	51	9
4	<b>8b</b> : Cl	−15→25	62	9
5	<b>8c</b> : F	−78	41	4
6	<b>8c</b> : F	−15→25	44	11

<sup>1</sup> The cycloadduct **7a** was obtained as a mixture of diastereomers (ds: 44/56~58/42).

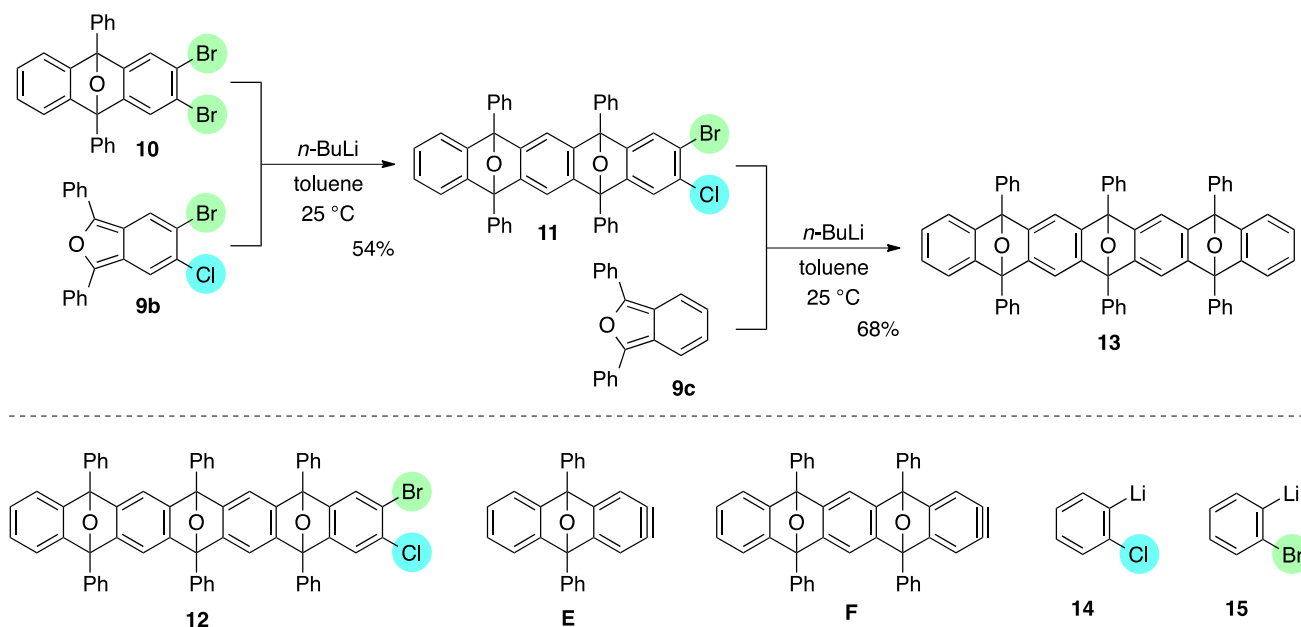
Further study revealed that 5,6-dibromo-1,3-diphenylisobenzofuran (**9a**) was also a suitable reactive partner, which cyclized with benzyne **B**, generated by treatment of iodobromide **8a** with *n*-BuLi (toluene, −15→25 °C), affording substituted epoxyanthracene **10** in 72% yield (Scheme 4).



**Scheme 4.** [2+4] cycloaddition of benzyne **B** and isobenzofuran **9a**.

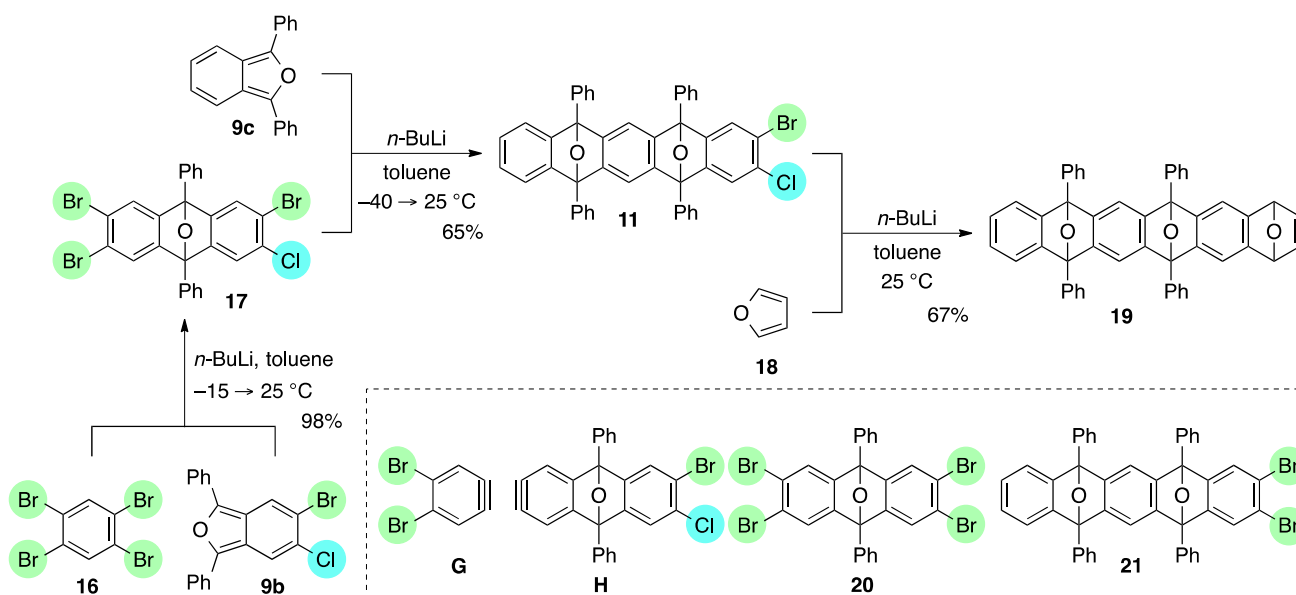
We next examined second [2+4] cycloaddition of aryne generated from the first cycloadduct. To explore another mode of selective halogen-lithium exchange of 1,2-haloarenes, *i.e.*, reactivity control by adjacent halogen (type 2 in Scheme 3) [38,39], two different halogens were introduced to isobenzofuran. Upon treatment of dibromide **10** with 1.3 equiv. of *n*-BuLi in the presence of 1.1 equiv. of 5-bromo-6-chloro-1,3-diphenylisobenzofuran (**9b**) [40] (toluene, 25 °C), aryne **E** was selectively generated and subsequent trapping with **9b** gave mono-cycloadduct **11** in 54% yield as a mixture of diastereomers (Scheme 5). In this case, bis-cycloadduct **12**, caused by the generation of aryne **F**, was produced in 16% yield. This observed site-selectivity in the bromine-lithium exchange among three bromides **9b**, **10**, and **11** was unexpected, because (2-chlorophenyl)lithium **14** was more thermodynamically stable than (2-bromophenyl)lithium **15** by existing of a more electron withdrawing chlorine atom, which would

suggest the favorable formation of aryne **F** over that of aryne **E** [41]. Aside from the unanticipated site-selectivity in this bromine-lithium exchange, further introduction of fused ring onto the dual cycloadduct **11** was realized by the third [2+4] cycloaddition of aryne **F** and isobenzofuran **9c** by treatment of **11** with *n*-BuLi under the similar conditions, affording polycyclic compound **13** in 66% yield, which is expected to be suitably converted to substituted heptacenes [42–45].



**Scheme 5.** Mono-directional [2+4] cycloadditions of arynes.

Moreover, it is worth mentioning that 1,2,4,5-tetrabromobenzene (**16**) nicely worked as a reactive platform [46–51], allowing bi-directional cycloadditions in an unsymmetrical manner (Scheme 6). The essential point of this sequential process is using 5-bromo-6-chloro-1,3-diphenylisobenzofuran (**9b**) to differentiate the reactivity of the two dihalogenated sites in the bis-aryne equivalent **17**, which was efficiently obtained by the first [2+4] cycloaddition of dibromobenzene **G** and isobenzofuran **9b**. It is notable that perfect site-selectivity was observed in the bromine-lithium exchange of **16**, selectively generating the dibromobenzene **G** [52]. The cycloadduct **17**, thus obtained, again underwent the selective bromine-lithium exchange at the dibromo side in **17**, as a related reaction of dibromide **10** and isobenzofuran **9b** (Scheme 5), generating the bromochlorobenzene **H**, which was intercepted by **9c** to afford the unsymmetrical cycloadduct **11** in 65% yield, accompanied by a formation of dual cycloadduct **21** (20%). Although the observed selectivity in the reaction of **17** was moderate (**11/21** = 3.2:1), use of bis-aryne equivalent **17** with an unsymmetric form turned out to be indispensable to discriminate the reactivity of the two dihalogenated sites in **17**, because the corresponding reaction of the symmetrical tetrabromide **20** resulted in the decreased selectivity in the formation of the desired mono-cycloadduct **21** and bis-cycloadduct **13** (**21/13** = 1.5:1). Final [2+4] cycloaddition of aryne **F**, generated from the bis-cycloadduct **11**, with furan **18** under the above-mentioned conditions was satisfied, efficiently affording the tris-cycloadduct **19** with a various synthetic opportunity for further introduction of fused rings and/or functionalization.



Scheme 6. Bi-directional [2+4] cycloadditions of aryne.

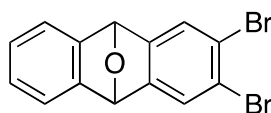
### 3. Experimental Section

#### General Information

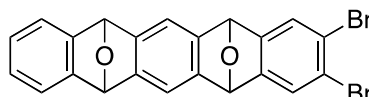
All experiments dealing with air- and moisture-sensitive compounds were conducted under an atmosphere of dry argon. Toluene (anhydrous; Wako Pure Chemical Industries, Ltd., Osaka, Japan) was used as received. For thin-layer chromatography (TLC) analysis, Merck pre-coated plates (silica gel 60 F<sub>254</sub>, Art 5715, 0.25 mm, Merck Japan, Tokyo, Japan) were used. For flash column chromatography, silica gel 60 N (spherical, neutral, 63–210  $\mu\text{m}$ ) from Kanto Chemical (Tokyo, Japan) was used. Silica gel preparative TLC (PTLC) was performed on Merck silica gel 60 PF<sub>254</sub> (Art 7747).

<sup>1</sup>H-NMR and <sup>13</sup>C-NMR were measured on a JNM ECA-300 and a JNM ECX-500II spectrometer (JEOL, Tokyo, Japan). Attenuated Total Reflectance Fourier Transformation Infrared (ATR-FTIR) spectra were recorded on a FT/IR-4200 FT-IR Spectrometer (JASCO, Tokyo, Japan). High resolution mass spectra were obtained with a JEOL JMS 700 spectrometer and a JEOL AccuTOF LC-plus JMS-T100LP. Melting point (mp) determinations were performed by using a MP-S3 instrument (Yanako, Kyoto, Japan) or a MPA100 Automated Melting Point System (OptiMelt, Sunnyvale, CA, USA) and are uncorrected.

Typical Procedure for [2+4] Cycloadditions of Aryne and Isobenzofuran: Synthesis of 2,3-Dibromo-9,10-dihydro-9,10-epoxyanthracene (**6a**). To a mixture of 1-bromo-2-iodobenzene (**8a**, 70.0 mg, 0.247 mmol) and isobenzofuran **1** (71.8 mg, 0.260 mmol) in toluene (2.0 mL) was added *n*-BuLi (1.60 M in *n*-hexane, 0.19 mL, 0.30 mmol) at  $-15^\circ\text{C}$ , and the reaction was warmed up to  $25^\circ\text{C}$ . After 5 min, the reaction was stopped by adding water. The products were extracted with EtOAc ( $\times 3$ ), and the combined organic extracts were washed with brine, dried ( $\text{Na}_2\text{SO}_4$ ), and concentrated in vacuo. The residue was purified by PTLC (hexane/EtOAc = 8/2) to give 2,3-dibromo-9,10-dihydro-9,10-epoxyanthracene (**6a**, 67.9 mg, 78.1%) as a white solid and 2,3-dibromo-5,7,12,14-tetrahydro-5,14:7,12-diepoxy-pentacene (**7a**, 1.2 mg, 1.0%, ds: 17/83) as a mixture of diastereomers.



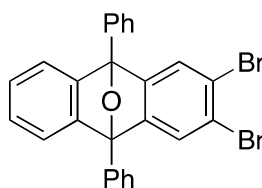
**Compound 6a:** Mp 208.5–209.1 °C (hexane/CHCl<sub>3</sub>); <sup>1</sup>H-NMR (CDCl<sub>3</sub>, δ) 6.01 (s, 2H), 7.06 (dd, 2H,  $J_1 = 3.1$  Hz,  $J_2 = 5.2$  Hz), 7.33 (dd, 2H,  $J_1 = 3.1$  Hz,  $J_2 = 5.2$  Hz), 7.55 (s, 2H); <sup>13</sup>C-NMR (CDCl<sub>3</sub>, δ) 82.0, 120.7, 121.6, 125.7, 126.5, 146.9, 149.2; IR (ATR) 3027, 1569, 1459, 1259, 1085, 953, 832, 762 cm<sup>-1</sup>; <sup>-</sup>HRMS (FAB)  $m/z$  351.8925 (351.8922 calcd for C<sub>14</sub>H<sub>8</sub>Br<sub>2</sub>O, M<sup>+</sup>).



**Compound 7a**, less polar diastereomer:  $R_f$  0.30 (hexane/CH<sub>2</sub>Cl<sub>2</sub> = 4/6); Mp decomposed at 300 °C; <sup>1</sup>H-NMR (CDCl<sub>3</sub>, δ) 5.90 (s, 2H), 5.95 (s, 2H), 7.00 (dd, 2H,  $J_1 = 3.1$  Hz,  $J_2 = 5.5$  Hz), 7.29 (dd, 2H,  $J_1 = 3.1$  Hz,  $J_2 = 5.5$  Hz), 7.31 (s, 2H), 7.53 (s, 2H); <sup>13</sup>C-NMR (CDCl<sub>3</sub>, δ) 81.9, 82.4, 114.2, 120.4, 121.6, 125.6, 126.0, 146.1, 147.8, 148.1, 149.2; IR (ATR) 3016, 1569, 1457, 1265, 1085, 949, 832, 772 cm<sup>-1</sup>; <sup>-</sup>HRMS (FAB)  $m/z$  468.9262 (468.9263 calcd for C<sub>22</sub>H<sub>13</sub>Br<sub>2</sub>O<sub>2</sub>, [M + H]<sup>+</sup>).

**Compound 7a**, more polar diastereomer:  $R_f$  0.13 (hexane/CH<sub>2</sub>Cl<sub>2</sub> = 4/6); Mp decomposed at 300 °C; <sup>1</sup>H-NMR (CDCl<sub>3</sub>, δ) 5.90 (s, 2H), 5.96 (s, 2H), 6.97 (dd, 2H,  $J_1 = 3.1$  Hz,  $J_2 = 5.2$  Hz), 7.27 (dd, 2H,  $J_1 = 3.1$  Hz,  $J_2 = 5.2$  Hz), 7.29 (s, 2H), 7.46 (s, 2H); <sup>13</sup>C-NMR (CDCl<sub>3</sub>, δ) 82.0, 82.5, 113.9, 120.5, 121.5, 125.6, 125.9, 146.0, 147.9, 149.2; IR (ATR) 3010, 1573, 1457, 1271, 1086, 952, 836, 754 cm<sup>-1</sup>; <sup>-</sup>HRMS (FAB)  $m/z$  468.9256 (468.9263 calcd for C<sub>22</sub>H<sub>13</sub>Br<sub>2</sub>O<sub>2</sub>, [M + H]<sup>+</sup>).

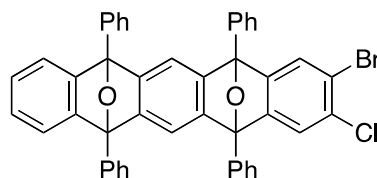
**2,3-Dibromo-9,10-diphenyl-9,10-epoxyanthracene (10).** According to the procedure described for the synthesis of cycloadduct **6a**, 1-bromo-2-iodobenzene (**8a**, 112 mg, 0.396 mmol), isobenzofuran **9a** (129 mg, 0.301 mmol) and *n*-BuLi (1.60 M in *n*-hexane, 0.25 mL, 0.40 mmol) gave, after purified by silica-gel flash column chromatography (hexane/CH<sub>2</sub>Cl<sub>2</sub>/Et<sub>2</sub>O = 98/1/1 → 96/3/1), cycloadduct **10** (110 mg, 72.4%) as a white solid.



**Compound 10:** Mp 167.6–168.5 °C (hexane/Et<sub>2</sub>O); <sup>1</sup>H-NMR (CDCl<sub>3</sub>, δ) 7.08 (dd, 2H,  $J_1 = 2.9$  Hz,  $J_2 = 5.7$  Hz), 7.38 (dd, 2H,  $J_1 = 2.9$  Hz,  $J_2 = 5.7$  Hz), 7.49–7.53 (m, 2H), 7.54 (s, 2H), 7.59–7.63 (m, 4H), 7.86–7.89 (m, 4H); <sup>13</sup>C-NMR (CDCl<sub>3</sub>, δ) 90.2, 120.7, 121.8, 125.6, 126.4, 126.5, 128.7, 129.0, 133.9, 149.2, 151.6; IR (ATR) 3030, 1599, 1499, 1295, 1036, 992, 871, 741 cm<sup>-1</sup>; <sup>-</sup>HRMS (DART)  $m/z$  502.9644 (502.9646 calcd for C<sub>26</sub>H<sub>17</sub>Br<sub>2</sub>O, [M + H]<sup>+</sup>).

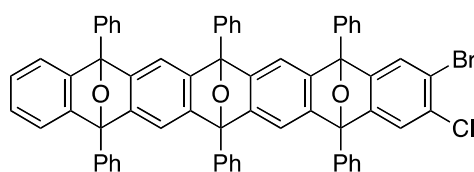
**2-Bromo-3-chloro-5,7,12,14-tetraphenyl-5,14:7,12-diepoxy-pentacene (11).** According to the procedure described for the synthesis of cycloadduct **6a**, cycloadduct **10** (75.6 mg, 0.150 mmol), isobenzofuran **9b** (63.2 mg, 0.165 mmol) and *n*-BuLi (1.60 M in *n*-hexane, 0.12 mL, 0.19 mmol) gave, after purification

by silica-gel flash column chromatography (hexane/CH<sub>2</sub>Cl<sub>2</sub>/Et<sub>2</sub>O = 96/3/1 → 88/9/3), 2-bromo-3-chloro-5,7,12,14-tetraphenyl-5,14:7,12-diepoxy-pentacene (**11**, 58.8 mg, 53.9%, ds. less polar/more polar = 46/54) and 2-bromo-3-chloro-5,7,12,14-tetraphenyl-5,14:7,12-diepoxy-pentacene (**12**, 23.7 mg, 15.9%) as a mixture of diastereomers, respectively. The diastereomers of **11** were separated by PTLC (hexane/toluene/CH<sub>2</sub>Cl<sub>2</sub>/Et<sub>2</sub>O = 82/10/6/2 X2), affording less polar **11** and more polar **11** as white solids.



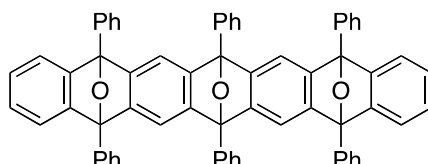
**Compound 11**, less polar: *R<sub>f</sub>* 0.38 (hexane/toluene/CH<sub>2</sub>Cl<sub>2</sub>/Et<sub>2</sub>O = 82/10/6/2, X2); Mp decomposed at 240 °C (MeOH/CHCl<sub>3</sub>); <sup>1</sup>H-NMR (CDCl<sub>3</sub>, δ) 6.96 (dd, 2H, *J*<sub>1</sub> = 2.9 Hz, *J*<sub>2</sub> = 5.2 Hz), 7.27 (dd, 2H, *J*<sub>1</sub> = 2.9 Hz, *J*<sub>2</sub> = 5.2 Hz), 7.29 (s, 1H), 7.33 (s, 2H), 7.44 (s, 1H), 7.46–7.51 (m, 4H), 7.56–7.60 (m, 8H), 7.77–7.79 (m, 4H), 7.83–7.86 (m, 4H); <sup>13</sup>C-NMR (CDCl<sub>3</sub>, δ) 90.2, 90.3, 90.5, 113.7, 119.3, 120.4, 122.6, 125.6, 125.8, 126.4, 126.6, 128.4, 128.7, 128.9, 129.1, 131.5, 133.70, 133.73, 134.6, 148.26, 148.34, 149.9, 150.15, 150.17, 150.6, 151.3; IR (ATR) 3059, 1607, 1500, 1308, 1083, 986, 867, 744 cm<sup>-1</sup>; <sup>-</sup>HRMS (ESI) *m/z* 749.0834 (749.0859 calcd for C<sub>46</sub>H<sub>28</sub>BrClNaO<sub>2</sub>, [M + Na]<sup>+</sup>).

**Compound 11**, more polar: *R<sub>f</sub>* 0.28 (hexane/toluene/CH<sub>2</sub>Cl<sub>2</sub>/Et<sub>2</sub>O = 82/10/6/2, X2); Mp decomposed at 230 °C (MeOH/CHCl<sub>3</sub>); <sup>1</sup>H-NMR (CDCl<sub>3</sub>, δ) 7.02 (dd, 2H, *J*<sub>1</sub> = 2.9 Hz, *J*<sub>2</sub> = 5.2 Hz), 7.30 (s, 2H), 7.32–7.35 (m, 3H), 7.43–7.49 (m, 5H), 7.52–7.57 (m, 8H), 7.75–7.77 (m, 4H), 7.81–7.84 (m, 4H); <sup>13</sup>C-NMR (CDCl<sub>3</sub>, δ) 90.2, 90.3, 90.5, 113.49, 113.51, 119.3, 120.5, 122.7, 125.6, 125.7, 126.4, 126.5, 128.3, 128.7, 128.8, 129.0, 131.5, 133.7, 133.8, 134.6, 148.2, 148.3, 149.9, 150.0, 150.3, 150.8, 151.6; IR (ATR) 3065, 1607, 1498, 1311, 1082, 989, 863, 746 cm<sup>-1</sup>; <sup>-</sup>HRMS (ESI) *m/z* 749.0876 (749.0859 calcd for C<sub>46</sub>H<sub>28</sub>BrClNaO<sub>2</sub>, [M + Na]<sup>+</sup>).



**Compound 12** (a mixture of four diastereomers): <sup>1</sup>H-NMR (CDCl<sub>3</sub>, δ) 6.90–7.01 (m, 8H), 7.19–7.33 (m, 24H), 7.36–7.60 (m, 80H), 7.66–7.83 (m, 48H); <sup>13</sup>C-NMR (CDCl<sub>3</sub>, δ) 90.0, 90.05, 90.07, 90.09, 90.11, 90.14, 90.17, 90.19, 90.36, 90.39, 90.46, 90.50, 113.3, 113.4, 113.47, 113.51, 113.7, 113.8, 119.2, 119.3, 119.5, 119.6, 120.08, 120.11, 120.2, 120.4, 122.4, 122.5, 122.7, 125.4, 125.5, 125.55, 125.62, 125.7, 125.8, 125.97, 126.00, 126.07, 126.12, 126.2, 126.3, 126.42, 126.44, 126.5, 126.57, 126.64, 126.7, 128.16, 128.21, 128.3, 128.4, 128.5, 128.59, 128.63, 128.66, 128.72, 128.8, 128.86, 128.90, 128.92, 129.00, 129.03, 131.4, 131.5, 131.58, 131.63, 133.68, 133.72, 133.76, 133.83, 133.87, 133.90, 134.3, 134.38, 134.44, 134.70, 134.73, 134.78, 134.80, 147.99, 148.03, 148.1, 148.2, 148.26, 148.30, 148.4, 148.9, 148.98, 149.02, 149.1, 149.2, 149.4, 149.49, 149.52, 149.70, 149.73, 149.78, 149.80, 149.86, 149.94, 149.96, 150.02, 150.2, 150.3, 150.35, 150.42, 150.5, 150.6, 151.18, 151.24, 151.37, 151.39; IR (ATR) 3062, 1606, 1499, 1307, 1082, 983, 885, 748 cm<sup>-1</sup>; <sup>-</sup>HRMS (ESI) *m/z* 1017.1756 (1017.1747 calcd for C<sub>66</sub>H<sub>40</sub>BrClNaO<sub>3</sub>, [M + Na]<sup>+</sup>).

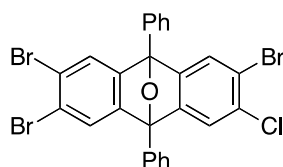
5,7,9,14,16,18-Hexaphenyl-5,18:7,16:9,14-triepoxyheptacene (**13**). According to the procedure described for the synthesis of cycloadduct **6a**, cycloadduct **11** (more polar) (35.1 mg, 0.0482 mmol), isobenzofuran **9c** (14.7 mg, 0.0544 mmol) and *n*-BuLi (1.60 M in *n*-hexane, 0.040 mL, 0.064 mmol) gave, after purification by silica-gel flash column chromatography (hexane/CH<sub>2</sub>Cl<sub>2</sub>/Et<sub>2</sub>O = 96/3/1→88/9/3), 5,7,9,14,16,18-hexaphenyl-5,18:7,16:9,14-triepoxyheptacene (**13**) as a mixture of diastereomers (29.0 mg, 68.0%, ds. less polar/more polar = 46/54). Those diastereomers were separated by PTLC (hexane/toluene/CH<sub>2</sub>Cl<sub>2</sub>/Et<sub>2</sub>O = 78/10/8/4, X4), affording less polar **13** and more polar **13** as white solids, respectively.



**Compound 13** (less polar): *R<sub>f</sub>* 0.55 (hexane/toluene/CH<sub>2</sub>Cl<sub>2</sub>/Et<sub>2</sub>O = 78/10/8/4, X4); Mp decomposed at 260 °C (MeOH/CHCl<sub>3</sub>); <sup>1</sup>H-NMR (CDCl<sub>3</sub>, δ): 6.92 (dd, 4H, *J*<sub>1</sub> = 2.9 Hz, *J*<sub>2</sub> = 5.2 Hz), 7.22 (s, 4H), 7.23 (dd, 4H, *J*<sub>1</sub> = 2.9 Hz, *J*<sub>2</sub> = 5.2 Hz), 7.44–7.49 (m, 6H), 7.52–7.56 (m, 12H), 7.72–7.75 (m, 4H), 7.79–7.82 (m, 8H); <sup>13</sup>C-NMR (CDCl<sub>3</sub>, δ) 90.4, 113.4, 120.3, 125.6, 126.5, 126.6, 128.2, 128.3, 128.8, 128.9, 134.6, 134.8, 149.2, 149.4, 150.1; IR (ATR) 3058, 1603, 1496, 1307, 974, 867, 747 cm<sup>-1</sup>; <sup>-</sup>HRMS (ESI) *m/z* 905.3020 (905.3032 calcd for C<sub>66</sub>H<sub>42</sub>NaO<sub>3</sub>, [M + Na]<sup>+</sup>).

**Compound 13** (more polar): *R<sub>f</sub>* 0.49 (hexane/toluene/CH<sub>2</sub>Cl<sub>2</sub>/Et<sub>2</sub>O = 78/10/8/4, X4); Mp decomposed at 250 °C (MeOH/CHCl<sub>3</sub>); <sup>1</sup>H-NMR (CDCl<sub>3</sub>, δ) 6.94 (dd, 2H, *J*<sub>1</sub> = 2.9 Hz, *J*<sub>2</sub> = 5.2 Hz), 6.96 (dd, 2H, *J*<sub>1</sub> = 2.9 Hz, *J*<sub>2</sub> = 5.2 Hz), 7.19 (s, 2H), 7.22–7.25 (m, 4H), 7.28 (s, 2H), 7.39–7.59 (m, 18H), 7.72–7.74 (m, 4H), 7.77–7.80 (m, 4H), 7.81–7.83 (m, 4H); <sup>13</sup>C-NMR (CDCl<sub>3</sub>, δ) 90.37, 90.39, 90.5, 113.2, 113.5, 120.2, 120.3, 125.7, 125.8, 126.4, 126.5, 126.6, 128.11, 128.13, 128.3, 128.6, 128.8, 134.5, 134.8, 134.9, 149.0, 149.1, 149.3, 149.6, 149.9, 150.1; IR (ATR) 3063, 1602, 1497, 1308, 977, 869, 747 cm<sup>-1</sup>; <sup>-</sup>HRMS (ESI) *m/z* 905.3028 (905.3032 calcd for C<sub>66</sub>H<sub>42</sub>NaO<sub>3</sub>, [M + Na]<sup>+</sup>).

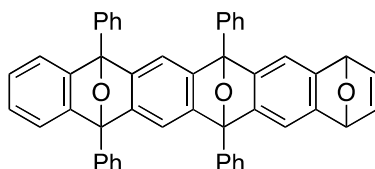
2,3,6-Tribromo-7-chloro-9,10-diphenyl-9,10-epoxyanthracene (**17**). According to the procedure described for the synthesis of cycloadduct **6a**, 1,2,4,5-tetrabromobenzene (**16**, 1.54 g, 3.91 mmol), isobenzofuran **9b** (1.00 g, 2.61 mmol) and *n*-BuLi (1.60 M in *n*-hexane, 2.50 mL, 4.00 mmol) gave, after purification by silica-gel flash column chromatography (hexane/CH<sub>2</sub>Cl<sub>2</sub>/Et<sub>2</sub>O = 96/3/1), 2,3,6-tribromo-7-chloro-9,10-diphenyl-9,10-epoxyanthracene (**17**, 1.58 g, 98.1%) as a white solid.



**Compound 17**: Mp 247.2–248.0 °C (hexane/CHCl<sub>3</sub>); <sup>1</sup>H-NMR (CDCl<sub>3</sub>, δ) 7.41 (s, 1H), 7.52–7.56 (m, 2H), 7.559 (s, 1H), 7.564 (s, 2H), 7.61–7.65 (m, 4H), 7.80–7.83 (m, 4H); <sup>13</sup>C-NMR (CDCl<sub>3</sub>, δ) 89.8, 90.0, 120.1, 122.5, 122.9, 125.9, 126.3, 129.1, 129.2, 132.3, 132.89, 132.92, 149.5, 150.3, 150.37, 150.44; IR (ATR) 3017, 1601, 1499, 1288, 1089, 987, 887, 746 cm<sup>-1</sup>; <sup>-</sup>HRMS (DART) *m/z* 614.8381 (614.8362 calcd for C<sub>26</sub>H<sub>15</sub>Br<sub>3</sub>ClO, [M + H]<sup>+</sup>).

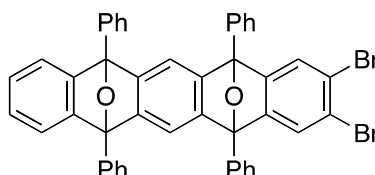
*2-Bromo-3-chloro-5,7,12,14-tetraphenyl-5,14:7,12-diepoxy-pentacene (11)*. According to the procedure described for the synthesis of cycloadduct **6a**, cycloadduct **17** (124 mg, 0.201 mmol), isobenzofuran **9c** (59.7 mg, 0.221 mmol) and *n*-BuLi (1.60 M in *n*-hexane, 0.15 mL, 0.24 mmol) gave, after purification by silica-gel flash column chromatography (hexane/CH<sub>2</sub>Cl<sub>2</sub>/Et<sub>2</sub>O = 96/3/1→88/9/3), cycloadduct **11** (94.3 mg, 64.7%, ds. less polar/more polar = 52/48) and cycloadduct **13** as a mixture of diastereomers (33.6 mg, 20.0%), respectively.

*1,4-Dihydro-6,8,13,15-tetraphenyl-1,4:6,15:8,13-triepoxyhexacene (19)*. According to the procedure described for the synthesis of cycloadduct **6a**, cycloadduct **11** (less polar) (67.9 mg, 0.0933 mmol), furan **18** (65 mg, 0.96 mmol) and *n*-BuLi (1.63 M in *n*-hexane, 0.075 mL, 0.12 mmol) gave, after purification by PTLC (hexane/CH<sub>2</sub>Cl<sub>2</sub>/acetone = 7/2/1), 1,4-dihydro-6,8,13,15-tetraphenyl-1,4:6,15:8,13-triepoxyhexacene (**19**) as a mixture of diastereomers (42.3 mg, 66.6%).



*Compound 19* (a mixture of two diastereomers): <sup>1</sup>H-NMR (CDCl<sub>3</sub>, δ) 5.50 (s, 2H), 5.52 (s, 2H), 6.88 (s, 2H), 6.91 (s, 2H), 6.92–6.95 (m, 4H), 7.13 (s, 2H), 7.19 (s, 2H), 7.23 (dd, 2H, *J*<sub>1</sub> = 2.9 Hz, *J*<sub>2</sub> = 5.2 Hz), 7.26 (dd, 2H, *J*<sub>1</sub> = 2.9 Hz, *J*<sub>2</sub> = 5.2 Hz), 7.29 (s, 2H), 7.33 (s, 2H), 7.44–7.49 (m, 8H), 7.54–7.59 (m, 16H), 7.79–7.87 (m, 16H); <sup>13</sup>C-NMR (CDCl<sub>3</sub>, δ) 82.2, 82.3, 90.47, 90.52, 113.40, 113.43, 113.6, 113.8, 120.2, 120.4, 125.6, 125.7, 126.5, 126.55, 126.60, 126.9, 128.3, 128.76, 128.81, 134.8, 134.9, 143.19, 143.22, 148.2, 148.3, 148.6, 148.8, 149.2, 149.5, 149.8, 150.0, 150.2; IR (ATR) 3062, 1602, 1499, 1308, 984, 848, 744, 700 cm<sup>-1</sup>; <sup>-</sup>HRMS (ESI) *m/z* 703.2233 (703.2249 calcd for C<sub>50</sub>H<sub>32</sub>NaO<sub>3</sub>, [M + Na]<sup>+</sup>).

*2,3-Dibromo-5,7,12,14-tetraphenyl-5,14:7,12-diepoxy-pentacene (21)*. According to the procedure described for the synthesis of cycloadduct **6a**, 2,3,6,7-tetrabromo-9,10-diphenyl-9,10-epoxyanthracene (**20**, 110 mg, 0.166 mmol) and isobenzofuran **9c** (49.5 mg, 0.183 mmol) and *n*-BuLi (1.63 M in *n*-hexane, 0.12 mL, 0.20 mmol) gave, after purification by silica-gel flash column chromatography (hexane/CH<sub>2</sub>Cl<sub>2</sub>/Et<sub>2</sub>O = 96/3/1→88/9/3), 2,3-dibromo-5,7,12,14-tetraphenyl-5,14:7,12-diepoxy-pentacene (**21**, 45.4 mg, 35.4%, ds. less polar/more polar = 48/52) and 2,3-dibromo-5,7,12,14-tetraphenyl-5,14:7,12-diepoxy-pentacene (**13**) as a mixture of diastereomers (35.0 mg, 23.9%), respectively.



*Compound 21* (less polar): *R*<sub>f</sub> 0.62 (hexane/toluene/CH<sub>2</sub>Cl<sub>2</sub>/Et<sub>2</sub>O = 82/10/6/2, X3); Mp decomposed at 250 °C (MeOH/CHCl<sub>3</sub>); <sup>1</sup>H-NMR (CDCl<sub>3</sub>, δ) 6.96 (dd, 2H, *J*<sub>1</sub> = 2.9 Hz, *J*<sub>2</sub> = 5.2 Hz), 7.27 (dd, 2H, *J*<sub>1</sub> = 2.9 Hz, *J*<sub>2</sub> = 5.2 Hz), 7.33 (s, 2H), 7.44 (s, 2H), 7.46–7.51 (m, 4H), 7.56–7.60 (m, 8H), 7.76–7.79 (m, 4H), 7.83–7.86 (m, 4H); <sup>13</sup>C-NMR (CDCl<sub>3</sub>, δ) 90.2, 90.5, 113.7, 120.4, 121.7, 125.6, 125.8, 126.4,

126.6, 128.4, 128.7, 128.9, 129.0, 133.7, 134.6, 148.3, 149.9, 150.2, 151.4; IR (ATR) 3059, 1606, 1499, 1308, 1033, 984, 866, 743  $\text{cm}^{-1}$ ;  $^{-}$ HRMS (ESI)  $m/z$  793.0333 (793.0354 calcd for  $\text{C}_{46}\text{H}_{28}\text{Br}_2\text{NaO}_2$ ,  $[\text{M} + \text{Na}]^+$ ).

**Compound 21** (more polar):  $R_f$  0.52 (hexane/toluene/ $\text{CH}_2\text{Cl}_2$ / $\text{Et}_2\text{O}$  = 82/10/6/2, X3); Mp decomposed at 250 °C (MeOH/ $\text{CHCl}_3$ );  $^1\text{H-NMR}$  ( $\text{CDCl}_3$ ,  $\delta$ ) 7.01 (dd, 2H,  $J_1 = 2.9$  Hz,  $J_2 = 5.2$  Hz), 7.31 (s, 2H), 7.33 (dd, 2H,  $J_1 = 2.9$  Hz,  $J_2 = 5.2$  Hz), 7.42–7.48 (m, 4H), 7.482 (s, 2H), 7.52–7.57 (m, 8H), 7.75–7.77 (m, 4H), 7.81–7.84 (m, 4H);  $^{13}\text{C-NMR}$  ( $\text{CDCl}_3$ ,  $\delta$ ) 90.2, 90.5, 113.5, 120.5, 121.7, 125.70, 125.74, 126.4, 126.6, 128.3, 128.7, 128.8, 129.0, 133.7, 134.7, 148.2, 150.0, 150.3, 151.7; IR (ATR) 3063, 1601, 1499, 1310, 1032, 983, 862, 745  $\text{cm}^{-1}$ ;  $^{-}$ HRMS (ESI)  $m/z$  793.0361 (793.0354 calcd for  $\text{C}_{46}\text{H}_{28}\text{Br}_2\text{NaO}_2$ ,  $[\text{M} + \text{Na}]^+$ ).

#### 4. Conclusions

Site-selective halogen-lithium exchange of 1,2-dihaloarenes allowed for the successive generation of benzynes and subsequent multiple [2+4] cycloadditions with various arynophiles to give highly functionalized polycyclic compounds, which were amenable to selective transformation en route to substituted polyacene derivatives. Further synthetic applications are under active investigation in our laboratories.

#### Supplementary Materials

Supplementary materials can be accessed at: <http://www.mdpi.com/1420-3049/20/10/19449/s1>.

#### Acknowledgments

This work was partially supported by the Grant-in-Aid for Scientific Research on Innovative Areas 2707 Middle Molecular Strategy from MEXT, Japan, and ACT-C from the Japan Science and Technology Agency.

#### Author Contributions

S.E. performed the experiments; S.E. and T.H. designed the experiments and wrote the paper.

#### Conflicts of Interest

The authors declare no conflict of interest.

#### References and Notes

1. Hoffmann, R.W. *Dehydrobenzene and Cycloalkynes*; Academic: New York, NY, USA, 1967.
2. Kessar, S.V. Nucleophilic coupling with arynes. In *Comprehensive Organic Synthesis*; Trost, B.M., Ed.; Pergamon: Oxford, UK, 1991; Volume 4, pp. 483–515.
3. Pellissier, H.; Santelli, M. The use of arynes in organic synthesis. *Tetrahedron* **2003**, *59*, 701–730.
4. Wenk, H.H.; Winkler, M.; Sander, W. One century of aryne chemistry. *Angew. Chem. Int. Ed.* **2003**, *42*, 502–528.

5. Yoshida, H.; Takaki, K. Aryne insertion reactions into carbon–carbon  $\sigma$ -bonds. *Synlett*, **2012**, *23*, 1725–1732.
6. Bhunia, A.; Yetra, S.R.; Biju, A.T. Recent advances in transition-metal-free carbon-carbon and carbon-heteroatom bond-forming reactions using arynes. *Chem. Soc. Rev.* **2012**, *41*, 3140–3152.
7. Dubrovskiy, A.V.; Markina, N.A.; Larock, R.C. Use of benzyne for the synthesis of heterocycles. *Org. Biomol. Chem.* **2013**, *11*, 191–218.
8. Hamura, T.; Chuda, Y.; Nakatsuji, Y.; Suzuki, K. Catalytic generation of arynes and trapping by nucleophilic addition and iodination. *Angew. Chem. Int. Ed.* **2012**, *51*, 3368–3372.
9. Haneda, H.; Eda, S.; Aratani, M.; Hamura, T. Dibromoisobenzofuran as a formal equivalent of didehydroisobenzofuran: Reactive platform for expeditious assembly of polycycles. *Org. Lett.* **2014**, *16*, 286–289.
10. Friedrichsen, W. Benzo[*c*]furans. *Adv. Heterocycl. Chem.* **1980**, *26*, 135–241.
11. Friedrichsen, W. Recent advances in the chemistry of benzo[*c*]furans and related compounds. *Adv. Heterocycl. Chem.* **1999**, *73*, 1–96.
12. Binger, P.; Wedemann, P.; Goddard, R.; Brinker, U.H. Cyclopropene: A new simple synthesis and Diels-Alder reactions with cyclopentadiene and 1,3-diphenylisobenzofuran. *J. Org. Chem.* **1996**, *61*, 6462–6464.
13. Rodrigo, R. Progress in the chemistry of isobenzofurans: Applications to the synthesis of natural products and polyaromatic hydrocarbons. *Tetrahedron* **1988**, *44*, 2093–2135.
14. Wong, H.N.C. Synthesis of novel benzenoid molecules by low-valent-titanium deoxygenation. *Acc. Chem. Res.* **1989**, *22*, 145–152.
15. Man, Y.-M.; Mak, T.C.W.; Wong, H.N.C. Synthesis of benzo-fused tetraphenylenes and crystal structure of a 4:1 clathrate inclusion compound of dibenzo[*b,h*]tetraphenylene with *p*-xylene. *J. Org. Chem.* **1990**, *55*, 3214–3221.
16. Chan, S.-H.; Yick, C.-Y.; Wong, H.N.C. 5,6-Bis(trimethylsilyl)benzo[*c*]furan: An isolable versatile building block for linear polycyclic aromatic compounds. *Tetrahedron* **2002**, *58*, 9413–9422.
17. Rainbolt, J.E.; Miller, G.P. 4,7-Diphenylisobenzofuran: A useful intermediate for the construction of phenyl-substituted acenes. *J. Org. Chem.* **2007**, *72*, 3020–3030.
18. Warrenner, R.N. The isolation of isobenzofuran, a stable but highly reactive molecule. *J. Am. Chem. Soc.* **1971**, *93*, 2346–2348.
19. Warrenner, R.N.; Shang, M.; Butler, D.N. A new stabilised form of isobenzofuran, rack-mounted on an alicyclophane. *Chem. Commun.* **2001**, 1550–1551, doi:10.1039/B104383H.
20. Sygula, A.; Sygula, R.; Rabideau, P.W. Isocorannulenofuran: A versatile building block for the synthesis of large buckybowls. *Org. Lett.* **2006**, *8*, 5909–5911.
21. Pei, B.J.; Chan, W.H.; Lee, A.W.M. Anthracene capped isobenzofuran: A synthon for the preparations of iptycenes and iptycene quinones. *Org. Lett.* **2011**, *13*, 1774–1777.
22. Hamura, T.; Nakayama, R. A one-pot preparation of 1,3-diarylisobenzofuran. *Chem. Lett.* **2013**, *42*, 1013–1015.
23. Asahina, K.; Matsuoka, S.; Nakayama, R.; Hamura, T. An efficient synthetic route to 1,3-bis(arylethynyl)isobenzofuran using alkoxybenzocyclobutenone as a reactive platform. *Org. Biomol. Chem.* **2014**, *12*, 9773–9776.

24. Cao, Y.; Wang, Xiao Y.; Wang, J.-Y.; Pei, J. Iron(III) chloride promoted cyclization: A facile approach to polycyclic aromatics for functional materials. *Synlett* **2014**, *25*, 313–323.
25. Reyes, E.; Uribe, U.; Carrillo, L.; Vicario, J.L. Transannular reactions in asymmetric total synthesis. *Tetrahedron* **2014**, *70*, 9461–9484.
26. Scott, L.T. Polycyclic aromatic hydrocarbon bowls, baskets, balls and tubes: Challenging targets for chemical synthesis. *Polycycl. Aromat. Compd.* **2010**, *30*, 247–259.
27. Clayden, J. Regioselective synthesis of organolithiums by X-Li exchange. Organolithiums: selectivity for synthesis. In *Tetrahedron Organic Chemistry Series*; Pergamon: Oxford, UK, 2002; Volume 23, pp. 111–147.
28. Beak, P.; Allen, D.J. Experimental evaluation of transition structure geometry for an aryl bromide-allyllithium exchange reaction: New information relevant to the reaction mechanism. *J. Am. Chem. Soc.* **1992**, *114*, 3420–3425.
29. Nájera, C.; Sansano, J.M.; Yus, M. Recent synthetic uses of functionalised aromatic and heteroaromatic organolithium reagents prepared by non-deprotonating methods. *Tetrahedron* **2003**, *59*, 9255–9303.
30. Dabrowski, M.; Kubicka, J.; Lulinski, S.; Serwatowski, J. Halogen-lithium exchange between substituted dihalobenzenes and butyllithium: Application to the regioselective synthesis of functionalized bromobenzaldehydes. *Tetrahedron* **2005**, *61*, 6590–6595.
31. Eda, S.; Eguchi, F.; Haneda, H.; Hamura, T. A new synthetic route to substituted tetracenes and pentacenes via stereoselective [4+2] cycloadditions of 1,4-dihydro-1,4-epoxynaphthalene and isobenzofuran. *Chem. Commun.* **2015**, *51*, 5963–5966.
32. Akita, R.; Kawanishi, K.; Hamura, T. Ring selective generation of isobenzofuran for divergent access to polycyclic aromatic compounds. *Org. Lett.* **2015**, *17*, 3094–3097.
33. Gilman, H.; Gorsich, R.D. Some reactions of *o*-halobromobenzenes with *n*-butyllithium. *J. Am. Chem. Soc.* **1956**, *78*, 2217–2222.
34. Chen, L.S.; Chen, G.J.; Tamborski, C. The synthesis and reactions of *ortho* bromophenyllithium. *J. Organomet. Chem.* **1980**, *193*, 283–292.
35. Caster, K.C.; Keck, C.G.; Walls, R.D. Synthesis of benzonorbornadienes: Regioselective benzyne formation. *J. Org. Chem.* **2001**, *66*, 2932–2936.
36. Coe, J.W.; Wirtz, M.C.; Bashore, C.G.; Candler, J. Formation of 3-halobenzyne: Solvent effects and cycloaddition adducts. *Org. Lett.* **2004**, *6*, 1589–1592.
37. Nagaki, A.; Ichinari, D.; Yoshida, J. Three-component coupling based on flash chemistry. Carbolithiation of benzyne with functionalized aryllithiums followed by reactions with electrophiles. *J. Am. Chem. Soc.* **2014**, *136*, 12245–12248.
38. Voss, G.; Gerlach, H. Regioselectiver brom/lithium-austausch bei 2,5-dibromo-1-nitrobenzol. Eine einfache synthese von 4-brom-2-nitrobenzaldehyd und 6,6'-dibromoindigo. *Chem. Ber.* **1989**, *122*, 1199–1201.
39. Stanetty, P.; Krumpak, B.; Rodler, I.K. Regioselectivity in sequential bromine-lithium exchange reactions of 2,4-dibromo-*N,N*-dimethylaniline. *J. Chem. Res.* **1995**, *9*, 342–343.
40. For preparation, see Supporting Information.
41. Hamura, T.; Arisawa, T.; Matsumoto, T.; Suzuki, K. Two-directional annelation: Dual benzyne cycloadditions starting from bis(sulfonyloxy)diiodobenzene. *Angew. Chem. Int. Ed.* **2006**, *45*, 6842–6844.

42. Bendikov, M.; Wudl, F.; Perepichka, D.F. Tetrathiafulvalenes, oligoacenes, and their buckminsterfullerene derivatives: The brick and mortar of organic electronics. *Chem. Rev.* **2004**, *104*, 4891–4946.
43. Anthony, J.E. Functionalized acenes and heteroacenes for organic electronics. *Chem. Rev.* **2006**, *106*, 5028–5048.
44. Anthony, J.E. The larger acenes: Versatile organic semiconductors. *Angew. Chem. Int. Ed.* **2008**, *47*, 452–483.
45. Bettinger, H.F. Electronic structure of higher acenes and polyacene: The perspective developed by theoretical analyses. *Pure Appl. Chem.* **2010**, *82*, 905–915.
46. Hart, H.; Ok, D. Synthesis of 1,5-diamino-1,5-dihydrobenzo[1,2-*d*:4,5-*d'*]bistriazole (DABT) and its use as a 1,4-benzadiyne equivalent. *J. Org. Chem.* **1986**, *51*, 979–986.
47. Hart, H.; Lai, C.-Y.; Nwokogu, G.; Shamouilian, S.; Teuerstein, A.; Zlotogorski, C. Bisannulation of arenes with bis-aryne equivalents. *J. Am. Chem. Soc.* **1980**, *102*, 6649–6651.
48. Chen, Y.-L.; Sun, J.-Q.; Wei, X.; Wong, W.-W.; Lee, A.W.M. Generation of synthetic equivalents of benzynes from benzobisoxadisiloles. *J. Org. Chem.* **2004**, *69*, 7190–7197.
49. Morton, G.E.; Barrett, A.G.M. 1,4-Difluoro-2,5-dimethoxybenzene as a precursor for iterative double benzyne-furan Diels-Alder reactions. *J. Org. Chem.* **2005**, *70*, 3525–3529.
50. Schuster, I.I.; Cracium, L.; Ho, D.M.; Pascal, R.A., Jr. Synthesis of a strained, air-sensitive, polycyclic aromatic hydrocarbon by means of a new 1,4-benzadiyne equivalent. *Tetrahedron* **2002**, *58*, 8875–8882.
51. Duong, H.M.; Bendikov, M.; Steiger, D.; Zhang, Q.; Sonmez, G.; Yamada, J.; Wudl, F. Efficient synthesis of a novel, twisted and stable, electroluminescent “twistacene”. *Org. Lett.* **2003**, *5*, 4433–4436.
52. This site selectivity in the bromine-lithium exchange is due to the electron withdrawal of the four bromo atoms in **16**, which leads to the selective generation of tribromophenyllithium. Subsequent elimination of lithium bromide from this intermediate produced dibromobenzyne **G**.

*Sample Availability:* Not available.

© 2015 by the authors; licensee MDPI, Basel, Switzerland. This article is an open access article distributed under the terms and conditions of the Creative Commons Attribution license (<http://creativecommons.org/licenses/by/4.0/>).

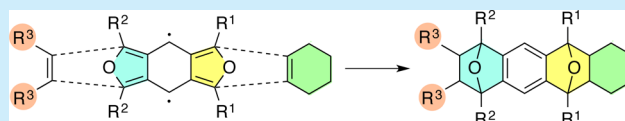
# Ring Selective Generation of Isobenzofuran for Divergent Access to Polycyclic Aromatic Compounds

Rie Akita, Kazuki Kawanishi, and Toshiyuki Hamura\*

Department of Applied Chemistry for Environment, School of Science and Technology, Kwansei Gakuin University, 2-1 Gakuen, Sanda, Hyogo 669-1337, Japan

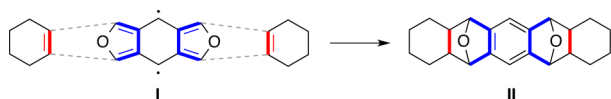
**S** Supporting Information

**ABSTRACT:** Ring selective generation of isobenzofuran, a formal equivalent to bis-isobenzofuran, was developed. Importantly, selective introduction of functionalities and/or fused rings in the isobenzofuran core by iterative cycloadditions can achieve the divergent construction of polycyclic compounds. This selective approach enables us to prepare a regioisomeric pair of pentacenes.



Construction of polycyclic structures with diverse functionalities is one of the important subjects often faced in the natural and unnatural product syntheses.<sup>1</sup> In this context, we were interested in the dual annulation and/or functionalization onto a reactive core ring<sup>2</sup> since it would allow for the rapid assembly of polycycles. In particular, we were intrigued by the use of bis-isobenzofuran **I**,<sup>3–5</sup> which could serve as a reactive platform for linearly fused polycyclic compounds **II** (Scheme 1).

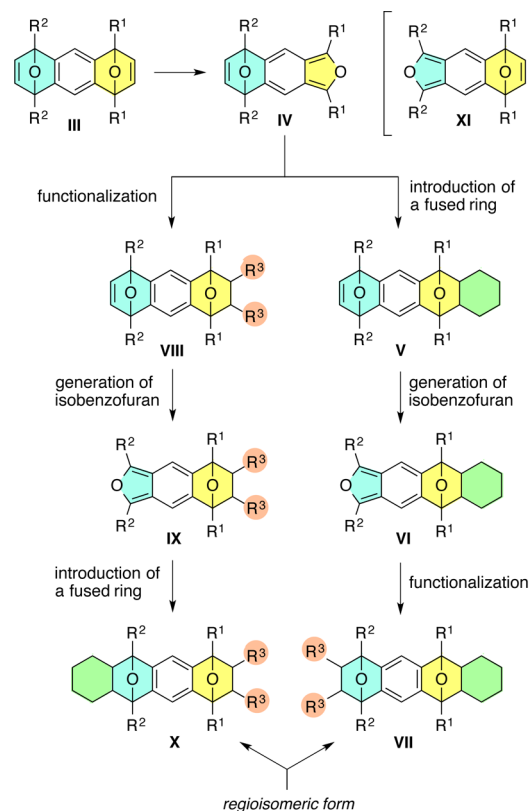
## Scheme 1. Dual Annulation of Bis-isobenzofuran



In this study, we focus on the formal use of bis-isobenzofuran **I** by sequential generation of two isobenzofurans from diepoxyanthracene **III** (Scheme 2). Selective introduction of functionalities and/or fused rings in **III** by iterative cycloadditions can achieve the divergent construction of polycyclic compounds. The fundamental issue that should be established in this process is the “ring selectivity”, that is, the relative susceptibilities of the two oxa-bicyclo rings in **III** toward the generation of isobenzofuran. If the more reactive oxa-bicyclo ring (yellow) in **III** would undergo selective Diels–Alder or retro-Diels–Alder reaction with 3,6-di(2-pyridyl)-1,2,4,5-tetrazine (vide infra), the isobenzofuran **IV**, selectively generated, can cyclize with a dienophile to give the [4 + 2] cycloadduct **V**. Subsequent second generation of isobenzofuran **VI** at the remaining oxa-bicyclo ring (blue) in **V** and trapping with a dienophile selectively affords the bis-cycloadduct **VII**. By switching the order of the dienophiles in each cycloaddition, the isomer **X** would also be accessible.

Now, we disclose the selective access to polycyclic aromatic compounds by using the *ring selective* generation of isobenzofurans. This divergent approach enables us to prepare a regioisomeric pair of substituted pentacenes, one of which

## Scheme 2. Ring Selective Generation and Trapping of Isobenzofuran



turned out to have higher solubility and stability, which is described in this communication.

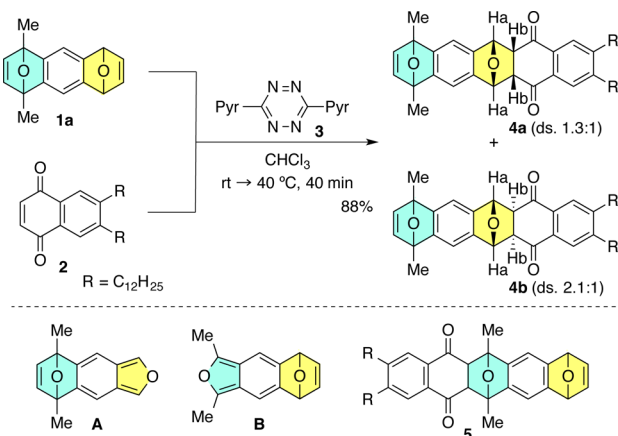
First, three diepoxyanthracenes **1a–1c**<sup>6</sup> with different substitution patterns on the epoxy rings were examined for

Received: May 10, 2015

Published: June 9, 2015

exploiting the ring selective generation of isobenzofurans. Upon heating of diepoxyanthracene **1a** with tetrazine **3** in the presence of naphthoquinone **2**<sup>7</sup> (CHCl<sub>3</sub>, 40 °C, 40 min), the less substituted oxa-bicyclo ring (yellow ring) underwent the exclusive generation of isobenzofuran **A** and subsequent cycloaddition of **A** with **2** to give the monocycloadduct **4** in high yield with perfect ring selectivity (Scheme 3). In this case,

**Scheme 3. Ring Selective Generation of Isobenzofuran from 1a**



the cycloadduct **5**, based on the generation of isobenzofuran **B**, was not produced at all.<sup>8</sup> In addition to the ring selectivity, this cycloaddition was stereoselective to give *endo* isomer **4a** as a major product (**4a/4b** = 80:20). The structure of **4a** was determined by <sup>1</sup>H NMR analysis, where an AA'XX' pattern of the aliphatic methine protons (two sets of doublet-of-doublet signals for H<sub>a</sub> and H<sub>b</sub>, J = 1.7, 3.5 Hz), characteristic as an *endo* isomer, was observed. In the case of cycloadduct **4b**, HMBC correlations revealed the connection between the naphthoquinone and the right epoxy ring in **1a**, differentiating **4b** from regioisomer **5**. Moreover, the absence of vicinal coupling between H<sub>a</sub> and H<sub>b</sub> in **4b** indicated the dihedral angle approached 90°, thereby determining the structure as an *exo* isomer.

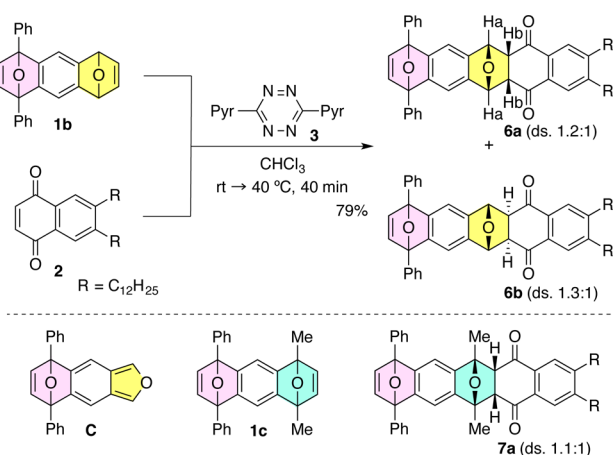
This observed ring selectivity in the generation of isobenzofuran **A** from the yellow ring over that of the blue ring can be explained by the facile nature of the interaction between the double bond in the less substituted oxa-bicyclo ring and the diene in tetrazine **3**.

Similarly, diepoxyanthracene **1b**, possessing the two phenyl groups in the left ring (pink ring), reacted with tetrazine **3** at the less substituted right ring to generate isobenzofuran **C**, which was intercepted with **2** to give cycloadducts **6a** and **6b** (**6a/6b** = 64:36), respectively (Scheme 4). Again, the structure of **6a** was confirmed by <sup>1</sup>H NMR spectroscopy, showing vicinal coupling of the two aliphatic protons, H<sub>a</sub> and H<sub>b</sub>. The *exo* isomer **6b** was determined after conversion to the pentacenequinone **11** (vide infra).

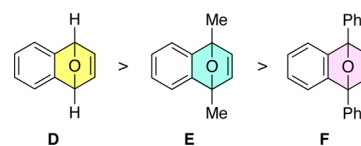
Moreover, ring selectivity was observed for the reaction of tetrasubstituted derivative **1c**, having methyl and phenyl groups at the two epoxy rings, which led to the selective formation of the *endo* cycloadduct **7** in moderate yield (43%).<sup>9</sup>

These results indicate the order of the reactivity of the epoxy ring: **D** > **E** > **F**, which is based on the steric effect of the substituents in each epoxy ring (Scheme 5).

**Scheme 4. Ring Selective Generation of Isobenzofurans from 1b and 1c**

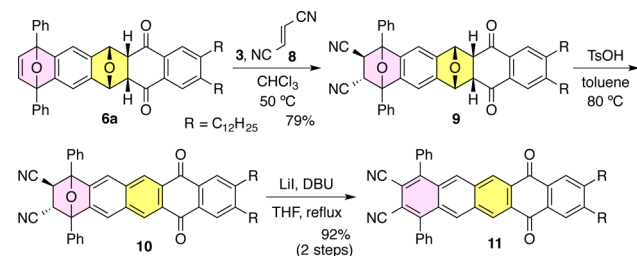


**Scheme 5. Order of the Reactivity**



The monocycloadducts, thus selectively obtained, were further functionalized by the second [4 + 2] cycloaddition (Scheme 6). For example, treatment of *endo* adduct **6a** with

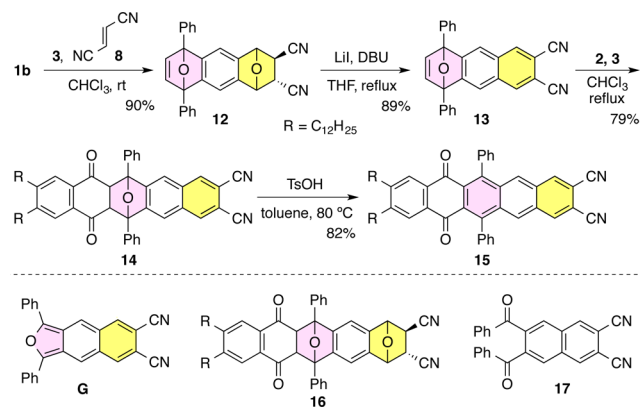
**Scheme 6. Second [4 + 2] Cycloaddition**



tetrazine **3** in the presence of fumaronitrile (**8**) (CHCl<sub>3</sub>, 50 °C) gave the [4 + 2] cycloadduct **9** as a mixture of diastereomers, which were smoothly converted to pentacenequinone **11** through the two-step sequence of aromatization. Upon treatment of cycloadduct **9** with TsOH (toluene, 80 °C), the dehydration occurred smoothly at the central epoxy ring to give the quinone **10**. Subsequent base-induced aromatization (LiI, DBU, THF, reflux)<sup>10</sup> at the remaining epoxy ring cleanly produced the pentacenequinone **11** in 92% yield.<sup>11</sup> Similar functionalization–aromatization protocol of the cycloadduct **6b** also gave **11** in high yield. At this stage, the structure of **6b** could be unambiguously determined as an *exo* isomer.

It is important to note that isomeric pentacenequinone **15** was selectively synthesized by switching the order of the addition of trapping agents in each cycloaddition (Scheme 7). The first [4 + 2] cycloaddition of isobenzofuran **C** with **8** at the less substituted yellow ring gave functionalized epoxyanthracene **13** after aromatization of the right epoxy ring in **12** under the basic conditions. Since the attempt at aromatization of the bis-cycloadduct **16** obtained by the dual cycloaddition of **1b** turned out to be unsuccessful, the monocycloadduct **12** was

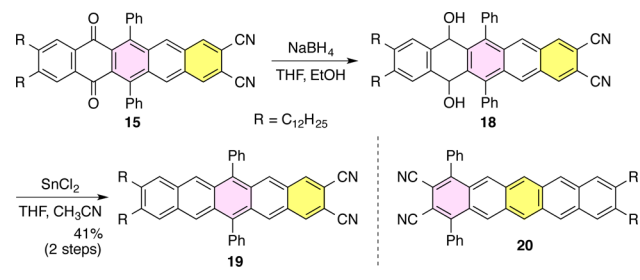
## Scheme 7. Second [4 + 2] Cycloaddition



aromatized before the second [4 + 2] cycloaddition. Epoxyanthracene **13**, thus obtained, was treated with tetrazine **3** to generate isonaphthofuran **G**,<sup>12</sup> a structurally attractive  $\pi$ -extended isoheterol, which was cleanly trapped with naphthoquinone **2** to give pentacenequinone **15** after acid treatment. For the conversion of **14** to **15**, prolonged reaction time was required to complete the aromatization because the retro-Diels–Alder reaction occurred upon heating of **14**.<sup>13</sup> In this case, insufficient reaction time caused the formation of the ring-cleaved oxidized diketone **17**.

Lastly, an important point to emphasize is that, as one of the synthetic applications, pentacenequinone **15** was converted to the pentacene **19** through the reduction of two carbonyl groups by treatment with NaBH<sub>4</sub> followed by Sn<sup>II</sup>-mediated reductive aromatization (Scheme 8). Attaching the two long alkyl chains

## Scheme 8. Selective Synthesis of Substituted Pentacenes



and the two cyano groups at the 2,3 and 9,10 positions sufficiently improved the solubility and the stability of the product in comparison with nonsubstituted pentacene.<sup>14</sup> Indeed, purification of **19** by preparative thin layer chromatography with a stringent exclusion of air and light gave the pure product, whose half-life turned out to be around 288 min.<sup>15,16</sup> In sharp contrast, pentacene **20**, an isomer of **19**, similarly synthesized by this two-step sequence, was fairly unstable and immediately underwent photo-oxidation.<sup>17,18</sup>

In summary, ring selective generation and iterative cycloaddition of isobenzofuran allowed us to rapidly construct functionalized polycyclic compounds, which were amenable to selective transformation en route to substituted pentacene derivatives. Further synthetic applications are under active investigation in our laboratories.

## ■ ASSOCIATED CONTENT

## S Supporting Information

Experimental procedures and compound characterization data. The Supporting Information is available free of charge on the ACS Publications website at DOI: 10.1021/acs-orglett.5b01364.

## ■ AUTHOR INFORMATION

## Corresponding Author

\*E-mail: thamura@kwansei.ac.jp.

## Author Contributions

R.A. and K.K. contributed equally.

## Notes

The authors declare no competing financial interest.

## ■ ACKNOWLEDGMENTS

This work was partially supported by ACT-C from Japan Science and Technology Agency. We also thank Individual Special Research A from Kwansai Gakuin University.

## ■ REFERENCES

- (1) For recent reviews, see: (a) Cao, Y.; Wang, X.-Y.; Wang, J.-Y.; Pei, J. *Synlett* **2014**, 25, 313. (b) Reyes, E.; Uria, U.; Carrillo, L.; Vicario, J. L. *Tetrahedron* **2014**, 70, 9461. (c) Scott, L. T. *Polycyclic Aromat. Compd.* **2010**, 30, 247.
- (2) For selective examples, see: (a) Hamura, T.; Chuda, Y.; Nakatsuji, Y.; Suzuki, K. *Angew. Chem., Int. Ed.* **2012**, 51, 3368. (b) Haneda, H.; Eda, S.; Aratani, M.; Hamura, T. *Org. Lett.* **2014**, 16, 286.
- (3) (a) Luo, J.; Hart, H. *J. Org. Chem.* **1988**, 53, 1341. (b) Qu, H.; Cui, W.; Li, J.; Shao, J.; Chi, C. *Org. Lett.* **2011**, 13, 924.
- (4) For preparation of isobenzofuran, see: (a) Warrener, R. N. *J. Am. Chem. Soc.* **1971**, 93, 2346. (b) Warrener, R. N.; Shang, M.; Butler, D. N. *Chem. Commun.* **2001**, 1550. (c) Sygula, A.; Sygula, R.; Rabideau, P. W. *Org. Lett.* **2006**, 8, 5909. (d) Pei, B. J.; Chan, W. H.; Lee, A. W. M. *Org. Lett.* **2011**, 13, 1774. (e) Hamura, T.; Nakayama, R. *Chem. Lett.* **2013**, 42, 1013. (f) Asahina, K.; Matsuoka, S.; Nakayama, R.; Hamura, T. *Org. Biomol. Chem.* **2014**, 12, 9773.
- (5) For selective synthetic applications of isobenzofuran, see: (a) Binger, P.; Wedemann, P.; Goddard, R.; Brinker, U. H. *J. Org. Chem.* **1996**, 61, 6462. (b) Rodrigo, R. *Tetrahedron* **1988**, 44, 2093. (c) Wong, H. N. C. *Acc. Chem. Res.* **1989**, 22, 145. (d) Man, Y.-M.; Mak, T. C. W.; Wong, H. N. C. *J. Org. Chem.* **1990**, 55, 3214. (e) Chan, S.-H.; Yick, C.-Y.; Wong, H. N. C. *Tetrahedron* **2002**, 58, 9413. (f) Rainbolt, J. E.; Miller, G. P. *J. Org. Chem.* **2007**, 72, 3020.
- (6) Diepoxyanthracenes **1a–1d** were prepared by the iterative [4 + 2] cycloadditions of benzyne and two kinds of furans. For details, see Supporting Information. See also: (a) Hart, H.; Ok, D. *J. Org. Chem.* **1986**, 51, 979. (b) Hart, H.; Lai, C.-Y.; Nwokogu, G.; Shamouilian, S.; Teuerstein, A.; Zlotogorski, C. *J. Am. Chem. Soc.* **1980**, 102, 6649.
- (7) For preparation, see Supporting Information.
- (8) Similar reaction of nonsubstituted diepoxyanthracene gave a sizable amount of the dual cycloadduct (20%) in addition to the desired monocycloadduct (47%).
- (9) The structure of the *endo* cycloadduct **7a** was determined by NOE. The chemical shifts of aromatic protons of **7a** are similar to those of the *endo* isomer **6a**.
- (10) For a related base-induced aromatization of 2,3-dicyanoepoxynaphthalenes, see: Polley, R.; Hanack, M. *J. Org. Chem.* **1995**, 60, 8278. See also ref 5e.
- (11) Double aromatization at the two epoxy rings in cycloadduct **9** under the acidic conditions (TsOH, CHCl<sub>3</sub>, 40 °C) was unsuccessful, giving a complex mixture of products.
- (12) (a) Smith, J. G.; Fogg, D. E.; Munday, I. J.; Sandborn, R. E.; Dibble, P. W. *J. Org. Chem.* **1988**, 53, 2942. (b) Mondal, R.; Shah, B. K.; Neckers, D. C. *J. Org. Chem.* **2006**, 71, 4085. See also ref 13.

- (13) Rainbolt, J. E.; Miller, G. P. *J. Org. Chem.* **2007**, *72*, 3020.
- (14) (a) Kaur, I.; Jia, W.; Kopreski, R. P.; Selvarasah, S.; Dokmeci, M. R.; Pramanik, C.; McGruer, N. E.; Miller, G. P. *J. Am. Chem. Soc.* **2008**, *130*, 16274. (b) Wang, J.; Liu, K.; Liu, Y. Y.; Song, C. L.; Shi, Z. F.; Peng, J. B.; Zhang, H. L.; Cao, X. P. *Org. Lett.* **2009**, *11*, 2563.
- (15) The photo-oxidative stability of pentacene **19** was investigated by exposure of  $2.0 \times 10^{-4}$  M CH<sub>2</sub>Cl<sub>2</sub> solution to ambient light and air at 25 °C and monitoring the reduction in the absorbance of the UV-vis spectra. See ref 14.
- (16) These results indicated that the existence of the phenyl groups at the 6 and 13 positions in the pentacene core were also important for stability.
- (17) For selected reports on the synthesis of 6,13-substituted pentacenes, see: (a) Anthony, J. E.; Brooks, J. S.; Eaton, D. L.; Parkin, S. R. *J. Am. Chem. Soc.* **2001**, *123*, 9482. (b) Payne, M. M.; Delcamp, J. H.; Parkin, S. R.; Anthony, J. E. *Org. Lett.* **2004**, *6*, 1609. (c) Swartz, C. R.; Parkin, S. R.; Bullock, J. E.; Anthony, J. E.; Mayer, A. C.; Malliaras, G. G. *Org. Lett.* **2005**, *7*, 3163. (d) Miao, Q.; Chi, X.; Xiao, S.; Zeis, R.; Lefenfeld, M.; Siegrist, T.; Steigerwald, M. L.; Nuckolls, C. *J. Am. Chem. Soc.* **2006**, *128*, 1340. (e) Ono, K.; Totani, H.; Hiei, T.; Yoshino, A.; Saito, K.; Eguchi, K.; Tomura, M.; Nishida, J.; Yamashita, Y. *Tetrahedron* **2007**, *63*, 9699. (f) Palayangoda, S. S.; Mondal, R.; Shah, B. K.; Neckers, D. C. *J. Org. Chem.* **2007**, *72*, 6584. (g) Wang, Y.; Fu, N.; Chan, S.; Lee, H.; Wong, H. N. C. *Tetrahedron* **2007**, *63*, 8586. (h) Lehnher, D.; McDonald, R.; Tykwinski, R. R. *Org. Lett.* **2008**, *10*, 4163. (i) Lehnher, D.; Murray, A. H.; McDonald, R.; Ferguson, M. J.; Tykwinski, R. R. *Chem.—Eur. J.* **2009**, *15*, 12580. (j) Kaur, I.; Jia, W.; Kopreski, R. P.; Selvarasah, S.; Dokmeci, M. R.; Pramanik, C.; McGruer, N. E.; Miller, G. P. *J. Am. Chem. Soc.* **2008**, *130*, 16274. (k) Wang, J.; Liu, K.; Liu, Y.; Song, C.; Shi, Z.; Peng, J.; Zhang, H.; Cao, X. *Org. Lett.* **2009**, *11*, 2563. (l) Tang, M. L.; Oh, J. H.; Reichardt, A. D.; Bao, Z. *J. Am. Chem. Soc.* **2009**, *131*, 3733. (m) Li, S.; Zhou, L.; Nakajima, K.; Kanno, K.; Takahashi, T. *Chem.—Asian J.* **2010**, *5*, 1620. (n) Eda, S.; Eguchi, F.; Haneda, H.; Hamura, T. *Chem. Commun.* **2015**, *51*, 5963. See also ref 2b.
- (18) For selected reviews on pentacenes, see: (a) Bendikov, M.; Wudl, F.; Perepichka, D. F. *Chem. Rev.* **2004**, *104*, 4891. (b) Anthony, J. E. *Chem. Rev.* **2006**, *106*, 5028. (c) Anthony, J. E. *Angew. Chem.* **2008**, *120*, 460; *Angew. Chem., Int. Ed.* **2008**, *47*, 452. (d) Bettinger, H. F. *Pure Appl. Chem.* **2010**, *82*, 905.



Cite this: DOI: 10.1039/c5cc00077g

Received 5th January 2015,  
Accepted 25th February 2015

DOI: 10.1039/c5cc00077g

www.rsc.org/chemcomm

# A new synthetic route to substituted tetracenes and pentacenes *via* stereoselective [4+2] cycloadditions of 1,4-dihydro-1,4-epoxynaphthalene and isobenzofuran†

Shohei Eda, Fumiaki Eguchi, Hiroshi Haneda and Toshiyuki Hamura\*

Stereoselective [4+2] cycloadditions of 1,4-dihydro-1,4-epoxynaphthalene and isobenzofuran were described. Among several possibilities, *syn-exo* and/or *anti-endo* isomers were selectively produced depending on the substitution pattern of the reactants. Importantly, the *syn-exo* isomer underwent acid promoted aromatization, affording the corresponding tetracene. These findings enabled us to prepare a substituted pentacene with electron withdrawing groups.

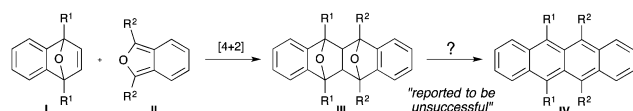
Due to the inherent strain, 1,4-epoxynaphthalenes **I** show potentially interesting reactivities in organic syntheses.<sup>1</sup> The [4+2] cycloaddition of **I** with dienes is one of their representative reactions for construction of polycyclic compounds.<sup>2</sup> Among various dienes, isobenzofuran **II**, a 10 $\pi$  electron system, is an attractive reactive partner of **I**, since it can readily cyclize with **I** to give diepoxytetracene **III**,<sup>3</sup> which can be viewed as an efficient precursor to substituted tetracenes (Scheme 1). However, conversion of **III** to tetracenes **IV** was reported to be unsuccessful, resulting in the formation of ring cleaved products.<sup>3b,d,4</sup> These unfortunate results discouraged the syntheses of various functionalized derivatives of **III**.

In this context, we recently exploited a one-pot synthetic method for 1,3-diarylisobenzofurans<sup>5,6</sup> by a sequential reaction of methyl 2-formylbenzoate with two identical or different aryl metal species.<sup>7</sup> In addition, successive [4+2] cycloadditions of benzyne and dibromoisobenzofuran were developed, allowing a rapid construction of polycyclic structures.<sup>8</sup> These findings can

offer various opportunities to open up a new way to polycyclic aromatic compounds.

In this study, we re-examined the [4+2] cycloaddition of 1,4-epoxynaphthalene and isobenzofuran to elucidate the stereochemical course of the reaction, and more importantly, to develop the synthetic utility of the cycloadducts (*vide supra*). The important points that were uncovered during the course of the investigation are that (1) *syn-exo* and/or *anti-endo* cycloadducts are selectively produced depending on the substitution patterns of the 1,4-epoxynaphthalene and isobenzofuran, and (2) the *syn-exo* isomer can be cleanly converted to the corresponding tetracene under the acidic conditions. These findings enable us to prepare a substituted pentacene with electron-withdrawing groups, which is described in this communication.

Table 1 shows the initial model reaction. Upon heating epoxynaphthalene **1** and diphenylisobenzofuran (**2**) in toluene at 110 °C, the [4+2] cycloaddition occurred smoothly to give the cycloadduct **3** in 96% yield (entry 1). In this case, *syn-exo* isomer **3aA** was selectively obtained as a major product, accompanied by a small amount of the *anti-endo* isomer **3aB**. The same reaction performed at lower reaction temperature slightly

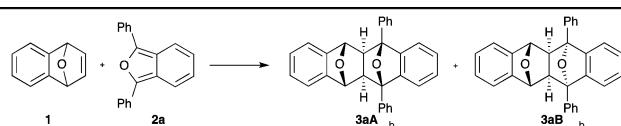


Scheme 1 The [4+2] cycloaddition of 1,4-epoxynaphthalene **I** and isobenzofuran **II**.

Department of Chemistry, School of Science and Technology,  
Kwansei Gakuin University, 2-1 Gakuen, Sanda, Hyogo 669-1337, Japan.  
E-mail: thamura@kwansei.ac.jp; Fax: +81-79-565-7591; Tel: +81-79-565-7591

† Electronic supplementary information (ESI) available: Experimental details and characterization data. See DOI: 10.1039/c5cc00077g

Table 1 Initial model study



Entry <sup>a</sup>	Solvent	Temp.	Time	Yield (%)	3aA : 3aB
1	Toluene	110	0.5 h	96	75 : 25
2	Toluene	25	8 h	86	79 : 21
3	Toluene	0	8 d	83	81 : 19
4	Benzene	80	3 h	95	77 : 23
5	Hexane	69	3.2 h	93	76 : 24
6	CH <sub>3</sub> CN	82	3.5 h	94	67 : 23
7	EtOH	78	2 h	96	76 : 24
8	THF	65	3.5 h	95	77 : 23

<sup>a</sup> 1.2 equiv. of **1** and 1.0 equiv. of **2a**. <sup>b</sup> *Syn* and *anti* represent the relative relationship between the two oxygen bridges.

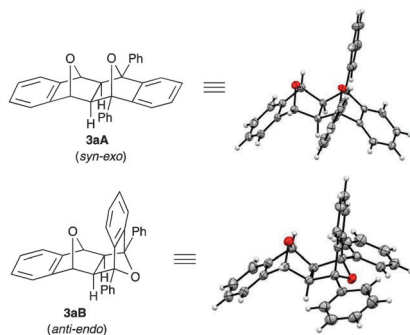


Fig. 1 X-ray structures of cycloadducts **3aA** and **3aB**. The thermal ellipsoids are scaled at a 50% probability level.

improved the *syn-exo* selectivity, although a prolonged reaction time was required to consume the starting material (entries 2 and 3). Use of other solvents showed little effect on the stereoselectivity (entries 4–8).

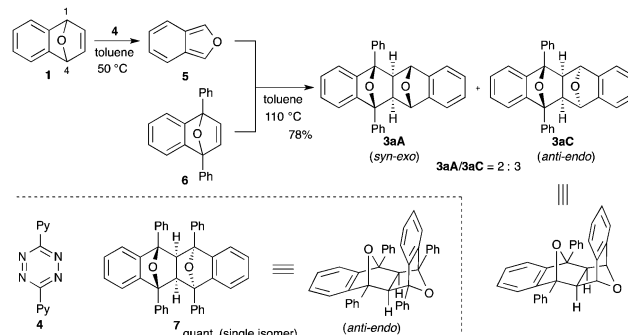
The observed stereoselectivity is due to the concave topology of the epoxynaphthalene **1**, which would force the isobenzofuran to approach along the convex side of **1**. The stereochemistry of each cycloadduct was determined by X-ray analysis (Fig. 1). These cycloadducts were thermally stable and the retro Diels–Alder reaction did not occur at all under the reaction conditions (toluene, 110 °C).

This [4+2] cycloaddition could be applicable to various substrate combinations (Table 2). Upon heating epoxynaphthalene **1** with diarylisobenzofurans **2b** and **2c**,<sup>9</sup> having a fluoro or a methoxy group on the aromatic ring at the *para* position (toluene, 110 °C, 0.5 h), the [4+2] cycloadditions occurred stereoselectively to give cycloadducts **3bA** and **3cA** as major products, respectively (entries 1 and 2). Isobenzofuran **2d**,<sup>9</sup> having a sterically congested *o*-tolyl group, cyclized slowly with **1** (110 °C, 30 h) to give cycloadduct **3d** in 82% yield (entry 3).

Table 2 [4+2] cycloaddition of epoxynaphthalene and isobenzofuran

Entry	Furan	Ar	R <sup>1</sup>	Product	Yield/%
1	<b>2b</b>		H	<b>3b</b>	94 (75:25) <sup>b</sup>
2	<b>2c</b>		H	<b>3c</b>	95 (76:24) <sup>b</sup>
3 <sup>a</sup>	<b>2d</b>		H	<b>3d</b>	82 (80:20) <sup>b</sup>
4	<b>2e</b>		F	<b>3e</b>	87 (57:43) <sup>b</sup>
5	<b>2f</b>		Cl	<b>3f</b>	97 (68:32) <sup>b</sup>
6	<b>2g</b>		OMe	<b>3g</b>	98 (76:24) <sup>b</sup>

<sup>a</sup> The reaction was performed for 30 h. <sup>b</sup> *syn-exo*:*anti-endo*.

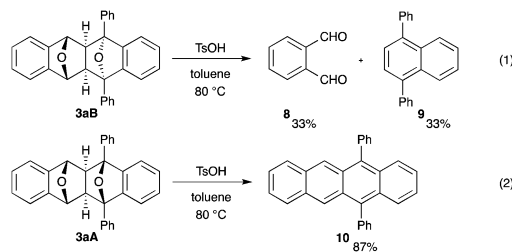


Scheme 2 Stereoselective [4+2] cycloaddition of 1,4-disubstituted epoxynaphthalene.

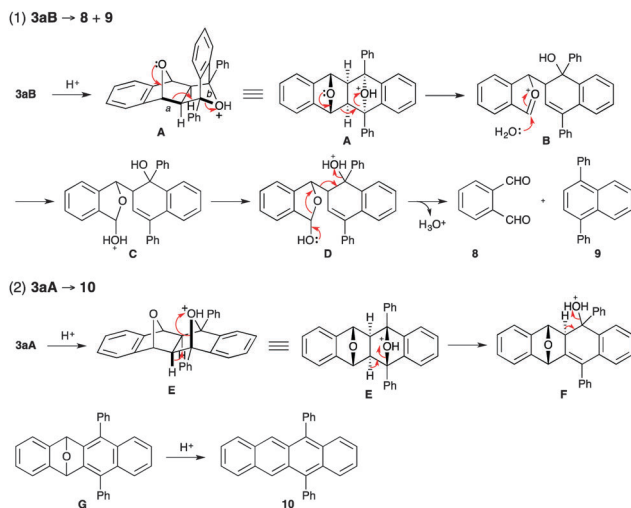
Furthermore, substituents at C<sub>5</sub> and C<sub>6</sub> positions on the isobenzofuran slightly influenced the stereoselectivity. The cycloadditions of isobenzofurans **2f** and **2g**, having a chloro or methoxy group, with **1** occurred smoothly to give the cycloadducts **3f** and **3g** with moderate stereoselectivities (entries 5 and 6). On the other hand, the corresponding reaction of fluoride **2e** resulted in poor selectivity (entry 4).

Further investigation revealed that introduction of the substituent at the C<sub>1</sub> and C<sub>4</sub> position in epoxynaphthalene switched the stereoselectivity (Scheme 2). Upon treatment of epoxynaphthalene **1** with tetrazine **4** in toluene at 50 °C, isobenzofuran **5** was generated,<sup>6c</sup> which was intercepted by 1,4-diphenylepoxynaphthalene **6** to give *anti-endo* isomer **3aC** as a major stereoisomer (**3aA**/**3aC** = 2:3). Remarkably, heating 1,4-diphenylepoxynaphthalene **6** and diphenylisobenzofuran **2a** in toluene at 110 °C gave *anti-endo* isomer **7** as an exclusive product, whose stereochemistry was unequivocally confirmed by X-ray analysis.<sup>10,11</sup>

We next focused our attention on the conversion of [4+2] cycloadducts to the corresponding tetracenes (Scheme 3). All attempts on acid promoted aromatization of *anti-endo* isomers **3B** to the corresponding tetracenes have failed. In these cases, however, ring cleavage occurred predominantly. For example, treatment of **3aB** with TsOH (toluene, 80 °C, 1.5 h) gave the phthalaldehyde **8** and diphenylnaphthalene **9** in 33% and 33% yields, respectively (eqn 1). In sharp contrast, we were pleased to find that the *syn-exo* isomer **3aA** could be cleanly aromatized under the same reaction conditions, affording substituted tetracene **10**<sup>12</sup> in 87% yield (eqn 2).



Scheme 3 Attempts on acid promoted aromatization of the [4+2] cycloadducts.



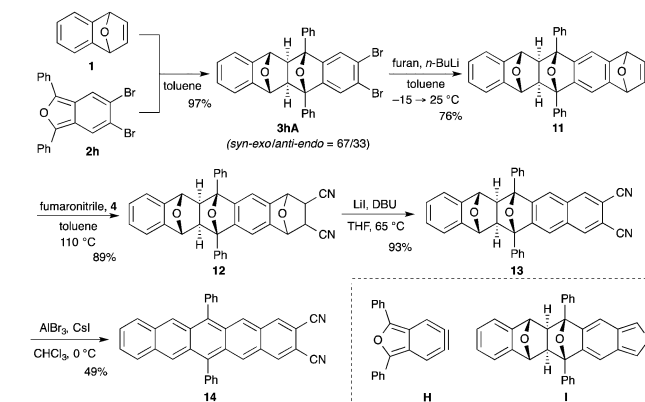
**Scheme 4** A possible reaction course to the ring cleaved or the aromatized products.

A possible reaction course of the [4+2] cycloadducts **3aA** and **3aB** to the ring cleaved or the aromatized products **8–10** is shown in Scheme 4.

The formation of the ring cleaved products **8** and **9** can be explained by Grob type fragmentation,<sup>13</sup> since the *anti* orientation of the two epoxide bridges in the protonated intermediate **A** would facilitate the cleavage of the carbon–carbon bond *a* and the carbon–oxygen bond *b* with an *anti*-periplanar relationship.<sup>3d</sup> The intermediate **B**, thus formed, underwent nucleophilic addition of water, and subsequent proton transfer and fragmentation of the resulting lactol **D** gave the phthalaldehyde (**8**) and 1,4-diphenyl-naphthalene (**9**).

On the other hand, the conversion of **3aA** to the tetracene **10** is ascribed to the *anti* orientation of the two protons on the bridge-head carbon with respect to the two epoxide bridges in **3aA**, which would facilitate the dehydration of the protonated intermediate **E**, affording the epoxytetracene **G**. Second acid induced aromatization of the epoxytetracene **G** led to the clean formation of the tetracene **10**.<sup>14</sup>

Lastly, an important point to emphasize is that this synthetic method could be applied to the synthesis of a substituted pentacene (Scheme 5).<sup>15</sup> Starting from dibromoisobenzofuran **2h**, which served as a synthetic equivalent of didehydroisobenzofuran **H**,<sup>8</sup> the precursor of pentacene was rapidly constructed by successive [4+2] cycloadditions. Thus, the first [4+2] cycloaddition of epoxynaphthalene **1** and isobenzofuran **2h** smoothly gave cycloadduct **3hA** in high yield. In this case, the *syn*-*exo* isomer was again a major stereoisomer. The second [4+2] cycloaddition of benzyne, generated by treatment of *syn*-*exo* isomer **3hA** with *n*-BuLi, and furan afforded the [4+2] cycloadduct **11**. Subsequent cyanation through the generation of isobenzofuran **I** by treatment of **11** with tetrazine **4** and its trapping with fumaronitrile gave the product **12** in 89% yield. The cycloadduct **12**, thus obtained, was converted to the corresponding tetraepoxypentacene **13** under the basic conditions (LiI, DBU, THF, 65 °C). Final acid-promoted aromatization of **13** under the above-mentioned



**Scheme 5** Synthesis of a substituted pentacene.

conditions, however, was not satisfied, affording the pentacene **14** only in 12% yield. Re-investigation of the aromatized conditions revealed that Lewis-acid promoted conditions ( $\text{AlBr}_3$ , CsI,  $\text{CHCl}_3$ , 0 °C)<sup>8</sup> improved the yield of the desired product **14**.<sup>16,17</sup>

In summary, stereoselective [4+2] cycloaddition of epoxy-naphthalene and isobenzofuran allowed rapid construction of highly functionalized diepoxytetracenes, which were amenable to selective transformation en route to substituted tetracene and pentacene derivatives. Further synthetic applications are under active investigation in our laboratories.

This work was supported by the MEXT and JST, ACT-C. The authors thank Prof. Hidehiro Uekusa (Tokyo Institute of Technology) for X-ray analysis and yasuko Tanaka (ICME, Kyusyu Univ.) for HRMS measurements.

## Notes and references

- For selective recent examples, see: (a) K. Villeneuve and W. Tam, *J. Am. Chem. Soc.*, 2006, **128**, 3514; (b) M. Ballantine, M. L. Menard and W. Tam, *J. Org. Chem.*, 2009, **74**, 7570; (c) J. Tsoung, K. Kramer, A. Zajdlik, C. Liebert and M. Lautens, *J. Org. Chem.*, 2011, **76**, 9031; (d) G. C. Tsui and M. Lautens, *Angew. Chem., Int. Ed.*, 2012, **51**, 5400; (e) J. Hu, Q.-J. Yang, J.-B. Xu, C. Huang, B.-M. Fan, J. Wang, C.-Y. Lin, Z.-X. Bian and A. S. C. Chan, *Org. Biomol. Chem.*, 2013, **11**, 814; (f) J. Hu, Q. Yang, L. Yu, J. Xu, S. Liu, C. Huang, L. Wang, Y. Zhou and B. Fan, *Org. Biomol. Chem.*, 2013, **11**, 2294.
- (a) A. Menzek, L. Kelebekli, A. Altumdas, E. Sahin and F. Polat, *Helv. Chim. Acta*, 2008, **91**, 2367; (b) D. Margetic, M. E. Maksic, P. Troselj and Z. Marinic, *J. Fluorine Chem.*, 2010, **131**, 408.
- (a) T. Sakai, K. Kanematsu and K. Iizuka, *Heterocycles*, 1975, **3**, 109; (b) H. Meier and B. Rose, *Liebigs Ann.*, 1997, **663**; (c) N. Pichon, A. H. Marchand, P. Mailliet and J. Maddaluno, *J. Org. Chem.*, 2004, **69**, 7220; (d) W.-X. Niu, E.-Q. Yang, Z.-F. Shi, X.-P. Cao and D. Kuck, *J. Org. Chem.*, 2012, **77**, 1422.
- To the best of our knowledge, only one example is reported for acid-induced aromatization of diepoxytetracene to corresponding tetracene derivatives. In this case, the stereochemistry of the starting material was not determined, see: T. E. Youssef and M. Hanack, *J. Porphyrins phthalocyanines*, 2002, **6**, 571.
- (a) A. O. Patil, A. J. Heeger and F. Wudl, *Chem. Rev.*, 1988, **88**, 183; (b) J. Roncali, *Chem. Rev.*, 1997, **97**, 173; (c) W. Friedrichsen, *Adv. Heterocycl. Chem.*, 1980, **26**, 135; (d) W. Friedrichsen, *Adv. Heterocycl. Chem.*, 1999, **73**, 1.
- For selective examples of the syntheses of isobenzofuran, see: (a) G. Wittig and L. Pohmer, *Chem. Ber.*, 1956, **89**, 1334; (b) M. P. Cava, M. J. Mitchell and A. A. Deana, *J. Org. Chem.*, 1960, **25**, 1481; (c) R. N. Warrenner, *J. Am. Chem. Soc.*, 1971, **93**, 2346; (d) J. T. Sharp and C. E. D. Skinner, *Tetrahedron Lett.*, 1986, **27**, 869; (e) Y. Kuminobu, Y. Nishina, C. Nakagawa and K. Takai, *J. Am. Chem. Soc.*, 2006, **128**, 12376; (f) S. T. Meek,

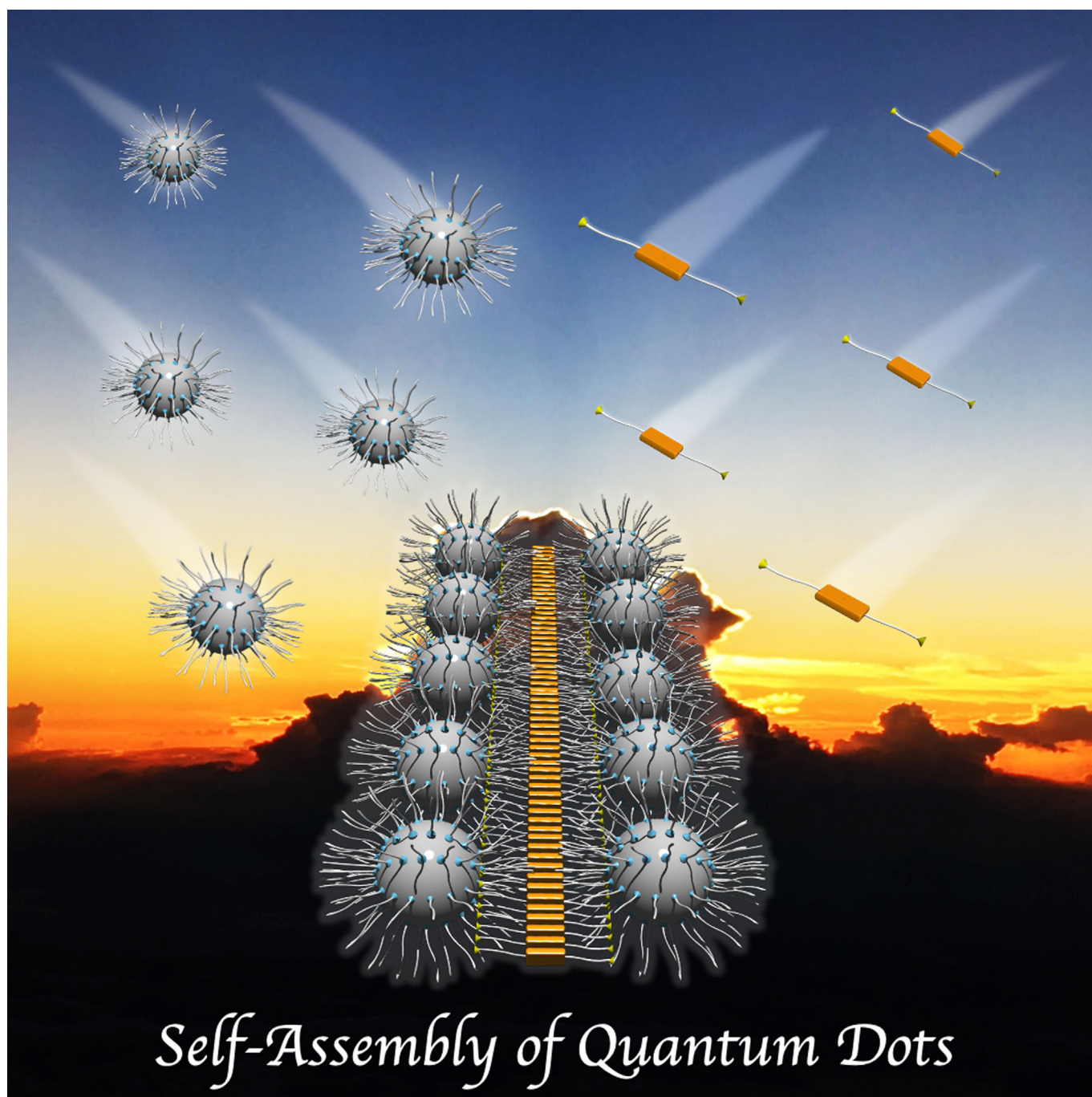
- E. E. Nesterov and T. M. Swager, *Org. Lett.*, 2008, **10**, 2991; (g) Y. Nishina, T. Kida and T. Ureshino, *Org. Lett.*, 2011, **13**, 3960.
- 7 (a) T. Hamura and R. Nakayama, *Chem. Lett.*, 2013, **42**, 1013; (b) K. Asahina, S. Matsuoka, R. Nakayama and T. Hamura, *Org. Biomol. Chem.*, 2014, **12**, 9773.
- 8 H. Haneda, S. Eda, M. Aratani and T. Hamura, *Org. Lett.*, 2014, **16**, 286.
- 9 For preparation of isobenzofurans, see ESI.† See also ref. 5a and 6.
- 10 For details, see ESI.†.
- 11 The [4+2] cycloaddition of 1,4-dimethylepoxynaphthalene and diphenylisobenzofuran **2a** also gave the corresponding *anti-endo* cycloadduct as a single stereoisomer.
- 12 (a) L. Zhou, K. Nakajima, K. Kanno and T. Takahashi, *Tetrahedron Lett.*, 2009, **50**, 2722; (b) T. Ohmura, A. Kijima and M. Sugimoto, *Org. Lett.*, 2011, **13**, 1238; (c) M. Chen, Y. Chen and Y. Liu, *Chem. Commun.*, 2012, **48**, 12189.
- 13 (a) C. A. Grob and P. W. Schiess, *Angew. Chem., Int. Ed. Engl.*, 1967, **6**, 1; (b) C. A. Grob, *Angew. Chem., Int. Ed. Engl.*, 1969, **8**, 535; (c) K. Prantz and J. Mulzer, *Chem. Rev.*, 2010, **110**, 3741.
- 14 The reducing agent that is responsible for producing **10** from the epoxytetracene **G**, which is probably produced as an initial product, is yet to be identified. See also ref. 8.
- 15 For selected reviews on acenes, see: (a) M. Bendikov, F. Wudl and D. F. Perepichka, *Chem. Rev.*, 2004, **104**, 4891; (b) J. E. Anthony, *Chem. Rev.*, 2006, **106**, 5028; (c) J. E. Anthony, *Angew. Chem., Int. Ed.*, 2008, **47**, 452; (d) H. F. Bettinger, *Pure Appl. Chem.*, 2010, **82**, 905.
- 16 For selected reports on synthesis of 6,13-substituted pentacenes, see: (a) J. E. Anthony, J. S. Brooks, D. L. Eaton and S. R. Parkin, *J. Am. Chem. Soc.*, 2001, **123**, 9482; (b) M. M. Payne, J. H. Delcamp, S. R. Parkin and J. E. Anthony, *Org. Lett.*, 2004, **6**, 1609; (c) C. R. Swartz, S. R. Parkin, J. E. Bullock, J. E. Anthony, A. C. Mayer and G. G. Malliaras, *Org. Lett.*, 2005, **7**, 3163; (d) Q. Miao, X. Chi, S. Xiao, R. Zeis, M. Lefenfeld, T. Siegrist, M. L. Steigerwald and C. Nuckolls, *J. Am. Chem. Soc.*, 2006, **128**, 1340; (e) K. Ono, H. Totani, T. Hiei, A. Yoshino, K. Saito, K. Eguchi, M. Tomura, J. Nishida and Y. Yamashita, *Tetrahedron*, 2007, **63**, 9699; (f) S. S. Palayangoda, R. Mondal, B. K. Shah and D. C. Neckers, *J. Org. Chem.*, 2007, **72**, 6584; (g) Y. Wang, N. Fu, S. Chan, H. Lee and H. N. C. Wong, *Tetrahedron*, 2007, **63**, 8586; (h) D. Lehnher, R. McDonald and R. R. Tykwinski, *Org. Lett.*, 2008, **10**, 4163; (i) D. Lehnher, A. H. Murray, R. McDonald, M. J. Ferguson and R. R. Tykwinski, *Chem. – Eur. J.*, 2009, **15**, 12580; (j) I. Kaur, W. Jia, R. P. Kopeski, S. Selvarasah, M. R. Dokmeci, C. Pramanik, N. E. McGruer and G. P. Miller, *J. Am. Chem. Soc.*, 2008, **130**, 16274; (k) J. Wang, K. Liu, Y. Liu, C. Song, Z. Shi, J. Peng, H. Zhang and X. Cao, *Org. Lett.*, 2009, **11**, 2563; (l) M. L. Tang, J. H. Oh, A. D. Reichardt and Z. Bao, *J. Am. Chem. Soc.*, 2009, **131**, 3733; (m) S. Li, L. Zhou, K. Nakajima, K. Kanno and T. Takahashi, *Chem. – Asian J.*, 2010, **5**, 1620.
- 17 The same reaction of **3aA** by treatment with AlBr<sub>3</sub> and CsI gave the tetracene **10** in 51% yield.

雑誌論文 1 3

## ■ Nanostructures

# Self-Assembly of Semiconductor Quantum Dots using Organic Templates

Mitsuaki Yamauchi\* and Sadahiro Masuo\*[a]



**Abstract:** Colloidal semiconductor nanocrystals, known as quantum dots (QDs), are regarded as brightly photoluminescent nanomaterials possessing outstanding photophysical properties, such as high photodurability and tunable absorption and emission wavelengths. Therefore, QDs have great potential for a wide range of applications, such as in photoluminescent materials, biosensors and photovoltaic devices. Since the development of synthetic methods for accessing high-quality QDs with uniform morphology and size, various types of QDs have been designed and synthesized, and their photophysical properties dispersed in solutions and at the single QD level have been reported in detail. In contrast to

dispersed QDs, the photophysical properties of assembled QDs have not been revealed, although the structures of the self-assemblies are closely related to the device performance of the solid-state QDs. Therefore, creating and controlling the self-assembly of QDs into well-defined nanostructures is crucial but remains challenging. In this Minireview, we discuss the notable examples of assembled QDs such as dimers, trimers and extended QD assemblies achieved using organic templates. This Minireview should facilitate future advancements in materials science related to the assembled QDs.

## Introduction

Nanocrystals consisting of several hundreds to thousands of atoms have been widely studied for electronic and optoelectronic applications due to their unique photophysical properties, which are dramatically different from those of the bulk material.<sup>[1]</sup> Among nanocrystals, colloidal semiconductor nanocrystals showing quantum size effects, known as quantum dots (QDs), are attractive as next-generation photoluminescent and optoelectronic nanomaterials.<sup>[2–5]</sup> Unlike organic photoluminescent dyes, QDs exhibit high photostability and a narrow emission line width, and their absorption and emission wavelengths can be tuned, and as a result, QDs are actively being studied for applications in various fields such as photoluminescent materials,<sup>[6–9]</sup> photovoltaic devices<sup>[10]</sup> and biosensing materials.<sup>[11–13]</sup> Owing to these in-depth investigations, the outstanding photophysical properties of both ensemble<sup>[1,14–17]</sup> and single QDs have been elucidated.<sup>[18–23]</sup>

Generally, QDs, such as CdSe/ZnS, have core/shell-type structures and are several nanometers in diameter.<sup>[24]</sup> The surface environment of the QDs is one of the most important factors for maintaining the performance of QD materials and thus, passivation by long aliphatic ligands such as oleic acid and oleylamine is used to protect QDs.<sup>[25]</sup> Hence, typical QDs preferentially disperse in good solvents. Basically, the ligands undergo dynamic adsorption and desorption on the QD surface due to the noncovalent bonds between the ligand and the QD core. This behavior enables the exchange of the native ligands with other adsorption molecules, which is called ligand exchange.<sup>[26,27]</sup> Recently, combinations of QDs and functional organic molecules such as chiral molecules,<sup>[28,29]</sup> photochromic molecules,<sup>[30–32]</sup>  $\pi$ -conjugated dyes,<sup>[33–40]</sup> fullerene-based molecules,<sup>[41–43]</sup> and self-assembling dyes<sup>[44]</sup> have been studied to

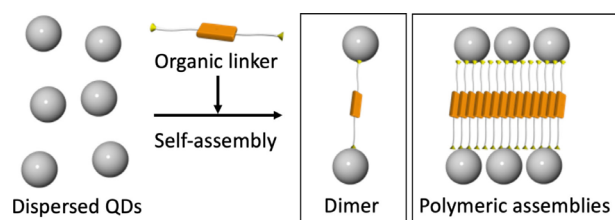
access additional properties and unique behaviors. For example, Jares-Erijman and co-workers reported photoswitchable QDs based on the photoisomerization of a diarylethene derivative, in which the emission intensity of the QDs can be controlled by a switch in the energy transfer between the QDs and diarylethene.<sup>[30]</sup> Castellano and co-workers reported pyrene-functionalized QDs exhibiting thermally activated delayed photoluminescence based on the triplet-triplet energy transfer.<sup>[38]</sup>

The photophysical properties of individual QD monomers can change in the assembled state of multiple QDs in concentrated solutions and solid materials, such as in two-dimensional films and three-dimensional superlattices.<sup>[45–47]</sup> In such assembled states, an inter-QD interaction can occur. Therefore, the performance and properties of the fabricated devices depend on the assembled structures of the QDs. For example, QD dimers show specific absorption and emission spectra that are different from those of QD monomers due to the presence of inter-QD interactions.<sup>[48]</sup> Furthermore, inter-QD interactions, such as energy and charge transfer, in the solid state can be tuned by changing the constituent elements of the QDs.<sup>[49]</sup> By exploiting the differences in the emission properties between the monomer and assembled states, Kanie and co-workers demonstrated the switching of assembly structure-dependent emission from CdS QDs covered with phenethyl ether-type dendrons in the liquid-crystal phase.<sup>[50]</sup> In addition, the long-range-ordered superlattices formed by self-assembling perovskite QDs can emit the intense and short light pulse with a red-shifted emission wavelength, so-called superfluorescence,<sup>[51]</sup> under a strong excitation.<sup>[52,53]</sup> Accordingly, the assembly of QDs can lead to novel properties that are never obtained with single QDs. Therefore, controlling the assembled structures of QDs is important. As a method for the assembly of semiconductor nanocrystals, ligand exchange reactions were applied by the research groups of Nakashima<sup>[54]</sup> and Wan.<sup>[55]</sup> However, although the functionalization of single QDs has progressed, examples of the self-assembly of QDs into supramolecular structures are extremely limited because a rational strategy for the self-assembly of QDs has not been reported. In this Minireview, we discuss the self-assembly of QDs into dimeric, trimeric and extended polymeric assemblies by

[a] Dr. M. Yamauchi, Prof. Dr. S. Masuo  
Department of Applied Chemistry for Environment  
Kwansei Gakuin University  
2-1 Gakuen, Sanda, Hyogo 669-1337 (Japan)  
E-mail: yamauchi@kwansei.ac.jp  
masuo@kwansei.ac.jp

 The ORCID identification number(s) for the author(s) of this article can be found under: <https://doi.org/10.1002/chem.201905807>.

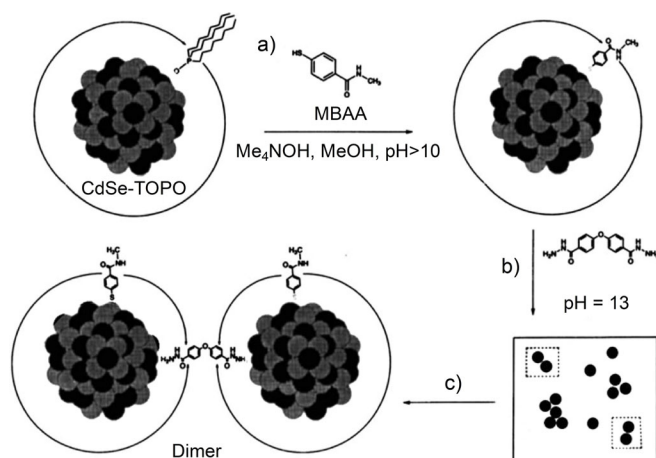
using organic templates, such as linker molecules and self-assembling molecules (Figure 1).



**Figure 1.** Schematic of the self-assembly of QDs into polymeric assemblies with organic linkers.

## Oligomerization of Quantum Dots via Organic Linkers

Dispersed QDs can be connected with organic linkers. Alivisatos and co-workers demonstrated the synthesis of oligomers of CdSe QDs using an organic linker with hydrazide groups and isolated the resulting dimers by size-selective precipitation (Figure 2).<sup>[56]</sup> In the first step, the authors synthesized monodis-

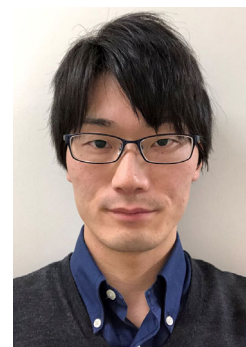


**Figure 2.** Schematic of the dimerization process of CdSe QDs with an organic linker. (a) The passivation process with *N*-methyl-4-sulfanylbenzamide (MBAA). (b) The cross-linking process by the addition of bis(acyl hydrazide). (c) The size-selective precipitation at pH > 10. Reprinted with permission from ref. [56]. Copyright 1997, Wiley-VCH.

perse CdSe QDs passivated with trioctylphosphine oxide (TOPO) as a ligand. To enhance the stability of the QDs, the TOPO ligand was replaced with thiol molecules with a polar end group through ligand exchange. In the second step, the thiol-passivated QDs were cross-linked upon the addition of a bis(acyl hydrazide) linker. As a result, QD monomers, dimers, trimers and oligomers were obtained and isolated by size-selective precipitation in MeOH/Et<sub>2</sub>O. Transmission electron microscopy (TEM) revealed that the purification afforded a dimer-rich solution (monomer:dimer:trimer = 2:7:1).

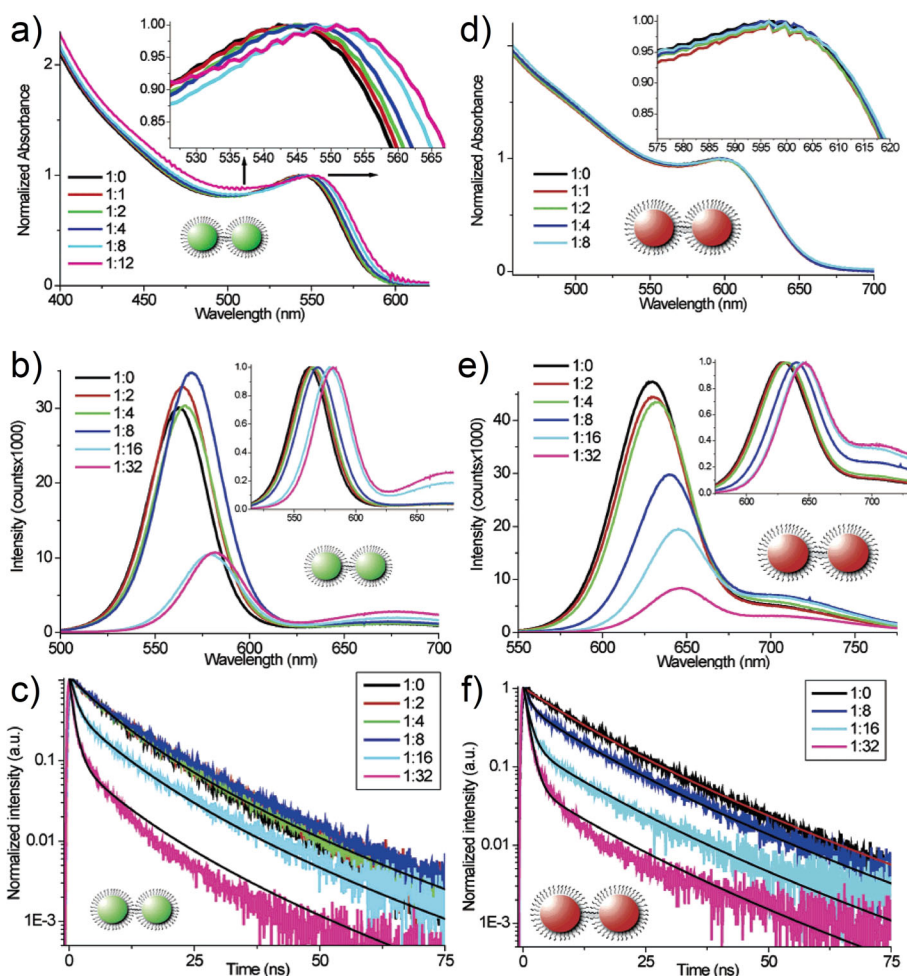
Koole and co-workers reported a simple method for cross-linking CdTe QDs into QD aggregates such as dimers and small oligomers, in which a short linker with two adhesion moieties, 1,6-hexanedithiol, was used to connect the QDs in solution.<sup>[57]</sup> These adhesion moieties, thiol groups, can form relatively strong bonds to the QD surface. As confirmed by Cryo-TEM analysis of the QD aggregates, not only dimer but also small oligomers were formed at higher QD/linker ratios (1:4, 8, 16). In the case of a green-emitting QD (gQD), the spectra of cross-linked gQDs were different from those of dispersed QDs. The absorption spectra showed a gradual redshift in the first absorption peak with spectral broadening as the fraction of linkers increased (Figure 3a). The photoluminescence (PL) spectra and the PL decay curves did not change up to a gQD/linker ratio of 1:8 (Figure 3b,c). Considering the redshift in the absorption peak, these results indicate the occurrence of strong electronic (tunneling) coupling between the gQDs in the linked gQD oligomers. The evidence of such electronic coupling was also obtained by quantum mechanical calculations on coupled QDs through an effective mass approach, in which the coupling energy decreased upon increasing the size of QDs. However, in the case of a cross-linked red-emitting QD (rQD), the absorption did not change as the fraction of linkers increased (Figure 3d). At a rQD/linker ratio of 1:8, the PL spectra showed lower PL intensity and a redshift in the PL peak (Figure 3e). Furthermore, the PL decay curves showed the emergence of a fraction with short lifetimes at the same rQD/linker ratio (Figure 3f). These results indicate the occurrence of

Mitsuaki Yamauchi received his Ph.D. degree in 2017 from Chiba University under the supervision of Prof. Shiki Yagai. During 2014–2017, he studied supramolecular polymerization of small molecules with the support of JSPS Research Fellowship for Young Scientists (DC1). Afterwards, he joined the group of Prof. Sadahiro Masuo at Department of Applied Chemistry for Environment, Kwansei Gakuin University as Assistant Professor. His current researches focus on the creation of stimuli-responsive supramolecular materials using semiconductor nanocrystals, organic dyes and their hybrids.



Sadahiro Masuo received his Ph.D. degree in 2002 from Osaka University under the supervision of Prof. Hiroshi Masuhara. From 2002 to 2004, he was working as a postdoctoral fellow in the group of Prof. Frans C. De Schryver at Katholieke Universiteit Leuven, where he learned single-molecule spectroscopy techniques. Afterwards, he joined the group of Prof. Akira Itaya at Kyoto Institute of Technology as Research associate. In 2010, he moved to Department of Chemistry, Kwansei Gakuin University as Associate Professor. Since 2016, he is Professor of Department of Applied Chemistry for Environment, Kwansei Gakuin University. His research interests are photo-functional materials such as organic-, inorganic nanocrystals using microspectroscopy techniques.





**Figure 3.** (a,d) Absorption and (b,e) PL spectra and (c,f) PL decay curves of cross-linked CdTe QDs with 1,6-hexanedithiol linkers in toluene at various QD/linker ratios; (a–c) gQD dimer, (d–f) rQD dimer. Reprinted with permission from ref. [57]. Copyright 2006, American Chemical Society.

energy transfer between the rQDs as a result of dipole-dipole interactions in the linked rQD dimers. Accordingly, the size of QDs can determine the inter-QD interactions in the QD aggregates, in which the smaller QDs are affected by the electronic coupling while the larger QDs prefer to occur the energy transfer.

Basché and co-workers reported a method for preparing QD dimers and trimers, which were synthesized with the help of a rigid dye linker consisting of a terylene diimide (TDI) with two dicarboxylic anchors (Figure 4a).<sup>[58]</sup> The dimerization and trimerization of QDs with oleic acid/oleylamine ligands was achieved through a ligand exchange reaction by mixing solutions of the monomeric QDs in toluene and the TDI in methanol. Furthermore, the authors demonstrated a powerful method for the separation of QD oligomers, such as dimers and trimers, by using density gradient ultracentrifugation based on cyclohexane-CCl<sub>4</sub> mixtures. The separated QD dimers were confirmed by high-resolution transmission electron microscopy (HR-TEM) images (Figure 4b). The PL spectrum displayed an emission from the QDs and the TDI moieties, which supports the dimerization of the QDs via a TDI linker (Figure 4c). Furthermore, the PL rise/decay curve showed that an increasing point on the

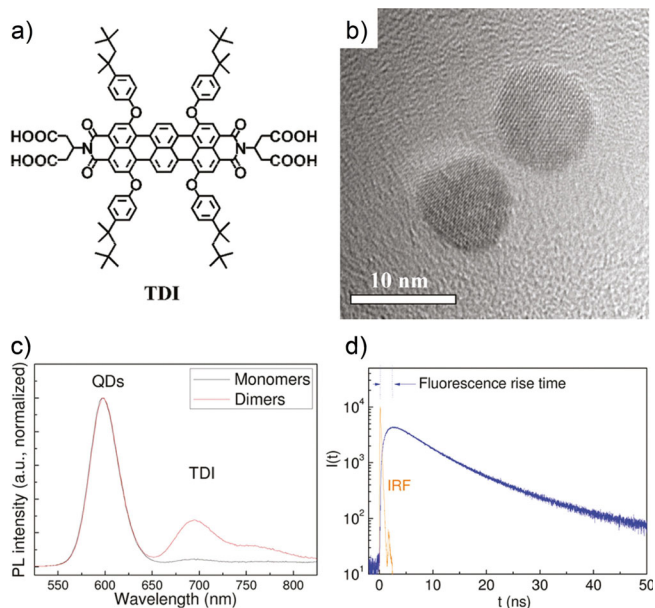
curve was shifted to a longer time relative to the instrumental response function (Figure 4d). This result indicates the presence of fluorescence resonance energy transfer.

## Self-Assembly of Quantum Dots via Template Molecules

Although QDs generally exist as in disperse state in solution, the evaporation of the solvent and the addition of self-assembling molecules can induce the formation of high-order supramolecular QD assemblies. In this section, we discuss such extended QD assemblies as surfaces or in solution.

### Self-assembly of quantum dots on the surface

Most QDs can self-assemble into QD-shape-dependent arrangements upon evaporation of the solvent. For example, colloidal QDs such as CdSe/ZnS form a hexagonal packing arrangement, while cubic QDs such as CsPbBr<sub>3</sub> form a tetragonal (cubic) arrangement. In this regard, the packing structures of self-assembled QDs can also depend on physical properties of ligands on the QD surface. Especially, controlling a distance be-

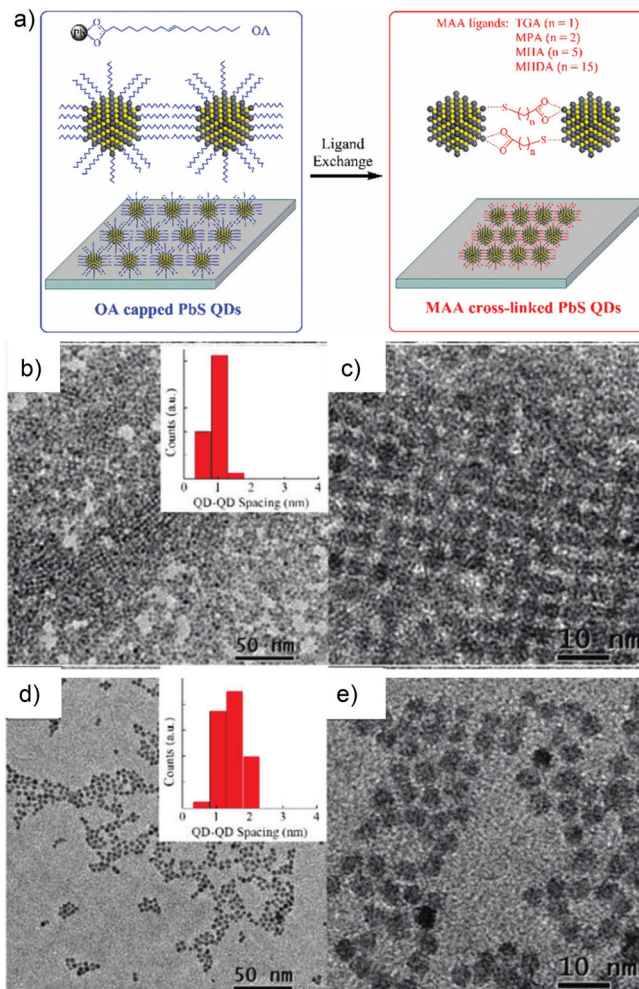


**Figure 4.** (a) Molecular structure of TDI. (b) TEM image of TDI-linked QD dimers. (c) PL spectra ( $\lambda_{\text{ex}} = 450$  nm) of the QD monomer and TDI-linked dimer. (d) PL rise/decay curve ( $\lambda_{\text{ex}} = 450$  nm) of the TDI-linked dimer (blue) with instrumental response function (IRF, orange). Reprinted with permission from ref. [58]. Copyright 2011, American Chemical Society.

tween QDs in solid state through the ligand exchange have been studied in detail for photovoltaic devices using PbS QDs.<sup>[59–65]</sup>

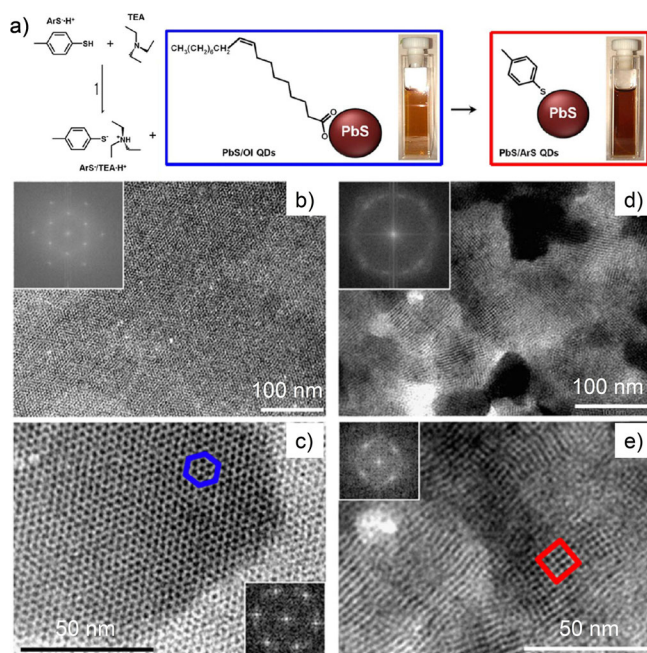
Shen and co-workers discussed the effect of ligands on PbS QDs in the self-assembled QD films and the device performance of fabricated solar cells.<sup>[66]</sup> The as-synthesized QDs were capped with oleic acid (OA-QD). For the ligand exchange, mercaptoalkanoic acid (MMA) such as 3-mercaptopropionic acid (MPA) and 6-mercaptohexanoic acid (MHA) were used as alternative ligands (Figure 5 a). The ligand exchange in solid state was confirmed by Fourier transform infrared (FT-IR) spectroscopy, in which a decrease in the  $\text{CH}_2$  stretching vibrational peaks and an absence of SH stretching vibrational peaks supported the ligand exchange. The TEM observation of the self-assembled QDs on ultrathin carbon substrates revealed that the QD-QD spacing of OA-QDs was ca. 3 nm while those of MPA-QDs and MHA-QDs were ca. 1.0 nm and 1.5 nm, respectively (Figure 5 b–e). These results indicate that the length of ligands can control the distances between QDs in the self-assembled states. As a result, the closely packed MPA-QD films exhibited the highest photon conversion efficiency in the solar cell device.

Giansante and co-workers reported controlling the self-assembly of PbS QDs on substrates by tuning the ligand.<sup>[67]</sup> Synthesized PbS QDs capped with oleic acid (PbS/OL QDs) underwent a ligand exchange reaction to afford arenethiolate-capped QDs (PbS/ArS QDs) by mixing *p*-methylbenzenethiol and triethylamine (Figure 6 a). The TEM images of the dried, self-assembled QDs, prepared under vapor-saturated conditions, reveal that the PbS/OL QDs form a hexagonal packing structure, while the PbS/ArS QDs self-assembled into cubic-like



**Figure 5.** (a) Schematic of the self-assembled PbS QD arrays before and after the solid-state ligand exchange with mercaptoalkanoic acid ligands. (b–e) TEM images of the self-assembled QDs capped with 3-mercaptopropionic acid (MPA) (b,c) and QDs capped with 6-mercaptohexanoic acid (MHA). (d,e) The inset histograms show the statistical data of QD-QD spacing. Reprinted with permission from ref. [66]. Copyright 2017, Royal Society of Chemistry.

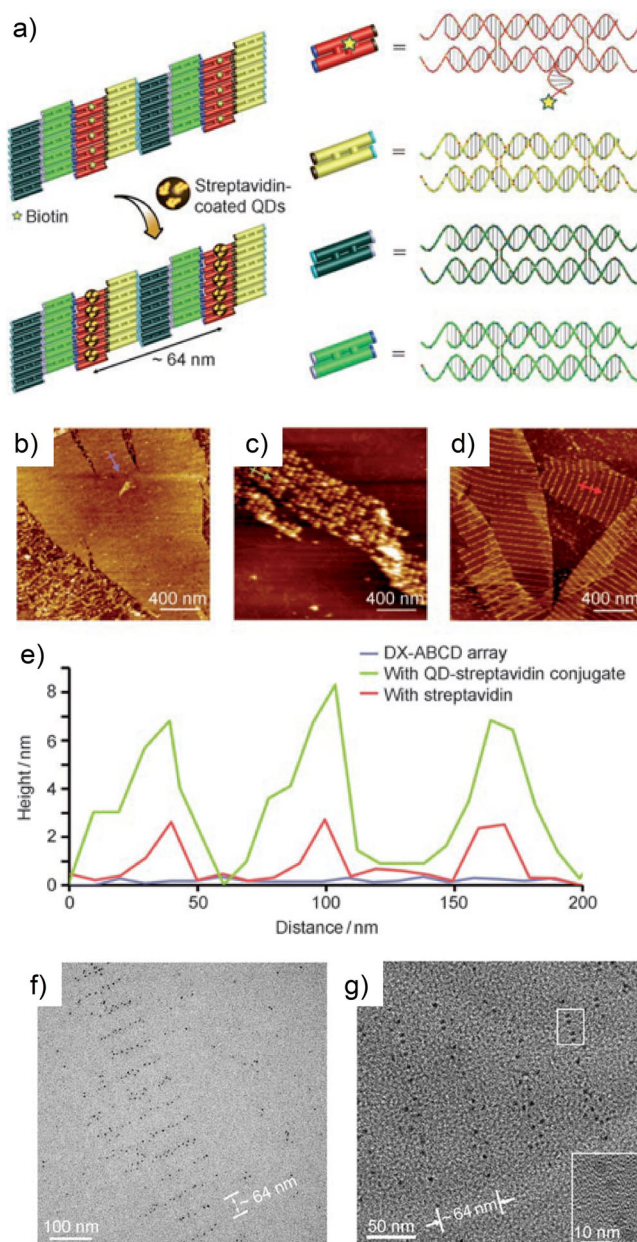
close-packed superlattices (Figure 6 b–e). The authors discussed the different packing structures as a function of the capping ligand, as the ligand plays an important role in controlling the self-assembled structure. For the self-assembly of PbS/OL QDs, the hydrophobic interactions between QDs is a driving force for the formation of a hexagonal packing structure. In contrast, PbS/ArS QDs self-assembled through  $\pi$ - $\pi$  stacking between aromatic moieties in the arenethiolate ligand into a tetragonal packing structure. Due to the different assembled structures, the distance between QDs and the morphology of the resulting films were different, leading to changes in charge-transport properties. These results suggest that controlling the assembled structures can be used to improve the optoelectronic properties of solids.



**Figure 6.** (a) Schematic of the ligand exchange behavior of PbS/OL QDs to PbS/ArS QDs. (b–e) TEM images of self-assembled PbS/OL QDs (b,c) and PbS/ArS QDs (d,e). Reprinted with permission from ref. [67]. Copyright 2013, American Chemical Society.

### Self-assembly of quantum dots assisted by template molecules

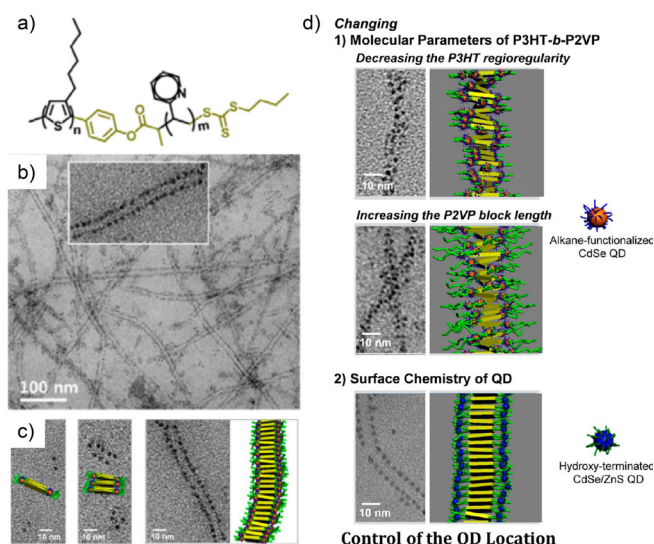
Unlike QDs, organic molecules exhibiting noncovalent interactions such as hydrogen bonding and  $\pi$ - $\pi$  stacking can spontaneously form supramolecular assemblies.<sup>[68–73]</sup> When self-assembling molecules are introduced to a QD system, they can facilitate the assembly of QDs. Yan and co-workers reported a strategy for constructing well-aligned two-dimensional (2D) nanopatterns of CdSe/ZnS core/shell QDs assisted by a DNA-tile-directed self-assembly (Figure 7a).<sup>[74]</sup> In this strategy, they used double-crossover DNA molecules with a biotin group, which serves as a binding moiety for streptavidin on the QDs, allowing the molecules to self-assemble into a 2D DNA array. The DNA 2D array structure was confirmed by AFM observation (Figure 7b). Upon mixing the array assemblies with streptavidin-coated QDs, the streptavidin molecules bind to the biotin, leading to the formation of QD-DNA coassemblies. The AFM images showed periodic stripes composed of QDs on a 2D DNA tile (Figure 7c). AFM cross-sectional analysis revealed that the QD arrays on DNA tiles have an average height of ca. 9 nm. Considering that the height of a streptavidin-bonding 2D DNA tile was ca. 2 nm (Figure 7d,e), the height of arranged QDs on a 2D DNA tile was estimated to be ca. 7 nm, which corresponds to the diameter of the individual QDs containing ligands (Figure 7e). The TEM images showed a periodic pattern of the QD arrays formed by DNA tiles, in which the DNA tiles were not visualized due to the low electron density (Figure 7f,g). A periodicity between the QD arrays was found to be ca. 64 nm. The periodicity was consistent with an estimated periodic distance between two neighboring biotin lines (Fig-



**Figure 7.** (a) Schematic of the formation of DNA-tile-assisted self-assembly of QDs. AFM images for determining the height of the DNA assembled tiles (b), QD arrays on DNA tiles (c) and streptavidin-bonding DNA tiles (d). (e) AFM cross-sectional analysis of the AFM images in b–d. (f, g) TEM images of the pattern of the QD arrays on the DNA tiles. Reprinted with permission from ref. [74]. Copyright 2008, Wiley-VCH.

ure 7a). These results demonstrated that the bottom-up approach using DNA self-assembly leading to programmable nanoarchitectures can be of great importance to rationally construct self-assembled QDs.

Lee and co-workers reported hybrid 1D nanowires composed of a poly(3-hexylthiophene)-*b*-poly(2-vinylpyridine) amphiphilic block copolymer (P3HT-*b*-P2VP, Figure 8a) and QDs, and the polymer allowed precise control over the location of the QDs.<sup>[75]</sup> Crystallization of the copolymers into nanowires occurred by the addition of a poor solvent (acetonitrile) into a polymer solution in good solvent (chloroform). Upon mixing

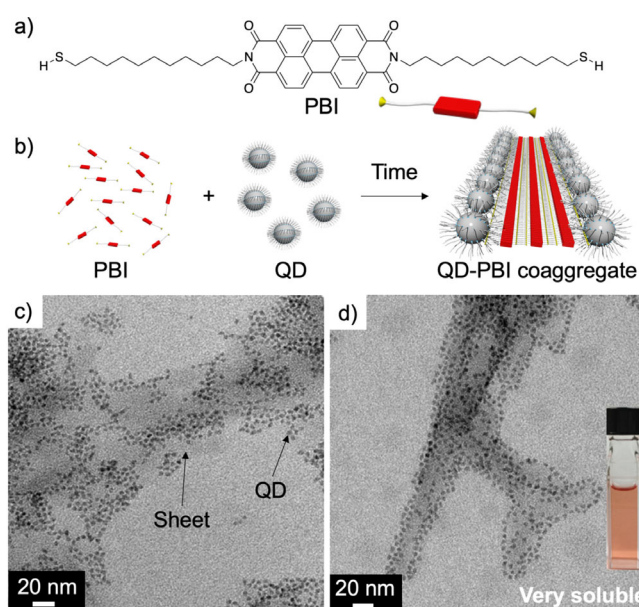


**Figure 8.** (a) Chemical structure of the P3HT-*b*-P2VP amphiphilic block copolymers. (b) TEM image of hybrid nanowires composed of block copolymers and CdSe QDs. (c) TEM images of the coaggregation process of the hybrid nanowires through the formation of dimeric seeds. (d) Schematic of precise control of QD location within the nanowires by changing the molecular parameters of block copolymers and surface condition of QDs. Reprinted with permission from ref. [75]. Copyright 2014, American Chemical Society.

the copolymers and QDs in the above procedure, solvophobic interactions between the aliphatic ligands on QDs and the aliphatic side chains of the copolymers could act as a driving force for the formation of hybrid coaggregates. The TEM images showed the formation of micrometer-long hybrid nanowires, in which the QDs were located with a constant inter-QD distance, which corresponds to the length of the copolymer, along the fiber axis of the P3HT-*b*-P2VP copolymers (Figure 8b). Furthermore, they investigated the coaggregation mechanism by TEM observations at different coaggregation stages. In the early stage of mixing, isolated QD dimers with a center-to-center distance of ca. 9 nm were observed (Figure 8c). In later stages, because the dimers served as seeds for further coaggregation, they self-assembled into long nanowires while maintaining the center-to-center distance of the QDs. These results indicate that the formation of stackable seeds plays an important role in the growth of 1D hybrid nanowires. Notably, the QD locations within the nanowires can be tuned by changing the molecular structures and controlling the surface properties of QDs (Figure 8d). When the regioregularity value of P3HT block copolymer was low, the mixture of QDs and copolymers formed hybrid nanowires with an irregular QD location due to the deterioration of uniform  $\pi$ - $\pi$  interactions between the polythiophene chains. Also, increasing P2VP block length resulted in the formation of hybrid nanowires in which QDs were located at central area of the nanowire. Moreover, upon changing the QD surface from the alkane-terminated (hydrophobic) CdSe QD to hydroxy-terminated (hydrophilic) CdSe/ZnS QD, the center-to-center distance between QD arrays in the hybrid nanowires became larger (ca.

12 nm). As the hydroxyl group of QD can connect with a pyridine moiety of the P2VP, the change of the distance occurred.

Yamauchi and Masuo demonstrated a strategy for the arrangement of CdSe/ZnS core/shell type QDs assisted by the self-assembly of organic, low-molecular-weight perylene bisimide (PBI) (Figure 9a,b).<sup>[76]</sup> In this molecular design, the PBI



**Figure 9.** (a) Chemical structures of PBI. (b) Schematic of the coaggregation process over time. (c, d) TEM images of the QD-PBI intermediates and coaggregates with QD arrangements. Reprinted with permission from ref. [76]. Copyright 2019, Wiley-VCH.

has thiol groups that can adhere to the QD surface, and the PBI moieties can generally form strong  $\pi$ - $\pi$  stacking interactions in nonpolar media. Upon mixing in  $\text{CHCl}_3$ /cyclohexane (1:9, v/v), the QDs and PBI molecules formed kinetically controlled QD-PBI intermediates without QD arrangements, as shown by the TEM image (Figure 9c). Upon aging for 1 h, they had converted into thermodynamically stable supramolecular coaggregates with QD arrangements. TEM observation revealed that the QDs were uniformly arranged along the sheet-like PBI aggregates (Figure 9d). Notably, the coaggregates show good solubility in nonpolar solvents, which suggests that QDs can serve as solubility-enhancing nanomaterials for organic molecular assemblies. Furthermore, the time-dependent coaggregation process was studied in detail by absorption spectroscopy. Hence, coaggregates with QD arrangements were found to form by a rearrangement of  $\pi$ - $\pi$  stacking of PBI over time. Such time-dependent assembly processes have been observed when involving multiple interactions like a combination of hydrogen-bonding and  $\pi$ - $\pi$  stacking. However, the time-change occurred in the assembly of PBI molecules without hydrogen-bonding moieties. This result indicates that the kinetic states in the assembly process of PBIs can be affected by an interaction with inorganic QDs. Accordingly, the supramolecular approach to form unique QD aggregates using the controllable self-assembly of small molecules can contrib-

ute to the construction of programable self-assembly of various nanoparticles.

## Conclusion and Outlook

In this Minireview, we focused on the self-assembly of QDs into supramolecular aggregates, such as dimeric QDs and extended QD arrays, supported by template molecules and substrates. For the dimerization of QDs, the use of organic linkers possessing two adhesion moieties, such as amino, carboxyl or thiol groups, is effective. In contrast, to construct high-order QD assemblies, the use of self-assembling molecules such as DNA and  $\pi$ -conjugated molecules is key to obtaining assemblies with QD arrangements.

Recently, synthetic methods for accessing QDs with various properties, such as high photoluminescent quantum yields and narrow emission bands, have been developed. When QDs with such outstanding properties are used in the solid state to fabricate emission and optoelectronic devices, the resulting supramolecular structures strongly affect the performance of the device. Accordingly, understanding and controlling the supramolecular structures of QDs could be crucial and allow the enhancement of material properties by tuning the supramolecular structures. In particular, the formation of assemblies of QDs in solution, so-called preorganization, can be an attractive platform for preparing high-order supramolecular materials through a bottom-up process. Despite their importance, examples for assembled QDs are still limited. In contrast to typical  $\pi$ -conjugated organic molecules, QDs have a sensitive surface and many adhesion points, making the precise control of QD arrangements quite difficult. This may impede further developments of QD materials. If the surface chemistry of QDs is well understood and well controlled, the field of assembled QDs as well as dispersed QDs will be more active. Accordingly, an enhancement in the device performance based on controlling the self-assembly of QDs can be realized. In addition, understanding and controlling the physical properties influenced by QD–QD interactions should be achievable through the rational control of QD-assembled states, that is, the distance between QDs, the location of QDs and the dimensions of QD assemblies. When the self-assembly of colloidal QDs is rationally controlled, the methodology can contribute to the creation of new photoluminescent and optoelectronic devices depending on the nanostructures. Hence, future progress in materials science related to the assembled nanoparticles containing not only QDs but also other colloids such as polymer nanoparticles and organic nanocrystals can be expected. In this regard, we look forward to seeing novel behaviors and outstanding functions of QD-based materials.

## Acknowledgements

This work was partially supported by Grants-in-Aid for Scientific Research (Nos. 18H01958 and 18K14195) from the Japan Society for the Promotion of Science (JSPS) and a Grant-in-Aid for

Scientific Research on Innovation Areas „Photosynergetics“ (No. 26107005) from MEXT, Japan.

## Conflict of interest

The authors declare no conflict of interest.

**Keywords:** hybrid materials · nanostructures · quantum dot · self-assembly · supramolecular chemistry

- [1] D. V. Talapin, J. S. Lee, M. V. Kovalenko, E. V. Shevchenko, *Chem. Rev.* **2010**, *110*, 389–458.
- [2] A. P. Alivisatos, *Science* **1996**, *271*, 933–937.
- [3] W. R. Algar, K. Susumu, J. B. Delehanty, I. L. Medintz, *Anal. Chem.* **2011**, *83*, 8826–8837.
- [4] C. R. Kagan, E. Lifshitz, E. H. Sargent, D. V. Talapin, *Science* **2016**, *353*, aac5523.
- [5] J. Owen, L. Brus, *J. Am. Chem. Soc.* **2017**, *139*, 10939–10943.
- [6] C. B. Murray, D. J. Norris, M. G. Bawendi, *J. Am. Chem. Soc.* **1993**, *115*, 8706–8715.
- [7] P. O. Anikeeva, J. E. Halpert, M. G. Bawendi, V. Bulovic, *Nano Lett.* **2009**, *9*, 2532–2536.
- [8] O. Chen, J. Zhao, V. P. Chauhan, J. Cui, C. Wong, D. K. Harris, H. Wei, H. S. Han, D. Fukumura, R. K. Jain, M. G. Bawendi, *Nat. Mater.* **2013**, *12*, 445–451.
- [9] M. K. Choi, J. Yang, T. Hyeon, D.-H. Kim, *Flexible Electronics* **2018**, *2*, 10.
- [10] A. J. Nozik, M. C. Beard, J. M. Luther, M. Law, R. J. Ellingson, J. C. Johnson, *Chem. Rev.* **2010**, *110*, 6873–6890.
- [11] M. Bruchez Jr., M. Moronne, P. Gin, S. Weiss, A. P. Alivisatos, *Science* **1998**, *281*, 2013–2016.
- [12] V. Biju, T. Itoh, A. Anas, A. Sujith, M. Ishikawa, *Anal. Bioanal. Chem.* **2008**, *391*, 2469–2495.
- [13] S. Zhang, R. Geryak, J. Geldmeier, S. Kim, V. V. Tsukruk, *Chem. Rev.* **2017**, *117*, 12942–13038.
- [14] F. García-Santamaría, Y. Chen, J. Vela, R. D. Schaller, J. A. Hollingsworth, V. I. Klimov, *Nano Lett.* **2009**, *9*, 3482–3488.
- [15] Y. Kobayashi, N. Tamai, *J. Phys. Chem. C* **2010**, *114*, 17550–17556.
- [16] S. J. Lim, M. U. Zahid, P. Le, L. Ma, D. Entenberg, A. S. Harney, J. Condeelis, A. M. Smith, *Nat. Commun.* **2015**, *6*, 8210.
- [17] C. Pu, H. Qin, Y. Gao, J. Zhou, P. Wang, X. Peng, *J. Am. Chem. Soc.* **2017**, *139*, 3302–3311.
- [18] Y. Chen, J. Vela, H. Htoon, J. L. Casson, D. J. Werder, D. A. Bussian, V. I. Klimov, J. A. Hollingsworth, *J. Am. Chem. Soc.* **2008**, *130*, 5026–5027.
- [19] B. Mahler, P. Spinicelli, S. Buil, X. Quelin, J. P. Hermier, B. Dubertret, *Nat. Mater.* **2008**, *7*, 659–664.
- [20] H. Naiki, S. Masuo, S. Machida, A. Itaya, *J. Phys. Chem. C* **2011**, *115*, 23299–23304.
- [21] S. Masuo, K. Kanetaka, R. Sato, T. Teranishi, *ACS Photonics* **2016**, *3*, 109–116.
- [22] H. Takata, H. Naiki, L. Wang, H. Fujiwara, K. Sasaki, N. Tamai, S. Masuo, *Nano Lett.* **2016**, *16*, 5770–5778.
- [23] A. L. Efros, D. J. Nesbitt, *Nat. Nanotechnol.* **2016**, *11*, 661–671.
- [24] R. Xie, U. Kolb, J. Li, T. Basche, A. Mews, *J. Am. Chem. Soc.* **2005**, *127*, 7480–7488.
- [25] D. A. Hines, P. V. Kamat, *ACS Appl. Mater. Interfaces* **2014**, *6*, 3041–3057.
- [26] A. S. Blum, M. H. Moore, B. R. Ratna, *Langmuir* **2008**, *24*, 9194–9197.
- [27] D. R. Baker, P. V. Kamat, *Langmuir* **2010**, *26*, 11272–11276.
- [28] M. Naito, K. Iwahori, A. Miura, M. Yamane, I. Yamashita, *Angew. Chem. Int. Ed.* **2010**, *49*, 7006–7009; *Angew. Chem.* **2010**, *122*, 7160–7163.
- [29] U. Tohgha, K. Varga, M. Balaz, *Chem. Commun.* **2013**, *49*, 1844–1846.
- [30] S. A. Diaz, G. O. Menéndez, M. H. Etchehon, L. Giordano, T. M. Jovin, E. A. Jares-Erijman, *ACS Nano* **2011**, *5*, 2795–2805.
- [31] Y. Akaishi, A. D. Pramata, S. Tominaga, S. Kawashima, T. Fukaminato, T. Kida, *Chem. Commun.* **2019**, *55*, 8060–8063.
- [32] L. Zhu, M. Q. Zhu, J. K. Hurst, A. D. Li, *J. Am. Chem. Soc.* **2005**, *127*, 8968–8970.

- [33] O. Schmelz, A. Mews, T. Basché, A. Herrmann, K. Müllen, *Langmuir* **2001**, *17*, 2861–2865.
- [34] H. Skaff, K. Sill, T. Emrick, *J. Am. Chem. Soc.* **2004**, *126*, 11322–11325.
- [35] P. T. Snee, R. C. Somers, G. Nair, J. P. Zimmer, M. G. Bawendi, D. G. Nocera, *J. Am. Chem. Soc.* **2006**, *128*, 13320–13321.
- [36] T. Ren, P. K. Mandal, W. Erker, Z. Liu, Y. Avlasevich, L. Puhl, K. Mullen, T. Basche, *J. Am. Chem. Soc.* **2008**, *130*, 17242–17243.
- [37] W. R. Algar, A. Khachatryan, J. S. Melinger, A. L. Huston, M. H. Stewart, K. Susumu, J. B. Blanco-Canosa, E. Oh, P. E. Dawson, I. L. Medintz, *J. Am. Chem. Soc.* **2017**, *139*, 363–372.
- [38] C. Mongin, P. Moroz, M. Zamkov, F. N. Castellano, *Nat. Chem.* **2018**, *10*, 225–230.
- [39] M. La Rosa, S. A. Denisov, G. Jonusauskas, N. D. McClenaghan, A. Credi, *Angew. Chem. Int. Ed.* **2018**, *57*, 3104–3107; *Angew. Chem.* **2018**, *130*, 3158–3161.
- [40] T. Uno, M. Koga, H. Sotome, H. Miyasaka, N. Tamai, Y. Kobayashi, *J. Phys. Chem. Lett.* **2018**, *9*, 7098–7104.
- [41] J. H. Bang, P. V. Kamat, *ACS Nano* **2011**, *5*, 9421–9427.
- [42] E. S. Shibu, A. Sonoda, Z. Tao, Q. Feng, A. Furube, S. Masuo, L. Wang, N. Tamai, M. Ishikawa, V. Biju, *ACS Nano* **2012**, *6*, 1601–1608.
- [43] E. Zenkevich, A. Stupak, C. Gohler, C. Krasselt, C. von Borzyskowski, *ACS Nano* **2015**, *9*, 2886–2903.
- [44] C. Wang, E. A. Weiss, *J. Am. Chem. Soc.* **2016**, *138*, 9557–9564.
- [45] A. L. Rogach, D. V. Talapin, E. V. Shevchenko, A. Kornowski, M. Haase, H. Weller, *Adv. Funct. Mater.* **2002**, *12*, 653–664.
- [46] D. Kim, S. Tomita, K. Ohshiro, T. Watanabe, T. Sakai, I. Y. Chang, K. Hyeon-Deuk, *Nano Lett.* **2015**, *15*, 4343–4347.
- [47] M. A. Boles, M. Engel, D. V. Talapin, *Chem. Rev.* **2016**, *116*, 11220–11289.
- [48] B. K. Hughes, J. L. Blackburn, D. Kroupa, A. Shabaev, S. C. Erwin, A. L. Efros, A. J. Nozik, J. M. Luther, M. C. Beard, *J. Am. Chem. Soc.* **2014**, *136*, 4670–4679.
- [49] N. Kholmicheva, N. Razgoniaeva, P. Yadav, A. Lahey, C. Erickson, P. Moroz, D. Gamelin, M. Zamkov, *J. Phys. Chem. C* **2017**, *121*, 1477–1487.
- [50] M. Matsubara, W. Stevenson, J. Yabuki, X. Zeng, H. Dong, K. Kojima, S. F. Chichibu, K. Tamada, A. Muramatsu, G. Ungar, K. Kanie, *Chem* **2017**, *2*, 860–876.
- [51] G. T. Noeli, J.-H. Kim, J. Lee, Y. Wang, A. K. Wójcik, S. A. McGill, D. H. Reitze, A. A. Belyanin, J. Kono, *Nat. Phys.* **2012**, *8*, 219–224.
- [52] G. Rainò, M. A. Becker, M. I. Bodnarchuk, R. F. Mahrt, M. V. Kovalenko, T. Stoferle, *Nature* **2018**, *563*, 671–675.
- [53] Y. Tong, E. P. Yao, A. Manzi, E. Bladt, K. Wang, M. Doblinger, S. Bals, P. Müller-Buschbaum, A. S. Urban, L. Polavarapu, J. Feldmann, *Adv. Mater.* **2018**, *30*, 1801117.
- [54] Y. Taniguchi, T. Takishita, T. Kawai, T. Nakashima, *Angew. Chem. Int. Ed.* **2016**, *55*, 2083–2086; *Angew. Chem.* **2016**, *128*, 2123–2126.
- [55] J. K. Sun, S. Huang, X. Z. Liu, Q. Xu, Q. H. Zhang, W. J. Jiang, D. J. Xue, J. C. Xu, J. Y. Ma, J. Ding, Q. Q. Ge, L. Gu, X. H. Fang, H. Z. Zhong, J. S. Hu, L. J. Wan, *J. Am. Chem. Soc.* **2018**, *140*, 11705–11715.
- [56] X. G. Peng, T. E. Wilson, A. P. Alivisatos, P. G. Schultz, *Angew. Chem. Int. Ed. Engl.* **1997**, *36*, 145–147; *Angew. Chem.* **1997**, *109*, 113–115.
- [57] R. Koole, P. Liljeroth, C. de Mello Donega, D. Vanmaekelbergh, A. Meijerink, *J. Am. Chem. Soc.* **2006**, *128*, 10436–10441.
- [58] X. Xu, S. Stottinger, G. Battagliarin, G. Hinze, E. Mugnaioli, C. Li, K. Mullen, T. Basche, *J. Am. Chem. Soc.* **2011**, *133*, 18062–18065.
- [59] M. Law, J. M. Luther, Q. Song, B. K. Hughes, C. L. Perkins, A. J. Nozik, *J. Am. Chem. Soc.* **2008**, *130*, 5974–5985.
- [60] Y. Liu, M. Gibbs, C. L. Perkins, J. Tolentino, M. H. Zarghami, J. Bustamante, Jr., M. Law, *Nano Lett.* **2011**, *11*, 5349–5355.
- [61] A. H. Ip, S. M. Thon, S. Hoogland, O. Voznyy, D. Zhitomirsky, R. Debnath, L. Levina, L. R. Rollny, G. H. Carey, A. Fischer, K. W. Kemp, I. J. Kramer, Z. Ning, A. J. Labelle, K. W. Chou, A. Amassian, E. H. Sargent, *Nat. Nanotechnol.* **2012**, *7*, 577–582.
- [62] M. Ono, T. Nishihara, T. Ihara, M. Kikuchi, A. Tanaka, M. Suzuki, Y. Kanemitsu, *Chem. Sci.* **2014**, *5*, 2696–2701.
- [63] C. H. Chuang, P. R. Brown, V. Bulovic, M. G. Bawendi, *Nat. Mater.* **2014**, *13*, 796–801.
- [64] D. Zhitomirsky, O. Voznyy, L. Levina, S. Hoogland, K. W. Kemp, A. H. Ip, S. M. Thon, E. H. Sargent, *Nat. Commun.* **2014**, *5*, 3803.
- [65] G. H. Carey, A. L. Abdelhady, Z. Ning, S. M. Thon, O. M. Bakr, E. H. Sargent, *Chem. Rev.* **2015**, *115*, 12732–12763.
- [66] J. Chang, Y. Ogomi, C. Ding, Y. H. Zhang, T. Toyoda, S. Hayase, K. Katayama, Q. Shen, *Phys. Chem. Chem. Phys.* **2017**, *19*, 6358–6367.
- [67] C. Giansante, L. Carbone, C. Giannini, D. Altamura, Z. Ameer, G. Maruccio, A. Loiudice, M. R. Belviso, P. D. Cozzoli, A. Rizzo, G. Gigli, *J. Phys. Chem. C* **2013**, *117*, 13305–13317.
- [68] F. J. M. Hoeben, P. Jonkheijm, E. W. Meijer, A. P. H. J. Schenning, *Chem. Rev.* **2005**, *105*, 1491–1546.
- [69] A. Ajayaghosh, V. K. Praveen, *Acc. Chem. Res.* **2007**, *40*, 644–656.
- [70] L. C. Palmer, S. I. Stupp, *Acc. Chem. Res.* **2008**, *41*, 1674–1684.
- [71] T. Aida, E. W. Meijer, S. I. Stupp, *Science* **2012**, *335*, 813–817.
- [72] F. Würthner, C. R. Saha-Moller, B. Fimmel, S. Ogi, P. Leowanawat, D. Schmidt, *Chem. Rev.* **2016**, *116*, 962–1052.
- [73] B. Adhikari, X. Lin, M. Yamauchi, H. Ouchi, K. Aratsu, S. Yagai, *Chem. Commun.* **2017**, *53*, 9663–9683.
- [74] J. Sharma, Y. Ke, C. Lin, R. Chhabra, Q. Wang, J. Nangreave, Y. Liu, H. Yan, *Angew. Chem. Int. Ed.* **2008**, *47*, 5157–5159; *Angew. Chem.* **2008**, *120*, 5235–5237.
- [75] Y. J. Kim, C. H. Cho, K. Paek, M. Jo, M. K. Park, N. E. Lee, Y. J. Kim, B. J. Kim, E. Lee, *J. Am. Chem. Soc.* **2014**, *136*, 2767–2774.
- [76] M. Yamauchi, S. Masuo, *Chem. Eur. J.* **2019**, *25*, 167–172.

Manuscript received: December 25, 2019

Revised manuscript received: February 18, 2020

Accepted manuscript online: February 26, 2020

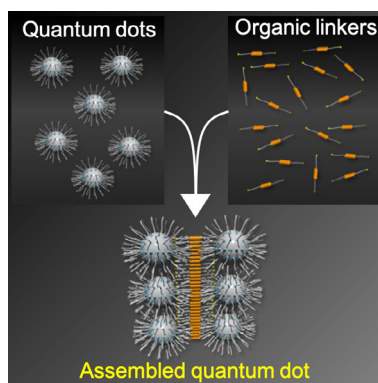
Version of record online: ■ ■ ■ 0000

## MINIREVIEW

## ■ Nanostructures

*M. Yamauchi,\* S. Masuo\**

■■ - ■■

**Self-Assembly of Semiconductor Quantum Dots using Organic Templates**

**Control over the self-assembly** of colloidal semiconductor nanocrystals, known as quantum dots (QDs), is a great challenge. In this Minireview, the self-assemblies of QDs with organic template molecules are highlighted (see figure), which should facilitate future advances in materials science related to assembled QDs.

**Self-assembly of semiconductor quantum dots** are realized by mixing organic template molecules with adhesion moieties to the surface of quantum dots. This Minireview highlights the strategies for the formation of assembled quantum dots such as dimers and trimers and extended assemblies, and their photophysical properties. For more information, see the Minireview by M. Yamauchi and S. Masuo on page ■■.

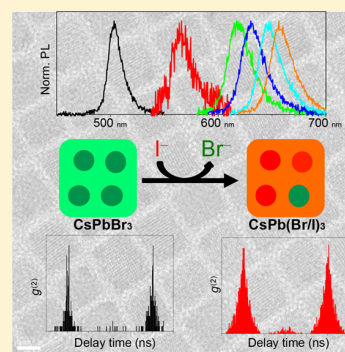
# In Situ Observation of Emission Behavior during Anion-Exchange Reaction of a Cesium Lead Halide Perovskite Nanocrystal at the Single-Nanocrystal Level

Hiroyuki Yoshimura, Mitsuaki Yamauchi,<sup>1B</sup> and Sadahiro Masuo<sup>\*1B</sup>

Department of Applied Chemistry for Environment, Kwansei Gakuin University, 2-1 Gakuen, Sanda, Hyogo 669-1337, Japan

## Supporting Information

**ABSTRACT:** Postsynthesis anion-exchange reaction of cesium lead halide ( $\text{CsPbX}_3$ ; X = Cl, Br, and I) perovskite nanocrystals (NCs) has emerged as a unique strategy to control band gap. Recently, the partially anion-exchanged  $\text{CsPb}(\text{Br}/\text{I})_3$  NC was reported to form an inhomogeneously alloyed heterostructure, which could possibly form some emission sites depending on the halide composition in the single NC. In this work, we observed the in situ emission behavior of single  $\text{CsPb}(\text{Br}/\text{I})_3$  NCs during the anion-exchange reaction. Photon-correlation measurements of the single NCs revealed that the mixed halide  $\text{CsPb}(\text{Br}/\text{I})_3$  NC exhibited single-photon emission. Even when irradiated with an intense excitation laser, the single NC exhibited single-photon emission with a photoluminescence spectrum of a single peak. These results suggested that the heterohalide compositions of the  $\text{CsPb}(\text{Br}/\text{I})_3$  NC do not form any emission sites with different band gap energies; instead, the NC forms emission sites with uniform band gap energy as a whole NC via quantum confinement.



Over the past few years, semiconducting lead halide perovskite nanocrystals (NCs) have emerged as one of the most interesting materials for optoelectronic applications.<sup>1–9</sup> In particular, fully inorganic lead halide perovskite NCs with the formula  $\text{CsPbX}_3$ , in which X is Cl, Br, or I, have been recently shown to exhibit outstanding optical properties. Such compounds are characterized by a broad tunable photoluminescence (PL) over the entire visible spectral region, a narrow full-width at half-maximum (fwhm) of the spectrum, and high PL quantum yields (PLQYs).<sup>10–18</sup> Because the upper valence band is predominately formed by the halide p-orbitals and the lower conduction band is formed by the overlap of Pb p-orbitals,<sup>10,19</sup> the PL wavelength of such perovskite NCs can be easily adjusted through compositional mixing of halogen elements, which is achieved by using different lead halide ratios in the synthesis of the NCs. In addition, a notable characteristic of perovskite NCs is the ability to control the PL wavelength through postsynthetic anion-exchange reaction of a single starting composition because of the more rigid nature of the cationic sublattice and the more mobile nature of anions in halide perovskites.<sup>20–26</sup> Anion exchange has emerged as a simple yet highly effective method to control the composition of  $\text{CsPbX}_3$  perovskite NCs, with X = Cl, Cl/Br mixed halide, Br, Br/I mixed halide, and I. This postsynthesis tunability of the halide composition can tune the band gap of  $\text{CsPbX}_3$  NCs throughout the entire visible region. The anion-exchange reactivity is not limited to the  $\text{CsPbX}_3$  perovskites; a similar behavior has been observed and exploited for a range of halide-based NCs, including hybrid organic–inorganic lead halide perovskites ( $\text{MAPbX}_3$ , MA =  $\text{CH}_3\text{NH}_3^+$ ), ternary bismuth halides ( $\text{MA}_3\text{Bi}_2\text{X}_9$ ), cesium antimony halides

( $\text{Cs}_3\text{Sb}_2\text{X}_9$ ), and elpasolites ( $\text{Cs}_2\text{AgBiX}_6$ ).<sup>27–31</sup> The postsynthesis anion-exchange reaction appears to be a ubiquitous and powerful feature of metal-halide NC chemistry, and the reaction is an important strategy to achieve desired material properties. Therefore, understanding such anion-exchange reactions that produce different halide and mixed halide perovskites is essential for both a fundamental understanding and optimized applications.

Generally, anion-exchanged NCs are assumed to possess a homogeneous composition; for example, mixed halide  $\text{CsPb}(\text{Br}/\text{I})_3$  NCs have the same composition across the NCs, forming a homogeneous alloy. Recently, Haque et al. investigated the distribution of halide anions inside the NCs after partial and complete anion exchange of  $\text{CsPbBr}_3$  NCs with  $\text{I}^-$  using variable energy hard X-ray photoemission spectroscopy.<sup>32</sup> They demonstrated that the anion exchange formed an inhomogeneously alloyed heterostructure with a higher concentration of the exchanged  $\text{I}^-$  on the surface of the NCs. Even for a completely anion-exchanged NC, which showed no further shift of the PL peak position in the presence of excess  $\text{I}^-$ , a significant amount of  $\text{Br}^-$  was still present at the core of the anion-exchanged NCs. If the  $\text{CsPb}(\text{Br}/\text{I})_3$  NC forms such heterostructures, then questions about the emission properties, particularly the emission sites in the single NC, arise, namely, whether the PL photons are emitted from both emission sites consisting of high and low concentrations of  $\text{I}^-$  with different energies or only a single photon is emitted from

**Received:** October 30, 2019

**Accepted:** December 8, 2019

**Published:** December 8, 2019

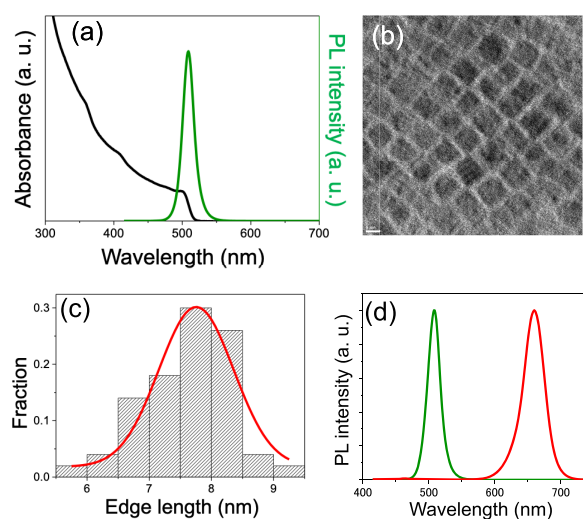
one emission site, acting as a single quantum dot,<sup>15,16,33–36</sup> with the energy due to quantum confinement depending on the mixed halide composition. Li et al. studied the evolution of the in situ PL during the anion-exchange reaction.<sup>37</sup> They observed two distinct PL peaks during the initial stage of the reaction after the addition of  $\text{PbI}_2$  precursor solution to  $\text{CsPbBr}_3$  NCs, suggesting that the reaction was inhomogeneous at the beginning and resulted in two or more different compositions. Regarding the inhomogeneity, they interpreted it as the halide compositions having NC-to-NC variations in the initial stage of the anion-exchange reaction, and finally, the halide composition reached a steady state and formed homogeneous NCs because of the high conductivity of  $\text{I}^-$ . However, the evolution of the in situ PL was measured for an NC ensemble, which obscures the inhomogeneity of the halide composition in individual NCs. To elucidate the emission property depending on the inhomogeneity, in situ observation at the single NC level is essential. Nevertheless, in situ PL observation during the anion-exchange reaction at the single NC level has not been realized thus far.

In this work, we investigated the emission properties, particularly the single-photon emission behavior, of the intermediate  $\text{CsPb}(\text{Br}/\text{I})_3$  NC, i.e., the mixed halide composition, during the anion-exchange reaction at the single NC level to reveal the emission site of the NC. We henceforth focus the discussion on the exchange route starting from  $\text{CsPbBr}_3$  NCs because of their stability and strong emission. The average edge length of the  $\text{CsPbBr}_3$  NCs was controlled to be ca. 7 nm, which was comparable to the Bohr diameter (7 nm),<sup>10</sup> to investigate the emission behavior of single NCs acting as quantum dots. Directly synthesized  $\text{CsPbBr}_3$  NCs were dispersed in a poly(methyl methacrylate) (PMMA) thin film to fix them, and then an octadecene solution with  $\text{PbI}_2$  as a halide precursor was dropped on the PMMA thin film under an optical microscope. In this way, we succeeded in observing the in situ emission behavior of single mixed halide  $\text{CsPb}(\text{Br}/\text{I})_3$  NCs during the anion-exchange reaction. We observed a gradual redshift of the single peak in the PL spectrum from the single NCs with time. The photon-correlation histogram obtained from the single NCs showed single-photon emission behavior, indicating the emission property of a quantum emitter even for the inhomogeneous anion composition of  $\text{CsPb}(\text{Br}/\text{I})_3$  NCs. Additionally, when multiple excitons were generated in a single NC by applying a higher excitation laser, single-photon emission behavior and a PL spectrum with a single peak were observed. These results indicated that the inhomogeneous halide composition during the anion-exchange reaction formed a uniform electronic state in the NCs, and the PL photons were emitted from only one emission site at the same time. In other words, the single NC with an inhomogeneous halide composition behaves as a single quantum dot because of quantum confinement depending on the halide composition.

$\text{CsPbBr}_3$  NCs were synthesized as described by Protesescu et al.,<sup>10</sup> with some minor adaptations (details are provided in the Supporting Information). Then, an anion-exchange reaction with  $\text{PbI}_2$  was carried out to replace the  $\text{Br}^-$  in the  $\text{CsPbBr}_3$  NCs with  $\text{I}^-$ . The anion-exchange reaction in solution was performed according to the following procedure:<sup>20</sup> A total of 2.78 g of  $\text{PbI}_2$  ( $6.03 \times 10^{-3}$  mol), 4.8 mL of oleic acid, and 4.8 mL of oleylamine were loaded into a three-necked round-bottom flask with 10 mL of octadecene, dried/degassed for 1 h at 120 °C under vacuum, and then stirred under argon gas at

120 °C until  $\text{PbI}_2$  was dissolved. Then, 1 mL of the  $\text{PbI}_2$  solution (0.31 mol/L) was injected into 2 mL of  $\text{CsPbBr}_3$  NC-dispersed toluene solution ( $4.2 \times 10^{-6}$  mol/L) with vigorous stirring at room temperature to replace  $\text{Br}^-$  with  $\text{I}^-$ . For the anion-exchange reaction of single NCs,  $\text{CsPbBr}_3$  NCs were dispersed in a PMMA thin film by spin-coating NC-dispersed PMMA/toluene solution onto a clean glass coverslip. The PMMA thin film with a ca. 30 nm thickness was prepared by spin-coating PMMA/toluene solution of 0.5 wt % at 3000 rpm. Typically, the number of NCs in the PMMA thin film was less than 10 NCs in an area of  $10 \mu\text{m} \times 10 \mu\text{m}$  to allow for isolation of a single NC with a confocal microscope. This sample was set on the stage of an inverted microscope, and then the above  $\text{PbI}_2$  solution was dropped on the sample, i.e., on the PMMA thin film. The PL behavior of isolated single NCs before and during the anion-exchange reaction was measured using a single NC spectroscopy setup<sup>38–40</sup> consisting of an inverted microscope, a picosecond pulsed laser (405 nm) as an excitation light source, a spectrometer with an EM-CCD camera, two single-photon counting avalanche photodiodes for photon-correlation measurement, and a time-correlated single-photon counting system (details are provided in the Supporting Information).

Figure 1 shows the absorption and PL spectra (a), a transmission electron microscopy (TEM) image (b), and the

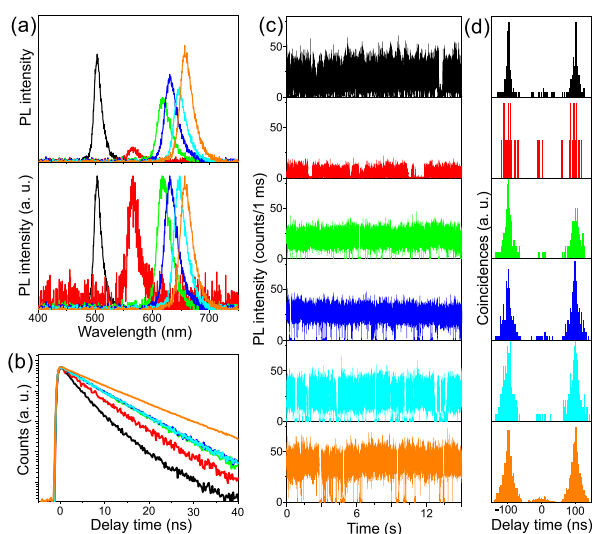


**Figure 1.** (a) Absorption (black) and PL (green; excited by 405 nm light) spectra of the synthesized  $\text{CsPbBr}_3$  NCs in toluene. (b) TEM image of the  $\text{CsPbBr}_3$  NCs. The scale bar in the image represents 5 nm. (c) Size distribution estimated from the TEM image. The size was estimated as the edge length of the cubic-shaped NCs. (d) PL spectra before (green) and after (red) the anion-exchange reaction.

size distribution of synthesized  $\text{CsPbBr}_3$  NCs estimated from the TEM image (c). The absorption spectrum showed a first peak at 500 nm (Figure 1a), from which the size of the NCs was calculated to be ca. 7.5 nm.<sup>14</sup> In the TEM image, cubic-shaped NCs were observed, and the average edge length of the NCs was estimated to be  $7.8 \pm 0.1$  nm (Figure 1c). This size is consistent with the size calculated with the absorption peak. From these results, we confirmed the formation of  $\text{CsPbBr}_3$  NCs. Then, the anion-exchange reaction of the  $\text{CsPbBr}_3$  NCs in solution was confirmed by injecting  $\text{PbI}_2$  solution into the

CsPbBr<sub>3</sub> NC-dispersed toluene solution under the condition of an overall halide ratio in the system,  $[\text{Br}]_{\text{parent}}/[\text{I}]_{\text{incoming}}$  of 1:10 (details are provided in the Supporting Information). The change in the PL spectrum due to the anion-exchange reaction is shown in Figure 1d. The parent CsPbBr<sub>3</sub> NCs in toluene exhibited a PL spectrum with a peak at 508 nm and a 20 nm fwhm. The PL spectrum was changed into a spectrum with a peak at 660 nm and a 37 nm fwhm by the 30 s anion-exchange reaction. No further spectral shift was observed for a longer reaction time and by adding excess PbI<sub>2</sub> solution. Therefore, in the CsPbBr<sub>3</sub> NCs, which showed a PL peak at 660 nm, almost all Br<sup>-</sup> was probably replaced with I<sup>-</sup>. When lower-concentration PbI<sub>2</sub> solutions were added to the CsPbBr<sub>3</sub> NCs, PL spectra with a single peak at an intermediate wavelength between 508 and 660 nm were observed, as reported in the literature (Figure S1 in the Supporting Information).<sup>20,22</sup> These results supported that the anion-exchange reaction of our CsPbBr<sub>3</sub> NCs possibly proceeded in the same manner as that for reported NCs.

The emission behavior of single CsPbBr<sub>3</sub> NCs dispersed in PMMA thin film was measured using a single NC measurement setup with a 23 W/cm<sup>2</sup> excitation power at 405 nm. The observed PL spectrum (a), PL decay curve (b), time trace of the PL intensity (c), and photon-correlation histogram (d) of a representative single NC are shown in Figure 2 in black. The



**Figure 2.** Emission behavior of a single CsPbBr<sub>3</sub> NC and the single NC during the anion-exchange reaction. (a) PL spectra (upper panel) and normalized PL spectra (bottom panel), (b) PL decay curve, (c) time traces of the PL intensity, and (d) photon-correlation histograms. Black, a single CsPbBr<sub>3</sub> NC before the anion-exchange reaction; red, 330 s; green, 560 s; blue, 700 s; light blue, 930 s; and orange, 3570 s after dropping PbI<sub>2</sub> solution onto the top of the sample.

single NC exhibited a PL spectrum with a peak at 503 nm and a 15 nm fwhm, which is narrower than the ensemble PL bandwidth (Figure S1 and Table S1). This result suggests a considerable contribution of size nonuniformity to the apparent PL bandwidth of the NC ensemble samples. The average lifetime was estimated to be 5.9 ns, which is consistent with reported values.<sup>10,19,37,41</sup> In the photon-correlation histogram, photon-detection events at delay time 0 ns were

much fewer than those at other delay times. The second-order correlation function  $g^{(2)}(0)$ , defined as the ratio of the number of detection events at a delay time of 0 ns to the average number of detection events at other delay times, provides information about the photon statistics in the PL emission; specifically, the probability of single-photon emission increases when  $g^{(2)}(0)$  approaches zero. In this case,  $g^{(2)}(0)$  was estimated to be 0.07, which indicated that the single NC emitted single photons, i.e., only one exciton (emission site) emitted a photon in an excitation process.<sup>15,16,33,41,42</sup>

To investigate the emission behavior, particularly the number of emission sites during the anion-exchange reaction, PbI<sub>2</sub> solution was drop-cast onto the top of the sample, and the change in the emission behavior of the single NC was observed in situ, as shown in Figure 2. The PL peak wavelength, fwhm of the PL spectrum, average PL lifetime, and  $g^{(2)}(0)$  obtained from the observations are summarized in Table 1. In this case,

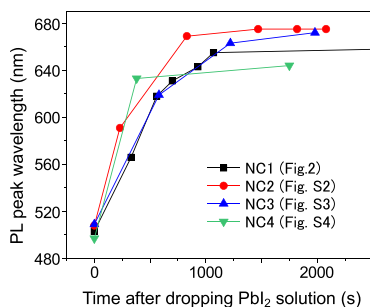
**Table 1.** PL Peak Wavelength, FWHM of the PL Spectrum, Average PL Lifetime, and  $g^{(2)}(0)$  Obtained from the Observed Emission Behavior of a Single NC during the Anion-Exchange Reaction

	PL peak (nm)	fwhm (nm)	average PL lifetime (ns)	$g^{(2)}(0)$
before reaction	503	14	5.9	0.07
during reaction				
330 s	566	18	10.3	0.21
560 s	618	24	11.9	0.05
700 s	631	24	11.9	0.06
930 s	643	22	12.1	0.03
3500 s	660	21	12.8	0.06

a PbI<sub>2</sub> solution with 15 000 times lower concentration than that for the anion-exchange reaction in solution was used to slow the reaction and observe the emission behavior of the single mixed halide CsPb(Br/I)<sub>3</sub> NC during the reaction. Additionally, we determined that the PMMA thin film was not damaged by the PbI<sub>2</sub> octadecene solution. At 330 s after dropping the PbI<sub>2</sub> solution (indicated by the red color in Figure 2), the single peak of the PL spectrum was red-shifted to 566 nm, and then the peak gradually red-shifted up to 660 nm with time until 3570 s as the Br<sup>-</sup> in the NC was replaced by I<sup>-</sup> (Figure 2a). No further redshift was observed over time. The red-shifted PL spectrum with a peak at 660 nm was the same as that observed for the anion-exchange reaction in solution with excess I<sup>-</sup> (Figures 1d and S1). These spectral shifts indicate that in situ PL observation of a single NC during the anion-exchange reaction was possible by fixing the single NCs in the PMMA thin film. Because the amorphous PMMA film possesses a free volume, I<sup>-</sup> can penetrate the PMMA film. Therefore, the anion-exchange reaction was achieved even for the CsPbBr<sub>3</sub> NCs dispersed in the PMMA thin film. Through the anion-exchange reaction, the fwhm of the PL spectra slightly increased (Figure 2a and Table 1). The PL intensity initially decreased, for example, the PL at 330 s, and then the intensity gradually increased with the redshift of the spectra (Figure 2a,c). This intensity change is consistent with the in situ PL observed for the anion-exchange reaction of the NC ensemble,<sup>22</sup> which may be attributed to the formation of defect sites due to the lattice mismatch arising from the anion exchange. However, the PL decay curves of such NCs (Figure 2b) exhibited no short lifetime component corresponding to

quenching of the exciton by defect sites. The lifetime gradually became longer with the redshift of the spectra, which is a similar trend as in the recent literature.<sup>10,19,37,43</sup>

In the photon-correlation histogram, the single mixed halide CsPb(Br/I)<sub>3</sub> NC during the anion-exchange reaction maintained a small center peak at the delay time of 0 ns and exhibited low  $g^{(2)}(0)$  values (Figure 2d and Table 1). This is the first observation of a real-time halogen exchange reaction in a single NC. In the histogram observed at 330 s, the contribution of the center peak was higher than that at other times because of the low signal-to-noise ratio due to the low PL intensity. These results clearly indicated that the CsPb(Br/I)<sub>3</sub> NC exhibited single-photon emission, i.e., only one emission site emitted photons even for the inhomogeneously alloyed heterostructure of halide anions.<sup>32</sup> This means that the CsPb(Br/I)<sub>3</sub> NC does not form any emission sites with low and high band gap energies depending on the composition of the Br/I ratio, and the NC forms an emission site with uniform band gap energy via quantum confinement depending on the Br/I ratio. Other single NCs also exhibited the same trend of the emission behavior, although the relationship between the spectral shift and the time, i.e., reaction rate, was different for each NC (see Figures S2–S4 and Table S1). This difference is probably due to the differences in the size of the parent CsPbBr<sub>3</sub> NCs and/or in the fixed position in the PMMA thin film. The relationships between the PL peak wavelength and the time obtained from 4 single NCs are shown in Figure 3. In

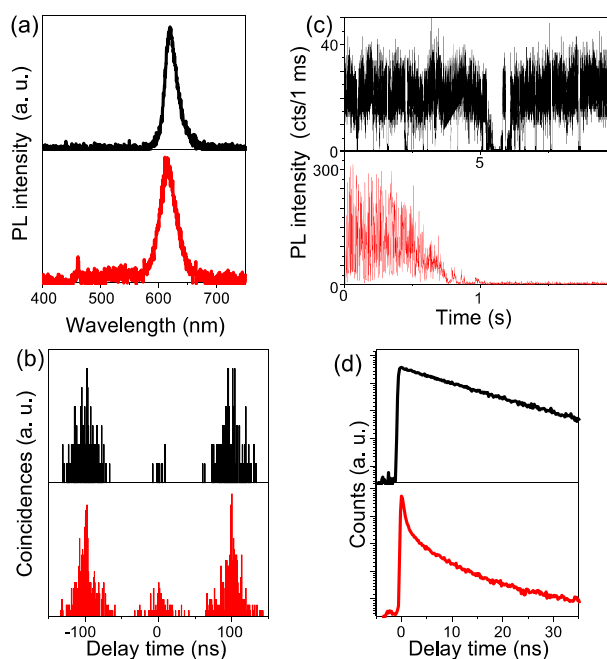


**Figure 3.** Shift of the PL peak wavelength during the anion-exchange reaction, obtained from the observed emission behavior of single NCs shown in Figure 2 (NC1) and Figures S2–S4 (NC2–4).

Figure 3, the PL peak wavelength at time 0 s (before the reaction) is different for each single NC. The PL peak wavelength depends on the size of the NC; that is, the single NC exhibiting a shorter PL peak has a smaller size. In Figure 3, the size of the single NCs increases in the order NC4, NC1, NC2, and NC3, and NC2 and NC3 have almost the same size. The final PL peak wavelength shift due to the anion-exchange reaction of a smaller NC was shorter than that of a larger NC. The final PL peak wavelengths of NC2 and NC3 were almost the same, while the reaction rates were different. Thus, the reaction rate depends on the size of the NC and fixed position in the PMMA thin film.

From the above results, we elucidated that the single mixed halide CsPb(Br/I)<sub>3</sub> NC exhibited single-photon emission. However, if the single NC forms both a higher band gap emission site with a high Br/I ratio and a lower band gap emission site with a lower Br/I ratio due to the heterogeneity of the Br/I ratio, then when energy transfer from the higher band gap site to the lower band gap site occurs, the observed

results should be the same as the present results. Thus, to investigate the possibility of the energy transfer, we measured the photon correlation of a single CsPb(Br/I)<sub>3</sub> NC using an intense excitation laser. When multiple excitons are generated in the single NC by irradiating it with the intense excitation laser, state filling will occur; that is, because the lower band gap site is occupied by an exciton due to energy transfer, an exciton also populates the higher band gap site. Thus, a PL spectrum with multiple peaks should be observed if the NC forms multiple emission sites with different energies. The emission behavior observed from a single CsPb(Br/I)<sub>3</sub> NC by irradiating it with low (23 W/cm<sup>2</sup>) and high (4 kW/cm<sup>2</sup>) excitation laser powers at 405 nm is shown in Figure 4. Using



**Figure 4.** PL spectra (a), photon-correlation histograms (b), time traces of the PL intensity, and PL decay curves observed by irradiating an NC with excitation powers of 23 W/cm<sup>2</sup> (black) and 4 kW/cm<sup>2</sup> (red).

these excitation powers, generation of 0.02 and 4 excitons/pulse, respectively, in the single NC was estimated from the calculations, taking into account the absorption cross-section of the CsPbBr<sub>3</sub> NC.<sup>12,14,19</sup> When the NC was irradiated with the intense laser, the PL intensity was increased (~300 cts/ms), and the survival time in the time trace of the PL intensity (Figure 4c) was shortened (~1 s). In the PL decay curve, the contribution of the short lifetime increased compared to the emission behavior observed under low-power excitation (Figure 4d). In the photon-correlation histogram (Figure 4b), the center peak at delay time 0 ns maintained a low value, i.e., single-photon emission, even under intense excitation laser irradiation, which indicated that an efficient Auger recombination process occurred between the generated excitons.<sup>43–47</sup> This Auger recombination and subsequent trion formation resulted in the appearance of the short lifetime and spiky trajectory of the PL intensity, i.e., frequent blinking in the time trace of the PL intensity.<sup>15,16,33,41,42,48–51</sup> Importantly, the PL spectra shown in Figure 4a exhibited a single peak even when the NC was excited by an intense excitation laser. From these

results, we can conclude that no energy transfer occurred in the CsPb(Br/I)<sub>3</sub> NC; that is, the CsPb(Br/I)<sub>3</sub> NC formed a uniform electronic state of the same band gap energy as a whole NC. In addition, no spectral shift due to light-induced phase segregation<sup>52</sup> was observed for the present size CsPb(Br/I)<sub>3</sub> NC. This result provides important insight into the phase segregation that results in instability and degradation of perovskite materials.

In conclusion, we succeeded in observing the emission behavior of a single CsPb(Br/I)<sub>3</sub> NC during the anion-exchange reaction. From the photon-correlation measurements of the single NCs obtained by applying low and high excitation powers, we elucidated that the single NCs exhibited single-photon emission despite the heterogeneity of the Br/I ratio in the single NCs. The size of the parent CsPbBr<sub>3</sub> NCs in the present work was 7.8 nm, which was comparable to the Bohr diameters of NCs (7 nm for CsPbBr<sub>3</sub> and 12 nm for CsPbI<sub>3</sub>).<sup>10</sup> Therefore, a single NC formed a uniform electronic state via quantum confinement depending on the Br/I ratio; that is, the single NC behaved as a quantum dot. The present results are quite reasonable and provide new insights into lead halide perovskite NCs, on which a great deal of research has been performed.

## ■ ASSOCIATED CONTENT

### Supporting Information

The Supporting Information is available free of charge at <https://pubs.acs.org/doi/10.1021/acs.jpcllett.9b03204>.

Details of synthesis and anion-exchange reaction, instrument setup, emission behavior of single NCs during the anion-exchange reaction (PDF)

## ■ AUTHOR INFORMATION

### Corresponding Author

\*E-mail: [masuo@kwansei.ac.jp](mailto:masuo@kwansei.ac.jp).

### ORCID

Mitsuaki Yamauchi: 0000-0003-0005-5960

Sadahiro Masuo: 0000-0003-4828-5968

### Notes

The authors declare no competing financial interest.

## ■ ACKNOWLEDGMENTS

This work was partially supported by Grants-in-Aid for Scientific Research (Nos. 18H01958 and 18K14195) from the Japan Society for the Promotion of Science (JSPS). TEM measurements were supported by Prof. Dr. K. Kamada and Dr. T. Uchida at National Institute of Advanced Industrial Science and Technology (AIST).

## ■ REFERENCES

- (1) Yakunin, S.; Protesescu, L.; Krieg, F.; Bodnarchuk, M. I.; Nedelcu, G.; Humer, M.; De Luca, G.; Fiebig, M.; Heiss, W.; Kovalenko, M. V. Low-Threshold Amplified Spontaneous Emission and Lasing from Colloidal Nanocrystals of Caesium Lead Halide Perovskites. *Nat. Commun.* **2015**, *6*, 8515.
- (2) Huang, H.; Chen, B. K.; Wang, Z. G.; Hung, T. F.; Susha, A. S.; Zhong, H. Z.; Rogach, A. L. Water Resistant CsPbX<sub>3</sub> Nanocrystals Coated with Polyhedral Oligomeric Silsesquioxane and Their Use as Solid State Luminophores in All-Perovskite White Light-Emitting Devices. *Chem. Sci.* **2016**, *7*, 5699–5703.
- (3) Li, G. R.; Rivarola, F. W. R.; Davis, N. J. L. K.; Bai, S.; Jellicoe, T. C.; de la Pena, F.; Hou, S. C.; Ducati, C.; Gao, F.; Friend, R. H.; et al.

Highly Efficient Perovskite Nanocrystal Light-Emitting Diodes Enabled by a Universal Crosslinking Method. *Adv. Mater.* **2016**, *28*, 3528–3534.

(4) Manser, J. S.; Christians, J. A.; Kamat, P. V. Intriguing Optoelectronic Properties of Metal Halide Perovskites. *Chem. Rev.* **2016**, *116*, 12956–13008.

(5) Meyns, M.; Peralvarez, M.; Heuer-Jungemann, A.; Hertog, W.; Ibanez, M.; Nafria, R.; Genc, A.; Arbiol, J.; Kovalenko, M. V.; Carreras, J.; et al. Polymer-Enhanced Stability of Inorganic Perovskite Nanocrystals and Their Application in Color Conversion LEDs. *ACS Appl. Mater. Interfaces* **2016**, *8*, 19579–19586.

(6) Huang, H.; Bodnarchuk, M. I.; Kershaw, S. V.; Kovalenko, M. V.; Rogach, A. L. Lead Halide Perovskite Nanocrystals in the Research Spotlight: Stability and Defect Tolerance. *ACS Energy Lett.* **2017**, *2*, 2071–2083.

(7) Panigrahi, S.; Jana, S.; Calmeiro, T.; Nunes, D.; Martins, R.; Fortunato, E. Imaging the Anomalous Charge Distribution Inside CsPbBr<sub>3</sub> Perovskite Quantum Dots Sensitized Solar Cells. *ACS Nano* **2017**, *11*, 10214–10221.

(8) Lee, S.; Park, J. H.; Nam, Y. S.; Lee, B. R.; Zhao, B. D.; Di Nuzzo, D.; Jung, E. D.; Jeon, H.; Kim, J. Y.; Jeong, H. Y.; et al. Growth of Nanosized Single Crystals for Efficient Perovskite Light-Emitting Diodes. *ACS Nano* **2018**, *12*, 3417–3423.

(9) Lin, K.; Xing, J.; Quan, L. N.; de Arquer, F. P. G.; Gong, X.; Lu, J.; Xie, L.; Zhao, W.; Zhang, D.; Yan, C.; et al. Perovskite Light-Emitting Diodes with External Quantum Efficiency Exceeding 20%. *Nature* **2018**, *562*, 245–248.

(10) Protesescu, L.; Yakunin, S.; Bodnarchuk, M. I.; Krieg, F.; Caputo, R.; Hendon, C. H.; Yang, R. X.; Walsh, A.; Kovalenko, M. V. Nanocrystals of Cesium Lead Halide Perovskites (CsPbX<sub>3</sub>, X = Cl, Br, and I): Novel Optoelectronic Materials Showing Bright Emission with Wide Color Gamut. *Nano Lett.* **2015**, *15*, 3692–3696.

(11) Akkerman, Q. A.; Motti, S. G.; Kandada, A. R. S.; Mosconi, E.; D'Innocenzo, V.; Bertoni, G.; Marras, S.; Kamino, B. A.; Miranda, L.; De Angelis, F.; et al. Solution Synthesis Approach to Colloidal Cesium Lead Halide Perovskite Nanoplatelets with Monolayer-Level Thickness Control. *J. Am. Chem. Soc.* **2016**, *138*, 1010–1016.

(12) De Roo, J.; Ibanez, M.; Geiregat, P.; Nedelcu, G.; Walravens, W.; Maes, J.; Martins, J. C.; Van Driessche, I.; Kovalenko, M. V.; Hens, Z. Highly Dynamic Ligand Binding and Light Absorption Coefficient of Cesium Lead Bromide Perovskite Nanocrystals. *ACS Nano* **2016**, *10*, 2071–2081.

(13) Liu, F.; Zhang, Y.; Ding, C.; Kobayashi, S.; Izuishi, T.; Nakazawa, N.; Toyoda, T.; Ohta, T.; Hayase, S.; Minemoto, T.; et al. Highly Luminescent Phase-Stable CsPbI<sub>3</sub> Perovskite Quantum Dots Achieving Near 100% Absolute Photoluminescence Quantum Yield. *ACS Nano* **2017**, *11*, 10373–10383.

(14) Maes, J.; Balcaen, L.; Drijvers, E.; Zhao, Q.; De Roo, J.; Vantomme, A.; Vanhaecke, F.; Geiregat, P.; Hens, Z. Light Absorption Coefficient of CsPbBr<sub>3</sub> Perovskite Nanocrystals. *J. Phys. Chem. Lett.* **2018**, *9*, 3093–3097.

(15) Hu, F.; Zhang, H.; Sun, C.; Yin, C.; Lv, B.; Zhang, C.; Yu, W. W.; Wang, X.; Zhang, Y.; Xiao, M. Superior Optical Properties of Perovskite Nanocrystals as Single Photon Emitters. *ACS Nano* **2015**, *9*, 12410–12416.

(16) Park, Y. S.; Guo, S.; Makarov, N. S.; Klimov, V. I. Room Temperature Single-Photon Emission from Individual Perovskite Quantum Dots. *ACS Nano* **2015**, *9*, 10386–10393.

(17) Swarnkar, A.; Chulliyil, R.; Ravi, V. K.; Irfanullah, M.; Chowdhury, A.; Nag, A. Colloidal CsPbBr<sub>3</sub> Perovskite Nanocrystals: Luminescence beyond Traditional Quantum Dots. *Angew. Chem., Int. Ed.* **2015**, *54*, 15424–15428.

(18) Aharonovich, I.; Englund, D.; Toth, M. Solid-State Single-Photon Emitters. *Nat. Photonics* **2016**, *10*, 631–641.

(19) Ravi, V. K.; Markad, G. B.; Nag, A. Band Edge Energies and Excitonic Transition Probabilities of Colloidal CsPbX<sub>3</sub> (X = Cl, Br, I) Perovskite Nanocrystals. *ACS Energy Lett.* **2016**, *1*, 665–671.

(20) Akkerman, Q. A.; D'Innocenzo, V.; Accornero, S.; Scarpellini, A.; Petrozza, A.; Prato, M.; Manna, L. Tuning the Optical Properties

of Cesium Lead Halide Perovskite Nanocrystals by Anion Exchange Reactions. *J. Am. Chem. Soc.* **2015**, *137*, 10276–10281.

(21) Bekenstein, Y.; Koscher, B. A.; Eaton, S. W.; Yang, P.; Alivisatos, A. P. Highly Luminescent Colloidal Nanoplates of Perovskite Cesium Lead Halide and Their Oriented Assemblies. *J. Am. Chem. Soc.* **2015**, *137*, 16008–16011.

(22) Nedelcu, G.; Protesescu, L.; Yakunin, S.; Bodnarchuk, M. I.; Grotevent, M. J.; Kovalenko, M. V. Fast Anion-Exchange in Highly Luminescent Nanocrystals of Cesium Lead Halide Perovskites (CsPbX<sub>3</sub>, X = Cl, Br, I). *Nano Lett.* **2015**, *15*, S635–S640.

(23) Guhrenz, C.; Benad, A.; Ziegler, C.; Haubold, D.; Gaponik, N.; Eychmuller, A. Solid-State Anion Exchange Reactions for Color Tuning of CsPbX<sub>3</sub> Perovskite Nanocrystals. *Chem. Mater.* **2016**, *28*, 9033–9040.

(24) Koscher, B. A.; Bronstein, N. D.; Olshansky, J. H.; Bekenstein, Y.; Alivisatos, A. P. Surface- vs Diffusion-Limited Mechanisms of Anion Exchange in CsPbBr<sub>3</sub> Nanocrystal Cubes Revealed through Kinetic Studies. *J. Am. Chem. Soc.* **2016**, *138*, 12065–12068.

(25) Creutz, S. E.; Crites, E. N.; De Siena, M. C.; Gamelin, D. R. Anion Exchange in Cesium Lead Halide Perovskite Nanocrystals and Thin Films Using Trimethylsilyl Halide Reagents. *Chem. Mater.* **2018**, *30*, 4887–4891.

(26) Imran, M.; Caligiuri, V.; Wang, M. J.; Goldoni, L.; Prato, M.; Krahne, R.; De Trizio, L.; Manna, L. Benzoyl Halides as Alternative Precursors for the Colloidal Synthesis of Lead-Based Halide Perovskite Nanocrystals. *J. Am. Chem. Soc.* **2018**, *140*, 2656–2664.

(27) Pellet, N.; Teuscher, J.; Maier, J.; Grätzel, M. Transforming Hybrid Organic Inorganic Perovskites by Rapid Halide Exchange. *Chem. Mater.* **2015**, *27*, 2181–2188.

(28) Jang, D. M.; Park, K.; Kim, D. H.; Park, J.; Shojaei, F.; Kang, H. S.; Ahn, J. P.; Lee, J. W.; Song, J. K. Reversible Halide Exchange Reaction of Organometal Trihalide Perovskite Colloidal Nanocrystals for Full-Range Band Gap Tuning. *Nano Lett.* **2015**, *15*, 5191–5199.

(29) Leng, M.; Chen, Z.; Yang, Y.; Li, Z.; Zeng, K.; Li, K.; Niu, G.; He, Y.; Zhou, Q.; Tang, J. Lead-Free, Blue Emitting Bismuth Halide Perovskite Quantum Dots. *Angew. Chem., Int. Ed.* **2016**, *55*, 15012–15016.

(30) Zhang, J.; Yang, Y.; Deng, H.; Farooq, U.; Yang, X. K.; Khan, J.; Tang, J.; Song, H. S. High Quantum Yield Blue Emission from Lead Free Inorganic Antimony Halide Perovskite Colloidal Quantum Dots. *ACS Nano* **2017**, *11*, 9294–9302.

(31) Creutz, S. E.; Crites, E. N.; De Siena, M. C.; Gamelin, D. R. Colloidal Nanocrystals of Lead-Free Double-Perovskite (Elpasolite) Semiconductors: Synthesis and Anion Exchange To Access New Materials. *Nano Lett.* **2018**, *18*, 1118–1123.

(32) Haque, A.; Ravi, V. K.; Shanker, G. S.; Sarkar, I.; Nag, A.; Santra, P. K. Internal Heterostructure of Anion-Exchanged Cesium Lead Halide Nanocubes. *J. Phys. Chem. C* **2018**, *122*, 13399–13406.

(33) Hu, F. R.; Yin, C. Y.; Zhang, H. C.; Sun, C.; Yu, W. W.; Zhang, C. F.; Wang, X. Y.; Zhang, Y.; Xiao, M. Slow Auger Recombination of Charged Excitons in Nonblinking Perovskite Nanocrystals without Spectral Diffusion. *Nano Lett.* **2016**, *16*, 6425–6430.

(34) Lounis, B.; Bechtel, H. A.; Gerion, D.; Alivisatos, P.; Moerner, W. E. Photon Antibunching in Single CdSe/ZnS Quantum Dot Fluorescence. *Chem. Phys. Lett.* **2000**, *329*, 399–404.

(35) Michler, P.; Imamoglu, A.; Mason, M. D.; Carson, P. J.; Strouse, G. F.; Buratto, S. K. Quantum Correlation among Photons from a Single Quantum Dot at Room Temperature. *Nature* **2000**, *406*, 968–970.

(36) Fernee, M. J.; Tamarat, P.; Lounis, B. Spectroscopy of Single Nanocrystals. *Chem. Soc. Rev.* **2014**, *43*, 1311–1337.

(37) Li, M.; Zhang, X.; Lu, S.; Yang, P. Phase Transformation, Morphology Control, and Luminescence Evolution of Cesium Lead Halide Nanocrystals in the Anion Exchange Process. *RSC Adv.* **2016**, *6*, 103382–103389.

(38) Takata, H.; Naiki, H.; Wang, L.; Fujiwara, H.; Sasaki, K.; Tamai, N.; Masuo, S. Detailed Observation of Multiphoton Emission Enhancement from a Single Colloidal Quantum Dot Using a Silver-Coated AFM Tip. *Nano Lett.* **2016**, *16*, 5770–5778.

(39) Naiki, H.; Uedao, T.; Wang, L.; Tamai, N.; Masuo, S. Multiphoton Emission Enhancement from a Single Colloidal Quantum Dot Using SiO<sub>2</sub>-Coated Silver Nanoparticles. *ACS Omega* **2017**, *2*, 728–737.

(40) Masuo, S.; Kanetaka, K.; Sato, R.; Teranishi, T. Direct Observation of Multiphoton Emission Enhancement from a Single Quantum Dot Using AFM Manipulation of a Cubic Gold Nanoparticle. *ACS Photonics* **2016**, *3*, 109–116.

(41) Raino, G.; Nedelcu, G.; Protesescu, L.; Bodnarchuk, M. I.; Kovalenko, M. V.; Mahrt, R. F.; Stoferle, T. Single Cesium Lead Halide Perovskite Nanocrystals at Low Temperature: Fast Single Photon Emission, Reduced Blinking, and Exciton Fine Structure. *ACS Nano* **2016**, *10*, 2485–2490.

(42) Yarita, N.; Tahara, H.; Ihara, T.; Kawawaki, T.; Sato, R.; Saruyama, M.; Teranishi, T.; Kanemitsu, Y. Dynamics of Charged Excitons and Biexcitons in CsPbBr<sub>3</sub> Perovskite Nanocrystals Revealed by Femtosecond Transient-Absorption and Single-Dot Luminescence Spectroscopy. *J. Phys. Chem. Lett.* **2017**, *8*, 1413–1418.

(43) Makarov, N. S.; Guo, S. J.; Isaienko, O.; Liu, W. Y.; Robel, I.; Klimov, V. I. Spectral and Dynamical Properties of Single Excitons, Biexcitons, and Trions in Cesium-Lead-Halide Perovskite Quantum Dots. *Nano Lett.* **2016**, *16*, 2349–2362.

(44) Castaneda, J. A.; Nagamine, G.; Yassitepe, E.; Bonato, L. G.; Voznyy, O.; Hoogland, S.; Nogueira, A. F.; Sargent, E. H.; Cruz, C. H. B.; Padilha, L. A. Efficient Biexciton Interaction in Perovskite Quantum Dots Under Weak and Strong Confinement. *ACS Nano* **2016**, *10*, 8603–8609.

(45) de Jong, E. M. L. D.; Yamashita, G.; Gomez, L.; Ashida, M.; Fujiwara, Y.; Gregorkiewicz, T. Multiexciton Lifetime in All-Inorganic CsPbBr<sub>3</sub> Perovskite Nanocrystals. *J. Phys. Chem. C* **2017**, *121*, 1941–1947.

(46) Eperon, G. E.; Jedlicka, E.; Ginger, D. S. Biexciton Auger Recombination Differs in Hybrid and Inorganic Halide Perovskite Quantum Dots. *J. Phys. Chem. Lett.* **2018**, *9*, 104–109.

(47) Mondal, N.; De, A.; Samanta, A. Biexciton Generation and Dissociation Dynamics in Formamidinium- and Chloride-Doped Cesium Lead Iodide Perovskite Nanocrystals. *J. Phys. Chem. Lett.* **2018**, *9*, 3673–3679.

(48) Utzat, H.; Shulenberg, K. E.; Achorn, O. B.; Nasilowski, M.; Sinclair, T. S.; Bawendi, M. G. Probing Linewidths and Biexciton Quantum Yields of Single Cesium Lead Halide Nanocrystals in Solution. *Nano Lett.* **2017**, *17*, 6838–6846.

(49) Li, B.; Huang, H.; Zhang, G.; Yang, C.; Guo, W.; Chen, R.; Qin, C.; Gao, Y.; Biju, V.; Rogach, A. L.; et al. Excitons and Biexciton Dynamics in Single CsPbBr<sub>3</sub> Perovskite Quantum Dots. *J. Phys. Chem. Lett.* **2018**, *9*, 6934–6940.

(50) Seth, S.; Ahmed, T.; Samanta, A. Photoluminescence Flickering and Blinking of Single CsPbBr<sub>3</sub> Perovskite Nanocrystals: Revealing Explicit Carrier Recombination Dynamics. *J. Phys. Chem. Lett.* **2018**, *9*, 7007–7014.

(51) Trinh, C. T.; Minh, D. N.; Ahn, K. J.; Kang, Y.; Lee, K.-G. Organic–Inorganic FAPbBr<sub>3</sub> Perovskite Quantum Dots as a Quantum Light Source: Single-Photon Emission and Blinking Behaviors. *ACS Photonics* **2018**, *5*, 4937–4943.

(52) Zhang, H.; Fu, X.; Tang, Y.; Wang, H.; Zhang, C.; Yu, W. W.; Wang, X.; Zhang, Y.; Xiao, M. Phase Segregation due to Ion Migration in All-Inorganic Mixed-Halide Perovskite Nanocrystals. *Nat. Commun.* **2019**, *10*, 1088.

## Crystallization-Induced Emission of Azobenzene Derivatives

Mitsuaki Yamauchi,\* Kosuke Yokoyama, Naoki Aratani, Hiroko Yamada, and Sadahiro Masuo\*

**Abstract:** Most azobenzene derivatives are utilized as well-defined photoresponsive materials, but their emission properties have not been of great interest as they are relatively poor. Here, we report crystallization-induced emission (CIE) based on the suppression of the photoisomerization of azobenzene derivatives. Although these molecules show negligible emission in solution, their microcrystals exhibit intense emission from the azobenzene moieties as a result of CIE. Upon rapid precipitation, fine particles with low crystallinity were kinetically formed and underwent CIE over time with a concomitant increase in crystallinity. Furthermore, we demonstrated “photocutting” of an emissive single crystal using a strong laser by a combination of CIE behavior and photomelting based on the photoisomerization of the azobenzene moiety. Our results regarding the CIE behavior of azobenzene derivatives in addition to their photoisomerization can provide a new platform for developing photoresponsive luminescent materials.

Photochromic molecules exhibiting reversible color changes upon light stimulation are of great importance to create stimuli-responsive materials.<sup>[1]</sup> Azobenzene derivatives are among the most famous photochromic molecules, and in solution, they photoisomerize between the *trans*- and *cis*-isomers with large structural transformations by UV- and visible-light irradiation.<sup>[1a]</sup> Due to their well-defined photo-reactivity, various azobenzene-functionalized molecules have been designed and synthesized as photoresponsive materials.<sup>[2]</sup> However, azobenzene is a nonemissive  $\pi$ -conjugated molecule because the energy associated with the excited state is predominately used for photoisomerization instead of emission.<sup>[3]</sup> Hence, the observation of emissions from simple azobenzene moieties is difficult. To achieve emission behavior, a drastic modification of the molecular structure<sup>[4]</sup> to suppress the photoisomerization is required. Aggregation and crystallization might be effective for the development of emissive azobenzenes since the associated dense packing can suppress photoisomerization.<sup>[5]</sup> This emission can be regarded as a result of the aggregation- or crystallization-induced emission (AIE or CIE).<sup>[6]</sup> The construction and control of

CIE from a simple azobenzene moiety, however, is still challenging.

Here, we demonstrate CIE with pyrene-functionalized azobenzene derivative **1** and 4,4'-dihydroxyazobenzene (**2**) (Figure 1). Although these molecules showed negligible



**Figure 1.** a) Chemical structures of azobenzene-pyrene dyad **1** and precursors **2** and **3**, and the synthesis of **1**. b) Schematic representation of the crystallization-induced emission (CIE) behavior of **1** as single crystals and as fine particles.

emission in solution, their microcrystals did as a result of CIE. Furthermore, kinetically formed fine particles of **1** exhibited an increased degree of crystallinity over time, leading to a significant enhancement in the intensity of the emission. Interestingly, photoirradiation of the emissive microcrystal with an intense 405-nm laser resulted in selective melting by photoisomerization of the azobenzene moiety, which allowed “photocutting” of the emissive microcrystal.

[\*] Dr. M. Yamauchi, K. Yokoyama, Prof. Dr. S. Masuo  
Department of Applied Chemistry for Environment  
Kwansei Gakuin University  
2-1 Gakuen, Sanda, Hyogo 669-1337 (Japan)  
E-mail: yamauchi@kwansei.ac.jp  
masuo@kwansei.ac.jp

Prof. Dr. N. Aratani, Prof. Dr. H. Yamada  
Division of Materials Science  
Nara Institute of Science and Technology  
8916-5 Takayama-cho, Ikoma 630-0192 (Japan)

Supporting information and the ORCID identification number(s) for the author(s) of this article can be found under:  
<https://doi.org/10.1002/anie.201908121>.

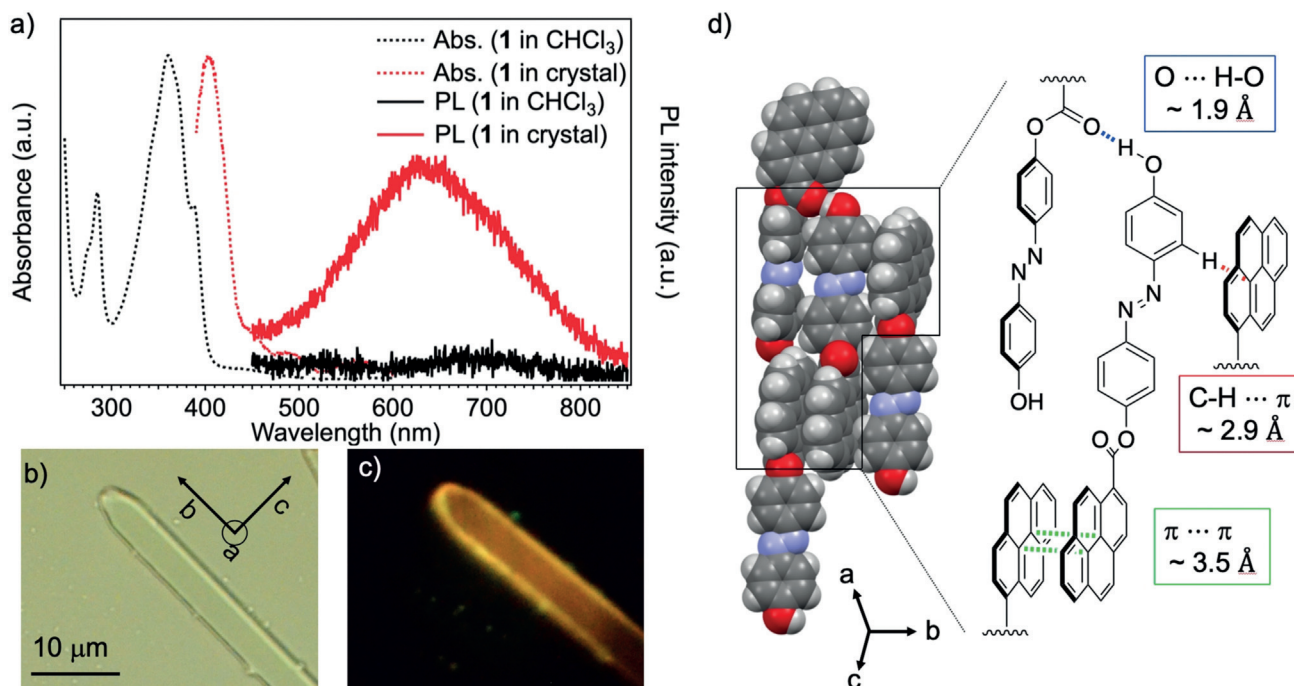
First, we found that **2** exhibited a broad emission ( $\lambda_{\max} \approx 610$  nm) in the crystalline state upon excitation at 405 nm under a microscope (Figure S1 in the Supporting Information). Such an emission in a longer-wavelength region is characteristic of an excimer-like emission of **2** in the crystal. Given that monomeric **2** in  $\text{CHCl}_3$  did not emit (Figure S1), this confirms CIE. The suppression of photoisomerization can play a key role in the CIE behavior of azobenzene derivatives. However, the low solubility of **2** in common solvents such as  $\text{CHCl}_3$  impeded further analyses and application. To improve the solubility, we designed the new pyrene-functionalized azobenzene derivative **1**. For this molecule, we expected that the azobenzene moiety can show not only photoisomerization in its monomeric state but also emission in the crystalline state, while the pyrene moiety can act as a strong  $\pi$ - $\pi$ -stacking moiety to increase the crystallinity. Compound **1** with a *trans*-azobenzene moiety was synthesized from **2** and 1-pyrenecarboxylic acid (**3**) as precursors according to Scheme S1. The products were characterized by  $^1\text{H}$  NMR and  $^{13}\text{C}$  NMR spectroscopy and ESI mass spectrometry (see Supporting Information). As expected, in addition to CIE behavior, **1** showed relatively good solubility due to a decrease in insoluble hydroxy ( $-\text{OH}$ ) groups, and this solubility enabled us to investigate the CIE behavior of the azobenzene moieties in detail as described below.

The UV/Vis-absorption spectrum of **1** in  $\text{CHCl}_3$  ( $c = 10 \mu\text{M}$ ) at  $20^\circ\text{C}$  showed bands at 285, 361, and 388 nm with a weak broad absorption at approximately 450 nm (Figure 2a). The broad absorption can be assigned to the  $n$ - $\pi^*$  transition of the *trans*-azobenzene moiety, while the other

peaks correspond to the overlap of the  $\pi$ - $\pi^*$  transition of the *trans*-azobenzene and pyrene moieties. Compared to precursors **2** and **3**, the bands of **1** are slightly red-shifted, suggesting a small change in the electronic state relative to the ground state (Figure S2a). Although the photoluminescent (PL)-spectroscopic measurements revealed that **3** showed strong emission at 394 and 412 nm in  $\text{CHCl}_3$  under excitation at 365 nm (photoluminescent quantum yield (PLQY) = 0.50), **1** showed extremely weak emission at 390 and 407 nm (PLQY = 0.001) (Figure S2b). The decrease in emission efficiency from the pyrene moiety is due to non-radiative deactivation by photoinduced electron transfer<sup>[7]</sup> and/or resonance energy transfer<sup>[8]</sup> between the pyrene and the azobenzene chromophores. Because the energy associated with the excited state is mainly utilized for the photoisomerization of azobenzene, the emission from the azobenzene moiety in solution was negligible (Figure 2a).

Upon preparing a concentrated  $\text{CHCl}_3$  solution of **1** ( $c \approx 3 \text{ mM}$ ) and cooling it down, crystalline objects were obtained. Observation of the objects on a glass substrate using an optical microscope revealed the formation of plate-shaped individual microcrystals (MCs; Figure 2b). The absorption spectrum of the MCs measured under an optical microscope exhibited a new band at 407 nm in a longer-wavelength region relative to the monomeric absorption band at 361 nm (Figures 2a and S3). This redshift is attributed to the crystallization of **1**.

The PL imaging under the microscope revealed that the MCs exhibited intense emission upon excitation with a 405 nm continuous-wave (CW) laser (Figure 2c). The PL



**Figure 2.** a) Absorption and PL spectra of **1** in  $\text{CHCl}_3$  and an individual MC under an optical microscope (PL: 405 nm pulsed laser excitation). Laser intensity at the focal point:  $\approx 1 \text{ Wcm}^{-2}$ . b) Transmission image and c) PL image of an individual MC under an optical microscopy with 405 nm CW laser excitation. Laser intensity at the crystal surface:  $\approx 2 \text{ Wcm}^{-2}$ . d) Crystal structure of **1**, monoclinic, space group:  $C2/c$  ( $a = 27.622(10) \text{ \AA}$ ,  $b = 7.973(3) \text{ \AA}$ ,  $c = 22.599(8) \text{ \AA}$ ,  $\beta = 119.551(6)^\circ$ ,  $V = 4329(3) \text{ \AA}^3$ ,  $Z = 8$ ,  $T = 296 \text{ K}$ ,  $R1 = 0.0593$ ,  $wR2 = 0.1130$ ,  $\text{GOF} = 1.005$ , calculated density:  $1.358 \text{ gcm}^{-3}$ ).

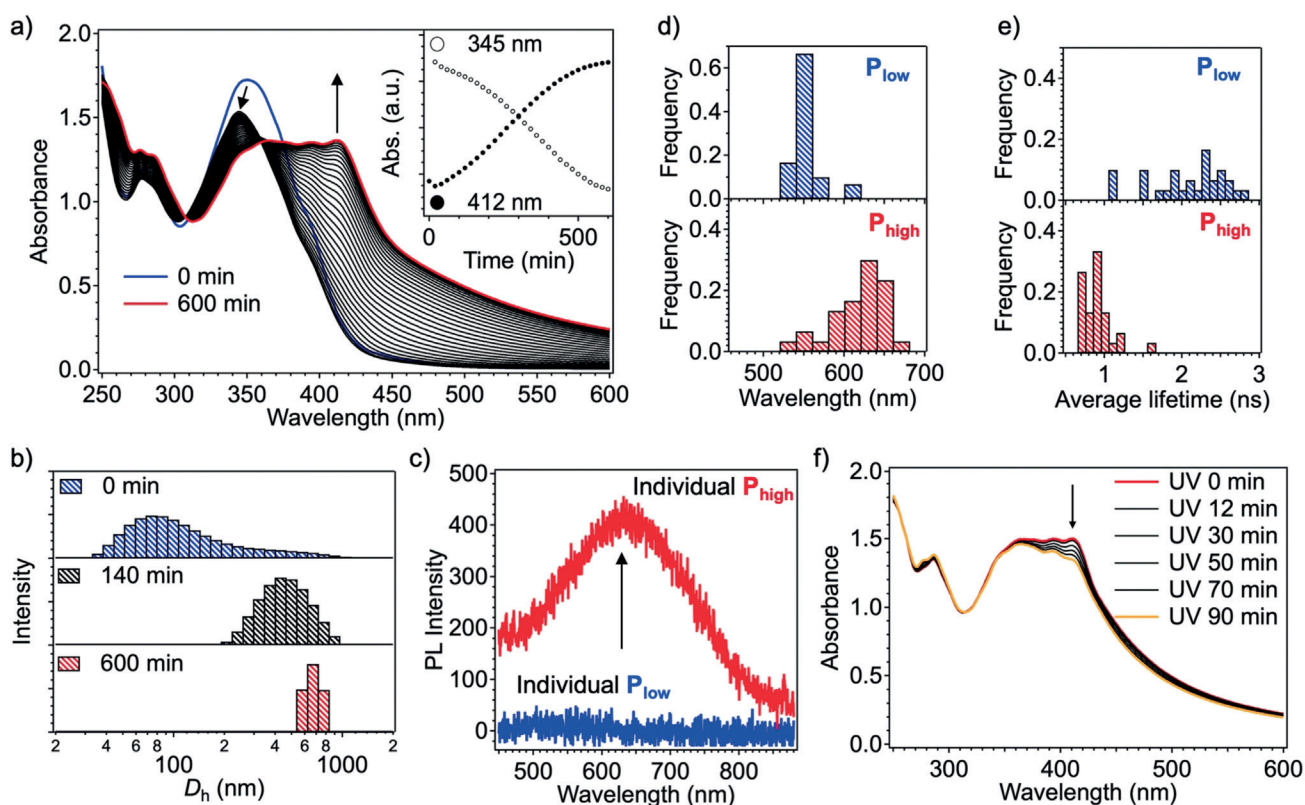
image suggests that the MCs emit strongly at the crystal edges, showing optical-waveguide behavior. In diluted  $\text{CHCl}_3$  solution, **1** showed a weak emission from the pyrene moiety under excitation at 365 nm (Figure S2b), while it was almost non-emissive under excitation at 405 nm (Figure 2a). At 405 nm, **1** has a higher contribution of the absorption of the azobenzene moiety compared with that of the pyrene moiety (Figure S2a,c). This result indicates that the emission from the azobenzene moiety was not observed in the monomeric state. Hence, the emission of the MCs can be regarded as CIE of the azobenzene moiety. To investigate the emission from the azobenzene moiety, we used a 405 nm excitation for measurements of PL spectra and decay curves from the following experiments. The PL-spectroscopic measurement of the MCs showed a broad excimer-like emission at  $\lambda_{\text{max}} = 640$  nm (Figure 2a). In the crystalline state, however, **2** and **3** showed absorption bands at 405 and 433 nm (**2**) and 350, 387, and 410 nm (**3**), and exhibited broad PL spectra ( $\lambda_{\text{max}} = 610$  nm, **2**) and relatively sharp spectra ( $\lambda_{\text{max}} = 515$  and 540 nm, **3**; see Figures S1 and S4). Considering the spectral shape and PL wavelength, the emission of the MCs originates from the azobenzene moieties. Notably, the emission wavelength of the MCs was red-shifted by  $\approx 30$  nm relative to that of crystalline **2**, and this shift is probably due to a change in the molecular packing caused by the presence of the pyrene unit. Based on an analysis of the PL-decay curves with PL spectra, the MCs showed a short average PL lifetime of 0.5 ns ( $\lambda_{\text{max}} = 640$  nm), while the average lifetimes of **2** and **3** in the crystal state were estimated to be 0.5 ns ( $\lambda_{\text{max}} = 610$  nm) and 2.9 ns ( $\lambda_{\text{max}} = 515$  nm), respectively (Figure S5). These results indicate that the emission from the azobenzene moiety in the crystal showed a short lifetime, while that from the pyrene moiety in the crystal had a longer lifetime. To further confirm that the emission of the MCs originates from the single-crystal phase, we measured the PL spectrum of an amorphous thin film prepared by spin-coating from a monomer solution in THF ( $c = 1$  mM) onto a glass substrate. As a result, the film was non-emissive under excitation with a 405 nm laser using the same laser intensity as for the measurements of the MCs. Upon increasing the laser intensity, a weak PL spectrum with a peak at 535 nm was detected, which is attributed to an emission from the pyrene moiety (Figure S6a). These results support that the emission from the azobenzene moiety stems from the single-crystal phase.

Single-crystal X-ray diffraction analysis of a large MC, prepared by re-crystallization in concentrated  $\text{CHCl}_3$  solution, revealed that the packing of **1** is monoclinic in the space group  $C2/c$  (Figure 2d, Figure S7, Table S1). The analysis suggests that **1** crystallizes through three intermolecular interactions: face-to-face  $\pi$ - $\pi$  stacking between the pyrene rings (distance between the closest carbon atoms ( $d_{\pi\cdots\pi}$ )  $\approx 3.5$  Å), CH- $\pi$  interactions between the hydrogen atom of the azobenzene ring and the pyrene ring (distance between the hydrogen atom and the closest carbon atom of pyrene ring ( $d_{\text{C-H}\cdots\pi}$ )  $\approx 2.9$  Å), and hydrogen bonding between the hydrogen atom of the hydroxy group and a carboxy oxygen ( $d_{\text{O-H}\cdots\text{O}}$ )  $\approx 1.9$  Å). At the azobenzene moiety, the CH- $\pi$  interactions and hydrogen bonds can directly contribute to the suppression of isomerization. Considering that the azobenzene

moiety in the crystal does not form  $\pi$ - $\pi$  interactions, the red-shift of the absorption band indicates an increase in the planarity of the azobenzene moiety compared to the conformation in solution.

Because **1** shows CIE, the intensity of the emission should depend on the degree of crystallinity. To confirm this hypothesis, we attempted to prepare fine particles with low crystallinity by reprecipitation.<sup>[9]</sup> To address this, 0.3 mL of a THF solution of **1** ( $c = 1$  mM) was quickly injected into 3 mL of pure water under vigorous stirring to form a suspension of the particles ( $c = 90$   $\mu\text{m}$ ) dispersed in THF/water (1:10, v/v). Notably, the resulting solution underwent a time change of intermolecular interactions, as confirmed by absorption measurements. The absorption spectrum of the fresh solution, recorded after injection and subsequent stirring for 5 min, exhibited an absorption-band maximum at 350 nm (Figure 3a). We regarded this spectrum as data at 0 min and monitored the spectral change every 20 min. After 20 min, the band blue-shifted slightly to 345 nm. This small shift implies the occurrence of a weak intermolecular interaction between the aromatic moieties, which corresponds to the formation of particles with low crystallinity (referred to as  $P_{\text{low}}$ ). As shown in Figure 3a, the absorption band of  $P_{\text{low}}$  clearly red-shifted and new structural bands at 362, 395, and 412 nm with an isosbestic point at 307 nm appeared. The absorbance at 345 and 412 nm showed a sigmoidal change over time, and the absorbance reached a plateau after 10 h. Such a change is characteristic for autocatalytic crystallization involving nucleation and growth processes.<sup>[10]</sup> This spectral change indicates an increase in crystallinity. The emergence of this red-shifted band is consistent with what was observed for the MCs (Figure 2a). The time-dependent dynamic light scattering (DLS) measurements indicated that the hydrodynamic diameter increased from 80 nm to 700 nm (Figure 3b). These results demonstrate that **1** kinetically formed  $P_{\text{low}}$ , which has a loosely packed structure, and it transformed into thermodynamically more stable submicron-particles with high crystallinity (referred to as  $P_{\text{high}}$ ). The higher degree of crystallinity of  $P_{\text{high}}$  was confirmed by polarized optical microscopic observation of  $P_{\text{low}}$  and  $P_{\text{high}}$  on a glass substrate, where  $P_{\text{high}}$  showed the formation of rod-like textures, while  $P_{\text{low}}$  did not show such a texture (Figure S8).

The PL spectra of individual  $P_{\text{low}}$  and  $P_{\text{high}}$ , spin-coated from their solutions onto glass substrates, obtained with pulsed laser excitation at 405 nm, showed an increase in the emission intensity of  $P_{\text{high}}$  (Figure 3c). To compare the emission behaviors of  $P_{\text{low}}$  and  $P_{\text{high}}$ , we measured the PL spectra and decay curves of many individual particles of  $P_{\text{low}}$  and  $P_{\text{high}}$ . Based on the measurement data, histograms corresponding to the PL wavelength and average lifetime are presented in Figure 3d,e. In comparison to  $P_{\text{high}}$ ,  $P_{\text{low}}$  exhibits weak emission with shorter emission wavelengths ( $\lambda_{\text{max}} \approx 550$  nm) and longer lifetimes ( $\tau = 2$ –4 ns). This result indicates that the emission originates from the pyrene moiety. The lack of emission from the azobenzene moiety is probably due to the low crystallinity of  $P_{\text{low}}$ . In contrast,  $P_{\text{high}}$  exhibited relatively strong emission with red-shifted wavelengths ( $\lambda_{\text{max}} \approx 630$  nm) and a shorter lifetime ( $\tau = 0.8$ –1 ns), which are indicative of emission from azobenzene moieties (Fig-



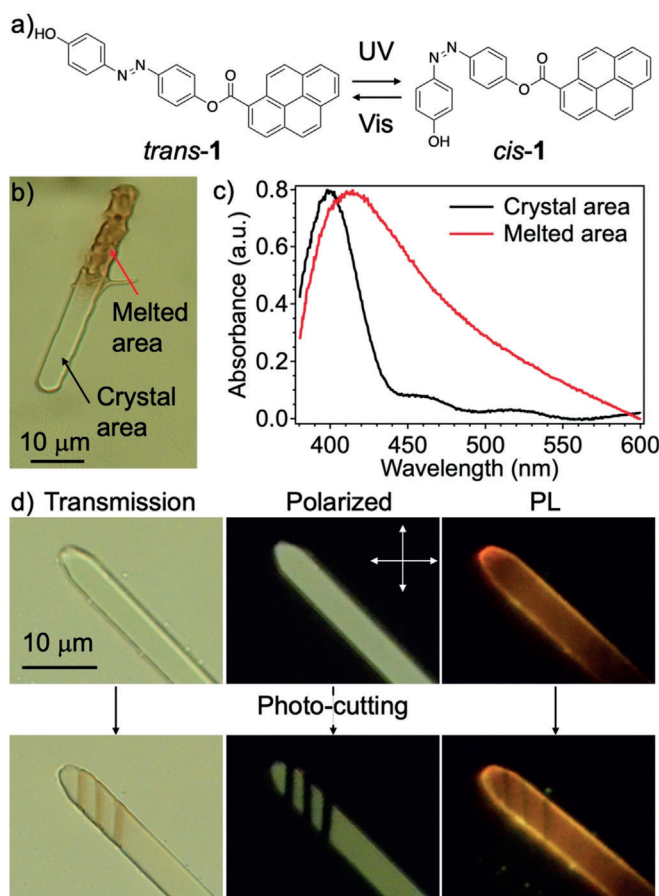
**Figure 3.** a) Time-dependent absorption spectra of **1** in THF/water (1:10, v/v) at 20°C. Inset: Absorbance as a function of time. b) DLS-derived distribution of particle sizes of **1** in THF/water (1:10, v/v) at 20°C. c) PL spectra of individual  $P_{\text{low}}$  and  $P_{\text{high}}$  under an optical microscope, obtained by spin-coating their solutions onto a glass substrate and exciting with a 405 nm pulsed laser. d), e) Histograms of PL wavelengths (d) and PL lifetimes (e) of  $P_{\text{low}}$  and  $P_{\text{high}}$ , based on data collected from at least 30 individual nanocrystals. Considering the weak emission of  $P_{\text{low}}$ , the more intense laser power was used. f) Change in the absorption spectrum of  $P_{\text{high}}$  in THF/water (1:10, v/v) at 20°C upon irradiation with 365 nm UV light.

ure 3 d,e). Notably, a similar change in the emission properties was observed under solvent-free conditions, that is, when  $P_{\text{low}}$  was left on the glass substrate and exposed to air for several weeks (Figure S9). This result suggests that the increase in crystallinity causing the CIE behavior was achieved by a molecular rearrangement in the same particle. Additionally, a change in emission behaviors was also observed when  $P_{\text{low}}$  was dried on the substrate under vacuum for several hours (Figure S10), indicating that the removal of solvent molecules from  $P_{\text{low}}$  induces an increase in crystallinity.

The increase in crystallinity should affect the photoisomerization efficiency of the azobenzene moiety because a large conformational change is required for the isomerization (Figure 4 a). In  $\text{CHCl}_3$ , monomeric **1** showed effective photoisomerization. Upon irradiation of the solution with 365 nm UV light ( $17 \text{ mW cm}^{-2}$ , LED lamp), the absorbance corresponding to the *trans*-azobenzene moiety at 365 nm gradually decreased (Figure S11 a). After UV irradiation for 5 s, **1** reached a photostationary state (PSS). Subsequent irradiation with 470 nm visible light ( $20 \text{ mW cm}^{-2}$ , LED lamp) caused an increase in the absorbance of **1** as a result of *cis*-to-*trans* isomerization (Figure S11 b). Compared to the monomer state,  $P_{\text{high}}$  in THF/water (1:10, v/v) exhibited very slow *trans*-to-*cis* photoisomerization, and the isomerization was not complete even after UV irradiation for 90 min; during this

time, a decrease in the absorbance of the azobenzene moiety at 415 nm was observed (Figure 3 f). This difference supports that crystallization can suppress isomerization. Unlike  $P_{\text{high}}$ , the MCs did not show photoisomerization by irradiation with the weak UV lamp (Figure S12). This is probably because molecules in the MCs are densely and homogeneously packed and thereby the MCs have higher crystallinity. In the case of  $P_{\text{high}}$ , the presence of  $\text{H}_2\text{O}$  may weaken the hydrogen bonds between molecules of **1**, resulting in a lower crystallinity of  $P_{\text{high}}$ .

Notably, we found that exposure to an intense 405 nm CW laser ( $100\text{--}400 \text{ W cm}^{-2}$ ) for several seconds melted the MCs with a change of color (Figure 4 b). The absorption spectrum of the melted area under a microscope showed the emergence of a slightly red-shifted band at 415 nm with a broad absorption region around approximately 450 nm (Figure 4 c). Given that the amorphous film consisting of *trans*-**1** had the absorption band at about 360 nm (Figure S6 b), the presence of red-shifting implies a formation of *cis*-azobenzene moiety. However,  $^1\text{H}$  NMR measurements of a solution, prepared by dissolving the mostly melted **1** in  $[\text{D}_8]\text{THF}$ , showed the formation of only *trans*-**1** (Figure S13). The absence of *cis*-**1** is presumably because a *cis*-to-*trans* thermal isomerization rapidly occurred upon dissolving melted **1** in  $[\text{D}_8]\text{THF}$ . In contrast, crystals of pyrene derivative **3**, which show strong



**Figure 4.** a) Molecular structures of *trans*-1 and *cis*-1. b) Transmission microphotograph of a melted individual MC by an optical microscope with a 405 nm CW laser ( $100 \text{ W cm}^{-2}$ ) in the exposed area with  $50 \mu\text{m}$  diameter through a wide field. c) Absorption spectra of an individual MC by an optical microscope before and after irradiation with a 405 nm CW laser ( $100 \text{ W cm}^{-2}$ ). d) Transmission, polarized, and PL microphotographs ( $\lambda_{\text{ex}} = 405 \text{ nm}$ ) of an individual MC by an optical microscope before and after photocutting with a 405 nm CW laser ( $\approx 4 \text{ kW cm}^{-2}$ ).

absorption around 405 nm, did not undergo such melting by the laser irradiation (Figures S4c and S14). This result indicates that a heat-induced melting of the MCs can be excluded and therefore the photoisomerization of the azobenzene moiety can guide the melting process. A similar facilitation of photoisomerization by intense laser irradiation was reported by Masuhara and co-workers. In their study, the simultaneous generation of many photoexcited molecules by the intense laser irradiation led to the photoisomerization of spironaphthooxazine derivatives in the crystal, which could not be induced by photoirradiation with low power.<sup>[11]</sup> Furthermore, the photoisomerization-induced melting of a solid composed of an azobenzene derivative was demonstrated by Norikane and co-workers.<sup>[12]</sup> In our system, emission from the azobenzene moieties and photomelting behavior were realized simultaneously. By exploiting the photomelting, we succeeded in the “photocutting” of an emissive individual MC by focused intense CW laser irradiation ( $0.4\text{--}4 \text{ kW cm}^{-2}$ ) (Figure 4d). The polarized optical

microscopic images show a disappearance of the texture in the melted area, indicating a lack of molecular order. The PL images suggest that photocutting provided non-emissive areas. The difference in the emission spectra of the crystalline and melted areas was confirmed by PL spectroscopy (Figure S15). When the MC was melted, the intensity of emission became significantly weaker due to a decrease in crystallinity. These results demonstrate that photoisomerization enables control over the emission properties of **1**.

In conclusion, we demonstrated the crystallization-induced emission behavior of pyrene-functionalized azobenzene derivative **1** in the single-crystal and monomeric states. Upon crystallization of **1** in concentrated  $\text{CHCl}_3$  into microcrystals, emission from the pyrene moieties observed in the monomeric solution disappeared and emission from the azobenzene moieties appeared. The fine particles prepared in THF/water (1:10, v/v) exhibited time-dependent CIE behavior in which particles with low crystallinity were formed kinetically and then, over time, transformed into thermodynamically stable crystalline particles exhibiting relatively intense emission. Moreover, we demonstrated the photoisomerization-induced cutting of an emissive microcrystal (photocutting) by irradiation with an intense CW laser as a combination of photoisomerization and CIE of the azobenzene moiety. The findings regarding the CIE behavior of azobenzene-functionalized molecules in addition to photoisomerization can provide a new platform for developing photoresponsive luminescent materials.

## Acknowledgements

This work was partially supported by Grants-in-Aid for Scientific Research (Nos. 18H01958, 18K14195 and 16H02286) from the Japan Society for the Promotion of Science (JSPS) and a Grant-in-Aid for Scientific Research on Innovation Areas “Photosynergetics” (No. 26107005) from MEXT, Japan. The authors thank Prof. Dr. Shirakawa and Ms. Ikeda at Kwansei Gakuin University for help with the ESI mass measurements. The DLS measurements were supported by Prof. Dr. S. Yagai at Chiba University.

## Conflict of interest

The authors declare no conflict of interest.

**Keywords:** Azobenzene · Crystallization-induced emission · Kinetics · Self-assembly

**How to cite:** *Angew. Chem. Int. Ed.* **2019**, *58*, 14173–14178  
*Angew. Chem.* **2019**, *131*, 14311–14316

[1] a) H. M. Bandara, S. C. Burdette, *Chem. Soc. Rev.* **2012**, *41*, 1809–1825; b) M. Irie, T. Fukaminato, K. Matsuda, S. Kobatake, *Chem. Rev.* **2014**, *114*, 12174–12277.

[2] a) S. Shinkai, T. Nakaji, T. Ogawa, K. Shigematsu, O. Manabe, *J. Am. Chem. Soc.* **1981**, *103*, 111–115; b) X. Liang, H. Asanuma, H. Kashida, A. Takasu, T. Sakamoto, G. Kawai, M. Komiyama, *J. Am. Chem. Soc.* **2003**, *125*, 16408–16415; c) T. Muraoka, K.

- Kinbara, Y. Kobayashi, T. Aida, *J. Am. Chem. Soc.* **2003**, *125*, 5612–5613; d) S. Tamesue, Y. Takashima, H. Yamaguchi, S. Shinkai, A. Harada, *Angew. Chem. Int. Ed.* **2010**, *49*, 7461–7464; *Angew. Chem.* **2010**, *122*, 7623–7626; e) A. Gopal, M. Hifsudheen, S. Furumi, M. Takeuchi, A. Ajayaghosh, *Angew. Chem. Int. Ed.* **2012**, *51*, 10505–10509; *Angew. Chem.* **2012**, *124*, 10657–10661; f) S. Yagai, M. Yamauchi, A. Kobayashi, T. Karatsu, A. Kitamura, T. Ohba, Y. Kikkawa, *J. Am. Chem. Soc.* **2012**, *134*, 18205–18208; g) M. Endo, T. Fukui, S. H. Jung, S. Yagai, M. Takeuchi, K. Sugiyasu, *J. Am. Chem. Soc.* **2016**, *138*, 14347–14353.
- [3] a) H. Rau, *Angew. Chem. Int. Ed. Engl.* **1973**, *12*, 224–235; *Angew. Chem.* **1973**, *85*, 248–258; b) A. Cembran, F. Bernardi, M. Garavelli, L. Gagliardi, G. Orlandi, *J. Am. Chem. Soc.* **2004**, *126*, 3234–3243.
- [4] J. Yoshino, N. Kano, T. Kawashima, *Chem. Commun.* **2007**, 559–561.
- [5] a) M. Shimomura, T. Kunitake, *J. Am. Chem. Soc.* **1987**, *109*, 5175–5183; b) K. Tsuda, G. C. Dol, T. Gensch, J. Hofkens, L. Latterini, J. W. Weener, E. W. Meijer, F. C. De Schryver, *J. Am. Chem. Soc.* **2000**, *122*, 3445–3452; c) J. Azuma, A. Shishido, T. Ikeda, N. Tamai, *Mol. Cryst. Liq. Cryst. Sci. Technol. Sect. A* **2006**, *314*, 83–88; d) B. K. Tsai, C. H. Chen, C. H. Hung, V. K. S. Hsiao, C. C. Chu, *J. Mater. Chem.* **2012**, *22*, 20874–20877; e) M. Han, S. J. Cho, Y. Norikane, M. Shimizu, A. Kimura, T. Tamagawa, T. Seki, *Chem. Commun.* **2014**, *50*, 15815–15818.
- [6] a) Y. Dong, J. W. Lam, A. Qin, Z. Li, J. Sun, H. H. Sung, I. D. Williams, B. Z. Tang, *Chem. Commun.* **2007**, 40–42; b) Y. Hong, J. W. Lam, B. Z. Tang, *Chem. Commun.* **2009**, 4332–4353; c) W. Z. Yuan, X. Y. Shen, H. Zhao, J. W. Y. Lam, L. Tang, P. Lu, C. Wang, Y. Liu, Z. Wang, Q. Zheng, J. Z. Sun, Y. Ma, B. Z. Tang, *J. Phys. Chem. C* **2010**, *114*, 6090–6099.
- [7] A. Kathiravan, K. Sundaravel, M. Jaccob, G. Dhinakaran, A. Rameshkumar, D. Arul Ananth, T. Sivasudha, *J. Phys. Chem. B* **2014**, *118*, 13573–13581.
- [8] M. Gascón-Moya, A. Pejoan, M. Izquierdo-Serra, S. Pittolo, G. Cabre, J. Hernando, R. Alibes, P. Gorostiza, F. Busque, *J. Org. Chem.* **2015**, *80*, 9915–9925.
- [9] a) H. Kasai, H. S. Nalwa, H. Oikawa, S. Okada, H. Matsuda, N. Minami, A. Kakuta, K. Ono, A. Mukoh, H. Nakanishi, *Jpn. J. Appl. Phys. Part 2* **1992**, *31*, L1132–L1134; b) H. Kasai, H. Kamatani, Y. Yoshikawa, S. Okada, H. Oikawa, A. Watanabe, O. Itoh, H. Nakanishi, *Chem. Lett.* **1997**, *26*, 1181–1182.
- [10] a) P. A. Bachmann, P. L. Luisi, J. Lang, *Nature* **1992**, *357*, 57–59; b) T. S. Balaban, J. Leitich, A. R. Holzwarth, K. Schaffner, *J. Phys. Chem. B* **2000**, *104*, 1362–1372.
- [11] T. Asahi, M. Suzuki, H. Masuhara, *J. Phys. Chem. A* **2002**, *106*, 2335–2340.
- [12] a) Y. Norikane, E. Uchida, S. Tanaka, K. Fujiwara, E. Koyama, R. Azumi, H. Akiyama, H. Kihara, M. Yoshida, *Org. Lett.* **2014**, *16*, 5012–5015; b) E. Uchida, R. Azumi, Y. Norikane, *Nat. Commun.* **2015**, *6*, 7310.

Manuscript received: June 30, 2019

Revised manuscript received: July 25, 2019

Accepted manuscript online: July 28, 2019

Version of record online: August 23, 2019

# Kinetically and Thermodynamically Controlled Nanostructures of Perylene-Substituted Lophine Derivatives

Ryosuke Usui,<sup>†</sup> Mitsuaki Yamauchi,<sup>‡,§</sup> Yukihide Ishibashi,<sup>§</sup> Osamu Tsutsumi,<sup>†</sup> Tsuyoshi Asahi,<sup>§</sup> Sadahiro Masuo,<sup>‡</sup> Naoto Tamai,<sup>‡,§</sup> and Yoichi Kobayashi<sup>\*,†,§</sup>

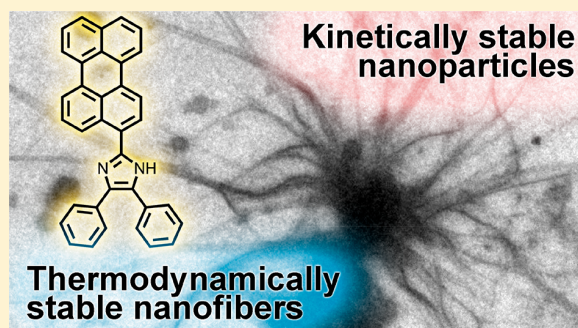
<sup>†</sup>Department of Applied Chemistry, College of Life Sciences, Ritsumeikan University, Kusatsu, Shiga 525-8577, Japan

<sup>‡</sup>Department of Chemistry, School of Science and Technology, Kwansei Gakuin University, Sanda, Hyogo 669-1337, Japan

<sup>§</sup>Department of Materials Science and Biotechnology, Graduate School of Science and Engineering, Ehime University, Matsuyama, Ehime 790-8577, Japan

## Supporting Information

**ABSTRACT:** Supramolecular assemblies have been extensively studied because of their fundamental insights into intermolecular interactions and their potential applications to optoelectronic devices. Among various molecular building units, 2,4,5-triphenylimidazole (lophine) has been extensively studied because the molecule itself gives chemiluminescence and bright fluorescence and because it forms various anisotropic nanostructures. While various potential applications such as to optoelectronic and lasing devices have been reported in lophine-based nanostructures, the relationship among molecular structures, nanostructures, and their optical properties remains elusive. This study reveals that the hydrogen bonding of the imidazole ring plays a crucial role for one-dimensional anisotropic nanostructures and their optical properties. The hydrogen bonding leads to thermodynamically stable nanofibers and gives a monomeric sharp emission, while it also induces ultrafast nonradiative relaxation. On the other hand, the  $\pi$ - $\pi$  interaction leads to kinetically favorable nanoparticles and gives a broad emission due to the excimer of the perylene moiety. The insight into the relationship among molecular structures, nanostructures, and optical properties are important for on-demand optical and electrical properties of lophine-based nanostructures.



## 1. INTRODUCTION

Supramolecular assemblies have been extensively studied not only because of their fundamental insights into intermolecular interactions and excitonic coupling<sup>1–3</sup> but also because of their potential applications to luminescent materials, field effect transistor (FET), artificial photosynthesis, and lasing devices.<sup>4–11</sup> Various supramolecular nanostructures have been reported by using different molecular units as building blocks such as cyanine, porphyrin, chlorophyll, and perylene bisimide. Among them, 2,4,5-triphenylimidazole (lophine) has been received considerable attention because the molecule itself has several fascinating properties such as chemiluminescence and highly bright fluorescence in solution and because it is used as a precursor for fading-speed-tunable photochromic molecules<sup>12–16</sup> and initiators for radical polymerizations.<sup>17</sup> The lophine framework forms various types of anisotropic nanostructures by the combination of the hydrogen bonding of the imidazole ring and  $\pi$ - $\pi$  interactions.<sup>18,19</sup> These microcrystals have been applied to optical waveguides, FET, and lasing devices.<sup>20–23</sup> Moreover, crystals of lophine derivatives show ferroelectricity,<sup>24,25</sup> and these microcrystals are promising for flexible ferroelectric materials.<sup>25</sup> Lophine

contains the N–H bond at the imidazole ring, which forms the hydrogen bond in solid states. The hydrogen bonds are supposed to play crucial roles in the molecular packing and their optical and electrical properties. However, the relationship among molecular structures, formed nanostructures, and their optical properties remain elusive. Recently, hydrogen-bond assisted self-assemblies have been applied to lasing devices and room temperature persistent luminescence.<sup>6,26,27</sup> The investigations of these structure-dependent optical properties are particularly important to realize the on-demand optical and electrical properties of lophine-based nanostructures.

In this study, we synthesized perylene-substituted lophine derivatives as shown in Figure 1 to investigate their nanostructure-dependent optical properties. The N–H bond of the imidazole ring of 1 is replaced with the phenyl ring in 2. The comparison of nanostructures and optical properties of these two compounds reveals the effect of the hydrogen

**Received:** February 12, 2019

**Revised:** March 26, 2019

**Published:** April 1, 2019

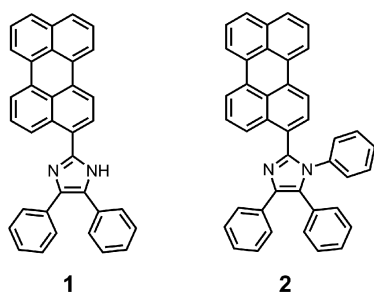


Figure 1. Molecular structures of 1 and 2.

bonding on the shape of nanostructures and optical properties. The perylene moiety acts as a molecular indicator for the aggregation because it gives characteristic emissions depending on the aggregation. We analyzed the relationship among molecular structures, shapes of nanostructures, and optical properties in detail by using femtosecond transient absorption spectroscopy and picosecond fluorescence decay measurements of solutions, nanostructures, and crystalline solids.

## 2. EXPERIMENTAL SECTION

**2.1. Materials.** All reagents were purchased from Tokyo Chemical Industry (TCI) and Wako Co. Ltd. and were used without further purification. All reactions were shielded from light. Column chromatography was performed on alumina gel (200 mesh, Wakogel).

**2.2. Syntheses and Preparations of Nanostructures.** *4,5-Diphenyl-2-perylene-1-yl-1H-imidazole (1).* 3-Perylenecarboxaldehyde (224.6 mg, 0.801 mmol), benzil (235.3 mg, 1.12 mmol), and ammonium acetate (940.3 mg, 12.2 mmol) were stirred at 80 °C in acetic acid (15 mL) for over 12 h. An orange precipitate was neutralized by adding ammonia–water and was collected by filtration (Kiryama No. 5B). The precipitate was washed with water and then ethanol. The residue was dried in vacuo to give an orange powder. The powder was purified by column chromatography on alumina gel using hexane/ethyl acetate (3/1) as eluent. Compound 1 was obtained as a yellow powder and the yield was 69%.  $^1\text{H}$  NMR (DMSO- $d_6$ , 400 MHz):  $\delta$  12.88 (s, 1H), 9.20 (d,  $J$  = 8.4 Hz, 1H), 8.50 (dd,  $J$  = 10.0, 8.0 Hz, 3H), 8.44 (d,  $J$  = 8.0 Hz, 1H), 8.02 (d,  $J$  = 8.0 Hz, 1H), 7.84 (dd,  $J$  = 8.4, 5.6 Hz, 2H), 7.73–7.56 (m, 7H), 7.47 (t,  $J$  = 7.2 Hz, 2H), 7.41–7.34 (m, 3H), 7.27 (t,  $J$  = 7.6 Hz, 1H), MALDI–TOF–MS:  $m/z$  471  $[\text{M} + \text{H}]^+$

*4,5-Diphenyl-2-perylene-1-yl-1-phenylimidazole (2).* 3-Perylenecarboxaldehyde (224.3 mg, 0.800 mmol), benzil (253.0 mg, 1.20 mmol), aniline (111 mg, 1.19 mmol), and ammonium acetate (385.0 mg, 4.99 mmol) were stirred at 110 °C in acetic acid (15 mL) for over 12 h. An orange precipitate was neutralized by adding ammonia–water. The precipitate was collected by filtration and then washed with water and ethanol. The residue was dried in vacuo to give an orange powder (60%).  $^1\text{H}$  NMR (DMSO- $d_6$ , 400 MHz):  $\delta$  8.41 (dd,  $J$  = 7.2, 4.8 Hz, 2H), 8.36 (d,  $J$  = 7.2 Hz, 1H), 8.25 (d,  $J$  = 8.0 Hz, 1H), 8.04 (d,  $J$  = 8.4 Hz, 1H), 7.83 (dd,  $J$  = 8.8, 3.2 Hz, 2H), 7.59–7.52 (m, 5H), 7.45 (d,  $J$  = 8.0 Hz, 1H), 7.33 (s, 5H), 7.31–7.26 (m, 2H), 7.22–7.11 (m, 6H), MALDI–TOF–MS:  $m/z$  546  $[\text{M} + \text{H}]^+$

Nanostructure solutions were prepared with reprecipitation methods.<sup>28,29</sup> Namely, the saturated tetrahydrofuran (THF) solution (200  $\mu\text{L}$ ) of the compounds was rapidly injected to 4

mL water and the solution was stirred vigorously at 298 or 338 K. By changing the heating temperature and durations during and after the reprecipitation method, several batches of different nanostructure solutions were prepared. Four types of nanostructure samples (#1 to #4) in each compound are introduced in this study. Nanostructures of #1 were prepared at 298 K, while those of #2 and #3 were prepared at 338 K and heated for 10 min at the same temperature. Nanostructures of #4 were prepared at 338 K and heated for 70 min at the same temperature. The effect of the amount of the THF solution on the size of nanostructures was shown in the [Supporting Information](#).

**2.3. Apparatus.** Proton nuclear magnetic resonance ( $^1\text{H}$  NMR) spectra were measured at 400 MHz on a JNM-ECS 400 MHz (JEOL). Matrix-assisted laser desorption ionization time-of-flight mass spectrometry (MALDI–TOF–MS) was performed with Axima-CFRplus (Shimadzu). The X-ray diffraction data of the crystalline solids were collected on the Ultima IV (Rigaku). Steady-state absorption and emission spectra were measured with UV-3600 (Shimadzu) and FP-6500 (JASCO), respectively. Transmission electron microscope (TEM) and field emission scanning electron microscope (FE-SEM) images were collected with JEM-3100FEF (JEOL) and SU9000 (HITACHI), respectively at Nara Institute of Science and Technology (NAIST). Fourier transform infrared (FTIR) absorption spectra were measured with FT/IR-6100 (JASCO) with the spectral resolution of 0.48  $\text{cm}^{-1}$ . The relative emission quantum yields of solutions were measured by using coumarin 153 in ethanol as a reference.<sup>30</sup> The absolute emission quantum yields of crystalline solids were measured by F-7000 (Hitachi) with a 415 nm excitation light. Emission decay measurements were conducted with the setup reported previously except the excitation light source.<sup>31</sup> A cavity-dumped Ti:sapphire laser (KM laboratories, 830 nm, 4 MHz) was passed through a frequency-doubled  $\beta\text{-BaB}_2\text{O}_4$  (BBO) crystal to generate 415 nm laser and the laser was used for the excitation pulse.

The emission behaviors of the single aggregate shown in [Figures 4 and S9–S11](#) were measured using a sample-scanning confocal microscope in combination with picosecond-pulsed laser excitation at 470 nm (10.0 MHz, 90 ps full width at half-maximum). Briefly, the excitation laser was focused on the isolated aggregate by an objective lens (NA 1.4; Olympus). The photons emitted from the sample were collected by a same objective lens and passed through a confocal pinhole and long-pass filter (LP02–488-RU-25; Semrock) and short-pass filter (FF01–650-SP-25; Semrock). Subsequently, half of the photons were detected with a spectrograph (SpectraPro2358; Acton Research Corporation) with a cooled CCD camera (PIXIS400B Princeton Instruments). The remaining half of the photons were detected by an avalanche photodiode (APD) single-photon-counting module (SPCM-AQR-14; PerkinElmer). The signal from the APD were connected via a router to a time-correlated single-photon counting board (SPC-630; Becker & Hickl) for lifetime measurements. All measurements were performed at room temperature in a dark room.

The emission decays were analyzed with least-squares analyses with multiple exponential decay functions. The instrumental response function (IRF) was convolved with the decay functions for the analyses of solutions and crystalline solids, while simple multiexponential decay functions were used for emission decays of single nanostructure because the IRF of these experiments is too broad to analyze the fast decay

component. Thus, the fast decay component of the emission decays of nanostructures was analyzed in detail by the emission decays of the solutions and crystalline solids. The goodness of the fitting was confirmed by the deviation (weighted residual) as shown below.<sup>30</sup>

$$D_k = \frac{N(t_k) - N_c(t_k)}{\sqrt{N(t_k)}}$$

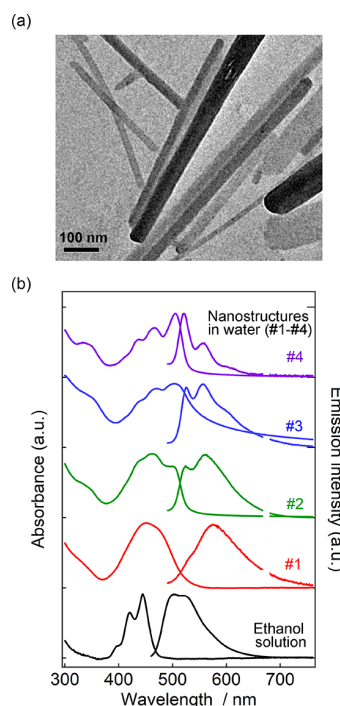
where,  $D_k$ ,  $N(t_k)$ , and  $N_c(t_k)$  indicate the deviation, the measured data, and calculated decay data using assumed parameter values of  $k$ th data points.

Steady-state absorption and emission spectra for single nanostructures shown in Figure S12 were measured by using another microspectroscopic setup. For the steady-state absorption measurements of single nanostructure, a femto-second white-light continuum was used as a probe light and focused with a 60× objective lens (NA 0.70). The white-light continuum was generated by focusing a 800 nm fundamental light of the amplified femtosecond Ti:sapphire laser pulse (Spectra-physics, Spitfire-ACE) into a 3 mm CaF<sub>2</sub> glass plate. The estimated beam diameter was 1 μm. The transmitted light was collimated with 20x objective lens. The intensity was detected with a fiber-coupled high-sensitive CCD camera (Andor, Newton DU970P) with a polychromator (Andor, Shamrock163). For steady-state emission measurement, a 450 nm laser diode (Thorlabs, CPS450) was employed as an excitation light. The excitation light was focused into the sample with the 60× objective lens. The beam diameter at the focal point was estimated to be 3 μm. The emission from a single nanostructure was collected with the same objective lens and passed through a confocal pinhole. The intensity was detected with the same CCD camera as the polychromator.

Transient absorption measurements were conducted by using the setup reported previously except the slight modifications of the excitation light source.<sup>32</sup> An optical parametric amplifier (OPA, TOPAS, Light conversion) was used to generate the 630 nm excitation pulse. The polarization of the pump beam is set at the magic angle (54.7°) with respect to that of the probe to eliminate polarization and photoselection effects.

### 3. RESULTS AND DISCUSSION

Figure 2a shows the transmission electron microscope (TEM) image of nanostructures of 1 prepared at 338 K during the reprecipitation method and heated at the same temperature for 10 min (the condition is the same as #2 and #3 in Figure 2b as explained later). Wide-field scanning electron microscope (SEM) images of nanostructures of 1 are shown in Figure S5. The TEM image shows that the thin and rigid nanofibers are formed by the reprecipitation methods. Wide field SEM images show that two types of nanostructures are mainly observed in the nanostructure solution, namely rectangular or cubic-like nanoparticles and nanofibers. The average diameter of thin nanofibers is approximately 15–40 nm, but thick nanofibers with the diameter of >50 nm are also observed. It appears that the thick nanofibers are formed by the bundle of multiple nanofibers. The average size of the nanoparticles are tens-of-nanometers. The length of nanofibers are micrometer scales. The nano beam electron diffraction (NBD) measurements show that several parts of nanostructures have crystallinity, although most parts of nanostructures are amorphous (Figure S5).

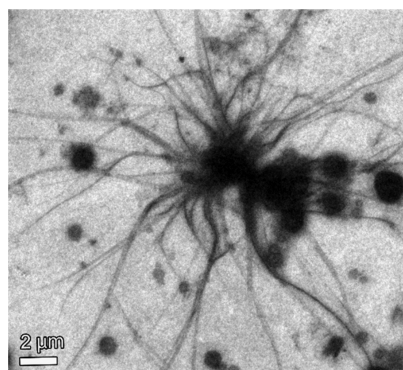


**Figure 2.** (a) TEM image of nanostructures of 1 prepared at 338 K and heated at the same temperature for 10 min (the condition is the same as #2 and #3 in part b). (b) Steady-state absorption and emission spectra of 1 in ethanol and nanostructures of 1 in water (#1-#4, see the Experimental Section for the detail of the sample preparations) at room temperature. The excitation wavelength is 450 nm. The emission spectra around 670 nm are omitted because of a noise by the instrument.

Figure 2b shows the steady-state absorption and emission spectra of 1 in ethanol and the nanostructure solution of 1 prepared in different conditions. In 1 dissolved in ethanol, the sharp absorption bands are observed at 420 and 450 nm, which are attributable to the  $\pi-\pi^*$  transition of the perylene moiety and the imidazole ring. The emission bands are observed at 503 and 523 nm upon excitation with 450 nm. The relative emission quantum yield is 0.70 by using coumarin 153 in ethanol as a reference. Nanostructures of #1 are prepared at 298 K by reprecipitation methods, while those of #2 and #3 are prepared at 338 K and heated for 10 min. Nanostructures of #4 are prepared at 338 K and heated for 70 min. It should be mentioned that the sample preparation conditions of #2 and #3 are the same but the obtained spectra are slightly different depending on batches. However, the clear tendency is observed in absorption and emission spectra depending on the heating condition. The absorption spectrum of #1, which is prepared at room temperature, is broadened and shifts to the red as compared to that in ethanol. The emission spectrum is also broadened and shifts to the red, and the Stokes shift largely increases (~100 nm). The broad and largely red-shifted emission spectrum is a characteristic feature of the excimer emission of  $\alpha$ -perylene crystals.<sup>33–35</sup> Therefore, we assign the broad emission band to the excimer emission of 1. This assignment is consistent with the emission decay measurements, where the longer emission lifetime is observed in the broad and red-shifted emission of nanostructures than that in ethanol as shown later. The longer emission lifetime than that

of the monomer is a typical characteristic for the excimer emission.

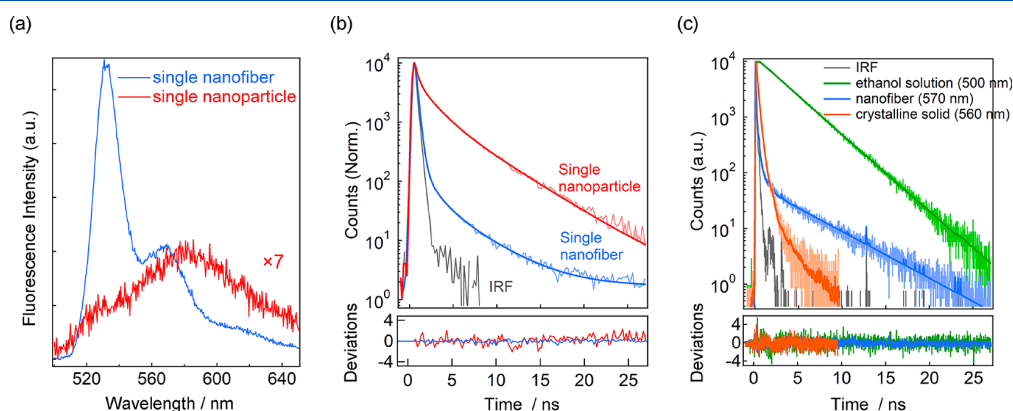
In #2 and #3, where the solutions are heated to 338 K for 10 min during the reprecipitation method, the additional absorption and emission bands appear at approximately 500 and 525 nm, respectively. Furthermore, #4, where the nanostructure solution is prepared at 338 K and heated for 70 min, has the sharper absorption and emission bands at 505 and 521 nm, respectively. The sharper absorption and emission spectra and slight red-shifted absorption spectra than those of monomer suggest that the well-aligned nanostructures are formed by heating. The crystalline solids of **1** formed by the recrystallization are needle-like microcrystals and give the similar sharp emission to that of #4 (Figure S13). The FTIR absorption spectrum of crystalline solids of **1** in a KBr plate has a broad absorption at 2600–3200  $\text{cm}^{-1}$ , while that of **2** does not (Figure S7). The broad absorption can be assigned to the N–H...N stretching mode of the imidazole ring following to the previous experimental and theoretical studies of imidazole.<sup>36</sup> It indicates that the solid state of **1** has the hydrogen bonding network. Moreover, the TEM measurement of the heated sample shows that the nanofibers grow radially from the aggregated nanoparticles as shown in Figure 3. The



**Figure 3.** TEM image of the nanostructure of **1** prepared at 338 K and heated at the same temperature for 70 min.

growth of nanofibers from nanoparticles by heating indicates that nanofibers are thermodynamically stable nanostructures

and that nanoparticles are kinetically formed nanostructures. This result also indicates that the broad excimer emission, which is mainly observed in the sample without heating (#1) of **1**, is originated from kinetically formed nanoparticles. It also indicates that the sharp absorption and emission spectra, which are mainly observed heated nanostructures of **1** (#4), are originated from thermodynamically formed nanofibers. Moreover, nanostructures of **2** do not give any monomer-like sharp emission, and give only the excimer-like broad emission irrespective of the heating duration as shown in the Supporting Information (Figure S8). **2** forms wrapped nanosheets by the reprecipitation method and the aspect ratio of the nanostructure is much smaller than that of the nanostructures of **1** (Figure S6). This result strongly suggests that the hydrogen bonding of the imidazole ring is the key interaction for anisotropic nanofibers and the monomeric sharp emission. The reason why the excimer molecular arrangement is kinetically preferable than the hydrogen bonding is most probably that the  $\pi$ – $\pi$  interaction of **1** is easily formed as compared to the hydrogen bonding. That is, various molecular arrangements can form the  $\pi$ – $\pi$  stacking in **1** (including metastable arrangements). On the other hand, the molecular arrangements which can form the hydrogen bond are restricted to the direction of the N–H bond of the imidazole ring. In the case of **1**, because the hydrogen bond is somehow stronger than the  $\pi$ – $\pi$  interaction, the heating process gradually converts the  $\pi$ -stacked molecular arrangements to the hydrogen-bonded molecular arrangement. The monomeric emission feature is observed in nanofibers most probably because the hydrogen bonding network inhibits the  $\pi$ -stacked arrangement. Moreover, since the molecular arrangement induced by the hydrogen bonding is restricted, it is expected that molecules in the hydrogen bonding network are well aligned. This is probably the reason why nanofibers formed by the hydrogen bonding network has the sharp absorption and emission spectra. The small Stokes-shift and sharp emission features are similar to that of  $\beta$ -perylene crystal, which is one of the metastable crystal phases of perylene.<sup>33,37</sup> In  $\beta$ -perylene crystal, the monomer-like sharp emission is observed because of the herringbone molecular alignment.<sup>33</sup> The shape-dependent optical properties of **1** are further investigated in single nanostructure emission spectroscopy.



**Figure 4.** (a) Emission spectra and (b) decays of a single nanofiber and a nanoparticle excited at 470 nm (the probe wavelength is 488–650 nm). (c) Emission decays of the nanostructure solution of **1** (#2), **1** in ethanol, and the crystalline solid of **1**. Values in bracket indicate the probe wavelength. The bottom figures of parts b and c indicate the deviations.

TEM measurements of nanostructures of **2** show that **2** forms wrapped nanosheets (Figure S6) as explained before. The lattice fringes are observed in TEM, and NBD measurements show the many parts of wrapped nanosheets have crystallinity. The absorption spectra of nanostructures of **2** do not change irrespective of heating duration once they are heated. This result suggests that wrapped nanosheets of **2** are thermodynamically stable nanostructures. All nanostructures of **2** give broad and red-shifted emissions assigned to the excimer emission irrespective of the heating conditions, although the emission peaks are slightly different depending on the sample preparations (Figure S8). Since **2** does not have the hydrogen bonding, it shows that the  $\pi$ - $\pi$  interaction is the origin for the excimer emission of nanostructures of **2**. The details of **2** are shown in Supporting Information.

The emission quantum yields of all nanostructures of **1** drastically decrease to  $<0.01$  as compared to that in ethanol solution (0.70). The emission quantum yields of **2** also decrease to 0.02–0.03 as compared to that in ethanol solution (0.92). However, the emission quantum yields of nanostructures of **2** are higher than those of **1**. The absolute emission quantum yields of the crystalline solids of **1** and **2** are 0.03 and 0.09, respectively. Emission decay measurements reveal that the drastic decrease in the emission quantum yields of nanostructures is due to the intrinsic nonradiative relaxation pathways induced by the hydrogen bonding and carrier trapping as discussed later.

To investigate the detail of shape dependent optical properties of nanostructures, single nanostructure emission measurements are conducted. The sample is prepared by spin coating the nanostructure solution to the glass substrate (see the Supporting Information for detail). Emission microscope images are shown in Figures S9–S12. As was observed in SEM and TEM measurements, two types of nanostructures, namely nanoparticles and nanofibers, are observed in **1**. Figure 4a shows single particle emission spectra of a nanofiber and a nanoparticle of **1**. The spectra are averaged by several nanostructures. The emission spectra of each nanostructure are shown in the SI. As was expected in the solution experiments, the nanofiber of **1** gives the sharp emission spectrum and the peak is located at 532 nm, which is similar to the emission spectrum of #4 (Figure 2b). This emission spectrum is also similar to that of needle-like crystalline solids of **1** formed by recrystallizations (Figure S13), although the emission peak of the crystalline solid is shifted to the red. The detail of the crystalline solids is shown in the Supporting Information. It also indicates that the nanofibers, which is formed by the hydrogen bond interaction, is the thermodynamically stable nanostructures. The emission spectrum of nanoparticles is broad and shifted to the red, which is similar to the excimer emission of the solution of #1. These single nanostructure experiments also show that the spectral change of the emission spectra from #1 to #4 upon heating at 338 K (Figure 2b) is due to the transformation of nanoparticles to thermodynamically stable nanofibers as shown in Figure 3. It should be mentioned that the emission spectra of single nanoparticle are different depending on the nanoparticles as shown in Figures S9 and S10. Since some spectra have a shoulder at around 525 nm, one of the reasons for the difference is probably due to the superposition of the small amount of the sharp nanofiber emission in some nanoparticles. Other possibilities may be due to the different molecular arrangement and the different local environments in different

nanoparticles. The emission spectra of nanostructure solutions of #2 and #3 are most probably composed of the superposition of individual emission spectra of nanoparticles and nanofibers.

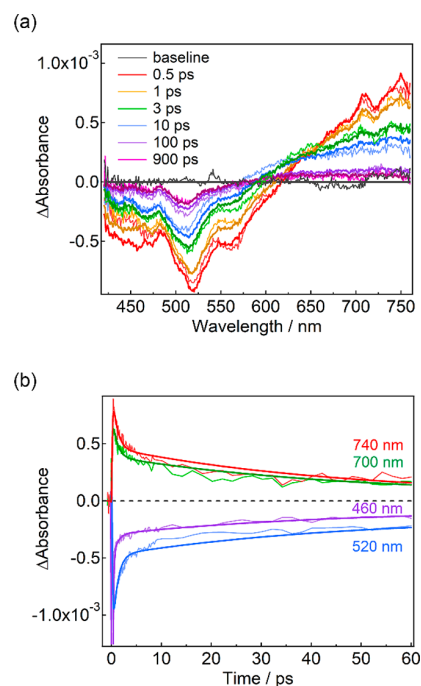
Figure 4b shows the emission decays of a single nanoparticle and a nanofiber excited at 465 nm. The emission decay of a single nanofiber of **1** has a large amplitude of the fast decay component and a small amplitude of the slow decay components. The emission decay of the single nanofiber is fitted with the three-exponential decay function. The lifetimes of the fast decay are within the instrumental response function (IRF,  $\sim 98\%$ ) and that of the slow decays are 1.2 ns ( $\sim 1.5\%$ ) and 4.2 ns ( $<1\%$ ). The slow decay components vary from  $\sim 2$ –10 ns in different nanostructures and these values also depend on the fitting condition because of the low signal-to-noise ( $S/N$ ) ratio. The emission decay of nanoparticles of **1** has much smaller amplitude of the fast decay component as compared to that of nanofibers. The emission decay of the single nanoparticle is fitted with the three-exponential decay function and the lifetimes are 600 ps (62%), 3.0 ns (34%), and 7.6 ns (4%). It is worth noting that nanoparticles of **1** and nanosheets of **2**, both of which give excimer emissions, do not have such a large and fast decay component (Figures S9–S11). It shows that the large amount of the fast decay component is characteristic for nanofibers of **1**. The effect of water can be excluded for the fast decay component because the sample of the single emission decay measurements is a dry film. It strongly suggests that the characteristic fast decay component of the nanofiber of **1** is due to the nonradiative relaxation induced by hydrogen bonding. The fast decay component (600 ps) of the nanoparticle of **1** is relatively slower and smaller than that of the nanofiber of **1** and the relatively slower decays are also observed in the emission decays of a single nanostructure of **2** (Figure S11). These results suggest that the relatively slower decay component in nanoparticles of **1** and nanostructures of **2** is originated from the carrier trapping. Although nanoparticles of **1** and nanostructures of **2** do not have such a fast decay component like nanofibers of **1**, these decays still contain the large amount of the fast decay components assigned to the carrier trapping. Moreover, the transient absorption spectroscopy shows that the additional fast decay components faster than the IRF (11 ps) is also observed in nanostructures of **2** as shown later. This result indicates that the low emission quantum yields of nanostructures are due to both contributions of the nonradiative relaxation pathways by the hydrogen bonding and carrier trapping. The emission decays are further investigated in ethanol solution, nanostructures (#2), and crystalline solids as shown in Figure 4c, where the faster IRF gives more detailed information on the emission decay processes. The excitation wavelength is set to 415 nm. The lifetime of the slower decay is 5.2 ns, which is slower than that of **1** dissolved in ethanol (the lifetime is 3.1 ns). Since #2 is composed of the mixture of nanoparticles and nanofibers, the slower decay is assigned to the excimer emission of the nanoparticles. Nanostructure solutions of #2 also show the similar emission decay to that of a single nanofiber. The decay of the nanostructure solution is analyzed with three exponential decay functions convolved by IRF with the time constants of 38 ps (92.2%), 460 ps (6.5%), and 5.2 ns (1.3%). The fast decay component is still almost the same as IRF, indicating that the further faster time scale is necessary to reveal the process. The emission decay of the crystalline solids has the characteristic fast decay component as similar to the fast decay component of the nanofiber. The

decay of the crystalline solids is analyzed with three exponential decay functions convolved by IRF, and the lifetimes are 120 ps (87.0%), 370 ps (12.8%), and 2.0 ns (0.2%). The lifetime of the fast decay is slightly slower than that of nanofibers and the emission of the crystalline solids mostly decays within 100 ps. It suggests that the crystalline solids have few excimer components and that the fiber-like nanostructures formed by the hydrogen bonding is the thermodynamically stable nanostructures.

On the other hand, the emission decay of nanostructures of **2** prepared at 338 K and heated for 10 min is almost identical to that of the crystalline solid of **2** (Figure S15). The decay of the nanostructure solution of **2** is fitted with the three exponential function convolved by IRF, and the lifetimes are 300 ps (69.4%), 1.9 ns (24.8%), and 8.0 ns (5.8%), respectively. It also shows that the nanosheets of **2** are thermodynamically stable nanostructures. The result is consistent with the fact that the absorption spectra of nanostructures of **2** do not change irrespective of heating durations after the preparation of nanostructures at 338 K.

To further investigate the ultrafast process of the hydrogen bond-induced nonradiative relaxations of **1**, femtosecond transient absorption measurements are conducted with a 400 nm excitation pulse. The transient absorption spectra are temporally analyzed with the sequential model of the global analyses. Transient absorption spectra of **1** and **2** dissolved in ethanol are shown in Figures S16 and S17. It is noted that the excitation of **1** and **2** in ethanol with 400 nm only excites the  $S_1$  state as shown in Figure 2b and Figure S8. The spectral evolutions of **1** and **2** in ethanol solution are very similar, indicating that the relaxation pathways are almost the same. Briefly, after the short-lived Franck–Condon (FC) state of the  $S_1$  state (1–2 ps), the  $S_1$  state with the lowest vibrational level is formed within tens-to-hundreds of picoseconds via vibrational cooling. The  $S_1$  gives the ground state bleaching and the stimulated emission signal. The excited state relaxes to the ground state mostly by the radiative transition because the emission quantum yields of both compounds are high.

Parts a and b of Figure 5 show the transient absorption spectra and dynamics of the nanostructure solution of **1** (#3 in Figure 2b) excited at 400 nm. The transient absorption spectra and dynamics of nanostructures of **2** are shown in Figure S19 for comparison. The time evolution of the transient absorption spectra are globally analyzed with the four-state sequential kinetic model.<sup>38</sup> The singular value decomposition (SVD) analyses give the evolution associated spectra, which indicate the differential absorption spectra of each species of the kinetic model. The thick lines indicate the fitted transient absorption spectra by the global analyses, while the thin and pale-color lines indicate the raw transient absorption spectra. The details of the analyses of the transient absorption spectra of Figure 5 are shown in the Figure S18. At 0.5 ps after the excitation, two negative signals are observed at 520 and 560 nm. The negative signal at 520 nm is probably assigned to the superposition of the ground state bleach and the stimulated emission signals of the  $\beta$ -crystal-like sharp monomeric emission, while the negative signal at 560 nm is assigned to the stimulated emission. The stimulated emission signal rapidly disappears with the time constant of 0.96 ps. On the other hand, such the ultrafast relaxation process is not observed in the transient absorption dynamics of nanostructures of **2** as shown in Figure S19. Therefore, it suggests that the nanofibers of **1** formed by the hydrogen bonding induces the ultrafast nonradiative



**Figure 5.** (a) Transient absorption spectra and (b) dynamics of the nanostructure solution (#3) of **1** excited at 400 nm ( $71 \mu\text{J cm}^{-2}$ ) of a femtosecond laser pulse. The thick lines indicate the fitted transient absorption spectra and decays by the global analyses, while the thin and pale-color lines indicate the raw transient absorption spectra and decays.

relaxation. As is shown in the emission spectrum of Figure 2b, #3 contains both nanoparticles and nanofibers. It is expected that the stimulated emission signal observed around 520–620 nm has two spectral components, the sharp and broad emission features. However, it was difficult to resolve these spectral components of the stimulated emission from the transient absorption spectra. One plausible reason may be the superposition of the broad excited state absorption, which obscure the stimulated emission of the broad excimer emission. The other reason might be due to the partial aggregations of nanofibers and nanoparticles in solutions. The TEM measurements show that the nanofibers are formed from the nanoparticles because nanofibers are thermodynamically stable nanostructures. The aggregation of nanofibers and nanoparticles may induce the ultrafast nonradiative decay process of nanoparticles by carrier diffusions to nanofibers. The ground state bleach signal of the nanostructure of **1** slightly recovers with the same time constant of the ultrafast nonradiative relaxation. However, the certain amount of the bleach signal still exists, indicating the generated electron and hole pair (exciton) is dissociated. The ultrafast dissociation of the exciton of nanostructures of **1** may indicate the efficient electrical properties as similar to other imidazole-based nanostructures. However, it is necessary to reduce the vibronic coupling by the hydrogen bonding to enhance the luminescent properties of these nanomaterials.

In summary, we synthesized perylene-substituted lophine derivatives and prepared different nanostructures depending on the  $\pi$ – $\pi$  interaction and the hydrogen bonding. The hydrogen bonding leads to thermodynamically stable nanofibers and gives the monomeric sharp emission, while it also

induces the ultrafast nonradiative relaxation. On the other hand, the  $\pi$ - $\pi$  interaction leads to kinetically favorable nanoparticles and gives the broad emission due to the excimer of the perylene moiety. The insight into the relationship among molecular structures, nanostructures, and optical properties are important for developing further photofunctional organic nanomaterials.

## ■ ASSOCIATED CONTENT

### Supporting Information

The Supporting Information is available free of charge on the ACS Publications website at DOI: 10.1021/acs.jpcc.9b01391.

Details of material characterizations ( $^1\text{H}$  NMR, HPLC, TEM, NBD, and XRD measurements) and optical properties of **1** and **2** (PDF)

## ■ AUTHOR INFORMATION

### Corresponding Author

\*(Y.K.) E-mail: ykobayas@fc.ritsumei.ac.jp.

### ORCID

Mitsuaki Yamauchi: 0000-0003-0005-5960

Yukihide Ishibashi: 0000-0002-4015-8828

Sadahiro Masuo: 0000-0003-4828-5968

Naoto Tamai: 0000-0002-7343-6564

Yoichi Kobayashi: 0000-0003-3339-3755

### Notes

The authors declare no competing financial interest.

## ■ ACKNOWLEDGMENTS

This work was supported partly by JSPS KAKENHI Grant Number JP26107010 in Scientific Research on Innovative Areas “photosynergetics”, JSPS KAKENHI Grant Number JP18K14194 and JP18H05263, and Izumi Science and Technology Foundation for Y.K. A part of this work was conducted in NAIST, supported by the Nanotechnology Platform Program (Synthesis of Molecules and Materials) of the Ministry of Education, Culture, Sports, Science, and Technology (MEXT), Japan. The authors acknowledge Dr. M. Fujihara at NAIST for TEM measurements, Mr. K. Ozaki, and Ms. Y. Kuroda at Ritsumeikan University for emission quantum yield measurements of crystalline solids, Ms. H. Tanaka at Ehime University for single nanostructure absorption and emission measurements, and Prof. H. Maeda, Prof. Y. Okada, and Prof. Y. Nagasawa at Ritsumeikan University for MALDI-TOF MS, HPLC, and emission spectrometry, respectively.

## ■ REFERENCES

- (1) Kasha, M.; Rawls, H. R.; El-Bayoumi, M. A. The Exciton Model in Molecular Spectroscopy. *Pure Appl. Chem.* **1965**, *11*, 371–392.
- (2) Hestand, N. J.; Spano, F. C. Expanded Theory of H- and J-Molecular Aggregates: The Effects of Vibronic Coupling and Intermolecular Charge Transfer. *Chem. Rev.* **2018**, *118*, 7069–7163.
- (3) Whitesides, G. M.; Mathias, J. P.; Seto, C. T. Molecular Self-Assembly and Nanochemistry: A Chemical Strategy for the Synthesis of Nanostructures. *Science* **1991**, *254*, 1312–1319.
- (4) Haketa, Y.; Maeda, H. Dimension-Controlled Ion-Pairing Assemblies Based on  $\pi$ -Electronic Charged Species. *Chem. Commun.* **2017**, *53*, 2894–2909.
- (5) Zhang, W.; Yao, J.; Zhao, Y. S. Organic Micro/Nanoscale Lasers. *Acc. Chem. Res.* **2016**, *49*, 1691–1700.

(6) Zhao, Y. S.; Fu, H.; Peng, A.; Ma, Y.; Liao, Q.; Yao, J. Construction and Optoelectronic Properties of Organic One-Dimensional Nanostructures. *Acc. Chem. Res.* **2010**, *43*, 409–418.

(7) Coffin, R. C.; Peet, J.; Rogers, J.; Bazan, G. C. Streamlined Microwave-Assisted Preparation of Narrow-Bandgap Conjugated Polymers for High-Performance Bulk Heterojunction Solar Cells. *Nat. Chem.* **2009**, *1*, 657–661.

(8) Hoeben, F. J. M.; Jonkheijm, P.; Meijer, E. W.; Schenning, A. P. H. J. About Supramolecular Assemblies of  $\pi$ -Conjugated Systems. *Chem. Rev.* **2005**, *105*, 1491–1546.

(9) Wasielewski, M. R. Photoinduced Electron Transfer in Supramolecular Systems for Artificial Photosynthesis. *Chem. Rev.* **1992**, *92*, 435–461.

(10) Yan, D.; Williams, G. R.; Zhao, M.; Li, C.; Fan, G.; Yang, H. Flexible Free-Standing Luminescent Two-Component Fiber Films with Tunable Hierarchical Structures Based on Hydrogen-Bonding Architecture. *Langmuir* **2013**, *29*, 15673–15681.

(11) Yan, D.; Jones, W.; Fan, G.; Wei, M.; Evans, D. G. Organic Microbelt Array Based on Hydrogen-Bond Architecture Showing Polarized Fluorescence and Two-Photon Emission. *J. Mater. Chem. C* **2013**, *1*, 4138–4145.

(12) Hayashi, T.; Maeda, K. Preparation of a New Phototropic Substance. *Bull. Chem. Soc. Jpn.* **1960**, *33*, 565–566.

(13) Hayashi, T.; Maeda, K.; Morinaga, M. The Mechanism of the Photochromism and Thermochromism of 2,2',4,4',5,5'-Hexaphenyl-1,1'-Biimidazolyl. *Bull. Chem. Soc. Jpn.* **1964**, *37*, 1563–1564.

(14) Kishimoto, Y.; Abe, J. A Fast Photochromic Molecule That Colors Only under UV Light. *J. Am. Chem. Soc.* **2009**, *131*, 4227–4229.

(15) Yamashita, H.; Ikezawa, T.; Kobayashi, Y.; Abe, J. Photochromic Phenoxyl-Imidazolyl Radical Complexes with Decoloration Rates from Tens of Nanoseconds to Seconds. *J. Am. Chem. Soc.* **2015**, *137*, 4952–4955.

(16) Kobayashi, Y.; Mutoh, K.; Abe, J. Fast Photochromic Molecules toward Realization of Photosynergetic Effects. *J. Phys. Chem. Lett.* **2016**, *7*, 3666–3675.

(17) Dessauer, R. *Photochemistry, History and Commercial Applications of Hexaarylbiimidazoles*; Elsevier: Delaware, 2006.

(18) Yan, D.; Patel, B.; Delori, A.; Jones, W.; Duan, X. The Formation of Hydrogen-Bond Facilitated Salts with Tunable Optical Properties: An Experimental and Theoretical Study of 2,4,5-Triphenylimidazole. *Cryst. Growth Des.* **2013**, *13*, 333–340.

(19) Yan, D.; Evans, D. G. Molecular Crystalline Materials with Tunable Luminescent Properties: From Polymorphs to Multi-Component Solids. *Mater. Horiz.* **2014**, *1*, 46–57.

(20) Zang, L.; Che, Y.; Moore, J. S. Conjugated Molecules: Adaptable Building Blocks for Organic Nanodevices. *Acc. Chem. Res.* **2008**, *41*, 1596–1608.

(21) Zhao, Y. S.; Peng, A.; Fu, H.; Ma, Y.; Yao, J. Nanowire Waveguides and Ultraviolet Lasers Based on Small Organic Molecules. *Adv. Mater.* **2008**, *20*, 1661–1665.

(22) One-Dimensional Nanostructures; Zhai, T.; Yao, J., Eds.; Wiley: New Jersey, 2013.

(23) Zhang, W.; Yan, Y.; Gu, J.; Yao, J.; Zhao, Y. S. Low-Threshold Wavelength-Switchable Organic Nanowire Lasers Based on Excited-State Intramolecular Proton Transfer. *Angew. Chem., Int. Ed.* **2015**, *54*, 7125–7129.

(24) Horiuchi, S.; Kagawa, F.; Hatahara, K.; Kobayashi, K.; Kumai, R.; Murakami, Y.; Tokura, Y. Above-Room-Temperature Ferroelectricity and Antiferroelectricity in Benzimidazoles. *Nat. Commun.* **2012**, *3*, 1306–1308.

(25) Owczarek, M.; Hujsak, K. A.; Ferris, D. P.; Prokofjevs, A.; Majerz, I.; Szklarz, P. A.; Zhang, H.; Sarjeant, A. A.; Stern, C. L.; Jakubas, R.; et al. Flexible Ferroelectric Organic Crystals. *Nat. Commun.* **2016**, *7*, 13108.

(26) Yan, D. Micro-/Nanostructured Multicomponent Molecular Materials: Design, Assembly, and Functionality. *Chem. - Eur. J.* **2015**, *21*, 4880–4896.

- (27) Zhou, B.; Yan, D. Hydrogen-Bonded Two-Component Ionic Crystals Showing Enhanced Long-Lived Room-Temperature Phosphorescence via TADF-Assisted Förster Resonance Energy Transfer. *Adv. Funct. Mater.* **2019**, *29*, 1807599.
- (28) Kasai, H.; Nalwa, H. S.; Oikawa, H.; Okada, S.; Matsuda, H.; Minami, N.; Kakuta, A.; Ono, K.; Mukoh, A.; Nakanishi, H. A Novel Preparation Method of Organic Microcrystals. *Jpn. J. Appl. Phys.* **1992**, *31*, L1132–L1134.
- (29) Kasai, H.; Kamatani, H.; Yoshikawa, Y.; Okada, S.; Oikawa, H.; Watanabe, A.; Itoh, O.; Nakanishi, H. Crystal Size Dependence of Emission from Perylene Microcrystals. *Chem. Lett.* **1997**, *26*, 1181–1182.
- (30) Lakowicz, J. R. *Principles of Fluorescence Spectroscopy*; 3rd ed.; Springer US: 2006.
- (31) Boens, N.; Qin, W.; Basarić, N.; Hofkens, J.; Ameloot, M.; Pouget, J.; Lefevre, J. P.; Valeur, B.; Gratton, E.; VandeVen, M.; et al. Fluorescence Lifetime Standards for Time and Frequency Domain Fluorescence Spectroscopy. *Anal. Chem.* **2007**, *79*, 2137–2149.
- (32) Kobayashi, Y.; Pan, L.; Tamai, N. Effects of Size and Capping Reagents on Auger Recombination Dynamics of CdTe Quantum Dots Auger Recombination Dynamics of CdTe QDs. *J. Phys. Chem. C* **2009**, *113*, 11783–11789.
- (33) Tanaka, J. The Electronic Spectra of Aromatic Molecular Crystals. II. The Crystal Structure and Spectra of Perylene. *Bull. Chem. Soc. Jpn.* **1963**, *36*, 1237–1249.
- (34) Chu, N. Y. C.; Kearns, D. Monomer Emission from Excimer Forming Crystals: Pyrene and Perylene. *Mol. Cryst. Liq. Cryst.* **1972**, *16*, 61–74.
- (35) Von Freydrorf, E.; Kinder, J.; Michel-Beyerle, M. E. On Low Temperature Fluorescence of Perylene Crystals. *Chem. Phys.* **1978**, *27*, 199–209.
- (36) Marechal, Y.; Witkowski, A. Infrared Spectra of H-Bonded Systems. *J. Chem. Phys.* **1968**, *48*, 3697–3705.
- (37) Tanaka, J.; Kishi, T.; Tanaka, M. Electronic Spectra of Perylene Crystals. *Bull. Chem. Soc. Jpn.* **1974**, *47*, 2376–2381.
- (38) Snellenburg, J. J.; Liptenok, S. P.; Seger, R.; Mullen, K. M.; van Stokkum, I. H. M. Glotaran: A Java-Based Graphical User Interface for the R Package TIMP. *J. Stat. Softw.* **2012**, *49*, 1–22.

## PAPER



Cite this: *Phys. Chem. Chem. Phys.*,  
2019, 21, 6348

## Photoconversion of 6,13- $\alpha$ -diketopentacene single crystals exhibiting light intensity-dependent morphological change†

Mitsuaki Yamauchi,<sup>a</sup> Yuya Miyamoto,<sup>a</sup> Mitsuharu Suzuki,<sup>b</sup> Hiroko Yamada<sup>b</sup> and Sadahiro Masuo<sup>b\*</sup>

Recently, we revealed that 6,13-dihydro-6,13-ethanopentacene-15,16-dione (PDK) could be quantitatively photoconverted into pentacene even in the crystal phase, accompanied by the destruction of the crystals. In this work, we investigated the relationship between the photoinduced morphological changes and the light intensity for the photoconversion at a single micrometre-sized crystal level. Photoirradiation with a strong intensity (over 100 kW cm<sup>-2</sup>) resulted in hole formation in a single crystal. When medium intensity (0.5–100 kW cm<sup>-2</sup>) was irradiated, destruction including separation and jumping of the crystal was observed. Absorption spectrum measurement of the single crystal revealed that when almost same number of pentacene was generated, the destruction was induced by the generated strain within crystal due to the stacking mismatch between the different molecules. Upon photoirradiation with a low intensity (below 0.5 kW cm<sup>-2</sup>), protruding pillar objects were observed on the crystal surface. This formation is a result of the surface movement of molecules through the relaxation of strain. Our results provide important insight into stimuli-responsive crystal materials and could contribute to the generation and application of remotely controllable smart materials.

Received 23rd October 2018,  
Accepted 17th December 2018

DOI: 10.1039/c8cp06594b

rsc.li/pccp

### Introduction

Controlling the morphology of functional materials with external photochemical and mechanical stimuli is of great importance for creating stimuli-responsive smart materials.<sup>1–15</sup> Single crystals composed of organic molecules that are morphologically controllable with light, however, are limited due to the molecular packing structures of solids.<sup>10–13</sup> With photoresponsive molecules, morphological changes in a single crystal can be achieved rationally with an external photostimulus. Unlike molecules under solution conditions, molecules packed in a crystal should interact, and unexpected morphological changes can be induced by photoirradiation. To date, prominent morphological photocontrol in single crystals using diarylethene and azobenzene units as general photochromic molecules has been reported. Irie and co-workers reported rapid and reversible shape control of single diarylethene crystals because of conformational changes caused by isomerization.<sup>10</sup> Norikane and co-workers reported an azobenzene single crystal exhibiting directional and continuous

motion driven by melting and crystallization of the crystal *via* photoisomerization.<sup>12</sup>

In contrast to these reversible systems with photochromic molecules, Yamada and co-workers synthesized a series of  $\alpha$ -diketone-type acene precursors exhibiting a one-way photoconversion, which is due to the release of CO molecules, in solution to form extended  $\pi$ -conjugated acenes.<sup>16–39</sup> Acenes are highly promising p-type organic semiconductors and have been the subject of extensive studies. However, acenes often have low solubility and stability, which poses major obstacles in the synthesis and processing of this class of compounds. The synthesized acene precursors are generally more soluble and stable than the corresponding acene compound, and their quantitative photoconversion can be achieved simply by photoirradiation in solution. With these acene precursors, the fabrication of high-performance organic field-effect transistors (OFETs) and photovoltaic devices have been demonstrated.<sup>25,29,31,32,35–40</sup>

Recently, our group investigated the photoconversion of 6,13-dihydro-6,13-ethanopentacene-15,16-dione (PDK), a representative acene precursor, into pentacene in the crystalline phase using spectroscopy techniques.<sup>13</sup> We clarified that the PDK could be quantitatively photoconverted into pentacene even in the crystalline phase upon sufficiently lengthy photoirradiation although the photoconversion rate in the crystalline phase was much slower than that in solution. Importantly, crystal destruction was observed

<sup>a</sup> Department of Applied Chemistry for Environment, Kwansai Gakuin University, 2-1 Gakuen, Sanda, Hyogo 669-1337, Japan. E-mail: masuo@kwansai.ac.jp

<sup>b</sup> Graduate School of Materials Science, Nara Institute of Science and Technology, Ikoma 630-0192, Japan

† Electronic supplementary information (ESI) available. See DOI: 10.1039/c8cp06594b

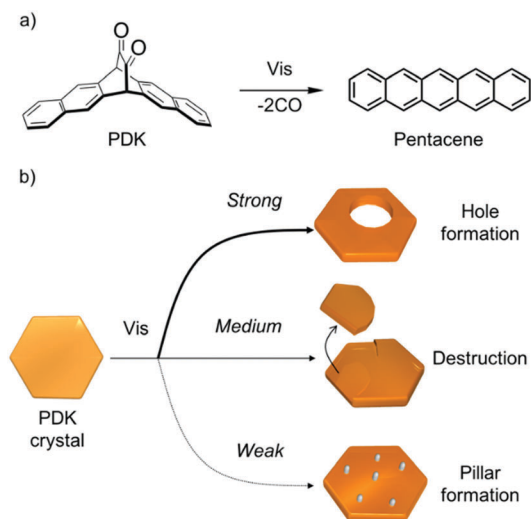


Fig. 1 (a) Chemical structure of PDK and its photoconversion into pentacene. (b) Schematic representation of the light-intensity-dependent morphological change of a single micrometre-sized PDK crystal.

during the photoconversion. This destruction is likely due to internal strain resulting from the change in molecular volume, *i.e.*, bent-shaped PDK into planar pentacene, during the photoconversion. These results indicated that the photoconversion of PDK in the crystalline phase is accompanied by a morphological change, *i.e.*, the quantitative photoconversion of the PDK is achieved by accompanying the destruction of the crystals. To elucidate the mechanism of these morphological changes, obtaining an understanding of this type of strain in molecules densely packed in crystal is necessary. Here, we report morphological changes in single micrometre-sized PDK crystals depending on light intensity for the photoconversion. Specifically, changes such as hole and pillar formation and destruction of the single crystal were observed by atomic force microscopy (AFM) (Fig. 1). Photoirradiation with a 488 nm continuous-wave (CW) laser with a very strong laser intensity resulted in hole formation in a single crystal. When medium intensity was irradiated, destruction including separation and jumping was observed. As the intensity was further decreased, protruding pillar objects were observed on the crystal surface without destruction. This unique morphology on the crystal is a result of the surface movement of molecules through the relaxation of strain generated by very slow photoconversion of PDK into pentacene.

## Experimental

PDK was synthesized according to a previous reported method.<sup>17</sup> Single micrometre-sized hexagonal crystals were prepared on a clean glass coverslip by drop-casting of a toluene solution and complete evaporation of the toluene in a dark room.

The morphological and spectroscopic changes of the single crystals were investigated under a confocal optical microscope combining with an AFM and spectroscopy systems (details in ESI†).<sup>41</sup> The coverslip on which the single crystals were formed was set on the stage of an inverted microscope. As a light source of the photoconversion, a 488 nm CW laser was introduced

through an objective lens. For the observation of an absorption spectrum of the single PDK micrometre-sized crystal, a halogen lamp for Köhler illumination system of the microscope was used as the incident light. The spectrum was measured using a spectrometer with a cooled CCD camera by the accumulation time of 5 s. All measurements were performed at room temperature in a dark room.

## Results and discussion

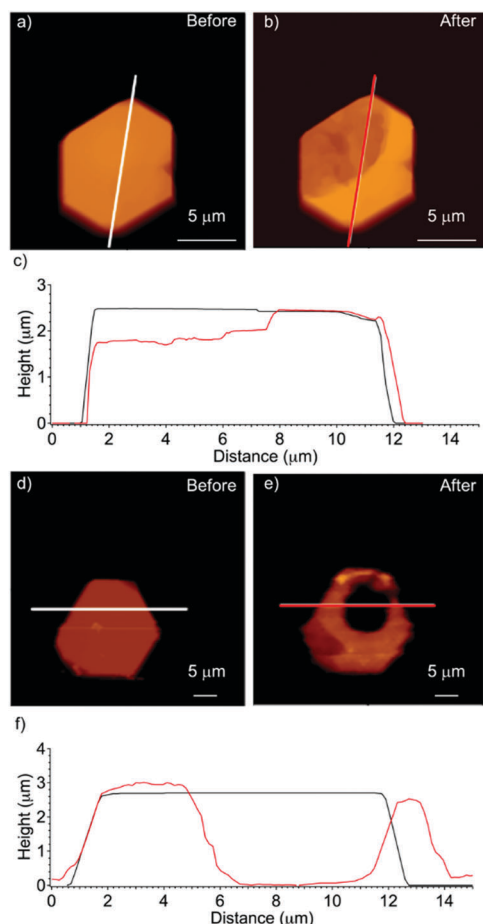
### Morphological changes induced by medium and strong laser intensity

In our previous work, we did not investigate the relationship between the morphological change and the light intensity.<sup>13</sup> When the 488 nm CW laser of a few tens  $\text{kW cm}^{-2}$  at a focal point was focused on the crystal, the destruction of the single crystal, including separation of a part of the crystal and jumping of the crystal was observed.<sup>13</sup> Here, we investigate the relationship between the morphological change and laser intensity.

Fig. 2(a–c) shows an example of the crystal destruction observed by photoirradiation with  $0.5 \text{ kW cm}^{-2}$  for 10 min. In this case, the separation of a part of the crystal was observed by the AFM measurement. Cross-sectional analysis reveals that the hollow possesses *ca.*  $1 \mu\text{m}$  in depth (Fig. 2c). Considering that the penetration depth of the laser is comparable to the thickness of the single crystal ( $< 3 \mu\text{m}$ ), the separation can be explained by strain within the crystal generated by the conversion of PDK to pentacene. The photoconverted pentacene acts as a mismatched stacking moiety within the PDK crystal, generating strain within the crystal. Moreover, an increase in the amount of strain can give rise to the separation of the crystal.

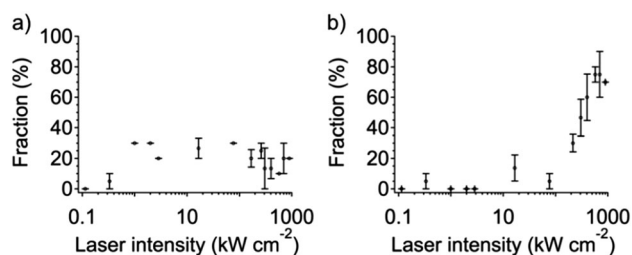
As the laser was strengthened to a very strong intensity, for example,  $960 \text{ kW cm}^{-2}$ , a well-defined hole was predominantly observed instead of destruction of the crystal after 10 min of photoirradiation, as visualized by AFM (Fig. 2d and e). The cross-sectional analysis shows that the irradiated single crystal has a hole with *ca.*  $7 \mu\text{m}$  diameter (Fig. 2f). In addition, the shape of the single crystal was maintained, but the edges of the crystal became smooth after hole formation. These results imply that movement of the molecules was induced by the strong laser beam. Almost all PDK molecules are converted into pentacene quickly in the case of a very strong laser intensity compared to with the case of a medium laser intensity. Furthermore, due to the very strong laser intensity, the temperature of the crystal increased, which may melt and sublimate the resulting pentacene, similar to laser ablation. This melting is consistent with the formation of a smooth edge after photoirradiation. Thus, the hole would be formed with the remaining molecules.

To evaluate the different morphological changes statistically, the frequency of destruction or hole formation under various intensities of  $0.1\text{--}1000 \text{ kW cm}^{-2}$  was observed and plotted as a function of laser intensity (Fig. 3a and b). At  $1\text{--}100 \text{ kW cm}^{-2}$ , *ca.* 30% of single PDK crystals exhibited separation and jumping (Fig. 3a). A strong laser beam with an intensity of  $100\text{--}1000 \text{ kW cm}^{-2}$ , however, resulted in a slight decrease in frequency. In contrast, although the



**Fig. 2** (a and b) AFM height images of a single micrometre-sized PDK crystal before (a) and after (b) photoirradiation with 0.5 kW cm<sup>-2</sup>. (c) AFM cross-sectional analysis along the white and red lines in (a and b). (d and e) AFM height images of a single micrometre-sized PDK crystal before (d) and after (e) photoirradiation with 960 kW cm<sup>-2</sup>. (f) AFM cross-sectional analysis along the white and red lines in (d and e).

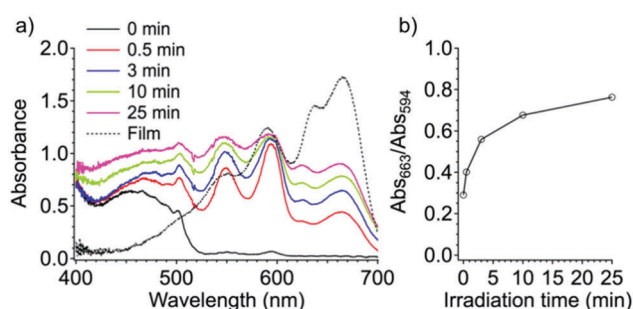
frequency of hole formation was quite low below 100 kW cm<sup>-2</sup>, as the laser intensity was increased, the frequency increased dramatically, resulting in 75% hole formation at 580 kW cm<sup>-2</sup> (Fig. 3b). The combination of separation and jumping resulted in almost all crystals exhibiting morphological changes above 580 kW cm<sup>-2</sup>. The existence of threshold values for hole formation and destruction suggest that the yield of pentacene in crystal plays an important role in the morphological changes.



**Fig. 3** (a and b) Frequency of photoinduced morphological changes: destruction behavior (a) and hole formation (b) as a function of laser intensity.

To reveal the relationship between the destruction and the number of converted molecules, we further investigated the photoinduced separation and jumping of the single micrometre-sized PDK crystals using UV/vis absorption spectroscopy. In this experiment, we employed a medium laser intensity (35 kW cm<sup>-2</sup>). The UV/vis spectra of a single crystal were recorded every 60 s with an accumulation time of 5 s during photoirradiation until the destruction of the crystal was observed. As a confocal microscope was used for this measurement, the spectra were detected from molecules in the confocal volume (hundreds nanometres wide and a few micrometres height). Examples of the observed UV/vis spectra are shown in Fig. 4a. In the case of this crystal, destruction of the crystal occurred after *ca.* 25 min of photoirradiation. Before photoconversion (0 min), the PDK crystal showed a broad absorption band at approximately 450 nm, which was assignable to the n-π\* transition of the diketone moiety of the PDK molecule. Upon photoirradiation, the absorption bands at 548 and 594 nm, which are attributed to the pentacene monomer, were increased. Furthermore, additional bands were also observed at approximately 625 and 663 nm. Considering that these bands were not detected in solution, the emergence of the bands is indicative of aggregation of planar pentacene *via* π-π stacking in the single crystal. Indeed, these aggregate bands are also observed in a pentacene-rich thin film (“Film” in Fig. 4a). Thus, compared to monomer band, the aggregate band should depend on the number of pentacene molecules formed by photoconversion.

To analyse the change in absorption up to the destruction of the crystal, the ratio of the monomer absorbance at 594 nm to the aggregate absorbance at 663 nm ( $A_{663}/A_{594}$ ) was plotted as a function of irradiation time (Fig. 4b). This plot shows an increase in the ratio upon photoirradiation, and the destruction of the crystal was observed when the ratio  $A_{663}/A_{594}$  reached *ca.* 0.7. Interestingly, almost the same ratios were obtained from 10 single crystals subjected to the same conditions. The presence of a critical point may mean that destruction occurs when almost same number of PDK molecules are converted to pentacene in the irradiated area. Notably, compared with the ratio in the pentacene-rich thin film ( $A_{663}/A_{594} = ca. 1.4$ , Fig. 4a), the ratio in a single crystal is low. This result indicates that the destruction of the crystal occurred before sufficient photoconversion of PDK into pentacene. Conversely, to achieve quantitative photoconversion,

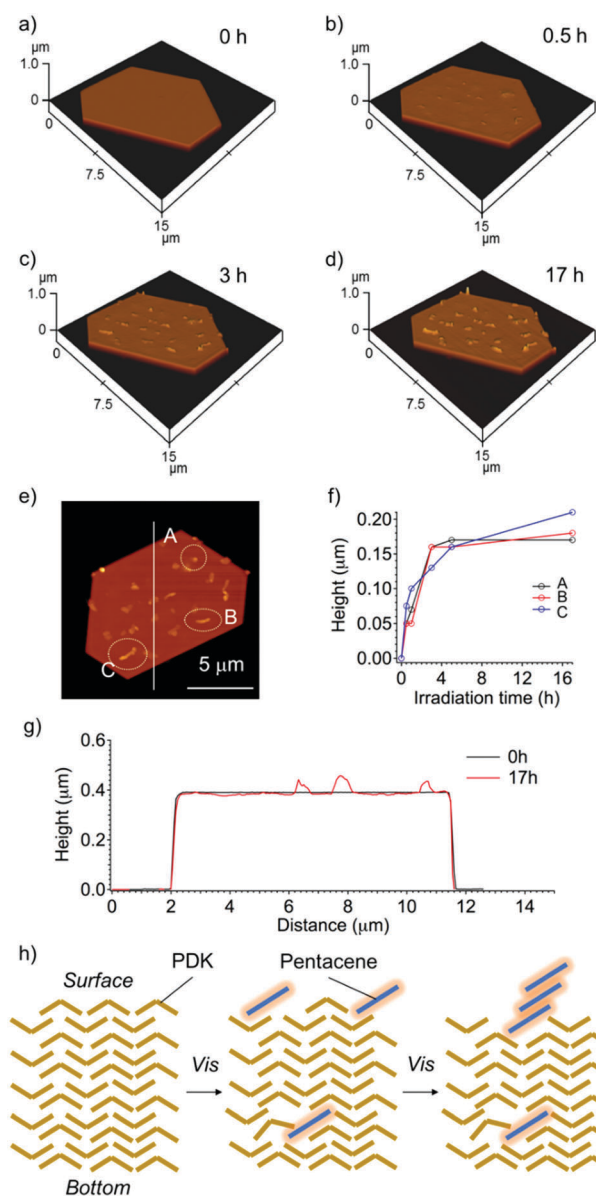


**Fig. 4** (a) UV/vis absorption spectra measured from a single PDK crystal and from a pentacene-rich film upon photoirradiation. (b) Plot of the  $A_{663}/A_{594}$  ratio as a function of irradiation time.

the destruction of the crystal was needed, as we reported previously.<sup>13</sup> Therefore, the destruction mechanism can be explained by an increase in strain within the crystal caused by the formation of pentacene; to relax this strain, the molecules need to move and rearrange.

### Morphological changes induced by weak light intensity

Although Fig. 3(a) shows that a very low laser intensity ( $<0.1 \text{ kW cm}^{-2}$ ) did not cause a clear morphological change in the single crystal, prolonged photoirradiation did lead to a unique morphological change, as observed by AFM imaging.



**Fig. 5** (a–d) 3D AFM images of a single PDK crystal upon photoirradiation for 0, 0.5, 3 and 17 h. (e) AFM height image of the crystal after 17 h photoirradiation. (f) Plot of height of pillars A–C as a function of irradiation time. (g) AFM cross-sectional analysis of the crystal before and after 17 h of photoirradiation along the white line in (e). (h) Schematic representation of the proposed mechanism for the formation of a pillar object on a single-crystal surface.

A 3D AFM image of a single PDK crystal before photoirradiation showed its flat surface (Fig. 5a). After 30 min of photoirradiation with  $0.15 \text{ W cm}^{-2}$  to the full face of crystal, protruding pillar objects were observed on the crystal surface (Fig. 5b). The individual pillars grew further over time, and the growth was monitored during 17 h of photoirradiation (Fig. 5a–d). As reported previously, pillar-like products were also observed upon photoirradiation of PDK amorphous thin film due to the crystallization of photoconverted pentacene.<sup>34</sup> In contrast to the previous condition, the present study indicates a different mechanism of the pillar formation occurred *via* a crystal-to-crystal transition without solvent around the crystal. The AFM cross-sectional analysis depending on the irradiation time supported the growth (Fig. 5e–g). Plotting the height as a function of irradiation time revealed a non-linear change. After 5 h, the change levelled off. Notably, as revealed by AFM cross-sectional analysis, the height of the crystal surface decreased evenly except for the pillars (Fig. 5g). This result demonstrates the movement and rearrangement of pentacene molecules generated on the surface (Fig. 5h). Because this surface morphological change was not observed under medium and strong laser beams, photoirradiation with a weak intensity for a long time was essential to promote the movement of the molecules. Importantly, the number of pillars was not changed during growth, implying that the first pillars formed act as a nucleus to elongate cooperatively. This cooperative mechanism is common in crystal growth, but photoinduced cooperative crystal growth on a single crystal surface is rare. To obtain insight into the resulting pillars, we performed X-ray diffraction measurements and microscopic absorption spectroscopy, but evidence that the pillars consist of only pentacene could not be obtained due to their very small size. On the basis of these results, surface molecules are easy to move and rearrange for the relaxation of strain, while inner molecules can suppress this movement due to the closely packed state. Although photoirradiation with a weak laser intensity did not afford destruction on this time scale, this situation of the inner molecule is similar to that when using a medium laser intensity. Thus, further photoirradiation, for example, for several days, may induce destruction.

## Conclusions

We demonstrated a photoinduced morphological change in a single micrometre-sized PDK crystal. In this change, the laser intensity affects the morphology of the crystal. Under photoirradiation with a visible laser beam, the V-shaped PDK molecules packed in the crystal undergo photoconversion into planar pentacene together with the release of CO molecules, resulting in the generation of strain within crystal due to the stacking mismatch between the different molecules. This strain leads to destruction, such as separation and jumping of the single PDK crystal. Interestingly, unexpected morphological changes such as hole and pillar formation occurred depending on the laser intensity. In the case of a very low intensity, as the formation of pentacene is slow, a large morphological change

does not occur even if low strain is generated, and the strain generated on the crystal surface can be relaxed by the movement of molecules. Indeed, under this condition, the very slow formation of pillars on the crystal surface was confirmed by AFM. The resulting pillar objects on a single crystal act as nuclei, and they cooperatively grow into a well-defined pillar object. In contrast, photoirradiation with a strong laser intensity resulted in the preferential formation of holes. Although the strain is indeed generated, much of the strain can be eliminated by sublimation because the production of pentacene is very rapid and high yielding. With an intermediate laser intensity, although the yield of pentacene is not so high that pentacene is sublimated, the strain in the crystal becomes very large due to the coexistence of PDK and pentacene, leading to destruction. These results indicate the importance of the degree of strain in a single crystal to the morphological changes. Our study demonstrates a fundamental insight into photoresponsive crystal materials and could contribute to the construction and development of remotely controllable smart materials.

## Conflicts of interest

There are no conflicts to declare.

## Acknowledgements

This work was partly supported by a Grant-in-Aid for Scientific Research (No. 18H01958, 18K14195 and 16H02286) from the Japan Society for the Promotion of Science (JSPS) and a Grant-in-Aid for Scientific Research on Innovation Areas "Photosynergetics" (No. 26107005) from MEXT, Japan. We also thank Mr S. Katao, NAIST for the X-ray single crystal structure analysis.

## References

- 1 F. D. Jochum and P. Theato, *Chem. Soc. Rev.*, 2013, **42**, 7468–7483.
- 2 X. Z. Yan, F. Wang, B. Zheng and F. H. Huang, *Chem. Soc. Rev.*, 2012, **41**, 6042–6065.
- 3 S. Yagai, T. Nakajima, K. Kishikawa, S. Kohmoto, T. Karatsu and A. Kitamura, *J. Am. Chem. Soc.*, 2005, **127**, 11134–11139.
- 4 N. Hosono, T. Kajitani, T. Fukushima, K. Ito, S. Sasaki, M. Takata and T. Aida, *Science*, 2010, **330**, 808–811.
- 5 Y. Sagara and T. Kato, *Angew. Chem., Int. Ed.*, 2008, **47**, 5175–5178.
- 6 H. Ito, T. Saito, N. Oshima, N. Kitamura, S. Ishizaka, Y. Hinatsu, M. Wakeshima, M. Kato, K. Tsuge and M. Sawamura, *J. Am. Chem. Soc.*, 2008, **130**, 10044–10045.
- 7 T. Seki, Y. Takamatsu and H. Ito, *J. Am. Chem. Soc.*, 2016, **138**, 6252–6260.
- 8 S. Yagai, S. Okamura, Y. Nakano, M. Yamauchi, K. Kishikawa, T. Karatsu, A. Kitamura, A. Ueno, D. Kuzuhara, H. Yamada, T. Seki and H. Ito, *Nat. Commun.*, 2014, **5**, 4013.
- 9 P. Naumov, S. C. Sahoo, B. A. Zakharov and E. V. Boldyreva, *Angew. Chem., Int. Ed.*, 2013, **52**, 9990–9995.
- 10 S. Kobatake, S. Takami, H. Muto, T. Ishikawa and M. Irie, *Nature*, 2007, **446**, 778–781.
- 11 E. Uchida, K. Sakaki, Y. Nakamura, R. Azumi, Y. Hirai, H. Akiyama, M. Yoshida and Y. Norikane, *Chem. – Eur. J.*, 2013, **19**, 17391–17397.
- 12 E. Uchida, R. Azumi and Y. Norikane, *Nat. Commun.*, 2015, **6**, 7310.
- 13 S. Masuo, K. Tanaka, M. Oe and H. Yamada, *Phys. Chem. Chem. Phys.*, 2014, **16**, 13483–13488.
- 14 M. Yamauchi, T. Ohba, T. Karatsu and S. Yagai, *Nat. Commun.*, 2015, **6**, 8936.
- 15 M. Yamauchi, N. Kanao, B. Adhikari, T. Karatsu and S. Yagai, *Chem. Lett.*, 2017, **46**, 111–114.
- 16 J. Strating, B. Zwanenburg, A. Wagenaar and A. C. Udding, *Tetrahedron Lett.*, 1969, **10**, 125–128.
- 17 H. Uno, Y. Yamashita, M. Kikuchi, H. Watanabe, H. Yamada, T. Okujima, T. Ogawa and N. Ono, *Tetrahedron Lett.*, 2005, **46**, 1981–1983.
- 18 H. Yamada, Y. Yamashita, M. Kikuchi, H. Watanabe, T. Okujima, H. Uno, T. Ogawa, K. Ohara and N. Ono, *Chem. – Eur. J.*, 2005, **11**, 6212–6220.
- 19 R. Mondal, B. K. Shah and D. C. Neckers, *J. Am. Chem. Soc.*, 2006, **128**, 9612–9613.
- 20 R. Mondal, R. M. Adhikari, B. K. Shah and D. C. Neckers, *Org. Lett.*, 2007, **9**, 2505–2508.
- 21 H. F. Bettinger, R. Mondal and D. C. Neckers, *Chem. Commun.*, 2007, 5209–5211.
- 22 H. Yamada, T. Okujima and N. Ono, *Chem. Commun.*, 2008, 2957–2974.
- 23 R. Mondal, A. N. Okhrimenko, B. K. Shah and D. C. Neckers, *J. Phys. Chem. B*, 2008, **112**, 11–15.
- 24 Y. W. Zhao, R. Mondal and D. C. Neckers, *J. Org. Chem.*, 2008, **73**, 5506–5513.
- 25 A. Masumoto, Y. Yamashita, S. Go, T. Kikuchi, H. Yamada, T. Okujima, N. Ono and H. Uno, *Jpn. J. Appl. Phys.*, 2009, **48**, 051505.
- 26 R. Mondal, C. Tonshoff, D. Khon, D. C. Neckers and H. F. Bettinger, *J. Am. Chem. Soc.*, 2009, **131**, 14281–14289.
- 27 S. Katsuta, H. Yamada, T. Okujima and H. Uno, *Tetrahedron Lett.*, 2010, **51**, 1397–1400.
- 28 C. Tonshoff and H. F. Bettinger, *Angew. Chem., Int. Ed.*, 2010, **49**, 4125–4128.
- 29 H. Yamada, C. Ohashi, T. Aotake, S. Katsuta, Y. Honsho, H. Kawano, T. Okujima, H. Uno, N. Ono, S. Seki and K. Nakayama, *Chem. Commun.*, 2012, **48**, 11136–11138.
- 30 T. Aotake, S. Ikeda, D. Kuzuhara, S. Mori, T. Okujima, H. Uno and H. Yamada, *Eur. J. Org. Chem.*, 2012, 1723–1729.
- 31 T. Motoyama, T. Kiyota, H. Yamada and K. Nakayama, *Sol. Energy Mater. Sol. Cells*, 2013, **114**, 156–160.
- 32 K.-i. Nakayama, C. Ohashi, Y. Oikawa, T. Motoyama and H. Yamada, *J. Mater. Chem. C*, 2013, **1**, 6244–6251.
- 33 H. F. Bettinger, R. Mondal, M. Krasowska and D. C. Neckers, *J. Org. Chem.*, 2013, **78**, 1851–1857.
- 34 S. Katsuta, H. Saeki, K. Tanaka, Y. Murai, D. Kuzuhara, M. Misaki, N. Aratani, S. Masuo, Y. Ueda and H. Yamada, *J. Mater. Chem. C*, 2014, **2**, 986–993.
- 35 M. Suzuki, T. Aotake, Y. Yamaguchi, N. Noguchi, H. Nakano, K.-i. Nakayama and H. Yamada, *J. Photochem. Photobiol., C*, 2014, **18**, 50–70.

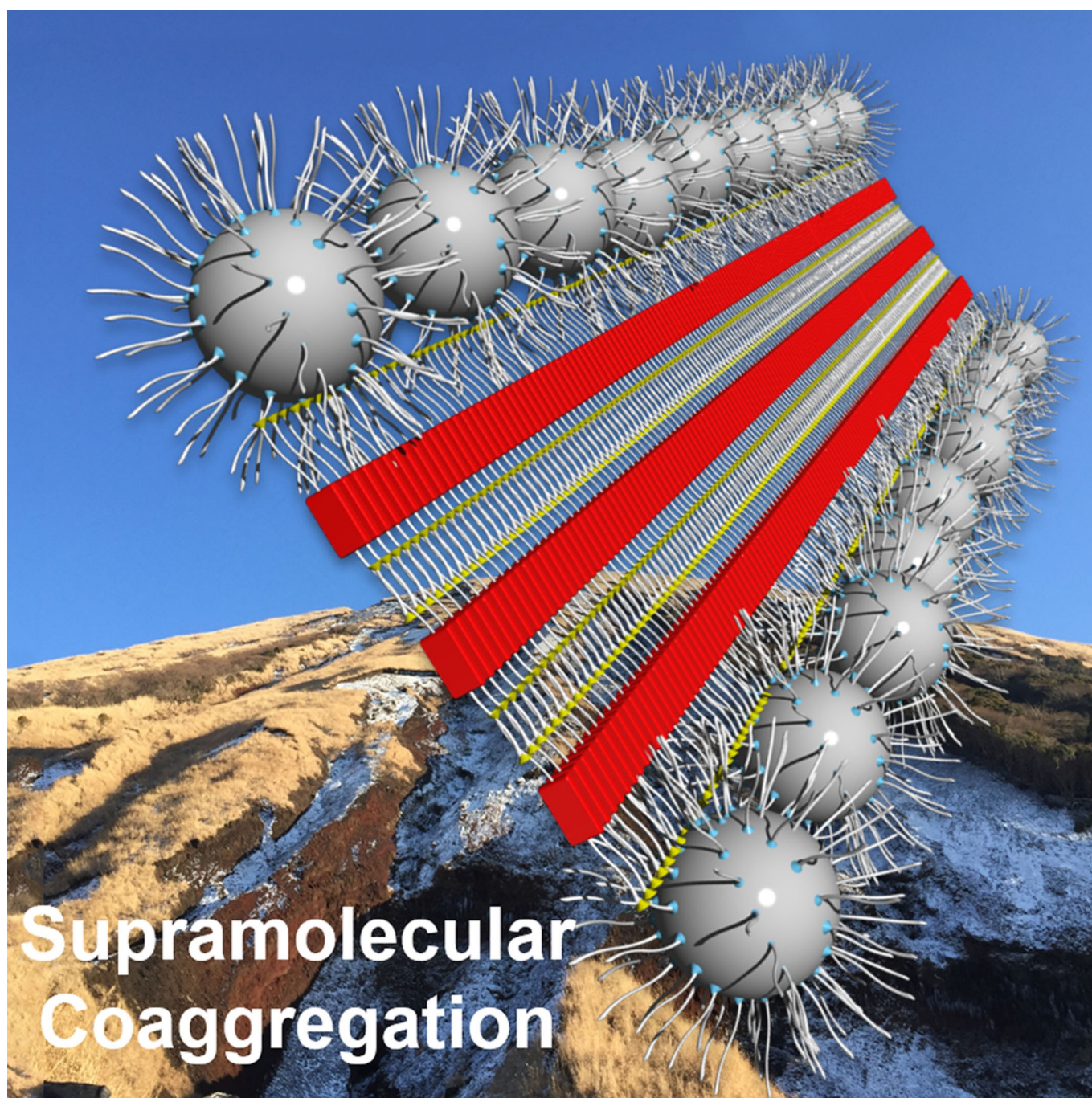
- 36 T. Motoyama, S. Sugii, S. Ikeda, Y. Yamaguchi, H. Yamada and K. Nakayama, *Jpn. J. Appl. Phys.*, 2014, **53**, 01AB02.
- 37 Y. Yamaguchi, M. Suzuki, T. Motoyama, S. Sugii, C. Katagiri, K. Takahira, S. Ikeda, H. Yamada and K. Nakayama, *Sci. Rep.*, 2014, **4**, 7151.
- 38 S. Masuo, W. Sato, Y. Yamaguchi, M. Suzuki, K. I. Nakayama and H. Yamada, *Photochem. Photobiol. Sci.*, 2015, **14**, 883–890.
- 39 M. Suzuki, Y. Yamaguchi, K. Takahashi, K. Takahira, T. Koganezawa, S. Masuo, K. Nakayama and H. Yamada, *ACS Appl. Mater. Interfaces*, 2016, **8**, 8644–8651.
- 40 C. Ohashi, H. Yamada and K. Nakayama, *Mol. Cryst. Liq. Cryst.*, 2013, **580**, 103–109.
- 41 S. Masuo, K. Kanetaka, R. Sato and T. Teranishi, *ACS Photonics*, 2016, **3**, 109–116.

雜誌論文 1 8

■ Supramolecular Chemistry | *Hot Paper* |

## Colloidal Quantum Dot Arrangement Assisted by Perylene Bisimide Self-Assembly

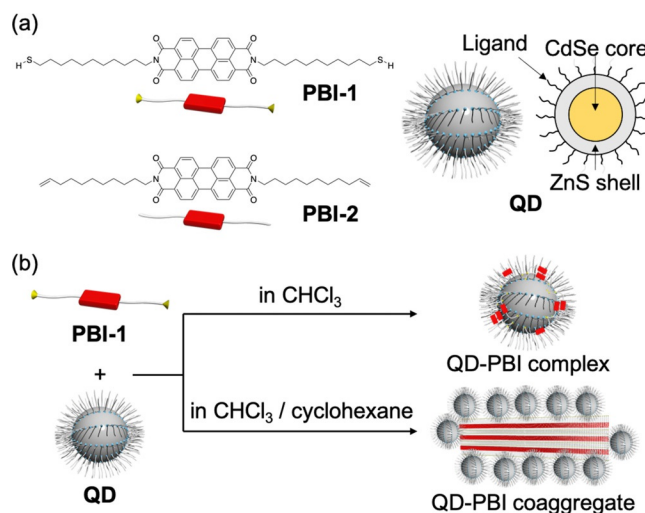
Mitsuaki Yamauchi\* and Sadahiro Masuo\*[a]



**Abstract:** Colloidal semiconductor nanocrystals, so-called quantum dots (QDs), are attractive as molecular-like smart nanomaterials, and their emission and optoelectronic properties in the dispersed state have been actively studied. The construction of supramolecular structures composed of multiple QDs, however, is still challenging. Here, a new strategy to form supramolecular QD structures via self-assembly of perylene bisimide (PBI) dyes is demonstrated. In a mixed solution, QDs and PBI undergo time-dependent fusion to form an isolated colloidal QD-PBI complex or a unique QD-PBI co-aggregate composed of QDs arranged along a sheet-like PBI nanostructure, and these dramatically different supramolecular structures can be controlled by the solvent polarity.

Combinations of multiple functional molecules are of great importance for the creation of nanomaterials with new desired functions. Among functional materials, colloidal semiconductor nanocrystals, so-called quantum dots (QDs), are attractive molecular-like smart nanomaterials with applications for biosensing<sup>[1]</sup> because of their outstanding emission and optoelectronic properties. The emission wavelength of QDs can be tuned synthetically by changing the size and composition of QDs.<sup>[2]</sup> Since synthetic methods to obtain QDs with uniform diameters were developed, the detailed photophysical properties of QDs have been revealed at ensemble<sup>[1b,3]</sup> and single QD levels.<sup>[4]</sup> For further progress in the field of nanocrystals, the surface chemistry of QDs<sup>[5]</sup> has been modified to realize new functions and applications by introducing functional organic molecules such as photochromic molecules<sup>[6]</sup> and fluorescent  $\pi$ -conjugated molecules.<sup>[7]</sup> To construct highly organized materials, understanding and controlling the supramolecular structures of QDs is important but remains challenging.

In sharp contrast, the self-assembly of artificial organic  $\pi$ -conjugated molecules is a powerful tool to create various extended nanostructures,<sup>[8]</sup> such as nanofibers,<sup>[9]</sup> nanotubes<sup>[10]</sup> and nanosheets.<sup>[11]</sup> When this prominent self-assembly mechanism is introduced to a QD system, indirect QD self-assembly should be realized. Here, we report a new strategy to construct supramolecular structures composed of QDs and perylene bisimide (PBI) dye,<sup>[8e,12]</sup> which possesses two thiol groups, and the solvent polarity of which affects the resulting supramolecular structures in this system (Figure 1). Our in-depth studies using spectroscopic and microscopic measurements revealed that in a polar solvent,  $\text{CHCl}_3$ , PBI molecules undergo time-dependent adhesion on the QD surface and weak  $\pi$ - $\pi$  stacking to form isolated QD-PBI colloidal complexes. In low polarity media



**Figure 1.** a) Chemical structures of **PBI-1**, **PBI-2** and **QD**. b) Schematic representation of **PBI-1** and **QD** complexation and co-aggregation.

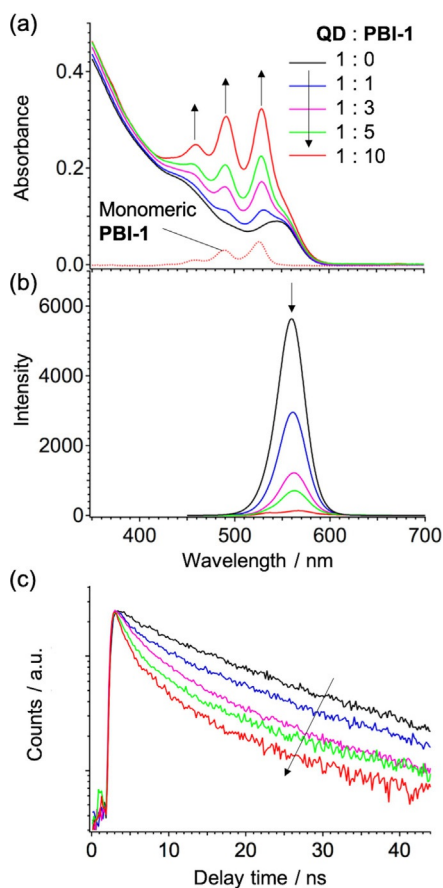
( $\text{CHCl}_3$ /cyclohexane), a mixture of QDs and PBI exhibits time-dependent co-aggregation to form unique QD-PBI co-aggregates composed of QDs arranged along sheet-like aggregates of PBI via kinetically generated nonuniform intermediates.

**PBI-1**, which possesses two thiol groups functionalized with long alkyl chains, and **PBI-2**, which does not possess thiol groups, were synthesized according to Scheme S1 (in the Supporting Information). The thiol group is introduced as an adhesion moiety to adhere to the Zn atom on the QD surface. The core/shell type CdSe/ZnS (two monolayers of ZnS) QDs capped with oleic acid and oleylamine ligands were synthesized by a reported procedure with minor modifications (see the Supporting Information). The morphology of the QDs was confirmed by transmission electron microscopy (TEM) imaging, and the QD diameter was estimated to be  $4.7 \pm 0.2$  nm (Figure S5). The UV/Vis absorption spectrum of the QDs in  $\text{CHCl}_3$  ( $[\text{QD}] = 0.5 \mu\text{M}$ ) displayed a first absorption band at 545 nm and a large absorption regime at lower wavelengths (Figure 2a). Upon mixing the QDs and **PBI-1** at a ratio of 1:1 with stirring for 5 hours, new bands characteristic of the PBI 0-0 and 0-1 vibronic transitions appeared at 531 nm and 491 nm (Figure 2a). A further increase in the **PBI-1** fraction to obtain a QD:PBI-1 ratio of 1:10 resulted in the emergence of the well-defined absorption bands of PBI. The intensity ratio of these transitions ( $A_{0-0}/A_{0-1} = 1.1$ ) of PBI moiety is smaller than that of monomeric **PBI-1** ( $A_{0-0}/A_{0-1} = 1.6$ ), indicating a weak interaction between PBI molecules caused by mixing.

The photoluminescence (PL) spectrum of the QDs in  $\text{CHCl}_3$  under excitation at 405 nm (at this wavelength, **PBI-1** has subtle absorption, while QD has large absorption) showed an emission at  $\lambda_{\text{max}} = 560$  nm (Figure 2b). Upon mixing the QDs with **PBI-1**, the emission intensity of the QDs decreased, resulting in almost complete quenching of PL at QD:PBI-1 = 1:10 (Figure 2b). The decay curves showed that the average PL lifetime decreased from 13.5 ns to 3.9 ns upon increasing the fraction of **PBI-1** (Figure 2c). Importantly, the PL intensity of the QDs and that of **PBI-1** decreased upon increasing the fraction

[a] Dr. M. Yamauchi, Prof. Dr. S. Masuo  
Department of Applied Chemistry for Environment  
Kwansei Gakuin University, 2-1 Gakuen, Sanda, Hyogo 669-1337 (Japan)  
E-mail: yamauchi@kwansei.ac.jp  
masuo@kwansei.ac.jp

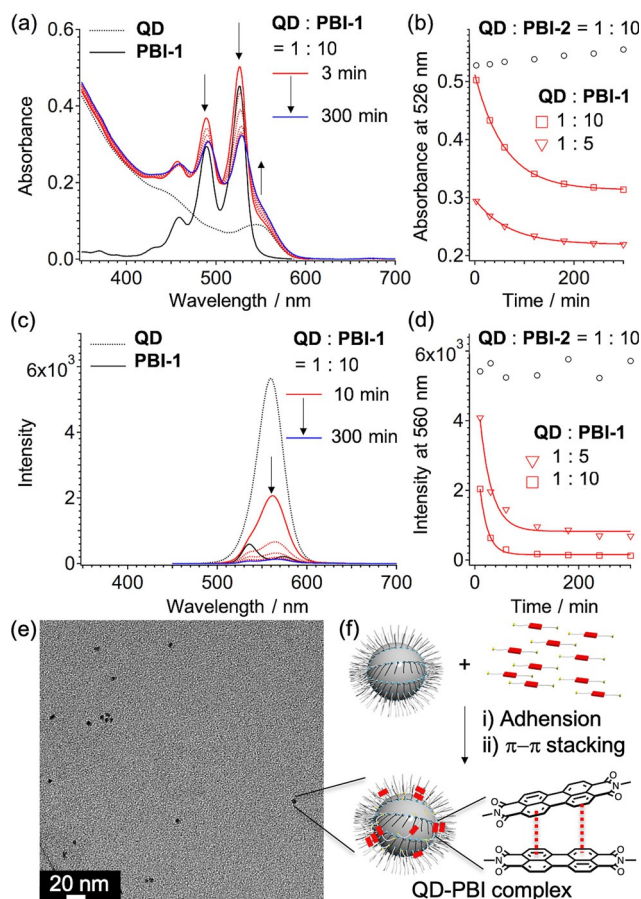
Supporting information and the ORCID identification number(s) for the author(s) of this article can be found under:  
<https://doi.org/10.1002/chem.201805119>.



**Figure 2.** a) UV/Vis absorption and b) PL spectra ( $\lambda_{\text{ex}} = 405 \text{ nm}$ ) and c) PL decay curves of mixtures ( $[\text{QD}] = 0.5 \mu\text{M}$ ) in  $\text{CHCl}_3$  with different ratios of **QD** and **PBI-1**. These solutions were measured after stirring for 5 hours.

of **PBI-1** (Figure S6). To ascertain the origin of this quenching, we mixed the **QDs** with 1-hexanethiol or **PBI-2** without thiol groups.<sup>[13]</sup> The PL intensities and decay curves of these mixtures were constant, even at ratios of 1:20 for 1-hexanethiol and 1:10 for **PBI-2** (Figure S7). These results imply that the quenching is induced by intermolecular interactions such as energy transfer between **PBI-1** and **QD** in the complex.<sup>[14]</sup> Considering the results, the change in the PL intensity can be regarded as indicative of **PBI-1** adhesion on the **QD** surface.

Interestingly, the complexation of the **QDs** and **PBI-1** at various ratios exhibited a change over time, as revealed by UV/Vis absorption studies (Figure 3a, Figure S8). Upon mixing (**QD:PBI-1** = 1:10), the UV/Vis spectrum at  $t = 3 \text{ min}$  showed the monomeric absorption bands of **PBI** moieties at 457, 489 and 526 nm. The time-dependent UV/Vis spectra under stirring revealed that the bands slightly redshifted and the absorption at approximately 550 nm increased. These changes are characteristic of weak  $\pi$ - $\pi$  stacking between **PBI** chromophores. As this change was not detected in the absence of **QDs**, we concluded that **PBI-1** undergoes  $\pi$ - $\pi$  stacking after adhesion of **PBI-1** on the **QD** surface. The PL spectra also exhibited a time-dependent decrease in intensity upon mixing at various ratios (Figure 3c, Figure S8). To analyze the **QD** and **PBI-1** complexation process, we plotted the absorbance at 526 nm to monitor



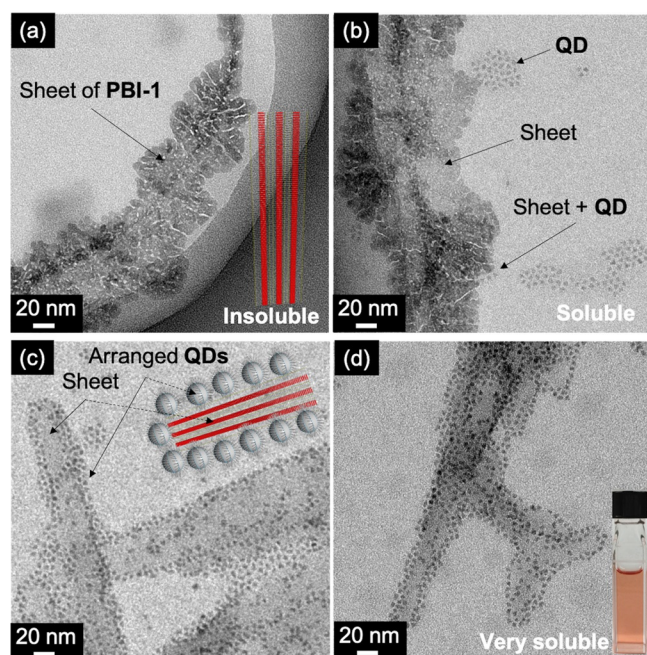
**Figure 3.** Time-dependent changes in the a) UV/Vis and c) PL spectra ( $\lambda_{\text{ex}} = 405 \text{ nm}$ ) of a mixture (**QD:PBI-1** = 1:10,  $[\text{QD}] = 0.5 \mu\text{M}$ ) in  $\text{CHCl}_3$  with stirring. Plots of b) the absorbance and d) PL intensity as a function of time. e) TEM image of the isolated complexes. f) Schematic representation of the complexation process.

for  $\pi$ - $\pi$  stacking and the PL intensity at 560 nm to monitor adhesion as a function of time. As mentioned previously, **QD** and **PBI-2** did not show a change over time due to no co-aggregation (Figure 3b,d). For complexation, the resulting absorbance and PL intensity plots have exponential changes (Figure 3b,d). First-order kinetic fitting of the experimental data affords rate constants of  $k = 0.015 \text{ min}^{-1}$  (**QD:PBI-1** = 1:5) and  $k = 0.017 \text{ min}^{-1}$  (**QD:PBI-1** = 1:10) for  $\pi$ - $\pi$  stacking and  $k = 0.044 \text{ min}^{-1}$  (**QD:PBI-1** = 1:5) and  $k = 0.066 \text{ min}^{-1}$  (**QD:PBI-1** = 1:10) for adhesion. These results suggest that **PBI-1** adheres to the **QD** surface as the initiation step, and then, the **PBI-1** molecules on the **QD** surface participate in weak  $\pi$ - $\pi$  stacking, which agrees with the conclusion mentioned above (Figure 3f).

TEM images of the complex (**QD:PBI-1** = 1:10) revealed the formation of isolated colloidal nanostructures but not polymeric extended aggregates (Figure 3e). The diameter of the complex was estimated to be ca. 5 nm, which is consistent with that of an isolated **QD** (Figure S5). This result indicates that two thiol groups may adhere to the same **QD** surface without acting as a linker to dimerize two **QDs**. Indeed, due to the intramolecularly closed nature of the structure, the dispersibility

of the complex was maintained, even upon increasing the concentration. Our results are different from a report by Basché and co-workers that demonstrated dimerization of QDs using terylene molecules with dicarboxylic groups as a linker.<sup>[15]</sup> This difference is probably due to the flexible long alkyl chains of PBI-1 that enable binding to the same QD surface.

To enhance  $\pi$ - $\pi$  stacking between PBI chromophores, we changed the solvent from  $\text{CHCl}_3$  to  $\text{CHCl}_3/\text{cyclohexane}$  (1:9, v/v). As PBI-1 is not directly soluble in nonpolar solvents, a  $\text{CHCl}_3$  solution of PBI-1 was prepared and then added to cyclohexane. Upon preparing the  $\text{CHCl}_3/\text{cyclohexane}$  solution of PBI-1 alone ( $[\text{PBI-1}] = 20 \mu\text{M}$ ), PBI-1 immediately precipitated due to the low solubility of the resulting supramolecular aggregates. TEM images of the precipitates show agglomerated sheet-like aggregates (Figure 4a, Figure S9). Notably, upon



**Figure 4.** TEM images of aggregates of a) PBI-1 and b–d) mixtures of PBI-1 and QD that formed in  $\text{CHCl}_3/\text{cyclohexane}$  (1:9 v/v). a) Aggregates of PBI-1 alone, b) mixtures of aggregated PBI-1 and QD, c) co-aggregates of PBI-1 and QD that formed as the solution became more concentrated b), and d) co-aggregates of PBI-1 and QD prepared by direct mixing.

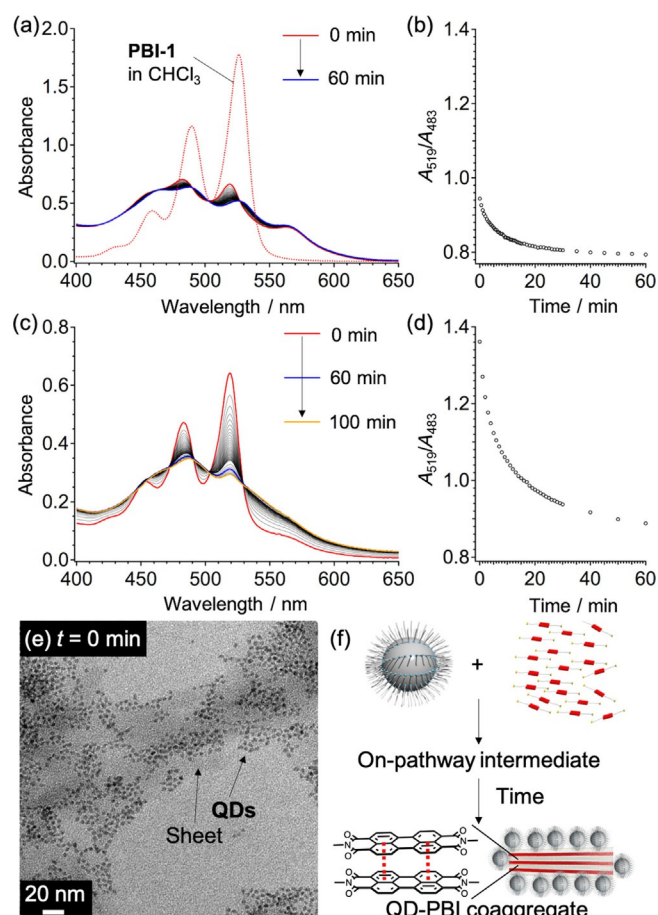
adding the QDs into the solution containing precipitates and shaking the solution ( $\text{QD}:\text{PBI-1} = 1:40$ ,  $[\text{QD}] = 0.5 \mu\text{M}$ ), the precipitates of PBI-1 re-dissolved, and the solution became homogeneous. The TEM images of the soluble aggregates show the sheets were thinner than the precipitate of PBI-1 alone, and partial adhesion of the QDs to the sheets was observed (Figure 4b, Figure S10). Accordingly, the enhancement of PBI-1 aggregate solubility is due to the presence of QDs. The QDs suppress the agglomeration of the sheets, indicating that the QDs act as a solubility-enhancement material. Notably, upon concentrating the solution under an argon flow, unique co-aggregates composed of QDs arranged along a thin sheet of PBI-1 were partially formed in addition to sole PBI-1 aggregates and

free QDs, as visualized by TEM (Figure 4c, Figure S11). In this solution, the dissolution of precipitated PBI-1 could lead to the formation of monomeric PBI-1. Thus, concentrating the resultant PBI-1 monomers induced co-aggregation with free QDs to create nanostructured co-aggregates. As shown in the inset of Figure 4c, the QDs undergo adhesion to the aggregated PBI-1 sheet via thiol groups located in the outside of the sheet to form the co-aggregates. Unlike the complexation in  $\text{CHCl}_3$ , the co-aggregate is based on the extended self-assembly of PBI-1 through a well-defined  $\pi$ - $\pi$  stacking.

Based on the above results, the presence of QDs in the early stage of PBI-1 aggregation is essential for the formation of such co-aggregates. To ensure PBI-1 interacts with QDs before PBI-1 aggregation, we prepared two solutions, monomeric PBI-1 in  $\text{CHCl}_3$  and QDs in cyclohexane, and mixed the two solutions ( $\text{QD}:\text{PBI-1} = 1:40$ ) in  $\text{CHCl}_3/\text{cyclohexane}$  (1:9, v/v). Upon mixing, the optically clear solution of the resulting PBI-1 aggregates containing QDs was stable over time, which was probably due to the interaction with the QDs. Interestingly, the TEM images exhibited the formation of nanostructured co-aggregates of PBI-1 and QD in good yield (Figure 4d, Figure S12). Previously, such an arrangement of nanoparticles has been achieved using functional polymers,<sup>[16]</sup> but to our knowledge, this is the first demonstration of nanoparticle arrangement using only synthetic small molecules.

To obtain insight into the mechanism of QD-PBI co-aggregate formation, we studied the kinetics of time-dependent co-aggregation using UV/Vis spectroscopy. Upon mixing, the UV/Vis spectrum at  $t = 0$  min showed a dramatic decrease in the absorption bands of the monomeric state at 457, 489 and 526 nm and the ratio  $A_{0-0} (519 \text{ nm})/A_{0-1} (483 \text{ nm})$  of PBI moiety decreased from 1.6 to 1.0 with the emergence of a new aggregate band at 562 nm (Figure 5a). This result indicates strong face-to-face (H-type)  $\pi$ - $\pi$  stacking between PBI chromophores.<sup>[12a]</sup> Furthermore, the bands gradually redshifted to 466, 488 and 525 nm with a decrease in the absorbance over 60 min, suggesting kinetically formed intermediates transformed into thermodynamically stable co-aggregates via a rearrangement. In the time change, the ratio  $A_{0-0}/A_{0-1}$  at  $t = 0$  min (1.0) gradually decreased to be 0.8 at  $t = 60$  min (Figure 5b). To determine whether the intermediate is an on-pathway or off-pathway product in the co-aggregation process, we investigated the concentration dependence of the kinetics. Upon decreasing the concentration ( $\text{QD}:\text{PBI-1} = 1:40$ ,  $[\text{QD}] = 0.25 \mu\text{M}$ ), the spectrum at  $t = 0$  min showed sharp absorption bands, suggesting the presence of monomeric PBI-1 (Figure 5c). The spectra exhibited a gradual change over time with an isosbestic point at 530 nm. The  $A_{0-0}/A_{0-1}$  gradually decreased from 1.4 (0 min) to 0.9 (60 min) (Figure 5d). Given that the kinetically formed intermediate was not stabilized by increasing the concentration, the intermediate can be regarded as an on-pathway product (Figure 5f).<sup>[17]</sup>

The direct observation of the intermediate was conducted by time-dependent TEM. The TEM image corresponding to the just mixed solution at  $t = 0$  min showed that the intermediate has a nonuniform morphology without an arrangement of QDs (Figure 5e). This result indicates that the on-pathway in-



**Figure 5.** a, c) Time-dependent changes in the UV/Vis spectra of the QD and PBI-1 mixture (QD:PBI-1 = 1:40, [QD] = a) 0.5  $\mu\text{m}$ , c) 0.25  $\mu\text{m}$ ) in  $\text{CHCl}_3$ /cyclohexane (1:9, v/v). b, d) Plots of the ratio absorbance at 519 nm ( $A_{519}$ ) / at 483 nm ( $A_{483}$ ) as a function of time. Data for b) and d) were taken from a) and c), respectively. e) TEM image of the QD-PBI intermediate. f) Schematic representation of the co-aggregation process.

intermediate undergoes a time-dependent rearrangement to form the co-aggregates with QD arrangements. It should be noted that supramolecular assembly kinetics have been mostly shown in the presence of multiple interactions, for example, a combination of  $\pi$ - $\pi$  stacking and hydrogen-bonding.<sup>[18]</sup> In contrast, the present study demonstrates unprecedented kinetics for the co-aggregation of PBI molecules without hydrogen-bonding units and colloidal inorganic nanocrystals. This rare behavior implies that a kinetic state in the self-assembly of PBI molecules is dominated by interactions with colloidal nanocrystals.

In conclusion, we revealed co-aggregation of inorganic QDs and PBI molecules, which are very different species, by spectroscopic and microscopic studies, and the solvent polarity affected the morphology of the co-aggregates. In the polar solvent  $\text{CHCl}_3$ , PBI-1 with thiol groups adhered to the QD surface, and weak  $\pi$ - $\pi$  stacking between PBI units occurred over time. As a result, a colloidal complex predominately formed. In sharp contrast, in low polarity media ( $\text{CHCl}_3$ /cyclohexane), PBI-1 and QD exhibited time-dependent co-aggregation into a unique nanostructure composed of QDs arranged along sheet aggregates

of PBI-1. The present results demonstrate a synergistic effect of the unexpected co-aggregation because the QDs can assist the dissolution of insoluble PBI-1, while the self-assembling ability of PBI-1 can guide the arrangement of the QDs. Research on further controlling the arrangement of nanocrystals based on a supramolecular assembly of organic molecules is ongoing in our laboratory.

## Acknowledgements

This work was partially supported by a Grant-in-Aid for Scientific Research (No. 18H01958, 18K14195 and 16H02286) from the Japan Society for the Promotion of Science (JSPS) and a Grant-in-Aid for Scientific Research on Innovation Areas "Photosynergetics" (No. 26107005) from MEXT, Japan. The authors thank Prof. Dr. T. Hamura and Dr. K. Kitamura at Kwansai Gakuin University for help with MS and NMR measurements. TEM measurements were provided by Prof. Dr. K. Kamada and Dr. T. Uchida at AIST.

## Conflict of interest

The authors declare no conflict of interest.

**Keywords:** kinetics · perylene · quantum dots · self-assembly · supramolecular chemistry

- [1] a) A. P. Alivisatos, *Science* **1996**, *271*, 933–937; b) D. V. Talapin, J. S. Lee, M. V. Kovalenko, E. V. Shevchenko, *Chem. Rev.* **2010**, *110*, 389–458; c) M. A. Boles, M. Engel, D. V. Talapin, *Chem. Rev.* **2016**, *116*, 11220–11289; d) S. Zhang, R. Geryak, J. Geldmeier, S. Kim, V. V. Tsukruk, *Chem. Rev.* **2017**, *117*, 12942–13038; e) J. Owen, L. Brus, *J. Am. Chem. Soc.* **2017**, *139*, 10939–10943.
- [2] J. J. Li, Y. A. Wang, W. Guo, J. C. Keay, T. D. Mishima, M. B. Johnson, X. Peng, *J. Am. Chem. Soc.* **2003**, *125*, 12567–12575.
- [3] S. J. Lim, M. U. Zahid, P. Le, L. Ma, D. Entenberg, A. S. Harney, J. Condeelis, A. M. Smith, *Nat. Commun.* **2015**, *6*, 8210.
- [4] a) S. Masuo, K. Kanetaka, R. Sato, T. Teranishi, *ACS Photonics* **2016**, *3*, 109–116; b) H. Takata, H. Naiki, L. Wang, H. Fujiwara, K. Sasaki, N. Tamai, S. Masuo, *Nano Lett.* **2016**, *16*, 5770–5778; c) H. Naiki, T. Ueda, L. Wang, N. Tamai, S. Masuo, *ACS Omega* **2017**, *2*, 728–737.
- [5] D. A. Hines, P. V. Kamat, *ACS Appl. Mater. Interfaces* **2014**, *6*, 3041–3057.
- [6] S. A. Díaz, G. O. Menéndez, M. H. Etchehon, L. Giordano, T. M. Jovin, E. A. Jares-Erijman, *ACS Nano* **2011**, *5*, 2795–2805.
- [7] a) O. Schmelz, A. Mews, T. Basché, A. Herrmann, K. Müllen, *Langmuir* **2001**, *17*, 2861–2865; b) C. Mongin, P. Moroz, M. Zamkov, F. N. Castellano, *Nat. Chem.* **2017**, *10*, 225–230; c) D. Kowerko, J. Schuster, N. Amecke, M. Abdel-Mottaleb, R. Dobrawa, F. Würthner, C. von Borczyskowski, *Phys. Chem. Chem. Phys.* **2010**, *12*, 4112–4123; d) C. Wang, E. A. Weiss, *J. Am. Chem. Soc.* **2016**, *138*, 9557–9564.
- [8] a) F. J. M. Hoeben, P. Jonkheijm, E. W. Meijer, A. P. H. J. Schenning, *Chem. Rev.* **2005**, *105*, 1491–1546; b) A. Ajayaghosh, V. K. Praveen, *Acc. Chem. Res.* **2007**, *40*, 644–656; c) L. C. Palmer, S. I. Stupp, *Acc. Chem. Res.* **2008**, *41*, 1674–1684; d) T. Aida, E. W. Meijer, S. I. Stupp, *Science* **2012**, *335*, 813–817; e) F. Würthner, C. R. Saha-Moller, B. Fimmel, S. Ogi, P. Leowanawat, D. Schmidt, *Chem. Rev.* **2016**, *116*, 962–1052; f) B. Adhikari, X. Lin, M. Yamauchi, H. Ouchi, K. Aratsu, S. Yagai, *Chem. Commun.* **2017**, *53*, 9663–9683.
- [9] a) F. Würthner, S. Yao, U. Beginn, *Angew. Chem. Int. Ed.* **2003**, *42*, 3247–3250; *Angew. Chem.* **2003**, *115*, 3368–3371; b) M. Yamauchi, T. Ohba, T. Karatsu, S. Yagai, *Nat. Commun.* **2015**, *6*, 8936; c) C. Roche, H. J. Sun, P. Leowanawat, F. Araoka, B. E. Partridge, M. Peterca, D. A. Wilson, M. E.

- Prendergast, P. A. Heiney, R. Graf, H. W. Spiess, X. Zeng, G. Ungar, V. Percec, *Nat. Chem.* **2016**, *8*, 80–89; d) M. Yamauchi, B. Adhikari, D. D. Prabhu, X. Lin, T. Karatsu, T. Ohba, N. Shimizu, H. Takagi, R. Haruki, S. I. Adachi, T. Kajitani, T. Fukushima, S. Yagai, *Chem. Eur. J.* **2017**, *23*, 5270–5280; e) M. J. Mayoral, C. Rest, V. Stepanenko, J. Schellheimer, R. Q. Albuquerque, G. Fernandez, *J. Am. Chem. Soc.* **2013**, *135*, 2148–2151; f) M. Kumar, P. Brocorens, C. Tonnele, D. Beljonne, M. Surin, S. J. George, *Nat. Commun.* **2014**, *5*, 5793.
- [10] a) J. P. Hill, W. Jin, A. Kosaka, T. Fukushima, H. Ichihara, T. Shimomura, K. Ito, T. Hashizume, N. Ishii, T. Aida, *Science* **2004**, *304*, 1481–1483; b) T. Shimizu, M. Masuda, H. Minamikawa, *Chem. Rev.* **2005**, *105*, 1401–1443; c) S. Yagai, M. Yamauchi, A. Kobayashi, T. Karatsu, A. Kitamura, T. Ohba, Y. Kikkawa, *J. Am. Chem. Soc.* **2012**, *134*, 18205–18208.
- [11] S. Shin, S. Lim, Y. Kim, T. Kim, T. L. Choi, M. Lee, *J. Am. Chem. Soc.* **2013**, *135*, 2156–2159.
- [12] a) K. Balakrishnan, A. Datar, T. Naddo, J. Huang, R. Oitker, M. Yen, J. Zhao, L. Zang, *J. Am. Chem. Soc.* **2006**, *128*, 7390–7398; b) C. Kulkarni, K. K. Bejagam, S. P. Senanayak, K. S. Narayan, S. Balasubramanian, S. J. George, *J. Am. Chem. Soc.* **2015**, *137*, 3924–3932.
- [13] S. F. Wuister, C. De Mello Donegá, A. Meijerink, *J. Phys. Chem. B* **2004**, *108*, 17393–17397.
- [14] J. E. Weaver, M. R. Dasari, A. Datar, S. Talapatra, P. Kohli, *ACS Nano* **2010**, *4*, 6883–6893.
- [15] X. Xu, S. Stottinger, G. Battagliarin, G. Hinze, E. Mugnaioli, C. Li, K. Mullen, T. Basche, *J. Am. Chem. Soc.* **2011**, *133*, 18062–18065.
- [16] a) Y. Zhao, K. Thorkelsson, A. J. Mastroianni, T. Schilling, J. M. Luther, B. J. Rancatore, K. Matsunaga, H. Jinnai, Y. Wu, D. Poulsen, J. M. Frechet, A. P. Alivisatos, T. Xu, *Nat. Mater.* **2009**, *8*, 979–985; b) W. Ma, H. Kuang, L. Xu, L. Ding, C. Xu, L. Wang, N. A. Kotov, *Nat. Commun.* **2013**, *4*, 2689; c) Y. J. Kim, C. H. Cho, K. Paek, M. Jo, M. K. Park, N. E. Lee, Y. J. Kim, B. J. Kim, E. Lee, *J. Am. Chem. Soc.* **2014**, *136*, 2767–2774.
- [17] R. L. Baldwin, *Fold. Des.* **1996**, *1*, R1–8.
- [18] a) P. A. Korevaar, S. J. George, A. J. Markvoort, M. M. Smulders, P. A. Hilbers, A. P. Schenning, T. F. De Greef, E. W. Meijer, *Nature* **2012**, *481*, 492–496; b) S. Ogi, K. Sugiyasu, S. Manna, S. Samitsu, M. Takeuchi, *Nat. Chem.* **2014**, *6*, 188–195; c) S. Ogi, V. Stepanenko, K. Sugiyasu, M. Takeuchi, F. Wurthner, *J. Am. Chem. Soc.* **2015**, *137*, 3300–3307; d) T. Fukui, S. Kawai, S. Fujinuma, Y. Matsushita, T. Yasuda, T. Sakurai, S. Seki, M. Takeuchi, K. Sugiyasu, *Nat. Chem.* **2016**, *9*, 493–499.

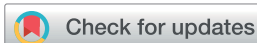
---

 Manuscript received: October 10, 2018

Revised manuscript received: October 31, 2018

Accepted manuscript online: November 6, 2018

Version of record online: December 4, 2018

Cite this: *RSC Adv.*, 2018, 8, 35237

## Improvement in interlayer structure of p–i–n-type organic solar cells with the use of fullerene-linked tetrabenzoporphyrin as additive†

Yuto Tamura,<sup>a</sup> Mitsuharu Suzuki,<sup>a</sup> Takaki Nakagawa,<sup>b</sup> Tomoyuki Koganezawa,<sup>c</sup> Sadahiro Masuo,<sup>b</sup> Hironobu Hayashi,<sup>a</sup> Naoki Aratani<sup>a</sup> and Hiroko Yamada<sup>\*a</sup>

The additive effect on small-molecule-based p–i–n-type devices has been little investigated so far. We focus on the improvement of the miscibility of tetrabenzoporphyrin (BP) and [6,6]-phenyl-C<sub>61</sub>-butyric acid methyl ester (PC<sub>61</sub>BM) blend film by addition of fullerene-linked tetrabenzoporphyrin (BP–C<sub>60</sub>) as an additive to the interlayer (i-layer). BP is one of the most promising p-type organic semiconductors, and BP films can be prepared readily by heating as-cast films of the precursor (a bicyclo[2.2.2]octadiene-fused porphyrin; CP), that results in changes from amorphous CP films to polycrystalline BP films. Because of the high crystallinity of BP, large BP grains on the scale of tens to hundreds of nanometers are generated in blend films of BP and PC<sub>61</sub>BM during film fabrication. We found that the addition of BP–C<sub>60</sub> as an additive (3, 5, 7, and 10 wt%) to the i-layer composed of BP and PC<sub>61</sub>BM improves the miscibility of BP and PC<sub>61</sub>BM. The power conversion efficiency of p–i–n-type organic solar cells consisting of a blend film of BP and PC<sub>61</sub>BM (i-layer) sandwiched by BP (p-layer) and PC<sub>61</sub>BM (n-layer) improved by up to 50% as compared to that of a control device after the addition of BP–C<sub>60</sub> to the i-layer. The film morphology was investigated using atomic force microscopy, fluorescence microspectroscopy, two-dimensional grazing-incident wide-angle X-ray diffraction measurements, and scanning electron microscopy. Interacting with both BP and PC<sub>61</sub>BM, the addition of BP–C<sub>60</sub> led to changes in the grain size as well as an increase in the size of the BP/PC<sub>61</sub>BM interface and hence effective charge separation in the p–i–n device. This morphological improvement is attributable to the ability of BP–C<sub>60</sub>, which exhibits the characteristics of both BP and C<sub>60</sub>, to promote the compatibility of BP and PC<sub>61</sub>BM. This study is a significant step towards the development of high-performance p–i–n-type solar cells and should pave the way for the fabrication of high-performance bulk-heterojunction layers in solution-processed organic photovoltaic devices.

Received 5th September 2018  
Accepted 6th October 2018

DOI: 10.1039/c8ra07398h

rsc.li/rsc-advances

## Introduction

Solution-processed organic solar cells (OSCs) are attracting increasing attention because of their unique properties, such as lightweight and flexible nature, as well as the fact that they can be fabricated by low-cost techniques such as roll-to-roll processing.<sup>1–5</sup> During the past decade, the power conversion efficiency (PCE) of lab-scale OSCs has shown rapid increases

because of the synergic evolution of photovoltaic materials (both p-type and n-type)<sup>6–13</sup> and device structures.<sup>14,15</sup> In addition to the developments of the materials and device structure, the optimization of the active layer structure is essential for ensuring the highest PCE in almost all cases. The bulk-heterojunction (BHJ)-type active layer, in which p-type and n-type materials are blended, has shown great promise for use in high-efficiency OSCs.<sup>16,17</sup> The two blended components form a large-area p–n junction, where exciton dissociation occurs at the interface. Further, the bi-continuous phases allow the ready hole and electron transport toward the respective electrodes. As a result, OSCs based on the BHJ continue to exhibit the highest PCE values of approximately 10–12%<sup>18–25</sup> and are the most widely studied OSCs. On the other hand, controlling the three-dimensional nanomorphology with the aim of optimizing the BHJ film remains a challenge. To date, several strategies have been suggested for ensuring this aim. They include the use of different processing solvents<sup>26</sup> and solvent additives<sup>27–29</sup> as well as thermal,<sup>30–34</sup> and solvent annealing.<sup>34–42</sup> However, these

<sup>a</sup>Division of Materials Science, Graduate School of Science and Technology, Nara Institute of Science and Technology, 8916-5 Takayama-cho, Ikoma, Nara 630-0192, Japan. E-mail: hyamada@ms.naist.jp

<sup>b</sup>Department of Applied Chemistry and Environment, Kwansai Gakuin University, 2-1 Gakuen, Sanda, Hyogo 669-1337, Japan

<sup>c</sup>Japan Synchrotron Radiation Research Institute, 1-1-1 Kouto, Sayo-cho, Sayo-gun, Hyogo 679-5198, Japan

† Electronic supplementary information (ESI) available: Out-of-plane XRD data, UV-vis absorption spectra of p–i–n devices, 1D line cut of 2D-GIWAXD patterns with line fitting, figures of BP crystal with (101) and (200) planes, and additional AFM, SEM, and STEM images. See DOI: 10.1039/c8ra07398h



strategies depend to a great extent on the properties of p- and n-type materials such as its solubility, crystallinity, and miscibility. The orientation of the molecules on the substrate and in active layer is also important.

The precursor approach is one of the most suitable methods for constructing effective active layers through a solution-based process. In this approach, highly soluble and non-aggregating precursor molecules of the target semiconductor materials are deposited on the substrate by a solution-based process and then converted *in situ* into the target material through thermal stimulation or photostimulation.<sup>43–52</sup> Since the conversion of the precursor into the semiconducting material involves a decrease in the solubility owing to the induced structural changes, a three-layered p–i–n structure with the above-mentioned vertical-phase separation can be achieved through solution-based processes.<sup>53–57</sup> Here, “i” stands for the interlayer between the p- and n-layers. Similar to the BHJ film, this layer consists of blended p- and n-type materials.

Tetrabenzoporphyrin (BP), which exhibits superior p-type semiconductor characteristics, is one of the most successful materials for the thermal precursor approach to construct p–i–n devices. The precursor of BP, a bicyclo[2.2.2]octadiene-fused porphyrin (CP),<sup>56</sup> is solution processable, and the obtained film can be transformed into a polycrystalline BP film by thermal annealing (Fig. 1). Matsuo and co-workers successfully demonstrated the interdigitated structure in a p–i–n device through this thermal precursor approach using BP and bis(dimethylphenylsilylmethyl)[60]fullerene, with the device exhibiting good performance.<sup>54</sup> In addition, Nguyen and co-workers investigated the nanoscale morphology of a p–i–n device based on BP and either [6,6]-phenyl-C<sub>61</sub>-butyric acid methyl ester (PC<sub>61</sub>BM) or [6,6]-phenyl-C<sub>61</sub>-butyric acid *n*-butyl ester.<sup>55</sup> Thus, there have been several reports on controlling the morphology during the thermal precursor approach using well-studied fullerene derivatives. On the other hand, there have been few studies on other strategies for modifying the structure of the i-layer during the thermal precursor approach. This is

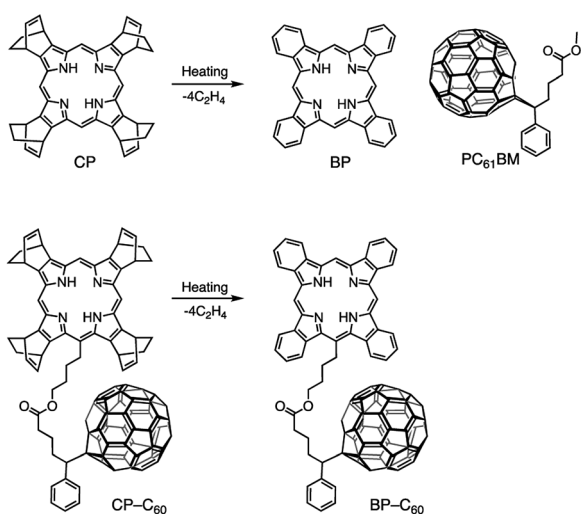


Fig. 1 Chemical transformation of CP into BP and CP-C<sub>60</sub> into BP-C<sub>60</sub> through heating and chemical structure of PC<sub>61</sub>BM.

probably due to the difficulty in inducing morphological changes in the robust BP film through additional annealing processes or by using solvent additives.

Several groups have explored the possibility of using fullerene-linked molecular additives for tuning the morphology of poly(3-hexylthiophene) (P3HT):PC<sub>61</sub>BM BHJ devices. A graft-block-type copolymer,<sup>58</sup> block copolymer,<sup>59–61</sup> fullerene-end capped P3HT,<sup>62</sup> fullerene-linked oligothiophene,<sup>63,64</sup> and pyrene-capped PC<sub>61</sub>BM<sup>65</sup> have been used as additives for this purpose. Since fullerene-linked materials can be preferentially placed at the interface between two distinct heterophased materials, the successful incorporation of these materials improves device performance by reducing the P3HT and/or PC<sub>61</sub>BM domain size and suppressing micrometer-sized separation. Further, the use of these additives also improves device storage stability. Thus, despite the significant differences in the chemical structures and properties of these additives, their addition has an undeniably positive effect on the device characteristics.

In the case of small-molecule-based p–i–n-type devices, the additive effect has not been investigated extensively, because intact crystalline blend films of BP and PC<sub>61</sub>BM tend to exhibit good storage stability without additives. However, these materials show poor miscibility also because of the high crystallinity. The discovery of a suitable additive to improve the miscibility of BP and PC<sub>61</sub>BM would significantly increase the PCE of BP:PC<sub>61</sub>BM OSCs because of the efficient charge separation. Recently, we reported a fullerene-linked BP (BP-C<sub>60</sub>) molecule as an OSC material based on the precursor approach using corresponding CP-type precursor (CP-C<sub>60</sub>), which can be quantitatively converted to BP-C<sub>60</sub> by heating (Fig. 1). We systematically investigated the effect of covalent linkage between the BP (p-material) and C<sub>60</sub> (n-material) units on the performance of solution-processed BHJ and p–i–n devices as well as the optical properties in solution.<sup>66,67</sup> Based on the studies on BP-C<sub>60</sub>, we expected BP-C<sub>60</sub> to be highly suitable for use as an additive of BP and PC<sub>61</sub>BM blend films because of the following reasons: (1) BP-C<sub>60</sub> exhibited effective intramolecular electron transfer between BP and C<sub>60</sub> in CH<sub>2</sub>Cl<sub>2</sub>. This result suggests that the addition of BP-C<sub>60</sub> to BP:PC<sub>61</sub>BM films would promote the effective charge generation. Devices based on BP-C<sub>60</sub> films showed better photovoltaic performance as compared to that of devices based on blended 1 : 1 BP:PC<sub>61</sub>BM films in the same conditions;<sup>67</sup> (2) crystallization does not occur during the thermal conversion of CP-C<sub>60</sub> into BP-C<sub>60</sub> at 160–220 °C (Fig. S1, ESI†) and BP-C<sub>60</sub> itself exhibits high homogeneity in film form and thus forms amorphous films; (3) because the additive is constructed with the same components with the p- and n-materials, it is well miscible in i-layer. The addition of BP-C<sub>60</sub> to BP:PC<sub>61</sub>BM films would inhibit the aggregation of BP to some extent, but each of BP and C<sub>60</sub> in BP-C<sub>60</sub> tend to gather BP and PC<sub>61</sub>BM, respectively, because of their crystallinity. Therefore the smaller domains will be obtained by adding the additive. Thus, an improvement in the PCE with addition of BP-C<sub>60</sub> is expected.

With these facts in mind, in this study, we demonstrate an effective approach for morphological control using BP-C<sub>60</sub> as an additive for BP:PC<sub>61</sub>BM-based p–i–n devices. The experimental results showed that, when added to the i-layer, BP-C<sub>60</sub> is



compatible with both BP and PC<sub>61</sub>BM and helps improve the film structure. After the addition of 5 wt% BP-C<sub>60</sub> to the i-layer, the PCE of the resulting p-i-n device increased by up to 50% with respect to that of a control p-i-n device. The fabricated films were investigated in detail using atomic force microscopy (AFM), fluorescence microspectroscopy, two-dimensional grazing-incident wide-angle X-ray diffraction (2D-GIWAXD) measurements, and scanning electron microscopy (SEM).

## Results and discussion

To begin with, the effect of BP-C<sub>60</sub> as a morphological additive for the internal BP:PC<sub>61</sub>BM layer in p-i-n devices was investigated. The p-i-n devices were prepared as shown in Fig. 2 (see Experimental for more details). The BP film for the p-layer was prepared on a (3,4-ethylenedioxythiophene):poly(4-styrenesulfonate) (PEDOT:PSS)-coated indium-tin-oxide (ITO) substrate by the spin-coating of CP followed by heating (thermal precursor approach). In the same manner, i-layers containing BP:PC<sub>61</sub>BM with and without BP-C<sub>60</sub> were prepared on the BP film by the spin-coating of a CP:PC<sub>61</sub>BM solution with and without CP-C<sub>60</sub> followed by heating. The obtained p-i-structure is labelled as Structure I. The n-layer of PC<sub>61</sub>BM was deposited on Structure I by spin-coating

a PC<sub>61</sub>BM solution and subsequent thermal annealing. Finally, the buffer and metal electrode were deposited on the n-layer to form the p-i-n devices, which contained different amounts of BP-C<sub>60</sub>. For microscopic observations of the BP structure on the p-layer, Structure I was rinsed by using a drop of chloroform on the substrate and subjecting it to spinning, then Structure II was obtained. The photovoltaic performances of the various p-i-n devices are listed in Table 1 and Fig. 3a. After the addition of BP-C<sub>60</sub> to the BP:PC<sub>61</sub>BM i-layer, the photovoltaic performance of the p-i-n devices was significantly enhanced.

For instance, the  $J_{SC}$ ,  $V_{OC}$ , and FF values were improved with an increase in the amount of the added BP-C<sub>60</sub> from 0 to 3 and 5 wt%, leading to increases in the PCE from 1.58 to 2.10 and 2.38%, respectively. On the other hand, when more than 7 wt% of BP-C<sub>60</sub> was added, the PCE value decreased slightly, to 2.22 and 2.18% at 7 and 10 wt%, respectively. It should be noted that the thickness of the i-layer barely changed, suggesting that the presence of BP-C<sub>60</sub> in the i-layer was responsible for the observed changes in the device performance. To elucidate the reason for the higher  $J_{SC}$  values of the BP-C<sub>60</sub>-containing p-i-n devices, their external quantum efficiency (EQE) spectra were measured and compared with that of the control p-i-n device (0 wt%), as shown in Fig. 3b. The BP-C<sub>60</sub>-containing devices showed higher EQE values for wavelengths of 340 nm, 400–500 nm, and 550–720 nm, even though the active layers in all the devices had the same photoabsorption capability (see Fig. S2, ESI†). Further, the p-i-n devices (3–10 wt%) show improved EQE values within the photoabsorption range of the BP:PC<sub>61</sub>BM blend as compared to that of the 0 wt% device. For example, the best-performing p-i-n device (5 wt%) exhibited quantum efficiencies that were 13%, 25%, and 30% higher than those of the 0 wt% device at 340, 455, and 615 nm, respectively. The charge transport ability of the films was evaluated by space-charge-limited current (SCLC) measurement, as shown in Table 1. Both of hole and electron mobilities ( $\mu_h$  and  $\mu_e$ , respectively) of active layers are two to three times improved by addition of additives. These improvements can be attributed to the effective carrier generation at the p-n interface area enlarged by addition of BP-C<sub>60</sub>.

To investigate the microscopic surface morphology of the i-layer, the Structure I of the various samples was investigated using AFM, as shown in Fig. 4a–e. Several grains can be seen on the film in all the AFM images. These grains are attributable to

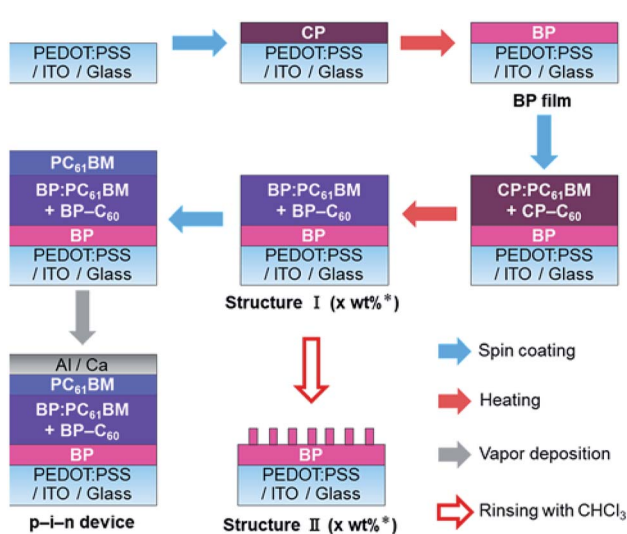


Fig. 2 Procedure of device fabrication (\* amount of BP-C<sub>60</sub> added was 0–10 wt%).

Table 1 Photovoltaic parameters of p-i-n devices<sup>a</sup> and hole and electron carrier mobilities ( $\mu_h$  and  $\mu_e$ ) measured by SCLC technique

BP-C <sub>60</sub> /wt%	i-layer thickness/nm	PCE <sup>b</sup> /% (PCE <sub>ave</sub> <sup>c</sup> /%)	$J_{SC}$ <sup>b</sup> /mA cm <sup>-2</sup>	$V_{OC}$ <sup>b</sup> /V	FF <sup>b</sup>	$R_s$ <sup>b</sup> /Ω cm <sup>2</sup>	$R_{sh}$ <sup>b,d</sup> /Ω cm <sup>2</sup>	$\mu_h/10^{-4}$ cm <sup>2</sup> V <sup>-1</sup> s <sup>-1</sup> (active-layer thickness/nm)	$\mu_e/10^{-4}$ cm <sup>2</sup> V <sup>-1</sup> s <sup>-1</sup> (active-layer thickness/nm)
0	65	1.58 (1.4 ± 0.1)	5.93	0.50	0.53	7	383	1.0 (109)	0.9 (103)
3	63	2.10 (2.02 ± 0.06)	6.29	0.56	0.60	10	795	2.0 (145)	2.1 (140)
5	67	2.38 (2.30 ± 0.08)	6.76	0.58	0.61	9	795	2.3 (138)	2.9 (129)
7	60	2.22 (2.12 ± 0.08)	6.91	0.56	0.58	9	600	1.6 (140)	2.7 (138)
10	64	2.18 (2.10 ± 0.06)	6.65	0.57	0.58	9	769	2.0 (130)	1.4 (148)

<sup>a</sup> Obtained under AM1.5G illumination at 100 mW cm<sup>-2</sup>. <sup>b</sup> Parameters of the best-performing cells. <sup>c</sup> Averages and standard deviations of four devices. <sup>d</sup>  $R_s$ : series resistance;  $R_{sh}$ : shunt resistance.



BP-rich domains. Nguyen *et al.* also reported similar grains on the surfaces of BP/BP:PC<sub>61</sub>BM films and, based on conductive and photoconductive AFM measurements, characterized these grains as being BP-rich domains.<sup>55</sup> In the case of Structure I (0 wt%), 1–2 μm-sized spot- and needle-like domains were observed, with the root-mean-square (RMS) surface roughness of the i-layer being 48.6 nm. This inhomogeneous distribution of the BP and PC<sub>61</sub>BM components is undesirable from the viewpoint of the photovoltaic process and was probably the reason this device exhibited the lowest PCE (1.58%) as well as a low FF value (0.53). On the other hand, the Structure I corresponding to the 3–10 wt% BP-C<sub>60</sub> devices were significantly smoother, with the markedly lower RMS roughness values at 33.5 nm (3 wt%), 12.0 nm (5 wt%), 20.5 nm (7 wt%), and 6.4 nm (10 wt%). In p-i-n devices based on BP:fullerene derivatives, the flatness of the i-layer plays a critical role in ensuring a homogeneous morphology of the n-layer required for improved performance.<sup>55,66,67</sup> This is because large, vertically oriented BP grains often extend through the n-layer, and PC<sub>61</sub>BM-uncovered BP features are formed on the n-layer and reach the electrode. In fact, the shunt resistances ( $R_{sh}$ ) in the p-i-n (3–10 wt%) devices with a flat n-layer were twice as high as that of the p-i-n (0 wt%) device (see Fig. S3, ESI†). In general,  $V_{OC}$  increases with an increase in the  $R_{sh}$ . Thus, the slight improvement in  $V_{OC}$  seen in the cases of the p-i-n (3–10 wt%) devices can be ascribed to these structural

differences between the i- and n-layers. Furthermore, needle-like grains that gradually became smaller with an increase in the BP-C<sub>60</sub> content were also observed. For instance, needle-like grains with a length of approximately 2 μm were present in the Structure I (3 and 5 wt%), whereas grains approximately 1 μm or smaller were seen in the Structure I (7 and 10 wt%). Considering that the typical exciton diffusion length in molecular organic materials is in the order of a few to tens of nanometers,<sup>68</sup> the grains placed in parallel on the substrates in all the films were too long to allow for efficient charge separation. However, the smoother surface and smaller grains observed in Structure I in the cases of the p-i-n (3–10 wt%) devices were more effective than those of control device Structure I (0 wt%).

Further investigations of the macrostructure of Structure I were performed using fluorescence microspectroscopy. As shown in Fig. 4f–j, the intensity of the fluorescence from BP decreased gradually as the proportion of BP-C<sub>60</sub> in the i-layer was increased. These data confirmed that the addition of BP-C<sub>60</sub> led to more effective quenching of excitons in the BP domains, thus improving the characteristics of the BP:PC<sub>61</sub>BM interface with respect to the generation of hole–electron pairs. In addition, the numerous bright spots observed in the control device Structure I (0 wt%) were absent from the Structure I samples containing BP-C<sub>60</sub>. This suggests that more homogeneous BP:PC<sub>61</sub>BM films were formed after the addition of BP-C<sub>60</sub>.

The crystallinity and molecular orientation of Structure I were investigated through 2D-GIWAXD measurements. The obtained diffraction patterns are shown in Fig. 4k–o. The 2D-GIWAXD patterns confirmed that the BP in Structure I was polycrystalline with a monoclinic unit cell having the  $P2_1/n$  space group, as also reported by Aramaki *et al.*<sup>69</sup> Further, the GIWAXD patterns of BP films have also been reported previously by Chabinyč *et al.*<sup>70</sup> The GIWAXD patterns of BP in all the Structure I samples were similar. Note that the arcs of the (101) and (200) planes of BP, which had the highest intensity, were observed at  $q_{xy} = 0.71$  and  $0.82 \text{ \AA}^{-1}$ , respectively. Further, because the (101) and (200) planes, their appearance along the  $q_{xy}$  axis suggested that vertically oriented herringbone-like columns of BP were present on the substrate, resulting in improved hole transport, as described in Fig. S5, ESI†. From these results, it can be concluded that the presence of BP-C<sub>60</sub> in the i-layer does not result in any changes in the orientation of the BP crystals. On the other hand, the crystallinity of BP decreased with the addition of a greater amount of BP-C<sub>60</sub>, since the full width at half maximum values of the (101) and (200) peaks as estimated by 1D vertical line cuts from 2D-GIWAXD data in the in-plane direction increased with an increase in the BP-C<sub>60</sub> concentration (see Fig. S4, ESI†). In addition, GIWAXD patterns ascribable to crystalline PC<sub>61</sub>BM<sup>71</sup> were observed at approximately  $q = 1.46, 1.39,$  and  $1.37 \text{ \AA}^{-1}$ . In contrast to the cases of the Structure I (0 and 3 wt%), crystalline PC<sub>61</sub>BM were barely visible in the Structure I (5 wt%) and were completely absent in the Structure I (7 and 10 wt%). These results confirm that BP-C<sub>60</sub> interacted with both BP and PC<sub>61</sub>BM to prevent crystallization in the active layer.

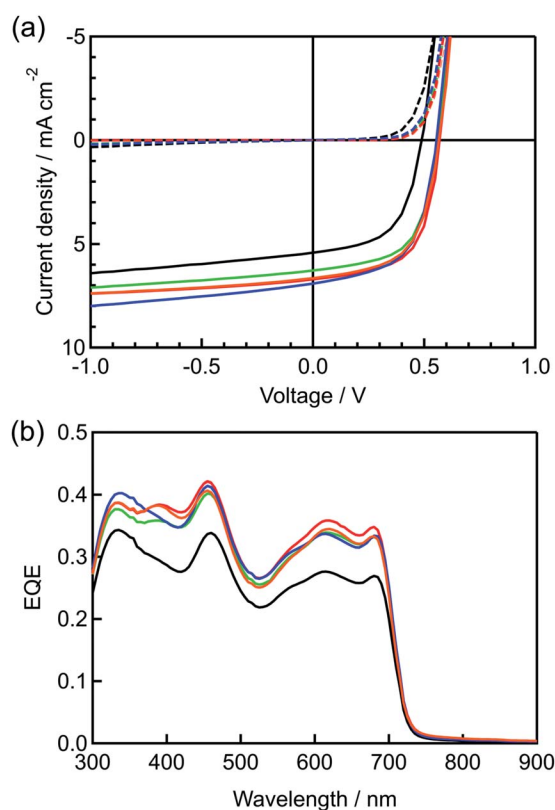


Fig. 3 Photovoltaic performances of the best devices fabricated using different amounts of BP-C<sub>60</sub>: (a) illuminated (solid line) and dark (dotted line)  $J$ - $V$  characteristics and (b) EQE spectra. 0 wt%: black; 3 wt%: green; 5 wt%: red; 7 wt%: blue; and 10 wt%: orange lines.



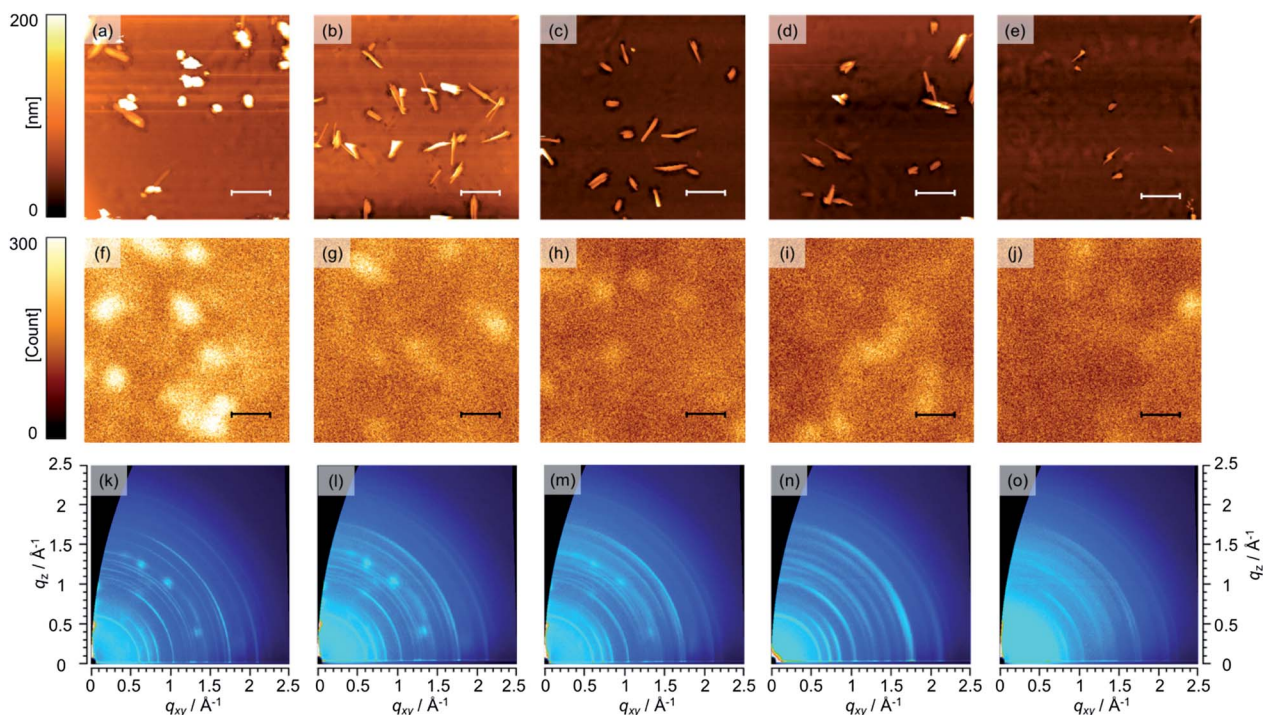


Fig. 4 AFM height images (top), fluorescence microspectroscopy images\* (middle), and 2D-GIWAXD patterns (bottom) of Structure I surfaces corresponding to different amounts of BP-C<sub>60</sub>: (a), (f), and (k) 0 wt%; (b), (g), and (l) 3 wt%; (c), (h), and (m) 5 wt%; (d), (i), and (n) 7 wt%; and (e), (j), and (o) 10 wt%. Scale bars correspond to 2  $\mu\text{m}$ . \*To detect fluorescence of BP, 405 nm laser was used as excitation source.

The interfacial structure of BP between the p- and i-layers was observed using SEM. For these investigations, Structure II was prepared by selectively washing away the PC<sub>61</sub>BM from the i-layer because BP does not dissolve readily in common organic solvents. Top-view SEM images of Structure II are shown in Fig. 5a–e. In contrast to the case for the BP film (see Fig. S6, ESI†), nanoscale textures were seen in BP. Further, Structure II (0 wt%) contained closely packed, columnar BP nanostructures with a diameter of approximately 20–60 nm. On the other hand, after BP-C<sub>60</sub> had been added to the i-layer, these features changed significantly. For instance, while Structure II (3 wt%) did exhibit a column-like nanostructure, its top edge was slightly sharper than that of Structure II (0 wt%). The finest features were observed in Structure II (5 wt%), which consisted of randomly shaped gaps with a diameter of approximately 10–40 nm. Structure II (7 wt%) also consisted of gaps, but the BP features were

more aggregated than in the case of Structure II (5 wt%). Finally, amorphous BP features were observed in Structure II (10 wt%). In order to determine the height of these features, cross-sectional observations were performed using scanning transmission electron microscopy (STEM). The measured heights of the features formed after the addition of BP-C<sub>60</sub> in various amounts were 27 nm (0 wt%), 26 nm (3 wt%), 28 nm (5 wt%), 24 nm (7 wt%), and 21 nm (10 wt%) (see Fig. S7, ESI†).

The nanoscale features observed by SEM suggested the size of the p–n interface was best for Structure II (5 wt%), thus enhancing charge separation and charge transport to the appropriate electrodes. The p–i–n (5 wt%) device exhibited the best performance, namely, an improved  $J_{\text{SC}}$  value at 6.81  $\text{mA cm}^{-2}$  and the highest FF value at 0.61. This result can be attributed to its i-layer structure, wherein there exists a balance between the charge-carrier generation and transport.

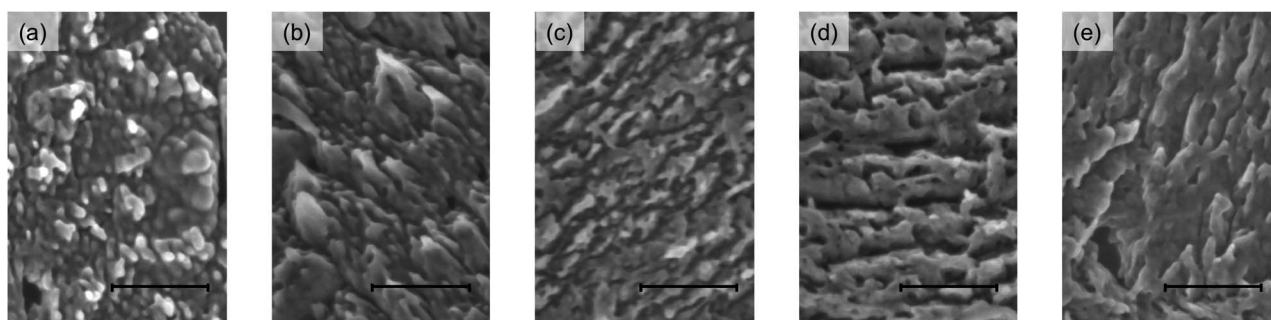


Fig. 5 SEM images of Structure II surfaces corresponding to devices with different amounts of BP-C<sub>60</sub>: (a) 0 wt%, (b) 3 wt%, (c) 5 wt%, (d) 7 wt%, and (e) 10 wt%. Scale bars correspond to 200 nm.



## Conclusions

In this work, we demonstrated that the structure of the i-layer of solution-processable p-i-n devices based on BP:PC<sub>61</sub>BM can be modified readily by adding a small amount of BP-C<sub>60</sub> to improve the device performance. The p-i-n devices containing BP-C<sub>60</sub> in the i-layer showed significantly improved performance (PCE = 2.38%) as compared to that of a device without BP-C<sub>60</sub> (PCE = 1.58%) and even surpassed the record performance of the BP:PC<sub>61</sub>BM-based p-i-n device (PCE = 2.0%) reported by Matsuo *et al.*<sup>54</sup> The presence of BP-C<sub>60</sub> in the i-layer affects the layer morphology, phase separation, and crystallinity. AFM and fluorescence microspectroscopy measurements suggested that, when BP-C<sub>60</sub> is introduced into the i-layer, the domain size is reduced, leading to the formation of a larger p-n interface for charge-carrier generation as well as smoother i- and n-layers, which result in better semiconducting behavior. In addition, the interfacial BP network, which was investigated by SEM, is also modified by the presence of BP-C<sub>60</sub>. However, the presence of excessive BP-C<sub>60</sub> can lead to the deterioration of the p-n interface and limit carrier transport in the active layer. On the other hand, despite the morphological changes induced with the addition of BP-C<sub>60</sub>, the crystal orientation does not change, but the crystallinity of both BP and PC<sub>61</sub>BM decreases gradually. Thus, it is essential to add BP-C<sub>60</sub> in the appropriate amount in order to ensure that it has the desired positive effect as a morphological additive.

For the high charge carrier mobility of small molecular organic semiconductors, good crystallinity with high transfer integral is critical. The good crystallinity also brings the stability of the organic electronic devices. On the other hand, the good crystallinity often disturbs the miscibility of donor and acceptor materials, that is necessary for effective charge generation in OPVs. BP is one of the superior and promising p-type organic semiconductors with high crystallinity and several groups reported the improvement of the miscibility of BP and acceptor materials by the derivatization of BP and PC<sub>61</sub>BM, as described in Introduction. However, it is important to improve the PCE performance without changing the chemical structure of BP and PC<sub>61</sub>BM, a standard combination, to give the general and universal information about the additive effect of connected donor-acceptor molecule to i-layer in small molecular OPVs.

The fact that fullerene-linked materials allow for the morphological control of solution-processed small molecules in thin films suggests that they have enormous potential for fabricating suitable heterojunctions. Although this study focused on the performance of p-i-n devices based on the BP:PC<sub>61</sub>BM system, the result that the addition of even a small amount of a fullerene-linked molecule can enhance the photovoltaic performance suggests a new opportunity for improving the performance of small-molecule-based OSCs.

## Experimental

### Materials

CP and CP-C<sub>60</sub> were prepared according to the reported procedures.<sup>56,67</sup>

### Thin film preparation and device fabrication for OSC

Patterned-ITO/glass substrates (20 mm × 25.0 mm, <15 Ω per square) were washed with running water and were ultrasonically cleaned in detergent, pure-water and isopropanol for 10 min each. After the substrates were dried, (3,4-ethylenedioxythiophene):poly(4-styrenesulfonate) (PEDOT:PSS, Clevios P VP AI4083) was spin-coated (3000 rpm, 30 s) under air followed by a thermal annealing treatment at 130 °C for 10 min. The substrates were transferred to a nitrogen-filled glove box (<10.0 ppm O<sub>2</sub> and H<sub>2</sub>O). The p-layer was prepared by spin coating (1500 rpm, 30 s) of a CP-solution (7 mg mL<sup>-1</sup> in chloroform) followed by heating (200 °C, 10 min) to effect the *in situ* conversion of CP to BP. The i-layers were deposited by spin coating (1500 rpm, 30 s) a CP:PC<sub>61</sub>BM (1 : 1.5 wt/wt)-solution (10 mg mL<sup>-1</sup>, chloroform) containing 0–10 wt% of CP-C<sub>60</sub> followed by heating (180 °C, 20 min) to effect the *in situ* conversion to BP:PC<sub>61</sub>BM containing BP-C<sub>60</sub>. The n-layer was prepared by spin coating (1500 rpm, 30 s) of PC<sub>61</sub>BM-solution (7 mg mL<sup>-1</sup> in chloroform), which was then annealed (195 °C, 10 min). After preparation of the active layers, the buffer layer (Ca, 5 nm) and counter electrode (Al, 50 nm) were vapor deposited at a high vacuum (<5.0 × 10<sup>-1</sup> Pa) through a shadow mask with a defined active area of 4 mm<sup>2</sup>. Finally, the fabricated organic solar cell was encapsulated with backing glasses using a UV-curable resin under nitrogen atmosphere.

### OSC performances

Current density–voltage (*J*-*V*) curves were measured using a Keithley 2611B SYSTEM Source Meter unit under AM1.5G illumination at an intensity of 100 mW cm<sup>-2</sup> using a solar simulator (Bunko-keiki, CEP-2000RP). The external quantum efficiency (EQE) spectra were obtained under illumination of monochromatic light using the same system.

### SCLC measurement

The SCLC device structures for hole-only and electron-only measurements were [ITO/MoO<sub>3</sub>/active layer/MoO<sub>3</sub>/Al] and [ITO/ZnO/active layer/LiF/Al], respectively. For hole only device, MoO<sub>3</sub> (15 nm) was vapor deposited on the cleaned ITO/glass substrate at high vacuum (<5.0 × 10<sup>-4</sup> Pa). For electron only device, ZnO film (28 nm) was prepared by sol-gel method using the ZnO precursor solution.<sup>29</sup> The ZnO precursor solution was spin coated (5000 rpm, 30 s) on the cleaned ITO/glass substrate followed by heating (300 °C, 1 h) under air condition to obtain the ZnO film. Then, substrates were transferred to a N<sub>2</sub>-filled glove box (<10.0 ppm O<sub>2</sub> and H<sub>2</sub>O). Each active layer was prepared by spin coating of CP:PC<sub>61</sub>BM solution with and without CP-C<sub>60</sub> in chloroform (14 mg mL<sup>-1</sup>) at 800 rpm for 30 s on ITO/MoO<sub>3</sub> (15 nm) or ITO/ZnO (28 nm), respectively. After spin coating, these films were heated in the same condition for the OPV device fabrication to convert to BP:PC<sub>61</sub>BM solution with and without BP-C<sub>60</sub> in the nitrogen-filled glove box. After preparation of the organic layers, MoO<sub>3</sub> (15 nm)/Al (50 nm) or LiF (1 nm)/Al (50 nm) were vapor deposited at high vacuum (<5.0 × 10<sup>-4</sup> Pa). Current–voltage (*J*-*V*) curves of fabricated SCLC devices were measured by



Keithley 2400 source-measure unit in air. To estimate the charge mobility, curve fitting was performed according to the formula as follows,

$$J = \frac{8}{9} \frac{\varepsilon \varepsilon_0 \mu V^3}{L^3}$$

where  $\varepsilon$  is the dielectric constant,  $\varepsilon_0$  is the permittivity of space,  $\mu$  is the charge mobility.  $V$  is the applied voltage, and  $L$  is the active layer thickness. The dielectric constant  $\varepsilon$  is assumed to be 3, which is atypical value for organic semiconductors.

### Film thickness

Active layer thickness was measured by a Surface Profiler ET200 (Kosaka Laboratory Ltd). The value was obtained as an average of 10 measurement points.

### Atomic force microscopy (AFM)

The surface morphology of organic films was observed by an SPA400, SPI3800N AFM (Seiko instruments Inc.) in tapping mode using silicon probes with a resonant frequency of  $\sim 138$  kHz and a force constant of  $16 \text{ N m}^{-1}$ .

### Scanning electron microscopy (SEM)

The surface texture of organic films was observed by an Ultra High-Resolution Scanning Electron Microscope SU9000 (Hitachi, Ltd.) with accelerating voltage of 1.0 kV. The sample film surface was not deposited with conductive materials for prevention of static charge. The thin-film samples for these measurements were prepared on PEDOT:PSS-coated ITO/glass substrates in the same manner as in the device fabrication described above.

### Scanning transmission electron microscopy (STEM)

The cross-sectional structure of organic films was observed by a HD-2700 (Hitachi, Ltd.) which combines an Energy Dispersive X-ray (EDX) spectroscopy Octane T Ultra W 100mm2SDD (AMETEK). For this measurement, Focused Ion Beam System FB2200 (Hitachi, Ltd.) has been used for site-specific preparation of cross sectional samples suitable for STEM analysis using the micro sampling technique.<sup>72</sup>

### Fluorescence microspectroscopy

The fluorescence from the Structure I was collected by an objective lens (60 $\times$ , N.A.:0.7, LUCPlanFLN, Olympus) and passed through a confocal pinhole (100  $\mu\text{m}$ ) and suitable filters. To detect the fluorescence of the BP, a 405 nm laser was used as an excitation source, and a long-pass filter (LP02-442RU, Semrock) and a short-pass filter (FF01-650/SP, Semrock) were used to cut the excitation laser beam and fluorescence from PC<sub>61</sub>BM, respectively. The detected fluorescence was split into two paths by a 50/50 beam splitter, and the two paths were detected using a spectrometer (SpectraPro2358, Acton Research Corporation) with a cooled CCD camera (PIXIS400B, Princeton Instruments) and an avalanche single-photon counting module (APD: SPCM-AQR-14, PerkinElmer). The signal from the APD was connected to a time-

correlated single-photon counting board (SPC-630, Becker & Hickl) for the fluorescence images.

### Two-dimensional grazing-incident wide-angle X-ray diffraction (2D-GIWAXD) measurements

D-GIWAXD measurements were performed in a HUBER multi-axis diffractometer installed in beamline BL-19B2 at Spring-8 (Hyogo, Japan). The X-ray beam was monochromatized by a double-crystal Si (111) monochromator, and the X-ray energy was 12.398 keV. Scattered X-rays from samples were detected by an X-ray photon counting pixel detector (PILATUS 300 K). The X-ray-beam incidence angle was set to  $0.12^\circ$ , and the sample-to-detector distance was about 174 mm. The thin-film samples for the GIWAXD measurements were prepared on ITO-coated glass substrates in the same manner as in the device fabrication described above. All of sample substrates were kept a certain size (10 mm  $\times$  10 mm) to receive a similar effect of the footprint.

### Conflicts of interest

There are no conflicts to declare.

### Acknowledgements

This work was partly supported by CREST, JST, Grants-in-Aid for Scientific Research (No. JP26105004, JP16H02286, JP16K17949 and JP17H03042) and the Grant-in-Aid for JSPS Research Fellow program for Young Scientists. We thank The Nippon Synthetic Chemical Industry Co., Ltd. (Osaka, Japan) for providing ethyl isocynoacetate, the starting material for the synthesis of CP. We also thank Mr K. Miyake of NAIST for assistance with the SEM and STEM measurements. The synchrotron experiments were performed at beamline BL-19B2 of the Spring-8 facility with the approval of the Japan Synchrotron Radiation Research Institute (JASRI) (Proposal No. 2017A1779).

### Notes and references

- 1 M. Kaltenbrunner, M. S. White, E. D. Glowacki, T. Sekitani, T. Someya, N. S. Sariciftci and S. Bauer, *Nat. Commun.*, 2012, **3**, 770.
- 2 F. C. Krebs, *Org. Electron.*, 2009, **10**, 761–768.
- 3 D. Angmo, S. A. Gevorgyan, T. T. Larsen-Olsen, R. R. Søndergaard, M. Hösel, M. Jørgensen, R. Gupta, G. U. Kulkarni and F. C. Krebs, *Org. Electron.*, 2013, **14**, 984–994.
- 4 G. A. dos Reis Benatto, B. Roth, M. Corazza, R. R. Søndergaard, S. A. Gevorgyan, M. Jørgensen and F. C. Krebs, *Nanoscale*, 2016, **8**, 318–326.
- 5 M. Finn, C. J. Martens, A. V. Zaretski, B. Roth, R. R. Søndergaard, F. C. Krebs and D. J. Lipomi, *Sol. Energy Mater. Sol. Cells*, 2018, **174**, 7–15.
- 6 H. Benten, D. Mori, H. Ohkita and S. Ito, *J. Mater. Chem. A*, 2016, **4**, 5340–5365.



- 7 S. Li, W. Liu, C.-Z. Li, M. Shi and H. Chen, *Small*, 2017, 1701120.
- 8 Y. Lin and X. Zhan, *Mater. Horiz.*, 2014, 1, 470.
- 9 Y. Lin and X. Zhan, *Adv. Energy Mater.*, 2015, 5, 150163.
- 10 I. Etzbarria, J. Ajuria and R. Pacios, *Org. Electron.*, 2015, 19, 34–60.
- 11 W. Chen, X. Yang, G. Long, X. Wan, Y. Chen and Q. Zhang, *J. Mater. Chem. C*, 2015, 3, 4698–4705.
- 12 H. Sun, X. Song, J. Xie, P. Sun, P. Gu, C. Liu, F. Chen, Q. Zhang, Z.-K. Chen and W. Huang, *ACS Appl. Mater. Interfaces*, 2017, 9, 29924–29931.
- 13 W. Chen and Q. Zhang, *J. Mater. Chem. C*, 2017, 5, 1275–1302.
- 14 Z. He, C. Zhong, S. Su, M. Xu, H. Wu and Y. Cao, *Nat. Photonics*, 2012, 6, 591–595.
- 15 J. You, L. Dou, K. Yoshimura, T. Kato, K. Ohya, T. Moriarty, K. Emery, C. C. Chen, J. Gao, G. Li and Y. A. Yang, *Nat. Commun.*, 2013, 4, 1410–1446.
- 16 A. J. Heeger, *Adv. Mater.*, 2014, 26, 10–28.
- 17 M. C. Scharber and N. S. Sariciftci, *Prog. Polym. Sci.*, 2013, 38, 1929–1940.
- 18 Z. He, B. Xiao, F. Liu, H. Wu, Y. Yang, S. Xiao, C. Wang, T. P. Russell and Y. Cao, *Nat. Photonics*, 2015, 9, 174–179.
- 19 J. Huang, J. H. Carpenter, C. Z. Li, J. S. Yu, H. Ade and A. K. Y. Jen, *Adv. Mater.*, 2016, 28, 967–974.
- 20 J. Huang, H. Wang, K. Yan, X. Zhang, H. Chen, C.-Z. Li and J. Yu, *Adv. Mater.*, 2017, 29, 1606729.
- 21 J. Huang, X. Zhang, D. Zheng, K. Yan, C.-Z. Li and J. Yu, *Sol. RRL*, 2017, 1, 1600008.
- 22 T. Kumari, S. M. Lee, S.-H. Kang, S. Chen and C. Yang, *Energy Environ. Sci.*, 2017, 10, 258–265.
- 23 S. Li, L. Ye, W. Zhao, S. Zhang, S. Mukherjee, H. Ade and J. Hou, *Adv. Mater.*, 2016, 28, 9423–9429.
- 24 Y. Liu, J. Zhao, Z. Li, C. Mu, W. Ma, H. Hu, K. Jiang, H. Lin, H. Ade and H. Yan, *Nat. Commun.*, 2014, 5, 5293.
- 25 F. Zhao, S. Dai, Y. Wu, Q. Zhang, J. Wang, L. Jiang, Q. Ling, Z. Wei, W. Ma, W. You, C. Wang and X. Zhan, *Adv. Mater.*, 2017, 29, 1700144.
- 26 M. A. Ruderer, S. Guo, R. Meier, H. Y. Chiang, V. Köstgens, J. Wiedersich, J. Perlich, S. V. Roth and P. Müller-Buschbaum, *Adv. Funct. Mater.*, 2011, 21, 3382–3391.
- 27 H. C. Liao, C. C. Ho, C. Y. Chang, M. H. Jao, S. B. Darling and W. F. Su, *Mater. Today*, 2013, 16, 326–336.
- 28 J. Peet, J. Y. Kim, N. E. Coates, W. L. Ma, D. Moses, A. J. Heeger and G. C. Bazan, *Nat. Mater.*, 2007, 6, 497–500.
- 29 M. Suzuki, Y. Yamaguchi, K. Takahashi, K. Takahira, T. Koganezawa, S. Masuo, K. Nakayama and H. Yamada, *ACS Appl. Mater. Interfaces*, 2016, 8, 8644–8651.
- 30 G. J. Zhao, Y. J. He and Y. Li, *Adv. Mater.*, 2010, 22, 4355–4358.
- 31 X. Yang and A. Uddin, *Renewable Sustainable Energy Rev.*, 2014, 30, 324–336.
- 32 O. K. Kwon, M. A. Uddin, J. H. Park, S. K. Park, T. L. Nguyen, H. Y. Woo and S. Y. Park, *Adv. Mater.*, 2016, 28, 910–916.
- 33 Q. Zhang, B. Kan, F. Liu, G. Long, X. Wan, X. Chen, Y. Zuo, W. Ni, H. Zhang, M. Li, Z. Hu, F. Huang, Y. Cao, Z. Liang, M. Zhang, T. P. Russell and Y. Chen, *Nat. Photonics*, 2014, 9, 35–41.
- 34 J. L. Wang, K. K. Liu, J. Yan, Z. Wu, F. Liu, F. Xiao, Z. F. Chang, W. H. Bin, Y. Cao and T. P. Russell, *J. Am. Chem. Soc.*, 2016, 138, 7687–7697.
- 35 G. Wei, S. Wang, K. Sun, M. E. Thompson and S. R. Forrest, *Adv. Energy Mater.*, 2011, 1, 184–187.
- 36 K. Wang, M. Azouz, M. Babics, F. Cruciani, T. Marszalek, Q. Saleem, W. Pisula and P. M. Beaujuge, *Chem. Mater.*, 2016, 28, 5415–5425.
- 37 J.-L. Wang, F. Xiao, J. Yan, Z. Wu, K.-K. Liu, Z.-F. Chang, R.-B. Zhang, H. Chen, H.-B. Wu and Y. Cao, *Adv. Funct. Mater.*, 2016, 26, 1803–1812.
- 38 J. L. Wang, Z. Wu, J.-S. Miao, K.-K. Liu, Z.-F. Chang, R.-B. Zhang, H.-B. Wu and Y. Cao, *Chem. Mater.*, 2015, 27, 4338–4348.
- 39 S. Miller, G. Fanchini, Y.-Y. Lin, C. Li, C.-W. Chen, W.-F. Su and M. Chhowalla, *J. Mater. Chem.*, 2008, 18, 306–312.
- 40 J. Miao, H. Chen, F. Liu, B. Zhao, L. Hu, Z. He and H. Wu, *Appl. Phys. Lett.*, 2015, 106, 183302.
- 41 S. Grob, A. N. Bartynski, A. Opitz, M. Gruber, F. Grassl, E. Meister, T. Linderl, U. Hörmann, C. Lorch, E. Moons, F. Schreiber, M. E. Thompson and W. Brütting, *J. Mater. Chem. A*, 2015, 3, 15700–15709.
- 42 K. Gao, W. Deng, L. Xiao, Q. Hu, Y. Kan, X. Chen, C. Wang, F. Huang, J. Peng, H. Wu, X. Peng, Y. Cao, T. P. Russell and F. Liu, *Nano Energy*, 2016, 30, 639–648.
- 43 T. Motoyama, S. Sugii, S. Ikeda, Y. Yamaguchi, H. Yamada and K. Nakayama, *Jpn. J. Appl. Phys.*, 2014, 53, 01AB02.
- 44 H. Yamada, C. Ohashi, T. Aotake, S. Katsuta, Y. Honsho, H. Kawano, T. Okujima, H. Uno, N. Ono, S. Seki and K. Nakayama, *Chem. Commun.*, 2012, 48, 11136–11138.
- 45 H. Yamada, Y. Yamaguchi, R. Katoh, T. Motoyama, T. Aotake, D. Kuzuhara, M. Suzuki, T. Okujima, H. Uno, N. Aratani and K. Nakayama, *Chem. Commun.*, 2013, 49, 11638–11640.
- 46 T. Motoyama, T. Kiyota, H. Yamada and K. Nakayama, *Sol. Energy Mater. Sol. Cells*, 2013, 114, 156–160.
- 47 N. Noguchi, S. Junwei, H. Asatani and M. Matsuoka, *Cryst. Growth Des.*, 2010, 10, 1848–1853.
- 48 A. S. Dhoot, S. Aramaki, D. Moses and A. J. Heeger, *Adv. Mater.*, 2007, 19, 2914–2918.
- 49 P. B. Shea, H. Yamada, N. Ono and J. Kanicki, *Thin Solid Films*, 2012, 520, 4031–4035.
- 50 H. Saeki, M. Misaki, D. Kuzuhara, H. Yamada and Y. Ueda, *Jpn. J. Appl. Phys.*, 2013, 52, 111601.
- 51 T. Uemeyama, K. Hirose, K. Noda, K. Matsushige, T. Shishido, H. Saarenpää, N. V. Tkachenko, H. Lemmetyinen, N. Ono and H. Imahori, *J. Phys. Chem. C*, 2012, 116, 17414–17423.
- 52 A. Hirao, T. Akiyama, T. Okujima, H. Yamada, H. Uno, Y. Sakai, S. Aramaki and N. Ono, *Chem. Commun.*, 2008, 39, 4714–4716.
- 53 Y. Yamaguchi, M. Suzuki, T. Motoyama, S. Sugii, C. Katagiri, K. Takahira, S. Ikeda, H. Yamada and K. Nakayama, *Sci. Rep.*, 2014, 4, 7151.
- 54 Y. Matsuo, Y. Sato, T. Niinomi, I. Soga, H. Tanaka and E. Nakamura, *J. Am. Chem. Soc.*, 2009, 131, 16048–16050.



- 55 M. Guide, X. D. Dang and T. Q. Nguyen, *Adv. Mater.*, 2011, **23**, 2313–2319.
- 56 S. Ito, T. Murashima, N. Ono and H. Uno, *Chem. Commun.*, 1998, **16**, 1661–1662.
- 57 M. Suzuki, Y. Yamaguchi, K. Uchinaga, K. Takahira, C. Quinton, S. Yamamoto, N. Nagami, M. Furukawa, K. Nakayama and H. Yamada, *Chem. Sci.*, 2018, **9**, 6614–6621.
- 58 K. Sivula, Z. T. Ball, N. Watanabe and J. M. J. Fréchet, *Adv. Mater.*, 2006, **18**, 206–210.
- 59 J. U. Lee, J. W. Jung, T. Emrick, T. P. Russell and W. H. Jo, *Nanotechnology*, 2010, **21**, 105201.
- 60 J. U. Lee, A. Cirpan, T. Emrick, T. P. Russell and W. H. Jo, *J. Mater. Chem.*, 2009, **19**, 1483–1489.
- 61 C. Yang, J. K. Lee, A. J. Heeger and F. Wudl, *J. Mater. Chem.*, 2009, **19**, 5416.
- 62 J. U. Lee, J. W. Jung, T. Emrick, T. P. Russell and W. H. Jo, *J. Mater. Chem.*, 2010, **20**, 3287.
- 63 J. B. Kim, K. Allen, S. J. Oh, S. Lee, M. F. Toney, Y. S. Kim, C. R. Kagan, C. Nuckolls and Y. L. Loo, *Chem. Mater.*, 2010, **22**, 5762–5773.
- 64 Y. C. Lai, T. Higashihara, J. C. Hsu, M. Ueda and W. C. Chen, *Sol. Energy Mater. Sol. Cells*, 2012, **97**, 164–170.
- 65 L. Chen, K. Yao and Y. Chen, *J. Mater. Chem.*, 2012, **22**, 18768.
- 66 Y. Tamura, H. Saeki, J. Hashizume, Y. Okazaki, D. Kuzuhara, M. Suzuki, N. Aratani and H. Yamada, *Chem. Commun.*, 2014, **50**, 10379–10381.
- 67 Y. Tamura, D. Kuzuhara, M. Suzuki, H. Hayashi, N. Aratani and H. Yamada, *J. Mater. Chem. A*, 2016, **4**, 15333–15342.
- 68 O. V. Mikhnenko, P. W. M. Blom and T.-Q. Nguyen, *Energy Environ. Sci.*, 2015, **8**, 1867–1888.
- 69 S. Aramaki and J. Mizuguchi, *Acta Crystallogr., Sect. E: Struct. Rep. Online*, 2003, **59**, o1556–o1558.
- 70 C. D. Liman, S. Choi, D. W. Breiby, J. E. Cochran, M. F. Toney, E. J. Kramer and M. L. Chabinyc, *J. Phys. Chem. B*, 2013, **117**, 14557–14567.
- 71 E. D. Gomez, K. P. Barteau, H. Wang, M. F. Toney and Y.-L. Loo, *Chem. Commun.*, 2011, **47**, 436–438.
- 72 R. J. Young and M. V. Moore, *Dual-Beam (FIB-SEM) Systems Techniques and Automated Applications*, 2005.



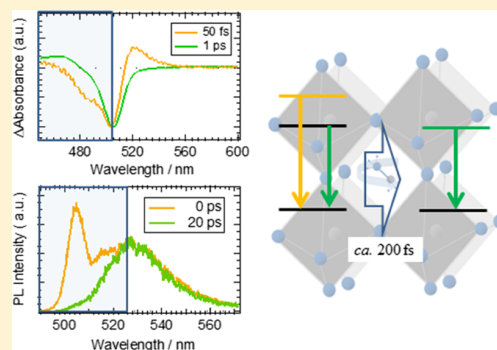
# Unraveling the Ultrafast Exciton Relaxation and Hidden Energy State in $\text{CH}_3\text{NH}_3\text{PbBr}_3$ Nanoparticles

Tetsuro Katayama,<sup>\*†</sup> Harunobu Suenaga, Tomoki Okuhata, Sadahiro Masuo,<sup>†</sup> and Naoto Tamai<sup>\*†</sup>

Department of Chemistry, School of Science and Technology, Kwansei Gakuin University, 2-1 Gakuen, Sanda, Hyogo 669-1337, Japan

**S** Supporting Information

**ABSTRACT:** Recently organic–inorganic lead-halide perovskite nanoparticles (NPs) have been attractive as low-cost and high-conversion-efficient solar cells and light-emitting diode. The generation of the exciton and dissociation into free carriers are quite important for primary photoelectric conversion processes. In this study, we have examined the initial exciton dynamics of  $\text{CH}_3\text{NH}_3\text{PbBr}_3$  (MAPbBr<sub>3</sub>) NPs by femtosecond transient absorption spectroscopy and picosecond time-resolved luminescence spectroscopy. The ultrafast exciton quenching with a time constant of 200 fs was observed, which may be related with longitudinal optical phonon and/or lurching motion of MA cation in the excited state. In addition, higher electronic state with a short lifetime was clearly detected by the excitation intensity dependence of time-resolved luminescence and transient absorption spectra. These findings of MAPbBr<sub>3</sub> NPs are very important not only for understanding the generation of charge carrier but also for constructing the high-efficiency charge separation and electric luminescence systems.



## INTRODUCTION

Recently organic–inorganic lead-halide perovskite materials have been attractive as low cost and high conversion efficient solar cells since the first report of 2009.<sup>1–5</sup> The generation of the exciton and the dissociation into free carriers are quite important for primary photoelectric conversion processes. Previously, the correlation between the generation of carriers and the oscillator strength of exciton on the ground state was discussed in the device of a perovskite solar cell by means of transient absorption microscopy.<sup>6</sup> The size effects of the perovskite crystal and nanoparticles (NPs) were also discussed with other time-resolved spectroscopy.<sup>7–10</sup> These phenomena were interpreted in terms of a large dielectric constant induced from the inhomogeneous surface charge following the photoexcitation.<sup>8</sup> Large dielectric constants can reduce the Coulombic attractive fields of electrons and holes. The drastic change of the Coulombic attractive fields of the electron and hole, following the photoexcitation, was also reported in vinyl<sup>11–13</sup> and  $\pi$ -conjugated polymers.<sup>14–16</sup> Thus, the process reducing the Coulombic attractive fields between electrons and holes is very important for photoelectric conversion systems. Even though the photoelectric conversion efficiency of  $\text{CH}_3\text{NH}_3\text{PbBr}_3$  (MAPbBr<sub>3</sub>) film was reported as over 10%,<sup>17</sup> the exciton binding energy of 60 meV reported for MAPbBr<sub>3</sub> of bulk crystal is higher than the thermal energy at room temperature (25 meV).<sup>18</sup> In addition, although the exciton binding energy of MAPbBr<sub>3</sub> NPs with an average size of 3.3 nm is 375 meV,<sup>19,20</sup> the photoelectric conversion efficiency of the solar cell device prepared with MAPbBr<sub>3</sub> NPs was reported as

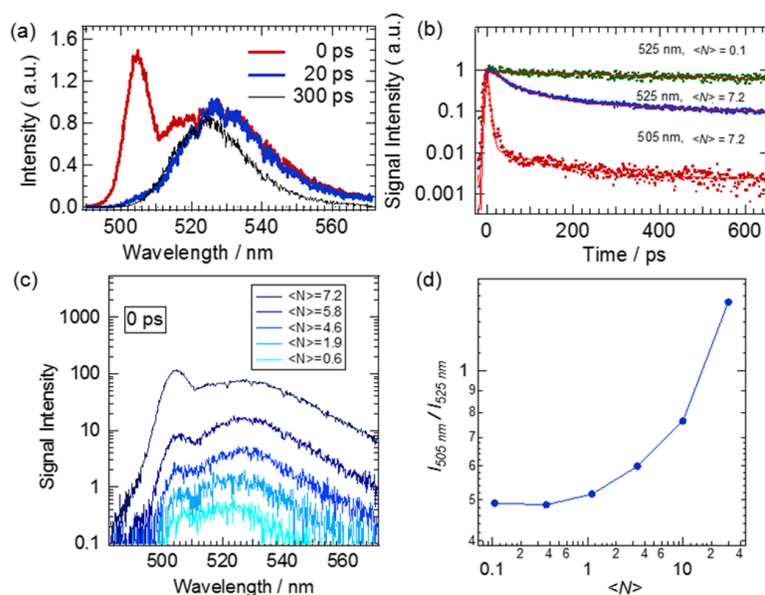
11%.<sup>21</sup> The internal conversion efficiency was over 80%. These high conversion efficiencies could not be simply explained by an exciton binding energy of NPs higher than the thermal energy at room temperature.

Single- and multiple-exciton dynamics of perovskite NPs have been reported by means of transient absorption and time-resolved luminescence measurements.<sup>22–25</sup> Scholes group first demonstrated the transient absorption dynamics of MAPbI<sub>3</sub> NPs.<sup>22</sup> Klimov group revealed the size dependence of Auger recombination of excitons in Cs-based quantum dots (QDs).<sup>23</sup> However, an initial stage of the relaxation of exciton has not been discussed because of the limitation of the monitoring wavelength and signal-to-noise ratio. In this study, we have examined the initial exciton dynamics by femtosecond transient absorption spectroscopy with a temporal resolution of 30 fs and picosecond time-resolved luminescence spectroscopy. The spectral change in the initial stage and the excitation intensity dependence of the luminescence spectra revealed the hidden electronic state and Coulombic screening between electron and hole in MAPbBr<sub>3</sub> NPs within a time constant of about 200 fs. This time constant is similar to a rotational “wobbling-in-a-cone” motion of MA cation molecules measured by femtosecond IR transient absorption spectroscopy and molecular dynamics (MD) calculation.<sup>26,27</sup> Comprehensive understanding of the exciton dynamics of NPs is very important not only for

**Received:** January 30, 2018

**Revised:** February 8, 2018

**Published:** February 12, 2018



**Figure 1.** (a) Time-resolved luminescence spectra (exc. at 480 nm,  $\langle N \rangle = 7.2$ ), (b) luminescence decay dynamics at 505 and 525 nm with different excitation intensities, (c) excitation intensity dependence of luminescence spectra of MAPbBr<sub>3</sub> QDs in toluene solution observed at 0 ps after excitation, and (d) luminescence intensity ratio of 505 nm against 525 nm ( $I_{505\text{nm}}/I_{525\text{nm}}$ ) of QDs as a function of the excitation intensity.

understanding the generation of charge carrier but also for constructing the high-efficiency charge-separation systems.

## EXPERIMENTAL SETUP

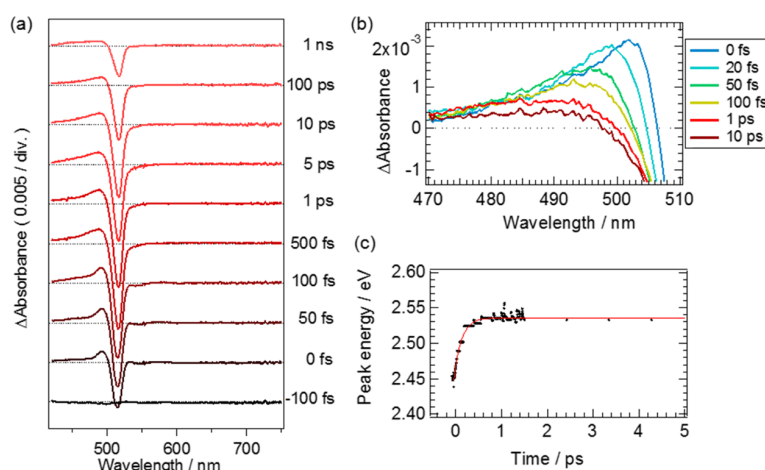
UV–vis absorption and luminescence spectra were recorded using a Hitachi U-4100 and Fluorolog-3 (Jobin Yvon Spex), respectively. The structures of MAPbBr<sub>3</sub> NPs were characterized by scanning transmission electron microscopy (STEM; Tecnai 20, 200 keV, FEI). Transient absorption spectra were measured by means of femtosecond pump-probe experiments. Light source was an amplified mode-locked Ti:sapphire laser (Solstice, Spectra-Physics), and the state-selective excitation experiments were performed by a noncollinear optical parametric amplifier (TOPAS-white, Light Conversion Ltd.). Excitation wavelengths were converted into 515 nm for transient absorption and 490 nm for time-resolved luminescence measurements. Transient absorption spectra were probed by delayed pulses of a femtosecond white-light continuum, generated by focusing a fundamental laser pulse into a CaF<sub>2</sub> plate. Probe light was detected by a C-MOS detector (Hamamatsu, PMA-20). The temporal resolution was ca. 30 fs. Time-resolved luminescence spectra were measured by using a streak camera with 1 kHz reputation rate (Hamamatsu, synchronous blanking unit M5678 and synchroscan sweep unit M5675). The temporal resolution was ca. 6 ps. Longer lifetime components were measured by a time-correlated single-photon counting method. The sample solution was agitated with a stirring bar during measurements.

Lead (II) bromide (PbBr<sub>2</sub>, Aldrich, 99.999%) methylamine hydrobromide (CH<sub>3</sub>NH<sub>2</sub> HBr, TCI, 99%), and *n*-otylamine (Wako, 98%) were purchased and used without further purification. NPs were synthesized by a reprecipitation method.<sup>19</sup> Before the measurements, the solution was centrifuged with a speed of 12 000 rpm. The supernatant was used for the transient absorption measurements. The solvent of redispersed NPs was toluene. Luminescence quantum yield was ca. 70%. Coumarin 343 in ethanol was used as the reference

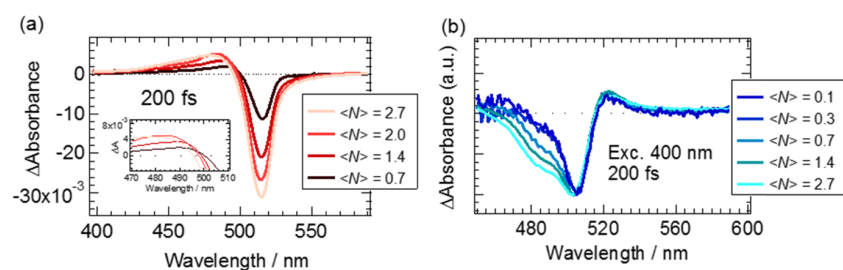
sample for determining the quantum yield of the luminescence. The average particle size of NPs was estimated to be  $5.5 \pm 0.5$  nm from STEM analyses, as shown Figure S1. Figure S1 shows the steady-state absorption and luminescence spectra of MAPbBr<sub>3</sub> NPs in toluene solution. The absorption and luminescence spectra of the centrifuged MAPbBr<sub>3</sub> NPs are apparently different from those of the precipitate in toluene solution. The lifetimes (amplitudes) of the centrifuged MAPbBr<sub>3</sub> NPs were estimated to be 8 ns (0.85) and 23 ns (0.15) from double exponential fits to the luminescence decay, as shown in Figure S2. The luminescence decay of redispersed MAPbBr<sub>3</sub> has much longer lifetime components over 200 ns as compared with MAPbBr<sub>3</sub> NPs because of the contribution of large-sized NPs.

## RESULTS AND DISCUSSION

**Time-Resolved Emission Spectra.** Figure 1a shows time-resolved luminescence for MAPbBr<sub>3</sub> NPs excited at 490 nm and detected at various delay times after excitation. Two luminescence peaks around 505 and 530 nm were observed just after excitation. The peak around at 505 nm disappeared very quickly within an instrument response function. The emission at 530 nm remained over 20 ps after excitation and then shifted to 525 nm within 300 ps. Figure 1b shows the luminescence decays observed at 505 and 525 nm with different excitation intensities. At lower excitation intensity of  $4.8 \times 10^{12}$  photon/cm<sup>2</sup> (average excitation number per NPs  $\langle N \rangle = 0.1$ , cross section at 480 nm was estimated as  $(2.2 \pm 0.7) \times 10^{14}$  cm<sup>2</sup> by using a general calculation method),<sup>23</sup> a single exponential decay was observed with a time constant longer than 2 ns. On the other hand, the luminescence decay at  $\langle N \rangle = 7.2$  was described by a sum of two exponential functions with a time constant of 55 ps (0.5) and 1.7 ns (0.5). The amplitude ratio between 55 ps and 1.7 ns increased with increasing the excitation intensity. The faster decay component of 55 ps is also observed in femtosecond transient absorption dynamics at higher excitation intensities, as illustrated in Figure S3. Thus,



**Figure 2.** (a) Transient absorption spectra for MAPbBr<sub>3</sub> QDs in toluene solution (exc. at 515 nm,  $\langle N \rangle = 0.7$ ), (b) transient absorption spectra within 1 ps after excitation (exc. at 515 nm,  $\langle N \rangle = 0.3$ ), and (c) peak energy shift of the positive signal around 500 nm.



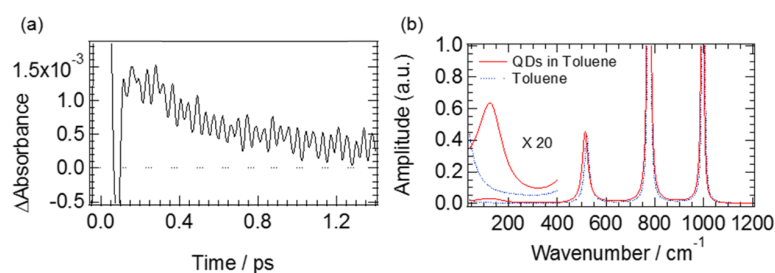
**Figure 3.** Excitation intensity dependence of transient absorption spectra for MAPbBr<sub>3</sub> QDs in toluene solution observed at 200 fs after excitation. (a) Excitation wavelength was at 515 nm and (b) at 400 nm.

the lifetime of 55 ps is probably because of biexciton Auger recombination. The binding energy of biexciton was estimated as  $\Delta XX = 21$  meV from the difference of luminescence maximum between spectral components of 55 ps and 1.7 ns by using global analysis, as shown in Figure S4. This value was close to the thermal energy of room temperature (25 meV). The excitation intensity dependence of luminescence spectra for MAPbBr<sub>3</sub> NPs just after the excitation (0 ps) is illustrated in Figure 1c. The peak at 505 nm was clearly observed at higher excitation intensity and the peak wavelength almost constant, irrespective of the excitation intensity. The ratio of the luminescence intensity of 505 nm against 525 nm is given in Figure 1d. As clearly shown in the figure, the ratio increases nonlinearly over  $\langle N \rangle = 2$ . Recently, Klimov group reported a similar luminescence behavior from multiexcitons in the Cs-based perovskite QDs (diameter = 6.3 to 11.2 nm), in which a new luminescence spectrum with a very short lifetime was superimposed at shorter wavelength region.<sup>23</sup> In addition, the luminescence spectrum from higher energy states was reported in iodine-based bulk perovskite film using a femtosecond optical Kerr gating method.<sup>24</sup> By considering the previous results, the spectrum at 505 nm is probably because of the luminescence from energy higher than the band-edge state of MAPbBr<sub>3</sub> NPs.

**Femtosecond TA Measurements.** For deciphering the ultrafast excitation dynamics in MAPbBr<sub>3</sub> NPs, femtosecond transient absorption spectroscopy was utilized. Figure 2a shows the time evolution of transient absorption spectra at low excitation intensity. Negative signal was observed immediately after excitation at 515 nm, and a positive absorption was

observed at 490 nm. Negative signals indicate the loss of the ground state, and a positive signal can be attributed to the photoinduced absorption (PA) of MAPbBr<sub>3</sub>.<sup>8</sup> Figure 2b illustrates PA spectra in the initial time region up to 10 ps. As clearly shown in the figure, the peak wavelength shifts to blue from 505 to 490 nm accompanied with the spectral broadening. The time constant of the spectral shift was estimated to be 200 fs with the energy shift of ca. 90 meV, as shown in Figure 2c. Previously, photoinduced giant dielectric constant was reported in the organic–inorganic halide perovskite system.<sup>28</sup> Increase of the dielectric constant should reduce the Coulombic attractive field between hole and electron pair, which was called “exciton quenching” in inorganic–organic perovskite crystal with MD simulation study.<sup>26</sup> In the calculation, the steady-state absorption spectrum changes from “QDs”-like to “bulk”-like spectrum without exciton absorption. The photoinduced exciton quenching might induce a negative signal as a result of disappearance of exciton absorption, and thus the blue-shift of PA signal in Figure 2b could be interpreted in terms of increase of the negative signal.

The exciton quenching was also observed with carrier–exciton interaction.<sup>8</sup> Thus, multiple excitons generated at higher excitation intensity might induce the exciton quenching originated from the electron/hole–exciton interaction. Figure 3a illustrates the excitation intensity dependence of the transient absorption spectra at 200 fs after 515 nm excitation. The PA spectrum shifted to blue with an increase in the excitation intensity. On the other hand, the maximum wavelength of the bleach signal around 515 nm does not change. This behavior suggests that the blue-shift of the



**Figure 4.** (a) Transient absorption dynamics of MAPbBr<sub>3</sub> QDs excited at 515 nm ( $\langle N \rangle = 2.0$ ) and observed at 490 nm. (b) Vibrational components of the vibrational components were calculated by maximum entropy method (MEM) from the residual component of the time profiles of transient absorbance at 490 nm. Residual component of the time profiles at 490 nm was obtained by means of fitting with an exponential function. Residual components and fast Fourier transform (FFT) spectra are shown in Figure S6.

absorption band around 490 nm is probably because of the Coulombic screening between electron and hole originated from the carrier–exciton interaction.<sup>21,22</sup> Thus, the blue-shift of the PA signal with a time constant of 200 fs in Figure 2b at low excitation intensity can be ascribed to exciton quenching. In addition, the existence of ultrafast rotational “wobbling-in-a-cone” motion of MA cation with a time constant of  $\sim 300$  fs in the excited state of bulk MAPbI<sub>3</sub> has been recently reported.<sup>26</sup> The Coulombic screening between electron and hole can be expected by the increase of dielectric constant induced by the oriental motion of MA cation.<sup>26,28</sup> Thus, the blue-shift of PA with a time constant of 200 fs in Figure 2b probably originated from change of dielectric constant with the ultrafast rotational motion of MA cation, although the time constant is a little faster than that in the bulk. Figure 3b shows the excitation intensity dependence of transient absorption spectra at 400 nm excitation. A positive signal around 525 nm was observed at 400 nm excitation. The new band might be resulted by the interference of 1P and 1S<sup>29</sup> with the red-shift of absorption edge. In addition, with the increase of the excitation intensity, the spectral width of the bleach signal greatly increased, and an additional peak appeared around 490 nm. This result indicates that the electronic state higher than 1S(e) is occupied with the increasing excitation intensity. It has been recently reported that the bleach shoulder shorter than 490 nm appeared at high excitation intensity, which was originated from the new trapping site with a lifetime of  $>10$  ns.<sup>30</sup> However, as shown in Figure S5, the shoulder at 490 nm disappeared with a time constant of ca. 200 fs. Hence, this behavior might not be caused from the trapping sites at higher excitation intensity. This behavior is explicable as the relaxation from higher electronic state, for example, 1P(e) reported as II–VI semiconductor QD systems.<sup>29,31</sup> The hidden electronic state might appear with luminescence at 505 nm and bleach signal at 490 nm with higher excitation intensity condition, just after the excitation. The relaxation time constant of hidden electronic state was almost the same as the initial spectral change of PA. Thus, the disappearance of hidden electronic state suggests the reduction of quantum confinements with increasing the dielectric constant in NPs. Slow hot-carrier relaxation and efficient hot-electron transfer dynamics with several hundred femtoseconds and a yield more than 80% in MAPbBr<sub>3</sub> perovskite nanocrystal have been reported.<sup>32</sup> Such an efficient hot-electron transfer probably progresses via hidden electronic state with a lifetime of 200 fs. The QD-like state might have an advantage for slow-carrier relaxation and electron-transfer reaction because of phonon bottleneck process.

**Coherent Longitudinal Optical Phonon Motions.** To reveal the Coulombic screening mechanism coupled with the phonon vibration of the perovskite, vibrational coherence of the perovskite NPs was precisely analyzed. Figure 4a shows the time profiles of the transient absorbance monitored at 490 nm. Vibrational coherence was observed in the transient signal, where several vibrational components were superimposed in the signal. Vibrational spectra were analyzed by an MEM, as shown in Figure 4b. Four peaks were observed and their energies were 1000, 780, 510, and 120 cm<sup>-1</sup> for MAPbBr<sub>3</sub> NPs. 1000, 780, and 510 cm<sup>-1</sup> were also observed in pure toluene. The low-frequency mode of 120 cm<sup>-1</sup> was not observed in the toluene solvent. Hence, the low-frequency mode is probably because of the phonon vibrational mode in perovskite. Previously, longitudinal optical (LO) phonon mode and lurching mode of MA cation was reported in the wavenumber region of 100–150 cm<sup>-1</sup> by resonance Raman spectroscopy of the perovskite NPs and a single crystal.<sup>33,34</sup> This frequency of LO phonon mode is similar to our experimental data, with a period of 120 cm<sup>-1</sup> also close to the time constant of exciton quenching. Thus, the phonon mode might assist the ion displacement of MA cation, inducing the Coulombic screening between electron and hole.

## CONCLUSIONS

In conclusion, ultrafast exciton dynamics in MAPbBr<sub>3</sub> NPs was observed by time-resolved luminescence and femtosecond transient absorption spectroscopy. The exciton quenching and hidden states were revealed by precise analyses of time-resolved spectroscopic data. These phenomena suggest the electronic state change from “QD”-like to “bulk”-like state with decreasing the quantum confinement effect. Vibrational coherence data with a period of 120 cm<sup>-1</sup> also suggest that the MA cation motion with LO phonon mode in NPs assists the exciton quenching. Such a dynamical Coulombic screening reduces the binding energy of exciton, leading to high electric charge separation and photoelectric conversion efficiency.

## ASSOCIATED CONTENT

### Supporting Information

The Supporting Information is available free of charge on the ACS Publications website at DOI: 10.1021/acs.jpcc.8b01051.

Scanning TEM image and steady-state absorption and luminescence spectra, luminescence decay, excitation intensity dependence of transient absorption decay, decay-associated spectra of the time-resolved luminescence, excitation intensity dependence of transient absorption, and FFT spectra (PDF)

## AUTHOR INFORMATION

## Corresponding Authors

\*E-mail: [tetsuro@kwansei.ac.jp](mailto:tetsuro@kwansei.ac.jp). Phone: +81-(0)79-565-8364 (T.K.).

\*E-mail: [tamai@kwansei.ac.jp](mailto:tamai@kwansei.ac.jp)(N.T.).

## ORCID

Tetsuro Katayama: 0000-0002-3214-2228

Sadahiro Masuo: 0000-0003-4828-5968

Naoto Tamai: 0000-0002-7343-6564

## Author Contributions

The manuscript was written through contributions from all authors. All authors have given approval to the final version of the manuscript.

## Notes

The authors declare no competing financial interest.

## ACKNOWLEDGMENTS

This work was supported by the JSPS KAKENHI (grant number; JP26107005 in Scientific Research on Innovative Areas “Photosynergetics” and 17K14084) and the CASIO foundation (grant number; 9347).

## REFERENCES

- (1) Kojima, A.; Teshima, K.; Shirai, Y.; Miyasaka, T. Organometal Halide Perovskites as Visible-light Sensitizers for Photovoltaic Cells. *J. Am. Chem. Soc.* **2009**, *131*, 6050–6051.
- (2) Lee, M. M.; Teuscher, J.; Miyasaka, T.; Murakami, T. N.; Snaith, H. J. Efficient Hybrid Solar Cells Based on Meso-superstructured Organometal Halide Perovskites. *Science* **2012**, *338*, 643–647.
- (3) Liu, M.; Johnston, M. B.; Snaith, H. J. Efficient Planar Heterojunction Perovskite Solar Cells by Vapor Deposition. *Nature* **2013**, *501*, 395–398.
- (4) Zhou, H.; Chen, Q.; Li, G.; Luo, S.; Song, T.-B.; Duan, H.-S.; Hong, Z.; You, J.; Liu, Y.; Yang, Y. Interface Engineering of Highly Efficient Perovskite Solar Cells. *Science* **2014**, *345*, 542–546.
- (5) Shi, D.; Adinolfi, V.; Comin, R.; Yuan, M.; Alaroussi, E.; Buin, A.; Chen, Y.; Hoogland, S.; Rothenberger, A.; Bakr, O. M.; et al. Low Trap-state Density and Long Carrier Diffusion in Organo Lead Trihalide Perovskite Single Crystals. *Science* **2015**, *347*, 519–522.
- (6) Katayama, T.; Jinno, A.; Takeuchi, E.; Ito, S.; Endo, M.; Wakamiya, A.; Murata, Y.; Ogomi, Y.; Hayase, S.; Miyasaka, H. Inhomogeneous Deactivation Process with UV Excitation in Submicron Grains of Lead Iodide Perovskite-Based Solar Cell as Revealed by Femtosecond Transient Absorption Microscopy. *Chem. Lett.* **2014**, *43*, 1656–1658.
- (7) de Quilletes, D. W.; Vorpahl, S. M.; Stranks, S. D.; Nagaoka, H.; Eperon, G. E.; Ziffer, M. E.; Snaith, H. J.; Ginger, D. S. Impact of Microstructure on Local Carrier Lifetime in Perovskite Solar Cells. *Science* **2015**, *348*, 683–686.
- (8) Grancini, G.; Kandada, A. R. S.; Frost, J. M.; Barker, A. J.; De Bastiani, M.; Gandini, M.; Marras, S.; Lanzani, G.; Walsh, A.; Petrozza, A. Role of Microstructure in the Electron-Hole Interaction of Hybrid Lead-Halide Perovskites. *Nat. Photonics* **2015**, *9*, 695–701.
- (9) Zhu, H.; Miyata, K.; Fu, Y.; Wang, J.; Joshi, P. P.; Niesner, D.; Williams, K. W.; Jin, S.; Zhu, X.-Y. Screening in Crystalline Liquids Protects Energetic Carriers in Hybrid Perovskites. *Science* **2016**, *353*, 1409–1413.
- (10) Even, J.; Pedesseau, L.; Katan, C. Analysis of Multivalley and Multibandgap Absorption and Enhancement of Free Carriers Related to Exciton Screening in Hybrid Perovskites. *J. Phys. Chem. C* **2014**, *118*, 11566–11572.
- (11) Katayama, T.; Ishibashi, Y.; Morii, Y.; Ley, C.; Brazard, J.; Lacombat, F.; Plaza, P.; Martin, M. M.; Miyasaka, H. Ultrafast Delocalization of Cationic States in Poly(N-vinylcarbazole) Solid Leading to Carrier Generation. *Phys. Chem. Chem. Phys.* **2010**, *12*, 4560–4563.
- (12) Katayama, T.; Ishibashi, Y.; Miyasaka, H. Direct Detection of Electron Transfer Processes in Photoconductive Poly(N-vinylcarbazole) Solid Film Doped with Electron Acceptors: Temperature Dependence of Femtosecond to Microsecond Dynamics. *J. Photochem. Photobiol., A* **2012**, *234*, 107–114.
- (13) Fushimi, T.; Ohkita, H.; Ito, S.; Yamamoto, M. Dynamical Formation of Intramolecular Carbazole Dimer Cations in Poly(methyl methacrylate) Solids below the Glass Transition Temperature. *Macromolecules* **2002**, *35*, 9523–9528.
- (14) Clarke, T. M.; Durrant, J. R. Charge photogeneration in organic solar cells. *Chem. Rev.* **2010**, *110*, 6736–6767.
- (15) Zhu, X.-Y.; Yang, Q.; Muntwiler, M. Charge-Transfer Excitons at Organic Semiconductor Surfaces and Interfaces. *Acc. Chem. Res.* **2009**, *42*, 1779–1787.
- (16) Gélinas, S.; Rao, A.; Kumar, A.; Smith, S. L.; Chin, A. W.; Clark, J.; van der Poll, T. S.; Bazan, G. C.; Friend, R. H. Ultrafast Long-Range Charge Separation in Organic Semiconductor Photovoltaic Diodes. *Science* **2014**, *343*, 512–516.
- (17) Heo, J. H.; Song, D. H.; Im, S. H. Planar CH<sub>3</sub>NH<sub>3</sub>PbBr<sub>3</sub> Hybrid Solar Cells with 10.4% Power Conversion Efficiency, Fabricated by Controlled Crystallization in the Spin-Coating Process. *Adv. Mater.* **2014**, *26*, 8179–8183.
- (18) Sestu, N.; Cadelano, M.; Sarritsu, V.; Chen, F.; Marongiu, D.; Piras, R.; Mainas, M.; Quochi, F.; Saba, M.; Bongiovanni, G.; et al. Absorption F-Sum Rule for the Exciton Binding Energy in Methylammonium Lead Halide Perovskites. *J. Phys. Chem. Lett.* **2015**, *6*, 4566–4572.
- (19) Zhang, F.; Zhong, H.; Chen, C.; Wu, X.-G.; Hu, X.; Huang, H.; Han, J.; Zou, B.; Dong, Y. Brightly Luminescent and Color-Tunable Colloidal CH<sub>3</sub>NH<sub>3</sub>PbX<sub>3</sub> (X = Br, I, Cl) Quantum Dots: Potential Alternatives for Display Technology. *ACS Nano* **2015**, *9*, 4533–4542.
- (20) Mali, S. S.; Shim, C. S.; Hong, C. K. Highly Stable and Efficient Solid-state Solar Cells Based on Methylammonium Lead Bromide (CH<sub>3</sub>NH<sub>3</sub>PbBr<sub>3</sub>) Perovskite Quantum Dots. *NPG Asia Mater.* **2015**, *7*, e208.
- (21) Tachikawa, T.; Karimata, I.; Kobori, Y. Surface Charge Trapping in Organolead Halide Perovskites Explored by Single-Particle Photoluminescence Imaging. *J. Phys. Chem. Lett.* **2015**, *6*, 3195–3201.
- (22) Hassan, Y.; Song, Y.; Pensack, R. D.; Abdelrahman, A. I.; Kobayashi, Y.; Winnik, M. A.; Scholes, G. D. Structure-Tuned Lead Halide Perovskite Nanocrystals. *Adv. Mater.* **2016**, *28*, 566–573.
- (23) Makarov, N. S.; Guo, S.; Isaienko, O.; Liu, W.; Robel, I.; Klimov, V. I. Spectral and Dynamical Properties of Single Excitons, Biexcitons, and Trions in Cesium–Lead-Halide Perovskite Quantum Dots. *Nano Lett.* **2016**, *16*, 2349–2362.
- (24) Chen, K.; Barker, A. J.; Morgan, F. L. C.; Halpert, J. E.; Hodgkiss, J. M. Effect of Carrier Thermalization Dynamics on Light Emission and Amplification in Organometal Halide Perovskites. *J. Phys. Chem. Lett.* **2015**, *6*, 153–158.
- (25) Manser, J. S.; Kamat, P. V. Band Filling with Free Charge Carriers in Organometal Halide Perovskites. *Nat. Photonics* **2014**, *8*, 737–743.
- (26) Mattoni, A.; Filippetti, A.; Saba, M. I.; Delugas, P. Methylammonium Rotational Dynamics in Lead Halide Perovskite by Classical Molecular Dynamics: The Role of Temperature. *J. Phys. Chem. C* **2015**, *119*, 17421–17428.
- (27) Bakulin, A. A.; Selig, O.; Bakker, H. J.; Rezus, Y. L.; Müller, C.; Glaser, T.; Lovrincic, R.; Sun, Z.; Chen, Z.; Jansen, T. L. C.; et al. Real-Time Observation of Organic Cation Reorientation in Methylammonium Lead Iodide Perovskites. *J. Phys. Chem. Lett.* **2015**, *6*, 3663–3669.
- (28) Juarez-Perez, E. J.; Sanchez, R. S.; Badia, L.; Garcia-Belmonte, G.; Kang, Y. S.; Sero, I. M.; Bisquert, J. Photoinduced Giant Dielectric Constant in Lead Halide Perovskite Solar Cells. *J. Phys. Chem. Lett.* **2014**, *5*, 2390–2394.
- (29) Sewall, S. L.; Franceschetti, A.; Cooney, R. R.; Zunger, A.; Kambhampati, P. Direct Observation of the Structure of Band-edge

Biexcitons in Colloidal Semiconductor CdSe Quantum Dots. *Phys. Rev. B: Condens. Matter Mater. Phys.* **2009**, *80*, 081310.

(30) Zheng, K.; Židek, K.; Abdellah, M.; Chen, J.; Chábera, P.; Zhang, W.; Al-Marri, M. J.; Pullerits, T. High Excitation Intensity Opens a New Trapping Channel in Organic–Inorganic Hybrid Perovskite Nanoparticles. *ACS Energy Lett.* **2016**, *1*, 1154–1161.

(31) Kobayashi, Y.; Nishimura, T.; Yamaguchi, H.; Tamai, N. Effect of Surface Defects on Auger Recombination in Colloidal CdS Quantum Dots. *J. Phys. Chem. Lett.* **2011**, *2*, 1051–1055.

(32) Li, M.; Bhaumik, S.; Goh, T. W.; Kumar, M. S.; Yantara, N.; Grätzel, M.; Mhaisalkar, S.; Mathews, N.; Sum, T. C. Slow Cooling and Highly Efficient Extraction of Hot Carrier in Colloidal Perovskite Nanocrystals. *Nat. Commun.* **2017**, *8*, 14350.

(33) Ledinský, M.; Löper, P.; Niesen, B.; Holovský, J.; Moon, S.-J.; Yum, J.-H.; De Wolf, S.; Fejfar, A.; Ballif, C. Raman Spectroscopy of Organic–Inorganic Halide Perovskites. *J. Phys. Chem. Lett.* **2015**, *6*, 401–406.

(34) Matsuishi, K.; Ishihara, T.; Onari, S.; Chang, Y. H.; Park, C. H. Optical Properties and Structural Phase Transitions of Lead-Halide based inorganic–organic 3D and 2D perovskite semiconductors under high pressure. *Phys. Status Solidi B* **2004**, *241*, 3328–3333.

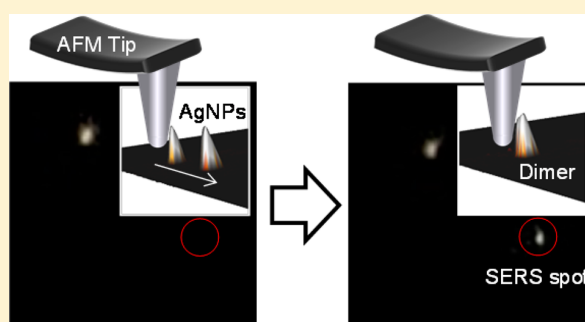
# In Situ Observation of Surface-Enhanced Raman Scattering from Silver Nanoparticle Dimers and Trimers Fabricated Using Atomic Force Microscopy Manipulation

Taisuke Fukui,<sup>†</sup> Hiroyuki Naiki,<sup>‡</sup> and Sadahiro Masuo<sup>\*,‡</sup>

<sup>†</sup>Department of Chemistry, and <sup>‡</sup>Department of Applied Chemistry for Environment, Kwansei Gakuin University, 2-1 Gakuen, Sanda, Hyogo 669-1337, Japan

## Supporting Information

**ABSTRACT:** The generation of surface-enhanced Raman scattering (SERS) was directly observed in situ during the fabrication of Ag nanoparticle (AgNP) dimers and trimers using atomic force microscopy (AFM) manipulation, and the size of the SERS hot spot was estimated using the super-resolution imaging technique. SERS from 4,4'-bipyridine was observed upon fabrication of the AgNP dimers and trimers using AFM manipulation. Then the SERS spots were analyzed by fitting with the point spread function for super-resolution imaging. The distribution of the centroid position of the SERS spot from the AgNP dimer was 9 nm along the *x*-axis and 8 nm along the *y*-axis, which represents the size of the SERS hot spot. The same technique was applied to the AgNP trimer. The obtained results are important not only for the SERS technique but also for other



plasmon enhancement techniques which are useful in a wide range of research areas.

## INTRODUCTION

Surface-enhanced Raman scattering (SERS) by metal nanostructures has great potential for use as an analytical technique in the fields of biomedicine,<sup>1,2</sup> molecular biology,<sup>3–5</sup> and environmental science<sup>6</sup> due to its ability to identify and confirm molecular components at the single-molecule level. Both experimental and theoretical approaches have demonstrated that SERS is strongly scattered from junctions in metal nanoparticle (MNP) aggregates.<sup>7–10</sup> Two main mechanisms have been suggested for the generation of SERS. The first mechanism is the so-called electrical mechanism, which is caused by the strong electric field of the localized surface plasmon resonance (LSPR) on the MNP aggregates.<sup>9–12</sup> Upon irradiating the aggregates with resonant light, a strong electric field is generated at the junction of the aggregates, which is called a hot spot. When molecules interact with the electric field at the hot spot through dipole–dipole coupling, the excitation and scattering field intensities of the Raman scattering from molecules located at the junctions increase (up to  $10^{10}$  times). The second mechanism is the so-called chemical mechanism, which consists of various effects, including the resonance Raman effect, the charge-transfer effect, and the adsorption effect.<sup>10,13,14</sup> Generally, the enhancement provided by the electrical mechanism is stronger than that from the chemical mechanism ( $\sim 10^4$  times). Combining the electrical and chemical effects, SERS enhancement from the MNP aggregates increases  $10^{14}$ -fold compared to conventional Raman scattering. Thus, the hot spot provided by the electrical

mechanism of SERS plays the most important role in enhancing the Raman scattering of molecules.

The importance of the SERS hot spot has been clarified through quantitative studies.<sup>7–10</sup> Itoh et al. investigated the necessity of the hot spot for the generation of SERS by combining SERS and scanning electron microscopy (SEM) observations. They demonstrated that AgNP dimers induced SERS, whereas SERS was not observed from the molecule adsorbed on a single AgNP. Thus, the presence of an AgNP junction was required to observe SERS. In addition, they confirmed polarization-dependent SERS generation, in which SERS was generated by irradiation with incident light at a polarization angle parallel to the long axis of the dimer.<sup>7,10</sup> This result also indicated that the generation of a hot spot was required to observe SERS. To examine the size and location of the hot spot, Willets et al. applied the super-resolution imaging technique, which has a spatial resolution of 5 nm, to AgNP dimers, trimers, and aggregates.<sup>8,9,15–18</sup> By analyzing the point spread function (PSF) of the SERS spot, they demonstrated that the SERS spot can be observed at the junction of the AgNP dimer and that the size of the SERS hot spot depended on the shape and size of the AgNPs; therefore, the morphology of the aggregates could be estimated by overcoming optical diffraction limitations.

**Received:** April 20, 2017

**Revised:** August 17, 2017

**Published:** August 21, 2017

In most reports, the influence of the hot spot on SERS has been investigated using self-assembled MNP aggregates; i.e., SERS was observed from self-assembled aggregates deposited on a substrate, which was prepared by facilitating aggregation in the suspension. For example, in the reports by Willets et al., the size of the SERS hot spot was estimated with the assumption that the hot spot is located at the junction.<sup>8,9,15–18</sup> No reports have achieved the in situ observation of hot spots resulting from the fabrication of MNP aggregates to accurately estimate the size of the hot spot. It would be interesting to determine whether SERS can be generated during the in situ fabrication of simple MNP aggregates, such as dimer and trimer structures. In principle, when MNP dimers are fabricated by combining two MNPs, SERS should be observed due to the generation of a hot spot. Atomic force microscopy (AFM) manipulation is a useful technique to observe in situ the generation of SERS during the fabrication of MNP dimers and trimers.<sup>19–21</sup> Previously, Tong et al. demonstrated SERS generation using AFM manipulation.<sup>19,20</sup> SERS was generated by aligning AuNPs with organic molecules or by moving an AuNP to the vicinity of a single carbon nanotube using the manipulation technique.

In this work, to confirm whether a SERS hot spot exists at a MNP junction and to estimate the size of the SERS hot spot, we observed in situ the generation of SERS from 4,4'-bipyridine from AgNP dimers and trimers prepared using AFM manipulation. 4,4'-Bipyridine was adsorbed on the AgNPs, and then single AgNPs were moved by AFM manipulation to fabricate AgNP dimer and trimer structures. SERS was observed during the fabrication of the AgNP dimers and trimers. The observed SERS spot was analyzed using the PSF and super-resolution imaging on the order of few nanometers, and the size of the hot spot was estimated. In situ observation using the AFM manipulation technique clarified the generation of the hot spot.

## EXPERIMENTAL SECTION

**Preparation of AgNPs with 4,4'-Bipyridine.** AgNPs (containing sodium citrate as stabilizer) and 4,4'-bipyridine were purchased from Sigma-Aldrich and Wako Pure Chemical Industries, respectively. All chemicals were used as received without further purification. An aqueous solution of 4,4'-bipyridine ( $2 \times 10^{-5}$  M) was mixed with an aqueous suspension of the AgNPs ( $2 \times 10^{-5}$  M) in a 1:1 volume ratio. The mixture was spin-coated onto a glass coverslip.

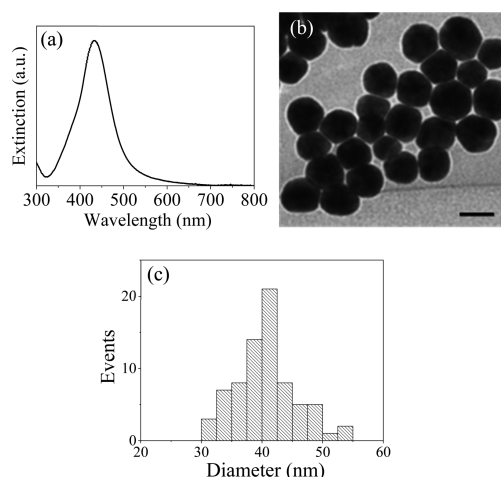
**Instrument Setup for SERS Measurement and Fabrication of AgNP Dimers and Trimers Using AFM Manipulation.** As the excitation light source for SERS measurement, a 532 nm continuous-wave laser (Spectra-Physics, Excelsior-532-50) was passed through a bandpass filter (Semrock, LL01-532-25) and subsequently introduced into an inverted microscope (Olympus, IX-71). Then the beam was reflected using a dichroic mirror (Semrock, FF555-Di02-25  $\times$  36) and focused onto the 100  $\mu$ m area of the sample using an oil-immersion objective lens (Olympus, 100 $\times$ , N.A:1.4). AFM manipulation of the AgNPs was realized using an AFM (JPK instruments, NanoWizard II) placed on top of the inverted microscope stage.<sup>21</sup> In addition to the three closed-loop, piezo-driven axes of the AFM, a two-axis, closed-loop, piezo-driven sample stage was employed. SERS from 4,4'-bipyridine was collected using the same objective lens and passed through a notch filter (Semrock, NF01-532U-25). The SERS image was obtained using an EM-CCD (Photometrics, Cascade II 512). The SERS spectra were also measured using a

spectrometer (Acton Research Corp., SpectraPro2358) with a cooled CCD camera (Princeton Instruments, PIXIS400B) by switching the optical path of the detected SERS using a mirror.

The AFM manipulation of the AgNPs along with detection of the accompanying SERS behavior of 4,4'-bipyridine was performed using the following procedure. Initially, a silicon AFM tip (Olympus, OMLC-AC160TS-R3) was coupled to the center of the focused excitation laser by adjusting the piezo of the AFM. Then the AFM topography and SERS images of the sample were measured before AFM manipulation. Subsequently, AgNP dimers and trimers were fabricated using the AFM tip to move one AgNP to the vicinity of another by moving the sample stage. Then, the AFM topography and SERS behavior of 4,4'-bipyridine from the AgNP dimers and trimers were measured. The AFM topography measurement and manipulation of the AgNPs were performed in tapping mode and contact mode, respectively. All measurements were performed at room temperature under ambient conditions.

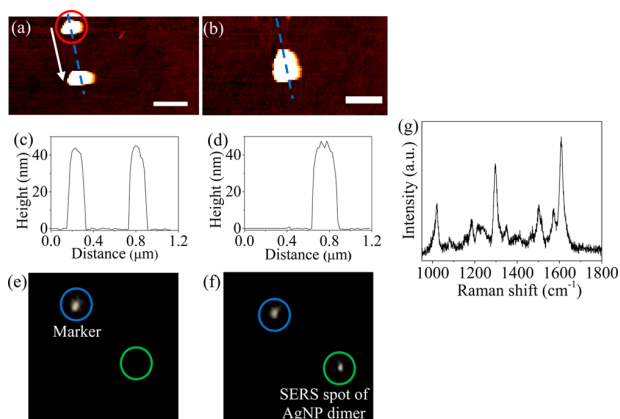
## RESULTS AND DISCUSSION

The AgNPs exhibited a peak LSPR wavelength at 433 nm (Figure 1a). A TEM image of the AgNPs, and a histogram of



**Figure 1.** (a) Extinction spectrum of an aqueous suspension of the AgNPs. (b) TEM image of the AgNPs. The scale bar in the image indicates 40 nm. (c) Histogram of the diameter of the AgNP.

the diameter of the AgNP estimated from the TEM image are shown Figure 1b and 1c, respectively. The average diameter was estimated to be 40 nm from the histogram. Figure 2 shows the AFM topography images (a and b) and cross sections (c and d) of the AgNPs before (a and c) and after (b and d) fabrication of the AgNP dimers through AFM manipulation. Before manipulation, the AgNP was far away from the other AgNP ( $\sim$ 400 nm), and the heights of the two AgNPs were estimated to be 44 nm (Figures 2a and c), which was similar to the diameter estimated from the TEM image. To fabricate the AgNP dimer, the first AgNP (red circle) was pushed to the second AgNP using the AFM tip, as shown by the arrow in Figure 2a, where the two AgNPs then combined into an AgNP dimer (Figure 2b). As the width of the AgNP dimer was larger than that of the single AgNP and the height did not change (Figure 2d), the two AgNPs were aligned in the  $x$ - $y$  plane. The SERS images before (e) and after (f) fabricating the AgNP dimer are shown in Figure 2. Before fabrication of the AgNP



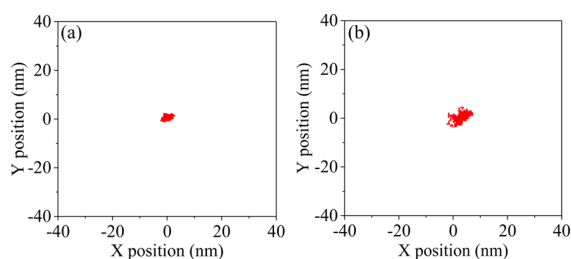
**Figure 2.** AFM topography of the AgNPs (a, b), cross sections of the blue dotted line in the topography images (c, d), and Raman scattering images (e, f) before (a, c, and e) and after (b, d, and f) fabricating the AgNP dimer by AFM manipulation. (g) SERS spectrum from the AgNP dimer. The scale bars in the images (a, b) indicate 300 nm.

dimer (Figure 2e), a bright spot can be observed in the upper left region (blue circle). The spot is attributed to the SERS of 4,4'-bipyridine with the aggregated AgNPs assembled during the sample preparation. The spot was used as a marker to show the appearance of a SERS spot upon fabrication of the AgNP dimer. After fabrication of the AgNP dimer, a new bright spot appeared in the lower right region (green circle). The appearance of the new bright spot after AFM manipulation is also shown in movie S1. To confirm that the new bright spot was attributed to the SERS from the 4,4'-bipyridine, the spectrum of the bright spot was recorded and is shown in Figure 2g. The observed spectrum exhibited Raman bands, which can be attributed to the vibrational modes of the 4,4'-bipyridine molecule at  $1018\text{ cm}^{-1}$  (ring breathing),  $1080\text{ cm}^{-1}$  (in-plane ring deformation, C–H bending),  $1240\text{ cm}^{-1}$  (in-plane C–H bending),  $1300\text{ cm}^{-1}$  (inter-ring stretching), and  $1612\text{ cm}^{-1}$  (ring stretching). The peak wavenumbers and shapes of the spectrum were consistent with the reported SERS spectrum of 4,4'-bipyridine.<sup>22–27</sup> Therefore, the new bright spot was attributed to SERS from 4,4'-bipyridine. Murakoshi et al. reported the SERS spectra of 4,4'-bipyridine enhanced by Ag dimer structure which was fabricated by vacuum deposition of Ag.<sup>26,27</sup> The wavenumbers of the vibrational modes of our SERS spectrum were completely consistent with those of the reported SERS spectra, which indicated that the 4,4'-bipyridine did not interact with sodium citrate, which contained our AgNP suspension as a stabilizer. In addition, the electric field enhancement of the AgNP dimer was investigated using the numerical simulation (details in the Supporting Information). By this simulation, we confirmed that the incident laser at 532 nm can be enhanced at the junction of the AgNPs by fabricating the AgNP dimer. From these results, SERS could be observed during the fabrication of the AgNP dimer using AFM manipulation.

For PSF analysis of the SERS spot, a photoluminescence (PL) spot from a single CdSe/ZnS quantum dot (QD; Invitrogen, core radius: 2.6 nm, emission peak wavelength: 605 nm) was first measured to estimate the spatial resolution of our measurement setup. A QD suspension in toluene ( $\sim 10^{-8}\text{ M}$ ) was spin-coated on a coverslip, and the PL spot of a single QD was detected. The PL spot was fitted by the PSF in eq 1 (further details are given in the Supporting Information)

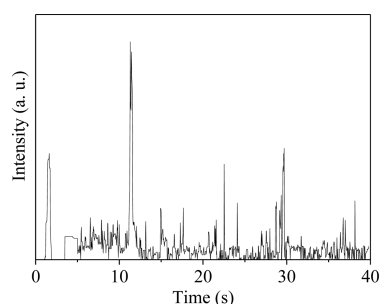
$$I(x, y) = I_0 \exp \left[ -\frac{1}{2w_x^2} \{ (x - x_0) \cos \theta - (y - y_0) \sin \theta \}^2 - \frac{1}{2w_y^2} \{ (x - x_0) \sin \theta + (y - y_0) \cos \theta \}^2 \right] I_{\text{B.G.}} \quad (1)$$

where  $I(x, y)$  is the intensity of the detected PL or SERS for a given position  $(x, y)$  in space,  $I_0$  is the SERS or PL intensities at the center of the fit,  $I_{\text{B.G.}}$  is the background intensity, and  $w_x$  and  $w_y$  are the width of the Gaussian along the  $x$ - and  $y$ -axis, respectively. Here, to consider the movement of the PL or SERS spot in the diagonal direction,  $\theta$  is defined as the angle of trajectory between a given position and the centroid positions  $(x_0, y_0)$  of the spot. The centroid positions of the spots were analyzed by fitting the PL and SERS spots using the eq 1. The distribution of the centroid positions estimated from the PL spots of a single QD is shown in Figure 3a. The  $x$ - and the  $y$ -



**Figure 3.** Distributions of the centroid positions of PL from a single QD (a) and SERS from the AgNP dimer (b) obtained by fitting each image frame using the PSF in eq 1.

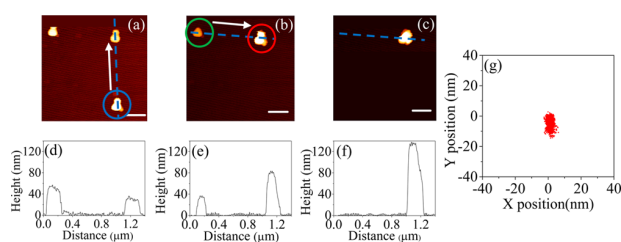
axis lengths of the distribution were estimated to be 5 and 3 nm, respectively. The slight elongation along the  $x$ -axis length was caused by lateral stage drift during the PL measurement. From these results, the spatial resolution of our measurement setup was estimated to be these values. The distribution of the centroid positions of the SERS spot from the AgNP dimer is shown in Figure 3b. The  $x$ - and  $y$ -axis lengths of the distribution were estimated to be 9 and 8 nm, respectively. Interestingly, the distribution of the centroid positions estimated from the SERS spot was larger than the spatial resolution. This result indicates the movement of the centroid positions of the SERS spot during the SERS measurement. This movement can be attributed to the thermal diffusion of 4,4'-bipyridine in the hot spot. Generally, SERS is generated at the hot spot of the MNPs through the enhancement of the excitation and scattering processes as follows:<sup>10,12,28,29</sup> (i) excitation light is absorbed by an MNP; (ii) the absorbed light energy excites a molecule through dipole–dipole coupling with the electric field of the hot spot; (iii) some of the excited energy in the molecule is converted into Raman scattering; (iv) a Raman scattering photon is scattered back from the molecule to the MNP; and (v) SERS is scattered from the MNP as plasmon-dipole radiation. Based on this process, SERS can be scattered from hot spots of MNPs. Hence, the molecule coupled with the hot spot is important to generating SERS. In our case, SERS was observed from the hot spot generated by fabricating an AgNP dimer using AFM manipulation. The time trace of the observed SERS intensity is shown in Figure 4. The time trace exhibited on and off states of SERS at millisecond to second time scales, i.e., the typical blinking behavior of



**Figure 4.** Time trace of the SERS intensity from the AgNP dimer obtained from movie S1.

SERS.<sup>12,28,29</sup> The blinking was partially attributed to the thermal diffusion of molecules in-and-out of the hot spot.<sup>12,28,29</sup> Hence, the thermal diffusion of 4,4'-bipyridine in the hot spot of the AgNP dimer induced the coupling and uncoupling of 4,4'-bipyridine with the electric field of the hot spot. In Figure 3b, the distribution of the centroid positions of the SERS spot was larger than the spatial resolution. This result indicated that 4,4'-bipyridine diffused in and out of the hot spot of the AgNP dimer and scattered SERS at the several positions in the hot spot. Therefore, the distribution of the centroid positions represented the size of the hot spot of the AgNP dimer. As shown in Figure 3b, the *x*-axis of the distribution of the centroid positions of the SERS spot was longer than the *y*-axis. As seen in the AFM image in Figure 2a, the boundary of the AgNP dimer between the two AgNPs was oblique, because the two AgNPs were moved from the upper left and lower right regions. Therefore, the distribution of the centroid positions of the SERS spot was also oblique. The generation of a hot spot was directly observed, and the size of the hot spot was estimated using a combination of AFM manipulation and super-resolution imaging.

Figure 5 shows the AFM topography images (a–c) and cross sections (d–f) of the AgNPs before (a, b, d, and e) and after (c



**Figure 5.** AFM topography images of the AgNPs (a–c) and cross sections of the blue dotted lines in the topography image (d–f) before (a, d) after fabricating the AgNP dimer (b, e) and after fabricating the AgNP trimer (c, f). (g) Distribution of the centroid positions of the SERS spot from the AgNP trimer obtained by fitting each image frame using the PSF in eq 1. The scale bars in images a–c indicate 300 nm.

and f) fabrication of the AgNP trimer via AFM manipulation. To fabricate the AgNP trimer, an AgNP with a height of 54 nm, shown in the lower right region (blue circle) of the AFM image, was pushed to an AgNP with a height of 34 nm, shown by an arrow in the upper right region in Figure 5a. Thus, an AgNP dimer (red circle) was fabricated, as shown in Figure 5b. The height of the fabricated AgNP dimer was estimated to be 80 nm, which was almost the sum of the two AgNPs (Figure 5d and e). This increase in height indicated that the AgNPs were

stacked. To fabricate the AgNP trimer, another AgNP with a height of 34 nm, shown in the upper left region (green circle), was pushed to the AgNP dimer, shown by an arrow in Figure 5b. Finally, the AgNP trimer was fabricated, as shown in Figure 5c. The height of the fabricated AgNP trimer was estimated to be 135 nm (Figure 5f), indicating that the three AgNPs were stacked in the vertical direction of the *x*–*y* plane. The distribution of the centroid positions of the SERS spot of the AgNP trimer is shown in Figure 5g. Because the AgNP trimer is aligned in the *x*–*y* plane, the two distributions of the centroid positions of SERS spot should be fully separated, as the distribution of the centroid positions was considerably smaller than the size of an AgNP, as indicated by the result of the AgNP dimer. For the present AgNP trimer, the distribution of the centroid positions was not separated in the *x*–*y* plane, which was caused by the AgNPs being stacked in the vertical direction, as shown in the AFM image in Figure 5c. Hence, because the hot spots overlapped in the *x*–*y* projection, a single distribution of the centroid positions was observed, as shown in Figure 5g. The distribution was estimated to be 8 nm along the *x*-axis and 16 nm along the *y*-axis. The distribution of the centroid positions was larger than that of AgNP dimer (Figure 3b). Interestingly, the obtained distribution of the centroid positions showed that the length of the *y*-axis was longer than that of the *x*-axis. For the AgNP dimer, the length of the *x*-axis was longer than that of the *y*-axis. Hence, the AgNP trimer would tilt in the *y*-axis direction. The hot spots were not fully overlapped in the *x*–*y* projection. Therefore, the distribution of the centroid positions was observed as a single spot and was larger than that of the AgNP dimer. From these results, the distribution and location of the hot spot strongly depend on the morphology of the MNP aggregates, as determined by the combination of AFM manipulation and the super-resolution imaging.

## CONCLUSIONS

The SERS spots of AgNP dimers and trimers with 4,4'-bipyridine fabricated by AFM manipulation were observed in situ, and the distributions of the centroid positions of the SERS spots were estimated by super-resolution imaging. The distribution of the centroids on the AgNP dimer was larger than the spatial resolution of our measurement set up. The distribution of the centroid positions was attributed to the thermal diffusion of 4,4'-bipyridine at the hot spot, and the thermal diffusion was confirmed through the observation of the blinking behavior of SERS. For the AgNP trimer, the distribution of the centroid positions was generated at one location and was larger than that of the AgNP dimer. The single distribution of the centroid positions resulted from the stacking of the three AgNPs in the vertical direction of the *x*–*y* plane and the overlapping of the hot spots in the *x*–*y* projection. Therefore, the size and location of a hot spot can be observed by AFM and super-resolution imaging using AFM manipulation. The direct observation of SERS obtained by the combination of AFM manipulation and super-resolution imaging provides further understanding of the generation of SERS hot spots.

## ASSOCIATED CONTENT

### Supporting Information

The Supporting Information is available free of charge on the ACS Publications website at DOI: 10.1021/acs.jpcc.7b03709.

Super-resolution imaging through point spread function fitting and numerical simulation of the AgNP dimer (PDF)

Movie of the in situ observation of SERS from an AgNP dimer fabricated using AFM manipulation (AVI)

## AUTHOR INFORMATION

### Corresponding Author

\*E-mail: masuo@kwansei.ac.jp.

### ORCID

Sadahiro Masuo: 0000-0003-4828-5968

### Notes

The authors declare no competing financial interest.

## ACKNOWLEDGMENTS

We thank Dr. Li Wang and Prof. Naoto Tamai (Department of Chemistry, Kwansai Gakuin University) for the numerical simulation of AgNPs. This work was partly supported by a Grant-in-Aid for Scientific Research (No. 26390023) from the Japan Society for the Promotion of Science (JSPS) and a Grant-in-Aid for Scientific Research on Innovation Areas "Photosynergetics" (No. 26107005) from MEXT, Japan.

## REFERENCES

- (1) Lane, L. A.; Qian, X.; Nie, S. SERS Nanoparticles in Medicine: From Label-Free Detection to Spectroscopic Tagging. *Chem. Rev.* **2015**, *115*, 10489–10529.
- (2) Song, J.; Huang, P.; Duan, H.; Chen, X. Plasmonic Vesicles of Amphiphilic Nanocrystals: Optically Active Multifunctional Platform for Cancer Diagnosis and Therapy. *Acc. Chem. Res.* **2015**, *48*, 2506–2515.
- (3) Driscoll, A. J.; Harpster, M. H.; Johnson, P. A. The Development of Surface-Enhanced Raman Scattering as a Detection Modality for Portable in Vitro Diagnostics: Progress and Challenges. *Phys. Chem. Chem. Phys.* **2013**, *15*, 20415–20433.
- (4) Schlucker, S. Surface-Enhanced Raman Spectroscopy: Concepts and Chemical Applications. *Angew. Chem., Int. Ed.* **2014**, *53*, 4756–4795.
- (5) Radziuk, D.; Moehwald, H. Prospects for Plasmonic Hot Spots in Single Molecule SERS Towards the Chemical Imaging of Live Cells. *Phys. Chem. Chem. Phys.* **2015**, *17*, 21072–21093.
- (6) Halvorson, R.; Vikesland, P. Surface-Enhanced Raman Spectroscopy (SERS) for Environmental Analyses. *Environ. Sci. Technol.* **2010**, *44*, 7749–7755.
- (7) Yoshida, K.; Itoh, T.; Tamaru, H.; Biju, V.; Ishikawa, M.; Ozaki, Y. Quantitative Evaluation of Electromagnetic Enhancement in Surface-Enhanced Resonance Raman Scattering from Plasmonic Properties and Morphologies of Individual Ag Nanostructures. *Phys. Rev. B: Condens. Matter Mater. Phys.* **2010**, *81*, 115406.
- (8) Weber, M. L.; Willets, K. A. Nanoscale Studies of Plasmonic Hot Spots Using Super-Resolution Optical Imaging. *MRS Bull.* **2012**, *37*, 745–751.
- (9) Willets, K. A. Super-Resolution Imaging of SERS Hot Spots. *Chem. Soc. Rev.* **2014**, *43*, 3854–3864.
- (10) Yamamoto, Y. S.; Itoh, T. Why and How Do the Shapes of Surface-Enhanced Raman Scattering Spectra Change? Recent Progress from Mechanistic Studies. *J. Raman Spectrosc.* **2016**, *47*, 78–88.
- (11) Campion, A.; Kambhampati, P. Surface-Enhanced Raman Scattering. *Chem. Soc. Rev.* **1998**, *27*, 241–250.
- (12) Yamamoto, Y. S.; Ishikawa, M.; Ozaki, Y.; Itoh, T. Fundamental Studies on Enhancement and Blinking Mechanism of Surface-Enhanced Raman Scattering (SERS) and Basic Applications of SERS Biological Sensing. *Front. Phys.* **2014**, *9*, 31–46.
- (13) Jensen, L.; Aikens, C. M.; Schatz, G. C. Electronic Structure Methods for Studying Surface-Enhanced Raman Scattering. *Chem. Soc. Rev.* **2008**, *37*, 1061–1073.
- (14) Morton, S. M.; Silverstein, D. W.; Jensen, L. Theoretical Studies of Plasmonics Using Electronic Structure Methods. *Chem. Rev.* **2011**, *111*, 3962–3994.
- (15) Stranahan, S. M.; Willets, K. A. Super-Resolution Optical Imaging of Single-Molecule SERS Hot Spots. *Nano Lett.* **2010**, *10*, 3777–3784.
- (16) Stranahan, S. M.; Titus, E. J.; Willets, K. A. SERS Orientational Imaging of Silver Nanoparticle Dimers. *J. Phys. Chem. Lett.* **2011**, *2*, 2711–2715.
- (17) Titus, E. J.; Weber, M. L.; Stranahan, S. M.; Willets, K. A. Super-Resolution SERS Imaging Beyond the Single-Molecule Limit: An Isotope-Edited Approach. *Nano Lett.* **2012**, *12*, 5103–5110.
- (18) Blythe, K. L.; Titus, E. J.; Willets, K. A. Objective-Induced Point Spread Function Aberrations and Their Impact on Super-Resolution Microscopy. *Anal. Chem.* **2015**, *87*, 6419–6424.
- (19) Tong, L.; Li, Z.; Zhu, T.; Xu, H.; Liu, Z. Single Gold-Nanoparticle-Enhanced Raman Scattering of Individual Single-Walled Carbon Nanotubes Via Atomic Force Microscope Manipulation. *J. Phys. Chem. C* **2008**, *112*, 7119–7123.
- (20) Tong, L.; Zhu, T.; Liu, Z. Atomic Force Microscope Manipulation of Gold Nanoparticles for Controlled Raman Enhancement. *Appl. Phys. Lett.* **2008**, *92*, 023109.
- (21) Masuo, S.; Kanetaka, K.; Sato, R.; Teranishi, T. Direct Observation of Multiphoton Emission Enhancement from a Single Quantum Dot Using Afm Manipulation of a Cubic Gold Nanoparticle. *ACS Photonics* **2016**, *3*, 109–116.
- (22) Akyüz, S.; Akyüz, T.; Dames, J. E. D. A Fourier-Transform Infrared and Laser-Raman Spectroscopic Investigation of 4,4'-Bipyridyl-Transition Metal (II) Tetracyanonickelate Clathrates. *J. Inclusion Phenom. Mol. Recognit. Chem.* **1996**, *26*, 111–117.
- (23) Muniz-Miranda, M. Surface Enhanced Raman Scattering of 4,4'-Bipyridine Adsorbed on Smooth Copper, Silver and Aluminium Surfaces Activated by Deposited Silver Particles. *J. Raman Spectrosc.* **1996**, *27*, 435–437.
- (24) Ould-Moussa, L.; Poizat, O.; Castellà-Ventura, M.; Buntinx, G.; Kassab, E. Ab Initio Computations of the Geometrical, Electronic, and Vibrational Properties of the Ground State, the Anion Radical, and the N,N'-Dihydro Cation Radical of 4,4'-Bipyridine Compared to Transient Raman Spectra. *J. Phys. Chem.* **1996**, *100*, 2072–2082.
- (25) Lim, J. K.; Joo, S.-K. Excitation-Wavelength Dependent Charge Transfer Resonance of Bipyridines on Silver Nanoparticles: Surface-Enhanced Raman Scattering Study. *Surf. Interface Anal.* **2007**, *39*, 684–690.
- (26) Sawai, Y.; Takimoto, B.; Nabika, H.; Ajito, K.; Murakoshi, K. Observation of a Small Number of Molecules at a Metal Nanogap Arrayed on a Solid Surface Using Surface-Enhanced Raman Scattering. *J. Am. Chem. Soc.* **2007**, *129*, 1658–1662.
- (27) Nagasawa, F.; Takase, M.; Nabika, H.; Murakoshi, K. Polarization Characteristics of Surface-Enhanced Raman Scattering from a Small Number of Molecules at the Gap of a Metal Nano-Dimer. *Chem. Commun.* **2011**, *47*, 4514–4516.
- (28) Kitahama, Y.; Tanaka, Y.; Itoh, T.; Ozaki, Y. Power-Law Analysis of Surface-Plasmon-Enhanced Electromagnetic Field Dependence of Blinking SERS of Thiocyanine or Thiocarbocyanine Adsorbed on Single Silver Nanoaggregates. *Phys. Chem. Chem. Phys.* **2011**, *13*, 7439–7448.
- (29) Itoh, T.; Biju, V.; Ishikawa, M. Surface-Enhanced Resonance Raman Scattering and Background Light Emission Coupled with Plasmon of Single Silver Nanoaggregates. *J. Chem. Phys.* **2006**, *124*, 134708.

Cite this: *J. Mater. Chem. A*, 2017, 5, 14003

## Side-chain engineering in a thermal precursor approach for efficient photocurrent generation†

Kohtaro Takahashi,<sup>a</sup> Daichi Kumagai,<sup>b</sup> Naoya Yamada,<sup>b</sup> Daiki Kuzuhara,<sup>a</sup> Yuji Yamaguchi,<sup>b</sup> Naoki Aratani,<sup>a</sup> Tomoyuki Koganezawa,<sup>c</sup> Sota Koshika,<sup>d</sup> Noriyuki Yoshimoto,<sup>d</sup> Sadahiro Masuo,<sup>e</sup> Mitsuharu Suzuki,<sup>a\*</sup> Ken-ichi Nakayama<sup>\*bf</sup> and Hiroko Yamada<sup>a\*</sup>

An ideal active-layer compound for bulk-heterojunction (BHJ) organic photovoltaic devices (OPVs) can assemble upon deposition to form the effective  $\pi$ - $\pi$  stacking that facilitates exciton diffusion and charge-carrier transport. It is also expected to possess high-enough miscibility for forming sufficient heterojunctions to ensure efficient charge separation. However, these characteristics are often not compatible in organic small-molecule semiconductors: compounds endowed with rich self- $\pi$ - $\pi$  interaction capacity tend to be poor in miscibility, or maybe even insoluble in extreme cases. Herein, we postulate that a thermal precursor approach can serve as a way out of this dilemma, provided that molecules are properly engineered. This work evaluates a series of diketopyrrolopyrrole (DPP)-tetrabenzoporphyrin (BP) conjugates named  $C_n$ -DPP-BP ( $n = 4, 6, 8$  or  $10$  depending on the length of alkyl groups on the DPP unit) as a p-type material in BHJ OPVs. These compounds are strongly aggregating and insoluble, thus processed *via* the thermal precursor approach in which the corresponding soluble derivatives ( $C_n$ -DPP-CP) are solution-processed into thin films and then converted to the target materials by *in situ* thermal reactions. The comparative study shows that the short-circuit current density largely depends on the length of alkyl substituents, ranging from  $0.88 \text{ mA cm}^{-2}$  with C10-DPP-BP to  $15.2 \text{ mA cm}^{-2}$  with C4-DPP-BP. Investigation into the structure of active layers through fluorescence-decay analysis, atomic-force microscopy, and two-dimensional grazing-incidence wide-angle X-ray diffractometry indicates that the introduction of shorter alkyl chains positively affects the miscibility and molecular orientation in BHJ layers. This trend is not fully parallel to those observed in the BHJ systems prepared through conventional solution techniques, and will provide a unique basis for devising a new class of high-performance OPV materials.

Received 13th May 2017  
Accepted 31st May 2017

DOI: 10.1039/c7ta04162d

rsc.li/materials-a

## 1. Introduction

The photon-to-electron conversion process in organic photovoltaic devices (OPVs) is accomplished by the synergetic actions of multiple materials.<sup>1</sup> The design of OPV materials is therefore multilateral, requiring careful consideration of the balance among various aspects of the overall photovoltaic process. For

instance, strong  $\pi$ - $\pi$  interaction is favourable in terms of facilitating exciton diffusion and charge-carrier transport, while it may also lead to excessive aggregation and phase separation which limit charge separation by reducing the heterojunction.<sup>2-6</sup> Accordingly, the compromise between efficient self-interaction and sufficient miscibility is often a critical factor in designing active-layer materials for OPVs.

On the other hand, precursor approaches provide unique opportunities in the engineering of small-molecule OPV materials.<sup>7-15</sup> In the preparation of small-molecule thin films by precursor approaches, soluble precursor compounds are solution-processed into the thin-film form and then converted to target materials by quantitative *in situ* chemical reactions. A typical example is the preparation of tetrabenzoporphyrin (BP) thin films. BP is an insoluble p-type semiconductor, while its thermal precursor 1,4:8,11:15,18:22,25-tetraethano-29H,31H-tetrabenzob[*b,g,l,q*]porphyrin (CP) is well soluble. Thus, thin films of BP can be prepared in a stepwise manner where CP is solution-deposited then thermally converted to BP.<sup>16-24</sup> By taking advantage of such precursor approaches, it is possible to

<sup>a</sup>Graduate School of Materials Science, Nara Institute of Science and Technology (NAIST), Ikoma, Japan. E-mail: hyamada@ms.naist.jp

<sup>b</sup>Department of Organic Device Engineering, Yamagata University, Yonezawa, Japan  
<sup>c</sup>Japan Synchrotron Radiation Research Institute (JASRI), SPring-8, Sayo, Japan

<sup>d</sup>Graduate School of Engineering, Iwate University, Morioka, Japan

<sup>e</sup>Department of Applied Chemistry for Environment, Kansai Gakuin University, Sanda, Japan

<sup>f</sup>Department of Material and Life Science, Osaka University, Suita, Japan

† Electronic supplementary information (ESI) available: Supplementary figures and tables, experimental details, UV-vis absorption spectra and <sup>1</sup>H and <sup>13</sup>C NMR spectra. CCDC for the crystal structure of C6-DPP-BP is 1491998. For ESI and crystallographic data in CIF or other electronic format see DOI: 10.1039/c7ta04162d

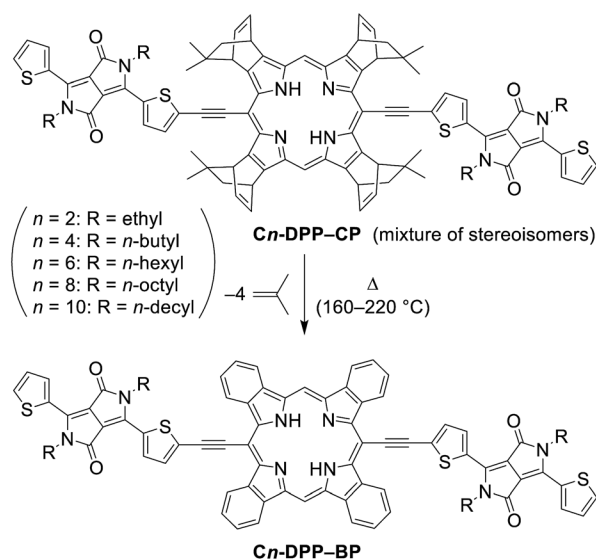
obtain well-performing small-molecule photovoltaic layers comprising highly crystalline, aggregating molecular semiconductors without sacrificing their intermolecular contacts. Matsuo *et al.* indeed employed the CP-to-BP conversion in the 2009 paper for preparing p-i-n-type organic photovoltaic layers having highly ordered crystalline nanophases that afforded a power-conversion efficiency (PCE) of 5.2%.<sup>20</sup> This was achieved by employing a specially designed n-type material named SIMEF, as well as carefully optimized thermal-annealing conditions and cathode buffer material. Notably, the 5.2% PCE was among the best achieved in small-molecule OPVs at that time, and still remains one of the highest reported for the OPVs having BP or its derivative in the active layer.

Meanwhile, the current state-of-the-art devices have achieved PCEs of over 10%,<sup>4,25–30</sup> and many research groups are working toward even higher efficiencies in order to realize practical applications of OPVs. Along these lines, we have envisioned that high-performance OPVs may be obtained by further exploiting the superior traits of BP (*e.g.*, high absorption coefficient,<sup>31</sup> good hole transport capability,<sup>32,33</sup> and exceptional stability<sup>34,35</sup>) in combination with the use of the thermal precursor approach for active-layer deposition.

A key task in this context is the enhancement of photocurrent-generation efficiency. BP has strong but rather narrow absorption bands, being transparent around 500–600 nm and over 700 nm.<sup>20,36</sup> In consequence of this limited photoabsorption window, short-circuit current density ( $J_{SC}$ ) values of BP-based OPVs have been relatively low; for instance, the p-i-n system reported by Matsuo *et al.* showed a  $J_{SC}$  of 10.5 mA cm<sup>-2</sup> at the maximum,<sup>20</sup> while the current-best cells typically afford  $J_{SC}$ s of 15–20 mA cm<sup>-2</sup>.<sup>4,25–30</sup> Thus, expansion of the absorption range is a primary factor in designing  $\pi$ -conjugated frameworks of BP-based photoabsorbers. Another important factor in improving  $J_{SC}$  is the substituent effect. It is well known that the photovoltaic performance of organic semiconductors largely depends not only on the structure of the main  $\pi$ -framework, but also on the structure and position of peripheral substituents. For instance, Shin *et al.* reported that the structural difference of alkyl chains on a diketopyrrolopyrrole (DPP)-based small-molecule system brought about a considerable variation in  $J_{SC}$  ranging from below 4 to over 8 mA cm<sup>-2</sup> and accordingly in PCE from 1.1 to 4.2%.<sup>37</sup> This and many other examples have demonstrated the strong impact of substituents on the charge-carrier generation and transport efficiencies in organic photovoltaic layers.<sup>37–40</sup>

With these in mind, we have designed a series of DPP-BP conjugates that can efficiently absorb at a wide range of wavelengths in the visible and near-infrared regions. These conjugates have linear alkyl chains on the DPP units, and are denoted as *C<sub>n</sub>*-DPP-BP in which *n* is either 2, 4, 6, 8, or 10 depending on the length of alkyl chains. *C<sub>n</sub>*-DPP-BPs are all insoluble in common organic solvents, and thus solution-deposited *via* the thermal precursor approach from the corresponding CP derivatives (Scheme 1).

The following sections compare bulk-heterojunction (BHJ) OPVs comprising *C<sub>n</sub>*-DPP-BP and [6,6]-phenyl-C<sub>61</sub>-butyric acid methyl ester (PC<sub>61</sub>BM), and reveal that the length of alkyl chains



Scheme 1 Formation of *C<sub>n</sub>*-DPP-BPs from the corresponding thermal precursors *C<sub>n</sub>*-DPP-CPs.

greatly affects the performance of the resulting devices. The  $J_{SC}$  ranges from 0.88 mA cm<sup>-2</sup> with C10-DPP-BP to 15.2 mA cm<sup>-2</sup> with C4-DPP-BP, resulting in PCEs of 0.19 and 5.2%, respectively. The origin of this large substituent impact is discussed based on analyses of the active layers by fluorescence decay measurements, atomic-force microscopy (AFM), and two-dimensional grazing-incidence wide-angle X-ray diffractometry (2D-GIWAXD). It is shown that the introduction of shorter alkyl chains suppresses the propensity of *C<sub>n</sub>*-DPP-BP molecules to form large aggregates and to adopt edge-on-mode geometry, which positively affects the photocurrent-generation efficiency in BHJ films. These results would provide a basis for molecular design in the thermal precursor approach toward preparing photovoltaic active layers with ideal morphology.

## 2. Results and discussion

### 2.1. Molecular design and synthesis

*C<sub>n</sub>*-DPP-BPs have an acceptor–donor–acceptor (A–D–A) structure in which BP and DPP serve as donor and acceptor units, respectively. The A–D–A configuration has been a widely employed molecular design to achieve desirable frontier-orbital energy levels and effective  $\pi$ -conjugation in state-of-the-art active-layer compounds for OPVs.<sup>41</sup> The DPP chromophore is chosen as the partner of BP, because DPP strongly absorbs around 550 nm at which BP's absorption valley is located.<sup>42</sup> The BP and DPP units are connected through the sterically non-demanding ethynylene linkage in order to minimize the steric hindrance between the benzo moieties and the *meso* substituents of BP. The geometry optimization by density functional theory (DFT) has predicted that *C<sub>n</sub>*-DPP-BPs possess relatively planar molecular conformations associated with efficient  $\pi$ -conjugation (Fig. S1, ESI†). A related molecular design has been employed for soluble small-molecule photoabsorbers based on the non-benzoannulated zinc porphyrin chromophore.<sup>43,44</sup>

The peripheral substituents of *C<sub>n</sub>*-DPP-BPs are kept minimal, namely, each molecule is equipped with only four linear, relatively short alkyl chains at the nitrogen atoms of DPP moieties. Accordingly, *C<sub>n</sub>*-DPP-BPs are all insoluble in common organic solvents. This molecular design is made possible by employing the precursor approach and is beneficial in that such large  $\pi$ -systems as *C<sub>n</sub>*-DPP-BPs do not require the heavy decoration with insulating solubilizing groups that are unnecessary in terms of the optimization of thin-film morphology and molecular packing.

The corresponding precursors *C<sub>n</sub>*-DPP-CPs have four dimethylethano bridges as thermally removable solubilizing units in order to ensure the sufficient solubility for synthesis and solution deposition.<sup>16,45,46</sup> Note that the original CP has four non-methylated ethano bridges which are often insufficient for solubilizing  $\pi$ -extended BP derivatives.

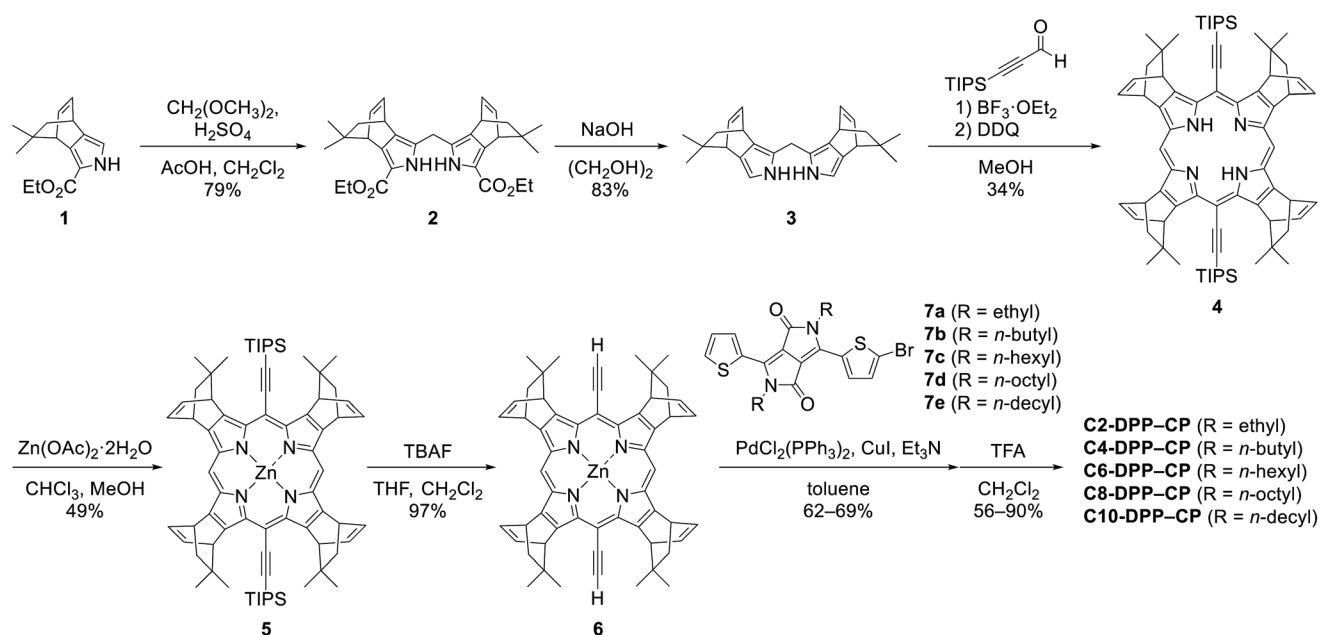
The synthesis of *C<sub>n</sub>*-DPP-CPs is summarized in Scheme 2. Pyrrole **1** was prepared according to the literature,<sup>46</sup> which was then subjected to the double condensation with dimethoxymethane and hydrolytic decarboxylation to form dipyrromethane **2**. The "2 + 2"-type MacDonald condensation of **2** with 3-triisopropylsilyl-2-propynal in the presence of  $\text{BF}_3 \cdot \text{OEt}_2$ <sup>47,48</sup> followed by the oxidation with 2,3-dichloro-5,6-dicyano-1,4-benzoquinone (DDQ) afforded porphyrin **4** in 34% yield. Here, while five diastereomers can possibly form depending on the relative orientation of the four dimethylethano bridges against the porphyrin plane, a mixture of only two diastereomers was used in the following step (see the synthesis procedure, ESI†). After insertion of a zinc(II) ion, the triisopropylsilyl (TIPS) groups were removed by the action of tetrabutylammonium fluoride (TBAF) to afford porphyrin **6**. The target thermal precursors *C<sub>n</sub>*-DPP-CPs were obtained by the Sonogashira coupling of zinc porphyrin **6** with brominated DPP derivatives **7a–7e**,<sup>49</sup> and the dezincification with trifluoroacetic acid.

The proper connectivity among the CP, DPP, and ethynylene units was confirmed by single-crystal X-ray diffraction analysis of C6-DPP-CP (Fig. S2 and Table S1, ESI†). The torsion angles between the porphyrin and DPP planes in the crystal structure are 10° and 17°. Similar planarity can be expected for *C<sub>n</sub>*-DPP-BPs after the thermal conversion, because the steric hindrance between the central porphyrin core and side units should not be much different before and after the extrusion of isobutylene units. Thermogravimetric traces of *C<sub>n</sub>*-DPP-CPs show that the thermally induced retro-Diels–Alder reactions to *C<sub>n</sub>*-DPP-BPs start around 130–140 °C (Fig. S3, ESI†).

## 2.2. Optical and electronic properties

The optical absorption spectra of thin films of BP and *C<sub>n</sub>*-DPP-BP are compared in Fig. 1. BP shows strong absorptions around 400 and 700 nm corresponding to the Soret and Q bands, respectively, while the absorption between these bands is weak and the absorption extends to merely about 720 nm. On the other hand, *C<sub>n</sub>*-DPP-BPs generally show broader absorption than BP with absorption edge wavelengths reaching well beyond 800 nm. The locations of absorption edges are slightly different among *C<sub>n</sub>*-DPP-BPs, indicating that there are minor differences in solid-state molecular arrangement depending on the length of alkyl chains.

The highest occupied molecular orbital (HOMO) levels of *C<sub>n</sub>*-DPP-BPs were determined by photoelectron spectrometry as  $-5.0$  or  $-5.1$  eV (Fig. S4, ESI†). The optical energy gap ( $E_g$ ) values were calculated from the absorption onsets of thin films as 1.44–1.47 eV, and the lowest unoccupied molecular orbital (LUMO) levels were calculated from these values to be  $-3.5$  to  $-3.7$  eV. As summarized in Table 1, the HOMO and LUMO levels of *C<sub>n</sub>*-DPP-BPs are lower than those of BP in the thin-film state by 0.1–0.2 and 0.3–0.5 eV, respectively.<sup>50</sup> Considering the general relationship between the open-circuit voltage ( $V_{oc}$ ) and



Scheme 2 Synthesis of *C<sub>n</sub>*-DPP-CPs. Starting material **1** and all the products were isolated and used as mixtures of stereoisomers.

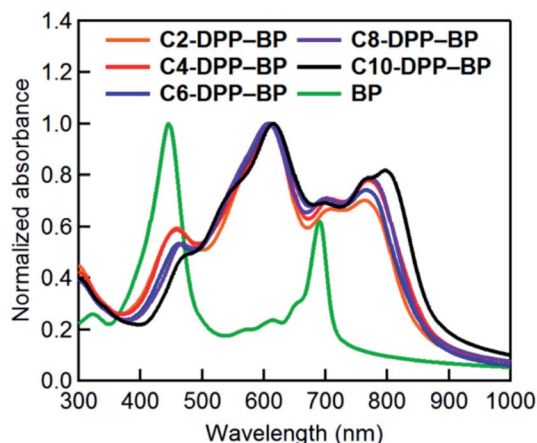


Fig. 1 Absorption spectra of BP and  $C_n$ -DPP-BP thin films.

Table 1 Optical and electronic properties of  $C_n$ -DPP-BPs and BP

Materials <sup>a</sup>	$\lambda_{\text{onset}}$ (nm)	$E_g^b$ (eV)	HOMO <sup>c</sup> (eV)	LUMO <sup>d</sup> (eV)
C2-DPP-BP	846	1.47	-5.0	-3.5
C4-DPP-BP	862	1.44	-5.0	-3.6
C6-DPP-BP	857	1.45	-5.0	-3.6
C8-DPP-BP	855	1.45	-5.0	-3.5
C10-DPP-BP	868	1.43	-5.1	-3.7
BP	716	1.73	-4.9	-3.2

<sup>a</sup> As thin films. <sup>b</sup> Calculated from  $\lambda_{\text{onset}}$ . <sup>c</sup> Determined by photoelectron spectroscopy in air. <sup>d</sup> Calculated as HOMO +  $E_g$ .

the HOMO level of the donor, the  $V_{\text{OC}}$ s of  $C_n$ -DPP-BP:PC<sub>61</sub>BM systems are expected to be higher than that of BP:PC<sub>61</sub>BM.

### 2.3. Photovoltaic performance

BHJ OPVs with a general device structure of [ITO/PEDOT:PSS/ $C_n$ -DPP-BP:PC<sub>61</sub>BM/Ca/Al] were fabricated *via* the thermal precursor approach using  $C_n$ -DPP-CPs as precursors of  $C_n$ -DPP-BPs. The relative amount against PC<sub>61</sub>BM, thermal conversion conditions, and concentration of cast solution were optimized for each  $C_n$ -DPP-BP (Tables S2–S13, ESI<sup>†</sup>). Unfortunately, thin films containing C2-DPP-BP were found too rough to be evaluated for OPV performance (Fig. S5, ESI<sup>†</sup>), thus C2-DPP-BP was not studied further.

The current-density-voltage ( $J$ - $V$ ) curves and external quantum efficiency (EQE) spectra of the best-performing cells are plotted in Fig. 2a and b, and the obtained photovoltaic parameters are summarized in Table 2. The best result was obtained with C4-DPP-BP affording the maximum PCE of 5.2% ( $J_{\text{SC}} = 15.2 \text{ mA cm}^{-2}$ ,  $V_{\text{OC}} = 0.67 \text{ V}$ , FF (fill factor) = 0.52). This efficiency is much higher than those obtained in BP:PC<sub>61</sub>BM and BP:PCBNB ( $\leq 0.1\%$ , PCBNB: [6,6]-phenyl-C<sub>61</sub>-butyric acid *n*-butyl ether).<sup>5,50</sup> Moreover, the 5.2% PCE is close to the best efficiencies reported so far for BP-based OPVs (5.2–5.4%) that have been achieved by using the specially designed n-type materials SIMEF<sup>20</sup> and (*o*-anisylsilylmethyl)(phenyl-silylmethyl)

[60]fullerene (SIMEF-Ph, *o*-An)<sup>51</sup> in optimized p-i-n-type active layers.

Notably, the  $J_{\text{SC}}$  of  $15.2 \text{ mA cm}^{-2}$  obtained in the C4-DPP-BP:PC<sub>61</sub>BM system is considerably higher than those in the BP:PC<sub>61</sub>BM ( $5.7\text{--}7.0 \text{ mA cm}^{-2}$ )<sup>20,32</sup> and BP:SIMEF systems ( $10.2\text{--}10.5 \text{ mA cm}^{-2}$ ).<sup>20,51</sup> The EQE spectrum shows that the photovoltaic response of the C4-DPP-BP:PC<sub>61</sub>BM device well exceeds 700 nm and reaches 850 nm where pristine BP does not absorb (Fig. 2b). This is apparently owing to the extended  $\pi$ -

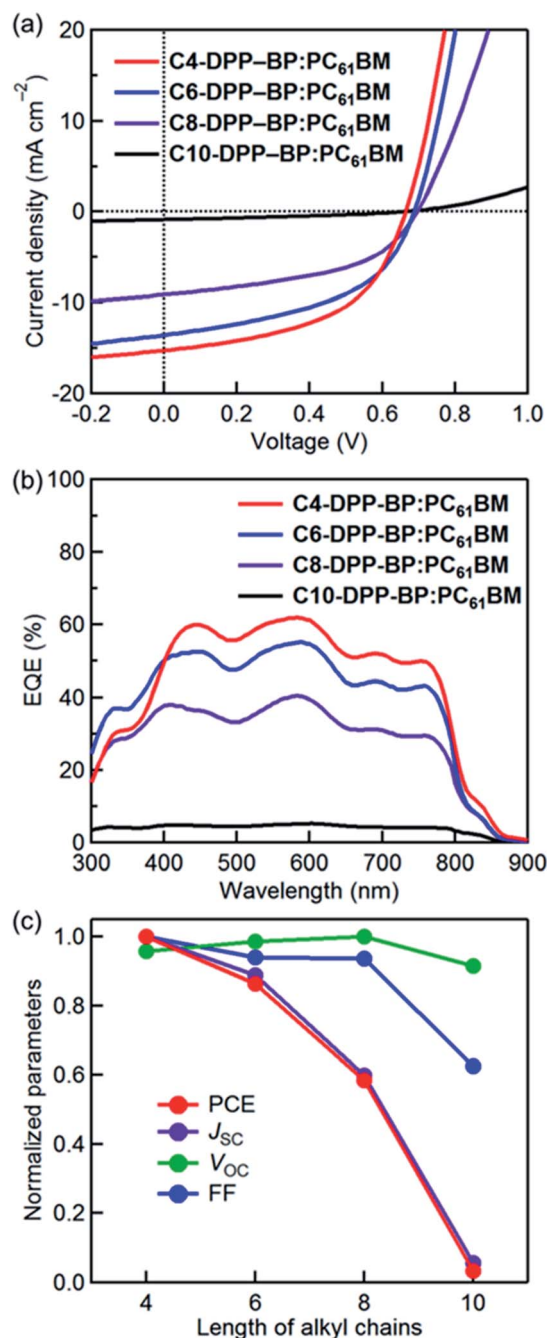


Fig. 2 (a)  $J$ - $V$  curves, (b) EQE spectra, and (c) normalized photovoltaic parameters of the best-performing BHJ cells. Measurements were performed under AM1.5G illumination at  $100 \text{ mW cm}^{-2}$ .

Table 2 Photovoltaic parameters of optimized *Cn*-DPP-BP:PC<sub>61</sub>BM OPVs<sup>a</sup> and hole mobilities in blend films

p-Type material	Thickness <sup>b</sup> (nm)	$J_{SC}$ <sup>c</sup> (mA cm <sup>-2</sup> )	$V_{OC}$ <sup>c</sup> (V)	FF <sup>c</sup>	PCE <sup>c</sup> (%)	PCE <sub>ave</sub> <sup>d</sup> (%)	$\mu_h$ (cm <sup>2</sup> V <sup>-1</sup> s <sup>-1</sup> )
C4-DPP-BP	105	15.2	0.67	0.52	5.2	5.0 ± 0.1	2.2 × 10 <sup>-4</sup>
C6-DPP-BP	115	13.6	0.69	0.49	4.5	4.4 ± 0.1	1.7 × 10 <sup>-4</sup>
C8-DPP-BP	115	9.1	0.70	0.48	3.1	3.0 ± 0.1	1.5 × 10 <sup>-4</sup>
C10-DPP-BP	115	0.88	0.66	0.33	0.19	0.18 ± 0.01	0.60 × 10 <sup>-4</sup>

<sup>a</sup> Obtained under AM1.5G illumination at 100 mW cm<sup>-2</sup>. <sup>b</sup> Active-layer thickness. <sup>c</sup> Parameters of the best-performing cells. <sup>d</sup> Averages and standard deviations of four devices.

conjugation with two DPP units, serving as a major contributing factor to the high  $J_{SC}$ . The  $V_{OC}$  of 0.67 V in the C4-DPP-BP:PC<sub>61</sub>BM system is slightly increased from those in BP:PC<sub>61</sub>BM devices (0.44–0.61 V),<sup>32,52</sup> reflecting the lower HOMO level of C4-DPP-BP (−5.0 eV) than that of BP (−4.9 eV). In addition, the FF of 0.52 is significantly improved from that of a BP:PC<sub>61</sub>BM BHJ device (0.23),<sup>5</sup> which is probably because of the superior morphology in the present case of C4-DPP-BP as compared to pristine BP (see Section 2.4). At the same time, however, the 0.52 FF is still lower as compared to those in the state-of-the-art cells which typically afford FFs around 0.7.<sup>4,25–30</sup> It has been reported that the FF can be improved by employing the p–i–n configuration rather than BHJ as the active-layer structure,<sup>14,50,52</sup> which may also be the case with C4-DPP-BP. This aspect is beyond the scope of the present work of obtaining a well-performing BHJ layer, and will be examined elsewhere.

Fig. 2c shows plots of normalized OPV parameters against the length of alkyl chains. The PCE decreases together with the  $J_{SC}$  as alkyl chains become longer from C4- to C10-DPP-BP, while the  $V_{OC}$  is essentially unchanged among all the four derivatives. The FF is constant around 0.5 with the C4-, C6-, and C8-derivatives, but considerably decreases to 0.33 in the case of C10-DPP-BP. In order to understand the observed dependence on the alkyl-chain length, the charge-transfer efficiency, charge-carrier mobility, and charge-recombination efficiency of each blend film were examined.

The charge-transfer efficiency was evaluated using a picosecond-pulsed laser excitation at 470 nm followed by the measurement of the average fluorescence lifetime ( $\tau_f$ ) in each BHJ layer (Fig. 3a). The obtained  $\tau_f$  values are smaller with shorter alkyl chains, namely, 0.45 ns for C4-DPP-BP:PC<sub>61</sub>BM, 0.48 ns for C6-DPP-BP:PC<sub>61</sub>BM, 0.54 ns for C8-DPP-BP:PC<sub>61</sub>BM, and 0.70 ns for C10-DPP-BP:PC<sub>61</sub>BM. This result suggests that more effective fluorescence quenching *via* charge separation occurs with shorter alkyl chains.<sup>16,36</sup> In other words, *Cn*-DPP-BPs are more finely mixed with PC<sub>61</sub>BM when the alkyl substituents on the DPP units are shorter.

Next, the hole mobility ( $\mu_h$ ) in each blend film was measured by the space-charge-limited current (SCLC) method in hole-only devices with a general structure of [ITO/PEDOT:PSS/*Cn*-DPP-BP:PC<sub>61</sub>BM/MoO<sub>3</sub>/Al] (Table 2, and Fig. S6, ESI<sup>†</sup>). The organic layers were deposited under the same conditions as those optimized for BHJ OPVs. The measurements have revealed that the  $\mu_h$  increases from 0.60 to 2.2 × 10<sup>-4</sup> cm<sup>2</sup> V<sup>-1</sup> s<sup>-1</sup> as the alkyl substituents become shorter from C10 to C4. Thus, the C4-DPP-BP:PC<sub>61</sub>BM blend is the best in terms of the efficiency of hole

transport toward the anode among the examined systems. Improvement in  $\mu_h$  generally leads to higher  $J_{SC}$  and FF values,<sup>29,44,53</sup> which is also the case for *Cn*-DPP-BP:PC<sub>61</sub>BM.

We then measured the variation in  $J_{SC}$  as a function of illumination intensity to evaluate the charge-recombination characteristics (Fig. 3b).<sup>54,55</sup> In general, the power-law dependence of  $J_{SC}$  upon light intensity is observed for OPVs, namely,  $J_{SC} \propto I^\alpha$  where  $\alpha$  is an exponential factor, and  $\alpha = 1$  indicates the efficient sweep out of carriers prior to recombination. The  $\alpha$  values are high for the C4-, C6-, and C8-DPP-BP:PC<sub>61</sub>BM devices, being 1, 1, and 0.98, respectively. On the other hand, the C10-DPP-BP:PC<sub>61</sub>BM device exhibited an  $\alpha$  of 0.88, suggesting that the bimolecular charge recombination is promoted in this case

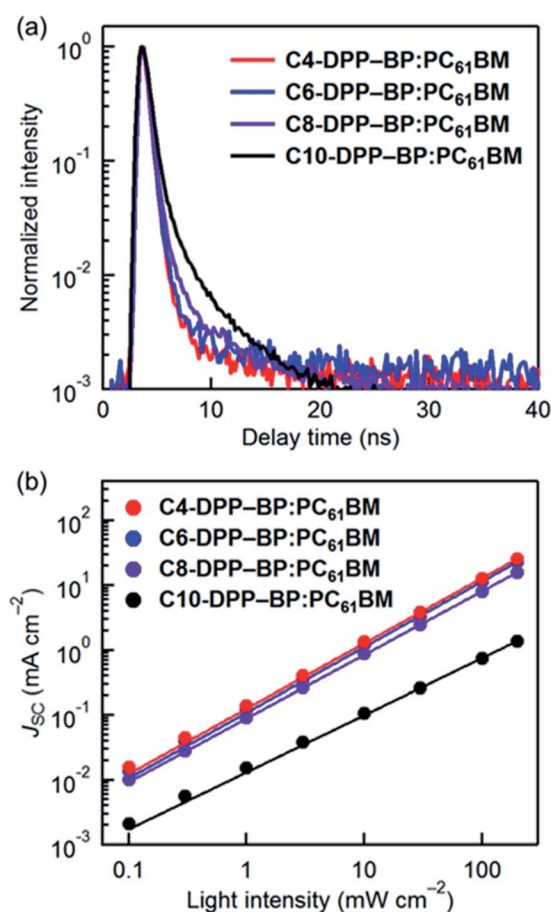


Fig. 3 (a) Fluorescence lifetime decay curves and (b) light-intensity dependency of  $J_{SC}$  for the optimized BHJ OPVs.

compared to other systems with shorter alkyl chains. Thus, the non-geminate charge recombination is suppressed when alkyl groups are shorter.

#### 2.4. Surface morphology

The surface morphologies of *C<sub>n</sub>*-DPP-BP:PC<sub>61</sub>BM films probed by AFM are shown in Fig. 4a–d. Pinholes, which lower the performance and stability of OPVs,<sup>56,57</sup> are noticeable in all the cases, although their depth and appearance frequency are largely dependent on the length of alkyl substituents. The depth of the deepest pinhole in each probed area is about 10, 12, 37, and 34 nm for the C4-, C6-, C8-, and C10-DPP-BP blend films, respectively (Fig. S7, ESI†). Pinholes or cracks are also noticeable in neat films of *C<sub>n</sub>*-DPP-BPs (Fig. S8, ESI†) and other previously reported BP derivatives deposited by the thermal precursor approach.<sup>15</sup> In all these cases, such morphological defects become more prominent when larger alkyl groups are introduced as substituents. These observations suggest that the formation of large structural defects in thin films would be facilitated as molecules become more mobile and easier to rearrange during the thermal conversion process.

We also observed the surface morphology of blend films after rinsing with toluene. Since *C<sub>n</sub>*-DPP-BPs are insoluble in toluene (Fig. S9, ESI†), it is possible to wash away PC<sub>61</sub>BM from the blend films and directly observe the morphology of remaining *C<sub>n</sub>*-DPP-BP domains (Fig. 4e–h).<sup>20,32</sup> Micrometer-sized grains exist in the cases of C8- and C10-DPP-BP, whereas grains are around 100 nm or smaller in the cases of C4- and C6-DPP-BP. These results are in accordance with the above postulation that longer alkyl chains would bring about higher molecular mobility during the thermal conversion process, resulting in more significant self-aggregation and formation of larger domains. Considering that typical exciton diffusion lengths in molecular organic materials are within the range of only a few to tens of nanometers,<sup>58</sup> the grains in C8- and

C10-DPP-BP:PC<sub>61</sub>BM films are too large to allow efficient charge separation.

#### 2.5. Molecular orientation and crystallinity

The molecular arrangement in *C<sub>n</sub>*-DPP-BP neat films and *C<sub>n</sub>*-DPP-BP:PC<sub>61</sub>BP blend films was analysed by 2D-GIWAXD measurements.<sup>59</sup> Fig. 5a–h, i and j show the 2D-GIWAXD images and their out-of-plane profiles, respectively (see Fig. S10, S11, Tables S14 and S15, ESI† for the exact peak positions and the corresponding *d*-spacing values).

The C4- and C6-DPP-BP neat films show combinations of a low-wavenumber diffraction in the in-plane direction ( $q_{xy} = 0.48 \text{ \AA}^{-1}$ ,  $d = 13 \text{ \AA}$ ) and a high-wavenumber diffraction in the out-of-plane direction ( $q_z = 1.79 \text{ \AA}^{-1}$ ,  $d = 3.5 \text{ \AA}$ ). The former diffraction roughly corresponds to the edge-to-edge dimension of the BP framework (Fig. S12, ESI†), and the latter to the  $\pi$ - $\pi$  stacking distance. Thus, these pairs of diffraction peaks indicate that molecules of C4- and C6-DPP-BP are arranged in face-on geometries in neat films, which is favourable for the out-of-plane carrier transport in OPVs.<sup>28</sup> The C8-DPP-BP neat film shows arc-shaped diffraction patterns at around  $q = 0.35 \text{ \AA}^{-1}$  ( $d = 18 \text{ \AA}$ ) and  $1.75 \text{ \AA}^{-1}$  ( $3.6 \text{ \AA}$ ) indicating random arrangement of crystallites.<sup>60</sup> A combination of a primary peak in the out-of-plane direction ( $q_z = 0.33 \text{ \AA}^{-1}$ ,  $d = 19 \text{ \AA}$ ) and a peak from the  $\pi$ - $\pi$  stacking in the in-plane direction ( $q_{xy} = 1.74 \text{ \AA}^{-1}$ ,  $d = 3.6 \text{ \AA}$ ) is apparent in the data of C10-DPP-BP neat film, suggesting that C10-DPP-BP molecules stack mainly in the edge-on mode. The C10-DPP-BP neat film also shows higher-order peaks in the out-of-plane direction ( $q_z = 0.65$  and  $0.94 \text{ \AA}^{-1}$ ) indicating a higher crystallinity as compared to the other neat films.

It is noteworthy that the molecular orientation in *C<sub>n</sub>*-DPP-BP neat films drastically changes only by altering the alkyl-chain length. Although the origin of this result is not clear at this moment, one possible factor is the aspect ratio of molecules.

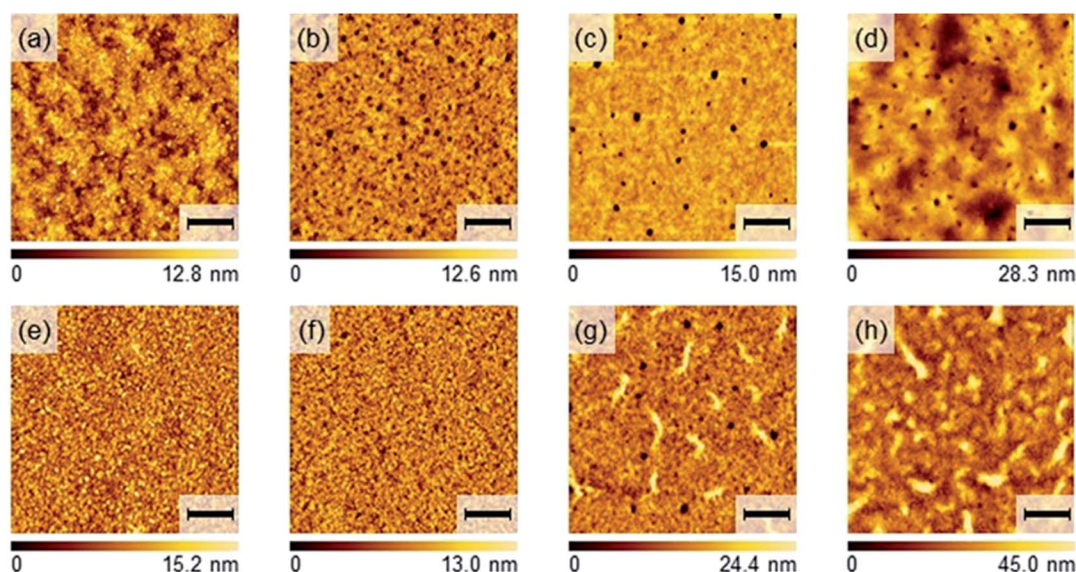


Fig. 4 Tapping-mode AFM images. (a) C4-DPP-BP:PC<sub>61</sub>BM, (b) C6-DPP-BP:PC<sub>61</sub>BM, (c) C8-DPP-BP:PC<sub>61</sub>BM, (d) C10-DPP-BP:PC<sub>61</sub>BM, (e) rinsed C4-DPP-BP:PC<sub>61</sub>BM, (f) rinsed C6-DPP-BP:PC<sub>61</sub>BM, (g) rinsed C8-DPP-BP:PC<sub>61</sub>BM, and (h) rinsed C10-DPP-BP:PC<sub>61</sub>BM. The scale bars correspond to 1  $\mu\text{m}$ .

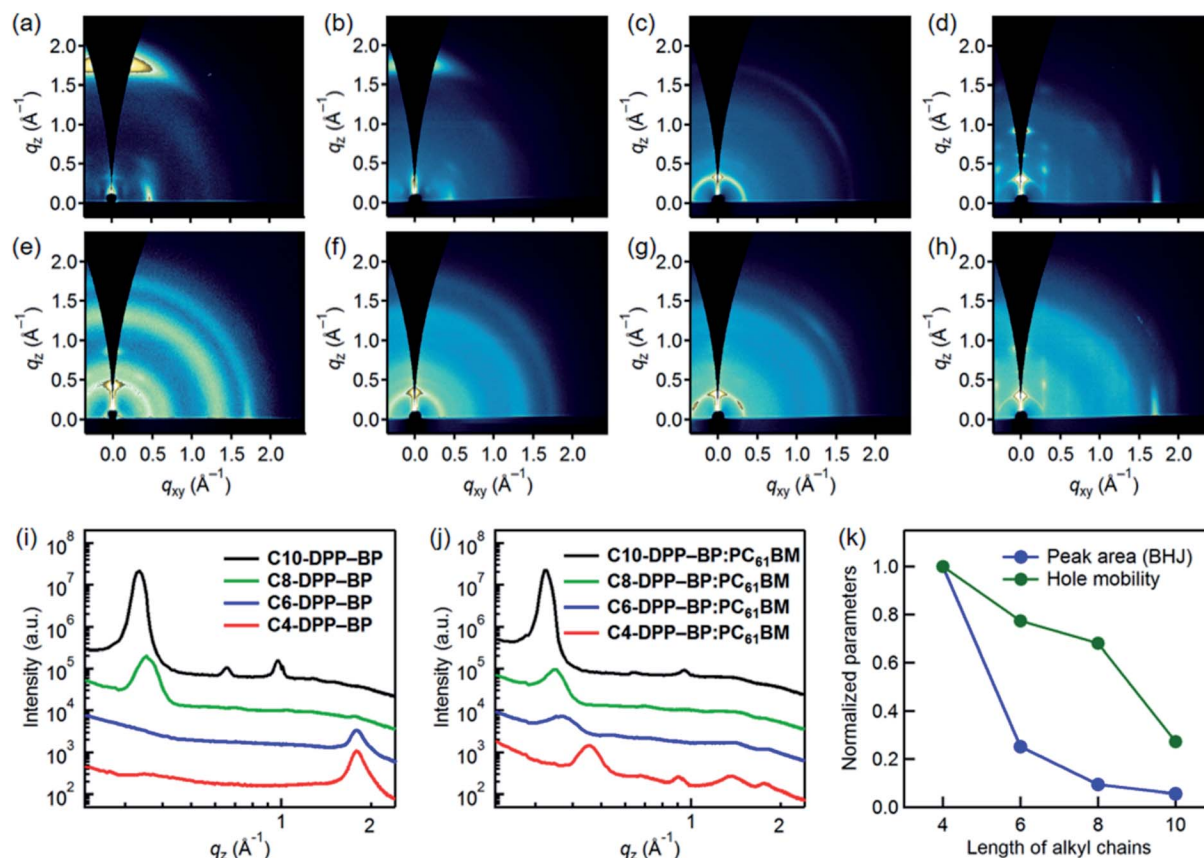


Fig. 5 2D-GIWAXD images of (a) C4-DPP-BP, (b) C6-DPP-BP, (c) C8-DPP-BP, (d) C10-DPP-BP, (e) C4-DPP-BP:PC<sub>61</sub>BM, (f) C6-DPP-BP:PC<sub>61</sub>BM, (g) C8-DPP-BP:PC<sub>61</sub>BM, (h) C10-DPP-BP:PC<sub>61</sub>BM; out-of-plane profiles of 2D-GIWAXD images of (i) the  $C_n$ -DPP-BP neat films and (j) the  $C_n$ -DPP-BP:PC<sub>61</sub>BM blend films; and (k) correlation of peak areas in out-of-plane profiles and hole mobilities in blend films with the alkyl-chain length.

The aspect ratio of  $C_n$ -DPP-BP molecules with extended alkyl chains increases from C10-DPP-BP to C4-DPP-BP (Fig. S13, ESI<sup>†</sup>), and the molecular orientation changes from edge-on to face-on as the ratio increases. Similar trends have been reported with solution-processable small molecules by Chen *et al.*<sup>29,61</sup> and Bazan *et al.*<sup>62,63</sup> In these reports, the molecular orientation in neat films changes from edge-on to face-on upon increasing the longer axis of molecules and thus the aspect ratio (Fig. S14 and S15, ESI<sup>†</sup>).

On the other hand, the edge-on orientation was found to be a preferred molecular arrangement regardless of the alkyl-chain length in the blend films (Fig. 5e-h). The diffraction pattern of the C10-DPP-BP:PC<sub>61</sub>BM film is very similar to that of the C10-DPP-BP neat film, demonstrating that C10-DPP-BP molecules take the edge-on geometry with high selectivity in the blend film as well (Fig. 5h, S10d and S11d, ESI<sup>†</sup>). Thus, the out-of-plane carrier transport should be inefficient in the C10-DPP-BP:PC<sub>61</sub>BM blend, which is reflected in the low  $J_{SC}$  and FF in the corresponding OPVs.<sup>64</sup> In the case of C8-DPP-BP:PC<sub>61</sub>BM, a relatively strong  $\pi$ - $\pi$  stacking peak ( $q = 1.74 \text{ \AA}^{-1}$ ,  $d = 3.61 \text{ \AA}$ ) is observed at  $20$ - $60^\circ$  from the  $q_{xy}$  axis, indicating that the effective charge-carrier paths based on C8-DPP-BP molecules point diagonally to the substrates (Fig. S16, ESI<sup>†</sup>). This orientation is less favourable for the charge extraction in OPVs than the exact face-on

orientation but would be better than the edge-on orientation. The  $\pi$ - $\pi$  stacking diffraction from the C6-DPP-BP:PC<sub>61</sub>BM film is arc-shaped, thus the charge-carrier transport *via* C6-DPP-BP molecules does not have a preferred orientation in this blend film. This type of molecular arrangement is often observed in efficient small-molecule BHJ OPVs.<sup>29,43</sup> The diffraction pattern of the C4-DPP-BP:PC<sub>61</sub>BM film is similar to that of the C6-DPP-BP:PC<sub>61</sub>BM film, while the diffraction intensity is higher for the former. The observed molecular arrangements in the blend films seem to be more or less reflecting those of  $C_n$ -DPP-BP neat films in which a derivative with shorter alkyl chains shows a stronger tendency to adopt the face-on geometry.

We then calculated the peak areas corresponding to the  $\pi$ - $\pi$  stacking of  $C_n$ -DPP-BP molecules in the out-of-plane direction in order to compare the populations of effective charge-carrier paths among the  $C_n$ -DPP-BP:PC<sub>61</sub>BM films. Note that the peak area serves as a relative measure of the crystallite volume within thin films.<sup>65</sup> The values were obtained by applying the Gaussian fitting to the out-of-plane profiles of 2D-GIWAXD images (Fig. S17, ESI<sup>†</sup>),<sup>66</sup> and found to increase as the alkyl-chain length decreases. The SCLC hole mobility roughly follows this trend (Fig. 5k), well demonstrating the positive impact of face-on stacking on the charge-carrier transport and thus  $J_{SC}$  and FF in OPVs.

### 3. Conclusions

This study has explored the side-chain effect on the photovoltaic performance of a series of small-molecule BHJ thin films prepared *via* the thermal precursor approach. The systematic evaluation of *Cn*-DPP-BP:PC<sub>61</sub>BM systems showed that the length of alkyl chains on *Cn*-DPP-BP molecules strongly influenced the efficiency of the resulting OPVs, namely, the PCE improved from 0.19 to 5.2% as the alkyl chains became shorter from *n*-decyl (C10) to *n*-butyl (C4). A large part of this change could be ascribed to  $J_{SC}$  that increased from 0.88 to 15.2 mA cm<sup>-2</sup>. The analyses of thin film properties confirmed that the best-performing compound C4-DPP-BP was superior to the longer-alkyl-chain derivatives in terms of both the charge-carrier generation and transport efficiencies owing to the more preferable morphology and  $\pi$ - $\pi$ -stacking orientation in the BHJ layer. On the other hand, the worst-performing derivative C10-DPP-BP formed extremely large aggregates and adopted the edge-on geometry in high selectivity, which would both adversely affect the charge-carrier generation and transport.

These observations with *Cn*-DPP-BPs are not fully parallel to those with conventional solution-processable small molecules. Specifically, solution-processable small molecules for BHJ OPVs usually require extensive decollation with bulky, flexible substituents to ensure solubility in the deposition solvent and miscibility with the partner material. By contrast, in the present case of the thermal precursor approach, the  $\pi$ -framework of DPP-BP conjugates requires as compact substituents as possible in order to form favourable morphology for the photovoltaic process. It is presumed that this result relates to the high tendency of *Cn*-DPP-BP molecules to self-aggregate and their mobility during the thermal conversion from CP to BP at relatively high temperatures of  $\geq 160$  °C.

Our capacity for controlling the morphology and molecular orientation in solution-processed small-molecule thin films will benefit from further study on the characteristics of the thermal precursor approach. Work along these lines is underway in our group.

### Acknowledgements

This work was supported by the CREST program of the Japan Science and Technology Agency (JST) (SM, KN, HY), Grants-in-Aid for Scientific Research (KAKENHI) (JP26105004 (HY), JP16K17949 (MS), JP17H03042 (NA), JP26390023 (SM), JP17H03134 (KN), and JP16H02286 (HY)) from the Japan Society for the Promotion of Science (JSPS), the program for promoting the enhancement of research universities in NAIST supported by the Ministry of Education, Culture, Sports, Science and Technology (MEXT), Grant-in-Aid for JSPS Research Fellow (JP16J04335, KT) and Foundation for NAIST (KT and MS). We acknowledge Nippon Synthetic Chem. Ind. (Osaka, Japan) for a gift of ethyl isocyanacetate, which was used for the preparation of the starting pyrrole. We also thank R. Abe and Ms Y. Nishikawa in NAIST for the analysis of 2D-GIWAXD images and mass spectroscopy, respectively. The synchrotron experiments were performed at beamlines BL19B2 and BL46XU in SPring-8 with the approval of

the Japan Synchrotron Radiation Research Institute (JASRI) (Proposal No. 2015A1683 (MS), 2015A1842 (KT), 2015A1965 (TK), and 2015B1769 (KT)).

### Notes and references

- 1 K. Leo, *Elementary Processes in Organic Photovoltaics*, Springer International Publishing, Switzerland, 2017.
- 2 K. L. Gu, Y. Zhou, X. Gu, H. Yan, Y. Diao, T. Kurosawa, B. Ganapathysubramanian, M. F. Toney and Z. Bao, *Org. Electron.*, 2017, **40**, 79–87.
- 3 O. K. Kwon, M. A. Uddin, J.-H. Park, S. K. Park, T. L. Nguyen, H. Y. Woo and S. Y. Park, *Adv. Mater.*, 2016, **28**, 910–916.
- 4 Y. Liu, J. Zhao, Z. Li, C. Mu, W. Ma, H. Hu, K. Jiang, H. Lin, H. Ade and H. Yan, *Nat. Commun.*, 2014, **5**, 5293.
- 5 Y. Tamura, H. Saeki, J. Hashizume, Y. Okazaki, D. Kuzuhara, M. Suzuki, N. Aratani and H. Yamada, *Chem. Commun.*, 2014, **50**, 10379–10381.
- 6 H. Najafzadeh, B. Lee, Q. Zhou, L. C. Feldman and V. Podzorov, *Nat. Mater.*, 2010, **9**, 938–943.
- 7 T. Umeyama, D. Matano, S. Shibata, J. Baek, S. Ito and H. Imahori, *ECS J. Solid State Sci. Technol.*, 2017, **6**, M3078–M3083.
- 8 K. Kawajiri, T. Kawanoue, M. Yamato, K. Terai, M. Yamashita, M. Furukawa, N. Aratani, M. Suzuki, K. Nakayama and H. Yamada, *ECS J. Solid State Sci. Technol.*, 2017, **6**, M3068–M3074.
- 9 T. Umeyama, S. Shibata and H. Imahori, *RSC Adv.*, 2016, **6**, 83758–83766.
- 10 Y. Tamura, D. Kuzuhara, M. Suzuki, H. Hayashi, N. Aratani and H. Yamada, *J. Mater. Chem. A*, 2016, **4**, 15333–15342.
- 11 M. Suzuki, Y. Yamaguchi, K. Takahashi, K. Takahira, T. Koganezawa, S. Masuo, K. Nakayama and H. Yamada, *ACS Appl. Mater. Interfaces*, 2016, **8**, 8644–8651.
- 12 C. Quinton, M. Suzuki, Y. Kaneshige, Y. Tatenaka, C. Katagiri, Y. Yamaguchi, D. Kuzuhara, N. Aratani, K. Nakayama and H. Yamada, *J. Mater. Chem. C*, 2015, **3**, 5995–6005.
- 13 S. Masuo, W. Sato, Y. Yamaguchi, M. Suzuki, K. Nakayama and H. Yamada, *Photochem. Photobiol. Sci.*, 2015, **14**, 883–890.
- 14 Y. Yamaguchi, M. Suzuki, T. Motoyama, S. Sugii, C. Katagiri, K. Takahira, S. Ikeda, H. Yamada and K. Nakayama, *Sci. Rep.*, 2014, **4**, 7151.
- 15 K. Takahashi, N. Yamada, D. Kumagai, D. Kuzuhara, M. Suzuki, Y. Yamaguchi, N. Aratani, K. Nakayama and H. Yamada, *J. Porphyrins Phthalocyanines*, 2015, **19**, 465–478.
- 16 Y. Zhen, H. Tanaka, K. Harano, S. Okada, Y. Matsuo and E. Nakamura, *J. Am. Chem. Soc.*, 2015, **137**, 2247–2252.
- 17 C. D. Liman, S. Choi, D. W. Breiby, J. E. Cochran, M. F. Toney, E. J. Kramer and M. L. Chabinyc, *J. Phys. Chem. B*, 2013, **117**, 14557–14567.
- 18 P. B. Shea, H. Yamada, N. Ono and J. Kanicki, *Thin Solid Films*, 2012, **520**, 4031–4035.
- 19 N. Noguchi, S. Junwei, H. Asatani and M. Matsuoka, *Cryst. Growth Des.*, 2010, **10**, 1848–1853.
- 20 Y. Matsuo, Y. Sato, T. Niinomi, I. Soga, H. Tanaka and E. Nakamura, *J. Am. Chem. Soc.*, 2009, **131**, 16048–16050.

- 21 P. B. Shea, L. R. Pattison, M. Kawano, C. Chen, J. Chen, P. Petroff, D. C. Martin, H. Yamada, N. Ono and J. Kanicki, *Synth. Met.*, 2007, **157**, 190–197.
- 22 P. B. Shea, J. Kanicki, L. R. Pattison, P. Petroff, M. Kawano, H. Yamada and N. Ono, *J. Appl. Phys.*, 2006, **100**, 034502.
- 23 S. Aramaki, Y. Sakai and N. Ono, *Appl. Phys. Lett.*, 2004, **84**, 2085–2087.
- 24 S. Ito, T. Murashima, N. Ono and H. Uno, *Chem. Commun.*, 1998, 1661–1662.
- 25 W. Zhao, D. Qian, S. Zhang, S. Li, O. Inganäs, F. Gao and J. Hou, *Adv. Mater.*, 2016, **28**, 4734–4739.
- 26 S. Li, L. Ye, W. Zhao, S. Zhang, S. Mukherjee, H. Ade and J. Hou, *Adv. Mater.*, 2016, **28**, 9423–9429.
- 27 Y. Jin, Z. Chen, S. Dong, N. Zheng, L. Ying, X.-F. Jiang, F. Liu, F. Huang and Y. Cao, *Adv. Mater.*, 2016, **28**, 9811–9818.
- 28 V. Vohra, K. Kawashima, T. Kakara, T. Koganezawa, I. Osaka, K. Takimiya and H. Murata, *Nat. Photonics*, 2015, **9**, 403–408.
- 29 B. Kan, M. Li, Q. Zhang, F. Liu, X. Wan, Y. Wang, W. Ni, G. Long, X. Yang, H. Feng, Y. Zuo, M. Zhang, F. Huang, Y. Cao, T. P. Russell and Y. Chen, *J. Am. Chem. Soc.*, 2015, **137**, 3886–3893.
- 30 J.-D. Chen, C. Cui, Y.-Q. Li, L. Zhou, Q.-D. Ou, C. Li, Y. Li and J.-X. Tang, *Adv. Mater.*, 2015, **27**, 1035–1041.
- 31 D. S. Berezin, O. V. Toldina and E. V. Kudrik, *Russ. J. Gen. Chem.*, 2003, **73**, 1309–1314.
- 32 M. Guide, X.-D. Dang and T.-Q. Nguyen, *Adv. Mater.*, 2011, **23**, 2313–2319.
- 33 N. Noguchi, S. Junwei, H. Asatani and M. Matsuoka, *Cryst. Growth Des.*, 2010, **10**, 1848–1853.
- 34 L. H. Hutter, B. J. Müller, K. Koren, S. M. Borisov and I. Klimant, *J. Mater. Chem. C*, 2014, **2**, 7589–7598.
- 35 V. Gottumukkala, O. Ongayi, D. G. Baker, L. G. Lomax and M. G. H. Vicente, *Bioorg. Med. Chem.*, 2006, **14**, 1871–1879.
- 36 S. Aramaki, Y. Sakai, R. Yoshiyama, K. Sugiyama, N. Ono and J. Mizuguchi, *Proc. SPIE*, 2004, **5522**, 27–35.
- 37 W. Shin, T. Yasuda, G. Watanabe, Y. S. Yang and C. Adachi, *Chem. Mater.*, 2013, **25**, 2549–2556.
- 38 Q. V. Hoang, C. E. Song, I.-N. Kang, S.-J. Moon, S. K. Lee, J.-C. Lee and W. S. Shin, *RSC Adv.*, 2016, **6**, 28658–28665.
- 39 A. Mishra, D. Popovic, A. Vogt, H. Kast, T. Leitner, K. Walzer, M. Pfeiffer, E. Mena-Osteritz and P. Bäuerle, *Adv. Mater.*, 2014, **26**, 7217–7223.
- 40 Y. S. Choi, T. J. Shin and W. H. Jo, *ACS Appl. Mater. Interfaces*, 2014, **6**, 20035–20042.
- 41 W. Ni, X. Wan, M. Li, Y. Wang and Y. Chen, *Chem. Commun.*, 2015, **51**, 4936–4950.
- 42 A. B. Tamayo, M. Tantiwiwat, B. Walker and T.-Q. Nguyen, *J. Phys. Chem. C*, 2008, **112**, 15543–15552.
- 43 K. Gao, L. Li, T. Lai, L. Xiao, Y. Huang, F. Huang, J. Peng, Y. Cao, F. Liu, T. P. Russell, R. A. J. Janssen and X. Peng, *J. Am. Chem. Soc.*, 2015, **137**, 7282–7285.
- 44 H. Qin, L. Li, F. Guo, S. Su, J. Peng, Y. Cao and X. Peng, *Energy Environ. Sci.*, 2014, **7**, 1397–1401.
- 45 H. Saeki, O. Kurimoto, H. Nakaoka, M. Misaki, D. Kuzuhara, H. Yamada, K. Ishida and Y. Ueda, *J. Mater. Chem. C*, 2014, **2**, 5357–5364.
- 46 T. Okujima, Y. Hashimoto, G. Jin, H. Yamada, H. Uno and N. Ono, *Tetrahedron*, 2008, **64**, 2405–2411.
- 47 K. Takahashi, D. Kuzuhara, N. Aratani and H. Yamada, *J. Photopolym. Sci. Technol.*, 2013, **26**, 213–216.
- 48 H. Yamada, K. Kushibe, T. Okujima, H. Uno and N. Ono, *Chem. Commun.*, 2006, 383–385.
- 49 S. Loser, C. J. Bruns, H. Miyauchi, R. P. Ortiz, A. Facchetti, S. I. Stupp and T. J. Marks, *J. Am. Chem. Soc.*, 2011, **133**, 8142–8145.
- 50 Y. Sato, T. Niinomi, M. Hashiguchi, Y. Matsuo and E. Nakamura, *Proc. SPIE*, 2007, **6656**, 66560U.
- 51 H. Tanaka, Y. Abe, Y. Matsuo, J. Kawai, I. Soga, Y. Sato and E. Nakamura, *Adv. Mater.*, 2012, **24**, 3521–3525.
- 52 M. Guide, J. D. A. Lin, C. M. Proctor, J. Chen, C. García-Cervera and T.-Q. Nguyen, *J. Mater. Chem. A*, 2014, **2**, 7890–7896.
- 53 L. Xiao, S. Chen, K. Gao, X. Peng, F. Liu, Y. Cao, W.-Y. Wong, W.-K. Wong and X. Zhu, *ACS Appl. Mater. Interfaces*, 2016, **8**, 30176–30183.
- 54 A. K. K. Kyaw, D. H. Wang, V. Gupta, W. L. Leong, L. Ke, G. C. Bazan and A. J. Heeger, *ACS Nano*, 2013, **7**, 4569–4577.
- 55 S. R. Cowan, A. Roy and A. J. Heeger, *Phys. Rev. B: Condens. Matter Mater. Phys.*, 2010, **82**, 245207.
- 56 A. W. Hains, Z. Liang, M. A. Woodhouse and B. A. Gregg, *Chem. Rev.*, 2010, **110**, 6689–6735.
- 57 B. Kippelen and J.-L. Brédas, *Energy Environ. Sci.*, 2009, **2**, 251–261.
- 58 O. V. Mikhnenko, P. W. M. Blom and T.-Q. Nguyen, *Energy Environ. Sci.*, 2015, **8**, 1867–1888.
- 59 P. Müller-Buschbaum, *Adv. Mater.*, 2014, **26**, 7692–7709.
- 60 I. Osaka and K. Takimiya, *Polymer*, 2015, **59**, A1–A15.
- 61 Q. Zhang, B. Kan, F. Liu, G. Long, X. Wan, X. Chen, Y. Zuo, W. Ni, H. Zhang, M. Li, Z. Hu, F. Huang, Y. Cao, Z. Liang, M. Zhang, T. P. Russell and Y. Chen, *Nat. Photonics*, 2015, **9**, 35–41.
- 62 J. A. Love, I. Nagao, Y. Huang, M. Kuik, V. Gupta, C. J. Takacs, J. E. Coughlin, L. Qi, T. S. van der Poll, E. J. Kramer, A. J. Heeger, T.-Q. Nguyen and G. C. Bazan, *J. Am. Chem. Soc.*, 2014, **136**, 3597–3606.
- 63 J. A. Love, C. M. Proctor, J. Liu, C. J. Takacs, A. Sharenko, T. S. van der Poll, A. J. Heeger, G. C. Bazan and T.-Q. Nguyen, *Adv. Funct. Mater.*, 2013, **23**, 5019–5026.
- 64 I. Osaka, T. Kakara, N. Takemura, T. Koganezawa and K. Takimiya, *J. Am. Chem. Soc.*, 2013, **135**, 8834–8837.
- 65 A. Sharenko, M. Kuik, M. F. Toney and T.-Q. Nguyen, *Adv. Funct. Mater.*, 2014, **24**, 3543–3550.
- 66 J. M. Szarko, J. Guo, Y. Liang, B. Lee, B. S. Rolczynski, J. Strzalka, T. Xu, S. Loser, T. J. Marks, L. Yu and L. X. Chen, *Adv. Mater.*, 2010, **22**, 5468–5472.



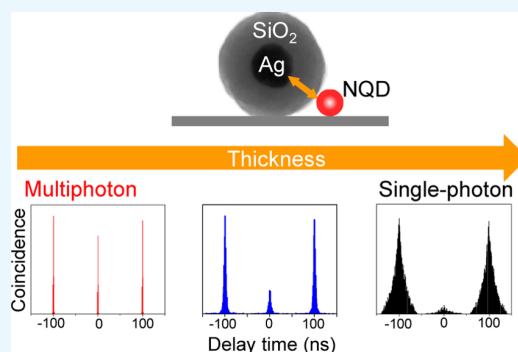
# Multiphoton Emission Enhancement from a Single Colloidal Quantum Dot Using SiO<sub>2</sub>-Coated Silver Nanoparticles

Hiroyuki Naiki,<sup>†</sup> Toshihisa Uedao,<sup>‡</sup> Li Wang,<sup>‡</sup> Naoto Tamai,<sup>‡</sup> and Sadahiro Masuo<sup>\*,†</sup>

<sup>†</sup>Department of Applied Chemistry for Environment and <sup>‡</sup>Department of Chemistry, Kwansei Gakuin University, 2-1 Gakuen, Sanda, Hyogo 669-1337, Japan

## Supporting Information

**ABSTRACT:** The enhancement of multiphoton emission from a single colloidal nanocrystal quantum dot (NQD) interacting with a plasmonic nanostructure was investigated using SiO<sub>2</sub>-coated silver nanoparticles (Ag/SiO<sub>2</sub>) as the plasmonic nanostructure. Using Ag/SiO<sub>2</sub> with five different SiO<sub>2</sub> shell thicknesses, we observed modification of the emission behavior depending on the distance between the NQD and silver nanoparticle (AgNP). The single-photon emission from a single NQD converted to multiphoton emission with a shortening of the emission lifetime as the NQD–AgNP distance decreased, whereas an increase and decrease in the emission intensity were observed. From the distance-dependent results, we concluded that the probability of multiphoton emission was increased by the quenching of the single-exciton state due to energy transfer from the NQD to the AgNP and that the emission intensity was modified by the enhancement of the excitation rate and quenching. These results indicate that the plasmonic nanostructure is very effective in controlling the emission photon statistics, that is, single- and multi-photon emission and the emission intensity from the single NQD, which is difficult to achieve in an NQD alone.



## INTRODUCTION

Colloidal nanocrystal quantum dots (NQDs) are dispersible nanoscale emitters that are of great interest because of their potential applications in a wide range of optoelectronic devices<sup>1–10</sup> and in biosensing.<sup>11–13</sup> The emission photon statistics, that is, single-photon emission and multiphoton emission, from a single NQD is an important optical property obtained as a result of multiexciton dynamics, which can be explained as follows. When multiple excitons are simultaneously generated in a single NQD, multiexciton states (MX), such as the triexciton state (TX) or biexciton state (BX), are formed, depending on the number of generated excitons. In the emission process, the excitons decay from the TX or BX to the single-exciton state (SX) by emitting a single photon on a picosecond time scale. Then, the remaining single-exciton decays from the SX to the ground state (GS) by emitting a single photon on a nanosecond time scale.<sup>14</sup> Thus, multiple photons can be emitted by this cascade emission. The obtained multiphoton emission can behave as an entangled photon pair, which is important for quantum information technologies.<sup>15</sup> However, when multiple excitons are generated, nonradiative Auger recombination occurs. The excitons decay nonradiatively from the MX to the SX.<sup>16</sup> Subsequently, the remaining single-exciton decays from the SX to the GS by emitting a single photon. Therefore, single-photon emission can be obtained via Auger recombination.<sup>17–20</sup> Single-photon emission is also important for quantum information technologies. Generally,

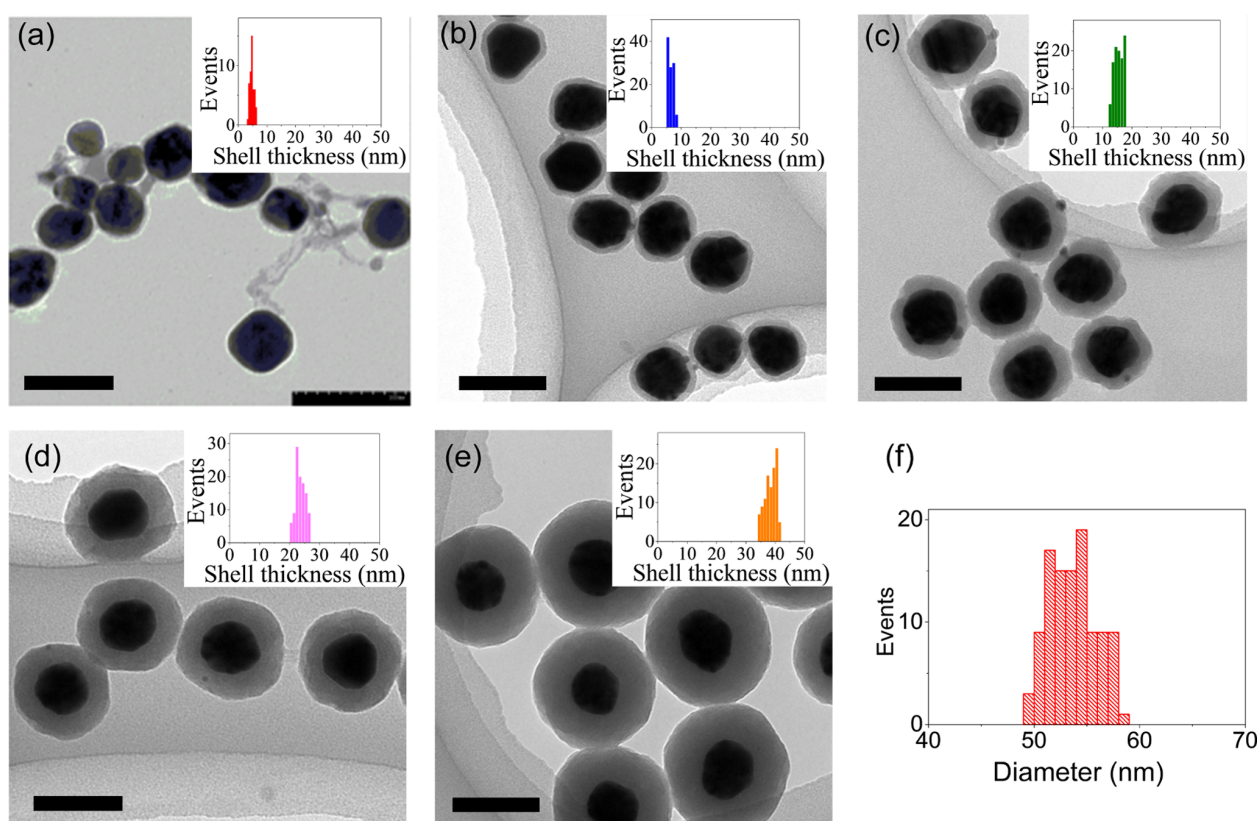
the emission photon statistics of an NQD are controlled by quantum confinement, which depends on the size, shape, and atomic composition of the NQDs themselves.

Recently, control of the photon statistics of NQDs using plasmonic nanostructures, that is, metallic nanostructures (MNSs), has received substantial attention. An increase in the probability of multiphoton emission through the interaction with MNS has been reported using various NQD–MNS systems.<sup>21–37</sup> Two mechanisms have been proposed to explain the increase in multiphoton emission. One is the enhancement of the multiphoton emission rate by enhancement of the radiative rate. Because of this enhancement, a single NQD–MNS can emit multiple photons before the excitons are annihilated by Auger recombination, that is, the quantum yield of the MX emission ( $\Phi_{MX}$ ) increases.<sup>21–25,27,30–34,36</sup> The other mechanism is the quenching of the SX by the MNS, that is, a decrease in the quantum yield of the SX emission ( $\Phi_{SX}$ ) rather than an actual increase in the  $\Phi_{MX}$ . This mechanism can be understood as follows: When the excitons are quenched by the MNS, due to energy or electron transfer, the quenching of the SX is more efficient than that of the MX because of the longer lifetime of the SX. Because of the decrease in  $\Phi_{SX}$ , the contribution of the MX emission increases. Consequently, the

**Received:** December 28, 2016

**Accepted:** February 21, 2017

**Published:** February 27, 2017



**Figure 1.** TEM images of Ag/SiO<sub>2</sub> with different shell thicknesses and histograms of each shell thickness. Average shell thickness: (a) 5, (b) 7, (c) 15, (d) 24, and (e) 38 nm. The scale bar in each image represents 100 nm. (f) A histogram of the diameters of the core AgNPs.

probability of the MX emission increases.<sup>28,37–40</sup> Although these two mechanisms were proposed, the details are not yet fully understood.

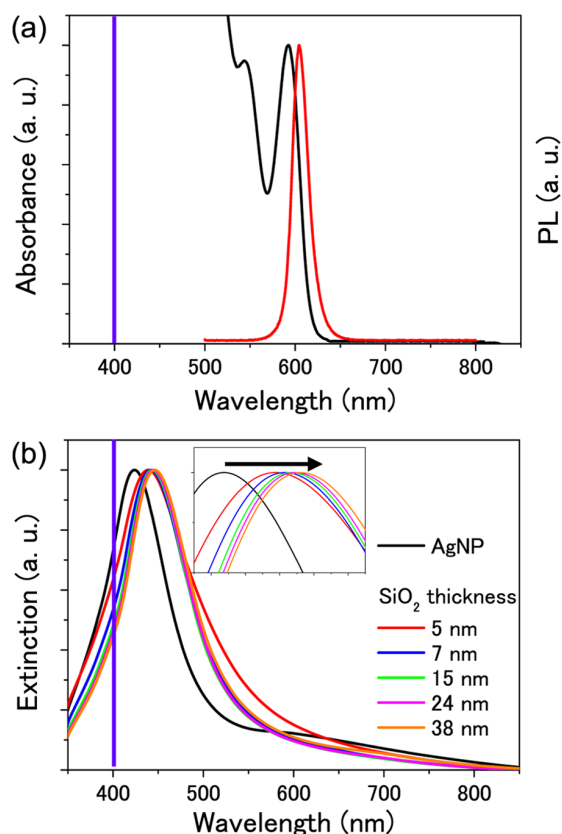
To elucidate the mechanism, a single NQD–MNS system in which the spectral overlap and distance are fully controlled is ideal. When the localized surface plasmon resonance (LSPR) band of the MNS overlaps the absorption spectrum of the nearby emitter, the excitation rate of the emitter is enhanced by the electric field of the localized surface plasmon (LSP) generated on the MNS by incident light. When the LSPR band overlaps with the emission spectrum of the emitter, the relaxation process, that is, radiative and nonradiative processes, of the emitter is enhanced by the dipole–dipole interaction between the emitter and MNS.<sup>41–45</sup> The enhancement factors strongly depend on the distance between the emitter and MNS. Although the relationship between the change in photon statistics and spectral overlap has often been discussed in the literature,<sup>22,24,25,31,36,46</sup> few reports have examined the dependence of the change in photon statistics on distance.<sup>31,37</sup> Coating the MNSs or NQDs with the dielectric material SiO<sub>2</sub> is an effective method for controlling the distance. Numerous studies have reported the modification of the PL intensity and lifetime of distance-controlled NQD–MNS systems using a SiO<sub>2</sub> shell.<sup>31,34,47–50</sup> However, only one report has examined the relationship between the photon statistics and distance.<sup>31</sup> In that work, the distance-dependent emission photon statistics was measured using SiO<sub>2</sub>-coated gold nanoparticles with 5 and 10 nm thick SiO<sub>2</sub> shells. To elucidate the mechanism of modification of the emission behavior of the NQDs using

MNSs systematically, further experimental results using different NQD–MNS systems are required.

In this work, to elucidate the relationship between photon statistics and distance and the mechanism of enhancement of MX emission, SiO<sub>2</sub>-coated silver (Ag/SiO<sub>2</sub>) nanoparticles with five different SiO<sub>2</sub> shell thicknesses were used to control the distance between a single NQD and a silver nanoparticle (AgNP). A dielectric SiO<sub>2</sub> spacer with a controlled thickness provides a simple means of tuning the interactions between a NQD and AgNP. To control the distance using the SiO<sub>2</sub>-shell thickness, using a single Ag/SiO<sub>2</sub> nanoparticle and single NQD and following a previously reported atomic force microscopy (AFM) manipulation technique<sup>36</sup> is ideal. However, the AFM manipulation of Ag/SiO<sub>2</sub> is hindered by the adsorption of Ag/SiO<sub>2</sub> onto the silicon AFM cantilever. Therefore, the emission photon statistics of single NQDs interacting with Ag/SiO<sub>2</sub> was detected for samples prepared by dispersing NQDs and Ag/SiO<sub>2</sub> nanoparticles on a coverslip by spin-coating.

## RESULTS AND DISCUSSION

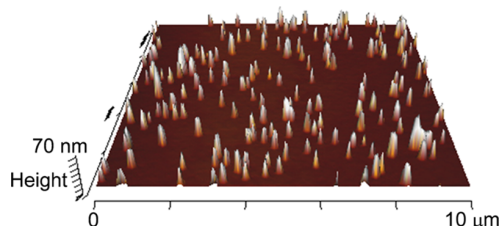
Transmission electron microscopy (TEM) images of Ag/SiO<sub>2</sub> nanoparticles with different shell thicknesses and histograms of each shell thickness and of the diameter of the core AgNPs are shown in Figure 1. The core AgNPs were almost spherical, and the average diameter was  $54 \pm 2$  nm (Figure 1f). The shell thicknesses were estimated as  $5 \pm 1$ ,  $7 \pm 1$ ,  $15 \pm 1$ ,  $24 \pm 2$ , and  $38 \pm 2$  nm from the TEM images. Figure 2 shows the absorption and PL spectra of the NQDs in toluene (a) and the extinction spectra of the prepared Ag/SiO<sub>2</sub> with different thicknesses (b). The LSPR band of the Ag/SiO<sub>2</sub> nanoparticles



**Figure 2.** (a) Absorption (black) and PL (red) spectra of CdSe/ZnS NQDs dispersed in toluene. (b) Extinction spectra of Ag/SiO<sub>2</sub> with different shell thicknesses dispersed in ethanol. The wavelength of the excitation laser (405 nm) is marked as a purple vertical line.

was shifted toward a longer wavelength as the thickness of the SiO<sub>2</sub> shell increased, as expected and previously observed by others.<sup>51,52</sup> Because the LSPR band greatly overlaps with the absorption spectrum of the NQDs, we expected that the excitation rate of the NQD would be enhanced by the isolated Ag/SiO<sub>2</sub> nanoparticles under 405 nm excitation. In addition, the relaxation process of the NQDs would also be enhanced because of the small overlap of the PL spectrum with the LSPR band. In an AFM topography image of the prepared sample (Figure 3), isolated Ag/SiO<sub>2</sub> was visualized, although some of the Ag/SiO<sub>2</sub> aggregated. Isolated NQDs were not observed, probably because the NQDs were close to the Ag/SiO<sub>2</sub> as a result of sample preparation by spin-coating.

Figure 4 shows representative emission behavior detected from an isolated NQD without Ag/SiO<sub>2</sub> (reference) (a–d) and

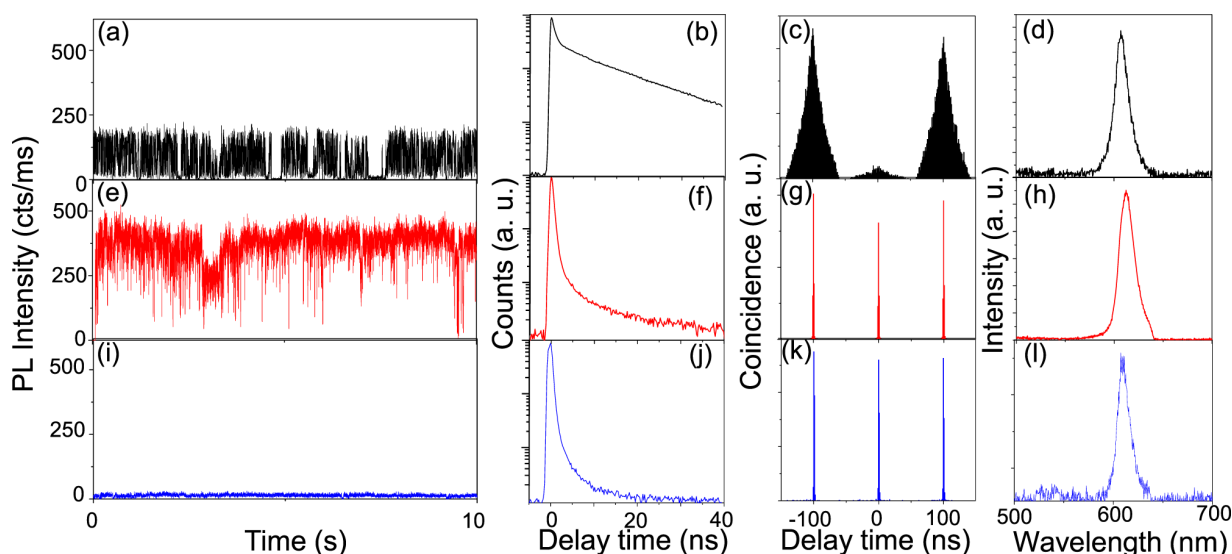


**Figure 3.** AFM topography image of the prepared NQD–Ag/SiO<sub>2</sub> sample.

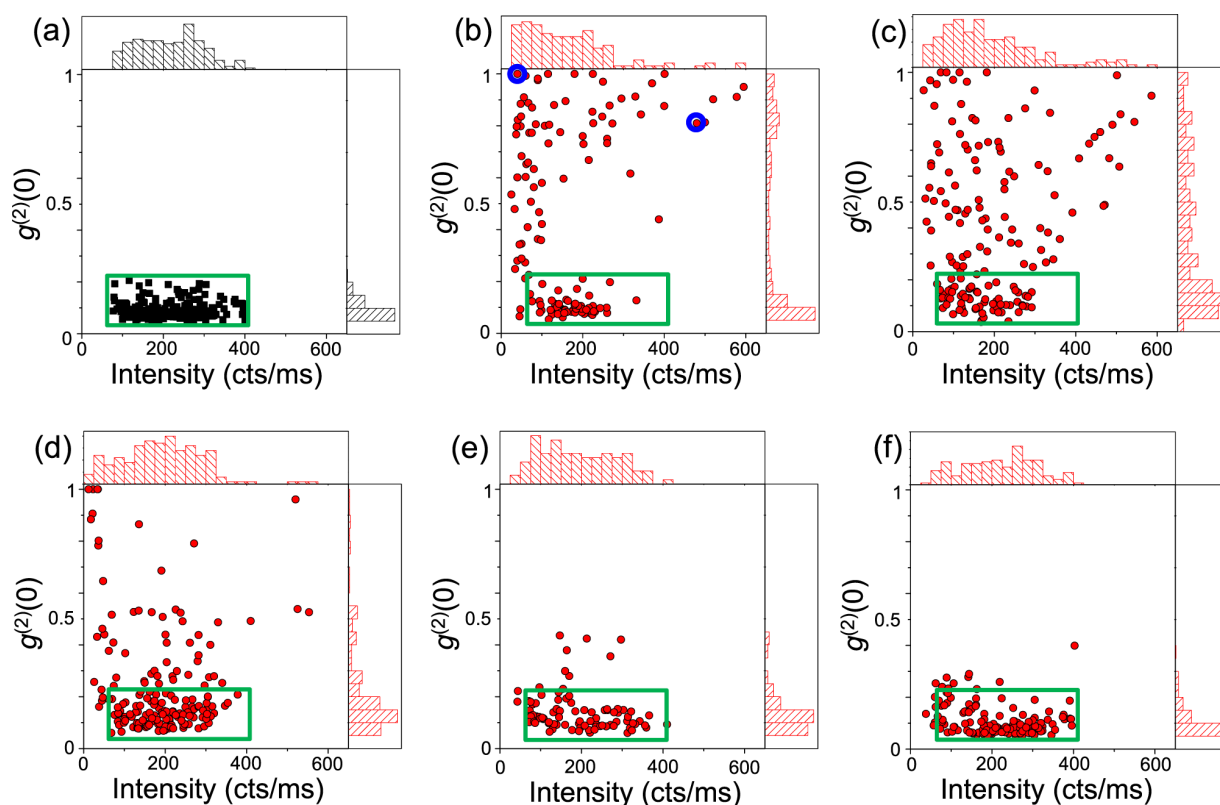
two isolated NQDs with Ag/SiO<sub>2</sub> particles with 5 nm thick shells (e–l) exposed to an excitation laser at 405 nm with an intensity of 710 W/cm<sup>2</sup>. The number of excitons generated in a single NQD by a single excitation pulse,  $\langle N \rangle$ , was estimated at 0.48 by taking into account the absorption cross-section of an NQD at 405 nm ( $1.1 \times 10^{-14}$  cm<sup>2</sup>) and the number of photons in the single excitation pulse. The time trace of the PL intensity obtained from the reference NQD displayed 200 counts/ms and characteristic blinking behavior (Figure 4a). The low-intensity level of blinking results from the quenching of the exciton by the charged state of the NQD.<sup>53</sup> The quenching process causes the short decay component of the PL decay curve. The PL decay curve shown in Figure 4b was fitted using a two-exponential function,  $I(t) = \alpha_1 \exp(-t/\tau_1) + \alpha_2 \exp(-t/\tau_2)$ , where  $\alpha$  and  $\tau$  represent the normalized amplitude and PL lifetime, respectively, with lifetimes of  $\tau_1 = 0.8$  ns ( $\alpha_1 = 60.0\%$ ) and  $\tau_2 = 18.1$  ns ( $\alpha_2 = 40.0\%$ ). The short lifetime,  $\tau_1 = 0.8$  ns, was obtained as a result of quenching of the exciton. In the photon correlation histogram (Figure 4c), the contribution of the center peak at a delay time of 0 ns was much lower than that of the other peaks at delay times of  $\pm 100$  ns. The second-order correlation function,  $g^{(2)}(0)$ , provides information about the emission photon statistics, that is, the probability of single-photon emission increases when  $g^{(2)}(0)$  is close to zero. In addition, the  $g^{(2)}(0)$  value corresponds to the efficiency of BX emission,  $\Phi_{\text{BX}}/\Phi_{\text{SX}}$ , at low excitation power (average NQD exciton occupancy  $\langle N \rangle \ll 1$ ).<sup>28,33</sup> At a high excitation power, such as that under excitation enhancement by the electric field of LSP (vide infra), the  $g^{(2)}(0)$  value does not correspond to the exact  $\Phi_{\text{BX}}/\Phi_{\text{SX}}$ . However, the increase in the  $g^{(2)}(0)$  value indicates the increase in the probability of multiphoton emission even at a high excitation power. Therefore, we use the  $g^{(2)}(0)$  value to show the modification of the photon statistics. The  $g^{(2)}(0)$  values were calculated as 0.09 in Figure 4c, thus indicating that the reference NQD exhibited single-photon emission.

Representative results for the two single NQDs with Ag/SiO<sub>2</sub> are shown in Figure 4e–l. For the single NQD shown in Figure 4e–h, the PL intensity increased compared to that of the reference. The time trace of the PL intensity displayed 480 counts/ms and a reduction of the low-intensity levels (Figure 4e), which has also been observed in previous reports using AgNP and gold nanoparticles (AuNPs) as MNSs.<sup>21,25,36</sup> The PL decay curve (Figure 4f) was fitted using a three-exponential function,  $I(t) = \alpha_1 \exp(-t/\tau_1) + \alpha_2 \exp(-t/\tau_2) + \alpha_3 \exp(-t/\tau_3)$ , with three lifetimes of 0.3 ns (85.4%), 1.4 ns (12.7%), and 6.7 ns (1.9%). Because the lifetime of 0.3 ns was the same as the instrument response function (IRF), the actual lifetime is probably shorter. Shortening of the lifetime indicated that the relaxation process of the NQD was modified by Ag/SiO<sub>2</sub>. In the photon correlation histogram (Figure 4g), the contribution of the center peak increased, and the  $g^{(2)}(0)$  value was estimated as 0.81. This result indicates that the probability of multiphoton emission increased compared to that of the reference, shown in Figure 4c.

For the single NQD shown in Figure 4i–l, the PL intensity decreased to 28 counts/ms with shortening of the PL lifetime. As the background count under this experimental condition was 0.3 counts/ms, the single NQD exhibited a low PL intensity. By fitting the PL decay curve (Figure 4j), three lifetimes were obtained: 0.3 ns (88.1%), 1.1 ns (10.4%), and 4.3 ns (1.4%). From Figure 4k, the  $g^{(2)}(0)$  value was estimated as 0.99, thus indicating that the probability of multiphoton



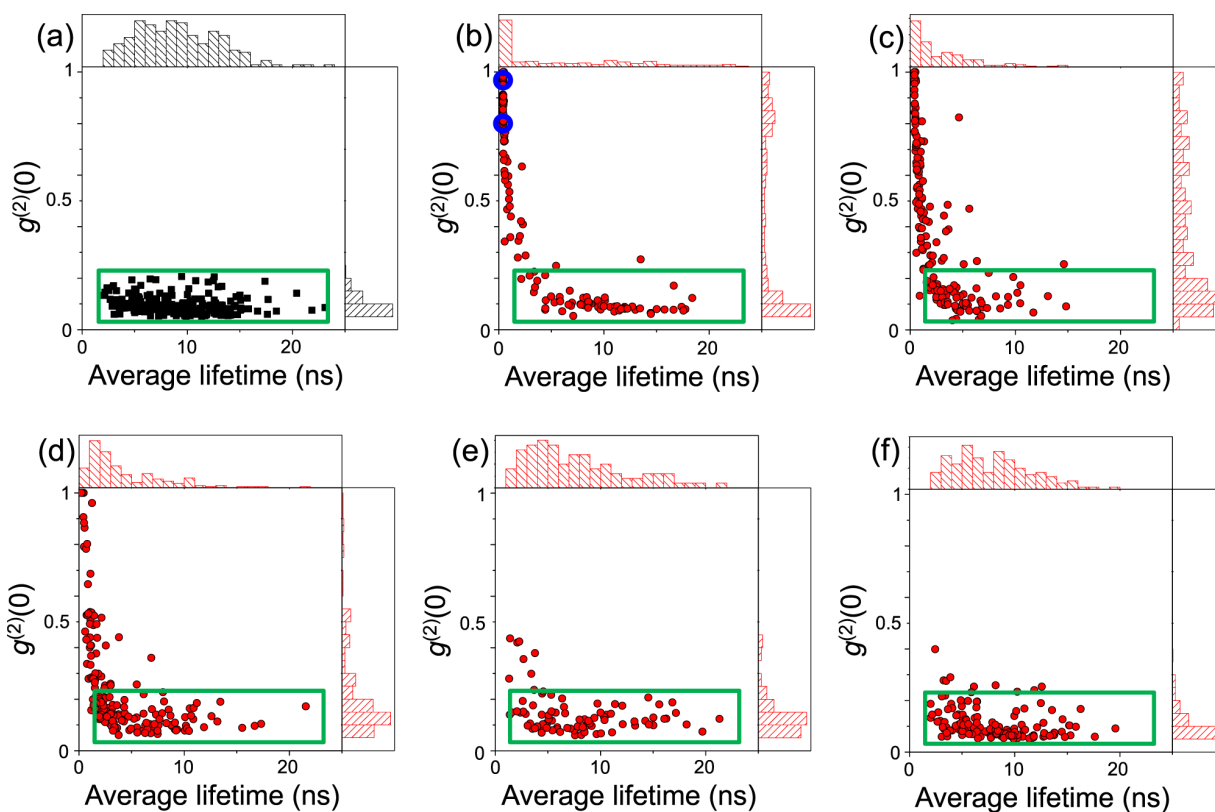
**Figure 4.** Time traces of PL intensity (a, e, i), PL decay curves (b, f, j), photon correlation histograms (c, g, k), and PL spectra (d, h, l) detected from a single NQD without Ag/SiO<sub>2</sub> (reference) (a–d) and from two single NQDs with Ag/SiO<sub>2</sub> with a 5 nm thick shells (e–l).



**Figure 5.** Correlations between the PL intensity and  $g^{(2)}(0)$  and histograms of the PL intensity and  $g^{(2)}(0)$  detected from individual NQDs without Ag/SiO<sub>2</sub> (a) and with Ag/SiO<sub>2</sub>, with shell thicknesses of 5 nm (b), 7 nm (c), 15 nm (d), 24 nm (e), and 38 nm (f). Each figure is based on more than 100 single NQD measurements.

emission was increased, similar to that for the single NQD shown in Figure 4g. In Figure 4h,l, no clear change in the PL spectra was observed compared with the reference (Figure 4d). Although the peak wavelengths of the spectra were different from those of the reference, the difference was within the spectral distribution of the individual NQDs. Because of the small shift in the BX and TX emission spectra compared with

the SX emission spectrum,<sup>14</sup> distinguishing the multiphoton emission spectrum from the SX emission spectrum at room temperature is difficult.<sup>21,36,37</sup> Although we considered the spectral change with respect to the full width at half-maximum, no significant change was observed. The observed increase in the  $g^{(2)}(0)$  value was attributed to the change in the PL behavior of the NQD because neither emission nor background



**Figure 6.** Correlations between the average lifetime and  $g^{(2)}(0)$  and histograms of the average lifetime and  $g^{(2)}(0)$  detected from individual NQDs without Ag/SiO<sub>2</sub> (a) and with Ag/SiO<sub>2</sub>, with shell thicknesses of 5 nm (b), 7 nm (c), 15 nm (d), 24 nm (e), and 38 nm (f). Each figure is based on more than 100 single NQD measurements.

scattering from Ag/SiO<sub>2</sub> was observed in Figure 4h,l. The above emission behavior, that is, a reduction in the blinking and increase in the probability of multiphoton emission with shortening of the lifetime, was identical to our previous results,<sup>21,25,36,37</sup> and the increase in the probability of multiphoton emission was also identical to that noted in prior reports.<sup>21–25,27–37</sup>

The above results are only representative examples obtained from single NQDs with and without Ag/SiO<sub>2</sub> dispersed on a coverslip. As we have reported recently, the direct observation of changes in the emission behavior with the approach of an MNS provides meaningful results, even if the results are obtained from a few individual NQDs.<sup>36,37</sup> However, in single NQD measurements, such as those shown in the present work, statistical data compiled from all results obtained from a large number of single NQDs was important to elucidate the essential emission behavior because the emission behavior of individual NQDs and NQD–Ag/SiO<sub>2</sub> interactions have broad heterogeneity. For example, in the sample, both aggregated and isolated Ag/SiO<sub>2</sub> were observed, as shown in Figure 3. Thus, the NQD–Ag/SiO<sub>2</sub> interaction strongly depends on each NQD–Ag/SiO<sub>2</sub> pair. In addition, the NQD–Ag/SiO<sub>2</sub> distance was not controlled in the sample. Therefore, we discuss the emission behavior of single NQDs on the basis of the statistical data in the following section.

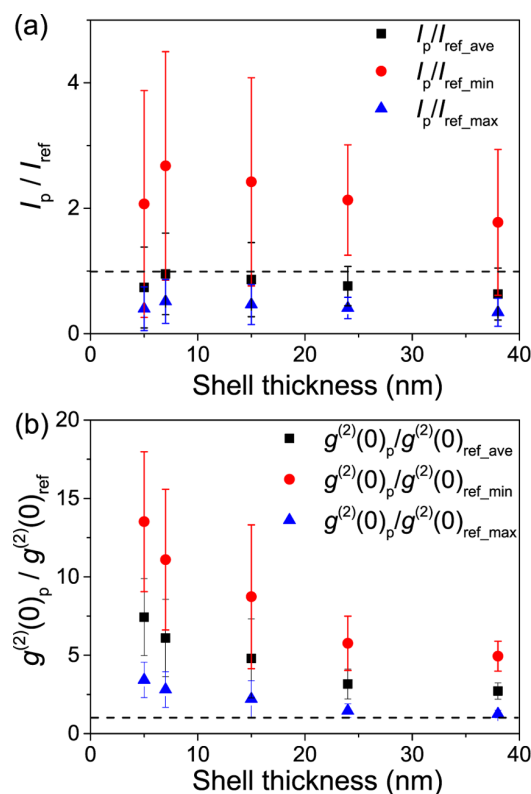
On the basis of the measurements shown in Figure 4, the correlations between  $g^{(2)}(0)$  and the PL intensity and between  $g^{(2)}(0)$  and the average lifetime detected from single NQDs are shown in Figures 5 and 6, respectively. The values obtained from the single NQDs with Ag/SiO<sub>2</sub> shown in Figure 4 are

marked by blue circles in Figures 5b and 6b. Each correlation was built from more than 100 single NQD measurements. The decay curves detected from the reference NQDs were fitted by single- or two-exponential functions, whereas the decay curves of the single NQDs with Ag/SiO<sub>2</sub> were fitted using two- or three-exponential functions. The average lifetime was calculated as follows:  $\alpha_1 \times \tau_1 + \alpha_2 \times \tau_2 + \alpha_3 \times \tau_3$ . In the case of the reference NQDs, the PL intensity and average lifetime were distributed in a range of 80–400 counts/ms and 2–23 ns, respectively (Figures 5a and 6a). Nearly all single NQDs exhibited  $g^{(2)}(0)$  values of less than 0.2, thus indicating that the single NQDs emitted single photons. These results represent the typical emission behavior of the single NQDs and were used as a reference. The distributions of the reference values are indicated by green squares in each correlation.

The single NQDs with Ag/SiO<sub>2</sub> exhibited large distributions of the correlations compared with the reference NQD. Among the single NQDs with Ag/SiO<sub>2</sub> with 5 nm thick shells (Figures 5b and 6b), a large number of single NQDs exhibited higher  $g^{(2)}(0)$  values than those of the reference. The single NQDs with higher  $g^{(2)}(0)$  values exhibited large distributions of PL intensity, in the range of 25–600 counts/ms (Figure 5b). However, single NQDs with a higher intensity than that of the reference (greater than 400 counts/ms) were rare, whereas the number of single NQDs with a lower intensity than that of the reference increased, as confirmed by the histogram of PL intensities shown in Figure 5b. As shown in Figure 6b, the single NQDs with higher  $g^{(2)}(0)$  values exhibited shorter average lifetimes compared to those of the reference, and the average lifetime decreased with increasing  $g^{(2)}(0)$  values. These

changes in emission behavior were caused by the interaction with Ag/SiO<sub>2</sub>. However, single NQDs with nearly identical  $g^{(2)}(0)$  values and average lifetimes to those of the reference were observed and are surrounded by green squares in Figures 5b and 6b. These NQDs probably did not interact with Ag/SiO<sub>2</sub> because these data were obtained from samples prepared by just dispersing the NQDs and Ag/SiO<sub>2</sub> on the coverslip by spin-coating. The contribution of the NQDs with higher  $g^{(2)}(0)$  values and shorter lifetimes decreased with increasing shell thickness. In the case of the single NQDs with Ag/SiO<sub>2</sub> with 7 nm thick shells, the contribution of the NQDs with  $g^{(2)}(0)$  greater than 0.8 slightly decreased in the  $g^{(2)}(0)$  histograms shown in Figures 5c and 6c. The contribution of the high  $g^{(2)}(0)$  further decreased with increasing shell thickness, that is, for 15 nm thick shells (Figures 5d and 6d) and 24 nm thick shells (Figures 5e and 6e), and most of the NQDs exhibited the same  $g^{(2)}(0)$  and average lifetime as those of the reference for 38 nm thick shells (Figures 5f and 6f). These results clearly indicated that the increase in  $g^{(2)}(0)$ , that is, the increase in the probability of multiphoton emission, is strongly dependent on the NQD–AgNP distance. We are convinced that the emission behaviors shown here were obtained from single NQDs because of the following reasons: (1) Using the same concentration of an NQD-dispersed solution, most NQDs were isolated in the case of the reference sample (Figures 5a and 6a). (2) In the case of NQDs with Ag/SiO<sub>2</sub> with SiO<sub>2</sub> shell thicknesses of 24 and 38 nm, most NQDs exhibited the emission behavior of single NQDs, that is, low  $g^{(2)}(0)$  values, as shown in Figures 6e,f and 7e,f, using the same concentration of an NQD-dispersed solution. (3) We checked the emission behavior by changing the concentration and measured the emission behavior at quite a low concentration. (4) In Figure 6b, a clear correlation between the average lifetime and  $g^{(2)}(0)$  value was observed, that is, an NQD with a lower average lifetime exhibited a higher  $g^{(2)}(0)$  value. Actually, it was reported that this type of correlation was observed even in the case of the aggregate of NQDs.<sup>54</sup> However, if the correlation shown in Figure 6b was caused by the aggregate, the correlation should not show distance dependence as shown in Figure 6. Therefore, the correlation was due to the interaction with Ag/SiO<sub>2</sub>.

Enhancements of the excitation rate and radiative rate can be considered to be part of the mechanism of increase of the PL intensity, whereas the decrease in the PL intensity is caused by enhancement of the nonradiative rate (quenching). Enhancements of the radiative and nonradiative rates result in shortening of the lifetime. Therefore, the observed increase in PL intensity with increasing  $g^{(2)}(0)$  and shortening of the lifetime can be explained by the enhancement of the radiative rate or by a combination of enhancement of the excitation rate and nonradiative rate. Similarly, the decrease in PL intensity with increasing  $g^{(2)}(0)$  and shortening of the lifetime can be explained by the enhancement of the nonradiative rate. As shown in Figure 2, the LSPR band of the isolated Ag/SiO<sub>2</sub> nanoparticles overlaps with the absorption and PL spectra of the NQD, although the spectral overlap between the LSPR and PL bands was smaller than the spectral overlap of the LSPR band with the absorption band, and the LSPR band was generated by 405 nm excitation. Thus, the combination of enhancement of the excitation rate and nonradiative rate is probably a more predominant mechanism of increase of the PL intensity. The AFM image revealed aggregation of some of the Ag/SiO<sub>2</sub> nanoparticles (Figure 3). The LSPR band of metallic



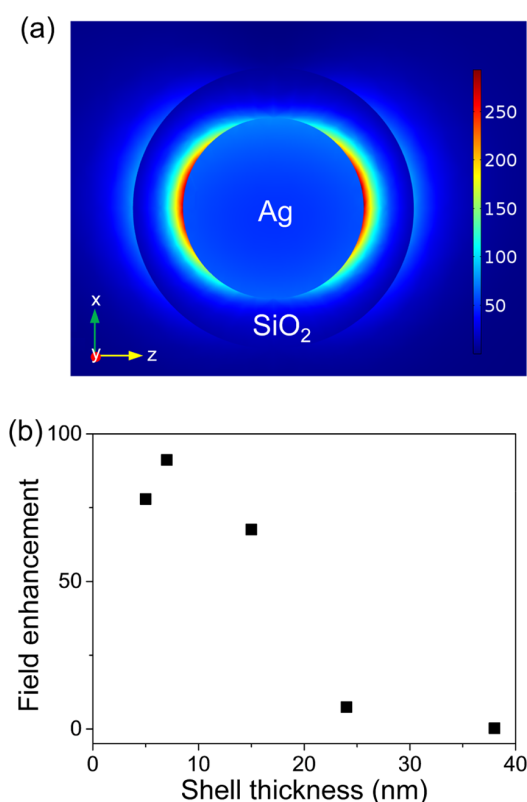
**Figure 7.** Enhancement factors of the PL intensity ( $I_p/I_{ref}$ ) (a) and  $g^{(2)}(0)$  value ( $g^{(2)}(0)_p/g^{(2)}(0)_{ref}$ ) (b) depending on the shell thickness. The subscripts “p” and “ref” refer to the NQDs with Ag/SiO<sub>2</sub> and reference NQDs, respectively.  $I_p$  and  $g^{(2)}(0)_p$  were estimated as the average values from the NQDs that exhibited higher  $g^{(2)}(0)$  values compared to those of the reference (outside the green square in Figures 5 and 6).  $I_{ref}$  and  $g^{(2)}(0)_{ref}$  were estimated as the average (black solid square), minimum (red solid circle), and maximum (blue solid triangle) values.

nanoparticles is known to be red-shifted by interactions between metallic nanoparticles.<sup>55–57</sup> In our sample, such aggregates should display a red-shifted LSPR band, depending on the condition of the aggregates, that is, the number of Ag/SiO<sub>2</sub> particles and the distance between the particles. Thus, for these aggregates, the spectral overlap between the LSPR and PL bands increased, whereas the spectral overlap between the LSPR and absorption bands decreased. This effect was probably responsible for the decrease in PL intensity due to the increase in the enhancement of the nonradiative rate and the decrease in the enhancement of the excitation rate. Unfortunately, our instrumental setup did not allow assignment of the LSPR bands of individual Ag/SiO<sub>2</sub> nanoparticles. However, the increase in the  $g^{(2)}(0)$  values was attributed to the enhancement of the relaxation process. We discuss the distance-dependent results below to elucidate the mechanism.

Figure 7 shows the enhancement factors of the PL intensity,  $I_p/I_{ref}$  (a), and  $g^{(2)}(0)$ ,  $g^{(2)}(0)_p/g^{(2)}(0)_{ref}$  (b), for single NQDs with Ag/SiO<sub>2</sub> as a function of shell thickness. The subscripts p and ref refer to the NQDs with Ag/SiO<sub>2</sub> and the reference NQDs, respectively. Estimation of the enhancement factors was complicated by the large distribution of the PL intensity and  $g^{(2)}(0)$  values for both the single NQDs with Ag/SiO<sub>2</sub> and the reference NQDs. Thus,  $I_p$  and  $g^{(2)}(0)_p$  were estimated as average values, except for the NQDs surrounded by the green

squares in Figures 5 and 6, to eliminate the NQDs that did not interact with Ag/SiO<sub>2</sub>. The following three combinations of values of  $I_{\text{ref}}$  and  $g^{(2)}(0)_{\text{ref}}$  were used: first, the average of all values,  $I_{\text{ref\_ave}} = 216$  counts/ms,  $g^{(2)}(0)_{\text{ref\_ave}} = 0.095$ ; second, the minimum value,  $I_{\text{ref\_min}} = 77$  counts/ms,  $g^{(2)}(0)_{\text{ref\_min}} = 0.052$ ; and third, the maximum value,  $I_{\text{ref\_max}} = 400$  counts/ms,  $g^{(2)}(0)_{\text{ref\_max}} = 0.206$ . Using these three combinations, the enhancement factors were estimated. The values of the enhancement factors for PL intensity shown in Figure 7a increased with decreasing shell thickness, and the enhancement factor reached the maximum value at a shell thickness of 7 nm for each of the three combinations of values. Then, the value decreased for the particles with 5 nm thick shells. In the case of  $g^{(2)}(0)$ , the enhancement factor increased with decreasing shell thickness (Figure 7b). This result indicates that the probability of multiphoton emission is enhanced with decreasing distance. To consider the enhancement mechanism, the dependence of the relative change in the enhancement factor of PL intensity on distance is important. Novotny et al. have investigated the distance-dependent PL intensity of a single organic molecule using a AuNP attached to the end of a pointed optical fiber and have also reported the distance-dependent enhancement factor of PL intensity, which was similar to our result.<sup>58,59</sup> Using theoretical analysis, Novotny et al. clearly demonstrated that the change in the PL intensity as a function of distance can be interpreted as arising from a combination of enhancement of the excitation rate by the LSP of the AuNP and quenching of the PL by resonance energy transfer from the single molecule to the AuNP.<sup>59</sup> These reports support the interpretation of our results primarily by the same mechanism, that is, a combination of enhancement of the excitation rate and quenching. Both the enhancement of the excitation rate and quenching increase with decreasing distance. As a result, enhancement of the PL intensity reaches a maximal value and then decreases at shorter distances. Enhancement of the radiative rate is a possible mechanism for the increase in the PL intensity. An increase in the PL intensity due to enhancement of the radiative rate has been observed previously.<sup>36</sup> However, in the case of enhancement of the radiative rate, the PL intensity should increase with decreasing distance, even at 5 nm. Therefore, our results in this work can be interpreted as arising from a combination of enhancement of the excitation rate and nonradiative rate. Because of this enhancement of the nonradiative rate, that is, the decrease in  $\Phi_{\text{SX}}$  by Ag/SiO<sub>2</sub> as the proposed mechanism, the probability of multiphoton emission increased. Because the efficiency of quenching increases with decreasing distance, the  $g^{(2)}(0)$  values increased with decreasing distance.

To confirm the influence of excitation rate enhancement by Ag/SiO<sub>2</sub> and, in particular, to obtain distance-dependent electric field enhancement, a numerical simulation of Ag/SiO<sub>2</sub> particles with different shell thicknesses was conducted (details in the Supporting Information (SI)).<sup>60,61</sup> The diameter of the AgNP was fixed as 54 nm, which was estimated as an average value from the TEM observation, and the shell thickness was varied to be 5, 7, 15, 24, and 38 nm. Figure 8a shows the distribution of the electric field enhancement of a Ag/SiO<sub>2</sub> particle with a 15 nm thick shell, as an example, obtained by the simulation for illumination at a wavelength similar to that of the excitation laser (405 nm) with the z-direction of the electric field. Electric field enhancement was defined as  $I = |E|^2/|E_0|^2$ , where  $E$  and  $E_0$  are the electric field intensity on Ag/SiO<sub>2</sub> and the light source, respectively. Field enhancement can be observed at the surface of the SiO<sub>2</sub> shell. Figure 8b shows



**Figure 8.** (a) Simulated distribution of the electric field enhancement of a Ag/SiO<sub>2</sub> nanoparticle with a 15 nm thick shell. (b) Electric field enhancement at the surface of the SiO<sub>2</sub> shell as a function of the SiO<sub>2</sub> shell thickness.

the electric field enhancement of 405 nm light at the surface of an SiO<sub>2</sub> shell with different thicknesses. The field enhancement decreased with increasing shell thickness, and the values at 24 and 34 nm were quite low (7.4 at 24 nm and 0.2 at 34 nm), thus indicating that field enhancement cannot be expected at 34 nm. This result is in good agreement with the experimental results shown in Figures 5 and 7, in which the PL intensity was not modified for the shell thickness of 38 nm.

## CONCLUSIONS

In this work, we observed modification of the emission behavior depending on the distance between NQDs and AgNPs using Ag/SiO<sub>2</sub> nanoparticles with different SiO<sub>2</sub> thicknesses to elucidate the mechanism of modification of the emission photon statistics. To eliminate the heterogeneity of each single NQD–Ag/SiO<sub>2</sub>, statistical results compiled from more than 100 single NQD measurements were used. The probability of multiphoton emission increased with decreasing lifetime as the distance decreased. In addition, the PL intensity increased and then decreased with decreasing distance. We determined that the modification of the emission behavior was primarily caused by the combination of excitation rate enhancement and nonradiative rate enhancement (quenching). Thus, the PL intensity was increased because of the excitation rate enhancement induced by the LSP of the AgNPs and the probability of multiphoton emission was increased by the quenching of SX induced by the resonance energy transfer from the NQD to the AgNP. Numerical calculation of the Ag/SiO<sub>2</sub> supported the excitation rate enhancement. In fact, the PL

intensity did not increase, as expected from the numerical calculation, because of the quenching of SX.

As results, the mechanism of modification of the emission behavior in this work was similar to that in the previous report, in which a silver-coated AFM tip was used as the plasmonic nanostructure.<sup>37</sup> Although the obtained results were similar, the present results are important to confirm the generality of the mechanism because we could obtain similar results using different plasmonic nanostructures. The present results also support the validity of the reported mechanism and indicate that the emission behavior of NQDs can be modified using plasmonic nanostructures by controlling the enhancement effects of the plasmonic nanostructure and the distance between the NQDs and nanostructure.

## EXPERIMENTAL SECTION

Monodisperse and well-defined AgNPs were prepared by the reduction of AgCl colloids with ascorbic acid.<sup>62</sup> Details are provided in the SI. The prepared spherical AgNPs were coated with a dielectric SiO<sub>2</sub> shell (Ag/SiO<sub>2</sub>) of five different thicknesses by a modified Stöber method (details in the SI).<sup>50,51</sup> The SiO<sub>2</sub> shell acts as a rigid, chemically inert, and electrically insulating spacer between the NQDs and AgNPs. The NQD–Ag/SiO<sub>2</sub> sample was prepared by first spin-coating an Ag/SiO<sub>2</sub>-dispersed ethanol solution onto a clean coverslip and then spin-coating a toluene solution of commercially available CdSe/ZnS core/shell NQDs (PL maximum wavelength: 605 nm; Invitrogen) onto the coverslip. To control the distance between the NQD and AgNP, adsorption and binding of the NQD onto Ag/SiO<sub>2</sub> using chemistry are favored methods. However, because these procedures damage the NQD surface and induce a low PL intensity, the samples in the present work were prepared by a simple spin-coating technique. The distance between the NQD and Ag/SiO<sub>2</sub> was not controlled in the sample. However, the minimum distance should be identical to the shell thickness. A reference sample composed of only isolated NQDs was prepared by spin-coating the NQD solution onto a clean coverslip. AFM topography images of the samples were obtained using an AFM (JPK Instruments, NanoWizard II) mounted on the microscope stage.<sup>36,37</sup>

The emission behaviors of the isolated NQDs were measured with a Hanbury-Brown and Twiss type photon correlation setup in combination with picosecond-pulsed laser excitation at 405 nm (10.0 MHz, 90 ps full width at half-maximum) under a sample-scanning confocal microscope.<sup>36,37</sup> Briefly, the excitation laser was focused on the single NQD by an objective lens (NA 1.4; Olympus) and the photons emitted from the NQD were collected by a same objective lens and passed through a confocal pinhole and long-pass filter (LP02-514RU; Semrock). Subsequently, half of the photons were detected with a spectrograph (SpectraPro2358; Acton Research Corporation) with a cooled CCD camera (PIXIS400B Princeton Instruments). The remaining half of the photons passed through a band-pass filter (FF01-607/36; Semrock) and were detected by two avalanche photodiode (APD) single-photon-counting modules (SPCM-AQR-14; PerkinElmer). A short-pass filter (ASAHI SPECTRA, SIX780) was put in front of one of two APDs to cut the near-infrared photons emitted from the APD accompanying the detection of the PL photons. The signals from the two APDs were connected via a router to a time-correlated single-photon counting board (SPC-630; Becker & Hickl) for Hanbury-Brown and Twiss type photon correlation

and lifetime measurements. By analyzing the obtained data with software designed in our laboratory, time traces of PL intensity, PL decay curves, and photon correlation histograms were simultaneously obtained for the single NQDs. The time-resolution of the lifetime measurement (IRF) was approximately 0.3 ns. All measurements were performed at room temperature under ambient conditions.

## ASSOCIATED CONTENT

### Supporting Information

The Supporting Information is available free of charge on the ACS Publications website at DOI: 10.1021/acsomega.6b00520.

Fabrication of SiO<sub>2</sub>-coated silver nanoparticles (Ag/SiO<sub>2</sub>); numerical simulation of the Ag/SiO<sub>2</sub> (PDF)

## AUTHOR INFORMATION

### Corresponding Author

\*E-mail: masuo@kwansei.ac.jp.

### ORCID

Naoto Tamai: 0000-0002-7343-6564

Sadahiro Masuo: 0000-0003-4828-5968

### Notes

The authors declare no competing financial interest.

## ACKNOWLEDGMENTS

This work was partly supported by JSPS KAKENHI Grant Number JP26390023, JP26107005 in Scientific Research on Innovation Areas “Photosynergetics”.

## REFERENCES

- (1) Klein, D. L.; Roth, R.; Lim, A. K. L.; Alivisatos, A. P.; McEuen, P. L. A Single-Electron Transistor Made from a Cadmium Selenide Nanocrystal. *Nature* **1997**, *389*, 699–701.
- (2) Klimov, V. I.; Mikhailovsky, A. A.; Xu, S.; Malko, A.; Hollingsworth, J. A.; Leatherdale, C. A.; Eisler, H.; Bawendi, M. G. Optical Gain and Stimulated Emission in Nanocrystal Quantum Dots. *Science* **2000**, *290*, 314–317.
- (3) Coe, S.; Woo, W. K.; Bawendi, M.; Bulovic, V. Electroluminescence from Single Monolayers of Nanocrystals in Molecular Organic Devices. *Nature* **2002**, *420*, 800–803.
- (4) Nozik, A. J. Quantum Dot Solar Cells. *Physica E* **2002**, *14*, 115–120.
- (5) Klimov, V. I. Mechanisms for Photogeneration and Recombination of Multiexcitons in Semiconductor Nanocrystals: Implications for Lasing and Solar Energy Conversion. *J. Phys. Chem. B* **2006**, *110*, 16827–16845.
- (6) Robel, I.; Subramanian, V.; Kuno, M.; Kamat, P. V. Quantum Dot Solar Cells. Harvesting Light Energy with CdSe Nanocrystals Molecularly Linked to Mesoscopic TiO<sub>2</sub> Films. *J. Am. Chem. Soc.* **2006**, *128*, 2385–2393.
- (7) Klimov, V. I.; Ivanov, S. A.; Nanda, J.; Achermann, M.; Bezel, I.; McGuire, J. A.; Piryatinski, A. Single-Exciton Optical Gain in Semiconductor Nanocrystals. *Nature* **2007**, *447*, 441–446.
- (8) Kamat, P. V. Quantum Dot Solar Cells. Semiconductor Nanocrystals as Light Harvesters. *J. Phys. Chem. C* **2008**, *112*, 18737–18753.
- (9) Qian, L.; Zheng, Y.; Xue, J. G.; Holloway, P. H. Stable and Efficient Quantum-Dot Light-Emitting Diodes Based on Solution-Processed Multilayer Structures. *Nat. Photonics* **2011**, *5*, 543–548.
- (10) Tang, J.; Sargent, E. H. Infrared Colloidal Quantum Dots for Photovoltaics: Fundamentals and Recent Progress. *Adv. Mater.* **2011**, *23*, 12–29.

- (11) Bruchez, M., Jr.; Moronne, M.; Gin, P.; Weiss, S.; Alivisatos, A. P. Semiconductor Nanocrystals as Fluorescent Biological Labels. *Science* **1998**, *281*, 2013–2016.
- (12) Chan, W. C.; Nie, S. Quantum Dot Bioconjugates for Ultrasensitive Nonisotopic Detection. *Science* **1998**, *281*, 2016–2018.
- (13) Alivisatos, P. The Use of Nanocrystals in Biological Detection. *Nat. Biotechnol.* **2004**, *22*, 47–52.
- (14) Fisher, B.; Caruge, J. M.; Zehnder, D.; Bawendi, M. Room-Temperature Ordered Photon Emission from Multiexciton States in Single CdSe Core-Shell Nanocrystals. *Phys. Rev. Lett.* **2005**, *94*, No. 087403.
- (15) Benson, O.; Santori, C.; Pelton, M.; Yamamoto, Y. Regulated and Entangled Photons from a Single Quantum Dot. *Phys. Rev. Lett.* **2000**, *84*, 2513.
- (16) Klimov, V. I.; Mikhailovsky, A. A.; McBranch, D. W.; Leatherdale, C. A.; Bawendi, M. G. Quantization of Multiparticle Auger Rates in Semiconductor Quantum Dots. *Science* **2000**, *287*, 1011–1013.
- (17) Lounis, B.; Bechtel, H. A.; Gerion, D.; Alivisatos, P.; Moerner, W. E. Photon Antibunching in Single CdSe/ZnS Quantum Dot Fluorescence. *Chem. Phys. Lett.* **2000**, *329*, 399–404.
- (18) Michler, P.; Imamoglu, A.; Mason, M. D.; Carson, P. J.; Strouse, G. F.; Buratto, S. K. Quantum Correlation among Photons from a Single Quantum Dot at Room Temperature. *Nature* **2000**, *406*, 968–970.
- (19) Messin, G.; Hermier, J. P.; Giacobino, E.; Desbiolles, P.; Dahan, M. Bunching and Antibunching in the Fluorescence of Semiconductor Nanocrystals. *Opt. Lett.* **2001**, *26*, 1891–1893.
- (20) Brokmann, X.; Giacobino, E.; Dahan, M.; Hermier, J. P. Highly Efficient Triggered Emission of Single Photons by Colloidal CdSe/ZnS Nanocrystals. *Appl. Phys. Lett.* **2004**, *85*, 712–714.
- (21) Masuo, S.; Naiki, H.; Machida, S.; Itaya, A. Photon Statistics in Enhanced Fluorescence from a Single CdSe/ZnS Quantum Dot in the Vicinity of Silver Nanoparticles. *Appl. Phys. Lett.* **2009**, *95*, No. 193106.
- (22) Mallek-Zouari, I.; Buil, S.; Quelin, X.; Mahler, B.; Dubertret, B.; Hermier, J. P. Plasmon Assisted Single Photon Emission of CdSe/CdS Nanocrystals Deposited on Random Gold Film. *Appl. Phys. Lett.* **2010**, *97*, No. 053109.
- (23) Vion, C.; Spinicelli, P.; Coolen, L.; Schwob, C.; Frigerio, J. M.; Hermier, J. P.; Maitre, A. E. Controlled Modification of Single Colloidal CdSe/ZnS Nanocrystal Fluorescence through Interactions with a Gold Surface. *Opt. Express* **2010**, *18*, 7440–7455.
- (24) Cannesson, D.; Mallek-Zouari, I.; Buil, S.; Quelin, X.; Javaux, C.; Mahler, B.; Dubertret, B.; Hermier, J. P. Strong Purcell Effect Observed in Single Thick-Shell CdSe/CdS Nanocrystals Coupled to Localized Surface Plasmons. *Phys. Rev. B* **2011**, *84*, No. 245423.
- (25) Naiki, H.; Masuo, S.; Machida, S.; Itaya, A. Single-Photon Emission Behavior of Isolated CdSe/ZnS Quantum Dots Interacting with the Localized Surface Plasmon Resonance of Silver Nanoparticles. *J. Phys. Chem. C* **2011**, *115*, 23299–23304.
- (26) Masuo, S.; Tanaka, T.; Machida, S.; Itaya, A. Photon Antibunching in Enhanced Photoluminescence of a Single CdSe/ZnS Nanocrystal by Silver Nanostructures. *J. Photochem. Photobiol., A* **2012**, *237*, 24–30.
- (27) Leblanc, S. J.; McClanahan, M. R.; Jones, M.; Moyer, P. J. Enhancement of Multiphoton Emission from Single CdSe Quantum Dots Coupled to Gold Films. *Nano Lett.* **2013**, *13*, 1662–1669.
- (28) Park, Y.-S.; Ghosh, Y.; Chen, Y.; Piryatinski, A.; Xu, P.; Mack, N. H.; Wang, H.-L.; Klimov, V. I.; Hollingsworth, J. A.; Htoon, H. Super-Poissonian Statistics of Photon Emission from Single CdSe-CdS Core-Shell Nanocrystals Coupled to Metal Nanostructures. *Phys. Rev. Lett.* **2013**, *110*, No. 117401.
- (29) Park, Y.-S.; Ghosh, Y.; Xu, P.; Mack, N. H.; Wang, H.-L.; Hollingsworth, J. A.; Htoon, H. Single-Nanocrystal Photoluminescence Spectroscopy Studies of Plasmon–Multiexciton Interactions at Low Temperature. *J. Phys. Chem. Lett.* **2013**, *4*, 1465–1470.
- (30) Yuan, C. T.; Wang, Y. C.; Cheng, H. W.; Wang, H. S.; Kuo, M. Y.; Shih, M. H.; Tang, J. Modification of Fluorescence Properties in Single Colloidal Quantum Dots by Coupling to Plasmonic Gap Modes. *J. Phys. Chem. C* **2013**, *117*, 12762–12768.
- (31) Dey, S.; Zhou, Y. D.; Tian, X. D.; Jenkins, J. A.; Chen, O.; Zou, S. L.; Zhao, J. An Experimental and Theoretical Mechanistic Study of Biexciton Quantum Yield Enhancement in Single Quantum Dots near Gold Nanoparticles. *Nanoscale* **2015**, *7*, 6851–6858.
- (32) Wang, F.; Karan, N. S.; Nguyen, H. M.; Ghosh, Y.; Hollingsworth, J. A.; Htoon, H. Coupling Single Giant Nanocrystal Quantum Dots to the Fundamental Mode of Patch Nanoantennas through Fringe Field. *Sci. Rep.* **2015**, *5*, No. 14313.
- (33) Wang, F.; Karan, N. S.; Nguyen, H. M.; Ghosh, Y.; Sheehan, C. J.; Hollingsworth, J. A.; Htoon, H. Correlated Structural-Optical Study of Single Nanocrystals in a Gap-Bar Antenna: Effects of Plasmonics on Excitonic Recombination Pathways. *Nanoscale* **2015**, *7*, 9387–9393.
- (34) Wang, F.; Karan, N. S.; Nguyen, H. M.; Mangum, B. D.; Ghosh, Y.; Sheehan, C. J.; Hollingsworth, J. A.; Htoon, H. Quantum Optical Signature of Plasmonically Coupled Nanocrystal Quantum Dots. *Small* **2015**, *11*, 5028–5034.
- (35) Dey, S.; Zhao, J. Plasmonic Effect on Exciton and Multiexciton Emission of Single Quantum Dots. *J. Phys. Chem. Lett.* **2016**, *7*, 2921–2929.
- (36) Masuo, S.; Kanetaka, K.; Sato, R.; Teranishi, T. Direct Observation of Multiphoton Emission Enhancement from a Single Quantum Dot Using AFM Manipulation of a Cubic Gold Nanoparticle. *ACS Photonics* **2016**, *3*, 109–116.
- (37) Takata, H.; Naiki, H.; Wang, L.; Fujiwara, H.; Sasaki, K.; Tamai, N.; Masuo, S. Detailed Observation of Multiphoton Emission Enhancement from a Single Colloidal Quantum Dot Using a Silver-Coated AFM Tip. *Nano Lett.* **2016**, *16*, 5770–5778.
- (38) Cheng, H. W.; Yuan, C. T.; Wang, J. S.; Lin, T. N.; Shen, J. L.; Hung, Y. J.; Tang, J.; Tseng, F. G. Modification of Photon Emission Statistics from Single Colloidal CdSe Quantum Dots by Conductive Materials. *J. Phys. Chem. C* **2014**, *118*, 18126–18132.
- (39) Gao, Y.; Roslyak, O.; Dervishi, E.; Karan, N. S.; Ghosh, Y.; Sheehan, C. J.; Wang, F.; Gupta, G.; Mohite, A.; Dattelbaum, A. M.; et al. Hybrid Graphene-Giant Nanocrystal Quantum Dot Assemblies with Highly Efficient Biexciton Emission. *Adv. Opt. Mater.* **2015**, *3*, 39–43.
- (40) Liu, J.; Kumar, P.; Hu, Y. W.; Cheng, G. J.; Irudayaraj, J. Enhanced Multiphoton Emission from CdTe/ZnS Quantum Dots Decorated on Single-Layer Graphene. *J. Phys. Chem. C* **2015**, *119*, 6331–6336.
- (41) Zhang, X.; Marocico, C. A.; Lunz, M.; Gerard, V. A.; Gun'ko, Y. K.; Lesnyak, V.; Gaponik, N.; Susha, A. S.; Rogach, A. L.; Bradley, A. L. Wavelength, Concentration, and Distance Dependence of Non-radiative Energy Transfer to a Plane of Gold Nanoparticles. *ACS Nano* **2012**, *6*, 9283–9290.
- (42) Reineck, P.; Gomez, D.; Ng, S. H.; Karg, M.; Bell, T.; Mulvaney, P.; Bach, U. Distance and Wavelength Dependent Quenching of Molecular Fluorescence by Au@SiO<sub>2</sub> Core-Shell Nanoparticles. *ACS Nano* **2013**, *7*, 6636–6648.
- (43) Chizhik, A. I.; Rother, J.; Gregor, I.; Janshoff, A.; Enderlein, J. Metal-Induced Energy Transfer for Live Cell Nanoscopy. *Nat. Photonics* **2014**, *8*, 124–127.
- (44) Zhang, X.; Marocico, C. A.; Lunz, M.; Gerard, V. A.; Gun'ko, Y. K.; Lesnyak, V.; Gaponik, N.; Susha, A. S.; Rogach, A. L.; Bradley, A. L. Experimental and Theoretical Investigation of the Distance Dependence of Localized Surface Plasmon Coupled Forster Resonance Energy Transfer. *ACS Nano* **2014**, *8*, 1273–1283.
- (45) Sun, D.; Tian, Y.; Zhang, Y. G.; Xu, Z. H.; Sfeir, M. Y.; Cutlet, M.; Gang, O. Light-Harvesting Nanoparticle Core-Shell Clusters with Controllable Optical Output. *ACS Nano* **2015**, *9*, 5657–5665.
- (46) Hoang, T. B.; Akselrod, G. M.; Mikkelsen, M. H. Ultrafast Room-Temperature Single Photon Emission from Quantum Dots Coupled to Plasmonic Nanocavities. *Nano Lett.* **2016**, *16*, 270–275.
- (47) Liu, N.; Prall, B. S.; Klimov, V. I. Hybrid Gold/Silica/Nanocrystal-Quantum-Dot Superstructures: Synthesis and Analysis of Semiconductor-Metal Interactions. *J. Am. Chem. Soc.* **2006**, *128*, 15362–15363.

- (48) Ma, X. D.; Fletcher, K.; Kipp, T.; Grzelczak, M. P.; Wang, Z.; Guerrero-Martinez, A.; Pastoriza-Santos, I.; Kornowski, A.; Liz-Marzan, L. M.; Mews, A. Photoluminescence of Individual Au/CdSe Nanocrystal Complexes with Variable Interparticle Distances. *J. Phys. Chem. Lett.* **2011**, *2*, 2466–2471.
- (49) Khanal, B. P.; Pandey, A.; Li, H.; Lin, Q. L.; Bae, W. K.; Luo, H. M.; Klimov, V. I.; Pietryga, J. M. Generalized Synthesis of Hybrid Metal-Semiconductor Nanostructures Tunable from the Visible to the Infrared. *ACS Nano* **2012**, *6*, 3832–3840.
- (50) Naiki, H.; Masuhara, A.; Masuo, S.; Onodera, T.; Kasai, H.; Oikawa, H. Highly Controlled Plasmonic Emission Enhancement from Metal-Semiconductor Quantum Dot Complex Nanostructures. *J. Phys. Chem. C* **2013**, *117*, 2455–2459.
- (51) Kobayashi, Y.; Katakami, H.; Mine, E.; Nagao, D.; Konno, M.; Liz-Marzan, L. M. Silica Coating of Silver Nanoparticles Using a Modified Stober Method. *J. Colloid Interface Sci.* **2005**, *283*, 392–396.
- (52) Aslan, K.; Wu, M.; Lakowicz, J. R.; Geddes, C. D. Fluorescent Core-Shell Ag@SiO<sub>2</sub> Nanocomposites for Metal-Enhanced Fluorescence and Single Nanoparticle Sensing Platforms. *J. Am. Chem. Soc.* **2007**, *129*, 1524–1525.
- (53) Galland, C.; Ghosh, Y.; Steinbruck, A.; Sykora, M.; Hollingsworth, J. A.; Klimov, V. I.; Htoon, H. Two Types of Luminescence Blinking Revealed by Spectroelectrochemistry of Single Quantum Dots. *Nature* **2011**, *479*, 203–208.
- (54) Shepherd, D. P.; Whitcomb, K. J.; Milligan, K. K.; Goodwin, P. M.; Gelfand, M. P.; Orden, A. V. Fluorescence Intermittency and Energy Transfer in Small Clusters of Semiconductor Quantum Dots. *J. Phys. Chem. C* **2010**, *114*, 14831–14837.
- (55) Gunnarsson, L.; Rindzevicius, T.; Prikulis, J.; Kasemo, B.; Kall, M.; Zou, S. L.; Schatz, G. C. Confined Plasmons in Nanofabricated Single Silver Particle Pairs: Experimental Observations of Strong Interparticle Interactions. *J. Phys. Chem. B* **2005**, *109*, 1079–1087.
- (56) Sheikholeslami, S.; Jun, Y. W.; Jain, P. K.; Alivisatos, A. P. Coupling of Optical Resonances in a Compositionally Asymmetric Plasmonic Nanoparticle Dimer. *Nano Lett.* **2010**, *10*, 2655–2660.
- (57) Barrow, S. J.; Funston, A. M.; Gómez, D. E.; Davis, T. J.; Mulvaney, P. Surface Plasmon Resonances in Strongly Coupled Gold Nanosphere Chains from Monomer to Hexamer. *Nano Lett.* **2011**, *11*, 4180–4187.
- (58) Anger, P.; Bharadwaj, P.; Novotny, L. Enhancement and Quenching of Single-Molecule Fluorescence. *Phys. Rev. Lett.* **2006**, *96*, No. 113002.
- (59) Bharadwaj, P.; Novotny, L. Spectral Dependence of Single Molecule Fluorescence Enhancement. *Opt. Express* **2007**, *15*, 14266–14274.
- (60) Wu, H. J.; Henzie, J.; Lin, W. C.; Rhodes, C.; Li, Z.; Sartorel, E.; Thorner, J.; Yang, P. D.; Groves, J. T. Membrane-Protein Binding Measured with Solution-Phase Plasmonic Nanocube Sensors. *Nat. Methods* **2012**, *9*, 1189–1191.
- (61) Wang, W.; Li, Z. P.; Gu, B. H.; Zhang, Z. Y.; Xu, H. X. Ag@SiO<sub>2</sub> Core-Shell Nanoparticles for Probing Spatial Distribution of Electromagnetic Field Enhancement Via Surface-Enhanced Raman Scattering. *ACS Nano* **2009**, *3*, 3493–3496.
- (62) Chen, B.; Jiao, X. L.; Chen, D. R. Size-Controlled and Size-Designed Synthesis of Nano/Submicrometer Ag Particles. *Cryst. Growth Des.* **2010**, *10*, 3378–3386.



Cite this: *Photochem. Photobiol. Sci.*, 2017, **16**, 489

## Modification of emission photon statistics from single quantum dots using metal/SiO<sub>2</sub> core/shell nanostructures†

Hiroyuki Naiki,\*‡<sup>a</sup> Hidetoshi Oikawa<sup>a</sup> and Sadahiro Masuo\*<sup>b</sup>

Emission photon statistics, *i.e.*, single-photon and multi-photon emissions, of isolated QDs is required for tailoring optoelectronic applications. In this article, we demonstrate that the emission photon statistics can be modified by the control of the spectral overlap of the QDs with the localized surface plasmon resonance (LSPR) of the metal nanoparticle (metal NP) and by the distance between the QD and the metal NP. Moreover, the contribution to the modification of the emission photon statistics, which is the excitation and emission enhancements and the quenching generated by the spectral overlap and the distance, is elucidated. By fabricating well-defined SiO<sub>2</sub>-coated AgNPs and AuNPs (metal/SiO<sub>2</sub>), the spectral overlap originated from the metal species of Ag and Au and the distance constituted by the thickness of the SiO<sub>2</sub> shell are controlled. The probability of single-photon emission of single QD was increased by the enhancement of the excitation rate *via* adjusting the distance using Ag/SiO<sub>2</sub> while the single-photon emission was converted to multi-photon emission by the effect of exciton quenching at a short distance and a small spectral overlap. By contrast, the probability of multi-photon emission was increased by enhancement of the multi-photon emission rate and the quenching *via* the spectral overlap using Au/SiO<sub>2</sub>. These results indicated the fundamental finding to control emission photon statistics in single QDs by controlling the spectral overlap and the distance, and understand the interaction of plasmonic nanostructures and single QD systems.

Received 13th September 2016,  
Accepted 21st November 2016

DOI: 10.1039/c6pp00342g

rsc.li/pps

## Introduction

Colloidal semiconductor quantum dots (QDs) have potential applications in solar energy conversion,<sup>1–3</sup> light emitting diodes,<sup>4–6</sup> quantum photon sources,<sup>7–15</sup> and sensing.<sup>16–18</sup> These devices are based on a wide range of high absorption cross-sections, photostabilities, and multi-exciton dynamics of QDs. Notably, unique emission behavior, such as single-photon emission<sup>7–9</sup> and multi-photon emission,<sup>10–15</sup> from a single QD has been observed using the photon-antibunching measurements because of the multi-exciton dynamics dominated by the Auger relaxation process. Multi-photon emission, such as bi-exciton emission, from individual QDs has been reported in detail. Nair *et al.* calculated the quantum yield of

bi-exciton emission from a single CdSe/CdZnS (core/shell) QD,<sup>10</sup> and Mangum *et al.* demonstrated multi-photon emission from CdSe/CdS QDs using their developed photon-antibunching measurement.<sup>13</sup>

Previously, we demonstrated multi-photon emission from a single CdSe/ZnS QD that interacted with Ag nanoparticles (AgNPs–QD).<sup>19–21</sup> Photoluminescence (PL) emission behavior was suggested on the basis of the multi-exciton being first generated in the single QD by the strong electric field of the LSPR of AgNPs, which is so-called “excitation enhancement”.<sup>22</sup> In the case of isolated single QDs, the multi-exciton decayed nonradiatively by the Auger recombination between excitons on the picosecond time scale (~100 ps);<sup>4</sup> as a result, a single-exciton remained. However, in the case of the AgNP–QD system, the multi-photon emission rate was accelerated by the AgNPs, which was caused by the enhanced radiative process called as “emission enhancement”<sup>23–26</sup> and/or quenching *via* energy transfer to AgNPs. Hence, the multi-photon emission rate could be faster than Auger recombination. As a result, the multi-photon emission from the single QDs was observed to interact with the AgNPs. Specifically, the emission enhancement by the AgNPs could alter the probability of multi-photon emission from individual QDs *via* a modified multi-exciton

<sup>a</sup>Institute of Multidisciplinary Research for Advanced Materials, Tohoku University, Katahira 2-1-1, Aoba-ku, Sendai 980-8577, Japan

<sup>b</sup>Department of Applied Chemistry for Environment, Kwansei Gakuin University, Gakuen 2-1, Sanda, Hyogo 669-1337, Japan

† Electronic supplementary information (ESI) available: Fig. S1: TEM images and the diameter histograms of Ag, Au, and SiO<sub>2</sub> NPs. See DOI: 10.1039/c6pp00342g

‡ Current address: Department of Applied Chemistry for Environment, Kwansei Gakuin University, Gakuen 2-1, Sanda, Hyogo 669-1337, Japan.

relaxation process.<sup>19–21</sup> In current reports, multi-photon emissions from isolated QDs have similarly been observed to substantially interact with metal nanostructures.<sup>27–34</sup> Cannesson *et al.*, LeBlanc *et al.*, Park *et al.*, Dey *et al.*, and Wang *et al.* have demonstrated this increase in the probability of multi-photon emission by investigating CdSe/CdS QDs with Au films,<sup>27</sup> CdSe/ZnS QDs with Au films,<sup>28</sup> CdSe/CdS QDs with Ag films,<sup>30</sup> CdSe/CdS QDs with Au/SiO<sub>2</sub>,<sup>33</sup> and CdSe/CdS/SiO<sub>2</sub> QDs with Au gap-nanoantennas.<sup>34</sup> Similar to our results, the multi-photon emission from individual QDs was enhanced by the interaction with the metal nanostructures.

So far, by using various types of metal nanostructures, the conversion of single-photon emission to multi-photon emission has been observed. In other words, the contributions of excitation and emission enhancements and quenching on modifying the emission photon statistics were unclear because the contribution depends on the geometry of the metal nanostructure–single QD system. Generally, the enhancements and the quenching depend on the spectral overlap and the distance between a metal nanostructure and a single QD in the system. Thus, to elucidate the influence of the enhancements and the quenching on modifying the emission photon statistics, the spectral overlap and the distance in the metal nanostructure–single QD system are required to be precisely and definitely controlled. In particular, with respect to the spectral overlap, the overlap between the absorption spectrum of the QDs and the LSPR band leads to excitation enhancement, whereas the overlap between the PL spectrum of the QD and the LSPR band induces the emission enhancement and the quenching. With regards to the distance, a shorter distance is better for excitation and emission enhancements because the electric-field intensity of the LSPR and the dipole–dipole interaction between the QD and the metal nanostructure increases with decreasing distance. Recently, we have demonstrated the modification of emission photon statistics by excitation and emission enhancements and quenching, overcoming the difficulty to precisely control the spectral overlap and the distance.<sup>35,36</sup> The spectral overlap was fixed by using a spectrally defined single metal nanostructure, such as a single cubic AuNP and a silver-coated atomic force microscopy tip (AgTip). In addition, the distance was controlled at a nanometer scale using an atomic force microscopy (AFM) system, bringing the single cubic AuNP and the AgTip close to a single QD. From these results, the emission photon statistics could be modified by the contribution of both the emission enhancement and the quenching, and controlled by adjusting the precise distance of AgTip to single QDs between 2 and 50 nm.

In this work, we elucidate the contribution of excitation and emission enhancements and quenching by modifying the emission photon statistics using SiO<sub>2</sub>-coated metal NPs (metal/SiO<sub>2</sub>). The single metal/SiO<sub>2</sub> adsorbed the single QD while controlling the spectral overlap and the distance. In previous reports, by using a spectrally defined single metal nanostructure and AFM system, the contribution of excitation and emission enhancements and quenching on modifying the emission photon statistics was investigated. In this approach,

by using metal/SiO<sub>2</sub> with well-controlled morphology and composition, the emission photon statistics is modified to adjust both the spectral overlap and the distance. The spectral overlap is controlled to use the different metal species, Ag and Au, on the metal/SiO<sub>2</sub>, which exhibit the LSPR band at different wavelengths. The distance is controlled by the shell thickness of SiO<sub>2</sub> ranging from 6 to 38 nm. From the results of modified emission photon statistics, the influence of the controlled spectral overlap and distance is clarified.

## Experimental section

### Chemicals

Silver nitrate, L-ascorbic acid, poly(vinyl pyrrolidone) (PVP,  $M_w$ : 40 000 and 360 000), sodium chloride, sodium hydroxide, sodium citrate, 50% dimethylamine solution (DA), HAuCl<sub>4</sub>·4H<sub>2</sub>O, and 28% ammonia solution were purchased from Wako Pure Chemical Industries Ltd. *N'*-(2-Aminoethyl)-*N*-(3-trimethoxysilyl propyl)ethane-1,2-diamine, 1,5-pentandiol (PD), and CdSe/ZnS QDs (Lumidot,  $\lambda_{em}$ : 610 nm) were purchased from Sigma-Aldrich. Tetraethylorthosilicate (TEOS) was purchased from Alfa Aesar Co. All chemicals were used as received, without further purification.

### Fabrication of Ag/SiO<sub>2</sub>-single QD systems

Well-defined AgNPs were prepared by the reduction of AgCl colloids with ascorbic acid according to a previously reported method.<sup>37</sup> First, 170 mg of PVP ( $M_w$ : 40 000) and 170 mg of silver nitrate were dissolved in 40 mL of pure water under stirring, and then 400  $\mu$ L of sodium chloride aqueous solution (5.0 M) was added and stirred for 15 min at room temperature under dark conditions. The resulting AgCl colloidal suspension was added to 360 mL of the reducing solution, which contained 2800 mg of L-ascorbic acid and 800 mg of sodium hydroxide. The mixture was further stirred for 2 h under dark conditions. The resulting AgNPs were collected by centrifugation at 8000g for 60 min and washed twice with pure water and ethanol, in sequence.

The prepared AgNPs were coated with SiO<sub>2</sub> shells with five different shell thicknesses using typical Stöber methods described elsewhere.<sup>37</sup> Then, 8 mL of AgNP suspension was diluted with 20 mL of ethanol and 750  $\mu$ L of 50% DA solution was added. After ultrasonication for 30 min to disperse the NPs completely, different amounts of the TEOS and ethanol solution (1 M: 50, 150, 300, 500, and 800  $\mu$ L) were added to form SiO<sub>2</sub> shells with different thicknesses, and the shells were grown for more than 12 h at 40 °C. Each Ag/SiO<sub>2</sub> sample was collected by centrifugation at 5000g for 30 min, washed with ethanol, and then re-dispersed in ethanol. The size and shape of the Ag/SiO<sub>2</sub> samples were characterized by transmission electron microscopy (TEM, H-7650, HITACHI).

To adsorb single CdSe/ZnS QDs onto the Ag/SiO<sub>2</sub> (Ag/SiO<sub>2</sub>-QDs), the shell surface of the Ag/SiO<sub>2</sub> was first modified with an aminosilane coupling agent. Four milliliters of Ag/SiO<sub>2</sub> suspension and 330  $\mu$ L of 50% DA solution were added to

6 mL of ethanol and then ultrasonicated for 30 min. *N*'-(2-Aminoethyl)-*N*-(3-trimethoxy-silylpropyl)ethane-1,2-diamine in ethanol solution (16  $\mu$ M, 190  $\mu$ L) was added to the NP suspensions and reacted for 15 h at 40 °C. The resulting amino-functionalized Ag/SiO<sub>2</sub> particles with different thicknesses were collected by centrifugation at 5000g for 10 min and re-dispersed in ethanol to adjust the absorbance to 0.25 to prepare a constant concentration. Subsequently, 3  $\mu$ L of QDs in ethanol (16.5  $\mu$ M) were added to the Ag/SiO<sub>2</sub> suspensions and ultrasonicated for 5 min. Finally, Ag/SiO<sub>2</sub>-QD suspensions were spin-coated onto coverslips at 3000 rpm for 90 s. Absorption and PL spectra were collected using a UV-vis absorption spectrophotometer (V-570, JASCO) and a PL spectrophotometer (F-7000, HITACHI), respectively.

### Fabrication of Au/SiO<sub>2</sub>-single QD systems

Highly spherical AuNPs were synthesized by a modified polyol method.<sup>38</sup> To tailor the spherical shape by underpotential deposition, 0.15 mL of silver nitrate in PD solution (0.04 M) and 6.0 mL of PVP ( $M_w$ : 360 000,  $2.7 \times 10^{-4}$  M) in PD solution were added to 11 mL of boiled PD. Subsequently, 3.0 mL of HAuCl<sub>4</sub>·4H<sub>2</sub>O in PD solution (0.1 M) were periodically added every 30 s for 15 min. The mixture, with a wine-red color, was refluxed for 5 h to form the desired AuNPs through an Ostwald ripening process. After the mixture was allowed to cool at room temperature, the resulting AuNPs were collected by centrifugation at 10 000g for 60 min and washed twice with ethanol and pure water, respectively. Finally, the product was re-dispersed in 40 mL of sodium citrate aqueous solution (0.05 M) to coat the shell. The obtained AuNPs were coated with SiO<sub>2</sub> shells using the Stöber method as well as the aforementioned method. Eight milliliters of AuNP suspension and 3 mL of 28% ammonia solution were added to 20 mL of ethanol. After ultrasonication for 30 min, different amounts of TEOS ethanol solution (1 M: 50, 70, 100, 180, and 250  $\mu$ L) were injected and reacted for 12 h at 40 °C. Formed Au/SiO<sub>2</sub> was collected again by centrifugation at 8000g for 30 min, washed with ethanol, and then re-dispersed in 28 mL of ethanol. To adsorb single CdSe/ZnS QDs onto Au/SiO<sub>2</sub> (Au/SiO<sub>2</sub>-QDs), the shell surface of the Au/SiO<sub>2</sub> was modified with aminosilane coupling agents, and single QDs were adsorbed onto amino-functionalized Au/SiO<sub>2</sub> following the same method used for the Ag/SiO<sub>2</sub>-QDs.

### Instrumental setup for single QD measurement

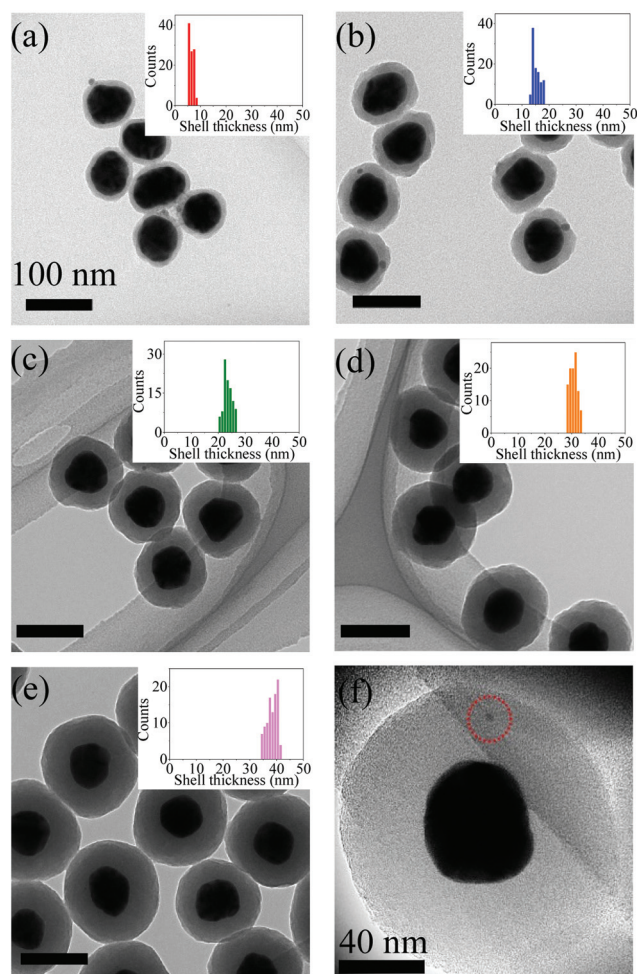
The PL properties of individual QDs were measured using a Hanbury-Brown and Twiss type photon correlation setup with a fs-pulsed laser excitation source and a homemade sample-scanning confocal microscope system. As an excitation light source, the frequency-doubled output (488 nm, 8.01 MHz, ~200 fs full-width at half-maximum (FWHM)) of a Ti:sapphire laser (976 nm, 80 MHz, 100 fs FWHM, Mai-Tai, Spectra-Physics) was circularly polarized by a Glan-Thomson polarizer and a  $\lambda/4$  waveplate. The laser beam was reflected by a dichroic mirror (Asahi Spectra) to introduce it into an inverted microscope (TE2000, Nikon), where it was focused onto the sample

by an oil-immersion objective lens (100 $\times$ , N.A.:1.3, Nikon). A PL image from the sample was recorded by raster scanning it over a focused incident laser spot. This focused spot was then moved to an isolated photoluminescent spot, which corresponded to an individual QD in the PL image, and the PL emission properties of isolated QDs were measured. The emitted photons from single QDs were collected by the same objective lens and were passed through a 100  $\mu$ m optical pinhole, a long-pass filter (LP02-514RU, Semrock), and a band-pass filter (FF01-607/36, Semrock) that were suitable for the PL band of the QD. The photons were then divided equally by a 50/50 non-polarizing beam-splitter cube into two beam paths and then detected by two avalanche single-photon counting modules (APD: SPCM-AQR-14, PerkinElmer). The signals from both APDs were connected to the router of a time-correlated single-photon counting (TCSPC) PC board (SPC630, Becker & Hickl). The signal from one of the APDs was delayed using a delay generator (DG535, Stanford Research) to compensate for the dead time of the TCSPC board. A synchronization signal, which detected part of the excitation laser, was used as a synchronization signal for PL lifetime measurement. Time-resolved data were acquired using a first-in-first-out mode, in which the arrival time after the beginning of the acquisition, the time delay between the start and stop pulses, and the detection channel were registered for each detected PL photon. The data were analyzed using a homemade LabVIEW routine that allowed the time traces of PL intensity and PL lifetime and the photon correlation histogram of the isolated QDs to be simultaneously measured.

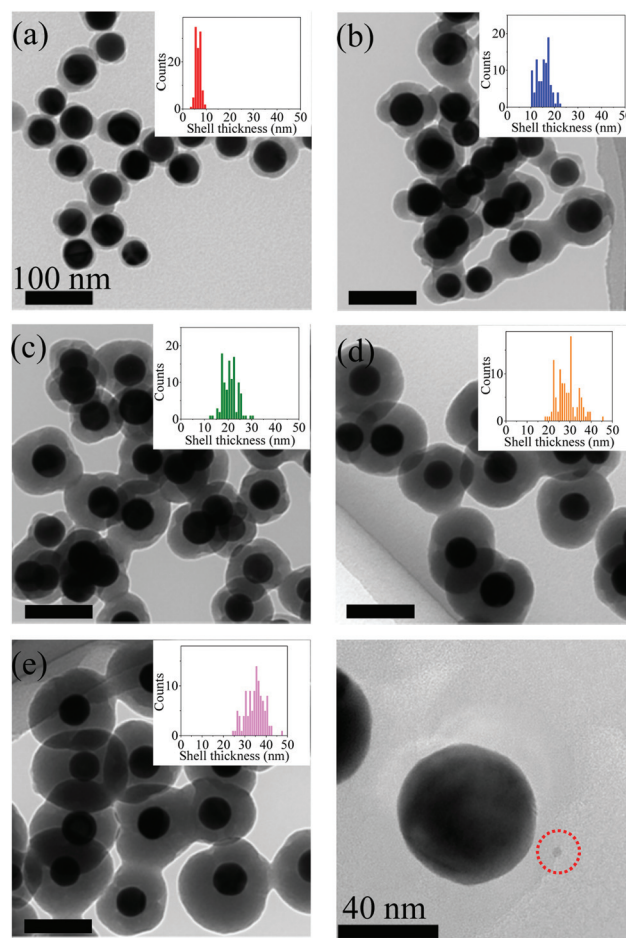
## Results and discussion

### Characterization of the prepared metal/SiO<sub>2</sub>

We have strategically concentrated on designing well-defined metal/SiO<sub>2</sub>-QD structures to control the contribution of the excitation and emission enhancements and the quenching. At close distances, exciton quenching, such as electron and energy transfers from the single QD to the metal nanostructure, is generated. Distances from 5 nm to 30 nm have been reported to be suitable for fluorescence enhancement as a result of the combination of the enhancements and the quenching by the metal nanostructures.<sup>22</sup> However, the ideal distance strongly depends on the size of the metal nanostructures. In addition, an increase in the probability of the multi-photon emission induced by the quenching of single-excitons has also been reported.<sup>29,32,35,36,39</sup> Hence, the selection of suitable metal species, the adjustment of the size and shape of metal nanostructures, and the distance between QDs and metal nanostructures are critical for modifying the emission photon statistics in the PL emission by controlling the contribution of excitation and emission enhancements and quenching. The average diameters of Ag and AuNPs in Ag/SiO<sub>2</sub> and Au/SiO<sub>2</sub> were estimated to be  $54 \pm 2$  nm and  $43 \pm 4$  nm, respectively, from TEM images shown in Fig. S1.† The TEM images of Ag/SiO<sub>2</sub> and Au/SiO<sub>2</sub> with histograms of the shell



**Fig. 1** TEM images and histograms of shell thicknesses of Ag/SiO<sub>2</sub> for different shell thicknesses. Average shell thickness: (a) 7 nm, (b) 15 nm, (c) 24 nm, (d) 31 nm, and (e) 38 nm. (f) HRTEM image of Ag/SiO<sub>2</sub>-QDs (average shell thickness: 38 nm). The single dot circled by a red-dotted line corresponds to a single QD.



**Fig. 2** TEM images and histograms of the shell thickness of Au/SiO<sub>2</sub> with different shell thicknesses. Average shell thickness: (a) 6 nm, (b) 15 nm, (c) 21 nm, (d) 29 nm, and (e) 35 nm. (f) HRTEM image of Au/SiO<sub>2</sub>-QDs (average shell thickness: 15 nm). The single dot circled by a red-dotted line corresponds to a single QD.

thickness are shown in Fig. 1 and 2, respectively. In particular, in the case of Au/SiO<sub>2</sub>, the shell thicknesses were inhomogeneous compared with those of Ag/SiO<sub>2</sub>. This inhomogeneity likely affected the PL emission behavior of single QDs (*vide infra*). However, for the average shell thicknesses, the thicknesses were successfully adjusted across a similar thickness range for Ag/SiO<sub>2</sub> and Au/SiO<sub>2</sub> (Ag/SiO<sub>2</sub>: 7 ± 1 nm, 15 ± 1 nm, 24 ± 2 nm, 31 ± 1 nm and 38 ± 2 nm; Au/SiO<sub>2</sub>: 6 ± 1 nm, 15 ± 3 nm, 21 ± 3 nm, 29 ± 5 nm and 35 ± 4 nm). We selected these shell thicknesses to investigate the optimal thickness for modification of the emission photon statistics *via* the metal NPs. The sizes of the metal NPs and their shell thicknesses are summarized in Table 1.

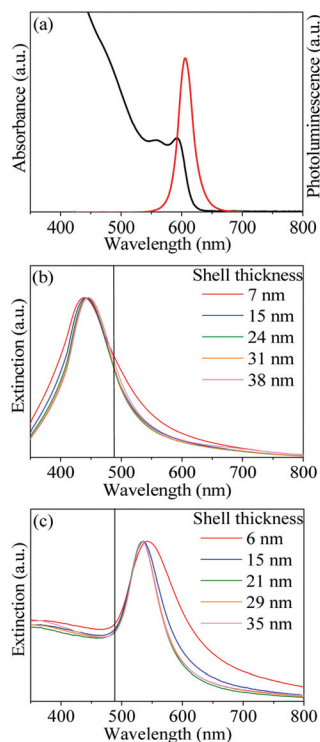
The absorption and PL spectra of CdSe/ZnS QDs dispersed in toluene and the extinction spectra of the prepared Ag/SiO<sub>2</sub> and Au/SiO<sub>2</sub> with various shell thicknesses are shown in Fig. 3(a–c), respectively; the peak wavelengths of the LSPR

**Table 1** Characterization results for Ag/SiO<sub>2</sub> and Au/SiO<sub>2</sub>

Metal/SiO <sub>2</sub>	Core size ± SD (nm)	Shell thickness ± SD (nm)	LSPR peak (nm)	Overlap area with emission spectrum of QDs (standardization%)
Ag	54 ± 2	7 ± 1	439	11.3
		15 ± 1	442	9.0
		24 ± 2	443	8.0
		31 ± 1	445	8.1
		38 ± 2	446	8.8
Au	43 ± 4	6 ± 1	542	25.5
		15 ± 3	535	17.7
		21 ± 3	534	14.3
		29 ± 5	534	15.0
		35 ± 4	534	14.9

SD is standard deviation.

spectra are summarized in Table 1. The absorption spectrum of the QD overlapped with the LSPR spectra of both Ag/SiO<sub>2</sub> and Au/SiO<sub>2</sub> for all shell thicknesses, which indicates that



**Fig. 3** (a) Absorption (black line) and photoluminescence spectra (red line) of CdSe/ZnS QDs dispersed in toluene. (b), (c) Extinction spectra of Ag/SiO<sub>2</sub> and Au/SiO<sub>2</sub> with different shell thicknesses. Black vertical lines indicate the excitation wavelength (488 nm).

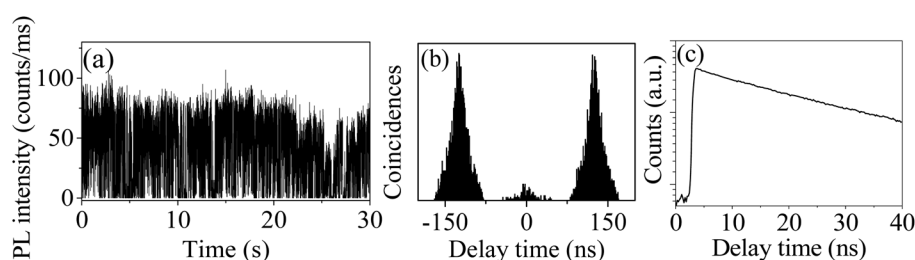
both Ag/SiO<sub>2</sub> and Au/SiO<sub>2</sub> have a potential to enhance the excitation rate of the QDs. However, a pulsed laser with a wavelength of 488 nm was used as the excitation light source in our experiments; therefore, the LSPR was excited for Ag/SiO<sub>2</sub>, but could not be excited efficiently for Au/SiO<sub>2</sub>. The emission enhancement is derived from the overlap between the LSPR and PL spectra of the QDs,<sup>23–26</sup> because the emission rate of the QDs is accelerated *via* the exciton-induced scattering of the LSPR from the metal NPs. Standardized overlap areas estimated from the spectra are also summarized in Table 1. The LSPR spectra of Ag/SiO<sub>2</sub> have little overlap with the PL emission spectrum of the QDs (8.0 to 11.3%). By

contrast, in the case of Au/SiO<sub>2</sub>, the overlap areas were estimated to be 14.3 to 25.5%, which is 1.3 to 3.2 times larger than that of Ag/SiO<sub>2</sub>. This difference in the overlap area is an important factor in controlling the emission photon statistics in PL emission.

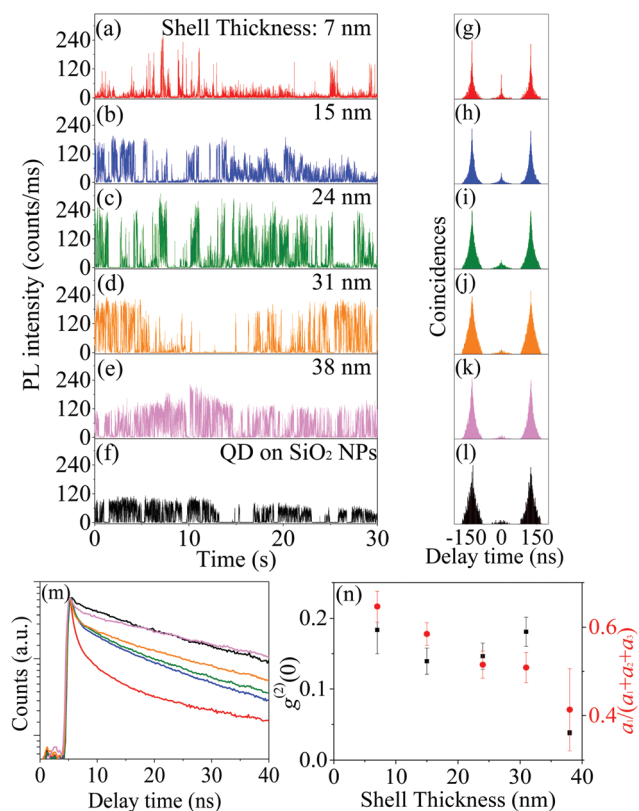
After a single QD was adsorbed onto the surface of each single metal/SiO<sub>2</sub> by electrostatic interaction, the adsorption of the single QD was confirmed by high-resolution TEM (HRTEM, JEM-3010, JEOL) images, as shown in Fig. 2(f) and 3(f). Black dots were observed on the shell, which were assigned to single QDs. The obtained Ag/SiO<sub>2</sub>-QD and Au/SiO<sub>2</sub>-QD systems were spin-coated onto glass coverslips to observe their PL emission behavior.

### Photon-antibunching behavior of single CdSe/ZnS QDs

We first investigated the PL emission behavior of the uncoupled single QDs as a control sample. The PL emission properties of single QDs were obtained using a sample-scanning confocal microscope in combination with a fs-pulsed laser excitation source (excitation wavelength: 488 nm; power: 0.21 kW cm<sup>-2</sup>) using the Hanbury-Brown and Twiss photon correlation setup. Fig. 4 shows the PL emission behavior of a representative single QD, *i.e.*, a time trace of the PL intensity (a), a photon correlation histogram (b), and a PL decay curve (c). The average number of excitons generated by a single excitation pulse was estimated as 0.22 by taking into account the number of photons per pulse and the absorption cross-section of the QD at the excitation wavelength ( $3.5 \times 10^{-15}$  cm<sup>2</sup> at 488 nm). In Fig. 4(a), typical PL blinking behavior was observed and the PL intensity at on-time was approximately 80 counts per ms. The average PL intensity estimated from 72 single QDs was 55 counts per ms. We estimated the PL lifetime as 17 ns by fitting the PL decay curve with a single exponential function,  $I(t) = \alpha \exp(-t/\tau)$ , where  $\alpha$  is the normalized amplitude and  $\tau$  is the PL lifetime. In the photon correlation histogram shown in Fig. 4(b), the detection events at a delay time of 0 ns ( $\tau = 0$ ) were lower than those at other delay times ( $\pm 125$  ns). In this work, the second-order correlation function  $g^{(2)}(0)$  is defined as the ratio of the number of detection events at  $\tau = 0$  to those at other delay times. The value of  $g^{(2)}(0)$  is known to be correlated with the multi-photon emission efficiency under low excitation conditions, *i.e.*, the  $g^{(2)}(0)$  value



**Fig. 4** Typical time trace of photoluminescence intensity (a), photon correlation histogram (b), and photoluminescence decay curve (c) detected simultaneously from a single QD under an applied excitation laser power of 0.21 kW cm<sup>-2</sup>.



**Fig. 5** Time traces of photoluminescence intensities (a–f), photon correlation histograms (g–l), photoluminescence decay curves (m) detected simultaneously from Ag/SiO<sub>2</sub>-QDs and QD on SiO<sub>2</sub> NPs, and dependence of averaged  $g^{(2)}(0)$  (black square) values and the contributions of amplitude for the shortest PL lifetime (red circle) on shell thickness (n). Shell thickness of 7 nm: (a), (g), and red line in (m), 15 nm: (b), (h), and blue line in (m), 24 nm: (c), (i), and red line in (m), 31 nm: (d), (j), and orange line in (m), 38 nm: (e), (k), and purple line in (m) and QD on SiO<sub>2</sub> NPs: (f), (l), and black line in (m). The excitation laser power was 0.21 kW cm<sup>-2</sup>.

increases when this efficiency is increased.<sup>29,34</sup> The  $g^{(2)}(0)$  value was estimated to be 0.07 from Fig. 4(b), which indicates that single QDs emitted single photons. These emission behaviors were typical among single QDs as control samples.

### Photon-antibunching behavior of metal/SiO<sub>2</sub>-QDs

Time traces of the PL intensities (a–e), the photon correlation histograms (g–k), and the PL decay curves (m) obtained from the most enhanced Ag/SiO<sub>2</sub>-QDs for each shell thickness are shown in Fig. 5. Most of the Ag/SiO<sub>2</sub>-QD systems exhibited higher PL intensities compared with the control sample because the LSPR of the Ag/SiO<sub>2</sub> interacted with QDs, resulting in excitation enhancement. (The averaged PL intensities are summarized in Table 2). Notably, the photon correlation histogram of the Ag/SiO<sub>2</sub>-QD with a shell thickness of 7 nm exhibited the highest center peak ( $g^{(2)}(0) = 0.19$  in Fig. 5f) and the PL decay was faster compared with those of other Ag/SiO<sub>2</sub>-QDs in Fig. 5(m). This indicates that the probability of a single-photon emission was decreased by Ag/SiO<sub>2</sub> with a 7 nm shell. The lower efficiency of single-photon emission was probably caused by the quenching of a single-exciton because of energy transfer from the single QD to the Ag/SiO<sub>2</sub>.<sup>29,32,35,36,39</sup> The decay curves were fit using a three-exponential function,

$$I(t) = \alpha_1 \exp(-t_1/\tau_1) + \alpha_2 \exp(-t_2/\tau_2) + \alpha_3 \exp(-t_3/\tau_3) \quad (1)$$

The PL lifetimes and the amplitudes of each decay component, and the averaged PL lifetimes obtained from the fitting are shown in Table 2. The shortest PL lifetimes were the same value as the instrument response function (IRF; 0.6 ns). Specifically, the shortest PL lifetime was likely much shorter than the IRF. The shortest PL lifetime was attributed to the energy transfer. To show the emission behaviors depending on the shell thickness, the averaged contribution of the amplitude for the shortest PL lifetime, *i.e.*,  $\alpha_1/(\alpha_1 + \alpha_2 + \alpha_3)$  and  $g^{(2)}(0)$  values estimated from all of the obtained data with respect to the shell thicknesses (around 20 each of Ag/SiO<sub>2</sub>-QD systems) is shown in Fig. 5(n). The large  $\alpha_1/(\alpha_1 + \alpha_2 + \alpha_3)$  value of the Ag/SiO<sub>2</sub>-QDs with the 7 nm shell indicates that the contribution from exciton quenching by energy transfer was higher than that of other Ag/SiO<sub>2</sub>-QD systems as shown in Fig. 5(n). Accelerated PL decay by exciton quenching has been reported to lead to a decreased probability of single-photon emission.<sup>29,32,35,36,39</sup> The aforementioned results obtained for the Ag/SiO<sub>2</sub>-QDs with the 7 nm shell are consistent with these reported results. The existence of single-exciton quenching in

**Table 2** Averaged PL intensities, PL lifetimes of each decay components, amplitudes, and averaged PL lifetimes of Ag/SiO<sub>2</sub>-QDs and Au/SiO<sub>2</sub>-QDs estimated by fitting three exponential functions

Metal/SiO <sub>2</sub>	Shell thickness (nm)	Averaged PL intensity (counts per ms)	$\tau_1$ (ns)	$\alpha_1$	$\tau_2$ (ns)	$\alpha_2$	$\tau_3$ (ns)	$\alpha_3$	$\tau_{ave}$ (ns)
Ag	7	115	0.6	0.80	3.4	0.16	17	0.04	1.8
	15	92	0.6	0.57	6.6	0.25	18	0.18	5.3
	24	108	0.6	0.43	5.0	0.24	17	0.33	6.9
	31	109	0.6	0.43	6.3	0.21	25	0.36	10.9
	38	89	0.6	0.25	7.7	0.31	20	0.44	11.4
Au	6	156	0.6	0.65	3.1	0.18	14	0.17	3.2
	15	96	0.6	0.72	2.7	0.21	11	0.07	1.7
	21	89	0.6	0.61	4.5	0.24	20	0.15	4.6
	29	104	0.6	0.63	3.3	0.22	11	0.15	2.7
	35	94	0.6	0.52	5.6	0.28	16	0.20	5.2

Ag/SiO<sub>2</sub>-QDs with the 7 nm shell is also supported by the blinking behavior of the PL emission. Because of the quenching of the single-exciton by the Ag/SiO<sub>2</sub>, the Ag/SiO<sub>2</sub>-QDs with the 7 nm shell exhibited more frequent blinking compared with Ag/SiO<sub>2</sub>-QDs with shells thicker than 15 nm.

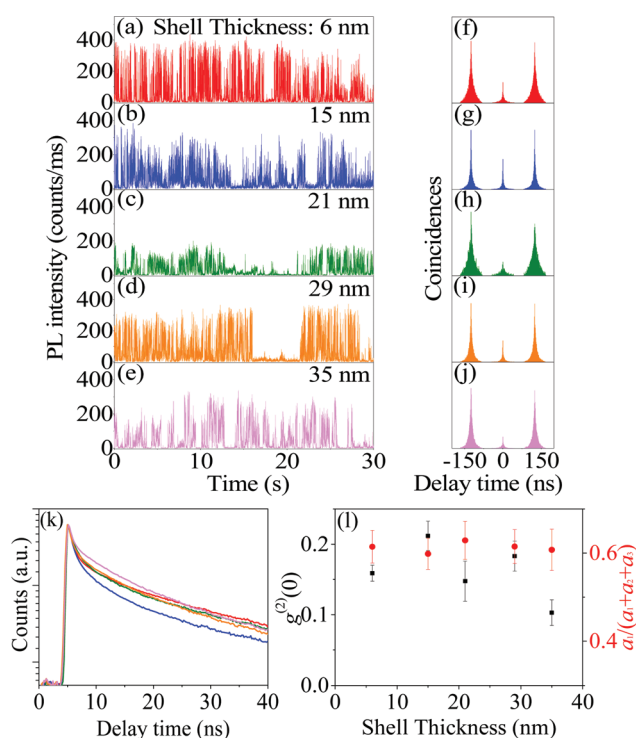
However, the Ag/SiO<sub>2</sub>-QD systems with shells thicker than 15 nm exhibited almost the same  $g^{(2)}(0)$  values as those of the control samples ( $g^{(2)}(0) = 0.10, 0.12, 0.06,$  and  $0.04$  in Fig. 5h–k, respectively). Hence, the efficiencies of single-photon emission in Ag/SiO<sub>2</sub>-QD systems with shells thicker than 15 nm decreased to those of the control samples. The PL intensities were much greater than that of the control sample but slower than that of the Ag/SiO<sub>2</sub>-QDs with shells of 7 nm thickness as shown in Fig. 5(m). The  $g^{(2)}(0)$  values decreased with increasing shell thickness, and the  $\alpha_1/(\alpha_1 + \alpha_2 + \alpha_3)$  values decreased with increasing shell thickness as well as the  $g^{(2)}(0)$  values as shown in Fig. 5(n), because the efficiency of the energy transfer depends on the distance. In the case of Ag/SiO<sub>2</sub>-QD systems with shells thicker than 15 nm, the contribution of the energy transfer was low. Therefore, the Ag/SiO<sub>2</sub>-QD systems with shells thicker than 15 nm exhibited single-photon emission behaviors due to a decrease in the contribution of exciton quenching, depending on the shell thickness. About the dependence of the PL intensity on the distance between an emitter and a metal NP, previously, Novotny *et al.* observed the change of the fluorescence intensity from a single organic molecule by the approach of a metal NP attached to the end of a pointed optical fiber. They reported the increase and the decrease in the fluorescence intensity with reducing distance between the single molecule and the metal NP.<sup>40,41</sup> By theoretical analysis, the change of the fluorescence intensity was caused by the combination of excitation enhancement and the quenching depending on the distance, same as ours. In the case of Ag/SiO<sub>2</sub>-QD systems, the PL intensities from Ag/SiO<sub>2</sub>-QD systems slightly increased with reducing distance compared to that in Novotny's reports. This increase in the PL intensity indicated that the excitation enhancement and the quenching *via* the energy transfer to the AgNPs probably occurred, however, these efficiencies were low.

To confirm whether the aforementioned results were caused by Ag/SiO<sub>2</sub>, a SiO<sub>2</sub> NP was used instead of Ag/SiO<sub>2</sub> (as shown in the TEM image of SiO<sub>2</sub> NPs in Fig. S1†). Single QDs were adsorbed onto SiO<sub>2</sub> NPs (QDs on SiO<sub>2</sub> NPs) of 50 nm in diameter, and the PL emission behaviors of the QDs on SiO<sub>2</sub> NPs were observed. Most of the QDs on SiO<sub>2</sub> NPs exhibited the same time trace of the PL intensity, photon correlation histogram, and PL lifetime as the control samples as shown in Fig. 5(f), (l), and (m), respectively. Therefore, the aforementioned emission behavior of the Ag/SiO<sub>2</sub>-QD system resulted from the interaction of the QDs with the Ag/SiO<sub>2</sub>.

In the case of the Ag/SiO<sub>2</sub>-QD system, the mechanism of PL emission behavior is summarized as follows: the excitation rate of QDs was increased by the electric field of the Ag/SiO<sub>2</sub>'s LSPR induced by a 488 nm excitation laser. As a consequence of this excitation enhancement, the probability of multi-

exciton generation increased. Subsequently, a non-radiative Auger recombination between excitons occurred within 100 ps<sup>4</sup> because the emission enhancement by the Ag/SiO<sub>2</sub> could be neglected. Therefore, single-photon emission with a higher PL intensity compared with that of the control sample was observed in Ag/SiO<sub>2</sub>-QD systems with shells of 15 to 38 nm thickness. However, quenching of the single-exciton by the Ag/SiO<sub>2</sub> caused an increase in the multi-photon emission and high frequency blinking behavior in the case of the 7 nm thick shell.

By contrast, Au/SiO<sub>2</sub>-QD systems exhibited markedly different emission photon statistics. Representative time traces of the PL intensity (a–e), the photon correlation histograms (f–j), the PL decay curves (k), and the dependence of averaged  $\alpha_1/(\alpha_1 + \alpha_2 + \alpha_3)$  values and the  $g^{(2)}(0)$  values estimated from all of the obtained data (around 20 each of Au/SiO<sub>2</sub>-QD systems) on shell thicknesses (l) of Au/SiO<sub>2</sub>-QDs for each shell thickness are shown in Fig. 6. All of the Au/SiO<sub>2</sub>-QD systems exhibited PL intensities greater than those of the control sample as well as the Ag/SiO<sub>2</sub>-QD systems. (These averaged PL intensities are summarized in Table 2). In contrast to the Ag/SiO<sub>2</sub>-QD systems, the center peaks in the photon correlation histograms of the Au/SiO<sub>2</sub>-QD systems, with the exception of the system



**Fig. 6** Time traces of photoluminescence intensities (a–e), photon correlation histograms (f–j), photoluminescence decay curves (k) detected simultaneously from Au/SiO<sub>2</sub>-QD, and dependence of averaged  $g^{(2)}(0)$  (black square) values and the contributions of amplitude for the shortest PL lifetime (red circle) on shell thickness (l). Shell thickness of 6 nm: (a), (f), and red line in (k), 15 nm: (b), (g), and blue line in (k), 21 nm: (c), (h), and red line in (k), 29 nm: (d), (i), and orange line in (k), and 35 nm: (e), (j), and purple line in (k). The excitation laser power was  $0.21 \text{ kW cm}^{-2}$ .

with the 35 nm thick shell, were greater ( $g^{(2)}(0) = 0.17, 0.30, 0.15, 0.21, \text{ and } 0.07$  as shown in Fig. 6f–j) than that of the control sample. The Au/SiO<sub>2</sub>-QDs with the 35 nm thick shell exhibited single-photon emission. Similar to the PL decays of the Ag/SiO<sub>2</sub>-QD systems, those of the Au/SiO<sub>2</sub>-QD systems were faster than that of the control sample. In Fig. 6(l), the  $g^{(2)}(0)$  values reduced with increasing shell thicknesses as well as in the case of Ag/SiO<sub>2</sub>-QD systems, while the correlation of the Au/SiO<sub>2</sub>-QD systems are weaker than that of the Ag/SiO<sub>2</sub>-QD systems. The  $\alpha_1/(\alpha_1 + \alpha_2 + \alpha_3)$  values of the Au/SiO<sub>2</sub>-QD systems slightly decreased with increasing shell thickness, which is the same tendency as the Ag/SiO<sub>2</sub>-QD systems shown in Fig. 6(l).

Meanwhile, the decrease in  $\alpha_1/(\alpha_1 + \alpha_2 + \alpha_3)$  values as a function of the shell thickness of the Au/SiO<sub>2</sub>-QD systems was less pronounced than that of the Ag/SiO<sub>2</sub>-QD systems. In addition, the  $\alpha_1/(\alpha_1 + \alpha_2 + \alpha_3)$  values for the Au/SiO<sub>2</sub>-QD systems remained higher even in the same shell thickness range contrary to the Ag/SiO<sub>2</sub>-QD systems. The high  $\alpha_1/(\alpha_1 + \alpha_2 + \alpha_3)$  values indicate that the energy transfer was more efficient as a consequence of the Au/SiO<sub>2</sub>-QD systems exhibiting a larger spectral overlap compared with the Ag/SiO<sub>2</sub>-QD systems. In the case of the Ag/SiO<sub>2</sub>-QD systems, the energy transfer caused the quenching, whereas the emission enhancement was mainly induced by the energy transfer in the Au/SiO<sub>2</sub>-QD systems. In the case of the Au/SiO<sub>2</sub>-QD systems, the PL intensities increased, although the excitation enhancement could be neglected. This increase in the PL intensity was caused by the emission enhancement. Specifically, the probability of the multi-photon emission was increased by the emission enhancement. Therefore, the  $g^{(2)}(0)$  values and the  $\alpha_1/(\alpha_1 + \alpha_2 + \alpha_3)$  values were higher than that of the Ag/SiO<sub>2</sub>-QD systems. However, as shown in Fig. 6(l), the dispersion of the  $g^{(2)}(0)$  and  $\alpha_1/(\alpha_1 + \alpha_2 + \alpha_3)$  values was large, although a negative correlation was observed. This large dispersion might be caused by the inhomogeneity in the shell thickness of the Au/SiO<sub>2</sub>. Depending on the position at which the single QDs are adsorbed, the distance between the QD and the AuNP varied. Therefore, large dispersion was observed because of the variation in this distance.

The mechanism of the multi-photon emission with an increase in the PL intensity of the Au/SiO<sub>2</sub>-QD systems is attributed to the enhancement of the multi-photon emission rate by the Au/SiO<sub>2</sub>. In the case of the Au/SiO<sub>2</sub>-QD system, the excitation enhancement can be neglected because the LSPR cannot be excited efficiently by the incident 488 nm laser. However, the multi-photon emission rate was accelerated because of emission enhancement by the Au/SiO<sub>2</sub>, and the multi-photon was emitted before the non-radiative Auger recombination. Hence, the emission enhancement resulted in the observed PL emission behavior. However, the interaction between the QDs and LSPR was weaker than that of the AgNP-QD system in previous reports.<sup>19–21</sup> Therefore, the PL decay curves were not reduced to the IRF, and the probability of multi-photon emission was lower than that of the reported AgNP-QD system. Similar to the Ag/SiO<sub>2</sub>-QD systems, Au/SiO<sub>2</sub>-

QD systems might have been quenched. However, the PL intensity of the Au/SiO<sub>2</sub>-QD system was much higher than that of the control sample. Specifically, the contribution of quenching to the increase in multi-photon emission was much lower. Therefore, the Au/SiO<sub>2</sub>-QD systems exhibited higher PL intensities and lower frequency of blinking compared to the Ag/SiO<sub>2</sub>-QDs with a 7 nm shell thickness.

## Conclusions

The results of our study provide evidence that Ag/SiO<sub>2</sub> and Au/SiO<sub>2</sub> can modify the emission photon statistics of single QDs by controlling the contribution of plasmonic effects, *i.e.*, excitation and emission enhancements and quenching, of metal NPs under the same excitation conditions. Specifically, Ag/SiO<sub>2</sub>-QDs can exhibit single-photon emission, whose efficiency was almost the same as the control samples with higher PL intensity due to the enhanced excitation rate of the Ag/SiO<sub>2</sub>-QD systems with shells of 15 nm to 38 nm in thickness. In the case of Ag/SiO<sub>2</sub>-QDs with a shell 7 nm in thickness, the high contribution of the exciton quenching in addition to this excitation enhancement caused the multi-photon emission with high frequency blinking. By contrast, Au/SiO<sub>2</sub> with shells of 6 nm to 29 nm in thickness can promote the multi-photon emission with higher PL intensity and low frequency blinking *via* an accelerated multi-photon emission rate by emission enhancement. The results presented herein suggest that the plasmonic nanostructures are suitable to modify the emission photon statistics of single QDs by controlling QD-plasmonic interaction.

## Acknowledgements

This work was partly supported by a Grant-in-Aid for Scientific Research on Priority Area “Strong Photons-Molecules Coupling Fields (No. 470)” from the Ministry of Education, Culture, Sports, Science and Technology, Japan, a Grant-in-Aid for the Japan Society for the Promotion of Science (JSPS) Fellows (No. 12J08034 to HN) and a Grant-in-Aid for Scientific Research (No. 26390023 to SM) from JSPS. Additionally, we wish to thank Professor Dr Hitoshi Kasai and Assistant Professor Dr Tsunenobu Onodera at Tohoku University for preparation and characterization of metal/SiO<sub>2</sub>-QD systems and Professor Dr Noriaki Ikeda at the Kyoto Institute of Technology for use of their measurement setup.

## Notes and references

- 1 R. Schaller and V. Klimov, High Efficiency Carrier Multiplication in PbSe Nanocrystals: Implications for Solar Energy Conversion, *Phys. Rev. Lett.*, 2004, **92**, 186601.
- 2 V. Klimov, Mechanisms for Photogeneration and Recombination of Multiexcitons in Semiconductor

- Nanocrystals: Implications for Lasing and Solar Energy Conversion, *J. Phys. Chem. B*, 2006, **110**, 16827–16845.
- 3 P. V. Kamat, Quantum Dot Solar Cells. The Next Big Thing in Photovoltaics, *J. Phys. Chem. Lett.*, 2013, **4**, 908–918.
  - 4 V. Klimov, A. A. Mikhailovsky, D. W. McBranch, C. A. Leatherdale and M. G. Bawendi, Quantization of Multiparticle Auger Rates in Semiconductor Quantum Dots, *Science*, 2000, **287**, 1011–1013.
  - 5 V. Klimov, A. A. Mikhailovsky, H. Xu, A. V. Malko, J. A. Hollingsworth, C. A. Leatherdale, H.-J. Eisler and M. G. Bawendi, Optical Gain and Stimulated Emission in Nanocrystal Quantum Dots, *Science*, 2000, **290**, 314–317.
  - 6 Y. Shirasaki, G. J. Supran, M. G. Bawendi and V. Bulović, Emergence of Colloidal Quantum-dot Light-emitting Technologies, *Nat. Photonics*, 2013, **7**, 13–23.
  - 7 B. Lounis, H. A. Bechtel, D. Gerion, A. P. Alivisatos and W. E. Moerner, Photon Antibunching in Single CdSe/ZnS Quantum Dot Fluorescence, *Chem. Phys. Lett.*, 2000, **329**, 399–404.
  - 8 P. Michler, A. Imamoglu, M. D. Mason, P. J. Carson, G. F. Strouse and S. K. Buratto, Quantum Correlation among Photons from a Single Quantum Dot at Room Temperature, *Nature*, 2000, **406**, 968–970.
  - 9 G. Messin, J. P. Hermier, E. Giacobino, P. Desbiolles and M. Dahan, Bunching and Antibunching in the Fluorescence of Semiconductor Nanocrystals, *Opt. Lett.*, 2001, **26**, 1891–1893.
  - 10 G. Nair, J. Zhao and M. G. Bawendi, Biexciton Quantum Yield of Single Semiconductor Nanocrystals from Photon Statistics, *Nano Lett.*, 2011, **11**, 1136–1140.
  - 11 Y.-S. Park, A. V. Malko, J. Vela, Y. Chen, Y. Ghosh, F. García-Santamaría, J. A. Hollingsworth, V. I. Klimov and H. Htoon, Near-Unity Quantum Yields of Biexciton Emission from CdSe/CdS Nanocrystals Measured Using Single-Particle Spectroscopy, *Phys. Rev. Lett.*, 2011, **106**, 187401.
  - 12 J. Zhao, O. Chen, D. B. Strasfeld and M. G. Bawendi, Biexciton Quantum Yield Heterogeneities in Single CdSe (CdS) Core (shell) Nanocrystals and its Correlation to Exciton Blinking, *Nano Lett.*, 2012, **12**, 4477–4483.
  - 13 B. D. Mangum, Y. Ghosh, J. A. Hollingsworth and H. Htoon, Disentangling the Effects of Clustering and Multi-exciton Emission in Second-order Photon Correlation Experiments, *Opt. Express*, 2013, **21**, 7419–7426.
  - 14 B. D. Mangum, S. Sampat, Y. Ghosh, J. A. Hollingsworth, H. Htoon and A. V. Malko, Influence of the Core Size on Biexciton Quantum Yield of Giant CdSe/CdS Nanocrystals, *Nanoscale*, 2014, **6**, 3712–3720.
  - 15 Y.-S. Park, W. K. Bae, J. M. Pietryga and V. Klimov, Auger Recombination of Biexcitons and Negative and Positive Triions in Individual Quantum Dots, *ACS Nano*, 2014, **8**, 7288–7296.
  - 16 M. Bruchez Jr., M. Moronne, P. Gin, S. Weiss and A. P. Alivisatos, Semiconductor Nanocrystals as Fluorescent Biological Labels, *Science*, 1998, **281**, 2013–2016.
  - 17 A. P. Alivisatos, The Use of Nanocrystals in Biological Detection, *Nat. Biotechnol.*, 2004, **22**, 47–52.
  - 18 I. L. Medintz, H. T. Uyeda, E. R. Goldman and H. Mattoussi, Quantum Dot Bioconjugates for Imaging, Labelling and Sensing, *Nat. Mater.*, 2005, **4**, 435–446.
  - 19 S. Masuo, H. Naiki, S. Machida and A. Itaya, Photon Statistics in Enhanced Fluorescence from a Single CdSe/ZnS Quantum Dot in the Vicinity of Silver Nanoparticles, *Appl. Phys. Lett.*, 2009, **95**, 193106.
  - 20 H. Naiki, S. Masuo, S. Machida and A. Itaya, Single-Photon Emission Behavior of Isolated CdSe/ZnS Quantum Dots Interacting with the Localized Surface Plasmon Resonance of Silver Nanoparticles, *J. Phys. Chem. C*, 2011, **115**, 23299–23304.
  - 21 S. Masuo, T. Tanaka, S. Machida and A. Itaya, Photon Antibunching in Enhanced Photoluminescence of a Single CdSe/ZnS Nanocrystal by Silver Nanostructures, *J. Photochem. Photobiol., A*, 2012, **237**, 24–30.
  - 22 J. R. Lakowicz, K. Ray, M. Chowdhury, H. Szmecinski, Y. Fu, J. Zhang and K. Nowaczyk, Plasmon-controlled Fluorescence: a New Paradigm in Fluorescence Spectroscopy, *Analyst*, 2008, **133**, 1308–1346.
  - 23 K. Okamoto, I. Niki, A. Shvartser, Y. Narukawa, T. Mukai and A. Scherer, Surface-plasmon-enhanced Light Emitters Based on InGaN Quantum Wells, *Nat. Mater.*, 2004, **3**, 601–605.
  - 24 Y. Chen, K. Munechika and D. S. Ginger, Dependence of Fluorescence Intensity on the Spectral Overlap between Fluorophores and Plasmon Resonant Single Silver Nanoparticles, *Nano Lett.*, 2007, **7**, 690–696.
  - 25 G. Laurent and T. Asahi, Enhancement of Excimer Fluorescence from Thin Dye Film by Single Gold Nanoparticles, *Chem. Lett.*, 2009, **38**, 332–333.
  - 26 K. Munechika, Y. Chen, A. F. Tillack, A. P. Kulkarni, I. J. Plante, A. M. Munro and D. S. Ginger, Spectral Control of Plasmonic Emission Enhancement from Quantum Dots near Single Silver Nanoprisms, *Nano Lett.*, 2010, **10**, 2598–2603.
  - 27 D. Canneson, I. Mallek-Zouari, S. Buil, X. Quélin, C. Javaux, B. Dubertret and J. P. Hermier, Enhancing the Fluorescence of Individual Thick Shell CdSe/CdS Nanocrystals by Coupling to Gold Structures, *New J. Phys.*, 2012, **14**, 063035.
  - 28 S. J. LeBlanc, M. R. McClanahan, M. Jones and P. J. Moyer, Enhancement of Multiphoton Emission from Single CdSe Quantum Dots Coupled to Gold Films, *Nano Lett.*, 2013, **13**, 1662–1669.
  - 29 Y.-S. Park, Y. Ghosh, Y. Chen, A. Piryatinski, P. Xu, N. Mack, H.-L. Wang, V. Klimov, J. A. Hollingsworth and H. Htoon, Super-Poissonian Statistics of Photon Emission from Single CdSe-CdS Core-Shell Nanocrystals Coupled to Metal Nanostructures, *Phys. Rev. Lett.*, 2013, **110**, 117401.
  - 30 Y.-S. Park, Y. Ghosh, P. Xu, N. H. Mack, H.-L. Wang, J. A. Hollingsworth and H. Htoon, Single-Nanocrystal Photoluminescence Spectroscopy Studies of Plasmon-Multiexciton Interactions at Low Temperature, *J. Phys. Chem. Lett.*, 2013, **4**, 1465–1470.
  - 31 C. T. Yuan, Y. C. Wang, H. W. Cheng, H. S. Wang, M. Y. Kuo, M. H. Shih and J. Tang, Modification of

- Fluorescence Properties in Single Colloidal Quantum Dots by Coupling to Plasmonic Gap Modes, *J. Phys. Chem. C*, 2013, **117**, 12762–12768.
- 32 H.-W. Cheng, C.-T. Yuan, J.-S. Wang, T.-N. Lin, J.-L. Shen, Y.-J. Hung, J. Tang and F.-G. Tseng, Modification of Photon Emission Statistics from Single Colloidal CdSe Quantum Dots by Conductive Materials, *J. Phys. Chem. C*, 2014, **118**, 18126–18132.
- 33 S. Dey, Y. Zhou, X. Tian, J. A. Jenkins, O. Chen, S. Zou and J. Zhao, An Experimental and Theoretical Mechanistic Study of Biexciton Quantum Yield Enhancement in Single Quantum Dots near Gold Nanoparticles, *Nanoscale*, 2015, **7**, 6851–6858.
- 34 F. Wang, N. S. Karan, H. M. Nguyen, Y. Ghosh, C. J. Sheehan, J. A. Hollingsworth and H. Htoon, Correlated Structural-optical Study of Single Nanocrystals in a Gap-bar Antenna: Effects of Plasmonics on Excitonic Recombination Pathways, *Nanoscale*, 2015, **7**, 9387–9393.
- 35 S. Masuo, K. Kanetaka, R. Sato and T. Teranishi, Direct Observation of Multiphoton Emission Enhancement from a Single Quantum Dot Using AFM Manipulation of a Cubic Gold Nanoparticle, *ACS Photonics*, 2016, **3**, 109–116.
- 36 H. Takata, H. Naiki, L. Wang, H. Fujiwara, K. Sasaki, N. Tamai and S. Masuo, Detailed Observation of Multiphoton Emission Enhancement from a Single Colloidal Quantum Dot Using a Silver-Coated AFM Tip, *Nano Lett.*, 2016, **16**, 5770–5778.
- 37 H. Naiki, A. Masuhara, S. Masuo, T. Onodera, H. Kasai and H. Oikawa, Highly Controlled Plasmonic Emission Enhancement from Metal-Semiconductor Quantum Dot Complex Nanostructures, *J. Phys. Chem. C*, 2013, **117**, 2455–2459.
- 38 C. I. Yoo, D. Seo, B. H. Chung, I. S. Chung and H. Song, A Facile One-Pot Synthesis of Hydroxyl-Functionalized Gold Polyhedrons by a Surface Regulating Copolymer, *Chem. Mater.*, 2009, **21**, 939–944.
- 39 Y. Gao, *et al.*, Hybrid Graphene-Giant Nanocrystal Quantum Dot Assemblies with Highly Efficient Biexciton Emission, *Adv. Opt. Mater.*, 2015, **3**, 39–43.
- 40 P. Bharadwaj and L. Novotny, Spectral Dependence of Single Molecule Fluorescence Enhancement, *Opt. Express*, 2001, **15**, 14266–14274.
- 41 P. Anger, P. Bharadwaj and L. Novotny, Enhancement and Quenching of Single-Molecule Fluorescence, *Phys. Rev. Lett.*, 2006, **96**, 113002.

## Detailed Observation of Multiphoton Emission Enhancement from a Single Colloidal Quantum Dot Using a Silver-Coated AFM Tip

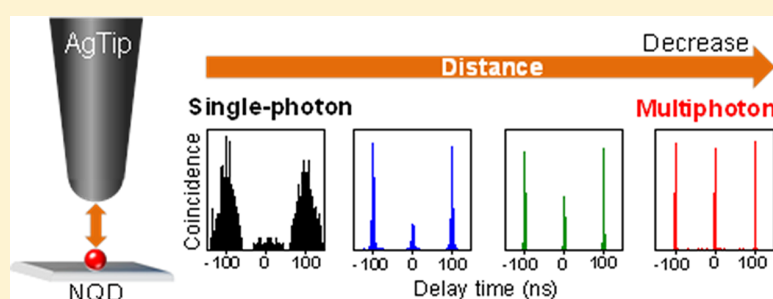
Hiroki Takata,<sup>†</sup> Hiroyuki Naiki,<sup>‡</sup> Li Wang,<sup>†</sup> Hideki Fujiwara,<sup>§</sup> Keiji Sasaki,<sup>§</sup> Naoto Tamai,<sup>†</sup> and Sadahiro Masuo<sup>\*,‡</sup>

<sup>†</sup>Department of Chemistry, Kwansai Gakuin University, 2-1 Gakuen, Sanda, Hyogo 669-1337, Japan

<sup>‡</sup>Department of Applied Chemistry for Environment, Kwansai Gakuin University, 2-1 Gakuen, Sanda, Hyogo 669-1337, Japan

<sup>§</sup>Research Institute for Electronic Science, Hokkaido University, Sapporo, 001-0020 Japan

### S Supporting Information



**ABSTRACT:** The enhancement of multiphoton emission from a single colloidal nanocrystal quantum dot (NQD) interacting with a plasmonic nanostructure was investigated using a silver-coated atomic force microscopy tip (AgTip) as the plasmonic nanostructure. Using the AgTip, which exhibited a well-defined localized surface plasmon (LSP) resonance band, we controlled the spectral overlap and the distance between the single NQD and the AgTip. The emission behavior of the single NQD when approaching the AgTip at the nanometer scale was measured using off-resonance (405 nm) and resonance (465 nm) excitation of the LSP. We directly observed the conversion of the single-photon emission from a single NQD to multiphoton emission with reduction of the emission lifetime at both excitation wavelengths as the NQD-AgTip distance decreased, whereas a decrease and increase in the emission intensity were observed at 405 and 465 nm excitation, respectively. By combining theoretical analysis and the numerical simulation of the AgTip, we deduced that the enhancement of the multiphoton emission was caused by the quenching of the single-exciton state due to the energy transfer from the NQD to the AgTip and that the emission intensity was increased by enhancement of the excitation rate due to the electric field of the LSP on the AgTip. These results provide evidence that the photon statistics and the photon flux from the single NQD can be manipulated by the plasmonic nanostructure through control of the spectral overlap and the distance.

**KEYWORDS:** Quantum dot, single photon, multiphoton, multiexciton, plasmon, tip enhancement

Modification of the emission photon statistics, i.e., single-photon emission/multiphoton emission, from a single colloidal nanocrystal quantum dot (NQD) using plasmonic nanostructures has attracted considerable attention from the viewpoint of fundamental science as a new phenomenon induced by a plasmonic nanostructure and from the viewpoint of applications for quantum information technologies.<sup>1–17</sup> NQDs are a unique class of tunable, dispersible fluorophores that have drawn intensive interest for their potential applications in a wide range of optoelectronic devices<sup>18–27</sup> and biological detection systems.<sup>28–30</sup> One of the particularly remarkable characteristics of the NQD is single-photon and multiphoton emission from a single NQD.

When multiple excitons are produced in a single NQD, they form a multiple exciton state (MX), such as a triexciton state (TX) or biexciton state (BX), through the Coulomb interaction between excitons. In the emission process, multiple photons

can be emitted by the cascade emission from the BX or TX to the ground state (GS) via a single exciton state (SX).<sup>31</sup> The emitted multiple photons can behave as an entangled photon pair, which is important for quantum information technologies.<sup>32</sup> However, when multiple excitons are produced in a single NQD, the excitons decay from the MX to the SX by nonradiative Auger recombination.<sup>33</sup> Subsequently, the remaining single exciton decays from the SX to the GS by emitting a single photon. Therefore, a single NQD can exhibit single-photon emission through Auger recombination.<sup>34–37</sup> Single-photon emission is also important for quantum information and communication technologies. Generally, the emission

**Received:** June 17, 2016

**Revised:** August 3, 2016

**Published:** August 8, 2016

photon statistics of the NQD are governed by the multiexciton dynamics based on the quantum confinement depending on the size, shape, and atomic composition of NQDs themselves. Researchers have recently demonstrated that the probability of multiphoton emission, i.e., BX emission, through interactions with plasmonic nanostructures can be increased.<sup>1–17</sup>

Plasmonic nanostructures, i.e., metallic nanostructures (MNSs), can enhance the excitation and the relaxation processes of nearby fluorophores. In the case of excitation enhancement, the excitation rate of the fluorophore can be enhanced by the electric field of the localized surface plasmon (LSP) generated on the MNS by incident light. For this enhancement, overlap of the absorption spectrum of the fluorophore with the localized surface plasmon resonance (LSPR) band is required. In the case of relaxation enhancement, both the radiative and the nonradiative rates of the fluorophore can be enhanced. For this enhancement, overlap of the photoluminescence (PL) spectrum of the fluorophore with the LSPR band is required. The LSP can be generated on the MNS by resonance energy transfer, and the LSP then decays radiatively or nonradiatively. The enhancement of the radiative and nonradiative rates, i.e., whether the LSP decays radiatively or nonradiatively, depends on the scattering properties of the MNS itself. The enhancement of the nonradiative process is referred to as quenching of the excitons.

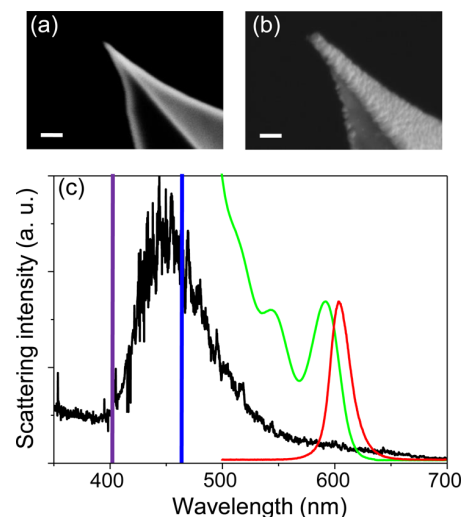
Increasing the probability of BX emission from a single NQD through interactions with MNSs requires consideration of the factors that enhance the relaxation process. Currently, two possibilities have been proposed. One mechanism involves enhancement of the BX emission rate by enhancing the radiative rate. With such an enhancement, the single NQD-MNS can emit multiphotons before the excitons are annihilated by Auger recombination.<sup>1,3–6,8,11–15,17</sup> The other mechanism is the quenching of SX by the MNS, i.e., a decrease in the PL quantum yield ( $\Phi_{\text{PL}}$ ) of SX emission ( $\Phi_{\text{SX}}$ ) rather than an actual increase in the  $\Phi_{\text{PL}}$  of the BX emission ( $\Phi_{\text{BX}}$ ). When the excitons are quenched by MNS via energy or electron transfer,<sup>9</sup> the quenching of SX is more efficient compared with the quenching of BX because of the longer lifetime of SX. As  $\Phi_{\text{SX}}$  decreases, the contribution of BX emission increases.<sup>9,38–40</sup> Although these two mechanisms have been proposed, the process has not yet been fully elucidated.

To elucidate the mechanism, a single NQD-MNS system in which both the spectral overlap and the distance are fully controlled would be used because the fluorophore–MNS interaction strongly depends on the spectral overlap and the distance between the fluorophore and MNS. However, no investigation using such systems has been reported. In this context, using atomic force microscopy (AFM) manipulation of a single Au nanocube (AuCube) with a well-defined shape and size to directly observe the change of the emission behavior of the single NQD, we previously reported that the photon statistics of the NQD were converted from single-photon emission to multiphoton emission because of the enhancement of the BX emission rate when approaching the AuCube.<sup>17</sup> This previous work clearly demonstrates that enhancement of the BX emission rate could be induced by the spectral overlap between the PL of the NQD and the LSPR of MNS. However, in the case of AFM manipulation, control of the distance between the single NQD and the AuCube with nanometer-scale precision was difficult.

In this work, to elucidate the control of the MX dynamics and subsequent photon statistics using an MNS, we used a

silver-coated AFM cantilever (AgTip) as an MNS. Distance control with nanometer-scale precision can be achieved through the use of an AFM system with an AgTip, as demonstrated previously.<sup>41–43</sup> In addition, using the AgTip, which exhibits a well-defined LSPR band, enabled control of both the distance and the spectral overlap. By observing the dependence of the emission behavior of single NQDs on the excitation wavelength and the NQD-AgTip distance, we elucidated in detail the mechanism of the control of NQD photon statistics by MNS.

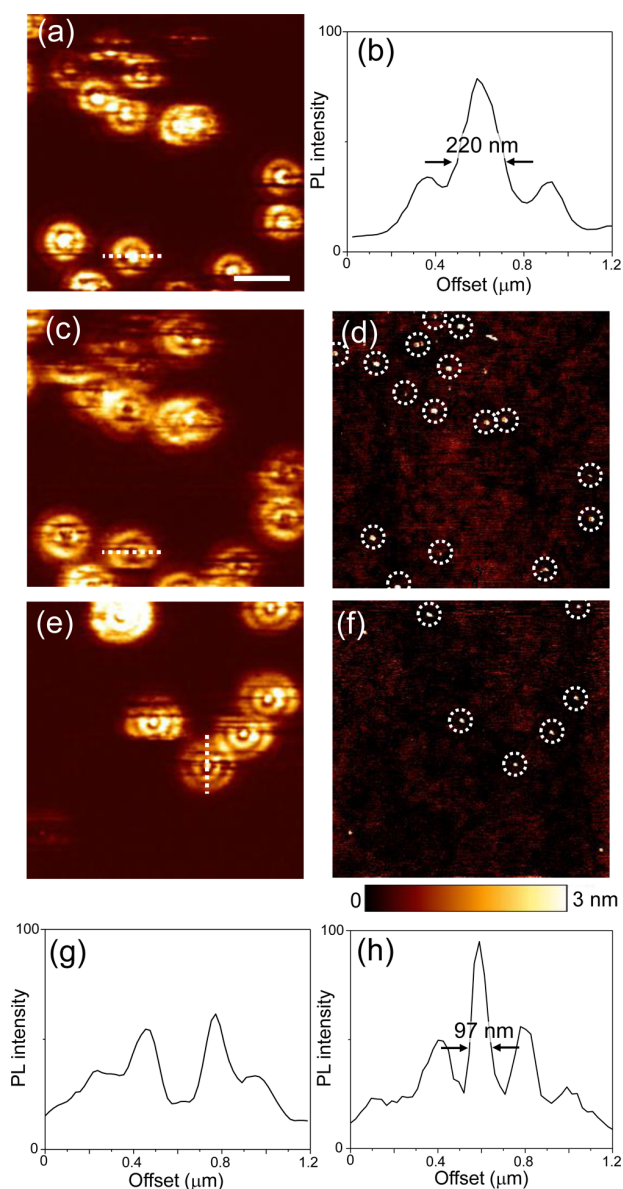
Figure 1 shows the scanning electron microscopy (SEM) images of an Si cantilever before sputtering (a) and after



**Figure 1.** Scanning electron microscopy (SEM) images of the Si cantilever before Ag sputtering (a) and after Ag sputtering (b). The scale bars in the images represent 100 nm. (c) A scattering spectrum of the AgTip (black line) and the absorption (green line) and PL (red line) spectra of the NQD dispersed in toluene. The vertical purple and blue lines indicate the 405 and 465 nm excitation wavelengths.

sputtering (b) with Ag. A comparison of these images confirms the coating of the cantilever by Ag. The tip radius of the AgTip,  $a$ , was estimated to be  $20 \leq a \leq 30$  nm from the SEM images. The scattering spectrum of the AgTip is shown in Figure 1c, along with the absorption and PL spectra of the NQD. The AgTip showed an LSPR band with a peak wavelength at 450 nm. The LSPR fully overlaps the absorption spectrum of the NQD and slightly overlaps the PL spectrum. In this work, 405 and 465 nm lasers were used as the excitation light source. On the basis of the spectral relationship, we expected that the excitation rate of the NQD could be enhanced by the electric field of the LSP generated on the AgTip at 465 nm excitation. The relaxation rate of the NQD could also be modified by the AgTip independent of the excitation wavelength because of the spectral overlap between the PL and LSPR.

The PL and AFM images of the single NQDs dispersed on a coverslip are summarized in Figure 2. Figure 2a shows a typical PL image of the individual NQDs measured at 405 nm excitation without advancing the AgTip. The individual NQDs exhibit a double-lobed PL intensity pattern, which is characteristic of radially polarized beam excitation.<sup>41,42,44</sup> From the cross-section of a single PL spot (Figure 2b), the double-lobed pattern was confirmed, and the full-width at half-maximum (fwhm) of the center lobe was estimated to be 220 nm. The PL and AFM images of the same area as that shown in image (a)



**Figure 2.** (a) A PL image of individual NQDs obtained at 405 nm excitation without the approach of the AgTip. (b) A cross-section of the single PL spot indicated by the dotted line in image a. (c, d) PL and AFM images of the individual NQDs obtained from the same area as image (a) at 405 nm excitation with an approaching AgTip. (e, f) PL and AFM images of the individual NQDs obtained at 465 nm excitation with an approaching AgTip. (g, h) Cross sections of the single PL spots indicated by the dotted lines in images c and e, respectively. The size of all images is  $5 \mu\text{m} \times 5 \mu\text{m}$ . The scale-bar in image (a) represents  $1 \mu\text{m}$ .

were then measured again by 405 nm excitation with advancement of the AgTip (Figure 2c,d). The center lobe of each PL spot disappeared with the approach of the AgTip (c). From the cross-section of a single PL spot (Figure 2g), the disappearance of the center lobe was clearly confirmed. This result indicates that the PL from the single NQDs was quenched; i.e., the nonradiative decay rate was enhanced by the approach of the AgTip at 405 nm excitation.

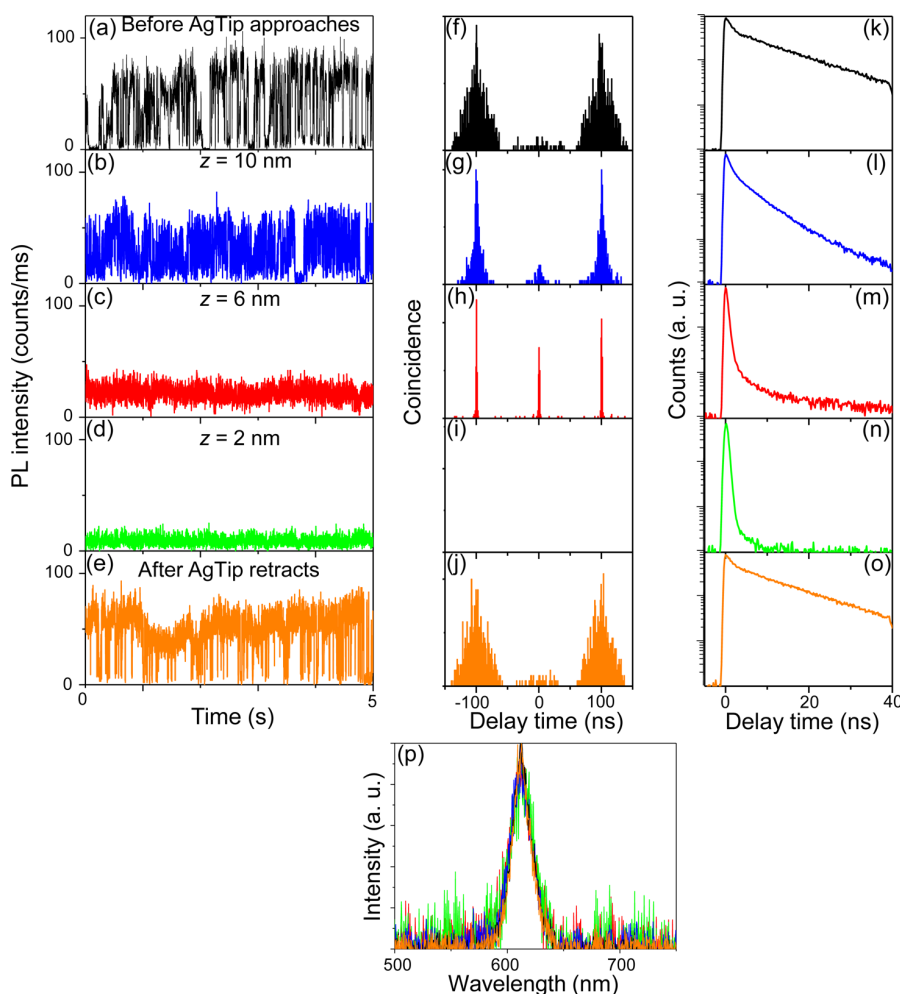
The PL and AFM images obtained from another area at 465 nm excitation with the approach of the AgTip are shown in

Figure 2e and f, respectively. In this case, the center lobe of the individual PL spots appeared in the PL image. From the cross-section of the single PL spot (Figure 2h), the fwhm of the center lobe was smaller (97 nm) than the cross-section (b) obtained at 405 nm excitation without advancing the AgTip. These results indicate that the PL was not quenched and that the spatial resolution of the PL image was increased<sup>41,42,45</sup> by the approach of the AgTip at 465 nm excitation. The significance of these results is that the PL was quenched and unquenched by 405 and 465 nm excitations, respectively. Below, the details of the emission behavior of the individual NQDs are discussed.

The representative emission behavior of a single NQD depending on the NQD-AgTip distance ( $z$ -distance) is summarized in Figure 3. The  $z$ -distance was defined as the distance from the top of the NQD to the top of the AgTip. These results were obtained from the same single NQD at 405 nm excitation. In the time traces of the PL intensity (Figure 3a–e), the PL intensity decreased with decreasing  $z$ -distance: 80 cts/ms (before approaching the AgTip; a); 60 cts/ms ( $z = 10$  nm; b); 30 cts/ms ( $z = 6$  nm; c); and 20 cts/ms ( $z = 2$  nm; d). When the AgTip was retracted, the intensity returned to the original intensity before the approach of the AgTip (80 cts/ms; e). In the PL decay curves (Figure 3k–o), the curves show faster decay with decreasing  $z$ -distance. The lifetime ( $\tau$ ) and the normalized amplitude of the lifetime ( $\alpha$ ) were estimated as follows by fitting with two- or three-exponential functions:  $\tau_1 = 1.2$  ns (30.0%) and  $\tau_2 = 25.0$  ns (70.0%) before the approach of the AgTip; 1.0 ns (56.8%), 5.6 (40.6%), and 17.8 ns (2.6%) for  $z = 10$  nm; 0.3 ns (99.2%) and 3.9 ns (0.8%) for  $z = 6$  nm; and 0.3 ns (99.9%) and 5.1 (0.1%) for  $z = 2$  nm. Because the shortest lifetime of 0.3 ns was the same as the instrument response function (IRF), the actual lifetime was probably much shorter than 0.3 ns. After the AgTip was retracted, the lifetime returned to almost the original values before the approach of the AgTip: 1.5 (28.3%) and 23.2 ns (71.7%). The decrease in the PL intensity with decreasing lifetime caused by the approach of the AgTip clearly indicates that the PL was quenched; i.e., the nonradiative decay rate of the NQD was enhanced by the AgTip as a result of the resonance energy transfer from the NQD to the AgTip (vide infra).

In the photon correlation histogram (Figure 3f–j), the second-order correlation function  $g^{(2)}(0)$ , which is defined as the ratio of the number of detection events at a delay time of 0 ns to the average number of detection events at other delay times, provides information about the photon statistics in the PL emission; specifically, the probability of single-photon emission increases when  $g^{(2)}(0)$  approaches zero. In addition, the  $g^{(2)}(0)$  value corresponds to the efficiency of BX emission,  $\Phi_{\text{BX}}/\Phi_{\text{SX}}$  at low excitation power, such as under our excitation conditions (the average NQD exciton occupancy  $\langle N \rangle \ll 1$ ).<sup>9,14</sup> The  $g^{(2)}(0)$  value increased with the approach of the AgTip: 0.09 before the approach of the AgTip, 0.17 for  $z = 10$  nm, and 0.85 for  $z = 6$  nm. In the case of  $z = 2$  nm, the PL intensity was too low for a photon correlation histogram to be constructed. After retracting the AgTip, the  $g^{(2)}(0)$  value returned to the original value of 0.08. These results indicate that the emission photon statistics changed from single-photon emission to multiphoton emission with the approach of the AgTip.

In the PL spectra (Figure 3p), no clear change of the spectra was observed. Because of the small red-shift of the BX emission spectrum compared with the SX emission spectrum,<sup>31,46</sup> distinguishing the BX emission spectrum from the SX emission

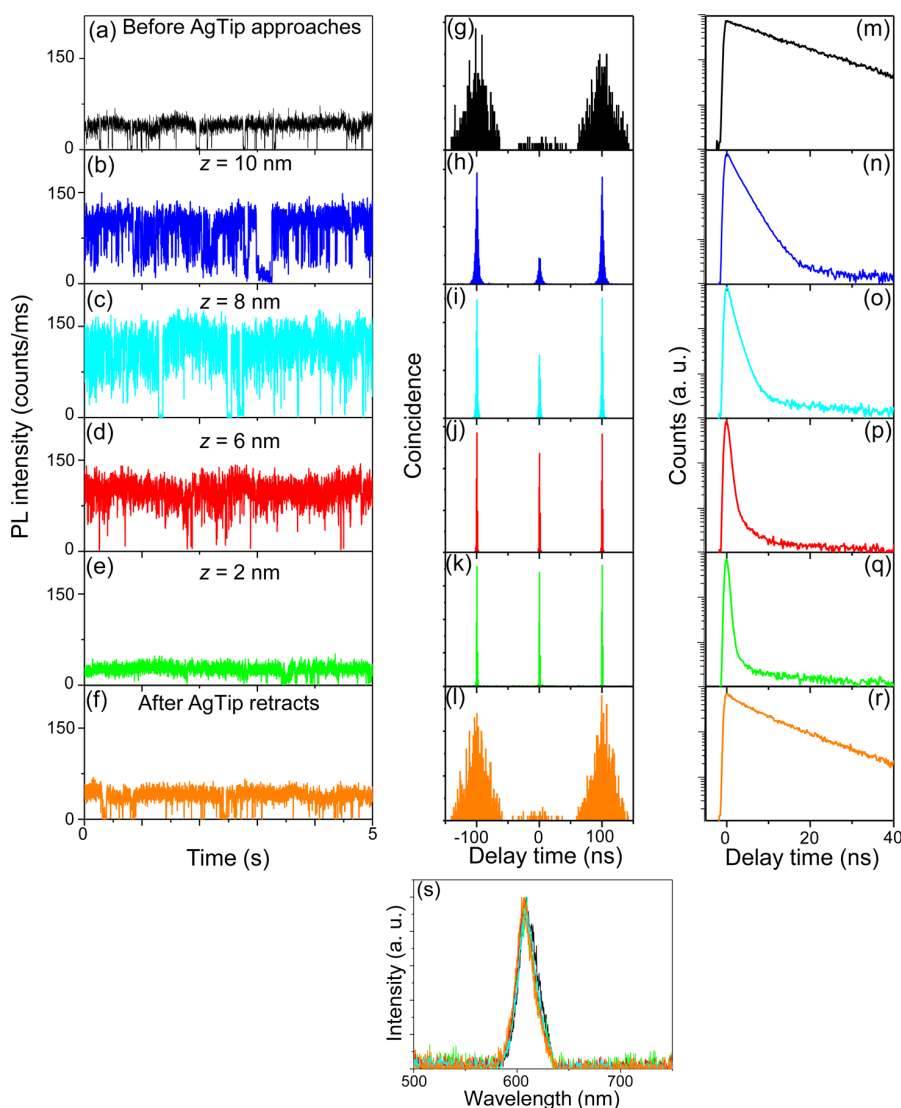


**Figure 3.** Time traces of the PL intensity (a–e), photon correlation histograms (f–j), PL decay curves (k–o), and the PL spectra (p) detected from the same single NQD depending on the  $z$ -distance at 405 nm excitation: (a, f, k, and black line in p) before the approach of the AgTip; (b, g, l, and blue line in p)  $z = 10$  nm; (c, h, m, and red line in p)  $z = 6$  nm; (d, i, n, and green line in p)  $z = 2$  nm; and (e, j, o, and orange line in p) after the AgTip was retracted.

spectrum is difficult at room temperature.<sup>1,17</sup> Similar changes in the emission behavior were observed from other single NQDs reproducibly, as shown in the Supporting Information (SI). The observed emission behavior can be interpreted as follows. In the case of 405 nm excitation, no excitation enhancement occurs because the LSP is not generated on the AgTip. By contrast, enhancement of the relaxation process, mainly enhancement of the nonradiative rate (quenching), occurs through the spectral overlap between the PL and LSPR band. Because quenching was observed at  $z \approx 10$  nm, the mechanism of the quenching is likely resonance energy transfer from the NQD to the AgTip rather than electron transfer. Thus, we concluded that the efficient quenching of the SX of the NQD caused the increase in the probability of the BX emission, as reported previously.<sup>9,38–40</sup>

In the case of 465 nm excitation, enhancement of the excitation rate is expected. In addition, the enhancement of the relaxation process also occurs, as in the case of the 405 nm excitation, because the spectral overlap between the PL and the LSPR is unchanged. The representative emission behavior of the single NQD observed at 465 nm excitation with the approach of the AgTip is shown in Figure 4. Unlike the 405 nm

excitation, the PL intensity from the single NQD increased with the approach of the AgTip: 60 cts/ms before the approach of the AgTip (a), increasing to 140 cts/ms for  $z = 10$  nm (b), 160 cts/ms for  $z = 8$  nm (c), and 140 cts/ms for  $z = 6$  nm (d). When the AgTip further approached the single NQD, i.e., at  $z = 2$  nm, the intensity decreased to 40 cts/ms. The intensity then returned to the same value as before the approach (60 cts/ms) after the AgTip was retracted. In the photon correlation histograms (Figures 4g–l), the  $g^{(2)}(0)$  value increased with the approach of the AgTip, as in the case of the 405 nm excitation; the  $g^{(2)}(0)$  value of 0.09 before the approach of the AgTip (g) increased to 0.29, 0.56, 0.88, and 0.92 for  $z = 10$  nm (h), 8 nm (i), 6 nm (j), and 2 nm (k), respectively. Thus, the probability of BX emission increased with decreasing  $z$ -distance. After the AgTip was retracted, the  $g^{(2)}(0)$  value returned to 0.09. The decay curves (Figures 4m–r) were also shortened with the approach of the AgTip: the 26.7 ns (100%) lifetime before advancing the AgTip was modified to 0.8 ns (17.9%), 2.3 ns (81.9%), and 21.2 ns (0.2%) for  $z = 10$  nm, to 0.7 ns (65.9%), 1.3 ns (34.0%), and 11.4 ns (0.1%) for  $z = 8$  nm, to 0.4 ns (99.5%) and 2.8 ns (0.5%) for  $z = 6$  nm, and to 0.3 ns (99.4%) and 2.7 ns (0.6%) for  $z = 2$  nm. After the AgTip was retracted,



**Figure 4.** Time traces of the PL intensity (a–f), photon correlation histograms (g–l), PL decay curves (m–r), and the PL spectra (s) detected from the same single NQD depending on the  $z$ -distance at 465 nm excitation: (a, g, m, and black line in s) before the approach of the AgTip; (b, h, n, and blue line in s)  $z = 10$  nm; (c, i, o, and right blue line in s)  $z = 8$  nm; (d, j, p, and red line in p)  $z = 6$  nm; (e, k, q, and green line in s)  $z = 2$  nm; and (f, l, r, and orange line in s) after the AgTip was retracted.

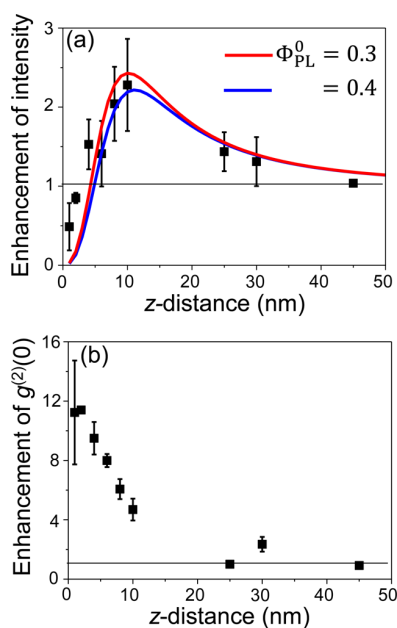
the lifetime increased to 2.8 ns (15.4%) and 17.3 ns (84.6%) and did not return to the original value before the AgTip was advanced (26.7 ns). This shortening of the lifetime was caused by damage to the NQD during the measurement.

In the PL spectra (Figure 4s), no change in the spectrum was observed, as in the case of 405 nm excitation. Interestingly, the PL intensity increased with the low probability of BX emission at  $z = 10$  nm, whereas in the cases of  $z = 8$  and 6 nm, the probability of BX emission increased with increasing intensity. Similar changes in the emission behavior with the approach of the AgTip were observed from other single NQDs, as shown in the SI. These results demonstrate that control of single-photon and multiphoton emission with increased intensity is possible through nanometer-scale control of the  $z$ -distance.

The emission behavior observed at 465 nm excitation can be interpreted as follows. With the enhancement of the excitation rate, the PL intensity increased because the LSP could be generated on the AgTip at 465 nm excitation. In addition, the

quenching of SX also occurred, which caused an increase in BX emission with decreased PL lifetime, as in the case of the 405 nm excitation. The details of the mechanism of the emission behavior are discussed below.

Figure 5 shows the enhancements of the PL intensity and  $g^{(2)}(0)$  value as a function of the  $z$ -distance built as average values of 10 single NQD measurements at 465 nm excitation. In Figure 5a, the PL intensity increased with decreasing  $z$ -distance, and the intensity reached the maximum value, i.e., enhancement of 2.3 times on average, near  $z \approx 10$  nm. The intensity then decreased as the  $z$ -distance decreased further. In Figure 5b, the  $g^{(2)}(0)$  value increased with decreasing  $z$ -distance below 10 nm. The maximum value of the enhancement was 10.5 times, on average, at  $z \approx 2$  nm. We discuss the mechanism of the change in the emission behavior induced by the approach of the AgTip using the enhancement of the PL intensity as a function of the  $z$ -distance (Figure 5a). Previously, Novotny et al. investigated the change of the PL intensity from a single



**Figure 5.** Enhancements of the PL intensity,  $I/I^0$  (a), and  $g^{(2)}(0)$  value,  $g^{(2)}(0)/g^{(2)}(0)^0$  (b), as a function of the  $z$ -distance. The superscript 0 indicates the values before the approach of the AgTip. These figures were built from the average results of 10 single NQD measurements at 465 nm excitation. The red and blue lines in panel a show the theoretical curves obtained by assuming  $\Phi_{\text{PL}}^0 = 30\%$  and  $40\%$ , respectively, with  $a = 20$  nm.

organic molecule by the approach of a gold nanoparticle (AuNP) attached to the end of a pointed optical fiber, and they reported an increase and a decrease in the PL intensity depending on the distance between the single molecule and the AuNP.<sup>41,43</sup> Using theoretical analysis, they clearly demonstrated that the change of the PL intensity as a function of the distance could be interpreted by the combination of the enhancement of the excitation rate by the LSP of the AuNP and the quenching of the PL by resonance energy transfer from the single molecule to the AuNP.<sup>43</sup> To elucidate the mechanism, we applied this theoretical analysis to the enhancement of the PL intensity (Figure 5a).

The enhancement of the PL intensity can be expressed as

$$\frac{I}{I^0} = \frac{\gamma_{\text{exc}} \Phi_{\text{PL}}}{\gamma_{\text{exc}}^0 \Phi_{\text{PL}}^0} \quad (1)$$

where  $\gamma_{\text{exc}}$  and  $\Phi_{\text{PL}}$  represent the excitation rate and the PL quantum yield, respectively, and the superscript "0" refers to the value without the approach of the AgTip. The enhancement of the PL intensity (Figure 5a) was fitted using eq 1. In eq 1, the enhancement of the excitation rate  $\frac{\gamma_{\text{exc}}}{\gamma_{\text{exc}}^0}$  by the electric field of the LSP can be expressed as

$$\frac{\gamma_{\text{exc}}}{\gamma_{\text{exc}}^0} = \left| 1 + 2 \frac{a^3}{(a+z)^3} \frac{\varepsilon(\omega_1) - 1}{\varepsilon(\omega_1) + 2} \right|^2 \quad (2)$$

where  $a$ ,  $z$ , and  $\varepsilon(\omega_1)$  refer to the tip radius of the AgTip, the distance between the single NQD and the AgTip, and the dielectric constant of Ag at the frequency  $\omega_1$  of the excitation wavelength (465 nm), respectively. In eq 1, the  $\Phi_{\text{PL}}$  of the single NQD interacting with the AgTip can be expressed as

$$\Phi_{\text{PL}} = \frac{\gamma_r/\gamma_r^0}{\gamma_r/\gamma_r^0 + \gamma_q/\gamma_r^0 + (1 - \Phi_{\text{PL}}^0)/\Phi_{\text{PL}}^0} \quad (3)$$

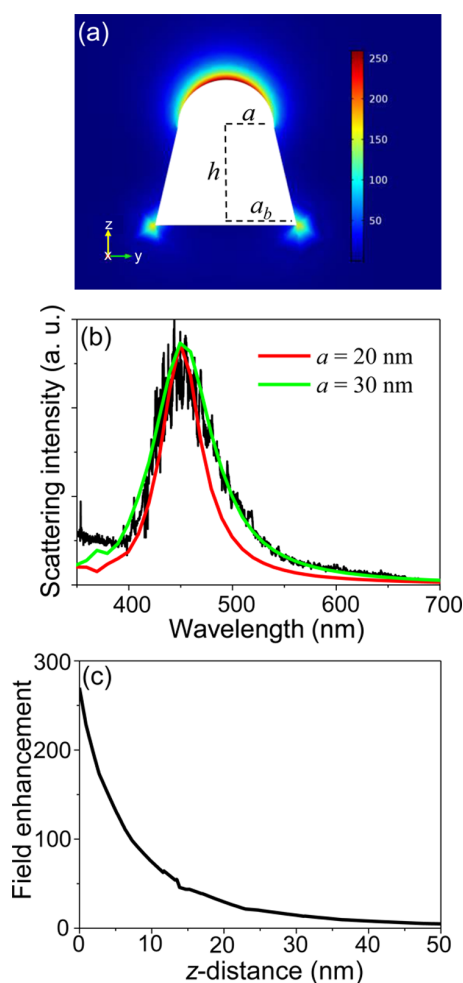
where  $\gamma_r$  refers to the radiative rate and  $\gamma_q$  indicates the additional nonradiative rate (quenching) of the single NQD by the energy transfer rate from the single NQD to the AgTip. Parameter  $\gamma_r/\gamma_r^0$  represents the enhancement of the radiative rate. In this work, we assumed  $\gamma_r/\gamma_r^0 = 1$  to exclude the enhancement of the radiative rate. In eq 3, the ratio  $\gamma_q/\gamma_r^0$  can be expressed as

$$\frac{\gamma_q}{\gamma_r^0} = \frac{3}{16} \text{Im} \frac{\varepsilon(\omega_2) - 1}{\varepsilon(\omega_2) + 1} \frac{1}{k_2^3 z^3} \frac{(P_x^2 + P_y^2 + 2P_z^2)}{|\mathbf{P}|^2} \quad (4)$$

where  $\varepsilon(\omega_2)$  and  $\kappa_2$  refer to the dielectric constant of Ag at the frequency  $\omega_2$  of the PL wavelength (610 nm) and the wavevector at  $\omega_2$ , respectively.  $\mathbf{P} = [P_x, P_y, P_z]$  is the dipole moment. In these equations,  $a$  and  $\Phi_{\text{PL}}^0$  were treated as adjustable parameters, whereas other values were treated as fixed parameters.<sup>47</sup>

The red and blue lines in Figure 5a show the theoretical curves obtained by assuming  $\Phi_{\text{PL}}^0 = 30\%$  and  $40\%$ , respectively, with  $a = 20$  nm. The theoretical curves are clearly in good agreement with the experimental results with reasonable  $\Phi_{\text{PL}}^0$  and  $a$  values. This result indicates that the observed change of the emission behavior can be interpreted by the combination of the excitation rate enhancement and the quenching by the resonance energy transfer from the NQD to the AgTip. Therefore, the increase in the probability of BX emission can be explained by the quenching of the SX due to energy transfer. Because the quenching rate increases with decreasing  $z$ -distance, the  $g^{(2)}(0)$  value increased with a decrease in the  $z$ -distance (Figure 5b). This quenching occurred independent of the excitation wavelength. Thus, the increase in BX emission was observed for both 405 and 465 nm excitation wavelengths. In the case of 465 nm excitation, enhancement of the excitation rate also occurred. Hence, the PL intensity increased with decreasing  $z$ -distance, and as the distance further decreased, the PL intensity decreased because of the contribution of energy transfer. In the case of 405 nm excitation, the PL intensity decreased with decreasing  $z$ -distance because no enhancement of the excitation rate occurred.

To confirm the validity of the aforementioned interpretation, i.e., enhancement of the excitation rate by LSP on the AgTip, we conducted numerical simulations of the AgTip. The primary difficulty in the simulations was the determination of the shape and effective length of the AgTip. Thus, the tip radius of the AgTip ( $a$ ) was fixed as  $a = 20$  and  $30$  nm, which was estimated from the SEM image of the AgTip, and the shape and the effective length were varied to reproduce the scattering spectrum of the AgTip (details in SI). We achieved good agreement between the simulated extinction spectrum and the observed scattering spectrum by assuming a cone-shaped AgTip with an effective length ( $h$ ) = 60 nm and a bottom radius ( $a_b$ ) = 44 nm. Figure 6a shows the distribution of the electric field enhancement of the cone-shaped AgTip obtained by the simulation for illumination at a wavelength similar to that of the excitation laser (465 nm) with  $z$ -direction of the electric field. The simulated extinction spectra of the AgTip are shown in Figure 6b, along with the scattering spectrum of the AgTip. The red and blue lines are the extinction spectra simulated under the assumptions of  $a = 20$  and  $30$  nm, respectively. The peak wavelengths of the extinction spectra



**Figure 6.** (a) Distribution of the electric field enhancement simulated by assuming a cone-shaped AgTip with  $a = 30$  nm,  $a_b = 44$  nm, and  $h = 60$  nm. (b) The extinction spectra simulated under the assumptions  $a = 20$  nm (red line) and 30 nm (green line) with the same  $a_b$  and  $h$  as panel a. The spectrum indicated by a black line shows the scattering spectrum of the AgTip. (c) The electric field enhancement as a function of the  $z$ -distance obtained from panel a. In this case,  $z$ -distance indicates the distance from the top of the AgTip.

were approximately the same, whereas the spectral widths were strongly dependent on  $a$ . The simulated spectrum corresponding to  $a = 30$  nm was in better agreement with the experimental scattering spectrum. Figure 6c shows the electric field enhancement as a function of the  $z$ -distance obtained from Figure 6a. From this result, we observed that the field enhancement increased below 50 nm. This result is in good agreement with the  $z$ -dependent PL intensity enhancement (Figure 5a), which is evidence that the PL intensity was increased by the electric field of LSP on the AgTip.

In this work, we observed the dependence of the emission behavior of single NQDs on the  $z$ -distance with the approach of an AgTip to elucidate the mechanism of the modification of the emission photon statistics. In the case of 405 nm excitation, the PL intensity decreased with decreasing lifetime and the probability of multiphoton emission increased with decreasing  $z$ -distance. In the case of 465 nm excitation, the PL intensity increased and then decreased with decreasing  $z$ -distance, whereas the lifetime was shortened and the probability of the

multiphoton emission increased with decreasing  $z$ -distance, similar to the behavior observed at 405 nm excitation. By comparing the experimental data with the results of theoretical calculations, we elucidated that the increase in the probability of the multiphoton emission was induced by the quenching of the SX by the resonance energy transfer from the NQD to the AgTip and that the enhancement of the PL intensity was induced by the enhancement of the excitation rate by the LSP on the AgTip. This mechanism differs from the previously reported enhancement of the BX emission rate by a plasmonic nanostructure.<sup>1,3–6,8,11–15,17</sup> Although the increase in the probability of the BX emission due to the quenching of SX has been previously reported, the PL intensity was decreased in the case of this enhancement.<sup>9,38–40</sup> However, in our case, enhanced multiphoton emission with enhanced PL intensity was observed by the combination of quenching of the SX and enhancement of the excitation rate. Furthermore, the photon statistics and the intensity were modified through control of the distance. These results clearly demonstrated that the emission photon statistics and the emission intensity could be modified by the distance, the spectral overlap, and the excitation wavelength, i.e., by combining the enhancement of the excitation rate, the radiative rate, and the nonradiative rates using the plasmonic nanostructure. An increase in the probability of multiphoton emission can be achieved via enhancement of the radiative and nonradiative rates, the intensity can be increased via enhancement of the excitation rate and the radiative rate, and the enhancement factor of these enhancements can be controlled by the distance.

**Methods.** Commercially available colloidal CdSe/ZnS core/shell NQDs (average core radius: 2.6 nm; maximum PL wavelength: 610 nm) were purchased from Invitrogen. The AgTip was prepared by sputtering Ag onto a silicon AFM cantilever with a 7 nm tip radius (Olympus, OMCL-AC160TS-R3). The scattering spectrum of the AgTip was measured by contacting the AgTip with a taper fiber coupled with a white light source,<sup>48</sup> and numerical simulations of the AgTip were conducted using finite element analysis. Details are provided in the SI. The sample was prepared by spin-coating a toluene solution of colloidal CdSe/ZnS NQDs onto a clean glass coverslip.

The PL emission behavior of the single NQD as a function of the NQD-AgTip distance ( $z$ -distance) was measured using an inverted confocal microscope (Olympus, IX-71) combining with an AFM system (JPK Instruments, NanoWizard II).<sup>17</sup> In addition to the three closed-loop piezo-driven axes of the AFM head, a two-axis, closed-loop piezo-driven sample stage was used. To produce the  $z$ -polarized excitation beam, the linear polarization of pulsed laser beams (405 and 465 nm, 10.0 MHz, 90 ps fwhm, PicoQuant) was converted to radial polarization by a converter (ARCOptix); the beam was then focused to a diffraction-limited spot on the sample using an objective lens (Olympus, NA 1.4). The excitation intensity was adjusted to produce 0.17 excitons/pulse in a single NQD by taking into account the excitation intensity and the absorption cross-section of the NQD. The photons emitted from the NQD were collected by the same objective lens and passed through a confocal pinhole and long-pass and a short-pass filters to remove the excitation laser and AFM laser. Subsequently, half of the photons were detected by a spectrograph (Acton Research Corporation, SpectraPro2358) equipped with a cooled CCD camera (Princeton Instruments, PIXIS400B). The remaining half of the photons were passed through a band-

pass filter and were detected by two avalanche single-photon counting modules (PerkinElmer, SPCM-AQR-14) for Hanbury-Brown and Twiss-type photon correlation and lifetime measurements. The time-resolution of the lifetime measurement IRF was approximately 0.3 ns. The details are provided in the SI.

The measurement procedure was as follows. Initially, the AgTip was coupled to the center of a focused laser by the piezo of the AFM head. AFM topography and PL images of the sample were collected simultaneously by scanning the sample stage. By choosing a PL spot corresponding to the single NQD in the PL image, we measured the emission behavior before advancing the AgTip. Subsequently, the same single NQD was selected in the AFM image, and the AgTip was advanced toward the single NQD to measure the dependence of the emission behavior on the *z*-distance. The *z*-distance was defined as the distance from the top of the NQD to the top of the AgTip. The distance was controlled by a closed-loop feedback system. The real-time displacement of the *z*-distance was monitored by the software of the AFM system. The AFM topography measurement and the approach of the AgTip were performed in tapping and contact modes, respectively. All measurements were performed at room temperature under ambient conditions.

## ■ ASSOCIATED CONTENT

### Supporting Information

The Supporting Information is available free of charge on the ACS Publications website at DOI: 10.1021/acs.nanolett.6b02479.

Instrument setup, scattering spectrum measurement of the AgTip, numerical simulation of the AgTip, and emission behavior of the single NQDs with an approach of the AgTip (PDF)

## ■ AUTHOR INFORMATION

### Corresponding Author

\*E-mail: masuo@kwansai.ac.jp.

### Notes

The authors declare no competing financial interest.

## ■ ACKNOWLEDGMENTS

We thank Prof. Tadaaki Kaneko, Mr. Koji Ashida, Mr. Daichi Dojima, and Mr. Satoshi Ito at Kansai Gakuin University for assistance with SEM observations. This work was partly supported by JSPS KAKENHI Grant Number JP26390023 and JP26107005 in Scientific Research on Innovation Areas "Photosynthetic".

## ■ ABBREVIATIONS

NQD, colloidal nanocrystal quantum dot; AgTip, silver-coated atomic force microscopy tip; AFM, atomic force microscopy; LSP, localized surface plasmon; LSPR, localized surface plasmon resonance; MX, multiexciton; TX, triexciton; BX, biexciton; SX, single exciton; GS, ground state; MNS, metallic nanostructure; PL, photoluminescence; SEM, scanning electron microscopy; AuCube, cubic gold nanoparticle; AuNP, gold nanoparticle; fwhm, full-width at half-maximum; IRF, instrument response function

## ■ REFERENCES

- (1) Masuo, S.; Naiki, H.; Machida, S.; Itaya, A. *Appl. Phys. Lett.* **2009**, *95*, 193106.
- (2) Yuan, C. T.; Yu, P.; Ko, H. C.; Huang, J.; Tang, J. *ACS Nano* **2009**, *3*, 3051–3056.
- (3) Mallek-Zouari, I.; Buil, S.; Quelin, X.; Mahler, B.; Dubertret, B.; Hermier, J. P. *Appl. Phys. Lett.* **2010**, *97*, 053109.
- (4) Vion, C.; Spinicelli, P.; Coolen, L.; Schwob, C.; Frigerio, J. M.; Hermier, J. P.; Maitre, A. E. *Opt. Express* **2010**, *18*, 7440–7455.
- (5) Cannesson, D.; Mallek-Zouari, I.; Buil, S.; Quelin, X.; Javaux, C.; Mahler, B.; Dubertret, B.; Hermier, J. P. *Phys. Rev. B: Condens. Matter Mater. Phys.* **2011**, *84*, 245423.
- (6) Naiki, H.; Masuo, S.; Machida, S.; Itaya, A. *J. Phys. Chem. C* **2011**, *115*, 23299–23304.
- (7) Masuo, S.; Tanaka, T.; Machida, S.; Itaya, A. *J. Photochem. Photobiol., A* **2012**, *237*, 24–30.
- (8) Leblanc, S. J.; McClanahan, M. R.; Jones, M.; Moyer, P. J. *Nano Lett.* **2013**, *13*, 1662–1669.
- (9) Park, Y.-S.; Ghosh, Y.; Chen, Y.; Piryatinski, A.; Xu, P.; Mack, N. H.; Wang, H.-L.; Klimov, V. I.; Hollingsworth, J. A.; Htoon, H. *Phys. Rev. Lett.* **2013**, *110*, 117401.
- (10) Park, Y.-S.; Ghosh, Y.; Xu, P.; Mack, N. H.; Wang, H.-L.; Hollingsworth, J. A.; Htoon, H. *J. Phys. Chem. Lett.* **2013**, *4*, 1465–1470.
- (11) Yuan, C. T.; Wang, Y. C.; Cheng, H. W.; Wang, H. S.; Kuo, M. Y.; Shih, M. H.; Tang, J. *J. Phys. Chem. C* **2013**, *117*, 12762–12768.
- (12) Dey, S.; Zhou, Y. D.; Tian, X. D.; Jenkins, J. A.; Chen, O.; Zou, S. L.; Zhao, J. *Nanoscale* **2015**, *7*, 6851–6858.
- (13) Wang, F.; Karan, N. S.; Nguyen, H. M.; Ghosh, Y.; Hollingsworth, J. A.; Htoon, H. *Sci. Rep.* **2015**, *5*, 14313.
- (14) Wang, F.; Karan, N. S.; Nguyen, H. M.; Ghosh, Y.; Sheehan, C. J.; Hollingsworth, J. A.; Htoon, H. *Nanoscale* **2015**, *7*, 9387–9393.
- (15) Wang, F.; Karan, N. S.; Nguyen, H. M.; Mangum, B. D.; Ghosh, Y.; Sheehan, C. J.; Hollingsworth, J. A.; Htoon, H. *Small* **2015**, *11*, 5028–5034.
- (16) Hoang, T. B.; Akselrod, G. M.; Mikkelsen, M. H. *Nano Lett.* **2016**, *16*, 270–275.
- (17) Masuo, S.; Kanetaka, K.; Sato, R.; Teranishi, T. *ACS Photonics* **2016**, *3*, 109–116.
- (18) Klein, D. L.; Roth, R.; Lim, A. K. L.; Alivisatos, A. P.; McEuen, P. L. *Nature* **1997**, *389*, 699–701.
- (19) Klimov, V. I.; Mikhailovsky, A. A.; Xu, S.; Malko, A.; Hollingsworth, J. A.; Leatherdale, C. A.; Eisler, H.; Bawendi, M. G. *Science* **2000**, *290*, 314–317.
- (20) Coe, S.; Woo, W. K.; Bawendi, M.; Bulovic, V. *Nature* **2002**, *420*, 800–803.
- (21) Nozik, A. J. *Phys. E* **2002**, *14*, 115–120.
- (22) Klimov, V. I. *J. Phys. Chem. B* **2006**, *110*, 16827–16845.
- (23) Robel, I.; Subramanian, V.; Kuno, M.; Kamat, P. V. *J. Am. Chem. Soc.* **2006**, *128*, 2385–2393.
- (24) Klimov, V. I.; Ivanov, S. A.; Nanda, J.; Achermann, M.; Bezel, I.; McGuire, J. A.; Piryatinski, A. *Nature* **2007**, *447*, 441–446.
- (25) Kamat, P. V. *J. Phys. Chem. C* **2008**, *112*, 18737–18753.
- (26) Qian, L.; Zheng, Y.; Xue, J. G.; Holloway, P. H. *Nat. Photonics* **2011**, *5*, 543–548.
- (27) Kramer, I. J.; Sargent, E. H. *Chem. Rev.* **2014**, *114*, 863–882.
- (28) Bruchez, M., Jr.; Moronne, M.; Gin, P.; Weiss, S.; Alivisatos, A. P. *Science* **1998**, *281*, 2013–2016.
- (29) Chan, W. C.; Nie, S. *Science* **1998**, *281*, 2016–2018.
- (30) Alivisatos, P. *Nat. Biotechnol.* **2004**, *22*, 47–52.
- (31) Fisher, B.; Caruge, J. M.; Zehnder, D.; Bawendi, M. *Phys. Rev. Lett.* **2005**, *94*, 087403.
- (32) Benson, O.; Santori, C.; Pelton, M.; Yamamoto, Y. *Phys. Rev. Lett.* **2000**, *84*, 2513.
- (33) Klimov, V. V.; Mikhailovsky, A. A.; McBranch, D. W.; Leatherdale, C. A.; Bawendi, M. G. *Science* **2000**, *287*, 1011–1013.
- (34) Lounis, B.; Bechtel, H. A.; Gerion, D.; Alivisatos, P.; Moerner, W. E. *Chem. Phys. Lett.* **2000**, *329*, 399–404.

- (35) Michler, P.; Imamoglu, A.; Mason, M. D.; Carson, P. J.; Strouse, G. F.; Buratto, S. K. *Nature* **2000**, *406*, 968–970.
- (36) Messin, G.; Hermier, J. P.; Giacobino, E.; Desbiolles, P.; Dahan, M. *Opt. Lett.* **2001**, *26*, 1891–1893.
- (37) Brokmann, X.; Giacobino, E.; Dahan, M.; Hermier, J. P. *Appl. Phys. Lett.* **2004**, *85*, 712–714.
- (38) Cheng, H. W.; Yuan, C. T.; Wang, J. S.; Lin, T. N.; Shen, J. L.; Hung, Y. J.; Tang, J.; Tseng, F. G. *J. Phys. Chem. C* **2014**, *118*, 18126–18132.
- (39) Gao, Y.; Roslyak, O.; Dervishi, E.; Karan, N. S.; Ghosh, Y.; Sheehan, C. J.; Wang, F.; Gupta, G.; Mohite, A.; Dattelbaum, A. M.; Doorn, S. K.; Hollingsworth, J. A.; Piryatinski, A.; Htoon, H. *Adv. Opt. Mater.* **2015**, *3*, 39–43.
- (40) Liu, J.; Kumar, P.; Hu, Y. W.; Cheng, G. J.; Irudayaraj, J. *J. Phys. Chem. C* **2015**, *119*, 6331–6336.
- (41) Anger, P.; Bharadwaj, P.; Novotny, L. *Phys. Rev. Lett.* **2006**, *96*, 113002.
- (42) Kuhn, S.; Hakanson, U.; Rogobete, L.; Sandoghdar, V. *Phys. Rev. Lett.* **2006**, *97*, 017402.
- (43) Bharadwaj, P.; Novotny, L. *Opt. Express* **2007**, *15*, 14266–14274.
- (44) Novotny, L.; Beversluis, M. R.; Youngworth, K. S.; Brown, T. G. *Phys. Rev. Lett.* **2001**, *86*, 5251–5254.
- (45) Gerton, J. M.; Wade, L. A.; Lessard, G. A.; Ma, Z.; Quake, S. R. *Phys. Rev. Lett.* **2004**, *93*, 180801.
- (46) Achermann, M.; Hollingsworth, J. A.; Klimov, V. I. *Phys. Rev. B: Condens. Matter Mater. Phys.* **2003**, *68*, 245302.
- (47) Johnson, P. B.; Christy, R. W. *Phys. Rev. B* **1972**, *6*, 4370–4379.
- (48) Ren, F.; Takashima, H.; Tanaka, Y.; Fujiwara, H.; Sasaki, K. *Opt. Express* **2013**, *21*, 27759–27769.

# Photoprecursor Approach Enables Preparation of Well-Performing Bulk-Heterojunction Layers Comprising a Highly Aggregating Molecular Semiconductor

Mitsuharu Suzuki,<sup>†</sup> Yuji Yamaguchi,<sup>‡</sup> Kohei Takahashi,<sup>‡</sup> Katsuya Takahira,<sup>‡</sup> Tomoyuki Koganezawa,<sup>#</sup> Sadahiro Masuo,<sup>‡</sup> Ken-ichi Nakayama,<sup>\*,‡</sup> and Hiroko Yamada<sup>\*,†</sup>

<sup>†</sup>Graduate School of Materials Science, Nara Institute of Science and Technology, 8916-5 Takayama-cho, Ikoma, Nara 630-0192, Japan

<sup>‡</sup>Department of Organic Device Engineering, Yamagata University, 4-3-16 Jonan, Yonezawa, Yamagata 992-8510, Japan

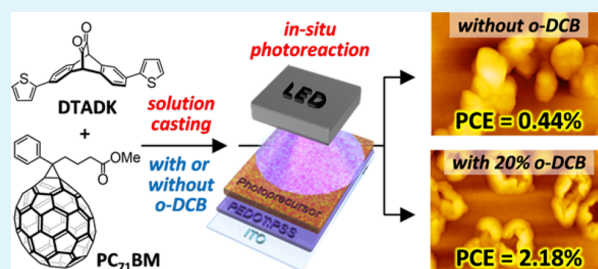
<sup>#</sup>Japan Synchrotron Radiation Research Institute, 1-1-1 Kouto, Sayo-cho, Sayo-gun, Hyogo 679-5198, Japan

<sup>‡</sup>Department of Applied Chemistry and Environment, Kwansei Gakuin University, 2-1 Gakuen, Sanda, Hyogo 669-1337, Japan

## S Supporting Information

**ABSTRACT:** Active-layer morphology critically affects the performance of organic photovoltaic cells, and thus its optimization is a key toward the achievement of high-efficiency devices. However, the optimization of active-layer morphology is sometimes challenging because of the intrinsic properties of materials such as strong self-aggregating nature or low miscibility. This study postulates that the “photoprecursor approach” can serve as an effective means to prepare well-performing bulk-heterojunction (BHJ) layers containing highly aggregating molecular semiconductors. In the photoprecursor approach, a photoreactive precursor compound is solution-deposited and then converted in situ to a semiconducting material. This study employs 2,6-di(2-thienyl)anthracene (DTA) and [6,6]-phenyl-C<sub>71</sub>-butyric acid methyl ester as p- and n-type materials, respectively, in which DTA is generated by the photoprecursor approach from the corresponding  $\alpha$ -diketone-type derivative DTADK. When only chloroform is used as a cast solvent, the photovoltaic performance of the resulting BHJ films is severely limited because of unfavorable film morphology. The addition of a high-boiling-point cosolvent, *o*-dichlorobenzene (*o*-DCB), to the cast solution leads to significant improvement such that the resulting active layers afford up to approximately 5 times higher power conversion efficiencies. The film structure is investigated by two-dimensional grazing-incident wide-angle X-ray diffraction, atomic force microscopy, and fluorescence microspectroscopy to demonstrate that the use of *o*-DCB leads to improvement in film crystallinity and increase in charge-carrier generation efficiency. The change in film structure is assumed to originate from dynamic molecular motion enabled by the existence of solvent during the in situ photoreaction. The unique features of the photoprecursor approach will be beneficial in extending the material and processing scopes for the development of organic thin-film devices.

**KEYWORDS:** organic solar cells, photoprecursor approach, morphology control, solution process,  $\alpha$ -diketones



## INTRODUCTION

The past decade has witnessed significant progress in organic photovoltaics. Indeed, power conversion efficiencies (PCEs) of >10% have already been achieved in several state-of-the-art cells.<sup>1–5</sup> Although improvements in material design<sup>6–17</sup> and device architecture<sup>18–22</sup> have greatly contributed to this progress, the optimization of active-layer morphology has also been a key factor.<sup>2,23–27</sup> To date, the most successful organic photovoltaic cells (OPVs) are of the bulk-heterojunction (BHJ) type, in which p- and n-type semiconductors are microscopically mixed to achieve a large p–n interface area in the active layer.<sup>28,29</sup> Solution-processed BHJ films are rarely used as deposited; rather, they are often subjected to a postdeposition treatment such as thermal or solvent-vapor annealing to form

favorable morphology for charge-carrier generation and transport.<sup>30–42</sup> Furthermore, it is common to employ a small amount of a high-boiling-point additive to induce a desirable degree of phase separation or crystallization.<sup>43–46</sup>

Despite the considerable efforts and accumulated technical knowledge, obtaining BHJ layers with ideal morphology remains a challenging task. The microscopic structure of a solution-processed blend film is greatly affected by various aspects of material properties and processing conditions such as solubility, crystallinity, miscibility, temperature, or solvent

**Received:** January 11, 2016

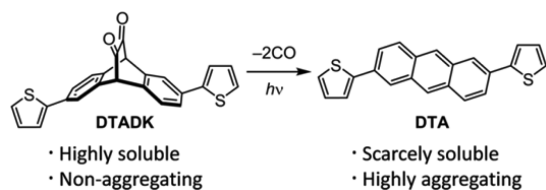
**Accepted:** March 17, 2016

**Published:** March 17, 2016

composition. Accordingly, the prediction of film morphology remains an issue, with no established general protocol for optimization. It is not rare that the photovoltaic response is severely limited because of poor film morphology, and common postdeposition treatments fail to address the problem. A typical example is when a BHJ composite comprises a material that is strongly self-aggregating and resistive to the formation of domains of suitable size for the photovoltaic process.

The precursor approach provides nonconventional means toward the achievement of effective active-layer structures through solution-based deposition processes.<sup>47–52</sup> In this approach, a well-soluble and nonaggregating precursor compound is solution-deposited on a substrate and then quantitatively converted in situ to a semiconducting material by an external stimulus such as heat or light. In pioneering work, Matsuo, Nakamura, and co-workers successfully demonstrated that photovoltaic active layers with highly ordered interpenetrating domains could be solution-processed by employing carefully optimized deposition conditions in the thermoprecursor approach where tetrabenzoporphyrin and bis-(dimethylphenylsilylmethyl)[60]fullerene (SIMEF) were used as p- and n-type materials, respectively.<sup>52</sup> More recently, we reported that the photoprecursor approach could serve as an effective method in the control of the vertical composition profile in photovoltaic active layers without any thermal treatment.<sup>48</sup> Specifically, the photovoltaic response of poorly performing BHJ layers was considerably improved by sandwiching them between neat p- and n-type materials to form a triple-layer structure. This multilayer structure was solution-processed by taking advantage of the drastic difference in solubility between acene-based p-type compounds and the corresponding  $\alpha$ -diketone-type photoprecursors, for example, 2,6-di(2-thienyl)anthracene (DTA, scarcely soluble) and its photoprecursor (DTADK, highly soluble), respectively (Scheme 1).

#### Scheme 1. Photochemical Generation of DTA from Its $\alpha$ -Diketone-Type Photoprecursor DTADK

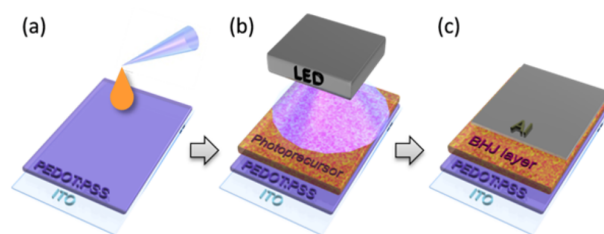


This contribution presents another strategy in the preparation of well-performing photovoltaic active layers via the photoprecursor approach focusing on a BHJ system consisting of DTA and [6,6]-phenyl- $C_{71}$ -butyric acid methyl ester ( $PC_{71}BM$ ). Whereas the photoprecursor DTADK is well miscible with  $PC_{71}BM$ , DTA is strongly self-aggregating. As such, DTA: $PC_{71}BM$  blend films prepared by the photoprecursor approach usually contain large DTA-rich grains affording poor photovoltaic performance.<sup>48,53</sup> We show that this problem can be greatly attenuated by using *o*-dichlorobenzene (*o*-DCB) as a cosolvent in cast solutions. Upon the addition of 20% of *o*-DCB, PCE in the resulting BHJ device is improved by up to 5 times, owing to the significant enhancement in short-circuit current density ( $J_{SC}$ ) and fill factor (FF). The obtained films are investigated by two-dimensional grazing-incident wide-angle X-ray diffraction (2D GIWAXD),

atomic force microscopy (AFM), and fluorescence microspectroscopy.

## RESULTS AND DISCUSSION

The OPVs examined in this study were fabricated as schematically described in Figure 1 (see the Experimental



**Figure 1.** Fabrication of BHJ OPVs by the photoprecursor approach: (a) spin-coating of DTADK: $PC_{71}BM$  blend solution on ITO/PEDOT:PSS; (b) photoirradiation to effect the conversion of DTADK to DTA; (c) vacuum deposition of Ca/Al to complete the device.

Section for more details). The DTA: $PC_{71}BM$  active layers were prepared by the photoprecursor approach using DTADK as a photoprecursor of DTA. The ratio between DTADK and  $PC_{71}BM$  in cast solutions was kept at 2:1 by weight, which afforded the best PCE when chloroform was used as a solo cast solvent.<sup>48</sup>

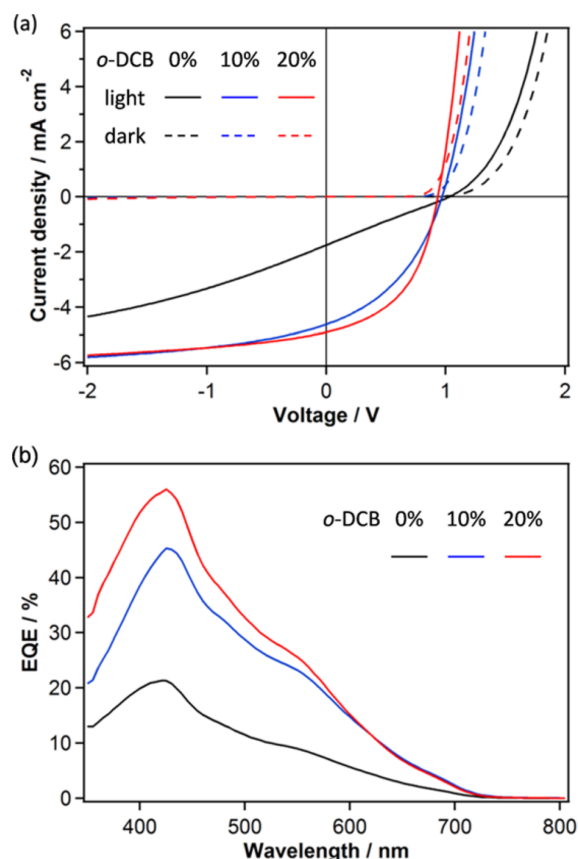
Morphology modification in the DTA: $PC_{71}BM$  blend can be completely different from that in common BHJ systems composed of a well-soluble p-type material and a fullerene-based n-type material. Solution-processable p-type materials are typically equipped with highly solubilizing alkyl groups, which allow the molecules to reorganize relatively easily during postdeposition annealing. These substituents also prevent excessive self-aggregation and ensure a certain degree of miscibility between p- and n-type materials. In relation to this, it is known that the self-organization behavior of p-type materials, rather than fullerene-based n-type materials, is often responsible for the morphology in BHJ films.<sup>2</sup> By contrast, DTA does not have solubilizing substituents, and its miscibility with  $PC_{71}BM$  is extremely low. Preliminary investigation revealed that commonly employed morphology-improvement techniques were not as effective for the DTA: $PC_{71}BM$  system as the new approach presented herein—that is, thermal annealing resulted in moderate improvements at best, whereas solvent-vapor annealing and addition of a small amount of high-boiling-point additive (1,8-diiodooctane) led to either a deterioration or very limited improvement in the photovoltaic performance (Table S1 in the Supporting Information (SI)).

In contrast, when *o*-DCB is added to the cast solution, the photovoltaic performance of the resulting DTA: $PC_{71}BM$  films is significantly enhanced. As shown in Table 1 and Figure 2a,  $J_{SC}$  and FF considerably improve as the amount of *o*-DCB increases from 0 to 10% and to 20%, leading to the increase in PCE from 0.44 to 1.79% and to 2.18%, respectively. The thickness of the active layers decreases with the increase of *o*-DCB content; thus, the improvement in  $J_{SC}$  can be attributed to the enhancement in charge-carrier generation or transport efficiency, which more than compensates for the decrease in photoabsorption capability of the active layer. It should be noted that the PCE is not improved as much when the active-layer thickness is decreased by using a lower concentration

**Table 1.** Photovoltaic Parameters of the BHJ OPVs Based on DTA and PC<sub>71</sub>BM<sup>a</sup>

entry	<i>o</i> -DCB (vol %)	active-layer thickness (nm)	$J_{SC}$ (mA cm <sup>-2</sup> )	$V_{OC}$ (V)	FF (%)	PCE (%)
1	0	106	1.75 (1.73 ± 0.05)	1.03 (1.03 ± 0.01)	24.4 (24.0 ± 0.3)	0.44 (0.43 ± 0.01)
2	10	90	4.62 (4.43 ± 0.22)	0.97 (0.98 ± 0.03)	39.9 (39.5 ± 2.1)	1.79 (1.70 ± 0.11)
3	20	66	4.90 (4.87 ± 0.03)	0.93 (0.95 ± 0.02)	47.7 (46.5 ± 1.6)	2.18 (2.16 ± 0.03)

<sup>a</sup>Showing the parameters of the best-performing cell in each case followed by the average of four devices in parentheses.



**Figure 2.** Characteristics of the best BHJ devices prepared using different amounts of *o*-DCB cosolvent: (a)  $J$ - $V$  curves (solid lines, under AM1.5G illumination at 100 mW cm<sup>-2</sup>; dashed lines, in the dark); (b) EQE spectra.

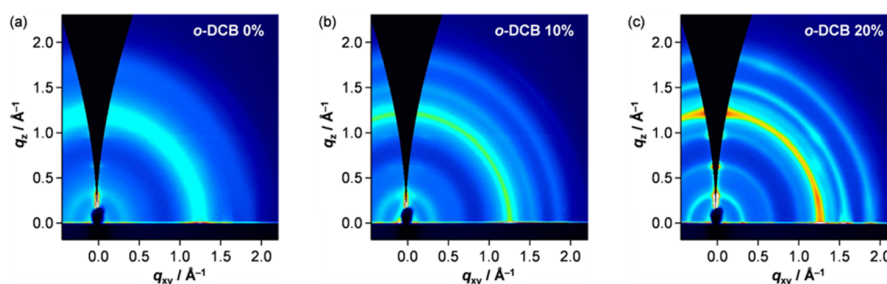
solution in chloroform (0.90% PCE with a 67 nm thick active layer),<sup>48</sup> indicating that the use of *o*-DCB is crucial for the observed improvement. The efficiency becomes slightly lower when 30% of *o*-DCB is used, with considerable leak current

observed at negative bias voltages below -1 V. This is presumably because the thickness of active layer excessively decreases (Table S2 and Figure S1 in the SI).

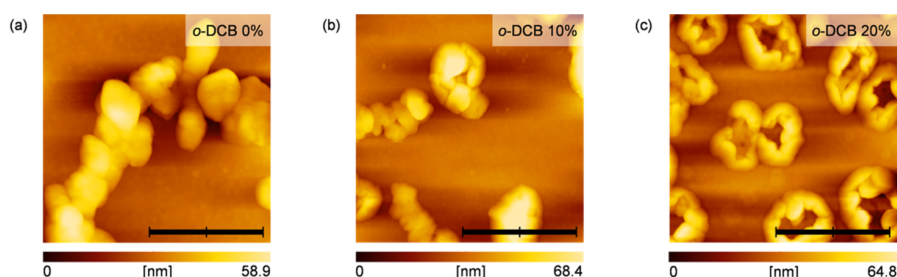
The external quantum efficiency (EQE) spectra of the champion cells prepared with 0, 10, and 20% *o*-DCB are plotted in Figure 2b. The 10% *o*-DCB device shows uniformly enhanced EQEs in the complete photoabsorption range of the DTA:PC<sub>71</sub>BM blend, in comparison with the device prepared without *o*-DCB. This observation can be explained by the improvement of the film morphology increasing the p-n interface and/or effective charge-carrier paths, which is similarly indicated by the increase in  $J_{SC}$  (from 1.75 to 4.62 mA cm<sup>-2</sup>) and FF (from 24.4 to 39.9%) (Table 1 and Figure 1a). The maximum quantum efficiency more than doubles from 21 to 45% at 425 nm; this improvement is highly respectable considering that the photoabsorption capability of the active layer is attenuated by the decrease in film thickness.

The maximum EQE is further enhanced to 56% at 425 nm when the amount of *o*-DCB cosolvent is increased to 20%. However, the apparent enhancement from the 10% *o*-DCB device is limited to wavelengths below 600 nm, whereas essentially no change is observed above that point. As the photoabsorption of DTA is dominant around the highest EQEs (400–430 nm),<sup>48</sup> effect of the increased *o*-DCB concentration is assumed to be more significant in the photovoltaic process initiated with the exciton generation in DTA rather than PC<sub>71</sub>BM. In other words, the structure of DTA domains is well below the full optimization when 10% *o*-DCB is used, leaving room for additional improvement by using higher amounts of *o*-DCB. Here again, the enhanced, and even unchanged, EQEs mean significant improvement in the efficiency of exciton-to-current conversion, considering the reduction in photoabsorption because of the smaller film thickness. Indeed, the estimated internal quantum efficiency (IQE) reaches ca. 90% at maximum for the cell prepared with 20% *o*-DCB (Figure S2), which is as high as that estimated with the same method for the system based on the high-performance polymer PTB7.<sup>54</sup>

In contrast to  $J_{SC}$  and FF, the open-circuit voltage ( $V_{OC}$ ) is relatively unaffected by the use of *o*-DCB cosolvent. Nonetheless, slight differences are noticeable; namely,  $V_{OC}$  gradually



**Figure 3.** GIWAXD data for the DTA:PC<sub>71</sub>BM blend films deposited by the photoprecursor approach on glass/ITO/PEDOT:PSS. The amounts of *o*-DCB cosolvent in cast solutions are (a) 0%, (b) 10%, and (c) 20%.



**Figure 4.** Tapping-mode AFM images of BHJ films deposited on glass/ITO/PEDOT:PSS by the photoprecursor approach with different amounts of *o*-DCB cosolvent: (a) 0%, RMS roughness = 9.3 nm; (b) 10%, RMS roughness = 10.6 nm; (c) 20%, RMS roughness = 10.6 nm. The scale bars correspond to 1  $\mu\text{m}$ .

decreases from 1.03 to 0.93 V in the champion devices (or from 1.03 to 0.95 V on average) as the *o*-DCB concentration increases from 0 to 20%. This difference may be ascribed to the change in film morphology induced by the use of cosolvent. There are many preceding studies in which  $V_{\text{OC}}$  slightly decreases upon film annealing associated with significant increases in  $J_{\text{SC}}$  and FF, for example, the papers by Neher et al.<sup>55</sup> and Ade et al.<sup>56</sup> on the PTB7:PC<sub>71</sub>BM system and the work by Palomares et al.<sup>57</sup> investigating the  $V_{\text{OC}}$  dependence on fullerene derivatives. The work by Palomares' group, in which a lower  $V_{\text{OC}}$  was attributed to a higher crystallinity of the p-type material caused by the interaction with n-type material, might be of particular relevance to the present case (see below). The group concluded that the difference in crystallinity affected the charge recombination dynamics and the electronic structure of the p-type material and, thus,  $V_{\text{OC}}$ .

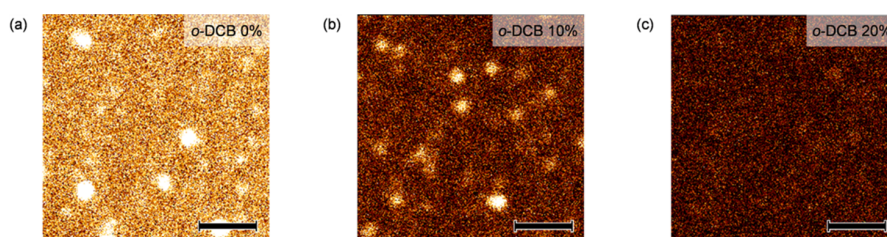
The crystallinity and molecular orientation in DTA:PC<sub>71</sub>BM films were investigated by 2D GIWAXD (Figure 3). The GIWAXD pattern of the film deposited without *o*-DCB is dominated by a broad halo around  $q = 1.3 \text{ \AA}^{-1}$ , which can be assigned to the Bragg diffraction of PC<sub>71</sub>BM (Figure 3a).<sup>58</sup> The appearance of this halo seems unchanged (intensity is hard to quantify because of the overlapping diffraction of DTA as described below) when *o*-DCB is added (Figure 3b,c). This indicates that the crystallinity of PC<sub>71</sub>BM domains does not change significantly by the use of the cosolvent.

The film deposited with 20% *o*-DCB shows a series of relatively strong diffractions around  $q_z = 0.33, 0.65, \text{ and } 1.0 \text{ \AA}^{-1}$  (Figure 3c). These diffractions can be assigned to the 200, 400, and 600 diffractions of DTA,<sup>59</sup> respectively, indicating the end-on stacking of DTA molecules. There are also relatively strong rings around  $q = 1.3$  (overlapping with the diffraction of PC<sub>71</sub>BM), 1.6, and 1.9  $\text{\AA}^{-1}$ , which correspond well with the 111, 020, and 121 diffractions of DTA, respectively.<sup>59</sup> The *b*- and *c*-axes correspond to the DTA herringbone stack, and thus the observed rings indicate that this stacking motif is randomly oriented within the film. As the charge-carrier mobility in DTA crystals is expected to be highest along the herringbone stack, those crystallites in which the herringbone stack extends toward electrodes should be the main contributors to the enhanced photovoltaic performance.

The surface morphology of the BHJ films was probed by AFM. The film prepared without *o*-DCB contains large grains surrounded by relatively flat regions to form a “sea–island” structure as previously reported (Figure 4a).<sup>48</sup> The lateral dimensions of these grains range up to several hundred nanometers, and the root-mean-square (RMS) surface roughness of the film is as high as 9.3 nm. On the basis of fluorescence microspectroscopy analysis, the “islands” are

seemingly DTA-rich, whereas the “sea” likely consists of relatively well-mixed DTA and PC<sub>71</sub>BM.<sup>53</sup> This inhomogeneous distribution of the two components is undesirable for the photovoltaic process and is probably the cause of the observed low PCE (0.44%) associated with a low FF (24.4%). On the other hand, the film surface is very smooth, and no large grains are observed before photoreaction (Figure S3a in the SI), clearly demonstrating that the photoprecursor DTADK is not as self-aggregating as DTA and well miscible with PC<sub>71</sub>BM under the employed deposition conditions. In addition, this observation shows that DTA molecules move considerably during the photoreaction in the solid state.

The surface roughness, in sharp contrast to the photovoltaic performance, changes minimally when 20% *o*-DCB is used in spin-coating (Figure 4c); namely, the 20% *o*-DCB film contains large grains, and its RMS roughness is 10.6 nm, being as high as that of the case without *o*-DCB (9.3 nm). An apparent difference, however, does exist between these two cases: grains aggregate randomly when no *o*-DCB is used, whereas they assemble to form flower-like objects when 20% *o*-DCB is added. Dried pre-photoreaction films are equally smooth in both cases (Figure S3a,c in the SI), and thus it is assumed that the existence of *o*-DCB during the photoreaction is the key to the formation of the observed structures. Note that the films prepared with *o*-DCB cosolvent are apparently wet right after deposition and are immediately subjected to the photoreaction. As DTADK is well soluble in *o*-DCB, considerable amounts of it should exist in the liquid part during the photoreaction, most likely at the saturation or a supersaturation concentration. Upon the photoinduced conversion from DTADK to DTA, the low-solubility product should immediately start to precipitate. Here, the decarbonylation of  $\alpha$ -diketone-type photoprecursors proceeds more smoothly when molecules are able to move more easily to accommodate the change in molecular structure associated with the reaction.<sup>60</sup> Thus, it can be supposed that the reaction is faster in the liquid part of wet films of DTADK:PC<sub>71</sub>BM blend, and the generated DTA precipitates while the solvent (mostly *o*-DCB) keeps extracting the remaining DTADK from the solid part. Such enhanced dynamics in wet films may have led to the formation of the flower-like structures. In relation to this, there are several models proposed to explain the formation of doughnut-shaped microstructures on solid surfaces, such as the bubble model, hole model, and spinodal dewetting model.<sup>61–67</sup> Especially relevant to the present case may be the example in which solvent entrapment poses a crucial effect in determining the morphology of multicomponent thin films containing a highly aggregating porphyrin derivative.<sup>61</sup>



**Figure 5.** Fluorescence microspectroscopy images of BHJ films deposited on glass/ITO/PEDOT:PSS by the photoprecursor approach with different amounts of *o*-DCB cosolvent: (a) 0%; (b) 10%; (c) 20%. All of the measurements were conducted with 405 nm excitation at an intensity of 56 W cm<sup>-2</sup>. The scale bars correspond to 5 μm. The color scale is defined as white for 100 counts and black for 0 count in all of the images.

When 10% *o*-DCB cosolvent is used, the resulting film shows a surface morphology that can be described as “between” the 0 and 20% cases (Figure 4b); therefore, the amount of *o*-DCB plays an important role in determining film morphology. It should also be mentioned that the presence of PC<sub>71</sub>BM is crucial in forming the observed structures, because neat DTA films do not show the flower-like motif (Figure S4 in the SI). In addition, the neat film prepared with 20% *o*-DCB contains large grains with well-defined polyhedral shapes, which are not observed in the corresponding blend film. Thus, PC<sub>71</sub>BM disturbs the formation of such relatively large DTA crystals, in accordance with the common observation that the film crystallinity is attenuated in BHJ films as compared to the corresponding neat films. These results indicate that DTA, PC<sub>71</sub>BM, and solvent molecules mutually affect each other in forming the observed microstructures. The process is in principle highly complex, involving many factors such as the kinetics of crystal nucleation and solvent evaporation or the effects of relative solubility and miscibility between different components. More detailed examination on these intriguing observations will be presented elsewhere.

The microstructure of thin films was further investigated by fluorescence microspectroscopy. As shown in Figure 5, the intensity of fluorescence from DTA significantly decreases as the *o*-DCB content in cast solution increases. The fluorescence lifetime also decreases with the increase of the *o*-DCB content (Figure S5 in the SI). These data clearly show that the use of *o*-DCB cosolvent has led to the effective suppression of the radiative quenching of excitons in DTA domains, presumably owing to the decrease in domain size and increase in p–n interface to facilitate the generation of hole–electron pairs. Here, a good part of DTA domains in the 20% *o*-DCB film would be much smaller than the micrometer regime, considering the commonly observed diffuse lengths of excitons in organic semiconductors (several tens of nanometers).<sup>68,69</sup> Thus, each grain of several hundreds of nanometers observed by AFM (Figure 4c) should consist of multiple smaller domains of DTA in good contact with PC<sub>71</sub>BM domains. This formation of sufficiently small DTA domains may be directly related to the enhanced film crystallinity induced by the use of *o*-DCB cosolvent. The “concentration”, and thus the number of nucleation sites as well, would be unusually high in wet films to severely limit the growth of each crystallite. Importantly, as mentioned above, neat DTA films prepared by the photoprecursor approach contain relatively large crystals that can be clearly distinguished by AFM (Figure S4c in the SI). Therefore, the formation of small DTA crystals in BHJ films should be due to the effect of not only residual *o*-DCB but also PC<sub>71</sub>BM.

## CONCLUSIONS

The present contribution has demonstrated that the photoprecursor approach enables preparation of well-performing BHJ layers containing the highly aggregating molecular semiconductor DTA. The key is using a high-boiling-point cosolvent for solution deposition. The PCE is improved from 0.44 to 2.18% associated with significant enhancement in FF and  $J_{SC}$  when 20% *o*-DCB is added to the cast solution. The 2.18% PCE is remarkable considering the limited photoabsorption capability of DTA that can absorb only up to 475 nm. It is reasonable to expect that much higher PCEs will be achieved by employing narrow band gap materials. Furthermore, it should be emphasized that the addition of the  $\alpha$ -diketone unit considerably improves the solubility of acene compounds, as exemplified well by the fact that DTADK is highly soluble in common organic solvents, whereas DTA is essentially insoluble. Thus, the precursor approach presented herein does not require heavy decoration of molecules with solubilizing alkyl groups, which can be beneficial in increasing crystallinity and photoabsorption coefficients of active layers to achieve high exciton/charge-carrier mobilities, and work along these lines is underway in our group.

The GIWAXD and fluorescence microspectroscopy analyses have indicated that the enhanced photovoltaic performance can be attributed to the improvement in crystallinity of DTA domains and increase in charge-carrier generation efficiency. High crystallinity is often not compatible with efficient charge-carrier generation in small-molecule BHJ films, because highly crystalline molecular materials tend to self-aggregate, forming large domains and limited p–n interfaces. Thus, this aspect sets the present method apart from simple solution deposition/drying and conventional annealing processes. In addition, AFM images show that grains assemble to form flower-like secondary structures when 20% of *o*-DCB is added to the cast solution. The control experiments have indicated that the existence of *o*-DCB and PC<sub>71</sub>BM during the photogeneration of DTA would be responsible for the evolution of the intriguing film morphology. The highly dynamic nature of the present process, which involves in situ chemical conversion associated with concomitant precipitation, dissolution, and crystallization, is unusual and can be of great interest in terms of the formation of organic microarchitectures. With all of these observations combined, we expect that the modified photoprecursor approach presented herein will add a new dimension to the solution processing methodology for organic semiconductors.

## EXPERIMENTAL SECTION

**Materials.** DTADK was synthesized according to the reported procedure.<sup>70</sup> The purity of DTADK was confirmed to be >99% by high-performance liquid chromatography (Inertsil ODS-3, detected by

absorption at 254 nm, acetonitrile as eluent). PC<sub>71</sub>BM was purchased from Luminescence Technology Corp. and used as received. Solvents were of reagent grade purchased from commercial vendors and used without further purification.

**Device Fabrication and Evaluation.** Indium–tin oxide (ITO)-patterned glass substrates (20 × 25 mm, 15 ohm per square) were cleaned by gentle rubbing with an acetone-soaked wipe for ca. 5 s, sonication in acetone and isopropanol for 10 min each, and exposure to boiling isopropanol for 10 min. The washed substrates were further treated in a UV–O<sub>3</sub> cleaner (Filgen, UV253 V8) for 20 min, and the poly(3,4-ethylenedioxythiophene):poly(4-styrenesulfonate) layer (PEDOT:PSS, Clevis P VP AI4083) was spin-coated at 5000 rpm for 40 s in air followed by a thermal annealing treatment at 120 °C for 20 min in air. The thickness of the resulting PEDOT:PSS layer was about 30 nm. The substrates were then transferred to a N<sub>2</sub>-filled glovebox (<0.5 ppm of O<sub>2</sub> and H<sub>2</sub>O) for preparation of the organic layers. DTA:PC<sub>71</sub>BM BHJ films were prepared by spin-coating of a DTADK:PC<sub>71</sub>BM (2:1 in weight) solution in chloroform containing 0–30 vol % *o*-DCB (12 mg mL<sup>-1</sup>, 800 rpm, 30 s), followed by photoirradiation (470 nm LED, 640 mW cm<sup>-2</sup>, 4 min). Finally, Ca (10 nm) and Al (80 nm) were vapor-deposited at high vacuum (~10<sup>-5</sup> Pa) through a shadow mask that defined an active area of 4.0 mm<sup>2</sup>. The general device structure was [ITO/PEDOT:PSS (30 nm)/DTA:PC<sub>71</sub>BM/Ca (10 nm)/Al (80 nm)].

Current–voltage (*J*–*V*) curves were measured using a Keithley 2400 source measurement unit under AM1.5G illumination at an intensity of 100 mW cm<sup>-2</sup> using a solar simulator (Bunko-keiki, CEP-2000TF). The external quantum efficiency (EQE) spectra were obtained under illumination of monochromatic light using the same system. The UV–vis absorption spectra of the organic films including the PEDOT:PSS layer were recorded using a JASCO V-650 spectrophotometer by the transmittance mode. The internal quantum efficiency (IQE) values were roughly estimated from the EQE and UV–vis absorption spectra according to the previously employed method by Yu et al.<sup>54</sup> Note that minor underestimation of IQE is expected with this method.

**Film Characterization.** The surface morphology of organic films was observed by an SII SPA400/SPI3800N atomic force microscope in tapping mode using a silicon probe with a resonant frequency of 138 kHz and a force constant of 16 N m<sup>-1</sup> (SII, SI-DF20). GIWAXD measurements were performed in a HUBER multiaxis diffractometer installed in beamline BL-19B2 or BL-46XU at SPring-8. The X-ray beam was monochromatized by a double-crystal Si(111) monochromator, and the X-ray energy was 12.398 keV. Scattered X-rays from samples were detected by an X-ray photon counting pixel detector (PILATUS 300 K). The X-ray-beam incidence angle was set to 0.12°, and the sample-to-detector distance was about 174 mm. The thin-film samples for the GIWAXD measurements were prepared on ITO-coated glass substrates in the same manner as in the device fabrication described above. Fluorescence microscopy measurements were conducted as previously described.<sup>53</sup>

## ■ ASSOCIATED CONTENT

### Supporting Information

The Supporting Information is available free of charge on the ACS Publications website at DOI: 10.1021/acsami.6b00345.

Additional OPV data, estimated internal quantum efficiencies, additional AFM images, and fluorescence decay curves (PDF)

## ■ AUTHOR INFORMATION

### Corresponding Authors

\*(K.N.) E-mail: nakayama@yz.yamagata-u.ac.jp.

\*(H.Y.) E-mail: hyamada@ms.naist.jp.

## Author Contributions

The manuscript was written through contributions of all authors. All authors have given approval to the final version of the manuscript. M.S. and Y.Y. contributed equally.

## Notes

The authors declare no competing financial interest.

## ■ ACKNOWLEDGMENTS

This research was supported by the CREST program of the Japan Science and Technology Agency (JST), Grants-in-Aid for Scientific Research (KAKENHI) 26600004 to M.S., 26390023 to S.M., and 25288092 and 26105004 to H.Y. from the Japan Society for the Promotion of Science (JSPS), Japan Regional Innovation Strategy Program by the Excellence (J-RISE) sponsored by JST, the Green Photonics Project in NAIST sponsored by the Ministry of Education, Culture, Sports, Science and Technology (MEXT), Japan, the program for promoting the enhancement of research universities in NAIST supported by MEXT, and Kansai Research Foundation for Technology Promotion (KRF). The synchrotron experiments were performed at beamlines BL-19B2 and BL-46XU in SPring-8 with the approval of the Japan Synchrotron Radiation Research Institute (JASRI) (Proposals 2015A1683, 2015A1842, 2015A1965, and 2015B1769).

## ■ REFERENCES

- (1) Vohra, V.; Kawashima, K.; Kakara, T.; Koganezawa, T.; Osaka, I.; Takimiya, K.; Murata, H. Efficient Inverted Polymer Solar Cells Employing Favourable Molecular Orientation. *Nat. Photonics* **2015**, *9*, 403–408.
- (2) Liu, Y.; Zhao, J.; Li, Z.; Mu, C.; Ma, W.; Hu, H.; Jiang, K.; Lin, H.; Ade, H.; Yan, H. Aggregation and Morphology Control Enables Multiple Cases of High-Efficiency Polymer Solar Cells. *Nat. Commun.* **2014**, *5*, 5293.
- (3) Chen, J.-D.; Cui, C.; Li, Y.-Q.; Zhou, L.; Ou, Q.-D.; Li, C.; Li, Y.; Tang, J.-X. Single-Junction Polymer Solar Cells Exceeding 10% Power Conversion Efficiency. *Adv. Mater.* **2015**, *27*, 1035–1041.
- (4) Chen, C.-C.; Chang, W.-H.; Yoshimura, K.; Ohya, K.; You, J.; Gao, J.; Hong, Z.; Yang, Y. An Efficient Triple-Junction Polymer Solar Cell Having a Power Conversion Efficiency Exceeding 11%. *Adv. Mater.* **2014**, *26*, 5670–5677.
- (5) Liu, Y.; Chen, C.-C.; Hong, Z.; Gao, J.; Yang, Y. (Michael); Zhou, H.; Dou, L.; Li, G.; Yang, Y. Solution-Processed Small-Molecule Solar Cells: Breaking the 10% Power Conversion Efficiency. *Sci. Rep.* **2013**, *3*, 3356.
- (6) Dennler, G.; Scharber, M. C.; Ameri, T.; Denk, P.; Forberich, K.; Waldauf, C.; Brabec, C. J. Design Rules for Donors in Bulk-Heterojunction Tandem Solar Cells—Towards 15% Energy-Conversion Efficiency. *Adv. Mater.* **2008**, *20*, 579–583.
- (7) Anthony, J. E. Small-Molecule, Nonfullerene Acceptors for Polymer Bulk Heterojunction Organic Photovoltaics. *Chem. Mater.* **2011**, *23*, 583–590.
- (8) Boudreaux, P.-L. T.; Najari, A.; Leclerc, M. Processable Low-Bandgap Polymers for Photovoltaic Applications. *Chem. Mater.* **2011**, *23*, 456–469.
- (9) Facchetti, A.  $\pi$ -Conjugated Polymers for Organic Electronics and Photovoltaic Cell Applications. *Chem. Mater.* **2011**, *23*, 733–758.
- (10) Walker, B.; Kim, C.; Nguyen, T.-Q. Small Molecule Solution-Processed Bulk Heterojunction Solar Cells. *Chem. Mater.* **2011**, *23*, 470–482.
- (11) Mishra, A.; Bäuerle, P. Small Molecule Organic Semiconductors on the Move: Promises for Future Solar Energy Technology. *Angew. Chem., Int. Ed.* **2012**, *51*, 2020–2067.
- (12) Coughlin, J. E.; Henson, Z. B.; Welch, G. C.; Bazan, G. C. Design and Synthesis of Molecular Donors for Solution-Processed

- High-Efficiency Organic Solar Cells. *Acc. Chem. Res.* **2014**, *47*, 257–270.
- (13) Lai, Y.-Y.; Cheng, Y.-J.; Hsu, C.-S. Applications of Functional Fullerene Materials in Polymer Solar Cells. *Energy Environ. Sci.* **2014**, *7*, 1866–1883.
- (14) Umeyama, T.; Imahori, H. Design and Control of Organic Semiconductors and Their Nanostructures for Polymer–Fullerene-Based Photovoltaic Devices. *J. Mater. Chem. A* **2014**, *2*, 11545–11560.
- (15) Ye, L.; Zhang, S.; Huo, L.; Zhang, M.; Hou, J. Molecular Design toward Highly Efficient Photovoltaic Polymers Based on Two-Dimensional Conjugated Benzodithiophene. *Acc. Chem. Res.* **2014**, *47*, 1595–1603.
- (16) Chen, W.; Yang, X.; Long, G.; Wan, X.; Chen, Y.; Zhang, Q. A Perylene Diimide (PDI)-Based Small Molecule with Tetrahedral Configuration as a Non-Fullerene Acceptor for Organic Solar Cells. *J. Mater. Chem. C* **2015**, *3*, 4698–4705.
- (17) Hu, B.; Li, M.; Chen, W.; Wan, X.; Chen, Y.; Zhang, Q. Novel Donor–Acceptor Polymers Based on 7-Perfluorophenyl-6H-[1,2,5]-thiadiazole[3,4-g]benzimidazole for Bulk Heterojunction Solar Cells. *RSC Adv.* **2015**, *5*, 50137–50145.
- (18) He, Z.; Zhong, C.; Su, S.; Xu, M.; Wu, H.; Cao, Y. Enhanced Power-Conversion Efficiency in Polymer Solar Cells Using an Inverted Device Structure. *Nat. Photonics* **2012**, *6*, 591–595.
- (19) Cao, W.; Xue, J. Recent Progress in Organic Photovoltaics: Device Architecture and Optical Design. *Energy Environ. Sci.* **2014**, *7*, 2123–2144.
- (20) Ameri, T.; Li, N.; Brabec, C. J. Highly Efficient Organic Tandem Solar Cells: A Follow up Review. *Energy Environ. Sci.* **2013**, *6*, 2390–2413.
- (21) Adebajo, O.; Maharjan, P. P.; Adhikary, P.; Wang, M.; Yang, S.; Qiao, Q. Triple Junction Polymer Solar Cells. *Energy Environ. Sci.* **2013**, *6*, 3150–3170.
- (22) Heremans, P.; Cheyns, D.; Rand, B. P. Strategies for Increasing the Efficiency of Heterojunction Organic Solar Cells: Material Selection and Device Architecture. *Acc. Chem. Res.* **2009**, *42*, 1740–1747.
- (23) Huang, Y.; Kramer, E. J.; Heeger, A. J.; Bazan, G. C. Bulk Heterojunction Solar Cells: Morphology and Performance Relationships. *Chem. Rev.* **2014**, *114*, 7006–7043.
- (24) Liu, F.; Gu, Y.; Shen, X.; Ferdous, S.; Wang, H.-W.; Russell, T. P. Characterization of the Morphology of Solution-Processed Bulk Heterojunction Organic Photovoltaics. *Prog. Polym. Sci.* **2013**, *38*, 1990–2052.
- (25) Brabec, C. J.; Heeney, M.; McCulloch, I.; Nelson, J. Influence of Blend Microstructure on Bulk Heterojunction Organic Photovoltaic Performance. *Chem. Soc. Rev.* **2011**, *40*, 1185–1199.
- (26) Yang, X.; Loos, J. Toward High-Performance Polymer Solar Cells: The Importance of Morphology Control. *Macromolecules* **2007**, *40*, 1353–1362.
- (27) Benanti, T. L.; Venkataraman, D. Organic Solar Cells: An Overview Focusing on Active Layer Morphology. *Photosynth. Res.* **2006**, *87*, 73–81.
- (28) Scharber, M. C.; Sariciftci, N. S. Efficiency of Bulk-Heterojunction Organic Solar Cells. *Prog. Polym. Sci.* **2013**, *38*, 1929–1940.
- (29) Dennler, G.; Scharber, M. C.; Brabec, C. J. Polymer-Fullerene Bulk-Heterojunction Solar Cells. *Adv. Mater.* **2009**, *21*, 1323–1338.
- (30) Zhang, X.; Zhan, C.; Yao, J. Non-Fullerene Organic Solar Cells with 6.1% Efficiency through Fine-Tuning Parameters of the Film-Forming Process. *Chem. Mater.* **2015**, *27*, 166–173.
- (31) Wu, F.-C.; Li, Y.-H.; Tsou, C.-J.; Tung, K.-C.; Yen, C.-T.; Chou, F.-S.; Tang, F.-C.; Chou, W.-Y.; Ruan, J.; Cheng, H.-L. Synergistic Effects of Binary-Solvent Annealing for Efficient Polymer–Fullerene Bulk Heterojunction Solar Cells. *ACS Appl. Mater. Interfaces* **2015**, *7*, 18967–18976.
- (32) Wang, J.-L.; Yin, Q.-R.; Miao, J.-S.; Wu, Z.; Chang, Z.-F.; Cao, Y.; Zhang, R.-B.; Wang, J.-Y.; Wu, H.-B.; Cao, Y. Rational Design of Small Molecular Donor for Solution-Processed Organic Photovoltaics with 8.1% Efficiency and High Fill Factor via Multiple Fluorine Substituents and Thiophene Bridge. *Adv. Funct. Mater.* **2015**, *25*, 3514–3523.
- (33) Wang, J.-L.; Wu, Z.; Miao, J.-S.; Liu, K.-K.; Chang, Z.-F.; Zhang, R.-B.; Wu, H.-B.; Cao, Y. Solution-Processed Diketopyrrolopyrrole-Containing Small-Molecule Organic Solar Cells with 7.0% Efficiency: In-Depth Investigation on the Effects of Structure Modification and Solvent Vapor Annealing. *Chem. Mater.* **2015**, *27*, 4338–4348.
- (34) Miao, J.; Chen, H.; Liu, F.; Zhao, B.; Hu, L.; He, Z.; Wu, H. Efficiency Enhancement in Solution-Processed Organic Small Molecule: Fullerene Solar Cells via Solvent Vapor Annealing. *Appl. Phys. Lett.* **2015**, *106*, 183302.
- (35) Huang, W.; Gann, E.; Cheng, Y.-B.; McNeill, C. R. In-Depth Understanding of the Morphology–Performance Relationship in Polymer Solar Cells. *ACS Appl. Mater. Interfaces* **2015**, *7*, 14026–14034.
- (36) Du, Z.; Chen, W.; Chen, Y.; Qiao, S.; Bao, X.; Wen, S.; Sun, M.; Han, L.; Yang, R. High Efficiency Solution-Processed Two-Dimensional Small Molecule Organic Solar Cells Obtained via Low-Temperature Thermal Annealing. *J. Mater. Chem. A* **2014**, *2*, 15904–15911.
- (37) Chen, H.; Hsiao, Y.-C.; Hu, B.; Dadmun, M. Control of Morphology and Function of Low Band Gap Polymer–bis-Fullerene Mixed Heterojunctions in Organic Photovoltaics with Selective Solvent Vapor Annealing. *J. Mater. Chem. A* **2014**, *2*, 9883–9890.
- (38) Sharma, G. D.; Suresh, P.; Sharma, S. S.; Vijay, Y. K.; Mikroyannidis, J. A. Effect of Solvent and Subsequent Thermal Annealing on the Performance of Phenylenevinylene Copolymer:PCBM Solar Cells. *ACS Appl. Mater. Interfaces* **2010**, *2*, 504–510.
- (39) Bull, T. A.; Pingree, L. S. C.; Jenekhe, S. A.; Ginger, D. S.; Luscombe, C. K. The Role of Mesoscopic PCBM Crystallites in Solvent Vapor Annealed Copolymer Solar Cells. *ACS Nano* **2009**, *3*, 627–636.
- (40) Miller, S.; Fanchini, G.; Lin, Y.-Y.; Li, C.; Chen, C.-W.; Su, W.-F.; Chhowalla, M. Investigation of Nanoscale Morphological Changes in Organic Photovoltaics during Solvent Vapor Annealing. *J. Mater. Chem.* **2008**, *18*, 306–312.
- (41) Nguyen, L. H.; Hoppe, H.; Erb, T.; Günes, S.; Gobsch, G.; Sariciftci, N. S. Effects of Annealing on the Nanomorphology and Performance of Poly(alkylthiophene):Fullerene Bulk-Heterojunction Solar Cells. *Adv. Funct. Mater.* **2007**, *17*, 1071–1078.
- (42) Kim, Y.; Choulis, S. A.; Nelson, J.; Bradley, D. D. C.; Cook, S.; Durrant, J. R. Device Annealing Effect in Organic Solar Cells with Blends of Regioregular Poly(3-hexylthiophene) and Soluble Fullerene. *Appl. Phys. Lett.* **2005**, *86*, 063502.
- (43) Schmidt, K.; Tassone, C. J.; Niskala, J. R.; Yiu, A. T.; Lee, O. P.; Weiss, T. M.; Wang, C.; Fréchet, J. M. J.; Beaujuge, P. M.; Toney, M. F. A Mechanistic Understanding of Processing Additive-Induced Efficiency Enhancement in Bulk Heterojunction Organic Solar Cells. *Adv. Mater.* **2014**, *26*, 300–305.
- (44) Dang, M. T.; Wuest, J. D. Using Volatile Additives to Alter the Morphology and Performance of Active Layers in Thin-Film Molecular Photovoltaic Devices Incorporating Bulk Heterojunctions. *Chem. Soc. Rev.* **2013**, *42*, 9105–9126.
- (45) Lee, J. K.; Ma, W. L.; Brabec, C. J.; Yuen, J.; Moon, J. S.; Kim, J. Y.; Lee, K.; Bazan, G. C.; Heeger, A. J. Processing Additives for Improved Efficiency from Bulk Heterojunction Solar Cells. *J. Am. Chem. Soc.* **2008**, *130*, 3619–3623.
- (46) Herath, N.; Das, S.; Keum, J. K.; Zhu, J.; Kumar, R.; Ivanov, I. N.; Sumpter, B. G.; Browning, J. F.; Xiao, K.; Gu, G.; Joshi, P.; Smith, S.; Lauter, V. Peculiarity of Two Thermodynamically-Stable Morphologies and Their Impact on the Efficiency of Small Molecule Bulk Heterojunction Solar Cells. *Sci. Rep.* **2015**, *5*, 13407.
- (47) Quinton, C.; Suzuki, M.; Kaneshige, Y.; Tatenaka, Y.; Katagiri, C.; Yamaguchi, Y.; Kuzuhara, D.; Aratani, N.; Nakayama, K.; Yamada, H. Evaluation of Semiconducting Molecular Thin Films Solution-Processed via the Photoprecursor Approach: The Case of Hexyl-Substituted Thienoanthracenes. *J. Mater. Chem. C* **2015**, *3*, 5995–6005.

- (48) Yamaguchi, Y.; Suzuki, M.; Motoyama, T.; Sugii, S.; Katagiri, C.; Takahira, K.; Ikeda, S.; Yamada, H.; Nakayama, K. Photoprecursor Approach as an Effective Means for Preparing Multilayer Organic Semiconducting Thin Films by Solution Processes. *Sci. Rep.* **2014**, *4*, 7151.
- (49) Suzuki, M.; Aotake, T.; Yamaguchi, Y.; Noguchi, N.; Nakano, H.; Nakayama, K.; Yamada, H. Synthesis and Photoreactivity of  $\alpha$ -Diketone-Type Precursors of Acenes and Their Use in Organic-Device Fabrication. *J. Photochem. Photobiol., C* **2014**, *18*, 50–70.
- (50) Saeki, H.; Misaki, M.; Kuzuhara, D.; Yamada, H.; Ueda, Y. Fabrication of Phase-Separated Benzoporphycene/[6,6]-Phenyl-C<sub>61</sub>-Butyric Acid Methyl Ester Films for Use in Organic Photovoltaic Cells. *Jpn. J. Appl. Phys.* **2013**, *52*, 111601.
- (51) Saeki, H.; Kurimoto, O.; Misaki, M.; Kuzuhara, D.; Yamada, H.; Ueda, Y. Thermal Conversion Behavior and Morphology Control of Benzoporphycene from a Novel Soluble Precursor. *Appl. Phys. Express* **2013**, *6*, 035601.
- (52) Matsuo, Y.; Sato, Y.; Niinomi, T.; Soga, I.; Tanaka, H.; Nakamura, E. Columnar Structure in Bulk Heterojunction in Solution-Processable Three-Layered P-I-N Organic Photovoltaic Devices Using Tetrabenzoporphyrin Precursor and Silylmethyl[60]fullerene. *J. Am. Chem. Soc.* **2009**, *131*, 16048–16050.
- (53) Masuo, S.; Sato, W.; Yamaguchi, Y.; Suzuki, M.; Nakayama, K.; Yamada, H. Evaluation of the Charge Transfer Efficiency of Organic Thin-Film Photovoltaic Devices Fabricated Using a Photoprecursor Approach. *Photochem. Photobiol. Sci.* **2015**, *14*, 883–890.
- (54) Liang, Y.; Xu, Z.; Xia, J.; Tsai, S.-T.; Wu, Y.; Li, G.; Ray, C.; Yu, L. For the Bright Future—Bulk Heterojunction Polymer Solar Cells with Power Conversion Efficiency of 7.4%. *Adv. Mater.* **2010**, *22*, E135–E138.
- (55) Kniepert, J.; Lange, I.; Heidbrink, J.; Kurpiers, J.; Brenner, T. J. K.; Koster, L. J. A.; Neher, D. Effect of Solvent Additive on Generation, Recombination, and Extraction in PTB7:PCBM Solar Cells: A Conclusive Experimental and Numerical Simulation Study. *J. Phys. Chem. C* **2015**, *119*, 8310–8320.
- (56) Collins, B. A.; Li, Z.; Tumbleston, J. R.; Gann, E.; McNeill, C. R.; Ade, H. Absolute Measurement of Domain Composition and Nanoscale Size Distribution Explains Performance in PTB7:PC71BM Solar Cells. *Adv. Energy Mater.* **2013**, *3*, 65–74.
- (57) Sánchez-Díaz, A.; Izquierdo, M.; Filippone, S.; Martin, N.; Palomares, E. The Origin of the High Voltage in DPM12/P3HT Organic Solar Cells. *Adv. Funct. Mater.* **2010**, *20*, 2695–2700.
- (58) Lu, L.; Chen, W.; Xu, T.; Yu, L. High-Performance Ternary Blend Polymer Solar Cells Involving Both Energy Transfer and Hole Relay Processes. *Nat. Commun.* **2015**, *6*, 7327.
- (59) Meng, H.; Sun, F.; Goldfinger, M. B.; Jaycox, G. D.; Li, Z.; Marshall, W. J.; Blackman, G. S. High-Performance, Stable Organic Thin-Film Field-Effect Transistors Based on Bis-5'-alkylthiophen-2'-yl-2,6-anthracene Semiconductors. *J. Am. Chem. Soc.* **2005**, *127*, 2406–2407.
- (60) Nakayama, K.; Ohashi, C.; Oikawa, Y.; Motoyama, T.; Yamada, H. Characterization and Field-Effect Transistor Performance of Printed Pentacene Films Prepared by Photoconversion of a Soluble Precursor. *J. Mater. Chem. C* **2013**, *1*, 6244–6251.
- (61) Burke, K. B.; Belcher, W. J.; Thomsen, L.; Watts, B.; McNeill, C. R.; Ade, H.; Dastoor, P. C. Role of Solvent Trapping Effects in Determining the Structure and Morphology of Ternary Blend Organic Devices. *Macromolecules* **2009**, *42*, 3098–3103.
- (62) Masuo, S.; Yoshikawa, H.; Asahi, T.; Masuhara, H.; Sato, T.; Jiang, D.-L.; Aida, T. Repetitive Contraction and Swelling Behavior of Gel-like Wire-Type Dendrimer Assemblies in Solution Layer by Photon Pressure of a Focused Near-Infrared Laser Beam. *J. Phys. Chem. B* **2002**, *106*, 905–909.
- (63) Masuo, S.; Yoshikawa, H.; Asahi, T.; Masuhara, H.; Sato, T.; Jiang, D.-L.; Aida, T. Fluorescent Doughnut-Like Assembling of Wire-Type Dendrimers Depending on Their Generation Numbers and Degrees of Polymerization. *J. Phys. Chem. B* **2001**, *105*, 2885–2889.
- (64) Latterini, L.; Blossey, R.; Hofkens, J.; Vanoppen, P.; De Schryver, F. C.; Rowan, A. E.; Nolte, R. J. M. Ring Formation in Evaporating Porphyrin Derivative Solutions. *Langmuir* **1999**, *15*, 3582–3588.
- (65) Herminghaus, S.; Jacobs, K.; Mecke, K.; Bischof, J.; Fery, A.; Ibn-Elhaj, M.; Schlagowski, S. Spinodal Dewetting in Liquid Crystal and Liquid Metal Films. *Science* **1998**, *282*, 916–919.
- (66) Hofkens, J.; Latterini, L.; Vanoppen, P.; Faes, H.; Jeuris, K.; De Feyter, S.; Kerimo, J.; Barbara, P. F.; De Schryver, F. C.; Rowan, A. E.; Nolte, R. J. M. Mesoscale Structure of Evaporated Porphyrin Thin Films: Porphyrin Wheel Formation. *J. Phys. Chem. B* **1997**, *101*, 10588–10598.
- (67) Schenning, A. P. H. J.; Benneker, F. B. G.; Geurts, H. P. M.; Liu, X. Y.; Nolte, R. J. M. Porphyrin Wheels. *J. Am. Chem. Soc.* **1996**, *118*, 8549–8552.
- (68) Tamai, Y.; Ohkita, H.; Benten, H.; Ito, S. Exciton Diffusion in Conjugated Polymers: From Fundamental Understanding to Improvement in Photovoltaic Conversion Efficiency. *J. Phys. Chem. Lett.* **2015**, *6*, 3417–3428.
- (69) Mikhnenko, O. V.; Blom, P. W. M.; Nguyen, T.-Q. Exciton Diffusion in Organic Semiconductors. *Energy Environ. Sci.* **2015**, *8*, 1867–1888.
- (70) Yamada, H.; Kawamura, E.; Sakamoto, S.; Yamashita, Y.; Okujima, T.; Uno, H.; Ono, N. Effective Photochemical Synthesis of an Air-Stable Anthracene-Based Organic Semiconductor from Its Diketone Precursor. *Tetrahedron Lett.* **2006**, *47*, 7501–7504.

# Direct Observation of Multiphoton Emission Enhancement from a Single Quantum Dot Using AFM Manipulation of a Cubic Gold Nanoparticle

Sadahiro Masuo,<sup>\*,†</sup> Keisuke Kanetaka,<sup>†</sup> Ryota Sato,<sup>‡</sup> and Toshiharu Teranishi<sup>‡</sup>

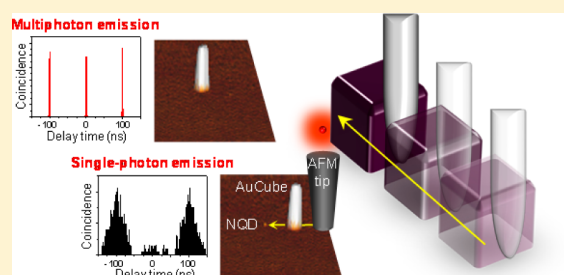
<sup>†</sup>Department of Applied Chemistry for Environment, Kwansei Gakuin University, 2-1 Gakuen, Sanda, Hyogo 669-1337, Japan

<sup>‡</sup>Institute for Chemical Research, Kyoto University, Gokasho, Uji, Kyoto 661-0011, Japan

## Supporting Information

**ABSTRACT:** The change of photon statistics in the fluorescence of a single CdSe/ZnS core/shell colloidal nanocrystal quantum dot (NQD) accompanying the atomic force microscopy (AFM) manipulation of a cubic Au nanoparticle (AuCube) was investigated to elucidate the effect of plasmonic nanostructures on the multiexciton dynamics of the NQD. Upon coupling to an AuCube of a well-defined size and shape, we directly observed the conversion of a single-photon emission from an individual NQD to a multiphoton emission, and this was accompanied by an increase in fluorescence intensity and a reduction in fluorescence lifetime. The multiphoton emission then returned to a single-photon emission upon separating the AuCube from the single NQD. The efficiency of the multiphoton emission was enhanced 6.9 times through the use of the AuCube. The enhancement of the multiphoton emission was attributable mainly to the augmentation of the biexciton emission rate. These results provide evidence that quantum dot photon statistics can be manipulated by plasmonic nanostructures, and NQD-plasmonic nanostructure systems can be desirable for many technological applications.

**KEYWORDS:** colloidal quantum dot, plasmonics, single photon, multiphoton, AFM manipulation, metal nanoparticle



Colloidal nanocrystal quantum dots (NQDs) are a unique class of tunable, dispersible fluorophores that are of great interest for applications in a wide range of optoelectronic devices.<sup>1–9</sup> An important and interesting exciton dynamics is the simultaneous existence of multiple excitons (MX) in a single NQD. MX can be generated upon the absorption of multiple photons that each have energy equal to the NQD band gap or upon the absorption of a single photon bearing at least twice the band gap energy.<sup>10–14</sup> The latter process is called multiple exciton generation (MEG). MEG, and the subsequent extraction of multiple carriers, represents a promising route to ultimately improve the power conversion efficiency of NQD-based photovoltaic cells.<sup>15–19</sup> Furthermore, the cascade emission from MX, that is, multiphoton emission from triexciton (TX) and biexciton (BX) states, is valued for its production of correlated photon pairs (also called entangled photons) to realize quantum information and communication technologies.<sup>20</sup>

However, when MX are generated in a single NQD, they can decay by nonradiative Auger recombination (AR), that is, the MX are reduced to a single exciton (SX) by AR<sup>21</sup> and are wastefully consumed. AR also causes the fluorescence blinking behavior that is known as Auger ionization.<sup>22</sup> Therefore, suppression of AR has been extensively studied for efficient use of the excitons.<sup>23–26</sup> On the other hand, AR facilitates single-

photon emission for the single NQD, that is, photon antibunching in the NQD fluorescence, because the surviving SX can emit a single photon even when MX are produced in an NQD.<sup>27–30</sup> The single-photon emission is also an important and interesting optical property of the single NQD for quantum information and communication technologies. Therefore, it is very important to control the MX dynamics for applications employing NQDs.

We previously reported that MX dynamics, that is, the probability of a multiphoton emission from MX and a single-photon emission from SX, can be modified through interactions of the NQD with metallic nanostructures.<sup>31–33</sup> By applying a photon-correlation measurement to a single CdSe/ZnS core/shell NQD coupled to silver nanoparticles (AgNPs), we revealed that the quantum yield (QY) of BX emission increased when the fluorescence lifetime was shortened to the instrument response function (0.4 ns). To explain this result, we proposed that, when BX are generated in a single NQD, BX emission and AR are competitive processes. A single NQD itself emits a single-photon even when BX are generated because the rate of AR is much faster than that of BX emission. The time scale of AR depends on the volume of the NQD. In the case of our

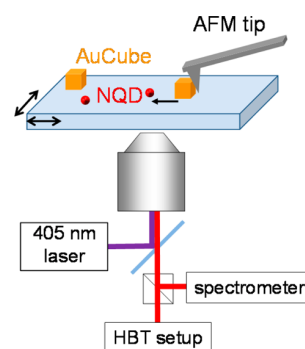
**Received:** September 4, 2015

**Published:** December 8, 2015

NQD (core radius: 2.6 nm), AR occurs within 100 ps.<sup>21</sup> In contrast, for single NQDs coupled with AgNPs, an enhanced emission of the BX occurs, and the BX emission can be emitted before AR. Therefore, a single NQD with a short lifetime (i.e., the rate of BX emission is faster than that of AR) exhibits an increase in the QY of BX emission, which also represents a decrease in the probability of photon antibunching.<sup>31,32</sup> These results indicate that the BX emission can be improved by the interaction with AgNPs; as a result, AR can be suppressed.

Recently, a similar enhancement of multiphoton emission was reported using combinations of CdSe/CdS-random gold<sup>34</sup> and silver<sup>35,36</sup> films, a CdSe/CdS-gold gap bar antenna structure,<sup>37</sup> a CdSe/ZnS-rough gold film,<sup>38</sup> and a CdSe/ZnS-plasmonic cavity, which consisted of a silver nanocube and a gold film.<sup>39</sup> These reports have clearly demonstrated an increased probability of multiphoton emission, that is, BX emission, from a single NQD via an interaction with metallic nanostructures. Two possibilities have been discussed to describe the mechanism behind these increases in the BX emission. One mechanism involves the enhancement of the BX emission rate by the metallic nanostructure, which is similar to our previous results mentioned above. Another is the quenching of SX emission by the metallic nanostructure, that is, a decrease in the QY of SX emission rather than an actual increase in the QY of BX emission<sup>36,40,41</sup> Thus, the interplay of NQDs and metallic nanostructures, particularly the influence of metallic nanostructures on the MX dynamics of the NQD, is not fully understood. Furthermore, the critical problem of these reports, including ours, is that the possibility of measuring a cluster of the NQDs cannot be excluded. When single NQDs are deposited onto a glass substrate or metallic film, then the individual NQDs tend to form clusters. Even when the NQDs are dispersed in a polymer thin film, such as poly(methyl methacrylate), a few tens of percents of the NQDs form clusters.<sup>39</sup> If a single cluster is measured in substitution of a single NQD, then the observed emission behavior can appear to be an enhancement of the multiphoton emission. To exclude this possibility and to understand the interaction between single NQDs and metallic nanostructures, one would have to directly observe changes in the emission behavior of a single NQD that accompany the interaction with a metallic nanostructure. To achieve this direct observation, atomic force microscopy (AFM) is the ideal technique to manipulate the metallic nanostructure. Indeed, changes in the emission behaviors of a single fluorescence sphere,<sup>42</sup> nitrogen vacancy center,<sup>43,44</sup> and NQD<sup>45</sup> approaching single metallic nanoparticles by AFM manipulation have clearly been observed in situ. However, photon statistics in the fluorescence from a single NQD utilizing AFM manipulation have never been reported.

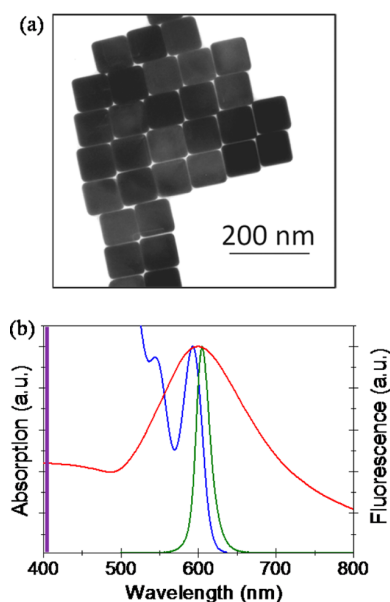
To elucidate the possibility of controlling MX dynamics using a metallic nanostructure, that is, the MX-metallic nanostructure interaction, AFM manipulation was employed in this study (Figure 1). The change in the fluorescence photon statistics of a single NQD by an approaching cubic gold nanoparticle (AuCube) was directly observed; in other words, the single-photon emission of an individual NQD was converted to multiphoton emission by the interaction with a metallic nanostructure. This result directly indicates that the MX dynamics can be controlled by interactions with metallic nanostructures.



**Figure 1.** Schematic of the experimental setup for AFM manipulation of a single AuCube.

## RESULTS AND DISCUSSION

A transmission electron microscopy (TEM) image of the AuCube is shown in Figure 2a. Monodispersed cubic Au

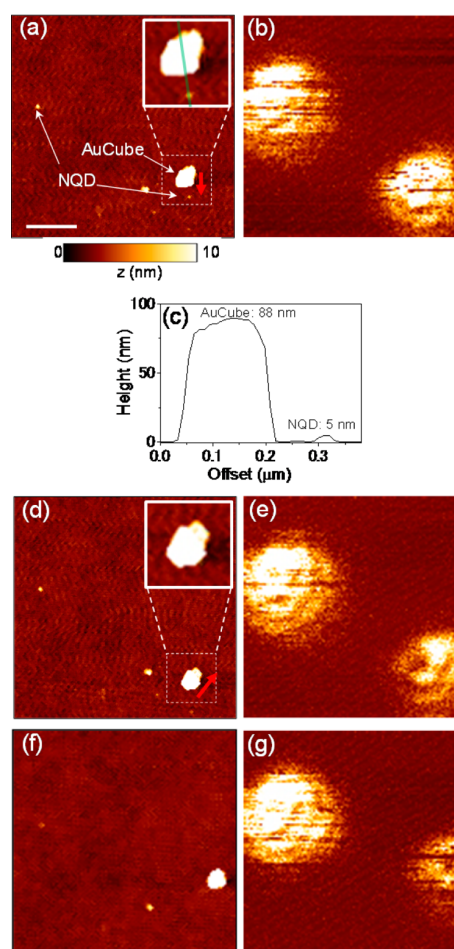


**Figure 2.** (a) Transmission electron microscopy image of monodispersed cubic Au nanoparticles (AuCubes). (b) An extinction spectrum of the AuCube colloidal solution (red), absorption (blue) and fluorescence (green) spectra of a CdSe/ZnS QD colloidal solution. The wavelength of the excitation laser is marked as a purple vertical line.

nanoparticles (AuCube) of a well-defined size and shape were confirmed by this image. The size of the AuCube was estimated as  $87 \pm 2.4$  nm from the TEM image. An extinction spectrum of the AuCube-dispersed aqueous solution is shown in Figure 2b with the absorption and fluorescence spectra of NQD in toluene. The localized surface plasmon resonance (LSPR) band of the AuCube overlaps with both the absorption and fluorescence spectra of the NQD. This indicates that both excitation and relaxation processes of the NQD can be enhanced with the AuCube by with choice of excitation wavelength. It is well-known that the fluorophore–metallic nanostructure interaction strongly depends on the spectral overlap and the distance between a fluorophore and a metallic nanostructure. When the absorption of the fluorophore

overlaps with the LSPR band, the excitation rate of the fluorophore can be augmented by the electric field of the LSPR generated by the excitation light. Similarly, when the fluorescence spectrum of the fluorophore overlaps with the LSPR band, this relaxation process can be enhanced. The enhanced relaxation process is interpreted as the resonant energy transfer from the excited state of the fluorophore to the metallic nanostructure through dipole–dipole interactions; therefore, the LSPR can be generated on the metallic nanostructure by energy transfer and then decays radiatively and nonradiatively. The fluorescence lifetime ( $\tau$ ) and the  $QY$  ( $\Phi$ ) of the “fluorophore–metallic nanostructure” system can be expressed as  $\tau = 1/(k_{r0} + k_{nr0} + k_{rp} + k_{nrp})$  and  $\Phi = (k_{r0} + k_{rp})/(k_{r0} + k_{nr0} + k_{rp} + k_{nrp})$ , where  $k_{r0}$  and  $k_{nr0}$  are the intrinsic radiative and nonradiative decay rates of the fluorophore, respectively, and  $k_{rp}$  and  $k_{nrp}$  are the radiative and nonradiative decay rates of the LSPR generated on a metallic nanostructure, respectively. When the distance between the fluorophore and the metallic nanostructure is closed, then electron transfer from the excited fluorophore to the metallic nanostructure should be considered. Under our experimental conditions, the LSPR could not be efficiently generated by the excitation laser (405 nm; Figure 2b). Therefore, the enhancement of the relaxation process was considered. The advantage of the well-defined AuCube is that there is little variation of the LSPR band in each AuCube; hence, we can simply consider the mechanism of the NQD–metallic nanostructure interaction.

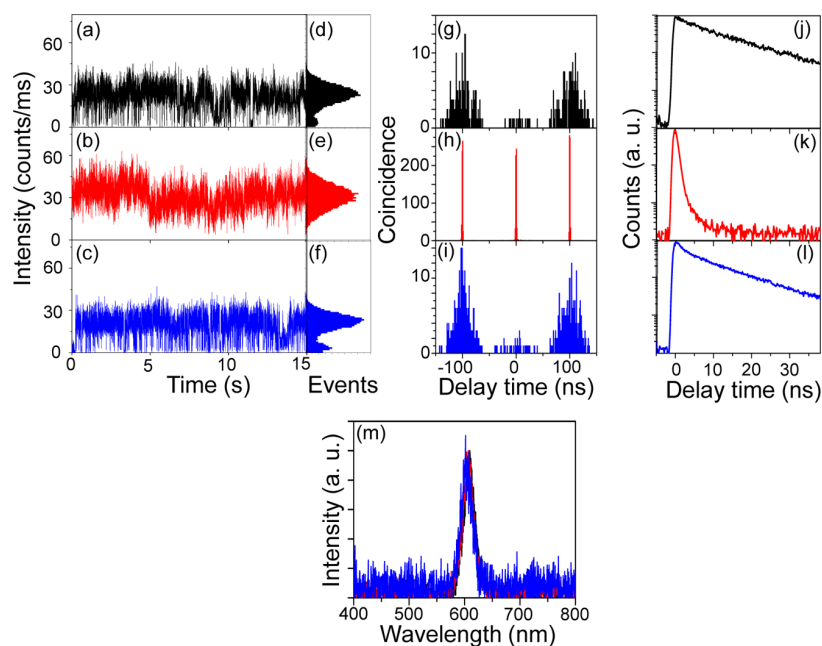
Figures 3 and 4 show the representative results of AFM manipulation of an AuCube and the accompanying emission behavior that was detected from a single NQD. In the AFM images, a big white object and small white dots correspond to a single AuCube and individual NQDs, respectively. The AuCube does not appear square-shaped because the end of the AFM tip was broken during manipulation of another AuCube, which led to the large radius of curvature for the probe. When the AFM image of an AuCube was observed by an AFM tip with a sharper radius of curvature, then the square shape of the AuCube was observed (see the Supporting Information, SI). The cross-section of a single NQD and a single AuCube from the expanded view inset in Figure 3a is shown in Figure 3c. The heights of the AuCube (88 nm) and NQD (5 nm) were in good agreement with the expected values. The center-to-center distance between the NQD and the AuCube was estimated to be 185 nm. The larger width of the AuCube (160 nm) compared to its height (88 nm) was due to the large curvature of the AFM tip. In the fluorescence images, the signals from individual NQDs were collected from the same NQD positions shown in the AFM image. The blank lines observed in the fluorescence images of the single NQDs are attributable to off-periods arising from fluorescence blinking. The AuCube was then pushed in the direction of the red arrow (Figure 3a) and approached the single NQD. After moving the AuCube near the NQD, the single NQD could not be visualized in the AFM image (Figure 3d). To estimate the center-to-center distance between the NQD and AuCube, we assumed that the single NQDs were fixed before and after the manipulation of the AuCube, and the position of another single NQD was used as the reference point. By this way, the center-to-center distance was estimated as 5 nm, indicating that the NQD physically overlapped (i.e., on the top of) with the AuCube or might be attached to the side of the AuCube. In the fluorescence image taken after manipulation (Figure 3e), the blank lines, which are associated with the blinking of a single NQD, disappeared.



**Figure 3.** AFM images (a, d, f) and fluorescence images (b, e, g) of the NQD–AuCube system before AFM manipulation of an AuCube (a, b), after AFM manipulation (d, e), and after the AuCube was pushed away from the NQD (f, g). (c) Cross sections of the AuCube and the NQD corresponding to the green line in the inset of (a). In (a) and (d), an AuCube was pushed in the direction indicated by the red arrows. The scale bar in image (a) represents 500 nm.

Subsequently, the AuCube was separated from the single NQD by pushing it in the direction of the arrow to demonstrate that the changes in the fluorescence were reversible. In the AFM image after the AuCube was pushed away (Figure 3f), the single NQD was not visualized, and the position of the fluorescence image of the NQD moved to the upper right (Figure 3g). These observations indicated that the NQD also moved when the AuCube was pushed away. However, it was assumed that the new position of the NQD with respect to the AuCube was of sufficient distance to prevent strong interactions (vide infra). In the fluorescence image, the characteristic blank lines due to the blinking reappeared.

The fluorescence behavior of the single NQD accompanying the above AFM manipulation of the AuCube is summarized in Figure 4. In this measurement, the polarization of the incident laser was aligned vertically in the image. Before moving the AuCube near the NQD, the time trace of the fluorescence intensity (Figure 4a) displayed the well-known fluorescence blinking behavior with distinct on/off periods, which resulted in a bimodal distribution for the corresponding count rate histogram (Figure 4d). The off-state, which is also called the



**Figure 4.** Time traces of fluorescence intensity (a–c), corresponding count rate histograms (d–f), photon correlation histograms (g–i), fluorescence decay curves (j–l), and fluorescence spectra (m) detected from a single NQD before the approach of the AuCube (a, d, g, j, and black line in m) after the approach of the AuCube (b, e, h, k, and red line in m), and after the AuCube was pushed away (c, f, i, l, and blue line in m).

dark-state or the gray-state, results from the quenching of the exciton by the charged state of a NQD that was previously ionized.<sup>46</sup> The quenching process leads to the bimodal distribution in the fluorescence intensity and the multi-exponential fluorescence decay. However, in the case of the single NQD measured here, the quenching was not especially high, and the decay curve (shown in Figure 4j) was well fitted using a single exponential function with a lifetime of 29.6 ns. The maximum fluorescence count of the single NQD was estimated as 47 counts/ms from Figure 4a. In the photon correlation histogram shown in Figure 4g, the contribution of the center peak at a delay time of 0 ns was lower than the other peaks at delay times  $\pm 100$  ns. In this work, the second-order correlation function,  $g^{(2)}(0)$ , was defined as the ratio of the number of detection events at the center peak to the average number of detection events at the other peaks. The value of  $g^{(2)}(0)$  indicates the probability of a single-photon emission, and this probability increases when  $g^{(2)}(0)$  is close to zero. It is known that the  $g^{(2)}(0)$  value corresponds to the efficiency of BX emission,  $\Phi_{\text{BX}}/\Phi_{\text{SX}}$  ( $\Phi_{\text{BX}}$  and  $\Phi_{\text{SX}}$  are QYs of the BX and SX, respectively), at low excitation power, such as with our excitation conditions (the average NQD exciton occupancy  $\langle N \rangle \ll 1$ ).<sup>36,37</sup> The  $g^{(2)}(0)$  values were calculated to be 0.14 for Figure 4g, indicating that the individual NQD exhibited single-photon emission, that is, photon antibunching. This fluorescence behavior is characteristic of the single NQD itself and was dramatically changed by interacting with the AuCube.

The fluorescence behavior of the single NQD in proximity of the AuCube is shown in Figure 4b,e,h,k,m. By maneuvering the AuCube close to the single NQD, a reduction of the off-states was observed in the time trace of the fluorescence intensity (Figure 4b). In the count rate histogram (Figure 4e), the reduction of the off-state can be seen in the reduction of the off peak in the bimodal distribution. The maximum fluorescence count of the single NQD increased from 47 to 60 counts/ms.

In the photon correlation histogram shown in Figure 4h, the contribution of the center peak increased dramatically, and the  $g^{(2)}(0)$  values increased to 0.97. This result indicates that the efficiency of the BX emission from the single NQD was  $6.9\times$  higher than that of the single NQD before approaching the AuCube. In Figure 4k, the fluorescence was decayed rapidly, and the two lifetimes of 0.4 ns (99.8%) and 2.5 ns (0.2%) were obtained by fitting the decay curve with a two exponential function. As the lifetime of 0.4 ns is the same as the instrument response function (IRF), the actual lifetime is probably shorter. Therefore, the lifetime was at least 74 times shorter than that of the isolated uncoupled NQD. In Figure 4m, no clear change in the fluorescence spectra was observed by moving the AuCube to near the single NQD. It was reported that the BX emission spectrum was about 15–20 meV red-shifted compared to the SX emission spectrum.<sup>47,48</sup> This energy difference corresponds to 4 to 6 nm red-shift of the BX emission spectrum for the NQD shown in Figure 4m. The full width at half-maximum (fwhm) value of the NQD spectrum before moving the AuCube near the NQD was 21 nm, which was much larger than the spectral shift. Therefore, it is difficult to distinguish the BX emission spectrum from the SX emission spectrum at room temperature. Because neither the emission nor the background scattering from the AuCube were observed in Figure 4m, the increase in the  $g^{(2)}(0)$  value and the disappearance of the off-state in the time trace were attributed to the change in the fluorescence behavior of the NQD. By placing the AuCube sufficiently close to the single NQD, the fluorescence intensity increased  $1.3\times$ , the efficiency of the BX emission increased  $6.9\times$ , and the fluorescence lifetime shortened. This fluorescence behavior is the same as what we reported for AgNPs,<sup>31,32</sup> and the increase in the efficiency of the BX emission is also the same as has been noted in prior reports.<sup>34–39,45</sup> The importance of the above results is that the change in the

fluorescence behavior was directly observed by manipulating the distance between an AuCube and a single NQD.

The fluorescence behavior of the single NQD after the AuCube was pushed away is shown in Figure 4c,f,i,l,m. It is clear that the fluorescence intensity, photon antibunching behavior, and decay curve were returned to those detected from the NQD before the approach of the AuCube, i.e., a maximum fluorescence count of 47 counts/ms, the reappearance of the off-state, a  $g^{(2)}(0)$  of 0.13, and fluorescence lifetimes of 1.8 ns (23%) and 22.0 ns (77%). The increased off-peak in the count rate histogram, the reduced lifetime (22.0 ns) when compared with the value obtained before the interaction with the AuCube (29.6 ns), and the appearance of an additional short 1.8 ns lifetime may be attributed to changes in the local environment around the NQD. This could indicate that the surface of the NQD was damaged by contact with the AuCube, the NQD was still weakly interacting with the AuCube, or both. The above results directly demonstrate that the efficiency of the BX emission was modified by a shortening of the fluorescence lifetime that resulted from interactions between the AuCube and the single NQD. Although we only show one example here, reproducible results were obtained and can be found in SI.

As mentioned above, the modification of the fluorescence behavior is likely a consequence of an enhancement in the multiexciton relaxation process because an improvement in the excitation process can be eliminated under our excitation conditions. As potential mechanisms for the increased efficiency of BX emission, both an enhancement of the emission rate from the BX state<sup>31,32,34,35,37–39</sup> and a drastic reduction in the  $\Phi_{SX}$  when compared with the BX,<sup>36,40,41</sup> predominantly by the quenching of the SX, have been reported. In the following, we estimate the AuCube-induced enhancement factors of the radiative and nonradiative (quenching) exciton processes.

By taking into account the enrichments of both excitation and relaxation processes of the NQD, the fluorescence enhancement factor ( $\eta_{PL}$ ) is written as

$$\eta_{PL} = \frac{I_p}{I_0} = \frac{\gamma_{exc,p} \Phi_p}{\gamma_{exc,0} \Phi_0} = \eta_{exc} \frac{\Phi_p}{\Phi_0} \quad (1)$$

where  $I$ ,  $\gamma_{exc}$ , and  $\Phi$  represent the fluorescence intensity, the excitation rate, and the fluorescence QY, respectively; the subscript 0 and p refer to the NQD without AuCube and with AuCube, respectively; and  $\eta_{exc} = \gamma_{exc,p}/\gamma_{exc,0}$  is the enhancement factor for the excitation rate. The enhancement for the QY is written as

$$\frac{\Phi_p}{\Phi_0} = \frac{k_{rp} k_{r0} + k_{nr0}}{k_{r0} k_{rp} + k_{nrp}} = \eta_r \frac{\tau_p}{\tau_0} \quad (2)$$

where  $k_r$ ,  $k_{nr}$ , and  $\tau$  represent radiative and nonradiative decay rates and the fluorescence lifetime, respectively, and  $\eta_r = k_{rp}/k_{r0}$  is the enhancement factor for the radiative decay rate. Under our excitation conditions, an enhancement of the excitation rate can probably be eliminated. Hence,  $\eta_{exc}$  should be unity in eq 1. From eqs 1 and 2, the  $\eta_r$  is written as

$$\eta_r \approx \frac{I_p \tau_0}{I_0 \tau_p} \quad (3)$$

It is clear that  $\tau_0/\tau_p = \Phi_0 \eta_r + (1 - \Phi_0) \eta_{nr}$ , where  $\eta_{nr} = k_{nrp}/k_{nr0}$  is the enhancement factor for the nonradiative decay rate. Therefore,  $\eta_{nr}$  can be written as

$$\eta_{nr} \approx \frac{(\tau_0/\tau_p) - \Phi_0 \eta_r}{1 - \Phi_0} \quad (4)$$

and  $\Phi_0$  strongly depends on each individual NQD. When we used  $\Phi_0 = 0.5$ , as well as  $I_0 = 47$  counts/ms,  $I_p = 60$  counts/ms,  $\tau_0 = 29.6$  ns, and  $\tau_p = 0.4$  ns, then the enhancement factors  $\eta_r = 95$  and  $\eta_{nr} = 54$  were obtained for a single NQD that interacted with an AuCube. As mentioned above,  $\tau_p = 0.4$  ns was estimated as the IRF because the decay curve was limited by the IRF. Hence,  $\tau_p$  is possibly much shorter than 0.4 ns. In this case, the enhancement factors  $\eta_r$  and  $\eta_{nr}$  become larger than 95 and 54, respectively. In addition to the above results, we have four more reproducible results about the fluorescence behavior of a single NQD accompanying the AFM manipulation of an AuCube. The observed fluorescence behavior, that is, the fluorescence intensity, fitting parameters of decay curves, and  $g^{(2)}(0)$  before and after the approach of the AuCube, and calculated  $\eta_r$  and  $\eta_{nr}$  about all five NQDs are summarized in Table S1 of SI. Using all results,  $\eta_r = 103 \pm 25$  and  $\eta_{nr} = 39 \pm 18$  were obtained. The calculated values indicate that both the enhancement of the BX emission rate and the quenching of the SX cause an increase in the efficiency of the BX emission upon the interaction of the NQD with the AuCube. In our results, the fluorescence intensity increased with the efficiency of the BX emission because the emission rate was enhanced by the AuCube, which indicates that the contribution of the enhanced emission rate is greater than the quenching of the SX. This result is quite different from an increase in BX emission resulting from the quenching of SX,<sup>36,40,41</sup> in which the fluorescence intensity would be much lower than that of the isolated uncoupled NQD. Our conclusion is also quite reasonable from the point of view of a reduction in off-states, as observed in the fluorescence time traces. As described above, the off-states were caused by the quenching of SX by the charged NQD which was generated by trapping of an electron of SX and also the AR-assisted ionization (Auger ionization).<sup>22,46</sup> In our case, the BX emission was enhanced by the AuCube and took place before AR could occur. In addition to the enhancement of the BX emission, the quenching of SX occurred, which suppressed the blinking.<sup>40,49,50</sup> Therefore, the off-states in the NQD fluorescence were reduced by the combination of the BX emission enhancement and the quenching of SX. The present results clearly demonstrate that the photon statistics and count rate of the fluorescence from a single NQD can be controlled by modifying the exciton relaxation process using metallic nanostructures.

## CONCLUSIONS

We directly demonstrated that the fluorescence behavior of a single NQD can be changed by proximate interactions with an AuCube. By manipulating the AuCube with an AFM manipulation, single-photon emission of the individual NQD was changed to multiphoton emission, and this was accompanied by an increase in the fluorescence intensity and a reduction in the fluorescence lifetime. The fluorescence behavior was then returned to its original state by separating the AuCube from the single NQD. Therefore, these results give direct evidence that single-photon and multiphoton NQD emissions can be modulated by metallic nanostructures. From an estimation of the enhancement factors for radiative and nonradiative (quenching) processes, which were based on the experimental data, the contribution of an increased BX

emission rate was greater than that associated with quenching. This in turn led to a BX emission with a higher fluorescence count when the AuCube was observed near the single NQD. It is known that the fluorophore–plasmonic nanostructure interaction strongly depends on the distance between the fluorophore and the plasmonic nanostructure. If it is possible to observe the fluorescence behavior depending on the distance, more knowledge can be obtained. To achieve the observation, the distance has to be controlled in a nanometer-scale precision. In the case of the AFM manipulation technique, however, the distance control was difficult. Therefore, we demonstrated only the changes in the fluorescence behavior accompanying the AFM manipulation. The present findings are important to understand NQD–plasmonic nanostructure interactions, particularly the control of MX dynamics for their efficient use.

## METHODS

Commercially available colloidal CdSe/ZnS core/shell NQD (average core radius: 2.6 nm; maximum fluorescence wavelength: 610 nm) were purchased from Invitrogen. Mono-disperse cubic Au nanoparticles (AuCube) of a well-defined size and shape were synthesized by a seed-mediated method, as reported in the literature.<sup>51</sup> The sample was prepared by spin-coating an aqueous AuCube dispersion and then a toluene solution of colloidal CdSe/ZnS NQDs onto a clean glass coverslip.

In situ manipulation of an AuCube and the detection of the fluorescence from a single NQD was realized by a home-built AFM (NanoWizard II, JPK instruments)/inverted confocal microscope (IX-71, Olympus) system (Figure 1). In addition to the three closed-loop piezo-driven axes of the AFM, a two axis, closed-loop, piezo-driven sample stage was employed. A linearly polarized pulsed laser beam (405 nm, 10.0 MHz, 90 ps fwhm, PicoQuant) with a power of 57 W/cm<sup>2</sup> was used as an excitation light source with the inverted microscope, and it was focused to a diffraction-limited spot on the sample by an objective lens (NA 1.4, Olympus). The number of excitons generated in a single NQD by a single excitation pulse was estimated to be 0.10 by taking into account the absorption cross-section of the NQD and the number of photons in a single excitation pulse. The fluorescence photons from the NQD were collected by the same objective lens and passed through a confocal pinhole and a long-pass filter to remove the excitation laser. Subsequently, half of the photons were detected by a spectrograph (SpectraPro2358, Acton Research Corporation) with a cooled CCD camera (PIXIS400B, Princeton Instruments). The remaining half of the photons were passed through a band-pass filter and were detected by two avalanche single-photon counting modules (SPCM-AQR-14, PerkinElmer) for Hanbury-Brown and Twiss-type photon correlation (HBT) and lifetime measurements. The time-resolution of the lifetime measurement (instrument response function: IRF) was approximately 0.4 ns. Details can be found in the SI.

The manipulation of a single AuCube and the detection of the fluorescence behavior of a single NQD were performed by the following procedure. Initially, a silicon AFM tip was coupled to the center of a focused excitation laser by the piezo of the AFM. Then, AFM topography and fluorescence images of the sample were measured simultaneously by scanning the sample stage. By choosing a fluorescence spot corresponding to the single NQD, the fluorescence behavior of the single NQD

was measured before AFM manipulation. A single AuCube was then moved to the individual NQD using the AFM tip and translating the sample stage. The AFM topography image was obtained, and the fluorescence behavior of the single NQD coupled to the AuCube was measured. Then, the AuCube was separated from the single NQD, and the fluorescence behavior of the single NQD was measured again. AFM topography measurement and AFM manipulation of the AuCube were performed in tapping and contact modes, respectively. All measurements were performed at room temperature under ambient conditions.

## ASSOCIATED CONTENT

### Supporting Information

The Supporting Information is available free of charge on the ACS Publications website at DOI: 10.1021/acsp Photonics.5b00496.

Instrumental setup, AFM image of AuCube and scanning electron microscopy images of an AFM tip, fluorescence behavior of a single NQD accompanying the AFM manipulation of an AuCube (PDF).

## AUTHOR INFORMATION

### Corresponding Author

\*E-mail: masuo@kwansei.ac.jp.

### Notes

The authors declare no competing financial interest.

## ACKNOWLEDGMENTS

This work was partly supported by a Grant-in-Aid for Scientific Research (No. 26390023) from the Japan Society for the Promotion of Science (JSPS) and a Grant-in-Aid for Scientific Research on Innovation Areas “Photosynergetics” (No. 26107005) from MEXT, Japan.

## ABBREVIATIONS

colloidal nanocrystal quantum dot:NQD; atomic force microscopy:AFM; cubic gold nanoparticle:AuCube; multiple excitons:MX; triexciton:TX; biexciton:BX; single exciton:SX; multiple exciton generation:MEG; Auger recombination:AR; silver nanoparticles:AgNPs; quantum yield:QY; instrument response function:IRF; transmission electron microscopy:TEM; localized surface plasmon resonance:LSPR; Hanbury-Brown and Twiss-type photon correlation:HBT

## REFERENCES

- (1) Klein, D. L.; Roth, R.; Lim, A. K. L.; Alivisatos, A. P.; McEuen, P. L. A single-electron transistor made from a cadmium selenide nanocrystal. *Nature* **1997**, *389*, 699–701.
- (2) Klimov, V. I.; Mikhailovsky, A. A.; Xu, S.; Malko, A.; Hollingsworth, J. A.; Leatherdale, C. A.; Eisler, H.; Bawendi, M. G. Optical gain and stimulated emission in nanocrystal quantum dots. *Science* **2000**, *290*, 314–317.
- (3) Coe, S.; Woo, W. K.; Bawendi, M.; Bulovic, V. Electroluminescence from single monolayers of nanocrystals in molecular organic devices. *Nature* **2002**, *420*, 800–803.
- (4) Klimov, V. I. Mechanisms for photogeneration and recombination of multiexcitons in semiconductor nanocrystals: implications for lasing and solar energy conversion. *J. Phys. Chem. B* **2006**, *110*, 16827–16845.
- (5) Robel, I.; Subramanian, V.; Kuno, M.; Kamat, P. V. Quantum dot solar cells. harvesting light energy with CdSe nanocrystals molecularly

linked to mesoscopic TiO<sub>2</sub> films. *J. Am. Chem. Soc.* **2006**, *128*, 2385–2393.

(6) Klimov, V. I.; Ivanov, S. A.; Nanda, J.; Achermann, M.; Bezel, I.; McGuire, J. A.; Piryatinski, A. Single-exciton optical gain in semiconductor nanocrystals. *Nature* **2007**, *447*, 441–446.

(7) Kamat, P. V. Quantum Dot Solar Cells. Semiconductor Nanocrystals as Light Harvesters. *J. Phys. Chem. C* **2008**, *112*, 18737–18753.

(8) Qian, L.; Zheng, Y.; Xue, J. G.; Holloway, P. H. Stable and efficient quantum-dot light-emitting diodes based on solution-processed multilayer structures. *Nat. Photonics* **2011**, *5*, 543–548.

(9) Bourzac, K. Quantum dots go on display. *Nature* **2013**, *493*, 283.

(10) Schaller, R. D.; Klimov, V. I. High efficiency carrier multiplication in PbSe nanocrystals: implications for solar energy conversion. *Phys. Rev. Lett.* **2004**, *92*, 186601.

(11) Ellingson, R. J.; Beard, M. C.; Johnson, J. C.; Yu, P.; Micic, O. I.; Nozik, A. J.; Shabaev, A.; Efros, A. L. Highly efficient multiple exciton generation in colloidal PbSe and PbS quantum dots. *Nano Lett.* **2005**, *5*, 865–871.

(12) Schaller, R. D.; Agranovich, V. M.; Klimov, V. I. High-efficiency carrier multiplication through direct photogeneration of multi-excitons via virtual single-exciton states. *Nat. Phys.* **2005**, *1*, 189–194.

(13) Murphy, J. E.; Beard, M. C.; Norman, A. G.; Ahrenkiel, S. P.; Johnson, J. C.; Yu, P. R.; Micic, O. I.; Ellingson, R. J.; Nozik, A. J. PbTe colloidal nanocrystals: Synthesis, characterization, and multiple exciton generation. *J. Am. Chem. Soc.* **2006**, *128*, 3241–3247.

(14) Beard, M. C.; Knutsen, K. P.; Yu, P.; Luther, J. M.; Song, Q.; Metzger, W. K.; Ellingson, R. J.; Nozik, A. J. Multiple Exciton Generation in Colloidal Silicon Nanocrystals. *Nano Lett.* **2007**, *7*, 2506–2512.

(15) Nozik, A. J. Quantum dot solar cells. *Phys. E* **2002**, *14*, 115–120.

(16) Law, M.; Beard, M. C.; Choi, S.; Luther, J. M.; Hanna, M. C.; Nozik, A. J. Determining the Internal Quantum Efficiency of PbSe Nanocrystal Solar Cells with the Aid of an Optical Model. *Nano Lett.* **2008**, *8*, 3904–3910.

(17) Pattantyus-Abraham, A. G.; Kramer, I. J.; Barkhouse, A. R.; Wang, X. H.; Konstantatos, G.; Debnath, R.; Levina, L.; Raabe, I.; Nazeeruddin, M. K.; Gratzel, M.; Sargent, E. H. Depleted-Heterojunction Colloidal Quantum Dot Solar Cells. *ACS Nano* **2010**, *4*, 3374–3380.

(18) Semonin, O. E.; Luther, J. M.; Choi, S.; Chen, H. Y.; Gao, J. B.; Nozik, A. J.; Beard, M. C. Peak External Photocurrent Quantum Efficiency Exceeding 100% via MEG in a Quantum Dot Solar Cell. *Science* **2011**, *334*, 1530–1533.

(19) Tang, J. A.; Sargent, E. H. Infrared Colloidal Quantum Dots for Photovoltaics: Fundamentals and Recent Progress. *Adv. Mater.* **2011**, *23*, 12–29.

(20) Benson, O.; Santori, C.; Pelton, M.; Yamamoto, Y. Regulated and Entangled Photons from a Single Quantum Dot. *Phys. Rev. Lett.* **2000**, *84*, 2513.

(21) Klimov, V. V.; Mikhailovsky, A. A.; McBranch, D. W.; Leatherdale, C. A.; Bawendi, M. G. Quantization of multiparticle Auger rates in semiconductor quantum dots. *Science* **2000**, *287*, 1011–1013.

(22) Efros, A. L.; Rosen, M. Random Telegraph Signal in the Photoluminescence Intensity of a Single Quantum Dot. *Phys. Rev. Lett.* **1997**, *78*, 1110.

(23) Htoon, H.; Malko, A. V.; Bussian, D.; Vela, J.; Chen, Y.; Hollingsworth, J. A.; Klimov, V. I. Highly emissive multiexcitons in steady-state photoluminescence of individual "giant" CdSe/CdS Core/Shell nanocrystals. *Nano Lett.* **2010**, *10*, 2401–2407.

(24) Osovsky, R.; Cheski, D.; Kloper, V.; Sashchiuk, A.; Kroner, M.; Lifshitz, E. Continuous-wave pumping of multiexciton bands in the photoluminescence spectrum of a single CdTe-CdSe core-shell colloidal quantum dot. *Phys. Rev. Lett.* **2009**, *102*, 197401.

(25) Wang, X. Y.; Ren, X. F.; Kahen, K.; Hahn, M. A.; Rajeswaran, M.; Maccagnano-Zacher, S.; Silcox, J.; Cragg, G. E.; Efros, A. L.; Krauss, T. D. Non-blinking semiconductor nanocrystals. *Nature* **2009**, *459*, 686–689.

(26) Garcia-Santamaria, F.; Chen, Y.; Vela, J.; Schaller, R. D.; Hollingsworth, J. A.; Klimov, V. I. Suppressed Auger recombination in "giant" nanocrystals boosts optical gain performance. *Nano Lett.* **2009**, *9*, 3482–3488.

(27) Lounis, B.; Bechtel, H. A.; Gerion, D.; Alivisatos, P.; Moerner, W. E. Photon antibunching in single CdSe/ZnS quantum dot fluorescence. *Chem. Phys. Lett.* **2000**, *329*, 399–404.

(28) Michler, P.; Imamoglu, A.; Mason, M. D.; Carson, P. J.; Strouse, G. F.; Buratto, S. K. Quantum correlation among photons from a single quantum dot at room temperature. *Nature* **2000**, *406*, 968–970.

(29) Messin, G.; Hermier, J. P.; Giacobino, E.; Desbiolles, P.; Dahan, M. Bunching and antibunching in the fluorescence of semiconductor nanocrystals. *Opt. Lett.* **2001**, *26*, 1891–1893.

(30) Brokmann, X.; Giacobino, E.; Dahan, M.; Hermier, J. P. Highly efficient triggered emission of single photons by colloidal CdSe/ZnS nanocrystals. *Appl. Phys. Lett.* **2004**, *85*, 712–714.

(31) Masuo, S.; Naiki, H.; Machida, S.; Itaya, A. Photon statistics in enhanced fluorescence from a single CdSe/ZnS quantum dot in the vicinity of silver nanoparticles. *Appl. Phys. Lett.* **2009**, *95*, 193106.

(32) Naiki, H.; Masuo, S.; Machida, S.; Itaya, A. Single-Photon Emission Behavior of Isolated CdSe/ZnS Quantum Dots Interacting with the Localized Surface Plasmon Resonance of Silver Nanoparticles. *J. Phys. Chem. C* **2011**, *115*, 23299–23304.

(33) Masuo, S.; Tanaka, T.; Machida, S.; Itaya, A. Photon antibunching in enhanced photoluminescence of a single CdSe/ZnS nanocrystal by silver nanostructures. *J. Photochem. Photobiol., A* **2012**, *237*, 24–30.

(34) Canneson, D.; Mallek-Zouari, I.; Buil, S.; Quelin, X.; Javaux, C.; Mahler, B.; Dubertret, B.; Hermier, J. P. Strong Purcell effect observed in single thick-shell CdSe/CdS nanocrystals coupled to localized surface plasmons. *Phys. Rev. B: Condens. Matter Mater. Phys.* **2011**, *84*, 245423.

(35) Park, Y.-S.; Ghosh, Y.; Xu, P.; Mack, N. H.; Wang, H.-L.; Hollingsworth, J. A.; Htoon, H. Single-Nanocrystal Photoluminescence Spectroscopy Studies of Plasmon–Multiexciton Interactions at Low Temperature. *J. Phys. Chem. Lett.* **2013**, *4*, 1465–1470.

(36) Park, Y.-S.; Ghosh, Y.; Chen, Y.; Piryatinski, A.; Xu, P.; Mack, N. H.; Wang, H.-L.; Klimov, V. I.; Hollingsworth, J. A.; Htoon, H. Super-Poissonian Statistics of Photon Emission from Single CdSe-CdS Core-Shell Nanocrystals Coupled to Metal Nanostructures. *Phys. Rev. Lett.* **2013**, *110*, 117401.

(37) Wang, F.; Karan, N. S.; Nguyen, H. M.; Ghosh, Y.; Sheehan, C. J.; Hollingsworth, J. A.; Htoon, H. Correlated structural-optical study of single nanocrystals in a gap-bar antenna: effects of plasmonics on exciton recombination pathways. *Nanoscale* **2015**, *7*, 9387–9393.

(38) Leblanc, S. J.; McClanahan, M. R.; Jones, M.; Moyer, P. J. Enhancement of Multiphoton Emission from Single CdSe Quantum Dots Coupled to Gold Films. *Nano Lett.* **2013**, *13*, 1662–1669.

(39) Yuan, C. T.; Wang, Y. C.; Cheng, H. W.; Wang, H. S.; Kuo, M. Y.; Shih, M. H.; Tang, J. Modification of Fluorescence Properties in Single Colloidal Quantum Dots by Coupling to Plasmonic Gap Modes. *J. Phys. Chem. C* **2013**, *117*, 12762–12768.

(40) Cheng, H. W.; Yuan, C. T.; Wang, J. S.; Lin, T. N.; Shen, J. L.; Hung, Y. J.; Tang, J.; Tseng, F. G. Modification of Photon Emission Statistics from Single Colloidal CdSe Quantum Dots by Conductive Materials. *J. Phys. Chem. C* **2014**, *118*, 18126–18132.

(41) Gao, Y.; Roslyak, O.; Dervishi, E.; Karan, N. S.; Ghosh, Y.; Sheehan, C. J.; Wang, F.; Gupta, G.; Mohite, A.; Dattelbaum, A. M.; Doorn, S. K.; Hollingsworth, J. A.; Piryatinski, A.; Htoon, H. Hybrid Graphene-Giant Nanocrystal Quantum Dot Assemblies with Highly Efficient Biexciton Emission. *Adv. Opt. Mater.* **2015**, *3*, 39–43.

(42) Bek, A.; Jansen, R.; Ringler, M.; Mayilo, S.; Klar, T. A.; Feldmann, J. Fluorescence enhancement in hot spots of AFM-designed gold nanoparticle sandwiches. *Nano Lett.* **2008**, *8*, 485–490.

(43) Schietinger, S.; Barth, M.; Aichele, T.; Benson, O. Plasmon-Enhanced Single Photon Emission from a Nanoassembled Metal-Diamond Hybrid Structure at Room Temperature. *Nano Lett.* **2009**, *9*, 1694–1698.

(44) Huck, A.; Kumar, S.; Shakoor, A.; Anderson, U. L. Controlled Coupling of a Single Nitrogen-Vacancy Center to a Silver Nanowire. *Phys. Rev. Lett.* **2011**, *106*, 096801.

(45) Ratchford, D.; Shafiei, F.; Kim, S.; Gray, S. K.; Li, X. Manipulating Coupling between a Single Semiconductor Quantum Dot and Single Gold Nanoparticle. *Nano Lett.* **2011**, *11*, 1049–1054.

(46) Galland, C.; Ghosh, Y.; Steinbruck, A.; Sykora, M.; Hollingsworth, J. A.; Klimov, V. I.; Htoon, H. Two types of luminescence blinking revealed by spectroelectrochemistry of single quantum dots. *Nature* **2011**, *479*, 203–208.

(47) Achermann, M.; Hollingsworth, J. A.; Klimov, V. I. Multiexcitons confined within a subexcitonic volume: Spectroscopic and dynamical signatures of neutral and charged biexcitons in ultrasmall semiconductor nanocrystals. *Phys. Rev. B: Condens. Matter Mater. Phys.* **2003**, *68*, 245302.

(48) Fisher, B.; Caruge, J. M.; Zehnder, D.; Bawendi, M. Room-temperature ordered photon emission from multiexciton states in single CdSe core-shell nanocrystals. *Phys. Rev. Lett.* **2005**, *94*, 087403.

(49) Matsumoto, Y.; Kanemoto, R.; Itoh, T.; Nakanishi, S.; Ishikawa, M.; Biju, V. Photoluminescence quenching and intensity fluctuations of CdSe-ZnS quantum dots on an Ag nanoparticle film. *J. Phys. Chem. C* **2008**, *112*, 1345–1350.

(50) Hamada, M.; Nakanishi, S.; Itoh, T.; Ishikawa, M.; Biju, V. Blinking suppression in CdSe/ZnS single quantum dots by TiO<sub>2</sub> nanoparticles. *ACS Nano* **2010**, *4*, 4445–4454.

(51) Eguchi, M.; Mitsui, D.; Wu, H. L.; Sato, R.; Teranishi, T. Simple reductant concentration-dependent shape control of polyhedral gold nanoparticles and their plasmonic properties. *Langmuir* **2012**, *28*, 9021–9026.



Cite this: *Photochem. Photobiol. Sci.*, 2015, **14**, 883

## Evaluation of the charge transfer efficiency of organic thin-film photovoltaic devices fabricated using a photoprecursor approach†

Sadahiro Masuo,<sup>\*a,d</sup> Wataru Sato,<sup>a</sup> Yuji Yamaguchi,<sup>b,d</sup> Mitsuharu Suzuki,<sup>c,d</sup> Ken-ichi Nakayama<sup>b,d</sup> and Hiroko Yamada<sup>c,d</sup>

Recently, a unique 'photoprecursor approach' was reported as a new option to fabricate a p-i-n triple-layer organic photovoltaic device (OPV) through solution processes. By fabricating the p-i-n architecture using two kinds of photoprecursors and a [6,6]-phenyl C<sub>71</sub> butyric acid methyl ester (PC<sub>71</sub>BM) as the donor and the acceptor, the p-i-n OPVs afforded a higher photovoltaic efficiency than the corresponding p-n devices and i-devices, while the photovoltaic efficiency of p-i-n OPVs depended on the photoprecursors. In this work, the charge transfer efficiency of the i-devices composed of the photoprecursors and PC<sub>71</sub>BM was investigated using high-sensitivity fluorescence microspectroscopy combined with a time-correlated single photon counting technique to elucidate the photovoltaic efficiency depending on the photoprecursors and the effects of the p-i-n architecture. The spatially resolved fluorescence images and fluorescence lifetime measurements clearly indicated that the compatibility of the photoprecursors with PC<sub>71</sub>BM influences the charge transfer and the photovoltaic efficiencies. Although the charge transfer efficiency of the i-device was quite high, the photovoltaic efficiency of the i-device was much lower than that of the p-i-n device. These results imply that the carrier generation and carrier transportation efficiencies can be increased by fabricating the p-i-n architecture.

Received 16th December 2014,  
Accepted 12th February 2015

DOI: 10.1039/c4pp00477a

www.rsc.org/ppps

## Introduction

Organic photovoltaic devices (OPVs) are an emerging technology with promising advantages, such as low cost, flexibility, light weight, transparency and large-area manufacturing compatibility.<sup>1–13</sup> A fundamental problem of organic materials is that carriers, such as excitons, electrons, and holes, tend to localize more in molecules than in inorganic semiconductor materials. Due to this tendency, the diffusion or hopping length of the carriers in organic materials is limited to a scale of nanometers. Therefore, the arrangement of the organic materials with nanometer-scale precision in the active layers of the OPVs is essential for constructing efficient photon-to-current energy conversion systems. In particular, the design of the donor-acceptor interface is of great importance to improve

the device performance of OPVs. Recent studies have achieved a power conversion efficiency (PCE) of 8–12% in bulk-heterojunction (BHJ) OPVs.<sup>14–16</sup> In addition to the design of the active layer, the vertical composition profile of the active layer significantly affects the efficiency of charge-carrier generation and transportation.<sup>17–19</sup> The vertical composition profile, layer by layer deposition of different materials, can be done straightforwardly *via* vacuum evaporation, while solution processes are practically challenging because of dissolution of the lower layers during the deposition of the upper layer.

Recently, some of authors have reported a unique 'photoprecursor approach' as a new option for layer-by-layer preparation of multicomponent organic semiconducting films through solution processes.<sup>20</sup> In this approach, soluble photoprecursors, 2,7-bis(thiophen-2-yl)-5,10-dihydro-5,10-ethanoanthracene-12,13-dione (DTADK) and 2,6-bis(5'-(2-ethylhexyl)-(2,2'-bithiophen)-5-yl)-9,10-dihydro-9,10-ethanoanthracene-11,12-dione (EH-DBTADK) (Fig. 1), were solution-deposited and then photoconverted *in situ* to a poorly soluble organic semiconductor. This approach enables solution-processing of the p-i-n triple-layer architecture that has been suggested to be effective in obtaining efficient OPVs. Both p-i-n OPVs fabricated using DTADK and EH-DBTADK afforded higher photovoltaic efficiencies than the corresponding p-n devices (double-

<sup>a</sup>Department of Chemistry, Kwansai Gakuin University, 2-1 Gakuen, Sanda, Hyogo 669-1337, Japan. E-mail: masuo@kwansai.ac.jp; Fax: +81-79-565-7341

<sup>b</sup>Department of Organic Device Engineering, Yamagata University, Yonezawa 992-8510, Japan

<sup>c</sup>Graduate School of Materials Science, Nara Institute of Science and Technology, Ikoma 630-0192, Japan

<sup>d</sup>CREST, Japan Science and Technology Agency (JST), Chiyoda-ku 102-0075, Japan

† Electronic supplementary information (ESI) available: Details of instrumental setup and phase AFM images of BHJ-OPVs. See DOI: 10.1039/c4pp00477a

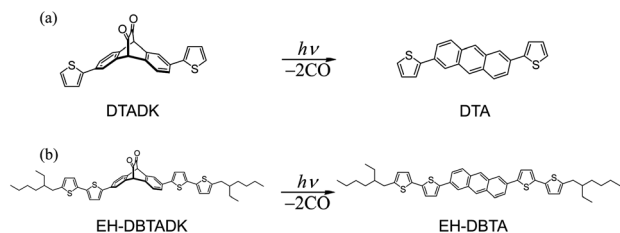


Fig. 1 Chemical structures of photoprecursors and their photoconversion to parent acenes.

layer of p- and n-type materials) and BHJ devices (p : n composite layer; i-layer), while the photovoltaic efficiency of p-i-n OPV composed of EH-DBTADK was much higher than that of DTADK.<sup>20</sup>

The photocurrent generation of OPVs consists of the following processes: (i) generation of excitons by absorbing photons (A), (ii) exciton diffusion and charge transfer at the interface (ED), (iii) charge separation by overcoming the charge recombination, *i.e.* the generation of holes and electrons at the interface (CS), and (iv) the collection of holes and electrons at the electrodes (CC). The external quantum efficiency (EQE) as a function of wavelength ( $\lambda$ ) is given using the efficiencies ( $\eta$ ) of these processes as follows:  $\text{EQE}(\lambda) = \eta\text{A}(\lambda) \times \eta\text{ED}(\lambda) \times \eta\text{CS}(\lambda) \times \eta\text{CC}(\lambda)$ . The efficiencies of these various processes must be optimized to create OPVs with high PCE; a high PCE cannot be achieved if even one of these processes has a low efficiency.

In this work, we investigated the charge transfer efficiency ( $\eta\text{ED}$ ) of the BHJ-OPVs (i-device) fabricated by DTADK and EH-DBTADK using a fluorescence microspectroscopy technique combined with the fluorescence lifetime and spectrum measurements to elucidate the difference in the photovoltaic efficiency depending on the photoprecursors and the effects of the p-i-n architecture. To investigate the charge transfer in OPVs, spectroscopic studies such as the fluorescence quenching,<sup>21–23</sup> transient absorption spectroscopy,<sup>24–27</sup> and spatially resolved imaging techniques<sup>28–32</sup> have been used. We employed a high-sensitivity fluorescence microspectroscopy technique to evaluate the  $\eta\text{ED}$  with sub-micrometer spatial resolution in the device. Using fluorescence images observed from micrometer-sized areas of the BHJ-OPVs and the fluorescence lifetimes detected at focal points in the images using a confocal fluorescence microscope, the spatially resolved  $\eta\text{ED}$  in the device was estimated accurately without being affected by the thickness of the active layer, the concentrations of donor/acceptor molecules, or other parameters. The correlation between the obtained  $\eta\text{ED}$  and photovoltaic efficiency is discussed.

## Experimental

### Materials

The chemical structures of the photoprecursors, DTADK and EH-DBTADK, and their photoconversion reactions are shown in Fig. 1. DTADK and EH-DBTADK were synthesized according

to the reported procedures.<sup>20,33</sup> The purities of these compounds were confirmed to be >99% by high performance liquid chromatography. [6,6]-Phenyl C<sub>71</sub> butyric acid methyl ester (PC<sub>71</sub>BM, >99%) was purchased from Luminescence Technology Corp. and used as received. Other reagents and solvents were reagent grade purchased from commercial vendors and used without further purification.

### Device fabrication and evaluation

PEDOT:PSS (Clevious™ AI4083, Heraeus) was spin-coated onto a clean ITO substrate. After baking in a vacuum at 120 °C for 10 min, the substrate was transferred to a nitrogen-filled glove box (<1 ppm O<sub>2</sub> and H<sub>2</sub>O). A chloroform solution, in which the photoprecursor as a p-type material and PC<sub>71</sub>BM as a n-type material were dissolved at a weight ratio of 2 : 1 (10 mg mL<sup>-1</sup>), was spin-coated at 800 rpm for 30 s. The photoprecursors in the mixed film were photoconverted into their parent acenes (DTADK into DTA, or EH-DBTADK into EH-DBTA) upon irradiation with a blue light-emitting diode (LED) lamp (wavelength: 470 nm, intensity: 200 mW cm<sup>-2</sup>, Edmund Optics), and Ca and Al were evaporated as cathodes. The device was then encapsulated with a glass lid. As references, neat films of the parent acenes were prepared from a solution of the photoprecursors (5 mg mL<sup>-1</sup>) without PC<sub>71</sub>BM in the same manner. The surface morphologies of the active layers in OPV devices and the neat film were evaluated by AFM measurement (NanoWizard®, JPK instruments). The photovoltaic performance was evaluated under AM 1.5G illumination with an intensity of 100 mW cm<sup>-2</sup> using a solar simulator system (CEP-2000, Bunkoukeiki). Details of the fabrication and evaluation of the devices were reported elsewhere.<sup>20,34,35</sup>

### Evaluation of charge transfer efficiency

The  $\eta\text{ED}$  of the prepared BHJ-OPVs was evaluated using a sample-scanning confocal microscope in combination with a picosecond-pulsed laser excitation (405 nm or 640 nm, 10 MHz, 100 ps FWHM, Picoquant). The fluorescence from the active layer of the OPV device was collected by an objective lens and passed through a confocal pinhole (100  $\mu\text{m}$ ) and suitable filters. To detect the fluorescence of the parent acenes, a 405 nm laser was used, and a long-pass filter and a short-pass filter were used to cut the excitation laser beam and fluorescence from PC<sub>71</sub>BM, respectively. The fluorescence of PC<sub>71</sub>BM was detected using a 640 nm laser, and a long-pass filter was used to cut the excitation laser beam. The detected fluorescence was split into two paths and were detected using a spectrometer with a cooled CCD camera and an avalanche single-photon counting module (APD: SPCM-AQR-14, Perkin-Elmer). The signal from the APD was connected to a time-correlated single-photon counting board. The time-resolution of the lifetime measurement, *i.e.* the instrumental response function (IRF) of the system, was estimated by the deconvolution analysis of a fluorescence decay curve of erythrosine in water, which has a reported fluorescence lifetime of 87 ps.<sup>36</sup> The estimated FWHM of the IRF was approximately 300 ps. The fluorescence images, lifetimes, and spectra of the

BHJ-OPVs were measured simultaneously using this setup. Details can be found in ESI.† All measurements were performed at room temperature under ambient conditions.

## Results and discussion

The photovoltaic performances of the BHJ-OPVs fabricated using the photoprecursors and PC<sub>71</sub>BM are summarized in Table 1. The short-circuit current ( $J_{SC}$ ) of the EH-DBTA:PC<sub>71</sub>BM device (3.71 mA cm<sup>-2</sup>) was significantly larger than that of the DTA:PC<sub>71</sub>BM device (2.38 mA cm<sup>-2</sup>). The value of  $J_{SC}$  can be determined as the integration of  $EQE(\lambda) = \eta_A(\lambda) \times \eta_{ED}(\lambda) \times \eta_{CS}(\lambda) \times \eta_{CC}(\lambda)$ , where  $\eta_{ED}(\lambda) \times \eta_{CS}(\lambda) \times \eta_{CC}(\lambda)$  is the internal quantum yield (IQE). The EQE, IQE, and UV-Vis absorption spectra measured from the two OPVs are shown in Fig. 2. The EQE and IQE of EH-DBTA:PC<sub>71</sub>BM are larger than those of DTA:PC<sub>71</sub>BM over the entire wavelength region. Hence, the  $J_{SC}$  of EH-DBTA:PC<sub>71</sub>BM was larger than that of DTA:PC<sub>71</sub>BM. In contrast, the open circuit voltage ( $V_{OC}$ ) of the DTA:PC<sub>71</sub>BM device was larger than that of the EH-DBTA:PC<sub>71</sub>BM device (Table 1). The larger  $V_{OC}$  of the DTA:PC<sub>71</sub>BM device is attributed to the larger HOMO-LUMO band-gap of DTA (2.67 eV) compared to that of EH-DBTA (2.42 eV). Thus, the difference between PCEs became smaller, with values of 0.68 and 0.85 obtained from the DTA:PC<sub>71</sub>BM and EH-DBTA:PC<sub>71</sub>BM devices, respectively. As noted above, the  $J_{SC}$  values of the two devices differed due to the difference in their IQEs. The IQE is determined by the  $\eta_{ED}$ ,  $\eta_{CS}$ , and  $\eta_{CC}$ . In the following discussion, the  $\eta_{ED}$ s in two OPVs will be evaluated using fluorescence microspectroscopy to establish the effect of the  $\eta_{ED}$  on the  $J_{SC}$  value in each device.

First, the  $\eta_{ED}$  in a BHJ-OPV fabricated using DTADK and PC<sub>71</sub>BM was investigated. The fluorescence images obtained from a 20 × 20 μm area in the OPV and DTA neat film are shown in Fig. 3. Fig. 3(a) corresponds to the fluorescence intensity distribution of DTA in the OPV observed by a 405 nm excitation. High- and low-intensity areas were both present across the device. The fluorescence intensity ( $I_f$ ) is expressed as follows:

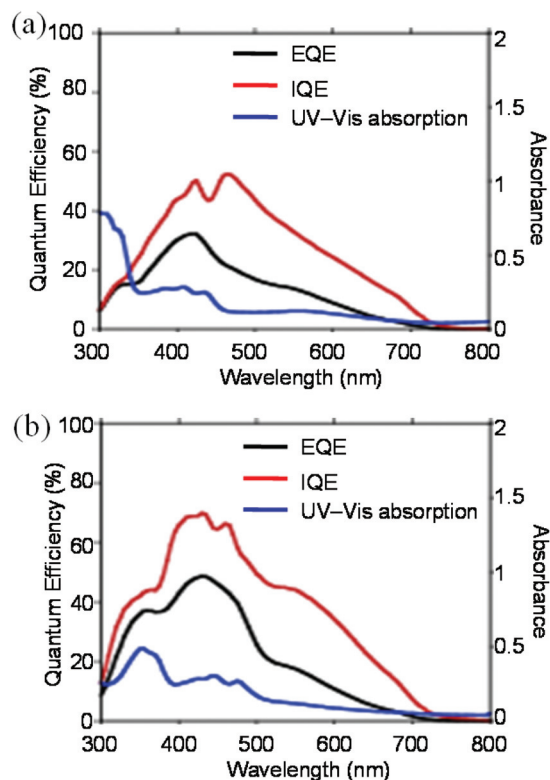
$$I_f = I_{ex} \alpha l \Phi_f \eta_{det} \quad (1)$$

where  $I_{ex}$  is the excitation intensity,  $\alpha$  is the absorption coefficient,  $l$  is the thickness of the sample (number of fluorescent molecules at the focal point),  $\Phi_f$  is the fluorescence quantum

**Table 1** Photovoltaic device performance of BHJ-OPVs consisting of photoprecursors and PC<sub>71</sub>BM<sup>a</sup>

	$J_{SC}/\text{mA cm}^{-2}$	$V_{OC}/\text{V}$	FF/%	PCE/%
DTA:PC <sub>71</sub> BM	2.38	1.06	26.8	0.68
EH-DBTA:PC <sub>71</sub> BM	3.71	0.78	29.4	0.85

<sup>a</sup> $J_{SC}$ : short circuit current,  $V_{OC}$ : open circuit current, FF: fill factor, PCE: power conversion efficiency.



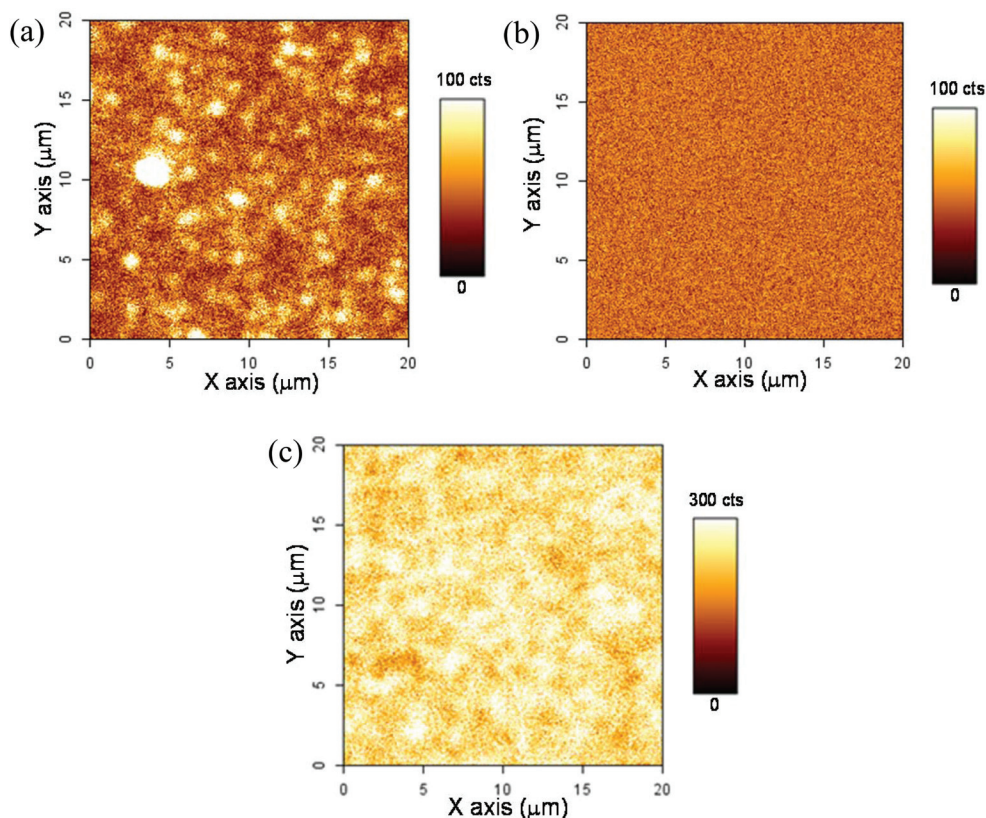
**Fig. 2** EQE( $\lambda$ ) (black), IQE( $\lambda$ ) (red), and UV-Vis absorption spectra (blue) measured from the OPVs consisting of DTA:PC<sub>71</sub>BM (a) and EH-DBTA:PC<sub>71</sub>BM (b).

yield, and  $\eta_{det}$  is the detection efficiency of the instrument.  $\Phi_f$  can be expressed as follows:

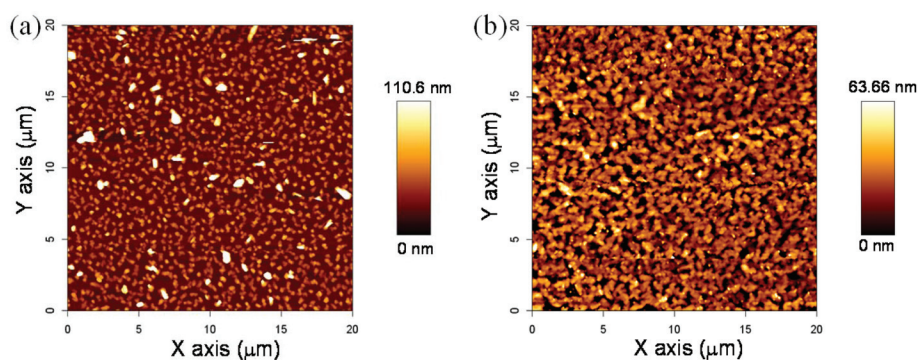
$$\Phi_f = \frac{k_r}{k_r + k_{nr} + k_{ED}} \quad (2)$$

where  $k_r$  and  $k_{nr}$  are the radiative and non-radiative decay rates, respectively, and  $k_{ED}$  is the charge transfer rate. When the fluorescence image was observed,  $I_{ex}$  and  $\eta_{det}$  were constants such that the heterogeneity of the fluorescence intensity was attributed to the difference in the thickness of the DTA layer and/or  $\Phi_f$  which varies depending on  $k_{ED}$  assuming that  $k_r$  and  $k_{nr}$  are constants. Fig. 3(c) shows the fluorescence image of a DTA neat film observed by a 405 nm excitation (note: the intensity-scale is different from that of BHJ-OPVs). This neat film showed a much higher fluorescence intensity, and the heterogeneity of the fluorescence intensity was also observed in the neat film, which indicated that the DTA did not form a uniform film.

AFM measurements were conducted to evaluate the film structures of the active layer of the OPV and the neat film. The obtained AFM images are shown in Fig. 4. Many broad peaks of several tens to a hundred nm in height were observed in the AFM images. The distance between the peaks was wider in the OPV device compared to that in the neat film due to the presence of PC<sub>71</sub>BM in the OPV device (*vide infra*). The fluorescence and AFM images indicated that DTA tended to



**Fig. 3** Fluorescence images observed from a BJJ-OPV consisting of DTA and PC<sub>71</sub>BM (a, b) and from a DTA neat film (c). Images (a, c) were observed by a 405 nm excitation with a 56 W cm<sup>-2</sup> intensity, and the image (b) was observed by a 640 nm excitation with a 4.5 kW cm<sup>-2</sup> intensity.

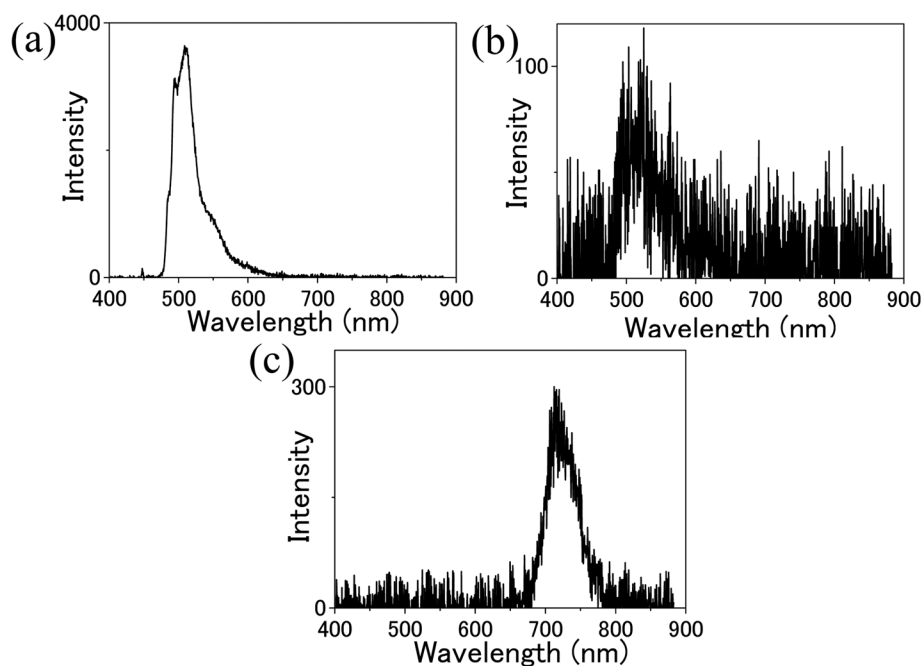


**Fig. 4** AFM images obtained from the OPV consisting of DTA and PC<sub>71</sub>BM (a) and a DTA neat film (b).

aggregate because of its high crystallinity.<sup>20</sup> The phase image of the active layer of the OPV is shown in Fig. S1 (a) in ESI.† The contrast of the phase image at the aggregates is different from other areas. This observation strongly supports that the aggregates have different film structures from other areas, *i.e.* the aggregates probably consist of a DTA crystalline structure. Therefore, the heterogeneity of the fluorescence image (Fig. 3a) was also due to the heterogeneity of DTA, as reflected in the difference in  $l$  in eqn (1). The bright areas in the fluorescence image (Fig. 3a) correspond to the aggregates of DTA peaked areas in the AFM image. The fluorescence spectra

observed from the bright and dark areas in the fluorescence image are shown in Fig. 5. Below 485 nm, the fluorescence spectra were cut off by a dichroic mirror that was inserted into the microscope to reflect the laser beam. The fluorescence peak at 510 nm was observed in both the bright and dark areas, although the signal-to-noise ratio in the spectrum measured in the dark area (Fig. 5b) was rather low. This peak was assigned to DTA.

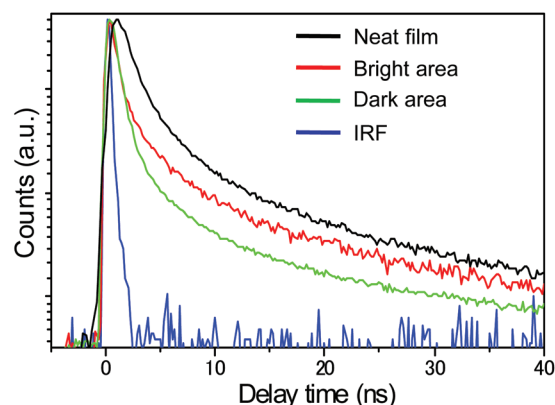
These fluorescence spectra indicate that DTA was present within the entire active layer of the device, although the distribution was heterogeneous because of its tendency to aggre-



**Fig. 5** Fluorescence spectra observed from the OPV consisting of DTA and PC<sub>71</sub>BM. Fluorescence spectra observed from a bright area (a) and a dark area (b) in the fluorescence image shown in Fig. 3(a) by a 405 nm excitation. (c) Fluorescence spectrum observed from the fluorescence image shown in Fig. 3(c) by a 640 nm excitation.

gate. Fig. 3(b) corresponds to the fluorescence intensity distribution of PC<sub>71</sub>BM in the active layer of the device observed by a 640 nm excitation. In contrast to Fig. 3(a), the heterogeneity was not observed. The fluorescence spectrum observed by a 640 nm excitation is shown in Fig. 5(c). The peak at 715 nm was characterized as representing PC<sub>71</sub>BM, and this spectrum was observed at all locations within the device. The fluorescence image and the spectrum observed by a 640 nm excitation indicate that PC<sub>71</sub>BM was uniformly distributed over the entire area of the active layer. It is well known that the PC<sub>71</sub>BM forms aggregates with several tens of nanometer-size. Such aggregates were probably formed in our devices. However, as the sizes of the aggregates were much smaller than the diffraction limit of light, the uniform fluorescence image of PC<sub>71</sub>BM was observed. These results demonstrate that the spatial distribution of DTA and PC<sub>71</sub>BM in the active layer can be observed by varying the excitation and detection wavelengths. However, the  $\eta$ ED information cannot be clearly obtained from the fluorescence images due to the non-uniform distribution of DTA in the active layer, although the decrease in the fluorescence intensity of BHJ-OPV (Fig. 3a) compared to the DTA neat film (Fig. 3c) is probably caused by the charge transfer.

The fluorescence lifetime measurements were conducted to evaluate the  $\eta$ ED of the OPVs. The fluorescence lifetime ( $\tau$ ) can be expressed as  $\tau_{\text{OPV}} = 1/(k_r + k_{\text{nr}} + k_{\text{ED}})$  for the OPV and as  $\tau_{\text{neat}} = 1/(k_r + k_{\text{nr}})$  for the neat film. Therefore, the contribution of  $k_{\text{ED}}$  can be estimated by comparing the lifetimes detected from the OPV and the neat film. The fluorescence decay curves observed from the OPV and DTA neat film by a 405 nm



**Fig. 6** Fluorescence decay curves observed from a DTA neat film (black) and a bright area (red) and dark area (green) in the fluorescence image of the OPV shown in Fig. 3(a) by a 405 nm excitation. The decay curve (blue) represents the instrument response function (IRF).

excitation are shown in Fig. 6. The decay curves were analyzed by fitting with three exponential functions as follows:

$$I(t) = \alpha_1 \exp(-t/\tau_1) + \alpha_2 \exp(-t/\tau_2) + \alpha_3 \exp(-t/\tau_3) \quad (3)$$

The fluorescence lifetimes ( $\tau$ ) and normalized amplitudes ( $\alpha$ ) obtained by the fitting are summarized in Table 2. The average lifetimes  $\langle \tau \rangle$  calculated by  $\alpha_1 \times \tau_1 + \alpha_2 \times \tau_2 + \alpha_3 \times \tau_3$  are also provided in this table. Fig. 6 illustrates that the decay curves detected from the OPV were shorter than that detected from the DTA neat film. The shortened lifetime indicates the

**Table 2** Fitting parameters for fluorescence decay curves<sup>a</sup>

		$\tau_1$ /		$\tau_2$ /		$\tau_3$ /		$\langle\tau\rangle$ /
		ns	$\alpha_1$	ns	$\alpha_2$	ns	$\alpha_3$	
DTA	Neat film	0.8	0.57	2.3	0.36	9.2	0.07	1.93
	OPV device							
	Bright area	0.5	0.66	2.2	0.26	10.1	0.08	1.71
	Dark area	0.4	0.93	2.1	0.06	7.0	0.01	0.57
EH-DBTA	Neat film	0.5	0.64	1.9	0.31	5.5	0.05	1.18
	OPV device	0.3	1.00	—	—	—	—	0.30

<sup>a</sup> Fluorescence decay curves were fitted with a sum of three exponential functions,  $I(t) = \alpha_1 \exp(-t/\tau_1) + \alpha_2 \exp(-t/\tau_2) + \alpha_3 \exp(-t/\tau_3)$ . The decay curve detected from the OPV device comprising of EH-DBTA and PC<sub>71</sub>BM was fitted with a single exponential function.  $\tau$  and  $\alpha$  represent the fluorescence lifetime and the normalized amplitude, respectively.  $\langle\tau\rangle$  is the averaged lifetime calculated by  $\alpha_1 \times \tau_1 + \alpha_2 \times \tau_2 + \alpha_3 \times \tau_3$ .

contribution of charge transfer in the device. The decay curve detected from a dark area was shorter than that detected from a bright area in the fluorescence image. In Table 2, the contribution of  $\tau_1$  in the decay curve detected from the dark area is greater than in the decay curve detected from the bright area. Hence, the average lifetime of the dark area is shorter than that of the bright area.

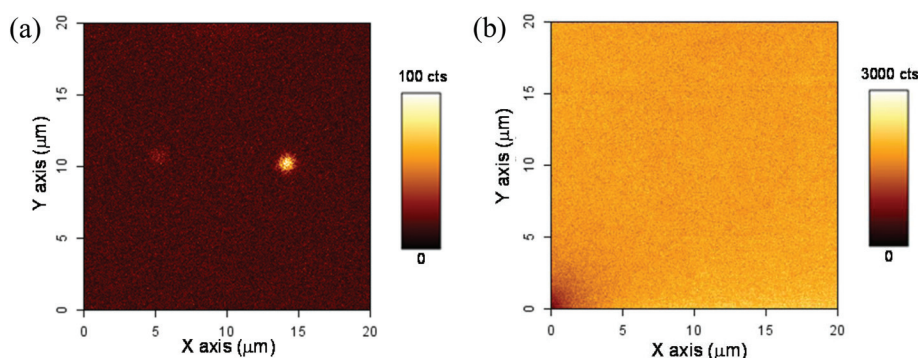
The difference in the decay curves observed in the bright and dark areas can be interpreted as follows. DTA formed aggregates in the bright areas in the fluorescence image, and the charge transfer only occurred at the surface of the aggregate, *i.e.* the excitons generated inside the aggregate did not contribute to the charge transfer. Therefore, the contribution of the short lifetime was lower and that of the fluorescence intensity was higher in the bright areas. In contrast, in the dark areas, the contribution of the charge transfer was higher than that in the bright areas because the lifetime was shorter. However, the decay curves detected from both areas still included long lifetimes of 2.2 and 10.1 ns for the bright area and 2.1 and 7.0 ns for the dark area. If the charge transfer occurs efficiently, the decay curve should be consistent with the instrument response function (IRF).

The  $\eta$ ED was estimated by comparing the average lifetimes  $\langle\tau\rangle$  as follows.  $\eta$ ED is expressed as  $\eta$ ED =  $k_{ED}/(k_r + k_{nr} + k_{ED})$ . The average lifetimes of the neat film  $\langle\tau_{neat}\rangle$  and OPV  $\langle\tau_{OPV}\rangle$  are expressed as  $\langle\tau_{neat}\rangle = 1/(k_r + k_{nr})$  and  $\langle\tau_{OPV}\rangle = 1/(k_r + k_{nr} + k_{ED})$ , respectively; thus,  $k_{ED} = 1/\langle\tau_{OPV}\rangle - 1/\langle\tau_{neat}\rangle$ , assuming that  $k_r$  and  $k_{nr}$  are constants in both the neat film and OPV. Therefore,  $\eta$ ED can be estimated using

$$\eta$$
ED =  $1 - \langle\tau_{OPV}\rangle / \langle\tau_{neat}\rangle$ . (4)

From Table 2, the average lifetimes in the bright area  $\langle\tau_{OPV\_B}\rangle$  and dark area  $\langle\tau_{OPV\_D}\rangle$  are 1.71 and 0.57 ns, respectively. Using these lifetimes, the  $\eta$ ED for the bright area and dark area can be estimated to be 0.11 and 0.70, respectively. ( $\eta$ ED = 0.84 is the maximum value in this estimation because our IRF was 0.3 ns.) These values indicate that only 11% and 70% of the excitons generated in the DTA caused the charge transfer in the bright and dark areas, respectively. One reason for this low efficiency was the low compatibility of DTA with PC<sub>71</sub>BM. As noted above, DTA tended to aggregate because of its high crystallinity. Therefore, there was a decrease in the interface between DTA and PC<sub>71</sub>BM, where the charge transfer occurs.

To improve the low compatibility, EH-DBTADK (Fig. 1b) which has branched alkyl-chains, was synthesized and used for device fabrication.<sup>20</sup> The fluorescence images observed from a BHJ-OPV fabricated using EH-DBTADK and PC<sub>71</sub>BM and from a neat film of EH-DBTA are shown in Fig. 7. In contrast to the DTA neat film, the heterogeneity of the fluorescence intensity was not observed in the image of the EH-DBTA neat film (Fig. 7b), indicating that EH-DBTA likely formed a uniform amorphous-like film because the crystallinity of EH-DBTA is lower than that of DTA. Therefore, the heterogeneity of the fluorescence intensity was not observed in the image of the OPV (Fig. 7a), although some fluorescence domains were observed. AFM images obtained from the OPV and the neat film are shown in Fig. 8. Although small, broad peaks were observed in the AFM image, the peaks were considerably smaller than those in the AFM images of the DTA (Fig. 4). A comparison of the AFM images of the OPV with those of the neat film illustrates that the peaks were smaller in



**Fig. 7** Fluorescence images observed from an OPV consisting of EH-DBTA and PC<sub>71</sub>BM (a) and from an EH-DBTA neat film (b) by a 405 nm excitation with a 56 W cm<sup>-2</sup> intensity.

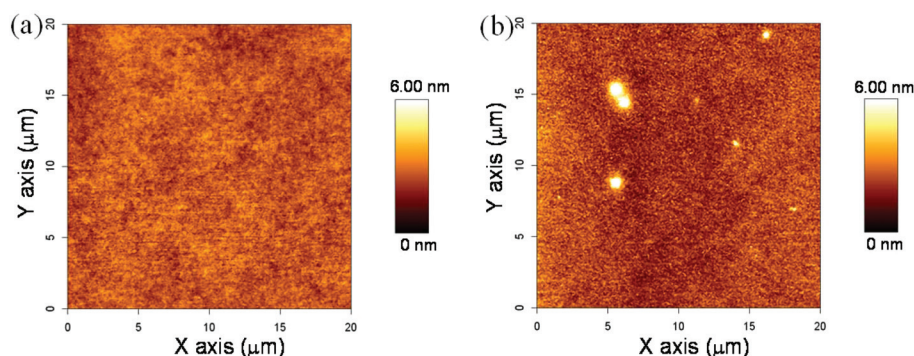


Fig. 8 AFM images obtained from the OPV consisting of EH-DBTA and PC<sub>71</sub>BM (a) and an EH-DBTA neat film (b).

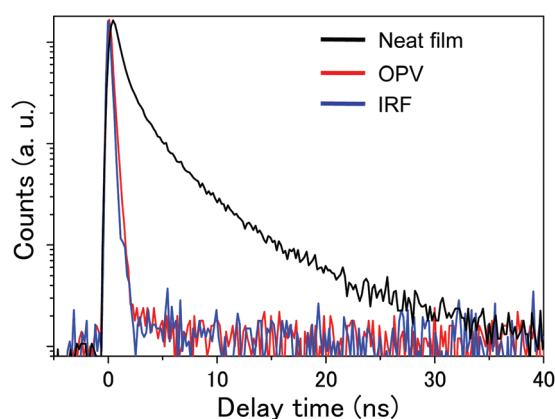


Fig. 9 Fluorescence decay curves observed from an EH-DBTA neat film (black) and the OPV (red) by a 405 nm excitation. The decay curve (blue) represents the instrument response function (IRF).

the OPV. In the phase AFM image shown in Fig. S1 (b),<sup>†</sup> the heterogeneity of the image was not observed.

These results indicate that EH-DBTA could be miscible with PC<sub>71</sub>BM due to improved compatibility. We presume that EH-DBTA is not mixed with PC<sub>71</sub>BM at the molecular level, *i.e.* both compounds form the nanometer-sized aggregates in the active layer. If the EH-DBTA is mixed with PC<sub>71</sub>BM at the molecular level, the photovoltaic performance cannot be observed. As the sizes of aggregates are considerably smaller than the diffraction limit of light, the uniform fluorescence intensity was observed in the fluorescence images. The fluorescence decay curves obtained from the EH-DBTA neat film and OPV are shown in Fig. 9. The decay curve detected from the OPV was considerably shorter than that detected from the EH-DBTA neat film and was nearly the same as the IRF. This result indicates that efficient charge transfer occurred in the OPV fabricated using EH-DBTADK and PC<sub>71</sub>BM and that the efficiency was higher than in the OPV comprised of DTA and PC<sub>71</sub>BM. The fluorescence lifetimes ( $\tau$ ), normalized amplitudes ( $\alpha$ ), and average lifetimes  $\langle\tau\rangle$  obtained by the fitting are summarized in Table 2. An  $\eta$ ED of 0.75 was obtained using eqn (1) with  $\langle\tau_{\text{OPV}}\rangle = 0.3$  ns and  $\langle\tau_{\text{neat}}\rangle = 1.18$  ns. The  $\eta$ ED of 0.75 reached the maximum value of our instrumental setup because the

$\langle\tau_{\text{OPV}}\rangle$  was the same as the IRF. Therefore, the  $\eta$ ED of the OPV device was over 75%. We can estimate the  $\eta$ ED more precisely using photo-detectors with high time resolution. The  $\eta$ ED was likely quite high, although it was not 100% because the fluorescence from EH-DBTA was still observed. These observations illustrate that efficient charge transfer occurred in the OPV device because EH-DBTA blended with PC<sub>71</sub>BM due to the low crystallinity of EH-DBTA.

As shown above, the  $\eta$ ED of the EH-DBTA:PC<sub>71</sub>BM device was considerably higher than that of the DTA:PC<sub>71</sub>BM device. This difference in  $\eta$ EDs is related to the IQE and  $J_{\text{SC}}$  of the devices. Fig. 2 indicates that the IQEs at 405 nm for the DTA:PC<sub>71</sub>BM and EH-DBTA:PC<sub>71</sub>BM devices were approximately 44% and 67%, respectively. From the fluorescence microspectroscopy measurements, the  $\eta$ ED at 405 nm for DTA:PC<sub>71</sub>BM was 11% in the bright area and 70% in the dark area, whereas the  $\eta$ ED for EH-DBTA:PC<sub>71</sub>BM was over 75%. The  $\eta$ EDs were reduced to the values of the IQEs by the contributions of the  $\eta$ CS and  $\eta$ CC, and the IQDs decreased to the values of the EQEs by the contribution of  $\eta$ A. For the BHJ-OPV considered here, the higher  $J_{\text{SC}}$  of the EH-DBTA:PC<sub>71</sub>BM device was attributed to the higher  $\eta$ ED due to the high compatibility between EH-DBTA and PC<sub>71</sub>BM using the high-sensitivity fluorescence microspectroscopy technique.

## Conclusions

The spatially resolved  $\eta$ ED of BHJ-OPVs fabricated using photoprecursors and PC<sub>71</sub>BM was estimated by observing the fluorescence images, spectra, and lifetimes using a confocal fluorescence microspectroscopy technique. For the BHJ-OPV composed of DTA and PC<sub>71</sub>BM, a lower and more heterogeneous  $\eta$ ED was clearly observed even though the DTA and PC<sub>71</sub>BM existed over the entire area of the active layer. This low, heterogeneous  $\eta$ ED was caused by the high crystallinity of DTA and the low compatibility of DTA with PC<sub>71</sub>BM. Therefore, for the OPV consisting of EH-DBTA, which has a low crystallinity, and PC<sub>71</sub>BM, the  $\eta$ ED was found to increase with an increase in  $J_{\text{SC}}$  and PCE. However, PCE was quite low (0.85) in spite of the high  $\eta$ ED. As a cause for the low PCE, the low efficiency of the carrier transportation from the BHJ layer to

the electrodes ( $\eta_{CC}$ ) can be considered. Recently, it was demonstrated that PCE can be increased to 2.83 by fabricating a p-i-n (p: DTA neat film, i: BHJ of EH-DBTA and PC<sub>71</sub>BM, n: PC<sub>71</sub>BM neat film) triple-layer architecture.<sup>20</sup> The present results indicate that the increase in the  $\eta_{CC}$  by fabricating p and n layers is a reason for the increase in the PCE of p-i-n OPV. In addition, the absorption efficiency ( $\eta_A$ ) and the amount of subsequent carrier generation also increase because of the increase in the interfaces of p-i and i-n. Therefore, the increase in the PCE was observed by fabricating the p-i-n architecture.

## Acknowledgements

This work was partially supported by CREST from the Japan Science and Technology Agency (JST), a Grant-in-Aid for Scientific Research (Grant no. 26390023 for SM), a Grant-in-Aid for Scientific Research (Grant no. 25288092 for HY) from the Japan Society for the Promotion of Science (JSPS), the Green Photonics Project in NAIST sponsored by the Ministry of Education, Culture, Sports, Science and Technology (MEXT), Japan, and the program for promoting the enhancement of research universities in NAIST supported by MEXT.

## References

- 1 Y. Y. Liang and L. P. Yu, *Acc. Chem. Res.*, 2010, **43**, 1227–1236.
- 2 P. M. Beaujuge and J. M. J. Frechet, *J. Am. Chem. Soc.*, 2011, **133**, 20009–20029.
- 3 D. Credgington and J. R. Durrant, *J. Phys. Chem. Lett.*, 2012, **3**, 1465–1478.
- 4 B. E. Hardin, H. J. Snaith and M. D. McGehee, *Nat. Photonics*, 2012, **6**, 162–169.
- 5 G. Li, R. Zhu and Y. Yang, *Nat. Photonics*, 2012, **6**, 153–161.
- 6 A. Mishra and P. Bauerle, *Angew. Chem., Int. Ed.*, 2012, **51**, 2020–2067.
- 7 H. J. Son, B. Carsten, I. H. Jung and L. P. Yu, *Energy Environ. Sci.*, 2012, **5**, 8158–8170.
- 8 H. X. Zhou, L. Q. Yang and W. You, *Macromolecules*, 2012, **45**, 607–632.
- 9 C. W. Tang, *Appl. Phys. Lett.*, 1986, **48**, 183.
- 10 N. S. Sariciftci, L. Smilowitz, A. J. Heeger and F. Wudl, *Synth. Met.*, 1993, **59**, 333–352.
- 11 N. S. Sariciftci, D. Braun, C. Zhang, V. I. Srdanov, A. J. Heeger, G. Stucky and F. Wudl, *Appl. Phys. Lett.*, 1993, **62**, 585.
- 12 J. J. M. Halls, C. A. Walsh, N. C. Greenham, E. A. Marseglia, R. H. Friend, S. C. Moratti and A. B. Holmes, *Nature*, 1995, **376**, 498–500.
- 13 G. Yu, J. Gao, J. C. Hummelen, F. Wudl and A. J. Heeger, *Science*, 1995, **270**, 1789–1791.
- 14 L. Dou, J. Gao, E. Richard, J. You, C. C. Chen, K. C. Cha, Y. He, G. Li and Y. Yang, *J. Am. Chem. Soc.*, 2012, **134**, 10071–10079.
- 15 Z. He, C. Zhong, X. Huang, W. Y. Wong, H. Wu, L. Chen, S. Su and Y. Cao, *Adv. Mater.*, 2011, **23**, 4636–4643.
- 16 J. You, L. Dou, K. Yoshimura, T. Kato, K. Ohya, T. Moriarty, K. Emery, C. C. Chen, J. Gao, G. Li and Y. Yang, *Nat. Commun.*, 2013, **4**, 1446.
- 17 M. Campoy-Quiles, T. Ferenczi, T. Agostinelli, P. G. Etchegoin, Y. Kim, T. D. Anthopoulos, P. N. Stavrinou, D. D. C. Bradley and J. Nelson, *Nat. Mater.*, 2008, **7**, 158–164.
- 18 Y. M. Nam, J. Huh and W. H. Jo, *J. Appl. Phys.*, 2011, **110**, 114521.
- 19 Z. G. Xiao, Y. B. Yuan, B. Yang, J. VanDerslice, J. H. Chen, O. Dyck, G. Duscher and J. S. Huang, *Adv. Mater.*, 2014, **26**, 3068–3075.
- 20 Y. Yamaguchi, M. Suzuki, T. Motoyama, S. Sugii, C. Katagiri, K. Takahira, S. Ikeda, H. Yamada and K. Nakayama, *Sci. Rep.*, 2014, **4**, 7151.
- 21 L. Schmidt-Mende, A. Fechtenkotter, K. Mullen, E. Moons, R. H. Friend and J. D. MacKenzie, *Science*, 2001, **293**, 1119–1122.
- 22 P. Peumans, A. Yakimov and S. R. Forrest, *J. Appl. Phys.*, 2004, **95**, 2938–2938.
- 23 H. Bente, M. Ogawa, H. Ohkita and S. Ito, *Adv. Funct. Mater.*, 2008, **18**, 1563–1572.
- 24 A. Furube, Z. S. Wang, K. Sunahara, K. Hara, R. Katoh and M. Tachiya, *J. Am. Chem. Soc.*, 2010, **132**, 6614–6615.
- 25 J. Guo, H. Ohkita, S. Yokoya, H. Bente and S. Ito, *J. Am. Chem. Soc.*, 2010, **132**, 9631–9637.
- 26 X. F. Wang, L. Wang, Z. Q. Wang, Y. W. Wang, N. Tamai, Z. R. Hong and J. Kido, *J. Phys. Chem. C*, 2013, **117**, 804–811.
- 27 S. Gelin, A. Rao, A. Kumar, S. L. Smith, A. W. Chin, J. Clark, T. S. van der Poll, G. C. Bazan and R. H. Friend, *Science*, 2014, **343**, 512–516.
- 28 Y. Q. Gao, T. P. Martin, A. K. Thomas and J. K. Grey, *J. Phys. Chem. Lett.*, 2010, **1**, 178–182.
- 29 J. H. Huang, F. C. Chien, P. L. Chen, K. C. Ho and C. W. Chu, *Anal. Chem.*, 2010, **82**, 1669–1673.
- 30 D. P. Ostrowski, M. S. Glaz, B. W. Goodfellow, V. A. Akhavan, M. G. Panthani, B. A. Korgel and D. A. V. Bout, *Small*, 2010, **6**, 2832–2836.
- 31 T. J. K. Brenner and C. R. McNeill, *J. Phys. Chem. C*, 2011, **115**, 19364–19370.
- 32 X. T. Hao, L. M. Hirvonen and T. A. Smith, *Methods Appl. Fluoresc.*, 2013, **1**, 015004.
- 33 H. Yamada, E. Kawamura, S. Sakamoto, Y. Yamashita, T. Okujima, H. Uno and N. Ono, *Tetrahedron Lett.*, 2006, **47**, 7501–7504.
- 34 T. Motoyama, T. Kiyota, H. Yamada and K. Nakayama, *Sol. Energy Mater. Sol. Cells*, 2013, **114**, 156–160.
- 35 T. Motoyama, S. Sugii, S. Ikeda, Y. Yamaguchi, H. Yamada and K. Nakayama, *Jpn. J. Appl. Phys.*, 2014, **53**, 01AB02.
- 36 M. Maus, M. Cotlet, J. Hofkens, T. Gensch, F. C. De Schryver, J. Schaffer and C. A. M. Seidel, *Anal. Chem.*, 2001, **73**, 2078–2086.



# Control of Circularly Polarized Luminescence by Orientation of Stacked $\pi$ -Electron Systems

Katsuaki Kikuchi,<sup>[a]</sup> Jun Nakamura,<sup>[a]</sup> Yuuya Nagata,<sup>[b]</sup> Hiromu Tsuchida,<sup>[c]</sup> Takahiro Kakuta,<sup>[c, d]</sup> Tomoki Ogoshi,<sup>[c, d]</sup> and Yasuhiro Morisaki<sup>\*,[a]</sup>

**Abstract:** Planar chiral building blocks based on 4,7,12,15-tetrasubstituted [2.2]paracyclophanes were obtained via a synthetic route involving an optical resolution step. Planar chiral enantiomers, comprising two fluorophores that were stacked to form a V-shaped higher-ordered structure, were synthesized from these building blocks. The V-shaped molecules emitted intense circularly polarized luminescence (CPL). Their chiroptical properties were compared with those of X-shaped molecules bearing the same two fluorophores stacked together. The CPL sign of the X-shaped molecule was opposite to that of the V-shaped molecule, which is supported by the theoretical results, indicating that the CPL sign can be controlled by the orientation of the stacked fluorophores.

Conjugated molecules exhibited interesting properties such as conductive and luminescent properties, and are being increasingly applied in various opto-electronic devices.<sup>[1]</sup> Recently, chiral conjugated molecules have received increased attention due to their chiroptical properties such as circularly polarized luminescence (CPL).<sup>[2]</sup> We have focused on planar chiral [2.2]paracyclophane skeletons<sup>[3–5]</sup> as optically active building blocks for the syntheses of chiral conjugated molecules<sup>[6]</sup> (polymers,<sup>[7]</sup> oligomers<sup>[8]</sup> and macrocycles).<sup>[9]</sup> Optical resolution

methods for 4,12-disubstituted<sup>[10]</sup> and 4,7,12,15-tetrasubstituted [2.2]paracyclophane compounds<sup>[9a,d,11]</sup> were developed, and then, a variety of chiral conjugated molecules have been synthesized. All molecules based on planar chiral [2.2]paracyclophanes exhibited excellent CPL profiles with large molar extinction coefficients ( $\epsilon$ ), high photoluminescence quantum efficiencies ( $\Phi_{\text{PL}}$ ), and large CPL dissymmetry factors ( $g_{\text{lum}}$ ), that are derived from the optically active second-ordered structures (V-,<sup>[8]</sup>  $\Delta$ -,<sup>[7a]</sup> X-,<sup>[12]</sup> and propeller-shaped structures<sup>[9a]</sup> as well as one-handed helix<sup>8</sup> and one-handed double helices).<sup>[9d]</sup>

In this study, new types of enantiopure [2.2]paracyclophane building blocks were synthesized and used to prepare the corresponding V-shaped compounds in order to compare their chiroptical properties with those of the X-shaped compounds. Same  $\pi$ -electron systems are stacked to form both V- and X-shaped structures, as shown in Figure 1. Orientation (in other words, stacking position) of two  $\pi$ -electron systems can be controlled using [2.2]paracyclophane-based chiral building blocks, leading to the control of chiroptical properties. The synthetic routes for production of V-shaped molecules and their optical properties are discussed in detail.

The synthetic route to the new type of 4,7,12,15-tetrasubstituted [2.2]paracyclophane (bis-(*para*)-pseudo-*ortho*-type [2.2]paracyclophane)<sup>[13]</sup> building blocks is shown in Scheme 1. 4,12-Dihydroxy[2.2]paracyclophane<sup>[14]</sup> (*rac*-1) was reacted with (1*S*,4*R*)-camphanic chloride to afford the corresponding diastereomers in 82% yield. After their reaction with Br<sub>2</sub> in the presence of iron, optical resolution was achieved by recrystallization and common silica gel (SiO<sub>2</sub>) column chromatography to separate the diastereomers (*R*<sub>p</sub>,1*S*,4*R*)-2 and (*S*<sub>p</sub>,1*S*,4*R*)-2 in 36% and 31% isolated yields, respectively. Gram-scale optical resolution was also possible to obtain both diastereomers. In previous studies, optical resolution was carried out after the reaction of *rac*-1 with (1*S*,4*R*)-camphanic chloride, and each separated diastereomer was brominated,<sup>[9d]</sup> as shown in Scheme S1 in the Supporting Information (SI). In the present study, optical resolution was carried out after bromination of the mixture of diastereomers; this modified route involves a single bromination step to prepare both diastereomers (*R*<sub>p</sub>,1*S*,4*R*)-2 and (*S*<sub>p</sub>,1*S*,4*R*)-2. Chromatograms of (*R*<sub>p</sub>,1*S*,4*R*)-2 and (*S*<sub>p</sub>,1*S*,4*R*)-2 obtained by chiral HPLC are shown in Figure S1 in SI, which indicate that the diastereomeric ratio was over 99.5%.

Chiral auxiliary of (*R*<sub>p</sub>,1*S*,4*R*)-2 was removed by its reaction with KOH to afford (*R*<sub>p</sub>)-3 (Scheme 1). After the workup, crude (*R*<sub>p</sub>)-3 was reacted with K<sub>2</sub>CO<sub>3</sub> and MeI to obtain new enantiopure chiral building block (*R*<sub>p</sub>)-4 in 91% isolated yield. The enantiomer (*S*<sub>p</sub>)-4 was also obtained in 88% isolated yield from (*S*<sub>p</sub>,1*S*,4*R*)-2.

[a] K. Kikuchi, Dr. J. Nakamura, Prof. Y. Morisaki  
Department of Applied Chemistry for Environment, School of Science and Technology  
Kwansei Gakuin University  
2-1 Gakuen, Sanda, Hyogo 669-1337 (Japan)  
E-mail: ymo@kwansei.ac.jp

[b] Dr. Y. Nagata  
Department of Synthetic Chemistry and Biological Chemistry, Graduate School of Engineering  
Kyoto University  
Nishikyo-ku, Kyoto 615-8510 (Japan)

[c] H. Tsuchida, Dr. T. Kakuta, Prof. T. Ogoshi  
Graduate School of Natural Science and Technology  
Kanazawa University  
Kakuma-machi, Kanazawa, Ishikawa 920-1192 (Japan)

[d] Dr. T. Kakuta, Prof. T. Ogoshi  
WPI Nano Life Science Institute  
Kanazawa University  
Kakuma-machi, Kanazawa, Ishikawa 920-1192 (Japan)

Supporting information and the ORCID identification number(s) for the author(s) of this article can be found under:  
<https://doi.org/10.1002/asia.201801741>.

This manuscript is part of a special issue on  $\pi$ -Conjugated Compounds for Molecular Materials. A link to the Table of Contents of the special issue will appear here when the complete issue is published.

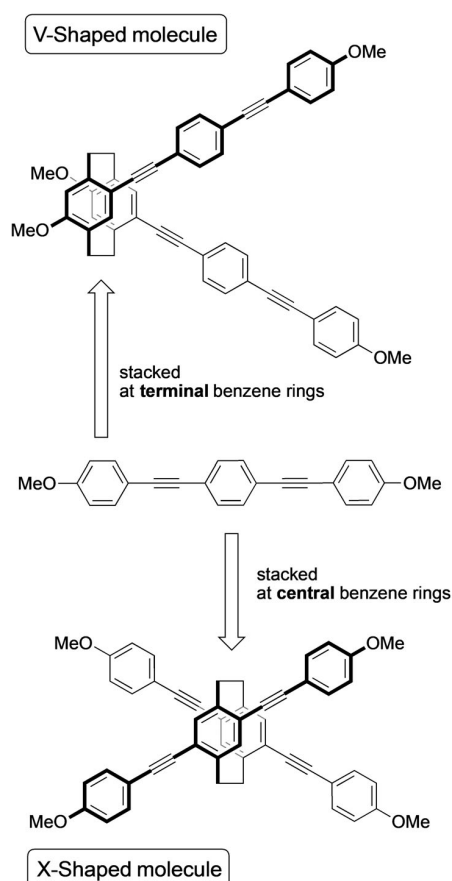
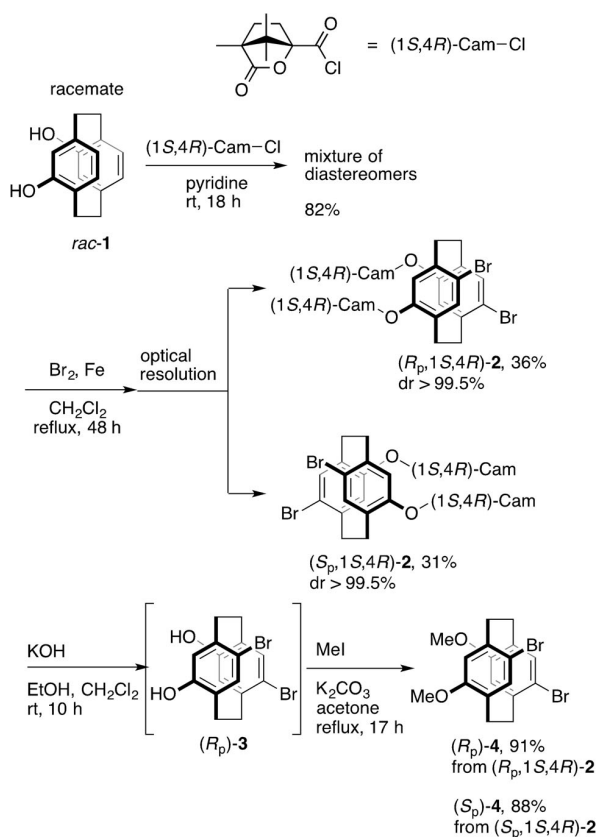


Figure 1. Structures of V-shaped and X-shaped molecules discussed in this work.

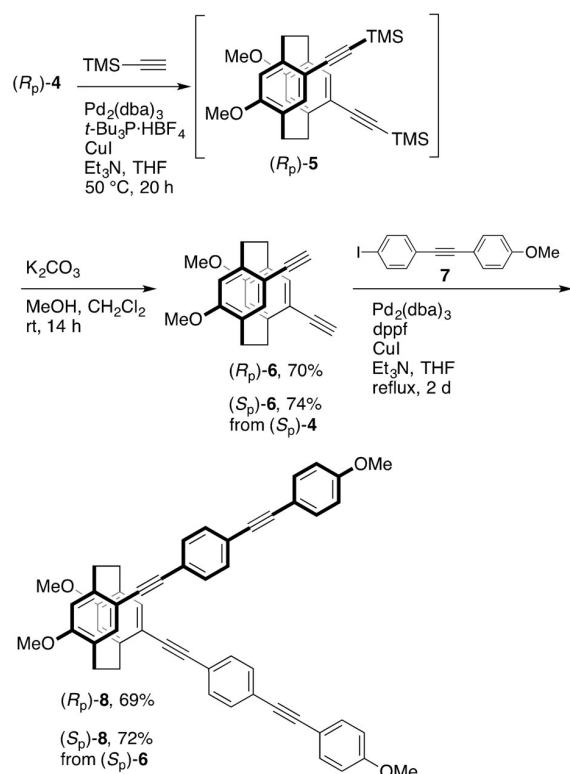
As shown in Scheme 2, the reaction of (*R<sub>p</sub>*)-**4** with trimethylsilylacetylene (TMS-acetylene) using Pd<sub>2</sub>(dba)<sub>3</sub> (dba = dibenzylideneacetone), tBu<sub>3</sub>P·HBF<sub>4</sub>, and CuI in Et<sub>3</sub>N and THF proceeded smoothly and afforded cross-coupling product (*R<sub>p</sub>*)-**5**, which was passed through a plug of SiO<sub>2</sub> column and used for the next reaction without further purification. The TMS groups of (*R<sub>p</sub>*)-**5** were easily removed by K<sub>2</sub>CO<sub>3</sub>/MeOH to afford new enantiopure chiral building block (*R<sub>p</sub>*)-**6** in 70% isolated yield from (*R<sub>p</sub>*)-**4**. Finally, the treatment of (*R<sub>p</sub>*)-**6** with **7** using a Pd/P/CuI catalytic system in Et<sub>3</sub>N and THF afforded the corresponding compound (*R<sub>p</sub>*)-**8** in 69% isolated yield. The enantiomer (*S<sub>p</sub>*)-**8** was also obtained following the same procedure (Scheme 2). The structures of new compounds in this study were confirmed by <sup>1</sup>H and <sup>13</sup>C NMR spectroscopy, and high-resolution mass spectrometry (HRMS). The detailed synthetic procedures as well as NMR spectra of the products are included in SI.

Chiral molecules (*R<sub>p</sub>*)- and (*S<sub>p</sub>*)-**8** are conjugated compounds in which two π-electron systems are stacked at terminal benzene rings to form a V-shaped secondary-ordered-structure. Their optical properties were compared with those of chiral molecules<sup>[12b]</sup> (*R<sub>p</sub>*)- and (*S<sub>p</sub>*)-**9** in which two π-electron systems are stacked at central benzene rings to form a X-shaped



Scheme 1. Optical resolution and transformations to produce planar chiral [2.2]paracyclophane building blocks.

second-order structure. The optical properties of both the enantiomers of **8** and **9** in the ground state were evaluated, and the UV and circular dichroism (CD) spectra, including data, are shown in Figure 2. In the UV spectrum of V-shaped molecule **8** in CHCl<sub>3</sub> (1.0 × 10<sup>-5</sup> M), the λ<sub>max</sub> was 345 nm with ε of 0.96 × 10<sup>5</sup> M<sup>-1</sup> cm<sup>-1</sup> (Figure 2A). In their CD spectra in CHCl<sub>3</sub> (1.0 × 10<sup>-5</sup> M), mirror image Cotton effects were observed in the absorption band. The Cotton effects of (*R<sub>p</sub>*)- and (*S<sub>p</sub>*)-**8** at the longest wavelength side were positive and negative, respectively.<sup>[15]</sup> On the other hand, UV spectrum of **9** is shown in Figure 2B. The absorption band was red-shifted in comparison with that of **8**, and its λ<sub>max</sub> was 361 nm with the ε of 0.68 × 10<sup>5</sup> M<sup>-1</sup> cm<sup>-1</sup> (Figure 2A). π-Electrons are delocalized through the two stacked π-electron systems, as explained by Bazan and co-workers,<sup>[16]</sup> leading to the red-shift in the UV spectra. In the CD spectra of (*R<sub>p</sub>*)- and (*S<sub>p</sub>*)-**9** (Figure 2B), more intense Cotton effects were observed. Their signs were opposite to those of (*R<sub>p</sub>*)- and (*S<sub>p</sub>*)-**8**; thus, the respective negative and positive Cotton effects at the longest wavelength side appeared for (*R<sub>p</sub>*)- and (*S<sub>p</sub>*)-**9**. Figures S7A and S7B show the CD spectra of (*S*)-isomers of **8** and **9** with the simulation results by time-dependent density functional theory (TD-DFT). These results indicate that the Cotton effects of V-shaped (*S<sub>p</sub>*)-**8** and X-shaped (*S<sub>p</sub>*)-**9** appear negative and positive, respectively, supporting the experimental results well.



Scheme 2. Synthesis of optically active V-shaped molecules.

Both chiral molecules of **8** and **9** emitted CPL with large  $g_{lum}$  values. Their CPL and PL spectra in  $CHCl_3$  ( $1.0 \times 10^{-5}$  M) are shown in Figure 3, and the PL decay curves are shown in Figure S6. The emission from V-shaped molecule **8** was observed with a peak top at 401 nm, and the absolute PL quantum yield ( $\Phi_{PL}$ ) was estimated to be 81% (Figure 3A). Intense CPL was observed at the emissive region, and the  $|g_{lum}|$  value was estimated to be  $1.3 \times 10^{-3}$ . The signs of  $(R_p)$ - and  $(S_p)$ -**8** were positive and negative, respectively, which are identical to those of the Cotton effects. The X-shaped molecule **9** in  $CHCl_3$  ( $1.0 \times 10^{-5}$  M) emitted PL with a peak top at 427 nm from the single component ( $\tau = 2.21$  ns with the  $\chi^2 = 1.12$ , Figure S6B), and the  $\Phi_{PL}$  value was 72%, as shown in Figure 3B. Slightly more intense CPL signals were observed in this case, and the  $|g_{lum}|$  value was calculated to be  $1.6 \times 10^{-3}$ . Also, an opposite CPL sign was observed; the respective signs of  $(R_p)$ - and  $(S_p)$ -**9** were negative and positive. As shown in Figure S8, the theoretical CPL spectra for  $(S_p)$ -isomers by TD-DFT supported the experimental results. Figure S9 shows the electronic transition dipole moments and magnetic transition dipole moments from S1 to S0 of  $(S_p)$ -**8** and **9**. The  $g_{lum}$  value is defined by  $4|\boldsymbol{\mu}||\mathbf{m}|\cos\theta/(|\boldsymbol{\mu}|^2 + |\mathbf{m}|^2)$ , where  $\boldsymbol{\mu}$  and  $\mathbf{m}$  represent electric and magnetic transition dipole moments, respectively, and the  $\theta$  is the angle between the  $\boldsymbol{\mu}$  and  $\mathbf{m}$ .<sup>[2,17]</sup> Basically, the  $|\mathbf{m}|^2$  can be neglected, and the  $g_{lum}$  simply represents  $4|\mathbf{m}|\cos\theta/|\boldsymbol{\mu}|$ . Thus,  $g_{lum}$  value is directly proportional to  $|\mathbf{m}|$  and inversely proportional to  $|\boldsymbol{\mu}|$ , while the  $\theta$  between the  $\boldsymbol{\mu}$  and  $\mathbf{m}$  is also an important factor.<sup>[2,17]</sup> The sign of a  $g_{lum}$  value is decided by the orientation

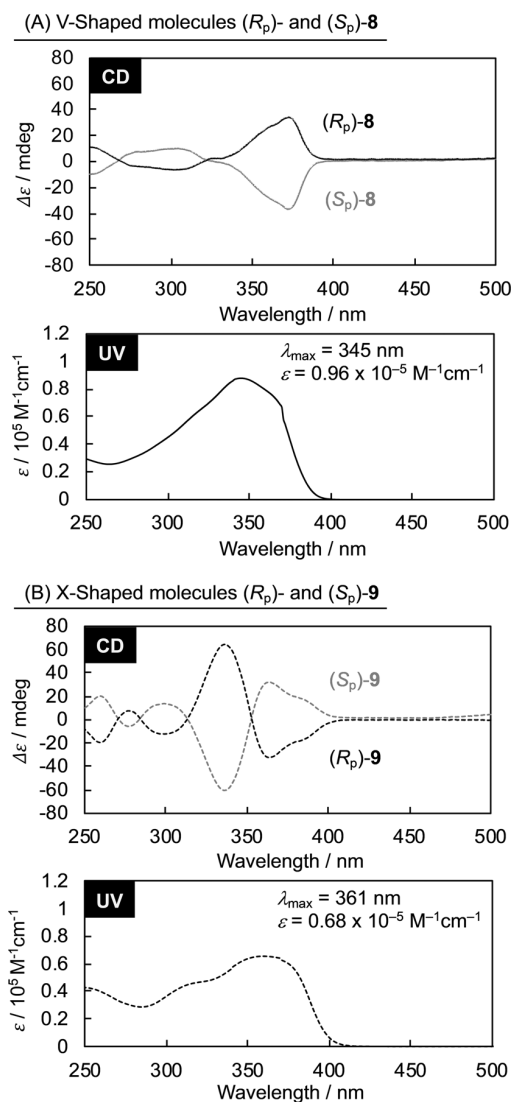
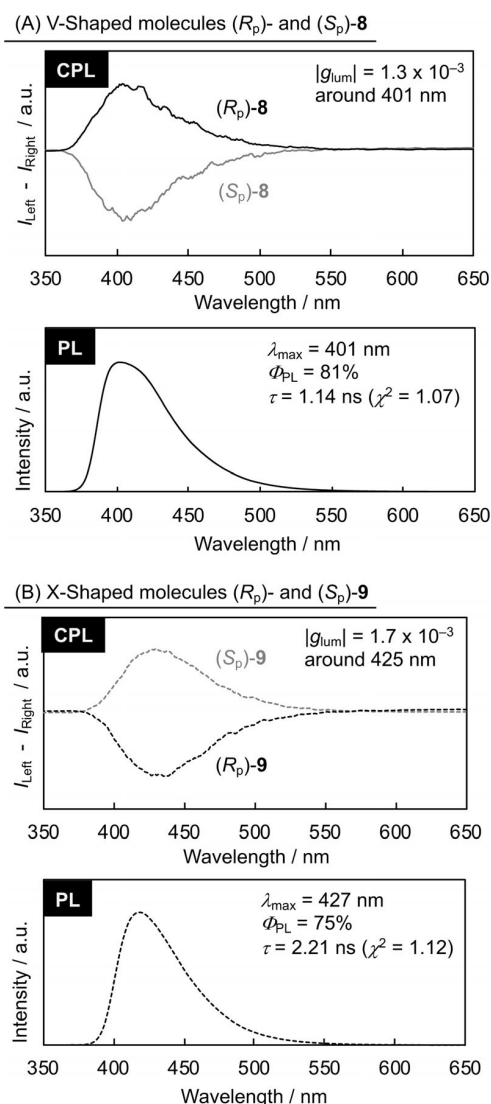


Figure 2. (A) UV-vis absorption and CD spectra of  $(R_p)$ - and  $(S_p)$ -**8** in  $CHCl_3$  ( $1.0 \times 10^{-5}$  M). (B) UV-vis absorption and CD spectra of  $(R_p)$ - and  $(S_p)$ -**9** in  $CHCl_3$  ( $1.0 \times 10^{-5}$  M).

of the dipole moments between  $\boldsymbol{\mu}$  and  $\mathbf{m}$ . As shown in Figure S9, the angle  $\theta$  between  $\boldsymbol{\mu}$  and  $\mathbf{m}$  of  $(S_p)$ -**8** was estimated to be  $144^\circ$ , and that of  $(S_p)$ -**9** was  $87^\circ$ .<sup>[18]</sup> Theoretical results suggested their negative and positive CPL signs for  $(S_p)$ -**8** and  $(S_p)$ -**9**, respectively, and supported the experimental results.

The important point of this study is that the orientation of two fluorophores decides the CPL sign. Stacking position of two fluorophores constructs the second-ordered structures such as V- and X-shaped orientations, leading to the opposite CPL signs, despite the same absolute configuration. Axially chiral molecules have achieved the CPL signal control, for example, by tuning the dihedral angle of binaphthyl units,<sup>[19]</sup> existence of neighboring groups,<sup>[20]</sup> and environmental changes.<sup>[21]</sup> This is the first study which reveals that a planar chiral molecule can control the CPL sign by changing the orientation of fluorophores.



**Figure 3.** (A) PL and CPL spectra of (*R<sub>p</sub>*)- and (*S<sub>p</sub>*)-**8** in CHCl<sub>3</sub> ( $1.0 \times 10^{-5}$  M). Excitation wavelength: absorption maximum for PL and 290 nm for CPL. (B) PL and CPL spectra of (*R<sub>p</sub>*)- and (*S<sub>p</sub>*)-**9** in CHCl<sub>3</sub> ( $1.0 \times 10^{-5}$  M). Excitation wavelength: absorption maximum for PL and 290 nm for CPL.

In conclusion, planar chiral building blocks based on bis-(*para*)-pseudo-*ortho*-type tetrasubstituted [2.2]paracyclophanes were prepared. Optically active molecules were synthesized from these enantiopure building blocks, resulting in two  $\pi$ -electron systems consisting of three benzene rings that are stacked at the terminal benzene rings to form a V-shaped structure. The V-shaped molecules emitted intense CPL with a high  $\Phi_{\text{PL}}$  (81%) and large  $g$  value ( $|g_{\text{lum}}| = 1.3 \times 10^{-3}$ ). Their optical properties were compared with those of corresponding X-shaped molecules, in which the same  $\pi$ -electron systems are stacked at the central benzene rings. The X-shaped molecules exhibited opposite CPL sign (as well as Cotton effect) as compared to that of the V-shaped molecules, and theoretical results supported the experimental results. Thus, stacking position of two  $\pi$ -electron systems leads to an opposite CPL signs

despite the same absolute configuration. In other words, the sign of CPL can be controlled by the orientation of the  $\pi$ -electron systems. These results suggest that the CPL sign can be controlled by the higher-ordered structure. Appropriate construction of the intermolecular orientations of  $\pi$ -electron systems in the solids, aggregates, and films can enhance the CPL intensity. However, even if a higher-ordered structure is constructed, there is the possibility that the CPL intensity may decrease due to the signal setoff, depending on the intermolecular orientations of  $\pi$ -electron systems (Figure S10). Recently, for example, it was reported that the  $g_{\text{lum}}$  value ( $|g_{\text{lum}}| = 2.5 \times 10^{-1}$ ) of the annealed thin film of optically active X-shaped molecule was 200 times greater than than the  $g_{\text{lum}}$  value ( $|g_{\text{lum}}| = 1.2 \times 10^{-3}$ ) in solution. Further preparation of optically active [2.2]paracyclophane-based compounds and construction of their higher-ordered structures are now in progress.

### Acknowledgements

This work was supported by Grant-in-Aid for Scientific Research on Innovative Areas (No. 17H05165 for Y.M. and 17H05148 for T.O.) “ $\pi$ -Figuration” from the Ministry of Education, Culture, Sports, Science and Technology, Japan. The financial support from the Nagase Science Technology Foundation is also acknowledged. Computation time was provided by the SuperComputer System, Institute for Chemical Research, Kyoto University. The authors are grateful to Professor Takuji Hatakeyama and Ms. Mayu Kameda (Department of Chemistry, School of Science and Technology, Kwansei Gakuin University) for PL decay studies.

### Conflict of interest

The authors declare no conflict of interest.

**Keywords:** [2.2]paracyclophane · circularly polarized luminescence · fluorophores · higher-ordered structures · planar chirality

- [1] For example, a) *Handbook of Conducting Polymers*, 3rd ed. (Eds.: T. A. Skotheim, R. L. Elsenbaumer, J. R. Reynolds), Marcel Dekker, New York, **2006**; b) *Organic Light Emitting Devices: Synthesis Properties and Application* (Eds.: K. Müellen, U. Scherf), Wiley-VCH, Weinheim, **2006**; c) *Organic Field-Effect Transistors* (Eds.: J. R. Groza, J. J. Locklin), CRC, Taylor & Francis, New York, **2007**; d) *Organic Photovoltaics: Materials, Device Physics, and Manufacturing Technologies* (Eds.: C. Brabec, V. Dyakonov, U. Scherf), Wiley-VCH, Weinheim, **2008**.
- [2] a) J. P. Riehl, F. S. Richardson, *Chem. Rev.* **1986**, *86*, 1–16; b) J. P. Riehl, F. Muller, *Comprehensive Chiroptical Spectroscopy*, Wiley, New York, **2012**.
- [3] a) C. J. Brown, A. C. Farthing, *Nature* **1949**, *164*, 915–916; b) D. J. Cram, H. Steinberg, *J. Am. Chem. Soc.* **1951**, *73*, 5691–5704.
- [4] a) *Cyclophane Chemistry: Synthesis Structures and Reactions* (Ed.: F. Vögtle), Wiley, Chichester, **1993**; b) *Modern Cyclophane Chemistry* (Eds.: R. Gleiter, H. Hopf), Wiley-VCH, Weinheim, **2004**; c) H. Hopf, *Angew. Chem. Int. Ed.* **2008**, *47*, 9808–9812; *Angew. Chem.* **2008**, *120*, 9954–9958.
- [5] a) D. J. Cram, N. L. Allinger, *J. Am. Chem. Soc.* **1955**, *77*, 6289–6294; b) V. Rozenberg, E. Sergeeva, H. Hopf in *Modern Cyclophane Chemistry* (Eds.: R. Gleiter, H. Hopf), Wiley-VCH, Weinheim, **2004**, pp. 435–462; c) G. J.

- Rowlands, *Org. Biomol. Chem.* **2008**, *6*, 1527–1534; d) S. E. Gibson, J. D. Knight, *Org. Biomol. Chem.* **2003**, *1*, 1256–1269; e) A. A. Aly, A. B. Brown, *Tetrahedron* **2009**, *65*, 8055–8089; f) J. Paradies, *Synthesis* **2011**, 3749–3766.
- [6] a) Y. Morisaki, Y. Chujo, *Angew. Chem. Int. Ed.* **2006**, *45*, 6430–6437; *Angew. Chem.* **2006**, *118*, 6580–6587; b) Y. Morisaki, Y. Chujo, *Polym. Chem.* **2011**, *2*, 1249–1257; c) Y. Morisaki, Y. Chujo, *Chem. Lett.* **2012**, *41*, 840–846; d) Y. Morisaki, S. Ueno, A. Saeki, A. Asano, S. Seki, Y. Chujo, *Chem. Eur. J.* **2012**, *18*, 4216–4224.
- [7] a) Y. Morisaki, R. Hifumi, L. Lin, K. Inoshita, Y. Chujo, *Polym. Chem.* **2012**, *3*, 2727–2730; b) Y. Morisaki, K. Inoshita, S. Shibata, Y. Chujo, *Polym. J.* **2015**, *47*, 278–281.
- [8] Y. Morisaki, K. Inoshita, Y. Chujo, *Chem. Eur. J.* **2014**, *20*, 8386–8390.
- [9] a) Y. Morisaki, M. Gon, T. Sasamori, N. Tokitoh, Y. Chujo, *J. Am. Chem. Soc.* **2014**, *136*, 3350–3353; b) M. Gon, Y. Morisaki, Y. Chujo, *J. Mater. Chem. C* **2015**, *3*, 521–529; c) M. Gon, H. Kozuka, Y. Morisaki, Y. Chujo, *Asian J. Org. Chem.* **2016**, *5*, 353–359; d) Y. Morisaki, R. Sawada, M. Gon, Y. Chujo, *Chem. Asian J.* **2016**, *11*, 2524–2527.
- [10] Y. Morisaki, R. Hifumi, L. Lin, K. Inoshita, Y. Chujo, *Chem. Lett.* **2012**, *41*, 990–992.
- [11] R. Sawada, M. Gon, J. Nakamura, Y. Morisaki, Y. Chujo, *Chirality* **2018**, *30*, 1109–1114.
- [12] a) M. Gon, Y. Morisaki, Y. Chujo, *Eur. J. Org. Chem.* **2015**, 7756–7762; b) M. Gon, Y. Morisaki, R. Sawada, Y. Chujo, *Chem. Eur. J.* **2016**, *22*, 2291–2298; c) M. Gon, R. Sawada, Y. Morisaki, Y. Chujo, *Macromolecules* **2017**, *50*, 1790–1802; d) Y. Sasai, H. Tsuchida, T. Kakuta, T. Ogoshi, Y. Morisaki, *Mater. Chem. Front.* **2018**, *2*, 791–795.
- [13] N. V. Vorontsova, V. I. Rozenberg, E. V. Sergeeva, E. V. Vorontsov, Z. A. Starikova, K. A. Lyssenko, H. Hopf, *Chem. Eur. J.* **2008**, *14*, 4600–4617.
- [14] G. Meyer-Eppler, E. Vogelsang, C. Benkhäuser, A. Schneider, G. Schnakenburg, A. Lützen, *Eur. J. Org. Chem.* **2013**, 4523–4532.
- [15] Sign of the Cotton effect of **8** can be explained by the exciton chirality method. For the exciton chirality method: see, N. Berova, K. Nakanishi in *Circular Dichroism: Principles and Applications 2nd ed.* (Eds.: N. Berova, K. Nakanishi, R. W. Woody), Wiley-VCH, New York, **2000**, pp. 337–382.
- [16] a) G. C. Bazan, W. J. Oldham, Jr., R. J. Lachicotte, S. Tretiak, V. Chernyak, S. Mukamel, *J. Am. Chem. Soc.* **1998**, *120*, 9188–9204; b) S. Wang, G. C. Bazan, S. Tretiak, S. Mukamel, *J. Am. Chem. Soc.* **2000**, *122*, 1289–1297; c) J. Zyss, I. Ledoux, S. Volkov, V. Chernyak, S. Mukamel, G. P. Bartholomew, G. C. Bazan, *J. Am. Chem. Soc.* **2000**, *122*, 11956–11962; d) G. P. Bartholomew, G. C. Bazan, *Acc. Chem. Res.* **2001**, *34*, 30–39; e) G. P. Bartholomew, G. C. Bazan, *Synthesis* **2002**, 1245–1255; f) G. P. Bartholomew, G. C. Bazan, *J. Am. Chem. Soc.* **2002**, *124*, 5183–5196; g) D. S. Seferos, D. A. Banach, N. A. Alcantar, J. N. Israelachvili, G. C. Bazan, *J. Org. Chem.* **2004**, *69*, 1110–1119; h) G. P. Bartholomew, M. Rumi, S. J. K. Pond, J. W. Perry, S. Tretiak, G. C. Bazan, *J. Am. Chem. Soc.* **2004**, *126*, 11529–11542; i) J. W. Hong, H. Y. Woo, G. C. Bazan, *J. Am. Chem. Soc.* **2005**, *127*, 7435–7443; j) G. C. Bazan, *J. Org. Chem.* **2007**, *72*, 8615–8635.
- [17] H. P. J. M. Dekkers in *Circular Dichroism: Principles and Applications, 2nd ed.* (Eds.: N. Berova, K. Nakanishi, R. W. Woody), Wiley-VCH, New York, **2000**, pp. 185–215.
- [18] Y. Nakakuki, T. Hirose, H. Sotome, H. Miyasaka, K. Matsuda, *J. Am. Chem. Soc.* **2018**, *140*, 4317–4326.
- [19] T. Kimoto, N. Tajima, M. Fujiki, Y. Imai, *Chem. Asian J.* **2012**, *7*, 2836–2841.
- [20] T. Amako, T. Kimoto, N. Tajima, M. Fujiki, Y. Imai, *RSC Adv.* **2013**, *3*, 6936–6944.
- [21] T. Kimoto, T. Amako, N. Tajima, R. Kuroda, M. Fujiki, Y. Imai, *Asian J. Org. Chem.* **2013**, *2*, 404–410.

Manuscript received: November 28, 2018

Revised manuscript received: January 7, 2019

Accepted manuscript online: January 8, 2019

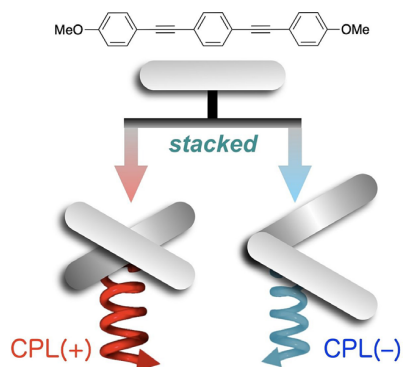
Version of record online: ■ ■ ■, 0000

## COMMUNICATION

Katsuaki Kikuchi, Jun Nakamura,  
Yuuya Nagata, Hiromu Tsuchida,  
Takahiro Kakuta, Tomoki Ogoshi,  
Yasuhiro Morisaki\*

■ ■ - ■ ■

Control of Circularly Polarized  
Luminescence by Orientation of  
Stacked  $\pi$ -Electron Systems



**CPL control:** Planar chiral 4,7,12,15-tetrasubstituted [2.2]paracyclophane building blocks were prepared. Chiral molecules, comprising of two fluorophores that were stacked to form a V-shaped higher-ordered structure, were synthesized from these building blocks. The V-shaped molecules emitted intense circularly polarized luminescence (CPL). The CPL sign of the X-shaped molecule was opposite to that of the V-shaped molecule, indicating that the CPL sign can be controlled by the orientation of the stacked fluorophores.



# Design of Thermochromic Luminescent Dyes Based on the Bis(*ortho*-carborane)-Substituted Benzobithiophene Structure

Kenta Nishino,<sup>[a]</sup> Yasuhiro Morisaki,<sup>[a, b]</sup> Kazuo Tanaka,<sup>\*[a]</sup> and Yoshiki Chujo<sup>[a]</sup>

**Abstract:** To obtain solid-state emissive materials having stimuli-responsive luminescent chromic properties without phase transition, benzobithiophenes modified with two *o*-carborane units having various substituents in the adjacent phenyl ring in *o*-carborane were designed and synthesized. Their emission colors were strongly affected not only by the substituents at the *para*-position of the phenyl ring but also

by molecular distribution in the solid state. In particular, the emission colors were changed by heating without crystal phase transition. It was proposed that their thermochromic properties were correlated not with isomerization but with the molecular motion at the distorted benzobithiophene moiety.

## Introduction

Thermochromic materials are versatile for thermometers, wide-tunable micro laser crystals and warning signals. There are many thermochromic dyes based on both organic and inorganic compounds such as liquid crystals,<sup>[1]</sup> stable radicals,<sup>[2]</sup> polymorphic compounds,<sup>[3]</sup> conjugated polymers,<sup>[4]</sup> leuco dyes,<sup>[5]</sup> Cu<sub>4</sub>I<sub>4</sub> clusters<sup>[6]</sup> and inorganic oxides.<sup>[7]</sup> Proposed mechanisms of these compounds are classified into 1) the changes in the structure by chemical reactions (i.e. neutral and biradical), 2) crystal phase transition (i.e. liquid crystals and polymorphic compounds), 3) switching of the energy back transfer (i.e. europium complexes), and 4) spin cross-over system (i.e. transition metal complexes).

Combination of “element-blocks”, which is defined as a minimum functional unit composed of heteroatoms, with conjugated system is one of valid strategies for fabricating advanced functions.<sup>[8]</sup> From this view point, the aryl-substituted *o*-carborane skeleton is a promising platform to obtain functional solid-state emissive materials.<sup>[9]</sup> From the first report on aggregation-induced emission (AIE) which can be detected only in the aggregation and condensed state,<sup>[10]</sup> the series of solid-state

emissive materials were discovered.<sup>[11]</sup> In particular, stimuli-responsive luminescent chromic behaviors were often found in these materials composed of the *o*-carborane “element-blocks”.<sup>[12]</sup> Therefore, a wide variety of luminescent chromism toward mechanical stresses, temperature changes and vapor fuming were demonstrated with the *o*-carborane-containing conjugated materials.<sup>[13]</sup> In these materials, luminescent chromism was generally caused by conformational or morphology changes in the solid materials. In order to obtain much sensitive materials, our next goal is to realize luminescent chromic behaviors without drastic structural changes as well as phase transition in the solid state.

We have reported synthesis and optical properties of bis(*o*-carborane)-substituted acenes.<sup>[12,14]</sup> Intense solid-state emission bands from the intramolecular charge transfer (ICT) state<sup>[15]</sup> in which the central aromatic system and the *o*-carborane unit, respectively worked as an electron donor and acceptor through the carbon in *o*-carborane can be observed in the solid state of these compounds. These *o*-carborane units also played a significant role in suppression of aggregation-caused quenching (ACQ) by disturbing intermolecular interaction because of steric hindrances. Except for luminescent properties, unique structural feature was found from the bis(*o*-carborane)-substituted aromatic ring. It should be remarked that the central anthracene moiety was critically distorted because of the bis(*o*-carborane) substitution according to the X-ray single crystal analyses.<sup>[12]</sup> From this fact, we presumed that electronic properties of the central distorted aromatic ring could be sensitive toward environmental factors, such as temperature and molecular morphology. In the cooling state or crystalline packing, molecular motions would be highly restricted. Thereby, the distorted center can work as an electron donor, and ICT emission is observable, similarly to the commodity system. Meanwhile, under heating condition or in the solution state, vigorous intramolecular motions should be induced around the distorted center. Therefore, solid-state emission can be varied by external stimuli through perturbation of the electronic state at the distorted center. Based on this assumption, we

[a] Dr. K. Nishino, Prof. Dr. Y. Morisaki, Prof. Dr. K. Tanaka, Prof. Dr. Y. Chujo  
Department of Polymer Chemistry  
Graduate School of Engineering  
Kyoto University  
Katsura, Nishikyo-ku, Kyoto 615-8510 (Japan)  
E-mail: tanaka@poly.synchem.kyoto-u.ac.jp

[b] Prof. Dr. Y. Morisaki  
Present address:  
Department of Applied Chemistry for Environment  
School of Science and Technology  
Kwansei Gakuin University  
2-1 Gakuen, Sanda, Hyogo 669-1337 (Japan)

 Supporting information and the ORCID identification number(s) for the author(s) of this article can be found under:  
<https://doi.org/10.1002/asia.201801529>

 This manuscript is part of a special issue on aggregation-induced emission. Click here to see the Table of Contents of the special issue.

designed the bis(*o*-carborane)-substituted molecule to demonstrate a luminescent chromic material without structural changes and phase transition.

Herein, synthesis and optical properties of bis(*o*-carborane)-substituted benzobithiophenes are reported. To clarify the structure-property relationship with luminescent behaviors, various substituents were introduced into the *para*-position of the adjacent phenyl ring in the *o*-carborane unit. From optical and structural analyses, it was found that the synthesized compounds had solid-state emission with the ICT characters, and especially, their emission colors were distinctly altered not only by the substituents at the *para*-position of the phenyl ring but also by molecular distribution in the solid state. Furthermore, thermochromic luminescent behaviors were obtained without crystal phase transition as we expected. Electronic structures at the distorted aromatic core created by the bis(*o*-carborane) substitution should be responsible for luminescent chromism.

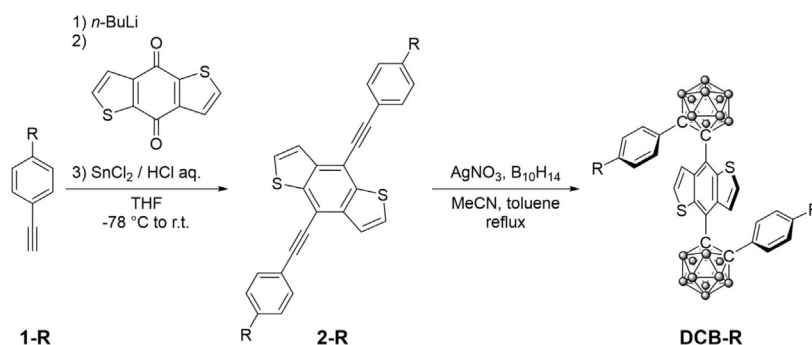
## Results and Discussion

Synthesis of **DCB-OMe** was performed by employing the previous method for the preparation of **DCB-R** (R=H, *t*Bu) as shown in Scheme 1.<sup>[16]</sup> Benzo[1,2-*b*:4,5-*b'*]dithiophene-4,8-dione was added to the THF solution of the lithiated ethynylbenzene derivative **1-OMe**. Following reduction with the quinone form of benzodithiophene by SnCl<sub>2</sub> in the HCl aq. solution, the diethynyl derivative **2-OMe** was obtained via the coupling reaction. After the decaborane insertion at the ethynyl moiety, **DCB-OMe** was obtained. **DCB-OH** was prepared by deprotection of the methoxy groups with BBr<sub>3</sub> (Scheme 2). All com-

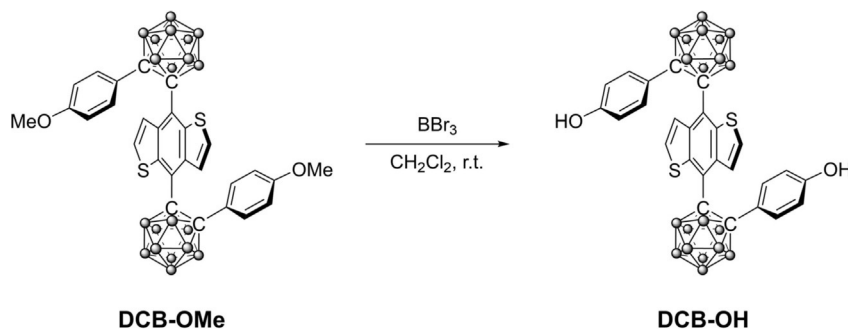
pounds were characterized by <sup>1</sup>H, <sup>11</sup>B and <sup>13</sup>C NMR spectroscopies (Charts S1–S9), elemental analyses and HRMS measurements. The products showed good stability and solubility in common organic solvents such as CHCl<sub>3</sub>, CH<sub>2</sub>Cl<sub>2</sub>, tetrahydrofuran (THF) and benzene. Thus, we concluded that the products should have the designed structures and enough stability for performing the series of measurements.

The X-ray single crystal analysis was applicable for determination of the structure of **DCB-OH** (Figure 1). The single crystal of **DCB-OH** was collected by recrystallization from benzene. Although the crystal incorporated benzene as a crystal solvent,  $\pi$ - $\pi$  interaction between benzene and aromatic rings was hardly observed. Therefore, electronic perturbations to **DCB-OH** by benzene should be negligible. Similarly to the crystal structure of **DCB-H** as reported in the previous study,<sup>[12]</sup> **DCB-OH** possessed the *cis*-type conformation in the crystal packing. In particular, it was found that **DCB-OH** had intermolecular and intramolecular hydrogen bonds. The distance of intermolecular and intramolecular hydrogen bonds were 1.907 and 1.938 Å, respectively. By the assistance with these hydrogen bonds, **DCB-OH** could be facilitated to form the *cis*-conformation and construct the dimeric structure.

From <sup>1</sup>H NMR spectroscopy, the conformations of the compounds were evaluated (Figure S1). In the previous report, it was demonstrated that **DCB-H** can form two types of structural isomers as the *cis*- and *trans*-conformations in the solution state although the *cis*-conformation was dominant in the crystal packing, and these structures were readily distinguishable by the signal patterns in the <sup>1</sup>H NMR spectra.<sup>[16]</sup> Based on this fact, next, to speculate the conformations of **DCB-OMe** and



Scheme 1. Synthesis of **DCB-R** (R=H, *t*Bu, CN, OMe).



Scheme 2. Synthesis of **DCB-OH**.

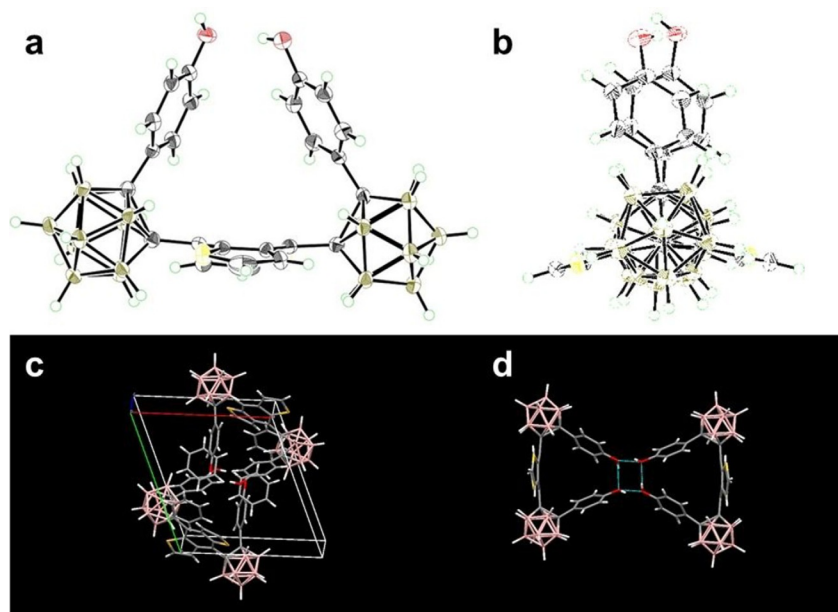


Figure 1. (a, b) ORTEP diagrams, (c) packing structure and (d) hydrogen bonds and dimeric structure of DCB-OH.

DCB-CN, variable-temperature  $^1\text{H}$  NMR spectra in  $\text{CD}_2\text{Cl}_2$  were measured (Figure S1). It was known that the signal peak at 8.5 ppm attributable to the *cis*-conformation was small even at low temperature. This result suggests that both compounds should form the *trans*-conformations. The energy differences between the *cis*- and *trans*-conformations of DCB-OMe were estimated by the calculation of thermodynamic parameters with the plot (Figure S2). As a result, it was observed that the enthalpy difference between both conformations was  $2.76 \text{ kJ mol}^{-1}$ , and the *trans*-conformation had more stable than the *cis*-one. Moreover, the peaks assigned to *cis*-conformation of DCB-CN were too small to prepare the plot. These data indicate that the DCB-OMe and DCB-CN should form the *trans*-conformation in the crystal state similarly to DCB-*t*Bu. It is likely that steric hindrances of the substituents contributed to formation of the *trans*-conformation.

The UV-vis absorption and photoluminescence (PL) spectra of DCB-R in THF ( $1.0 \times 10^{-5} \text{ M}$ ) were measured (Figure S3, Table 1). All samples showed the identical absorption spectra. The absorption bands in longer wavelength region had the peaks around 400 nm. These data suggest that the substituent group at the *para* position of the phenyl ring should slightly influence on the electronic structure in the ground state. In contrast, emission wavelengths of DCB-R were varied by the substituents. In particular, introduction of cyano groups induced red-shifted emission (Figure S3 b). Electron-withdrawing ability of the *o*-carborane units can be enhanced by cyano groups via the  $\sigma^*-\pi^*$  conjugation on the C–C bonds in the *o*-carborane unit. Thereby, the emission band should be influenced. It was presumed that emission should be originated from the ICT state according to the previous reports on photophysical properties of the aryl-substituted *o*-carborane derivatives.<sup>[9]</sup> To confirm this mechanism, UV-vis absorption and PL spectra were recorded in various solvents. Corresponding to

Table 1. Wavelengths of maximum absorbance and emission efficiencies of DCB-R under various conditions.							
R	$\lambda_{\text{abs}}$	$\lambda_{\text{THF}}$ [nm] <sup>[a]</sup>	$\Phi_{\text{PL}}$ <sup>[a,b]</sup>	$\lambda_{\text{agg}}$ [nm]	$\Phi_{\text{PL}}$ <sup>[b]</sup>	$\lambda_{\text{cry}}$ [nm]	$\Phi_{\text{PL}}$ <sup>[b]</sup>
H	403	682	0.12	638	0.23	614	0.90
OH	408	670	0.12	627	0.72	611	0.94
<i>t</i> Bu	404	698	0.03	615	0.43	586	0.67
OMe	406	686	0.02	628	0.25	563	0.64
CN	407	727	< 0.01	648	0.17	645	0.32

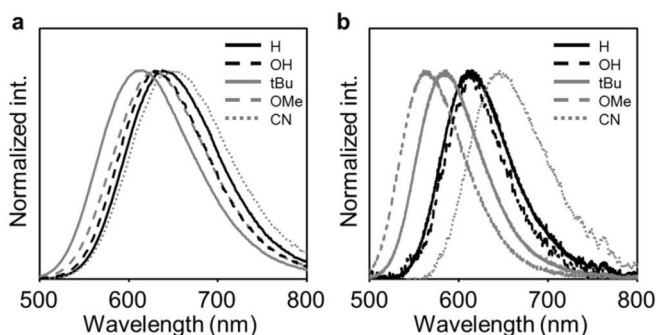
[a]  $1.0 \times 10^{-5} \text{ M}$ . [b] Determined as an absolute value with the integration sphere method.

the results from these previous reports,<sup>[9]</sup> the peak positions of absorption bands were detected at the similar positions, while bathochromic shifts were induced by increasing solvent polarity in the PL spectra (Figure S4, Table 2). From the Lippert–Mataga plots in which the extent of slopes of the fitting line represents the degree of the ICT character in the emission, it was shown that DCB-R showed the emission bands from the ICT state. Since the *o*-carborane units can work as a strong electron-accepting unit toward the central benzodithiophene unit, formation of the ICT state should proceed in the excited state.

Solid-state PL spectra of DCB-R were recorded at room temperature. Figure 2 shows the PL spectra in the crystalline state, and the results are listed in Table 1. All compounds showed blue-shifted emission compared to those in the THF solutions. It was implied that re-orientation energy could decrease in the aggregation with *o*-carboranes, and stabilization of the ICT state by solvation could be reduced.<sup>[17]</sup> As a result, blue-shifted emission bands were detected. The first impressive point is the peak positions of emission bands. Compared to the THF solutions, DCB-*t*Bu, DCB-OMe and DCB-CN which had the *trans*-

**Table 2.** Summary of changes in optical properties of DCB-R by altering solvent types.

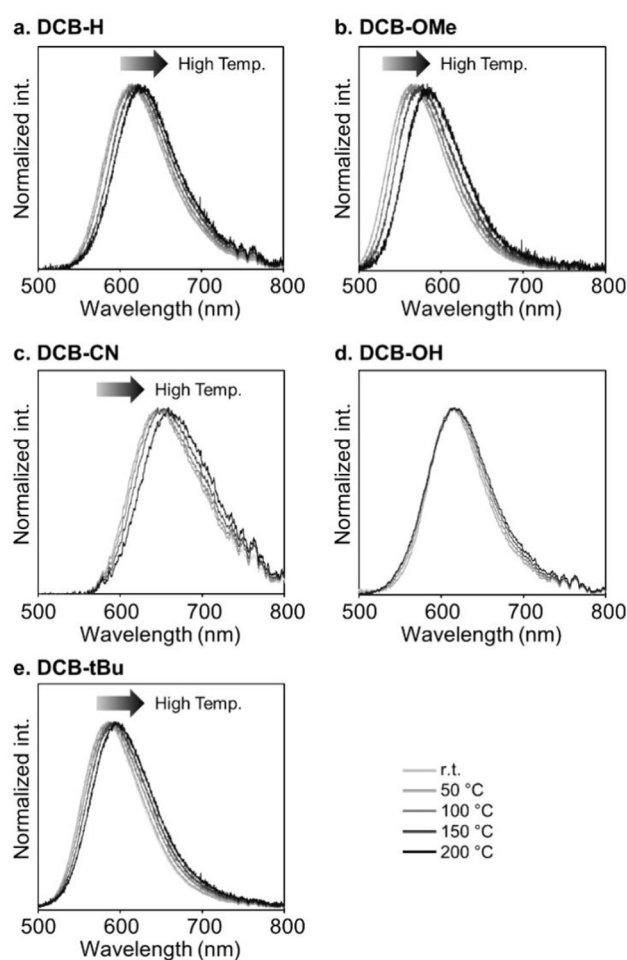
Solvent	DCB-H			DCB-tBu			DCB-OMe			DCB-CN			DCB-OH		
	$\lambda_{ab}$ [nm]	$\lambda_{PL}$ [nm]	$\Delta\lambda$ [cm <sup>-1</sup> ]	$\lambda_{ab}$ [nm]	$\lambda_{PL}$ [nm]	$\Delta\lambda$ [cm <sup>-1</sup> ]	$\lambda_{ab}$ [nm]	$\lambda_{PL}$ [nm]	$\Delta\lambda$ [cm <sup>-1</sup> ]	$\lambda_{ab}$ [nm]	$\lambda_{PL}$ [nm]	$\Delta\lambda$ [cm <sup>-1</sup> ]	$\lambda_{ab}$ [nm]	$\lambda_{PL}$ [nm]	$\Delta\lambda$ [cm <sup>-1</sup> ]
<i>n</i> -hexane	396	603	8668	402	614	8588	400	610	8606	401	624	8912	394	592	8488
benzene	401	658	9740	405	666	9676	406	668	9660	407	682	9907	401	639	9288
CHCl <sub>3</sub>	400	660	9848	404	670	9827	404	661	9623	405	686	10114	398	635	9377
THF	403	682	10151	404	689	10238	406	686	10053	406	727	10875	402	671	9972
CH <sub>2</sub> Cl <sub>2</sub>	400	681	10315	405	692	10240	405	685	10092	408	703	10285	398	658	9928
MeCN	402	714	10870	405	722	10840	404	709	10648	405	764	11602	397	686	10611



**Figure 2.** PL spectra in (a) the aggregation and (b) the crystalline state of DCB-R at room temperature.

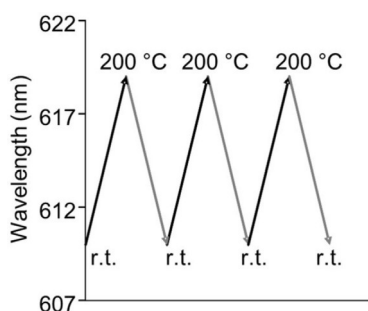
conformation presented emission bands in the shorter wavelength region than DCB-H and DCB-OH. In the previous report on the crystal packing of DCB-tBu, it was found that intramolecular twist was induced at the benzobithiophene moiety.<sup>[16]</sup> This conformational distortion should disturb electronic conjugation, followed by emission in the shorter wavelength region. Similar intramolecular twists could occur in DCB-OMe and DCB-CN. Another feature in the luminescent property was the dependency of emission efficiency on the conformation. Because of larger emission efficiencies in the crystalline state than those in the solution, it was clearly indicated that DCB-R had crystallization-induced emission enhancement properties. Moreover, in the crystalline state, the emission efficiencies of DCB-H and DCB-OH were relatively higher than those of DCB-tBu, DCB-OMe and DCB-CN. Although the *o*-carborane units located at both sides of the benzodithiophene moiety would suppress ACQ, lower emission properties could be caused by the intramolecular twist in the *trans* conformation of DCB-tBu, DCB-OMe and DCB-CN.

Stimuli-responsiveness of solid-state emission properties of DCB-R was evaluated by adding various types of external stimuli to the crystalline samples (Figures 3, 4, 5 and S5). Initially, thermochromic luminescent behaviors were investigated (Figure 3). The emission bands showed bathochromic shifts as temperature increased, and consequently luminescent color was gradually changed by heating (Figure S5). As a representative result, DCB-OMe showed the emission band around 570 nm at room temperature, and the bathochromic shift by 20 nm was observed by heating at 200 °C. In particular, it should be emphasized that this luminescent chromism pro-



**Figure 3.** Variable-temperature normalized PL spectra with solid DCB-R samples. All samples were placed on the cover glass and heated by a hot plate.

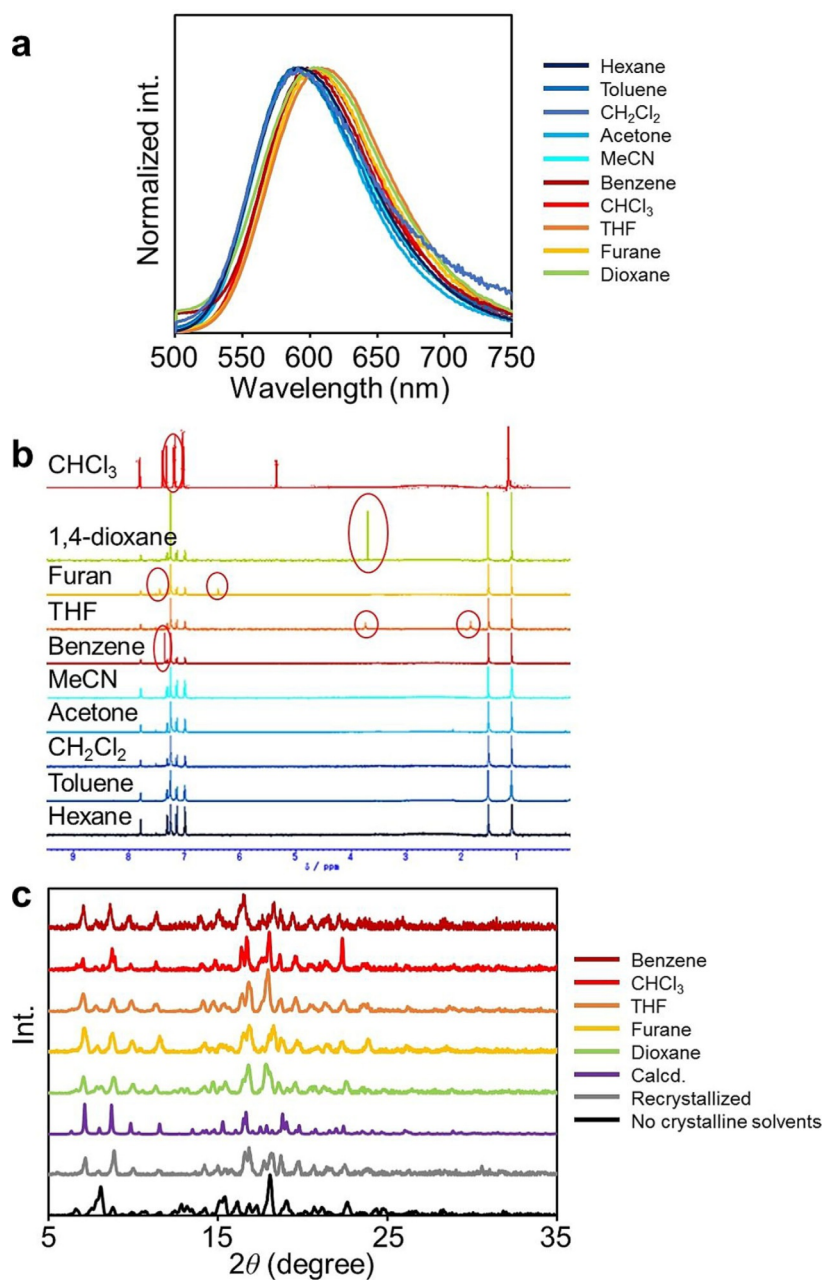
ceeded rapidly and repeatedly (Figure 4). The degree of luminescent chromism seemed to be independent of the conformations. Moreover, from DSC measurements, phase transitions were not observed in the detection temperature range from 0 to 220 °C (Figure S6). It is assumed that intramolecular motions might be induced by heating especially at the benzodithiophene moiety in which distortion of the molecular plane and twists between the connections with the *o*-carborane units were induced.<sup>[16]</sup> Indeed, emission intensities of all compounds decreased as temperature increased (Figure S7). This fact also supports that intramolecular motions should be activated by



**Figure 4.** Thermochromism of solid-state emission during stepwise heating and cooling cycles was performed with DCB-H.

heating, and luminescent properties were critically influenced. The crystalline sample of DCB-OH showed slight luminescent chromism. It is likely that intermolecular and intramolecular hydrogen bonds suppressed molecular motions even at high temperature.

The stimuli-responsiveness of the crystalline sample of DCB-*t*Bu toward another external stimulus such as fuming with organic volatile compounds (VOCs) was able to be examined owing to the largest value of emission efficiency in the crystalline state. Interestingly, emission color was changed by exposing other solvents such as benzene, CHCl<sub>3</sub>, THF, furan and 1,4-dioxane (Figure 5 a). In contrast, emission bands were insensitive to vapors of *n*-hexane, toluene, CH<sub>2</sub>Cl<sub>2</sub>, acetone and



**Figure 5.** (a) PL spectra (b) <sup>1</sup>H NMR spectra in CDCl<sub>3</sub> for CHCl<sub>3</sub>-fumed sample and CD<sub>2</sub>Cl<sub>2</sub> for others (red circles: solvent peaks of CHCl<sub>3</sub>, dioxane, furan, THF and benzene, respectively) and (c) PXRD patterns of DCB-*t*Bu after exposing with various solvents.

MeCN. From the  $^1\text{H}$  NMR measurements, it was found that the former solvents can be incorporated into the crystal packing (Figure 5b). Furthermore, from the powder X-ray diffraction analyses, different patterns were obtained from that of DCB-tBu with these encapsulated solvents (Figure 5c). Hence, it is suggested that vapochromic luminescent behaviors of DCB-tBu should be originated from the crystal-crystal phase transition by insertion of fumed VOCs into the crystal packing. Morphology changes could be reflected to luminescent chromism via the alteration of electronic structures of DCB-tBu.

The similar tendencies of a peak position and emission efficiency were also observed by the formation of amorphous states (Table 1). Aggregation was induced by the 100-folds dilution of the THF solution containing  $1.0 \times 10^{-3} \text{ M}$  DCB-R with deionized water. In the aggregation state, all compounds also demonstrated blue-shifted emission with larger emission efficiency compared to those in the THF solutions. These data mean that DCB-R should have the aggregation-induced emission enhancement (AIEE) property. Similarly to the crystalline samples, the molecules having the *trans*-conformation provided emission bands in the shorter wavelength region with larger emission efficiency. Intramolecular distortion could be responsible for optical properties. Significant AIEE was observed from DCB-OH. It is likely that intermolecular interaction could be disturbed by the hydrogen bond formation.

## Conclusions

Stimuli-responsiveness in the solid-state emissive properties of DCB-R via a unique process is demonstrated. Structural diversity was obtained from the derivatives with various types of substituents. In particular, these molecules showed rapid and reversible thermochromic luminescence in the crystalline state. From the series of analyses, a plausible mechanism was suggested. By heating, molecular motions should be activated in the crystalline packing. Then, the space to form thermally-stable conformations could be generated. As a result, extension of conjugated systems could occur, resulting in the bathochromic shifts of luminescence bands. Owing to small structural changes, rapid and reversible responses can be obtained. This strategy to tune luminescent color and to realize thermochromism could be useful for the construction the chemical sensors, smart windows, multi-color lasers and molecular thermometers.

## Acknowledgements

This work was partially supported by the Asahi Glass Foundation (for K.T.) and a Grant-in-Aid for Scientific Research (B) (JP17H03067) and (A) (JP17H01220), for Scientific Research on Innovative Areas "New Polymeric Materials Based on Element-Blocks (No.2401)" (JP24102013) and for Challenging Research (Pioneering) (JP18H05356).

## Conflict of interest

The authors declare no conflict of interest.

**Keywords:** carboranes • crystal packing • luminescence • photoluminescence • thermochromic materials • solid-state emission

- [1] I. Sage, *Liq. Cryst.* **2011**, *38*, 1551–1561.
- [2] a) Y. Morita, S. Suzuki, K. Fukui, S. Nakazawa, H. Kitagawa, H. Kishida, H. Okamoto, A. Naito, A. Sekine, Y. Ohashi, M. Shiro, K. Sasaki, D. Shiomi, K. Sato, T. Takui, K. Nakasuji, *Nat. Mater.* **2008**, *7*, 48–51; b) S. Matsumoto, T. Higashiyama, H. Akutsu, S. Nakatsuji, *Angew. Chem. Int. Ed.* **2011**, *50*, 10879–10883; *Angew. Chem.* **2011**, *123*, 11071–11075.
- [3] a) M. C. Torralba, M. Cano, J. A. Campo, J. V. Heras, E. Pinilla, M. R. Torres, *J. Organomet. Chem.* **2001**, *633*, 91–104; b) P. U. Biedermann, J. J. Stezowski, I. Agranat, *Chem. Eur. J.* **2006**, *12*, 3345–3354; c) S. Long, S. Parkin, M. A. Siegler, A. Cammers, T. Li, *Cryst. Growth Des.* **2008**, *8*, 4006–4013; d) P. Naumov, S. C. Lee, N. Ishizawa, Y. G. Jeong, I. H. Chung, S. Fukuzumi, *J. Phys. Chem. A* **2009**, *113*, 11354–11366.
- [4] a) R. R. Chance, R. H. Baughman, H. Müller, C. J. Eckhardt, *J. Chem. Phys.* **1977**, *67*, 3616–3618; b) R. R. Chance, *Macromolecules* **1980**, *13*, 396–398; c) A. Seeboth, D. Löttsch, R. Ruhmann, O. Muehling, *Chem. Rev.* **2014**, *114*, 3037–3068.
- [5] R. Kulčar, M. Friškovec, N. Hauptman, A. Vesel, M. K. Gunde, *Dyes Pigm.* **2010**, *86*, 271–277.
- [6] a) H. Kitagawa, Y. Ozawa, K. Toriumi, *Chem. Commun.* **2010**, *46*, 6302–6304; b) P. D. Harvey, M. Knorr, *Macromol. Rapid Commun.* **2010**, *31*, 808–826; c) S. Perruchas, C. Tard, X. F. Le Goff, A. Fargues, A. Garcia, S. Kahlal, J.-Y. Saillard, T. Gacoin, J.-P. Boilot, *Inorg. Chem.* **2011**, *50*, 10682–10692.
- [7] P. Kiri, G. Hyett, B. Russell, *Adv. Mater. Lett.* **2010**, *1*, 86–105.
- [8] a) Y. Chujo, K. Tanaka, *Bull. Chem. Soc. Jpn.* **2015**, *88*, 633–643; b) M. Gon, K. Tanaka, Y. Chujo, *Polym. J.* **2018**, *50*, 109–126.
- [9] a) H. Naito, K. Nishino, Y. Morisaki, K. Tanaka, Y. Chujo, *Angew. Chem. Int. Ed.* **2017**, *56*, 254–259; *Angew. Chem.* **2017**, *129*, 260–265; b) K. Nishino, H. Yamamoto, K. Tanaka, Y. Chujo, *Org. Lett.* **2016**, *18*, 4064–4067; c) H. Naito, K. Nishino, Y. Morisaki, K. Tanaka, Y. Chujo, *J. Mater. Chem. C* **2017**, *5*, 10047–10054; d) K. Nishino, K. Uemura, K. Tanaka, Y. Chujo, *Molecules* **2017**, *22*, 2009–2018; e) K. Nishino, Y. Morisaki, K. Tanaka, Y. Chujo, *New J. Chem.* **2017**, *41*, 10550–10554; f) H. Naito, K. Uemura, Y. Morisaki, K. Tanaka, Y. Chujo, *Eur. J. Org. Chem.* **2018**, 1885–1890; g) K. Nishino, K. Uemura, K. Tanaka, Y. Chujo, *New J. Chem.* **2018**, *42*, 4210–4214.
- [10] a) K. Kokado, Y. Chujo, *Macromolecules* **2009**, *42*, 1418–1420; b) K. Tanaka, K. Nishino, S. Ito, H. Yamane, K. Suenaga, K. Hashimoto, Y. Chujo, *Faraday Discuss.* **2017**, *196*, 31–42.
- [11] a) V. I. Bregadze, *Chem. Rev.* **1992**, *92*, 209–223; b) M. Scholz, E. Hey-Hawkins, *Chem. Rev.* **2011**, *111*, 7035–7062; c) R. Núñez, M. Terrés, A. Ferrer-Ugalde, F. F. d. Biani, F. Teixidor, *Chem. Rev.* **2016**, *116*, 14307–14378; d) F. Issa, M. Kassiou, L. M. Rendina, *Chem. Rev.* **2011**, *111*, 5701–5722; e) R. Núñez, I. Romero, F. Teixidor, C. Viñas, *Chem. Soc. Rev.* **2016**, *45*, 5147–5173; f) R. Furue, T. Nishimoto, I. S. Park, J. Lee, T. Yasuda, *Angew. Chem. Int. Ed.* **2016**, *55*, 7171–7175; *Angew. Chem.* **2016**, *128*, 7287–7291; g) S. Inagi, K. Hosoi, T. Kubo, N. Shida, T. Fuchigami, *Electrochemistry* **2013**, *81*, 368–370; h) D. Tu, P. Leong, S. Guo, H. Yan, C. Lu, Q. Zhao, *Angew. Chem. Int. Ed.* **2017**, *56*, 11370–11374; *Angew. Chem.* **2017**, *129*, 11528–11532; i) M. R. Son, Y.-J. Cho, S.-Y. Kim, H.-J. Son, D. W. Cho, S. O. Kang, *Phys. Chem. Chem. Phys.* **2017**, *19*, 24485–24492; j) Y. Chen, J. Guo, X. Wu, D. Jia, F. Tong, *Dyes Pigm.* **2018**, *148*, 180–188; k) A. Ferrer-Ugalde, J. Cabrera-González, E. J. Juárez-Pérez, F. Teixidor, E. Pérez-Inestrosa, J. M. Montenegro, R. Sillanpää, M. Haukka, R. Núñez, *Dalton Trans.* **2017**, *46*, 2091–2104; l) Z. Wang, T. Wang, C. Zhang, M. G. Humphrey, *Phys. Chem. Chem. Phys.* **2017**, *19*, 12928–12935; m) X. Li, Y. Yin, H. Yan, C. Lu, *Chem. Asian J.* **2017**, *12*, 2207–2210; n) S. Mukherjee, P. Thilagar, *Chem. Commun.* **2016**, *52*, 1070–1093; o) L. Böhlting, A. Brockhinke, J. Kahlert, L. Weber, R. A. Harder, D. S. Yufit, J. A. K. Howard, J. A. H. MacBride, M. A. Fox, *Eur. J. Inorg. Chem.* **2016**, 403–412; p) B. H.

- Choi, J. H. Lee, H. Hwang, K. M. Lee, M. H. Park, *Organometallics* **2016**, *35*, 1771–1777; q) D. Tu, P. Leong, Z. Li, R. Hu, C. Shi, K. Y. Zhang, H. Yan, Q. Zhao, *Chem. Commun.* **2016**, *52*, 12494–12497; r) M. Chaari, Z. Kelemen, J. G. Planas, F. Teixidor, D. Choquesillo-Lazarte, A. B. Salah, C. Viñas, R. Núñez, *J. Mater. Chem. C* **2018**, *6*, 11336–11347; s) J. C. Axtell, K. O. Kirlikovali, P. I. Djurovich, D. Jung, V. T. Nguyen, B. Munekiyo, A. T. Royappa, A. M. Spokoyny, *J. Am. Chem. Soc.* **2016**, *138*, 15758–15765; t) K. O. Kirlikovali, J. C. Axtell, K. Anderson, P. I. Djurovich, A. L. Rheingold, A. M. Spokoyny, *Organometallics* **2018**, *37*, 3122–3131; u) A. M. Prokhorov, T. Hofbeck, R. Czerwieńiec, A. F. Suleymanova, D. N. Kozhevnikov, H. Yersin, *J. Am. Chem. Soc.* **2014**, *136*, 9637–9642; v) Y. H. Lee, J. Park, J. Lee, S. U. Lee, M. H. Lee, *J. Am. Chem. Soc.* **2015**, *137*, 8018–8021; w) T. Kim, H. Kim, K. M. Lee, Y. S. Lee, M. H. Lee, *Inorg. Chem.* **2013**, *52*, 160–168; x) N. V. Nghia, J. Oh, J. Jung, M. H. Lee, *Organometallics* **2017**, *36*, 2573–2580.
- [12] H. Naito, Y. Morisaki, Y. Chujo, *Angew. Chem. Int. Ed.* **2015**, *54*, 5084–5087; *Angew. Chem.* **2015**, *127*, 5173–5176.
- [13] a) K. Nishino, K. Hashimoto, K. Tanaka, Y. Morisaki, Y. Chujo, *Sci. China Chem.* **2018**, *61*, 940–946; b) H. Mori, K. Nishino, K. Wada, Y. Morisaki, K. Tanaka, Y. Chujo, *Mater. Chem. Front.* **2018**, *2*, 573–579; c) K. Nishino, H. Yamamoto, K. Tanaka, Y. Chujo, *Asian J. Org. Chem.* **2017**, *6*, 1818–1822.
- [14] H. Naito, K. Nishino, Y. Morisaki, K. Tanaka, Y. Chujo, *Chem. Asian J.* **2017**, *12*, 2134–2138.
- [15] a) K. Kokado, Y. Chujo, *J. Org. Chem.* **2011**, *76*, 316–319; b) L. A. Boyd, W. Clegg, R. C. B. Copley, M. G. Davidson, M. A. Fox, T. G. Hibbert, J. A. K. Howard, A. Mackinnon, R. J. Peace, K. Wade, *Dalton Trans.* **2004**, 2786–2799; c) S. Kwon, K.-R. Wee, Y.-J. Cho, S. O. Kang, *Chem. Eur. J.* **2014**, *20*, 5953–5960.
- [16] K. Nishino, K. Uemura, K. Tanaka, Y. Morisaki, Y. Chujo, *Eur. J. Org. Chem.* **2018**, 1507–1512.
- [17] Q. Wu, T. Zhang, Q. Peng, D. Wang, Z. Shuai, *Phys. Chem. Chem. Phys.* **2014**, *16*, 5545–5552.

Manuscript received: October 17, 2018

Revised manuscript received: November 16, 2018

Accepted manuscript online: November 16, 2018

Version of record online: November 28, 2018

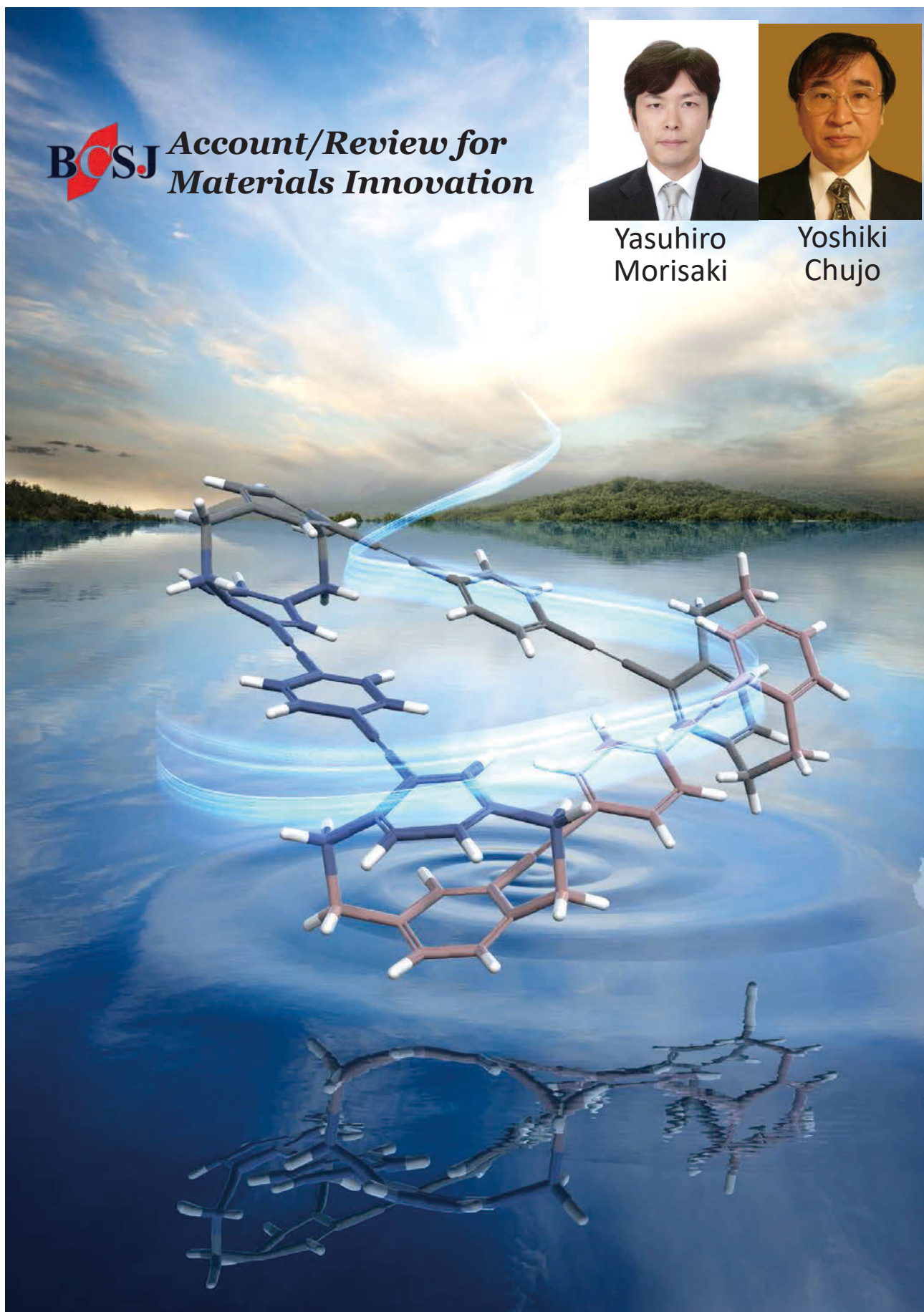
**BCSJ** *Account/Review for  
Materials Innovation*



Yasuhiro  
Morisaki



Yoshiki  
Chujo



## Planar Chiral [2.2]Paracyclophanes: Optical Resolution and Transformation to Optically Active $\pi$ -Stacked Molecules

Yasuhiro Morisaki\*<sup>1</sup> and Yoshiki Chujo\*<sup>2</sup>

<sup>1</sup>Department of Applied Chemistry for Environment, School of Science and Technology, Kwansai Gakuin University, 2-1 Gakuen, Sanda, Hyogo 669-1337, Japan

<sup>2</sup>Department of Polymer Chemistry, Graduate School of Engineering, Kyoto University, Nishikyo-ku, Kyoto 615-8510, Japan

E-mail: ymo@kwansai.ac.jp (Y. Morisaki), chujo@poly.synchem.kyoto-u.ac.jp (Y. Chujo)

Received: September 5, 2018; Accepted: October 19, 2018; Web Released: November 3, 2018



### Yasuhiro Morisaki

Yasuhiro Morisaki is Professor at Kwansai Gakuin University. He graduated from Kyoto University in 1995, and then, he received his Ph.D. from Kyoto University in 2000. After a six-month postdoctoral stay at Osaka National Research Institute, he joined the group of Professor Yoshiki Chujo as Assistant Professor at Kyoto University in 2000. From 2004 to 2005, he carried out postdoctoral work at the University of Alberta. He became Lecturer at Kyoto University in 2008 and Full Professor at Kwansai Gakuin University in 2015. His research interests focus on polymer and organic synthesis, in particular, cyclophane chemistry.



### Yoshiki Chujo

Yoshiki Chujo is Professor Emeritus of Kyoto University. He completed his Ph.D. at Kyoto University in 1980 and then joined Nagoya University as Assistant Professor in 1981. In 1983, he joined the group of J. McGrath at Virginia Polytechnic Institute as a postdoctoral research fellow. He returned to Kyoto University as Lecturer in 1986 and was a Professor of polymer chemistry there from 1994 to 2018. His research interests focus on polymer synthesis, inorganic polymers, and polymeric hybrid materials. He was a project leader of the Grant-in-Aid for Scientific Research on Innovative Areas "New Polymeric Materials Based on Element-Blocks", MEXT, Japan (2012–2018).

### Abstract

In this article, our recent results from practical optical resolution methods of disubstituted and tetrasubstituted [2.2]paracyclophane compounds and their transformations are described. The obtained enantiopure [2.2]paracyclophane compounds have been used as chiral building blocks to prepare optically active  $\pi$ -stacked molecules.  $\pi$ -Stacked molecules construct optically active second-ordered structures, such as V-, N-, M-, X-, triangle-shaped, and one-handed double helical structures, due to the orientation of stacked  $\pi$ -electron systems. They emit circularly polarized luminescence (CPL) by photo-excitation. [2.2]Paracyclophane-based chiral  $\pi$ -stacked molecules in this article emit brightly owing to good photoluminescence (PL) quantum efficiencies as well as large molar extinction coefficients. In particular, emission is of course CPL with a large dissymmetry factor ( $g_{\text{lum}}$  value). It is basically difficult to achieve CPL with high brightness, high PL efficiency, and

large  $g_{\text{lum}}$  value by using other chiral scaffolds; therefore, planar chiral [2.2]paracyclophane is an ideal scaffold to be an excellent CPL emitters.

**Keywords:** Planar chirality | [2.2]Paracyclophane | Circularly polarized luminescence

### 1. Introduction

Cyclophane is a general term for cyclic compounds containing at least one aromatic ring in the main chain skeleton and are well-known, particularly in the field of synthetic organic chemistry.<sup>1</sup> The typical example is [2.2]paracyclophane. [2.2]Paracyclophane was synthesized and isolated for the first time in 1949 as a pyrolysis product of *para*-xylene.<sup>2</sup> In 1951, a direct synthesis from 1,4-bis-bromomethylbenzene by Wurtz-type intramolecular cyclization reaction was reported,<sup>3</sup>

and various synthetic methods have been developed after that. [2.2]Paracyclophane has a unique  $\pi$ -stacked structure in which two benzene rings are fixed in the *para*-position with two ethylene chains, and there have been many studies on its reactivities and physical properties in the field of organic chemistry.<sup>1</sup>

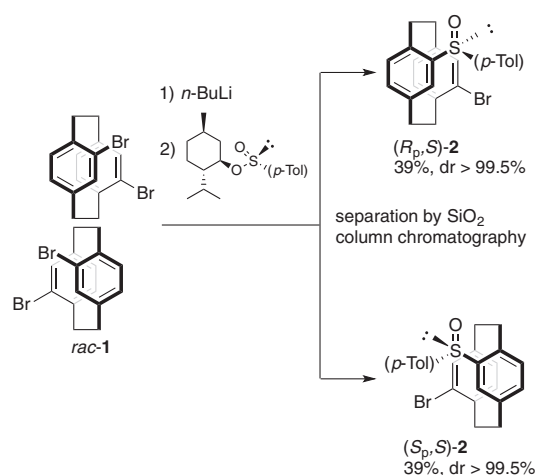
On the other hand, there are not many examples where [2.2]paracyclophane was effectively utilized in the field of polymer chemistry and materials chemistry.<sup>4–7</sup> Under such circumstances, the authors have focused on the  $\pi$ -stacked structure of [2.2]paracyclophane and synthesized various conjugated polymers and oligomers possessing [2.2]paracyclophane in the main chain.<sup>4</sup> In other words, by repeatedly incorporating pseudo-*para*-disubstituted [2.2]paracyclophane into the conjugated polymer main chain, we have synthesized  $\pi$ -electron-systems-stacked polymers in which the  $\pi$ -electron systems were partially stacked. Since their physical properties continuously change depending on the number of the stacked  $\pi$ -electron systems,<sup>8</sup> they were named through-space conjugated polymers. In addition, by precisely designing the stacked  $\pi$ -electron systems (by controlling the energy bandgaps as well as overlap integrals of the stacked  $\pi$ -electron systems), we achieved highly efficient (energy transfer efficiency ( $\Phi_{ET}$ ) > 0.99 and the rate of energy transfer ( $k_{ET}$ ) >  $10^{12}$  s<sup>-1</sup>) unidirectional fluorescence resonance energy transfer (FRET) through space. Thus, [2.2]paracyclophane-based through-space conjugated polymers and oligomers can act as single molecular wires.<sup>9</sup>

[2.2]Paracyclophane has two benzene rings fixed at a close distance (approximately 3.0 Å); therefore, the rotational movement of the benzene rings is suppressed. By introducing a substituent at appropriate positions of the benzene ring(s), the resulting [2.2]paracyclophane becomes a structurally stable planar chiral compound.<sup>10</sup> Such planar chirality of [2.2]paracyclophane has been utilized as a chiral auxiliary or chiral ligand in the field of synthetic organic chemistry and organometallic chemistry; however, it has not been used in the fields of polymer chemistry and materials chemistry.

The authors focused attention on the planar chirality of [2.2]paracyclophane and have applied it to polymer chemistry and materials chemistry, not only to develop practical optical resolution methods of [2.2]paracyclophane compounds, but also to use them as chiral building blocks. In this article, we wish to introduce our latest results, focusing on the synthesis of optically active disubstituted and tetrasubstituted [2.2]paracyclophanes and the preparation of optically active  $\pi$ -electron-systems-stacked molecules for their application in optoelectronic materials.

## 2. Optical Resolution of Disubstituted [2.2]Paracyclophane and Syntheses of Optically Active $\pi$ -Stacked Molecules

The authors reported the synthesis and properties of through-space conjugated polymers incorporating not only pseudo-*para*-disubstituted [2.2]paracyclophane, but also pseudo-*ortho*-disubstituted [2.2]paracyclophane in the main chain.<sup>11</sup> Therefore, we started our research with the idea of synthesizing an optically-active through-space conjugated polymer using an optically-active pseudo-*ortho*-disubstituted [2.2]paracyclophane compound as a co-monomer. However, after examin-



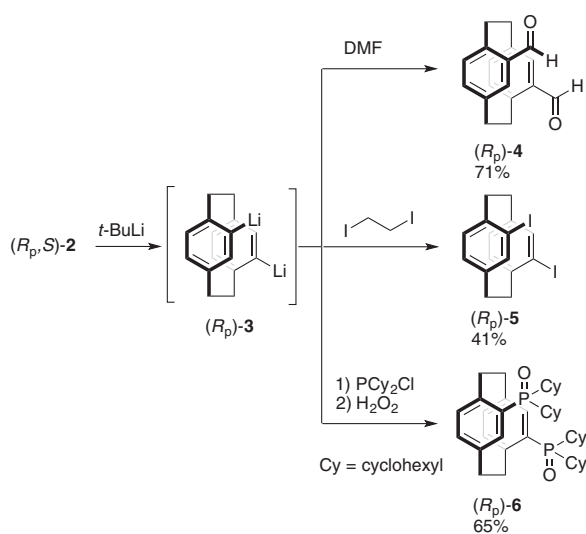
**Scheme 1.** Optical resolution of pseudo-*ortho*-disubstituted [2.2]paracyclophane.

ing optical resolution methods of pseudo-*ortho*-disubstituted [2.2]paracyclophane reported previously,<sup>12</sup> we found it difficult to conclude that any of them were practical for application to our strategy. For this reason, we started by working on developing a new optical resolution method (Scheme 1).

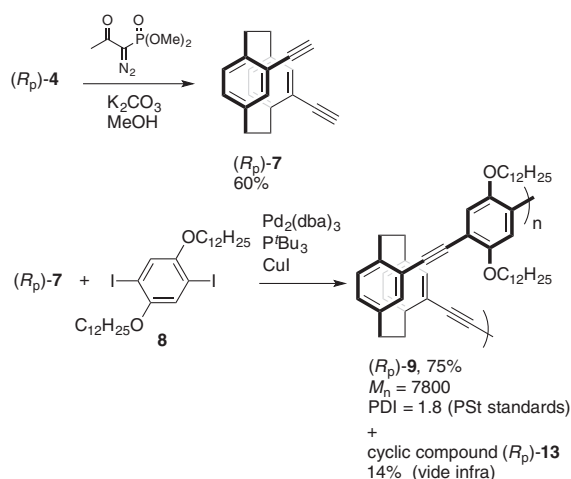
Racemic pseudo-*ortho*-dibromo[2.2]paracyclophane *rac-1* was monolithiated by reaction with *n*-butyllithium (*n*-BuLi), and by allowing (1*R*,2*S*,5*R*)-(–)-menthyl-*p*-toluenesulfinate to react with this, we obtained the diastereomers (*R<sub>p</sub>*,*S*)- and (*S<sub>p</sub>*,*S*)-**2** (the planar chirality *R* and *S* is represented by *R<sub>p</sub>* and *S<sub>p</sub>*, respectively). These were separable by simple column chromatography using silica gel, and each could be isolated with 39% yield.<sup>13</sup> The absolute configuration was determined by X-ray crystallography.

When the isolated diastereomers were reacted with (*t*-butyllithium) *t*-BuLi, not only did the lithium-halogen exchange reaction proceed, but the lithium-sulfur exchange reaction also proceeded,<sup>10c,14,15</sup> which led to the formation of the chiral dilithiated intermediate **3** (Scheme 2). The subsequent reaction with dimethylformamide (DMF) gave optically active pseudo-*ortho*-diformyl[2.2]paracyclophane **4**. Intermediate **3** could be reacted with various electrophiles (e.g., diiodoethane or phosphine chloride) instead of DMF to give corresponding planar chiral molecules (Scheme 2).<sup>13</sup> That is, we can say that the diastereomers (*R<sub>p</sub>*,*S*)- and (*S<sub>p</sub>*,*S*)-**2** are parent compounds capable of creating a wide variety of planar chiral [2.2]paracyclophanes and that this method is a practical optical resolution method. (*R<sub>p</sub>*)- and (*S<sub>p</sub>*)-diformyl[2.2]paracyclophanes (*R<sub>p</sub>*)- and (*S<sub>p</sub>*)-**4** could be separated by chiral column chromatography using a Chiralpak IA column; thus, their chromatographic optical resolution is also possible.<sup>13</sup>

Pseudo-*ortho*-diethynyl[2.2]paracyclophane **7** was synthesized using the optically active compound **4**, by the Chira-Bestmann reagent (Scheme 3).<sup>16</sup> Next, using compound **7** as the co-monomer, Sonogashira-Hagihara coupling<sup>17</sup> polymerization with diiodobenzene derivative **8** was carried out to obtain the corresponding optically active through-space conjugated polymer **9**.<sup>18</sup> Evaluation of chiroptical properties (chiral optical properties) of polymer **9** revealed the intense circularly



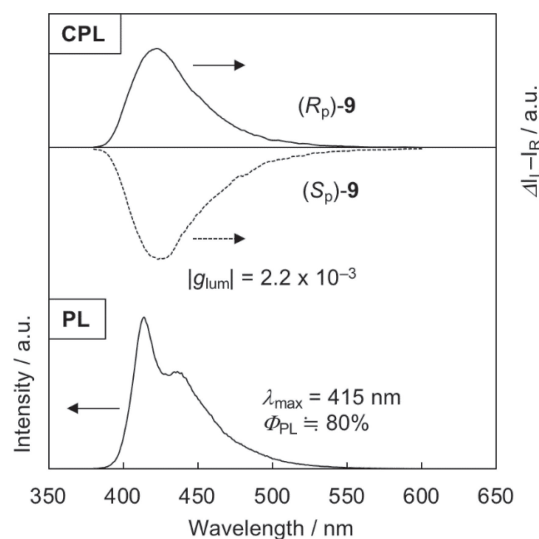
**Scheme 2.** Transformation of (*R<sub>p</sub>*,*S*)-**2** to various planar chiral compounds.



**Scheme 3.** Synthesis of optically active polymer.

polarized luminescence (CPL) in the emission region ( $\Phi_{\text{PL}}$  = absolute PL quantum yield) of the stacked  $\pi$ -electron system in a dilute chloroform solution (Figure 1). CPL is a phenomenon where there is a difference in the emission intensity between left-handed and right-handed circularly polarized light, and this difference is evaluated using a normalized value as the anisotropic factor:  $g_{\text{lum}}$  value = [(emission intensity of left-handed CPL) – (emission intensity of right-handed CPL)] / (emission intensity).<sup>19</sup> The  $|g_{\text{lum}}|$  value for polymer **9** at  $\lambda_{\text{PL,max}}$  was estimated to be  $2.2 \times 10^{-3}$ .

To better understand the behavior of CPL of polymer **9**, we decided to investigate the chiroptical properties using oligomers with well-defined molecular weight.<sup>20</sup> Optically active [2.2]paracyclophanes **5** and **7** were employed as building blocks to synthesize the optically active oligomers **10–13**, as shown in Figure 2. In other words, chiroptical properties were investigated by synthesizing two to four  $\pi$ -electron-system-layered structures and a cyclic structure in which three  $\pi$ -



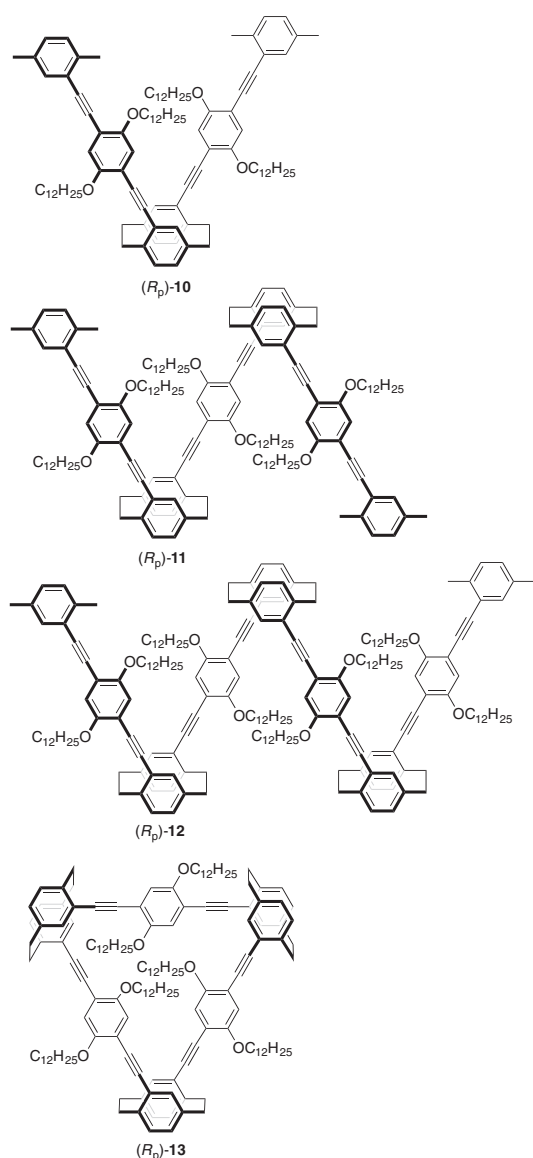
**Figure 1.** CPL and PL spectra of (*R<sub>p</sub>*)- and (*S<sub>p</sub>*)-**9** in  $\text{CHCl}_3$  ( $10 \times 10^{-5}$  M) excited at 290 nm for CPL and  $\lambda_{\text{abs,max}}$  for PL.

electron-systems are layered (isolated as a by-product of Scheme 3<sup>18</sup>).

Table 1 shows the absolute anisotropic factors of absorbance:  $g_{\text{abs}}$  value = [(molar absorption coefficient of left-handed circular polarized light) – (molar absorption coefficient of right-handed circular polarized light)] / (molar absorption coefficient) at  $\lambda_{\text{abs,max}}$  calculated from the circular dichroism (CD) spectra of the synthesized optically active oligomers, and the  $|g_{\text{lum}}|$  values at  $\lambda_{\text{PL,max}}$  calculated from CPL spectra. As a result, for **10** to **12**, the  $g_{\text{abs}}$  value showed a substantially constant value of  $3.0 \times 10^{-3}$ , regardless of the number of stacked  $\pi$ -electron systems. It is suggested that linearly  $\pi$ -stacked structures of **10–12** can adopt various conformations in the dilute solution in the ground state, leading to the constant  $g_{\text{abs}}$  values that reflected the optically-active V-shaped skeleton of the cyclophane moiety. Since the  $g_{\text{abs}}$  value is a normalized value, it can be understood that there is no change in the value as the number of stacked  $\pi$ -electron systems increases. Contrarily, the  $g_{\text{lum}}$  values of **10** to **12** increased depending on the number of stacked  $\pi$ -electron systems. This result indicates that some sort of chirality is induced in addition to the optically active V-shaped structure of the cyclophane moiety in the excited state.

On the other hand, we observed a difference in the  $g_{\text{abs}}$  values of linear  $\pi$ -stacked trimer **11** and the cyclic  $\pi$ -stacked trimer **13**, where the  $g_{\text{abs}}$  value of **13** was larger than that of **11**. The cyclic structure forms a fixed optically-active triangle (fixed optically-active second-ordered structure), whereas the linear  $\pi$ -stacked structure adopts various conformations in the ground state. That is, it can be surmised that the cyclic structure exhibited a large  $g_{\text{abs}}$  value as the chirality of the second-ordered structure was contributed to the optically active V-shaped structure.

Interestingly, the  $g_{\text{lum}}$  values of the linearly  $\pi$ -stacked trimer **11** and the cyclic trimer **13** were identical. This indicated that both adopt the same or similar structure in the excited



**Figure 2.** Structures of oligomers. ( $R_p$ )-Isomers are shown.

**Table 1.** Absolute  $g$  values of oligomers

oligomer	$ g_{\text{abs}} $	$ g_{\text{lum}} $
<b>10</b>	$2.9 \times 10^{-3}$	$1.8 \times 10^{-3}$
<b>11</b>	$3.0 \times 10^{-3}$	$2.2 \times 10^{-3}$
<b>12</b>	$3.0 \times 10^{-3}$	$2.6 \times 10^{-3}$
<b>13</b>	$3.7 \times 10^{-3}$	$2.2 \times 10^{-3}$

state. *para*-Arylene, *para*-arylene-vinylene and *para*-arylene-ethynylene, etc., are known to form a planar structure by excitation.<sup>21</sup> This is because the quinoid structure contributes in the excited state, and the rotatable single bond gains double bond features. Considering the excited state of the linearly  $\pi$ -stacked trimers in this manner, since each of the three  $\pi$ -electron systems assumes a planar structure, the molecule should form either a zigzag structure or a helical structure (foldamer) (Figure 3). The  $g_{\text{lum}}$  values of **11** and **13** being the

identical; thus, it is speculated that in the excited state, molecule **11** forms a structure similar to a cyclic structure, that is, a one-handed helical structure (= optically active second-ordered structure).

Although we cannot conclude that whole polymer **9** forms a one-handed helical structure in the excited state, helical contribution should be present. As such, the optically active through-space conjugated polymer was thought to exhibit intense CPL even in the dilute solution to form an optically active second-ordered structure (one-handed helix). This is the first example of a planar chiral molecule emitting CPL and also that employs optically active [2.2]paracyclophane in the field of polymer and materials chemistry. After our report on development of optical resolution of pseudo-*ortho*-disubstituted [2.2]paracyclophane by the diastereomer method in 2012, Lützen and coworkers reported the chromatographic optical resolution of pseudo-*ortho*-disubstituted [2.2]paracyclophane and syntheses of various optically active compounds in 2013.<sup>22</sup> Hasegawa and coworkers also reported the chromatographic optical resolution of pseudo-*ortho*-disubstituted [2.2]paracyclophane in 2014 and the application in a chiral dopant for liquid crystals in 2017.<sup>23</sup>

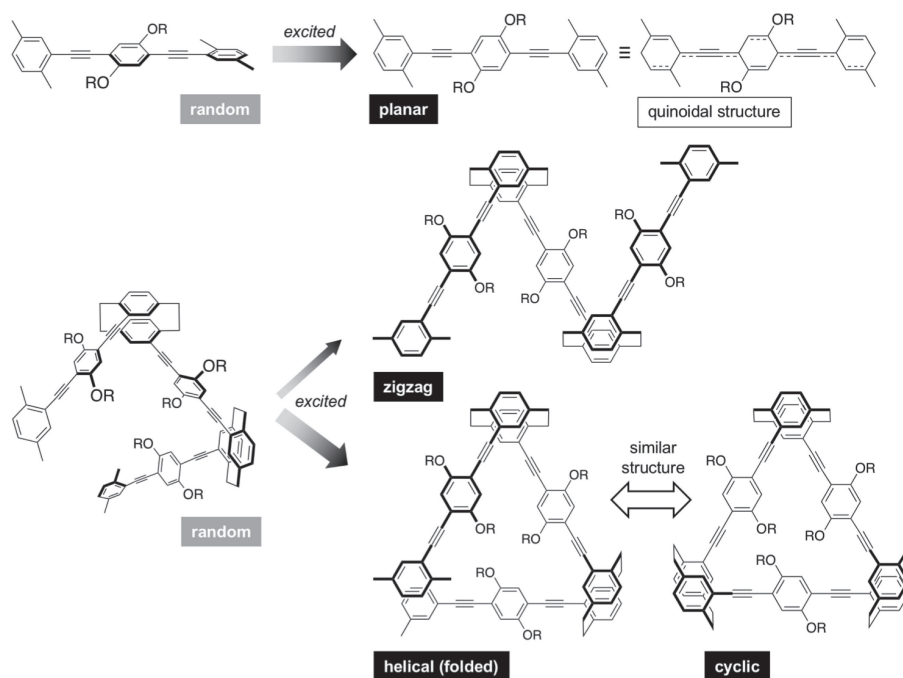
### 3. Optical Resolution of 4,7,12,15-Tetrasubstituted [2.2]Paracyclophane and Syntheses of Optically Active $\pi$ -Stacked Molecules

The authors' next target was tetrasubstituted [2.2]paracyclophane. We focused on the synthesis and applications of optically active X-shaped molecules and studied the optical resolution of 4,7,12,15-tetrasubstituted [2.2]paracyclophane. Scheme 4 shows the optical resolution method developed,<sup>24</sup> the racemate 4,7,12,15-tetrabromo[2.2]paracyclophane *rac*-**14** was synthesized by improving upon a previous report.<sup>25</sup> One of the bromo groups was converted to a hydroxy group to synthesize *rac*-**15**, and its reaction with (1*S*,4*R*)-(-)-camphoric chloride afforded the diastereomers ( $R_p$ ,1*S*,4*R*)-**16** and ( $S_p$ ,1*S*,4*R*)-**16**. The absolute configuration could be determined by X-ray crystallography. The diastereomers could be separated in gram-scale by simple column chromatography using silica gel.

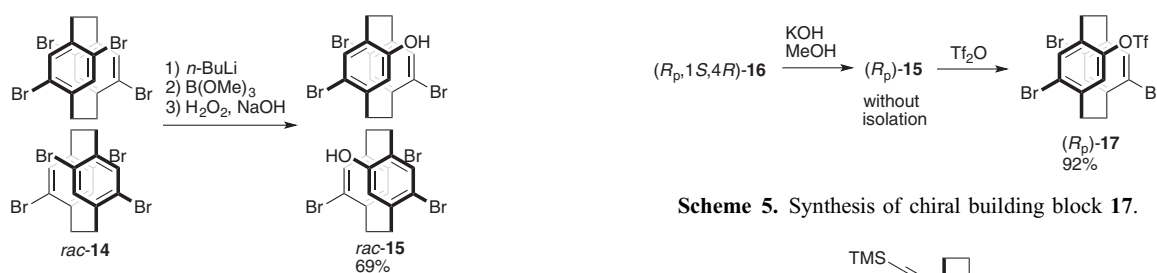
The chiral auxiliary was removed by hydrolysis, yielding the optically active phenol **15** (Scheme 5). The optically active 4,7,12,15-tetrasubstituted [2.2]paracyclophane **17** was synthesized by reacting **15** with trifluoromethanesulfonic anhydride, in view of cross-coupling using a Pd catalyst.

As shown in Scheme 6, Sonogashira-Hagihara coupling between the optically-active compound **17** with trimethylsilyl (TMS) acetylene was carried out. This led to the triyne **18** selectively in high yield, where only the bromo group in compound **17** reacted through the  $\text{Pd}_2(\text{dba})_3/\text{P}^t\text{Bu}_3$  catalyst system (dba = dibenzylideneacetone and  $\text{P}^t\text{Bu}_3$  = tri(*t*-butyl)phosphine). The trifluoromethylsulfonyl group was reacted with TMS acetylene using a  $\text{PdCl}_2(\text{dppf})$  catalyst (dppf = 1,1'-bis(diphenylphosphino)ferrocene) to synthesize the optically active tetrayne **19**. The TMS groups were removed easily to provide the target optically active compound 4,7,12,15-tetraethynyl[2.2]paracyclophane **20**.

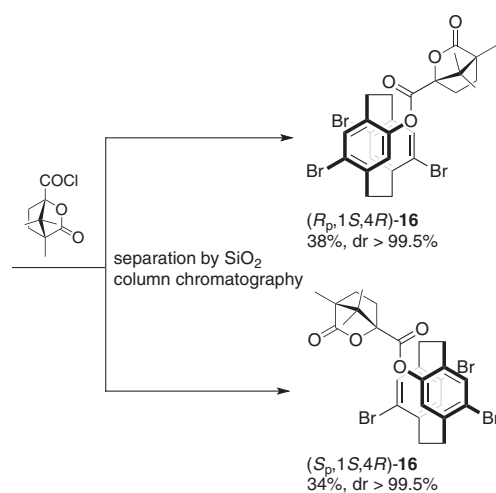
Cyclic compound **22** was synthesized via **21** using optically active 4,7,12,15-tetraethynyl[2.2]paracyclophane **20** as a chiral building block (Scheme 7). Evaluation of the chiroptical



**Figure 3.** Plausible conformations of the monomeric unit and linear trimer in the ground and excited states.

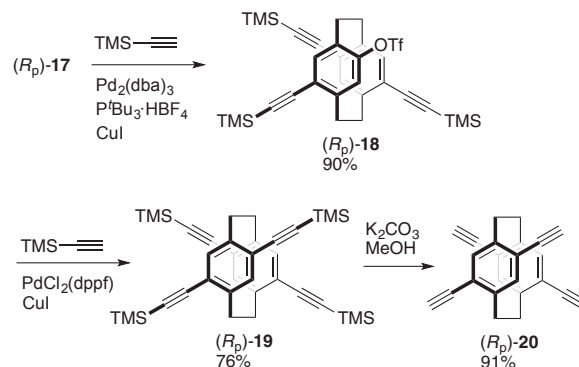


**Scheme 5.** Synthesis of chiral building block **17**.



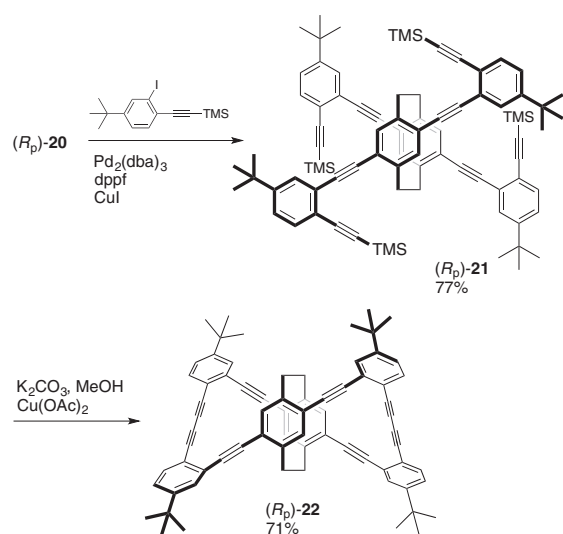
**Scheme 4.** Optical resolution of 4,7,12,15-tetrabromo [2.2]paracyclophane.

properties of the optically active compound **22** revealed that large chirality was induced in both the ground state and the excited state. The specific rotation was approximately 1,500 (c 0.5, CHCl<sub>3</sub>), and the molar ellipticity reached 3,000,000

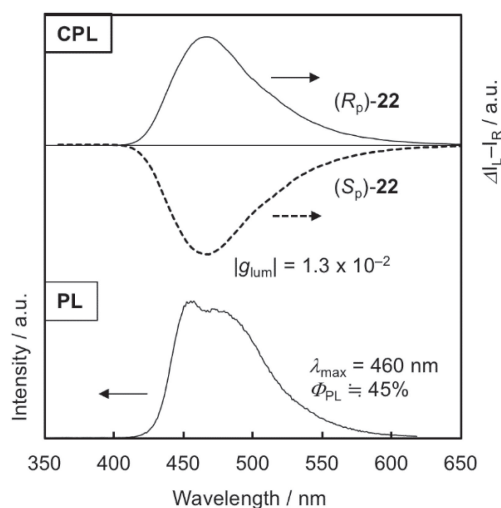


**Scheme 6.** Synthesis of optically active 4,7,12,15-tetraethynyl[2.2]paracyclophane **20**.

deg·cm<sup>2</sup>dmol<sup>-1</sup>. Indeed, compound **22** emitted CPL (spectra are shown in Figure 4), and the  $|g_{lum}|$  value at  $\lambda_{PL,max}$  was on the order of 10<sup>-2</sup>. This is a very large  $g_{lum}$  value for a mono-dispersed organic molecule in solution. In addition to the planar chirality of [2.2]paracyclophane, the optically active second-order structure (optically active propeller-shaped structure) seems to contribute greatly to the induction of chirality in the excited state. Although the fluorescence quantum yield was 45%, the molar absorption coefficient being 130,000 M<sup>-1</sup>cm<sup>-1</sup>



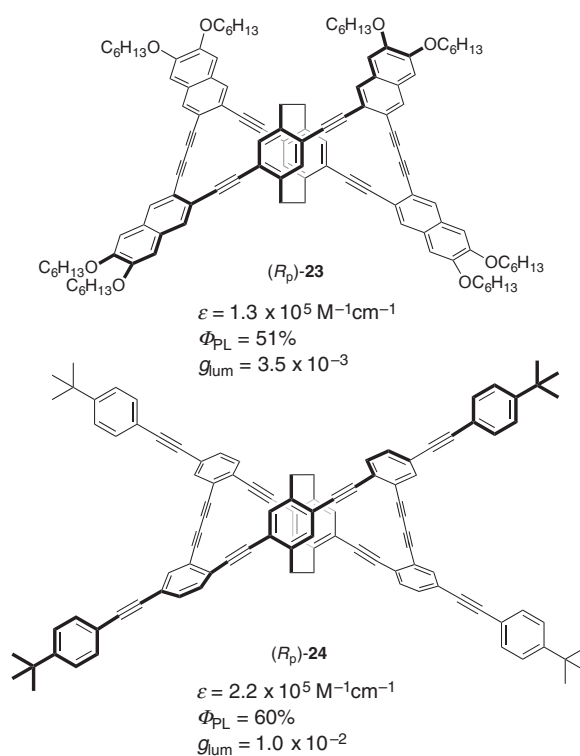
**Scheme 7.** Synthesis of optically active propeller-shaped compound **22**.



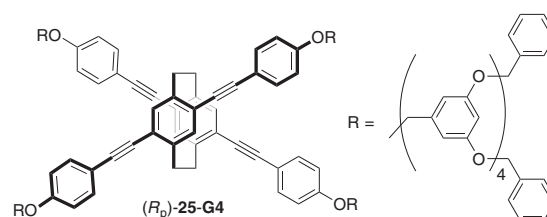
**Figure 4.** CPL and PL spectra of (*R<sub>p</sub>*)- and (*S<sub>p</sub>*)-**22** in  $\text{CHCl}_3$  ( $10 \times 10^{-6}\text{M}$ ) excited at 314nm for CPL and  $\lambda_{\text{abs,max}}$  for PL.

meant that the compound absorbed light sufficiently; thus, compound **22** is a molecule that emits highly intense CPL. In addition, optically active propeller-shaped molecules **23**<sup>26</sup> and **24**<sup>27</sup> were synthesized by molecular modification (Figure 5). Both compounds showed a large molar absorption coefficient, good fluorescence quantum yield, and large CPL  $g_{\text{lum}}$  value. In particular, **24** exhibited a large  $g_{\text{lum}}$  value on the order of  $10^{-2}$ , and it is an excellent CPL-emitting molecule based on the molar absorption coefficient and the fluorescence quantum yield.

Although the optically active molecules introduced thus far emit highly intense CPL in a dilute solution, their fluorescence quantum yield is remarkably lowered in the solid state due to general aggregation-caused quenching. We solved the quenching problem by using optically active **20** as a chiral building block to construct an X-shaped  $\pi$ -stacked structure, placing it in

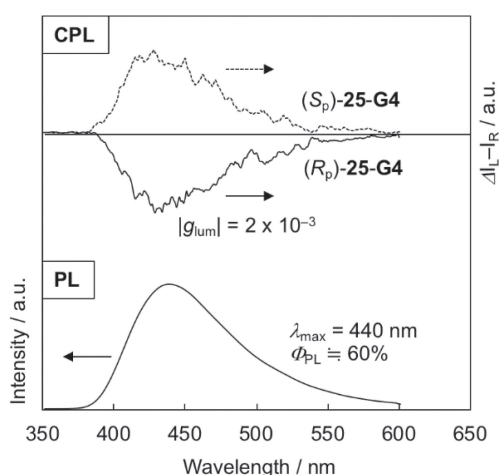


**Figure 5.** Structures and optical data of propeller-shaped cyclic compounds **23** and **24**.

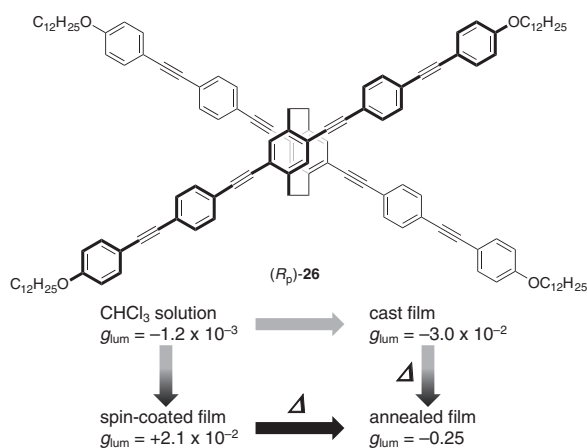


**Figure 6.** Structure of fourth-generation dendrimer (*R<sub>p</sub>*)-**25-G4**.

the core of a dendrimer.<sup>28</sup> Fréchet-type dendron having a large number of phenyl groups was employed for light-harvesting,<sup>29</sup> and first to fourth generation dendrimers **25-G<sub>n</sub>** ( $n = 1$  to  $4$ ) were prepared by the convergent approach. As a representative example, Figure 6 shows the fourth-generation dendrimer (*R<sub>p</sub>*)-**25-G4**. The second to fourth generation dendrimers showed very good film formability, and when the thin film was excited in the absorption region of the benzene ring, we observed emission with high intensity fluorescence from the optically active X-shaped core unit. Figure 7 shows the emission spectrum of the (*R<sub>p</sub>*)-**25-G4** thin film and the CPL spectra of both enantiomers. The fluorescence quantum yield of the thin film was estimated to be 60%, which was almost the same as that of 66% in the dilute solution. It is the result of the core being isolated by dendrons, thereby suppressing the aggregation-caused quenching. The emission was of course CPL, and the  $g_{\text{lum}}$  value at  $\lambda_{\text{PL,max}}$  was approximately  $2 \times 10^{-3}$ . Owing to the light-harvesting effect of the benzene rings on the surface of the dendrimer, it was possible to create a thin film that emits CPL



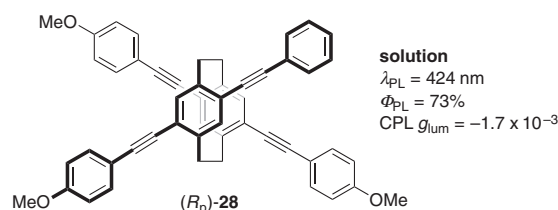
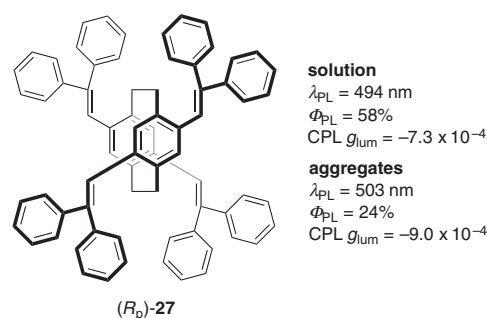
**Figure 7.** CPL and PL spectra of (*R<sub>p</sub>*)-25-G4 films, excited at 279 nm.



**Figure 8.** Structure of X-shaped molecule (*R<sub>p</sub>*)-26 and its CPL profiles.

with high intensity, high efficiency, and high dissymmetry factor.

Figure 8 shows an optically active X-shaped molecule (*R<sub>p</sub>*)-26,<sup>30</sup> which was synthesized using (*R<sub>p</sub>*)-20 as the chiral building block. This compound emitted CPL with a fluorescence quantum yield of 87% in dilute solution, and its  $g_{lum}$  value at  $\lambda_{PL,max}$  was  $-1.2 \times 10^{-3}$ . The  $g_{lum}$  value of the thin film formed by the spin-coating method exhibited the opposite sign and was estimated to be  $+2.1 \times 10^{-2}$ , which was larger by one order of magnitude. Furthermore, when the spin-coated film was annealed for 5 h at 90 °C, it showed a negative  $g_{lum}$  value again, and the  $g_{lum}$  value reaching  $-0.25$ , which is very large on the order of  $10^{-1}$ . On the other hand, the  $g_{lum}$  value of the thin film formed by the casting method was a negative value as in solution and was still one order of magnitude larger ( $-3.0 \times 10^{-2}$ ). When annealed in the same manner, the sign was reversed, showing the same value ( $-0.25$ ) as that of the spin-coated film. We believe that an optically active higher-ordered structure was formed in the thin film by van der Waals force of the long alkyl chains and  $\pi$ - $\pi$  interactions, and a



**Figure 9.** Structures of X-shaped molecules **27** and **28**, and their CPL profiles.

bis-(*para*)-pseudo-*ortho*-type      bis-(*para*)-pseudo-*meta*-type



**Figure 10.** Structures of bis-(*para*)-pseudo-*ortho*-type and bis-(*para*)-pseudo-*meta*-type tetrasubstituted [2.2]paracyclophanes.

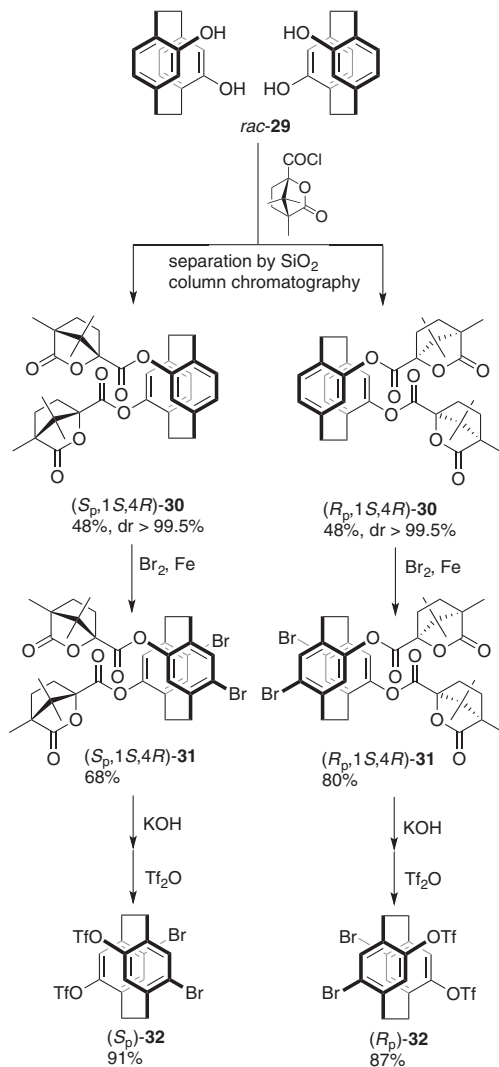
thermodynamically stable higher-ordered structure was formed by annealing.

Compounds (*R<sub>p</sub>*)-27 and (*R<sub>p</sub>*)-28 are X-shaped molecules synthesized using the optically active 4,7,12,15-tetrasubstituted [2.2]paracyclophane, (*R<sub>p</sub>*)-17, as the chiral building block (Figure 9). (*R<sub>p</sub>*)-27 is a  $\pi$ -electron system consisting of two arylene-vinylene layers, and we found that it also emitted CPL with relatively good fluorescence quantum yield not only in a dilute solution, but also in the aggregated state. The  $g_{lum}$  value of its CPL was estimated to be  $-9.0 \times 10^{-4}$ .<sup>31</sup> By combining (*R<sub>p</sub>*)-17 with a chemoselective Sonogashira-Hagihara coupling<sup>24</sup> with a  $Pd_2(dba)_3/P^tBu_3$  catalyst system, we could obtain X-shaped molecules like (*R<sub>p</sub>*)-28 consisting of heterogeneous  $\pi$ -electron systems.<sup>32</sup> We showed that it is possible to layer heterogeneous  $\pi$ -electron systems that have various electron-accepting and electron-donating groups introduced to it.

#### 4. Synthesis of Bis-(*para*)-pseudo-*ortho*-tetrasubstituted [2.2]Paracyclophane and Syntheses of Optically Active $\pi$ -Stacked Molecules

Furthermore, to synthesize a wide variety of stacked  $\pi$ -electron systems, we decided to synthesize a bis-(*para*)-pseudo-*ortho*-tetrasubstituted [2.2]paracyclophane derivative (Figure 10, left) as an optically active building block. We synthesized the racemic bisphenol *rac*-29 as a starting material and reacted this with (1*S*,4*R*)-(-)-camphanic chloride, to

produce the diastereomers (*R<sub>p</sub>*,1*S*,4*R*)-**30** and (*S<sub>p</sub>*,1*S*,4*R*)-**30** (Scheme 8).<sup>12d,33</sup> The absolute configuration was confirmed by X-ray crystallography. Both were readily isolated by simple column chromatography using silica gel. When each diaster-



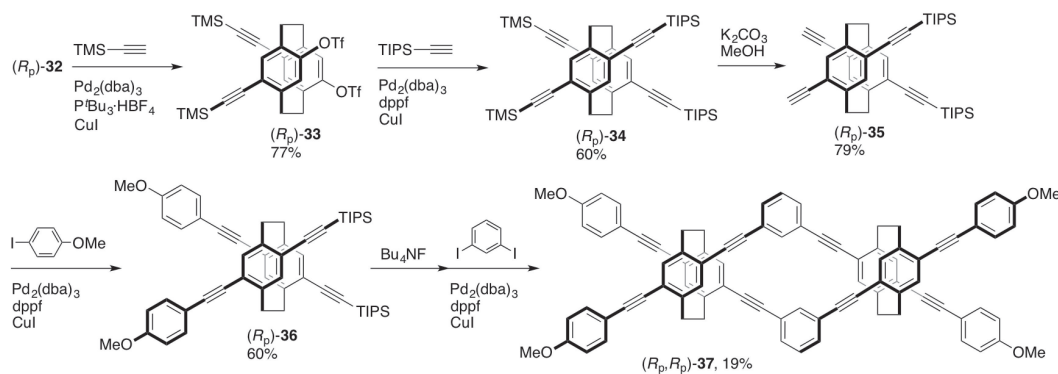
**Scheme 8.** Synthesis of bis-(*para*)-pseudo-*ortho*-4,7,12,15-tetrasubstituted [2.2]paracyclophanes.

omer **30** was reacted with bromine with an iron catalyst, we obtained (*R<sub>p</sub>*,1*S*,4*R*)-**31** and (*S<sub>p</sub>*,1*S*,4*R*)-**31**, where bromine was selectively substituted to the *para*-position of the oxygen substituent. Following the removal of the chiral auxiliary groups by saponification, reaction with trifluoromethanesulfonic anhydride in the presence of pyridine provided an optically active bis-(*para*)-pseudo-*ortho*-type tetrasubstituted [2.2]paracyclophane compound **32** in view of cross-coupling by Pd catalyst.<sup>33</sup>

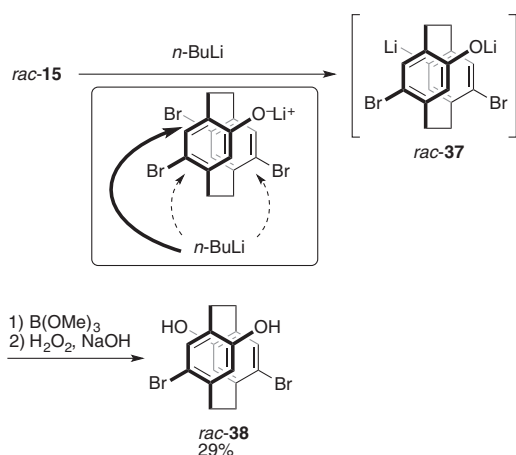
When we attempted the Sonogashira-Hagihara coupling of (*R<sub>p</sub>*)-**32** with TMS acetylene using the Pd<sub>2</sub>(dba)<sub>3</sub>/P<sup>t</sup>Bu<sub>3</sub> catalyst system, as expended, only the bromo-group reacted to provide the diene (*R<sub>p</sub>*)-**33** in good yield (Scheme 9). The trifluoromethylsulfonyl group was reacted with triisopropylsilyl (TIPS) acetylene using a Pd<sub>2</sub>(dba)<sub>3</sub>/dppf catalyst system to afford optically active tetrayne (*R<sub>p</sub>*)-**34**. Subsequently, reacting this compound with K<sub>2</sub>CO<sub>3</sub>/MeOH allowed the selective removal of the TMS group to afford (*R<sub>p</sub>*)-**35**, which was then subjected to Sonogashira-Hagihara coupling with *p*-iodoanisole to give (*R<sub>p</sub>*)-**36**. The TIPS group was removed by Bu<sub>4</sub>NF, and coupling with *m*-diiodobenzene provided (*R<sub>p</sub>*,*R<sub>p</sub>*)-**37** comprising two optically active cyclophanes. (*R<sub>p</sub>*,*R<sub>p</sub>*)-**37** forms a one-handed double helical structure in which boomerang-shaped arylene-ethynylene containing five benzene rings is stacked at the second and fourth phenylene moieties. (*R<sub>p</sub>*,*R<sub>p</sub>*)-**37** exhibited an absorption maximum at 379 nm, and the molar absorption coefficient was estimated to be  $1.25 \times 10^5 \text{ M}^{-1} \text{ cm}^{-1}$ . This compound also emitted high-intensity CPL (fluorescence quantum yield = 62%,  $g_{\text{lum}}$  value =  $1.6 \times 10^{-3}$ ).

### 5. Synthesis of Bis-(*para*)-pseudo-*meta*-tetrasubstituted [2.2]Paracyclophane

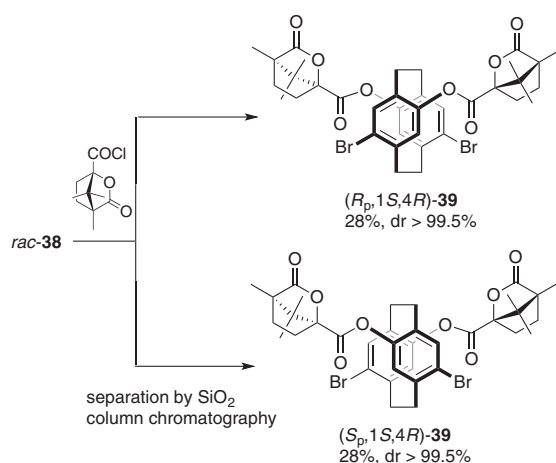
Recently, we successfully synthesized enantiopure bis-(*para*)-pseudo-*meta*-tetrasubstituted [2.2]paracyclophane derivatives (Figure 10, right) as new chiral building blocks.<sup>34</sup> On the other hand, Lützen and coworkers reported the chromatographic optical resolution of pseudo-*meta*-disubstituted [2.2]-paracyclophanes in 2014.<sup>35</sup> We used *rac*-**15** as the starting material and obtained the dilithiated compound *rac*-**37** by reaction with *n*-BuLi. By adding B(OMe)<sub>3</sub> to this compound and treating with H<sub>2</sub>O<sub>2</sub>/NaOH, the dibromodihydroxy[2.2]-paracyclophane *rac*-**38** was prepared (Scheme 10). After the initial lithium-hydrogen exchange to form phenoxide, the subsequent lithium-halogen exchange occurred preferentially at the pseudo-*meta*-position due to electronic factors. The structure



**Scheme 9.** Synthesis of one-handed double helical compound **37**.



**Scheme 10.** Synthesis of bis-(*para*)-pseudo-*meta*-type [2.2]paracyclophane **38**.



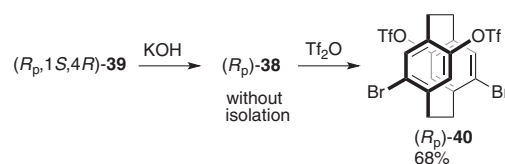
**Scheme 11.** Optical resolution of bis-(*para*)-pseudo-*meta*-type [2.2]paracyclophane.

of *rac-38* was determined by single crystal X-ray structural analysis, and we confirmed the synthesis of bis-(*para*)-pseudo-*meta*-type tetrasubstituted [2.2]paracyclophane.

We applied the diastereomer approach for the optical resolution (Scheme 11). Bisphenol *rac-38* was reacted with (1*S*,4*R*)-(–)-camphanic chloride, and the diastereomers (*R<sub>p</sub>*,1*S*,4*R*)-**39** and (*S<sub>p</sub>*,1*S*,4*R*)-**39** could be separated by column chromatography using silica gel. The absolute configuration was also determined by X-ray crystallography. The reaction of **39** with KOH and the subsequent reaction with trifluoromethanesulfonic anhydride afforded enantiopure bis-(*para*)-pseudo-*meta*-type tetrasubstituted [2.2]paracyclophane **40**, in view of cross-coupling using Pd catalyst (Scheme 12). We confirmed that indeed, when using the Pd<sub>2</sub>(dba)<sub>3</sub>/P<sup>t</sup>Bu<sub>3</sub> catalyst system, only the bromo-group of **40** reacted chemoselectively.

## 6. Conclusion

As discussed above, the authors have focused on the planar chirality of [2.2]paracyclophane compounds with substituents and developed practical methods for optical resolution primarily using the diastereomer approach. Various optically active  $\pi$ -



**Scheme 12.** Synthesis of bis-(*para*)-pseudo-*meta*-4,7,12,15-type building block.

stacked molecules, oligomers, and polymers were synthesized using the obtained optically active disubstituted and tetrasubstituted [2.2]paracyclophane compounds as chiral building blocks. We proposed that construction of the optically active higher-ordered structures in the excited state, derived from structurally stable planar chiral cyclophanes, is important for high-performance CPL. This is the first example that has applied planar chiral [2.2]paracyclophanes to the field of polymer chemistry and materials chemistry.

The  $\pi$ -electron system created by [2.2]paracyclophane shows a different emission mechanism depending on the conjugation length of the stacked  $\pi$ -electron system.<sup>4,36</sup> If the conjugation length is extended, one would observe emission from the  $\pi$ -electron system itself, instead of excimer-like emission, despite the  $\pi$ -stacked structure in proximity. Fluorescence profiles such as lifetime and quantum efficiency remain unchanged from the monomer, no matter how many  $\pi$ -electron systems are layered. The  $\pi$ -electron systems in the stacked compounds shown in this paper have sufficiently extended  $\pi$ -conjugation length, and they all exhibited bright fluorescence with good fluorescence quantum yield as well as large molar extinction coefficient. In addition, the light emitted is CPL with very large anisotropic factor in an organic molecule. It is difficult to express CPL that is compatible simultaneously with high fluorescence intensity, high quantum efficiency, and high anisotropy in other chiral scaffolds. We believe the planar chiral cyclophane skeleton to be an ideal scaffold for CPL.

Almost all research results discussed above were carried out with students in the Chujo laboratory. We would like to thank them for their efforts. We also thank students and coworkers at Kwansei Gakuin University. The authors are grateful to Professor Kazuo Akagi (Ritsumeikan University) Professor Tomoki Ogoshi (Kanazawa University) for CD and CPL measurements and valuable discussions. The authors are grateful to Professor Naoto Tamai (Kwansei Gakuin University) for PL lifetime measurements. This work was supported by Grant-in-Aid for Young Scientists (A) (No. 24685018), for Scientific Research on Innovative Area (No. 15H00733) “Element-Blocks”, and for Scientific Research on Innovative Area (No. 15H00992 and 17H05165) “ $\pi$ -Figuration” from the Ministry of Education, Culture, Sports, Science and Technology, Japan.

## References

- 1 a) F. Vögtle, *Cyclophane Chemistry: Synthesis, Structures and Reactions*, John Wiley & Sons, Chichester, **1993**. b) *Modern Cyclophane Chemistry*, ed. by R. Gleiter, H. Hopf, Wiley-VCH, Weinheim, **2004**. doi:10.1002/3527603964.
- 2 C. J. Brown, A. C. Farthing, *Nature* **1949**, *164*, 915.
- 3 D. J. Cram, H. Steinberg, *J. Am. Chem. Soc.* **1951**, *73*,

5691.

- 4 a) Y. Morisaki, Y. Chujo, *Angew. Chem., Int. Ed.* **2006**, *45*, 6430. b) Y. Morisaki, Y. Chujo, *Prog. Polym. Sci.* **2008**, *33*, 346. c) Y. Morisaki, Y. Chujo, *Bull. Chem. Soc. Jpn.* **2009**, *82*, 1070. d) Y. Morisaki, Y. Chujo, *Polym. Chem.* **2011**, *2*, 1249. e) Y. Morisaki, Y. Chujo, *Chem. Lett.* **2012**, *41*, 840.
- 5 S. Mizogami, S. Yoshimura, *J. Chem. Soc., Chem. Commun.* **1985**, 1736.
- 6 a) L. Guyard, P. Audebert, *Electrochem. Commun.* **2001**, *3*, 164. b) L. Guyard, P. Audebert, W. R. Dolbier, Jr., J.-X. Duan, *J. Electroanal. Chem.* **2002**, *537*, 189.
- 7 a) F. Salhi, B. Lee, C. Metz, L. A. Bottomley, D. M. Collard, *Org. Lett.* **2002**, *4*, 3195. b) F. Salhi, D. M. Collard, *Adv. Mater.* **2003**, *15*, 81. c) S. P. Jagtap, D. M. Collard, *J. Am. Chem. Soc.* **2010**, *132*, 12208.
- 8 Y. Morisaki, S. Ueno, A. Saeki, A. Asano, S. Seki, Y. Chujo, *Chem.—Eur. J.* **2012**, *18*, 4216.
- 9 a) Y. Morisaki, N. Kawakami, T. Nakano, Y. Chujo, *Chem.—Eur. J.* **2013**, *19*, 17715. b) Y. Morisaki, N. Kawakami, T. Nakano, Y. Chujo, *Chem. Lett.* **2014**, *43*, 426. c) Y. Morisaki, N. Kawakami, S. Shibata, Y. Chujo, *Chem.—Asian J.* **2014**, *9*, 2891. d) Y. Morisaki, S. Shibata, Y. Chujo, *Can. J. Chem.* **2017**, *95*, 424.
- 10 a) D. J. Cram, N. L. Allinger, *J. Am. Chem. Soc.* **1955**, *77*, 6289. b) V. Rozenberg, E. Sergeeva, H. Hopf, in *Modern Cyclophane Chemistry*, ed. by R. Gleiter, H. Hopf, Wiley-VCH, Weinheim, Germany, **2004**, pp. 435–462. doi:10.1002/3527603964.ch17. c) G. J. Rowlands, *Org. Biomol. Chem.* **2008**, *6*, 1527. d) S. E. Gibson, J. D. Knight, *Org. Biomol. Chem.* **2003**, *1*, 1256. e) A. A. Aly, A. B. Brown, *Tetrahedron* **2009**, *65*, 8055. f) J. Paradies, *Synthesis* **2011**, 3749.
- 11 Y. Morisaki, N. Wada, M. Arita, Y. Chujo, *Polym. Bull.* **2009**, *62*, 305.
- 12 a) P. J. Pye, K. Rossen, R. A. Reamer, N. N. Tsou, R. P. Volante, P. J. Reider, *J. Am. Chem. Soc.* **1997**, *119*, 6207. b) K. Rossen, P. J. Pye, A. Maliakal, R. P. Volante, *J. Org. Chem.* **1997**, *62*, 6462. c) R. Zhuravsky, Z. Starikova, E. Vorontsov, V. Rozenberg, *Tetrahedron: Asymmetry* **2008**, *19*, 216. d) B. Jiang, X.-L. Zhao, *Tetrahedron: Asymmetry* **2004**, *15*, 1141. e) P. G. Jones, J. Hillmer, H. Hopf, *Acta Crystallogr., Sect. E* **2003**, *59*, o24. f) D. Pamperin, H. Hopf, C. Syldat, M. Pietzsch, *Tetrahedron: Asymmetry* **1997**, *8*, 319. g) D. Pamperin, B. Ohse, H. Hopf, M. Pietzsch, *J. Mol. Catal. B: Enzym.* **1998**, *5*, 317. h) D. C. Braddock, I. D. MacGilp, B. G. Perry, *J. Org. Chem.* **2002**, *67*, 8679.
- 13 Y. Morisaki, R. Hifumi, L. Lin, K. Inoshita, Y. Chujo, *Chem. Lett.* **2012**, *41*, 990.
- 14 J. Clayden, in *Organolithiums: Selectivity for Synthesis*, Pergamon, Oxford, **2002**, p. 141–142.
- 15 a) P. B. Hitchcock, G. J. Rowlands, R. Parmar, *Chem. Commun.* **2005**, 4219. b) R. Parmar, M. P. Coles, P. B. Hitchcock, G. J. Rowlands, *Synthesis* **2010**, 4177.
- 16 a) S. Ohira, *Synth. Commun.* **1989**, *19*, 561. b) S. Müller, B. Liepold, G. J. Roth, H. J. Bestmann, *Synlett* **1996**, 521.
- 17 a) K. Sonogashira, Y. Tohda, N. Hagihara, in *Handbook of Organopalladium Chemistry for Organic Synthesis*, ed. by E. Negishi, Wiley-Interscience, New York, **2002**, pp. 493–529. doi:10.1002/0471212466.ch22.
- 18 Y. Morisaki, R. Hifumi, L. Lin, K. Inoshita, Y. Chujo, *Polym. Chem.* **2012**, *3*, 2727.
- 19 a) J. P. Riehl, F. S. Richardson, *Chem. Rev.* **1986**, *86*, 1. b) J. P. Riehl, F. Muller, *Comprehensive Chiroptical Spectroscopy*, Wiley and Sons, New York, **2012**, Ch. 3. doi:10.1002/9781118120187.ch3.
- 20 Y. Morisaki, K. Inoshita, Y. Chujo, *Chem.—Eur. J.* **2014**, *20*, 8386.
- 21 a) J. L. Brédas, B. Thémans, J. M. André, *Phys. Rev. B* **1982**, *26*, 6000. b) K. Pichler, D. A. Halliday, D. D. C. Bradley, P. L. Bum, R. H. Friend, A. B. Holmes, *J. Phys.: Condens. Matter* **1993**, *5*, 7155. c) S. Karabunarliev, M. Baumgarten, E. R. Bittner, K. Müllen, *J. Chem. Phys.* **2000**, *113*, 11372.
- 22 G. Meyer-Eppler, E. Vogelsang, C. Benkhäuser, A. Schneider, G. Schnakenburg, A. Lützen, *Eur. J. Org. Chem.* **2013**, 4523.
- 23 a) K. Kobayakawa, M. Hasegawa, H. Sasaki, J. Endo, H. Matsuzawa, K. Sako, J. Yoshida, Y. Mazaki, *Chem.—Asian J.* **2014**, *9*, 2751. b) M. Hasegawa, K. Kobayakawa, H. Matsuzawa, T. Nishinaga, T. Hirose, K. Sako, Y. Mazaki, *Chem.—Eur. J.* **2017**, *23*, 3267.
- 24 Y. Morisaki, M. Gon, T. Sasamori, N. Tokitoh, Y. Chujo, *J. Am. Chem. Soc.* **2014**, *136*, 3350.
- 25 H.-F. Chow, K.-H. Low, K. Y. Wong, *Synlett* **2005**, 2130.
- 26 M. Gon, H. Kozuka, Y. Morisaki, Y. Chujo, *Asian J. Org. Chem.* **2016**, *5*, 353.
- 27 M. Gon, Y. Morisaki, Y. Chujo, *J. Mater. Chem. C* **2015**, *3*, 521.
- 28 M. Gon, Y. Morisaki, R. Sawada, Y. Chujo, *Chem.—Eur. J.* **2016**, *22*, 2291.
- 29 a) C. J. Hawker, J. M. J. Fréchet, *J. Am. Chem. Soc.* **1990**, *112*, 7638. b) J. M. J. Fréchet, *Science* **1994**, *263*, 1710. c) J. M. J. Fréchet, C. J. Hawker, in *Comprehensive Polymer Science, Second Supplement*, ed. by G. Allen, Pergamon, Elsevier Science, Oxford, **1996**, pp. 71–132. doi:10.1016/B978-0-08-096701-1.00242-1.
- 30 M. Gon, R. Sawada, Y. Morisaki, Y. Chujo, *Macromolecules* **2017**, *50*, 1790.
- 31 M. Gon, Y. Morisaki, Y. Chujo, *Chem.—Eur. J.* **2017**, *23*, 6323.
- 32 Y. Sasai, H. Tsuchida, T. Kakuta, T. Ogoshi, Y. Morisaki, *Mater. Chem. Front.* **2018**, *2*, 791.
- 33 Y. Morisaki, R. Sawada, M. Gon, Y. Chujo, *Chem.—Asian J.* **2016**, *11*, 2524.
- 34 R. Sawada, M. Gon, J. Nakamura, Y. Morisaki, Y. Chujo, *Chirality* **2018**, *30*, 1109.
- 35 G. Meyer-Eppler, R. Sure, A. Schneider, G. Schnakenburg, S. Grimme, A. Lützen, *J. Org. Chem.* **2014**, *79*, 6679.
- 36 a) S. Wang, G. C. Bazan, S. Tretiak, S. Mukamel, *J. Am. Chem. Soc.* **2000**, *122*, 1289. b) G. P. Bartholomew, G. C. Bazan, *Acc. Chem. Res.* **2001**, *34*, 30. c) G. P. Bartholomew, G. C. Bazan, *Synthesis* **2002**, 1245. d) J. W. Hong, H. Y. Woo, B. Liu, G. C. Bazan, *J. Am. Chem. Soc.* **2005**, *127*, 7435. e) G. C. Bazan, *J. Org. Chem.* **2007**, *72*, 8615.

Communication

# $\pi$ -Stacked Polymer Consisting of a Pseudo-*meta*-[2.2]Paracyclophane Skeleton

Hazuki Maeda <sup>1</sup>, Mayu Kameda <sup>2</sup>, Takuji Hatakeyama <sup>2</sup> and Yasuhiro Morisaki <sup>1,\*</sup>

<sup>1</sup> Department of Applied Chemistry for Environment, School of Science and Technology, Kwansei Gakuin University, 2-1 Gakuen, Sanda, Hyogo 669-1337, Japan; ebk97584@kwansei.ac.jp

<sup>2</sup> Department of Chemistry, School of Science and Technology, Kwansei Gakuin University, 2-1 Gakuen, Sanda, Hyogo 669-1337, Japan; mqu.oq@kwansei.ac.jp (M.K.); hatake@kwansei.ac.jp (T.H.)

\* Correspondence: ymo@kwansei.ac.jp

Received: 27 August 2018; Accepted: 2 October 2018; Published: 12 October 2018



**Abstract:** A novel  $\pi$ -stacked polymer based on a pseudo-*meta*-linked [2.2]paracyclophane moieties was synthesized by Sonogashira-Hagihara coupling. The UV-vis absorption spectra of the synthesized polymer and model compounds revealed an extension of the conjugation length owing to the through-space conjugation. The optical properties of the  $\pi$ -stacked dimer with the pseudo-*meta*-linked [2.2]paracyclophane unit were compared with those of the corresponding dimers with the pseudo-*ortho*- and pseudo-*para*-linked [2.2]paracyclophane units.

**Keywords:** [2.2]paracyclophane;  $\pi$ -stacked polymer; through-space conjugation

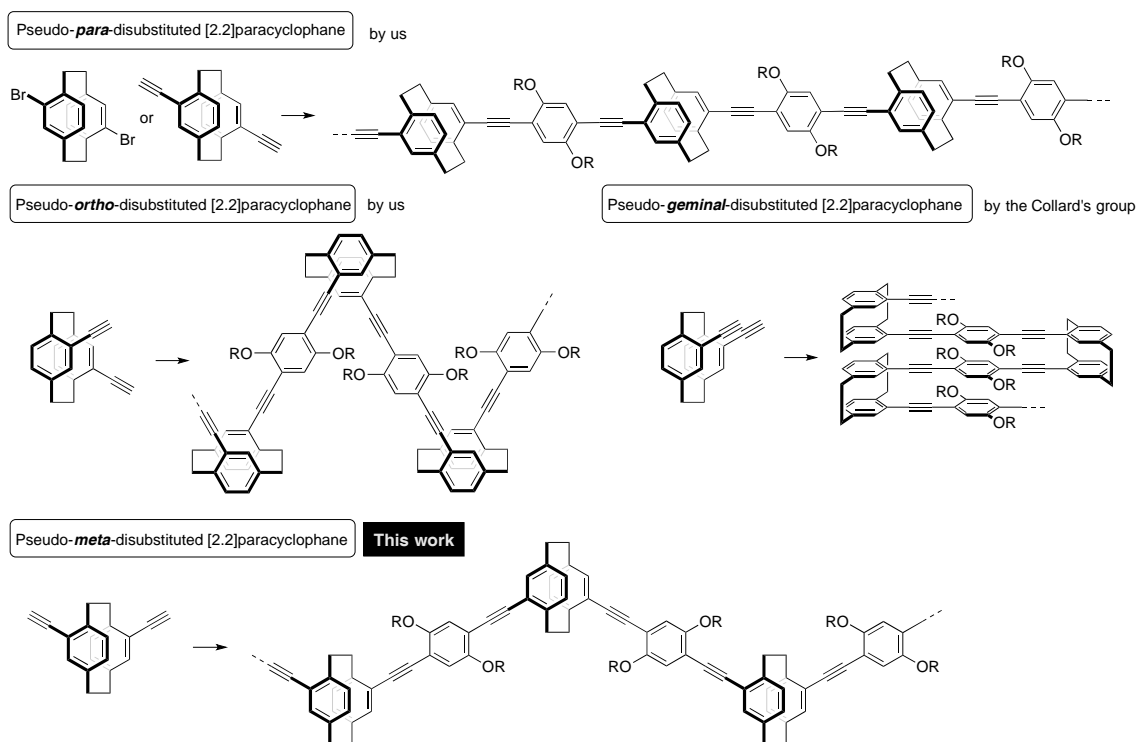
## 1. Introduction

“Cyclophane” is the general term for cyclic compounds that include at least one aromatic ring (arylene unit) in the cyclic skeleton. [2.2]Paracyclophane is a representative cyclophane comprising of two *p*-phenylenes and two ethylene chains [1–4]. The two phenylenes are stacked in proximity; the distance between phenylene rings is approximately 3 Å. Although [2.2]paracyclophanes are well-known and have been actively studied in the field of synthetic organic chemistry, they have not been sufficiently applied in the fields of polymer and materials chemistry.

Our interests have focused on the unique structures of [2.2]paracyclophane, repeatedly incorporating their molecular skeletons into  $\pi$ -conjugated polymer backbones through the use of disubstituted [2.2]paracyclophane compounds as comonomers [5–10]. For example, as shown in Figure 1, we synthesized a new type of conjugated polymer based on the pseudo-*para*-disubstituted [2.2]paracyclophane skeleton from pseudo-*para*-dibromo or diethynyl [2.2]paracyclophane [5,6,10]. The [2.2]paracyclophane unit provided a void space in the conjugated polymer main chain, leading to a partly  $\pi$ -stacked structure. The UV-vis absorption spectra of the corresponding oligomers as well as polymers with various molecular weights were red-shifted as the number of stacked  $\pi$ -electron systems increased [10]. Thus, we named this class of  $\pi$ -stacked polymers “through-space conjugated polymers”.

Pseudo-*ortho*-diethynyl[2.2]paracyclophane was also used as a comonomer to prepare the corresponding zigzag-shaped through-space conjugated polymer [7]. Pseudo-*ortho*-disubstituted [2.2]paracyclophanes are planar chiral compounds. After the successful development of an optical resolution method [11], we synthesized optically active through-space conjugated polymers [12,13]. This polymer emitted intense circularly polarized luminescence by photo-excitation due to the formation of a one-handed helix in the excited state.

Collard and coworkers prepared through-space conjugated polymers consisting of the pseudo-*geminal*-disubstituted [2.2]paracyclophane backbone, in which the  $\pi$ -electron systems were fully  $\pi$ -stacked and strongly interacted with each other in the polymer [14].



**Figure 1.** Poly(*p*-arylene-ethynylene) (PAE) type of [2.2]paracyclophane-containing through-space conjugated polymers containing various disubstituted [2.2]paracyclophane isomers.

With this background, our next target was very simple: That is, the synthesis of a through-space conjugated polymer incorporating pseudo-*meta*-disubstituted [2.2]paracyclophane units in the main chain. Very recently, Yu et al. reported tetraphenylethene-based conjugated polymers containing pseudo-*meta*-disubstituted [2.2]paracyclophane, which exhibited aggregation-induced emission [15]. From the viewpoint of a systematic study of poly(*p*-arylene-ethynylene) (PAE)-types of [2.2]paracyclophane-containing through-space conjugated polymers, we pursued the synthesis of the pseudo-*meta*-analogue. Herein, we report the preparation of the through-space conjugated polymer with the pseudo-*meta*-disubstituted [2.2]paracyclophane repeating units, and a comparison of its optical properties with those of the pseudo-*para*- and pseudo-*ortho*-disubstituted [2.2]paracyclophane-containing polymers.

## 2. Materials and Methods

### 2.1. Materials

[2.2]Paracyclophane (**1**), Br<sub>2</sub>, trimethylsilylacetylene, Pd<sub>2</sub>(dba)<sub>3</sub> (dba = dibenzylideneacetone), (*t*-Bu)<sub>3</sub>P·HBF<sub>4</sub>, dppf (1,1'-bis(diphenylphosphino)ferrocene), CuI, and K<sub>2</sub>CO<sub>3</sub> were commercially available compounds and used without purification. CCl<sub>4</sub> and MeOH were commercially available solvents and used without purification. Super dehydrated tetrahydrofuran (THF) was purchased and used without purification. Et<sub>3</sub>N was used after distillation over KOH.

Compounds *p*-**2** [16,17], *m*-**2** [16,17], *m*-**3** [18], and *m*-**4** [17,18] were known compounds; however, our synthetic procedures and results are shown. Compounds **5** [19,20] and **6** [13] were prepared via procedures described in the literature. Reported data [13] of *o*-**D1** (enantiopure *R<sub>p</sub>*-isomer) was used in this manuscript. Synthetic route and the data of *p*-**D1** were reported [10]; however, it was prepared and the data was collected again for this study.

## 2.2. Methods

$^1\text{H}$  and  $^{13}\text{C}$  NMR spectra were recorded on a JEOL JNM ECA-300 instrument at 300 MHz and a JEOL JNM ECX-500II instrument at 125 MHz, respectively. Samples were analyzed via thin layer chromatography (TLC) using silica gel 60 Merck F<sub>254</sub> plates. Column chromatography was performed with Wakogel C-300 SiO<sub>2</sub>. Flash column chromatography and recyclable preparative high-performance liquid chromatography (HPLC) were carried out on a YMC LC Forte/R system. High-resolution mass (HRMS) spectra were obtained on a JEOL JMS-S3000 spectrometer for matrix assisted desorption/ionization (MALDI) with 7,7,8,8-tetracyanoquinodimethane (TCNQ) as a matrix. Gel permeation chromatography (GPC) was carried out on a JASCO EXTREMA GPC system with TSKgel G3000H<sub>XL</sub> and G4000 H<sub>XL</sub> columns using THF as an eluent after calibration with standard polystyrene samples. UV-vis spectra were recorded on a JASCO V-730 spectrophotometer, and samples were analyzed in CHCl<sub>3</sub> at room temperature. Photoluminescence (PL) spectra and excitation spectra were recorded on a JASCO FP-8500 spectrofluorometer, and samples were analyzed in CHCl<sub>3</sub> at room temperature. The absolute PL quantum efficiency was calculated on a JASCO FP8500 with an ILF-835 integrating sphere. The PL lifetime measurement was performed on a Hamamatsu Photonics Quantaaurus-Tau fluorescence lifetime spectrometer system. Thermogravimetric analysis (TGA) was made on a Seiko EXSTAR 6000 instrument (10 °C/min) under N<sub>2</sub>. Differential scanning calorimetry (DSC) analysis was carried out on a Seiko DSC200 instrument at heating and cooling rate of 10 °C/min under N<sub>2</sub>.

## 2.3. Synthetic Procedures

### 2.3.1. Synthesis of *m*-2

[2.2]Paracyclophane (**1**) (21.7 g, 0.10 mol) was dissolved in CCl<sub>4</sub> (300 mL), and Br<sub>2</sub> (100 g, 0.63 mol) in CCl<sub>4</sub> (30 mL) was added dropwise at 55 °C. During the reaction, a white solid was formed. After 2 h of stirring, the reaction mixture was cooled to room temperature, and the aqueous saturated solution of NaHSO<sub>3</sub> was added. The white solid (*p*-**2**, 13.7 g, 38 mmol, 36%) was removed by filtration. The organic layer of the filtrate was dried by a rotary evaporator, and the residue was purified by recrystallization from hexane to obtain *m*-**2** (10.9 g, 30 mmol, 29%) as a white crystal. The  $^1\text{H}$  and  $^{13}\text{C}$  NMR data were matched with the reported values [16,17].

### 2.3.2. Synthesis of *m*-3

A mixture of *m*-**2** (0.56 mg, 1.5 mmol), Pd<sub>2</sub>(dba)<sub>3</sub> (0.17 g, 0.19 mmol), (*t*-Bu)<sub>3</sub>P·HBF<sub>4</sub> (97 mg, 0.34 mmol), CuI (51 mg, 0.27 mmol), THF (20 mL) and Et<sub>3</sub>N (20 mL) was placed in a round-bottom flask equipped with a magnetic stirring bar. After degassing the reaction mixture several times, trimethylsilylacetylene (3.0 mL) was added to the mixture. The reaction was carried out at reflux temperature for 24 h with stirring. After the reaction mixture was cooled to room temperature, precipitates were removed by filtration, and the solvent was removed with a rotary evaporator. The residue was purified by column chromatography on SiO<sub>2</sub> (CHCl<sub>3</sub>/hexane = 1/4 *v/v* as an eluent) to afford *m*-**3** (0.51 g, 1.3 mmol, 92%) as a pale yellow solid. *R*<sub>f</sub> = 0.43 (CHCl<sub>3</sub>/hexane = 1/4 *v/v*). The  $^1\text{H}$  NMR data were matched with the reported values [18].

### 2.3.3. Synthesis of *m*-4

K<sub>2</sub>CO<sub>3</sub> (2.0 g, 14 mmol) was added to a suspension of *m*-**3** (0.81 g, 2.0 mmol) in MeOH (35 mL). After the mixture was stirred for 24 h at room temperature, H<sub>2</sub>O and CHCl<sub>3</sub> were added to the reaction mixture. The organic layer was extracted with CHCl<sub>3</sub> and washed with brine. The combined organic layer was dried over MgSO<sub>4</sub>. MgSO<sub>4</sub> was removed by filtration, and the solvent was removed with a rotary evaporator. The residue was purified by column chromatography on SiO<sub>2</sub> (CHCl<sub>3</sub>/hexane = 1/2 *v/v* as an eluent) to afford *m*-**4** (0.48 g, 1.9 mmol, 92%) as a white solid. *R*<sub>f</sub> = 0.52 (CHCl<sub>3</sub>/hexane = 1/2 *v/v*). The  $^1\text{H}$  NMR data were matched with the reported values [17,18].

### 2.3.4. Synthesis of *m*-P1

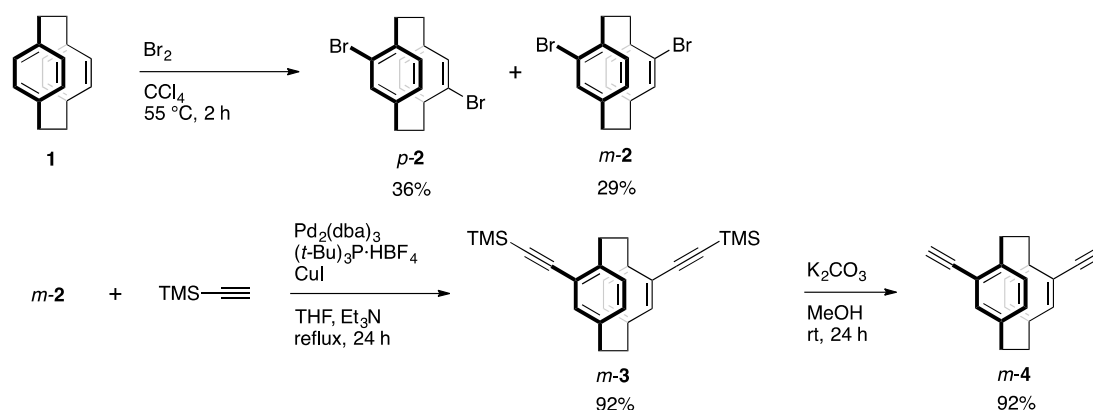
A mixture of *m*-4 (39 mg, 0.15 mmol), **5** (11 mg, 0.15 mmol), Pd<sub>2</sub>(dba)<sub>3</sub> (10 mg, 0.011 mmol), (t-Bu)<sub>3</sub>P·HBF<sub>4</sub> (9.2 mg, 0.032 mmol), CuI (5.4 mg, 0.028 mmol), THF (1.5 mL) and Et<sub>3</sub>N (1.5 mL) was placed in a Schlenk tube equipped with a magnetic stirring bar. After degassing the reaction mixture several times, polymerization was carried out at reflux temperature for 48 h with stirring. After the reaction mixture was cooled to room temperature, precipitates were removed by filtration, and the solvent was removed with a rotary evaporator. The residue was purified by reprecipitation three times from CHCl<sub>3</sub> and MeOH (good and poor solvent, respectively) to afford *m*-P1 (86 mg, 0.12 mmol, 81%) as an orange solid. <sup>1</sup>H NMR (CDCl<sub>3</sub>, 300 MHz) δ 0.86 (br), 1.24 (br), 1.56 (br), 1.96 (br), 2.99 (br), 3.12 (br), 3.24 (br), 3.66 (br), 4.11 (br), 6.53 (br), 6.66 (br), 7.07 (br), 7.17 (br) ppm; <sup>13</sup>C NMR (CDCl<sub>3</sub>, 125 MHz) δ 14.1, 22.7, 26.2, 29.3 (m), 31.9, 33.0, 35.0, 69.5, 70.3, 88.9, 89.8, 94.5, 95.0, 114.0, 116.2, 122.7, 125.8, 128.4, 129.0, 130.8, 132.2, 132.3, 136.5, 139.3, 142.8, 153.6 ppm. <sup>1</sup>H and <sup>13</sup>C NMR spectra are shown in Figures S1 and S2, respectively.

### 2.3.5. Synthesis of *m*-D1

A mixture of *m*-4 (10.9 mg, 0.043 mmol), **6** (70.5 mg, 0.100 mmol), Pd<sub>2</sub>(dba)<sub>3</sub> (5.4 mg, 0.006 mmol), dppf (8.4 mg, 0.015 mmol), CuI (3.8 mg, 0.020 mmol), THF (2.0 mL) and Et<sub>3</sub>N (2.0 mL) was placed in a Schlenk tube equipped with a magnetic stirring bar. After degassing the reaction mixture several times, the reaction was carried out at reflux temperature for 48 h with stirring. After the reaction mixture was cooled to room temperature, precipitates were removed by filtration, and the solvent was removed with a rotary evaporator. The residue was purified by a recyclable HPLC (CHCl<sub>3</sub> as an eluent) to afford *m*-D1 (38.5 mg, 0.027 mmol, 64%) as a yellow solid. <sup>1</sup>H NMR (CDCl<sub>3</sub>, 300 MHz) δ 0.86 (t, 7.2 Hz, 3H), 0.88 (t, 6.9 Hz, 3H), 1.25 (br, 32H), 1.54 (m, 4H), 1.89 (m, 4H), 2.32 (s, 3H), 2.52 (s, 3H), 2.98 (m, 1H), 3.09 (m, 1H), 3.25 (m, 1H), 3.63 (m, 1H), 4.05 (t, 6.3 Hz, 2H), 4.09 (t, 6.6 Hz, 2H), 6.52 (d, 7.8 Hz, 1H), 6.64 (s, 1H), 7.04 (m, 3H), 7.13 (d, 7.8 Hz, 2H), 7.36 (s, 1H) ppm; <sup>13</sup>C NMR (CDCl<sub>3</sub>, 125 MHz) δ 14.1, 20.3, 20.8, 22.7, 26.2, 29.5 (m), 31.6, 31.9, 33.0, 35.0, 69.2, 69.4, 89.6, 89.7, 94.1, 94.9, 113.9, 116.0, 116.4, 1230, 125.7, 129.2, 129.3, 130.8, 132.2, 134.9, 136.4, 137.2, 139.3, 142.8, 153.4, 153.5 ppm. HRMS (MALDI) calcd. for C<sub>100</sub>H<sub>136</sub>O<sub>4</sub> M<sup>+</sup>: 1401.0433, found 1401.0433. <sup>1</sup>H and <sup>13</sup>C NMR spectra are shown in Figures S3 and S4, respectively. GPC curves of *m*-P1 and *m*-D1 are shown in Figure S5.

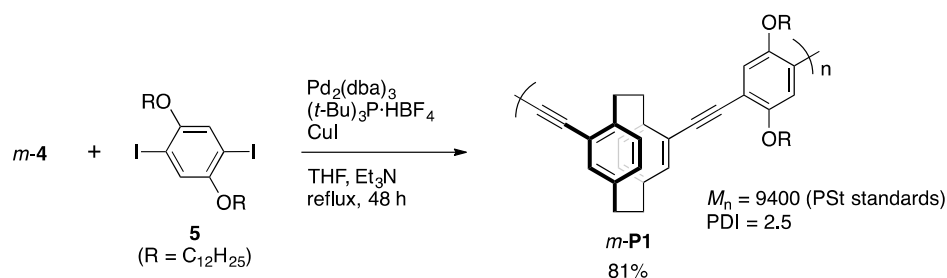
## 3. Results and Discussions

The synthetic route to the key monomer is shown in Scheme 1. Commercially available [2.2]paracyclophane (**1**) was reacted with Br<sub>2</sub> in CCl<sub>4</sub> at around 55 °C for 2 h to afford dibrominated [2.2]paracyclophanes. Pseudo-*p*-isomer *p*-2 was precipitated during the reaction and could be obtained by filtration in 36% isolated yield. Pseudo-*m*-isomer *m*-2 existed mainly in the filtrate, and was isolated by recrystallization in 29% yield. Sonogashira-Hagihara coupling [21] of *m*-2 with trimethylsilylacetylene proceeded smoothly using a Pd<sub>2</sub>(dba)<sub>3</sub>/(t-Bu)<sub>3</sub>P/CuI catalytic system to afford *m*-3 in 92% isolated yield, and the successive removal of TMS groups by K<sub>2</sub>CO<sub>3</sub>/MeOH afforded *m*-4 in 92% yield. Akita and coworkers reported the synthesis of *m*-3 from *m*-2 by the Sonogashira-Hagihara coupling using the PdCl<sub>2</sub>(PPh<sub>3</sub>)<sub>2</sub>/CuI catalytic system (33%) and the removal of TMS groups with Bu<sub>4</sub>NF to obtain *m*-4 (79%) [18]; thus, the total yield of *m*-4 from *m*-2 was 26%. In addition, Hopf and coworkers independently synthesized *m*-4 in total 55% isolated yield from *m*-2 via pseudo-*m*-diformyl[2.2]paracyclophane [17]. Our present method improves the isolated yield of *m*-4 from *m*-2, affording the total 85% yield. On the other hand, Lützen and coworkers reported the synthesis of optically active *m*-4 from the corresponding enantiopure pseudo-*m*-diformyl[2.2]paracyclophane in high isolated yield, although chromatographic chiral resolution of the precursor was required [22].



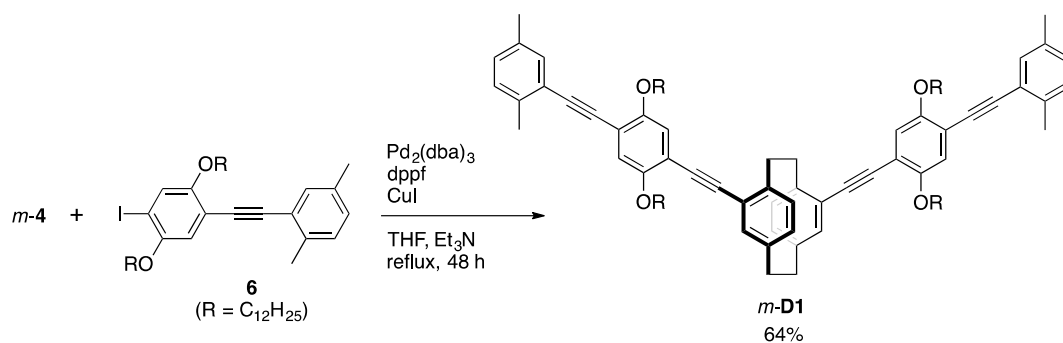
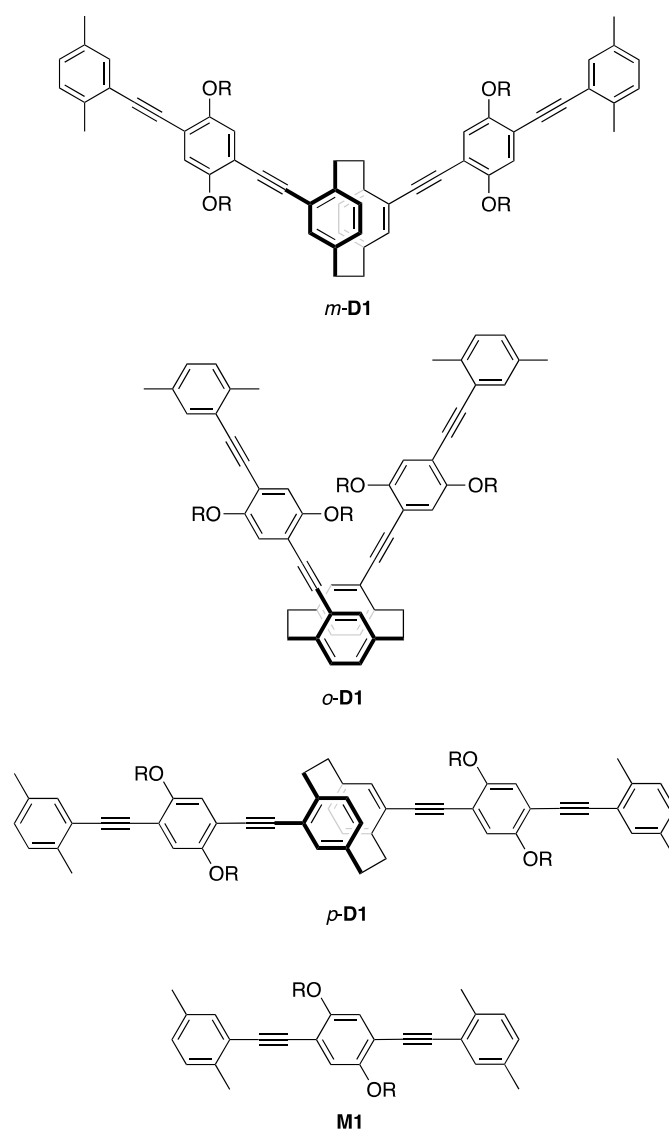
**Scheme 1.** Synthesis of pseudo-*m*-diethynyl[2.2]paracyclophane *m-4*.

As shown in Scheme 2, the target polymer was synthesized via Sonogashira-Hagihara coupling using the same catalytic system as that of the synthesis of *m-3*. The reaction of *m-4* with diiodobenzene derivative **5** afforded the corresponding  $\pi$ -stacked polymer *m-P1* in 81% isolated yield. Once the polymer was precipitated, all of the polymer solid was not dissolved in solvents. The structure of the  $\text{CHCl}_3$ -soluble part (84.2 wt/v %) of *m-P1* was confirmed by the  $^1\text{H}$  and  $^{13}\text{C}$  NMR spectra that were recorded in its  $\text{CDCl}_3$  solution. The number average molecular weight ( $M_n$ ) and polydispersity index (PDI) of the soluble part of *m-P1* in  $\text{CHCl}_3$  were estimated via gel permeation chromatography (GPC) to be 9400 and 2.5, respectively, using polystyrene (PSt) standards. A thin film was obtained from the  $\text{CHCl}_3$  solution by the casting or spin-coating method. The polymer showed thermal stability; 5 wt % weight loss was observed at 298 °C by TGA analysis (Figure S11, Supplementary Materials). As shown in Figure S12 (Supplementary Materials), in the DSC analysis, glass transition temperature ( $T_g$ ) and crystallization temperature ( $T_c$ ) were observed at around 60 and 170 °C by the first scan, respectively, whereas no peaks appeared in the second scan. Thus, the polymer showed sufficient thermal stability.



**Scheme 2.** Synthesis of  $\pi$ -stacked polymer *m-P1*.

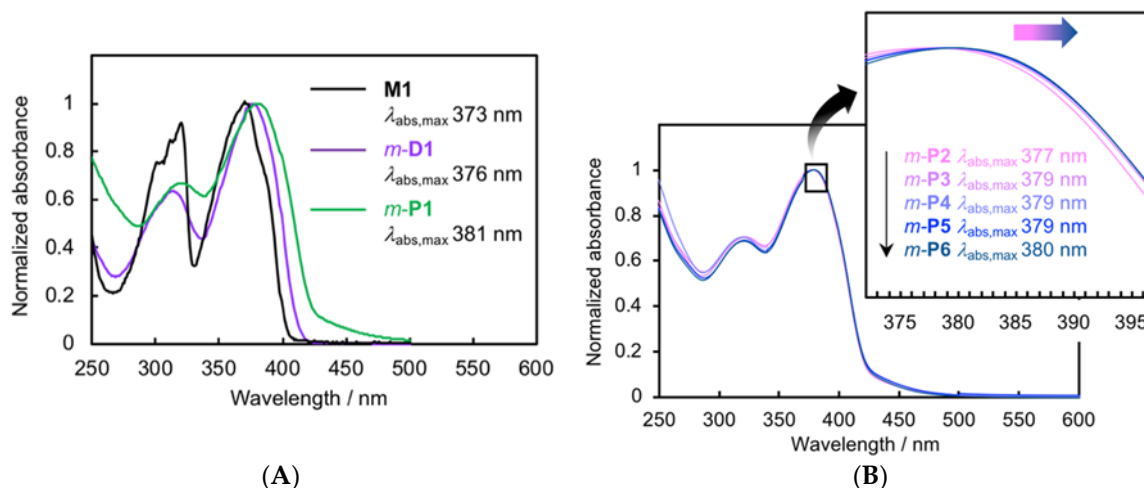
Scheme 3 shows the synthesis of  $\pi$ -stacked dimer *m-D1* as a model compound. The reaction of *m-4* with compound **6** using a  $\text{Pd}_2(\text{dba})_3/\text{dppf}/\text{CuI}$  catalytic system afforded *m-D1* in 64% isolated yield, in which two PAE-type- $\pi$ -electron systems are stacked at the terminal xylyl units. Previously, we prepared the stereoisomers of the  $\pi$ -stacked dimers, as shown in Figure 2.  $\pi$ -Stacked dimer *o-D1* comprises a pseudo-*o*-linked [2.2]paracyclophane skeleton, in which two PAE-type- $\pi$ -electron systems are stacked and oriented at an angle of 60°.  $\pi$ -Stacked dimer *p-D1* incorporates the pseudo-*p*-linked [2.2]paracyclophane skeleton. Finally, we prepared **M1** as the monomeric PAE-type-model compound (Figure 2).

Scheme 3. Synthesis of  $\pi$ -stacked dimer  $m\text{-D1}$ .

**Figure 2.** Structures of  $\pi$ -stacked dimers,  $m$ -,  $o$ -,  $p$ -D1 and monomeric model compound **M1** ( $R = \text{C}_{12}\text{H}_{25}$ ).

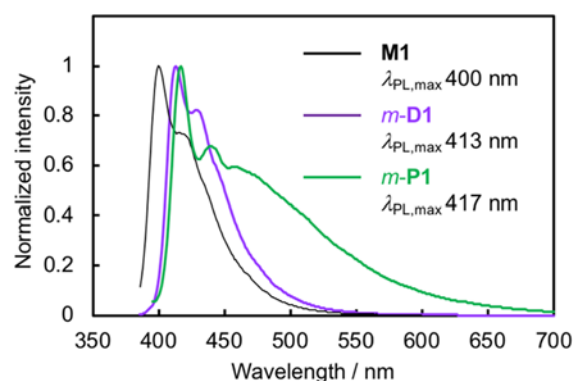
Figure 3A shows the UV-vis absorption spectra of **M1**,  $m\text{-D1}$ , and the soluble part of  $m\text{-P1}$  in  $\text{CHCl}_3$  at room temperature. **M1** exhibited a typical  $\pi\text{-}\pi^*$  absorption band with an absorption maximum ( $\text{abs}_{\text{max}}$ ) at 373 nm. The absorption spectra of  $m\text{-D1}$  and  $m\text{-P1}$  are slightly red-shifted, with  $\text{abs}_{\text{max}}$  values of 376 and 381 nm, respectively. The tailing band appeared in the spectrum of  $m\text{-P1}$  from 425

to 500 nm due to the intermolecular  $\pi$ - $\pi$  interactions of the aggregated polymer chains. This tailing band was also observed in the *m*-P1 casting film (Figure S8, Supplementary Materials). Polymer solution of *m*-P1 in CHCl<sub>3</sub> was separated by recyclable HPLC into five polymer solutions *m*-P2-P6 with  $M_n$  values of 3800, 5000, 7000, 10,000, and 15,000, respectively. In their UV-vis absorption spectra of *m*-P2-P6 shown in Figure 3B, minimal red-shift was observed as the  $M_n$  increased. For example, the  $\lambda_{\text{abs,max}}$  of *m*-P2 ( $M_n$  of 3800) was 377 nm, whereas that of *m*-P6 ( $M_n$  of 15000) was 380 nm. Thus, through-space conjugation was observed in the  $\pi$ -stacked polymers consisting of the pseudo-*meta*-linked [2.2]paracyclophanes.

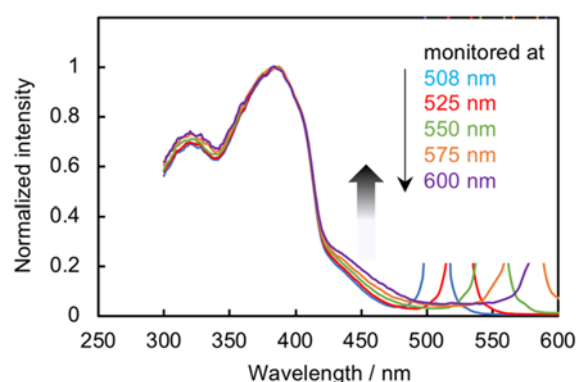


**Figure 3.** (A) UV-vis absorption spectra of **M1**, *m*-D1, and the soluble part of *m*-P1 in CHCl<sub>3</sub> ( $1.0 \times 10^{-5}$  M for **M1** and *m*-D1, and  $0.84 \times 10^{-5}$  M for *m*-P1); (B) UV-vis absorption spectra of *m*-P2-P6 in CHCl<sub>3</sub>.

Photoluminescence (PL) spectra of **M1**, *m*-D1, and the soluble part of *m*-P1 CHCl<sub>3</sub> solutions were obtained by excitation at  $\lambda_{\text{abs,max}}$  at room temperature; the spectra are shown in Figure 4. **M1** emitted efficiently with a PL quantum efficiency ( $\Phi_{\text{PL}}$ ) of 0.72; the PL spectrum exhibited a clear vibronic structure. The PL spectrum of *m*-D1 was identical to that of **M1**, albeit red-shifted slightly with a  $\Phi_{\text{PL}}$  of 0.73. The PL decay curve of *m*-D1 was fitted with a single exponential relation and the lifetime value ( $\tau$ ) was 1.27 ns with  $\chi^2 = 1.00$  (Figure S6, Supplementary Materials), which was almost same as that of **M1** ( $\tau = 1.24$  ns,  $\chi^2 = 1.00$ ). Pseudo-*meta*-linked  $\pi$ -stacked-dimer *m*-D1 emits from the chromophore state rather than from the phane state [23–27], in other words, simple PL from a PAE-type-monomeric unit is observed rather than an excimer-like emission from the two stacked  $\pi$ -electron systems. This behavior was identical to those of the pseudo-*para*- and pseudo-*ortho*-linked dimers (*p*-D1 and *o*-D1) (vide infra). The PL spectrum of *m*-P1 was similar to those of **M1** and *m*-D1; however, further PL was observed at longer-wavelength ( $\sim 460$  nm) in addition to the shorter-wavelength PL with vibronic structure, and the  $\Phi_{\text{PL}}$  was estimated to be 0.11. In addition, a broad PL spectrum was obtained in the *m*-P1 film (Figure S9, Supplementary Materials). The PL decay curve at 575 nm could be fitted with the double exponential relation with  $\chi^2$  of 1.06, and the  $\tau$  values were estimated to be 1.06 ns and 3.52 ns (Figure S7, Supplementary Materials). The longer lifetimes arose from the emission from the intermolecular  $\pi$ - $\pi$  interactions of the aggregated polymer chains. The excitation spectra of *m*-P1 were monitored at 508, 525, 550, 575, and 600 nm; namely, the broad PL band at the longer wavelength, as shown in Figure 5. As the monitored wavelength grew longer, the intensity of the tailing peak increased, which supports the tailing peak in the UV-vis absorption spectrum (Figure 3A). That of *m*-P1 film exhibited the clear tailing peak at the longer wavelength (Figure S10, Supplementary Materials), which was monitored at around 540 nm. The broad longer wavelength peaks of *m*-P1 (Figures 3A and 4) are derived from the intermolecular  $\pi$ - $\pi$  interactions of the aggregated polymer chains in the ground and excited states, respectively.

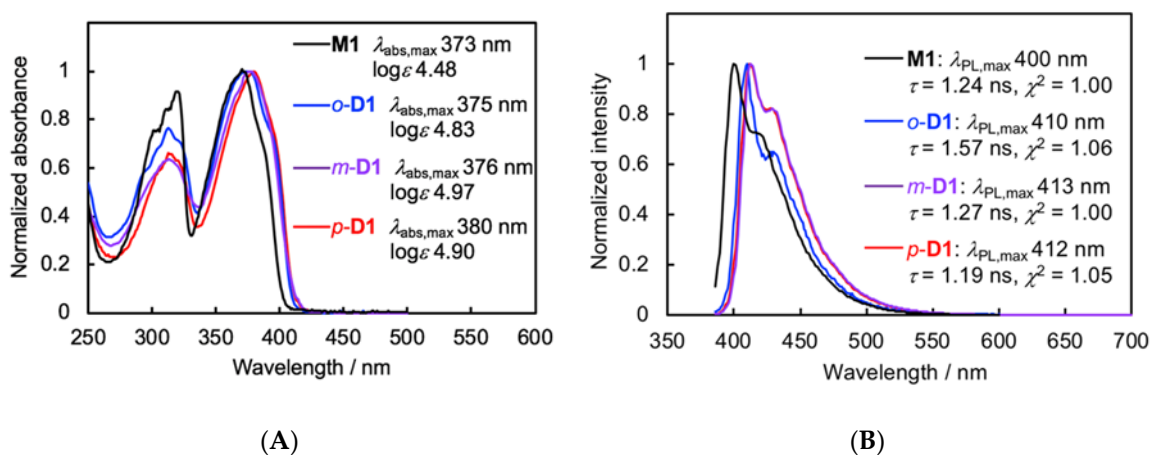


**Figure 4.** PL spectra of **M1**, *m*-**D1**, and the soluble part of *m*-**P1** in  $\text{CHCl}_3$  ( $1.0 \times 10^{-5}$  M for **M1** and *m*-**D1**, and  $0.84 \times 10^{-5}$  M for *m*-**P1**), excited at each  $\lambda_{\text{abs,max}}$ .



**Figure 5.** Excitation spectra of the soluble part of *m*-**P1** in  $\text{CHCl}_3$  ( $0.84 \times 10^{-5}$  M) at room temperature, monitored at 508, 525, 550, 575, and 600 nm. Intensities were normalized at peak tops around 380 nm.

The optical properties of **M1** and the  $\pi$ -stacked dimers *o*-, *m*-, and *p*-**D1** were compared, and the UV-vis absorption and PL spectra are shown in Figure 6A,B, respectively. The UV-vis absorption and PL spectra for the  $\pi$ -stacked dimers were red-shifted in comparison with those of **M1** due to the through-space conjugation. Essential differences in the optical properties among the dimers were not found:  $\lambda_{\text{abs,max}}$  was observed near 375 nm, and  $\lambda_{\text{PL,max}}$  appeared near 410 nm. These results indicate that the molecular orbital of the corresponding  $\pi$ -stacked unit is not influenced by the orientation of the  $\pi$ -stacked units despite the  $\pi$ -stacked structure in the ground as well as the excited state, although a small peak shift is observed in comparison with **M1** owing to the through-space conjugation.



**Figure 6.** (A) UV-vis absorption spectra of **M1**, *o*-**D1**, *m*-**D1**, and *p*-**D1** in  $\text{CHCl}_3$  ( $1.0 \times 10^{-5}$  M); (B) PL spectra of **M1**, *o*-**D1**, *m*-**D1**, and *p*-**D1** in  $\text{CHCl}_3$  ( $1.0 \times 10^{-5}$  M), excited at each  $\lambda_{\text{abs,max}}$ .

#### 4. Conclusions

Pseudo-*meta*-diethynyl[2.2]paracyclophane, prepared by a modified synthetic method, was used as a monomer in the synthesis of a  $\pi$ -stacked PAE-type-polymer consisting of pseudo-*meta*-linked [2.2]paracyclophane. The absorption spectra of the  $\pi$ -stacked polymers after separation by recyclable HPLC as well as a  $\pi$ -stacked dimer were gradually red-shifted as the number of  $\pi$ -stacked units increased, indicating the through-space conjugation. The  $\pi$ -stacked polymer exhibited a broad absorption band derived from the intermolecular  $\pi$ - $\pi$  interactions in addition to the  $\pi$ - $\pi^*$  transition band. PL from the intermolecular  $\pi$ - $\pi$  interactions was also observed. No essential differences in optical properties among the  $\pi$ -stacked molecules comprising pseudo-*o*-, *m*-, and *p*-linked [2.2]paracyclophanes were observed. It was reported that pseudo-*m*-linked [2.2]paracyclophane is symmetry-allowed for electron transport [28]. The present polymer can be a promising candidate to function as a single molecular wire that transfers electron effectively. In addition, the pseudo-*m*-disubstituted [2.2]paracyclophane is optically active due to its planar chirality. The synthesis of optically active  $\pi$ -stacked polymers from enantiopure pseudo-*m*-disubstituted [2.2]paracyclophane is currently in progress.

**Supplementary Materials:** The following are available online at <http://www.mdpi.com/2073-4360/10/10/1140/s1>, Figure S1:  $^1\text{H}$  NMR spectrum of *m*-P1, Figure S2:  $^{13}\text{C}$  NMR spectrum of *m*-P1, Figure S3:  $^1\text{H}$  NMR spectrum of *m*-D1, Figure S4:  $^{13}\text{C}$  NMR spectrum of *m*-D1, Figure S5: GPC curves of *m*-P1 and *m*-D1, Figure S6: PL decay curve of *m*-D1, Figure S7: PL decay curve of *m*-P1, Figure S8: UV-vis absorption spectrum of *m*-P1 film, Figure S9: PL spectrum of *m*-P1 film excited at 381 nm, Figure S10: Excitation spectrum of *m*-P1 film monitored at 541 nm, Figure S11: TGA curve of *m*-P1, and Figure S12: DSC thermograms of *m*-P1.

**Funding:** This work was supported by Grant-in-Aid for Scientific Research on Innovative Areas (No. 17H05165 for Y.M. and No. 17H05164 for T.H.) “ $\pi$ -Figuration” from the Ministry of Education, Culture, Sports, Science and Technology, Japan. The financial support from the Nagase Science Technology Foundation is also acknowledged.

**Acknowledgments:** The authors are grateful to Kazuo Tanaka and Masayuki Gon (Department of Polymer Chemistry, Graduate School of Engineering, Kyoto University) for TGA and DSC analyses.

**Conflicts of Interest:** The authors declare no conflict of interest.

#### References

1. Vögtle, F. *Cyclophane Chemistry: Synthesis, Structures and Reactions*; John Wiley & Sons: Chichester, UK, 1993; ISBN 978-0471931997.
2. Gleiter, R.; Hopf, H. (Eds.) *Modern Cyclophane Chemistry*; Wiley-VCH: Weinheim, Germany, 2004; ISBN 978-3527307135.
3. Brown, C.J.; Farthing, A.C. Preparation and Structure of Di-*p*-Xylylene. *Nature* **1949**, *164*, 915–916. [[CrossRef](#)]
4. Cram, D.J.; Steinberg, H. Macro Rings. I. Preparation and Spectra of the Paracyclophanes. *J. Am. Chem. Soc.* **1951**, *73*, 5691–5704. [[CrossRef](#)]
5. Morisaki, Y.; Chujo, Y. Synthesis of Novel  $\pi$ -Conjugated Polymers Having [2.2]Paracyclophane Skeleton in the Main Chain. Extension of  $\pi$ -Conjugated Length via the Through-Space. *Macromolecules* **2002**, *35*, 587–589. [[CrossRef](#)]
6. Morisaki, Y.; Chujo, Y. Through-Space Conjugated Polymers Based on Cyclophanes. *Angew. Chem. Int. Ed.* **2006**, *45*, 6430–6437. [[CrossRef](#)] [[PubMed](#)]
7. Morisaki, Y.; Wada, N.; Arita, M.; Chujo, Y. Synthesis of Through-space Conjugated Polymers Containing the Pseudo-*ortho*-Linked [2.2]Paracyclophane Moiety. *Polym. Bull.* **2009**, *62*, 305–314. [[CrossRef](#)]
8. Morisaki, Y.; Chujo, Y. Through-Space Conjugated Polymers Consisting of [2.2]Paracyclophane. *Polym. Chem.* **2011**, *2*, 1249–1257. [[CrossRef](#)]
9. Morisaki, Y.; Chujo, Y.  $\pi$ -Electron-system-layered Polymers Based on [2.2]Paracyclophane. *Chem. Lett.* **2012**, *41*, 840–846. [[CrossRef](#)]
10. Morisaki, Y.; Ueno, S.; Saeki, A.; Asano, A.; Seki, S.; Chujo, Y.  $\pi$ -Electron-system-layered Polymer: Through-space Conjugation and Properties as a Single Molecular Wire. *Chem. Eur. J.* **2012**, *18*, 4216–4224. [[CrossRef](#)] [[PubMed](#)]

11. Morisaki, Y.; Hifumi, R.; Lin, L.; Inoshita, K.; Chujo, Y. Practical Optical Resolution of Planar Chiral Pseudo-*ortho*-disubstituted [2.2]Paracyclophane. *Chem. Lett.* **2012**, *41*, 990–992. [[CrossRef](#)]
12. Morisaki, Y.; Hifumi, R.; Lin, L.; Inoshita, K.; Chujo, Y. Through-space Conjugated Polymers Consisting of Planar Chiral Pseudo-*ortho*-linked [2.2]Paracyclophane. *Polym. Chem.* **2012**, *3*, 2727–2730. [[CrossRef](#)]
13. Morisaki, Y.; Inoshita, K.; Chujo, Y. Planar Chiral Through-space Conjugated Oligomers: Synthesis and Characterization of Chiroptical Properties. *Chem. Eur. J.* **2014**, *20*, 8386–8390. [[CrossRef](#)] [[PubMed](#)]
14. Jagtap, S.P.; Collard, D.M. Multitiered 2D  $\pi$ -Stacked Conjugated Polymers Based on Pseudo-Geminal Disubstituted [2.2]Paracyclophane. *J. Am. Chem. Soc.* **2010**, *132*, 12208–12209. [[CrossRef](#)] [[PubMed](#)]
15. Yu, C.-Y.; Hsu, C.-C. Synthesis, Characterization and Aggregation-Induced Emission of Alternating Copolymers Containing Cyclophanes and Tetraphenylethenes. *Polymer* **2018**, *137*, 30–37. [[CrossRef](#)]
16. Reich, H.J.; Cram, D.J. Macro rings. XXXVII. Multiple Electrophilic Substitution Reactions of [2.2]Paracyclophanes and Interconversions of Polysubstituted Derivatives. *J. Am. Chem. Soc.* **1969**, *91*, 3527–3533. [[CrossRef](#)]
17. Bondarenko, L.; Dix, I.; Hinrichs, H.; Hopf, H. Cyclophanes. Part LII: Ethynyl[2.2]paracyclophanes—New Building Blocks for Molecular Scaffolding. *Synthesis* **2004**, 2751–2759.
18. Tanaka, Y.; Ozawa, T.; Inagaki, A.; Akita, M. Redox-active Polyiron Complexes with Tetra(ethynylphenyl) ethene and [2,2]Paracyclophane Spacers Containing Ethynylphenyl Units: Extension to Higher Dimensional Molecular Wire. *Dalton Trans.* **2007**, 928–933. [[CrossRef](#)] [[PubMed](#)]
19. Li, H.; Powell, D.R.; Hayashi, R.K.; West, R. Poly((2,5-dialkoxy-*p*-phenylene)ethynylene-*p*-phenyleneethynylene)s and Their Model Compounds. *Macromolecules* **1998**, *31*, 52–58. [[CrossRef](#)]
20. Moroni, M.; Moigne, J.L. Rigid Rod Conjugated Polymers for Nonlinear Optics. 1. Characterization and Linear Optical Properties of Poly(aryleneethynylene) Derivatives. *Macromolecules* **1994**, *27*, 562–571. [[CrossRef](#)]
21. Tohda, Y.; Sonogashira, K.; Hagihara, N. A Convenient Synthesis of Acetylenes: Catalytic Substitutions of Acetylenic Hydrogen with Bromoalkenes, Iodoarenes and Bromopyridines. *Tetrahedron Lett.* **1975**, *16*, 4467–4470.
22. Meyer-Eppler, G.; Sure, R.; Schneider, A.; Schnakenburg, G.; Grimme, S.; Lützen, A. Synthesis, Chiral Resolution, and Absolute Configuration of Dissymmetric 4,15-Difunctionalized [2.2]Paracyclophanes. *J. Org. Chem.* **2014**, *79*, 6679–6687. [[CrossRef](#)] [[PubMed](#)]
23. Wang, S.; Bazan, G.C.; Tretiak, S.; Mukamel, S. Oligophenylenevinylene Phane Dimers: Probing the Effect of Contact Site on the Optical Properties of Bichromophoric Pairs. *J. Am. Chem. Soc.* **2000**, *122*, 1289–1297. [[CrossRef](#)]
24. Bartholomew, G.P.; Bazan, G.C. Bichromophoric Paracyclophanes: Models for Interchromophore Delocalization. *Acc. Chem. Res.* **2001**, *34*, 30–39. [[CrossRef](#)] [[PubMed](#)]
25. Bartholomew, G.P.; Bazan, G.C. Strategies for the Synthesis of ‘Through-Space’ Chromophore Dimers Based on [2.2]Paracyclophane. *Synthesis* **2002**, 1245–1255. [[CrossRef](#)]
26. Hong, J.W.; Woo, H.Y.; Bazan, G.C. Solvatochromism of Distyrylbenzene Pairs Bound Together by [2.2]Paracyclophane: Evidence for a Polarizable “Through-Space” Delocalized State. *J. Am. Chem. Soc.* **2005**, *127*, 7435–7443. [[CrossRef](#)] [[PubMed](#)]
27. Bazan, G.C. Novel Organic Materials Through Control of Multichromophore Interactions. *J. Org. Chem.* **2007**, *72*, 8615–8635. [[CrossRef](#)] [[PubMed](#)]
28. Li, X.; Staykov, A.; Yoshizawa, K. Orbital Views on Electron-Transport Properties of Cyclophanes: Insight into Intermolecular Transport. *Bull. Chem. Soc. Jpn.* **2012**, *85*, 181–188. [[CrossRef](#)]



© 2018 by the authors. Licensee MDPI, Basel, Switzerland. This article is an open access article distributed under the terms and conditions of the Creative Commons Attribution (CC BY) license (<http://creativecommons.org/licenses/by/4.0/>).

# Synthesis of enantiopure planar chiral bis-(*para*)-pseudo-*meta*-type [2.2]paracyclophanes

Risa Sawada<sup>1</sup> | Masayuki Gon<sup>1</sup> | Jun Nakamura<sup>2</sup> | Yasuhiro Morisaki<sup>1,2</sup>  | Yoshiki Chujo<sup>1</sup>

<sup>1</sup>Department of Polymer Chemistry, Graduate School of Engineering, Kyoto University, Kyoto, Japan

<sup>2</sup>Department of Applied Chemistry for Environment, School of Science and Technology, Kwansei Gakuin University, Sanda, Japan

## Correspondence

Yasuhiro Morisaki, Department of Applied Chemistry for Environment, School of Science and Technology, Kwansei Gakuin University, 2-1 Gakuen, Sanda, Hyogo 669-1337, Japan.  
Email: ymo@kwansei.ac.jp

Yoshiki Chujo, Department of Polymer Chemistry, Graduate School of Engineering, Kyoto University, Nishikyoku, Kyoto 615-8510, Japan.  
Email: chujo@poly.synchem.kyoto-u.ac.jp

## Abstract

A new type of planar chiral (*R<sub>p</sub>*)- and (*S<sub>p</sub>*)-4,7,12,15-tetrasubstituted [2.2]paracyclophanes was prepared from racemic 4,7,12,15-tetrabromo[2.2]paracyclophane as the starting substrate. Regioselective lithiation and transformations afforded racemic bis-(*para*)-pseudo-*meta*-type [2.2]paracyclophane (4,15-dibromo-7,12-dihydroxy[2.2]paracyclophane). Its optical resolution was performed by the diastereomer method using a chiral camphanoyl group as the chiral auxiliary. The diastereoisomers were readily isolated by simple silica gel column chromatography, and the successive hydrolysis afforded (*R<sub>p</sub>*)- and (*S<sub>p</sub>*)-bis-(*para*)-pseudo-*meta*-type [2.2]paracyclophanes ((*R<sub>p</sub>*)- and (*S<sub>p</sub>*)-4,15-dibromo-7,12-dihydroxy[2.2]paracyclophanes). They can be used as pseudo-*meta*-substituted chiral building blocks.

## KEYWORDS

chiral auxiliary, chiral building block, diastereomer, optical resolution, regioselectivity

## 1 | INTRODUCTION

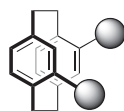
[2.2]Paracyclophane<sup>1–5</sup> consists of two phenylene units that are facing and stacking in proximity. The rotary motion of the benzene rings is restricted. Therefore, [2.2]paracyclophanes with substituent(s) can be planar chiral compounds depending on the substitution position(s),<sup>6–11</sup> and the planar chirality of [2.2]paracyclophane compounds is conformationally stable owing to the restricted rotary motion. Thus far, their primary use has been chiral auxiliaries in the fields of organic and organometallic chemistry. We have focused on the planar chirality of [2.2]paracyclophane and developed optical resolution methods for 4,12-disubstituted<sup>12–21</sup> and 4,7,12,15-tetrasubstituted<sup>22–24</sup> [2.2]paracyclophanes (Figure 1). Recently, we synthesized the bis-(*para*)-pseudo-*ortho*-type of optically active 4,7,12,15-tetrasubstituted [2.2]paracyclophane (Figure 1).<sup>23</sup> They were used as chiral building blocks to prepare various optically active  $\pi$ -conjugated compounds, leading to circularly polarized luminescence (CPL) with large dissymmetry factors.<sup>22,23,25–32</sup>

Thus, their planar chirality of [2.2]paracyclophane can be applied in the fields of polymer and materials chemistry. To produce a wider variety of planar chiral [2.2]paracyclophane compounds, this paper reports the preparation of new bis-(*para*)-pseudo-*meta*-type optically active 4,7,12,15-tetrasubstituted [2.2]paracyclophanes, which are planar chiral molecules with C<sub>2</sub> symmetry (Figure 1). Moreover, their optical resolution method and the synthesis of chiral building blocks are described.

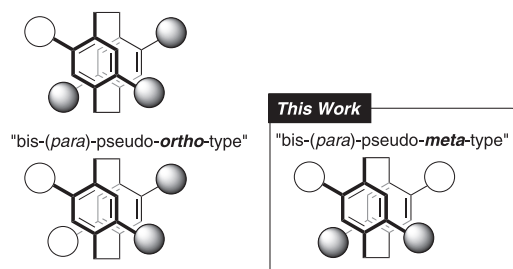
## 2 | RESULTS AND DISCUSSION

The synthetic route to racemic bis-(*para*)-pseudo-*meta*-type 4,7,12,15-tetrasubstituted [2.2]paracyclophane is shown in Scheme 1. Racemic 4,7,12,15-tetrabromo[2.2]paracyclophane (*rac*-1) was prepared as the precursor by a modified version of Chow's method.<sup>33</sup> We have already synthesized racemic tribromo[2.2]paracyclophane (*rac*-2) in 69% isolated yield from *rac*-1.<sup>22</sup> Compound *rac*-2 was then reacted with 2.3 equivalent of *n*-BuLi, and successive

## 4,12-Disubstituted [2.2]paracyclophane



## 4,7,12,15-Tetrasubstituted [2.2]paracyclophanes



**FIGURE 1** 4,12-Disubstituted and 4,7,12,15-tetrasubstituted [2.2]paracyclophane skeletons

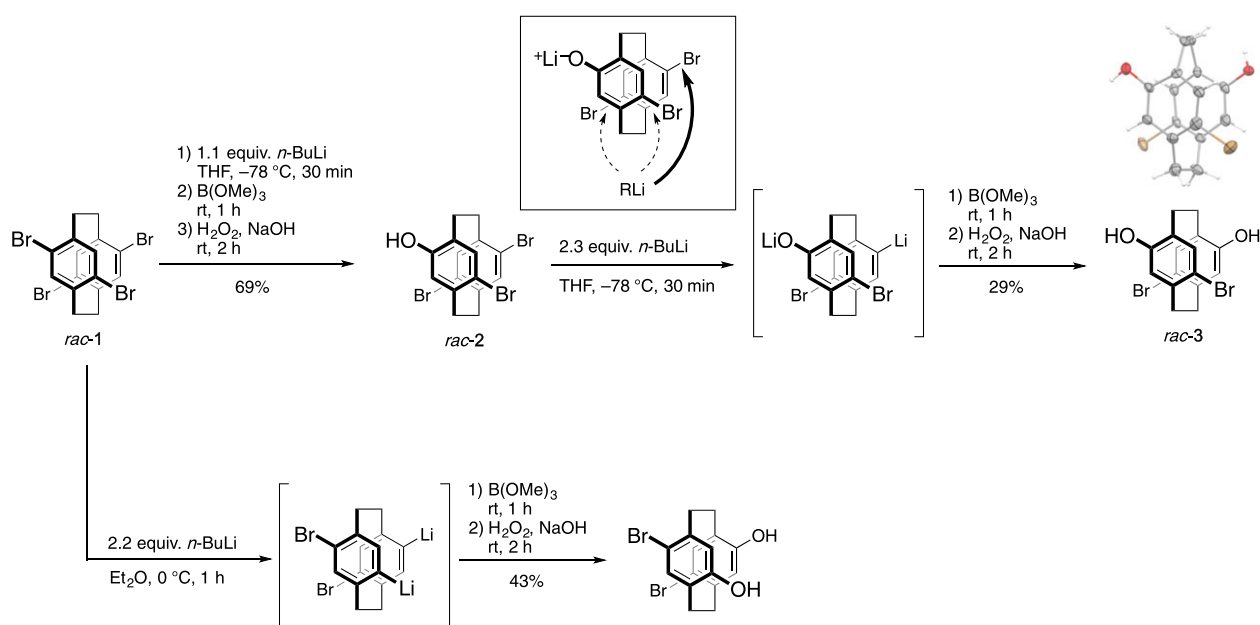
reactions with  $B(OMe)_3$  and  $H_2O_2/NaOH$  afforded the target compound, namely, bis-(*para*)-pseudo-*meta*-type 4,15-dibromo-7,12-dihydroxy[2.2]paracyclophane (*rac*-3) in 29% isolated yield. In terms of reaction mechanism, first, the phenol in *rac*-2 was reacted with *n*-BuLi to form lithium phenoxide. The next attack of *n*-BuLi occurred dominantly at the pseudo-*meta*-position due to the electronic effect (Scheme 1); thus, a bromo group at the pseudo-*meta*-position was replaced with lithium. The structure of *rac*-3 was confirmed by X-ray crystallography. A pair of enantiomers was crystallized instead of spontaneous resolution (Figure S9).

On the other hand, one-pot reaction of *rac*-1 with 2.2 equivalent of *n*-BuLi was also performed to obtain *rac*-3,

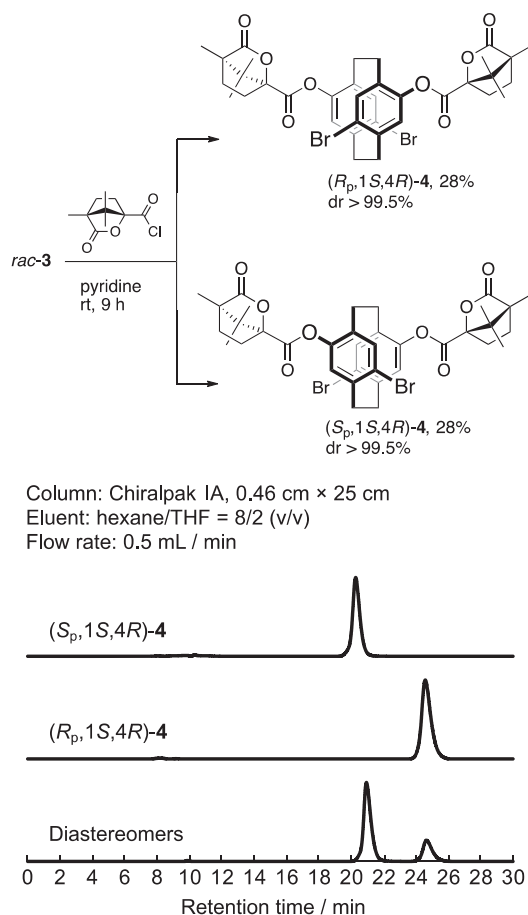
as shown in Scheme 1. However, the second attack of *n*-BuLi occurred regioselectively at the pseudo-*ortho*-position (Scheme 1), affording the bis-(*para*)-pseudo-*ortho*-type dilithio[2.2]paracyclophane intermediate. The treatment with  $B(OMe)_3$  and  $H_2O_2/NaOH$  afforded the corresponding 4,12-dibromo-7,15-dihydroxy[2.2]paracyclophane in 43% isolated yield.

The optical resolution was simply performed by the diastereomer method using camphanoyl chloride. Since optical resolution of racemic PHANOL (4,12-dihydroxy[2.2]paracyclophane) using camphanoyl chloride had been achieved by Jiang and Zhao,<sup>16</sup> we also applied (1*S*,4*R*)-camphanoyl chloride as the chiral auxiliary to *rac*-3, as shown in Figure 2. The obtained diastereomers **4** could be readily separated by a common  $SiO_2$  column chromatography. Figure 2 includes the chromatograms of separated diastereomers ( $R_p$ ,1*S*,4*R*)-**4** and ( $S_p$ ,1*S*,4*R*)-**4** (retention time gap = approximately 4.5 min) and of the mixture by a chiral column using Chiralpak IA, indicating that the ratios of both diastereomers were over 99.5%. Although single crystal of each diastereomer could not be obtained, the X-ray crystallography data were sufficient to determine their absolute configuration (Figure S10).

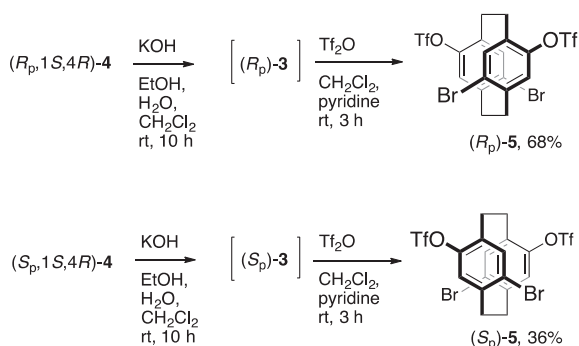
As shown in Scheme 2, the camphanoyl groups were removed by hydrolysis using KOH. Without purification, the obtained 4,15-dibromo-7,12-dihydroxy[2.2]paracyclophane (*rac*-3) was reacted with  $Tf_2O$  to obtain ( $R_p$ )- and ( $S_p$ )-4,15-dibromo-7,12-trifluoromethanesulfonyloxy[2.2]paracyclophanes (( $R_p$ )-**5** and ( $S_p$ )-**5**, respectively), which can be used as chiral building blocks for various optically active  $\pi$ -conjugated compounds by transition metal-catalyzed cross-couplings.



**SCHEME 1** Synthetic route to bis-(*para*)-pseudo-*meta*-isomer, *rac*-3, and the bis-(*para*)-pseudo-*ortho*-isomer



**FIGURE 2** Synthesis of  $(R_p,1S,4R)$ -**4** and  $(S_p,1S,4R)$ -**4** (optical resolution method) and their chromatograms



**SCHEME 2** Transformation of  $(R_p,1S,4R)$ -**4** and  $(S_p,1S,4R)$ -**4**

### 3 | CONCLUSION

In conclusion, planar chiral bis-*(para)*-pseudo-*meta*-type 4,7,12,15-tetrasubstituted [2.2]paracyclophanes were synthesized. Two synthetic routes to the racemic 4,15-dibromo-7,12-dihydroxy[2.2]paracyclophane were developed from racemic 4,7,12,15-tetrabromo[2.2]paracyclophane as a precursor. Optical resolution was achieved by the diastereomer method using optically

active camphanoyl chloride as a chiral auxiliary. Thus, enantiopure bis-*(para)*-pseudo-*meta*-type [2.2]paracyclophane was successfully produced in addition to the bis-*(para)*-pseudo-*ortho*-isomer. Removal of the camphanoyl unit and successive transformations afforded bis-*(para)*-pseudo-*meta*-type [2.2]paracyclophane chiral building blocks. As members of the planar chiral [2.2]paracyclophane family, they could be used to construct a wide variety of optically active  $\pi$ -stacked molecules.

## 4 | EXPERIMENTAL SECTION

### 4.1 | General

$^1\text{H}$  and  $^{13}\text{C}$  spectra were recorded on a JEOL EX400 or AL400 instrument. Samples were analyzed in  $\text{CDCl}_3$ , and the chemical shift values were expressed relative to  $\text{Me}_4\text{Si}$  as an internal standard. Analytical thin-layer chromatography (TLC) was performed with silica gel 60 Merck F<sub>254</sub> plates. Column chromatography was performed with Wakogel C-300  $\text{SiO}_2$ . High-resolution mass spectrometry (HRMS) for diastereomers **4** and enantiomers **5** was performed at the Technical Support Office at Kyoto University, and the HRMS spectra were obtained on a JEOL JMS-MS700 spectrometer for electrospray ionization (ESI). High-resolution mass spectrometry for racemic compound **3** was performed at Ehime University, and the HRMS spectrum was obtained on a JEOL JMS-MS700 spectrometer for fast atom bombardment (FAB). Diastereomer ratio (dr) was confirmed by a high-performance liquid chromatography (TOSOH UV-8020) equipped with a Daicel Chiralpak® IA column (0.46 cm  $\times$  25 cm; solvent flow rate, 0.5 mL/min). Specific rotations ( $[\alpha]_D^{25}$ ) were measured with a HORIBA SEPA-500 polarimeter.

### 4.2 | Materials

Compounds *rac*-**1**<sup>22,33</sup> and *rac*-**2**<sup>22</sup> were prepared as described in the literature. *n*-BuLi in hexane (1.6M),  $\text{B}(\text{OMe})_3$ ,  $\text{H}_2\text{O}_2$ , NaOH, (1*S*,4*R*)-camphanoyl chloride, KOH, and  $\text{Tf}_2\text{O}$  were commercially available compounds, and they were used without purification. Tetrahydrofuran (THF) and  $\text{Et}_2\text{O}$  were purchased and purified by the Glass Contour solvent purification system. Pyridine was purchased and used after distillation over KOH.

### 4.3 | Synthetic procedures

#### 4.3.1 | Synthesis of *rac*-**3** via *rac*-**2**

A solution of *n*-BuLi (1.60M in hexane, 3.6 mL, 5.7 mmol) was slowly added to a solution of *rac*-**2** (1.14 g, 2.47 mmol)

in THF (30 mL) at  $-78^{\circ}\text{C}$ . After 30 minutes,  $\text{B}(\text{OMe})_3$  (5.2 mL, 47 mmol) was added and the mixture was stirred 1 hour at  $-78^{\circ}\text{C}$  to room temperature. Aqueous solution of NaOH and aqueous solution of  $\text{H}_2\text{O}_2$  were added. The mixture was stirred for 2 hours at room temperature. To the yellow reaction mixture was added saturated aqueous  $\text{NH}_4\text{Cl}$  solution, and the organic layer was extracted 3 times with  $\text{CH}_2\text{Cl}_2$ . The combined organic layer was washed with brine and dried over  $\text{MgSO}_4$ .  $\text{MgSO}_4$  was removed by filtration, and the solvent was removed with a rotary evaporator. The residue was purified by column chromatography on  $\text{SiO}_2$  (hexane/ $\text{EtOAc}$  = 4/1 as an eluent,  $R_f$  = 0.24) to afford *rac*-**3** (284 mg, 0.71 mmol, 29%) as a white powder.

$^1\text{H}$  NMR ( $\text{CDCl}_3$ , 500 MHz)  $\delta$  2.76–2.88 (m, 4H), 3.03–3.11 (m, 2H), 3.18–3.26 (m, 2H), 4.70 (s, 2H), 6.26 (s, 2H), 7.06 (s, 2H) ppm;  $^{13}\text{C}$  NMR ( $\text{CDCl}_3$ , 125 MHz)  $\delta$  28.1, 33.6, 117.9, 119.5, 126.7, 135.2, 141.0, 153.7 ppm. HRMS (FAB) calcd. for  $\text{C}_{16}\text{H}_{14}^{79}\text{Br}_2\text{O}_2$   $[\text{M}]^+$ : 395.9361, found 395.9353. Calcd. for  $\text{C}_{16}\text{H}_{14}^{79}\text{Br}^{81}\text{BrO}_2$   $[\text{M}]^+$ : 397.9340, found 397.9352. Calcd. for  $\text{C}_{16}\text{H}_{14}^{81}\text{Br}_2\text{O}_2$   $[\text{M}]^+$ : 399.9320, found 399.9325.

### 4.3.2 | Synthesis of 4,12-dibromo-7,15-dihydroxy[2.2]paracyclophane from *rac*-**1**

A solution of *n*-BuLi (1.6M in hexane, 4.1 mL, 6.6 mmol) was slowly added to a solution of *rac*-**1** (1.53 g, 2.95 mmol) in  $\text{Et}_2\text{O}$  (80 mL) at  $0^{\circ}\text{C}$ . After 1 hour,  $\text{B}(\text{OMe})_3$  (1.7 mL, 15.2 mmol) was added at  $0^{\circ}\text{C}$  and then warmed to room temperature. After 1 hour, aqueous solution of NaOH and aqueous  $\text{H}_2\text{O}_2$  were added, and the mixture was stirred for 40 minutes at room temperature. To the reaction mixture was added saturated aqueous  $\text{NH}_4\text{Cl}$  solution, and the organic layer was extracted 3 times with  $\text{CH}_2\text{Cl}_2$ . The combined organic layer was washed with brine and dried over  $\text{Na}_2\text{SO}_4$ .  $\text{Na}_2\text{SO}_4$  was removed by filtration, and the solvent was evaporated. The residue was purified by column chromatography on  $\text{SiO}_2$  ( $\text{CHCl}_3$ / $\text{EtOAc}$  = 5:1 as an eluent,  $R_f$  = 0.23) to afford 4,12-dibromo-7,15-dihydroxy[2.2]paracyclophane (509 mg, 1.28 mmol, 43%) as a white powder.<sup>23</sup>

### 4.3.3 | Synthesis of (*R*<sub>p</sub>,1*S*,4*R*)-**4** and (*S*<sub>p</sub>,1*S*,4*R*)-**4**

A mixture of *rac*-**3** (284 mg, 0.71 mmol) and (1*S*,4*R*)-camphanoyl chloride (371 mg, 1.7 mmol) was placed in a round-bottom flask equipped with magnetic stirring bar. After degassing the reaction mixture several times, dehydrated pyridine (35 mL) was added and the mixture was stirred at room temperature for 9 hours. After addition of 5M HCl (35 mL), the organic layer was extracted

with  $\text{CH}_2\text{Cl}_2$  and washed with 1M HCl, saturated aqueous  $\text{NaHCO}_3$ , and brine. The combined organic layer was dried over  $\text{MgSO}_4$ .  $\text{MgSO}_4$  was removed by filtration, and the solvent was removed with a rotary evaporator. The residue was purified by column chromatography on  $\text{SiO}_2$  ( $\text{CHCl}_3$ / $\text{EtOAc}$  = 20/1 v/v as an eluent) to give (*R*<sub>p</sub>,1*S*,4*R*)-**4** and (*S*<sub>p</sub>,1*S*,4*R*)-**4** as a white solid. The recrystallization from  $\text{CHCl}_3$  and MeOH (good and poor solvent, respectively) was performed to obtain optically pure products: (*R*<sub>p</sub>,1*S*,4*R*)-**4** (150 mg, 0.20 mmol, 28%) and (*S*<sub>p</sub>,1*S*,4*R*)-**4** (149 mg, 0.19 mmol, 28%).

(*R*<sub>p</sub>,1*S*,4*R*)-**4**. Yield: 28%.  $R_f$  = 0.20 ( $\text{CHCl}_3$ /hexane = 9/1 v/v). Colorless needle crystal.  $^1\text{H}$  NMR ( $\text{CDCl}_3$ , 400 MHz)  $\delta$  1.10 (s, 6H), 1.18 (s, 6H), 1.21 (s, 6H), 1.78–1.85 (m, 2H), 2.00–2.09 (m, 2H), 2.25–2.35 (m, 2H), 2.55–2.63 (m, 2H), 2.70–2.83 (m, 2H), 2.94–3.18 (m, 4H), 3.22–3.34 (m, 2H), 6.80 (s, 2H), 7.12 (s, 2H) ppm;  $^{13}\text{C}$  NMR ( $\text{CDCl}_3$ , 100 MHz)  $\delta$  9.7, 16.7, 16.9, 29.0, 29.9, 31.2, 32.7, 54.3, 54.9, 90.6, 123.6, 125.2, 132.5, 135.9, 140.8, 148.0, 164.8, 177.6 ppm. HRMS (ESI) calcd. for  $\text{C}_{36}\text{H}_{38}\text{Br}_2\text{O}_8\text{Na}$   $[\text{M} + \text{Na}]^+$ : 779.0826, found 779.0831.  $[\alpha]_D^{23}$  =  $-32.1$  (*c* 0.1,  $\text{CHCl}_3$ ). Retention time of liquid chromatography:  $t$  = 24.6 minutes (Chiralpak<sup>®</sup> IA, hexane/THF = 8/2 v/v).

(*S*<sub>p</sub>,1*S*,4*R*)-**4**. Yield: 28%.  $R_f$  = 0.40 ( $\text{CHCl}_3$ / $\text{EtOAc}$  = 20/1 v/v). Colorless needle crystal.  $^1\text{H}$  NMR ( $\text{CDCl}_3$ , 400 MHz)  $\delta$  1.14 (s, 6H), 1.20 (s, 6H), 1.24 (s, 6H), 1.72–1.82 (m, 2H), 1.96–2.05 (m, 2H), 2.15–2.21 (m, 2H), 2.51–2.60 (m, 2H), 2.80–3.10 (m, 6H), 3.20–3.30 (m, 2H), 6.76 (s, 2H), 7.10 (s, 2H) ppm;  $^{13}\text{C}$  NMR ( $\text{CDCl}_3$ , 100 MHz)  $\delta$  9.7, 16.6, 17.3, 28.8, 29.9, 30.8, 32.7, 54.6, 55.0, 90.7, 123.6, 125.5, 132.8, 135.9, 140.7, 148.1, 165.1, 177.8 ppm. HRMS (ESI) calcd. for  $\text{C}_{36}\text{H}_{38}\text{Br}_2\text{O}_8\text{Na}$   $[\text{M} + \text{Na}]^+$ : 779.0826, found 779.0831.  $[\alpha]_D^{23}$  = 34.0 (*c* 0.1,  $\text{CHCl}_3$ ). Retention time of liquid chromatography:  $t$  = 20.3 minutes (Chiralpak<sup>®</sup> IA, hexane/THF = 8/2 v/v).

### 4.3.4 | Synthesis of (*R*<sub>p</sub>)-**5** and (*S*<sub>p</sub>)-**5**

KOH (62.1 mg, 1.1 mmol) in  $\text{H}_2\text{O}$  (1 mL) was added to a solution of (*R*<sub>p</sub>,1*S*,4*R*)-**4** (80.0 mg, 0.11 mmol) in EtOH (3 mL) and  $\text{CH}_2\text{Cl}_2$  (4 mL). After the mixture was stirred for 10 hours at room temperature, the reaction mixture was quenched by the addition of 5M HCl. The organic layer was extracted with  $\text{CH}_2\text{Cl}_2$  and washed with saturated aqueous  $\text{NaHCO}_3$  and brine. The combined organic layer was dried over  $\text{MgSO}_4$ .  $\text{MgSO}_4$  was removed by filtration, and the solvent was removed with a rotary evaporator to obtain (*R*<sub>p</sub>)-**3**, which was used without purification. Compound (*R*<sub>p</sub>)-**3** was placed in a 100-mL two-neck round-bottom flask equipped with a magnetic stirring bar, and  $\text{CH}_2\text{Cl}_2$  (10 mL), dehydrated pyridine (0.50 mL, 6.0 mmol), and  $\text{Tf}_2\text{O}$  (0.088 mL, 0.53 mmol) were added at  $0^{\circ}\text{C}$ . After stirring for 3 hours at room

temperature, the reaction mixture was quenched by the addition of 5M HCl. The organic layer was extracted with  $\text{CH}_2\text{Cl}_2$  and washed with 5M HCl, saturated aqueous  $\text{NaHCO}_3$ , and brine. The combined organic layer was dried over  $\text{MgSO}_4$ .  $\text{MgSO}_4$  was removed by filtration, and the solvent was removed with a rotary evaporator. The residue was purified by column chromatography on  $\text{SiO}_2$  ( $\text{CHCl}_3/\text{hexane} = 4/1$  as an eluent) to afford ( $R_p$ )-**5** (47.4 mg, 0.075 mmol, 68%) as a white solid.

$R_f = 0.25$  ( $\text{CHCl}_3/\text{hexane} = 4/1$ ).  $^1\text{H NMR}$  ( $\text{CDCl}_3$ , 400 MHz)  $\delta$  2.84–2.94 (m, 2H), 3.03–3.12 (m, 2H), 3.27–3.38 (m, 4H), 6.91 (s, 2H), 7.11 (s, 2H) ppm;  $^{13}\text{C NMR}$  ( $\text{CDCl}_3$ , 100 MHz)  $\delta$  29.7, 32.7, 118.6 (q,  $J_{\text{C-F}} = 318$  Hz), 125.4, 126.3, 133.5, 136.5, 142.2, 147.4 ppm. HRMS (ESI) calcd. for  $\text{C}_{18}\text{H}_{11}\text{Br}_2\text{F}_6\text{O}_6\text{S}_2$  [ $\text{M} - \text{H}$ ] $^-$ : 658.8268, found 658.8261.  $[\alpha]_{\text{D}}^{23} = -26.0$  ( $c$  0.2,  $\text{CHCl}_3$ ).

The synthetic procedure of ( $S_p$ )-**5** is the same as that of ( $R_p$ )-**5** in 36% isolated yield. HRMS (ESI) calcd. for  $\text{C}_{18}\text{H}_{11}\text{Br}_2\text{F}_6\text{O}_6\text{S}_2$  [ $\text{M} - \text{H}$ ] $^-$ : 658.8268, found 658.8287.  $[\alpha]_{\text{D}}^{23} = +26.1$  ( $c$  0.2,  $\text{CHCl}_3$ ).

## ACKNOWLEDGMENTS

This work was partly supported by Grant-in-Aid for Scientific Research on Innovative Areas (no. 17H05165) “ $\pi$ -Figuration” from the Ministry of Education, Culture, Sports, Science and Technology, Japan, and by Iketani Science and Technology Foundation. M.G. appreciates Research Fellowships (no. 14J02514) from the Japan Society for the Promotion of Science for Young Scientists.

## ORCID

Yasuhiro Morisaki  <http://orcid.org/0000-0002-9125-2670>

## REFERENCES

- Vögtle F (Ed). *Cyclophane Chemistry: Synthesis, Structures and Reactions*. Chichester: John Wiley & Sons; 1993.
- Gleiter R, Hopf H (Eds). *Modern Cyclophane Chemistry*. Weinheim: Wiley-VCH; 2004.
- Hopf H. [2.2]Paracyclophanes in polymer chemistry and materials science. *Angew Chem Int Ed*. 2008;47(51):9808–9812.
- Brown CJ, Farthing AC. Preparation and structure of di-*p*-xylylene. *Nature*. 1949;164(4178):915–916.
- Cram DJ, Steinberg H. Macro rings. I. Preparation and spectra of the paracyclophanes. *J Am Chem Soc*. 1951;73(12):5691–5704.
- Cram DJ, Allinger NL. Macro rings. XII. Stereochemical consequences of steric compression in the smallest paracyclophane. *J Am Chem Soc*. 1955;77(23):6289–6294.
- Rozenberg V, Sergeeva E, Hopf H. Cyclophanes as templates in stereoselective synthesis. In: Gleiter R, Hopf H, eds. *Modern Cyclophane Chemistry*. Weinheim: Wiley-VCH; 2004:435–462.
- Rowlands GJ. The synthesis of enantiomerically pure [2.2]paracyclophane derivatives. *Org Biomol Chem*. 2008;6(9):1527–1534.
- Gibson SE, Knight JD. [2.2]Paracyclophane derivatives in asymmetric catalysis. *Org Biomol Chem*. 2003;1(8):1256–1269.
- Aly AA, Brown AB. Asymmetric and fused heterocycles based on [2.2]paracyclophane. *Tetrahedron*. 2009;65(39):8055–8089.
- Paradies J. [2.2]Paracyclophane derivatives: synthesis and application in catalysis. *Synthesis*. 2011;2011(23):3749–3766.
- Morisaki Y, Hifumi R, Lin L, Inoshita K, Chujo Y. Practical optical resolution of planar chiral pseudo-*ortho*-disubstituted [2.2]paracyclophane. *Chem Lett*. 2012;41(9):990–992.
- Pye PJ, Rossen K, Reamer RA, Tsou NN, Volante RP, Reider PJ. A new planar chiral bisphosphine ligand for asymmetric catalysis: highly enantioselective hydrogenations under mild conditions. *J Am Chem Soc*. 1997;119(26):6207–6208.
- Rossen K, Pye PJ, Maliakal A, Volante RP. Kinetic resolution of *rac*-4,12-dibromo[2.2]paracyclophane in a palladium [2.2]phanephos catalyzed amination. *J Org Chem*. 1997;62(19):6462–6463.
- Zhuravsky R, Starikova Z, Vorontsov E, Rozenberg V. Novel strategy for the synthesis of chiral pseudo-*ortho*-substituted hydroxy[2.2]paracyclophane-based ligands from the resolved 4-bromo-12-hydroxy[2.2]paracyclophane as a parent compound. *Tetrahedron Asym*. 2008;19(2):216–222.
- Jiang B, Zhao XL. A simple and efficient resolution of ( $\pm$ )-4,12-dihydroxy[2.2]paracyclophane. *Tetrahedron Asym*. 2004;15(7):1141–1143.
- Jones PG, Hillmer J, Hopf H. (*S*)-4,16-Dihydroxymethyl-[2.2]paracyclophane bis-(1*S*)-camphanoate. *Acta Crystallogr*. 2003; E59:o24–o25.
- Pamperin D, Hopf H, Sylatk C, Pietzsch M. Synthesis of planar chiral [2.2]paracyclophanes by biotransformations: kinetic resolution of 4-formyl-[2.2]paracyclophane by asymmetric reduction. *Tetrahedron Asym*. 1997;8(2):319–325.
- Pamperin D, Ohse B, Hopf H, Pietzsch M. Synthesis of planar-chiral [2.2]paracyclophanes by biotransformations: screening for hydrolase activity for the kinetic resolution of 4-acetoxy-[2.2]paracyclophane. *J Mol Cat B Enzymatic*. 1998;5(1–4):317–319.
- Braddock DC, MacGilp ID, Perry BG. Improved synthesis of ( $\pm$ )-4,12-dihydroxy[2.2]paracyclophane and its enantiomeric resolution by enzymatic methods: planar chiral (*R*)- and (*S*)-phenol. *J Org Chem*. 2002;67(24):8679–8681.
- Meyer-Eppler G, Vogelsang E, Benkhäuser C, Schneider A, Schnakenburg G, Lützen A. Synthesis, chiral resolution, and absolute configuration of dissymmetric 4,12-difunctionalized [2.2]paracyclophanes. *Eur J Org Chem*. 2013;21:4523–4532.
- Morisaki Y, Gon M, Sasamori T, Tokitoh N, Chujo Y. Planar chiral tetrasubstituted [2.2]paracyclophane: optical resolution and functionalization. *J Am Chem Soc*. 2014;136(9):3350–3353.
- Morisaki Y, Sawada R, Gon M, Chujo Y. New type of planar chiral [2.2]paracyclophanes and construction of one-handed double helices. *Chem Asian J*. 2016;11(18):2524–2527.

24. Vorontsova NV, Rozenberg VI, Sergeeva EV, et al. Symmetrically tetrasubstituted [2.2]paracyclophanes: their systematization and regioselective synthesis of several types of bis-bifunctional derivatives by double electrophilic substitution. *Chem Eur J*. 2008;14(15):4600-4617.
25. Morisaki Y, Hifumi R, Lin L, Inoshita K, Chujo Y. Through-space conjugated polymers consisting of planar chiral pseudo-ortho-linked [2.2]paracyclophane. *Polym Chem*. 2012;3(10):2727-2730.
26. Morisaki Y, Inoshita K, Chujo Y. Planar chiral through-space conjugated oligomers: synthesis and characterization of chiroptical properties. *Chem Eur J*. 2014;20(27):8386-8390.
27. Gon M, Morisaki Y, Chujo Y. Optically active cyclic compounds based on planar chiral [2.2]paracyclophane: extension of the conjugated systems and chiroptical properties. *J Mater Chem C*. 2015;3(3):521-529.
28. Gon M, Morisaki Y, Chujo Y. Highly emissive circularly polarized luminescence from optically active conjugated dimers consisting of planar chiral [2.2]paracyclophane. *Eur J Org Chem*. 2015;(35):7756-7762.
29. Gon M, Kozuka H, Morisaki Y, Chujo Y. Optically active cyclic compounds based on planar chiral [2.2]paracyclophane: extension of the  $\pi$ -surface with naphthalene units. *Asian J Org Chem*. 2016;5(3):353-359.
30. Gon M, Morisaki Y, Sawada R, Chujo Y. Synthesis of optically active X-shaped conjugated compounds and dendrimers based on planar chiral [2.2]paracyclophane, leading to highly emissive circularly polarized luminescence materials. *Chem Eur J*. 2016;22(7):2291-2298.
31. Gon M, Sawada R, Morisaki Y, Chujo Y. Enhancement and controlling the signal of circularly polarized luminescence based on a planar chiral tetrasubstituted [2.2]paracyclophane framework in aggregation system. *Macromolecules*. 2017;50(5):1790-1802.
32. Gon M, Morisaki Y, Chujo Y. Optically active phenylethene dimers based on planar chiral tetrasubstituted [2.2]paracyclophane. *Chem Eur J*. 2017;23(26):6323-6329.
33. Chow HF, Low KH, Wong KY. An improved method for the regiospecific synthesis of polysubstituted [2.2]paracyclophanes. *Synlett*. 2005;(14):2130-2134.

## SUPPORTING INFORMATION

Additional supporting information may be found online in the Supporting Information section at the end of the article.

**How to cite this article:** Sawada R, Gon M, Nakamura J, Morisaki Y, Chujo Y. Synthesis of enantiopure planar chiral bis-(*para*)-pseudo-*meta*-type [2.2]paracyclophanes. *Chirality*. 2018;30: 1109–1114. <https://doi.org/10.1002/chir.23010>

## •ARTICLES•

SPECIAL TOPIC: Aggregation-induced Emission

August 2018 Vol.61 No.8: 940–946

<https://doi.org/10.1007/s11426-018-9258-y>

## Comparison of luminescent properties of helicene-like bibenzothiophenes with *o*-carborane and 5,6-dicarba-*nido*-decaborane

Kenta Nishino<sup>1</sup>, Kazushi Hashimoto<sup>1</sup>, Kazuo Tanaka<sup>1\*</sup>, Yasuhiro Morisaki<sup>1,2</sup> & Yoshiki Chujo<sup>1\*</sup><sup>1</sup>Department of Polymer Chemistry, Graduate School of Engineering, Kyoto University, Katsura Kyoto 615-8510, Japan;<sup>2</sup>Department of Applied Chemistry for Environment, School of Science and Technology, Kwansei Gakuin University, Sanda Hyogo 669-1337, Japan

Received February 16, 2018; accepted April 16, 2018; published online July 3, 2018

This article describes comparison of the anchoring effect on electronic properties of the helicene-like bibenzothiophene between *o*-carborane and 5,6-dicarba-*nido*-decaborane. The *o*-carborane and *nido*-decaborane-fused bibenzothiophenes were simultaneously obtained in the same reaction and successfully isolated. Initially, the X-ray single crystal analysis revealed that the helicene-like distorted structure was realized in the *nido*-decaborane-fused bibenzothiophene. From optical measurements in the solution state, distinct different characteristics depending on the type of anchors were observed. It was summarized that the absorption and luminescent properties originated from weak  $\pi$ -conjugation at the bibenzothiophene moiety in the *o*-carborane-fused compound were obtained, whereas robust  $\pi$ -conjugation and significant emission from the intramolecular charge transfer state were detected from the *nido*-decaborane-fused compound. These data can be explained by the theoretical results that  $\pi$ -conjugation was restrictedly developed within the bibenzothiophene moiety in frontier orbitals of the *o*-carborane-fused compound. In contrast,  $\pi$ -conjugation can be constructed even through the distorted bibenzothiophene because of the *nido*-decaborane unit. Moreover, the intramolecular charge transfer state should be realized because of electronic interaction involving the *nido*-decaborane unit in the excited state. Furthermore, it was demonstrated that the *nido*-decaborane-fused compound possessed solid-state emission and mechanochromic luminescent properties. The  $\pi$ -conjugation on the distorted structure supported by the *nido*-decaborane anchor should play a significant role in suppressing aggregation-caused quenching followed by presenting solid-state emission with stimuli responsiveness.

**carborane, helicene, mechanochromism, aggregation-induced emission**

**Citation:** Nishino K, Hashimoto K, Tanaka K, Morisaki Y, Chujo Y. Comparison of luminescent properties of helicene-like bibenzothiophenes with *o*-carborane and 5,6-dicarba-*nido*-decaborane. *Sci China Chem*, 2018, 61: 940–946, <https://doi.org/10.1007/s11426-018-9258-y>

### 1 Introduction

$\pi$ -Conjugated system involving “element-blocks”, which are defined as a minimum functional unit composed of heteroatoms [1,2], has large possibility to express unique functions originated from intrinsic properties of each ele-

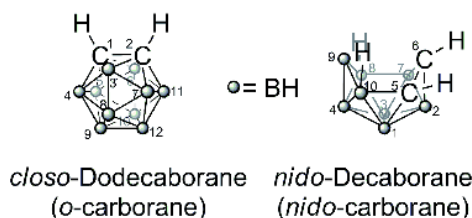
ment. For example, by introducing organoboron compounds into  $\pi$ -conjugation, opto-electronic properties are found such as intense emission, sharp spectra, charge-carrier ability, and high durability toward photo-degradation [3]. From this stand point, *o*-carborane (C<sub>2</sub>H<sub>12</sub>B<sub>10</sub>) is one of attractive and a versatile “element-block” especially for constructing robust conjugation system [4–9]. *o*-Carborane is an icosahedral boron cluster containing two adjacent carbon atoms in the cage. Because of high rigidity and chemical stability, *o*-

\*Corresponding authors (email: [tanaka@poly.synchem.kyoto-u.ac.jp](mailto:tanaka@poly.synchem.kyoto-u.ac.jp); [chujo@poly.synchem.kyoto-u.ac.jp](mailto:chujo@poly.synchem.kyoto-u.ac.jp))

carborane has been used such for enhancement of durability of an organic compound [10]. It has been recently reported that *o*-carborane can work as an anchor for improving molecular rigidity [11]. By fusing the *o*-carborane unit with  $\pi$ -conjugated molecules, molecular motions can be efficiently suppressed. As a result, significant characteristics of robust conjugation such as vibrational peaks were observed in optical spectra [11]. Furthermore, since *o*-carborane works as a strong electron-withdrawing unit when bonded at the carbon atom, the energy level of lowest unoccupied molecular orbitals can be lowered [12–15]. This function would be applicable for designing narrow band-gap materials. Thus, construction of novel electronic conjugation system involving *o*-carborane with aromatic rings is promising strategies not only for encountering new photochemical properties but also for obtaining advanced functional luminescent materials.

Commodity organic luminophores often show intense emission only in the diluted solution and suffer from drastic decrease in emission efficiency in the aggregation state. This phenomenon, aggregation-caused quenching (ACQ), is the one of critical limitations especially in the application of organic luminophores for optoelectronic devices in which organic materials are required to show intense emission in the condensed state. Although recent reports indicated that the *o*-carborane substitution can play a significant role in presenting quantitative emission efficiencies [10,16,17], critical ACQ still occurred in the expanded  $\pi$ -conjugated system supported by the *o*-carborane anchoring [18].

Herein, another role of the anchoring effect by steric boron clusters to the fused conjugated system is illustrated. The simultaneous synthesis of the bibenzothiophene derivatives having the fused *o*-carborane **CB** and 5,6-dicarba-*nido*-decaborane **NB** was accomplished (Scheme 1), and their properties were investigated. Initially, it was confirmed from the X-ray single crystal analysis that **NB** had the helicene-like distorted bibenzothiophene moiety. From optical measurements in the solution state, it was shown that  $\pi$ -conjugation should be insufficiently developed within the bibenzothiophene moiety in **CB**, meanwhile **NB** presented expanded  $\pi$ -conjugation through the whole molecule and bright emission with charge transfer (CT) character. Computational calculation results proposed that conjugation system should be obtained only at the bibenzothiophene moiety in **CB**, whereas electronic delocalization could occur through the whole **NB**. Furthermore, it was also demonstrated that **NB** had solid-state emission and mechanochromic luminescence (MCL). Steric hindrances of the distorted bibenzothiophene and the sphere carborane unit should be responsible for suppressing ACQ followed by exhibiting aggregation-induced emission (AIE) which is emission enhancement by the solidification. This is the first example, to the best of our knowledge, to demonstrate un-

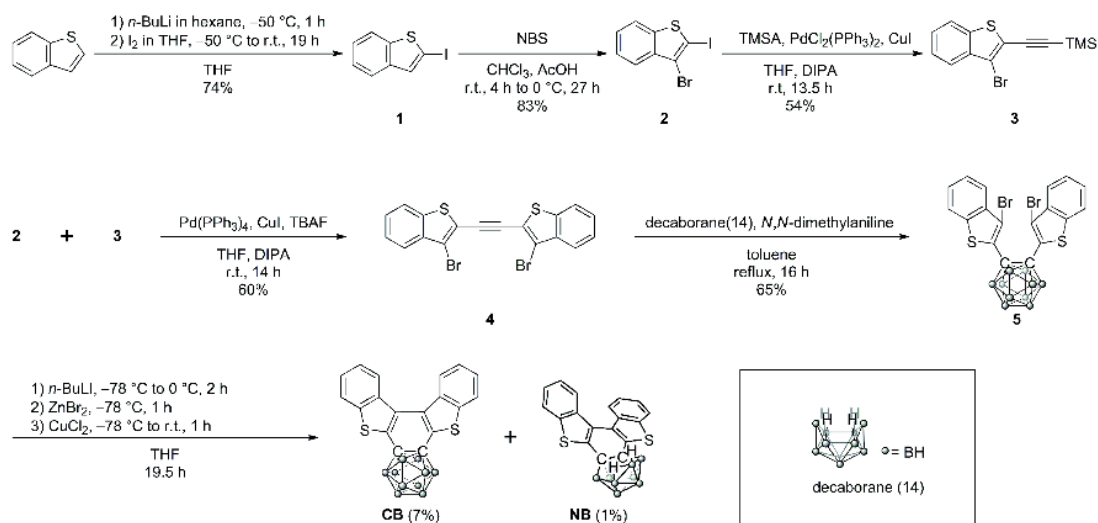


**Scheme 1** Chemical structures of the boron cluster compounds used in this article.

ique contribution of the *nido*-decaborane unit not only as an electron-conjugating anchor to extension of  $\pi$ -conjugated system but also as a robust bridge to formation of the helicene-like structure with solid-state emissive properties by suppressing ACQ.

## 2 Results and discussion

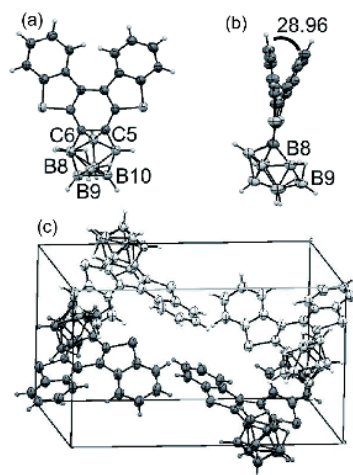
The synthesis of the  $\pi$ -conjugated molecules having boron clusters is shown in Scheme 2. The ethynyl compound **3** [19] was synthesized and coupled with **2** to afford **4** through the Sonogashira-Hagihara coupling reaction. From the alkyne insertion of decaborane with *N,N*-dimethylaniline as a Lewis base, the *o*-carborane derivative **5** was obtained in 65%. Finally, the intramolecular cyclization reaction of **5** was accomplished with *n*-BuLi, ZnBr<sub>2</sub> and CuCl<sub>2</sub> to afford *o*-carborane **CB** and 5,6-dicarba-*nido*-decaborane **NB** having the open-cage cluster structure in 7% and 1% isolated yields, respectively. Both products were able to be isolated with silica gel column chromatography although the apparent retention factor values were identical in the analytical thin-layer chromatography. Due to low reactivity in the ring-closing reaction and generation of the butylated byproducts at the benzothiophene moieties, reaction yields were low. Both compounds were characterized by <sup>1</sup>H, <sup>11</sup>B and <sup>13</sup>C NMR spectroscopy and high resolution mass spectroscopy (HRMS) (Charts S1–S6, Supporting Information online). From both compounds, the expected spectra were obtained in these analyses, indicating progress of ring fusion followed by formation of the bibenzothiophene moiety. Additionally, in the <sup>1</sup>H NMR spectra of **NB**, there were two specific peaks at –2 and –3 ppm. These peaks were assigned to the bridging hydrogens in the *nido*-decaborane unit according to the literature (Scheme 1) [20]. Moreover, from the <sup>11</sup>B NMR spectrum, the similar peak pattern was obtained with that of the previous reported the 5,6-dicarba-*nido*-decaborane derivative [21]. From these data, we concluded that **CB** and **NB** had *o*-carborane and *nido*-decaborane skeletons, respectively. The products showed good stability and solubility in common organic solvents such as CHCl<sub>3</sub>, CH<sub>2</sub>Cl<sub>2</sub>, hexane and benzene, while degradation proceeded in tetrahydrofuran (THF) and polar solvents such as acetonitrile and



**Scheme 2** Synthesis of **CB** and **NB**.

water. Therefore, optical data in the solution state were collected in the former solvents. In particular, transformation from **CB** to **NB** was suggested by monitoring  $^1\text{H}$  NMR spectra in deuterated THF at room temperature (Figure S1, Supporting Information online). It was proposed that once **CB** was formed and then partially transformed to **NB** during the reaction in THF. The 5,6-dicarba-*nido*-decaborane derivatives were synthesized [22,23], and their metal complexes [24–32] and reactivities [33–36] were investigated. However, although their optical properties were examined by Hanji and Geanangel in 1982 [37], electronic interaction with other  $\pi$ -conjugation units and influence on the electronic property of  $\pi$ -conjugated system are still veiled. Thus, further experiments were executed to clarify optical properties of **NB**.

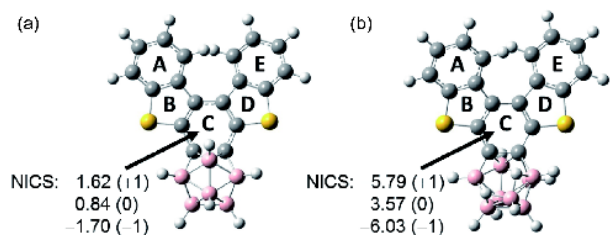
The single crystal sample of **NB** applicable for an X-ray diffraction study was obtained by slow evaporation with the  $\text{CHCl}_3$  solution. Figure 1 shows the oak ridge thermal ellipsoid plot (ORTEP) diagram of **NB**. The bridging hydrogens were located between B8 and B9 and B9 and B10. The C–C bond in the carborane moiety was 1.47 Å (Table S1, Supporting Information online). This bond length was shorter than those in the reported aromatic ring-fused *o*-carborane and *nido*-decaborane derivatives [38]. In addition, the C–C bonds around central ring were 1.37–1.47 Å (Figure 1(a)). These six bond lengths were also shorter than those of common C–C single bonds and longer than those of double ones. From these bond lengths, it was assumed that the 6-membered central ring could have aromaticity. Another impressive feature of **NB** in the crystal is the fact that the helicene-like structure was formed at the bibenzothiophene moiety. From the side view, it was obviously indicated that the distorted structure was realized at the bibenzothiophene moiety (Figure 1(b)). The angle between both fused benzene



**Figure 1** ORTEP drawings of **NB**. Thermal ellipsoids are scaled to the 50% probability level.

rings was  $29.0^\circ$ . Moreover, according to the previous report, it was known that *nido*-decaborane has chirality [37]. Therefore, similarly to helicenes, helicity should be generated in **NB** because of the combination with chirality in the *nido*-decaborane unit and the distortion at the bibenzothiophene moiety [37]. Finally, in the crystalline packing, **NB** showed the two types of stereoisomers (Figure 1(c)). These structural features induced by tight binding with the *nido*-decaborane unit could be beneficial for presenting solid-state emission by disturbing intermolecular interaction followed by ACQ in the condensed state [39,40].

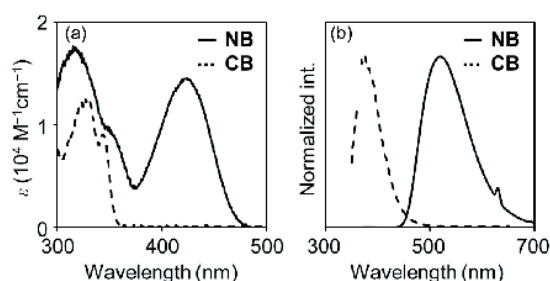
To estimate aromaticity, the nucleus-independent chemical shift (NICS) values of the rings were calculated (Figure 2, Table S2). The NICS( $x$ ) value represents the degree of deshielding at the dummy atom which is located at  $x$  Å height over the center of the ring. Especially, the NICS(+1) and



**Figure 2** NICS values of (a) **CB** and (b) **NB**. Current strengths are given in units of that for benzene (color online).

NICS(-1) values are typical indicators of aromaticity [41,42]. If NICS(+1) and NICS(-1) are under -5, the calculation result means that the ring has aromaticity. According to the NICS values of **NB**, the NICS(+1) and NICS(-1) values of the fused ring (ring C) were -5.79 and -6.03, respectively. These small NICS values suggest that the fused ring should have aromaticity. Furthermore, it was shown that the other rings (A, B, D and E) should also possess aromaticity (Figure S2). These results indicate that robust conjugation should be developed on the distorted bibenzothiophene moiety. The C-C bond in the *nido*-decaborane unit could contribute to developing conjugated system with the aromatic rings. In contrast, the NICS values of ring C in **CB** were much smaller than those in **NB** (-1.62 (+1), -0.84 (0) and -1.70 (-1)). These data mean that the ring C in **CB** should have slight aromaticity. Moreover, it was presumed that conjugation system between benzothiophenes could be suppressed. Similarly to the previous *o*-carborane derivative composed of the fused bibenzothiophene moiety, the *o*-carborane-fused bond might be unfavorable for the formation of an aromatic ring due to extension of bond length [18]. Furthermore, due to the distortion, extension of  $\pi$ -conjugation should be disturbed.

Next, the optical measurements of both compounds were performed (Table 1). To compare the electronic structure with previous *o*-carborane derivatives, UV-Vis absorption spectra were initially measured in the diluted solution (Figure 3(a)). The absorption bands attributable to the  $\pi$ - $\pi^*$  transition at the bibenzothiophene moiety were observed from the solution containing **CB**, and multiple sharp bands assigned to vibrational peaks were not obtained. This fact represents that electronic conjugation was insufficiently developed in the bibenzothiophene moiety. **NB** presented quite a different spectrum from **CB**. Interestingly, the absorption



**Figure 3** UV-Vis absorption and PL spectra of (a) **CB** and (b) **NB** in hexane ( $1.0 \times 10^{-5}$  M). Excitation wavelengths were  $\lambda_{\max}$  in the absorption spectra.

band attributable to the  $\pi$ - $\pi^*$  transitions was found from the solution containing **NB** in the longer wavelength region around 425 nm. Band-gap energy ( $E_g$ ) values estimated from the absorption edge in the spectra were far smaller (+2.64 eV in hexane) than that from **CB** (+3.49 eV in hexane), indicating that **NB** had narrower band gap energy than **CB**. In other words, in spite of the distorted bibenzothiophene structure, efficient electron delocalization should occur through **NB** owing to the anchoring effect of the *nido*-decaborane unit. It was implied that electronic conjugation could be constructed involving a whole molecule in **NB**.

Photoluminescence (PL) spectra were recorded with the solution samples containing **NB** and **CB** (Figure 3(b)). Similarly to absorption spectra, large bathochromic shift in the emission band was observed from **NB**. The emission band was observed from **CB** with the peak around 380 nm in all solvents. Slight solvent dependency of peak positions on solvent types was detected (Figure S3, Table S4). The conjugation should be effectively expanded within the bibenzothiophene moiety in the excited state. In contrast, the broad emission band was detected from the solution containing **NB** in the red-shifted region. In particular, positions of the emission bands were red-shifted by increasing solvent polarity. In hexane, **NB** showed the emission band with the peak at 521 nm. It was shown that the peak was observed at 552 nm in the  $\text{CH}_2\text{Cl}_2$  solution. To gather information on the emission mechanism, the Lippert-Mataga plot was prepared according to the empirical formula (Figure S4). The degree of the CT character in the emission property can be estimated from the slope of a fitting line. Since linear relationship was obtained in the plot, it was indicated that emission of **NB** should be exhibited via the CT state. In the previous works on electronic structures of other *o*-carborane-fused poly-

**Table 1** Optical and electronic properties of **CB** and **NB**

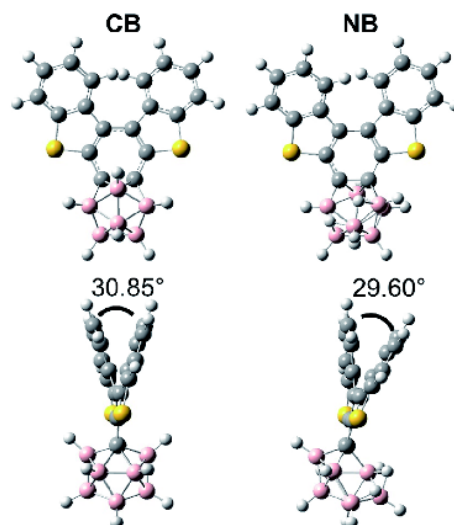
	solution in hexane <sup>a)</sup>					crystal		scratched	
	$\lambda_{\text{abs}}$ (nm)	$\epsilon$ ( $\text{M}^{-1} \text{cm}^{-1}$ )	$E_g$ (eV) <sup>b)</sup>	$\lambda_{\text{PL}}$ (nm) <sup>c)</sup>	$\Phi_{\text{PL}}$ <sup>d)</sup>	$\lambda_{\text{PL}}$ (nm) <sup>c)</sup>	$\Phi_{\text{PL}}$ <sup>d)</sup>	$\lambda_{\text{PL}}$ (nm) <sup>c)</sup>	$\Phi_{\text{PL}}$ <sup>d)</sup>
<b>CB</b>	344	8,600	3.49	376	<0.01	— <sup>e)</sup>	— <sup>e)</sup>	— <sup>e)</sup>	— <sup>e)</sup>
<b>NB</b>	425	15,000	2.64	521	0.64	556	0.49	547	0.57

a)  $1.0 \times 10^{-5}$  M; b) estimated from the absorption edge in the absorption spectra; c) excited at  $\lambda_{\text{abs}}$ ; d) determined as an absolute value with the integration sphere method; e) not detectable.

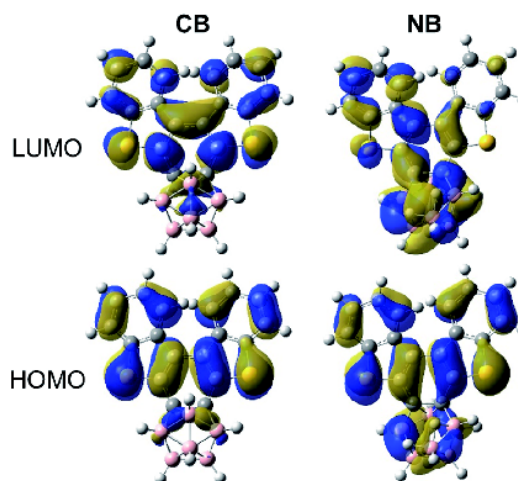
cyclic systems,  $\pi$ -conjugation was delocalized largely at the polycyclic units [11,18]. Indeed, **CB** also presented limited conjugation system with in the bibenzothiophene moiety in this article, and weak emission from the locally-excited state was detected. Furthermore, the *nido*-carborane derivatives which were obtained by the single boron-atom abstraction and had negative charges showed strong electron-donating ability [43]. In contrast, it was found that the *nido*-decaborane unit in **NB** should be incorporated into  $\pi$ -conjugated system through a distorted molecular structure. In addition, significant emission with the CT character was detected. Distinct different electronic structures should be realized between both compounds.

To obtain deeper insight into the optical properties, quantum calculations were performed for estimating the molecular orbitals by using density functional theory (DFT) for the ground state (GS) and time dependent-DFT (TD-DFT) for the excited state (ES). The structures of both compounds were optimized at the B3LYP/6-31+G(d,p) level in both states (Figure 4). The optimized structure of **NB** including the distorted bibenzothiophene moiety in the GS showed good agreement with the result of the single crystal analysis. Moreover, the structure in the ES was almost identical to that in the GS (Figure S5). This fact implies that the initial structure could be preserved in the excited state. The calculated transitions in the absorption process are shown in Table S3. The calculated absorption peaks showed good agreement with experimental results. From the calculation with **NB**, two significant transitions with large oscillator strengths were predicted at 318 and 425 nm. From the absorption spectrum, the absorption bands around 315 and 425 nm were clearly observed. In the spectrum of **CB**, the theoretical results were corresponded to the experimental data (exp. 330 and 344 nm; calcd. 319 and 324 nm). These two agreements between the optimized structure and the actual structure in the crystal packing and between theoretical and experimental optical data suggest high reliability of the calculation results. This means that the optimized structure of **CB** could be reasonable although the molecular conformation of **CB** in the crystal packing was not determined. From this stand point, similarly to the distorted structure of **NB**, it was proposed that the bibenzothiophene moiety in **CB** also possessed low planarity. It is likely that development of  $\pi$ -conjugation should be restricted by intramolecular distortion in **CB**.

Figure 5 shows the molecular orbitals of both molecules in the GS, and clear differences were illustrated. It was proposed that electronic orbitals in **CB** were developed mainly at the bibenzothiophene moiety both in highest occupied molecular orbital (HOMO) and lowest unoccupied molecular orbital (LUMO). Meanwhile, in the HOMO level of **NB**, molecular orbitals were delocalized through a whole molecule. It should be remarked that molecular orbitals were lo-



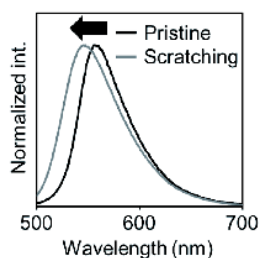
**Figure 4** Optimized structures of **CB** (left) and **NB** (right) in the ground state calculated at the B3LYP/6-31+G(d,p) level (color online).



**Figure 5** Calculated molecular orbitals of **CB** and **NB** at the B3LYP/6-31+G(d,p)//B3LYP/6-31+G(d,p) level (color online).

calated at the carborane unit and the half of conjugated unit in the LUMO level. Moreover, the molecular orbitals that corresponded to the emission transition were almost identical to HOMO and LUMO. From this calculation result, the CT character in emission of **NB** can be explained. The transition should proceed from localized LUMO to delocalized HOMO involving the *nido*-decaborane unit. Hence, strong emission with the CT character was observed only from **NB**.

Finally, solid-state emission and MCL properties were evaluated with the crystalline samples (Figure 6, Table 1). The pristine crystalline sample was prepared from recrystallization from  $\text{CHCl}_3/\text{MeOH}$ , and the scratched sample was prepared by scratching the pristine sample with an agate mortar until shiny particles disappeared. **CB** showed



**Figure 6** PL spectra of NB before and after scratching.

emission under detectable level, whereas the pristine crystalline sample of NB presented intense yellow emission with the emission maximum wavelength at 556 nm. After scratching the crystal, the emission peak appeared at 547 nm. The absolute photoluminescence quantum efficiency ( $\Phi_{\text{PL}}$ ) of the scratched sample ( $\Phi_{\text{PL}}=0.57$ ) was relatively larger than that of the pristine sample ( $\Phi_{\text{PL}}=0.49$ ). According to the blue-shifted emission and higher quantum efficiency, it was proposed that the MCL property of NB might be caused by the separation of intermolecular interactions by scratching similarly to those of boron complexes [44]. The distorted structure in NB could play important roles in facilitating morphology changes as well as suppressing ACQ by disturbing intermolecular interaction in the crystal packing [39,40]. On the other hand, ACQ should be caused in CB by intermolecular interaction due to high molecular planarity in the bibenzothiophene moiety.

### 3 Conclusions

The unexpected structure and electronic properties were clarified with the *nido*-decaborane-fused bibenzothiophene which can introduce distortion without loss of electronic conjugation. So far, the fusion with the *o*-carborane unit was able only to enhance molecular planarity and rigidity at the polycyclic moiety. On the other hand, it was clearly indicated that the *nido*-decaborane anchor was capable of constructing  $\pi$ -conjugation regardless of structural distortion by participating as an electron-withdrawing unit, and bright emission with the CT character can be generated. Furthermore, it was suggested that the helicene-like distorted structure including the *nido*-decaborane anchor should be favorable for suppressing ACQ followed by presenting solid-state emission and MCL. Our findings could be valid design tactics not only for constructing distorted  $\pi$ -conjugated structures but also for preparing solid-state emissive molecules with stimuli-responsive chromic properties. Moreover, although enantiomers were not separated in this study, introduction of the *nido*-decaborane anchor might be a tool for inducing chirality or helicity in nanostructures.

**Acknowledgements** This work was supported by Konica Minolta Science

and Technology Foundation (for K.T.) and a Grant-in-Aid for Scientific Research on Innovative Areas “New Polymeric Materials Based on Element-Blocks (No.2401)” (JP24102013).

**Supporting information** The supporting information is available online at <http://chem.scichina.com> and <http://link.springer.com/journal/11426>. The supporting materials are published as submitted, without typesetting or editing. The responsibility for scientific accuracy and content remains entirely with the authors.

- 1 Chujo Y, Tanaka K. *Bull Chem Soc Jpn*, 2015, 88: 633–643
- 2 Tanaka K, Chujo Y. *NPG Asia Mater*, 2015, 7: e223
- 3 Gon M, Tanaka K, Chujo Y. *Polym J*, 2018, 50: 109–126
- 4 Naito H, Nishino K, Morisaki Y, Tanaka K, Chujo Y. *Angew Chem Int Ed*, 2017, 56: 254–259
- 5 Nishino K, Yamamoto H, Tanaka K, Chujo Y. *Asian J Org Chem*, 2017, 6: 1818–1822
- 6 Nishino K, Uemura K, Gon M, Tanaka K, Chujo Y. *Molecules*, 2017, 22: 2009–2018
- 7 Nishino K, Uemura K, Tanaka K, Chujo Y. *New J Chem*, 2018, 42: 4210–4214
- 8 Mori H, Nishino K, Wada K, Morisaki Y, Tanaka K, Chujo Y. *Mater Chem Front*, 2018, 2: 573–579
- 9 Naito H, Uemura K, Morisaki Y, Tanaka K, Chujo Y. *Eur J Org Chem*, 2018, 2018: 1885–1890
- 10 Naito H, Nishino K, Morisaki Y, Tanaka K, Chujo Y. *Chem Asian J*, 2017, 12: 2134–2138
- 11 Nishino K, Hashimoto K, Tanaka K, Morisaki Y, Chujo Y. *Tetrahedron Lett*, 2016, 57: 2025–2028
- 12 Cho YJ, Kim SY, Cho M, Han WS, Son HJ, Cho DW, Kang SO. *Phys Chem Chem Phys*, 2016, 18: 9702–9708
- 13 Kim SY, Cho YJ, Jin GF, Han WS, Son HJ, Cho DW, Kang SO. *Phys Chem Chem Phys*, 2015, 17: 15679–15682
- 14 Wang Z, Jiang P, Wang T, Moxey GJ, Cifuentes MP, Zhang C, Humphrey MG. *Phys Chem Chem Phys*, 2016, 18: 15719–15726
- 15 Kwon S, Wee KR, Cho YJ, Kang SO. *Chem Eur J*, 2014, 20: 5953–5960
- 16 Nishino K, Yamamoto H, Tanaka K, Chujo Y. *Org Lett*, 2016, 18: 4064–4067
- 17 Naito H, Nishino K, Morisaki Y, Tanaka K, Chujo Y. *J Mater Chem C*, 2017, 5: 10047–10054
- 18 Tanaka K, Nishino K, Ito S, Yamane H, Suenaga K, Hashimoto K, Chujo Y. *Faraday Discuss*, 2017, 196: 31–42
- 19 Huang PY, Chen LH, Chen YY, Chang WJ, Wang JJ, Lii KH, Yan JY, Ho JC, Lee CC, Kim C, Chen MC. *Chem Eur J*, 2013, 19: 3721–3728
- 20 Štibr B, Teixidor F, Viñas C, Fusek Ji. *J Organomet Chem*, 1998, 550: 125–130
- 21 Štibr B, Hermánek S, Janousek Z, Plzák Z, Dolanský J, Plešek J. *Polyhedron*, 1982, 1: 822–824
- 22 Rietz RR, Schaeffer R. *J Am Chem Soc*, 1973, 95: 6254–6262
- 23 Lawrence SH, Wermer JR, Boocock SK, Banks MA, Keller PC, Shore SG. *Inorg Chem*, 1986, 25: 367–372
- 24 Jung CW, Hawthorne MF. *J Am Chem Soc*, 1980, 102: 3024–3032
- 25 Barker GK, Garcia MP, Green M, Pain GN, Stone FGA, Jones SKR, Welch AJ. *J Chem Soc Chem Commun*, 1981, 652
- 26 Štibr B, Linek A, Hašek J. *Acta Crystallogr B Struct Crystallogr Cryst Chem*, 1982, 38: 3147–3149
- 27 Barker GK, Godfrey NR, Green M, Parge HE, Stone FGA, Welch AJ. *J Chem Soc Chem Commun*, 1983, 277–279
- 28 Barker GK, Green M, Stone FGA, Wolsey WC, Welch AJ. *J Chem Soc Dalton Trans*, 1983, 2063–2069
- 29 Bown N, Grüner B, Štibr B, Fontaine XLR, Thornton-Pett M, Kennedy JD. *J Organomet Chem*, 2000, 614–615: 269–282
- 30 Pisareva IV, Dolgushin FM, Tok OL, Konoplev VE, Suponitsky KY, Yanovsky AI, Chizhevsky IT. *Organometallics*, 2001, 20: 4216–4220

- 31 Štíbr B, Holub J, Bakardjiev M, Hnyk D, Tok OL, Milius W, Wrackmeyer B. *Eur J Inorg Chem*, 2002, 2002: 2320–2326
- 32 Balagurova EV, Pisareva IV, Smol'yakov AF, Dolgushin FM, Godovikov IA, Chizhevsky IT. *Inorg Chem*, 2016, 55: 11193–11200
- 33 Bakardjiev M, Holub J, Štíbr B, Císarová I. *Dalton Trans*, 2010, 39: 4186–4190
- 34 Štíbr B. *J Organomet Chem*, 2015, 798: 30–35
- 35 Bakardjiev M, Štíbr B, Holub J, Padělková Z, Růžička A. *Organometallics*, 2015, 34: 450–454
- 36 Tok OL, Bakardjiev M, Štíbr B, Hnyk D, Holub J, Padělková Z, Růžička A. *Inorg Chem*, 2016, 55: 8839–8843
- 37 Hani R, Geanangel RA. *Polyhedron*, 1982, 1: 824–826
- 38 Powley SL, Rosair GM, Welch AJ. *Dalton Trans*, 2016, 45: 11742–11752
- 39 Oyama H, Nakano K, Harada T, Kuroda R, Naito M, Nobusawa K, Nozaki K. *Org Lett*, 2013, 15: 2104–2107
- 40 Matsuno T, Koyama Y, Hiroto S, Kumar J, Kawai T, Shinokubo H. *Chem Commun*, 2015, 51: 4607–4610
- 41 Schleyer PR, Maerker C, Dransfeld A, Jiao H, van Eikema Hommes NJR. *J Am Chem Soc*, 1996, 118: 6317–6318
- 42 Schleyer PR, Manoharan M, Wang ZX, Kiran B, Jiao H, Puchta R, van Eikema Hommes NJR. *Org Lett*, 2001, 3: 2465–2468
- 43 Nishino K, Morisaki Y, Tanaka K, Chujo Y. *New J Chem*, 2017, 41: 10550–10554
- 44 Yoshii R, Suenaga K, Tanaka K, Chujo Y. *Chem Eur J*, 2015, 21: 7231–7237

**Luminescent Carboranes** | *Very Important Paper* |

**VIP Enhancement of Luminescence Efficiencies by Thermal Rearrangement from *ortho*- to *meta*-Carborane in Bis-Carborane-Substituted Acenes**

 Hirofumi Naito,<sup>[a]</sup> Kyoya Uemura,<sup>[a]</sup> Yasuhiro Morisaki,<sup>[a][‡]</sup> Kazuo Tanaka,<sup>\*[a]</sup> and Yoshiki Chujo<sup>\*[a]</sup>

**Abstract:** In a previous study we synthesized a series of bis-*o*-carborane-modified acenes and revealed various unique luminescence properties, such as highly efficient solid-state emission and luminochromism. Here we report further enhancement of the luminescence efficiencies of bis-*o*-carborane-modified acenes by thermally induced structural rearrangement from *ortho*- to *meta*-carborane. We found that the thermal rearrangement of the anthracene derivative **1** occurred close to the melting point and gave luminescent products. From a detailed investigation of the product obtained from **1**, the transformation of the molecular structure was proven by X-ray crystallography. In addition, the analytical data indicated that rearrangement

caused by heating at 300 °C occurred at only one of the two *o*-carborane units. In accord with the results of theoretical investigations of the transition states of **1** by quantum chemical calculations, we propose that the thermal rearrangement could proceed because of a low activation energy in the first rearrangement step due to the presence of the anthracene. On the basis of optical measurements, enhancements of not only luminescence efficiencies but also aggregation-induced emission were observed. Furthermore, we have demonstrated that this strategy for enhancing emission properties is applicable to the corresponding tetracene derivative, resulting in a deep-red luminescent dye.

**Introduction**

To obtain functional organic materials, one promising strategy is to utilize an “element block”, which is defined as a minimum functional unit composed of heteroatoms.<sup>[1]</sup> For example, by connecting luminescent boron “element blocks” to an environment-sensitive unit, various types of stimuli-responsive materials have been readily constructed according to pre-programmed designs. Based on this strategy, *o*-carborane is recognized as a versatile “element block”, especially for the design of solid-state luminescent materials with chromic properties.<sup>[2–4]</sup> Carborane (C<sub>2</sub>B<sub>10</sub>H<sub>12</sub>) is an icosahedral cluster compound consisting of 10 boron atoms and 2 carbon atoms.<sup>[5–10]</sup> Based on their unique features, such as their boron-rich content and high thermal and chemical stability, the applications of carboranes in the fields of medicinal chemistry and materials science have been extensively studied.<sup>[5–10]</sup>

More recently, *o*-carborane has attracted attention as a key unit for optically functional materials.<sup>[11–38]</sup> *o*-Carborane is

known to act as an electron acceptor because of the electron-deficient nature of the three-center two-electron bonds when an electron donor is bonded to a carbon,<sup>[39,40]</sup> and bright emission from the induced charge-transfer (ICT) state can be obtained upon combination with electron-donating units.<sup>[41]</sup> It should be mentioned that bright emission from this ICT state has often been observed even in the solid state by suppressing aggregation-caused quenching (ACQ).<sup>[42–46]</sup> Moreover, emission enhancements by solidification have been detected.<sup>[42–48]</sup> Additionally, it has been found that some solid-state emissive *o*-carborane derivatives show luminescent chromic behavior towards external stimuli such as heating, vapor fuming, and scratching.<sup>[47]</sup> On the basis of results of a series of mechanical studies, it has been proposed that intramolecular vibration of the C–C bond in the *o*-carborane unit and rotation at the connecting bond should be responsible for emission enhancements in the condensed state and luminescent chromism, respectively.

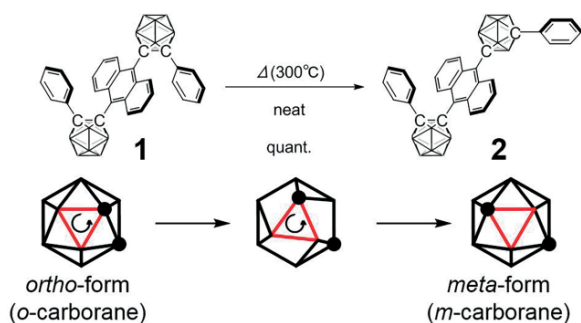
In this work we have synthesized bis-*o*-carborane-modified acenes<sup>[48,49]</sup> and observed enhanced luminescence by the unique thermally induced structural transformation of an *o*-carborane into a *m*-carborane, which is a structural isomer of *o*-carborane possessing two carbon atoms at the 1,7-positions. By heating the anthracene derivative **1** at 300 °C, an irreversible luminescent color change was detected and a luminescent product was successfully isolated. It was revealed by single-crystal X-ray diffraction analysis of the product that one of the two *o*-carborane units had rearranged to *m*-carborane **2** (Scheme 1). The results of a theoretical investigation suggested

[a] Department of Polymer Chemistry, Graduate School of Engineering, Kyoto University, Katsura, Nishikyo-ku, Kyoto 615-8510, Japan  
E-mail: tanaka@poly.synchem.kyoto-u.ac.jp  
chujo@poly.synchem.kyoto-u.ac.jp  
http://poly.synchem.kyoto-u.ac.jp/

[‡] Present address: Department of Applied Chemistry for Environment, School of Science and Technology, Kwansei Gakuin University, 2–1 Gakuen, Sanda, Hyogo 669–1337, Japan

Supporting information and ORCID(s) from the author(s) for this article are available on the WWW under <https://doi.org/10.1002/ejoc.201800151>.

that the transformation can proceed due to a lowering effect of the anthracene moiety on the energy barrier of the transition. Furthermore, it has been demonstrated that the isomerization can improve emission efficiencies both in solution and the solid state. Finally, we also observed that this strategy is applicable to the deep-red luminescent molecule composed of tetracene rather than anthracene. So far, *m*-carboranes have often simply been used as an electron-accepting unit in commodity luminescent dyes presenting ACQ. In this study we have demonstrated that the thermal rearrangement to *m*-carborane can be a facile strategy for enhancing luminescence properties.



Scheme 1. Thermally induced rearrangement in *o*-carborane.

## Results and Discussion

It has been reported that some *m*-carborane derivatives have been generated by thermal rearrangements of *o*-carborane.<sup>[5,50–53]</sup> By heating above 425 °C, *o*-carborane was irreversibly transformed into the more stable *m*-carborane. Since the discovery of *o*-carborane and its thermal rearrangement to *m*-carborane, many researchers have studied the mechanism of the transformation experimentally and theoretically.<sup>[5,50–53]</sup> Recently, computational analyses were performed by Brown and Mckee.<sup>[52]</sup> Accordingly, it was proposed that the rearrangement proceeds by a triangular-face rotation (TFR) process (Scheme 1). High thermal stability of the carborane boron–aryl carbon bond was suggested in the gas-phase rearrangement of 3-aryl-*o*-carborane to 2- and 4-aryl-*m*-carboranes at 550–600 °C under vacuum.<sup>[54]</sup> In *C,C'*-bis-substituted *o*-carboranes with bulky groups, cage rearrangement occurred at a lower temperature. Bond cleavage could be assisted by steric repulsion between the substituents, for example, 1,2-(RPh<sub>2</sub>Si)<sub>2</sub>C<sub>2</sub>B<sub>10</sub>H<sub>10</sub> (R = Me, Cl) and 1,2-(ClMe<sub>2</sub>Si)<sub>2</sub>C<sub>2</sub>B<sub>10</sub>H<sub>10</sub> underwent isomerization to the corresponding *m*-carborane derivatives at 260 and 280 °C, respectively.<sup>[55,56]</sup> In contrast, bond cleavage of the aryl–C(cage) bond was initiated in 1-phenyl-*o*-carborane at 300 °C.<sup>[57]</sup> Thus, in general, thermal rearrangements of 1- and/or 2-aryl-*o*-carboranes hardly occur.

Taking account the potential isomerization of *o*-carborane, we have also investigated the thermal reactivity of bis-*o*-carborane-modified acenes. Syntheses were performed according to previous reports,<sup>[48,49]</sup> and we initially prepared the red-luminescent crystal of the anthracene derivative **1** incorporating CHCl<sub>3</sub> as a solvent of crystallization. The powder sample of **1**·CHCl<sub>3</sub> was heated at 300 °C for 10 min in a DSC apparatus,

and the thermal behavior was monitored. Figure 1 shows the TGA and DSC profiles of **1**·CHCl<sub>3</sub> under N<sub>2</sub>. In the DSC profile, the endothermic peaks observed at around 120 and 272 °C can be attributed to the loss of solvent molecules and the melting point, respectively. It should be noted that a large exothermic peak can be observed at 276 °C. In the TGA profile, a loss of mass can be observed above 340 °C, which suggests that the exothermic reaction occurs at around the melting point of **1**. The residue in the pan of the DSC apparatus was analyzed by HPLC in chloroform and a significant single peak was detected (see Chart S1 in the Supporting Information). After collection, an orange product with almost the same red-luminescence property was isolated by HPLC. The resulting product **2** showed good stability and solubility in common organic solvents such as chloroform, dichloromethane, and tetrahydrofuran. Thereby, conventional characterization methods in organic synthesis such as NMR spectroscopy and mass spectrometry were applicable (see the Exptl. Sect. and Charts S2–S4). Further analyses were performed on **2**.

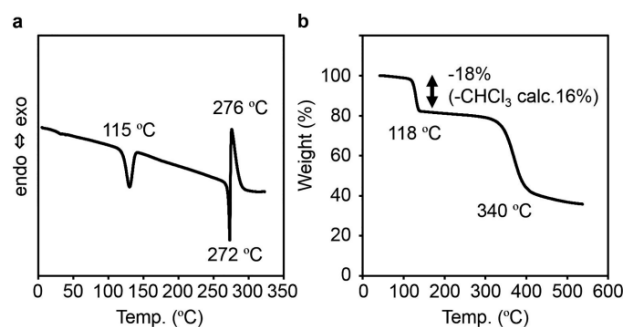


Figure 1. (a) DSC thermogram and (b) TGA curve of **1**·CHCl<sub>3</sub> recorded at a heating rate of 10 °C/min under a N<sub>2</sub> atmosphere.

The <sup>1</sup>H and <sup>11</sup>B NMR spectra of **1** and **2** were recorded and compared (see Figures S1 and S2 in the Supporting Information). The <sup>1</sup>H NMR spectrum of **2** indicates that a single chemical component was generated. The signal peaks corresponding to the 1,4,7,8-positions of the anthracene moiety shifted from 8.60 ppm to 8.79 and 9.16 ppm, and a broad peak derived from *B*-H hydrogens of the carborane cluster was detected. These data indicate that the exothermic reaction is not pyrolysis but a transformation in which the carborane cluster is maintained. By heating to over 320 °C, the signals disappeared, which indicates that decomposition rather than a second rearrangement occurred.

The molecular structure of **2** was confirmed by X-ray crystallography (Figure 2 and Table S1 in the Supporting Information). A single crystal of **2** suitable for X-ray crystallography was obtained by slow evaporation of a CHCl<sub>3</sub>/MeOH solution containing **2**. Surprisingly, only one *o*-carborane moiety rearranged to *m*-carborane. The crystal structure of **2** shows that the anthracene ring forms a  $\pi$ -stacked dimer with the neighboring anthracene, similarly to its precursor **1** (see Figure S3).<sup>[49]</sup> The overlapping area of the two  $\pi$ -stacked anthracenes was estimated to be 16 %, and the distance between the centers of each anthracene is 4.44 Å, which is much shorter than that in **1**-solvent. This is probably because the phenyl ring connected

to the *m*-carborane moiety is spatially distant from the adjacent anthracene moiety, thereby reducing the steric repulsion between the two molecules. From a comparison of the crystal packing before and after the rearrangement,<sup>[49]</sup> we propose that the rearrangement could proceed at the phenyl ring that is isolated from the  $\pi$ -dimer of the central anthracenes because of less structural restriction. The ring strain in the anthracene moiety of **2** was evaluated through the ring deformation angles  $\alpha$  and  $\beta$  with respect to the central ring. The  $\alpha$  and  $\beta$  values for **2** are 19.3 and 3.28°, respectively, which are similar to those of **1**-solvent (see Table S2). Intermolecular  $\pi$ - $\pi$  stacking between the anthracene rings and the steric hindrance of the phenyl-substituted *o*-carboranes in the  $\pi$ -stacked dimer induced these large deformation angles, just as in the case of **1**-solvent. Another structural isomer, in which both *o*-carborane moieties have rearranged to *m*-carboranes, was not detected in the <sup>1</sup>H NMR spectrum. This implies that the activation energy of this second isomerization could be higher than that of the first one.

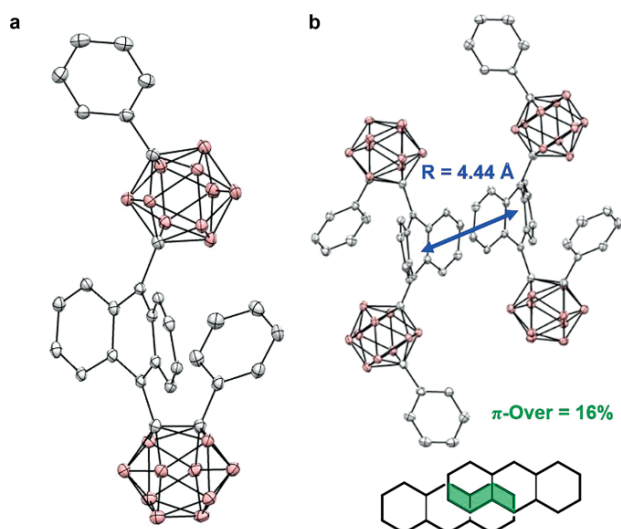


Figure 2. (a) Molecular structure and (b)  $\pi$ -dimer formation of **2** determined by X-ray crystallography.

To investigate the rearrangement process theoretically, quantum chemical calculations were performed (Figure 3). Transition-state calculations were carried out according to the calculation procedure of Brown and McKee.<sup>[52]</sup> Target species were optimized at the B3LYP/6-31G(d) level of theory and frequency calculations were carried out at the same level to confirm whether they are stationary points. In addition, zero-point energies, entropies, and thermal correction data were obtained. Single-point electronic energies were then calculated at the B3LYP/6-311+G(2d,p) level of theory. The enthalpies of the species at 298 K were used to calculate the enthalpies at 500 and 800 K, and these values were then used to determine the absolute free energies at 298, 500, and 800 K. The optimized structures showed good agreement with those determined by X-ray diffraction. Therefore, the calculated parameters were used in the theoretical study. According to the TFR model, transition states were proposed and the energy level of each transition-state

structure was estimated.<sup>[52]</sup> As models, the rearrangements of *o*-carborane (**o-Cb**), 1-phenyl-*o*-carborane (**Ph-o-Cb**), 1-anthracenyl-*o*-carborane (**Ant-o-Cb**), and 1-anthracenyl-2-phenyl-*o*-carborane (**Ant-Ph-o-Cb**) were surveyed by using the same method of calculation to assess the effect of substituents on the rearrangement process (see Scheme S1, Figures S4 and S5, and Tables S3 and S4 in the Supporting Information). The activation energies of the *ortho*-to-*meta* transformation for **o-Cb** and **Ph-o-Cb** were estimated to be 203.0 and 203.5 kJ/mol, respectively, whereas those of **Ant-o-Cb** and **Ant-Ph-o-Cb** were calculated to be 141.7 and 148.5 kJ/mol, respectively, which indicates that the introduction of the anthracene moiety decreases the activation energy. As shown experimentally, it is likely that steric repulsion facilitates the isomerization by lowering the activation energy.<sup>[49]</sup> It should be noted that this lowering of the activation energy should play a significant role in the rearrangement process. Calculations of the rearrangement of **1** revealed the initial rotation of the phenyl-*o*-carborane moiety, as represented in **TS1**. Moreover, the successive *ortho*-to-*meta* rearrangement is observed in **TS2** with an activation energy of 103.0 kJ/mol, which is approximately half the activation energy of the isomerization of **o-Cb**. This significantly lower activation energy strongly suggests the preference for thermal rearrangement over decomposition. Furthermore, the activation energy of the second *ortho*-to-*meta* isomerization (**TS3**) was calculated to be 131.1 kJ/mol, which is higher than that of the first isomerization process. These data clearly indicate that the second rearrangement process would compete with the decomposition process because of the high activation energy. Hence, the isomer containing the bis-*m*-carborane was scarcely obtained after heating.

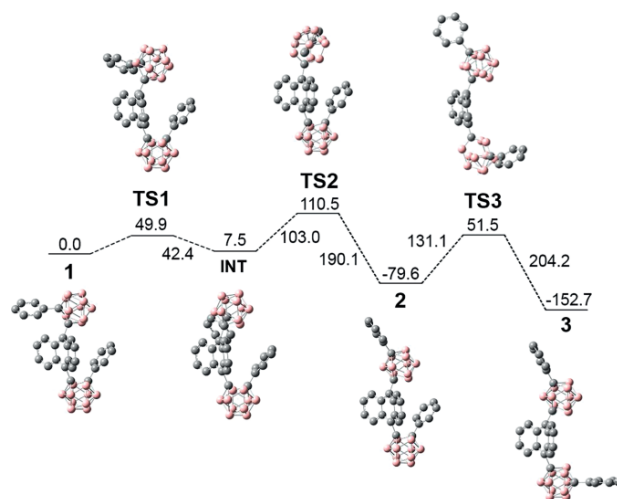


Figure 3. Calculated relative free energies and geometries of **1**.

Cyclic voltammograms (CVs) were collected for **1** and **2** (see Figure S6 in the Supporting Information). The CV of compound **1** shows two reduction peaks corresponding to reduction to the dianion and then the tetraanion.<sup>[58–60]</sup> In contrast, the CV of **2** shows three distinct reduction peaks. The first two reduction peaks for **2** are the reductions to the monoanion radical and then the dianion. The third reduction of **2** should be lower

after the formation of the *m*-carborane cluster. The diaryl-*m*-carborane should be more difficult to reduce than diaryl-*o*-carborane.<sup>[12]</sup> The first reduction potential of  $-0.64$  V for **1** is remarkable because it is approximately 0.5 V easier to reduce **1** than a bis-carborane assembly identical to **1** but with a tetrafluorophenylene instead of the anthracenylene bridge.<sup>[58]</sup> The LUMO energy levels were estimated from the peak onset potentials in the UV/Vis spectra, and the HOMO energy levels were calculated from the LUMO energy level and the band-gap energy estimated from the absorption edge (see Table S5). Compounds **1** and **2** both showed remarkably low-lying LUMO energy levels of  $-4.16$  and  $-4.13$  eV, respectively. It is likely that the introduction of two carborane moieties is responsible for the lowering of the energy levels of both frontier orbitals.

The effect of the rearrangement process on the optical properties was also examined. Figure 4a shows the UV/Vis absorption and photoluminescence (PL) spectra of **1** and **2** in THF solution ( $1.0 \times 10^{-5}$  M). Both absorption spectra exhibit bands with peaks at around 280 and 450 nm, attributable to typical  $\pi$ - $\pi^*$  transitions in phenyl and anthracene moieties, respectively. Meanwhile, a distinct difference was observed in the PL spectra of **1** and **2**. Although both compounds present emission from the ICT state at similar positions, at around 650 nm, the emission intensity is significantly greater for **2** compared with **1** (Table 1 and Figure S7 in the Supporting Information).<sup>[49]</sup> Notably, the absolute PL quantum efficiency ( $\Phi_{\text{PL}}$ ) of **2** is 0.19, which is much higher than that of **1** ( $\Phi_{\text{PL}} < 0.01$ ). Additionally, aggregation-induced emission enhancement (AIEE) is clearly demonstrated for **2** in the aggregated state [THF/H<sub>2</sub>O, 1:99 (v/v),  $1.0 \times 10^{-5}$  M]. Furthermore, **2** shows stronger emission in the crystalline state ( $\Phi_{\text{PL}} = 0.59$ ) than those in solution and aggregation. It has been suggested in previous reports that 1-anthracenyl-2-phenyl-*o*-carborane shows almost no emission in THF solution due to excitation deactivation through intramolecular vibration of the C-C bond in the *o*-carborane unit.<sup>[44]</sup> In the *meta* form, these vibrational motions would be absent. As a result, emission enhancements can be observed in solution following isomerization. In the aggregated state, the *m*-carborane unit could play a critical role in the suppression of ACQ, leading to emission enhancement without a shift of the peak because of steric hindrance. In the crystalline state, the stacking of the anthracene moiety is enhanced after thermal rearrangement due to the shorter distance between the two units in **2** compared with in **1**. Therefore, a slight decrease in the emission efficiency and a redshift of the emission band should be induced.

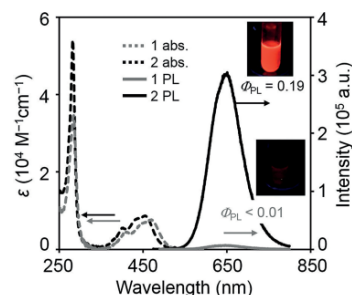


Figure 4. UV/Vis absorption and PL spectra of **1** and **2** in THF ( $1.0 \times 10^{-5}$  M). Excitation wavelengths were the  $\lambda_{\text{abs,max}}$ . The photos were taken under UV irradiation (365 nm).

Finally, to evaluate the generality of emission enhancement triggered by thermal rearrangement, we similarly heated the corresponding naphthalene and tetracene derivatives.<sup>[48]</sup> A similar DSC profile was obtained only for the tetracene derivative (see Figures S8 and S9 in the Supporting Information), and a luminescent product was obtained. On the basis of this result, several tens of milligrams of the tetracene derivative were heated and the product was analyzed. In summary, similarly to the anthracene derivative, the pristine tetracene derivative shows low emission in all states due to intermolecular interactions of the distant aromatic rings of the *o*-carborane units,<sup>[48,61–63]</sup> and significant emission was observed after heating (Table 1, Table S6, and Figure S10). In the solution state, the emission band was observed at a shorter wavelength than that of the anthracene derivatives. This suggests that the original emission from tetracene should be recovered by heating. As a result, the emission band was detected in a similar wavelength region to that of the pristine tetracene (450–650 nm). This implies that the single *o*-carborane unit does not entirely deactivate the excitation, resulting in emission enhancement after the thermal rearrangement. In the solid state before heating, emission bands at a longer wavelength with low emission efficiencies were observed, which indicates that intermolecular interactions followed by ACQ occurs. After heating, blueshifted emission bands were observed in the aggregation and crystalline samples, which indicates the suppression of stacking. The intermolecular interactions could be disturbed by the *m*-carborane leading to emission enhancement in the solid state. These results suggest two issues. First, because thermal rearrangement occurs in broader acenes such as anthracene and tetracene, electronic interactions between the *o*-carborane unit and the bridging acene moiety should play a positive role in reducing

Table 1. Optical properties of the modified acenes before and after heating.<sup>[a]</sup>

	$\lambda_{\text{PL}}$ [nm]			$\Phi_{\text{PL}}$ <sup>[b]</sup>		
	THF <sup>[c]</sup>	Aggregation <sup>[d]</sup>	Crystal	THF <sup>[c]</sup>	Aggregation <sup>[d]</sup>	Crystal
<b>1</b>	647	643	628 <sup>[e]</sup>	<0.01	0.08	0.77 <sup>[e]</sup>
<b>2</b>	652	642	632	0.19	0.38	0.59
Tetracene <sup>[f]</sup>	–	759	742	–	0.01	<0.01
After heating <sup>[g]</sup>	568	657	670	0.30	0.07	0.07

[a] Excited at the corresponding  $\lambda_{\text{abs,max}}$ . [b] Determined as an absolute value by the integration sphere method. [c]  $c = 1.0 \times 10^{-5}$  M at room temperature. [d]  $c = 1.0 \times 10^{-5}$  M in THF/H<sub>2</sub>O (1:99) at room temperature. [e] The data were collected from the crystal incorporating chloroform (1-CHCl<sub>3</sub>). [f] See ref.<sup>[46]</sup> [g] Product from the tetracene derivative obtained after heating at 300 °C for 10 min.

the energy barriers in the thermal reactions. Secondly, emission enhancement by thermal rearrangement may occur in different molecules.

## Conclusions

Unexpected emission enhancement from bis-*o*-carborane-modified acenes has been observed upon heating. From a mechanistic study of the anthracene derivative, it was found that *ortho*-to-*meta* isomerization occurred. X-ray crystallography revealed that one of the two *o*-carborane units in **1** rearranged to *m*-carborane, and that two molecules of **2** formed a  $\pi$ -stacked dimer in the crystal packing, just like **1**. The thermal rearrangement process was simulated by quantum chemical calculations, and two important issues were found. First, the introduction of the anthracene moiety can lower the activation energy of the rearrangement. Secondly, greater thermal assistance should be needed for isomerization of the second *o*-carborane unit. Therefore, only one *o*-carborane moiety rearranged to *m*-carborane. Moreover, compound **2** shows enhanced luminescence properties both in solution and the crystalline state, and AIEE behavior was observed. Finally, similar luminescence enhancement was also detected in the corresponding tetracene derivative. Aryl-modified carboranes are known to be a versatile platform for obtaining functional luminescent materials showing highly efficient solid-state emission and luminescent chromic behavior. Thus, this rearrangement reaction extends the number of compounds in the material library. Our findings from this work could be useful in the design of thermally resistant solid-state emissive materials with multichromic characteristics based on *o*-carborane derivatives.

## Experimental Section

**General:**  $^1\text{H}$ ,  $^{13}\text{C}$ , and  $^{11}\text{B}$  NMR spectra were recorded with a JEOL JNM-EX400 instrument at 400, 100, and 128 MHz, respectively. The  $^1\text{H}$  and  $^{13}\text{C}$  chemical shifts are expressed relative to  $\text{Me}_4\text{Si}$  as internal standard, and the  $^{11}\text{B}$  chemical shifts were expressed relative to  $\text{BF}_3\cdot\text{Et}_2\text{O}$  as external standard. High-resolution mass spectra (HRMS) were obtained with a Thermo Fisher Scientific EXACTIVE spectrometer by means of atmospheric pressure chemical ionization (APCI). Analytical TLC was performed with silica gel 60 Merck F254 plates. Column chromatography was performed with Wakogel C-300 silica gel. UV/Vis absorption spectra were recorded with a SHIMADZU UV3600 spectrophotometer. Photoluminescence (PL) spectra were obtained with a Horiba FluoroMax-4 luminescence spectrometer; absolute PL quantum efficiencies ( $\Phi_{\text{PL}}$ ) were determined by using a Horiba FL-3018 Integrating Sphere. Differential scanning calorimetry (DSC) thermograms were recorded with a Seiko DSC200 instrument using approximately 1.5 mg of samples at a heating rate of  $10\text{ }^\circ\text{C}/\text{min}$  under  $\text{N}_2$ . Thermogravimetric analysis (TGA) was carried out by using a Seiko EXSTAR 6000 instrument at a heating rate of  $10\text{ }^\circ\text{C}/\text{min}$  under  $\text{N}_2$ . Cyclic voltammetry (CV) was carried out with a BAS CV-50W electrochemical analyzer in DMF containing 0.1 M of sample and 0.1 M of  $\text{Bu}_4\text{NClO}_4$  with a glassy carbon working electrode, a Pt counter electrode, an Ag/AgCl ( $\text{Ag}/\text{Ag}^+$ ) reference electrode, and a ferrocene/ferrocenium external reference. Recyclable preparative HPLC was performed by using a Japan Analytical Indus-

try LC-918R instrument (JAIGEL-1HH and 2HH columns) using  $\text{CHCl}_3$  as eluent (flow rate:  $7.5\text{ mL}/\text{min}$ ).

### Synthesis of Compound **2**

**Neat Conditions Under  $\text{N}_2$ :** Compound **1**- $\text{CHCl}_3$  (3.6 mg,  $4.9\text{ }\mu\text{mol}$ ) was heated at  $300\text{ }^\circ\text{C}$  for 10 min under  $\text{N}_2$  by using DSC apparatus to obtain **2** (2.2 mg,  $3.6\text{ }\mu\text{mol}$ , 73 %). Further purification for optical measurements was carried out by HPLC ( $\text{CHCl}_3$  as an eluent). A single crystal of **2** suitable for X-ray crystallography was obtained by slow evaporation from  $\text{CHCl}_3/\text{MeOH}$ .  $^1\text{H}$  NMR (400 MHz,  $\text{CD}_2\text{Cl}_2$ ):  $\delta = 9.16$  (d,  $J = 9.0\text{ Hz}$ , 2 H, Ar-H), 8.79 (d,  $J = 9.0\text{ Hz}$ , 2 H, Ar-H), 7.43 (t,  $J = 7.3\text{ Hz}$ , 2 H, Ar-H), 7.29 (tt,  $J = 8.8, J = 3.3\text{ Hz}$ , 7 H, Ar-H), 6.85 (t,  $J = 4.0\text{ Hz}$ , 2 H, Ar-H), 6.74 (d,  $J = 7.3\text{ Hz}$ , 3 H, Ar-H), 4.39–1.65 (br., 20 H, B-H) ppm.  $^{13}\text{C}$  NMR (100 MHz,  $\text{CD}_2\text{Cl}_2$ ):  $\delta = 135.4, 134.9, 131.9, 131.6, 131.4, 131.2, 130.7, 129.4, 128.7, 128.6, 128.3, 126.0, 125.7, 125.1, 124.1, 122.3, 96.4, 90.8, 77.7, 77.6$  ppm.  $^{11}\text{B}$  NMR (128 MHz,  $\text{CD}_2\text{Cl}_2$ ):  $\delta = 1.1, 0.1, -2.3, -3.3, -9.3, -10.2$  ppm. HRMS (APCI): calcd. for  $\text{C}_{30}\text{H}_{38}\text{B}_{20}$  [ $\text{M} + \text{H}$ ] $^+$  619.4977; found 619.4970.

**Neat Conditions Under Air:** Crystals of **1**- $\text{CHCl}_3$  (3.2 mg,  $4.4\text{ }\mu\text{mol}$ ) were placed between two glass slides and heated at  $290\text{ }^\circ\text{C}$  for 5 min under air by using a hot plate. After cooling, further purification was carried out by HPLC ( $\text{CHCl}_3$  as eluent) to obtain **2** (1.8 mg,  $2.9\text{ }\mu\text{mol}$ , 66 %).

**Solution Conditions:** Compound **1**- $\text{CHCl}_3$  (11.8 mg,  $16\text{ }\mu\text{mol}$ ) was dissolved in squalane (3 mL) and heated at  $290\text{ }^\circ\text{C}$  for 2 h under Ar with stirring. After cooling, squalane was removed by silica gel column chromatography with hexane as eluent to yield compound **2** (4.9 mg,  $8.0\text{ }\mu\text{mol}$ , 50 %).

**Calculation Methods:** Transition-state calculations were carried out with the Gaussian 09 suite of programs<sup>[64]</sup> using the calculation procedure of Brown and McKee.<sup>[52]</sup> Target species were optimized at the B3LYP/6-31G(d) level of theory and frequency calculations were carried out at the same level to confirm whether they are stationary points. In addition, zero-point energies, entropies, and thermal correction data were obtained. Single-point electronic energies were then calculated at the B3LYP/6-311+G(2d,p) level of theory. The enthalpies of the species at 298 K were applied to the enthalpy at 500 and 800 K, and these values were used to determine the absolute free energies at 298, 500, and 800 K.

CCDC 1561095 (for **2**) contains the supplementary crystallographic data for this paper. These data can be obtained free of charge from The Cambridge Crystallographic Data Centre.

## Acknowledgments

This work was partially supported by the Konica Minolta Science and Technology Foundation (for K. T.) and a Grant-in-Aid for Scientific Research in Innovative Areas ("New Polymeric Materials Based on Element-Blocks, No. 2401", JSPS KAKENHI Grant Number JP24102013).

**Keywords:** Functional organic materials · Carboranes · Rearrangement · Luminescence · Aggregation · Acenes

- [1] Y. Chujo, K. Tanaka, *Bull. Chem. Soc. Jpn.* **2015**, *88*, 633–643.
- [2] K. Nishino, K. Hashimoto, K. Tanaka, Y. Morisaki, Y. Chujo, *Tetrahedron Lett.* **2016**, *57*, 2025–2028.
- [3] Y. Morisaki, M. Tominaga, T. Ochiai, Y. Chujo, *Chem. Asian J.* **2014**, *9*, 1247–1251.
- [4] K. Nishino, Y. Morisaki, K. Tanaka, Y. Chujo, *New J. Chem.* **2017**, *41*, 10550–10554.

- [5] R. N. Grimes, "Icosahedral carboranes:  $1,2\text{-C}_2\text{B}_{10}\text{H}_{12}$ " in *Carboranes* (Ed.: R. N. Grimes), 2nd ed., Academic Press, New York, **1970**.
- [6] V. I. Bregadze, *Chem. Rev.* **1992**, *92*, 209–223.
- [7] A. González-Campo, E. J. Juárez-Pérez, C. Viñas, B. Boury, R. Sillanpää, R. Kivekäs, R. Núñez, *Macromolecules* **2008**, *41*, 8458–8466.
- [8] F. Issa, M. Kassiou, L. M. Rendina, *Chem. Rev.* **2011**, *111*, 5701–5722.
- [9] G. Li, S. Azuma, S. Sato, H. Minegishi, H. Nakamura, *Bioorg. Med. Chem. Lett.* **2015**, *25*, 2624–2628.
- [10] G. Li, S. Azuma, S. Sato, H. Minegishi, H. Nakamura, *J. Organomet. Chem.* **2015**, *798*, 189–195.
- [11] R. Núñez, M. Tarrés, A. Ferrer-Ugalde, F. F. d. Biani, F. Teixidor, *Chem. Rev.* **2016**, *116*, 14307–14378.
- [12] L. Böhring, A. Brockhinke, J. Kahlert, L. Weber, R. A. Harder, D. S. Yufit, J. A. K. Howard, J. A. H. MacBride, M. A. Fox, *Eur. J. Inorg. Chem.* **2016**, 403–412.
- [13] L. Weber, J. Kahlert, R. Brockhinke, L. Böhring, A. Brockhinke, H.-G. Stammer, B. Neumann, R. A. Harder, M. A. Fox, *Chem. Eur. J.* **2012**, *18*, 8347–8357.
- [14] L. Weber, J. Kahlert, R. Brockhinke, L. Böhring, J. Halama, A. Brockhinke, H.-G. Stammer, B. Neumann, C. Nervi, R. A. Harder, M. A. Fox, *Dalton Trans.* **2013**, *42*, 10982–10996.
- [15] J. Kahlert, L. Böhring, A. Brockhinke, H.-G. Stammer, B. Neumann, L. M. Rendina, P. J. Low, L. Weber, M. A. Fox, *Dalton Trans.* **2015**, *44*, 9766–9781.
- [16] Y.-J. Cho, S.-Y. Kim, M. Cho, W.-S. Han, H.-J. Son, D. W. Cho, S. O. Kang, *Phys. Chem. Chem. Phys.* **2016**, *18*, 9702–9708.
- [17] S.-Y. Kim, Y.-J. Cho, G. F. Jin, W.-S. Han, H.-J. Son, D. W. Cho, S. O. Kang, *Phys. Chem. Chem. Phys.* **2015**, *17*, 15679–15682.
- [18] K.-R. Wee, Y.-J. Cho, S. Jeong, S. Kwon, J.-D. Lee, I.-H. Suh, S. O. Kang, *J. Am. Chem. Soc.* **2012**, *134*, 17982–17990.
- [19] B. H. Choi, J. H. Lee, H. Hwang, K. M. Lee, M. H. Park, *Organometallics* **2016**, *35*, 1771–1777.
- [20] R. Furue, T. Nishimoto, I. S. Park, J. Lee, T. Yasuda, *Angew. Chem. Int. Ed.* **2016**, *55*, 7171–7175.
- [21] M. Uebe, A. Ito, Y. Kameoka, T. Sato, K. Tanaka, *Chem. Phys. Lett.* **2015**, *633*, 190–194.
- [22] Y. Kameoka, M. Uebe, A. Ito, T. Sato, K. Tanaka, *Chem. Phys. Lett.* **2014**, *615*, 44–49.
- [23] S. Inagi, K. Hosoi, T. Kubo, N. Shida, T. Fuchigami, *Electrochemistry* **2013**, *81*, 368–370.
- [24] Z. Wang, P. Jiang, T. Wang, G. J. Moxey, M. P. Cifuentes, C. Zhang, M. G. Humphrey, *Phys. Chem. Chem. Phys.* **2016**, *18*, 15719–15726.
- [25] J. J. Peterson, A. R. Davis, M. Were, E. B. Coughlin, K. R. Carter, *ACS Appl. Mater. Interfaces* **2011**, *3*, 1796–1799.
- [26] L. Zhu, W. Lv, S. Liu, H. Yan, Q. Zhao, W. Huang, *Chem. Commun.* **2013**, *49*, 10638–10640.
- [27] D. Tu, P. Leong, Z. Li, R. Hu, C. Shi, K. Y. Zhang, H. Yan, Q. Zhao, *Chem. Commun.* **2016**, *52*, 12494–12497.
- [28] W. Zhang, Y. Luo, Y. Xu, L. Tian, M. Li, R. He, W. Shen, *Dalton Trans.* **2015**, *44*, 18130–18137.
- [29] S. Mukherjee, P. Thilagar, *Chem. Commun.* **2016**, *52*, 1070–1093.
- [30] X. Li, H. Yan, Q. Zhao, *Chem. Eur. J.* **2016**, *22*, 1888–1898.
- [31] J. Park, Y. H. Lee, J. Y. Ryu, J. Lee, M. H. Lee, *Dalton Trans.* **2016**, *45*, 5667–5675.
- [32] Y. H. Lee, J. Park, S.-J. Jo, M. Kim, J. Lee, S. U. Lee, M. H. Lee, *Chem. Eur. J.* **2015**, *21*, 2052–2061.
- [33] A. M. Prokhorov, T. Hofbeck, R. Czerwieniec, A. F. Suleymanova, D. N. Kozhevnikov, H. Yersin, *J. Am. Chem. Soc.* **2014**, *136*, 9637–9642.
- [34] N. Shin, S. Yu, J. H. Lee, H. Hwang, K. M. Lee, *Organometallics* **2017**, *36*, 1522–1529.
- [35] N. V. Nghia, J. Oh, J. Jung, M. H. Lee, *Organometallics* **2017**, *36*, 2573–2580.
- [36] J. J. Schwartz, A. M. Mendoza, N. Wattanatorn, Y. Zhao, V. T. Nguyen, A. M. Spokoyny, C. A. Mirkin, T. Baše, P. S. Weiss, *J. Am. Chem. Soc.* **2016**, *138*, 5957–5967.
- [37] K. O. Kirlikovali, J. C. Axtell, A. Gonzalez, A. C. Phung, S. I. Khan, A. M. Spokoyny, *Chem. Sci.* **2016**, *7*, 5132–5138.
- [38] A. M. Prokhorov, P. A. Slepukhin, V. L. Rusinov, V. N. Kalinin, D. N. Kozhevnikov, *Chem. Commun.* **2011**, *47*, 7713–7715.
- [39] A. M. Spokoyny, C. W. Machan, D. J. Clingerman, M. S. Rosen, M. J. Wiesner, R. D. Kennedy, C. L. Stern, A. A. Sarjeant, C. A. Mirkin, *Nat. Chem.* **2011**, *3*, 590–596.
- [40] A. C. Serino, M. E. Anderson, L. M. A. Saleh, R. M. Dzedzic, H. Mills, L. K. Heidenreich, A. M. Spokoyny, P. S. Weiss, *ACS Appl. Mater. Interfaces* **2017**, *9*, 34592–34596.
- [41] K. Kokado, Y. Chujo, *J. Org. Chem.* **2011**, *76*, 316–319.
- [42] H. Naito, K. Nishino, Y. Morisaki, K. Tanaka, Y. Chujo, *Angew. Chem. Int. Ed.* **2017**, *56*, 254–259.
- [43] K. Nishino, H. Yamamoto, K. Tanaka, Y. Chujo, *Org. Lett.* **2016**, *18*, 4064–4067.
- [44] H. Naito, K. Nishino, Y. Morisaki, K. Tanaka, Y. Chujo, *J. Mater. Chem. C* **2017**, *8*, 10047–10054.
- [45] K. Nishino, K. Tanaka, Y. Chujo, *Molecules* **2017**, *22*, 2009–2018.
- [46] K. Tanaka, K. Nishino, S. Ito, H. Yamane, K. Suenaga, K. Hashimoto, Y. Chujo, *Faraday Discuss.* **2017**, *196*, 31–42.
- [47] K. Nishino, H. Yamamoto, K. Tanaka, Y. Chujo, *Asian. J. Org. Chem.* **2017**, *6*, 1818–1822.
- [48] H. Naito, K. Nishino, Y. Morisaki, K. Tanaka, Y. Chujo, *Chem. Asian J.* **2017**, *12*, 2134–2138.
- [49] H. Naito, Y. Morisaki, Y. Chujo, *Angew. Chem. Int. Ed.* **2015**, *54*, 5084; *Angew. Chem.* **2015**, *127*, 5173–5087.
- [50] H. D. Kaesz, R. Bau, H. A. Beall, W. N. Lipscomb, V. I. Bregadze, *J. Am. Chem. Soc.* **1967**, *89*, 4218–4220.
- [51] H. Hart, W. N. Lipscomb, *J. Am. Chem. Soc.* **1969**, *91*, 771–772.
- [52] C. A. Brown, M. L. McKee, *J. Mol. Model.* **2006**, *12*, 653–664.
- [53] I. J. Sugden, D. F. Plant, R. G. Bell, *Chem. Commun.* **2013**, *49*, 975–977.
- [54] V. N. Kalinin, N. I. Kobel'kova, L. I. Zakharkin, *J. Organomet. Chem.* **1979**, *172*, 391–395.
- [55] V. N. Kalinin, B. A. Izmailov, A. A. Kazantsev, L. I. Zhdanov, L. I. Zakharkin, *Zh. Obshch. Khim.* **1984**, *54*, 1208–1209.
- [56] R. M. Salinger, C. L. Frye, *Inorg. Chem.* **1965**, *4*, 1815–1816.
- [57] L. I. Zakharkin, V. N. Kalinin, T. N. Balykova, P. N. Gribkova, V. V. Korshak, *J. Gen. Chem. USSR (Engl. Transl.)* **1973**, *43*, 2249–2254.
- [58] J. Kahlert, H.-G. Stammer, B. Neumann, R. A. Harder, L. Weber, M. A. Fox, *Angew. Chem. Int. Ed.* **2014**, *53*, 3702; *Angew. Chem.* **2014**, *126*, 3776–3705.
- [59] L. Weber, J. Kahlert, L. Böhring, A. Brockhinke, H.-G. Stammer, B. Neumann, R. A. Harder, P. J. Low, M. A. Fox, *Dalton Trans.* **2013**, *42*, 2266–2281.
- [60] K.-R. Wee, Y.-J. Cho, J. K. Song, S. O. Kang, *Angew. Chem. Int. Ed.* **2013**, *52*, 9682; *Angew. Chem.* **2013**, *125*, 9864–9685.
- [61] H. Mori, K. Nishino, K. Wada, Y. Morisaki, K. Tanaka, Y. Chujo, *Mater. Chem. Front.* **2018**, *2*, 573–579.
- [62] K. Nishino, K. Uemura, K. Tanaka, Y. Chujo, *New J. Chem.* **2018**, *42*, 4210–4214.
- [63] K. Nishino, K. Uemura, K. Tanaka, Y. Morisaki, Y. Chujo, *Eur. J. Org. Chem.* **2018**, 1507–1512.
- [64] M. J. Frisch, G. W. Trucks, H. B. Schlegel, G. E. Scuseria, M. A. Robb, J. R. Cheeseman, G. Scalmani, V. Barone, B. Mennucci, G. A. Petersson, H. Nakatsuji, M. Caricato, X. Li, H. P. Hratchian, A. F. Izmaylov, J. Bloino, G. Zheng, J. L. Sonnenberg, M. Hada, M. Ehara, K. Toyota, R. Fukuda, J. Hasegawa, M. Ishida, T. Nakajima, Y. Honda, O. Kitao, H. Nakai, T. Vreven, J. A. Montgomery Jr., J. E. Peralta, F. Ogliaro, M. Bearpark, J. J. Heyd, T. Brothers, K. N. Kudin, V. N. Staroverov, R. Kobayashi, J. Normand, K. Raghavachari, A. Rendell, J. C. Burant, S. S. Iyengar, J. Tomasi, M. Cossi, N. Rega, J. M. Millam, M. Klene, J. E. Knox, J. B. Cross, V. Bakken, C. Adamo, J. Jaramillo, R. Gomperts, R. E. Stratmann, O. Yazyev, A. J. Austin, R. Cammi, C. Pomelli, J. W. Ochterski, R. L. Martin, K. Morokuma, V. G. Zakrzewski, G. A. Voth, P. Salvador, J. J. Dannenberg, S. Dapprich, A. D. Daniels, Ö. Farkas, J. B. Foresman, J. V. Ortiz, J. Cioslowski, D. J. Fox, *Gaussian 09, Revision D.01*, Gaussian, Inc., Wallingford, CT, **2009**.

Received: January 29, 2018



## RESEARCH ARTICLE



Cite this: *Mater. Chem. Front.*, 2018, 2, 791

Received 27th December 2017,  
Accepted 31st January 2018

DOI: 10.1039/c7qm00613f

rs.c.li/frontiers-materials

## Synthesis of optically active $\pi$ -stacked compounds based on planar chiral tetrasubstituted [2.2]paracyclophane†

Yusaku Sasai,<sup>a</sup> Hiromu Tsuchida,<sup>b</sup> Takahiro Kakuta,<sup>b</sup> Tomoki Ogoshi<sup>id</sup><sup>bc</sup> and Yasuhiro Morisaki<sup>id</sup><sup>\*a</sup>

Optically active X-shaped compounds based on planar chiral [2.2]paracyclophane were synthesized. These compounds composed of two different  $\pi$ -electron systems stacked at central aromatic rings through chemoselective Sonogashira–Hagihara coupling. The optical and chiroptical properties of the obtained compounds were investigated, which exhibited large molar absorption coefficients, good photoluminescence quantum efficiency, and intense circularly polarized luminescence (CPL) with large dissymmetry factors on the order of  $10^{-3}$ , indicating that the compounds are excellent CPL emitters.

### Introduction

[2.2]Paracyclophane is a unique molecule consisting of face-to-face benzene rings in proximity; the distance between the two benzene rings is approximately 3.0 Å.<sup>1</sup> [2.2]Paracyclophane has been utilized as a scaffold to construct  $\pi$ -stacked structures; various  $\pi$ -electron systems can be stacked in a molecule. 4,12-Disubstituted and 4,7,12,15-tetrasubstituted [2.2]paracyclophanes are representative scaffolds, as shown in Fig. 1.<sup>2</sup> For example, when using 4,12-disubstituted [2.2]paracyclophane to construct a  $\pi$ -stacked structure, the terminal benzene rings of the  $\pi$ -electron systems are stacked (Fig. 1a). Using 4,7,12,15-tetrasubstituted [2.2]paracyclophane as a scaffold, the central phenylenes of the  $\pi$ -electron systems are stacked (Fig. 1b). Thus, the  $\pi$ -stacked position of the  $\pi$ -electron system can be tuned by the choice of the [2.2]paracyclophane scaffold.

[2.2]Paracyclophane compounds with substituent(s) exhibit planar chirality due to the restricted rotational motion of the  $\pi$ -stacked benzene rings, depending on the substitution positions.<sup>3</sup> 4,12-Disubstituted and 4,7,12,15-tetrasubstituted [2.2]paracyclophanes are also planar chiral compounds. Recently, we have developed a practical optical resolution of 4,12-disubstituted

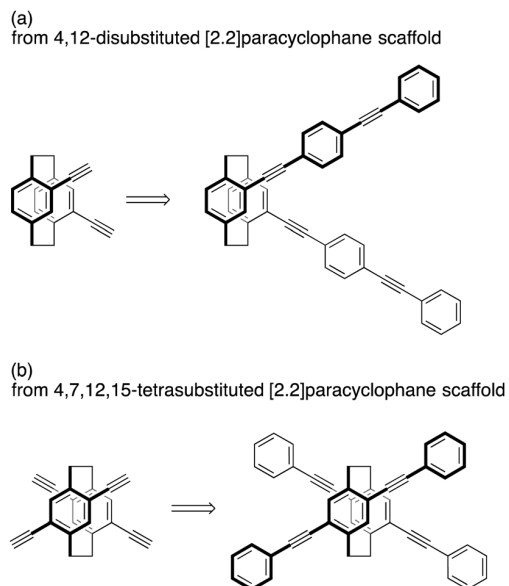


Fig. 1 [2.2]Paracyclophane scaffolds to construct  $\pi$ -stacked structures.

[2.2]paracyclophane<sup>4,5</sup> and the first optical resolution of 4,7,12,15-tetrasubstituted [2.2]paracyclophane,<sup>6,7</sup> leading to enantiopure scaffolds to synthesize optically active compounds with higher-ordered chiral structures. In that study, optically active V-shaped,<sup>4</sup> X-shaped,<sup>8</sup> 8-shaped,<sup>6a,b</sup> and double-helical<sup>6c</sup> compounds were synthesized which emit excellent circularly polarized luminescence (CPL) by photo-excitation.

The optical resolution of 4,7,12,15-tetrasubstituted [2.2]paracyclophane is carried out with 4-hydroxy-7,12,15-tribromo[2.2]paracyclophane (*rac-1*) using a chiral auxiliary, and then, the

<sup>a</sup> Department of Applied Chemistry for Environment, School of Science and Technology, Kwansei Gakuin University, 2-1 Gakuen, Sanda, Hyogo 669-1337, Japan. E-mail: ymo@kwansei.ac.jp

<sup>b</sup> Graduate School of Natural Science and Technology, Kanazawa University, Kakuma-machi, Kanazawa, Ishikawa 920-1192, Japan

<sup>c</sup> WPI Nano Life Science Institute, Kanazawa University, Kakuma-machi, Kanazawa, 920-1192, Japan

† Electronic supplementary information (ESI) available: Experimental details including synthetic procedures, characterization, and NMR spectra. See DOI: 10.1039/c7qm00613f

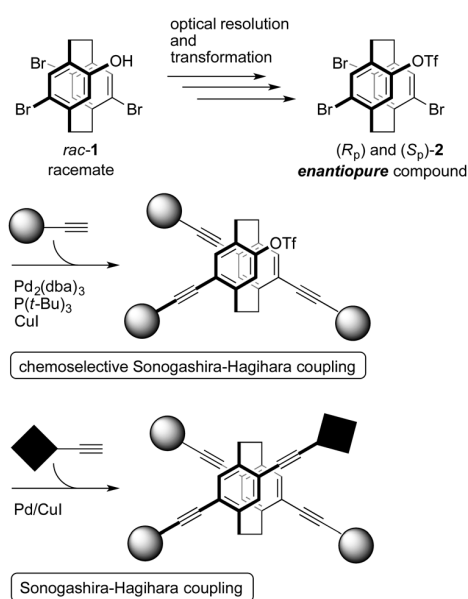


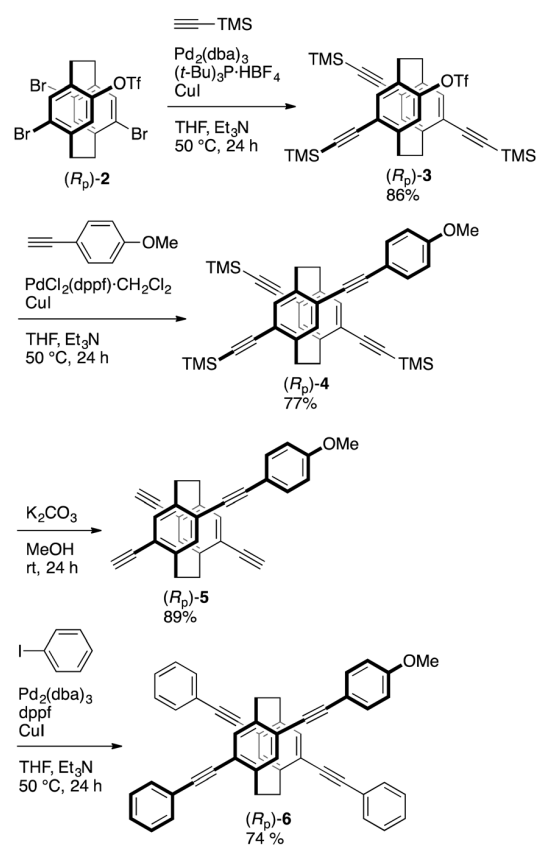
Fig. 2 Strategy to obtain X-shaped compounds with different  $\pi$ -electron systems.

hydroxyl group is converted to the trifluoromethylsulfonyl group to afford enantiopure compound **2** (Fig. 2).<sup>6a</sup> The catalytic system,  $\text{Pd}_2(\text{dba})_3/\text{P}(t\text{-Bu})_3/\text{CuI}$ , was found for chemoselective Sonogashira–Hagihara coupling;<sup>9</sup> only bromo groups reacted, and the trifluoromethylsulfonyl group remained (Fig. 2).<sup>6a</sup> This chemoselective coupling makes it possible to synthesize new types of X-shaped compounds with different  $\pi$ -electron systems stacked in molecules (Fig. 2). In this study, we demonstrate the stacking of different  $\pi$ -electron systems (*p*-phenylene ethynyls) consisting of three benzene rings at the central phenylene units. The synthetic routes and optical properties of the obtained  $\pi$ -stacked compounds are also shown.

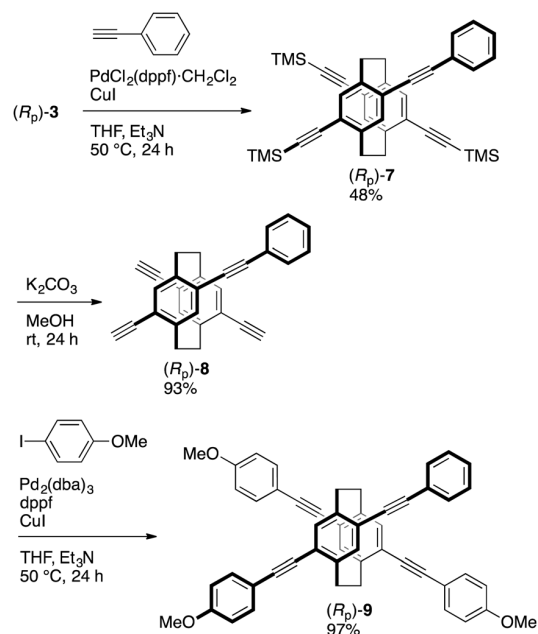
## Results and discussion

Schemes 1 and 2 show the synthetic routes to the target X-shaped compounds with different  $\pi$ -electron systems stacked; the synthetic routes from  $(R_p)$ -**2**<sup>6a</sup> are also shown. Chemoselective Sonogashira–Hagihara coupling of  $(R_p)$ -**2** with trimethylsilylacetylene in the presence of catalytic amounts of  $\text{Pd}_2(\text{dba})_3$  (dba = dibenzylideneacetone),  $(t\text{-Bu})_3\text{P}\cdot\text{HBF}_4$ , and  $\text{CuI}$  afforded triyne  $(R_p)$ -**3** in 86% isolated yield, as shown in Scheme 1. Sonogashira–Hagihara coupling of  $(R_p)$ -**3** with *p*-methoxyphenylacetylene using  $\text{PdCl}_2(\text{dppf})\cdot\text{CH}_2\text{Cl}_2$  (dppf = 1,1'-bis(diphenylphosphino)ferrocene) and  $\text{CuI}$  afforded the corresponding tetrayne  $(R_p)$ -**4** in 77% isolated yield. The trimethylsilyl group could be readily removed by reaction with  $\text{K}_2\text{CO}_3$  in MeOH to obtain  $(R_p)$ -**5** in 89% isolated yield. Finally, Sonogashira–Hagihara coupling of  $(R_p)$ -**5** with iodobenzene using  $\text{Pd}_2(\text{dba})_3$ , dppf, and  $\text{CuI}$  afforded the target compound  $(R_p)$ -**6** in 74% isolated yield, as shown in Scheme 1.<sup>10</sup>

The same synthetic strategy produced the other target compound  $(R_p)$ -**9** (Scheme 2). Triyne  $(R_p)$ -**3** was reacted with



Scheme 1 Synthesis of  $(R_p)$ -**6**.



Scheme 2 Synthesis of  $(R_p)$ -**9**.

phenylacetylene using  $\text{PdCl}_2(\text{dppf})\cdot\text{CH}_2\text{Cl}_2$  and  $\text{CuI}$  to obtain tetrayne  $(R_p)$ -**7** in 48% isolated yield. Its trimethylsilyl groups

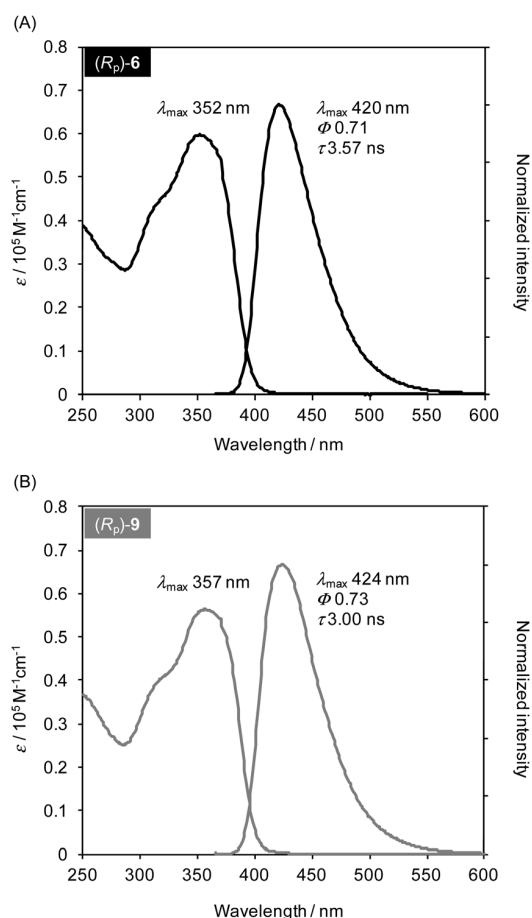


Fig. 3 UV and PL spectra of (A) ( $R_p$ )-**6** and (B) ( $R_p$ )-**9** in  $\text{CHCl}_3$  ( $1.0 \times 10^{-5}$  M, excited at each absorption maximum for the PL spectrum).

were also removed by  $\text{K}_2\text{CO}_3$  in MeOH to obtain ( $R_p$ )-**8** in 93% isolated yield. Sonogashira–Hagihara coupling of ( $R_p$ )-**8** with *p*-iodoanisole using  $\text{Pd}_2(\text{dba})_3$ , dppf, and CuI afforded compound ( $R_p$ )-**9** in 97% isolated yield, as shown in Scheme 2.<sup>10</sup>

The optical properties of compounds (both enantiomers) **6** and **9** were evaluated by ultraviolet (UV) and photoluminescence (PL) spectroscopies. Fig. 3 shows the UV and PL spectra of ( $R_p$ )-**6** and ( $R_p$ )-**9** in their dilute  $\text{CHCl}_3$  solutions ( $1.0 \times 10^{-5}$  M). Both compounds exhibited similar optical behaviours. Their peak tops in the UV spectra were at 352 nm and 357 nm, respectively, and those in the PL spectra appeared at 420 nm and 424 nm, respectively. The absolute PL quantum efficiencies ( $\Phi_{\text{lum}}$ ) of ( $R_p$ )-**6** and ( $R_p$ )-**9** were estimated to be 0.71 and 0.73, respectively. PL lifetime decay curves were fitted with a single exponential equation, and their lifetimes ( $\tau$ ) were calculated to be 3.57 ns and 3.00 ns, respectively. In addition, we have prepared two kinds of optically active X-shaped compounds: without a methoxy group<sup>8a</sup> and with four methoxy groups<sup>8b</sup> (Table S1 in the ESI†). As the number of methoxy groups increased, the spectra were slightly red-shifted,  $\Phi$  values improved, and  $\tau$  values decreased. The PL spectra of ( $R_p$ )-**6** and ( $R_p$ )-**9** were broad without any vibronic structure, and the  $\tau$  values were relatively long ( $>3$  ns). It is

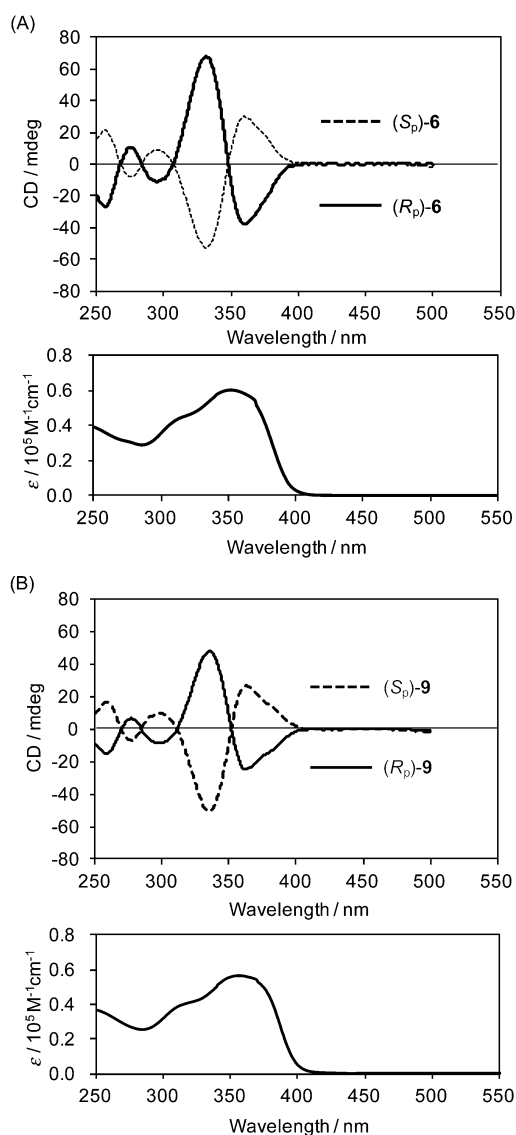


Fig. 4 CD and UV spectra of (A) enantiomers of **6** and (B) enantiomers of **9** in  $\text{CHCl}_3$  ( $1.0 \times 10^{-5}$  M).

known that the excited state is delocalized in the whole molecule in the case of close energy levels between through-bond and through-space states.<sup>2b,d,e,i,j</sup> Thus, the emission mechanisms of ( $R_p$ )-**6** and ( $R_p$ )-**9** are identical to those of previous studies, and there are no essential differences among these compounds.

The chiroptical properties of both enantiomers of **6** and **9** were investigated using circular dichroism (CD) and CPL spectra. The CD and the absorption spectra of both enantiomers of **6** and **9** in dilute  $\text{CHCl}_3$  ( $1.0 \times 10^{-5}$  M) are shown in Fig. 4A and B. In both cases, the absorption peaks around 350 nm are the typical  $\pi$ - $\pi^*$  transition bands of *p*-phenylene-ethynylenes, and clear Cotton effects were observed in the absorption bands. As shown in the CD spectra, chirality was induced in the arylene-ethynylene moieties by the planar chiral [2.2]paracyclophane moiety.

Fig. 5 shows the CPL and PL spectra of (*S*<sub>p</sub>)- and (*R*<sub>p</sub>)-**6** and **9** in dilute CHCl<sub>3</sub> (1.0 × 10<sup>-5</sup> M), and the *g*<sub>lum</sub> spectra are also included. The *g*<sub>lum</sub> is given by the following equation:  $2(I_{\text{left}} - I_{\text{right}})/(I_{\text{left}} + I_{\text{right}})$ , where *I*<sub>left</sub> and *I*<sub>right</sub> indicate the luminescence intensities of left- and right-handed CPL, respectively.<sup>11,12</sup> Both compounds **6** and **9** exhibited mirror image spectra. Positive and negative signals were observed for (*S*<sub>p</sub>)- and (*R*<sub>p</sub>)-isomers, respectively. These behaviours were the same as those reported in previous studies (Table S1 in the ESI<sup>†</sup>). The positive/negative signals were identical to those of the longest wavelength in the corresponding CD spectra, indicating the same orientations of dipole moments between electric and magnetic transitions in the ground and excited states. The absolute *g*<sub>lum</sub> values between the enantiomers of **6** and **9** were estimated to be approximately 1.5 × 10<sup>-3</sup> and 1.7 × 10<sup>-3</sup>,

respectively. Compounds **6** and **9** exhibited relatively large ε and good Φ<sub>lum</sub> (>0.7), in addition to the large *g*<sub>lum</sub> value on the order of 10<sup>-3</sup>. Therefore, optically active X-shaped compounds are promising CPL materials.

## Conclusions

In summary, planar chiral [2.2]paracyclophane-based optically active X-shaped compounds were synthesized. Different π-electron systems could be stacked at the central phenylene units by the chemo-selective Sonogashira–Hagihara coupling using a Pd<sub>2</sub>(dba)<sub>3</sub>/(*t*-Bu)<sub>3</sub>P/CuI catalytic system. Although essential differences between compounds consisting of different π-electron systems and the same π-electron systems were not observed, the compounds exhibited good emission behaviours, resulting in an excellent CPL emitter with a large ε, good Φ<sub>lum</sub>, and a large *g*<sub>lum</sub> value on the order of 10<sup>-3</sup>. The strategy in this study can stack two different π-electron systems; thus, our next target is the synthesis of optically active π-stacked compounds consisting of strong donor and acceptor π-electron systems. In addition, the systematic synthesis of planar chiral [2.2]paracyclophane-based optically active compounds by changing the stacking position<sup>4c</sup> and orientation of the stacked-π-electron systems will be studied to elucidate the CPL emission mechanism of the planar chiral [2.2]paracyclophane.

## Conflicts of interest

There are no conflicts to declare.

## Acknowledgements

This work was supported by Grants-in-Aid for Scientific Research on Innovative Areas (No. 17H05165 for Y. M. and 17H05148 for T. O.) “π-Figuration” from the Ministry of Education, Culture, Sports, Science and Technology, Japan. The financial support from the Nagase Science and Technology Foundation is also acknowledged. The authors are grateful to Professor Naoto Tamai (Department of Chemistry, School of Science and Technology, Kwansei Gakuin University) for PL lifetime measurements.

## Notes and references

- (a) F. Vögtle, *Cyclophane Chemistry: Synthesis, Structures and Reactions*, John Wiley & Sons, Chichester, 1993; (b) *Modern Cyclophane Chemistry*, ed. R. Gleiter and H. Hopf, Wiley-VCH, Weinheim, Germany, 2004; (c) H. Hopf, *Angew. Chem., Int. Ed.*, 2008, **47**, 9808–9812.
- Representative examples are shown. (a) G. C. Bazan, W. J. Oldham Jr., R. J. Lachicotte, S. Tretiak, V. Chernyak and S. Mukamel, *J. Am. Chem. Soc.*, 1998, **120**, 9188–9204; (b) S. Wang, G. C. Bazan, S. Tretiak and S. Mukamel, *J. Am. Chem. Soc.*, 2000, **122**, 1289–1297; (c) J. Zyss, I. Ledoux, S. Volkov, V. Chernyak, S. Mukamel, G. P. Bartholomew and G. C. Bazan, *J. Am. Chem. Soc.*, 2000, **122**, 11956–11962;

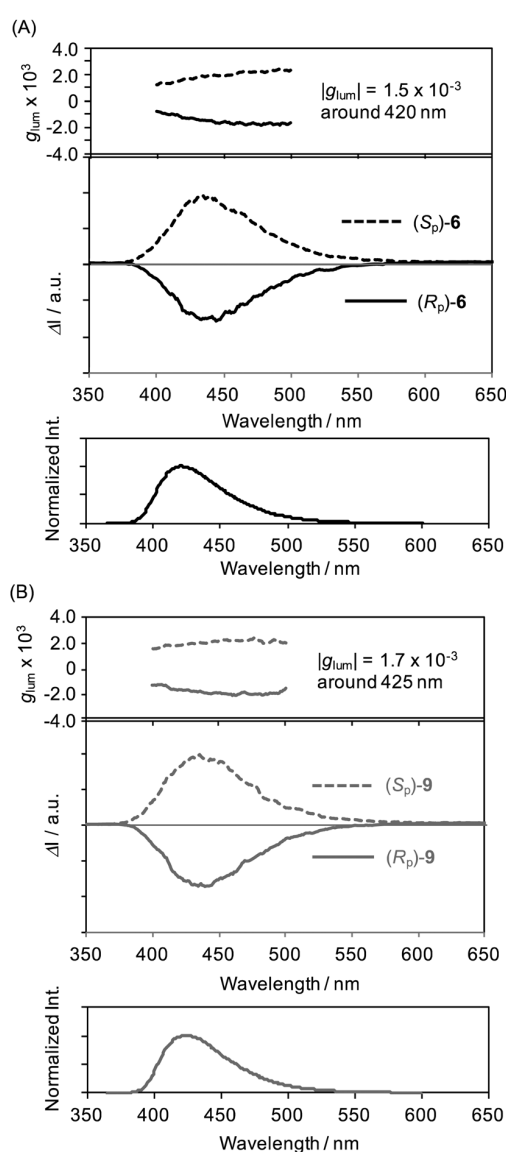


Fig. 5 CPL and PL spectra, including *g*<sub>lum</sub> spectra, of (A) enantiomers of **6** and (B) enantiomers of **9** in CHCl<sub>3</sub> (1.0 × 10<sup>-5</sup> M, excited at 280 nm).

- (d) G. P. Bartholomew and G. C. Bazan, *Acc. Chem. Res.*, 2001, **34**, 30–39; (e) G. P. Bartholomew and G. C. Bazan, *Synthesis*, 2002, 1245–1255; (f) G. P. Bartholomew and G. C. Bazan, *J. Am. Chem. Soc.*, 2002, **124**, 5183–5196; (g) D. S. Seferos, D. A. Banach, N. A. Alcantar, J. N. Israelachvili and G. C. Bazan, *J. Org. Chem.*, 2004, **69**, 1110–1119; (h) G. P. Bartholomew, M. Rumi, S. J. K. Pond, J. W. Perry, S. Tretiak and G. C. Bazan, *J. Am. Chem. Soc.*, 2004, **126**, 11529–11542; (i) J. W. Hong, H. Y. Woo and G. C. Bazan, *J. Am. Chem. Soc.*, 2005, **127**, 7435–7443; (j) G. C. Bazan, *J. Org. Chem.*, 2007, **72**, 8615–8635.
- 3 (a) D. J. Cram and N. L. Allinger, *J. Am. Chem. Soc.*, 1955, **77**, 6289–6294; (b) V. Rozenberg, E. Sergeeva and H. Hopf, in *Modern Cyclophane Chemistry*, ed., R. Gleiter and H. Hopf, Wiley-VCH, Weinheim, Germany, 2004, pp. 435–462; (c) G. J. Rowlands, *Org. Biomol. Chem.*, 2008, **6**, 1527–1534; (d) S. E. Gibson and J. D. Knight, *Org. Biomol. Chem.*, 2003, **1**, 1256–1269; (e) A. A. Aly and A. B. Brown, *Tetrahedron*, 2009, **65**, 8055–8089; (f) J. Paradies, *Synthesis*, 2011, 3749–3766.
- 4 (a) Y. Morisaki, R. Hifumi, L. Lin, K. Inoshita and Y. Chujo, *Chem. Lett.*, 2012, **41**, 990–992; (b) Y. Morisaki, R. Hifumi, L. Lin, K. Inoshita and Y. Chujo, *Polym. Chem.*, 2012, **3**, 2727–2730; (c) Y. Morisaki, K. Inoshita and Y. Chujo, *Chem. – Eur. J.*, 2014, **20**, 8386–8390.
- 5 For other optical resolutions of 4,12-disubstituted [2.2]paracyclophane, see: (a) P. J. Pye, K. Rossen, R. A. Reamer, N. N. Tsou, R. P. Volante and P. J. Reider, *J. Am. Chem. Soc.*, 1997, **119**, 6207–6208; (b) K. Rossen, P. J. Pye, A. Maliakal and R. P. Volante, *J. Org. Chem.*, 1997, **62**, 6462–6463; (c) R. Zhuravsky, Z. Starikova, E. Vorontsov and V. Rozenberg, *Tetrahedron: Asymmetry*, 2008, **19**, 216–222; (d) B. Jiang and X.-L. Zhao, *Tetrahedron: Asymmetry*, 2004, **15**, 1141–1143; (e) P. G. Jones, J. Hillmer and H. Hopf, *Acta Crystallogr., Sect. E: Struct. Rep. Online*, 2003, **59**, o24–o25; (f) D. Pamperin, H. Hopf, C. Syldatk and M. Pietzsch, *Tetrahedron: Asymmetry*, 1997, **8**, 319–325; (g) D. Pamperin, B. Ohse, H. Hopf and M. Pietzsch, *J. Mol. Catal. B: Enzym.*, 1998, **5**, 317–319; (h) D. C. Braddock, I. D. MacGilp and B. G. Perry, *J. Org. Chem.*, 2002, **67**, 8679–8681; (i) G. Meyer-Eppler, E. Vogelsang, C. Benkhäuser, A. Schneider, G. Schnakenburg and A. Lützen, *Eur. J. Org. Chem.*, 2013, 4523–4532.
- 6 (a) Y. Morisaki, M. Gon, T. Sasamori, N. Tokitoh and Y. Chujo, *J. Am. Chem. Soc.*, 2014, **136**, 3350–3353; (b) M. Gon, Y. Morisaki and Y. Chujo, *J. Mater. Chem. C*, 2015, **3**, 521–529; (c) Y. Morisaki, R. Sawada, M. Gon and Y. Chujo, *Chem. – Asian J.*, 2016, **11**, 2524–2527.
- 7 The optical resolution of *rac*-4,5,15,16-tetrasubstituted [2.2]-paracyclophane was reported: N. V. Vorontsova, V. I. Rozenberg, E. V. Sergeeva, E. V. Vorontsov, Z. A. Starikova, K. A. Lyssenko and H. Hopf, *Chem. – Eur. J.*, 2008, **14**, 4600–4617.
- 8 (a) M. Gon, Y. Morisaki and Y. Chujo, *Eur. J. Org. Chem.*, 2015, 7756–7762; (b) M. Gon, Y. Morisaki, R. Sawada and Y. Chujo, *Chem. – Eur. J.*, 2016, **22**, 2291–2298; (c) M. Gon, Y. Morisaki and Y. Chujo, *Chem. – Eur. J.*, 2017, **23**, 6323–6329.
- 9 (a) Y. Tohda, K. Sonogashira and N. Hagihara, *Tetrahedron Lett.*, 1975, **16**, 4467–4470; (b) K. Sonogashira, in *Handbook of Organopalladium Chemistry for Organic Synthesis*, ed. E. Negishi, Wiley-Interscience, New York, 2002, pp. 493–529.
- 10 Chemoselective Sonogashira–Hagihara coupling of **2** with arylacetylenes instead of trimethylsilyl acetylene is possible. In this study, trimethylsilyl acetylene was employed due to the easy removal of unreacted (excess amount) trimethylsilylacetylene and 1,4-bis(trimethylsilyl)-1,3-butadiyne as a byproduct by evaporation and column chromatography.
- 11 For reviews, see: (a) H. Maeda and Y. Bando, *Pure Appl. Chem.*, 2013, **85**, 1967–1978; (b) J. Kumar, T. Nakashima, H. Tsumatori and T. Kawai, *J. Phys. Chem. Lett.*, 2014, **5**, 316–321; (c) E. M. Sánchez-Carnereo, A. R. Agarrabeitia, F. Moreno, B. L. Maroto, G. Muller, M. J. Ortiz and S. de la Moya, *Chem. – Eur. J.*, 2015, **21**, 13488–13500; (d) F. Zinna and L. Di Bari, *Chirality*, 2015, **27**, 1–13; (e) G. Longhi, E. Castiglioni, J. Koshoubu, G. Mazzeo and S. Abbate, *Chirality*, 2016, **28**, 696–707.
- 12 Very recently, excellent CPL-emitting organic molecules with large  $g_{lum}$  values on the order of  $10^{-1}$  were reported. S. Sato, A. Yoshii, S. Takahashi, S. Furumi, M. Takeuchi and H. Isobe, *Proc. Natl. Acad. Sci. U. S. A.*, 2017, **114**, 13097–13101.

## Luminescent Carborane

# Modulation of the *cis*- and *trans*-Conformations in Bis-*o*-carborane Substituted Benzodithiophenes and Emission Enhancement Effect on Luminescent Efficiency by Solidification

Kenta Nishino,<sup>[a]</sup> Kyoya Uemura,<sup>[a]</sup> Kazuo Tanaka\*<sup>[a]</sup> Yasuhiro Morisaki,<sup>[a][‡]</sup> and Yoshiki Chujo\*<sup>[a]</sup>

**Abstract:** Bis-carborane-substituted benzo[1,2-*b*:4,5-*b'*]dithiophenes (DCB-R, where R = H, *t*Bu) were synthesized and characterized. Their three-dimensional conformations were tuned by introducing the *tert*-butyl substituent at the *para*-positions of the phenyl rings. Both molecules showed emission enhancement behavior, especially in the solid state. The emission quantum efficiencies were over 0.90 in the crystalline state. More-

over, it was shown that the efficiency of DCB-*t*Bu was over 0.70 in the amorphous state. From structural analyses and mechanistic investigations, it was proposed that the *tert*-butyl substituents play a critical role in the formation of the *trans*-conformation followed by suppression of aggregation-caused quenching because of the *o*-carborane units located at each plane of the benzodithiophene ring.

## Introduction

Most luminescent organic dyes suffer from a critical decrease in emission efficiency upon aggregation (aggregation-caused quenching, ACQ). Even though intense luminescence can be observed in the solution state, optical properties were often spoiled through ACQ by intermolecular interactions in the solid state. One promising platform to overcome the ACQ problem is a class of aggregation-induced emission (AIE)-active boron complexes, which show significant emission not in the dilute state but in aggregation.<sup>[1–3]</sup> Intense solid-state luminescent properties originating from AIE were found and applied for developing the conjugated materials, including polymers.<sup>[4]</sup> Additionally, based on environment-responsive intensity changes of the AIE-active materials, various types of film-type luminescent materials and sensors can be fabricated.<sup>[5–7]</sup>

It has been reported that some of the *o*-carborane<sup>[8–13]</sup> derivatives presented AIE<sup>[14–21]</sup> and can be applied as a solid-state luminescent material.<sup>[22–34]</sup> We have also focused on the aryl-modified *o*-carboranes as a scaffold for constructing luminescent “element-block”,<sup>[35,36]</sup> which is defined as a minimum functional unit composed of heteroatoms.<sup>[37–40]</sup> The *o*-carborane cluster is a boron cluster composed of three-center two-electron bonds, and acts as a strong electron-withdrawing group

when bonding through the carbon atoms.<sup>[41–51]</sup> Thereby, bright emission from the intramolecular charge transfer (ICT) state can be generated by combination of *o*-carborane and electron-rich aryl substituents.<sup>[52–55]</sup> Especially, even in the crystalline state, the CT emission can often be preserved by inhibiting ACQ because of the steric sphere shape of the *o*-carborane units. Thus, a variety of highly-emissive crystalline materials composed of aryl-connected *o*-carborane structures have been obtained.<sup>[56–58]</sup> Moreover, it is known that electronic structures were drastically changed by rotation at the *o*-carborane unit.<sup>[59,60]</sup> Furthermore, it was found that these materials showed stimuli-responsive luminescent chromism toward external mechanical forces and environmental factors such as temperature.<sup>[61]</sup> However, in these materials, emission quenching often occurred particularly in the amorphous state, although solid-state emission through the AIE mechanism was maintained to some extent. Intermolecular interaction could be severe at the aryl moiety in the random distribution. This unexpected emission quenching is a crucial limitation in the application of AIE-active materials to stimuli-responsive solid-state luminescent sensors by burying significant color changes. Thus, our next goal is to demonstrate preservation of the solid-state emission of AIE-active molecules from the conformation changes.

Herein, we designed bis-carborane-substituted benzo[1,2-*b*:4,5-*b'*]dithiophenes DCB-R (R = H, *t*Bu). The benzodithiophene moiety in DCB-R would be isolated by the phenyl rings located at the adjacent position in the *o*-carborane units from intermolecular interaction in the condensed state. From the structural analyses, it was found that DCB-H and DCB-*t*Bu formed the *cis*- and *trans*-conformations because of the degree of steric hindrance at the *para*-positions of the phenyl rings, respectively. Both molecules showed emission enhancement behaviors in the solid state, and especially in the crystalline

[a] Department of Polymer Chemistry, Graduate School of Engineering, Kyoto University, Katsura, Nishikyo-ku, Kyoto 615-8510, Japan  
E-mail: tanaka@poly.synchem.kyoto-u.ac.jp  
chujo@poly.synchem.kyoto-u.ac.jp  
http://poly.synchem.kyoto-u.ac.jp/

[‡] Present address: Department of Applied Chemistry for Environment, School of Science and Technology, Kwansei Gakuin University, 2-1 Gakuen, Sanda, Hyogo 669-1337, Japan

Supporting information and ORCID(s) from the author(s) for this article are available on the WWW under <https://doi.org/10.1002/ejoc.201701641>.

state. Furthermore, it was observed that these emission intensities were maintained even in the amorphous state.

## Results and Discussion

Scheme 1 shows the synthesis of DCB-R (R = H, *t*Bu). Initially, benzo[1,2-*b*:4,5-*b'*]dithiophene-4,8-dione was added to a tetrahydrofuran (THF) solution of the lithiated ethynylbenzene derivatives **1**-R. Then the quinone form of benzodithiophene was reduced by SnCl<sub>2</sub> in aq. HCl solution, and the diethynyl derivatives **2**-R were obtained through coupling reaction. The decaborane(14) insertion reaction was carried out to obtain the DCB-R. All compounds were characterized by <sup>1</sup>H, <sup>11</sup>B, and <sup>13</sup>C NMR spectroscopy, elemental analyses and HRMS measurements. The products showed good stability and solubility in common organic solvents such as CHCl<sub>3</sub>, CH<sub>2</sub>Cl<sub>2</sub>, THF, and benzene. Thus, we concluded that the products should have the designed structures and sufficient stability for performing the series of measurements.

From the <sup>1</sup>H NMR spectrum of DCB-H in CD<sub>2</sub>Cl<sub>2</sub> at 30 °C, broad signal peaks were observed, whereas at -30 °C, remarkable peaks were detected (Figure 1). Moreover, these spectrum changes proceeded reversibly by varying detection temperature. These data indicate that DCB-H can form the two types of structural isomers. These peaks were assigned by <sup>1</sup>H-<sup>1</sup>H COSY (Figure S1). At -30 °C, the peaks at 8.4, 7.7, 7.1, and 6.8 ppm were assigned to signals from conformation A; peaks at 7.8, 7.4, 7.2, and 7.0 ppm were attributable to those from conformation B. Especially, the peak at 8.4 ppm in the spectrum of conformation A showed upfield shift to 7.8 ppm in conformation B. The shielding effect on the benzo[1,2-*b*:4,5-*b'*]dithiophene unit could be induced by the benzene rings. Additionally, the existing ratio of conformation A was twofold larger than that of conformation B at -30 °C, and this ratio was also changed by temperature alteration. To estimate the height of the energy barrier for the isomerization, the logarithm of the existing ratio in DCB-H against inverse temperature was prepared (Figure S2). From this plot, thermodynamic parameters were calculated, and it was found that conformation A was 4.02 kJ/mol more stable than conformation B. Given the small energy gap, DCB-H formed both conformations and showed broad peaks in the

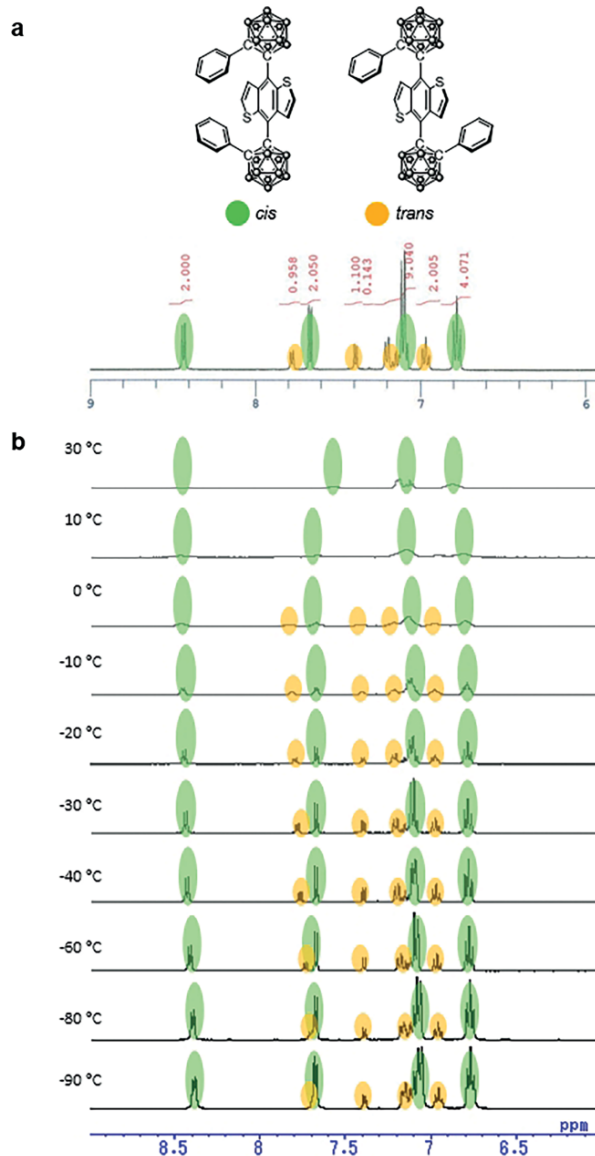
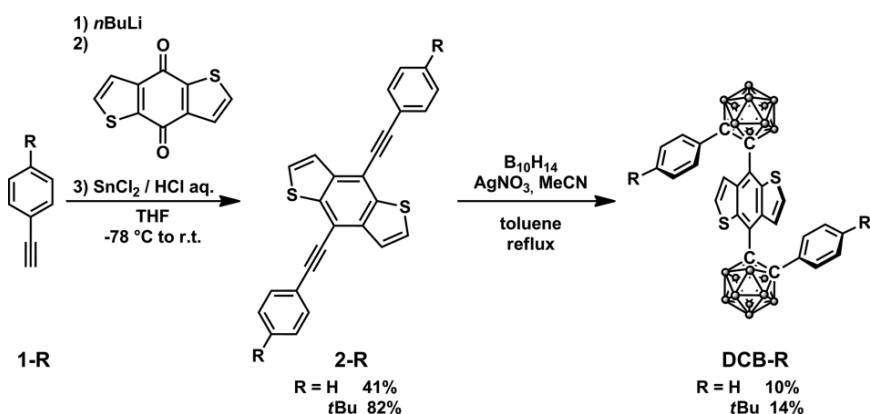


Figure 1. (a) Characterization of the <sup>1</sup>H NMR spectrum of DCB-H and (b) variable-temperature <sup>1</sup>H NMR spectra in CD<sub>2</sub>Cl<sub>2</sub>.



Scheme 1. Synthesis of DCB-R.

NMR spectrum in the solution at room temperature. On the other hand, DCB-*t*Bu showed sharp peaks at 7.8, 7.4, 7.2, 7.0 ppm in CD<sub>2</sub>Cl<sub>2</sub> at room temperature. These peaks were almost identical to those from conformation B of DCB-H. In particular, there were no peaks around 8.5 ppm that were specific for conformation A. These data indicate that very little DCB-*t*Bu forms conformation A-like structure. It was proposed that the steric effect of the *tert*-butyl groups could play a critical role in suppression of conformation changes.

To support the above speculation on the structures of these isomers, X-ray single-crystal analyses were executed. Single crystals were obtained by recrystallization from benzene for DCB-H and benzene/EtOH mix solvents for DCB-*t*Bu. Figures S3a–c show ORTEP diagrams of DCB-H. Although probability levels were low due to thermal motion, it was observed that the benzene rings that were connected to the next carbon position in the *o*-carborane moiety were distributed in the same direction. In addition, highly symmetric structures were observed. DCB-H formed the *cis*-conformation in the crystal state, whereas it was clear that DCB-*t*Bu had the *trans*-conformation (Figures S3d–f). These observations suggest that conformations A and B should be the *cis*- and *trans*-conformations, respectively. The structure of DCB-*t*Bu should be immobilized in the *trans*-conformation because of steric bulk of the *tert*-butyl groups. In contrast, DCB-H possessed the *cis*-conformation, and at –30 °C the *trans*-conformation of DCB-H appeared. The carbon–carbon bond in the *o*-carborane unit in DCB-H was 1.817 Å. This bond length was much longer than that in DCB-*t*Bu (1.795 Å). From the packing structure, the benzo[1,2-*b*:4,5-*b'*]dithiophene moiety showed less interaction with other benzo[1,2-*b*:4,5-*b'*]dithiophene units than the reported anthracene derivative.<sup>[61]</sup> It was implied that a smaller size of benzo[1,2-*b*:4,5-*b'*]dithiophene than that of anthracene might be responsible for suppression of intermolecular interaction in the crystal packing.

The electronic properties in the *cis*- and *trans*-conformations were calculated by using density functional theory (DFT) at the B3LYP/6-31G(d) level (Figure 2). Correspondingly, it was revealed that the *cis*-DCB-H had a smaller energy than *trans*-DCB-H, whereas the energy of *trans*-DCB-*t*Bu was smaller than that of the *cis*-derivative. These differences should be caused by the steric effect of the *tert*-butyl groups at the *para*-position of the phenyl rings. In addition, the optimized structure of *trans*-DCB-H seemed to involve significant strain. It is implied that a  $\pi$ – $\pi$  interaction between the phenyl ring and benzo[1,2-*b*:4,5-*b'*]dithiophene group could be formed.

The UV/Vis absorption spectra of DCB-R in THF (1.0 × 10<sup>–5</sup> M) were measured (Figure S4, Table S1). All samples showed identical absorption spectra (Table 1). The absorption bands in the longer wavelength region had peaks around 400 nm. These data suggest that the substituent group at the *para*-position of the phenyl ring should have a slight influence on the electronic structure in the ground state. Figure 3 shows the emission properties of DCB-R in THF solutions and water suspensions (THF/water = 1:99). In the clear solution, both molecules showed the broad emission bands around 700 nm ( $\Phi_{\text{PL}} = 0.12$ ). The  $\lambda_{\text{em}}$  of DCB-H presented an emission band with a peak at 682 nm. This

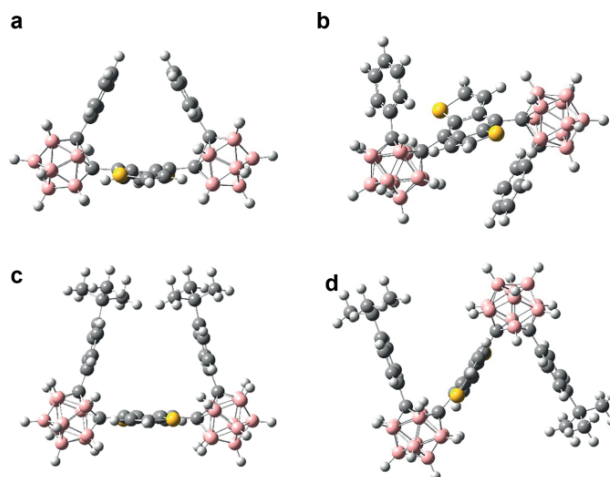


Figure 2. Optimized structures of (a) *cis*-DCB-H, (b) *trans*-DCB-H, (c) *cis*-DCB-*t*Bu and (d) *trans*-DCB-*t*Bu calculated at the B3LYP/6-31G(d) level.

value was shorter than that of DCB-*t*Bu ( $\lambda_{\text{em}} = 698$  nm). In contrast, the  $\lambda_{\text{em}}$  of DCB-H in the water suspension was longer than that of DCB-*t*Bu (638 nm for DCB-H and 615 nm for DCB-*t*Bu). Additionally, the  $\Phi_{\text{PLs}}$  of DCB-H and DCB-*t*Bu were 0.23 and 0.72, respectively. Hence, both molecules had aggregation-induced emission enhancement (AIEE) behavior in which emission efficiency is enhanced by solidification. By changing solvent polarity in the optical measurements, peak positions in both UV/Vis absorption and emission spectra were monitored (Figure S5 and Table S2). Similar to the ICT emission, typical peak shifts to the longer-wavelength region were observed only in the emission spectra by increasing solvent polarity, whereas almost no peak shifts were detected in the absorption spectra.

Table 1. Summary of emission properties of DCB-R.

R	THF <sup>[a]</sup>		Water		Crystal		Amorphous	
	$\lambda_{\text{em}}$ [nm]	$\Phi_{\text{PL}}^{\text{[b]}}$	$\lambda_{\text{em}}$ [nm]	$\Phi_{\text{PL}}^{\text{[b]}}$	$\lambda_{\text{em}}$ [nm]	$\Phi_{\text{PL}}^{\text{[b]}}$	$\lambda_{\text{em}}$ [nm]	$\Phi_{\text{PL}}^{\text{[b]}}$
H	682	0.12	638	0.23	617	0.90	n.d. <sup>[c]</sup>	n.d. <sup>[c]</sup>
<i>t</i> Bu	698	0.12	615	0.72	591	0.94	618	0.71

[a] 1.0 × 10<sup>–5</sup> M. [b] Measured with the integrated sphere method. [c] Not detected due to pyrolysis.

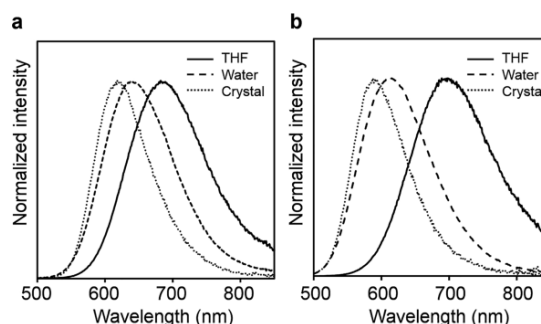


Figure 3. PL spectra of (a) DCB-H and (b) DCB-*t*Bu in THF solution (solid line), aggregation (dashed line), and crystalline (dotted line) states.

In the plots between Stokes shifts to solvent polarity, significant slopes were found in the fitting lines from both compounds (Figure S6). These results clearly indicate that the emission bands from DCB-R should originate from the ICT state. According to previous reports, the electron-accepting nature of the *o*-carborane unit plays a critical role in formation of the ICT state with the electron-donating benzodithiophene moieties.<sup>[61]</sup>

The solid-state emission was then evaluated in the crystal state. The powder samples were prepared by recrystallization from CHCl<sub>3</sub>/MeOH. Based on <sup>1</sup>H NMR spectra and TGA measurements (Figure S7), the crystal of DCB-*t*Bu included CHCl<sub>3</sub> as a crystal solvent. CHCl<sub>3</sub> was removed by heating at 200 °C for 1 h before optical measurements. It was confirmed that almost no degradation or isomerization proceeded in this temperature range (Figure S7). Table 1 shows the emission properties of DCB-H and DCB-*t*Bu in the crystal in the absence of solvent molecules, aggregation, and THF solutions (Figure 3). The emission spectra of DCB-H and DCB-*t*Bu in the crystal state showed blueshifted emission bands from those in the THF solution and water suspension (617 nm for DCB-H and 591 nm for DCB-*t*Bu). These blueshifts could be caused by a decrease of the reorientation energy.<sup>[62]</sup> The  $\Phi_{\text{PL}}$  values of DCB-H and DCB-*t*Bu were 0.90 and 0.94, respectively, and these were higher than those in the water suspension. These data clearly indicate that these molecules should have crystallization-induced emission enhancement (CIEE) properties.<sup>[4,56–58]</sup> In the crystal packing, extension at the C–C bond in the *o*-carborane unit after excitation, which causes emission quenching in the diluted solution, should be highly restricted. Thus, it is likely that an increase in emission efficiency was induced by crystallization.

In the THF solution, DCB-H showed emission in the shorter wavelength region than DCB-*t*Bu, whereas solid-state emission of DCB-H in both the water suspension and crystal was observed in the longer wavelength region. To obtain deeper insight on these behaviors, calculations of the excited states were performed by using time-dependent density functional theory (TD-DFT) at the B3LYP/6-31G(d) level. It was confirmed that the *cis*-conformation of DCB-H was also more stable than the *trans*-derivative in the excited state. Figure 4 presents the molecular orbitals of *cis*-DCB-H and *trans*-DCB-*t*Bu in the excited state. Both molecules showed  $\sigma^*-\pi^*$  conjugations at the C–C bond in the *o*-carborane unit. According to the previous studies, it was illustrated that the conjugated system involving the C–C bonds are the origin of the AIEE properties.<sup>[37–40]</sup> Thus, both molecules showed bright solid-state emission properties. The calculated transfer energies (corresponded transitions, wavelengths) of *cis*-DCB-H and *trans*-DCB-*t*Bu for the emission were 1.90 eV (MO-162: LUMO  $\rightarrow$  MO-161: HOMO, 653 nm) and 1.81 eV (MO-194: LUMO  $\rightarrow$  MO-193: HOMO, 684 nm), respectively. These values showed good agreement with the emission spectra in THF solution. On the other hand, in the crystalline state, the width of band gap of *trans*-DCB-*t*Bu seemed to be larger than that of *cis*-DCB-H. In the crystal packing of DCB-*t*Bu, a critical intramolecular twist was found (Figure S6). This conformational distortion is more likely to increase band gap energy. Thus, the emission band of DCB-*t*Bu in the crystalline state could be detected in the shorter wavelength region, although

the calculations indicated a narrower band gap from *trans*-DCB-*t*Bu than *cis*-DCB-H.

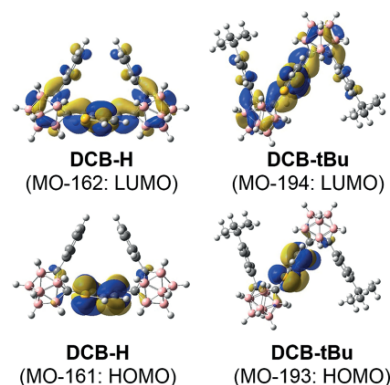


Figure 4. Calculated molecular orbitals of DCB-R.

Finally, the emission properties in the amorphous state were evaluated. Initially, thermal decomposition and melting temperatures were determined with TGA and DSC, respectively (Figure S7). Based on these data, the amorphous state was realized by rapid cooling with the melted sample according to the powder X-ray diffraction data (Figure S8). From the <sup>1</sup>H NMR spectra, it was confirmed that less significant degradation or isomerization were detected (Figure S7). It was found that emission from DCB-H was below the level of detection, whereas DCB-*t*Bu generated a spectrum that was almost identical to that in the water suspension around 618 nm (Table 1). It was longer than that in the crystal state. It should be emphasized that a significant  $\Phi_{\text{PL}}$  value (0.72) was obtained in the amorphous state. These data demonstrate that DCB-*t*Bu is a highly efficient luminogen in the amorphous state.

A plausible scenario to explain the large  $\Phi_{\text{PL}}$  values of DCB-*t*Bu in water suspension and the amorphous state is illustrated in Figure 5. Luminescence from both molecules was obtained from the transition from the intramolecular charge transfer state in the conjugation system involving the benzodithiophene moiety as a donor and *o*-carboranes as an acceptor via  $\sigma^*-\pi^*$  conjugation.<sup>[37–40]</sup> According to the <sup>1</sup>H NMR spectra, DFT-calculations and single-crystal structural data, DCB-*t*Bu should form the *trans*-conformation. This conformation is favorable for protecting the benzodithiophene moiety from intermolecular interaction such as  $\pi-\pi$  stacking even in the condensed state. On the other hand, since the benzodithiophene moiety was exposed in DCB-H, intermolecular interaction should be formed, followed by ACQ. Therefore, only DCB-*t*Bu maintained high lu-

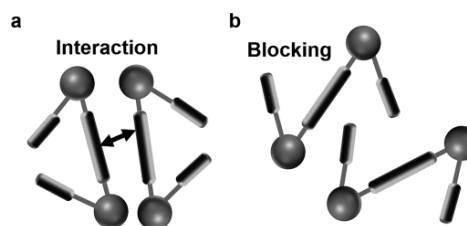


Figure 5. Proposed schematic models of intermolecular interactions in the solid samples of (a) DCB-H and (b) DCB-*t*Bu.

minescence ability in the disordered solids such as amorphous solids.

## Conclusions

Synthesis, structures, and optical properties of dual *o*-carborane substituted benzodithiophenes are described. The preferred structures of DCB derivatives were tuned by the substituents at the *para*-positions of the phenyl rings attached to the adjacent carbon atom in the *o*-carborane units. From the synthesized molecules, AIEE and CIEE properties were demonstrated. Moreover, both molecules showed intense emission bands in the crystal state with  $\Phi_{\text{PL}} > 0.90$  around 600 nm. In particular, DCB-*t*Bu also showed high emission properties in water suspension and amorphous states with  $\Phi_{\text{PL}} > 0.70$  caused by the isolation from intermolecular interaction in the *trans*-conformation. The improvement of emission efficiencies in the amorphous state is of importance in the practical use as printed devices and bio-probes. Given these unique optical properties in the solid state, it is suggested that both molecules could be promising "element blocks" for constructing advanced stimuli-responsive solid materials as well as for receiving AIE-active materials according to preprogrammed designs.

## Experimental Section

**General:** All reagents such as ethynylbenzene, 4-*tert*-butylethynylbenzene, *n*BuLi (1.6 M in hexane), SnCl<sub>2</sub>, HCl (1.0 M in water), decaborane, AgNO<sub>3</sub>, anhydrous toluene and acetonitrile (MeCN) were obtained from commercial sources and used without further purification. Tetrahydrofuran (THF) was purchased and purified with a two-column solid-state purification system (Glass Contour Solvent System, Joerg Meyer, Irvine, CA). <sup>1</sup>H, <sup>13</sup>C, and <sup>11</sup>B NMR spectra were recorded with a JEOL JNM-EX400 instrument at 400, 100, and 128 MHz, respectively. Variable-temperature <sup>1</sup>H NMR and <sup>1</sup>H-<sup>1</sup>H COSY NMR spectra were recorded with a JEOL-ECS400 instrument at 400 MHz. The <sup>1</sup>H chemical shift values are expressed relative to Me<sub>4</sub>Si in CDCl<sub>3</sub> or CH<sub>2</sub>Cl<sub>2</sub> in CD<sub>2</sub>Cl<sub>2</sub> as an internal standard. The <sup>13</sup>C shift values are expressed relative to CHCl<sub>3</sub> in CDCl<sub>3</sub> or CH<sub>2</sub>Cl<sub>2</sub> in CD<sub>2</sub>Cl<sub>2</sub> as an internal standard. The <sup>11</sup>B chemical shift values are expressed relative to BF<sub>3</sub>·Et<sub>2</sub>O as an external standard. High-resolution mass spectra (HRMS) were obtained with a Thermo Fisher Scientific EXACTIVE spectrometer for atmospheric pressure chemical ionization (APCI). Analytical thin-layer chromatography (TLC) was performed with silica gel 60 Merck F254 plates. Column chromatography was performed with Wakogel C-300 silica gel. UV/Vis absorption spectra were obtained with a SHIMADZU UV3600 spectrophotometer. Photoluminescence (PL) spectra were obtained with a Horiba FluoroMax-4 luminescence spectrometer; absolute PL quantum efficiencies ( $\Phi_{\text{PL}}$ ) were determined with a Horiba FL-3018 Integrating Sphere. X-ray crystal structure analyses were performed with a Rigaku R-Axis RAPID imaging plate area detector with graphite monochromated Mo-K $\alpha$  radiation ( $\lambda = 0.71069 \text{ \AA}$ ) at  $-180 \text{ }^\circ\text{C}$ . The structures were solved and refined by SHELXT. X-ray diffraction (XRD) data were obtained with a Rigaku MiniFlex diffractometer using Cu-K $\alpha$  radiation in a range of  $2^\circ \leq 2\theta \leq 50^\circ$  at intervals of  $0.01^\circ$  at a scanning rate of  $0.25^\circ\text{min}^{-1}$ .

**Preparation of 4,8-Di(arylethynyl)-benzo[1,2-*b*:4,5-*b'*]dithiophenes (2-R); General Procedure:** 4-Ethynylaryl (3 equiv.) was dissolved in THF under Ar atmosphere, then *n*BuLi (1.6 M hexane,

3 equiv.) was added at  $-78 \text{ }^\circ\text{C}$  and the solution was stirred. After 1 h, benzo[1,2-*b*:4,5-*b'*]dithiophene-4,8-dione (1 equiv.) was added in one portion and the mixture was stirred for 6 h at room temperature. Finally, after adding an excess of a HCl solution of SnCl<sub>2</sub>, a colored solid precipitated. The solid was filtered and washed with MeOH, to give the corresponding product 2-R.

**2-H:** Yield: 41 %; yellow solid. <sup>1</sup>H NMR (CDCl<sub>3</sub>, 400 MHz):  $\delta = 7.71$  (d,  $J = 5.4 \text{ Hz}$ , 2 H), 7.70–7.67 (m, 4 H), 7.59 (d,  $J = 5.6 \text{ Hz}$ , 2 H), 7.42–7.37 (m, 6 H) ppm. <sup>13</sup>C NMR (CDCl<sub>3</sub>, 100 MHz):  $\delta = 140.4, 138.3, 131.8, 128.5, 123.2, 112.0, 99.2, 85.7$  ppm. HRMS (APCI):  $m/z$  calcd. for C<sub>26</sub>H<sub>14</sub>S<sub>2</sub> [M + H]<sup>+</sup>: 391.0610; found: 391.0603.

**2-*t*Bu:** Yield: 82 %; yellow solid. <sup>1</sup>H NMR (CDCl<sub>3</sub>, 400 MHz):  $\delta = 7.71$  (dd,  $J = 5.5, 1.4 \text{ Hz}$ , 2 H), 7.62 (dd,  $J = 8.4, 1.5 \text{ Hz}$ , 4 H), 7.57 (dd,  $J = 5.6, 1.4 \text{ Hz}$ , 2 H), 7.44 (dd,  $J = 8.3, 1.2 \text{ Hz}$ , 4 H), 1.36 (s, 18 H) ppm. <sup>13</sup>C NMR (CDCl<sub>3</sub>, 100 MHz):  $\delta = 152.3, 140.3, 138.2, 131.6, 128.0, 125.5, 123.3, 119.9, 112.1, 99.4, 85.1, 34.9, 31.2$  ppm. HRMS (APCI):  $m/z$  calcd. for C<sub>34</sub>H<sub>30</sub>S<sub>2</sub> [M + H]<sup>+</sup>: 503.1862; found: 503.1854.

**Preparation of 4,8-Di(2-arylcarborane-1-yl)-benzo[1,2-*b*:4,5-*b'*]dithiophenes (DCB-R); General Procedure:** Decaborane (5 equiv.) was dissolved in MeCN under Ar atmosphere and heated at  $50 \text{ }^\circ\text{C}$  for 1 h. After the solution turned yellow, toluene was added. Then AgNO<sub>3</sub> (5 equiv.) and 1-R were added in one portion, and the solution was heated to reflux over 3 d. The black (or dark-red) residue was filtered off and the solution was evaporated. The crude residue was purified by silica gel column chromatography. After recrystallization by CHCl<sub>3</sub> and MeOH, 2-R was obtained as colored crystals.

**DCB-H:** Yield: 10 %; orange crystal. <sup>1</sup>H NMR (CD<sub>2</sub>Cl<sub>2</sub>, 400 MHz):  $\delta = 7.58$  (s, 2 H), 7.15 (d, 11 H), 6.87 (s, 7 H), 3.4–1.6 (br., 20 H) ppm. <sup>13</sup>C NMR (CDCl<sub>3</sub>, 100 MHz):  $\delta = 144.2, 140.9, 131.3, 131.2, 129.9, 129.7, 128.6, 127.4, 124.1, 90.9, 64.2$  ppm. <sup>11</sup>B NMR (CD<sub>2</sub>Cl<sub>2</sub>, 128 MHz):  $\delta = -0.5, -0.4, -3.0, -4.2, -8.6, -9.6$  ppm. HRMS (APCI):  $m/z$  calcd. for C<sub>26</sub>H<sub>34</sub>B<sub>20</sub>S<sub>2</sub> [M + H]<sup>+</sup>: 631.4106; found: 631.4105. C<sub>26</sub>H<sub>34</sub>B<sub>20</sub>S<sub>2</sub>: C, 49.82; H, 5.47; found: C, 46.64; H, 5.35.

**DCB-*t*Bu:** Orange crystals were obtained. CHCl<sub>3</sub> was contained as crystal solvent. CHCl<sub>3</sub> was removed by heating at  $150 \text{ }^\circ\text{C}$  for 1 h to give yellow crystals. Yield: 14 %. <sup>1</sup>H NMR (CD<sub>2</sub>Cl<sub>2</sub>, 400 MHz):  $\delta = 7.81$  (d,  $J = 6.4 \text{ Hz}$ , 2 H), 7.39 (d,  $J = 6.1 \text{ Hz}$ , 2 H), 7.18 (d,  $J = 8.6 \text{ Hz}$ , 4 H), 7.02 (d,  $J = 8.6 \text{ Hz}$ , 4 H), 3.90–1.60 (br., 20 H), 1.11 (s, 18 H) ppm. <sup>13</sup>C NMR (CD<sub>2</sub>Cl<sub>2</sub>, 100 MHz):  $\delta = 154.5, 143.8, 141.0, 129.6, 128.4, 126.7, 126.0, 123.3, 87.1, 77.9, 34.9, 31.0$  ppm. <sup>11</sup>B NMR (CD<sub>2</sub>Cl<sub>2</sub>, 128 MHz):  $\delta = -1.3, -4.2, -9.0$  ppm. HRMS (APCI):  $m/z$  calcd. for C<sub>34</sub>H<sub>51</sub>B<sub>20</sub>S<sub>2</sub> [M + H]<sup>+</sup>: 743.5358; found: 743.5330. C<sub>34</sub>H<sub>51</sub>B<sub>20</sub>S<sub>2</sub>: C, 55.25; H, 6.82; found: C, 55.18; H, 6.70.

CCDC 1583956 (for DCB-H), and 1583957 (for DCB-*t*Bu) contain the supplementary crystallographic data for this paper. These data can be obtained free of charge from The Cambridge Crystallographic Data Centre.

## Acknowledgments

This work was partially supported by The Institute for Synthetic Organic Chemistry (for K. T.) and a Grant-in-Aid for Scientific Research on Innovative Areas "New Polymeric Materials Based on Element-Blocks (No. 2401)" (JSPS KAKENHI Grant Number JP24102013).

**Keywords:** Carboranes · Aggregation-induced emission · Solid-state structures · Luminescence

[1] A. Iida, S. Yamaguchi, *Chem. Commun.* **2009**, 3002–3004.

- [2] A. Wakamiya, K. Mori, S. Yamaguchi, *Angew. Chem. Int. Ed.* **2007**, *46*, 4273–4276; *Angew. Chem.* **2007**, *119*, 4351.
- [3] C.-H. Zhao, A. Wakamiya, Y. Inukai, S. Yamaguchi, *J. Am. Chem. Soc.* **2006**, *128*, 15934–15935.
- [4] K. Tanaka, Y. Chujo, *NPG Asia Mater.* **2015**, *7*, e223.
- [5] C. A. DeRosa, S. A. Seaman, A. S. Mathew, C. M. Gorick, Z. Fan, J. N. Demas, S. M. Peirce, C. L. Fraser, *ACS Sens.* **2016**, *1*, 1366–1373.
- [6] T. Butler, W. A. Morris, J. Samonica-Kosicka, C. L. Fraser, *ACS Appl. Mater. Interfaces* **2016**, *8*, 1242–1251.
- [7] C. A. DeRosa, M. Kolpaczynska, C. Kerr, M. L. Daly, W. A. Morris, C. L. Fraser, *ChemPlusChem* **2017**, *82*, 399–406.
- [8] V. I. Bregadze, *Chem. Rev.* **1992**, *92*, 209–223.
- [9] M. Scholz, E. Hey-Hawkins, *Chem. Rev.* **2011**, *111*, 7035–7062.
- [10] F. Issa, M. Kassiou, L. M. Rendina, *Chem. Rev.* **2011**, *111*, 5701–5722.
- [11] R. Núñez, I. Romero, F. Teixidor, C. Viñas, *Chem. Soc. Rev.* **2016**, *45*, 5147–5173.
- [12] R. Núñez, M. Terrés, A. Ferrer-Ugalde, F. F. d. Biani, F. Teixidor, *Chem. Rev.* **2016**, *116*, 14307–14378.
- [13] R. N. Grimes, *Carboranes*, 2nd ed., Academic Press, Amsterdam, **2011**, pp. 301–540.
- [14] R. Furue, T. Nishimoto, I. S. Park, J. Lee, T. Yasuda, *Angew. Chem. Int. Ed.* **2016**, *55*, 7171–7175; *Angew. Chem.* **2016**, *128*, 7287.
- [15] S. Inagi, K. Hosoi, T. Kubo, N. Shida, T. Fuchigami, *Electrochemistry* **2013**, *81*, 368–370.
- [16] M. R. Son, Y.-J. Cho, S.-Y. Kim, H.-J. Son, D. W. Cho, S. O. Kang, *Phys. Chem. Chem. Phys.* **2017**, *19*, 24485–24492.
- [17] D. Tu, P. Leong, S. Guo, H. Yan, C. Lu, Q. Zhao, *Angew. Chem. Int. Ed.* **2017**, *56*, 11370–11374; *Angew. Chem.* **2017**, *129*, 7728.
- [18] Y. Chen, J. Guo, X. Wu, D. Jia, F. Tong, *Dyes Pigm.* **2018**, *148*, 180–188.
- [19] A. Ferrer-Ugalde, J. Cabrera-González, E. J. Juárez-Pérez, F. Teixidor, E. Pérez-Inestrosa, J. M. Montenegro, R. Sillanpää, M. Haukka, R. Núñez, *Dalton Trans.* **2017**, *46*, 2091–2104.
- [20] Z. Wang, T. Wang, C. Zhang, M. G. Humphrey, *Phys. Chem. Chem. Phys.* **2017**, *19*, 12928–12935.
- [21] X. Li, Y. Yin, H. Yan, C. Lu, *Chem. Asian J.* **2017**, *12*, 2207–2210.
- [22] X. Li, H. Yan, Q. Zhao, *Chem. Eur. J.* **2016**, *22*, 1888–1898.
- [23] S. Mukherjee, P. Thilagar, *Chem. Commun.* **2016**, *52*, 1070–1093.
- [24] L. Böhring, A. Brockhinke, J. Kahlert, L. Weber, R. A. Harder, D. S. Yufit, J. A. K. Howard, J. A. H. MacBride, M. A. Fox, *Eur. J. Inorg. Chem.* **2016**, 403–412.
- [25] L. Weber, J. Kahlert, R. Brockhinke, L. Böhring, J. Halama, A. Brockhinke, H.-G. Stammer, B. Neumann, C. Nervi, R. A. Harder, M. A. Fox, *Dalton Trans.* **2013**, *42*, 10982–10996.
- [26] J. Kahlert, L. Böhring, A. Brockhinke, H.-G. Stammer, B. Neumann, L. M. Rendina, P. J. Low, L. Weber, M. A. Fox, *Dalton Trans.* **2015**, *44*, 9766–9781.
- [27] B. H. Choi, J. H. Lee, H. Hwang, K. M. Lee, M. H. Park, *Organometallics* **2016**, *35*, 1771–1777.
- [28] M. Eo, M. H. Park, T. Kim, Y. Do, M. H. Lee, *Polymer* **2013**, *54*, 6321–6328.
- [29] T. Kim, H. Kim, K. M. Lee, Y. S. Lee, M. H. Lee, *Inorg. Chem.* **2013**, *52*, 160–168.
- [30] J. J. Peterson, A. R. Davis, M. Were, E. B. Coughlin, K. R. Carter, *ACS Appl. Mater. Interfaces* **2011**, *3*, 1796–1799.
- [31] D. Tu, P. Leong, Z. Li, R. Hu, C. Shi, K. Y. Zhang, H. Yan, Q. Zhao, *Chem. Commun.* **2016**, *52*, 12494–12497.
- [32] W. Zhang, Y. Luo, Y. Xu, L. Tian, M. Li, R. He, W. Shen, *Dalton Trans.* **2015**, *44*, 18130–18137.
- [33] L. Zhu, X. Tang, Q. Yu, W. Lv, H. Yan, Q. Zhao, W. Huang, *Chem. Eur. J.* **2015**, *21*, 4721–4730.
- [34] K.-R. Wee, Y.-J. Cho, S. Jeong, S. Kwon, J.-D. Lee, I.-H. Suh, S. O. Kang, *J. Am. Chem. Soc.* **2012**, *134*, 17982–17990.
- [35] Y. Chujo, K. Tanaka, *Bull. Chem. Soc. Jpn.* **2015**, *88*, 633–643.
- [36] M. Gon, K. Tanaka, Y. Chujo, *Polym. J.* <https://doi.org/10.1038/pj.2017.56>.
- [37] K. Tanaka, K. Nishino, S. Ito, H. Yamane, K. Suenaga, K. Hashimoto, Y. Chujo, *Faraday Discuss.* **2017**, *196*, 31–42.
- [38] K. Nishino, K. Hashimoto, K. Tanaka, Y. Morisaki, Y. Chujo, *Tetrahedron Lett.* **2016**, *57*, 2025–2028.
- [39] K. Nishino, Y. Morisaki, K. Tanaka, Y. Chujo, *New J. Chem.* **2017**, *41*, 10550–10554.
- [40] K. Nishino, H. Yamamoto, K. Tanaka, Y. Chujo, *Asian J. Org. Chem.* <https://doi.org/10.1002/ajoc.201700390>.
- [41] D. K. You, J. H. Lee, B. H. Choi, H. Hwang, M. H. Lee, K. M. Lee, M. H. Par, *Eur. J. Inorg. Chem.* **2017**, *2017*, 2496–2503.
- [42] L. Zhu, W. Lv, S. Liu, H. Yan, Q. Zhao, W. Huang, *Chem. Commun.* **2013**, *49*, 10638–10640.
- [43] J.-F. Nicoud, F. Bolze, X.-H. Sun, A. Hayek, P. Baldeck, *Inorg. Chem.* **2011**, *50*, 4272–4278.
- [44] M. Uebe, A. Ito, Y. Kameoka, T. Sato, K. Tanaka, *Chem. Phys. Lett.* **2015**, *633*, 190–194.
- [45] Y. Kameoka, M. Uebe, A. Ito, T. Sato, K. Tanaka, *Chem. Phys. Lett.* **2014**, *615*, 44–49.
- [46] K. Rajavelu, P. Rajakumar, M. Sudip, R. Kothandaraman, *New J. Chem.* **2016**, *40*, 10246–10258.
- [47] F. Teixidor, G. Barberà, A. Vaca, R. Kivekäs, R. Sillanpää, J. Oliva, C. Viñas, *J. Am. Chem. Soc.* **2005**, *127*, 10158–10159.
- [48] R. Núñez, P. Farràs, F. Teixidor, C. Viñas, R. Sillanpää, R. Kivekäs, *Angew. Chem. Int. Ed.* **2006**, *45*, 1270–1272; *Angew. Chem.* **2006**, *118*, 1292.
- [49] F. Teixidor, R. Núñez, C. Viñas, R. Sillanpää, R. Kivekäs, *Angew. Chem. Int. Ed.* **2000**, *39*, 4290–4292; *Angew. Chem.* **2000**, *112*, 4460.
- [50] A. Weller, *Nat. Chem.* **2011**, *3*, 590–596.
- [51] A. M. Spokoiny, C. D. Lewis, G. Teverovskiy, S. L. Buchwald, *Organometallics* **2012**, *31*, 8478–8481.
- [52] Y.-J. Cho, S.-Y. Kim, M. Cho, W.-S. Han, H.-J. Son, D. W. Cho, S. O. Kang, *Phys. Chem. Chem. Phys.* **2016**, *18*, 9702–9708.
- [53] S.-Y. Kim, Y.-J. Cho, G. F. Jin, W.-S. Han, H.-J. Son, D. W. Cho, S. O. Kang, *Phys. Chem. Chem. Phys.* **2015**, *17*, 15679–15682.
- [54] Z. Wang, P. Jiang, T. Wang, G. J. Moxey, M. P. Cifuentes, C. Zhang, M. G. Humphrey, *Phys. Chem. Chem. Phys.* **2016**, *18*, 15719–15726.
- [55] S. Kwon, K.-R. Wee, Y.-J. Cho, S. O. Kang, *Chem. Eur. J.* **2014**, *20*, 5953–5960.
- [56] H. Naito, K. Nishino, Y. Morisaki, K. Tanaka, Y. Chujo, *J. Mater. Chem. C* **2017**, *5*, 10047–10054.
- [57] K. Nishino, H. Yamamoto, K. Tanaka, Y. Chujo, *Org. Lett.* **2016**, *18*, 4064–4067.
- [58] H. Naito, K. Nishino, Y. Morisaki, K. Tanaka, Y. Chujo, *Chem. Asian J.* **2017**, *12*, 2134–2138.
- [59] L. Weber, J. Kahlert, R. Brockhinke, L. Böhring, A. Brockhinke, J.-G. Stammer, B. Neumann, R. A. Harder, M. A. Fox, *Chem. Eur. J.* **2012**, *18*, 8347–8357.
- [60] H. Naito, K. Nishino, Y. Morisaki, K. Tanaka, Y. Chujo, *Angew. Chem. Int. Ed.* **2017**, *56*, 254–259; *Angew. Chem.* **2017**, *129*, 260.
- [61] H. Naito, Y. Morisaki, Y. Chujo, *Angew. Chem. Int. Ed.* **2015**, *54*, 5084–5087; *Angew. Chem.* **2015**, *127*, 5173.
- [62] Q. Wu, T. Zhang, Q. Peng, D. Wang, Z. Shuai, *Phys. Chem. Chem. Phys.* **2014**, *16*, 5545–5552.

Received: November 26, 2017



## RESEARCH ARTICLE

View Article Online  
View Journal | View IssueCite this: *Mater. Chem. Front.*,  
2018, 2, 573

# Modulation of luminescence chromic behaviors and environment-responsive intensity changes by substituents in bis-*o*-carborane-substituted conjugated molecules†

Hiroki Mori, Kenta Nishino, Keisuke Wada, Yasuhiro Morisaki, Kazuo Tanaka \* and Yoshiki Chujo\*

Two types of multi-functional emissive bis-*o*-carborane-substituted 1,4-bis(phenylethynyl)benzene molecules were synthesized, and their optical properties were investigated in detail. The pristine *o*-carborane-substituted molecule **CBH** simultaneously exhibited dual emission from the locally excited (LE) and twisted intramolecular charge transfer (TICT) states in solution. Originating from changes in the intensity ratios between both emission bands, clear solvatochromic and thermochromic behaviors were observed. Surprisingly, TICT emission was observed even in the solid state. Aggregation- and crystallization-induced emission enhancement (AIEE and CIEE, respectively) were also presented by **CBH**. These solid-state emission enhancements could be derived from the suppression of aggregation-caused quenching (ACQ) by the bulky cage structure and the spherical shape of *o*-carborane. Next, we also synthesized the methyl-substituted derivative (**CBMe**) and found environment-resistant highly-efficient emission in both the solution and solid states. Finally, **CBMe** presented mechanochromic luminescence in the solid state. The substituent effects on the optical properties are discussed.

Received 23rd October 2017,  
Accepted 10th January 2018

DOI: 10.1039/c7qm00486a

rsc.li/frontiers-materials

## Introduction

Incorporation of optically-functional “element-blocks”, which are defined as a minimum functional unit containing heteroatoms,<sup>1,2</sup> is a promising strategy not only for obtaining bright luminescent materials but also for showing stimuli-responsive characteristics. For example, a series of luminescent conjugated molecules and polymers has recently been developed based on luminescent boron “element-blocks”.<sup>3–5</sup> By introducing aggregation-induced emission (AIE)-active “element-blocks”<sup>6–8</sup> into the conjugated main-chain, solid-state luminescence<sup>9–13</sup> and AIE properties<sup>14,15</sup> were realized in the “element-block polymers”. Furthermore, by employing stimuli-responsive luminescent “element-blocks”, chemical sensors and environment-sensitive luminescent chromism were also accomplished.<sup>16–23</sup> Therefore, discovery and exploration of unique characteristics

from “element-blocks” is a topic with high relevance, especially in material science as well as in fundamental photochemistry.

From this stand point, *o*-carborane,<sup>24–29</sup> which is a cluster compound containing two carbon and ten boron atoms, is a potential “element-block”<sup>30–32</sup> for constructing a conjugated system because of its unique solid-state luminescence properties.<sup>33–51</sup> Moreover, it is known that the *o*-carborane units work as a strong electron acceptor when connected at the carbon.<sup>52,53</sup> Therefore, by combination with electron-donating aryl units, intense emission from the intramolecular charge transfer (ICT) state was often obtained.<sup>52</sup> In particular, it has been revealed that *o*-carborane can play a significant role in presenting solid-state emission in various systems by suppressing ACQ.<sup>33–51</sup> It was proposed that the steric structure of *o*-carborane should play a critical role in avoiding ACQ by disturbing intermolecular interactions with the chromophore unit. Owing to this advantage of the *o*-carborane unit, this ICT emission can often be detected from *o*-carborane derivatives with high emission efficiencies even in the solid state where emission properties were often spoiled *via* the ACQ process.<sup>54–58</sup> Furthermore, it was suggested from theoretical investigation that the electronic state of the *o*-carborane unit should vary by its rotation.<sup>59</sup> Especially, the electron-accepting ability of *o*-carborane critically depends on the angle between the C–C bond in the *o*-carborane unit and the aryl substituent.<sup>52</sup>

Department of Polymer Chemistry, Graduate School of Engineering,  
Kyoto University, Katsura, Nishikyo-ku, Kyoto 615-8510, Japan.

E-mail: tanaka@poly.synchem.kyoto-u.ac.jp, chujo@poly.synchem.kyoto-u.ac.jp

† Electronic supplementary information (ESI) available. CCDC 1581419. For ESI and crystallographic data in CIF or other electronic format see DOI: 10.1039/c7qm00486a

‡ Present address: Department of Applied Chemistry for Environment, School of Science and Technology, Kwansai Gakuin University, 2-1 Gakuen, Sanda, Hyogo 669-1337, Japan.

Based on this fact, luminescent chromism has been accomplished with  $\pi$ -conjugated aryl-substituted *o*-carborane structures.<sup>60,61</sup> Thus, the construction and evaluation of new conjugation systems connected with *o*-carborane are of great significance to discover unique photochemical phenomena as well as to develop advanced optical materials.

Herein, we present the syntheses and optical properties of bis-*o*-carborane-substituted 1,4-bis(phenylethynyl)benzene having multi-functional emissive properties. Two types of *o*-carborane derivatives with or without the methyl substituent at the adjacent carbon to the aryl moiety were prepared for evaluating the influence of molecular motion on electronic structures. From optical measurements in the solution and solid states, it was found that drastic changes can be induced by the substituents. In the absence of the substituents, dual emission from the LE and TICT states in the solution state, AIEE, CIEE and solvato- and thermochromism were observed. In contrast, the *o*-carborane derivative having methyl substituents showed constant intense emission in both the solution and solid states and mechanochromic luminescence behavior. These various useful luminescence properties can be explained by the degree of molecular motion and the structures being controlled by the substituent effect.

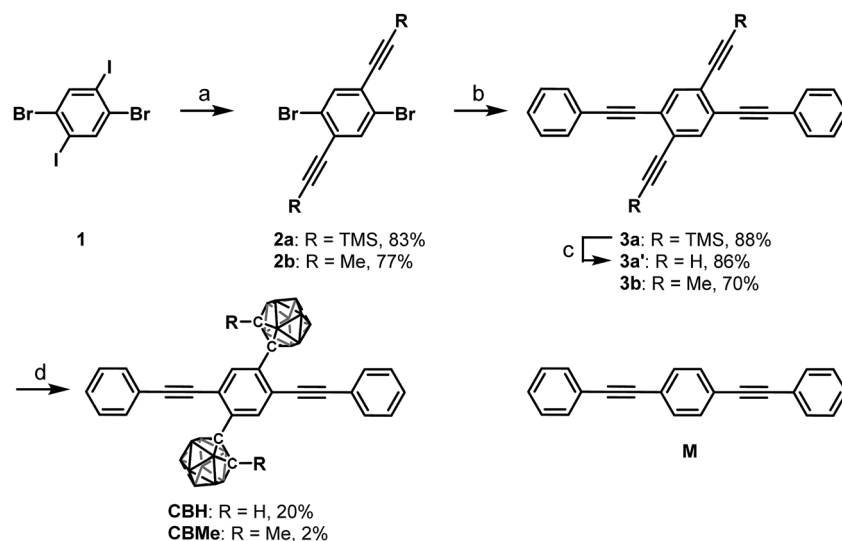
## Results and discussion

According to Scheme 1, bis-*o*-carborane and methylated *o*-carborane-substituted 1,4-bis(phenylethynyl)benzene **CBH** and **CBMe** were synthesized, respectively. It was presumed that the molecular rotation at the *o*-carborane units would be disturbed by the methyl substituent at the adjacent position. The two steps of the Sonogashira–Hagihara coupling reactions from 1,4-dibromo-2,5-diiodobenzene (**1**) to 1,4-bis(2'-phenylethyn-1'-yl)-2,5-bis(2'-trimethylsilylethyn-1''-yl)benzene (**3a**) followed by the deprotection

of  $K_2CO_3$  afforded 1,4-diethynyl-2,5-bis(2'-phenylethyn-1'-yl)benzene (**3a'**). Then, treatment with decaborane ( $B_{10}H_{14}$ ) in the presence of *N,N*-dimethylaniline and the successive regioselective alkyne-insertion reaction afforded **CBH**. Similarly, **CBMe** was also synthesized by the two steps of the Pd-catalyzed coupling reactions followed by the alkyne-insertion reaction with decaborane, although the reaction yield was low due to steric hindrance. **CBH** and **CBMe** were stable to  $H_2O$ , air, and heat in both the solution and solid states at least for half a year. The structures of the obtained compounds were characterized by  $^1H$ ,  $^{11}B$  and  $^{13}C$  NMR spectroscopies and high-resolution mass analyses (Charts S1–S6, ESI $^\dagger$ ).

The structure of **CBH** was successfully confirmed by the X-ray crystallographic analysis (Fig. 1, Table S1, ESI $^\dagger$ ). The dihedral angle C2–C1–C3–C4 ( $\varphi$ ) of **CBH** was  $21^\circ$ . This fact indicates that the 1,4-bis(phenylethynyl)benzene moiety has approximately a co-planar structure including the C1–C2 bond. In the crystal packing diagrams, **CBH** showed  $\pi$ -stacks with a distance of 4.190 Å between the phenyl rings of 1,4-bis(phenylethynyl)benzene moieties. It was presumed that steric repulsion of bulky icosahedral carborane clusters could be responsible for these structures.

The electronic properties of **CBH** in the ground state were examined by UV-vis absorption measurements. Fig. 2a shows the UV-vis absorption spectra of **CBH** and the model compound **M** (1,4-bis(phenylethynyl)benzene) in THF solution ( $1.0 \times 10^{-5}$  M). **CBH** exhibited a large absorption band in the UV region ( $\epsilon > 35\,000\ M^{-1}\ cm^{-1}$ ) assigned to the  $\pi$ – $\pi^*$  transition in the 1,4-bis(phenylethynyl)benzene moiety that corresponded to that of **M**. As listed in Table 1, the absorption band of **CBH** ( $\lambda_{max} = 344\ nm$ ) was obtained in a longer wavelength region compared to that of **M** ( $\lambda_{max} = 320\ nm$ ). It was proposed that the effect of the strong electron-accepting character of *o*-carborane can contribute to constructing a significant electronic interaction



**Scheme 1** Synthesis of **CBH** and **CBMe**. <sup>a</sup> Reagents and conditions: (a) ethynyl compound, Pd(PPh<sub>3</sub>)<sub>4</sub>, CuI, THF, <sup>i</sup>Pr<sub>2</sub>NH, r.t., 36 h; (b) phenylacetylene, Pd(PPh<sub>3</sub>)<sub>4</sub>, CuI, THF, Et<sub>3</sub>N, reflux, 22 h for **3a**, 48 h for **3b**; (c) K<sub>2</sub>CO<sub>3</sub>, THF, MeOH, r.t., 4 h; (d) decaborane, *N,N*-dimethylaniline, toluene, reflux, 7 d for **CBH**, 5 d for **CBMe**.

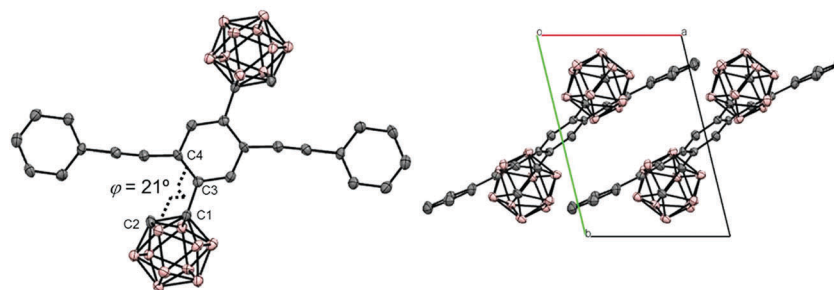


Fig. 1 Molecular structure and packing diagrams of **CBH** (hydrogen atoms are omitted for clarity, and thermal ellipsoids are displayed at 30% probability).

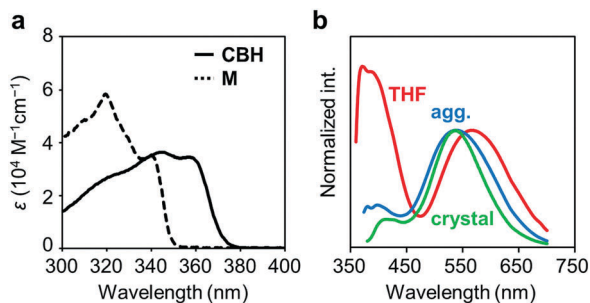


Fig. 2 (a) UV-vis absorption spectra of **CBH** and **M** ( $1.0 \times 10^{-5}$  M) and (b) normalized PL spectra of **CBH** in THF solution ( $1.0 \times 10^{-5}$  M), aggregates (THF/H<sub>2</sub>O v/v = 1/99 solution,  $1.0 \times 10^{-5}$  M) and the crystal.

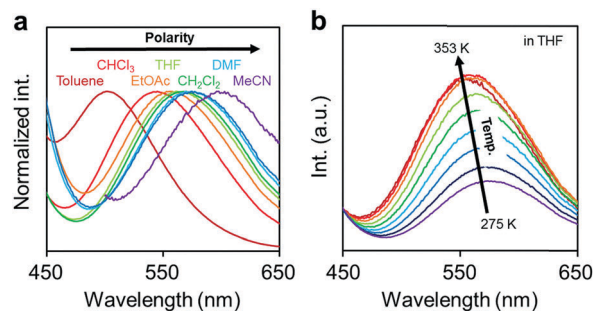


Fig. 3 (a) Solvent and (b) temperature-dependent peak shifts in the PL spectra of the solutions containing **CBH** ( $1.0 \times 10^{-6}$  M).

Table 1 Summary of optical properties of the compounds

	THF <sup>a</sup>		Aggregation <sup>b</sup>				Crystal		
	$\lambda_{\text{abs}}$ [nm]	$\epsilon$ [M <sup>-1</sup> cm <sup>-1</sup> ]	$E_{\text{g}}^c$ [eV]	$\lambda_{\text{em}}$ [nm]	$\Phi_{\text{PL}}^d$	$\lambda_{\text{em}}$ [nm]	$\Phi_{\text{PL}}^d$	$\lambda_{\text{em}}$ [nm]	$\Phi_{\text{PL}}^d$
<b>CBH</b>	344	36 300	3.33	371, 566	0.30	538	0.36	537	0.57
<b>CBMe</b>	368	39 200	3.23	540	0.84	542	0.81	493	0.78
<b>M</b>	320	58 500	3.55	347	0.95	— <sup>e</sup>	— <sup>e</sup>	— <sup>e</sup>	— <sup>e</sup>

<sup>a</sup> Measured in THF solution ( $1.0 \times 10^{-5}$  M). <sup>b</sup> Measured in THF/H<sub>2</sub>O v/v = 1/99 solution ( $1.0 \times 10^{-5}$  M). <sup>c</sup> Calculated from the onset value in the absorption spectra. <sup>d</sup> Determined as an absolute value with the integration sphere method. <sup>e</sup> Not detectable.

between the conjugated moiety and the *o*-carborane unit, followed by the peak shift *via* extension of  $\pi$ -conjugation to the whole molecule.

Next, the emission properties of **CBH** were investigated. The most impressive point was the dual-emissive property of **CBH** in the solution (Fig. 2b). Sharp emission bands with vibrational structures and broad ones were observed with peaks at around 370 nm and 570 nm, respectively. According to the previous reports, it was presumed that the aryl-modified *o*-carboranes can present ICT emission.<sup>52</sup> To elucidate the emission mechanism of **CBH**, optical spectra in various solvents (toluene, CHCl<sub>3</sub>, EtOAc, THF, CH<sub>2</sub>Cl<sub>2</sub>, DMF and MeCN) were measured, and the Lippert–Mataga plots were prepared (Fig. 3a and Fig. S1, Table S2, ESI<sup>†</sup>). By increasing solvent polarity, solvatochromism was detected only from the bands around 570 nm. These data including the degree of Stokes shifts calculated with

the position of the absorption bands clearly indicate that the emission bands around 370 nm and 570 nm are from the LE and ICT states, respectively. Lower emission efficiencies were obtained from the modified carboranes than from **M**. It is known that molecular motions including rotation at the connecting bond to the aryl moiety and vibration at the C–C bond in the *o*-carborane unit in the solution state should induce excitation deactivation along non-radiation processes.<sup>30</sup> Thus, emission annihilation was observed.

To evaluate the TICT character, the influence of molecular rotation on luminescence properties was examined by changing temperature. Thermochromic luminescence properties were observed. From the spectra in Fig. 3b, it was shown that the intensity of the emission band from the ICT state was enhanced by heating. This is reasonable because the transition from LE to ICT should be assisted by heating. Furthermore, it should be noted that only the LE emission was detected in the frozen state at 77 K where the molecular structure should be fixed at the initial state (Fig. S2, ESI<sup>†</sup>). This result means that structural alteration from the planar conformation, which can provide the LE emission, should proceed in the excited state followed by the exhibition of the ICT emission. From these data, the luminescence mechanism of **CBH** can be summarized. In the ground state, the planar conformation is dominant, leading to the LE emission. On exposure to photo-excitation, molecular rotation occurs, resulting in the formation of the ICT state. Finally, the emission band with environmental responsivity in the longer wavelength region was observed. Due to steric hindrance of the 1,4-bis(phenylethynyl)benzene moiety, rotation

was disturbed to some extent. Thus, the dual emissive property was obtained.

The solid-state emission properties of **CBH** were evaluated (Fig. 2b and Table 1). Interestingly, larger emission efficiencies were observed in both the aggregation state prepared by adding water to the THF solution and in the crystalline state. These data confirm that **CBH** has AIEE and CIEE properties. Similarly to the previous reports on aryl-modified *o*-carboranes, the *o*-carborane units should inhibit intermolecular motions in the condensed state because of steric hindrances. Thereby, ACQ was suppressed. In the previous report, it was shown that the formation of the TICT state was allowed even in the crystalline state. To evaluate the possibility of solid-state TICT formation with **CBH**, a photoluminescence (PL) spectrum was monitored at 77 K (Fig. S3, ESI<sup>†</sup>). Obviously, the emission band from the ICT state disappeared and only the LE emission was obtained. The same discussion based on the TICT mechanism should be applicable to that in the solution.

Next, by introducing the methyl groups at the adjacent carbon in the *o*-carborane units, the influence on optical properties was investigated. Synthesis was performed according to Scheme 1, and the characterization data indicated that the product has the desired structure. Unfortunately, a suitable single-crystal sample for X-ray crystallography was not obtained. However, it was suggested that the molecular structure should be fixed to the twisted conformation, which is similar to the structure in the TICT state.

Several comparison studies were carried out for evaluating the influence of the substituent effect on electronic properties. Fig. 4a shows the UV-vis absorption spectra of **CBMe** in THF solution ( $1.0 \times 10^{-5}$  M). The sharp peak around 260 nm and the broad peak around 370 nm assigned to the  $\pi$ - $\pi^*$  transition band of the 1,4-bis(phenylethynyl)benzene moieties were observed. The values of the optical band gaps ( $E_g$ ), which were estimated from the onset wavelength of the UV-vis absorption spectra, were in the order of **CBH** > **CBMe** (Table 1). The LUMO energy level was estimated from cyclic voltammetry (Fig. S4, ESI<sup>†</sup>) peak onset potentials, and the HOMO energy level was calculated from the LUMO energy level and the band gap energy estimated from the absorption edge (Table S3, ESI<sup>†</sup>). **CBH** and **CBMe** showed low-lying LUMO energy levels,  $-3.06$  eV and  $-3.18$  eV, respectively. By introducing the adjacent methyl groups into the *o*-carborane units, the molecular structure is anchored at the twisted conformation. According to the previous work, the electron-accepting ability of *o*-carborane is maximized at the twisted conformation.<sup>52</sup> Thus, a low-lying LUMO was realized, as observed in the cyclic voltammograms, leading to the narrower band-gap energy of **CBMe** than that of **CBH**.

The emission properties of **CBMe** were evaluated in various states (Fig. 4b). From the THF solution, a single emission band was observed with a peak at around 550 nm. From the PL spectra in various solvents followed by the analysis with the Lippert–Mataga plots, it was indicated that this broad emission band should result from the ICT state (Fig. S5, ESI<sup>†</sup>). Interestingly, **CBMe** showed high quantum efficiencies in the aggregate

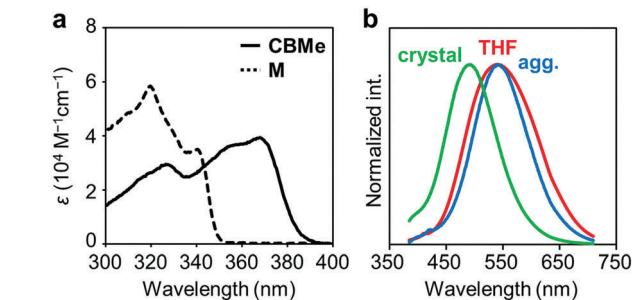


Fig. 4 (a) UV-vis absorption spectra of **CBMe** and **M** ( $1.0 \times 10^{-5}$  M) and (b) normalized PL spectra of **CBMe** in THF solution ( $1.0 \times 10^{-5}$  M), aggregates (THF/H<sub>2</sub>O v/v = 1/99 solution,  $1.0 \times 10^{-5}$  M) and the crystal.

state ( $\Phi_{\text{PL}} = 0.81$ ), the crystalline state ( $\Phi_{\text{PL}} = 0.78$ ) and even in solution ( $\Phi_{\text{PL}} = 0.84$ ). It is assumed that excitation deactivation induced by the intramolecular motion at the *o*-carborane unit could be restricted by the substituent effect.<sup>55</sup> Furthermore, the molecular structure was fixed at the twisted conformation. As a consequence, ICT should be efficiently induced in the excited state. This speculation can be supported by the result from the solid-state emission at 77 K (Fig. S6, ESI<sup>†</sup>). Significant changes were hardly obtained by cooling the crystalline sample of **CBMe**. Molecular motions should be effectively suppressed by the methyl substituent.

Another notable point was the difference in emission wavelengths between the amorphous and crystalline samples (Fig. 4b and Table 1). It should be mentioned that the crystalline sample of **CBMe** provided the emission band in a shorter wavelength region than those in the amorphous state as well as in solution. In other words, **CBMe** was expected to present environment-sensitive luminescence properties. By taking into consideration this assumption, the mechanochromic luminescence properties were examined with **CBMe**. The crystalline sample was pounded in a mortar until the detectable peaks were eliminated in the X-ray diffraction analysis (Fig. S7, ESI<sup>†</sup>). During the mechanical treatments, the optical spectra were monitored (Fig. 5). Initially, the emission band was observed at 493 nm ( $\Phi_{\text{PL}} = 0.78$ ). It was shown that the peak position was shifted to a longer wavelength region by the treatment ( $\lambda_{\text{em}} = 516$  nm,  $\Phi_{\text{PL}} = 0.61$ ). These data clearly indicate that **CBMe** has mechanochromic luminescence properties. Compared with the aggregation experiment with **CBMe**, as shown in Fig. 4, the emission band shift proceeded to the reverse direction by the formation of an amorphous state. In the solution-based system, solvent polarity should be responsible for emission properties. Therefore, the blue-shift might be induced by being surrounded by hydrophobic molecules. In the solid state, the degree of molecular packing should play a critical role in the electronic states. Because of bulky units including *o*-carboranes and methyl groups in **CBMe**, intermolecular interactions might be disturbed in the crystal packing, and blue-shifted emission was obtained. By the mechanical treatment, the molecular distribution should be randomized, and subsequently stabilization of energy levels by  $\pi$ -stacking followed by red-shifted emission could be realized. This scenario was also

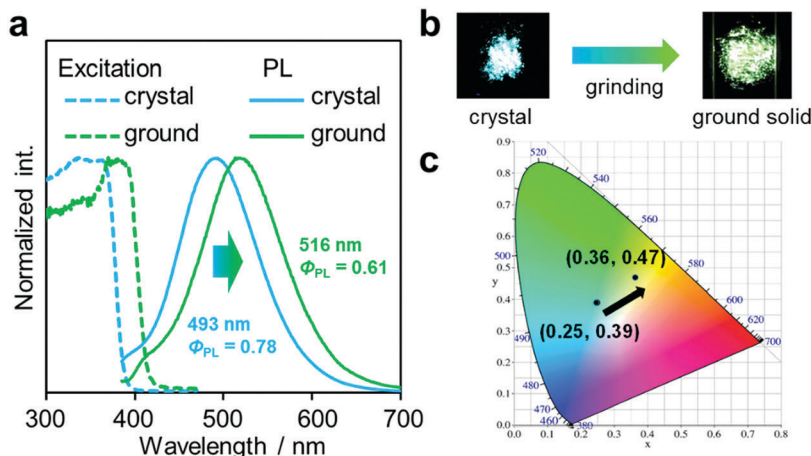


Fig. 5 (a) PL and excitation spectra of the solid samples of **CBMe**. (b) Pictures of the solid samples under UV irradiation before and after grinding. (c) Luminescent colors of the samples on the CIE diagram.

supported by the blue-shifted excitation spectrum. In the ground state, non-specific interactions could be formed. In the commodity mechanochromic luminescent materials, critical reduction of emission efficiencies was often induced after grinding, whereas **CBMe** presented a slight reduction of emission efficiency. The spherical molecular shape of *o*-carborane should be responsible for exhibiting environment-resistant intense emission by suppressing ACQ.

To deeply understand the TICT behavior of **CBH**, quantum chemical calculations were performed at the B3LYP/6-31+G(d)//B3LYP/6-31+G(d) level. Two geometries having planar ( $\varphi = 180^\circ$ ) and twisted ( $\varphi = 96^\circ$ ) conformers were obtained from the estimation for the optimized  $S_1$  structure of **CBH**. The molecular orbitals involved in the electronic transition are shown in Fig. 6. It was found that the  $S_1$ - $S_0$  electronic transition in both conformers should be mainly derived from the lowest unoccupied molecular orbital (LUMO) to the highest occupied molecular orbital (HOMO); 95% for the planar and 98% for the twisted conformers. HOMOs in both conformers and the LUMO in the planar conformer were mainly on the 1,4-bis(phenylethynyl)benzene moiety, while the LUMO in the twisted conformer was significantly delocalized to the *o*-carborane unit. These results strongly support that the emission from the LE and ICT states was derived from the planar and twisted conformers, respectively. The calculated emission wavelengths for the LE and TICT states were 400 nm and 733 nm, respectively. In addition, the C-C bond length in the *o*-carborane unit was 1.66 Å in the planar conformer and 2.40 Å in the twisted conformer, indicating that stronger electron-withdrawing should occur in the twisted conformer.<sup>52</sup> This fact corresponded to the ICT character of the emission band from the twisted conformer. Finally, we evaluated the possibility of solid-state TICT in the crystalline state. From the calculation with the structure determined by X-ray crystallography ( $\varphi = 21^\circ$ ), it was shown that the HOMO and LUMO were localized mainly at the 1,4-bis(phenylethynyl)benzene moiety. Moreover, according to the experimental result, the calculated emission wavelength was 395 nm. From these data, it was

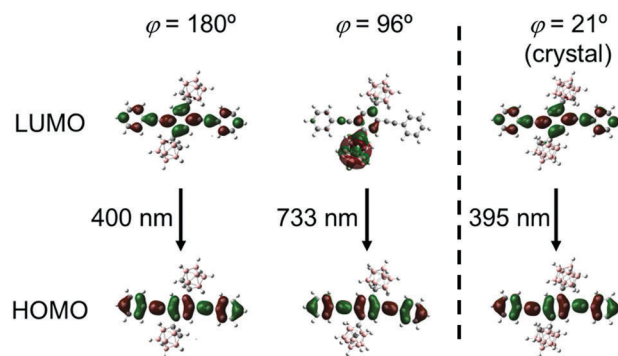


Fig. 6 Frontier orbitals involved in the  $S_1$ - $S_0$  transition for **CBH** at different 1,4-bis(phenylethynyl)benzene orientations ( $\varphi = 180^\circ$ ,  $96^\circ$  and  $21^\circ$ ).

proposed that **CBH** can exhibit only emission from the LE state. Indeed, the corresponding emission band was obtained at 77 K; meanwhile, the emission from the ICT state was mainly observed in the far longer wavelength region (Fig. S3, ESI<sup>†</sup>). These data strongly suggest that **CBH** should form the TICT excited state even in the crystalline state.

The  $S_0$ - $S_1$  electronic transition was investigated by using the same level of calculation (Fig. 7). Compared with the model compound **M**, the energy levels of both the HOMO and LUMO of **CBH** were lower by 0.56 eV and 0.76 eV, respectively. The large decreases in energy levels of the frontier orbitals could be presumably derived from the strong electron-withdrawing character of the *o*-carborane unit, resulting in a lower band gap than **M**. These results showed good agreement with the red-shift of the absorption maximum and electrochemical data of **CBH** (Fig. 2 and Fig. S4, ESI<sup>†</sup>).

To support the optical properties of **CBMe**, DFT and TD-DFT calculations were carried out at the B3LYP/6-31+G(d)//B3LYP/6-31+G(d) level (Fig. S8 and S9, ESI<sup>†</sup>). From the structural optimization, an almost perpendicular conformation to the C-C bond in *o*-carborane ( $\varphi = 97^\circ$ ) was obtained and the transition wavelength was almost the same as that in the absorption spectrum. As shown in the results from the TD-DFT calculation, the

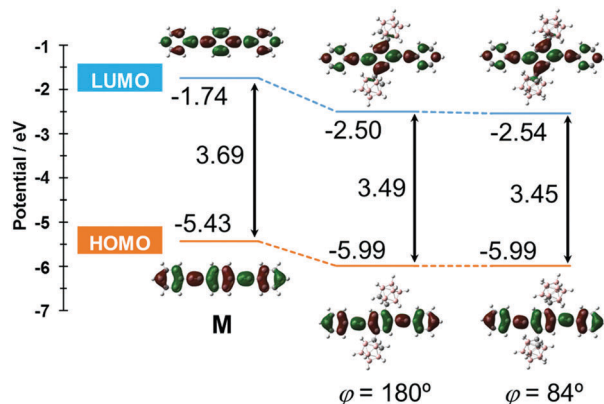


Fig. 7 Frontier orbitals involved in the  $S_0$ - $S_1$  transition and their energy levels for **CBH** and **M** at the B3LYP/6-31+G(d) level of theory.

frontier orbitals involved in the  $S_1$ - $S_0$  transition were mainly derived from the LUMO to HOMO transition (98%). The HOMO was found mostly on the 1,4-bis(phenylethynyl)benzene unit, while the LUMO was localized on the *o*-carborane unit with substantial orbital contribution, which is similar to the case of **CBH** (Fig. 6). These results strongly suggest that the emission around 490 nm originates from the ICT excited state. In addition, the LUMO partly existed on the C-H bond in the methyl group. This fact implies that the electron donation of the C-H antibonding orbital ( $\sigma^*$ ) of the methyl group into the  $\sigma^*$  orbital on C-C in *o*-carborane could decrease the electron-withdrawing ability of the *o*-carborane unit.<sup>52</sup> This effect could induce a slightly higher LUMO level followed by a larger band gap, and it is implied that the observation of the emission band in the shorter wavelength region compared to that of **CBH** could be induced (Table S4, ESI†). The calculations for emission wavelengths of the ICT emission (733 nm for **CBH** and 692 nm for **CBMe**) also supported this issue. Due to the presence of the methyl group on the adjacent carbon in the *o*-carborane unit, the molecular conformation is restricted. As a result, limitation to the ICT character can be induced, followed by relatively-blue-shifted emission compared to that of the H-substituted compound, according to the previous report on emission properties of the series of anthracene-*o*-carborane dyads with various substituents.<sup>55</sup> A similar tendency in the emission wavelength was also suggested in this study.

## Conclusion

It was demonstrated that the methyl substituent in the *o*-carborane unit dramatically influenced optical properties including luminescent color, emission intensity and sensitivity to external stimuli and environmental responsiveness in the bis-*o*-carborane-substituted 1,4-bis(phenylethynyl)benzene system. Basically, these changes can be explained by the degree of molecular motions and structures determined by the substituents. As a consequence, a variety of useful functions for developing advanced optical materials were obtained. Furthermore, according to computer calculation data, it was implied that dual *o*-carborane units might individually play different

roles from each other in the electronic conjugation in the excited state. This speculation could be valid for establishing design strategies not only to precisely control emission efficiencies by external stimuli and environmental factors but also to increase the diversity of luminescence chromic behaviors.

## Conflicts of interest

There are no conflicts to declare.

## Acknowledgements

This work was partially supported by The Kyoto Technoscience Center (for K. T.) and a Grant-in-Aid for Scientific Research on Innovative Areas “New Polymeric Materials Based on Element-Blocks (No. 2401)” (JSPS KAKENHI Grant Number JP24102013).

## References

- 1 Y. Chujo and K. Tanaka, *Bull. Chem. Soc. Jpn.*, 2015, **88**, 633–643.
- 2 M. Gon, K. Tanaka and Y. Chujo, *Polym. J.*, 2018, **50**, 109–126.
- 3 K. Tanaka and Y. Chujo, *NPG Asia Mater.*, 2015, **7**, e223.
- 4 H. Yamane, S. Ohtani, K. Tanaka and Y. Chujo, *Tetrahedron Lett.*, 2017, **58**, 2989–2992.
- 5 H. Yamane, K. Tanaka and Y. Chujo, *Tetrahedron Lett.*, 2015, **56**, 6786–6790.
- 6 K. Suenaga, K. Tanaka and Y. Chujo, *Chem. – Eur. J.*, 2017, **23**, 1409–1414.
- 7 M. Yamaguchi, S. Ito, A. Hirose, K. Tanaka and Y. Chujo, *J. Mater. Chem. C*, 2016, **3**, 5314–5319.
- 8 M. Yamaguchi, S. Ito, A. Hirose, K. Tanaka and Y. Chujo, *Mater. Chem. Front.*, 2017, **1**, 1573–1579.
- 9 K. Tanaka and Y. Chujo, *Macromol. Rapid Commun.*, 2012, **33**, 1235–1255.
- 10 R. Yoshii, A. Nagai, K. Tanaka and Y. Chujo, *Macromol. Rapid Commun.*, 2014, **35**, 1315–1319.
- 11 K. Tanaka, T. Yanagida, A. Hirose, H. Yamane, R. Yoshii and Y. Chujo, *RSC Adv.*, 2015, **5**, 96653–96659.
- 12 H. Yeo, K. Tanaka and Y. Chujo, *Macromolecules*, 2016, **49**, 8899–8904.
- 13 H. Yamane, S. Ito, K. Tanaka and Y. Chujo, *Polym. Chem.*, 2016, **7**, 2799–2807.
- 14 R. Yoshii, K. Tanaka and Y. Chujo, *Macromolecules*, 2014, **47**, 2268–2278.
- 15 S. Ito, A. Hirose, M. Yamaguchi, K. Tanaka and Y. Chujo, *Polymers*, 2017, **9**, 68–78.
- 16 A. Hirose, K. Tanaka, R. Yoshii and Y. Chujo, *Polym. Chem.*, 2015, **6**, 5590–5595.
- 17 K. Suenaga, R. Yoshii, K. Tanaka and Y. Chujo, *Macromol. Chem. Phys.*, 2016, **217**, 414–417.
- 18 R. Yoshii, K. Suenaga, K. Tanaka and Y. Chujo, *Chem. – Eur. J.*, 2015, **21**, 7231–7237.

- 19 K. Suenaga, K. Tanaka and Y. Chujo, *Eur. J. Org. Chem.*, 2017, 5191–5196.
- 20 S. Ohtani, M. Gon, K. Tanaka and Y. Chujo, *Chem. – Eur. J.*, 2017, 23, 11827–11833.
- 21 T. Matsumoto, H. Takamine, K. Tanaka and Y. Chujo, *Mater. Chem. Front.*, 2017, 1, 2368–2375.
- 22 K. Suenaga, K. Tanaka and Y. Chujo, *Chem. – Eur. J.*, 2017, 23, 1409–1414.
- 23 S. Ito, A. Hirose, M. Yamaguchi, K. Tanaka and Y. Chujo, *J. Mater. Chem. C*, 2016, 3, 5564–5571.
- 24 V. I. Bregadze, *Chem. Rev.*, 1992, 92, 209–223.
- 25 M. Scholz and E. Hey-Hawkins, *Chem. Rev.*, 2011, 111, 7035–7062.
- 26 F. Issa, M. Kassiou and L. M. Rendina, *Chem. Rev.*, 2011, 111, 5701–5722.
- 27 R. Núñez, I. Romero, F. Teixidor and C. Viñas, *Chem. Soc. Rev.*, 2016, 45, 5147–5173.
- 28 R. Núñez, M. Terrés, A. Ferrer-Ugalde, F. F. D. Biani and F. Teixidor, *Chem. Rev.*, 2016, 116, 14307–14378.
- 29 R. N. Grimes, *Carboranes*, Academic Press, Amsterdam, 2nd edn, 2011, pp. 301–540.
- 30 K. Tanaka, K. Nishino, S. Ito, H. Yamane, K. Suenaga, K. Hashimoto and Y. Chujo, *Faraday Discuss.*, 2017, 196, 31–42.
- 31 K. Nishino, K. Hashimoto, K. Tanaka, Y. Morisaki and Y. Chujo, *Tetrahedron Lett.*, 2016, 57, 2025–2028.
- 32 K. Nishino, Y. Morisaki, K. Tanaka and Y. Chujo, *New J. Chem.*, 2017, 15, 10550–10554.
- 33 X. Li, H. Yan and Q. Zhao, *Chem. – Eur. J.*, 2016, 22, 1888–1898.
- 34 S. Mukherjee and P. Thilagar, *Chem. Commun.*, 2016, 52, 1070–1093.
- 35 L. Böhling, A. Brockhinke, J. Kahlert, L. Weber, R. A. Harder, D. S. Yufit, J. A. K. Howard, J. A. H. MacBride and M. A. Fox, *Eur. J. Inorg. Chem.*, 2016, 403–412.
- 36 L. Weber, J. Kahlert, R. Brockhinke, L. Böhling, J. Halama, A. Brockhinke, H.-G. Stammler, B. Neumann, C. Nervi, R. A. Harder and M. A. Fox, *Dalton Trans.*, 2013, 42, 10982–10996.
- 37 J. Kahlert, L. Böhling, A. Brockhinke, H.-G. Stammler, B. Neumann, L. M. Rendina, P. J. Low, L. Weber and M. A. Fox, *Dalton Trans.*, 2015, 44, 9766–9781.
- 38 Y.-J. Cho, S.-Y. Kim, M. Cho, W.-S. Han, H.-J. Son, D. W. Cho and S. O. Kang, *Phys. Chem. Chem. Phys.*, 2016, 19, 9702–9708.
- 39 S.-Y. Kim, Y.-J. Cho, G. F. Jin, W.-S. Han, H.-J. Son, D. W. Cho and S. O. Kang, *Phys. Chem. Chem. Phys.*, 2015, 17, 15679–15682.
- 40 K.-R. Wee, Y.-J. Cho, S. Jeong, S. Kwon, J.-D. Lee, I.-H. Suh and S. O. Kang, *J. Am. Chem. Soc.*, 2012, 134, 17982–17990.
- 41 B. H. Choi, J. H. Lee, H. Hwang, K. M. Lee and M. H. Park, *Organometallics*, 2016, 35, 1771–1777.
- 42 R. Furue, T. Nishimoto, I. S. Park, J. Lee and T. Yasuda, *Angew. Chem., Int. Ed.*, 2016, 55, 7171–7175.
- 43 M. Uebe, A. Ito, Y. Kameoka, T. Sato and K. Tanaka, *Chem. Phys. Lett.*, 2015, 633, 190–194.
- 44 Y. Kameoka, M. Uebe, A. Ito, T. Sato and K. Tanaka, *Chem. Phys. Lett.*, 2014, 615, 44–49.
- 45 M. Eo, M. H. Park, T. Kim, Y. Do and M. H. Lee, *Polymer*, 2013, 54, 6321–6328.
- 46 T. Kim, H. Kim, K. M. Lee, Y. S. Lee and M. H. Lee, *Inorg. Chem.*, 2013, 52, 160–168.
- 47 A. Ferrer-Ugalde, J. Cabrera-González, E. J. Juárez-Pérez, F. Teixidor, E. Pérez-Inestrosa, J. M. Montenegro, R. Sillanpää, M. Haukka and R. Núñez, *Dalton Trans.*, 2017, 46, 2091–2104.
- 48 J. J. Peterson, A. R. Davis, M. Were, E. B. Coughlin and K. R. Carter, *ACS Appl. Mater. Interfaces*, 2011, 3, 1796–1799.
- 49 D. Tu, P. Leong, Z. Li, R. Hu, C. Shi, K. Y. Zhang, H. Yan and Q. Zhao, *Chem. Commun.*, 2016, 52, 12494–12497.
- 50 W. Zhang, Y. Luo, Y. Xu, L. Tian, M. Li, R. He and W. Shen, *Dalton Trans.*, 2015, 44, 18130–18137.
- 51 L. Zhu, X. Tang, Q. Yu, W. Lv, H. Yan, Q. Zhao and W. Huang, *Chem. – Eur. J.*, 2015, 21, 4721–4730.
- 52 H. Naito, K. Nishino, Y. Morisaki, K. Tanaka and Y. Chujo, *Angew. Chem., Int. Ed.*, 2017, 56, 254–259.
- 53 R. Núñez, P. Farràs, F. Teixidor, C. Viñas, R. Sillanpää and R. Kivekäs, *Angew. Chem., Int. Ed.*, 2006, 45, 1270–1272.
- 54 K. Nishino, H. Yamamoto, K. Tanaka and Y. Chujo, *Org. Lett.*, 2016, 18, 4064–4067.
- 55 H. Naito, K. Nishino, Y. Morisaki, K. Tanaka and Y. Chujo, *Chem. – Asian J.*, 2017, 12, 2134–2138.
- 56 H. Naito, K. Nishino, Y. Morisaki, K. Tanaka and Y. Chujo, *J. Mater. Chem. C*, 2017, 4, 10047–10054.
- 57 J. Cabrera-González, S. Bhattacharyya, B. Milián-Medina, F. Teixidor, N. Farfán, R. Arcos-Ramos, V. Vargas-Reyes, J. Gierschner and R. Núñez, *Eur. J. Inorg. Chem.*, 2017, 4575–4580.
- 58 D. Tu, P. Leong, S. Guo, H. Yan, C. Lu and Q. Zhao, *Angew. Chem., Int. Ed.*, 2017, 56, 11370–11374.
- 59 L. Weber, J. Kahlert, R. Brockhinke, L. Böhling, A. Brockhinke, H.-G. Stammler, B. Neumann, R. A. Harder and M. A. Fox, *Chem. – Eur. J.*, 2012, 18, 8347–8357.
- 60 H. Naito, Y. Morisaki and Y. Chujo, *Angew. Chem., Int. Ed.*, 2015, 54, 5084–5087.
- 61 K. Nishino, H. Yamamoto, K. Tanaka and Y. Chujo, *Asian J. Org. Chem.*, 2017, 6, 1818–1822.

Cite this: *New J. Chem.*, 2017, 41, 10550Received 7th July 2017,  
Accepted 3rd August 2017

DOI: 10.1039/c7nj02438j

rsc.li/njc

## Electron-donating abilities and luminescence properties of tolane-substituted *nido*-carboranes†

Kenta Nishino, Yasuhiro Morisaki,‡ Kazuo Tanaka  and Yoshiki Chujo\* 

The luminescence properties of *nido*-carborane (7,8-dicarba-*nido*-carborate anion)-substituted tolane derivatives were investigated. It was shown that the *nido*-carborane unit acted as an electron-donating group in all derivatives, and their emission colors can be tuned by the substituents at the tolane moiety. According to theoretical investigation, it was proposed that frontier orbitals were distinctly separated by the twisted structure of the methyl substituents at the *nido*-carborane unit. Thus, in the absorption spectra, drastic changes were obtained because the HOMO–LUMO transition was forbidden. These structural and electrical substituent effects should serve as good guidelines for designing optoelectronic materials based on *nido*-carboranes.

### Introduction

$\pi$ -Conjugated systems involving “element-blocks”, which are defined as a minimum functional unit composed of heteroatoms, are attractive candidates for receiving unique optically-functional materials.<sup>1</sup> From this viewpoint, a series of boron clusters<sup>2–6</sup> have gathered much attention especially for obtaining luminescent materials.<sup>7–34</sup> As a representative example, *o*-carborane (C<sub>2</sub>H<sub>12</sub>B<sub>10</sub>) derivatives in combination with conjugated molecules showed bright emission only in the aggregation state (aggregation-induced emission, AIE).<sup>35,36</sup> Owing to the bulkiness of *o*-carborane, aggregation-caused quenching (ACQ), which is often observed from commodity organic luminescent dyes, can be suppressed.<sup>37–39</sup> In addition, because of the strong electron-deficient nature of *o*-carborane, intense emission from the intramolecular charge transfer (ICT) state can be often obtained even in the solid state.<sup>40</sup> Furthermore, by controlling the morphology in the solid sample, luminescence color tuning and stimuli-responsive luminescence chromism were achieved.<sup>41</sup> Therefore, comprehension of electronic structures and luminescence mechanism of *o*-carborane-containing conjugated molecules is essential.<sup>42–44</sup>

*o*-Carborane can be transformed into *nido*-carborane species in the presence of strong nucleophiles. For example, a 7,8-dicarba-*nido*-undecaborate anion (*nido*-carborane) was obtained by eliminating the boron atom with a fluoride anion.<sup>45</sup> Based on this reaction, a series of *nido*-carborane derivatives has been

prepared and applied as BNCT materials<sup>46</sup> and catalysts composed of metal complexes with ruthenium, titanium, and zirconium.<sup>47</sup> In recent years, emissive materials concerning *nido*-carboranes were reported.<sup>48</sup> Based on the above elimination reaction of the boron atom from *o*-carborane followed by drastic changes in the luminescence color, fluoride sensing was accomplished. We also have synthesized *nido*-species obtained from diaryl-fused dibenzocarboranes.<sup>49</sup> They showed strong emission both in the solution and crystal states.<sup>49</sup> However, there are still very few examples that afford *nido*-carborane anion-based optical materials. In particular, the electronic properties of the *nido*-carborane unit in the  $\pi$ -conjugated system has been veiled. Therefore, it should be of great significance to collect systematic information on the electronic interaction of *nido*-carborane anions with conjugation units for realizing advanced optically-functional materials based on the *nido*-carborane unit as a versatile “element-block”.

Herein, synthesis and characteristics of *nido*-carborane-substituted tolane are presented. From a series of optical measurements and theoretical investigations with the synthesized compounds, contribution of electronic interaction was examined. In particular, it was suggested that the electron-donating ability of the *nido*-carborane unit should critically depend on the dihedral angle toward the tolane moiety. To obtain systematic information on this phenomenon, further molecules were designed and synthesized. Finally, modulation of electronic interaction based on the tunable electron-donating ability of the *nido*-carborane unit was demonstrated.

### Results and discussion

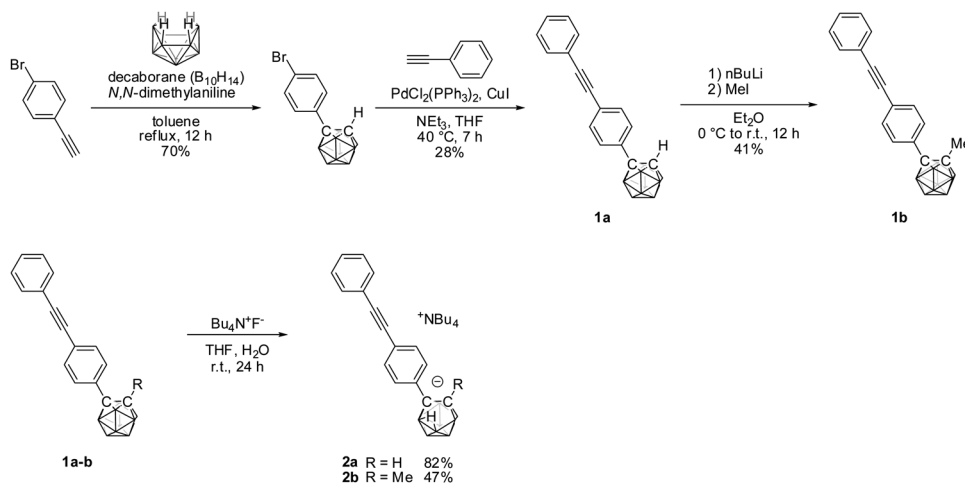
Synthesis of the *nido*-carborane derivative is shown in Scheme 1. 4-Bromo-*o*-carboranylbenzene was obtained by the addition of

Department of Polymer Chemistry, Graduate School of Engineering, Kyoto University, Katsura, Nishikyo-ku, Kyoto 615-8510, Japan.

E-mail: chujo@chujo.synchem.kyoto-u.ac.jp

† Electronic supplementary information (ESI) available. See DOI: 10.1039/c7nj02438j

‡ Present address: Department of Applied Chemistry for Environment, School of Science and Technology, Kwansai Gakuin University, 2-1 Gakuen, Sanda, Hyogo 669-1337, Japan.

Scheme 1 Synthesis of the *nido*-carborane-substituted tolanes.

decaborane with *p*-bromoethynylbenzene. Next, the Sonogashira-Hagihara coupling reaction was performed, and *o*-carboranyltoluene **1a** was obtained in 28% yield. Then, **1a** was reacted with *n*-BuLi and MeI to obtain (1-methyl-*o*-carboran-2-yl)toluene **1b**. Finally, one boron atom was eliminated from the *o*-carborane unit by treating with a THF solution of tetrabutylammonium fluoride, and *nido*-carborane was obtained. All compounds were characterized using  $^1\text{H}$ ,  $^{13}\text{C}$  and  $^{11}\text{B}$  NMR spectra and high resolution mass measurements. In the  $^1\text{H}$  NMR spectra of **2**, there was a specific peak at  $-2$  ppm (see the ESI $^\dagger$ ). These peaks were assigned to the bridging hydrogens in the *nido*-carborane unit according to the literature.<sup>50–52</sup> From these characterization data, we concluded that the products should have desired structures. The *nido*-carboranyltoluene anions with a tetraalkylammonium cation were stable to heat, oxygen, moisture and light, while the anion with a potassium cation was relatively reactive toward oxygen and light. It was assumed that steric hindrances of counter anions might contribute to improving their stability. Thus, all measurements were performed using ammonium salts in this study.

To gather information on their electronic properties in the ground state, UV-vis absorption spectra were recorded in the THF solutions at room temperature (Fig. 1a and Table 1). **2a** showed a broad absorption band with peaks at 287 and 313 nm, while **2b** showed a specific band with a peak at 289 nm with an

Table 1 Optical properties of *nido*-carboranes in THF solutions<sup>a</sup>

	$\lambda_{\text{ab}}$ (nm)	$\epsilon$ ( $\text{M}^{-1} \text{cm}^{-1}$ )	$E_{\text{g}}^b$ (eV)	$\lambda_{\text{PL}}$ (nm)	$\Phi_{\text{PL}}^c$	$\tau$ (ns)	$k_{\text{r}}$ ( $10^8 \text{ s}^{-1}$ )	$k_{\text{nr}}$ ( $10^8 \text{ s}^{-1}$ )
<b>2a</b>	313	29 000	3.50	447	0.59	4.5	1.31	0.91
<b>2b</b>	289	37 000	3.51	474	0.29	7.2	0.40	0.99
<b>2c</b>	317	35 000	3.56	430	0.45	3.3	1.36	1.67
<b>2d</b>	339	23 000	3.21	525	0.11	1.1	1.00	8.09

<sup>a</sup> Measured using  $10 \times 10^{-5} \text{ M}$ . <sup>b</sup> Calculated from the absorption edge. <sup>c</sup> Determined as an absolute value.

extinction coefficient of about  $37\,000 \text{ M}^{-1} \text{cm}^{-1}$ . Moreover, the extinction coefficient of **2b** at 313 nm was too small to be compared with that of **2a** although **2b** showed a higher coefficient at 289 nm than **2a**. However, the energy gaps between the highest occupied molecular orbital (HOMO) and the lowest unoccupied molecular orbital (LUMO) which were calculated from the absorption band edge were almost identical (**2a**: 3.50 eV, **2b**: 3.51 eV). This result suggests that there should be little differences in energy levels and be sure differences in transition probabilities.

In the photoluminescence (PL) spectra, **2b** showed a red-shifted emission compared to **2a** (Fig. 1b). However, the quantum efficiency ( $\Phi_{\text{PL}}$ ) of **2b** was smaller than that of **2a** (Table 1). To quantitatively evaluate kinetics in the decay processes, the rate constants of radiative ( $k_{\text{r}}$ ) and non-radiative decay processes ( $k_{\text{nr}}$ ) were estimated using  $\Phi_{\text{PL}}$  and fluorescence lifetime ( $\tau$ ) values according to the following equations:

$$k_{\text{r}} = \Phi_{\text{PL}}/\tau \quad (1)$$

$$k_{\text{nr}} = (1 - \Phi_{\text{PL}})/\tau \quad (2)$$

As shown in Table 1,  $k_{\text{nr}}$  values were almost identical, while  $k_{\text{r}}$  of **2a** was about three times larger than that of **2b**. This result suggests that low  $\Phi_{\text{PL}}$  and long  $\tau$  of **2b** were caused by low  $k_{\text{r}}$ .

In a previous report, it was shown that aromatic molecule-connecting *o*-carboranes presented significant emission from the ICT state.<sup>40</sup> To examine ICT characters of **2a** and **2b**, Lippert–Mataga plots were prepared according to the empirical

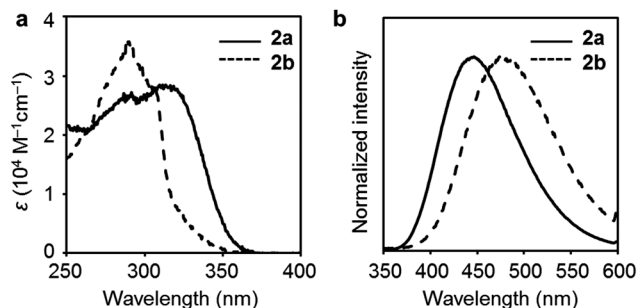


Fig. 1 (a) UV-vis absorption and (b) PL spectra of **2a** (solid line) and **2b** (dashed line) in THF solutions ( $1.0 \times 10^{-5} \text{ M}$ ). Excitation wavelengths for recording PL spectra were at 300 nm.

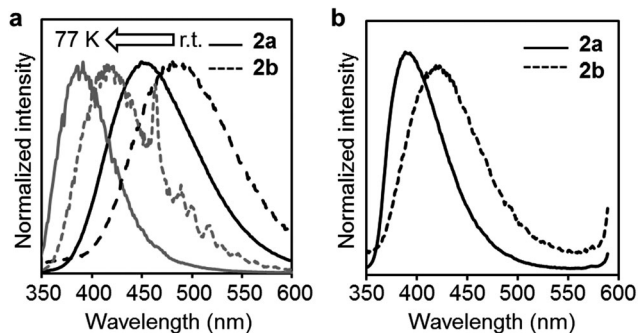


Fig. 2 PL spectra of **2a** (solid line) and **2b** (dashed line) in (a) 2-MeTHF solutions ( $1.0 \times 10^{-5}$  M) at r.t. (black) and 77 K (gray) and (b) the crystalline state.

formula (see the ESI<sup>†</sup>). By changing solvents, UV-vis absorption and PL spectra were monitored, and the degree of peak shifts in PL spectra was evaluated. The degree of ICT can be estimated from the slope of a fitting line (Fig. S1 and Tables S1–S3, ESI<sup>†</sup>). In addition, the dipole moments in the excited state were approximately calculated using hypothetical Onsager radii and estimated dipole moments in the ground state. Significant dependencies of the Stokes shift ( $\Delta\nu$ ) values were observed using a solvent polarity parameter (Lippert polarity parameter;  $\Delta f$ ). These data mean that the PL properties of **2a** and **2b** should include the ICT characters because of the electron-donating ability of the *nido*-carborane unit. The PL spectra of **2** were obtained in the frozen and crystalline states (Fig. 2). The emission spectra were blue-shifted at 77 K compared to those at room temperature in 2-methyl-THF (2-MeTHF) (Fig. 2a). Moreover, these blue-shifted emission bands were also observed in the crystalline-state PL spectra compared to the emission in the THF solution (Fig. 2b). These blue-shifted emissions could have originated from a decrease of the re-orientation energy of solvents as is often observed in the ICT luminophores. Hence, from these data, it was suggested that emission of **2** should be obtained from the ICT state.

To obtain deeper insight into their optical properties, quantum calculations were performed for estimating the molecular orbitals by using density functional theory (DFT) for the ground state (GS) and time dependent-DFT (TD-DFT) for the excited state (ES). The calculations were performed at the CAM-B3LYP/6-31+G(d,p)//B3LYP/6-31G(d,p) level.<sup>53</sup> The optimized structures in the GS are shown in Fig. 3. In this figure,  $\varphi$  means the dihedral angle between the C–C bond in the *nido*-carborane unit and that in the benzene ring, and  $l$  means the C–C bond in the *nido*-carborane unit. The dihedral angles in **2a** and **2b** were calculated to be  $158^\circ$  and  $107^\circ$ , respectively. The much twisted conformation of **2b** was originated from the steric effect of the methyl group at the *nido*-carborane unit. The calculated absorption transitions are summarized in Table S4 (ESI<sup>†</sup>). Accordingly, the absorption peaks at 313 and 287 nm of **2a** were assigned to  $S_0 \rightarrow S_1$  and  $S_0 \rightarrow S_2$  transitions, respectively. Therefore, these transitions corresponded to the HOMO  $\rightarrow$  LUMO and HOMO–1  $\rightarrow$  LUMO transitions, respectively. The molecular orbitals are also shown in Fig. 3. The HOMO–1 of **2a** was

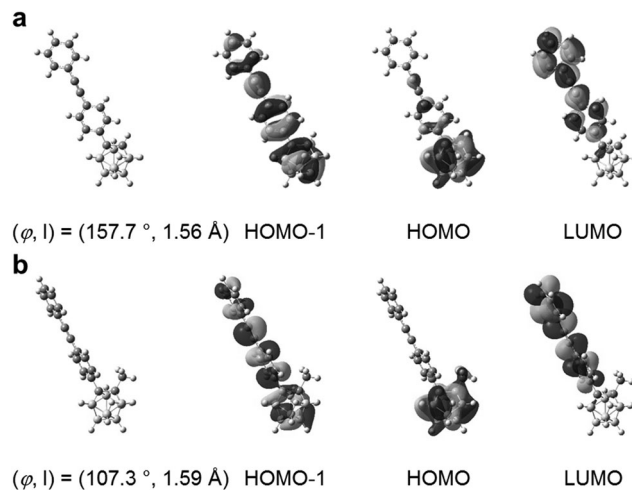


Fig. 3 Optimized structures in the ground state, where  $\varphi$  is the dihedral angle between *nido*-carborane and tolane, and  $l$  is the C–C bond length in the *nido*-carborane unit, and molecular orbitals of (a) **2a** and (b) **2b** in major absorption transitions. Calculations were performed at the CAM-B3LYP/6-31+G(d,p)//B3LYP/6-31G(d,p) level.

delocalized through the entire molecule. Most of the HOMO existed on the *nido*-carborane unit, and some of the orbital was located at the tolane moiety. Moreover, the LUMO was located at the tolane moiety. Because of the elongation of the HOMO to the tolane moiety, the high oscillator strength of **2a** for the  $S_0 \rightarrow S_1$  transition was obtained (0.9612). Furthermore,  $S_0 \rightarrow S_1$  and  $S_0 \rightarrow S_2$  transitions of **2b** also corresponded to the HOMO  $\rightarrow$  LUMO and HOMO–1  $\rightarrow$  LUMO, and the locations of HOMO–1 and LUMO were similar to those of **2a**. However, the HOMO of **2b** was localized at the *nido*-carborane unit because of its highly twisted structure. Hence, the oscillator strength of **2b** for the  $S_0 \rightarrow S_1$  transition was smaller than that of **2a**, and indeed the extinction coefficient of **2b** at 320 nm should be extremely small.

The optimized structure in the ES is shown in Fig. 4. Interestingly, the optimized structure of **2a** in the ES was changed compared with that in the GS. The dihedral angle was  $88^\circ$ , and this value was identical to that of **2b** ( $88^\circ$ ). This structural change in the dihedral angle in the ES was also observed in the calculation results with other aryl-substituted *o*-carborane dyads (Table S5, ESI<sup>†</sup>).<sup>37–39</sup> The calculated emission properties of **2a** and **2b** were 459 and 469 nm, respectively, and these corresponded to the experimental results. The molecular orbitals in the emission transition are also presented in Fig. 4. Both of their HOMOs were located at the *nido*-carborane unit, and LUMOs were located at the tolane moiety. Since the HOMO of **2b** was also located at the methyl group, the energy level of the HOMO became larger than that of **2a**. Thus, the band gap energy of **2b** could become smaller, and the red-shifted emission was indeed compared to **2a**. It can be summarized from these results that the *nido*-carborane unit should work as an electron-donating substituent.

To evaluate the degree of electron-donating ability and to demonstrate color tuning, additional substituent groups were

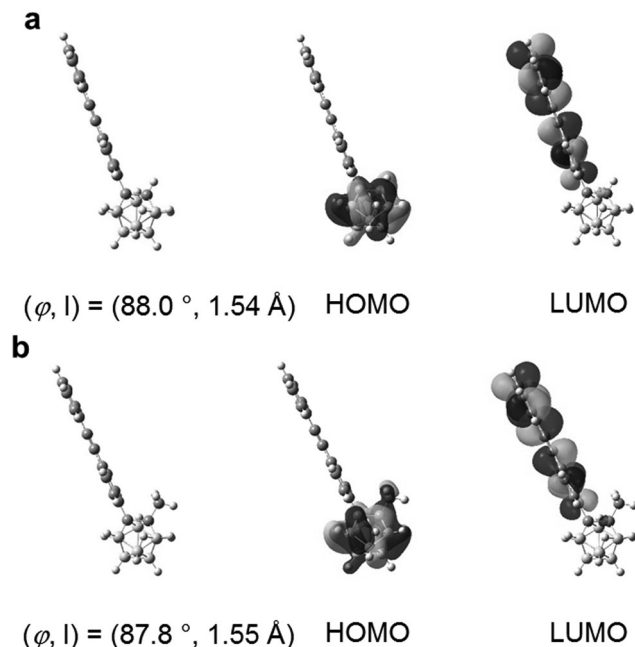
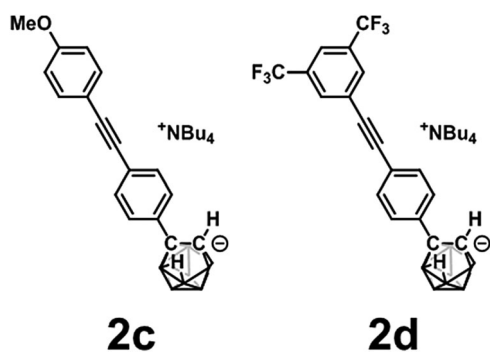


Fig. 4 Optimized structures in the excited state, where  $\varphi$  is the dihedral angle between *nido*-carborane and tolane, and  $l$  is the C–C bond length in the *nido*-carborane unit, and molecular orbitals of (a) **2a** and (b) **2b** in major emission transitions. Calculations were performed at the CAM-B3LYP/6-31+G(d,p)//B3LYP/6-31G(d,p) level.

introduced into the opposite end in the tolane moiety toward *nido*-carborane. Based on this idea, **2a** derivatives were designed and synthesized (Scheme 2). The electron-donating (methoxy, **2c**) and electron-withdrawing (trifluoromethyl, **2d**) groups were attached to the tolane moiety. The UV-vis absorption and PL spectra were recorded (Fig. 5 and Table 1). It was shown that the absorption peaks and edges and emission peaks were red-shifted from **2d**. It is likely that electronic interaction would be enhanced *via* the strong electron-donating and withdrawing system. As a result, bathochromic shifts were detected in optical spectra. In **2c**, the emission band was observed at a similar position to that in **2a** in the PL spectrum. This fact implies that a similar degree of electron donation might occur in **2c** with **2a**. This result means that the *nido*-carborane unit is capable of working as an electron-donating unit. Furthermore, it was



Scheme 2 Chemical structures of **2c** and **2d**.

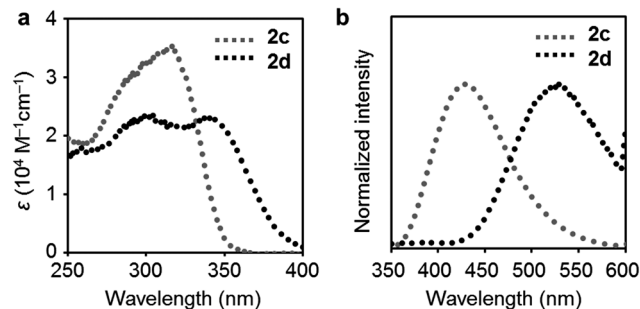


Fig. 5 (a) UV-vis absorption and (b) PL spectra of **2c** and **2d** in the THF solutions ( $1.0 \times 10^{-5}$  M). Excitation wavelengths for recording PL spectra were at 300 nm.

demonstrated that the optical properties of *nido*-carborane-connected aryl groups can be tuned by the substituent effect.

## Conclusion

The optical properties of the *nido*-carborane-substituted tolane derivatives are discussed. The methyl group at the carbon position in the *nido*-carborane unit showed steric effects and inhibited the rotation of the tolane unit in the ground state. Hence, the extinction coefficient drastically decreased as theoretical investigation suggested. Moreover, the radiative deactivation was suppressed, and the lifetime of the excited species was extended. From the PL spectra in various solvents, the substituent effect and calculated results, the ICT emission originating from the electron-donating ability of the *nido*-carborane unit was observed. These results could be useful for designing luminescent and charge separation materials based on the *nido*-carborane unit.

## Acknowledgements

This work was partially supported by the Konica Minolta Science and Technology Foundation (for K. T.) and a Grant-in-Aid for Scientific Research on Innovative Areas “New Polymeric Materials Based on Element-Blocks (No. 2401)” (JSPS KAKENHI Grant Number JP24102013).

## References

- 1 Y. Chujo and K. Tanaka, *Bull. Chem. Soc. Jpn.*, 2015, **88**, 633.
- 2 (a) R. N. Grimes, *Icosahedral carboranes: 1,2-C<sub>2</sub>B<sub>10</sub>H<sub>12</sub>, Carboranes*, 2nd edn, 2011, ch. 9, pp. 301–540; (b) V. I. Bregadze, *Chem. Rev.*, 1992, **92**, 209.
- 3 A. González-Campo, E. J. Juárez-Pérez, C. Viñas, B. Boury, R. Sillanpää, R. Kivekäs and R. Núñez, *Macromolecules*, 2008, **41**, 8458.
- 4 F. Issa, M. Kassiou and L. M. Rendina, *Chem. Rev.*, 2011, **111**, 5701.
- 5 G. Li, S. Azuma, S. Sato, H. Minegishi and H. Nakamura, *Bioorg. Med. Chem. Lett.*, 2015, **25**, 2624.
- 6 G. Li, S. Azuma, S. Sato, H. Minegishi and H. Nakamura, *J. Organomet. Chem.*, 2015, **798**, 189.

- 7 R. Núñez, M. Tarrés, A. Ferrer-Ugalde, F. F. D. Biani and F. Teixidor, *Chem. Rev.*, 2016, **116**, 14307.
- 8 L. Böhling, A. Brockhinke, J. Kahlert, L. Weber, R. A. Harder, D. S. Yufit, J. A. K. Howard, J. A. H. MacBride and M. A. Fox, *Eur. J. Inorg. Chem.*, 2016, 403.
- 9 L. Weber, J. Kahlert, R. Brockhinke, L. Böhling, A. Brockhinke, H.-G. Stammer, B. Neumann, R. A. Harder and M. A. Fox, *Chem. – Eur. J.*, 2012, **18**, 8347.
- 10 L. Weber, J. Kahlert, R. Brockhinke, L. Böhling, J. Halama, A. Brockhinke, H.-G. Stammer, B. Neumann, C. Nervi, R. A. Harder and M. A. Fox, *Dalton Trans.*, 2013, **42**, 10982.
- 11 J. Kahlert, L. Böhling, A. Brockhinke, H.-G. Stammer, B. Neumann, L. M. Rendina, P. J. Low, L. Weber and M. A. Fox, *Dalton Trans.*, 2015, **44**, 9766.
- 12 Y.-J. Cho, S.-Y. Kim, M. Cho, W.-S. Han, H.-J. Son, D. W. Cho and S. O. Kang, *Phys. Chem. Chem. Phys.*, 2016, **19**, 9702.
- 13 S.-Y. Kim, Y.-J. Cho, G. F. Jin, W.-S. Han, H.-J. Son, D. W. Cho and S. O. Kang, *Phys. Chem. Chem. Phys.*, 2015, **17**, 15679.
- 14 K.-R. Wee, Y.-J. Cho, S. Jeong, S. Kwon, J.-D. Lee, I.-H. Suh and S. O. Kang, *J. Am. Chem. Soc.*, 2012, **134**, 17982–17990.
- 15 B. H. Choi, J. H. Lee, H. Hwang, K. M. Lee and M. H. Park, *Organometallics*, 2016, **35**, 1771.
- 16 R. Furue, T. Nishimoto, I. S. Park, J. Lee and T. Yasuda, *Angew. Chem., Int. Ed.*, 2016, **55**, 7171.
- 17 M. Uebe, A. Ito, Y. Kameoka, T. Sato and K. Tanaka, *Chem. Phys. Lett.*, 2015, **633**, 190.
- 18 Y. Kameoka, M. Uebe, A. Ito, T. Sato and K. Tanaka, *Chem. Phys. Lett.*, 2014, **615**, 44.
- 19 S. Inagi, K. Hosoi, T. Kubo, N. Shida and T. Fuchigami, *Electrochemistry*, 2013, **81**, 368.
- 20 Z. Wang, P. Jiang, T. Wang, G. J. Moxey, M. P. Cifuentes, C. Zhang and M. G. Humphrey, *Phys. Chem. Chem. Phys.*, 2016, **18**, 15719.
- 21 J. J. Peterson, A. R. Davis, M. Were, E. B. Coughlin and K. R. Carter, *ACS Appl. Mater. Interfaces*, 2011, **3**, 1796.
- 22 L. Zhu, W. Lv, S. Liu, H. Yan, Q. Zhao and W. Huang, *Chem. Commun.*, 2013, **49**, 10638.
- 23 D. Tu, P. Leong, Z. Li, R. Hu, C. Shi, K. Y. Zhang, H. Yan and Q. Zhao, *Chem. Commun.*, 2016, **52**, 12494.
- 24 W. Zhang, Y. Luo, Y. Xu, L. Tian, M. Li, R. He and W. Shen, *Dalton Trans.*, 2015, **44**, 18130.
- 25 S. Mukherjee and P. Thilagar, *Chem. Commun.*, 2016, **52**, 1070.
- 26 X. Li, H. Yan and Q. Zhao, *Chem. – Eur. J.*, 2016, **22**, 1888.
- 27 J. Park, Y. H. Lee, J. Y. Ryu, J. Lee and M. H. Lee, *Dalton Trans.*, 2016, **45**, 5667.
- 28 Y. H. Lee, J. Park, S.-J. Jo, M. Kim, J. Lee, S. U. Lee and M. H. Lee, *Chem. – Eur. J.*, 2015, **21**, 2052.
- 29 A. M. Prokhorov, T. Hoffbeck, R. Czerwieńiec, A. F. Suleymanova, D. N. Kozhevnikov and H. Yersin, *J. Am. Chem. Soc.*, 2014, **136**, 9637.
- 30 N. Shin, S. Yu, J. H. Lee, H. Hwang and K. M. Lee, *Organometallics*, 2017, **36**, 1522.
- 31 N. V. Nghia, J. Oh, J. Jung and M. H. Lee, *Organometallics*, 2017, **36**, 2573.
- 32 J. J. Schwartz, A. M. Mendoza, N. Wattanatorn, Y. Zhao, V. T. Nguyen, A. M. Spokoyny, C. A. Mirkin, T. Baše and P. S. Weiss, *J. Am. Chem. Soc.*, 2016, **138**, 5957.
- 33 K. O. Kirlikovali, J. C. Axtell, A. Gonzalez, A. C. Phung, S. I. Khan and A. M. Spokoyny, *Chem. Sci.*, 2016, **7**, 5132.
- 34 A. M. Prokhorov, P. A. Slepukhin, V. L. Rusinov, V. N. Kalinin and D. N. Kozhevnikov, *Chem. Commun.*, 2011, **47**, 7713.
- 35 K. Kokado and Y. Chujo, *Macromolecules*, 2009, **42**, 1418.
- 36 K. Tanaka, K. Nishino, S. Ito, H. Yamane, K. Suenaga, K. Hashimoto and Y. Chujo, *Faraday Discuss.*, 2017, **196**, 31.
- 37 H. Naito, K. Nishino, Y. Morisaki, K. Tanaka and Y. Chujo, *Angew. Chem., Int. Ed.*, 2017, **56**, 254.
- 38 K. Nishino, H. Yamamoto, K. Tanaka and Y. Chujo, *Org. Lett.*, 2016, **18**, 4064.
- 39 H. Naito, K. Nishino, Y. Morisaki, K. Tanaka and Y. Chujo, *Chem. – Asian J.*, DOI: 10.1002/asia.201700815.
- 40 K. Kokado and Y. Chujo, *J. Org. Chem.*, 2010, **76**, 316.
- 41 H. Naito, Y. Morisaki and Y. Chujo, *Angew. Chem., Int. Ed.*, 2015, **54**, 5084.
- 42 K. Nishino, K. Hashimoto, K. Tanaka, Y. Morisaki and Y. Chujo, *Tetrahedron Lett.*, 2016, **57**, 2025–2028.
- 43 Y. Morisaki, M. Tominaga, T. Ochiai and Y. Chujo, *Chem. – Asian J.*, 2014, **9**, 1247–1251.
- 44 Y. Morisaki, M. Tominaga and Y. Chujo, *Chem. – Eur. J.*, 2012, **18**, 11251–11257.
- 45 R. N. Grimes, Eleven-vertex carboranes: 11-Vertex open clusters, *Carboranes*, Academic Press, New York, 2nd edn, 2011, ch. 9, p. 187.
- 46 J. Valliant, K. Guenther, A. King, P. Morel, P. Schaffer, O. Sogbein and K. Stephenson, *Coord. Chem. Rev.*, 2002, **232**, 173.
- 47 H. Wang, Y. Wang, H.-W. Li and Z. Xie, *Organometallics*, 2001, **20**, 5110.
- 48 M. H. Park, K. M. Lee, T. Kim, Y. Do and M. H. Lee, *Chem. – Asian J.*, 2011, **6**, 1362.
- 49 M. Tominaga, K. Nishino, Y. Morisaki and Y. Chujo, *J. Organomet. Chem.*, 2015, **789**, 165.
- 50 B. Štíbr, F. Teixidor, C. Viñas and J. Fusek, *J. Organomet. Chem.*, 1998, **550**, 125.
- 51 C. Shi, H. Sun, X. Tang, W. Lv, H. Yan, Q. Zhao, J. Wang and W. Huang, *Angew. Chem., Int. Ed.*, 2013, **52**, 13434.
- 52 F. Lerouge, A. Ferrer-Ugalde, C. Viñas, F. Teixidor, R. Sillanpää, A. Abreu, E. Xochitiotzi, N. Farfán and R. Núñez, *Dalton Trans.*, 2011, **40**, 7541.
- 53 M. J. Frisch, *et al.*, *Gaussian 09, Revision D.01*, Gaussian, Inc., Wallingford CT, 2009.



Cite this: *J. Mater. Chem. C*, 2017, 5, 10047

## Highly-efficient solid-state emissions of anthracene–*o*-carborane dyads with various substituents and their thermochromic luminescence properties†

Hirofumi Naito, Kenta Nishino, Yasuhiro Morisaki,‡ Kazuo Tanaka  and Yoshiki Chujo\*

This manuscript describes the synthesis and optical properties of a series of anthracenyl-*o*-carborane dyads exhibiting highly-efficient luminescence with various types of substituent groups at the adjacent carbon atom of *o*-carborane. The restricted rotational motion of the anthracene moiety and the ideal orientation for intramolecular charge transfer from the anthracene moiety to the carborane cluster resulted in yellow and orange emissions ( $\lambda_{em} = 563$  nm and 604 nm) with approximately 100% absolute fluorescence quantum efficiencies in the crystalline state of the methyl- and trimethylsilyl (TMS)-substituted dyads, respectively. In addition, clear thermochromic luminescence properties were also observed. Computer calculations were carried out to investigate the influence of the substituent effect on emission efficiency.

Received 16th June 2017,  
Accepted 5th September 2017

DOI: 10.1039/c7tc02682j

rsc.li/materials-c

## Introduction

Solid-state emissive organic molecules are promising materials not only for fabricating advanced opto-electronic devices such as flexible displays but also for preparing film-type chemical sensors.<sup>1,2</sup> However, most of the organic dyes suffer from aggregation-caused quenching (ACQ) in the condensed state.<sup>3</sup> Due to non-specific intermolecular interactions in the condensed state, most of the emission which can be clearly observed in the diluted solution is often spoiled. To overcome the ACQ problem, organoboron compounds and boron complexes are potential and versatile candidates.<sup>4</sup> Based on the strategy to modify luminescent molecules containing boron with bulky substituents, solid-state emission was achieved *via* suppression of ACQ.<sup>5</sup> Furthermore, recent studies have shown that some boron-containing molecules were able to present aggregation-induced emission (AIE) behaviors in which enhanced emission was achieved only in the condensed state by suppressing molecular motions.<sup>6</sup> Therefore, many researchers

have so far devoted their efforts towards exploring versatile molecular skeletons to improve solid-state emissive properties based on these strategies.

*o*-Carborane is a polyhedral boron cluster containing two adjacent carbon atoms in the cluster cage which has unique properties such as a neutron capturing ability and thermal and chemical stability.<sup>7</sup> In particular, various types of optical materials have recently been developed with *o*-carborane derivatives.<sup>8</sup> From the first report on AIE-active *o*-carborane derivatives,<sup>9</sup> we regarded *o*-carborane as an AIE-active “element-block”,<sup>10</sup> which is defined as a minimum functional unit composed of heteroatoms, and prepared a series of solid-state emissive materials.<sup>11</sup> According to the mechanistic studies on the optical properties of solid-state emissive *o*-carboranes, it was revealed that electronic conjugation with the aryl moiety was necessary for photo-excitation and emission.<sup>9</sup> The emission bands originate from the intramolecular charge transfer (ICT) state in which the *o*-carborane unit usually works as an electron-accepting unit because of the electron-deficient nature of boron clusters composed of 3-center 2-electron bonds.<sup>9</sup> It was suggested that ICT occurs more effectively than in the parallel orientation when  $\pi$ -conjugated planes are perpendicular to the C–C bond of *o*-carborane.<sup>11</sup> Moreover, it was proposed that intramolecular vibration at the C–C bond in *o*-carborane critically induced emission annihilation *via* electronic conjugation involving the  $\sigma^*-\pi^*$  interaction.<sup>9</sup> Therefore, in the aggregation state, intense emission can be achieved not only by restricting non-radiation decay caused by intramolecular vibration but also by suppressing

Department of Polymer Chemistry, Graduate School of Engineering, Kyoto University, Katsura, Nishikyo-ku, Kyoto 615-8510, Japan.  
E-mail: chujo@chujo.synchem.kyoto-u.ac.jp

† Electronic supplementary information (ESI) available. CCDC 1556482–1556485. For ESI and crystallographic data in CIF or other electronic format see DOI: 10.1039/c7tc02682j

‡ Present address: Department of Applied Chemistry for Environment, School of Science and Technology, Kwansei Gakuin University, 2-1 Gakuen, Sanda, Hyogo 669-1337, Japan.

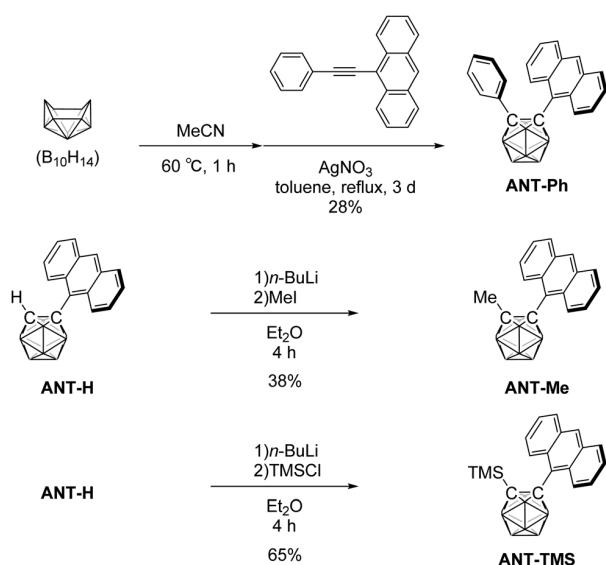
ACQ owing to the steric hindrance of the *o*-carborane unit toward intermolecular interactions in the condensed state. Based on these results, we next sought to achieve red-shifted emission based on the aryl-modified *o*-carborane system. However, by expanding the aryl moiety, a red-shift of the emission bands should be readily induced; meanwhile, ACQ also occurred due to intermolecular interactions at the expanded  $\pi$ -conjugated

system. Therefore, there were huge difficulties in achieving red-shifted emission from the aryl-modified *o*-carborane.

Herein, the solid-state emission and thermochromic luminescence properties of anthracene-modified *o*-carborane dyads are described. The modified anthracene-*o*-carborane dyads were designed based on the strategy for improving solid-state emission of the reported molecule by suppressing intramolecular motions.<sup>11</sup> To effectively utilize the bulkiness of *o*-carborane for inhibiting intermolecular interactions such as  $\pi$ -stacking and by suppressing molecular motions in the excited state, various types of substituents were introduced into the adjacent carbon atom in the *o*-carborane unit to the connecting point with anthracene. It was shown that the synthesized dyads showed yellow and orange emissions ( $\lambda_{\text{em}} = 563$  nm and 604 nm) with excellent emission quantum efficiencies in the crystalline state (approximately 100%). Even in the polymer matrix, almost quantitative emission efficiency was achieved. Furthermore, it was found that these dyads showed clear thermochromic luminescence properties. Their electronic properties and molecular structures are discussed here.

## Results and discussion

It was reported that rotation at the connection between *o*-carborane and anthracene in **ANT-H** should proceed in the excited state followed by the formation of the twisted induced charge transfer (TICT) state.<sup>11</sup> Subsequently, bright ICT emission was generated in this twisted conformation even from the crystalline



Scheme 1 Synthesis of anthracene-substituted *o*-carboranes.

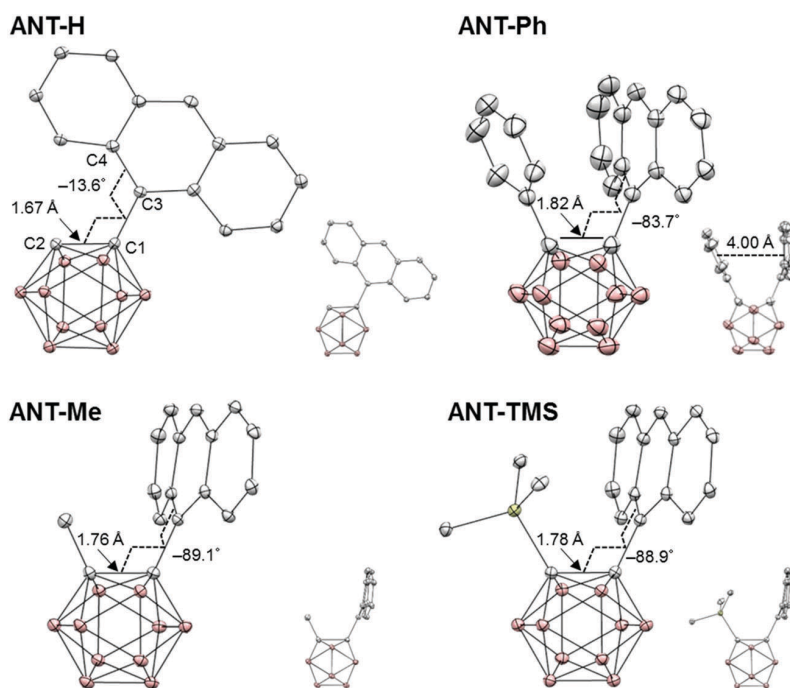


Fig. 1 Molecular structures of the *o*-carborane dyads (hydrogen atoms are omitted for clarity, and thermal ellipsoids are displayed at 30% probability). Side views are also shown.

state ( $\Phi_{\text{PL}} = 0.38$ ). Based on this result, we presumed that the improvement of emission efficiencies in the solid state could be capable of fixing a molecular conformation at the twisted structure by eliminating the energy-consumable process with mechanical motions in the excited state. To evaluate the validity of this idea, we designed and synthesized dyads with various substituents.

The anthracenyl-*o*-carborane dyads were synthesized from **ANT-H** according to Scheme 1.<sup>11</sup> **ANT-Ph** was obtained by the

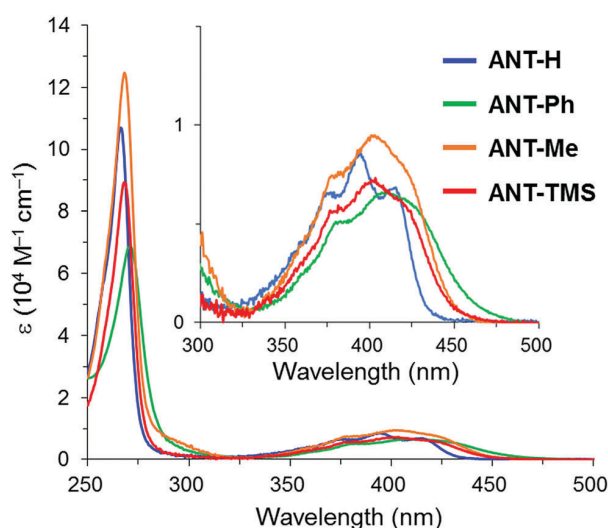


Fig. 2 UV-vis absorption spectra of the dyads in THF ( $1.0 \times 10^{-5}$  M).

alkyne-insertion reaction with decaborane ( $\text{B}_{10}\text{H}_{14}$ ). Lithiation of **ANT-H** with *n*-butyllithium followed by the reaction with methyl iodide and trimethylsilyl chloride afforded **ANT-Me** and **ANT-TMS** in 38% and 65%, respectively. The obtained compounds were stable to air and light and showed decomposition under detectable levels for more than one year under ambient conditions. The structures of the obtained compounds were identified by NMR spectroscopy and single crystal X-ray crystallography. From these results, it was concluded that the desired products were obtained and had stability high enough for the series of measurements.

Fig. 1 shows the molecular structures of the dyads (Tables S1–S3, ESI<sup>†</sup>). It was shown in a previous report that the dihedral angle C2–C1–C3–C4 ( $\varphi$ ) of **ANT-H** was  $-13.6^\circ$ , which means the anthracene moiety should be roughly co-planar with the C1–C2 bond.<sup>11</sup> In contrast, the dihedral angles ( $\varphi$ ) of **ANT-Ph**, **ANT-Me**, and **ANT-TMS** were almost  $-90^\circ$ . It is likely that the steric hindrances of the adjacent substituents determine the twisted conformation. Furthermore, the C1–C2 bond lengths were dependent on the adjacent substituents: 1.67 Å for **ANT-H**, 1.82 Å for **ANT-Ph**, 1.76 Å for **ANT-Me**, and 1.78 Å for **ANT-TMS**. It was proposed that the C1–C2 bond could be subject to the electronic interaction of the substituents. Moreover, the anthracene moiety in **ANT-Ph** was more tilted toward the adjacent substituent than those of **ANT-Me** and **ANT-TMS**, indicating that the intramolecular  $\pi$ – $\pi$  interaction between the anthracene and benzene moieties exists in the crystal structure geometry.

UV-vis absorption spectra of the dyads were measured in THF ( $1.0 \times 10^{-5}$  M, Fig. 2). The sharp peaks around 270 nm and

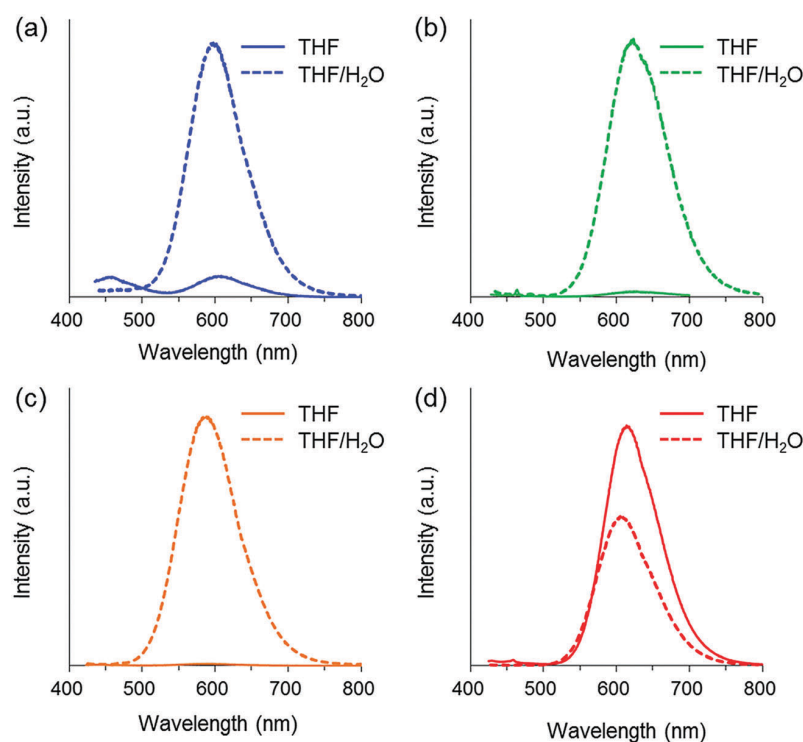


Fig. 3 PL spectra of (a) **ANT-H**, (b) **ANT-Ph**, (c) **ANT-Me** and (d) **ANT-TMS** in THF ( $1.0 \times 10^{-5}$  M) and aggregates (THF/ $\text{H}_2\text{O}$  v/v = 1/99 solution,  $1.0 \times 10^{-5}$  M).

broad peaks around 400 nm with vibrational structures were assigned to the  $\pi$ - $\pi^*$  transition band of the anthracene moiety. The values of the optical band gaps ( $E_g$ ), which were estimated from the onset wavelength in the spectra, were in the order of **ANT-H** > **ANT-Me** > **ANT-TMS** > **ANT-Ph**. It was observed that bathochromic shifts in the absorption edge correlated with the C-C bond length of the *o*-carborane unit (Fig. 1). This trend might have originated from the electron donating ability of the substituents.<sup>12</sup>

The energy levels of the frontier orbitals were estimated using cyclic voltammetry (CV). From the LUMO levels estimated from the peak onset potentials, HOMO levels were determined (Table S4, ESI<sup>†</sup>). All compounds showed remarkably low-lying LUMO energy levels in the region from -3.59 eV to -3.80 eV. Because of the strong electron withdrawing character of the *o*-carborane unit, the energy levels of the LUMO should be decreased.

Photoluminescence (PL) spectra were compared in the THF solution and aggregation (THF/H<sub>2</sub>O = 1/99 (v/v), Fig. 3). According to a previous report, aryl-modified *o*-carborane dyads showed intramolecular charge transfer (ICT) emission around 550–600 nm not in the solution state but in the condensed state because of the effective suppression of the vibrational motion at the *o*-carborane unit.<sup>9</sup> Indeed, **ANT-H** showed dual emission

around 450 nm and 600 nm with a quantum efficiency ( $\Phi_{\text{PL}}$ ) of 0.02.<sup>11</sup> In the ground state, the molecule had a parallel conformation and presented LE emission, whereas twisting occurred in the excited state, followed by the ICT emission. In the crystalline state of **ANT-H**, the parallel conformation should partially remain due to structural restriction. Therefore, the small LE band was obtained. Correspondingly, **ANT-Ph** and **ANT-Me** also showed weak emission around 600 nm ( $\Phi_{\text{PL}} < 0.01$ ). Meanwhile, in the aggregation formed by adding water to the THF solution, strong emission around 600–630 nm appeared with higher quantum efficiencies ( $\Phi_{\text{PL}} = 0.18$ – $0.29$ ), indicating typical AIE characters. **ANT-TMS** showed strong emission in both THF and THF/H<sub>2</sub>O solutions ( $\Phi_{\text{PL}} = 0.55$  and  $0.37$ , respectively), despite the fact that the emission of general *o*-carborane-based compounds should be quenched in solution because of the vibrational motion of the C1–C2 bond of *o*-carborane. It was suggested that the bulkiness of the TMS substituent could inhibit the rotational motions of the anthracene moiety in the excited states even in the solution state. Therefore, strong emission was observed even in the THF solution.

Fig. 4 shows the PL spectra in the crystalline state. It was found that the quantum efficiencies of the dyads significantly increased by introducing the adjacent substituents (Table 1). It should be emphasized that **ANT-Me** and **ANT-TMS** showed highly-efficient solid-state emission. It was known that **ANT-H** can emit from the TICT state by rotating the *o*-carborane unit even in the crystalline state. This geometrical change could also cause a non-radiative deactivation process. In contrast, the adjacent substituents should prohibit intramolecular rotation by structural restriction, leading to the disturbance of a non-radiative deactivation. Therefore, higher emission efficiencies were observed from the dyads with the substituents. To extend the applicability of these solid-state luminescent *o*-carboranes as film materials, the molecules were loaded onto poly(methyl methacrylate) (PMMA) matrices. Accordingly, **ANT-TMS** presented quantitative emission efficiency. These materials hold promise as highly-efficient luminophores in organic light-emitting devices.

To further comprehend their optical properties, quantum chemical calculations were carried out. The electronic transitions of the absorption and emission for each compound are shown in Table 2 and summarized in Fig. 5. The optimized structures were in good agreement with the geometry determined by X-ray crystallography. Fig. S1 (ESI<sup>†</sup>) shows the frontier orbitals and the energies of the dyads. The HOMOs and LUMOs in each dyad were mainly located on the anthracene  $\pi$  and  $\pi^*$  orbitals, respectively.

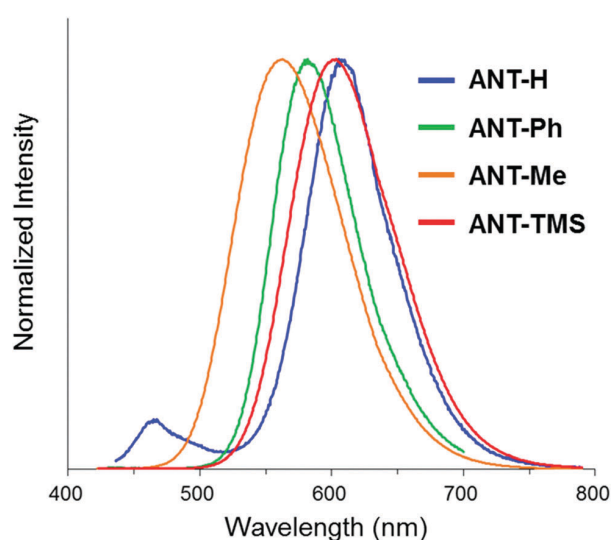


Fig. 4 PL spectra of the dyads in the crystalline state at room temperature.

Table 1 Optical properties of the dyads<sup>a</sup>

Compound	$\lambda_{\text{PL,max}}$ (nm)				$\Phi_{\text{PL}}^e$			
	THF <sup>b</sup>	THF/H <sub>2</sub> O = 1/99 <sup>c</sup>	PMMA film <sup>d</sup>	Crystalline state	THF <sup>b</sup>	THF/H <sub>2</sub> O = 1/99 <sup>c</sup>	PMMA film <sup>d</sup>	Crystalline state
<b>ANT-H</b>	459, 609	598	583	606	0.02	0.18	0.18	0.38
<b>ANT-Ph</b>	624	624	593	582	< 0.01	0.21	0.41	0.81
<b>ANT-Me</b>	588	587	563	563	< 0.01	0.29	0.63	> 0.99
<b>ANT-TMS</b>	614	605	586	604	0.55	0.37	> 0.99	0.97

<sup>a</sup> Excited at each  $\lambda_{\text{abs,max}}$ . <sup>b</sup>  $1.0 \times 10^{-5}$  M at room temperature. <sup>c</sup>  $1.0 \times 10^{-5}$  M at room temperature. <sup>d</sup> Dispersed in PMMA (10 wt%). <sup>e</sup> Absolute photoluminescence quantum efficiencies.

In LUMOs, some contribution of the carborane C–C antibonding orbital ( $\sigma^*$ ) was observed, indicating the  $\sigma^*-\pi^*$  conjugation.<sup>11</sup> TD-DFT calculations predicted the  $S_0-S_1$  transition of the dyads to be the  $\pi-\pi^*$  transition of the anthracene moiety with an oscillator strength of 0.1901–0.2175. After relaxation on the  $S_1$  potential surface, the LUMO was mainly on the *o*-carborane unit with substantial orbital contribution. Finally, the  $S_1-S_0$  transition was characterized as charge transfer from the *o*-carborane unit to the

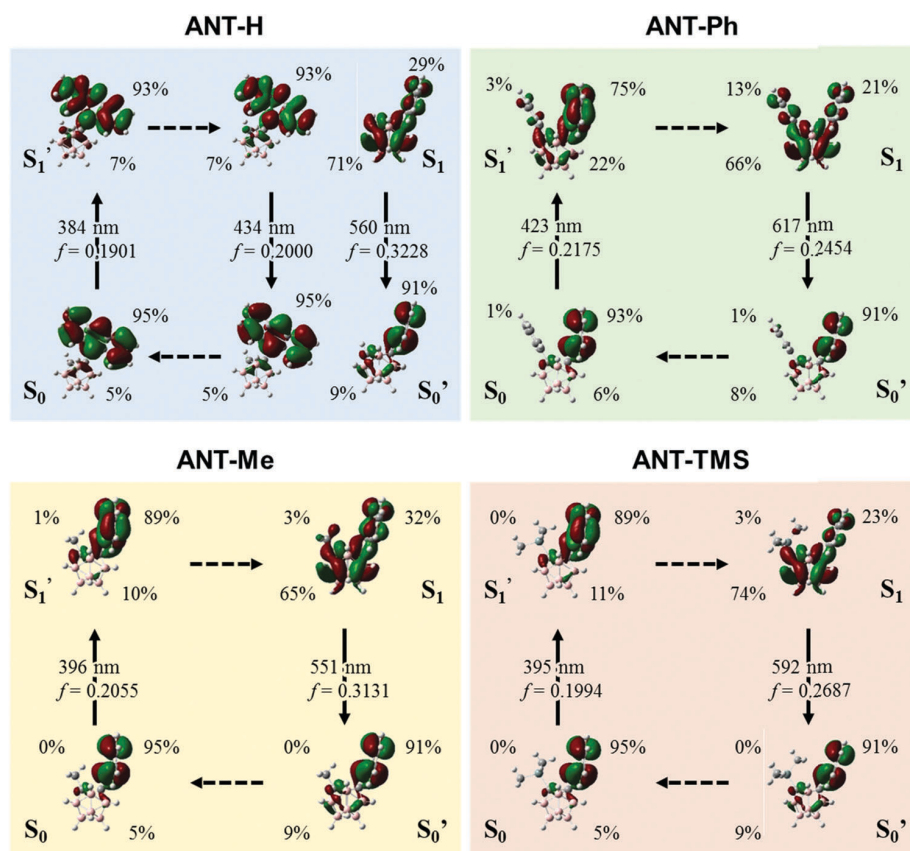
anthracene moiety. This result represents that the emission bands from the dyads should have originated from the transitions from the ICT state similarly to the emission mechanism of **ANT-H**.<sup>11</sup> According to the orbital composition in the LUMOs of the  $S_1$  optimized geometry, the orbital composition of the phenyl group in **ANT-Ph** (13%) was found to be higher than those of the methyl and TMS groups (3% and 3%, respectively). Similar results were observed in previous reports.<sup>13</sup> It implies that the phenyl group could make a weak electronic interaction with the anthracene moiety and/or the *o*-carborane unit in the excited state. As a result, the red-shifted emission band with a lower quantum efficiency of **ANT-Ph** was obtained in the aggregation state compared to those of **ANT-Me** and **ANT-TMS**.

Thermochromic behaviors in luminescence from the dyads were investigated with the crystalline samples. PL spectra were monitored on the hot plate by increasing the temperature from 50 °C to 200 °C (Fig. 6). According to the thermogravimetric analysis, it was shown that thermal degradation proceeded before melting (Table S3, ESI†). In particular, **ANT-H** showed the lowest decomposition temperature ( $T_d = 200$  °C) of the four compounds, and emission annihilation was correspondingly observed over 200 °C (Fig. S4a, ESI†). Therefore, we evaluated the thermochromic luminescence properties below 200 °C. Luminescence color changes were observed by heating. Furthermore, the optical properties were reversibly recovered

**Table 2** Calculated absorption (Abs.) and emission (Em.) data for anthracenyl-*o*-carboranes

		$\lambda_{\max}$ (nm)	$\Delta E$ (eV)	Oscillator strength ( $f$ )	Transition <sup>a</sup>
<b>ANT-H</b>	Abs.	385	3.22	0.1901	H → L (92%)
	Em.	434	2.86	0.2000	L → H (92%)
		560	2.21	0.3228	L → H (95%)
<b>ANT-Ph</b>	Abs.	423	2.93	0.2175	H → L (90%)
	Em.	617	2.01	0.2454	L → H (97%)
<b>ANT-Me</b>	Abs.	396	3.13	0.2055	H → L (93%)
	Em.	551	2.25	0.3131	L → H (95%)
<b>ANT-TMS</b>	Abs.	395	3.14	0.1994	H → L (93%)
	Em.	592	2.10	0.2687	L → H (96%)

<sup>a</sup> H = HOMO and L = LUMO, and percentages represent the proportion in this transition.



**Fig. 5** Absorption and emission processes of the dyads.

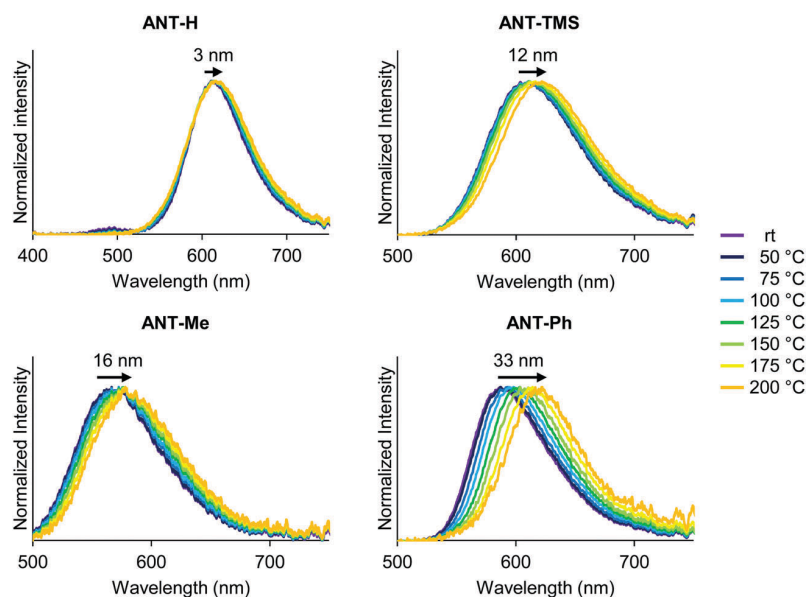


Fig. 6 Thermochromic luminescence behaviors of the powder samples of the *o*-carborane dyads during heating from 50 °C to 200 °C.

by cooling to room temperature, and these processes can be repeated many times. In the spectra, obviously, bathochromic shifts were observed by heating only from the dyads with the adjacent substituents. In particular, **ANT-Ph** showed the largest shift in this study. Crystal packing should be released by thermal motions at the substituents, followed by larger structural relaxation than that at room temperature. As a consequence, the probability of forming the favorable conformation to construct  $\pi$ -conjugation could be increased. Thus, bathochromic shifts should be detected in the higher temperature region. The phenyl group would be the suitable functional group for extending the conjugated system. Hence, the largest color change could be induced. By increasing the temperature, the emission intensity decreased (Fig. S4 and S5, ESI<sup>†</sup>). It is likely that molecular tumbling could be activated, followed by emission annihilation. In summary, these data indicate that the adjacent substituents contribute not only to the enhancement of solid-state emission efficiencies but also to the addition of stimuli-responsiveness toward temperature change.

## Conclusion

Anthracene-substituted *o*-carborane dyads were synthesized and fully characterized. Introduction of adjacent substituents such as phenyl, methyl, and TMS groups facilitated the formation of a perpendicular conformation at the anthracene moiety toward the C-C bond of *o*-carborane, leading to the enhancement of emission efficiencies in the crystalline state. In particular, **ANT-Me** and **ANT-TMS** showed excellent quantum efficiencies in the crystalline state. **ANT-TMS** showed strong fluorescence even in the solution and PMMA matrix because of the suppression of the non-radiative deactivation by the bulky TMS substituent. These data propose the validity of the

anthracene-substituted *o*-carborane skeleton as a platform for constructing solid-state luminescent materials. Furthermore, **ANT-Ph** showed the largest shift in the thermochromic luminescence behaviors. Our materials and concept should be useful as a guideline for designing luminescent solid materials with stimuli-responsive chromic properties.

## Conflicts of interest

There are no conflicts to declare.

## Acknowledgements

This work was partially supported by The Kyoto Technoscience Center (for K. T.) and a Grant-in-Aid for Scientific Research on Innovative Areas “New Polymeric Materials Based on Element-Blocks (No. 2401)” (JSPS KAKENHI Grant Number JP24102013).

## References

- (a) F. F. Vidor, T. Meyers and U. Hilleringmann, *Electronics*, 2015, **4**, 480–506; (b) S. K. Gupta, P. Jha, A. Singh, M. M. Chehim and D. K. Aswal, *J. Mater. Chem. C*, 2015, **3**, 8468–8479.
- (a) O. Ostroverkhova, *Chem. Rev.*, 2016, **116**, 13279–13412; (b) A. Hirose, K. Tanaka, R. Yoshii and Y. Chujo, *Polym. Chem.*, 2015, **6**, 5590–5595; (c) R. Yoshii, A. Hirose, K. Tanaka and Y. Chujo, *J. Am. Chem. Soc.*, 2014, **136**, 18131–18139.
- (a) W. H. Melhuish, *J. Phys. Chem.*, 1961, **65**, 229–235; (b) S. A. Jenekhe and J. A. Osaheni, *Science*, 1994, **265**, 765–768; (c) K. Suenaga, K. Tanaka and Y. Chujo, *Eur. J. Org. Chem.*, 2017, **2017**, 5191–5196; (d) S. Ohtani,

- M. Gon, K. Tanaka and Y. Chujo, *Chem. – Eur. J.*, 2017, **23**, 11827–11833.
- 4 (a) D. Frath, J. Massue, G. Ulrich and R. Ziessel, *Angew. Chem., Int. Ed.*, 2014, **53**, 2290–2310; (b) S. Mukherjee and P. Thilagar, *J. Mater. Chem. C*, 2016, **4**, 2647–2662; (c) S. Xiao, Q. Cao and F. Dan, *Curr. Org. Chem.*, 2012, **16**, 2970–2981; (d) K. Tanaka and Y. Chujo, *Macromol. Rapid Commun.*, 2012, **33**, 1235–1255; (e) K. Tanaka and Y. Chujo, *NPG Asia Mater.*, 2015, **7**, e223.
- 5 (a) C.-H. Zhao, E. Sakuda, A. Wakamiya and S. Yamaguchi, *Chem. – Eur. J.*, 2009, **15**, 10603–10612; (b) A. Wakamiya, K. Mori and S. Yamaguchi, *Angew. Chem., Int. Ed.*, 2007, **46**, 4273–4276; (c) C.-H. Zhao, A. Wakamiya and S. Yamaguchi, *Macromolecules*, 2007, **40**, 3898–3900.
- 6 (a) C. Glotzbach, N. Gödeke, R. Fröhlich, C.-G. Daniliuc, S. Saito, S. Yamaguchi and E.-U. Würthwein, *Dalton Trans.*, 2015, **44**, 9659–9671; (b) C. F. A. Gomez-Duran, R. Hu, G. Feng, T. Li, F. Bu, M. Arseneault, B. Liu, E. Peña-Cabrera and B. Z. Tang, *ACS Appl. Mater. Interfaces*, 2015, **7**, 15168–15176; (c) Y. Kubota, S. Tanaka, K. Funabiki and M. Matsui, *Org. Lett.*, 2012, **14**, 4682–4685; (d) S. Mukherjee and P. Thilagar, *Chem. – Eur. J.*, 2014, **20**, 9052–9062; (e) L. Wang, Z. Zhang, X. Cheng, K. Ye, F. Li, Y. Wang and H. Zhang, *J. Mater. Chem. C*, 2015, **3**, 499–505; (f) Q. Liu, X. Wang, H. Yan, Y. Wu, Z. Li, S. Gong, P. Liu and Z. Liu, *J. Mater. Chem. C*, 2015, **3**, 2953–2959; (g) L. Quan, Y. Chen, X.-J. Lv and W.-F. Fu, *Chem. – Eur. J.*, 2012, **18**, 14599–14604; (h) M. Yamaguchi, S. Ito, A. Hirose, K. Tanaka and Y. Chujo, *Mater. Chem. Front.*, 2017, **1**, 1573–1579; (i) K. Suenaga, K. Tanaka and Y. Chujo, *Chem. – Eur. J.*, 2017, **23**, 1409–1414; (j) K. Suenaga, R. Yoshii, K. Tanaka and Y. Chujo, *Macromol. Chem. Phys.*, 2016, **217**, 414–417; (k) K. Tanaka, T. Yanagida, A. Hirose, H. Yamane, R. Yoshii and Y. Chujo, *RSC Adv.*, 2015, **5**, 96653–96659; (l) R. Yoshii, K. Suenaga, K. Tanaka and Y. Chujo, *Chem. – Eur. J.*, 2015, **21**, 7231–7237.
- 7 (a) R. N. Grimes, *Carboranes*, Academic Press, Amsterdam, 2nd edn, 2011, pp. 301–540; (b) V. I. Bregadze, *Chem. Rev.*, 1992, **92**, 209–223; (c) M. Scholz and E. Hey-Hawkins, *Chem. Rev.*, 2011, **111**, 7035–7062; (d) R. Núñez, M. Terrés, A. Ferrer-Ugalde, F. F. d. Biani and F. Teixidor, *Chem. Rev.*, 2016, **116**, 14307–14378; (e) A. González-Campo, E. J. Juárez-Pérez, C. Viñas, B. Boury, R. Sillanpää, R. Kivekäs and R. Núñez, *Macromolecules*, 2008, **41**, 8458–8466; (f) F. Issa, M. Kassiou and L. M. Rendina, *Chem. Rev.*, 2011, **111**, 5701–5722; (g) G. Li, S. Azuma, S. Sato, H. Minegishi and H. Nakamura, *Bioorg. Med. Chem. Lett.*, 2015, **25**, 2624–2628; (h) G. Li, S. Azuma, S. Sato, H. Minegishi and H. Nakamura, *J. Organomet. Chem.*, 2015, **798**, 189–195; (i) R. Núñez, I. Romero, F. Teixidor and C. Viñas, *Chem. Soc. Rev.*, 2016, **45**, 5147–5173.
- 8 (a) L. Böhling, A. Brockhinke, J. Kahlert, L. Weber, R. A. Harder, D. S. Yuffit, J. A. K. Howard, J. A. H. MacBride and M. A. Fox, *Eur. J. Inorg. Chem.*, 2016, 403–412; (b) L. Weber, J. Kahlert, R. Brockhinke, L. Böhling, A. Brockhinke, H.-G. Stammer, B. Neumann, R. A. Harder and M. A. Fox, *Chem. – Eur. J.*, 2012, **18**, 8347–8357; (c) L. Weber, J. Kahlert, R. Brockhinke, L. Böhling, J. Halama, A. Brockhinke, H.-G. Stammer, B. Neumann, C. Nervi, R. A. Harder and M. A. Fox, *Dalton Trans.*, 2013, **42**, 10982–10996; (d) J. Kahlert, L. Böhling, A. Brockhinke, H.-G. Stammer, B. Neumann, L. M. Rendina, P. J. Low, L. Weber and M. A. Fox, *Dalton Trans.*, 2015, **44**, 9766–9781; (e) Y.-J. Cho, S.-Y. Kim, M. Cho, W.-S. Han, H.-J. Son, D. W. Cho and S. O. Kang, *Phys. Chem. Chem. Phys.*, 2016, **19**, 9702–9708; (f) S.-Y. Kim, Y.-J. Cho, G. F. Jin, W.-S. Han, H.-J. Son, D. W. Cho and S. O. Kang, *Phys. Chem. Chem. Phys.*, 2015, **17**, 15679–15682; (g) K.-R. Wee, Y.-J. Cho, S. Jeong, S. Kwon, J.-D. Lee, I.-H. Suh and S. O. Kang, *J. Am. Chem. Soc.*, 2012, **134**, 17982–17990; (h) B. H. Choi, J. H. Lee, H. Hwang, K. M. Lee and M. H. Park, *Organometallics*, 2016, **35**, 1771–1777; (i) R. Furue, T. Nishimoto, I. S. Park, J. Lee and T. Yasuda, *Angew. Chem., Int. Ed.*, 2016, **55**, 7171–7175; (j) M. Uebe, A. Ito, Y. Kameoka, T. Sato and K. Tanaka, *Chem. Phys. Lett.*, 2015, **633**, 190–194; (k) Y. Kameoka, M. Uebe, A. Ito, T. Sato and K. Tanaka, *Chem. Phys. Lett.*, 2014, **615**, 44–49; (l) S. Inagi, K. Hosoi, T. Kubo, N. Shida and T. Fuchigami, *Electrochemistry*, 2013, **81**, 368–370; (m) Z. Wang, P. Jiang, T. Wang, G. J. Moxey, M. P. Cifuentes, C. Zhang and M. G. Humphrey, *Phys. Chem. Chem. Phys.*, 2016, **18**, 15719–15726; (n) J. J. Peterson, A. R. Davis, M. Were, E. B. Coughlin and K. R. Carter, *ACS Appl. Mater. Interfaces*, 2011, **3**, 1796–1799; (o) L. Zhu, W. Lv, S. Liu, H. Yan, Q. Zhao and W. Huang, *Chem. Commun.*, 2013, **49**, 10638–10640; (p) D. Tu, P. Leong, Z. Li, R. Hu, C. Shi, K. Y. Zhang, H. Yan and Q. Zhao, *Chem. Commun.*, 2016, **52**, 12494–12497; (q) W. Zhang, Y. Luo, Y. Xu, L. Tian, M. Li, R. He and W. Shen, *Dalton Trans.*, 2015, **44**, 18130–18137; (r) S. Mukherjee and P. Thilagar, *Chem. Commun.*, 2016, **52**, 1070–1093; (s) X. Li, H. Yan and Q. Zhao, *Chem. – Eur. J.*, 2016, **22**, 1888–1898; (t) J. Park, Y. H. Lee, J. Y. Ryu, J. Lee and M. H. Lee, *Dalton Trans.*, 2016, **45**, 5667–5675; (u) Y. H. Lee, J. Park, S.-J. Jo, M. Kim, J. Lee, S. U. Lee and M. H. Lee, *Chem. – Eur. J.*, 2015, **21**, 2052–2061; (v) X. Li, X. Tong, Y. Yin, H. Yan, C. Lu, W. Huang and Q. Zhao, *Chem. Sci.*, 2017, **8**, 5930–5940; (w) L. Zhu, X. Tang, Q. Yu, W. Lv, H. Yan, Q. Zhao and W. Huang, *Chem. – Eur. J.*, 2015, **21**, 4721–4730; (x) A. Ferrer-Ugalde, A. González-Campo, C. Viñas, J. Rodríguez-Romero, R. Santillan, N. Farfán, R. Sillanpää, A. Sousa-Pedrares, R. Núñez and F. Teixidor, *Chem. – Eur. J.*, 2014, **20**, 9940–9951; (y) J. Cabrera-González, C. Viñas, M. Haukka, S. Bhattacharyya, J. Gierschner and R. Núñez, *Chem. – Eur. J.*, 2016, **22**, 13588–13598; (z) A. Ferrer-Ugalde, E. J. Juárez-Pérez, F. Teixidor, C. Viñas and R. Núñez, *Chem. – Eur. J.*, 2013, **19**, 17021–17030.
- 9 (a) K. Kokado and Y. Chujo, *J. Org. Chem.*, 2010, **76**, 316–319; (b) K. Kokado and Y. Chujo, *Macromolecules*, 2009, **42**, 1418–1420; (c) K. Tanaka, K. Nishino, S. Ito, H. Yamane, K. Suenaga, K. Hashimoto and Y. Chujo, *Faraday Discuss.*, 2017, **196**, 31–42.
- 10 (a) Y. Chujo and K. Tanaka, *Bull. Chem. Soc. Jpn.*, 2015, **88**, 633–643; (b) K. Nishino, K. Hashimoto, K. Tanaka, Y. Morisaki

- and Y. Chujo, *Tetrahedron Lett.*, 2016, **57**, 2025–2028; (c) K. Nishino, H. Yamamoto, K. Tanaka and Y. Chujo, *Org. Lett.*, 2016, **18**, 4064–4067; (d) H. Naito, Y. Morisaki and Y. Chujo, *Angew. Chem., Int. Ed.*, 2015, **54**, 5084–5087; (e) H. Naito, K. Nishino, Y. Morisaki, K. Tanaka and Y. Chujo, *Chem. – Asian J.*, 2017, **12**, 2134–2138.
- 11 H. Naito, K. Nishino, Y. Morisaki, K. Tanaka and Y. Chujo, *Angew. Chem., Int. Ed.*, 2017, **56**, 254–259.
- 12 (a) J. M. Oliva, N. L. Allan, P. R. Schleyer, C. Viñas and F. Teixidor, *J. Am. Chem. Soc.*, 2005, **127**, 13538–13547; (b) I. V. Glukhov, M. Y. Antipin and K. A. Lyssenko, *Eur. J. Inorg. Chem.*, 2004, 1379–1384; (c) J. Llop, C. Viñas, J. Oliva, F. Teixidor, M. A. Flores, R. Kivekas and R. Sillanpää, *J. Organomet.*, 2002, **657**, 232–238; (d) H. J. Bae, H. Kim, K. M. Lee, T. Kim, Y. S. Lee, Y. Do and M. H. Lee, *Dalton Trans.*, 2014, **43**, 4978–4985.
- 13 (a) A. Ferrer-Ugalde, E. J. Juárez-Pérez, F. Teixidor, C. Viñas, R. Sillanpää, E. Pérez-Inestrosa and R. Núñez, *Chem. – Eur. J.*, 2012, **18**, 544–553; (b) A. Ferrer-Ugalde, J. Cabrera-González, E. J. Juárez-Pérez, F. Teixidor, E. Pérez-Inestrosa, J. M. Montenegro, R. Sillanpää, M. Haukka and R. Núñez, *Dalton Trans.*, 2017, **46**, 2091–2104.

VIP

Luminescence Color Tuning from Blue to Near Infrared of Stable Luminescent Solid Materials Based on Bis-*o*-Carborane-Substituted OligoacenesHirofumi Naito,<sup>[a]</sup> Kenta Nishino,<sup>[a]</sup> Yasuhiro Morisaki,<sup>[a, b]</sup> Kazuo Tanaka,<sup>[a]</sup> and Yoshiki Chujo<sup>\*[a]</sup>

**Abstract:** Aryl-substituted *o*-carboranes have shown highly efficient solid-state emission in previous studies. To demonstrate color tuning of the solid-state emission in an aryl-*o*-carborane-based system, bis-*o*-carborane-substituted oligoacenes were synthesized and their properties were systematically investigated. Optical and electrochemical measurements revealed efficient decreases in energy band gaps and lowest unoccupied molecular orbital (LUMO) levels by adding a number of fused benzene rings for the extension

of  $\pi$ -conjugation. As a consequence, bright solid-state emission was observed in the region from blue to near infrared (NIR). Furthermore, various useful features were obtained from the modified *o*-carboranes as an optical material. The naphthalene derivatives exhibited aggregation-induced emission (AIE) and almost 100% quantum efficiency in the crystalline state. Furthermore, it was shown that the tetracene derivative with NIR-emissive properties had high durability toward photo-bleaching under UV irradiation.

## Introduction

Functionalized oligoacenes have attracted growing attention in recent years because of their wide applicability in areas such as luminescent and semiconducting materials.<sup>[1]</sup> Anthracenes and tetracenes are widely used for ion-sensing<sup>[2]</sup> or light-emitting diodes (LEDs),<sup>[3]</sup> and larger oligoacenes such as pentaacenes are promising candidates for field-effect transistors because of their exceptionally high charge transport properties.<sup>[4]</sup> Generally, oligoacenes are sensitive to air and light to undergo oxidation or photodegradation.<sup>[5]</sup> To overcome this low stability, two general approaches are known as thermodynamic and kinetic stabilization. Introduction of steric substituent such as a trialkylsilyl group inhibited oxidation and dimerization of oligoacenes.<sup>[6]</sup> Additionally, conjugation of electron-withdrawing substituents such as a trifluoromethyl group stabilized the HOMO level, leading to suppression of reactivity toward

oxygen and photodegradation. Based on these approaches, highly stable oligoacenes can be obtained.<sup>[6]</sup>

*o*-Carborane (C<sub>2</sub>H<sub>12</sub>B<sub>10</sub>) is a polyhedral boron-carbon cluster in which two carbon atoms are arranged in an adjacent position.<sup>[7]</sup> Recently, various types of luminescent materials have been constructed based on modified *o*-carboranes.<sup>[8]</sup> We also have paid attention to *o*-carborane as a luminescent "element-block",<sup>[9a]</sup> which is defined as a minimum functional unit composed of heteroatoms, for preparing optically functional solid materials.<sup>[9]</sup> In the previous reports, the aggregation-induced emission (AIE) property of  $\pi$ -conjugated *o*-carboranes was discovered, and their mechanism was clarified.<sup>[10]</sup> Accordingly, intramolecular charge transfer (ICT) occurs from the  $\pi$ -conjugated moieties to the C1-C2 bond of *o*-carborane quenches the emission in solution, whereas the freezing of the C1-C2 bond vibration causes emission in aggregates.<sup>[10]</sup> In particular, concentration quenching was also efficiently suppressed by steric hindrance of the sphere-shaped *o*-carborane unit. Based on this mechanism, a wide variety of solid-state emission including luminescent chromic behaviors were accomplished by suppressing energy-consuming vibration.<sup>[11]</sup> For example, by restricting intramolecular motions by the substituent effect, highly efficient emission (emission efficiency,  $\Phi_{\text{PL}} > 0.99$ ) was observed from yellow to red regions.<sup>[12]</sup> From these results, it is presumed that *o*-carborane can be used for improving stability of oligoacenes kinetically and thermodynamically because of both bulkiness of the sphere shape and electron-deficient nature, respectively. Our next goal is to demonstrate another role of *o*-carborane in enhancement of stability of luminescent organic units. Moreover, since the ICT emission generally appears in the longer wavelength region, it is challenging to

[a] H. Naito, Dr. K. Nishino, Prof. Y. Morisaki, Dr. K. Tanaka, Prof. Y. Chujo  
Department of Polymer Chemistry  
Graduate School of Engineering  
Kyoto University  
Katsura, Nishikyo-ku, Kyoto 615-8510 (Japan)  
E-mail: chujo@chujo.synchem.kyoto-u.ac.jp

[b] Prof. Y. Morisaki  
Present address:  
Department of Applied Chemistry for Environment  
School of Science and Technology,  
Kwansei Gakuin University  
2-1 Gakuen, Sanda, Hyogo 669-1337 (Japan)

Supporting information and the ORCID identification number(s) for the author(s) of this article can be found under <https://doi.org/10.1002/asia.201700815>.

obtain highly efficient blue emission from the solid sample of *o*-carboranes.

Herein, bis-*o*-carborane-substituted oligoacenes (Figure 1) were synthesized, and their optical properties as colorful solid-

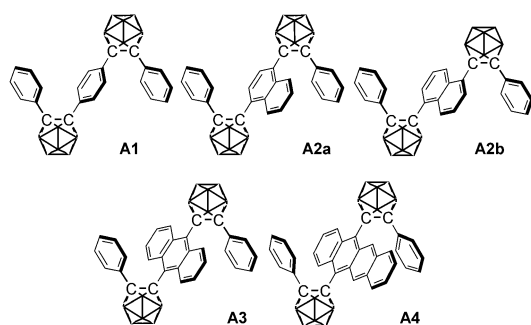
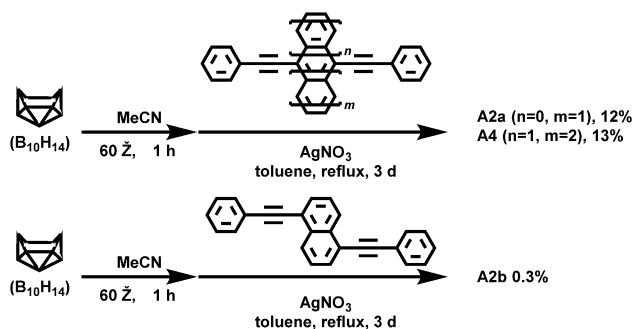


Figure 1. Bis-*o*-carborane-substituted oligoacenes used in this study.

state luminescent materials were examined. From the series of measurements for evaluating electronic properties, it was shown that addition of the number of fused benzene rings at the bridge between *o*-carboranes critically induced decreases in energy band gaps and LUMO levels originated from the expansion of  $\pi$ -conjugated system. As a result, bright solid-state emission was accomplished in the region from blue to near infrared (NIR). Furthermore, it was observed that the naphthalene derivatives exhibited the AIE property and almost 100% quantum efficiency in the crystalline state. Moreover, the tetracene derivative having NIR-emissive property had high durability toward photo-bleach. This study presents further feasibility of *o*-carborane as an “element-block” for realizing advanced optical materials.

## Results and Discussion

As shown in Scheme 1, **A2a**, **A2b** and **A4** were synthesized from decaborane ( $B_{10}H_{14}$ ) and corresponding 9,10-di(phenylethynyl)oligoacene using  $AgNO_3$  as a Lewis acid.<sup>[13]</sup> The structures of the obtained compounds were characterized by NMR spectroscopy and the X-ray crystallography. The obtained compounds were highly stable toward oxygen and light and easily dissolved in common organic solvents such as  $CHCl_3$ ,  $CH_2Cl_2$ ,



Scheme 1. Synthesis of **A1**–**A4**.

tetrahydrofuran (THF), and toluene. **A1** and **A3** were synthesized according to the literature.<sup>[11a,14]</sup>

Single crystals of **A2a** and **A4** suitable for X-ray diffraction studies were obtained from slow evaporation of  $CHCl_3$  and  $C_6H_6$  solution, respectively (Tables S2 and S3). Figure 2 shows

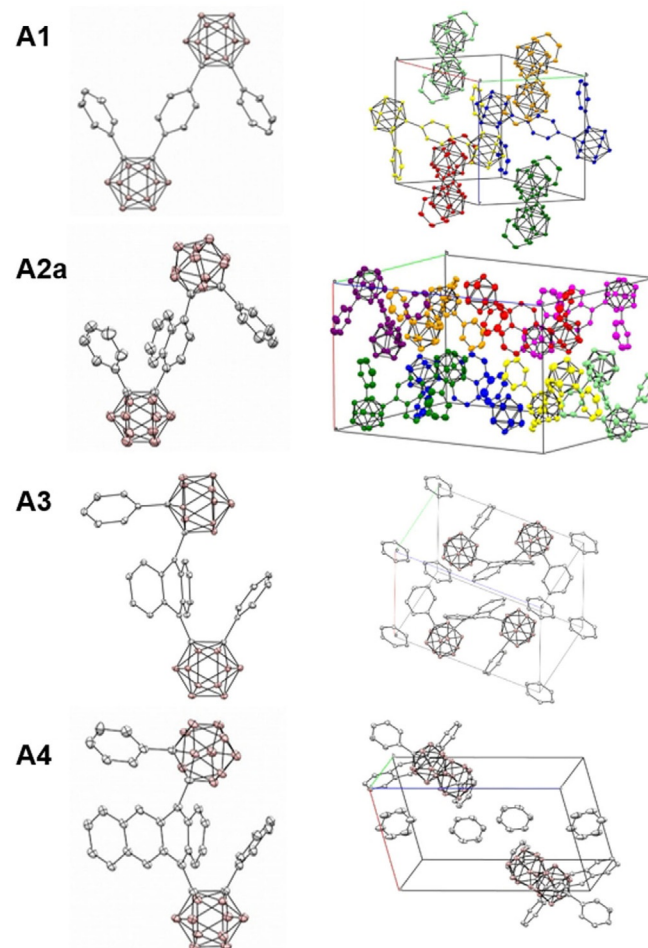
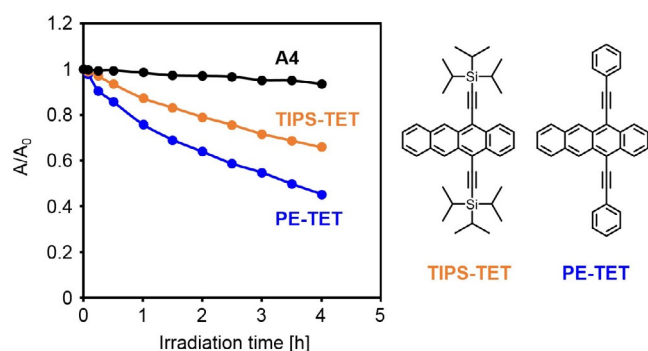


Figure 2. Molecular structures and packing diagrams of **A1**, **A2a**, **A3**· $C_6H_6$ , and **A4**·( $C_6H_6$ )<sub>2</sub> (hydrogen atoms are omitted for clarity, and thermal ellipsoids are displayed at 30% probability).

the molecular structures and packing diagrams of the compounds. The tetracene rings of two molecules of **A4** formed a  $\pi$ -stacked dimer like **A3**.<sup>[11a]</sup> The overlapping area of two  $\pi$ -stacked tetracenes was estimated as 13%, while **A1**, **A2a** and **A2b** hardly form a  $\pi$ -stacked dimer and intermolecular  $\pi$ - $\pi$  stacking. The core benzene and naphthalene rings were sterically hindered by two phenyl-*o*-carborane units, whereas anthracene and tetracene rings of **A3** and **A4** were highly distorted because of the steric repulsion between the oligoacene moiety and two carborane units.<sup>[11a]</sup> Thus, the core rings in **A3** and **A4** were isolated. Another impressive point was the ring deformation in the central oligoacene moiety. Obviously, the tetracene ring in the **A4**·( $C_6H_6$ )<sub>2</sub> crystal was significantly distorted, and the ring deformation angles  $\alpha$  and  $\beta$  values to the ring of tetracene connected to *o*-carboranes in **A4**·( $C_6H_6$ )<sub>2</sub> were

20.2° and 7.2°, respectively. These large deformation angles were caused by  $\pi$ - $\pi$  interaction between the tetracene rings and steric hindrance of the phenyl-substituted *o*-carboranes in the  $\pi$ -stacked dimer. This is comparable to the distorted anthracene derivatives and is the largest distortion angle, to the best of our knowledge, for tetracene derivatives.<sup>[11a,15]</sup> The aromaticity of the tetracene rings in the **A4**-(C<sub>6</sub>H<sub>6</sub>)<sub>2</sub> crystals was evaluated by the calculation of nucleus-independent chemical shifts (NICS) as listed in Table S1 in the Supporting Information. It was suggested that the aromaticity should be maintained according to these NICS values.

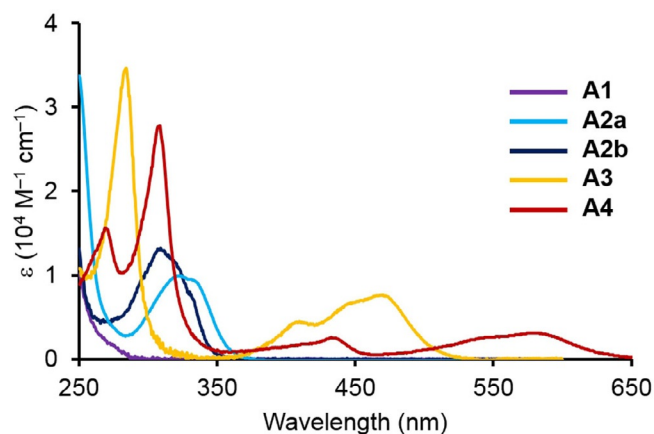
Oligoacenes including tetracene are readily oxidized or decomposed by light irradiation. To evaluate the protection effect of the carborane units toward undesired degradation, thermal and photo-stability of **A4** were investigated. Thermogravimetric analysis (TGA) showed that decomposition started at approximately 310 °C, and 5 wt% weight loss was observed at 334 °C under N<sub>2</sub> (Figure S1). The decomposition of the unsubstituted tetracene starts at around 140 °C.<sup>[16]</sup> Thus, the thermal stability was significantly enhanced by introducing the carborane units. The durability of **A4** toward photo-irradiation was investigated by monitoring the absorbance decay at  $\lambda_{\text{max}}$  in the aerated C<sub>6</sub>H<sub>5</sub>Cl solution during exposing to white light using a xenon lamp (150 W) at room temperature (Figure 3).<sup>[17]</sup> Compared to bis(phenylethynyl)tetracene (**PE-TET**) and bis(tri-



**Figure 3.** Photostability of tetracene derivatives in the C<sub>6</sub>H<sub>5</sub>Cl solution. UV-vis absorption peaks around 580 nm for **A4**, 540 nm for **TIPS-TET**, and 550 nm for **PE-TET**, respectively, were monitored under white light at room temperature.

isopropylsilylethynyl)tetracene (**TIPS-TET**), **A4** exhibited much higher stability, demonstrating the effectiveness of introduction of the carborane units. Additionally, photo-induced dimerization of the tetracene units in **A4**-(C<sub>6</sub>H<sub>6</sub>)<sub>2</sub> crystal hardly occurred even under UV light irradiation in air, where the pristine tetracene should be rapidly consumed. Thus, it was clearly indicated that the tetracene ring was stabilized thermodynamically and kinetically by the *o*-carborane units. Electron-withdrawing ability and steric hindrance of the phenyl-substituted *o*-carborane should play critical roles in stabilization of the tetracene moiety.

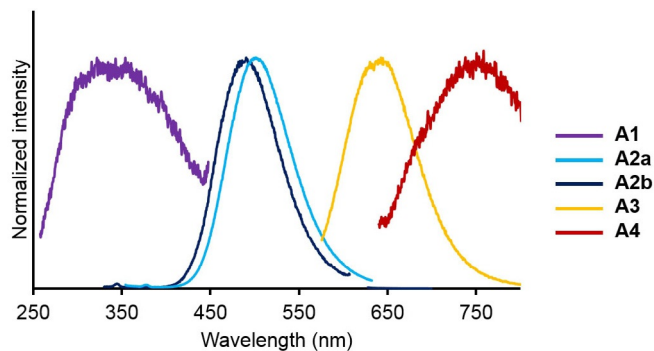
Figure 4 shows the UV-vis absorption spectra of **A1-A4** in THF (1.0 × 10<sup>-5</sup> M). The values of the energy band gap ( $E_g$ ) which was estimated from the onset wavelength in the spec-



**Figure 4.** UV-vis absorption spectra of **A1-A4** in THF (1.0 × 10<sup>-5</sup> M).

trum were red-shifted in the order of the length of oligoacene, indicating that the  $\pi$ -conjugation system was extended regardless of introduction of the carborane units. The LUMO energy levels were estimated from the cyclic voltammogram (CV) peak onset potentials, and the HOMO energy levels were calculated from the LUMO energy level and the band gap energy estimated from the absorption edge (Table S4). All compounds showed remarkably low-lying LUMO energy levels compared to the corresponding oligoacenes. It is likely that the strong electron-withdrawing character of the *o*-carborane unit should be responsible for lowering LUMO levels. In particular, LUMO levels of **A3** and **A4** were calculated to be -4.16 eV and -4.25 eV, respectively. These values are similar to that of C<sub>60</sub> (-4.2 eV), implying possibility as efficient electron-accepting materials.

Photoluminescence (PL) spectra were obtained in solution (1.0 × 10<sup>-5</sup> M) and aggregate (THF/H<sub>2</sub>O = 1/99 (v/v), 1.0 × 10<sup>-5</sup> M) states (Figure 5). In THF, **A1** and **A4** showed subtle emission, and **A2a**, **A2b** and **A3** showed weak emission at around 550 nm, 530 nm and 650 nm, respectively. Meanwhile, aggregates of **A1** and **A4** showed emission around 350 and 750 nm, respectively, and **A2a**, **A2b** and **A3** showed intense emission. These data indicate that all compounds should have the AIE property. PL spectra in the crystalline state were also mea-



**Figure 5.** PL spectra of *o*-carboranes in aggregates (THF/H<sub>2</sub>O v/v = 1/99 solution, 1.0 × 10<sup>-5</sup> M). Excited at 224, 334, 309, 471, and 586 nm for **A1**, **A2a**, **A2b**, **A3** and **A4**, respectively.

sured, and their absolute fluorescence quantum efficiencies are shown in Table 1. In the crystalline state, **A2a** and **A2b** showed remarkably high quantum efficiencies. In particular, **A2b** presented clear blue emission. From these data, it can be

**Table 1.** Optical properties of **A1–A4**.<sup>[a]</sup>

Compound	THF <sup>[b]</sup>		THF/H <sub>2</sub> O = 1/99 <sup>[b]</sup>		Crystal	
	$\lambda_{em}$ [nm]	$\Phi_{PL}$ <sup>[c]</sup>	$\lambda_{em}$ [nm]	$\Phi_{PL}$ <sup>[c]</sup>	$\lambda_{em}$ [nm]	$\Phi_{PL}$ <sup>[c]</sup>
<b>A1</b>	n.d. <sup>[d]</sup>	n.d. <sup>[d]</sup>	322	n.d. <sup>[d]</sup>	397	n.d. <sup>[d]</sup>
<b>A2a</b>	549	0.04	501	0.23	486	> 0.99
<b>A2b</b>	530	< 0.01	491	0.53	468	> 0.99
<b>A3</b> <sup>[e]</sup>	647	< 0.01	643	0.08	613 <sup>[f]</sup>	0.81
<b>A4</b>	n.d. <sup>[d]</sup>	< 0.01	759	0.01	742	< 0.01

[a] Excited at each  $\lambda_{abs,max}$ . [b]  $1.0 \times 10^{-5}$  M at room temperature. [c] Determined as an absolute quantum efficiency. [d] Not detected. [e] Ref. [11a]. [f] Collected from the benzene incorporated crystal (1-C<sub>6</sub>H<sub>6</sub>).

said that highly efficient blue luminescence was obtained in the solid state. The absorption band and emission band were completely separated because of the strong intramolecular charge transfer (ICT) character. X-ray crystallography of **A2** indicates that intermolecular  $\pi$ - $\pi$  interaction hardly existed because of bulkiness of the phenyl-*o*-carborane moieties, which can inhibit the non-radiative deactivation and lead to high quantum efficiency. On the other hand, in the case of **A1** and **A4**, the absorption and emission band could be partially overlapped, furthermore, **A3** and **A4** formed a  $\pi$ -stacked dimer in the crystals which can cause non-radiative deactivation. Thus, the quantum efficiencies became in the order of **A2** > **A3** > **A1**  $\approx$  **A4**.

For further understanding the electronic structures, density-functional theory (DFT) calculations were carried out at the B3LYP/6-31G(d)//B3LYP/6-31G(d) level of the theory by employing the Gaussian 09 suite program.<sup>[18]</sup> Figure S6 represents the frontier molecular orbitals as well as their energy levels of each oligoacene. The energy levels of HOMO and LUMO levels of each oligoacene decreased with respect to the corresponding unsubstituted oligoacenes, and the HOMO–LUMO band gaps of bis-*o*-carborane-substituted oligoacenes decreased from 5.39 eV for **A1** to 2.20 eV for **A4**, which was in agreement with the results from CV and UV-vis absorption measurements. The electron-withdrawing property of the *o*-carborane unit should be responsible for perturbation toward energy levels. The HOMOs in **A2–A4** were mainly located on the central oligoacene moieties, whereas the HOMO in **A1** was mainly on the terminal benzene rings. This could be attributed to the reason that the benzene rings of both sides were stabilized by one carborane, while the central benzene ring was strongly stabilized by two carborane units, thus the major contribution of the HOMO came from the terminal benzene rings.<sup>[19]</sup> Significant features observed in the *o*-carborane derivatives were also proposed in this study. From electronic interaction between the  $\sigma^*$  orbital of the carborane C–C bond and the  $\pi^*$  orbital of the central oligoacene, it was shown that  $\sigma^*$ - $\pi^*$  conjugation which can stabilize the LUMO levels was constructed.

TD-DFT calculation predicted the  $S_0$ - $S_1$  transitions in all compounds could be mainly derived from the transition between HOMO and LUMO with high oscillator strengths of 0.1070–0.2945 (Table S5). These features were similar to the previous *o*-carborane derivatives.

## Conclusions

Highly stable oligoacenes were successfully synthesized and characterized. Naphthalene derivatives **A2** showed intense blue emission with high quantum efficiencies in the crystalline state. Compounds **A3** and **A4** exhibited remarkably low LUMO levels comparable to fullerene because two electron-withdrawing *o*-carboranes were directly connected to the oligoacene moieties. Highly distorted structures of acenes in the crystals were observed in **A3** and **A4** by the  $\pi$ -stack dimer formation. Furthermore, it was demonstrated that durability of the tetracene moiety was dramatically improved by the bis-*o*-carborane substitution. This work exhibits the effectiveness of the introduction of the carborane cluster for stabilizing oligoacenes as well as for enhancing solid-state emissive properties.

## Acknowledgements

This work was partially supported by the Konica Minolta Science and Technology Foundation (for K.T.) and a Grant-in-Aid for Scientific Research on Innovative Areas “New Polymeric Materials Based on Element-Blocks (No.2401)” (JSPS KAKENHI Grant Number JP24102013).

## Conflict of interest

The authors declare no conflict of interest.

**Keywords:** aggregation-induced emission · anthracene · carborane · solid-state emission · tetracene

- [1] a) J. E. Anthony, *Chem. Rev.* **2006**, *106*, 5028–5048; b) J. E. Anthony, *Angew. Chem. Int. Ed.* **2008**, *47*, 452–483; *Angew. Chem.* **2008**, *120*, 460–492; c) F. Silvestri, A. Marrocchi, M. Seri, C. Kim, T. J. Marks, A. Facchetti, A. Taticchi, *J. Am. Chem. Soc.* **2010**, *132*, 6108–6123.
- [2] a) J. Y. Kwon, Y. J. Jang, S. K. Kim, K.-H. Lee, J. S. Kim, J. Yoon, *J. Org. Chem.* **2004**, *69*, 5155–5157; b) J. Yoon, S. K. Kim, N. J. Singh, J. W. Lee, Y. J. Yang, K. Chellappan, K. S. Kim, *J. Org. Chem.* **2004**, *69*, 581–583.
- [3] a) S.-K. Kim, B. Yang, Y. Ma, J.-H. Lee, J.-W. Park, *J. Mater. Chem.* **2008**, *18*, 3376–3384; b) P.-I. Shih, C.-Y. Chuang, C.-H. Chien, E. W.-G. Diau, C.-F. Shu, *Adv. Funct. Mater.* **2007**, *17*, 3141–3146; c) E.-A. You, Y.-G. Ha, Y.-S. Choi, J.-H. Choi, *Synth. Met.* **2005**, *153*, 209–212; d) C. Santato, R. Capelli, M. A. Loi, M. Murgia, F. Ciccoira, V. A. L. Roy, P. Stallinga, R. Zamboni, C. Rost, S. F. Karg, M. Muccini, *Synth. Met.* **2004**, *146*, 329–334.
- [4] a) D. H. Kim, D. Y. Lee, H. S. Lee, W. H. Lee, Y. H. Kim, J. I. Han, K. Cho, *Adv. Mater.* **2007**, *19*, 678–682; b) T. B. Singh, F. Meghdadi, S. Günes, N. Marjanovic, G. Horowitz, P. Lang, S. Bauer, N. S. Sariciftci, *Adv. Mater.* **2005**, *17*, 2315–2320.
- [5] a) C. S. Foote, *Acc. Chem. Res.* **1968**, *1*, 104–110; b) R. Debestani, K. J. Ellis, M. E. Sigman, *J. Photochem. Photobiol. A* **1995**, *86*, 231–239; c) W. Fudickar, T. Linker, *J. Am. Chem. Soc.* **2012**, *134*, 15071–15082.
- [6] a) J. E. Anthony, D. L. Eaton, S. R. Parkin, *Org. Lett.* **2002**, *4*, 15–18; b) B. Purushothaman, S. R. Parkin, M. J. Kendrick, D. David, J. W. Ward, L. Yu,

- N. Stingelin, O. D. Jurchescu, O. Ostroverkhova, J. E. Anthony, *Chem. Commun.* **2012**, 48, 8261–8263.
- [7] a) R. N. Grimes, *Carboranes*, Elsevier, **2016**, Chap. 9, pp. 301–540; b) V. I. Bregadze, *Chem. Rev.* **1992**, 92, 209–223; c) A. González-Campo, E. J. Juárez-Pérez, C. Viñas, B. Boury, R. Sillanpää, R. Kivekäs, R. Núñez, *Macromolecules* **2008**, 41, 8458–8466; d) F. Issa, M. Kassiou, L. M. Rendina, *Chem. Rev.* **2011**, 111, 5701–5722; e) G. Li, S. Azuma, S. Sato, H. Minegishi, H. Nakamura, *Bioorg. Med. Chem. Lett.* **2015**, 25, 2624–2628; f) G. Li, S. Azuma, S. Sato, H. Minegishi, H. Nakamura, *J. Organomet. Chem.* **2015**, 798, 189–195.
- [8] a) L. Böhling, A. Brockhinke, J. Kahlert, L. Weber, R. A. Harder, D. S. Yufit, J. A. K. Howard, J. A. H. MacBride, M. A. Fox, *Eur. J. Inorg. Chem.* **2016**, 403–412; b) L. Weber, J. Kahlert, R. Brockhinke, L. Böhling, A. Brockhinke, H.-G. Stammer, B. Neumann, R. A. Harder, M. A. Fox, *Chem. Eur. J.* **2012**, 18, 8347–8357; c) L. Weber, J. Kahlert, R. Brockhinke, L. Böhling, J. Halama, A. Brockhinke, H.-G. Stammer, B. Neumann, C. Nervi, R. A. Harder, M. A. Fox, *Dalton Trans.* **2013**, 42, 10982–10996; d) J. Kahlert, L. Böhling, A. Brockhinke, H.-G. Stammer, B. Neumann, L. M. Rendina, P. J. Low, L. Weber, M. A. Fox, *Dalton Trans.* **2015**, 44, 9766–9781; e) Y.-J. Cho, S.-Y. Kim, M. Cho, W.-S. Han, H.-J. Son, D. W. Cho, S. O. Kang, *Phys. Chem. Chem. Phys.* **2016**, 18, 9702–9708; f) S.-Y. Kim, Y.-J. Cho, G. F. Jin, W.-S. Han, H.-J. Son, D. W. Cho, S. O. Kang, *Phys. Chem. Chem. Phys.* **2015**, 17, 15679–15682; g) K.-R. Wee, Y.-J. Cho, S. Jeong, S. Kwon, J.-D. Lee, I.-H. Suh, S. O. Kang, *J. Am. Chem. Soc.* **2012**, 134, 17982–17990; h) B. H. Choi, J. H. Lee, H. Hwang, K. M. Lee, M. H. Park, *Organometallics* **2016**, 35, 1771–1777; i) R. Furue, T. Nishimoto, I. S. Park, J. Lee, T. Yasuda, *Angew. Chem. Int. Ed.* **2016**, 55, 7171–7175; *Angew. Chem.* **2016**, 128, 7287–7291; j) M. Uebe, A. Ito, Y. Kameoka, T. Sato, K. Tanaka, *Chem. Phys. Lett.* **2015**, 633, 190–194; k) Y. Kameoka, M. Uebe, A. Ito, T. Sato, K. Tanaka, *Chem. Phys. Lett.* **2014**, 615, 44–49; l) S. Inagi, K. Hosoi, T. Kubo, N. Shida, T. Fuchigami, *Electrochemistry* **2013**, 81, 368–370; m) Z. Wang, P. Jiang, T. Wang, G. J. Moxey, M. P. Cifuentes, C. Zhang, M. G. Humphrey, *Phys. Chem. Chem. Phys.* **2016**, 18, 15719–15726; n) J. J. Peterson, A. R. Davis, M. Were, E. B. Coughlin, K. R. Carter, *ACS Appl. Mater. Interfaces* **2011**, 3, 1796–1799; o) L. Zhu, W. Lv, S. Liu, H. Yan, Q. Zhao, W. Huang, *Chem. Commun.* **2013**, 49, 10638–10640; p) D. Tu, P. Leong, Z. Li, R. Hu, C. Shi, K. Y. Zhang, H. Yan, Q. Zhao, *Chem. Commun.* **2016**, 52, 12494–12497; q) W. Zhang, Y. Luo, Y. Xu, L. Tian, M. Li, R. He, W. Shen, *Dalton Trans.* **2015**, 44, 18130–18137; r) S. Mukherjee, P. Thilagar, *Chem. Commun.* **2016**, 52, 1070–1093; s) X. Li, H. Yan, Q. Zhao, *Chem. Eur. J.* **2016**, 22, 1888–1898; t) J. Park, Y. H. Lee, J. Y. Ryu, J. Lee, M. H. Lee, *Dalton Trans.* **2016**, 45, 5667–5675; u) Y. H. Lee, J. Park, S.-J. Jo, M. Kim, J. Lee, S. U. Lee, M. H. Lee, *Chem. Eur. J.* **2015**, 21, 2052–2061; v) A. M. Prokhorov, T. Hofbeck, R. Czerwieńiec, A. F. Suleymanova, D. N. Kozhevnikov, H. Yersin, *J. Am. Chem. Soc.* **2014**, 136, 9637–9642; w) N. Shin, S. Yu, J. H. Lee, H. Hwang, K. M. Lee, *Organometallics* **2017**, 36, 1522–1529; x) N. V. Nghia, J. Oh, J. Jung, M. H. Lee, *Organometallics* <https://doi.org/10.1021/acs.organomet.7b00139>; y) J. J. Schwartz, A. M. Mendoza, N. Wattanatorn, Y. Zhao, V. T. Nguyen, A. M. Spokoynny, C. A. Mirkin, T. Baše, P. S. Weiss, *J. Am. Chem. Soc.* **2016**, 138, 5957–5967; z) K. O. Kirlikovali, J. C. Axtell, A. Gonzalez, A. C. Phung, S. I. Khan, A. M. Spokoynny, *Chem. Sci.* **2016**, 7, 5132–5138; aa) A. M. Prokhorov, P. A. Slepukhin, V. L. Rusinov, V. N. Kalinin, D. N. Kozhevnikov, *Chem. Commun.* **2011**, 47, 7713–7715.
- [9] a) Y. Chujo, K. Tanaka, *Bull. Chem. Soc. Jpn.* **2015**, 88, 633–643; b) K. Nishino, K. Hashimoto, K. Tanaka, Y. Morisaki, Y. Chujo, *Tetrahedron Lett.* **2016**, 57, 2025–2028; c) R. Núñez, M. Tarrés, A. Ferrer-Ugalde, F. F. de Biani, F. Teixidor, *Chem. Rev.* **2016**, 116, 14307–14378.
- [10] a) K. Kokado, Y. Chujo, *J. Org. Chem.* **2011**, 76, 316–319; b) K. Kokado, Y. Chujo, *Macromolecules* **2009**, 42, 1418–1420; c) K. Tanaka, K. Nishino, S. Ito, H. Yamane, K. Suenaga, K. Hashimoto, Y. Chujo, *Faraday Discuss.* **2017**, 196, 31–42.
- [11] a) H. Naito, Y. Morisaki, Y. Chujo, *Angew. Chem. Int. Ed.* **2015**, 54, 5084–5087; *Angew. Chem.* **2015**, 127, 5173–5176; b) H. Naito, K. Nishino, Y. Morisaki, K. Tanaka, Y. Chujo, *Angew. Chem. Int. Ed.* **2017**, 56, 254–259; *Angew. Chem.* **2017**, 129, 260–265.
- [12] K. Nishino, H. Yamamoto, K. Tanaka, Y. Chujo, *Org. Lett.* **2016**, 18, 4064–4067.
- [13] a) R. Schaeffer, *J. Am. Chem. Soc.* **1957**, 79, 1006–1007; b) A. Toppino, A. R. Genady, M. E. El-Zaria, J. Reeve, F. Mostofian, J. Kent, J. F. Valliant, *Inorg. Chem.* **2013**, 52, 8743–8749.
- [14] C. Songkram, K. Takaishi, K. Yamaguchi, H. Kagechika, Y. Endo, *Tetrahedron Lett.* **2001**, 42, 6365–6368.
- [15] H. Kawai, T. Suzuki, M. Ohkita, T. Tsuji, *Chem. Eur. J.* **2000**, 6, 4177–4187.
- [16] G. Norwitz, M. E. Everett, M. T. Gurbarg, *Thermochim. Acta* **1975**, 12, 227–232.
- [17] C. Kim, P.-Y. Huang, J.-W. Jhuang, M.-C. Chen, J.-C. Ho, T.-S. Hu, J.-Y. Yan, L.-H. Chen, G.-H. Lee, A. Facchetti, T. J. Marks, *Org. Electron.* **2010**, 11, 1363–1375.
- [18] Gaussian 09, Revision D.01, M. J. Frisch, G. W. Trucks, H. B. Schlegel, G. E. Scuseria, M. A. Robb, J. R. Cheeseman, G. Scalmani, V. Barone, B. Menonucci, G. A. Petersson, H. Nakatsuji, M. Caricato, X. Li, H. P. Hratchian, A. F. Izmaylov, J. Bloino, G. Zheng, J. L. Sonnenberg, M. Hada, M. Ehara, K. Toyota, R. Fukuda, J. Hasegawa, M. Ishida, T. Nakajima, Y. Honda, O. Kitao, H. Nakai, T. Vreven, J. A. Montgomery, Jr., J. E. Peralta, F. Ogliaro, M. Bearpark, J. J. Heyd, E. Brothers, K. N. Kudin, V. N. Staroverov, R. Kobayashi, J. Normand, K. Raghavachari, A. Rendell, J. C. Burant, S. S. Iyengar, J. Tomasi, M. Cossi, N. Rega, J. M. Millam, M. Klene, J. E. Knox, J. B. Cross, V. Bakken, C. Adamo, J. Jaramillo, R. Gomperts, R. E. Stratmann, O. Yazyev, A. J. Austin, R. Cammi, C. Pomelli, J. W. Ochterski, R. L. Martin, K. Morokuma, V. G. Zakrzewski, G. A. Voth, P. Salvador, J. J. Dannenberg, S. Dapprich, A. D. Daniels, Ö. Farkas, J. B. Foresman, J. V. Ortiz, J. Cio-slowski, D. J. Fox, Gaussian, Inc., Wallingford CT, **2009**.
- [19] H. J. Bae, H. Kim, K. M. Lee, T. Kim, Y. S. Lee, Y. Do, M. H. Lee, *Dalton Trans.* **2014**, 43, 4978–4985.

Manuscript received: June 2, 2017

Accepted manuscript online: June 26, 2017

Version of record online: July 11, 2017

## COMMUNICATION



Cite this: *Chem. Commun.*, 2017, 53, 8304

Received 9th May 2017,  
Accepted 28th June 2017

DOI: 10.1039/c7cc03615a

rsc.li/chemcomm

## A silver(i)-induced higher-ordered structure based on planar chiral tetrasubstituted [2.2]paracyclophane†

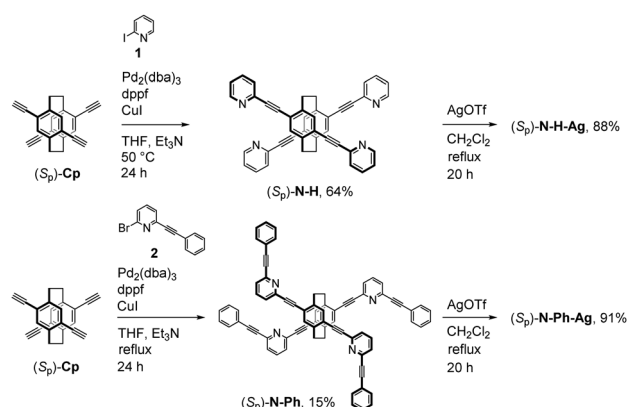
Masayuki Gon,<sup>‡</sup> Yasuhiro Morisaki<sup>‡</sup> and Yoshiki Chujo\*<sup>‡</sup>

Optically active phenylene–ethynylene dimers with pyridine groups based on a planar chiral 4,7,12,15-tetrasubstituted [2.2]paracyclophane were synthesized. The chiral conformation was controlled by pyridine–Ag(i) coordinations. After Ag(i) coordination, the resulting higher-ordered structure dramatically enhanced the signal intensity of circular dichroism (CD) and decreased that of circularly polarized luminescence (CPL).

Stimuli-responsive materials have potential for various applications to sensors,<sup>1</sup> bioprobes,<sup>2</sup> shape memory,<sup>3</sup> and self-assembly.<sup>4</sup> Especially, stimuli-responsive enantiopure compounds received much attention for next-generation materials with advanced techniques based on chirality because their chiroptical properties are informative and sensitive to structural change.<sup>5</sup> Non-covalent interaction between a substrate and an additive is often used as a stimulus and that should be effective for the dynamic control of higher-ordered formation.<sup>6</sup> Cozzi, Siegel and coworkers suggested a novel direction for the design of a double-helical structure with a chiral template and a metal-ion-coordination method.<sup>7</sup> To construct the higher-ordered structure, Ag(i)–pyridine coordination<sup>8</sup> was available because of the high affinity between Ag(i) and the nitrogen of pyridine in a dilute solution. Otera and coworkers, using the binaphthyl structure as a chiral template, constructed a double-helical structure based on rigid arylene–ethynylene groups with the pyridine–Ag(i) coordination.<sup>9</sup> They confirmed the formation of the double-helical structure with the spectral change in circular dichroism (CD) spectra. In spite of the convenience of pyridine–Ag(i) systems, optically active structures were limited. In this research, as a new chiral template, we focused

on a planar chiral 4,7,12,15-tetrasubstituted [2.2]paracyclophane framework.<sup>10,11</sup> The chirality of [2.2]paracyclophane is located in the center of the scaffold and the highly symmetrical structure has the advantage of  $\pi$ -conjugation-based chiroptical properties. Recently, our research group reported optical resolution methods of the planar chiral [2.2]paracyclophanes and revealed their unique chiroptical properties, especially the circularly polarized luminescence (CPL) properties.<sup>11a</sup> Herein, we designed a phenylene–ethynylene system containing pyridinyl groups using the planar chiral 4,7,12,15-tetrasubstituted [2.2]paracyclophane as the chiral template.

Scheme 1 shows the synthesis of the target planar chiral compounds (*S<sub>p</sub>*)-N-H, N-H-Ag, N-Ph and N-Ph-Ag from (*S<sub>p</sub>*)-4,7,12,15-tetraethynyl[2.2]paracyclophanes (*S<sub>p</sub>*)-Cp.<sup>11a</sup> In this scheme, only the reactions of the (*S<sub>p</sub>*)-isomers are shown; the (*R<sub>p</sub>*)-isomers were synthesized under the same conditions as those for (*R<sub>p</sub>*)-Cp. A Sonogashira–Hagihara coupling reaction<sup>12</sup> of (*S<sub>p</sub>*)-Cp was carried out with 2-iodopyridine **1** in the catalytic system of Pd<sub>2</sub>(dba)<sub>3</sub>/CuI using 1,1'-bis(diphenylphosphino)-ferrocene (dppf) as a phosphine ligand to obtain compound (*S<sub>p</sub>*)-N-H in 64% isolated yield. Using the same procedure, (*S<sub>p</sub>*)-N-Ph was obtained in 15% isolated yield. The reaction was carried out



Scheme 1 Synthesis of (*S<sub>p</sub>*)-N-H, N-Ph, (*S<sub>p</sub>*)-N-H-Ag and N-Ph-Ag.

Department of Polymer Chemistry, Graduate School of Engineering, Kyoto University, Katsura, Nishikyo-ku, Kyoto 615-8510, Japan.

E-mail: chujo@chujo.synchem.kyoto-u.ac.jp

† Electronic supplementary information (ESI) available. CCDC 1548564 and 1548569. For ESI and crystallographic data in CIF or other electronic format see DOI: 10.1039/c7cc03615a

‡ Present address: Department of Applied Chemistry for Environment, School of Science and Technology, Kwansai Gakuin University, 2-1 Gakuen, Sanda, Hyogo 669-1337, Japan.

under reflux conditions because the reactivity of bromide in compounds **2** was less than that of iodide in compound **1**. Using the (*S<sub>p</sub>*)-**N-H** and (*S<sub>p</sub>*)-**N-Ph**, Ag(I) coordination reactions were carried out in the presence of excess of AgOTf to obtain (*S<sub>p</sub>*)-**N-H-Ag** and (*S<sub>p</sub>*)-**N-Ph-Ag**, respectively. The structures of all new compounds in this study were confirmed by <sup>1</sup>H and <sup>13</sup>C NMR spectroscopy, high-resolution mass spectrometry (HRMS), and elemental analysis; the detailed synthetic procedures and NMR data are shown in the ESI.†

The Ag(I) coordination was confirmed by <sup>1</sup>H NMR spectra. Fig. 1 shows the <sup>1</sup>H NMR spectra of (*S<sub>p</sub>*)-**N-H**, (*S<sub>p</sub>*)-**N-H-Ag**, (*S<sub>p</sub>*)-**N-Ph** and (*S<sub>p</sub>*)-**N-Ph-Ag** in CD<sub>2</sub>Cl<sub>2</sub>. Simple <sup>1</sup>H NMR spectra were obtained both before and after the Ag(I) coordination due to the highly symmetrical structure of the tetrasubstituted [2.2]paracyclophane, which simplified the spectral analysis. The <sup>1</sup>H NMR spectrum of (*S<sub>p</sub>*)-**N-H-Ag** indicated downfield shifts of H<sub>a</sub>, H<sub>b</sub>, H<sub>c</sub> and H<sub>d</sub> relative to those of (*S<sub>p</sub>*)-**N-H**. The pyridine units, H<sub>a</sub>, H<sub>b</sub>, and H<sub>c</sub>, were downfield-shifted relative to those of (*S<sub>p</sub>*)-**N-Ph**. On the other hand, H<sub>d</sub> and H<sub>e</sub> showed clear upfield shifts. This is because of the shield effect of the benzene rings due to the face-to-face structure. H<sub>f</sub> exhibited almost the same chemical shift. It is considered that the downfield shift by Ag(I) coordination and the upfield shift by the benzene rings might be balanced. H' denotes aromatic protons of [2.2]paracyclophane. The difference in solubility also suggested the formation of the Ag(I) complexation. (*S<sub>p</sub>*)-**N-H-Ag** was dissolved in CH<sub>3</sub>CN, whereas (*S<sub>p</sub>*)-**N-H** was not dissolved in CH<sub>3</sub>CN. (*S<sub>p</sub>*)-**N-Ph-Ag** was dissolved in MeOH, whereas (*S<sub>p</sub>*)-**N-Ph** was not dissolved in MeOH. Although HRMS spectra detected the Ag(I)-coordinated species, only the mono-coordinated ones were monitored.<sup>9</sup> (*R<sub>p</sub>*)-Isomers showed the same behaviors as those of (*S<sub>p</sub>*)-isomers.

The structure of *rac*-**N-H-Ag** was confirmed by a single crystal X-ray analysis. Fig. 2 shows ORTEP drawings of *rac*-**N-H** and *rac*-**N-H-Ag**. Four nitrogen atoms of *rac*-**N-H** directed outside of the structure, whereas the nitrogen atoms of *rac*-**N-H-Ag** directed inside of the structure. Two nitrogen atoms of pyridine groups were coordinated to Ag(I) with the *trans* geometry. The angle of N(1)-Ag(1)-N(2) was found to be 174.7°, whereas that of N(3)-Ag(2)-N(4) was 161.6° to form a slightly bent structure because of the interaction between the OTf group and Ag(I).

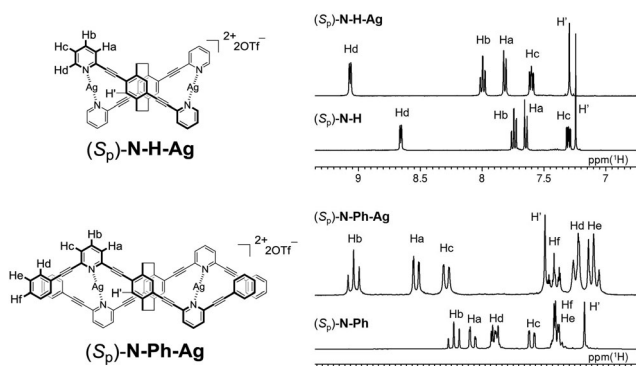


Fig. 1 <sup>1</sup>H NMR spectra of (A) (*S<sub>p</sub>*)-**N-H** and (*S<sub>p</sub>*)-**N-H-Ag**, (B) (*S<sub>p</sub>*)-**N-Ph** and (*S<sub>p</sub>*)-**N-Ph-Ag** in CD<sub>2</sub>Cl<sub>2</sub>.

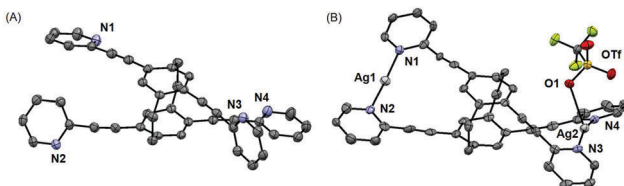


Fig. 2 ORTEP drawings of (A) *rac*-**N-H** and (B) *rac*-**N-H-Ag** (50% probability for thermal ellipsoids). Hydrogen atoms, CH<sub>2</sub>Cl<sub>2</sub> and one of the OTf groups are omitted for clarity. All data are shown in the ESI.†

As a result, the structure of *rac*-**N-H-Ag** was constructed by taking two Ag(I)s into *rac*-**N-H**. In this research, the single crystal X-ray structure of **N-Ph-Ag** was not obtained. Judging from the crystal structure of **N-H-Ag** and the chemical shifts of <sup>1</sup>H NMR, the two pyridyl groups should coordinate to the Ag(I) in a linear fashion in the structure of **N-Ph-Ag**. The details and plausible structure are discussed in another section.

The optical properties of both enantiomers **N-H** and **N-Ph** as well as their Ag(I) complexes **N-Ag** and **N-Ph-Ag** were evaluated. The optical and chiroptical data are summarized in Table 1. The UV-vis absorption spectra and the photoluminescence (PL) spectra were obtained in dilute CH<sub>2</sub>Cl<sub>2</sub> solutions ( $1.0 \times 10^{-5}$  M). Fig. S9 (ESI†) and the bottom spectra of Fig. 3 show the UV-vis absorption spectra of **N-H** and **N-Ph**, and the Ag(I) complexes, **N-H-Ag** and **N-Ph-Ag**. All of the absorption spectra changed after Ag(I) coordination. The absorption spectra of Ag(I) complexes exhibited a bathochromic shift compared with those of non-coordination compounds due to the increase in planarity (Fig. 2). It was estimated that the predicted conformation of **N-Ph-Ag** had  $\pi$ - $\pi$  stacking at the edge of the benzene rings. However, the interaction was too weak to detect the UV-vis absorption spectra. Fig. S10 (ESI†) and the bottom spectra of Fig. 4 show the PL spectra of **N-H**, **N-Ph**, **N-Ag** and **N-Ph-Ag**. In the PL spectrum of **N-Ag**, a little bathochromic shift compared with that of **N-H** was observed owing to the difference of the planarity. **N-Ph** showed almost the same properties as those of **N-H**.

The chiroptical properties of the ground and excited states of (*S<sub>p</sub>*)- and (*R<sub>p</sub>*)-**N-H** and **N-Ph**, (*S<sub>p</sub>*)- and (*R<sub>p</sub>*)-**N-H-Ag** and **N-Ph-Ag** were investigated by CD and CPL spectroscopies. The spectra were obtained in dilute CH<sub>2</sub>Cl<sub>2</sub> solutions ( $1.0 \times 10^{-5}$  M). Chiroptical data, such as the dissymmetry factor<sup>13</sup> of absorbance ( $g_{\text{abs}}$ ) and that of luminescence ( $g_{\text{lum}}$ ), are summarized in Table 1. Fig. 3 shows the CD and UV-vis absorption spectra of (*S<sub>p</sub>*)- and (*R<sub>p</sub>*)-**N-H** and **N-Ph**, and the Ag(I) complexes, (*S<sub>p</sub>*)- and (*R<sub>p</sub>*)-**N-H-Ag** and **N-Ph-Ag**. In all cases, mirror-image Cotton effects were observed in the CD spectra. The shapes of the spectra of (*S<sub>p</sub>*)-**N-H** and (*S<sub>p</sub>*)-**N-H-Ag** were similar. This is because some conformational change was observed in the ground state as shown in the results of the single crystal X-ray analysis. On the other hand, the maximum absolute  $g_{\text{abs}}$  value of (*S<sub>p</sub>*)-**N-Ph** was enhanced after the Ag(I) coordination. The maximum absolute  $g_{\text{abs}}$  values were estimated to be  $4.1 \times 10^{-3}$  for (*S<sub>p</sub>*)-**N-H**,  $4.6 \times 10^{-3}$  for (*S<sub>p</sub>*)-**N-Ag**,  $2.5 \times 10^{-3}$  for (*S<sub>p</sub>*)-**N-Ph** and  $7.0 \times 10^{-3}$  for (*S<sub>p</sub>*)-**N-Ph-Ag**, suggesting the major structural change between **N-Ph** and **N-Ph-Ag** in the ground state. Fig. 4 shows the CPL and

Table 1 Optical properties: spectroscopic data

	$\lambda_{\text{abs}}^a/\text{nm}$	$\lambda_{\text{lum}}^a/\text{nm}$	$\Phi_{\text{lum}}^b$	$ g_{\text{abs,max}} ^{c,d}/10^{-3}$	$g_{\text{abs}}^{c,e}/10^{-3}$	$g_{\text{lum}}^{c,e}/10^{-3}$ at $\lambda_{\text{lum}}$
$(S_p)$ - <b>N-H</b>	342	421	0.59	4.1	-1.8	-2.8
$(S_p)$ - <b>N-H-Ag</b>	378	427	0.24	4.6	-2.8	-2.5
$(S_p)$ - <b>N-Ph</b>	276, 356	417	0.56	2.5	-0.74	-1.2, +0.25 (at 524 nm)
$(S_p)$ - <b>N-Ph-Ag</b>	285, 393	424	0.35	7.0	+2.6	+0.27 (at 476 nm)

<sup>a</sup> In  $\text{CH}_2\text{Cl}_2$  ( $1.0 \times 10^{-5}$  M); excited at absorption maxima for PL. <sup>b</sup> Absolute PL quantum efficiency. <sup>c</sup> Ref. 13. <sup>d</sup> Maximum value of  $g_{\text{abs}}$ . <sup>e</sup> At the first Cotton effect.

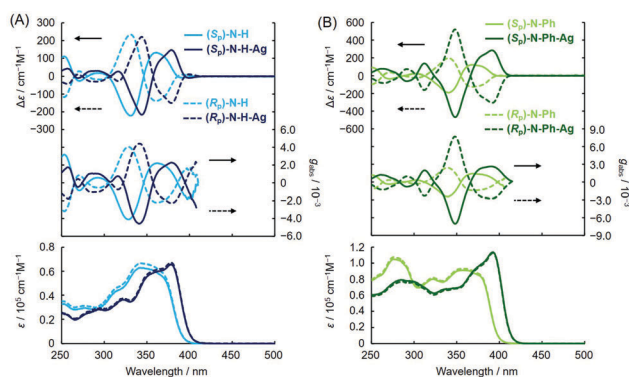


Fig. 3 CD (top),  $g_{\text{abs}}$  (middle), and UV-vis absorption (bottom) spectra of (A) **N-H**, **N-H-Ag**, (B) **N-Ph**, **N-Ph-Ag** in dilute  $\text{CH}_2\text{Cl}_2$  ( $1.0 \times 10^{-5}$  M).

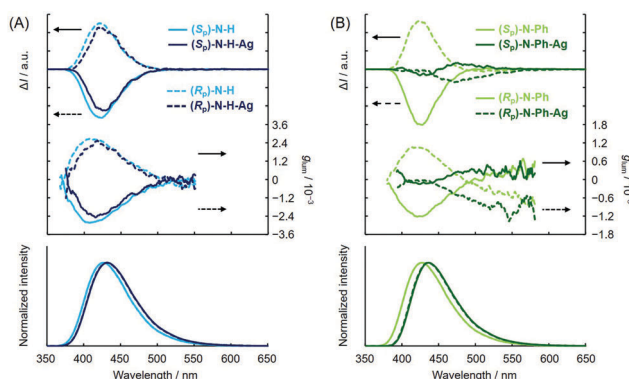


Fig. 4 CPL (top),  $g_{\text{lum}}$  (middle), and PL (bottom) spectra of (A) **N-H** and **N-H-Ag**, (B) **N-Ph** and **N-Ph-Ag** in dilute  $\text{CH}_2\text{Cl}_2$  ( $1.0 \times 10^{-5}$  M). Excitation wavelength was 300 nm.

PL spectra of  $(S_p)$ - and  $(R_p)$ -**N-H** and **N-Ph**,  $(S_p)$ - and  $(R_p)$ -**N-H-Ag** and **N-Ph-Ag**. Mirror-image CPL spectra were observed for the enantiomers. The shapes of the CPL spectra of  $(S_p)$ -**N-H** and  $(S_p)$ -**N-H-Ag** were similar with the same reason as the CD results. In the  $(S_p)$ -**N-Ph** system, two peaks were observed. One was a strong negative signal at around 420 nm ( $g_{\text{lum}} = -1.2 \times 10^{-3}$ ) and the other was a weak positive signal at around 530 nm ( $g_{\text{lum}} = +0.25 \times 10^{-3}$ ). The former was derived from the same structure with  $(S_p)$ -**N-H**. The latter might be derived from the  $\pi$ - $\pi$  interaction of phenylene-ethynylene moieties. Indeed, from a PL lifetime measurement monitored at 600 nm, the second and longer fluorescence lifetime component was detected (Fig. S11, ESI<sup>†</sup>). The difference of signal of the first Cotton effect from CD and CPL of  $(S_p)$ -**N-Ph** suggested the different formation in the

ground state and in the excited state. Interestingly, the CPL signal of  $(S_p)$ -**N-Ph-Ag** was nearly silent at the PL peak top, and the  $g_{\text{lum}}$  value of the longer wavelength (around 530 nm) was similar to that of  $(S_p)$ -**N-Ph**. It is difficult to understand the reason for the disappearance of the CPL signal. One of the reasons that should be considered is that the first Cotton effect of the CD spectra disappeared in comparison with that of  $(S_p)$ -**N-Ph**. That is, the resulting folded conformation decreased the CPL signal from the [2.2]paracyclophane scaffold. Therefore, we might detect the only CPL signal derived from the  $\pi$ - $\pi$  interaction of phenylene-ethynylene moieties. The signs of the first Cotton effect of CD and more intense signals of CPL spectra of  $(S_p)$ -**N-H**, **N-H-Ag** and **N-Ph** were identical.<sup>14</sup> However, since the bands were too weak to observe from Fig. 3 and 4, expanded views are added as Fig. S18 (ESI<sup>†</sup>).

Fig. S12 (ESI<sup>†</sup>) shows the predicted structures of the  $\text{Ag}(I)$  complexes. Two conformations are considered to be plausible higher-ordered structures; one is a zigzag type and the other is a double-helical type because a symmetrical structure is suggested by  $^1\text{H}$  and  $^{13}\text{C}$  NMR spectra in the dilute solution. The experimental result that the excimer of  $(S_p)$ -**N-Ph** showed the same sign at the first Cotton effect with  $(S_p)$ -**N-Ph-Ag** in the CPL spectra supported the zigzag conformation because the double-helical formation is difficult to construct in the excited state of  $(S_p)$ -**N-Ph**. The energy of the ground-state structure of the double-helical conformation was estimated to be more stable by  $44.0 \text{ kJ mol}^{-1}$  than that of the zigzag conformation from density functional theory (DFT) (Fig. S13, ESI<sup>†</sup>). The difference of the energy is enough to form the double-helical conformation dominantly. In addition, the double-helical structure is obviously less distorted when compared with the crystal structure of **N-H-Ag**. Therefore, both conformations are acceptable and it is difficult to decide which one is dominant in the solution. The structure is still under investigation.

In order to reveal the coordination behavior, the titration of the  $\text{AgOTf}$  solution to  $(S_p)$ -**N-H** and **N-Ph** was carried out in a dilute mixed  $\text{CH}_2\text{Cl}_2/\text{DMF} = 95/5$  v/v solution ( $1.0 \times 10^{-5}$  M). DMF was used for the preparation of the  $\text{AgOTf}$  solution because  $\text{CH}_2\text{Cl}_2$  is not a good solvent for  $\text{AgOTf}$ . Fig. S14 and S15 (ESI<sup>†</sup>) show the results of the titration of  $(S_p)$ -**N-H** and **N-Ph** monitored using the CD and CPL spectra, respectively. As a result, the spectral change was completed by the addition of about 5.0 eq. of  $\text{AgOTf}$  and the final spectra shape was identified with those of  $(S_p)$ -**N-H-Ag** and **N-Ph-Ag** discussed in the above section. Interestingly, the  $g_{\text{abs}}$  and  $g_{\text{lum}}$  values of  $(S_p)$ -**N-H** were lowered by 2.0 eq. titration of  $\text{AgOTf}$  and that was

recovered by 4.0 eq. titration of AgOTf (Fig. S14, ESI†). The mono-coordinate asymmetry species might reduce the chirality in the excited state. In all cases, 5.0 eq. of AgOTf was necessary for finishing the titration (Fig. S19, ESI†) and that was excess of the coordination number predicted from the single crystal X-ray analysis of (*S<sub>p</sub>*)-**N-H**. This is because the coordination is not as strong as the quantitative coordination. The contribution of Ag(I)- $\pi$  interaction<sup>6j,15</sup> might be considerable. From those results, it was confirmed that the spectral change was caused by the Ag(I) coordination and the chirality was gradually enhanced by constructing a higher-ordered structure in the ground state. The same titration spectra of (*R<sub>p</sub>*)-isomers are shown in Fig. S16 and S17 (ESI†), and mirror-image results as the (*S<sub>p</sub>*)-isomers were observed.

In summary, enantiopure phenylene-ethynylene dimers with pyridine groups based on a planar chiral 4,7,12,15-tetra-substituted[2.2]paracyclophane were synthesized. Comparing the **N-H** system with the **N-Ph** one, the large conformational change and the resulting higher-ordered structure varied with the chiroptical properties. In this research, we succeeded in observing a large enhancement in signal intensity of the CD and the disappearance of the signal of the CPL. The experimental data and theoretical calculations provided a zigzag or a double-helical conformation in the **N-Ph-Ag** system as the plausible higher-ordered structure. Transient change of chirality was observed by the titration of AgOTf and the final spectra were identified with the spectra of Ag(I) coordination structures. This study is useful for the applications of the dimers to chiral-based switching materials, such as chiroptical sensing systems.

This work was supported by Grant-in-Aid for Young Scientists (A) (no. 24685018) from the Ministry of Education, Culture, Sports, Science and Technology (MEXT) of Japan. M. G. appreciates Research Fellowships (no. 14J02514) from the Japan Society for the Promotion of Science for Young Scientists. The authors are grateful to Professor Kazuo Akagi and Dr Kazuyoshi Watanabe (Department of Polymer Chemistry, Graduate School of Engineering, Kyoto University) for CPL data analysis and valuable discussions.

## Notes and references

- (a) M. Akita, *Organometallics*, 2011, **30**, 43–51; (b) Y. Sagara and T. Kato, *Nat. Chem.*, 2009, **1**, 605–610.
- H. Shigemitsu and I. Hamachi, *Chem. – Asian J.*, 2015, **10**, 2026–2038.
- H. Meng and G. Li, *Polymer*, 2013, **54**, 2199–2221.
- (a) A. J. McConnell, C. S. Wood, P. P. Neelakandan and J. R. Nitschke, *Chem. Rev.*, 2015, **115**, 7729–7793; (b) Z. Qi and C. A. Schalley, *Acc. Chem. Res.*, 2014, **47**, 2222–2233; (c) X. Yan, F. Wang, B. Zheng and F. Huang, *Chem. Soc. Rev.*, 2012, **41**, 6042–6065.
- (a) G. A. Hembury, V. V. Borovkov and Y. Inoue, *Chem. Rev.*, 2008, **108**, 1–73; (b) M. Iwamura, Y. Kimura, R. Miyamoto and K. Nozaki, *Inorg. Chem.*, 2012, **51**, 4094–4098; (c) H. Maeda and Y. Bando, *Pure Appl. Chem.*, 2013, **85**, 1967–1978; (d) M. Liu, L. Zhang and T. Wang, *Chem. Rev.*, 2015, **115**, 7304–7397; (e) L. Liu, N. Ousaka, M. Horie, F. Mamiya and E. Yashima, *Chem. Commun.*, 2016, **52**, 11752–11755; (f) Y. Suzuki, T. Nakamura, H. Iida, N. Ousaka and E. Yashima, *J. Am. Chem. Soc.*, 2016, **138**, 4852–4859; (g) S. Yamamoto, H. Iida and E. Yashima, *Angew. Chem., Int. Ed.*, 2013, **52**, 6849–6853.
- (a) Y. Haketa, Y. Bando, K. Takaishi, M. Uchiyama, A. Muranaka, M. Naito, H. Shibaguchi, T. Kawai and H. Maeda, *Angew. Chem., Int. Ed.*, 2012, **51**, 7967–7971; (b) H. Maeda, W. Hane, Y. Bando, Y. Terashima, Y. Haketa, H. Shibaguchi, T. Kawai, M. Naito, K. Takaishi, M. Uchiyama and A. Muranaka, *Chem. – Eur. J.*, 2013, **19**, 16263–16271; (c) H. Maeda, T. Shirai, Y. Bando, K. Takaishi, M. Uchiyama, A. Muranaka, T. Kawai and M. Naito, *Org. Lett.*, 2013, **15**, 6006–6009; (d) H. Maeda, T. Nishimura, A. Tsujii, K. Takaishi, M. Uchiyama and A. Muranaka, *Chem. Lett.*, 2014, **43**, 1078–1080; (e) S. Sairenji, S. Akine and T. Nabeshima, *Dalton Trans.*, 2016, **45**, 14902–14906; (f) S. Akine, S. Sairenji, T. Taniguchi and T. Nabeshima, *J. Am. Chem. Soc.*, 2013, **135**, 12948–12951; (g) S. Akine, S. Hotate and T. Nabeshima, *J. Am. Chem. Soc.*, 2011, **133**, 13868–13871; (h) M. Yamamura, J. Miyake, Y. Imamura and T. Nabeshima, *Chem. Commun.*, 2011, **47**, 6801–6803; (i) S. Akine, T. Matsumoto and T. Nabeshima, *Chem. Commun.*, 2008, 4604–4606; (j) S. P. Morcillo, D. Miguel, L. Alvarez de Cienfuegos, J. Justicia, S. Abbate, E. Castiglioni, C. Bour, M. Ribagorda, D. J. Cardenas, J. M. Paredes, L. Crovotto, D. Choquesillo-Lazarte, A. J. Mota, M. C. Carreno, G. Longhi and J. M. Cuerva, *Chem. Sci.*, 2016, **7**, 5663–5670.
- (a) C. R. Woods, M. Benaglia, J. S. Siegel and F. Cozzi, *Angew. Chem., Int. Ed. Engl.*, 1996, **35**, 1830–1833; (b) R. Annunziata, M. Benaglia, M. Cinquini, F. Cozzi, C. R. Woods and J. S. Siegel, *Eur. J. Org. Chem.*, 2001, 173–180.
- (a) Q. Li, F. Huang, Y. Fan, Y. Wang, J. Li, Y. He and H. Jiang, *Eur. J. Inorg. Chem.*, 2014, 3235–3244; (b) N. Schultheiss, C. L. Barnes and E. Bosch, *Cryst. Growth Des.*, 2003, **3**, 573–580; (c) P. Sengupta, H. Zhang and D. Y. Son, *Inorg. Chem.*, 2004, **43**, 1828–1830; (d) E. Bosch, C. L. Barnes, N. L. Brennan, G. L. Eakins and B. E. Breyfogle, *J. Org. Chem.*, 2008, **73**, 3931–3934; (e) N. L. Brennan, C. L. Barnes and E. Bosch, *Inorg. Chim. Acta*, 2010, **363**, 3987–3992; (f) K. J. Kilpin, M. L. Gower, S. G. Telfer, G. B. Jameson and J. D. Crowley, *Inorg. Chem.*, 2011, **50**, 1123–1134; (g) Q. Ren, C. G. Reedy, E. A. Terrell, J. M. Wieting, R. W. Wagie, J. P. Asplin, L. M. Doyle, S. J. Long, M. T. Everard, J. S. Sauer, C. E. Baumgart, J. S. D'Acchioli and N. P. Bowling, *J. Org. Chem.*, 2012, **77**, 2571–2577.
- A. Orita, T. Nakano, D. L. An, K. Tanikawa, K. Wakamatsu and J. Otera, *J. Am. Chem. Soc.*, 2004, **126**, 10389–10396.
- (a) F. Vögtle, *Cyclophane Chemistry: Synthesis, Structures and Reactions*, John Wiley & Sons, Chichester, 1993; (b) *Modern Cyclophane Chemistry*, ed. R. Gleiter and H. Hopf, Wiley-VCH, Weinheim, Germany, 2004.
- (a) Y. Morisaki, M. Gon, T. Sasamori, N. Tokitoh and Y. Chujo, *J. Am. Chem. Soc.*, 2014, **136**, 3350–3353; (b) M. Gon, Y. Morisaki and Y. Chujo, *J. Mater. Chem. C*, 2015, **3**, 521–529; (c) M. Gon, Y. Morisaki and Y. Chujo, *Eur. J. Org. Chem.*, 2015, 7756–7762; (d) M. Gon, Y. Morisaki, R. Sawada and Y. Chujo, *Chem. – Eur. J.*, 2016, **22**, 2291–2298; (e) M. Gon, H. Kozuka, Y. Morisaki and Y. Chujo, *Asian J. Org. Chem.*, 2016, **5**, 353–359; (f) Y. Morisaki, R. Sawada, M. Gon and Y. Chujo, *Chem. – Asian J.*, 2016, **11**, 2524–2527; (g) M. Gon, R. Sawada, Y. Morisaki and Y. Chujo, *Macromolecules*, 2017, **50**, 1790–1802; (h) M. Gon, Y. Morisaki and Y. Chujo, *Chem. – Eur. J.*, 2017, **23**, 6323–6329.
- (a) Y. Tohda, K. Sonogashira and N. Hagihara, *Tetrahedron Lett.*, 1975, **16**, 4467–4470; (b) K. Sonogashira, in *Handbook of Organopalladium Chemistry for Organic Synthesis*, ed. E. Negishi, Wiley-Interscience, New York, 2002, pp. 493–529.
- $g_{\text{abs}} = \Delta\epsilon/\epsilon$  ( $\Delta\epsilon = \epsilon_{\text{left}} - \epsilon_{\text{right}}$ ).  $\epsilon_{\text{left}}$  and  $\epsilon_{\text{right}}$  indicate absorbances of left and right handed circularly polarized light, respectively.  $g_{\text{lum}} = \Delta I/I$  ( $\Delta I = I_{\text{left}} - I_{\text{right}}$ ).  $I_{\text{left}}$  and  $I_{\text{right}}$  indicate luminescence intensities of left and right handed CPL, respectively.
- (a) S. Abbate, G. Longhi, F. Lebon, E. Castiglioni, S. Superchi, L. Pisani, F. Fontana, F. Torricelli, T. Caronna, C. Villani, R. Sabia, M. Tommasini, A. Lucotti, D. Mendola, A. Mele and D. A. Lightner, *J. Phys. Chem. C*, 2014, **118**, 1682–1695; (b) Y. Liu, J. Cerezo, G. Mazzeo, N. Lin, X. Zhao, G. Longhi, S. Abbate and F. Santoro, *J. Chem. Theory Comput.*, 2016, **12**, 2799–2819.
- (a) M. Munakata, L. P. Wu and G. L. Ning, *Coord. Chem. Rev.*, 2000, **198**, 171–203; (b) V. J. Chebny and R. Rathore, *J. Am. Chem. Soc.*, 2007, **129**, 8458–8465; (c) J. M. Maier, P. Li, J. Hwang, M. D. Smith and K. D. Shimizu, *J. Am. Chem. Soc.*, 2015, **137**, 8014–8017; (d) A. Martin-Lasanta, L. Alvarez de Cienfuegos, A. Johnson, D. Miguel, A. J. Mota, A. Orte, M. J. Ruedas-Rama, M. Ribagorda, D. J. Cardenas, M. Carmen Carreno, A. M. Echavarren and J. M. Cuerva, *Chem. Sci.*, 2014, **5**, 4582–4591.

# Oxygen-Bridged Diphenylnaphthylamine as a Scaffold for Full-Color Circularly Polarized Luminescent Materials

Hidetaka Nishimura,<sup>†</sup> Kazuo Tanaka,<sup>‡</sup> Yasuhiro Morisaki,<sup>§</sup> Yoshiki Chujo,<sup>‡</sup> Atsushi Wakamiya,<sup>\*,†,||</sup> and Yasujiro Murata<sup>\*,†</sup>

<sup>†</sup>Institute for Chemical Research, Kyoto University, Uji, Kyoto 611-0011, Japan

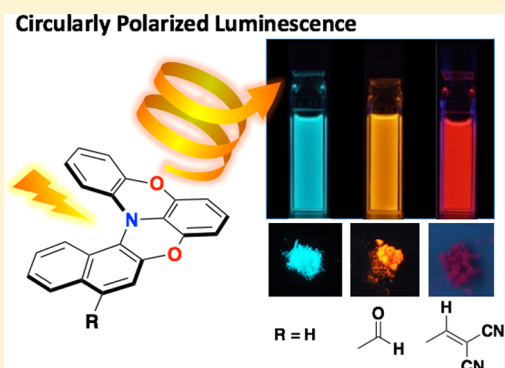
<sup>‡</sup>Department of Polymer Chemistry, Graduate School of Engineering, Kyoto University, Katsura, Nishikyo-ku, Kyoto 615-8510, Japan

<sup>§</sup>Department of Applied Chemistry for Environment, School of Science and Technology, Kwansai Gakuin University, 2-1 Gakuen, Sanda, Hyogo 669-1337, Japan

<sup>||</sup>Precursory Research for Embryonic Science and Technology (PRESTO) Japan Science and Technology Agency, 4-1-8 Honcho, Kawaguchi, Saitama 332-0012, Japan

## Supporting Information

**ABSTRACT:** An oxygen-bridged diphenylnaphthylamine with a helical shape was designed and synthesized as a key scaffold for circularly polarized luminescent (CPL) materials. The introduction of electron-withdrawing groups, such as formyl and 2,2-dicyanovinyl substituents at the naphthyl moiety in this skeleton effectively decreases the LUMO level and thus allows a tuning of the band gap. The prepared model compounds exhibit intense CPL signals with a dissymmetry factor ( $g$  value) of  $10^{-3}$  both in  $\text{CH}_2\text{Cl}_2$  solutions and in the solid states. The emission colors of these derivatives are influenced both by the substituents as well as by solvent effects, covering the whole visible region from blue to deep red.



## INTRODUCTION

Circularly polarized luminescence (CPL) refers to the differential emission of right- and left-handed circularly polarized light by chiral molecular systems,<sup>1</sup> and has attracted substantial attention on account of numerous potential applications, such as 3D optical displays,<sup>2</sup> CPL lasers,<sup>3</sup> chiral recognition,<sup>4</sup> and asymmetric photosynthesis.<sup>5</sup> Several types of CPL-emitting organic molecules have been developed so far, and these can be classified into small organic molecules,<sup>6</sup> polymers,<sup>7</sup> transition metal complexes,<sup>8</sup> and lanthanide complexes.<sup>4c,9</sup> Among these, small organic molecules have the advantage that their photophysical properties can be potentially tuned by the structural design. Nevertheless, examples of materials, whose CPL wavelength is tunable, are still limited.<sup>6b,i,7f,i</sup>

We have recently reported the synthesis of a partially oxygen-bridged triphenylamine as a key skeleton for hole-transporting materials, in which three benzene rings are constrained in a quasiplanar structure by two oxygen-tethers.<sup>10</sup> In addition to their hole-transporting ability, these compounds display intense fluorescence, thus promising potential as emissive materials. DFT calculations at the B3LYP/6-31G(d) level of theory suggested an inversion energy of 9.1 kcal/mol for the flipping of the nontethered phenyl rings in this skeleton, indicating that the two phenyl rings can easily flip in the gas phase or in solution at ambient temperature. Upon expanding the skeleton and thus increasing the steric hindrance, the ring flipping can be

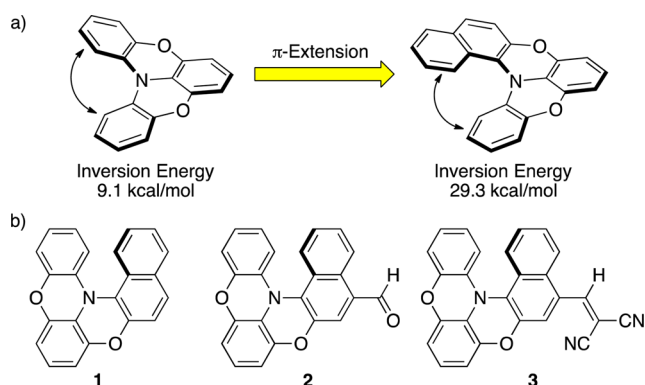
suppressed to allow isolation of the corresponding helical isomers. For example, DFT calculations suggested that the replacement of one phenyl ring with a naphthyl ring in this oxygen-bridged triphenylamine skeleton increases the inversion barrier to 29.3 kcal/mol, indicating the possibility of optical resolution for this skeleton (Figure 1a).

Considering the intense fluorescence of oxygen-bridged triarylamines, this skeleton can be used as a scaffold for CPL materials. Based on this notion, we have designed and synthesized oxygen-bridged diphenylnaphthylamine **1** and its derivatives **2–3**, which contain electron-withdrawing groups at the naphthyl ring (Figure 1b). We anticipated that the introduction of the naphthyl ring into this asymmetric system, together with varying substituents attached should induce deflection in the HOMO and LUMO to enhance the intramolecular charge transfer character, which should enable the development of emission-color-tunable CPL systems.

**Synthesis of Oxygen-Bridged Diphenylnaphthylamine Derivatives.** Oxygen-bridged diphenylnaphthylamine **1** was synthesized by our previously reported method, using a stepwise N-arylation followed by a 2-fold intramolecular nucleophilic aromatic cyclization (Scheme 1a).<sup>10</sup> A Buchwald–Hartwig arylation of 2,6-difluoroaniline with *o*-iodoani-

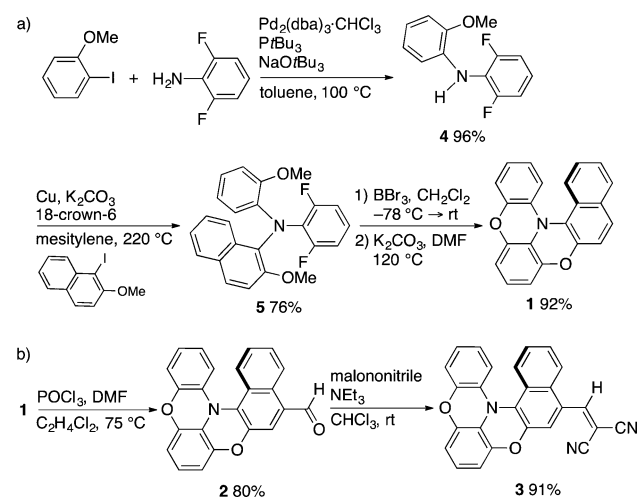
Received: March 2, 2017

Published: April 21, 2017



**Figure 1.** (a) Molecular design for the CPL materials in this study, together with calculated ring inversion energies. (b) Chemical structures of 1–3.

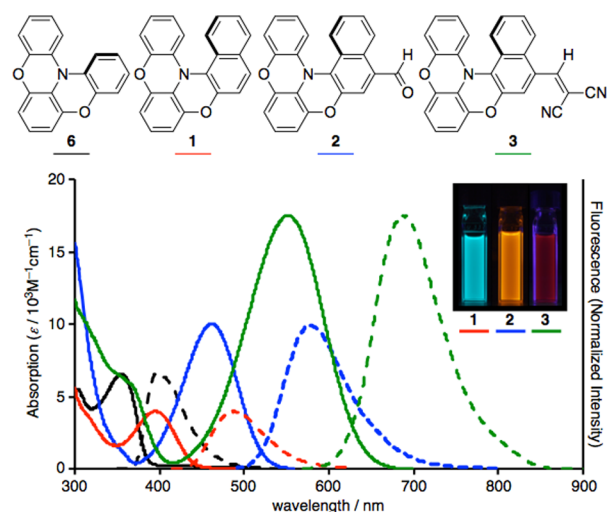
### Scheme 1. Synthesis of 1–3



sole selectively afforded monoarylated difluoroaniline **4** in 96% yield. Subsequently, an Ullmann arylation of **4** with 1-iodo-2-methoxynaphthalene<sup>11</sup> using Cu and K<sub>2</sub>CO<sub>3</sub> furnished bisarylated difluoroaniline **5** in 76% yield. After removal of the methyl groups in **5** with BBr<sub>3</sub>, treatment with K<sub>2</sub>CO<sub>3</sub> in DMF at 120 °C yielded oxygen-bridged diphenyl-naphthylamine **1** as yellow solids in 92%.

Derivatives **2** and **3**, which are functionalized at the 4-position of the naphthyl moiety, were easily prepared by subjecting **1** to the selective Vilsmeier–Haack reaction (Scheme 1b). Accordingly, treatment of **1** with POCl<sub>3</sub> in DMF selectively afforded monoformyl derivative **2** in 80% yield as orange solids. The reaction of **2** with malononitrile in the presence of triethylamine afforded mono-2,2-dicyanovinyl derivative **3** in 91% yield as purple solids. Compounds **1–3** were characterized by NMR spectroscopy, HRMS, and elemental analysis.

**Photophysical Properties in CH<sub>2</sub>Cl<sub>2</sub>.** Subsequently, we examined the photophysical properties of **1–3** in CH<sub>2</sub>Cl<sub>2</sub> (Figure 2, Table 1). In UV–vis absorption spectrum, diphenyl-naphthylamine **1** shows a relatively weak absorption band at  $\lambda_{\text{abs}} = 395$  nm ( $\log \epsilon = 3.60$ ), which is red-shifted by 40 nm compared to that of oxygen-bridged triphenylamine **6** ( $\lambda_{\text{abs}} = 355$  nm,  $\log \epsilon = 3.81$ ). Furthermore, formyl derivative **2** ( $\lambda_{\text{abs}} = 461$  nm,  $\log \epsilon = 4.00$ ) and 2,2-dicyanovinyl derivative **3** ( $\lambda_{\text{abs}} = 552$  nm,  $\log \epsilon = 4.24$ ) display significant bathochromic shifts



**Figure 2.** UV–vis absorption spectra (solid line) and fluorescence spectra (dashed line) of 1–3 and **6** in CH<sub>2</sub>Cl<sub>2</sub>. The photograph shows the emission of 1–3.

**Table 1.** Photophysical Parameters for 1–3 and **6** in CH<sub>2</sub>Cl<sub>2</sub><sup>a</sup>

	$\lambda_{\text{abs}}$ [nm] ( $\log \epsilon$ )	$\lambda_{\text{em}}$ [nm]	$\Phi^b$	$\tau$ [s]	$k_r$ [s <sup>-1</sup> ]	$k_{\text{nr}}$ [s <sup>-1</sup> ]
1	395 (3.60)	488	0.86	25.4	$3.4 \times 10^7$	$5.5 \times 10^6$
2	461 (4.00)	580	0.44	6.76	$6.5 \times 10^7$	$8.3 \times 10^7$
3	552 (4.24)	685	0.09	1.16	$7.8 \times 10^7$	$7.8 \times 10^8$
6	355 (3.81)	399	0.19	3.43	$5.5 \times 10^7$	$2.4 \times 10^8$

<sup>a</sup> $c = 10^{-5}$  M. <sup>b</sup>Absolute quantum yields determined by a calibrated sphere system.

of their absorption bands, accompanied by increased molar absorption coefficients.

In the fluorescence spectra obtained from these CH<sub>2</sub>Cl<sub>2</sub> solutions, triphenylamine **6** shows moderate emission at  $\lambda_{\text{em}} = 399$  nm ( $\Phi = 0.19$ ,  $\tau = 3.43$  ns; Table 1), while diphenyl-naphthylamine **1** exhibits an intense blueish green emission at  $\lambda_{\text{em}} = 488$  nm ( $\Phi = 0.86$ ) with a large Stokes shift (4825 cm<sup>-1</sup>). The lifetime of this emission ( $\tau = 25.4$  ns) is relatively long compared to other  $\pi$ -conjugated systems. The introduction of electron-withdrawing groups into formyl derivative **2** and 2,2-dicyanovinyl derivative **3** cause a significant red-shift on their emission bands at  $\lambda_{\text{em}} = 580$  nm (orange,  $\Phi = 0.44$ ,  $\tau = 6.76$  ns) and  $\lambda_{\text{em}} = 685$  nm (deep red,  $\Phi = 0.09$ ,  $\tau = 1.16$  ns), respectively. These are red-shifted by 92 and 197 nm relative to that of **1**, respectively, while maintaining large Stokes shifts of 4451 for **2** and 3517 cm<sup>-1</sup> for **3**, respectively. Under these conditions, radiative ( $k_r$ ) and nonradiative ( $k_{\text{nr}}$ ) rate constants were determined;  $k_r = 3.4 \times 10^7$  s<sup>-1</sup> and  $k_{\text{nr}} = 5.5 \times 10^6$  s<sup>-1</sup> for **1**,  $k_r = 6.5 \times 10^7$  s<sup>-1</sup> and  $k_{\text{nr}} = 8.3 \times 10^7$  s<sup>-1</sup> for **2**, as well as  $k_r = 7.8 \times 10^7$  s<sup>-1</sup> and  $k_{\text{nr}} = 7.8 \times 10^8$  s<sup>-1</sup> for **3**, respectively.

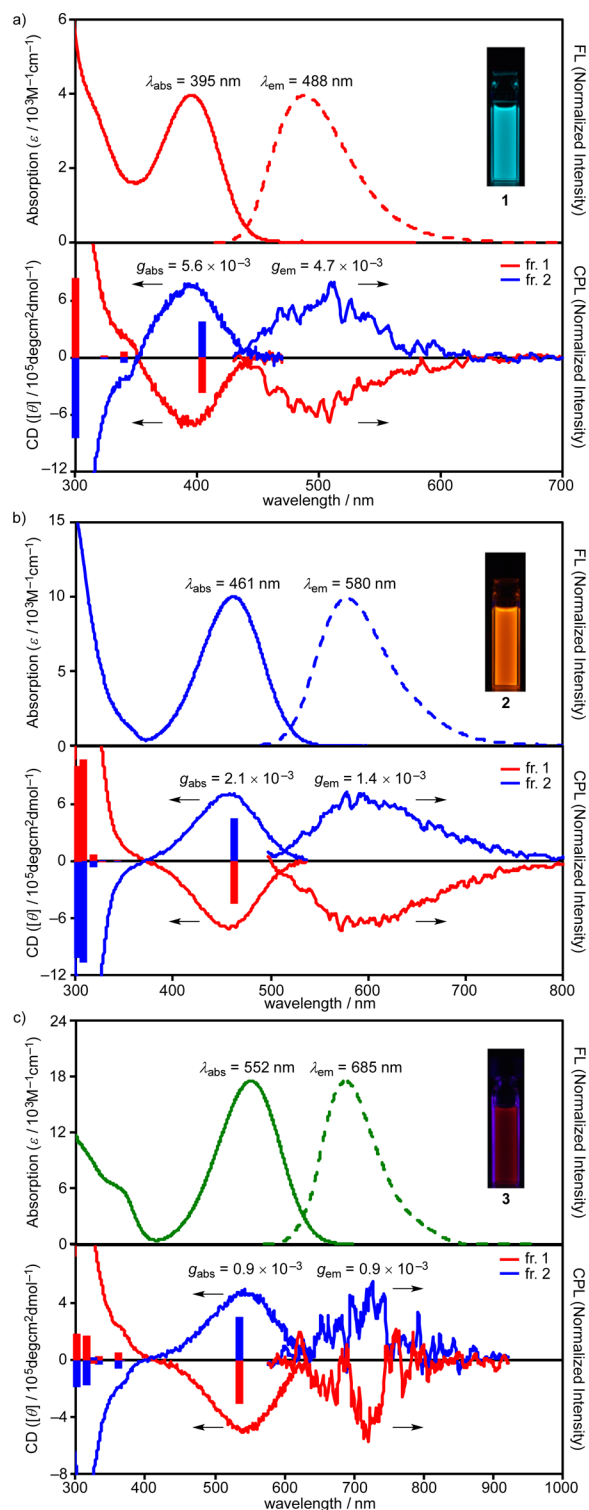
**Chiroptical Properties in CH<sub>2</sub>Cl<sub>2</sub>.** To examine the chiroptical properties of **1–3**, which are expected to arise from their helical structure, preparative chiral HPLC with CHIRALPAK-IF was used to achieve the optical resolution of **1–3** in order to obtain their enantiomers in pure form (Figures S4–S6). As predicted by DFT calculations, all enantiomers of **1–3** were stable under ambient conditions, and racemization was not observed at room temperature. In order to experimentally examine the chiral stability of **1–3**, monitoring

study was conducted on the racemization in toluene at 100 °C for 1 and 80 °C for 2 and 3. Every hour, the changes in the ratio of each fraction of the enantiomer were monitored using HPLC with CHIRALPAK-IF (Figure S7). According to these results, the ring inversion energies were determined to be 29.0 kcal/mol for 1, 27.6 kcal/mol for 2, and 27.1 kcal/mol for 3, respectively. These are quantitatively in good agreement with the values predicted by DFT calculations (B3LYP/6-31G(d)); 29.3 kcal/mol for 1, 27.8 kcal/mol for 2, and 26.4 kcal/mol for 3, respectively (Figures S1–S3).

With the pure enantiomers of 1–3 in hand, the chiroptical properties of 1–3 were investigated by circular dichroism (CD) and CPL spectroscopy in CH<sub>2</sub>Cl<sub>2</sub> solutions (Figure 3 and Table S1). CD spectroscopy of the (*P*)- and (*M*)-helices of 1–3 revealed clear Cotton effects for the corresponding absorption bands, i.e., they are mirror images of each other. Specifically, the first eluted fractions of 1–3 (fraction 1) exhibited a (–) Cotton effect, while the second eluted fraction (fraction 2) exhibited a (+) Cotton effect at 400–600 nm (Figure 3). On the basis of a comparison with the results of the TD-DFT calculations, a (*P*)-helix was assigned to the first fraction, and an (*M*)-helix to the second fraction of enantiomerically pure 1–3. In the CPL spectra, 1–3 exhibit substantial signals, owing to their helicity in addition to their strong emissive properties. In general, the degree of CD and CPL intensity is determined by the dissymmetry factor (*g*), which is defined as  $g_{\text{abs}} = 2(\epsilon_L - \epsilon_R)/(\epsilon_L + \epsilon_R)$  for CD and as  $g_{\text{em}} = 2(I_L - I_R)/(I_L + I_R)$  for CPL, respectively. Therein,  $\epsilon_L$ ,  $\epsilon_R$ ,  $I_L$ , and  $I_R$  refer to the absorption and emission intensities for left- and right-handed light, respectively. By measuring the CD signals for each of the pure enantiomers of 1–3 in CH<sub>2</sub>Cl<sub>2</sub>,  $g_{\text{abs}}$  values of  $5.6 \times 10^{-3}$  for 1,  $2.1 \times 10^{-3}$  for 2, and  $0.9 \times 10^{-3}$  for 3 were obtained, and the CPL signals delivered  $g_{\text{em}}$  values of  $4.7 \times 10^{-3}$  for 1,  $1.4 \times 10^{-3}$  for 2, and  $0.9 \times 10^{-3}$  for 3, respectively. Compared to previously reported small organic molecules,<sup>6</sup> these values are relatively high, suggesting the utility of oxygen-bridged diphenylnaphthylamine as a scaffold for CPL materials.

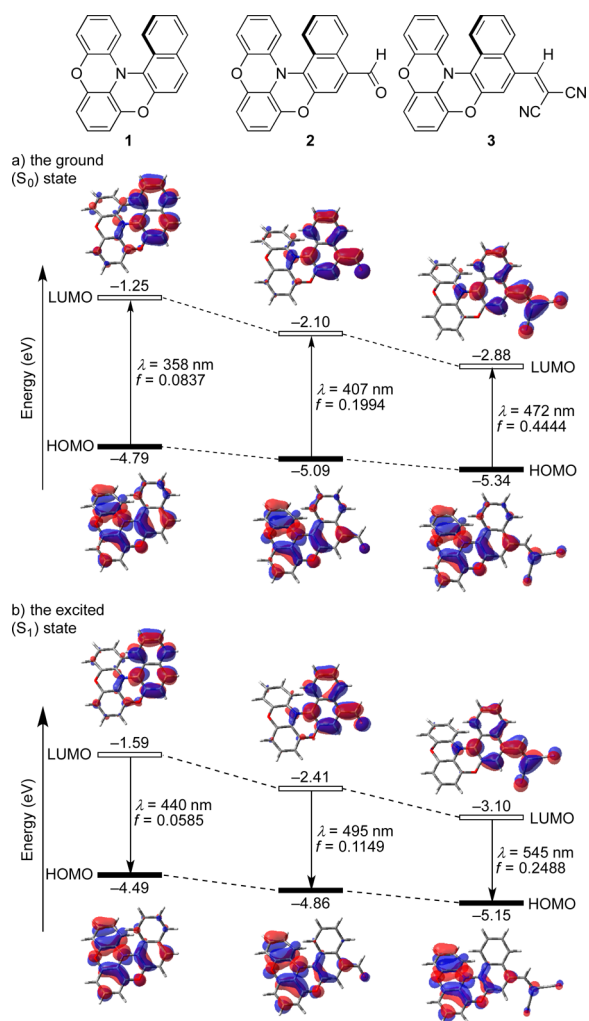
**Electronic Structures.** To gain deeper insight into the electronic structures, as well as the photophysical and chiroptical properties of oxygen-bridged diphenylnaphthylamines, DFT and TD-DFT calculations were carried out on 1–3 at the B3LYP/6-31G(d) level of theory, and the results are summarized in Figure 4a. The Kohn–Sham (KS)-HOMO of 1 (–4.79 eV) is delocalized over the entire skeleton, whereas the KS-LUMO (–1.25 eV) of 1 is mainly located on the naphthalene ring. Accordingly, the electron-withdrawing groups attached to the naphthyl moieties in 2 and 3 further delocalize the KS-LUMOs, and thus effectively decrease the energy levels in formyl derivative 2 (KS-LUMO: –2.10 eV) and 2,2-dicyanovinyl derivative 3 (KS-LUMO: –2.88 eV). In contrast, the KS-HOMO levels (2: –5.09 eV; 3: –5.34 eV) decrease moderately, which leads to narrower HOMO–LUMO gaps in 2 and 3 relative to that of 1. These differences in the electronic structure were confirmed by cyclic voltammetry measurements (Figure S8). Upon introduction of electron-withdrawing groups, the reduction potentials show significant shifts in positive direction ( $E_{\text{pc}} = -2.92$  for 1, –2.06 for 2, and –1.66 V vs Fc/Fc<sup>+</sup> for 3), whereas the shifts of the oxidation potentials are only moderate ( $E_{1/2} = +0.36$  for 1, +0.50 for 2, and +0.50 V vs Fc/Fc<sup>+</sup> for 3).

The TD-DFT calculations on the S<sub>0</sub> ground states indicate that the longest absorption for 1–3 should be assigned to



**Figure 3.** UV–vis absorption (solid) and fluorescence (dashed) spectra (top), and CD and CPL spectra (bottom) for (a) 1, (b) 2, and (c) 3 in CH<sub>2</sub>Cl<sub>2</sub>. The red and blue bars show the calculated CD bands (CAM-B3LYP/6-31G(d)) for the (*P*)- and (*M*)-helices, respectively. The transition energies have been calibrated using a factor of 0.88. Photographs show the emission of 1–3.

$\pi$ – $\pi^*$  transitions from the HOMO to the LUMO. Reflecting the narrow HOMO–LUMO gaps in 2 and 3, the wavelengths for the longest absorption of 2 (407 nm,  $f = 0.1994$ ) and 3 (472 nm,  $f = 0.4444$ ) are red-shifted compared to that of 1 (358 nm,



**Figure 4.** Pictorial presentation of the frontier orbitals, a plot of the Kohn–Sham HOMO and LUMO energy levels, and the optical transition with oscillator strength for the optimized structures of (a) the ground ( $S_0$ ) states (TD-CAM-B3LYP/6-31G(d)//B3LYP/6-31G(d)) and (b) the excited ( $S_1$ ) states (TD-CAM-B3LYP/6-31G(d)//TD-B3LYP/6-31G(d)) of 1–3.

$f = 0.0837$ ), and are accompanied by a larger oscillator strength. These results are qualitatively consistent with the observed absorption spectra of 1–3. The rather small oscillator strength obtained for the longest absorption in 1–3 suggests a non-negligible contribution of the intramolecular charge transfer (ICT) transition character induced by the deflection in the HOMO and LUMO.

In order to discuss the emission properties, theoretical calculations were also conducted on the  $S_1$  excited states of 1–3. The structures of the  $S_1$  excited states were optimized at the TD-B3LYP/6-31G(d) level of theory, and the emission properties were evaluated by single-point calculations at the TD-CAM-B3LYP/6-31G(d) level of theory for the optimized structures of the  $S_1$  states (Figure 4b).<sup>6d,13</sup> Similarly to the  $S_0$  states, the deflection in the KS-HOMO and KS-LUMO on the  $S_1$  excited states is observed for 1–3, corroborating that an ICT character should be induced in the excited states. The more significant deflection of the KS-HOMO and KS-LUMO in the  $S_1$  excited state leads to smaller oscillator strength values (emission) for 1 (440 nm,  $f = 0.0585$ ), 2 (495 nm,  $f = 0.1149$ ), and 3 (545 nm,  $f = 0.2488$ ), thus increasing the ICT character

compared to those in the  $S_0$  ground state (absorption). Such small oscillator strength values in the  $S_1$  state may explain the rather long lifetimes due to the small radiative rate constants ( $\sim 10^7$  s). Nevertheless, 1 exhibits an intense emission band with a high quantum yield ( $\lambda_{\text{em}} = 488$  nm,  $\Phi = 0.86$ ,  $\tau = 25.4$  ns), which is based on a well-suppressed nonradiative rate constant ( $\sim 10^6$  s), although the reason behind this phenomenon is not clear yet.

The chiroptical  $g$  values for CD and CPL could also be estimated by TD-DFT calculations at the TD-CAM-B3LYP/6-31G(d) level of theory on the  $S_0$  ground and  $S_1$  excited states of the optimized structures (Table 2). The  $g$  values were evaluated

**Table 2.** Theoretical Chiroptical Parameters for 1–3

	state	$\lambda$ [nm]	$D$ [ $10^{-36}$ esu $^2$ cm $^2$ ]	$R$ [ $10^{-40}$ esu $^2$ cm $^2$ ]	$ g $ [ $10^{-3}$ ]
1	$S_0$	358	6.37	105	6.6 (5.6) <sup>a</sup>
	$S_1$	440	5.47	72.9	5.3 (4.7) <sup>a</sup>
2	$S_0$	407	17.3	117	2.7 (2.1) <sup>a</sup>
	$S_1$	495	12.1	80.2	2.7 (1.4) <sup>a</sup>
3	$S_0$	472	44.6	130	1.2 (0.9) <sup>a</sup>
	$S_1$	545	28.9	90.8	1.3 (0.9) <sup>a</sup>

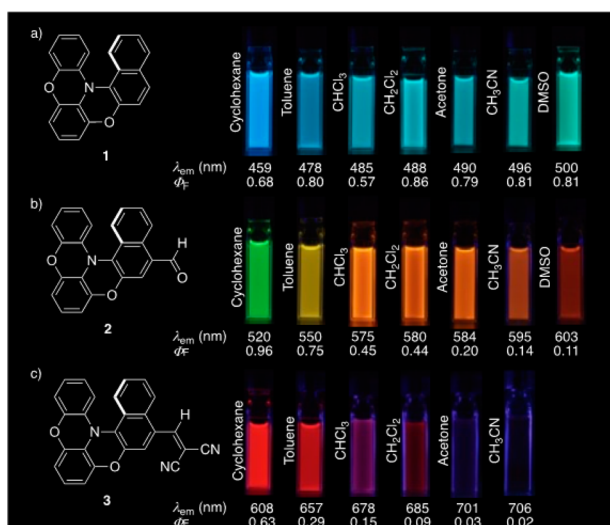
<sup>a</sup>Experimental  $g$  values obtained for  $\text{CH}_2\text{Cl}_2$  solutions.

according to the following equation:  $g = 4R/D$ , where  $D$  and  $R$  denominate the dipole and rotatory strength, respectively.<sup>14</sup>  $D$  is defined by the oscillator strength ( $f$ ) and the corresponding excitation energy ( $\nu/\text{cm}^{-1}$ ) as follows (eq 1):

$$D = \frac{3he^2}{8\pi^2\nu m_e c} f \quad (1)$$

where  $h$  is the Planck constant ( $6.626 \times 10^{-34}$  J s $^{-1}$ ),  $e$  the electron charge ( $4.80 \times 10^{-10}$  esu),  $m_e$  the electron mass ( $9.11 \times 10^{-31}$  kg), and  $c$  the speed of light ( $3.00 \times 10^{10}$  cm s $^{-1}$ ).  $R$  was evaluated directly by TD-DFT calculations, and the results for 1–3 are summarized in Table 2. The obtained TD-DFT-derived  $g_{\text{abs}}$  and  $g_{\text{em}}$  values for 1–3 are quantitatively in good agreement with the experimental values, supporting the validity of the present theoretical calculations. These results thus demonstrate the utility of this method for the prediction of CD and CPL parameters for newly synthesized compounds.

**Solvent Dependency in Fluorescence.** As previously discussed, the theoretical calculations suggest that an ICT character is induced in the excited states. Hence, we examined the solvent effect on the photophysical properties of 1–3. The data are summarized in Supporting Information. The corresponding Lippert–Mataga plots<sup>15</sup> show that the differences in the dipole moment from  $S_0$  to  $S_1$  ( $\Delta\mu$ ) are 8.8 for 1, 10.0 for 2, and 11.4 D for 3 (Figure S36), which demonstrates the induced ICT character especially in the excited state  $S_1$ . As a consequence of such an induced ICT character, 1–3 exhibit significant red-shifts of their emission bands with increasing solvent polarity (Figure 5). In cyclohexane, the emission of 1–3 is blue ( $\lambda_{\text{em}} = 459$  nm), light green (520 nm), and red (608 nm), respectively. In polar solvents, such as  $\text{CH}_3\text{CN}$  or DMSO, the emission of 1–3 is green ( $\lambda_{\text{em}} = 500$  nm in DMSO), red (600 nm in DMSO), and deep red (706 nm in  $\text{CH}_3\text{CN}$ ), respectively. Interestingly, these emissions cover the whole visible region, thus displaying full-color emission (Figure 5). The fluorescence quantum yields of these compounds are varied in these solvents (Figure 5). The maximum quantum yields were obtained for 1 ( $\Phi_{\text{F}} = 0.86$ ) in  $\text{CH}_2\text{Cl}_2$  and for 2 ( $\Phi_{\text{F}}$

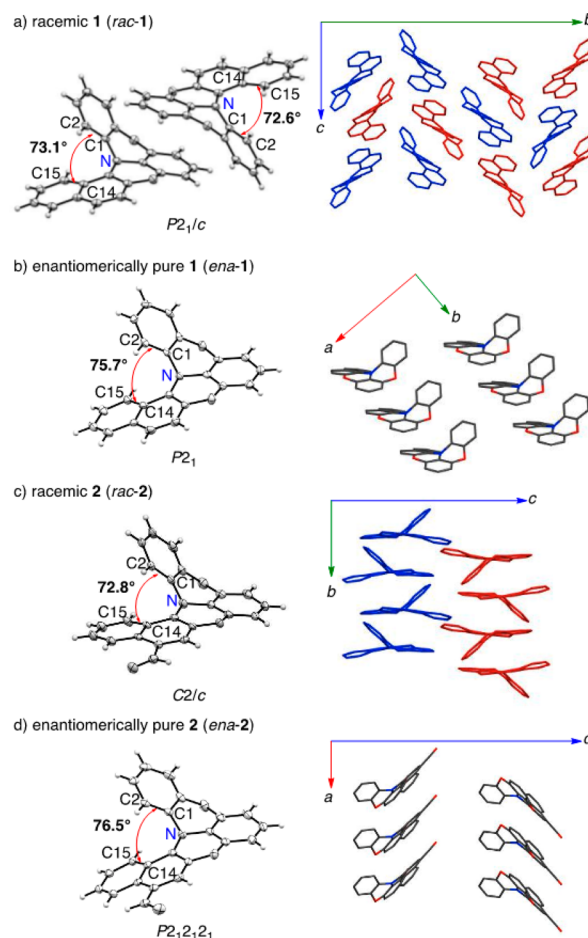


**Figure 5.** Photographs of emission and emission wavelengths and quantum yields for (a) **1**, (b) **2**, and (c) **3** in a variety of solvent.

= 0.96) and **3** ( $\Phi_F = 0.63$ ) in cyclohexane. The pure enantiomers of **2** and **3** in cyclohexane exhibit comparable  $g_{abs}$  and  $g_{em}$  values to those in  $\text{CH}_2\text{Cl}_2$  in their CD and CPL spectra, respectively ( $g_{abs}$ :  $1.9 \times 10^{-3}$  for **2**, and  $1.1 \times 10^{-3}$  for **3**,  $g_{em}$ :  $1.7 \times 10^{-3}$  for **2**, and  $0.9 \times 10^{-3}$  for **3**, Figures S31–S32).

**Single Crystal X-ray Structure.** Single crystal X-ray structural analyses were carried out on racemic crystals (*rac-1* and *rac-2*) as well as enantiomerically pure crystals (*ena-1* and *ena-2*) in order to determine any potential difference in the molecular structure and packing motifs that could affect the solid-state properties (Figure 6). Due to the lack of heavy elements in the compounds used in this study, the absolute structures for the enantiomerically pure crystals could not be unambiguously determined, as they are usually obtained by a Flack parameter with anomalous X-ray scattering. Thus, the absolute structures for each of the enantiomers of **1–3** were determined on the basis of a comparison between the TD-DFT calculations and the CD spectra in solution (*vide supra*). The crystal structure analyses confirmed that all molecules of **1** and **2** in both racemic and enantiomerically pure crystals have helical structures with dihedral angles ( $\angle\text{C2–C1–C14–C15}$ ) of  $72.6^\circ$  and  $73.1^\circ$  for *rac-1*,  $75.7^\circ$  for *ena-1*,  $72.8^\circ$  for *rac-2*, and  $76.5^\circ$  for *ena-2*, which are in good agreement with those of the optimized structures from the DFT calculations (**1**:  $72.3^\circ$ , **2**:  $73.4^\circ$ ). The small differences in the dihedral angles could be attributed to packing forces. In the packing structure, a one-dimensional columnar structure with slipped  $\pi$ -stacking was observed for both racemic and enantiomerically pure crystals. The *rac-1* crystals contain two independent molecules per unit cell, which form a pair in a columnar stacking structure. In the case of *rac-2* crystals, (*P*)- and (*M*)-helices of **2** form independent columnar structures, which are aligned alternately. In the packing structure of enantiomerically pure crystals, by adopting a slipped  $\pi$ -stacking in these columnar structures, the cofacial distances for the central benzene rings (*ena-1*: 3.44 Å; *ena-2*: 3.33 Å) are shorter than those in the racemic crystals (*rac-1*: 3.68 Å; *rac-2*: 3.62 Å).

**Fluorescence Properties in the Solid State.** Subsequently, we examined the fluorescence properties of **1–3** in the solid state for both the racemic and enantiomerically pure crystals. On account of the differences in packing motifs,



**Figure 6.** X-ray crystal structures: ORTEP drawings (50% probability for thermal ellipsoids) and packing structures for (a) *rac-1*, (b) *ena-1*, (c) *rac-2*, and (d) *ena-2*. The *P*- and *M*-helices in the racemic crystals are shown in red and blue, respectively.

crystals of **1–3** exhibit different emission behavior depending on the racemic mixtures or the enantiomerically pure compounds (Table 3, Figures S19, S21, and S23). Whereas both crystals of *rac-1* and *ena-1* show similar blueish green emission (*rac-1*:  $\lambda_{em} = 480$  nm; *ena-1*: 482 nm), the quantum yield of *ena-1* ( $\Phi = 0.55$ ) is significantly higher than that of *rac-1* ( $\Phi = 0.35$ ). In case of **2** and **3**, the differences in the

**Table 3.** Photophysical and Chiroptical Parameters for **1–3** in the Solid State

	state	$\lambda_{abs}$ [nm]	$\lambda_{em}$ [nm]	$\Phi^a$	$\tau$ [ns]	$ g_{em}  \cdot 10^{-3}$
<i>rac-1</i> <sup>b</sup>	crystal		480	0.35	15.1	
	nanoparticle <sup>d</sup>	401	487	0.41	15.9	4.5
<i>ena-1</i> <sup>c</sup>	crystal		482	0.55	11.1	
	nanoparticle <sup>d</sup>	469	583	0.13	4.99	1.5
<i>rac-2</i> <sup>b</sup>	crystal		572	0.09	9.29	
	nanoparticle <sup>d</sup>	469	585	0.14	6.44	
<i>ena-2</i> <sup>c</sup>	crystal		585	0.14	6.44	
	nanoparticle <sup>d</sup>	469	583	0.13	4.99	1.5
<i>rac-3</i> <sup>b</sup>	crystal		735	0.09	2.21	
<i>ena-3</i> <sup>c</sup>	crystal		706	0.02	3.07	
	nanoparticle <sup>d</sup>	572	669	<0.01	1.28	2.8

<sup>a</sup>Absolute quantum yields determined by a calibrated sphere system. <sup>b</sup>Racemic compound. <sup>c</sup>Enantiomerically pure compound. <sup>d</sup>Nanoparticles of the enantiomer dispersed in water.

fluorescence wavelengths as well as the quantum yields were found to be more significant between the racemic mixture and the enantiomers. Thus, crystals of *rac-2* and *ena-2* exhibit different emission colors: while *rac-2* shows yellowish orange emission ( $\lambda_{em} = 572$  nm,  $\Phi = 0.09$ ), the emission of *ena-2* is slightly red-shifted to orange ( $\lambda_{em} = 585$  nm,  $\Phi = 0.14$ ). Microcrystalline powders of *rac-3* and *ena-3* also exhibit different emission wavelengths in the near-IR (*rac-3*:  $\lambda_{em} = 735$  nm,  $\Phi = 0.02$ ) or deep red region (*ena-3*:  $\lambda_{em} = 706$  nm,  $\Phi = 0.08$ ). As shown in Table 3, the emission lifetimes for *rac-1* and *ena-1* are longer than those of the other compounds, similar to those in solution. The lifetime of *ena-1* ( $\tau = 11.1$  ns) is shorter than that of *rac-1* ( $\tau = 15.1$  ns), leading to an increase of the radiative rate constant for *ena-1*, while maintaining a similar nonradiative rate constant ( $k_r = 5.0 \times 10^7$ ,  $k_{nr} = 4.1 \times 10^7$ ) relative to that of *rac-1* ( $k_r = 2.3 \times 10^7$ ,  $k_{nr} = 4.3 \times 10^7$ ). These effects, which arise from the different packing structures, result in the observed higher quantum yield for *ena-1*.

**Chiroptical Properties in the Solid State.** In order to examine the chiroptical properties of 1–3 in the solid state, we prepared nanoparticles of the enantiomerically pure crystals of *ena-1–3* dispersed in water by a rapid reprecipitation method.<sup>12</sup> DLS measurements of the thus prepared dispersions in water confirmed the formation of nanoparticles of *ena-1–3* with an average size of ca. 100 nm (Figure S18). The emission behavior of the nanoparticles of *ena-1–3* was qualitatively similar to that observed for the crystals of *ena-1–3* (Table 3), suggesting the formation of the similar packing structure to crystals even in nanoparticle.

In the CD spectra for the nanoparticles of enantiomerically pure *ena-1–3*, Cotton effects were observed in the form of mirror images, similar to the case in solution (Figures S28–S30). For the nanoparticles of *ena-1–3*,  $g_{abs}$  values of  $3.6 \times 10^{-3}$  (*ena-1*),  $2.1 \times 10^{-3}$  (*ena-2*), and  $4.3 \times 10^{-3}$  (*ena-3*) were observed. In the CPL spectra, the nanoparticles of *ena-1–3* also exhibit CPL activity with  $g_{em}$  values of  $4.5 \times 10^{-3}$  (*ena-1*),  $1.5 \times 10^{-3}$  (*ena-2*), and  $2.5 \times 10^{-3}$  (*ena-3*), respectively, which are comparable to those in  $CH_2Cl_2$  solution. These results indicate potential use of these compounds in CPL materials even in the solid state.

## CONCLUSIONS

In summary, we have developed oxygen-bridged diphenyl-naphthylamine skeleton having helical structure and three derivatives 1–3 containing different functional groups were synthesized and examined their optical properties both in solution and in the solid-state. In solution, 1–3 exhibited full-color emission from blue to deep red with medium to high fluorescence quantum yield with the selection of the appropriate organic solvents by the change of their intramolecular charge transfer character in the excited state. In addition, the enantiomers of 1–3 also exhibited CPL signals with good  $g_{em}$  values of  $\sim 10^{-3}$ . In the crystalline states, all of 1–3 showed different optical properties between racemic mixtures and enantiomers due to their different packing motifs and such behaviors were also observed in the aqueous nanoparticles. Furthermore, the enantiomers of 1–3 also exhibited CPL activity even in the solid state and the nanoparticles of 1–3 exhibited comparable  $g_{abs}$  values ( $\sim 10^{-3}$ ) with those in solutions. We believe that such easily tuning of emission colors by the selection of substituents and good CPL activity both in solution and in the solid-state indicate usefulness of this oxygen-bridged dipe-

nylnaphthylamine skeleton for applications as functional materials in the field of organic electronics.

## EXPERIMENTAL SECTION

**General Considerations.** All reactions were carried out under an argon atmosphere. Thin layer chromatography (TLC) was performed on plates coated with 0.25 mm thick silica gel 60F-254 (Merck). Column chromatography was performed using PSQ 60B (Fuji Silysia). Preparative gel permeation chromatography (GPC) was performed with a JAI LC-918 system equipped with a RI-50 detector, a JAIGEL-2H column (20 mm ID  $\times$  600 mm), and a 1H column (20 mm ID  $\times$  600 mm) using toluene as eluent (flow rate: 3.8 mL/min). Melting points (m.p.) were measured on a Yanaco Micro Melting Point Apparatus. <sup>1</sup>H and <sup>13</sup>C NMR spectra were recorded with a JEOL ECA 500 (500 MHz for <sup>1</sup>H and 125 MHz for <sup>13</sup>C) spectrometer. The NMR chemical shifts are reported in ppm with reference to residual protons and carbons of  $CDCl_3$  ( $\delta$  7.26 ppm in <sup>1</sup>H NMR, and  $\delta$  77.00 ppm in <sup>13</sup>C NMR). FAB and EI mass spectra were performed with a JEOL JMS-MS700 V by the Joint Usage/Research Center (JURC) at the ICR, Kyoto Univ. Elemental analyses were performed by the JURC at the ICR, Kyoto Univ. Cyclic voltammetry (CV) was performed on a ALS/chi-620C electrochemical analyzer with the CV cell consisting of a glassy carbon electrode, a Pt wire counter electrode, and an Ag/AgNO<sub>3</sub> reference electrode. The measurement was carried out under argon atmosphere using  $CH_2Cl_2$  solution samples (1.0 mM) with 0.1 M tetrabutylammonium hexafluorophosphate ( $Bu_4N^+PF_6^-$ ) as a supporting electrolyte. The redox potentials were calibrated with ferrocene as an internal standard. UV–vis absorption measurements were performed with a Shimadzu UV-3150 spectrometer, in degassed spectral grade solvents. Fluorescence measurements were performed with a HORIBA FluoroMax 4P-NIR. Quantum yields were determined with a Hamamatsu Photonics Quantaurus QY C11347 with calibrated integrating sphere system. Circular dichroism (CD) measurements were performed with a JASCO J-820 spectropolarimeter at room temperature. Circularly polarized luminescence (CPL) measurements were performed with a JASCO CPL-200S spectropolarimeter at room temperature. Dynamic light scattering (DLS) measurements were performed at room temperature on an ELS-ZA2 (Otsuka Electronics Co., Ltd.) with a semiconductor laser (50 nW) as a light source. The particle size distribution was derived using the CONTIN algorithm.

**Computation Methods.** DFT calculations for optimization of the geometries and estimation of inversion barrier as well as TD-DFT calculations for transitions and optimization of the excited states were conducted using the Gaussian 09 program.<sup>16</sup>

**Materials Synthesis.** *2,6-Difluoro-N-(2-methoxyphenyl)-N-(2-methoxynaphthalenyl)aniline* (5). The mixture of 4 (1.16 g, 4.93 mmol), 1-iodo-2-methoxynaphthalene (1.69 g, 5.93 mmol),  $K_2CO_3$  (1.61 g, 11.7 mmol), copper powder (0.562 g, 8.85 mmol), and 18-crown-6 (0.138 g, 0.524 mmol) was dissolved in mesitylene (8.0 mL). The mixture was stirred at 220 °C for 46 h. The insoluble materials were filtered off, and the solids were washed with  $CH_2Cl_2$  (50 mL). After addition of 1 M  $NH_4Cl$  aq. to the filtrate, the aqueous phase was extracted with  $CH_2Cl_2$  (10 mL  $\times$  3). The organic phase was washed with water and brine, dried over  $Na_2SO_4$ , filtered off, and concentrated under reduced pressure. The obtained crude product was purified by silica gel column chromatography ( $CH_2Cl_2$ :hexane = 1:3,  $R_f$  = 0.18) to give 1.47 g (3.77 mmol) of 5 in 76% yield as white solids: mp 156.1–157.1 °C; <sup>1</sup>H NMR (500 MHz,  $CD_2Cl_2$ ):  $\delta$  7.88 (d, <sup>3</sup>J(H,H) = 8.0 Hz, 1H), 7.82 (d, <sup>3</sup>J(H,H) = 9.0 Hz, 1H), 7.80 (dd, <sup>3</sup>J(H,H) = 7.5 Hz, <sup>4</sup>J(H,H) = 1.5 Hz, 1H), 7.33 (d, <sup>3</sup>J(H,H) = 8.5 Hz, 1H), 7.36–7.29 (m, 2H), 6.97–6.92 (m, 2H), 6.93 (td, <sup>3</sup>J(H,H) = 8.0 Hz, <sup>4</sup>J(H,H) = 1.5 Hz, 1H), 6.80 (t, <sup>3</sup>J(H,H) = 10.0 Hz, 1H), 6.77 (t, <sup>3</sup>J(H,H) = 10.0 Hz, 1H), 6.68 (ddd, <sup>3</sup>J(H,H) = 7.5 Hz, <sup>3</sup>J(H,H) = 6.5 Hz, <sup>4</sup>J(H,H) = 2.0 Hz, 1H), 6.57 (dd, <sup>3</sup>J(H,H) = 7.5 Hz, <sup>4</sup>J(H,H) = 1.5 Hz, 1H), 3.71 (s, 3H), 3.63 (s, 3H); <sup>13</sup>C NMR (125 MHz,  $CD_2Cl_2$ ):  $\delta$  158.9 (dd, <sup>1</sup>J(C,F) = 248 Hz, <sup>3</sup>J(C,F) = 106 Hz), 154.9, 152.4, 137.7, 132.4, 130.2, 128.9, 128.4, 128.3, 126.9, 126.3 (t, <sup>2</sup>J(C,F) = 12.5 Hz), 124.2, 123.6, 123.2, 123.0 (t, <sup>3</sup>J(C,F) = 9.5 Hz), 122.3, 121.3, 120.5, 115.4,

112.9, 111.5 (d,  $^2J(\text{C},\text{F}) = 22.0$  Hz), 57.0, 56.2; HRMS (EI, Magnetic Sector) ( $m/z$ ): [ $\text{M}^+$ ] calcd. for  $\text{C}_{24}\text{H}_{19}\text{F}_2\text{NO}_2$ , 391.1378; found, 391.1393; Elemental analysis calcd. (%) for  $\text{C}_{24}\text{H}_{19}\text{F}_2\text{NO}_2$ : C 73.65, H 4.89, N 3.58; found: C 73.74, H 4.94, N 3.72.

**Naphtho[2,1-b][1,4]oxazino[2,3,4-kl]phenoxazine (1).** **5** (1.12 g, 2.87 mmol) was dissolved in dry  $\text{CH}_2\text{Cl}_2$  (45 mL).  $\text{BBr}_3$  (0.600 mL, 6.33 mmol) was added to the solution at  $-78$  °C. The mixture was slowly warmed up to room temperature and further stirred for 12 h. The reaction mixture was poured into water and extracted with ethyl acetate (15 mL  $\times$  3). The combined organic phase was washed with brine, dried over  $\text{Na}_2\text{SO}_4$ , filtered off, and concentrated under reduced pressure to give 1.30 g of the crude product as white solids, which was used without further purification. These solids were dissolved in DMF (85 mL). After addition of  $\text{K}_2\text{CO}_3$  (1.21 g, 8.75 mmol), the mixture was stirred at 120 °C for 24 h. The resulting insoluble materials were filtered off and washed with  $\text{CH}_2\text{Cl}_2$  (25 mL), and the filtrate was concentrated under reduced pressure. The obtained solids were dissolved in  $\text{CH}_2\text{Cl}_2$  (30 mL). After addition of 1 M HCl aq. (30 mL), the mixture was extracted with  $\text{CH}_2\text{Cl}_2$  (10 mL  $\times$  3) and washed with brine. The organic phase was dried over  $\text{Na}_2\text{SO}_4$ , filtered off, and concentrated under reduced pressure. The obtained crude product was dissolved in  $\text{CH}_2\text{Cl}_2$ . After being passed through a short pad of silica gel, the crude product was purified by silica gel column chromatography ( $\text{CH}_2\text{Cl}_2$ :hexane = 1:3,  $R_f = 0.64$ ) to give 855 mg (2.64 mmol) of **1** in 92% yield as yellow solids: mp 182.1–183.1 °C;  $^1\text{H}$  NMR (500 MHz,  $\text{CDCl}_3$ ):  $\delta$  7.78 (d,  $^3J(\text{H},\text{H}) = 8.0$  Hz, 1H), 7.57 (d,  $^3J(\text{H},\text{H}) = 9.0$  Hz, 1H), 7.44 (d,  $^3J(\text{H},\text{H}) = 8.1$  Hz, 1H), 7.37 (td,  $^3J(\text{H},\text{H}) = 7.0$  Hz,  $^4J(\text{H},\text{H}) = 1.0$  Hz, 1H), 7.29 (td,  $^3J(\text{H},\text{H}) = 7.0$  Hz,  $^4J(\text{H},\text{H}) = 1.0$  Hz, 1H), 7.15 (d,  $^3J(\text{H},\text{H}) = 9.0$  Hz, 1H), 7.06 (dd,  $^3J(\text{H},\text{H}) = 8.0$  Hz,  $^4J(\text{H},\text{H}) = 1.5$  Hz, 1H), 6.95 (td,  $^3J(\text{H},\text{H}) = 7.5$  Hz,  $^4J(\text{H},\text{H}) = 1.0$  Hz, 1H), 6.86 (t,  $^3J(\text{H},\text{H}) = 8.0$  Hz, 1H), 6.85 (td,  $^3J(\text{H},\text{H}) = 7.5$  Hz,  $^4J(\text{H},\text{H}) = 1.0$  Hz, 2H), 6.68 (dd,  $^3J(\text{H},\text{H}) = 8.0$  Hz,  $^4J(\text{H},\text{H}) = 1.0$  Hz, 1H), 6.60 (dd,  $^3J(\text{H},\text{H}) = 8.0$  Hz,  $^4J(\text{H},\text{H}) = 1.5$  Hz, 1H), 6.42 (dd,  $^3J(\text{H},\text{H}) = 8.0$  Hz,  $^4J(\text{H},\text{H}) = 1.5$  Hz, 1H);  $^{13}\text{C}$  NMR (125 MHz,  $\text{CDCl}_3$ ):  $\delta$  148.6, 148.1, 146.3, 145.4, 134.4, 131.4, 128.5, 125.7, 125.3, 124.8, 124.6, 124.0, 123.9, 123.7, 123.1, 122.7, 119.9, 117.7, 117.0, 115.9, 111.5, 111.0; HRMS (EI, Magnetic Sector) ( $m/z$ ): [ $\text{M}^+$ ] calcd. for  $\text{C}_{22}\text{H}_{13}\text{NO}_2$ , 323.0941; found, 323.0943; Elemental analysis calcd. (%) for  $\text{C}_{22}\text{H}_{13}\text{NO}_2$ : C 81.72, H 4.05, N 4.33; found: C 81.45, H 4.06, N 4.24.

**4-Formylnaphtho[2,1-b][1,4]oxazino[2,3,4-kl]phenoxazine (2).** Phosphoryl chloride (940  $\mu\text{L}$ , 10.1 mmol) was added to dry DMF (2 mL) at 0 °C and the solution was stirred for 15 min. **1** (163 mg, 0.505 mmol) was dissolved in dry  $\text{C}_2\text{H}_4\text{Cl}_2$  (2 mL). The DMF solution was added to the  $\text{C}_2\text{H}_4\text{Cl}_2$  solution. The mixture was heated at 75 °C for 6 h. The reaction mixture was neutralized by sat.  $\text{Na}_2\text{CO}_3$  aq. (40 mL) and extracted with  $\text{CH}_2\text{Cl}_2$  (20 mL  $\times$  3). The organic phase was washed with brine, dried over  $\text{Na}_2\text{SO}_4$ , filtered off, and concentrated under reduced pressure. The obtained crude product was purified by silica gel column chromatography ( $\text{CH}_2\text{Cl}_2$ :hexane = 1:2,  $R_f = 0.10$ ) to give 142 mg (0.405 mmol) of **2** in 80% yield as orange solids. mp 177.7–178.7 °C;  $^1\text{H}$  NMR (500 MHz,  $\text{CD}_2\text{Cl}_2$ ):  $\delta$  10.27 (s, 1H), 9.17 (d,  $^3J(\text{H},\text{H}) = 8.0$  Hz, 1H), 7.65 (s, 1H), 7.57 (td,  $^3J(\text{H},\text{H}) = 8.0$  Hz,  $^4J(\text{H},\text{H}) = 1.5$  Hz, 1H), 7.56 (dd,  $^3J(\text{H},\text{H}) = 8.5$  Hz,  $^4J(\text{H},\text{H}) = 1.5$  Hz, 1H), 7.36 (td,  $^3J(\text{H},\text{H}) = 8.0$  Hz,  $^4J(\text{H},\text{H}) = 1.5$  Hz, 1H), 7.10 (dd,  $^3J(\text{H},\text{H}) = 8.0$  Hz,  $^4J(\text{H},\text{H}) = 1.0$  Hz, 1H), 7.03 (td,  $^3J(\text{H},\text{H}) = 8.0$  Hz,  $^4J(\text{H},\text{H}) = 1.5$  Hz, 1H), 6.94 (t,  $^3J(\text{H},\text{H}) = 8.0$  Hz, 1H), 6.87 (td,  $^3J(\text{H},\text{H}) = 8.0$  Hz,  $^4J(\text{H},\text{H}) = 1.0$  Hz, 1H), 6.72 (d,  $^3J(\text{H},\text{H}) = 8.0$  Hz, 1H), 6.65 (d,  $^3J(\text{H},\text{H}) = 8.5$  Hz, 1H), 6.46 (d,  $^3J(\text{H},\text{H}) = 8.0$  Hz, 1H);  $^{13}\text{C}$  NMR (125 MHz,  $\text{CD}_2\text{Cl}_2$ ):  $\delta$  191.2, 149.0, 148.1, 145.7, 145.6, 133.3, 129.9, 128.5, 128.1, 127.5, 126.6, 126.2, 125.5, 125.4, 124.9, 124.4, 124.3, 123.6, 123.0, 117.7, 116.9, 112.2, 111.5; HRMS (FAB, Magnetic Sector) ( $m/z$ ): [ $\text{M}^+$ ] calcd. for  $\text{C}_{23}\text{H}_{13}\text{NO}_3$ , 351.0895; found, 351.0890; Elemental analysis calcd. (%) for  $\text{C}_{23}\text{H}_{13}\text{NO}_3$ : C 78.62, H 3.73, N 3.99; found: C 78.44, H 3.91 N 3.97.

**4-(2,2-Dicyanovinyl)naphtho[2,1-b][1,4]oxazino[2,3,4-kl]phenoxazine (3).** **2** (26.9 mg, 0.0766 mmol) and malononitrile (14.1 mg, 0.213 mmol) were dissolved in dry  $\text{CHCl}_3$  (7.5 mL).  $\text{NEt}_3$  (24

$\mu\text{L}$ ) was added to the solution and the mixture was stirred at room temperature for 5 h. The obtained crude products were absorbed on silica gel and purified by silica gel column chromatography ( $\text{CH}_2\text{Cl}_2$ :hexane = 1:1,  $R_f = 0.25$ ) to give 27.9 mg (0.0699 mmol) of **3** in 91% yield as purple solids: mp 290.4–291.4 °C;  $^1\text{H}$  NMR (500 MHz,  $\text{CD}_2\text{Cl}_2$ ):  $\delta$  8.54 (s, 1H), 8.09 (s, 1H), 7.99 (d,  $^3J(\text{H},\text{H}) = 8.5$  Hz, 1H), 7.59 (d,  $^3J(\text{H},\text{H}) = 8.5$  Hz, 1H), 7.58 (td,  $^3J(\text{H},\text{H}) = 8.0$  Hz,  $^4J(\text{H},\text{H}) = 1.5$  Hz, 1H), 7.37 (td,  $^3J(\text{H},\text{H}) = 8.0$  Hz,  $^4J(\text{H},\text{H}) = 1.0$  Hz, 1H), 7.11 (dd,  $^3J(\text{H},\text{H}) = 8.0$  Hz,  $^4J(\text{H},\text{H}) = 2.0$  Hz, 1H), 7.06 (td,  $^3J(\text{H},\text{H}) = 8.0$  Hz,  $^4J(\text{H},\text{H}) = 2.0$  Hz, 1H), 6.96 (t,  $^3J(\text{H},\text{H}) = 8.5$  Hz, 1H), 6.89 (td,  $^3J(\text{H},\text{H}) = 8.0$  Hz,  $^4J(\text{H},\text{H}) = 2.0$  Hz, 1H), 6.74 (dd,  $^3J(\text{H},\text{H}) = 8.5$  Hz,  $^4J(\text{H},\text{H}) = 1.0$  Hz, 1H), 6.68 (dd,  $^3J(\text{H},\text{H}) = 8.0$  Hz,  $^4J(\text{H},\text{H}) = 1.0$  Hz, 1H), 6.46 (dd,  $^3J(\text{H},\text{H}) = 8.0$  Hz,  $^4J(\text{H},\text{H}) = 2.0$  Hz, 1H);  $^{13}\text{C}$  NMR (125 MHz,  $\text{CDCl}_3$ ):  $\delta$  153.9, 148.6, 147.5, 145.4, 145.0, 132.2, 130.5, 128.2, 127.6, 126.0, 125.4, 125.0, 124.5, 124.0, 123.34, 123.30, 122.7, 122.0, 118.9, 117.7, 116.7, 114.4, 113.1, 112.1, 111.4, 81.6; HRMS (FAB, Magnetic Sector) ( $m/z$ ): [ $\text{M}^+$ ] calcd. for  $\text{C}_{26}\text{H}_{13}\text{N}_3\text{O}_2$ , 399.1002; found, 399.1008; Elemental analysis calcd. (%) for  $\text{C}_{26}\text{H}_{13}\text{N}_3\text{O}_2$ : C 78.19, H 3.28, N 10.52; found: C 77.91, H 3.58, N 10.15.

## ■ ASSOCIATED CONTENT

### Supporting Information

The Supporting Information is available free of charge on the ACS Publications website at DOI: 10.1021/acs.joc.7b00511.

Figures and tables for photophysical properties, optical resolution, X-ray crystal structure analysis, electrochemical properties, DFT calculations, and characterization data (PDF)

## ■ AUTHOR INFORMATION

### Corresponding Authors

\*wakamiya@scl.kyoto-u.ac.jp

\*yasujiro@scl.kyoto-u.ac.jp

### ORCID

Kazuo Tanaka: 0000-0001-6571-7086

Atsushi Wakamiya: 0000-0003-1430-0947

Yasujiro Murata: 0000-0003-0287-0299

### Notes

The authors declare no competing financial interest.

## ■ ACKNOWLEDGMENTS

This study was partially supported by the Japanese Science and Technology Agency (JST) via PRESTO, the Grant-in-Aid for Scientific Research on Innovative Areas “New Polymeric Materials Based on Element-Blocks (No. 2401)” (24102013), and Scientific Research (B) (JP26288093). We would like to thank Prof. T. Kawabata and Prof. T. Furuta (ICR Kyoto Univ.) for the CD measurements, Dr. M. Gon and Ms. R. Sawada for advice on the CPL measurements, and Dr. K. Sakakibara and Prof. Y. Tsujii for advice on the DLS measurements. The synchrotron single-crystal X-ray analysis was carried out on the BL38B1 beamline of SPring-8 with the approval of JASRI (2013A1489).

## ■ REFERENCES

- (a) Riehl, J. P.; Richardson, F. S. *J. Chem. Phys.* **1976**, *65*, 1011. (b) Richardson, F. S.; Riehl, J. P. *Chem. Rev.* **1977**, *77*, 773. (c) Riehl, J. P.; Richardson, F. S. *Chem. Rev.* **1986**, *86*, 1.
- (a) Dyreklev, P.; Berggren, M.; Inganäs, O.; Andersson, M. R.; Wennerström, O.; Hjertberg, T. *Adv. Mater.* **1995**, *7*, 43. (b) Schadt, M. *Annu. Rev. Mater. Sci.* **1997**, *27*, 305. (c) Peeters, E.; Christiaans, M. P. T.; Janssen, R. A. J.; Schoo, H. F. M.; Dekkers, H. P. J. M.; Meijer, E. W. *J. Am. Chem. Soc.* **1997**, *119*, 9909. (d) Montali, A.; Bastiaansen, C.;

- Smith, P.; Weder, C. *Nature* **1998**, *392*, 261. (e) Chen, S. H.; Katsis, D.; Schmid, A. W.; Mastrangelo, J. C.; Tsutsui, T.; Blanton, T. N. *Nature* **1999**, *397*, 506. (f) Grell, M.; Oda, M.; Whitehead, K. S.; Asimakis, A.; Neher, D.; Bradley, D. D. C. *Adv. Mater.* **2001**, *13*, 577.
- (3) (a) Furumi, S. *Chem. Rec.* **2010**, *10*, 394. (b) Topf, R. D. M.; McCall, M. W. *Phys. Rev. A: At., Mol., Opt. Phys.* **2014**, *90*, 053824.
- (4) (a) Li, Z.-B.; Sabat, M.; Hyacinth, M.; Pu, L.; Lin, J. *J. Org. Chem.* **2007**, *72*, 4905. (b) Muller, G. *Dalton Trans.* **2009**, 9692. (c) Liu, N.-N.; Song, S.; Li, D.-M.; Zheng, Y.-S. *Chem. Commun.* **2012**, *48*, 4908. (d) Yuasa, J.; Ohno, T.; Tsumatori, H.; Shiba, R.; Kamikubo, H.; Kataoka, M.; Hasegawa, Y.; Kawai, T. *Chem. Commun.* **2013**, *49*, 4604.
- (5) (a) Feringa, B. L.; van Delden, R. A. *Angew. Chem., Int. Ed.* **1999**, *38*, 3418. (b) Sato, I.; Yamashima, R.; Kadowaki, K.; Yamamoto, J.; Shibata, T.; Soai, K. *Angew. Chem., Int. Ed.* **2001**, *40*, 1096. (c) Podlech, J.; Gehring, T. *Angew. Chem., Int. Ed.* **2005**, *44*, 5776. (d) Kawasaki, T.; Soai, K. *Bull. Chem. Soc. Jpn.* **2011**, *84*, 879.
- (6) (a) Sánchez-Carnerero, E. M.; Agarrabeitia, A. R.; Moreno, F.; Maroto, B. L.; Muller, G.; Ortiz, M. J.; de la Moya, S. *Chem. - Eur. J.* **2015**, *21*, 13488. and references cited therein. (b) Sakai, H.; Shinto, S.; Kumar, J.; Araki, Y.; Sakanoue, T.; Takenobu, T.; Wada, T.; Kawai, T.; Hasobe, T. *J. Phys. Chem. C* **2015**, *119*, 13937. (c) Matsuno, T.; Koyama, Y.; Hiroto, S.; Kumar, J.; Kawai, T.; Shinokubo, H. *Chem. Commun.* **2015**, *51*, 4607. (d) Imagawa, T.; Hirata, S.; Totani, K.; Watanabe, T.; Vacha, M. *Chem. Commun.* **2015**, *51*, 13268. (e) Alnoman, R. B.; Rihn, S.; O'Connor, D. C.; Black, F. A.; Costello, B.; Waddell, P. G.; Clegg, W.; Peacock, R. D.; Herrebout, W.; Knight, J. G.; Hall, M. J. *Chem. - Eur. J.* **2016**, *22*, 93. (f) Kögel, J. F.; Kusaka, S.; Sakamoto, R.; Iwashima, T.; Tsuchiya, M.; Toyoda, R.; Matsuoka, R.; Tsukamoto, T.; Yuasa, J.; Kitagawa, Y.; Kawai, T.; Nishihara, H. *Angew. Chem., Int. Ed.* **2016**, *55*, 1377. (g) Yamamoto, Y.; Sakai, H.; Yuasa, J.; Araki, Y.; Wada, T.; Sakanoue, T.; Takenobu, T.; Kawai, T.; Hasobe, T. *Chem. - Eur. J.* **2016**, *22*, 4263. (h) Gon, M.; Morisaki, Y.; Sawada, R.; Chujo, Y. *Chem. - Eur. J.* **2016**, *22*, 2291. (i) Li, M.; Lu, H.-Y.; Zhang, C.; Shi, L.; Tang, Z.; Chen, C.-F. *Chem. Commun.* **2016**, *52*, 9921. (j) Saikawa, M.; Nakamura, T.; Uchida, J.; Yamamura, M.; Nabeshima, T. *Chem. Commun.* **2016**, *52*, 10727. (k) Oyama, H.; Akiyama, M.; Nakano, K.; Naito, M.; Nobusawa, K.; Nozaki, K. *Org. Lett.* **2016**, *18*, 3654. (l) Katayama, T.; Nakatsuka, S.; Hirai, H.; Yasuda, N.; Kumar, J.; Kawai, T.; Hatakeyama, T. *J. Am. Chem. Soc.* **2016**, *138*, 5210.
- (7) (a) Watanabe, K.; Akagi, K. *Sci. Technol. Adv. Mater.* **2014**, *15*, 044203. and references cited therein. (b) Goto, H.; Akagi, K. *Angew. Chem., Int. Ed.* **2005**, *44*, 4322. (c) Fukao, S.; Fujiki, M. *Macromolecules* **2009**, *42*, 8062. (d) Nakano, Y.; Liu, Y.; Fujiki, M. *Polym. Chem.* **2010**, *1*, 460. (e) Morisaki, Y.; Hifumi, R.; Lin, L.; Inoshita, K.; Chujo, Y. *Polym. Chem.* **2012**, *3*, 2727. (f) Watanabe, K.; Osaka, I.; Yorozyua, S.; Akagi, K. *Chem. Mater.* **2012**, *24*, 1011. (g) Ma, X.; Azeem, E. A.; Liu, X.; Cheng, Y.; Zhu, C. *J. Mater. Chem. C* **2014**, *2*, 1076. (h) Zhang, S.; Sheng, Y.; Wei, G.; Quan, Y.; Cheng, Y.; Zhu, C. *Polym. Chem.* **2015**, *6*, 2416. (i) Li, F.; Wang, Y.; Wang, Z.; Cheng, Y.; Zhu, C. *Polym. Chem.* **2015**, *6*, 6802.
- (8) (a) Meskers, S. C. J.; Dekkers, H. P. J. M.; Rapenne, G.; Sauvage, J.-P. *Chem. - Eur. J.* **2000**, *6*, 2129. (b) Schaffner-Hamann, C.; von Zelewsky, A.; Barbieri, A.; Barigelletti, F.; Muller, G.; Riehl, J. P.; Neels, A. *J. Am. Chem. Soc.* **2004**, *126*, 9339. (c) Oyler, K. D.; Coughlin, F. J.; Bernhard, S. *J. Am. Chem. Soc.* **2007**, *129*, 210.
- (9) (a) Zinna, F.; Di Bari, L. *Chirality* **2015**, *27*, 1. and references cited therein. (b) de Bettencourt-Dias, A.; Viswanathan, S.; Rollett, A. *J. Am. Chem. Soc.* **2007**, *129*, 15436. (c) Bozoklu, G.; Marchal, C.; Gateau, C.; Pécaut, J.; Imbert, D.; Mazzanti, M. *Chem. - Eur. J.* **2010**, *16*, 6159. (d) Kitchen, J. A.; Barry, D. E.; Mercks, L.; Albrecht, M.; Peacock, R. D.; Gunnlaugsson, T. *Angew. Chem., Int. Ed.* **2012**, *51*, 704. (e) Yuasa, J.; Ueno, H.; Kawai, T. *Chem. - Eur. J.* **2014**, *20*, 8621.
- (10) (a) Wakamiya, A.; Nishimura, H.; Fukushima, T.; Suzuki, F.; Saeki, A.; Seki, S.; Osaka, I.; Sasamori, T.; Murata, M.; Murata, Y.; Kaji, H. *Angew. Chem., Int. Ed.* **2014**, *53*, 5800. (b) Nishimura, H.; Ishida, N.; Shimazaki, A.; Wakamiya, A.; Saeki, A.; Scott, L. T.; Murata, Y. *J. Am. Chem. Soc.* **2015**, *137*, 15656. (c) Nishimura, H.; Fukushima, T.; Wakamiya, A.; Murata, Y.; Kaji, H. *Bull. Chem. Soc. Jpn.* **2016**, *89*, 726.
- (d) Wakamiya, A.; Nishimura, H.; Murata, Y. *Yuki Gosei Kagaku Kyokaiishi* **2016**, *74*, 1128.
- (11) Yamamoto, T.; Toyota, K.; Morita, N. *Tetrahedron Lett.* **2010**, *51*, 1364.
- (12) (a) Kasai, H.; Nalwa, H. S.; Oikawa, H.; Okada, S.; Matsuda, H.; Minami, N.; Kakuta, A.; Ono, K.; Mukoh, A.; Nakanishi, H. *Jpn. J. Appl. Phys.* **1992**, *31*, L1132. (b) Kasai, H.; Kamatani, H.; Okada, S.; Oikawa, H.; Matsuda, H.; Nakanishi, H. *Jpn. J. Appl. Phys.* **1996**, *35*, L221. (c) Kasai, H.; Oikawa, H.; Okada, S.; Nakanishi, H. *Bull. Chem. Soc. Jpn.* **1998**, *71*, 2597.
- (13) (a) Affeldt, R. F.; Iglesias, R. S.; Rodembusch, F. S.; Russowsky, D. *J. Phys. Org. Chem.* **2012**, *25*, 769. (b) Cui, X.; Charaf-Eddin, A.; Wang, J.; Le Guennic, B.; Zhao, J.; Jacquemin, D. *J. Org. Chem.* **2014**, *79*, 2038. (c) Yamaguchi, E.; Fukazawa, A.; Kosaka, Y.; Yokogawa, D.; Irle, S.; Yamaguchi, S. *Bull. Chem. Soc. Jpn.* **2015**, *88*, 1545.
- (14) (a) Bing, Y.; Selassie, D.; Paradise, R. H.; Isborn, C.; Kramer, N.; Sadilek, M.; Kaminsky, W.; Kahr, B. *J. Am. Chem. Soc.* **2010**, *132*, 7454. (b) Longhi, G.; Castiglioni, E.; Abbate, S.; Lebon, F.; Lightner, D. A. *Chirality* **2013**, *25*, 589.
- (15) (a) Mataga, N.; Kaifu, Y.; Koizumi, M. *Bull. Chem. Soc. Jpn.* **1955**, *28*, 690. (b) Mataga, N.; Kaifu, Y.; Koizumi, M. *Bull. Chem. Soc. Jpn.* **1956**, *29*, 465. (c) Lippert, E. *Z. Elektrochem.* **1957**, *61*, 962.
- (16) Frisch, M. J.; Trucks, G. W.; Schlegel, H. B.; Scuseria, G. E.; Robb, M. A.; Cheeseman, J. R.; Scalmani, G.; Barone, V.; Mennucci, B.; Petersson, G. A.; Nakatsuji, H.; Caricato, M.; Li, X.; Hratchian, H. P.; Izmaylov, A. F.; Bloino, J.; Zheng, G.; Sonnenberg, J. L.; Hada, M.; Ehara, M.; Toyota, K.; Fukuda, R.; Hasegawa, J.; Ishida, M.; Nakajima, T.; Honda, Y.; Kitao, O.; Nakai, H.; Vreven, T.; Montgomery, J. A., Jr.; Peralta, J. E.; Ogliaro, F.; Bearpark, M.; Heyd, J. J.; Brothers, E.; Kudin, K. N.; Staroverov, V. N.; Kobayashi, R.; Normand, J.; Raghavachari, K.; Rendell, A.; Burant, J. C.; Iyengar, S. S.; Tomasi, J.; Cossi, M.; Rega, N.; Millam, J. M.; Klene, M.; Knox, J. E.; Cross, J. B.; Bakken, V.; Adamo, C.; Jaramillo, J.; Gomperts, R.; Stratmann, R. E.; Yazyev, O.; Austin, A. J.; Cammi, R.; Pomelli, C.; Ochterski, J. W.; Martin, R. L.; Morokuma, K.; Zakrzewski, V. G.; Voth, G. A.; Salvador, P.; Dannenberg, J. J.; Dapprich, S.; Daniels, A. D.; Farkas, Ö.; Foresman, J. B.; Ortiz, J. V.; Cioslowski, J.; Fox, D. J. *Gaussian 09*, Revision D.01; Gaussian, Inc.: Wallingford, CT, 2009.

## Luminescence

## Optically Active Phenylethene Dimers Based on Planar Chiral Tetrasubstituted [2.2]Paracyclophane

Masayuki Gon,<sup>[a]</sup> Yasuhiro Morisaki,<sup>\*,[a, b]</sup> and Yoshiki Chujo<sup>\*,[a]</sup>

**Abstract:** Optically active phenylethene dimers based on a planar chiral 4,7,12,15-tetrasubstituted [2.2]paracyclophane were synthesized. We succeeded in controlling the molecular motion by binding luminophores in close proximity with the [2.2]paracyclophane scaffold. For example, aggregation-induced emission (AIE)-active luminophores were converted to show intense photoluminescence (PL) even in a diluted solution at room temperature and the resulting compound worked as a single-molecule thermoresponsible material around room temperature. Because of the AIE-active unit,

the molecular motion could be easily activated by heating, leading to variable and reversible PL intensity. Furthermore, the  $\pi$ -conjugated systems with the planar chirality of 4,7,12,15-tetrasubstituted [2.2]paracyclophane provided excellent characteristics on circular dichroism (CD) and circularly polarized luminescence (CPL). The obtained dimers showed high CPL performances both in a diluted solution and in an aggregation state. We succeeded in proving that simple molecular designs composed of only carbon and hydrogen atoms could create versatile optical functionalities.

## Introduction

The establishment of molecular design for controlling luminescent properties in  $\pi$ -conjugated systems is of much importance for applications not only to improve performances of organic optoelectronic devices<sup>[1]</sup> but also to produce optical sensors.<sup>[2]</sup> In the majority of organic luminescent molecules, strong emission can be observed only in a diluted solution, and weak or no emission in an aggregation state. This behavior is called aggregation-caused quenching (ACQ).<sup>[3]</sup> In particular, in planar molecules, ACQ is critically induced by strong intermolecular  $\pi$ - $\pi$  interactions that promote radiationless deactivation by exciton delocalization or excimer formation.<sup>[4]</sup> In contrast, recent reports presented another class of compounds that exhibits the opposite luminescent characteristics. Aggregation-induced emission (AIE) active molecules show subtle emission in the solution state, whereas bright emission can be observed in the aggregation state. It has been proposed that radiationless deactivation processes should be caused by vigorous intramolecular motion in the solution state. By suppressing the molecular motion in the aggregation state, strong emission can be recovered, leading to significant solid-state emissions.<sup>[5]</sup> Because of

the versatility of these switching properties, a wide variety of optical sensors have been developed.<sup>[6]</sup>

A large number of stimuli-responsive materials based on AIE behaviors have been constructed.<sup>[5e]</sup> The target-selective emission enhancements can be achieved by the immobilization of the movable units in AIE-active molecules with covalent or noncovalent bonds triggered by the target recognition.<sup>[7]</sup> Additionally, AIE properties were also varied corresponding to drastic environmental changes such as freezing of matrices,<sup>[8]</sup> polarity alteration,<sup>[9]</sup> and addition of external forces.<sup>[10]</sup> These systems were applicable for sensitive environmental sensors. Although various methodologies have been established so far, there is much room to explore precise control of molecular stacking and reflect external stimuli in the degree of stacking as optical property changes. Our target is to develop a single molecular system involving the stacking unit with luminescent properties and to realize stimuli-responsive materials toward environmental factors. A 4,7,12,15-tetrasubstituted [2.2]paracyclophane framework<sup>[11]</sup> makes it possible to control the orientation and the number of stacking molecules. In addition, the behavior was easily detected by the optical and chiroptical properties because the [2.2] paracyclophane scaffold can arrange two luminophores in close proximity at the chiral position without losing the PL performance.<sup>[12]</sup> Chiroptical properties, such as CD and CPL spectra measurements, provide detailed information about the molecular conformation and intermolecular interaction in the ground and excited state, respectively.<sup>[13]</sup> Exploring the system is important not just for understanding the interaction of  $\pi$ -conjugated molecules but also for producing functional materials, for example, high-performance CPL or stimuli-responsive materials. CPL is the phenomenon by which a chiral compound emits circularly polarized light and it is available for optically active light. Recently,

[a] Dr. M. Gon, Prof. Y. Morisaki, Prof. Y. Chujo  
Department of Polymer Chemistry  
Graduate School of Engineering, Kyoto University  
Nishikyo-ku, Katsura, Kyoto 615-8510 (Japan)  
E-mail: ymo@kwansei.ac.jp  
chujo@chujo.synchem.kyoto-u.ac.jp

[b] Prof. Y. Morisaki  
Present address: School of Science and Technology  
Kwansei Gakuin University, 2-1 Gakuen, Sanda  
Hyogo 669-1337 (Japan)

Supporting information for this article can be found under:  
<http://dx.doi.org/10.1002/chem.201605598>.

CPL has received much attention for its potential applications as a light source for 3D displays, in biochemistry, and for chirality induction in the field of organic synthesis and optical cryptography. For these reasons, we selected the optically active [2.2]paracyclophane framework and investigated the behaviors of ACQ and AIE monomers and dimers both in the dilute solution state and in the aggregation state.

Herein, we synthesized the mono- and diphenylethene-derivative monomers (**MPh1** and **MPh2**) and dimers (**DPh1** and **DPh2**) based on a planar chiral 4,7,12,15-tetrasubstituted [2.2]paracyclophane (Figure 1). **MPh1** includes a scaffold for ex-

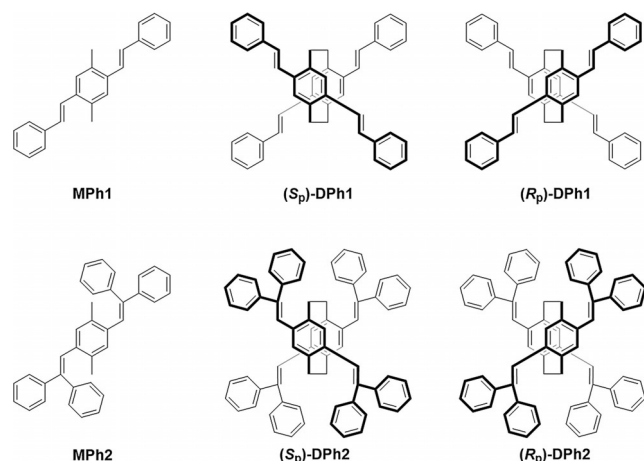


Figure 1. Structures of **MPh1**, **DPh1**, **MPh2**, and **DPh2**.

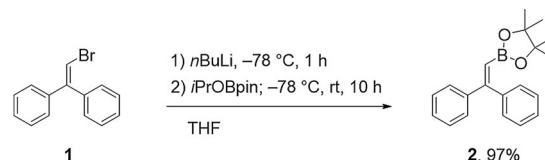
hibiting ACQ properties, while **MPh2** possesses a framework for exhibiting AIE properties.<sup>[14]</sup> By connecting two **MPh1** molecules to form the [2.2]paracyclophane framework, the resulting **DPh1** provided strong emission in the diluted solution and weak emission in the aggregation state, which was the same as the properties of **MPh1**. In contrast, **DPh2** showed strong emission even in the diluted solution and moderate emission in the aggregation state. This result means that the stacking formation with **MPh2** induced distinctly different optical properties from the single molecular unit. Furthermore, it was demonstrated that **DPh2** showed thermoresponsive photoluminescence (PL) changes around room temperature in the diluted solution. Moreover, because of the planar chirality of the dimers, **DPh1** and **DPh2** presented high-performance CPL profiles in diluted solutions and in the aggregation state. From these results, it can be expected that the tetrasubstituted [2.2]paracyclophane framework promises to be a fundamental molecular unit with the simple composition of the only carbon and hydrogen atoms for receiving stimuli-responsive as well as optically active materials.

## Experimental Section

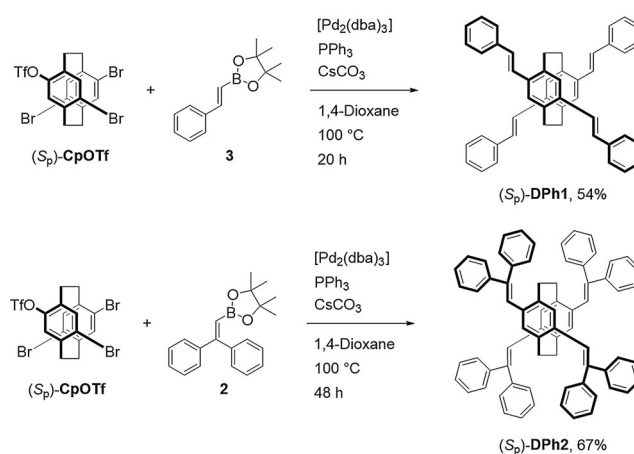
### Syntheses

The optical resolution of planar chiral 4,7,12,15-tetrasubstituted [2.2]paracyclophane was carried out using the diastereomer

method that we previously developed, and the obtained enantiopure compounds were converted to the corresponding (*S<sub>p</sub>*)- and (*R<sub>p</sub>*)-4,7,12-tribromo-15-(trifluoromethanesulfonate)[2.2]paracyclophanes ((*S<sub>p</sub>*)-**CpOTf**, (*R<sub>p</sub>*)-**CpOTf**).<sup>[12d]</sup> The synthetic routes to the target optically active cyclic compounds are shown in Schemes 1 and 2. According to the previous study on the syntheses of **DPh1**

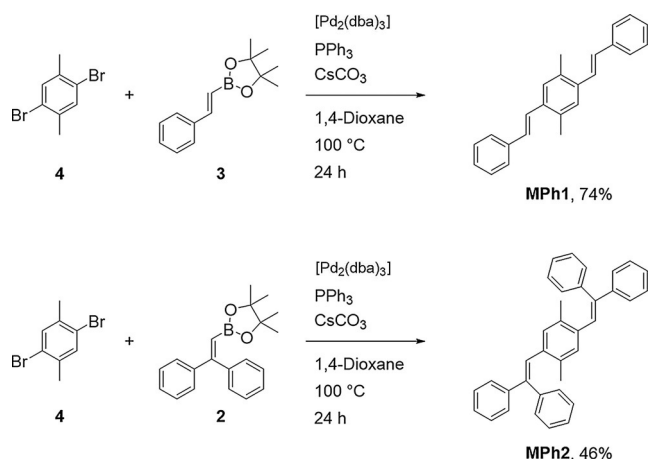


Scheme 1. Synthesis of compound **2**.



Scheme 2. Synthesis of planar chiral dimers (*S<sub>p</sub>*)-**DPh1** and **DPh2**.

and **MPh1**,<sup>[15]</sup> we modified the synthetic route to obtain optically active dimer compounds. A bromide of compound **1**<sup>[16]</sup> was converted to a boronate ester to obtain compound **2** in 97% isolated yield. Compound **2** was readily used in the Suzuki–Miyaura coupling<sup>[17]</sup> (Scheme 1). Scheme 2 shows the synthesis of the target planar chiral dimers **DPh1** and **DPh2**. In this scheme, only the reactions of the (*S<sub>p</sub>*)-isomers are shown; the (*R<sub>p</sub>*)-isomers were synthesized under identical conditions with (*R<sub>p</sub>*)-**CpOTf**. Suzuki–Miyaura coupling of (*S<sub>p</sub>*)-**CpOTf** carried out with *trans*-2-(4,4,5,5-tetramethyl-1,3,2-dioxaborolan-2-yl)styrene **3** in the catalytic system of [Pd<sub>2</sub>(dba)<sub>3</sub>]/PPh<sub>3</sub> (dba = dibenzylideneacetone) by using CsCO<sub>3</sub> as a base to afford (*S<sub>p</sub>*)-**DPh1** in 54% isolated yield. Using the same procedure, (*S<sub>p</sub>*)-**DPh2** was also prepared in 67% isolated yield. In the case of (*S<sub>p</sub>*)-**DPh2**, unreacted OTf groups were converted to OH groups to remove byproducts by silica gel column chromatography. Details are shown in the Supporting Information. Scheme 3 shows the syntheses of the monomeric model compounds, **MPh1** and **MPh2**, which are the half units of the dimers, **DPh1** and **DPh2**, respectively. As shown in Scheme 3, the same procedure as Scheme 1 was available for **MPh1** and **MPh2**, and the isolated yields of these molecules were 74 and 46%, respectively. The structures of all new compounds in this study were confirmed by <sup>1</sup>H and <sup>13</sup>C NMR spectroscopies, HRMS, and elemental analysis. The detailed synthetic procedures and NMR spectra are shown in the Supporting Information.



Scheme 3. Synthesis of model compounds **MPh1** and **MPh2**.

## Results and Discussion

### Optical properties

The optical properties of both enantiomers of  $\pi$ -conjugated dimers, **DPh1** and **DPh2** as well as their monomeric model compounds **MPh1** and **MPh2** were evaluated (Table 1). Figure 2 shows the UV/Vis absorption spectra of the compounds in diluted solutions (1,4-dioxane,  $1.0 \times 10^{-5}$  M) and the aggregation state produced in the poor solvent system (1,4-dioxane/H<sub>2</sub>O = 1/99 v/v,  $1.0 \times 10^{-5}$  M). Maximum values of the molar extinction coefficient of **DPh1** and **MPh1** in diluted solutions were larger than those in the aggregation state. In addition, the edges in the absorption band were observed in the redshifted wavelength region in the aggregation state. It is likely that intermolecular interaction should occur in the aggregation state. In the aggregation state of **MPh1**, the shoulder peak was observed at around 400 nm which was longer than the peak top wavelength of the dimer, **DPh1**, in the dilute solution state. Two reasons were probable for the explanation of the phenomenon. One is the difference of stacking formation between **DPh1** in the dilution state and **MPh1** in the aggregation state. **MPh1** could form face-to-face stacking whereas **DPh1** formed X-shaped stacking and the former interaction

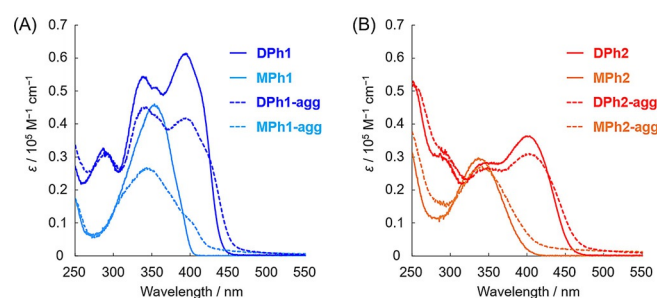


Figure 2. UV/Vis absorption spectra in 1,4-dioxane (solid line) and 1,4-dioxane/H<sub>2</sub>O = 1:99 v/v (dotted line) ( $1.0 \times 10^{-5}$  M). A) **DPh1** and **MPh1**; B) **DPh2** and **MPh2**.

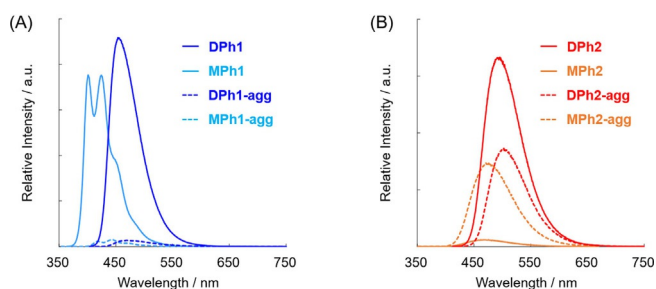
was stronger than the latter one. The other is the number of the interacted molecules. In the aggregation state of **MPh1**, two or more molecules could interact with each other. Conversely, from the comparison with **DPh2** and **MPh2**, a smaller change of maximum values of molar extinction coefficient was obtained than those with **DPh1** and **MPh1**. In the **DPh2** and **MPh2** systems, intermolecular interaction could be disturbed because of steric hindrance. The peak top wavelengths of absorption bands of **DPh1** (395 nm) and **DPh2** (403 nm) were redshifted in comparison to those of the monomers **MPh1** (353 nm) and **MPh2** (337 nm), respectively. Through-space conjugation via the [2.2]paracyclophane framework should be responsible for the redshifts of the absorption bands in the dimers.<sup>[18]</sup> The peak top wavelength of **MPh2** was shorter than that of **MPh1** although **MPh2** possesses larger numbers of the phenyl rings than those in **MPh1**. It is suggested that structural distortion could be induced in **MPh2** by steric hindrance, resulting in the restriction of conjugation length. However, a peak top wavelength of **DPh2** was observed in the longer wavelength region compared to that of **DPh1**. It is proposed that the molecular planarity could be improved by the dimerization via the [2.2]paracyclophane framework. Those data imply the existence of the restriction of molecular motion.

Figure 3 shows the PL spectra of the compounds in the diluted solution (1,4-dioxane,  $1.0 \times 10^{-5}$  M) and the aggregation state (1,4-dioxane/H<sub>2</sub>O = 1:99 v/v,  $1.0 \times 10^{-5}$  M). ACQ was clearly

Table 1. Optical properties of the compounds.

	$\lambda_{\text{abs}}$ [nm] <sup>[c]</sup>	$\lambda_{\text{lum}}$ [nm] <sup>[d]</sup>	$\tau$ [ns] <sup>[e]</sup>	$\chi^2$	$\Phi_{\text{lum}}$ <sup>[f]</sup>	$k_r$ [s <sup>-1</sup> ] <sup>[g]</sup>	$k_{\text{nr}}$ [s <sup>-1</sup> ] <sup>[g]</sup>
<b>DPh1</b> <sup>[a]</sup>	395	455	3.28	1.02	0.78	$2.4 \times 10^8$	$6.7 \times 10^7$
<b>DPh1-agg</b> <sup>[b]</sup>	394	470	0.24 (80.9%) 1.59 (19.1%)	1.58	0.03	$1.3 \times 10^{8[\text{h}]}$	$4.0 \times 10^{9[\text{h}]}$
<b>MPh1</b> <sup>[a]</sup>	353	401, 424	1.40	1.09	0.87	$6.2 \times 10^8$	$9.3 \times 10^7$
<b>MPh1-agg</b> <sup>[b]</sup>	344	443	0.24 (80.6%) 0.88 (19.4%)	1.44	0.13	$5.4 \times 10^{8[\text{h}]}$	$3.6 \times 10^{9[\text{h}]}$
<b>DPh2</b> <sup>[a]</sup>	403	494	2.60	1.17	0.58	$2.2 \times 10^8$	$1.6 \times 10^8$
<b>DPh2-agg</b> <sup>[b]</sup>	403	503	1.40	1.13	0.24	$1.7 \times 10^8$	$5.4 \times 10^8$
<b>MPh2</b> <sup>[a]</sup>	337	468	0.19	1.19	0.04	$2.1 \times 10^8$	$5.1 \times 10^9$
<b>MPh2-agg</b> <sup>[b]</sup>	341	473	2.30	1.07	0.56	$2.4 \times 10^8$	$1.9 \times 10^8$

[a] In 1,4-dioxane. [b] In 1,4-dioxane/H<sub>2</sub>O = 1:99 v/v. [c]  $1.0 \times 10^{-5}$  M. [d]  $1.0 \times 10^{-6}$  M, excited at absorption maxima. [e] Emission lifetime at  $\lambda_{\text{lum}}$ . [f] Absolute PL quantum efficiency. [g]  $k_r = \Phi_{\text{lum}}/\tau$ ,  $k_{\text{nr}} = (1 - \Phi_{\text{lum}})/\tau$ . [h] Calculated by using the major component.



**Figure 3.** PL spectra in 1,4-dioxane (solid line) and 1,4-dioxane/H<sub>2</sub>O = 1:99 v/v (dotted line) ( $1.0 \times 10^{-5}$  M). A) **DPh1** and **MPh1**; B) **DPh2** and **MPh2**.

observed from **DPh1** ( $\Phi_{\text{lum}}=0.78$  in diluted solution,  $\Phi_{\text{lum}}=0.03$  in aggregation state) and **MPh1** ( $\Phi_{\text{lum}}=0.87$  in diluted solution,  $\Phi_{\text{lum}}=0.13$  in aggregation state). Intermolecular interaction should occur in the planar conformations. Interestingly, **MPh2** showed AIE properties ( $\Phi_{\text{lum}}=0.04$  in diluted solution,  $\Phi_{\text{lum}}=0.56$  in the aggregation state); however, **DPh2** provided good PL properties in both solution and aggregation states ( $\Phi_{\text{lum}}=0.58$  in diluted solution,  $\Phi_{\text{lum}}=0.24$  in aggregation state). To comprehend the unique optical properties of **MPh2** and **DPh2**, detailed analyses were executed.

In the most of AIE-active molecules, the degree of molecular motion in the excited state plays a significant role in AIE properties. To confirm the effect of molecular motion, kinetic information was gathered from the calculations of radiative ( $k_r$ ) and nonradiative rate constants ( $k_{\text{nr}}$ ) with PL lifetime measurements (Table 1 and Figure S11, Supporting Information). In diluted solutions, the  $k_r$ s of **DPh2** and **MPh2** were almost the same ( $k_r=2.2 \times 10^8$  for **DPh2**,  $2.1 \times 10^8$  for **MPh2**), whereas the  $k_{\text{nr}}$  of **DPh2** was much smaller than that of **MPh2** ( $k_{\text{nr}}=1.6 \times 10^8$  for **DPh2**,  $5.1 \times 10^9$  for **MPh2**). These data clearly indicate that intramolecular motion should occur in **MPh2**. In addition, the rigid and stable [2.2]paracyclophane framework suppressed molecular motion in the excited state, leading to a smaller  $k_{\text{nr}}$  than that of **MPh2**. In the relationship of the  $k_{\text{nr}}$ s of **DPh1** ( $k_{\text{nr}}=6.7 \times 10^7$ ) and **MPh1** ( $k_{\text{nr}}=9.3 \times 10^7$ ), the same tendency was observed. In summary, **DPh2** should intrinsically have luminescent properties both in the solution and aggregation states. However, because of molecular planarity as suggested in the UV/Vis absorption spectrum, some degree of ACQ was induced via the intermolecular  $\pi$ - $\pi$  interaction in the aggregation state. Therefore, the moderate level of emission can be observed. The  $k_{\text{nr}}$  of **DPh1** was smaller than that of **DPh2** because the highly planar structure of **DPh1** made an efficient extension of the  $\pi$ -conjugated system and that contributed to the rigid conformation. In the PL spectra, the wavelength of the peak top of **MPh2** was shorter than that of **MPh1** in spite of the fact that the opposite result was obtained in the UV/Vis absorption spectra. Considering that the PL spectrum of **MPh1** exhibited a vibrational structure whereas that of **MPh2** did not show it, in the case of **MPh2**, structure relaxation occurred in the excited state, which led to a redshifted PL spectrum.

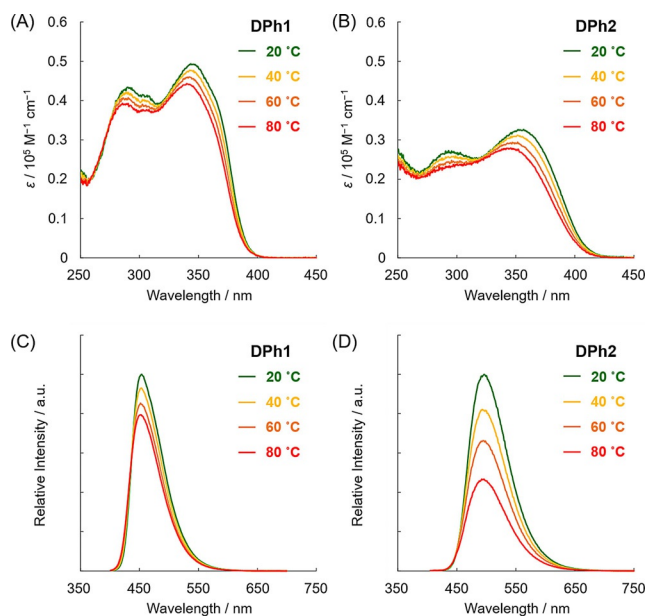
### Variable-temperature PL measurements

Variable-temperature UV/Vis absorption and PL measurements were carried out to obtain further information on the suppression of the molecular motion by the [2.2]paracyclophane framework. These spectra were obtained in the diluted toluene solution ( $1.0 \times 10^{-5}$  M for absorption and  $1.0 \times 10^{-6}$  M for the PL measurements) at 20, 40, 60, and 80 °C. Relative PL quantum efficiencies were calculated by using the absolute PL quantum efficiency in 1,4-dioxane at 25 °C as a standard (Table 2). In the

Table 2. Relative PL quantum efficiencies. <sup>[a,b]</sup>				
	20 [°C]	40 [°C]	60 [°C]	80 [°C]
<b>DPh1</b>	0.70	0.68	0.65	0.63
<b>DPh2</b>	0.51	0.44	0.39	0.29

[a] In toluene ( $1.0 \times 10^{-6}$  M excited at absorption maximum). [b] Relative PL quantum efficiencies were calculated from absolute PL quantum efficiencies of **DPh1** and **DPh2** in 1,4-dioxane (Table 1), respectively.

UV/Vis absorption spectra (Figures 4A and B), by increasing the temperature, the molar extinction coefficients of **DPh1** and **DPh2** decreased, and the wavelengths of absorption maxima were blueshifted. The effective conjugation length should be shortened by the molecular motion of the phenyl rings. In the PL spectra, the intensity of **DPh2** drastically decreased by increasing the temperature (Figures 4C and D). The PL quantum efficiencies of **DPh1** and **DPh2** decreased 9 and 43% by increasing the temperature from 20 to 80 °C, respectively, and they were recovered by cooling. These results represent that the molecular motion of the phenyl rings in **DPh2** was sup-



**Figure 4.** UV/Vis and PL variable-temperature spectra in toluene ( $1.0 \times 10^{-5}$  M for UV/Vis and  $1.0 \times 10^{-6}$  M for PL, excited at absorption maximum) at 20, 40, 60, and 80 °C; A) UV/Vis spectra of **DPh1**; B) UV/Vis spectra of **DPh2**; PL spectra of **DPh1**; PL spectra of **DPh2**.

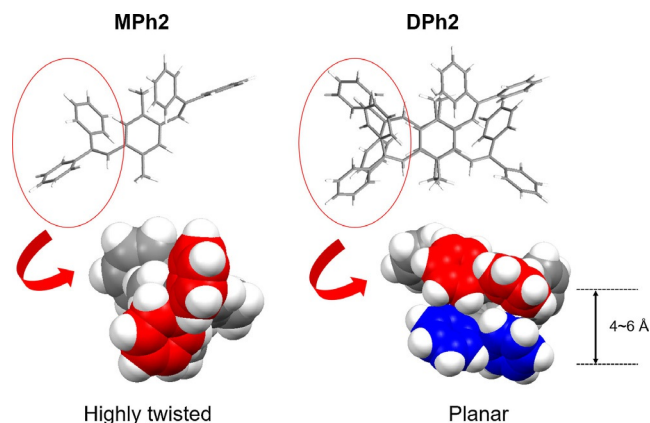
pressed at room temperature. By increasing the solution temperature, the molecular motion should be activated, resulting in acceleration of nonradiative deactivation. Taking advantage of the sensitivity of AIE-active molecules and rigidity of [2.2]paracyclophane frameworks, we successfully synthesized the single-molecule thermoresponsive material. Although several thermoresponsive systems with AIE-active molecule were reported, most of them were constructed based on a sol-gel transition or a composite system.<sup>[19]</sup> Three-dimensionally binding AIE-active molecules in close proximity with covalent bonds is a new strategy and the results are expected to contribute to a development of single-molecule optical sensors.

### Dispersion of the dimers in polystyrene film

To investigate the effect of molecular motion on ACQ, **DPh1** and **DPh2** were dispersed in polystyrene ( $M_n = 80,000$ , PDI = 2.6) films, and their optical properties were monitored. The films including 1, 2, 5, 10, 20, 40, 60, 80, and 100 wt% of **DPh1** and **DPh2** in polystyrene were prepared with a spin-coat method from 40  $\mu\text{L}$   $\text{CHCl}_3$  solution ( $1.0 \times 10^{-3}$  M of **DPh1** and **DPh2** in polystyrene). The results are summarized in Figure S12 and Table S1, Supporting Information. **DPh1** and **DPh2** exhibited high absolute PL quantum efficiencies in the 1 wt% films ( $\Phi_{\text{lum}} = 0.86$  and 0.80, respectively). The  $\Phi_{\text{lum}}$  value of the 1 wt% film of **DPh2** was much higher than that in the diluted solution ( $\Phi_{\text{lum}} = 0.58$ ). This result indicates that the molecular motion of **DPh2** was largely stopped in the film and was active in the dilute solution. Conversely, the molecular motion of **DPh1** was highly restricted even in the dilute solution state because similar  $\Phi_{\text{lum}}$  values were obtained both in the dilute solution state ( $\Phi_{\text{lum}} = 0.79$ ) and in the 1 wt% film state. The  $\Phi_{\text{lum}}$  of **DPh1** dropped rapidly from 2 to 20 wt% films ( $\Phi_{\text{lum}} = 0.79$  for 2 wt%, 0.55 for 5 wt%, 0.42 for 10 wt%, 0.26 for 20 wt%), and the 40, 60, 80, and 100 wt% films showed low  $\Phi_{\text{lum}}$  values ( $\Phi_{\text{lum}} < 0.1$ ). It is likely that ACQ should occur in these films. On the other hand, when increasing the rate of **DPh2** in polystyrene films, the decrease of the  $\Phi_{\text{lum}}$  was moderate. A high  $\Phi_{\text{lum}}$  value was kept in the 2 wt% film ( $\Phi_{\text{lum}} = 0.82$ ) and it decreased from the 5 wt% film ( $\Phi_{\text{lum}} = 0.69$ ). Finally, the  $\Phi_{\text{lum}}$  value reached 0.27 in the 100 wt% film, which was pure **DPh2**. This value was almost identical to the aggregate of **DPh2** ( $\Phi_{\text{lum}} = 0.24$ ). Therefore, it was suggested that the decrease of  $\Phi_{\text{lum}}$  in the aggregate of **DPh2** was caused by ACQ. Although a decrease of  $\Phi_{\text{lum}}$  occurred, the obtained **DPh2** films provided good PL quantum efficiencies even in the condensed state and those results can be an advantage for obtaining high brightness films.

### Molecular models

In **DPh2**, experimental optical data strongly suggested the existence of suppression of the molecular motion between two luminophores stacked at the [2.2]paracyclophane unit. Further information about the molecular motion was evaluated by DFT. The structures of **MPh2** and **DPh2** were optimized at the BLYP/def2-TZVPP level. Resulting molecular structures are



**Figure 5.** Molecular models of **MPh2** and **DPh2**. The structure was optimized by DFT at BLYP/def2-TZVPP levels.

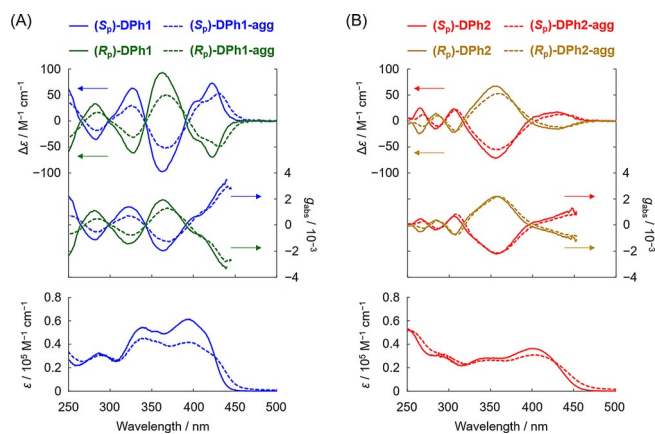
shown in Figure 5. From the molecular models, it was clearly shown that the optimized structure of **MPh2** was highly twisted, whereas that of **DPh2** was relatively planar because of the intramolecular stacking. The two luminophores were located at the distance of 4–6 Å, which was sufficient to inhibit the free rotation. The restriction of the molecular motion corresponded to the high  $\Phi_{\text{lum}}$  value of **DPh2** in the diluted solution. However, in the aggregation state, the ACQ should occur. The highly twisted structure of **MPh2** should be favorable for maintaining molecular motions in the solution and avoiding ACQ in the aggregation, leading to the AIE behavior. Thus, it is summarized that the stacking at the [2.2]paracyclophane unit should contribute to enhancing molecular planarity even in the presence of multiple hindered groups, leading to unique emission behaviors.

### Chiroptical properties

Finally, the chiroptical properties of the ground and excited states of **DPh1** and **DPh2** were investigated by CD and CPL spectroscopies, respectively. Chiroptical data such as CD and CPL dissymmetry factor<sup>[20]</sup> ( $g_{\text{abs}}$  and  $g_{\text{lum}}$ , respectively) are summarized in Table 3. Figure 6 shows the CD and absorption spectra of both enantiomers of **DPh1** and **DPh2** in the diluted solution (1,4-dioxane,  $1.0 \times 10^{-5}$  M) and in the aggregation state (1,4-dioxane/ $\text{H}_2\text{O} = 1:99$  v/v,  $1.0 \times 10^{-5}$  M). From both enantio-

Table 3. Chiroptical properties: Spectroscopic data of ( $S_p$ )-isomers.		
	$g_{\text{abs}}^{[a]}/10^{-3}$	$g_{\text{lum}}^{[b]}/10^{-3}$
( $S_p$ )- <b>DPh1</b>	+3.5	+3.7
( $S_p$ )- <b>DPh1-agg</b>	+3.0	+4.3
( $S_p$ )- <b>DPh2</b>	+1.0	+0.73
( $S_p$ )- <b>DPh2-agg</b>	+0.87	+0.90

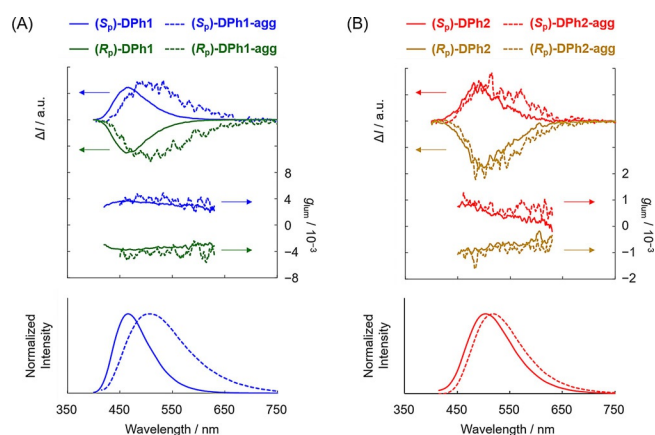
[a]  $g_{\text{abs}} = 2\Delta\epsilon/\epsilon$ , in which  $\Delta\epsilon$  indicates differences of absorbance between left- and right-handed circularly polarized light, respectively. The  $g_{\text{abs}}$  value of the first peak top was estimated. [b]  $g_{\text{lum}} = 2(I_{\text{left}} - I_{\text{right}})/(I_{\text{left}} + I_{\text{right}})$ , in which  $I_{\text{left}}$  and  $I_{\text{right}}$  indicate luminescence intensities of left- and right-handed CPL, respectively. The average  $g_{\text{lum}}$  value of the around peak top was estimated.



**Figure 6.** CD,  $g_{\text{abs}}$ , and absorption spectra in 1,4-dioxane (solid line) and in 1,4-dioxane/H<sub>2</sub>O = 1:99 v/v (dotted line) ( $1.0 \times 10^{-5}$  M). A) (*S<sub>p</sub>*)- and (*R<sub>p</sub>*)-DPh1; B) (*S<sub>p</sub>*)- and (*R<sub>p</sub>*)-DPh2.

mer solutions, mirror-image Cotton effects were observed clearly in the CD spectra. In the diluted solution, the  $g_{\text{abs}}$  values of the first Cotton effect were estimated to be  $+3.5 \times 10^{-3}$  for (*S<sub>p</sub>*)-DPh1 and  $+1.0 \times 10^{-3}$  for (*S<sub>p</sub>*)-DPh2, respectively. In the aggregation state, the  $g_{\text{abs}}$  values of the first Cotton effect were estimated to be  $+3.0 \times 10^{-3}$  for (*S<sub>p</sub>*)-DPh1 and  $+0.87 \times 10^{-3}$  for (*S<sub>p</sub>*)-DPh2, respectively. When these compounds formed the aggregates, the  $g_{\text{abs}}$  values for (*S<sub>p</sub>*)- and (*R<sub>p</sub>*)-DPh1 decreased and the pattern of the Cotton effect was redshifted in all regions, whereas those for (*S<sub>p</sub>*)- and (*R<sub>p</sub>*)-DPh2 remained in almost all regions. This result also indicates a stronger intermolecular interaction of DPh1 and a weaker intermolecular interaction of DPh2 because the structure of DPh1 was planar and that of DPh2 was twisted.

The CPL spectra of both enantiomers of DPh1 and DPh2 in the diluted solution (1,4-dioxane,  $1.0 \times 10^{-5}$  M) and in the aggregation state (1,4-dioxane/H<sub>2</sub>O = 1:99 v/v,  $1.0 \times 10^{-5}$  M) are shown in Figure 7. Mirror-image CPL spectra were obtained from the enantiomers. The  $g_{\text{lum}}$  values were estimated to be  $+3.7 \times 10^{-3}$  for (*S<sub>p</sub>*)-DPh1 and  $+0.73 \times 10^{-3}$  for (*S<sub>p</sub>*)-DPh2 in the diluted solution, and  $+4.3 \times 10^{-3}$  for (*S<sub>p</sub>*)-DPh1 and  $+0.90 \times$



**Figure 7.** CPL,  $g_{\text{lum}}$ , and PL spectra in 1,4-dioxane (solid line) and 1,4-dioxane/H<sub>2</sub>O = 1:99 v/v (dotted line) ( $1.0 \times 10^{-5}$  M). A) (*S<sub>p</sub>*)- and (*R<sub>p</sub>*)-DPh1; B) (*S<sub>p</sub>*)- and (*R<sub>p</sub>*)-DPh2. Excitation wavelength: 350 nm.

$10^{-3}$  for (*S<sub>p</sub>*)-DPh2 in the aggregation state. In the aggregation systems of (*S<sub>p</sub>*)- and (*R<sub>p</sub>*)-DPh1, CPL peak tops were redshifted, and the  $g_{\text{lum}}$  values increased because of intermolecular interaction in the excited state. On the other hand, small changes were observed in the CPL peak top and  $g_{\text{lum}}$  values of (*S<sub>p</sub>*)-DPh2 due to weak intermolecular interaction in the excited state. In the diluted solution, DPh1 exhibited excellent CPL profiles ( $\epsilon_{\text{max}} = 61,000 \text{ M}^{-1} \text{ cm}^{-1}$ ,  $\Phi_{\text{lum}} = 0.78$  and  $g_{\text{lum}} = +3.7 \times 10^{-3}$  for (*S<sub>p</sub>*)-DPh1,  $\epsilon_{\text{max}}$ : maximum of molar extinction coefficient) in comparison to the recently reported CPL compounds.<sup>[14a]</sup> On the other hand, in the aggregation state, DPh2 showed good CPL profiles ( $\epsilon_{\text{max}} = 31,000 \text{ M}^{-1} \text{ cm}^{-1}$ ,  $\Phi_{\text{lum}} = 0.24$  and  $g_{\text{lum}} = +0.90 \times 10^{-3}$  for (*S<sub>p</sub>*)-DPh2).

## Conclusion

Optically active phenylene dimers, DPh1 and DPh2, were synthesized with a planar chiral 4,7,12,15-tetrasubstituted [2.2]paracyclophane. From the series of experimental data and theoretical calculations, it is strongly suggested that molecular motion can be efficiently regulated by stacking with two luminophores in close proximity by the [2.2]paracyclophane unit even in the presence of multiple steric hindered groups. As a result, unique luminescent behaviors were monitored during phase transition. By increasing the temperature, PL intensity of DPh2 decreased sensitively. Subsequently, the intensity was recovered by cooling. Moreover, DPh1 and DPh2 showed good chiroptical properties and dissymmetry factors on the order of approximately  $10^{-3}$ . DPh1 had excellent CPL profiles in the diluted solution, and DPh2 had good CPL profiles in the aggregation state. Those effects originate from the planar chiral, rigid, and stable 4,7,12,15-tetrasubstituted[2.2]paracyclophane scaffold. Since these results are realized only with carbon and hydrogen atoms, the [2.2]paracyclophane unit could be a versatile building block for constructing advanced optical materials with multiple functions.

## Acknowledgements

This work was supported by a Grant-in-Aid for Young Scientists (A) (no. 24685018) from the Ministry of Education, Culture, Sports, Science and Technology (MEXT) of Japan. M.G. appreciates Research Fellowships (no. 14J02514) from the Japan Society for the Promotion of Science for Young Scientists. The authors are grateful to Professor Kazuo Akagi and Dr. Kazuyoshi Watanabe (Department of Polymer Chemistry, Graduate School of Engineering, Kyoto University) for CPL data analysis and valuable discussions.

**Keywords:** aggregation-induced emission · chirality · conjugation · luminescence · paracyclophanes

[1] a) *Organic Light Emitting Devices: Synthesis Properties and Application* (Eds.: K. Müellen, U. Scherf), Wiley-VCH, Weinheim, 2006; b) *Organic Photovoltaics: Materials, Device Physics, and Manufacturing Technologies* (Eds.: C. Brabec, V. Dyakonov, U. Scherf), Wiley-VCH, Weinheim, 2008.

- [2] X. Wang, O. S. Wolfbeis, R. J. Meier, *Chem. Soc. Rev.* **2013**, *42*, 7834–7869.
- [3] S. W. Thomas, G. D. Joly, T. M. Swager, *Chem. Rev.* **2007**, *107*, 1339–1386.
- [4] S. A. Jenekhe, J. A. Osaheni, *Science* **1994**, *265*, 765–768.
- [5] a) *Aggregation-induced emission: Fundamentals* (Eds.: A. Qin, B. Z. Tang), Wiley, New York, **2013**; b) *Aggregation-induced emission: Applications* (Eds.: A. Qin, B. Z. Tang), Wiley, New York, **2013**; c) J. Luo, Z. Xie, J. W. Y. Lam, L. Cheng, H. Chen, C. Qiu, H. S. Kwok, X. Zhan, Y. Liu, D. Zhu, B. Z. Tang, *Chem. Commun.* **2001**, 1740–1741; d) Y. Hong, J. W. Y. Lam, B. Z. Tang, *Chem. Soc. Rev.* **2011**, *40*, 5361–5388; e) J. Mei, N. L. C. Leung, R. T. K. Kwok, J. W. Y. Lam, B. Z. Tang, *Chem. Rev.* **2015**, *115*, 11718–11940.
- [6] a) J. Wu, W. Liu, J. Ge, H. Zhang, P. Wang, *Chem. Soc. Rev.* **2011**, *40*, 3483–3495; b) Y. Cai, L. Li, Z. Wang, J. Z. Sun, A. Qin, B. Z. Tang, *Chem. Commun.* **2014**, *50*, 8892–8895; c) A. Hirose, K. Tanaka, R. Yoshii, Y. Chujo, *Polym. Chem.* **2015**, *6*, 5590–5595; d) R. Yoshii, A. Hirose, K. Tanaka, Y. Chujo, *J. Am. Chem. Soc.* **2014**, *136*, 18131–18139.
- [7] a) C. Li, T. Wu, C. Hong, G. Zhang, S. Liu, *Angew. Chem. Int. Ed.* **2012**, *51*, 455–459; *Angew. Chem.* **2012**, *124*, 470–474; b) J. Liang, R. T. K. Kwok, H. Shi, B. Z. Tang, B. Liu, *ACS Appl. Mater. Interfaces* **2013**, *5*, 8784–8789; c) Y. Hong, H. Xiong, J. W. Y. Lam, M. Häußler, J. Liu, Y. Yu, Y. Zhong, H. H. Y. Sung, I. D. Williams, K. S. Wong, B. Z. Tang, *Chem. Eur. J.* **2010**, *16*, 1232–1245; d) L. Xu, Z. Zhu, X. Zhou, J. Qin, C. Yang, *Chem. Commun.* **2014**, *50*, 6494–6497; e) D. Ding, J. Liang, H. Shi, R. T. K. Kwok, M. Gao, G. Feng, Y. Yuan, B. Z. Tang, B. Liu, *J. Mater. Chem. B* **2014**, *2*, 231–238.
- [8] a) K. Suenaga, R. Yoshii, K. Tanaka, Y. Chujo, *Macromol. Chem. Phys.* **2016**, *217*, 414–421; b) K. Kokado, A. Nagai, Y. Chujo, *Macromolecules* **2010**, *43*, 6463–6468.
- [9] a) P. Alam, M. Karanam, D. Bandyopadhyay, A. R. Choudhury, I. R. Laskar, *Eur. J. Inorg. Chem.* **2014**, 3710–3719; b) J. J. Peterson, A. R. Davis, M. Werre, E. B. Coughlin, K. R. Carter, *ACS Appl. Mater. Interfaces* **2011**, *3*, 1796–1799.
- [10] a) R. Yoshii, K. Suenaga, K. Tanaka, Y. Chujo, *Chem. Eur. J.* **2015**, *21*, 7231–7237; b) M. Yamaguchi, S. Ito, A. Hirose, K. Tanaka, Y. Chujo, *J. Mater. Chem. C* **2016**, *4*, 5314–5319; c) H. Yuan, K. Wang, K. Yang, B. Liu, B. Zou, *J. Phys. Chem. Lett.* **2014**, *5*, 2968–2973; d) H. Imoto, K. Kizaki, S. Watase, K. Matsukawa, K. Naka, *Chem. Eur. J.* **2015**, *21*, 12105–12111; e) X. Y. Shen, Y. J. Wang, E. Zhao, W. Z. Yuan, Y. Liu, P. Lu, A. Qin, Y. Ma, J. Z. Sun, B. Z. Tang, *J. Phys. Chem. C* **2013**, *117*, 7334–7347.
- [11] a) *Cyclophane Chemistry: Synthesis Structures and Reactions* (Ed.: F. Vçgtle), Wiley, Chichester, **1993**; b) *Modern Cyclophane Chemistry* (Eds.: R. Gleiter, H. Hopf), Wiley-VCH, Weinheim, **2004**.
- [12] a) Y. Morisaki, R. Hifumi, L. Lin, K. Inoshita, Y. Chujo, *Chem. Lett.* **2012**, *41*, 990–992; b) Y. Morisaki, R. Hifumi, L. Lin, K. Inoshita, Y. Chujo, *Polym. Chem.* **2012**, *3*, 2727–2730; c) Y. Morisaki, K. Inoshita, Y. Chujo, *Chem. Eur. J.* **2014**, *20*, 8386–8390; d) Y. Morisaki, M. Gon, T. Sasamori, N. Tokitoh, Y. Chujo, *J. Am. Chem. Soc.* **2014**, *136*, 3350–3353; e) M. Gon, Y. Morisaki, Y. Chujo, *J. Mater. Chem. C* **2015**, *3*, 521–529; f) M. Gon, Y. Morisaki, Y. Chujo, *Eur. J. Org. Chem.* **2015**, 7756–7762; g) M. Gon, H. Kozuka, Y. Morisaki, Y. Chujo, *Asian J. Org. Chem.* **2016**, *5*, 353–359; h) M. Gon, Y. Morisaki, R. Sawada, Y. Chujo, *Chem. Eur. J.* **2016**, *22*, 2291–2298; i) Y. Morisaki, R. Sawada, M. Gon, Y. Chujo, *Chem. Asian J.* **2016**, *11*, 2524–2527.
- [13] a) E. M. Sánchez-Carnerero, A. R. Agarrabeitia, F. Moreno, B. L. Maroto, G. Muller, M. J. Ortiz, S. de la Moya, *Chem. Eur. J.* **2015**, *21*, 13488–13500; b) J. Roose, B. Z. Tang, K. S. Wong, *Small* **2016**, *12*, 6495–6512; c) J. Kumar, T. Nakashima, T. Kawai, *J. Phys. Chem. Lett.* **2015**, *6*, 3445–3452; d) H. Maeda, Y. Bando, *Pure Appl. Chem.* **2013**, *85*, 1967–1978.
- [14] K. Itami, Y. Ohashi, J. Yoshida, *J. Org. Chem.* **2005**, *70*, 2778–2792.
- [15] B. König, B. Knieriem, A. Meijere, *Chem. Ber.* **1993**, *126*, 1643–1650.
- [16] A. Annunziata, C. Galli, P. Gentili, A. Guarnieri, M. Beit-Yannai, Z. Rappoport, *Eur. J. Org. Chem.* **2002**, *13*, 2136–2143.
- [17] N. Miyaoura, K. Yamada, A. Suzuki, *Tetrahedron Lett.* **1979**, *20*, 3437–3440.
- [18] a) S. Wang, G. C. Bazan, S. Tretiak, S. Mukamel, *J. Am. Chem. Soc.* **2000**, *122*, 1289–1297; b) G. P. Bartholomew, G. C. Bazan, *Acc. Chem. Res.* **2001**, *34*, 30–39; c) G. P. Bartholomew, G. C. Bazan, *Synthesis* **2002**, 1245–1255; d) G. P. Bartholomew, G. C. Bazan, *J. Am. Chem. Soc.* **2002**, *124*, 5183–5196; e) D. S. Seferos, D. A. Banach, N. A. Alcantar, J. N. Israelachvili, G. C. Bazan, *J. Org. Chem.* **2004**, *69*, 1110–1119; f) G. P. Bartholomew, M. Rumi, S. J. K. Pond, J. W. Perry, S. Tretiak, G. C. Bazan, *J. Am. Chem. Soc.* **2004**, *126*, 11529–11542; g) J. W. Hong, H. Y. Woo, G. C. Bazan, *J. Am. Chem. Soc.* **2005**, *127*, 7435–7443; h) G. C. Bazan, *J. Org. Chem.* **2007**, *72*, 8615–8635.
- [19] a) M. Wang, D. Zhang, G. Zhang, D. Zhu, *Chem. Phys. Lett.* **2009**, *475*, 64–67; b) J. Liang, Z. Chen, J. Yin, G.-A. Yu, S. H. Liu, *Chem. Commun.* **2013**, 49, 3567–3569; c) W. Guan, J. Lu, W. Zhou, C. Lu, *Chem. Commun.* **2014**, *50*, 11895–11898; d) N. Song, D.-X. Chen, Y.-C. Qiu, X.-Y. Yang, B. Xu, W. Tian, Y.-W. Yang, *Chem. Commun.* **2014**, *50*, 8231–8234; e) H. Zheng, C. Li, C. He, Y. Q. Dong, Q. Liu, P. Qin, C. Zeng, H. Wang, *J. Mater. Chem. C* **2014**, *2*, 5829–5835; f) L. Zang, H. Shang, D. Wei, S. Jiang, *Sens. Actuators B* **2013**, *185*, 389–397; g) Y. Xu, P. Xue, D. Xu, X. Zhang, X. Liu, H. Zhou, J. Jia, X. Yang, F. Wang, R. Lu, *Org. Biomol. Chem.* **2010**, *8*, 4289–4296; h) Q. Chen, D. Zhang, G. Zhang, X. Yang, Y. Feng, Q. Fan, D. Zhu, *Adv. Funct. Mater.* **2010**, *20*, 3244–3251; i) T. Han, X. Feng, J. Shi, B. Tong, Y. Dong, J. W. Y. Lam, Y. Dong, B. Z. Tang, *J. Mater. Chem. C* **2013**, *1*, 7534–7539; j) Y. Jiang, X. Yang, C. Ma, C. Wang, Y. Chen, F. Dong, B. Yang, K. Yu, Q. Lin, *ACS Appl. Mater. Interfaces* **2014**, *6*, 4650–4657.
- [20] A CD dissymmetry factor is defined as  $g_{\text{abs}} = 2\Delta\epsilon/\epsilon$ , in which  $\Delta\epsilon$  indicates differences of absorbance between left- and right-handed circularly polarized light. CPL dissymmetry factor is defined as  $g_{\text{lum}} = 2(I_{\text{left}} - I_{\text{right}})/(I_{\text{left}} + I_{\text{right}})$ , in which  $I_{\text{left}}$  and  $I_{\text{right}}$  indicate luminescence intensities of left- and right-handed CPL, respectively.

Manuscript received: November 30, 2016

Accepted Article published: January 25, 2017

Final Article published: February 22, 2017

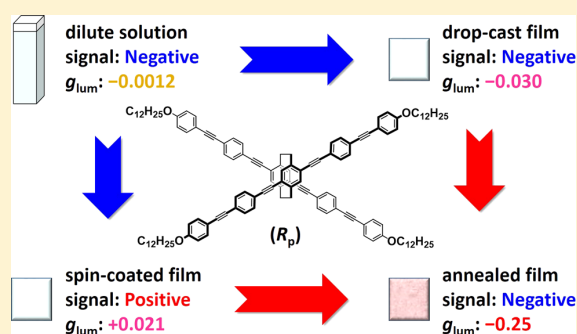
# Enhancement and Controlling the Signal of Circularly Polarized Luminescence Based on a Planar Chiral Tetrasubstituted [2.2]Paracyclophane Framework in Aggregation System

Masayuki Gon,<sup>1</sup> Risa Sawada, Yasuhiro Morisaki,\* and Yoshiki Chujo\*

Department of Polymer Chemistry, Graduate School of Engineering, Kyoto University, Nishikyo-ku, Katsura, Kyoto 615-8510, Japan

## Supporting Information

**ABSTRACT:** Optically active  $\pi$ -conjugated oligo(*p*-phenylene ethynylene) dimers with a planar chiral 4,7,12,15-tetrasubstituted [2.2]paracyclophane were synthesized. We investigated the optical and chiroptical properties of the racemic and optically active compounds by UV–vis absorption, photoluminescence (PL), circular dichroism (CD), and circularly polarized luminescence (CPL) measurements in the ground and excited states. Aggregates were prepared by the self-assembly in the mixed  $\text{CHCl}_3/\text{MeOH}$  solution, a spin-coated film, a drop-cast film, and the annealed films. In the dilute solution, the dimers exhibited good chiroptical properties, such as dissymmetry factors ( $g_{\text{abs}}$  and  $g_{\text{lum}}$ ) in  $10^{-3}$  order, large absorption coefficient, and high absolute PL quantum efficiency. In the aggregation state, UV–vis absorption and PL measurements suggested that one of the dimers formed J-aggregates and the others constructed parallel H-aggregates or inclined H-aggregates as kinetically stable self-assemblies. Those differences were caused by the length of  $\pi$ -conjugation and the strength of the intermolecular  $\pi$ – $\pi$  interaction. Transmission electron microscope (TEM) observations indicated the formation of the regular aggregates, and the aggregates made fiber structure. The spin-coated films and drop-cast films showed opposite CPL signal, and the values of dissymmetry factors reached  $10^{-2}$  order. The annealing process provided the thermodynamically stable forms to the films, and the  $g_{\text{lum}}$  values of the drop-cast thick films were drastically enhanced. Consequently, the  $g_{\text{lum}}$  values reached  $10^{-1}$  order (maximum:  $|g_{\text{lum}}| = 0.27$ ). Those are one of the largest  $g_{\text{lum}}$  values of the organic compounds in the self-assembly system. All properties observed in this study are attributed to the planar and high symmetrical X-shaped structure of the planar chiral 4,7,12,15-tetrasubstituted [2.2]paracyclophane framework. This is the first report realizing  $g_{\text{lum}}$  in  $10^{-1}$  order using the self-assembly system based on planar chirality as the only chiral source.



## INTRODUCTION

The molecular design of  $\pi$ -conjugated systems is essential to afford excellent optical properties in photoluminescent materials, optoelectronic devices, and organic thin film solar cell.<sup>1–4</sup> Many researchers have explored and developed effective  $\pi$ -conjugated systems for controlling the device performances. As one of the methods of controlling the properties, there is construction of higher-ordered structure with self-assembly. Various properties could be obtained from a single compound by tuning strength of an intermolecular interaction. In the case of  $\pi$ -conjugated materials, the main interaction is  $\pi$ – $\pi$  interaction which has been used for adding extra properties to the materials.<sup>5–10</sup> For example, J-aggregates and H-aggregates are representative higher-ordered structures and they are widely known as showing specific optical properties.<sup>11,12</sup> Considering the case of the optically active  $\pi$ -conjugated compounds, their aggregates show different properties from the monomeric system, and sometimes the improvement of chiroptical properties could be observed. Usually, the change of the chiroptical properties is detected by the spectral change of circularly dichroism (CD). For example, it is reported that regularly higher-ordered chiral structures,

such as helix structure, can improve chiroptical properties of self-assembly in the ground state.<sup>13–19</sup> In these days, circularly polarized luminescence (CPL) is focused as another chiroptical property. CPL is the phenomenon that optically active compounds emit circularly polarized light. The optically active light has high potentiality for the application to functional materials, for example, the light source of 3D display, in the field of biochemistry, chirality induction in the field of organic synthesis, and optical cryptography. Therefore, a lot of molecules have been designed to obtain high performance on chiroptical properties, such as big dissymmetry factor of luminescence ( $g_{\text{lum}}$ ), large molar extinction coefficient ( $\epsilon_{\text{abs}}$ ), and high photoluminescence quantum efficiency ( $\Phi_{\text{lum}}$ ).<sup>20–56</sup> It should be noted that the CPL properties could be enhanced by regularly higher-ordered chiral structures based on low molecular weight compounds<sup>56–68</sup> and polymers<sup>37–54</sup> in the excited state. In addition, chirality could be controlled by the self-assembly between kinetically and

**Received:** December 29, 2016

**Revised:** February 16, 2017

**Published:** February 24, 2017

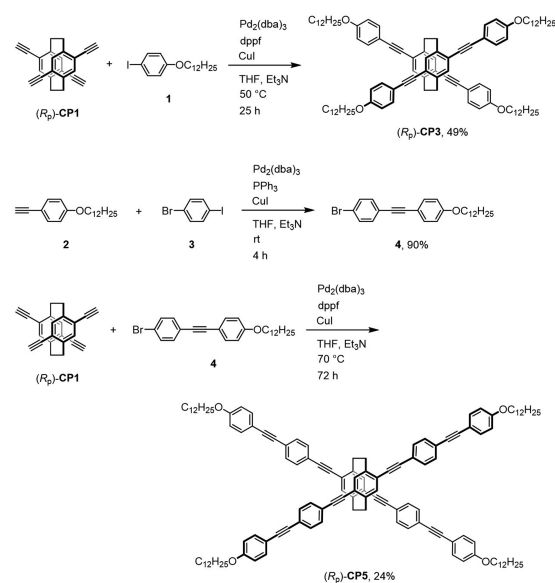
thermodynamically stable aggregates.<sup>69</sup> From those reports, it could be seen that almost all chiral aggregates were based on indirect chirality induction, such as modification by chiral substituents in a side chain, or based on torsion structure, such as helicity and axial chirality. If there are chirality based on planar structure, it should be realized to make strong and effective chiral aggregates by direct induction of chirality and stable intermolecular  $\pi$ - $\pi$  interaction. Recently, we reported the planar chiral 4,7,12,15-tetrasubstituted [2.2]paracyclophane framework<sup>70–72</sup> which stacked two chromophores in the chiral position.<sup>31–36</sup> The framework has good planarity and symmetrical structure, and the chirality center is located at the center of the compound. Hence, the planar chiral 4,7,12,15-tetrasubstituted [2.2]paracyclophane framework is one of the most important structures for investigating the behavior of self-assembly on chirality. In this work, we used oligo(*p*-phenylene ethynylene) units as rigid and planar chromophores which were easy to interact intermolecularly. Dodecyloxy groups were introduced to oligo(*p*-phenylene ethynylene) unit to support intermolecular interaction. The chromophores are stacked in an X-shaped form which induces twisted but planar chirality in the self-assembly. Therefore, it is expected to exhibit different properties from racemic and chiral compounds in their aggregation states. We investigated the optical and chiroptical properties of the racemic and optically active oligo(*p*-phenylene ethynylene) dimers with the planar chiral [2.2]paracyclophane framework using UV–vis absorption, PL, CD, and CPL measurements. Self-assembled aggregates were prepared in the mixed CHCl<sub>3</sub>/MeOH solutions, the spin-coated films, drop-cast films, and annealed films. TEM observation indicated that the aggregates arranged regularly. We succeeded in the observation of chirality inversion of self-assembled aggregates of the spin-coated and drop-cast films with  $g_{lum}$  in 10<sup>-2</sup> order. The annealing process enhanced the  $g_{lum}$  values up to the 10<sup>-1</sup> order (maximum:  $|g_{lum}| = 0.27$ ) regardless of the film preparation methods. We tried to interpret the mechanism with theoretical calculation and optical and chiroptical spectroscopic data.

## RESULTS AND DISCUSSION

**Synthesis.** The optical resolution of planar chiral 4,7,12,15-tetrasubstituted [2.2]paracyclophane was carried out using the diastereomer method we previously developed, and the obtained enantiopure compounds were converted to the corresponding (*R<sub>p</sub>*)- and (*S<sub>p</sub>*)-4,7,12,15-tetraethynyl[2.2]paracyclophanes.<sup>31</sup> The synthetic routes to the target optically active cyclic compounds are shown in Schemes 1 and 2. Compound 3 was purchased and used without further purification. Compounds 1, 2, 5, 6, and 7 were synthesized according to the literature (see Supporting Information). Dodecyloxy groups in CP3 and CP5 were introduced to form assembly with an aggregate condition. 2-Ethylhexyl groups in M3 and M5 were introduced to provide the target compounds with solubility in organic solvents, such as THF, CHCl<sub>3</sub>, CH<sub>2</sub>Cl<sub>2</sub>, and toluene because M3 and M5 substituted by dodecyloxy groups had poor solubility in organic solvents.

Scheme 1 shows the syntheses of the target planar chiral dimers CP3 and CP5, respectively. In this scheme, only the reactions of the (*R<sub>p</sub>*)-isomers are shown; the (*S<sub>p</sub>*)-isomers were synthesized under identical conditions from (*R<sub>p</sub>*)-CP1. The Sonogashira–Hagihara coupling reaction<sup>73,74</sup> was carried out with (*R<sub>p</sub>*)-CP1 and 1-dodecyloxy-4-iodobenzene (1) in the catalytic system of Pd<sub>2</sub>(dba)<sub>3</sub>/CuI (dba = dibenzylideneacetone) using 1,1'-bis(diphenylphosphino)ferrocene (dppf) as a phosphine

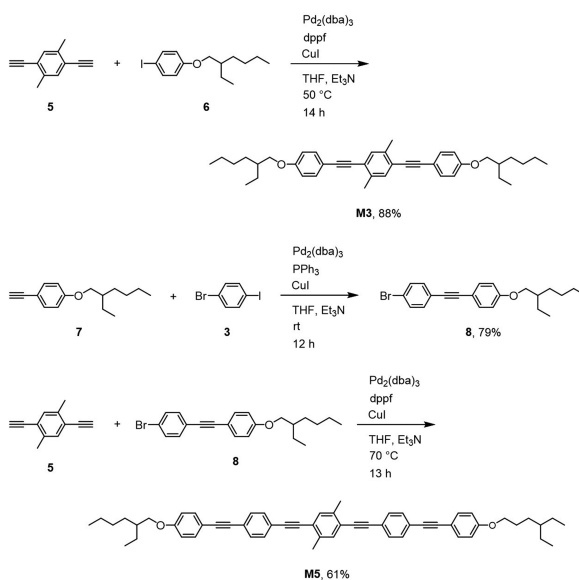
Scheme 1. Synthesis of (*R<sub>p</sub>*)-CP3 and (*R<sub>p</sub>*)-CP5



ligand to obtain compound (*R<sub>p</sub>*)-CP3 in 49% isolated yield. Iodide of 1-bromo-4-iodobenzene 3 was reacted chemoselectively with 1-dodecyloxy-4-ethynylbenzene (2) to afford compound 4 in 90% isolated yield. With the same procedure as (*R<sub>p</sub>*)-CP3, Sonogashira–Hagihara coupling of (*R<sub>p</sub>*)-CP1 and 4 was carried out to obtain (*R<sub>p</sub>*)-CP5 in 24% isolated yield.

Scheme 2 shows the syntheses of the monomers M3 and M5 as model compounds of CP3 and CP5, respectively.

Scheme 2. Synthesis of Model Compounds M3 and M5



Using 2,5-diethynyl-*p*-xylene (5) as a starting compound, M3 and M5 were prepared with the same procedure as the synthesis of (*R<sub>p</sub>*)-CP3 and (*R<sub>p</sub>*)-CP5. Isolated yields were 88% for M3 and 61% for M5. The structures of all new compounds in this study were confirmed by <sup>1</sup>H and <sup>13</sup>C NMR spectroscopy,

high-resolution mass spectrometry (HRMS), and elemental analysis; the detailed synthetic procedures and NMR spectra are shown in the [Supporting Information](#).

**Optical Properties in the Dilute Solution.** The optical properties of both enantiomers of CP3 and CP5 as well as their monomers M3 and M5 were evaluated. The optical and chiroptical data are summarized in [Tables 1 and 2](#), respectively.

**Table 1. Optical Properties: Spectroscopic Data of (*R<sub>p</sub>*)-Isomers**

	$\lambda_{\text{abs}}^a/\text{nm}$ ( $\epsilon/10^5 \text{ M}^{-1} \text{ cm}^{-1}$ )	$\lambda_{\text{lum}}^b/\text{nm}$	$\tau^c/\text{ns}$ ( $\chi^2$ )	$\Phi_{\text{lum}}^d$
CP3	366 (0.73)	415	2.05 (1.13)	0.65
CP5	386 (1.39)	425	0.88 (1.01)	0.87
M3	338 (0.54), 363 (0.97)	368	0.77 (1.00)	0.51
M5	363 (0.97)	399	0.61 (1.11)	0.87

<sup>a</sup>In CHCl<sub>3</sub> ( $1.0 \times 10^{-5}$  M). <sup>b</sup>In CHCl<sub>3</sub> ( $1.0 \times 10^{-6}$  M), excited at absorption maxima. <sup>c</sup>Emission lifetime at  $\lambda_{\text{lum}}$ . <sup>d</sup>Absolute PL quantum efficiency.

**Table 2. Chiroptical Properties: Spectroscopic Data of (*S<sub>p</sub>*)-Isomers and (*R<sub>p</sub>*)-Isomers**

	$g_{\text{abs}}/10^{-3}$ at $\lambda_{\text{abs}}^a$	$g_{\text{lum}}/10^{-3}$ at $\lambda_{\text{lum, max}}^b$
( <i>R<sub>p</sub></i> )-CP3	-1.2	-1.7
( <i>S<sub>p</sub></i> )-CP3	+1.3	+1.6
( <i>R<sub>p</sub></i> )-CP5	-1.1	-1.2
( <i>S<sub>p</sub></i> )-CP5	+1.1	+1.1

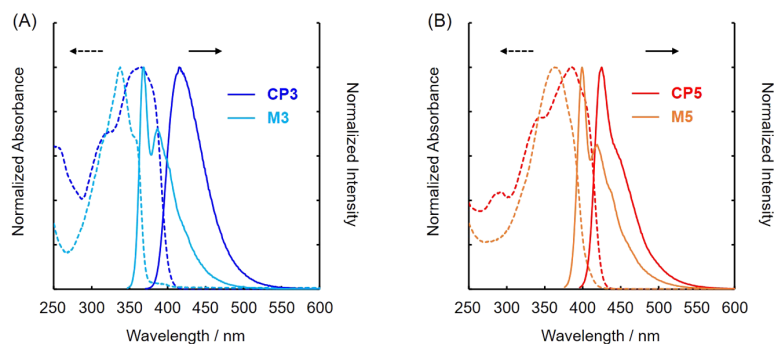
<sup>a</sup>The  $g_{\text{abs}}$  value of the first peak top was estimated. <sup>b</sup>Maximum of  $g_{\text{lum}}$  was estimated.

[Figures 1A and 1B](#) show the UV-vis absorption spectra and photoluminescence (PL) spectra of dimers (CP3 and CP5) and the monomers (M3 and M5) in the dilute CHCl<sub>3</sub> solutions ( $1.0 \times 10^{-5}$  M for UV and  $1.0 \times 10^{-6}$  M for PL). As shown in [Figure 1A](#), the absorption maximum of CP3 (366 nm) exhibited bathochromic shift compared with that of M3 (338 nm). This effect was caused by the through-space conjugation via the [2.2]paracyclophane framework in the ground state.<sup>72</sup> In PL spectra, the same bathochromic effect was observed between CP3 (415 nm) and M3 (368 nm). This indicates through-space conjugation occurred in the excited state. [Figure 1B](#) shows the comparison of the spectra of CP5 and M5. Although the bathochromic shift is shown in the UV-vis absorption (CP5: 386 nm; M5: 363 nm) and PL (CP5: 425 nm; M5: 399 nm) spectra, the shift was shorter than that of CP3 and M3, and monomer-like spectra were obtained. When the monomer

conjugation length of the dimer extends, the property becomes similar to the monomeric compound. This effect was previously reported in the literature on the oligo(*p*-phenylene vinylene) systems.<sup>72</sup> PL lifetime measurement supported these results. PL lifetime ( $\tau$ ) and  $\chi^2$  parameters are summarized in [Table 1](#), and the decay curves are shown in the [Supporting Information](#) ([Figure S13](#)). The PL lifetime ( $\tau$ ) of CP3 ( $\tau = 2.05$  ns) was far longer than that of M3 ( $\tau = 0.77$  ns), whereas the  $\tau$  of CP5 ( $\tau = 0.88$  ns) was similar to that of M5 ( $\tau = 0.61$  ns). An absolute PL quantum efficiency ( $\Phi_{\text{lum}}$ ) was enhanced by the rigid structure of the [2.2]paracyclophane unit, and CP5 exhibited high absolute PL quantum efficiency ( $\Phi_{\text{lum}} = 0.87$ ).

**Chiroptical Properties in the Dilute Solution.** The chiroptical properties in the ground and excited states of CP3 and CP5 were investigated by circular dichroism (CD) and CPL spectroscopy, respectively. The chiroptical data including CD and CPL dissymmetry factor ( $g_{\text{abs}}$  and  $g_{\text{lum}}$ , respectively) are summarized in [Table 2](#). CD dissymmetry factor is defined as  $g_{\text{abs}} = \Delta\epsilon/\epsilon$  ( $\Delta\epsilon = \epsilon_{\text{left}} - \epsilon_{\text{right}}$ ), where  $\epsilon_{\text{left}}$  and  $\epsilon_{\text{right}}$  indicate absorbances of left- and right-handed circularly polarized light, respectively. CPL dissymmetry factor is defined as  $g_{\text{lum}} = \Delta I/I$  ( $\Delta I = I_{\text{left}} - I_{\text{right}}$ ), where  $I_{\text{left}}$  and  $I_{\text{right}}$  indicate luminescence intensities of left- and right-handed CPL, respectively. Although the only properties of (*R<sub>p</sub>*)-isomers are discussed here, (*S<sub>p</sub>*)-isomers exhibited the same properties as (*R<sub>p</sub>*)-isomers except for the fact that inverse signals were obtained between (*R<sub>p</sub>*)-isomers and (*S<sub>p</sub>*)-isomers. [Figure 2](#) shows the CD and the UV-vis absorption spectra of both enantiomers of CP3 and CP5 in the dilute CHCl<sub>3</sub> ( $1.0 \times 10^{-5}$  M). Mirror-image Cotton effects were observed in both of CD spectra, and the  $g_{\text{abs}}$  values of the first Cotton effect were estimated to be  $-1.2 \times 10^{-3}$  for (*R<sub>p</sub>*)-CP3 and  $-1.1 \times 10^{-3}$  for (*R<sub>p</sub>*)-CP5. The  $g_{\text{abs}}$  values of (*R<sub>p</sub>*)-CP3 and (*R<sub>p</sub>*)-CP5 were similar in the ground state. The CPL spectra of both enantiomers of CP3 and CP5 in the dilute CHCl<sub>3</sub> ( $1.0 \times 10^{-5}$  M) are shown in [Figure 3](#). Intense mirror-image CPL spectra were obtained. The  $g_{\text{lum}}$  values were calculated to be  $-1.7 \times 10^{-3}$  for (*R<sub>p</sub>*)-CP3 and  $-1.2 \times 10^{-3}$  for (*R<sub>p</sub>*)-CP5. Considering that CP5 exhibited excellent absolute PL quantum efficiency ( $\Phi_{\text{lum}} = 0.87$ ), CP5 is a promising candidate for a CPL emitter.

**Optical Properties in the Aggregation State.** Planar  $\pi$ -conjugated compounds containing long alkyl chains often make self-assembly due to the  $\pi$ - $\pi$  stacking and van der Waals interactions. Chirality are sometimes enhanced by making higher-ordered structure with self-assembly. In this section, the chirality of CP3 and CP5 in the aggregation state was investigated by optical (UV-vis absorption and PL) and chiroptical (CD and CPL)



**Figure 1.** UV-vis absorption spectra in the dilute CHCl<sub>3</sub> ( $1.0 \times 10^{-5}$  M) and PL spectra in the dilute CHCl<sub>3</sub> ( $1.0 \times 10^{-6}$  M, excited at absorption maximum): (A) CP3 and M3; (B) CP5 and M5.

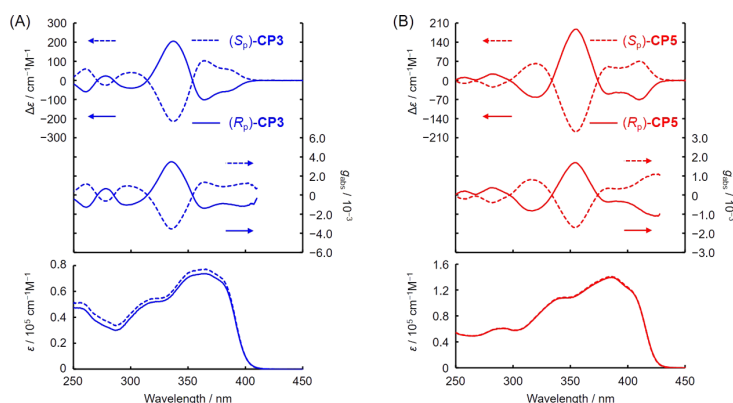


Figure 2. CD (top),  $g_{\text{abs}}$  (middle), and UV-vis absorption (bottom) spectra in the dilute  $\text{CHCl}_3$  ( $1.0 \times 10^{-5}$  M): (A) CP3 and (B) CP5.

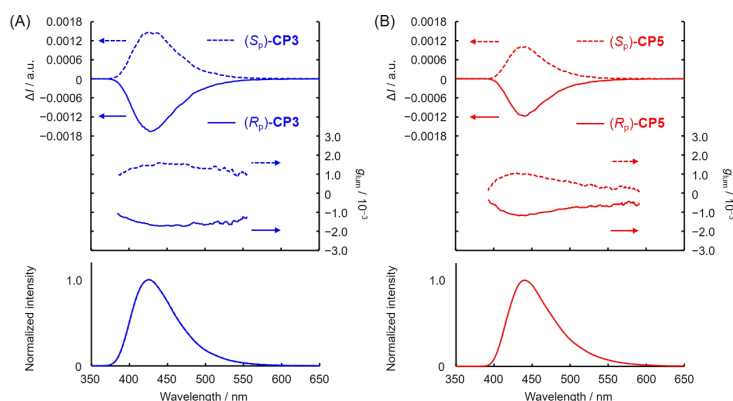


Figure 3. CPL (top),  $g_{\text{lum}}$  (middle), and PL (bottom) spectra of in the dilute  $\text{CHCl}_3$  ( $1.0 \times 10^{-5}$  M): (A) CP3 and (B) CP5, excited at 300 nm.

Table 3. Optical and Chiroptical Spectroscopic Data of (A) *rac*-CP3 and (B)  $(R_p)$ -CP3 and  $(S_p)$ -CP3 in the Aggregation State or the Film State

CHCl <sub>3</sub> :MeOH or film	(A) <i>rac</i> -CP3							
	10:0	5:5	4:6	3:7	2:8	1:9	film <sup>a</sup>	
$\lambda_{\text{abs}}/\text{nm}$	364	362	362	362	360	338	357, 398	
$\lambda_{\text{lum}}/\text{nm}$	417	419	422	420	418	431	435	
$\Phi_{\text{lum}}^b$	0.61	0.84	0.85	0.85	0.57	0.20	0.20	
CHCl <sub>3</sub> :MeOH or film	(B) $(R_p)$ -CP3 and $(S_p)$ -CP3							
	10:0	5:5	4:6	3:7	2:8	1:9	film <sup>a</sup>	
	$\lambda_{\text{abs}}/\text{nm}$	365	360	363	359	361	357	400
	$\lambda_{\text{lum}}/\text{nm}$	415	418	418	418	419	425	436
	$\Phi_{\text{lum}}^{b,c}$	0.65	0.86	0.86	0.72	0.28	0.19	0.22
	$(R_p)$ : $g_{\text{abs}}^d/10^{-3}$	-1.2	-1.3	-1.3	-1.7	-1.1	-0.72	-11
	$(R_p)$ : $g_{\text{lum}}^e/10^{-3}$	-1.7	-1.8	-1.9	-1.9	-1.9	-1.6	-7.9
	$(S_p)$ : $g_{\text{abs}}^d/10^{-3}$	+1.3	+1.2	+1.5	+1.3	+0.91	+0.51	+10
$(S_p)$ : $g_{\text{lum}}^e/10^{-3}$	+1.6	+1.4	+1.5	+1.4	+1.3	+1.6	+11	

<sup>a</sup>Spin-coated film prepared from  $\text{CHCl}_3$  solution ( $3.4 \times 10^{-3}$  M). <sup>b</sup>Absolute PL quantum efficiency. <sup>c</sup>Measured with the  $(R_p)$ -isomer. <sup>d</sup>The  $g_{\text{abs}}$  value of the first peak top was estimated. <sup>e</sup>Maximum of  $g_{\text{lum}}$  was estimated.

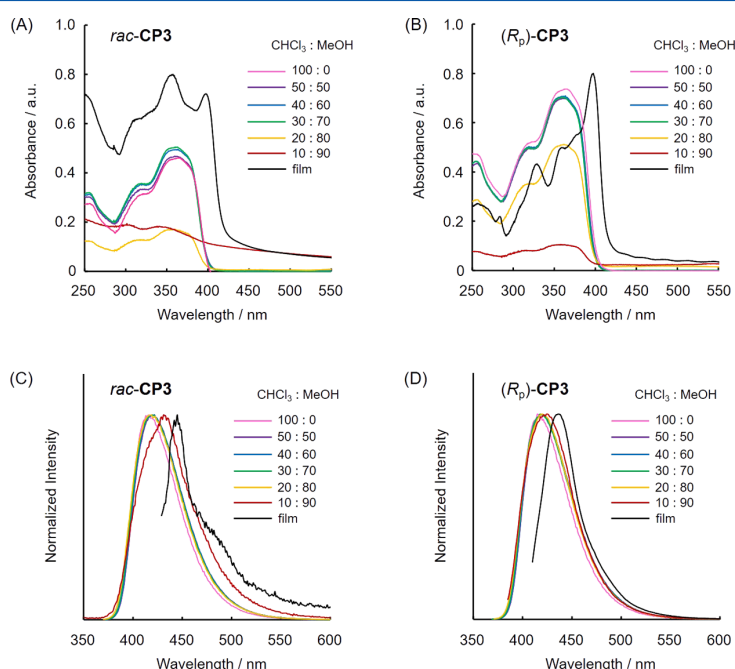
measurements. The spectroscopic data are summarized in Tables 3 and 4. Preparation methods of films are shown in the Supporting Information. Although almost all the same data and mirror-image spectra in chiroptical measurements were obtained between  $(R_p)$ - and  $(S_p)$ -isomers, some values were a little different. This is because subtly different preparation condition affected the aggregate formation. Ideally, they should be the same and mirror image data.

Figures 4 and 5 show the UV-vis absorption spectra and PL spectra of CP3 and CP5 in the mixed  $\text{CHCl}_3/\text{MeOH}$  solutions ( $1.0 \times 10^{-5}$  M) and in the spin-coated films. The spectroscopic data are summarized in Tables 3 and 4. As shown in Figures 4A and 4B, the absorbance clearly decreased in the  $\text{CHCl}_3/\text{MeOH} = 20/80$  v/v solution both in *rac*-CP3 and in  $(R_p)$ -CP3. This indicates that aggregation occurred from this ratio of the mixed  $\text{CHCl}_3/\text{MeOH}$  solution. In the spin-coated films, the specific

Table 4. Optical and Chiroptical Spectroscopic Data of ( $R_p$ )-CP5 in the Aggregation State or the Film State

(A) <i>rac</i> -CP5								
CHCl <sub>3</sub> :MeOH or film	10:0	6:4	5:5	4:6	3:7	2:8	1:9	film <sup>a</sup>
$\lambda_{\text{abs}}/\text{nm}$	385	382	362	274	274	277	275	331
$\lambda_{\text{lum}}/\text{nm}$	424	425	424	451	453	455	459	467
$\Phi_{\text{lum}}^b$	0.84	0.94	0.47	0.17	0.12	0.11	0.08	0.10
(B) ( $R_p$ )-CP5 and ( $S_p$ )-CP5								
CHCl <sub>3</sub> :MeOH or film	10:0	5:5	4:6	3:7	2:8	1:9	film <sup>a</sup>	
$\lambda_{\text{abs}}/\text{nm}$	386	382	387	379	381	385	339	
$\lambda_{\text{lum}}/\text{nm}$	425	425	431	453	455	458	462	
$\Phi_{\text{lum}}^{b,c}$	0.82	0.89	0.43	0.20	0.13	0.13	0.19	
( $R_p$ ): $g_{\text{abs}}^d/10^{-3}$	-1.1	-1.1	+8.2	+6.0	+4.1	+3.5	+4.4	
( $R_p$ ): $g_{\text{lum}}^e/10^{-3}$	-1.2	-1.1	+1.1	+3.4	+3.3	+2.7	+2.0	
( $S_p$ ): $g_{\text{abs}}^d/10^{-3}$	+1.1	+1.0	-8.7	-5.9	-4.4	-1.8	-2.3	
( $S_p$ ): $g_{\text{lum}}^e/10^{-3}$	+1.1	+0.87	-2.1	-2.9	-2.2	-2.8	-1.3	

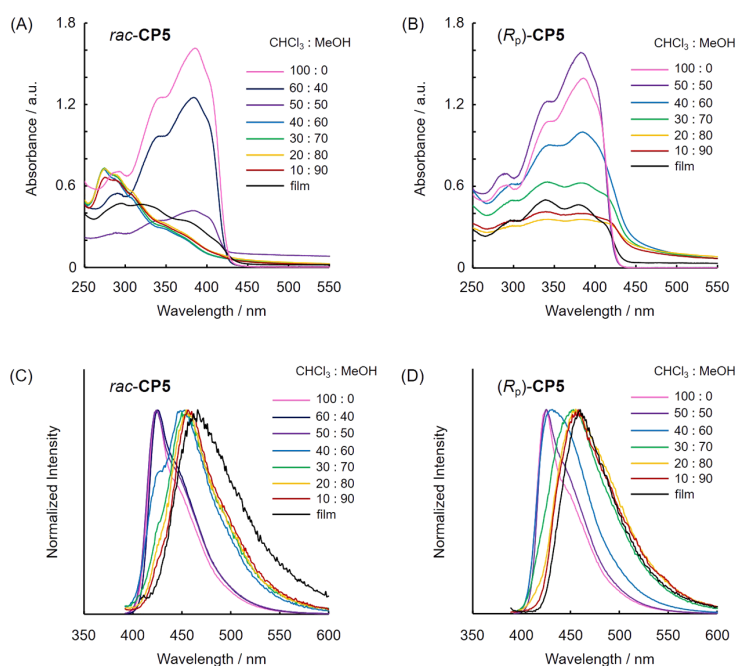
<sup>a</sup>Spin-coated film prepared from CHCl<sub>3</sub> solution ( $3.4 \times 10^{-3}$  M). <sup>b</sup>Absolute PL quantum efficiency. <sup>c</sup>Measured with the ( $R_p$ )-isomer. <sup>d</sup>The  $g_{\text{abs}}$  value of the first peak top was estimated. <sup>e</sup>Maximum of  $g_{\text{lum}}$  was estimated.



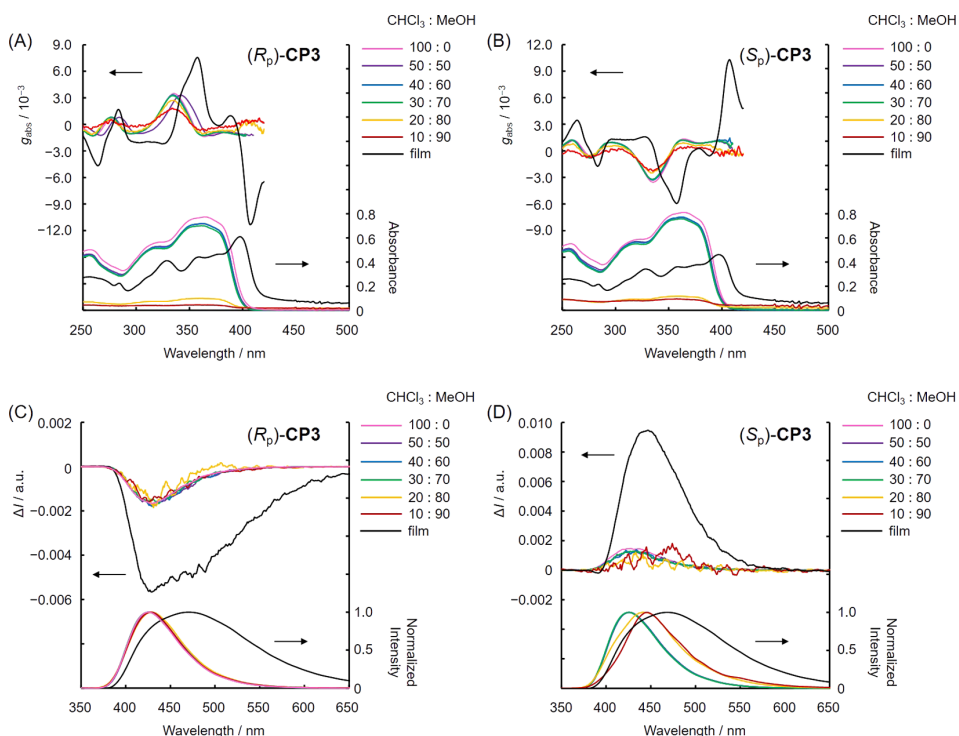
**Figure 4.** UV-vis absorption and PL spectra in CHCl<sub>3</sub>/MeOH = 100/0, 50/50, 40/60, 30/70, 20/80, and 10/90 v/v ( $1.0 \times 10^{-5}$  M) and a spin-coated film prepared from CHCl<sub>3</sub> ( $3.4 \times 10^{-3}$  M): (A) UV-vis absorption spectra of *rac*-CP3 and (B) ( $R_p$ )-CP3. The absorbance of the spin-coated film was normalized at a baseline of the absorbance of aggregation in CHCl<sub>3</sub>/MeOH = 10/90 v/v. (C) PL spectra of *rac*-CP3 and (D) ( $R_p$ )-CP3, excited at absorption maximum.

peaks of J-aggregates<sup>11,12</sup> were observed at 398 nm for *rac*-CP3 and 400 nm for ( $R_p$ )-CP3. Figures 4C and 4D show the PL spectra of *rac*-CP3 and ( $R_p$ )-CP3. The peak tops were gradually bathochromic-shifted because of the  $\pi$ - $\pi$  interaction in the aggregates in the excited state, and relatively sharp spectra were obtained in the spin-coated films of *rac*-CP3 and ( $R_p$ )-CP3. These results also support the fact of the formation of J-aggregates. Considering the results of UV-vis absorption and PL spectra, ( $R_p$ )-CP3 formed J-aggregates clearly. Figures 5A and 5B show the UV-vis absorption spectra of *rac*-CP5 and ( $R_p$ )-CP5. In the case of *rac*-CP5, by increasing the ratio of MeOH in the mixed CHCl<sub>3</sub>/MeOH solution, the absorbance from 300 to 430 nm decreased, and the absorbance from

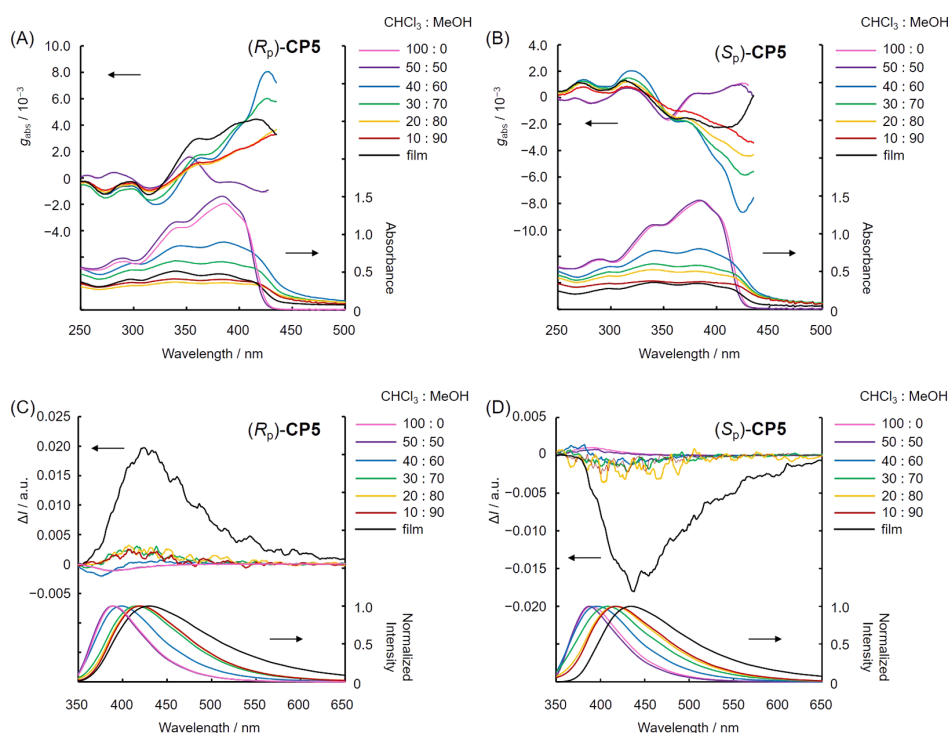
250 to 300 nm increased. These results indicate that the formation of H-aggregates,<sup>11,12</sup> and the spin-coated films exhibited almost the same behavior. On the other hand, ( $R_p$ )-CP5 did not show the same behavior. The absorbance of ( $R_p$ )-CP5 aggregates decreased due to the intermolecular  $\pi$ - $\pi$  interaction of the aggregates (vide infra). In the PL spectra (Figures 5C and 5D), the peak tops were gradually bathochromic-shifted because of the intermolecular  $\pi$ - $\pi$  interaction in the excited state. Larger bathochromic shift was observed in CP5 than in CP3 because the  $\pi$ - $\pi$  interaction of five benzene rings of CP5 was stronger than that of three benzene rings of CP3. In addition, the larger bathochromic effect indicates the existence of H-aggregation.<sup>11</sup> ( $S_p$ )-CP3 and



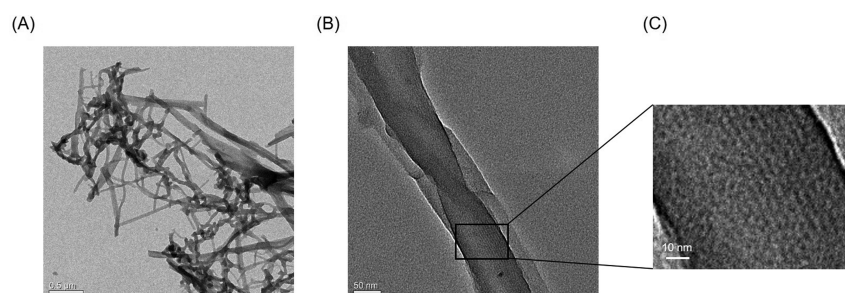
**Figure 5.** UV-vis absorption and PL spectra in CHCl<sub>3</sub>/MeOH = 100/0, 60/40, 50/50, 40/60, 30/70, 20/80, and 10/90 v/v ( $1.0 \times 10^{-5}$  M) and a spin-coated film prepared from CHCl<sub>3</sub> ( $3.4 \times 10^{-3}$  M): (A) UV-vis absorption spectra of *rac*-CP5 and (B) (*R<sub>p</sub>*)-CP5. The absorbance of the spin-coated film was normalized at a baseline of the absorbance of aggregation in CHCl<sub>3</sub>/MeOH = 10/90 v/v. (C) PL spectra of *rac*-CP5 and (D) (*R<sub>p</sub>*)-CP5, excited at absorption maximum.



**Figure 6.** CD and CPL spectra in CHCl<sub>3</sub>/MeOH = 100/0, 50/50, 40/60, 30/70, 20/80, and 10/90 v/v ( $1.0 \times 10^{-5}$  M) and a spin-coated film prepared from CHCl<sub>3</sub> ( $3.4 \times 10^{-3}$  M): (A) CD spectra of (*R<sub>p</sub>*)-CP3 and (B) (*S<sub>p</sub>*)-CP3; (C) PL spectra of (*R<sub>p</sub>*)-CP3 and (D) (*S<sub>p</sub>*)-CP3, excited at 300 nm.



**Figure 7.** CD and CPL spectra in  $\text{CHCl}_3/\text{MeOH} = 100/0, 50/50, 40/60, 30/70, 20/80,$  and  $10/90$  v/v ( $1.0 \times 10^{-5}$  M) and a spin-coated film prepared from  $\text{CHCl}_3$  ( $3.4 \times 10^{-3}$  M): (A) CD spectra of  $(R_p)$ -CP5 and (B)  $(S_p)$ -CP5; (C) PL spectra of  $(R_p)$ -CP5 and (D)  $(S_p)$ -CP5, excited at 300 nm.



**Figure 8.** TEM images of  $(R_p)$ -CP5: (A) low magnification for observing the entire self-assembled structure, (B, C) high magnification for observing a fiber structure and a stripe pattern.

**Table 5.**  $g_{\text{abs}}$  Values of  $(R_p)$ - and  $(S_p)$ -CP3 and -CP5 in Film States

film state	spin-coated film <sup>a</sup>		drop-cast thin film <sup>a</sup>	
	before annealing	after annealing <sup>b</sup>	before annealing	after annealing <sup>b</sup>
$(R_p)$ -CP3	-0.010 <sup>c</sup>	-0.0088 <sup>c</sup>	-0.12 <sup>d</sup>	-0.017 <sup>d</sup>
$(S_p)$ -CP3	+0.010 <sup>c</sup>	+0.013 <sup>c</sup>	+0.11 <sup>d</sup>	+0.016 <sup>d</sup>
$(R_p)$ -CP5	+0.0012 <sup>c</sup>	-0.15 <sup>e</sup>	-0.0021 <sup>e</sup>	-0.15 <sup>e</sup>
$(S_p)$ -CP5	-0.0010 <sup>c</sup>	+0.11 <sup>e</sup>	+0.00062 <sup>e</sup>	+0.15 <sup>e</sup>

<sup>a</sup>Films prepared from  $\text{CHCl}_3$  solution ( $3.4 \times 10^{-3}$  M). <sup>b</sup>CP3: annealing at 65 °C for 3 h; CP5: annealing at 90 °C for 5 h. <sup>c</sup>The  $g_{\text{abs}}$  value of the first peak top was estimated. <sup>d</sup>The  $g_{\text{abs}}$  value at 450 nm was estimated. <sup>e</sup>The  $g_{\text{abs}}$  value at 455 nm was estimated.

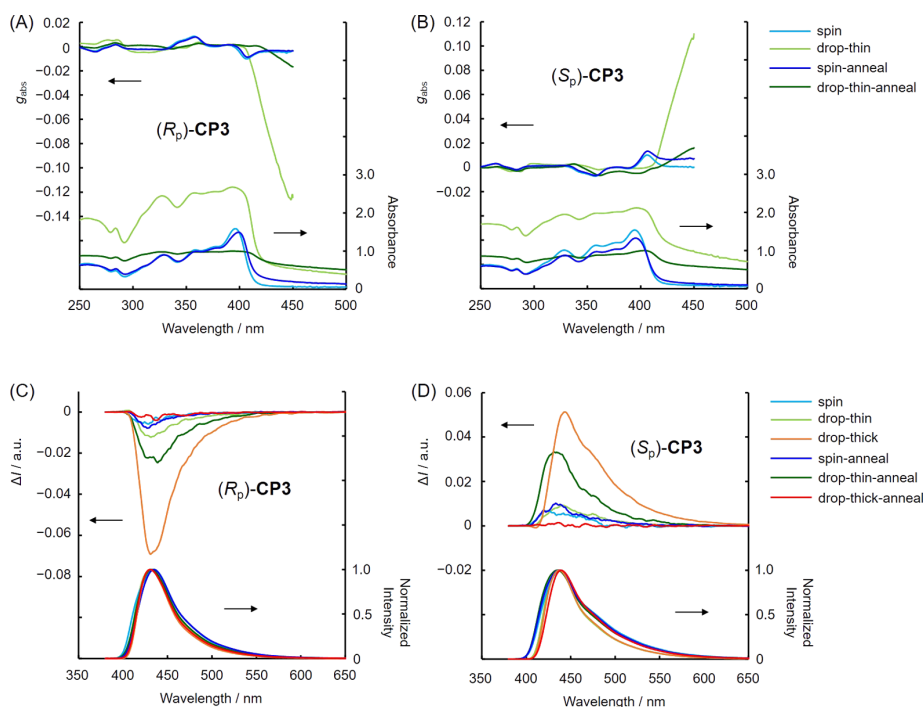
$(S_p)$ -CP5 have the same properties with  $(R_p)$ -CP3 and  $(R_p)$ -CP5, respectively, and the spectra of  $(S_p)$ -CP3 and  $(S_p)$ -CP5 are shown in Figure S14.

**Chiroptical Properties in the Aggregation State.** The chiroptical properties of CP3 and CP5 in the aggregation states were also investigated by circular dichroism (CD) and CPL spectroscopy. Chiroptical data are also summarized in Tables 3 and 4. Figures 6A and 6B show the CD and UV-vis absorption spectra of both enantiomers of CP3 in the mixed  $\text{CHCl}_3/\text{MeOH}$  solutions ( $1.0 \times 10^{-5}$  M) and in the spin-coated films. When evaluation of  $g_{\text{abs}}$  values in the aggregation state and film state, baseline increase of UV-vis absorption spectra due to scattering underestimated the true  $g_{\text{abs}}$  values. We estimated the absorption value of the baseline increase by scattering to be 0.01 judged from the UV-vis experimental data because there were no or little wavelength dependability. Therefore, in the calculation of  $g_{\text{abs}}$  values of the turbid or film samples, if the absorption at 500 nm was over 0.01, it was modified to be 0.01 and used as baseline. This is because there was no absorption of the samples at 500 nm. Figures 6A and 6B show the spectra of  $(R_p)$ -CP3 and  $(S_p)$ -CP3, respectively.

Table 6.  $g_{\text{lum}}$  Values of ( $R_p$ )- and ( $S_p$ )-CP3 and -CP5 in Film States

film state	spin-coated film <sup>a</sup>		drop-cast thin film <sup>a</sup>		drop-cast thick film <sup>a</sup>	
	before annealing	after annealing <sup>b</sup>	before annealing	after annealing <sup>b</sup>	before annealing	after annealing <sup>b</sup>
( $R_p$ )-CP3	-0.0061	-0.0087	-0.012	-0.026	-0.075	-0.0043
( $S_p$ )-CP3	+0.0056	+0.010	+0.0096	+0.034	+0.056	+0.0015
( $R_p$ )-CP5	+0.021	-0.12	-0.0086	-0.17	-0.030	-0.25
( $S_p$ )-CP5	-0.014	+0.13	+0.016	+0.13	+0.011	+0.27

<sup>a</sup>Prepared from  $\text{CHCl}_3$  solution ( $3.4 \times 10^{-3}$  M). <sup>b</sup>CP3: annealing at 65 °C for 3 h; CP5: annealing at 90 °C for 5 h.



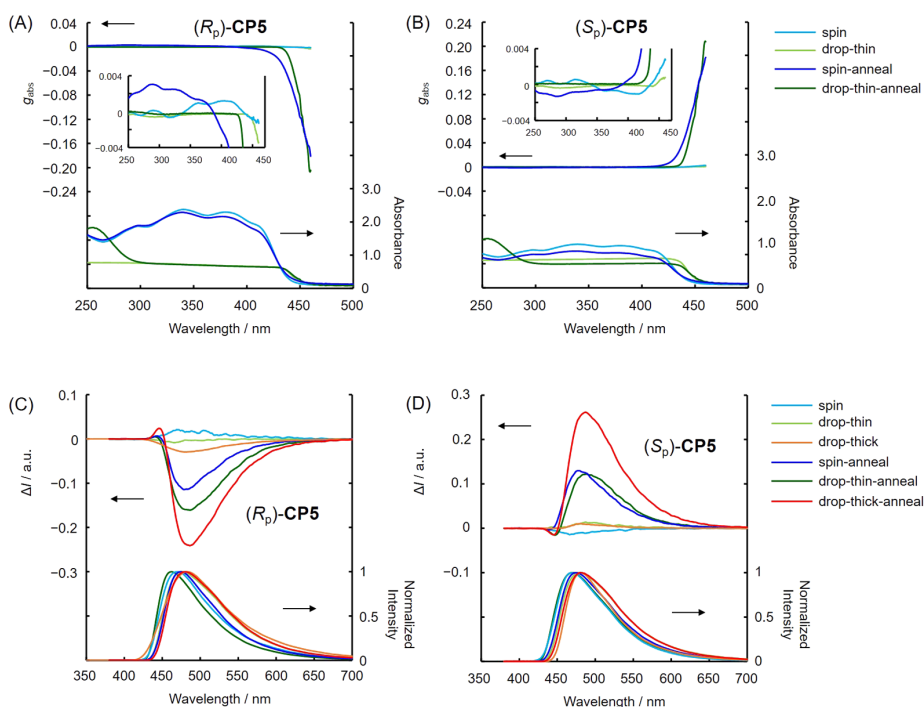
**Figure 9.** CD and CPL spectra in the spin-coated film and the drop-cast film. The spin-coated film prepared from  $\text{CHCl}_3$  ( $3.4 \times 10^{-3}$  M), drop-cast thin film prepared from  $\text{CHCl}_3$  ( $3.4 \times 10^{-3}$  M, 30  $\mu\text{L} \times 5$  times), and drop-cast thick film prepared from  $\text{CHCl}_3$  ( $3.4 \times 10^{-3}$  M, 30  $\mu\text{L} \times 15$  times). (A) CD spectra of ( $R_p$ )-CP3 and (B) ( $S_p$ )-CP3; (C) CPL spectra of ( $R_p$ )-CP3 and (D) ( $S_p$ )-CP3, excited at 350 nm.

In both CD spectra, mirror-image Cotton effects were observed. As shown in Figure 6, by increasing the ratio of MeOH, the  $g_{\text{abs}}$  values decreased. On the other hand, the largest  $g_{\text{abs}}$  values were obtained at the specific peak of J-aggregates in the spin-coated films, and the  $g_{\text{abs}}$  values were estimated to be  $-1.1 \times 10^{-2}$  for ( $R_p$ )-CP3 and  $+1.0 \times 10^{-2}$  for ( $S_p$ )-CP3. They were 9.2 and 7.7 times larger than those in the dilute solutions, respectively. The enhancement of the  $g_{\text{abs}}$  values was caused by chiral J-aggregates of CP3 in the ground state. The CPL spectra of both enantiomers of CP3 in the mixed  $\text{CHCl}_3/\text{MeOH}$  solutions ( $1.0 \times 10^{-5}$  M) and in the spin-coated films are shown in Figures 6C and 6D. Intense mirror-image CPL spectra were obtained for the enantiomers. As shown in the CD spectra, the largest  $g_{\text{lum}}$  values were observed in the spin-coated films, and they were calculated to be  $-7.9 \times 10^{-3}$  for ( $R_p$ )-CP3 and  $+1.1 \times 10^{-2}$  for ( $S_p$ )-CP3. They were 4.6 and 6.9 times larger than those in the dilute solutions, respectively. This improvement of the chirality in the spin-coated films was attributed to the J-aggregate formation.

Figures 7A and 7B show the CD and absorption spectra of both enantiomers of CP5 in the mixed  $\text{CHCl}_3/\text{MeOH}$  solutions ( $1.0 \times 10^{-5}$  M) and in the spin-coated films. Mirror-image

Cotton effects were obtained in both CD spectra. Unlike the case of CP3, by increasing the ratio of MeOH, signal inversion of the  $g_{\text{abs}}$  values occurred at the first Cotton effect. This effect was caused by the exciton couplings<sup>75–78</sup> of the intermolecular  $\pi-\pi$  interaction, and the details are discussed in the Mechanism section. The largest  $g_{\text{abs}}$  value was observed in the mixed solution  $\text{CHCl}_3/\text{MeOH} = 40/60$  v/v. They were estimated to be  $+8.2 \times 10^{-3}$  for ( $R_p$ )-CP5 and  $-8.7 \times 10^{-3}$  for ( $S_p$ )-CP5, which were 7.4 and 7.9 times larger than in the dilute solutions, respectively. The CPL spectra of both enantiomers of CP5 in the mixed  $\text{CHCl}_3/\text{MeOH}$  solutions ( $1.0 \times 10^{-5}$  M) and in the spin-coated films are shown in Figures 7C and 7D. As can be seen in the CD spectra, signal inversion was observed in the CPL spectra. The largest  $g_{\text{lum}}$  value was obtained in the spin-coated films instead of the  $\text{CHCl}_3/\text{MeOH} = 40/60$  v/v solution. They were calculated to be  $+2.0 \times 10^{-2}$  for ( $R_p$ )-CP5 and  $-1.3 \times 10^{-2}$  for ( $S_p$ )-CP5, which were 17 and 12 times larger than those in the dilute solutions, respectively. Exciton couplings in the excited state would contribute to the improvement of the chirality in the spin-coated films.

**TEM Observations.** In order to observe aggregate formation, TEM observation was carried out. We selected the aggregate sample of ( $R_p$ )-CP5 in  $\text{CHCl}_3/\text{MeOH} = 40/60$  v/v solution



**Figure 10.** CD and CPL spectra in the spin-coated film and the drop-cast film. The spin-coated film prepared from  $\text{CHCl}_3$  ( $3.4 \times 10^{-3}$  M), drop-cast thin film prepared from  $\text{CHCl}_3$  ( $3.4 \times 10^{-3}$  M,  $30 \mu\text{L} \times 5$  times), and drop-cast thick film prepared from  $\text{CHCl}_3$  ( $3.4 \times 10^{-3}$  M,  $30 \mu\text{L} \times 15$  times). (A) CD spectra of  $(R_p)$ -CP5 and (B)  $(S_p)$ -CP5; (C) CPL spectra of  $(R_p)$ -CP5 and (D)  $(S_p)$ -CP5, excited at 350 nm.

**Table 7. Absolute Quantum Efficiency of Prepared Films<sup>a</sup>**

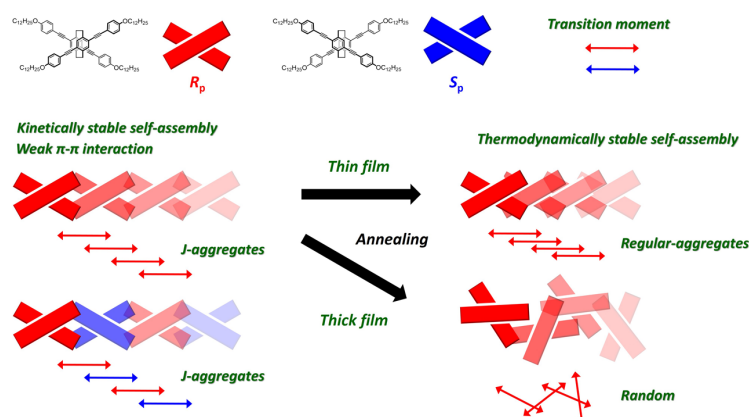
film state	spin-coated film <sup>b</sup>		drop-cast thin film <sup>b</sup>	
	before annealing	after annealing <sup>c</sup>	before annealing	after annealing <sup>c</sup>
$(R_p)$ -CP3	0.36	0.38	0.39	0.39
$(S_p)$ -CP3	0.31	0.32	0.34	0.34
$(R_p)$ -CP5	0.09	0.06	0.53	0.09
$(S_p)$ -CP5	0.13	0.05	0.58	0.09

<sup>a</sup>Absorption rate was approximately 60%–90%, and thick film was removed because the absorption was saturated. <sup>b</sup>Films prepared from  $\text{CHCl}_3$  solution ( $3.4 \times 10^{-3}$  M). <sup>c</sup>CP3: annealing at  $65^\circ\text{C}$  for 3 h; CP5: annealing at  $90^\circ\text{C}$  for 5 h.

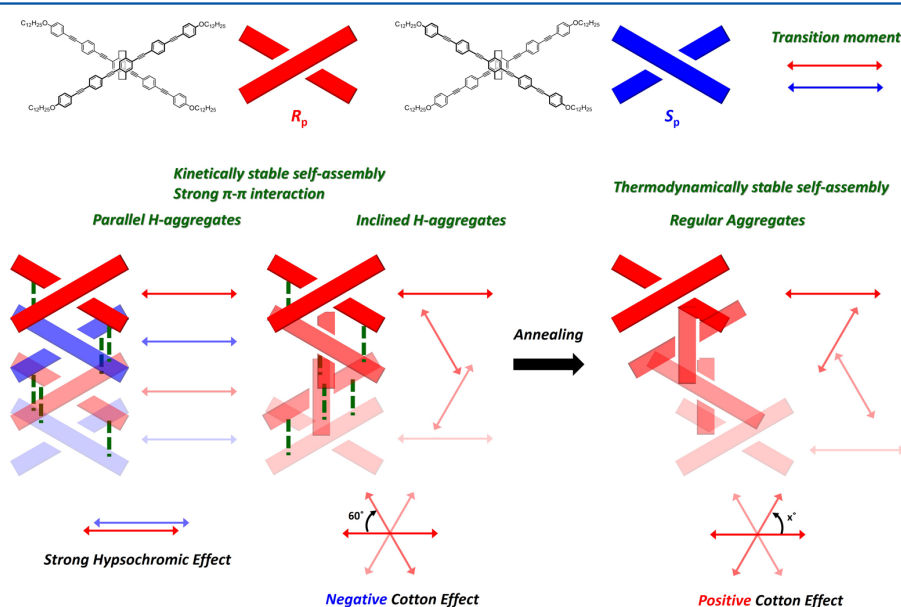
because the  $g$  values of CP5 were larger than that of CP3 and signal inversion occurred with that condition. TEM samples were prepared by depositing one drop of  $(R_p)$ -CP5 in  $\text{CHCl}_3/\text{MeOH} = 40/60$  v/v ( $1.0 \times 10^{-5}$  M) solution on a 200 mesh copper grid covered with a carbon film and dried to remove the solvent at room temperature. TEM images are shown in Figure 8. Clearly shown in the figure,  $(R_p)$ -CP5 made a fiber formation. The diameter of the fiber was about 50–100 nm, and the length of the fiber was over a micrometer (Figure 8A). In addition, a striped pattern was observed in the fibers (Figure 8B). Intervals between striped patterns were about 3 nm, which is identified with the molecular length of oligo(*p*-phenylene ethynylene) units of CP5 (Figure 8C). This indicates that  $(R_p)$ -CP5 arranged regularly, and the aggregates made the fiber formation. It is difficult to decide more detail of the formation (e.g., parallel or inclined H-aggregation); however, we can conclude that the enhancement and inversion of the chirality derived from such a self-assembled formation of planar chiral tetrasubstituted [2.2]paracyclophane derivatives.

**Properties of Annealing Films.** Three types of films—spin-coated film, drop-cast thin film, and drop-cast thick film—were prepared to investigate the chirality of the self-assembly. The details of the film preparation methods are shown in the Supporting Information. CD and CPL measurements were carried out, and the spectroscopic data are summarized in Tables 5 and 6. In CD spectra, the scattering effect of the drop-cast film was too large to evaluate the true  $g_{\text{abs}}$  values. However, we calculated the  $g_{\text{abs}}$  values with the same method as the aggregation section because we could obtain valid information about the chiroptical properties from the CD spectra.

Figures 9A and 9B show the CD spectra of  $(R_p)$ -CP3 and  $(S_p)$ -CP3, respectively. The spectra of the drop-cast thick films were not included in the figure because the absorbance was too large to measure. The spin-coated films and the annealing films exhibited almost same profiles. The  $g_{\text{abs}}$  value of the drop-cast thin films decreased after annealing. On the other hand, in the CPL spectra (Figure 9C,D), annealing process enhanced the  $g_{\text{lum}}$  values of the drop-cast thin films. The phenomena are attributed to the difference of the intermolecular interaction between in the ground state and that in the excited state. However, it is very difficult to understand. The largest  $g_{\text{abs}}$  values in the ground state were obtained from the drop-cast thin films before annealing, and the  $g_{\text{abs}}$  values were estimated to be  $-0.12$  for  $(R_p)$ -CP3 and  $+0.11$  for  $(S_p)$ -CP3 at 450 nm. The absorption band was too weak to be observed in the UV–vis absorption spectra because it was derived from the intermolecular  $\pi$ – $\pi$  interaction. The largest  $g_{\text{lum}}$  values were observed in the drop-cast thick films before annealing, and they were estimated to be  $-0.075$  for  $(R_p)$ -CP3 and  $+0.056$  for  $(S_p)$ -CP3. In the case of the drop-cast thick films, the  $g_{\text{lum}}$  values decreased after annealing because chiral self-assembly was disordered by heating.



**Figure 11.** Proposal mechanism of self-assembly of CP3. The direction of transition dipole moment was estimated by TD-DFT (B3LYP/6-31G(d,p)//B3LYP/6-31G(d,p)).



**Figure 12.** Proposal mechanism of self-assembly of CP5. The direction of transition dipole moment was estimated by TD-DFT (B3LYP/6-31G(d,p)//B3LYP/6-31G(d,p)).

Figures 10A and 10B show the CD spectra of ( $R_p$ )-CP5 and ( $S_p$ )-CP5, respectively. The  $g_{\text{abs}}$  values of the spin-coated films and the drop-cast thin films were enhanced at the weak absorption band at the longest wavelength after annealing. This behavior was not seen in the CP3 systems. The signal was inverse compared with the aggregates in the spin-coated films before annealing or mixed  $\text{CHCl}_3/\text{MeOH}$  solution systems. These results indicate that the different aggregation formed in the spin-coated and drop-cast films before annealing. Annealing formed the stable aggregation regardless of the film preparation methods. The largest  $g_{\text{abs}}$  values in the ground state were obtained in the drop-cast thin films after annealing, and the  $g_{\text{abs}}$  values were estimated to be  $-0.15$  for ( $R_p$ )-CP5 and  $+0.15$  for ( $S_p$ )-CP5 at 455 nm. In addition,  $g_{\text{abs}}$  values of the spin-coated thin films and the drop-cast thin films were similarly after annealing. In the CPL spectra (Figure 10C,D), the largest  $g_{\text{lum}}$  values in the excited state were observed in the drop-cast thick

films after annealing, and the  $g_{\text{lum}}$  values were estimated to be  $-0.25$  for ( $R_p$ )-CP5 and  $+0.27$  for ( $S_p$ )-CP5. In the case of CP5, the chirality was enhanced by annealing. Those are one of the largest  $g_{\text{lum}}$  values in the self-assembled organic compounds.<sup>39,42,43,47,48</sup> Absolute PL quantum efficiency was calculated; however, absorptions of these films were too large to obtain correct values. The calculated absolute PL quantum efficiencies are summarized in Table 7.

**Mechanism.** The mechanism of the self-assembly and chirality are discussed here. A spin-coated method formed a kinetically stable film, and a drop-cast method formed a thermodynamically stable film. The annealing method moved the films to more stable forms. The transition dipole moment was estimated by time-dependent density functional theory (TD-DFT) at the B3LYP/6-31G(d,p)//B3LYP/6-31G(d,p) levels. In this section, we used the only transition dipole moment to simplify the system and describe signal inversion. The origin of the

chiroptical property based on 4,7,12,15-tetrasubstituted [2.2]paracyclophane scaffolds was difficult to predict from the theoretical calculation, and that is under investigation.

Figure 11 shows the proposal mechanism of self-assembly of CP3. The reason for decrease of chirality of CP3 in the drop-cast thick films is that the interaction of dodecyloxy groups was very large and CP3 made random aggregates. Dodecyloxy chains of the thin films did not move drastically than those of the thick films; therefore, the chirality was slightly enhanced by forming rigid aggregates. UV–vis absorption spectra of thin films of CP3 before and after annealing (Figure 9A) support this proposal. The shape of the spectra was almost similar, but the molar extinction coefficient decreased because of the strong intermolecular interaction. In the case of the spin-coated films, the spectra remained before and after annealing because the J-aggregates were stable at 65 °C.

Figure 12 shows the proposal mechanism of the self-assembly of CP5. As shown in Figure 5, *rac*-CP5 formed H-aggregates, while (*R<sub>p</sub>*)-CP5 did not form it. These were spin-coated films, and the aggregates made kinetically stable forms. The main interaction was  $\pi$ – $\pi$  interaction of five benzene rings. Figure 12 shows the intermolecular  $\pi$ – $\pi$  interaction of *rac*-CP5 and (*R<sub>p</sub>*)-CP5. As shown clearly in the structure, the arrangement of transition dipole moment was different between *rac*-CP5 and (*R<sub>p</sub>*)-CP5. *rac*-CP5 exhibited parallel H-aggregates, but (*R<sub>p</sub>*)-CP5 exhibited inclined H-aggregates.<sup>79</sup> When the inclined H-aggregates arrange the transition moment in approximately 60° described in Figure 12, a positive Cotton effect was observed due to exciton coupling. Therefore, CD and CPL signal in the aggregation state was inverse compared with in the dilute solution (Figure 7). The drop-cast and annealing methods moved the films to thermodynamically stable forms. The main interaction is not  $\pi$ – $\pi$  interaction, and the inclined H-aggregates were slightly changed to overlap the dodecyloxy chain. As a result, exciton coupling was inverse compared with the kinetically stable form (Figure 10), although the regular form was not clear (the angle might be 0° <  $\alpha$  < 90°). In addition, the annealing process made the interaction stronger and the chirality was enhanced drastically.

## CONCLUSION

Optically active  $\pi$ -conjugated oligo(*p*-phenylene ethynylene) dimers with a planar chiral [2.2]paracyclophane were synthesized. In the dilute solution, CP3 and CP5 exhibited good chiroptical properties,  $g_{\text{abs}}$  and  $g_{\text{lum}}$  values in 10<sup>−3</sup> order. Especially, CP5 exhibited excellent CPL profiles ( $\epsilon_{\text{abs}} = 139\,000\text{ M}^{-1}\text{ cm}^{-1}$ ,  $\Phi_{\text{lum}} = 0.87$ , and  $|g_{\text{lum}}| = 1.2 \times 10^{-3}$ ). Under the kinetically stable condition, racemic and optically active CP3 formed J-aggregates, whereas, *rac*-CP5 formed parallel H-aggregates and optically active CP5 formed inclined H-aggregates because of the difference of the strength of the intermolecular  $\pi$ – $\pi$  interaction. CP5 showed unique chiroptical properties. For example, signal inversion occurred depending on the degree of the aggregation. Theoretical calculation supported the interpretation of the signal inversion mechanism. TEM observations revealed that (*R<sub>p</sub>*)-CP5 made fiber formation in the mixed CHCl<sub>3</sub>/MeOH = 40/60 v/v solution and provided the evidence of the regular aggregates. The  $g_{\text{lum}}$  values reached 10<sup>−2</sup> order in the opposite signal between the spin-coated films and the drop-cast films. The annealing method moved the films to the thermodynamically stable forms. The  $g_{\text{lum}}$  values of the drop-cast thick films of CP5 were drastically enhanced after annealing, and the  $g_{\text{lum}}$  values reached 10<sup>−1</sup> order (maximum:  $|g_{\text{lum}}| = 0.27$ )

regardless of the film preparation methods. Those are one of the largest  $g_{\text{lum}}$  values in the self-assembled organic compounds. These properties are attributed to the unique X-shaped chirality of the planar chiral 4,7,12,15-tetrasubstituted [2.2]-paracyclophane framework. This is the first report realizing 10<sup>−1</sup> order  $g_{\text{lum}}$  values with the self-assembled system using the planar chirality as the only chiral source. These behaviors in the dilute solution and in the aggregates are promised to be useful for the CPL application for various devices.

## ASSOCIATED CONTENT

### Supporting Information

The Supporting Information is available free of charge on the ACS Publications website at DOI: 10.1021/acs.macromol.6b02798.

Experimental details; Figures S1–S14 (PDF)

## AUTHOR INFORMATION

### Corresponding Authors

\*E-mail: ymo@kwansei.ac.jp (Y.M.).

\*E-mail: chujo@chujo.synchem.kyoto-u.ac.jp (Y.C.).

### ORCID

Masayuki Gon: 0000-0002-5540-5908

### Present Address

Y.M.: School of Science and Technology, Kwansai Gakuin University, 2-1 Gakuen, Sanda, Hyogo 669-1337, Japan.

### Notes

The authors declare no competing financial interest.

## ACKNOWLEDGMENTS

This work was supported by Grant-in-Aid for Young Scientists (A) (no. 24685018) from the Ministry of Education, Culture, Sports, Science and Technology (MEXT) of Japan. M.G. appreciates Research Fellowships (no. 14J02514) from the Japan Society for the Promotion of Science for Young Scientists. We are grateful to Professor Kazuo Akagi and Dr Kazuyoshi Watanabe (Department of Polymer Chemistry, Graduate School of Engineering, Kyoto University) for CPL data analysis and valuable discussions. TEM observation was supported by Kyoto University Nano Technology Hub in “Nanotechnology Platform Project” sponsored by the Ministry of Education, Culture, Sports, Science and Technology (MEXT), Japan.

## REFERENCES

- (1) *Handbook of Conducting Polymers*, 3rd ed.; Skotheim, T. A., Elsenbaumer, R. L., Reynolds, J. R., Eds.; Marcel Dekker: New York, 2006.
- (2) *Organic Light Emitting Devices: Synthesis, Properties and Application*; Müllen, K., Scherf, U., Eds.; Wiley-VCH: Weinheim, 2006.
- (3) *Organic Field-Effect Transistors*; Groza, J. R., Locklin, J. J., Eds.; CRC Press Taylor & Francis Group: New York, 2007.
- (4) *Organic Photovoltaics: Materials, Device Physics, and Manufacturing Technologies*; Brabec, C., Dyakonov, V., Scherf, U., Eds.; Wiley-VCH: Weinheim, 2008.
- (5) Hoeberl, F. J. M.; Jonkheijm, P.; Meijer, E. W.; Schenning, A. P. H. J. About Supramolecular Assemblies of  $\pi$ -Conjugated Systems. *Chem. Rev.* **2005**, *105*, 1491–1546.
- (6) Zang, L.; Che, Y.; Moore, J. S. One-Dimensional Self-Assembly of Planar  $\pi$ -Conjugated Molecules: Adaptable Building Blocks for Organic Nanodevices. *Acc. Chem. Res.* **2008**, *41*, 1596–1608.
- (7) Frauenrath, H.; Jahnke, E. A General Concept for the Preparation of Hierarchically Structured  $\pi$ -Conjugated Polymers. *Chem. - Eur. J.* **2008**, *14*, 2942–2955.

- (8) Vogelsang, J.; Adachi, T.; Brazard, J.; Vanden Bout, D. A.; Barbara, P. F. Self-assembly of highly ordered conjugated polymer aggregates with long-range energy transfer. *Nat. Mater.* **2011**, *10*, 942–946.
- (9) Ortony, J. H.; Chatterjee, T.; Garner, L. E.; Chworos, A.; Mikhailovsky, A.; Kramer, E. J.; Bazan, G. C. Self-Assembly of an Optically Active Conjugated Oligoelectrolyte. *J. Am. Chem. Soc.* **2011**, *133*, 8380–8387.
- (10) Cabanetos, C.; El Labban, A.; Bartelt, J. A.; Douglas, J. D.; Mateker, W. R.; Fréchet, J. M. J.; McGehee, M. D.; Beaujuge, P. M. Linear Side Chains in Benzo[1,2-b:4,5-b']dithiophene–Thieno[3,4-c]pyrrole-4,6-dione Polymers Direct Self-Assembly and Solar Cell Performance. *J. Am. Chem. Soc.* **2013**, *135*, 4656–4659.
- (11) Spano, F. C. The Spectral Signatures of Frenkel Polarons in H- and J-Aggregates. *Acc. Chem. Res.* **2010**, *43*, 429–439.
- (12) Würthner, F.; Kaiser, T. E.; Saha-Möller, C. R. J-Aggregates: From Serendipitous Discovery to Supramolecular Engineering of Functional Dye Materials. *Angew. Chem., Int. Ed.* **2011**, *50*, 3376–3410.
- (13) Koe, J. R.; Fujiki, M.; Motonaga, M.; Nakashima, H. Cooperative Helical Order in Optically Active Poly(diarylsilylenes). *Macromolecules* **2001**, *34*, 1082–1089.
- (14) Schenning, A. P. H. J.; Jonkheijm, P.; Peeters, E.; Meijer, E. W. Hierarchical Order in Supramolecular Assemblies of Hydrogen-Bonded Oligo(*p*-phenylene vinylene)s. *J. Am. Chem. Soc.* **2001**, *123*, 409–416.
- (15) George, S. J.; Ajayaghosh, A.; Jonkheijm, P.; Schenning, A. P. H. J.; Meijer, E. W. Coiled-Coil Gel Nanostructures of Oligo(*p*-phenylenevinylene)s: Gelation-Induced Helix Transition in a Higher-Order Supramolecular Self-Assembly of a Rigid  $\pi$ -Conjugated System. *Angew. Chem., Int. Ed.* **2004**, *43*, 3422–3425.
- (16) Ajayaghosh, A.; Varghese, R.; George, S. J.; Vijayakumar, C. Transcription and Amplification of Molecular Chirality to Oppositely Biased Supramolecular  $\pi$  Helices. *Angew. Chem., Int. Ed.* **2006**, *45*, 1141–1144.
- (17) Ajayaghosh, A.; Varghese, R.; Mahesh, S.; Praveen, V. K. From Vesicles to Helical Nanotubes: A Sergeant-and-Soldiers Effect in the Self-Assembly of Oligo(*p*-phenyleneethynylene)s. *Angew. Chem., Int. Ed.* **2006**, *45*, 7729–7732.
- (18) Cardolaccia, T.; Li, Y.; Schanze, K. S. Phosphorescent Platinum Acetylacetonate Organogelators. *J. Am. Chem. Soc.* **2008**, *130*, 2535–2545.
- (19) Nowacki, B.; Oh, H.; Zanlorenzi, C.; Jee, H.; Baev, A.; Prasad, P. N.; Akcelrud, L. Design and Synthesis of Polymers for Chiral Photonics. *Macromolecules* **2013**, *46*, 7158–7165.
- (20) Field, J. E.; Muller, G.; Riehl, J. P.; Venkataraman, D. Circularly Polarized Luminescence from Bridged Triarylamine Helicenes. *J. Am. Chem. Soc.* **2003**, *125*, 11808–11809.
- (21) Kawai, T.; Kawamura, K.; Tsumatori, H.; Ishikawa, M.; Naito, M.; Fujiki, M.; Nakashima, T. Circularly Polarized Luminescence of a Fluorescent Chiral Binaphthylene–Perylenebiscarboxydiimide Dimer. *ChemPhysChem* **2007**, *8*, 1465–1468.
- (22) Kaseyama, T.; Furumi, S.; Zhang, X.; Tanaka, K.; Takeuchi, M. Hierarchical Assembly of a Phthalhydrazide-Functionalized Helicene. *Angew. Chem., Int. Ed.* **2011**, *50*, 3684–3687.
- (23) Maeda, H.; Bando, Y.; Shimomura, K.; Yamada, I.; Naito, M.; Nobusawa, K.; Tsumatori, H.; Kawai, T. Chemical-Stimuli-Controllable Circularly Polarized Luminescence from Anion-Responsive  $\pi$ -Conjugated Molecules. *J. Am. Chem. Soc.* **2011**, *133*, 9266–9269.
- (24) Sawada, Y.; Furumi, S.; Takai, A.; Takeuchi, M.; Noguchi, K.; Tanaka, K. Rhodium-Catalyzed Enantioselective Synthesis, Crystal Structures, and Photophysical Properties of Helically Chiral 1,1'-Bitriphenylenes. *J. Am. Chem. Soc.* **2012**, *134*, 4080–4083.
- (25) Haketa, Y.; Bando, Y.; Takaishi, K.; Uchiyama, M.; Muranaka, A.; Naito, M.; Shibaguchi, H.; Kawai, T.; Maeda, H. Asymmetric Induction in the Preparation of Helical Receptor–Anion Complexes: Ion-Pair Formation with Chiral Cations. *Angew. Chem., Int. Ed.* **2012**, *51*, 7967–7971.
- (26) Oyama, H.; Nakano, K.; Harada, T.; Kuroda, R.; Naito, M.; Nobusawa, K.; Nozaki, K. Facile Synthetic Route to Highly Luminescent Sila[7]helicene. *Org. Lett.* **2013**, *15*, 2104–2107.
- (27) Nakamura, K.; Furumi, S.; Takeuchi, M.; Shibuya, T.; Tanaka, K. Enantioselective Synthesis and Enhanced Circularly Polarized Luminescence of S-Shaped Double Azahelicenes. *J. Am. Chem. Soc.* **2014**, *136*, 5555–5558.
- (28) Morisaki, Y.; Inoshita, K.; Chujo, Y. Planar-Chiral Through-Space Conjugated Oligomers: Synthesis and Characterization of Chiroptical Properties. *Chem. - Eur. J.* **2014**, *20*, 8386–8390.
- (29) Sakai, H.; Shinto, S.; Kumar, J.; Araki, Y.; Sakanoue, T.; Takenobu, T.; Wada, T.; Kawai, T.; Hasobe, T. Highly Fluorescent [7]-Carbohelicene Fused by Asymmetric 1,2-Dialkyl-Substituted Quinoxaline for Circularly Polarized Luminescence and Electroluminescence. *J. Phys. Chem. C* **2015**, *119*, 13937–13947.
- (30) Saikawa, M.; Nakamura, T.; Uchida, J.; Yamamura, M.; Nabeshima, T. Synthesis of figure-of-eight helical bisBODIPY macrocycles and their chiroptical properties. *Chem. Commun.* **2016**, *52*, 10727–10730.
- (31) Morisaki, Y.; Gon, M.; Sasamori, T.; Tokitoh, N.; Chujo, Y. Planar Chiral Tetrasubstituted [2.2]Paracyclophane: Optical Resolution and Functionalization. *J. Am. Chem. Soc.* **2014**, *136*, 3350–3353.
- (32) Gon, M.; Morisaki, Y.; Chujo, Y. Optically Active Cyclic Compounds Based on Planar Chiral [2.2]Paracyclophane: Extension of the Conjugated Systems and Chiroptical Properties. *J. Mater. Chem. C* **2015**, *3*, 521–529.
- (33) Gon, M.; Morisaki, Y.; Chujo, Y. Highly Emissive Circularly Polarized Luminescence from Optically Active Conjugated Dimers Consisting of Planar Chiral [2.2]Paracyclophane. *Eur. J. Org. Chem.* **2015**, *2015* (35), 7756–7762.
- (34) Gon, M.; Morisaki, Y.; Sawada, R.; Chujo, Y. Synthesis of Optically Active X-Shaped Conjugated Compounds and Dendrimers Based on Planar Chiral [2.2]Paracyclophane, Leading to Highly Emissive Circularly Polarized Luminescence. *Chem. - Eur. J.* **2016**, *22*, 2291–2298.
- (35) Gon, M.; Kozuka, H.; Morisaki, Y.; Chujo, Y. Optically Active Cyclic Compounds Based on Planar Chiral [2.2]Paracyclophane with Naphthalene Units. *Asian J. Org. Chem.* **2016**, *5*, 353–359.
- (36) Morisaki, Y.; Sawada, R.; Gon, M.; Chujo, Y. New Type of Planar Chiral [2.2]Paracyclophanes and Construction of One-Handed Double Helices. *Chem. - Asian J.* **2016**, *11*, 2524–2527.
- (37) Peeters, E.; Christiaans, M. P. T.; Janssen, R. A. J.; Schoo, H. F. M.; Dekkers, H. P. J. M.; Meijer, E. W. Circularly Polarized Electroluminescence from a Polymer Light-Emitting Diode. *J. Am. Chem. Soc.* **1997**, *119*, 9909–9910.
- (38) Satrijo, A.; Meskers, S. C. J.; Swager, T. M. Probing a Conjugated Polymer's Transfer of Organization-Dependent Properties from Solutions to Films. *J. Am. Chem. Soc.* **2006**, *128*, 9030–9031.
- (39) Wilson, J. N.; Steffen, W.; McKenzie, T. G.; Lieser, G.; Oda, M.; Neher, D.; Bunz, U. H. F. Chiroptical Properties of Poly(*p*-phenyleneethynylene) Copolymers in Thin Films: Large *g*-Values. *J. Am. Chem. Soc.* **2002**, *124*, 6830–6831.
- (40) Langeveld-Voss, B. M. W.; Janssen, R. A.; Christiaans, M. P. T.; Meskers, S. C. J.; Dekkers, H. P. J. M.; Meijer, E. W. Circular Dichroism and Circular Polarization of Photoluminescence of Highly Ordered Poly{3,4-di[(*S*)-2-methylbutoxy]thiophene}. *J. Am. Chem. Soc.* **1996**, *118*, 4908–4909.
- (41) Oda, M.; Nothofer, H.-G.; Lieser, G.; Scherf, U.; Meskers, S. C. J.; Neher, D. Circularly Polarized Electroluminescence from Liquid-Crystalline Chiral Polyfluorenes. *Adv. Mater.* **2000**, *12*, 362–365.
- (42) Oda, M.; Nothofer, H.-G.; Scherf, U.; Šunjić, V.; Richter, D.; Regenstein, W.; Meskers, S. C. J.; Neher, D. Chiroptical Properties of Chiral Substituted Polyfluorenes. *Macromolecules* **2002**, *35*, 6792–6798.
- (43) Goto, H.; Akagi, K. Optically Active Conjugated Polymers Prepared from Achiral Monomers by Polycondensation in a Chiral Nematic Solvent. *Angew. Chem., Int. Ed.* **2005**, *44*, 4322–4328.
- (44) Hayasaka, H.; Miyashita, T.; Tamura, K.; Akagi, K. Helically  $\pi$ -Stacked Conjugated Polymers Bearing Photoresponsive and Chiral Moieties in Side Chains: Reversible Photoisomerization-Enforced Switching Between Emission and Quenching of Circularly Polarized Fluorescence. *Adv. Funct. Mater.* **2010**, *20*, 1243–1250.
- (45) Fukao, S.; Fujiki, M. Circularly Polarized Luminescence and Circular Dichroism from Si–Si-Bonded Network Polymers. *Macromolecules* **2009**, *42*, 8062–8067.

- (46) Yu, J.-M.; Sakamoto, T.; Watanabe, K.; Furumi, S.; Tamaoki, N.; Chen, Y.; Nakano, T. Synthesis and efficient circularly polarized light emission of an optically active hyperbranched poly(fluorenevinylene) derivative. *Chem. Commun.* **2011**, *47*, 3799–3801.
- (47) Watanabe, K.; Sakamoto, T.; Taguchi, M.; Fujiki, M.; Nakano, T. A chiral  $\pi$ -stacked vinyl polymer emitting white circularly polarized light. *Chem. Commun.* **2011**, *47*, 10996–10998.
- (48) Hirahara, T.; Yoshizawa-Fujita, M.; Takeoka, Y.; Rikukawa, M. Highly Efficient Circularly Polarized Light Emission in the Green Region from Chiral Polyfluorene–Thiophene Thin Films. *Chem. Lett.* **2012**, *41*, 905–907.
- (49) Watanabe, K.; Koyama, Y.; Suzuki, N.; Fujiki, M.; Nakano, T. Gigantic chiroptical enhancements in polyfluorene copolymers bearing bulky neomenthyl groups: importance of alternating sequences of chiral and achiral fluorene units. *Polym. Chem.* **2014**, *5*, 712–717.
- (50) Nakano, Y.; Liu, Y.; Fujiki, M. Ambidextrous circular dichroism and circularly polarised luminescence from poly(9,9-di-*n*-decylfluorene) by terpene chirality transfer. *Polym. Chem.* **2010**, *1*, 460–469.
- (51) Kawagoe, Y.; Fujiki, M.; Nakano, Y. Limonene magic: noncovalent molecular chirality transfer leading to ambidextrous circularly polarised luminescent  $\pi$ -conjugated polymers. *New J. Chem.* **2010**, *34*, 637–647.
- (52) Morisaki, Y.; Hifumi, R.; Lin, L.; Inoshita, K.; Chujo, Y. Through-space conjugated polymers consisting of planar chiral pseudo-*ortho*-linked [2.2]paracyclophane. *Polym. Chem.* **2012**, *3*, 2727–2730.
- (53) Nagata, Y.; Nishikawa, T.; Suginome, M. Chirality-switchable circularly polarized luminescence in solution based on the solvent-dependent helix inversion of poly(quinoxaline-2,3-diyl)s. *Chem. Commun.* **2014**, *50*, 9951–9953.
- (54) Shiraki, T.; Tsuchiya, Y.; Noguchi, T.; Tamaru, S.; Suzuki, N.; Taguchi, M.; Fujiki, M.; Shinkai, S. Creation of Circularly Polarized Luminescence from an Achiral Polyfluorene Derivative through Complexation with Helix-Forming Polysaccharides: Importance of the *meta*-Linkage Chain for Helix Formation. *Chem. - Asian J.* **2014**, *9*, 218–222.
- (55) Maeda, H.; Bando, Y. Recent progress in research on stimuli-responsive circularly polarized luminescence based on  $\pi$ -conjugated molecules. *Pure Appl. Chem.* **2013**, *85*, 1967–1978.
- (56) Kumar, J.; Nakashima, T.; Kawai, T. Circularly Polarized Luminescence in Chiral Molecules and Supramolecular Assemblies. *J. Phys. Chem. Lett.* **2015**, *6*, 3445–3452.
- (57) Imai, Y.; Kawaguchi, K.; Harada, T.; Sato, T.; Ishikawa, M.; Fujiki, M.; Kuroda, R.; Matsubara, Y. Solid-state optical properties of a chiral supramolecular fluorophore consisting of chiral (1*R*,2*R*)-1,2-diphenylethylenediamine and fluorescent carboxylic acid derivatives. *Tetrahedron Lett.* **2007**, *48*, 2927–2930.
- (58) Imai, Y.; Murata, K.; Asano, N.; Nakano, Y.; Kawaguchi, K.; Harada, T.; Sato, T.; Fujiki, M.; Kuroda, R.; Matsubara, Y. Selective Formation and Optical Property of a  $2_1$ -Helical Columnar Fluorophore Composed of Achiral 2-Anthracenecarboxylic Acid and Benzylamine. *Cryst. Growth Des.* **2008**, *8*, 3376–3379.
- (59) Tsumatori, H.; Nakashima, T.; Kawai, T. Observation of Chiral Aggregate Growth of Perylene Derivative in Opaque Solution by Circularly Polarized Luminescence. *Org. Lett.* **2010**, *12*, 2362–2365.
- (60) Liu, J.; Su, H.; Meng, L.; Zhao, Y.; Deng, C.; Ng, J. C. Y.; Lu, P.; Faisal, M.; Lam, J. W. Y.; Huang, X.; Wu, H.; Wong, K. S.; Tang, B. Z. What makes efficient circularly polarised luminescence in the condensed phase: aggregation-induced circular dichroism and light emission. *Chem. Sci.* **2012**, *3*, 2737–2747.
- (61) Ng, J. C. Y.; Liu, J.; Su, H.; Hong, Y.; Li, H.; Lam, J. W. Y.; Wong, K. S.; Tang, B. Z. Complexation-induced circular dichroism and circularly polarised luminescence of an aggregation-induced emission luminogen. *J. Mater. Chem. C* **2014**, *2*, 78–83.
- (62) Kumar, J.; Nakashima, T.; Tsumatori, H.; Kawai, T. Circularly Polarized Luminescence in Chiral Aggregates: Dependence of Morphology on Luminescence Dissymmetry. *J. Phys. Chem. Lett.* **2014**, *5*, 316–321.
- (63) Kumar, J.; Nakashima, T.; Kawai, T. Inversion of Supramolecular Chirality in Bichromophoric Perylene Bisimides: Influence of Temperature and Ultrasound. *Langmuir* **2014**, *30*, 6030–6037.
- (64) Ng, J. C. Y.; Li, H.; Yuan, Q.; Liu, J.; Liu, C.; Fan, X.; Li, B. S.; Tang, B. Z. Valine-containing silole: synthesis, aggregation-induced chirality, luminescence enhancement, chiral-polarized luminescence and self-assembled structures. *J. Mater. Chem. C* **2014**, *2*, 4615–4621.
- (65) Ikeda, T.; Takayama, M.; Kumar, J.; Kawai, T.; Haino, T. Novel helical assembly of a Pt(II) phenylbipyridine complex directed by metal–metal interaction and aggregation-induced circularly polarized emission. *Dalton Trans.* **2015**, *44*, 13156–13162.
- (66) Li, H.; Zheng, X.; Su, H.; Lam, J. W. Y.; Sing Wong, K.; Xue, S.; Huang, X.; Huang, X.; Li, B. S.; Tang, B. Z. Synthesis, optical properties, and helical self-assembly of a bivaline-containing tetraphenylethene. *Sci. Rep.* **2016**, *6*, 19277.
- (67) Li, F.; Li, Y.; Wei, G.; Wang, Y.; Li, S.; Cheng, Y. Circularly Polarized Luminescence of Chiral Perylene Diimide Based Enantiomers Triggered by Supramolecular Self-Assembly. *Chem. - Eur. J.* **2016**, *22*, 12910–12915.
- (68) Katoono, R.; Suzuki, T. Planar chiral desymmetrization of a two-layered cyclophane and control of dynamic helicity through the arrangement of two nonstereogenic centers. *Chem. Commun.* **2016**, *52*, 1029–1031.
- (69) Liu, M.; Zhang, L.; Wang, T. Supramolecular Chirality in Self-Assembled Systems. *Chem. Rev.* **2015**, *115*, 7304–7397.
- (70) *Cyclophane Chemistry: Synthesis, Structures and Reactions*; Vögtle, F., Ed.; John Wiley & Sons: Chichester, 1993.
- (71) *Modern Cyclophane Chemistry*; Gleiter, R.; Hopf, H., Eds.; Wiley-VCH: Weinheim, 2004.
- (72) Bazan, G. C. Novel Organic Materials through Control of Multichromophore Interactions. *J. Org. Chem.* **2007**, *72*, 8615–8635.
- (73) Tohda, Y.; Sonogashira, K.; Hagihara, N. A convenient synthesis of acetylenes: catalytic substitutions of acetylenic hydrogen with bromoalkenes, iodoarenes and bromopyridines. *Tetrahedron Lett.* **1975**, *16*, 4467–4470.
- (74) Sonogashira, K. In *Handbook of Organopalladium Chemistry for Organic Synthesis*; Negishi, E., Ed.; Wiley-Interscience: New York, 2002; pp 493–529.
- (75) Person, R. V.; Monde, K.; Humpf, H.; Berova, N.; Nakanishi, K. A new approach in exciton-coupled circular dichroism (ECCD)—insertion of an auxiliary stereogenic center. *Chirality* **1995**, *7*, 128–135.
- (76) Freedman, T. B.; Cao, X.; Dukor, R. K.; Nafie, L. A. Absolute configuration determination of chiral molecules in the solution state using vibrational circular dichroism. *Chirality* **2003**, *15*, 743–758.
- (77) Berova, N.; Bari, L. D.; Pescitelli, G. Application of electronic circular dichroism in configurational and conformational analysis of organic compounds. *Chem. Soc. Rev.* **2007**, *36*, 914–931.
- (78) van Dijk, L.; Bobbert, P. A.; Spano, F. C. Extreme Sensitivity of Circular Dichroism to Long-Range Excitonic Couplings in Helical Supramolecular Assemblies. *J. Phys. Chem. B* **2010**, *114*, 817–825.
- (79) Peyratout, C.; Daehne, L. Aggregation of thiocyanine derivatives on polyelectrolytes. *Phys. Chem. Chem. Phys.* **2002**, *4*, 3032–3039.

## Solid-State Emission

International Edition: DOI: 10.1002/anie.201609656

German Edition: DOI: 10.1002/ange.201609656

Solid-State Emission of the Anthracene-*o*-Carborane Dyad from the Twisted-Intramolecular Charge Transfer in the Crystalline State

Hirofumi Naito, Kenta Nishino, Yasuhiro Morisaki, Kazuo Tanaka, and Yoshiki Chujo\*

**Abstract:** The emission process of the *o*-carborane dyad with anthracene originating from the twisted intramolecular charge transfer (TICT) state in the crystalline state is described. The anthracene-*o*-carborane dyad was synthesized and its optical properties were investigated. Initially, the dyad had aggregation- and crystallization-induced emission enhancement (AIEE and CIEE) properties via the intramolecular charge transfer (ICT) state. Interestingly, the dyad presented the dual-emissions assigned to both locally excited (LE) and ICT states in solution. From the mechanistic studies and computer calculations, it was indicated that the emission band from the ICT should be attributable to the TICT emission. Surprisingly, even in the crystalline state, the TICT emission was observed. It was proposed from that the compact sphere shape of *o*-carborane would allow for rotation even in the condensed state.

In some donor-acceptor-type organic compounds, intramolecular charge transfer (ICT) proceeds with drastic conformational changes, such as twisting at the bridge between electron-donating and -accepting units in the excited state. Sometimes, emission can be observed from this twisted intramolecular charge transfer (TICT) state.<sup>[1]</sup> The TICT emission is versatile, especially for developing bio-sensing materials.<sup>[2]</sup> Because the intensity and the peak position of the TICT emission are greatly affected by environmental factors, such as solvent polarity, temperature, and viscosity, sensing systems these parameters have been designed.<sup>[2]</sup> Indeed, TICT-based fluorophores are powerful tools for monitoring structural alterations of biomolecules.<sup>[3]</sup> In addition, by regulating the mobility of the molecules, dual emission peaks derived from locally-excited (LE) and TICT states were simultaneously observed in a single spectrum.<sup>[4]</sup> Based on the intrinsic differences of responsivity toward environmental factors between LE and TICT emissions, various types of unique optical sensors with luminescent chromism properties and ratiometric behaviors have been accomplished.<sup>[3]</sup> However, very few molecules present TICT emission in the

solid state because of two critical factors: concentration quenching and structural restriction in the condensed state. Thus, the application of the TICT mechanism for optoelectronic devices is still limited.

*o*-Carborane (C<sub>2</sub>H<sub>12</sub>B<sub>10</sub>) is an icosahedral boron cluster containing two adjacent carbon atoms in the cage. Owing to the intrinsic properties of the boron cluster, *o*-carborane derivatives have been used as a building block for neutron-capturing agents and for improving thermal and chemical stabilities of organic materials.<sup>[5]</sup> It was demonstrated that *o*-carborane derivatives tethered to the  $\pi$ -conjugated unit at the C1 (and/or C2) position exhibited aggregation-induced emission (AIE) properties; intramolecular charge transfer (ICT) from the  $\pi$ -conjugated moieties to the C1–C2 bond of *o*-carborane quenches the emission in solution,<sup>[6]</sup> whereas emission can be recovered by freezing the C1–C2 bond vibration in the aggregates.<sup>[7]</sup> Therefore, *o*-carborane is regarded as an AIE-inducible element block, which is defined as a functional unit composed of heteroatoms, for receiving AIE-active materials and highly-efficient solid-state emissions.<sup>[8,9]</sup> Since the discovery of AIE property of *o*-carborane-based conjugated compounds, many research groups have focused on their opto-electronic properties.<sup>[10]</sup> Recently, Fox and co-workers revealed the relationship between the electronic states and the conformation of  $\pi$ -conjugated units to the C1–C2 bond of an *o*-carborane cluster; that is, when  $\pi$ -conjugated planes are twisted to the C1–C2 bond of an *o*-carborane, intramolecular charge transfer occurs more efficiently than in the parallel conformer.<sup>[11]</sup> By making use of this unique character, emission behaviors from LE to ICT can be controlled by changing the conformation of the  $\pi$ -conjugation unit.<sup>[12]</sup> Several recent studies have reported the TICT emission from the *o*-carborane derivatives.<sup>[13]</sup> More recently, the pyrene-*o*-carborane dyads can present not only AIE-based solid-state emissions but also dual emissive properties.<sup>[13a]</sup> Especially in the solution state, the emission bands from the TICT state were obtained. Furthermore, significant emission from the ICT state was detected in the crystalline state. However, because of its low crystallinity, structural information was not obtained and a detailed mechanism in the solid-state emission was not clarified. Thus, to confirm the existence of the TICT process in the crystalline state with *o*-carborane derivatives, further examples must be examined.

Herein, the TICT emission in the crystalline state from the anthracene-*o*-carborane dyad is reported. Initially, the dyad was synthesized and dual emission from LE and TICT states was observed in the solution state. Surprisingly, it was shown that the dyad had both AIEE and CIEE properties attributable to the TICT emission band. The data from the X-ray single-crystal analysis and computer calculations suggested

[\*] H. Naito, K. Nishino, Y. Morisaki, K. Tanaka, Y. Chujo

Department of Polymer Chemistry

Graduate School of Engineering

Kyoto University

Katsura, Nishikyo-ku, Kyoto 615-8510 (Japan)

E-mail: chujo@chujo.synchem.kyoto-u.ac.jp

Y. Morisaki

Department of Applied Chemistry for Environment

School of Science and Technology

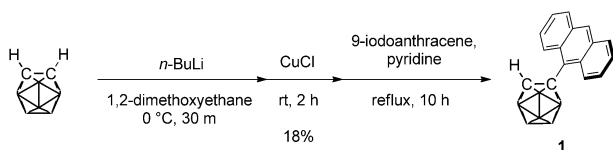
Kwansei Gakuin University

2-1 Gakuen, Sanda, Hyogo 669-1337 (Japan)

Supporting information for this article can be found under:  
<http://dx.doi.org/10.1002/anie.201609656>.

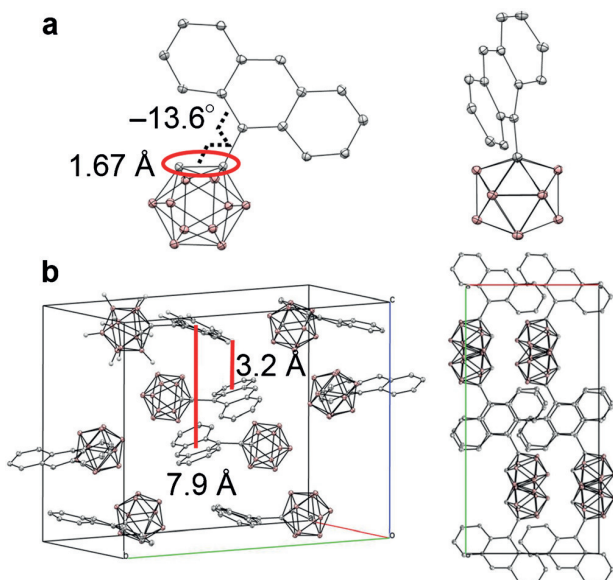
that the rotation at the carborane moiety should occur even in the crystalline state, leading to the CIEE behavior. This is the first example, to our knowledge, to confirm the TICT emission in the crystal packing based on the *o*-carborane derivative.

The synthesis of the *o*-carborane dyad **1** was performed according to Scheme 1. The treatment of *o*-carborane with *n*-butyllithium and subsequent Ullmann-type coupling with 9-iodoanthracene<sup>[14]</sup> afforded compound **1** in 18% yield. The product was characterized by <sup>1</sup>H, <sup>11</sup>B, and <sup>13</sup>C NMR and a mass measurement. The product showed good stability toward air and light under ambient conditions, and good solubility in common organic solvents such as CHCl<sub>3</sub>, CH<sub>2</sub>Cl<sub>2</sub>, THF, and toluene. From these observations, it was concluded that the product possessed the desired structure and stability high enough for optical measurements.



**Scheme 1.** Synthesis of **1**.

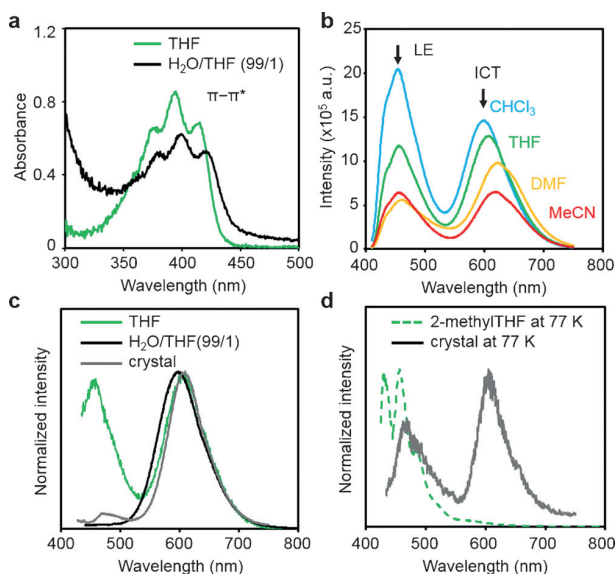
A single-crystal sample of **1** for an X-ray diffraction study was obtained by slow evaporation in CHCl<sub>3</sub>. Figure 1a shows the molecular structure of **1**. The dihedral angle between the anthracene and *o*-carborane moieties was  $-13.6^\circ$ . This means that the anthracene moiety should have the co-planar distribution to the C–C bond in the *o*-carborane moiety. In Figure 1b, the crystal packing diagram is presented. It was found that the distance between C–H and the anthracene ring was 3.2 Å. The intermolecular distance of the anthracene



**Figure 1.** a) Molecular structures and b) packing diagrams of **1** (hydrogen atoms are omitted for clarity, and thermal ellipsoids are displayed at 30% probability).

rings was 7.9 Å, although both rings showed good overlapping. These data suggest that the CH- $\pi$  interaction should be formed in the crystalline packing, while slight  $\pi$ - $\pi$  stacking occurs with the anthracene moiety. Because of the bulky icosahedral *o*-carborane cluster, intermolecular interactions could be weakened in the crystals.

To examine the optical properties of compound **1**, UV/Vis absorption measurements were evaluated. Figure 2a shows the spectra of **1** ( $1.0 \times 10^{-5}$  M) in THF solution and in a poor solvent (H<sub>2</sub>O with 1 vol% THF) to form aggregates of **1**. In THF, broad absorption bands around 400 nm were observed



**Figure 2.** a) UV/Vis absorption spectra of **1** ( $1.0 \times 10^{-5}$  M) in THF and in the poor solvent (THF/H<sub>2</sub>O v/v = 1/99). b) PL spectra of **1** in various solvents. c) PL spectra of **1** ( $1.0 \times 10^{-5}$  M) in the THF solution, aggregates, and crystalline states at room temperature, and d) in 2-MeTHF and crystalline state at 77 K.

attributable to the  $\pi$ - $\pi^*$  transition in the anthracene moiety. In the poor solvent, the absorption spectrum of **1** was red-shifted and became broader compared to that in THF. This should be the result of intermolecular interactions in the aggregates. Absorption spectra were also recorded in other solvents, such as CHCl<sub>3</sub>, THF, DMF, and acetonitrile (Figure S4). Because changes in the position of absorption bands in the spectra were hardly observed, this indicated that the electronic structures in the ground state can be preserved from polarity changes.

To elucidate the emission properties of **1**, photoluminescence (PL) spectra were measured in various solvents, such as CHCl<sub>3</sub>, THF, DMF, and acetonitrile (Figure 2b). Significant characteristics were revealed from the spectra. The first impressive point was dual emissions from the solution samples in all of the solvents. The emission bands around 600 nm were bathochromically shifted by increasing the solvent polarity. In contrast, the emission band around 450 nm was hardly influenced by changing solvent types. To analyze these differences in the response to solvent polarity,

the Lippert–Mataga plots were prepared with the values of the Stokes shift against the solvent polarizability,  $\Delta f$ , according to the Lippert–Mataga equation (Figure S5).<sup>[15]</sup> It was indicated that the slope of the approximate line prepared from the emission band around 450 nm was almost zero. On the other hand, the significant keen slope was obtained from the plots with the peak positions observed around 600 nm. These data indicate that the luminescent bands around 450 nm and 600 nm should be assigned to the LE state of the anthracene moiety and the ICT state in the whole molecule, respectively. It should be mentioned that the LE emission can be generally observed only under frozen or structurally-restricted environmental conditions.<sup>[2a,16]</sup> In this study, the dyad presented emission from the LE state. This implied that the energy barriers could be small in the rotation of the anthracene moiety. From the variable-temperature PL spectra, the difference of energy levels between LE and ICT states ( $\Delta H$ ) was estimated as 0.72 kcal mol<sup>-1</sup> (Figure S6).<sup>[17]</sup> This result raises the possibility of a transition from ICT to LE states at room temperature in the excited state.

In the aggregation and crystalline state, it was found that intensity of the ICT emission band significantly increased (Figure 2c). In the THF solution, weak emission was observed ( $\Phi_{\text{PL}}=0.02$ ). It was shown that the dyad had strong emissions both in the aggregation and crystalline states ( $\Phi_{\text{PL}}=0.18$  and 0.38, respectively). These data clearly indicate that the *o*-carborane–anthracene dyad is the AIE- and CIE-active molecule. It should be emphasized that intense ICT emission was observed even in the crystalline state. Interestingly, according to the result from X-ray crystal analysis in Figure 1, it was confirmed that the anthracene moiety should possess the parallel conformation along the C1–C2 bond in the *o*-carborane, which is an unfavorable steric distribution for the formation of the ICT state.<sup>[11,13]</sup> This fact strongly suggests that the rotation of *o*-carborane should be induced in the crystalline packing, leading to the ICT emission band around 600 nm. In other words, the TICT process should occur even in the crystalline state. To verify this assumption, PL spectra of **1** at 77 K were recorded. In the frozen matrix of 2-MeTHF with  $1.0 \times 10^{-5}$  M concentration, the intense LE emission derived from the anthracene moiety was observed around 450 nm with clear vibrational structures. Moreover, ICT emission around 600 nm was hardly detected. As a result, in the crystalline state at 77 K, the relatively intensity ratio of the LE emission toward ICT was larger than that at room temperature. It is likely that the rotation of the carborane moiety is suppressed in frozen media and in the crystalline state at low temperature, resulting in the expression of the LE emission. On the contrary, the LE emission gradually decreased in high temperature range (Figure S7). It was assumed that the rotation could be thermally enhanced by heating. These data also strongly support that the emission band around 600 nm should originate from the TICT state. In general, organic compounds were unable to exhibit TICT emissions in the crystalline state because the spaces are usually too small to have a large geometrical change in the excited state for the formation of the TICT state. Owing to the compact sphere shape of *o*-carborane, the rotation could proceed after photo-excitation. Additionally, aggregation-

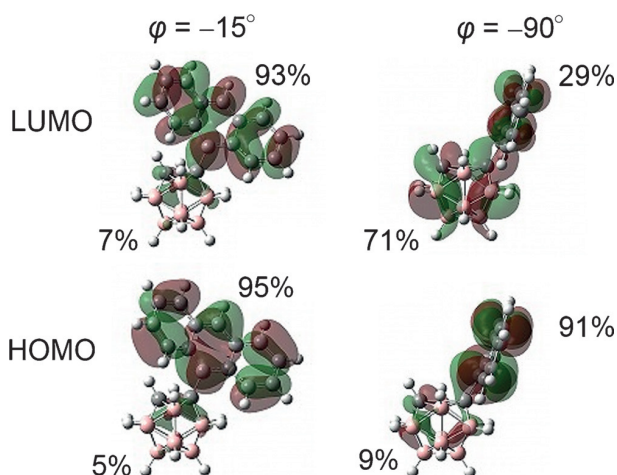
caused quenching (ACQ) was effectively avoided. Thus, the TICT emission can be obtained from the dyad even in the well-ordered packing state. From the PL decay measurements, it was shown that the lifetimes of LE emission in THF solution and in the crystalline state were similar, whereas that of TICT emission in the crystalline state was 3-times longer than that in THF (Table 1). It is likely that there is a higher energetic barrier to the rotation in the crystalline state than that in solution.

**Table 1:** Results from PL decay studies with **1** in the THF solution and crystalline states.

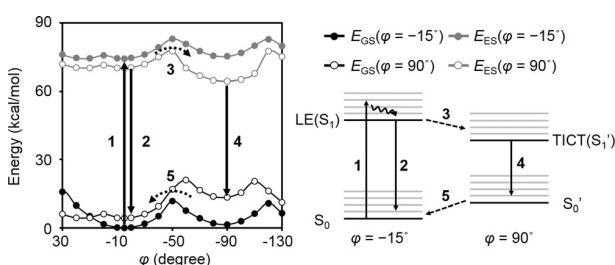
Condition	$\Phi_{\text{PL}}$	$\lambda_{\text{em}}$ [nm]	$\tau$ [ns]	$\chi^2$
THF solution	0.02	454	1.070	1.135
		605	2.797	1.160
Crystal	0.38	468	0.939	1.150
		603	7.965	1.121

According to the previous studies on AIE and CIE materials, intramolecular motions and vibrations played critical roles in the deactivation of the excited state of chromophores.<sup>[18]</sup> In this experiment, significant emission can be observed in the solid state with molecular rotation in the excited state. This strongly supports that the deactivation in the excited state of the AIE-active aryl-carborane systems should be induced not by the rotation but by the vibration at the C1–C2 bond in the *o*-carborane moiety.<sup>[7]</sup>

For insights into the relationship between the conformation and optical properties, quantum calculations were performed by using density functional theory (DFT) and time-dependent DFT (TD-DFT) at the B3LYP/6-31G(d)//B3LYP/6-31G(d) level. By altering the angle ( $\varphi$ ) between the anthracene plane and the C1–C2 bond in *o*-carborane, changes in the electronic properties were monitored. Two optimized S1 geometries with planar ( $\varphi = -15^\circ$ ) and twisted ( $\varphi = -90^\circ$ ) distributions were obtained (Figure 3). In both conformers, it was revealed that the S1-S0 electronic transition was mainly derived from lowest unoccupied molecular orbital (LUMO) to highest occupied molecular orbital (HOMO) (93 % and 95 % for planar and twisted conformers, respectively). Next, the electronic structures in both conformers were investigated. The HOMOs in both conformers and LUMO in the planar conformer were localized on the anthracene moiety. In contrast, the LUMO in the twisted conformer was significantly delocalized to the *o*-carborane moiety. This result also strongly supports that the emission from the planar and twisted conformers should be derived from the LE and CT states, respectively. The calculated emission wavelengths for the LE and TICT states were 433 nm and 561 nm, respectively. These values showed good agreement with the experimental results. Moreover, the C1–C2 bond length in the *o*-carborane moiety was 1.67 Å at  $\varphi = -15^\circ$  and 2.37 Å at  $\varphi = -90^\circ$ . Consistent with previous reports, it was demonstrated that the molecular distribution played important roles in the degree of electronic interaction between the  $\pi$ -conjugation unit and *o*-carborane.<sup>[11,13]</sup>



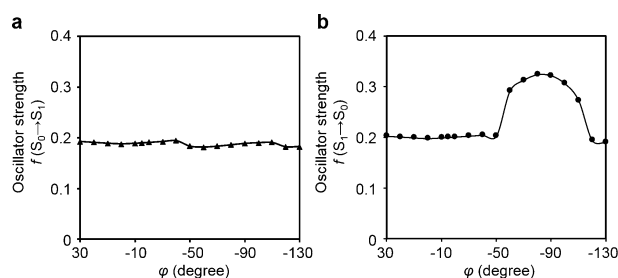
**Figure 3.** Frontier orbitals and proportions of localized electron orbitals in each unit of the S1 state of **1** with the planar ( $\varphi = -15^\circ$ ) and twisted ( $\varphi = -90^\circ$ ) distributions.



**Figure 4.** Energy levels of the ground and excited states of **1** with variable dihedral angles  $\varphi$  calculated at the B3LYP/6-31G(d) level and schematic images of absorption and emission processes.

The potential energy curves were calculated by varying the dihedral angle  $\varphi$  (Figure 4).<sup>[19]</sup> Figure 4 shows those results on each conformation in the gas phase. The  $E_{GS}(\varphi = -15^\circ)$  potential energy curve indicates that the most stable conformer was a planar conformer ( $\varphi = -15^\circ$ ), which is in good agreement with the angle ( $\varphi = -13.6^\circ$ ) determined by X-ray structural analysis. The second stable point was a twisted conformer ( $\varphi = -90^\circ$ ) that was  $1.5 \text{ kcal mol}^{-1}$  higher in energy. The rotation barrier was calculated as  $12 \text{ kcal mol}^{-1}$ . From these data, it is proposed that upon excitation at the planar conformer (process 1 in Figure 4), a fast vibrational relaxation process occurs ( $-15^\circ$  to  $90^\circ$ ). Subsequently, two deactivation paths are considered; one is the emission from the LE state (process 2), and the other is from the TICT state (process 3, and then 4). Because the rotation barrier in the excited state was  $8 \text{ kcal mol}^{-1}$ , it is assumed that the TICT state is readily accessible.

The changes in the oscillator strength for absorption (S0-S1) and emission (S1-S0) were evaluated by altering the dihedral angle  $\varphi$ . As shown in Figure 5a, the oscillator strength in the S0-S1 transition was constant at around 0.20. This means that rotation of the anthracene moiety should have less influence on the absorption properties. In contrast, in the emission process, it was obviously shown that the



**Figure 5.** Oscillator strength changes in the first electronic transition a) S0→S1 and b) S1→S0 by the rotation.

oscillator strength significantly depends on  $\varphi$  (Figure 5b). The larger oscillator strength was more significantly observed in the twisted conformer than that of the planar one. This corresponds to the assumption that strong emission can be observed from the twisted conformer. Because the degree of the oscillator strength was maintained through all of the angles, it is implied that LE emission might occur regardless of the anthracene distribution, resulting in the dual emission behavior.

The rotational energy barriers in the crystal packing in both excited and ground states was estimated from theoretical calculations (Figure S10).<sup>[20]</sup> The crystal packing was modeled by employing the quantum mechanics and molecular mechanics (QM/MM) method. One central molecule was treated as a QM molecule using the TD-DFT method, and the surrounding molecules were modeled using the universal force field (GAFF). The model was built by cutting a cluster, as shown in Figure S10. From this approach, the rotational energy barriers for the ground and excited states in the crystal packing were calculated to be 20 and  $19 \text{ kcal mol}^{-1}$ , respectively (Table 2). These values indicate that the increases in the energy barrier were obtained relative to the single-molecule model. However, these low values suggest that the *o*-carborane moiety in **1** could be capable of rotating in the crystal structure, presumably due to the spherical shape of *o*-carborane.<sup>[21]</sup> These data also suggest that the emission band around 600 nm in the crystalline state should be the TICT emission.

**Table 2:** Calculated rotation barrier for each model.

Model	Rotation Barrier [ $\text{kcal mol}^{-1}$ ]	
	Ground State	Excited State
Single-molecule	11.70	7.57
QM/MM model	19.74	18.54

The *o*-carborane-anthracene dyad was synthesized, and it was found that the dyad exhibited the TICT emissions both in the solution and crystalline states. From the quantum chemical calculations and dynamics evaluations, it was suggested that the rotation at the *o*-carborane moiety can proceed smoothly owing to the compact spherical shape of carborane, leading to the TICT process even in the densely packing state. There are several significant issues to be

emphasized: First, the new emission mechanism from *o*-carborane, such as TICT, is confirmed from the experimental results. So far, various types of *o*-carborane-based luminescent molecules have been developed from the CT emission. In this study, we demonstrated the emission via the dynamic state, including the twisting in the excited state from *o*-carborane derivatives. Second, the AIE- and CIE-active material was obtained. Finally, we demonstrated a solid-state luminescent molecule. Our findings could be feasible not only for presenting unique photophysical properties in the solid state, but also for preparing film-type optical sensors based on intrinsic stimuli-responsivity of TICT emission.

### Acknowledgements

This work was partially supported by a Grant-in-Aid for Scientific Research on Innovative Areas “New Polymeric Materials Based on Element-Blocks (No.2401)” (JSPS KAKENHI Grant Number JP24102013).

**Keywords:** aggregation-induced emission · carboranes · intramolecular charge transfer

**How to cite:** *Angew. Chem. Int. Ed.* **2017**, *56*, 254–259  
*Angew. Chem.* **2017**, *129*, 260–265

- [1] a) E. Lippert, W. Lüder, H. Boss in *Advances in Molecular Spectroscopy* (Ed.: A. Marngini), Pergamon Press, Oxford, **1962**, p. 443; b) A. Siemiarz, Z. R. Grabowski, A. Krówczynski, M. Asher, M. Ottolenghi, *Chem. Phys. Lett.* **1977**, *51*, 315–320; c) Z. R. Grabowski, K. Rotkiewicz, A. Siemiarz, *J. Lumin.* **1979**, *18–19*, Part 1, 420–424; d) Z. R. Grabowski, K. Rotkiewicz, W. Rettig, *Chem. Rev.* **2003**, *103*, 3899–4032; e) J. Wu, W. Liu, J. Ge, H. Zhang, P. Wang, *Chem. Soc. Rev.* **2011**, *40*, 3483–3495; f) K. Hamasaki, H. Ikeda, A. Nakamura, A. Ueno, F. Toda, I. Suzuki, T. Osa, *J. Am. Chem. Soc.* **1993**, *115*, 5035–5040.
- [2] a) S. Sasaki, S. Suzuki, W. M. C. Sameera, K. Igawa, K. Morokuma, G. Konishi, *J. Am. Chem. Soc.* **2016**, *138*, 8194–8206; b) N. P. F. Barthes, I. A. Karpenko, D. Dziuba, M. Spadafora, J. Auffret, A. P. Demchenko, Y. Mely, R. Benhida, B. Y. Michel, A. Burger, *RSC Adv.* **2015**, *5*, 33536–33545.
- [3] a) A. Okamoto, K. Tainaka, K. Nishiza, I. Saito, *J. Am. Chem. Soc.* **2005**, *127*, 13128–13129; b) A. Suzuki, N. Nemoto, I. Saito, Y. Saito, *Org. Biomol. Chem.* **2014**, *12*, 660–666; c) J. Feng, K. Tian, D. Hu, S. Wang, S. Li, Y. Zeng, Y. Li, G. Yang, *Angew. Chem. Int. Ed.* **2011**, *50*, 8072–8076; *Angew. Chem.* **2011**, *123*, 8222–8226; d) H. Dong, Y. Wei, W. Zhang, C. Wei, C. Zhang, J. Yao, Y. S. Zhao, *J. Am. Chem. Soc.* **2016**, *138*, 1118–1121; e) Y. Wei, H. Dong, C. Wei, W. Zhang, Y. Yan, Y. S. Zhao, *Adv. Mater.* **2016**, *28*, 7424–7429; f) H. Dong, C. Zhang, J. Yao, Y. S. Zhao, *Chem. Asian J.* **2016**, *11*, 2656–2661.
- [4] a) A. Ito, S. Ishizaka, N. Kitamura, *Phys. Chem. Chem. Phys.* **2010**, *12*, 6641–6649; b) R. Hu, E. Lager, A. Aguilar-Aguilar, J. Liu, J. W. Y. Lam, H. H. Y. Sung, I. D. Williams, Y. Zhong, K. S. Wong, E. Peña-Cabrera, B. Z. Tang, *J. Phys. Chem. C* **2009**, *113*, 15845–15853.
- [5] a) R. N. Grimes, *Carboranes*, 2nd ed. Academic Press, London, **2011**; b) V. I. Bregadze, *Chem. Rev.* **1992**, *92*, 209–223; c) F. Issa, M. Kassiou, L. M. Rendina, *Chem. Rev.* **2011**, *111*, 5701–5722; d) J. Valliant, K. Guenther, A. King, P. Morel, P. Schaffer, O. Sogbein, K. Stephenson, *Coord. Chem. Rev.* **2002**, *232*, 173–230; e) M. Scholz, E. Hey-Hawkins, *Chem. Rev.* **2011**, *111*, 7035–7062; f) J. Yue, Y. Li, Y. Zhao, D. Xiang, Y. Dai, *Polym. Degrad. Stab.* **2016**, *129*, 286–295; g) S. Qi, H. Wang, G. Han, Z. Yang, X. Zhang, S. Jiang, Y. Lu, *J. Appl. Polym. Sci.* **2016**, *133*, 43488; h) R. Otero, S. Seoane, R. Sigüeiro, A. Y. Belorusova, M. A. Maestro, R. Pérez-Fernández, N. Rochel, A. Mourinho, *Chem. Sci.* **2016**, *7*, 1033–1037; i) H. Nakamura, L. Tazaki, D. Kanoh, S. Sato, *Pure Appl. Chem.* **2015**, *87*, 143–154; j) G. Z. Li, S. Azuma, S. Sato, H. Minegishi, H. Nakamura, *Bioorg. Med. Chem. Lett.* **2015**, *25*, 2624–2628; k) H. Nakamura, L. Tasaki, D. Kanoh, S. Sato, H. S. Ban, *Dalton Trans.* **2014**, *43*, 4941–4944; l) B. P. Dash, R. Satapathy, J. A. Maguire, N. S. Hosmane, *Boron Science: New Technologies and Applications* (Ed.: N. S. Hosmane), CRC, Boca Raton, FL, **2011**; m) K. O. Kirlikovali, J. C. Axtell, A. Gonzalez, A. C. Phung, S. I. Khan, A. M. Spokoyny, *Chem. Sci.* **2016**, *7*, 5132–5138; n) J. J. Schwartz, A. M. Mendoza, N. Wattanatorn, Y. Zhao, V. T. Nguyen, A. M. Spokoyny, C. A. Mirkin, T. Baše, P. S. Weiss, *J. Am. Chem. Soc.* **2016**, *138*, 5957–5967.
- [6] a) N. Tsuboya, M. Lamrani, R. Hamasaki, M. Ito, M. Mitsushishi, T. Miyashita, Y. Yamamoto, *J. Mater. Chem.* **2002**, *12*, 2701–2705; b) J. O. Huh, H. Kim, K. M. Lee, Y. S. Lee, Y. Do, M. H. Lee, *Chem. Commun.* **2010**, *46*, 1138–1140; c) K. Lee, M. J. O. Huh, T. Kim, Y. Do, M. H. Lee, *Dalton Trans.* **2011**, *40*, 11758–11764; d) K. Kokado, Y. Chujo, *Dalton Trans.* **2011**, *40*, 1919–1923; e) L. A. Boyd, W. Clegg, R. C. B. Copley, M. G. Davidson, M. A. Fox, T. G. Hibbert, J. A. K. Howard, A. Mackinnon, R. J. Peace, K. Wade, *Dalton Trans.* **2004**, 2786–2799; f) S. Kwon, K.-R. Wee, Y.-J. Cho, S. O. Kang, *Chem. Eur. J.* **2014**, *20*, 5953–5960.
- [7] K. Kokado, Y. Chujo, *Macromolecules* **2009**, *42*, 1418–1420.
- [8] Y. Chujo, K. Tanaka, *Bull. Chem. Soc. Jpn.* **2015**, *88*, 633–643.
- [9] a) S. Mukherjee, P. Thilagar, *Chem. Commun.* **2016**, *52*, 1070–1093; b) H. Naito, Y. Morisaki, Y. Chujo, *Angew. Chem. Int. Ed.* **2015**, *54*, 5084–5087; *Angew. Chem.* **2015**, *127*, 5173–5176; c) R. Furue, T. Nishimoto, I. S. Park, J. Lee, T. Yasuda, *Angew. Chem. Int. Ed.* **2016**, *55*, 7171–7175; *Angew. Chem.* **2016**, *128*, 7287–7291; d) X. Li, H. Yan, Q. Zhao, *Chem. Eur. J.* **2016**, *22*, 1888–1898; e) S. Inagi, K. Hosoi, T. Kubo, N. Shida, T. Fuchigami, *Electrochemistry* **2013**, *81*, 368–370; f) H.-Q. Wang, W.-Y. Wang, X.-Y. Fang, L. Wang, C.-L. Zhu, Z.-Z. Chen, H. Chen, Y.-Q. Qiu, *J. Mol. Graphics Modell.* **2016**, *67*, 111–118; g) L. Böhling, A. Brockhinke, J. Kahlert, L. Weber, R. A. Harder, D. S. Yufit, J. A. K. Howard, J. A. H. MacBride, M. A. Fox, *Eur. J. Inorg. Chem.* **2016**, 403–412; h) Y. Kim, S. Park, Y. H. Lee, J. Jung, S. Yoo, M. H. Lee, *Inorg. Chem.* **2016**, *55*, 909–917; i) B. H. Choi, J. H. Lee, H. Hwang, K. M. Lee, M. H. Park, *Organometallics* **2016**, *35*, 1771–1784; j) K. Nishino, K. Hashimoto, K. Tanaka, Y. Morisaki, Y. Chujo, *Tetrahedron Lett.* **2016**, *57*, 2025–2028; k) Y.-J. Cho, S.-Y. Kim, M. Cho, W.-S. Han, H.-J. Son, D. W. Cho, S. O. Kang, *Phys. Chem. Chem. Phys.* **2016**, *18*, 9702–9708; l) L. Zhu, X. Tang, Q. Yu, W. Lv, H. Yan, Q. Zhao, W. Huang, *Chem. Eur. J.* **2015**, *21*, 4721–4730; m) J. J. Peterson, A. R. Davis, M. Werre, E. B. Coughlin, K. R. Carter, *ACS Appl. Mater. Interfaces* **2011**, *3*, 1796–1799; n) Z. Wang, P. Jiang, T. Wang, G. J. Moxey, M. P. Cifuentes, C. Zhang, M. G. Humphrey, *Phys. Chem. Chem. Phys.* **2016**, *18*, 15719–15726; o) A. Pitto-Barry, A. South, A. Rodger, N. P. E. Barry, *Dalton Trans.* **2016**, *45*, 1763–1768; p) K. Kokado, Y. Chujo, *J. Org. Chem.* **2011**, *76*, 316–319.
- [10] a) J. J. Peterson, M. Werre, Y. C. Simon, E. B. Coughlin, K. R. Carter, *Macromolecules* **2009**, *42*, 8594–8598; b) B. P. Dash, R. Satapathy, E. R. Gaillard, K. M. Norton, J. A. Maguire, N. Chug, N. S. Hosmane, *Inorg. Chem.* **2011**, *50*, 5485–5493; c) A. R. Davis, J. J. Peterson, K. R. Carter, *ACS Macro Lett.* **2012**, *1*, 469–472; d) K.-R. Wee, W.-S. Han, D. W. Cho, S. Kwon, C. Pac, S. O. Kang, *Angew. Chem. Int. Ed.* **2012**, *51*, 2677–2680; *Angew. Chem.* **2012**, *124*, 2731–2734; e) K.-R. Wee, Y.-J. Cho, S. Jeong, S. Kwon, J.-D. Lee, I.-H. Suh, S. O. Kang, *J. Am. Chem. Soc.* **2012**, *134*, 17982–17990; f) F. Lerouge, A. Ferrer-Ugalde, C.

- Viñas, F. Teixidor, R. Sillanpää, A. Abreu, E. Xochitiotzi, N. Farfán, R. Santillan, R. Núñez, *Dalton Trans.* **2011**, *40*, 7541–7550; g) R. A. Harder, J. A. H. MacBride, G. P. Rivers, D. Yufit, A. E. Goeta, J. A. K. Howard, K. Wade, M. A. Fox, *Tetrahedron* **2014**, *70*, 5182–5189; h) J. Kahlert, H.-G. Stammler, B. Neumann, R. A. Harder, L. Weber, M. A. Fox, *Angew. Chem. Int. Ed.* **2014**, *53*, 3702–3705; *Angew. Chem.* **2014**, *126*, 3776–3779.
- [11] a) L. Weber, J. Kahlert, R. Brockhinke, L. Böhling, A. Brockhinke, H.-G. Stammler, B. Neumann, R. A. Harder, M. A. Fox, *Chem. Eur. J.* **2012**, *18*, 8347–8357; b) L. Weber, J. Kahlert, L. Böhling, A. Brockhinke, H.-G. Stammler, B. Neumann, R. A. Harder, P. J. Low, M. A. Fox, *Dalton Trans.* **2013**, *42*, 2266–2281; c) J. Kahlert, L. Böhling, A. Brockhinke, H.-G. Stammler, B. Neumann, L. M. Rendina, P. J. Low, L. Weber, M. A. Fox, *Dalton Trans.* **2015**, *44*, 9766–9781.
- [12] a) S.-Y. Kim, A.-R. Lee, G. F. Jin, Y.-J. Cho, H.-J. Son, W.-S. Han, S. O. Kang, *J. Org. Chem.* **2015**, *80*, 4573–4580; b) L. Weber, J. Kahlert, R. Brockhinke, L. Böhling, J. Halama, A. Brockhinke, H. G. Stammler, B. Neumann, C. Nervi, R. A. Harder, P. J. Low, M. A. Fox, *Dalton Trans.* **2013**, *42*, 10982–10996; c) J. Park, Y. H. Lee, J. Y. Ryu, J. Lee, M. H. Lee, *Dalton Trans.* **2016**, *45*, 5667–5675; d) K.-R. Wee, Y.-J. Cho, J. K. Song, S. O. Kang, *Angew. Chem. Int. Ed.* **2013**, *52*, 9682–9685; *Angew. Chem.* **2013**, *125*, 9864–9867.
- [13] a) K. Nishino, H. Yamamoto, K. Tanaka, Y. Chujo, *Org. Lett.* **2016**, *18*, 4064–4067; b) S.-Y. Kim, Y.-J. Cho, G. F. Jin, W.-S. Han, H.-J. Son, D. W. Cho, S. O. Kang, *Phys. Chem. Chem. Phys.* **2015**, *17*, 15679–15682.
- [14] M. Shao, P. Dongare, L. N. Dawe, D. W. Thompson, Y. Zhao, *Org. Lett.* **2010**, *12*, 3050–3053.
- [15] a) E. Lippert, W. Rettig, V. Bonacic-Koutecky, F. Heisel, J. A. Miehe, *Adv. Chem. Phys.* **1987**, *68*, 1–173; b) B. Valeur, *Molecular Fluorescence*, Wiley-VCH, Weinheim, **2002**.
- [16] a) K. Tanaka, J.-H. Jeon, K. Inafuku, Y. Chujo, *Bioorg. Med. Chem.* **2012**, *20*, 915–919; b) K. Tanaka, K. Inafuku, S. Adachi, Y. Chujo, *Macromolecules* **2009**, *42*, 3489–3492.
- [17] B. Stevens, M. I. Ban, *Trans. Faraday Soc.* **1964**, *60*, 1515–1523.
- [18] J. Mei, N. L. C. Leung, R. T. K. Kwok, J. W. Y. Lam, B. Z. Tang, *Chem. Rev.* **2015**, *115*, 11718–11940.
- [19] V. I. Stsiapura, A. A. Maskevich, V. A. Kuzmitsky, K. K. Tur-overov, I. M. Kuznetsova, *J. Phys. Chem. A* **2007**, *111*, 4829–4835.
- [20] Q. Wu, T. Zhang, Q. Peng, D. Wang, Z. Shuai, *Phys. Chem. Chem. Phys.* **2014**, *16*, 5545–5552.
- [21] a) T.-A. V. Khuong, H. Dang, P. D. Jarowski, E. F. Maverick, M. A. Garcia-Garibay, *J. Am. Chem. Soc.* **2007**, *129*, 839–845; b) J. Vacek, J. Michl, *Proc. Natl. Acad. Sci. USA* **2010**, *107*, 14973–14977; c) S. Sato, T. Yamasaki, H. Isobe, *Proc. Natl. Acad. Sci. USA* **2014**, *111*, 8374–8379; d) P. Commins, M. A. Garcia-Garibay, *J. Org. Chem.* **2014**, *79*, 1611–1619; e) Y. Inagaki, K. Yamaguchi, W. Setaka, *RSC Adv.* **2014**, *4*, 58624–58630.

Manuscript received: October 2, 2016

Final Article published: December 1, 2016

# $\pi$ -Conjugated polymer-layered structures: synthesis and self-assembly

Yuichi Tsuji, Yasuhiro Morisaki<sup>1</sup> and Yoshiki Chujo

$\pi$ -Conjugated polymers capped with a boronic acid end-functional group were synthesized by chain-growth Suzuki–Miyaura polycondensation. The obtained polymers were reacted with a  $\pi$ -stacked-polymer scaffold, developed in our previous work. Despite their bulkiness, the conjugated polymers were efficiently introduced into the polymer scaffold. The spectroscopic and optical characterization of the obtained graft polymers in the solid state revealed that the original  $\pi$ -conjugated polymers were stacked in a single polymer chain. Although excluded volume effects prevented significant intermolecular interactions between the polyfluorenes, the introduced polythiophenes formed intermolecular  $\pi$ -stacked structures. Direct observations of the obtained graft polymers showed that the graft polymers self-assembled into the spherical or fiber structures depending on the introduced polymers, whereas no ordered structures were formed by the same polymers before the polymer reaction.

*Polymer Journal* (2017) 49, 203–208; doi:10.1038/pj.2016.89; published online 28 September 2016

## INTRODUCTION

Because of the formation of highly ordered structures, the supramolecular self-assembly of  $\pi$ -conjugated compounds<sup>1,2</sup> can provide new functionalities and lead to unique optoelectronic properties.<sup>3–11</sup> Because  $\pi$ -conjugated compounds tend to aggregate by  $\pi$ - $\pi$  stacking, the introduction of non-covalent interactions at appropriate positions increases their association constants and facilitates the formation of higher-ordered structures.<sup>12,13</sup> For example, supramolecular gels can be formed through intermolecular interactions such as hydrogen bonds,<sup>14,15</sup> and multiple long alkyl chains facilitate columnar stacking along the  $\pi$ -stacking direction of supramolecular assemblies<sup>16–19</sup> (Figure 1a). A variety of assembled structures can be formed through covalent linkages between  $\pi$ -conjugated units (Figure 1b). Flexible linkers enable intramolecular folding, and the resulting folded molecules can adopt unique morphologies such as fibers<sup>20–22</sup> and two-dimensional nanosheets.<sup>23</sup> Conjugated linkers extended the  $\pi$ -conjugation length and the conjugated polymers can form nanofibers through their strong  $\pi$ - $\pi$  interactions.<sup>24,25</sup>

Among the different types of linkers, hairpin-shaped rigid linkers can promote the formation of intramolecular  $\pi$ -stacked structures.<sup>26–30</sup> We have recently reported the synthesis of polymers with layered aromatic rings using a xanthenes scaffold as a hairpin-shaped linker; these polymers exhibit intramolecular  $\pi$ -stacked structures with multiple aromatic rings stacked along a single polymer chain.<sup>31–36</sup> They can be regarded as the assembly of several small  $\pi$ -conjugated units. However, owing to the small size of the

$\pi$ -conjugated moieties and to the bulkiness of the xanthenes scaffold, their intermolecular interactions were relatively weak. Recently, we reported a versatile polymer reaction method for the construction of aromatic ring-layered structures.<sup>37</sup> This method enables the production of  $\pi$ -stacked structures for a wide variety of  $\pi$ -electron systems. Herein, we used  $\pi$ -conjugated polymers as the stacked  $\pi$ -electron systems and an aromatic ring-layered polymer as a scaffold to synthesize  $\pi$ -conjugated polymer-layered structures, in which the  $\pi$ -conjugated polymers were grafted on the aromatic ring-layered scaffold. The rigid scaffold holds the  $\pi$ -conjugated polymers in a  $\pi$ - $\pi$  stacking arrangement; the ordered structure of which enhances the intermolecular interactions between the polymers, resulting in the formation of spherical- or fiber-like structures.

## RESULTS AND DISCUSSION

We applied catalyst-transfer Suzuki–Miyaura coupling<sup>38–43</sup> to synthesize end-functionalized poly(3-hexylthiophene) (P3HT) and poly(fluorene) (PF). As shown in Scheme 1, polymerization of AB-type monomers **2** and **3** with the palladium initiator **1** ( $[\text{monomer}]_0/[\mathbf{1}]_0 = 20$ ) was used to prepare boron-masking<sup>44</sup> polymers **P3HT-BDAN** and **PF-BDAN**. End-functionalization of the one terminal of the polymer was confirmed by <sup>1</sup>H NMR using the signals arising from the end-functionalized pyrenes and matrix-assisted laser desorption/ionization time-of-flight mass spectrometry. The values for the degree of polymerization of **P3HT-BDAN** and **PF-BDAN** were estimated to be 20 and 18, respectively, with almost 100% regioregularity (Supplementary

Department of Polymer Chemistry, Graduate School of Engineering, Kyoto University, Kyoto, Japan

<sup>1</sup>Current address: Department of Applied Chemistry for Environment, School of Science and Technology, Kwansai Gakuin University, 2-1 Gakuen, Sanda, Hyogo 669-1337, Japan.

Correspondence: Professor Y. Morisaki or Professor Y. Chujo, Department of Applied Chemistry for Environment, Kwansai Gakuin University, 2-1 Gakuen, Sanda, Hyogo 669-1337 Japan.

E-mail: ymo@kwansai.ac.jp or chujo@chujo.synchem.kyoto-u.ac.jp

Received 10 July 2016; revised 3 August 2016; accepted 3 August 2016; published online 28 September 2016

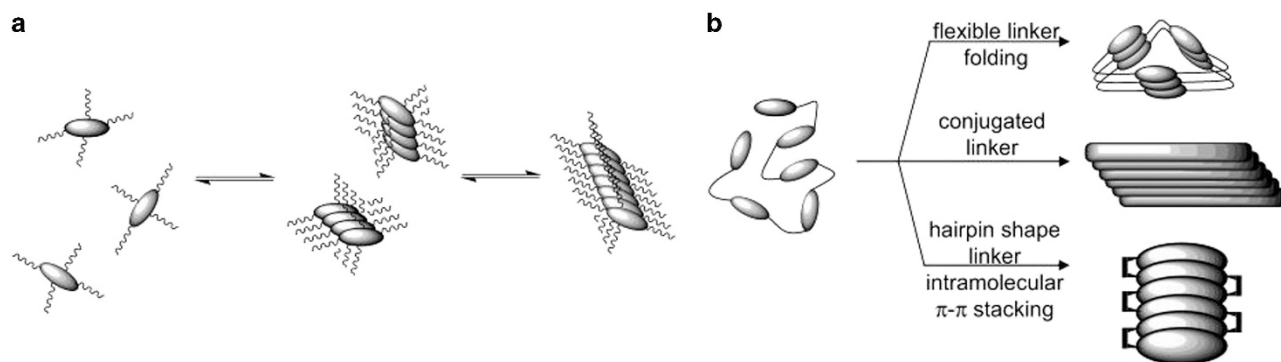
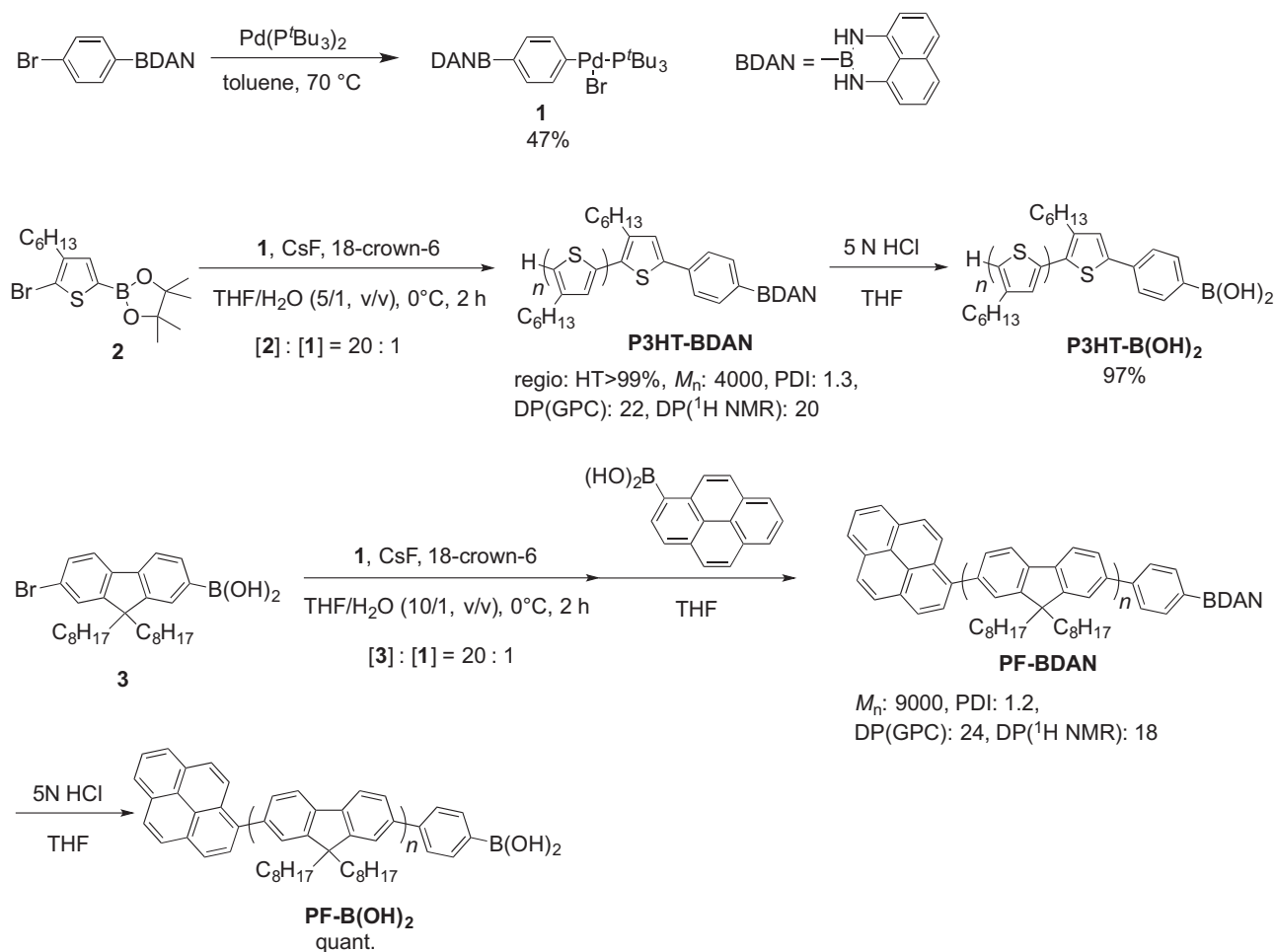


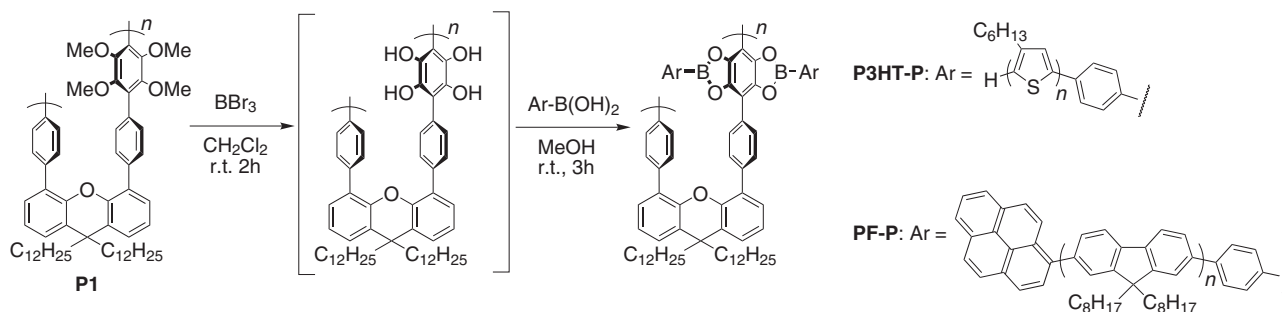
Figure 1 Examples of self-assemblies: (a) conjugated compounds and (b) covalently bonded conjugated compounds.



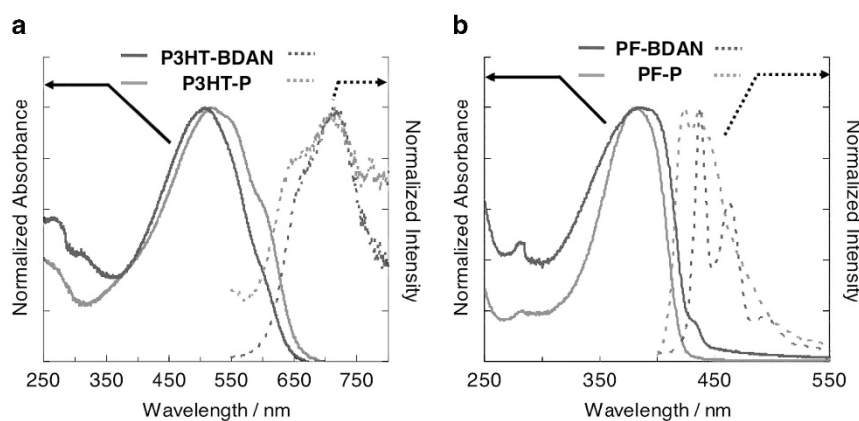
Scheme 1 Synthesis of a Pd initiator and end-functionalized polymers. GPC, gel-permeation chromatography; <sup>1</sup>H NMR, proton nuclear magnetic resonance.

Figure S3–S6 and Supplementary Figure S13–S16). After the deprotection of boronic acid, the polymer reaction of the polymer precursor (aromatic ring-layered polymer) **P1** with **P3HT-B(OH)<sub>2</sub>** or **PF-B(OH)<sub>2</sub>** was carried out under conditions similar to those reported in the literature (Scheme 2).<sup>37</sup> Grafting of P3HT and PF polymers to the scaffold was confirmed by Fourier Transform-Infrared (FT-IR) spectroscopy and gel-permeation chromatography, as shown in Supplementary Figure S15–S17. Only the peak arising from boronate

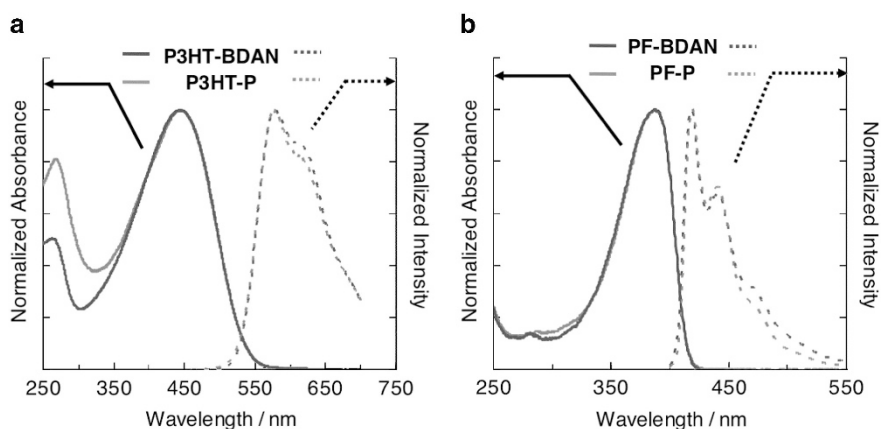
esters at  $1350\text{ cm}^{-1}$  was observed in both cases, with no peaks corresponding to the unreacted hydroxyl groups, and the molecular weights of the grafted polymers **P3HT-P** and **PF-P** were found to be much larger than those of **P3HT-BDAN** and **PF-BDAN**. The polymer reaction thus proceeded almost quantitatively, despite the low concentration of the boronic acid moiety in both **P3HT-B(OH)<sub>2</sub>** and **PF-B(OH)<sub>2</sub>**. Structures of all new compounds were confirmed by <sup>1</sup>H and <sup>13</sup>C NMR spectra (Supplementary Figure S1–S12).



**Scheme 2** Polymer reactions of **P1** to synthesize  $\pi$ -conjugated polymer-stacked polymers **P3HT-B(OH)<sub>2</sub>** and **PF-B(OH)<sub>2</sub>**.



**Figure 2** UV-vis absorption and fluorescence spectra of (a) **P3HT-P** and **P3HT-BDAN** in  $\text{CHCl}_3$  ( $1.0 \times 10^{-5}$  M), and (b) **PF-P** and **PF-BDAN** in  $\text{CHCl}_3$  ( $1.0 \times 10^{-5}$  M). UV-vis, ultraviolet-visible.

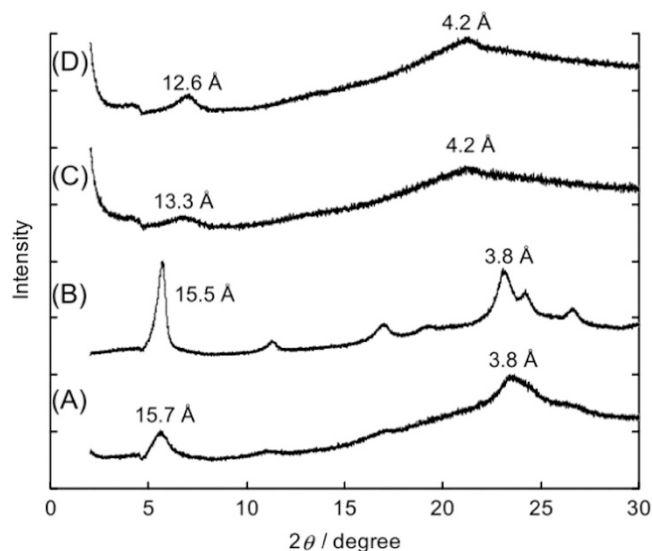


**Figure 3** UV-vis absorption (solid line) and fluorescence (dashed line) spectra of (a) **P3HT-P** film and **P3HT-BDAN** film, and (b) **PF-P** film and **PF-BDAN** film. UV-vis, ultraviolet-visible.

The ultraviolet-visible absorption and fluorescence spectra of the polymers were measured in diluted  $\text{CHCl}_3$  solutions, with no significant differences emerging in the optical properties measured before and after the polymer reactions (Figure 2). Because the degree of polymerization of the original polymers was sufficiently large and similar to the reported effective conjugation length,<sup>45,46</sup> the intramolecular interactions within the introduced polymers had little influence on their electronic state. On the other hand, significant differences were observed in the cast films (Figure 3). Polymer **P3HT-BDAN** was randomly aggregated in the solid state; its absorption peaks were

broadened and red-shifted owing to the intermolecular  $\pi$ - $\pi$  interactions. The fluorescence emission intensity also decreased and the corresponding spectrum was red-shifted. The main absorption peak of **P3HT-P** exhibited a further red-shift compared with that of **P3HT-BDAN**, with an absorption shoulder  $\sim 600$  nm corresponding to the crystalline **P3HT** domains in a single polymer chain.<sup>47</sup> In addition, hardly any emission was detected from **P3HT-P**. These results suggest that the **P3HT** units in **P3HT-P** adopted a well-stacked and more ordered arrangement in the solid state owing to the presence of the xanthene-based polymer scaffold. The X-ray diffraction profile of

**P3HT-P** indicated a phase I pattern<sup>48</sup> in which the hexyl chains of P3HT adopted a lamellar packing, and the  $\pi$ - $\pi$  stacking distance among P3HT chains was estimated to be 3.8 Å (Figure 4). However, the crystallinity of the **P3HT-P** film seemed to decrease. Even though **P3HT-BDAN** also exhibited a phase I pattern, the X-ray diffraction peak associated with the  $\pi$ - $\pi$  stacking of P3HT units was different; in particular, the intramolecular  $\pi$ - $\pi$  stacking peak of **P3HT-P** in a single polymer chain was strong, and its intensity was similar to that of the peak associated with the lamellar alkyl chains. This was owing to

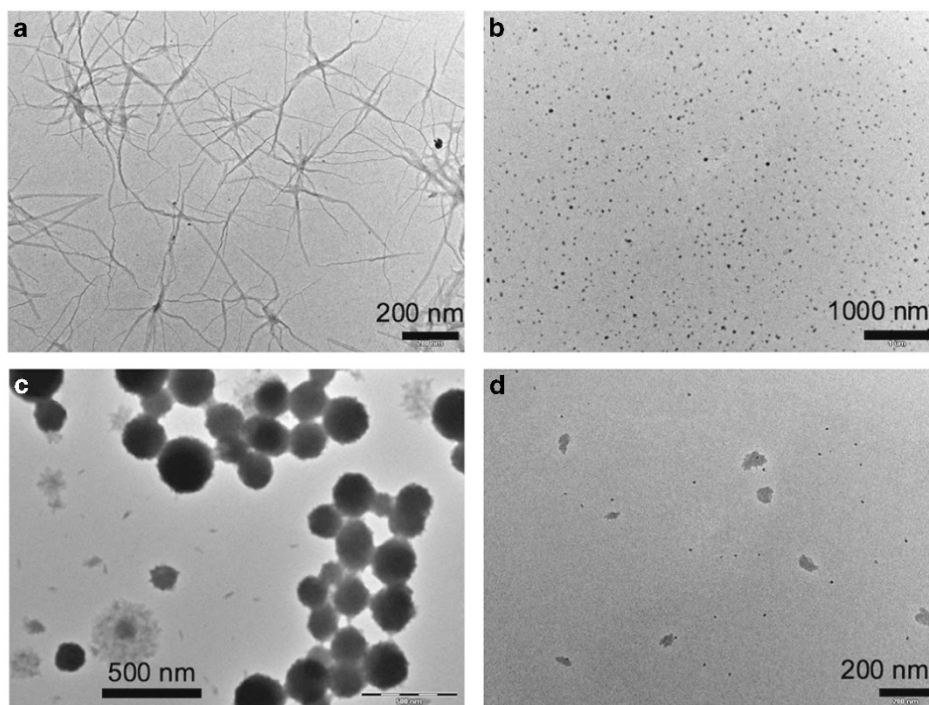


**Figure 4** X-ray powder diffraction patterns of (A) **P3HT-P**, (B) **P3HT-BDAN**, (C) **PF-P** and (D) **PF-BDAN**. Peaks are labeled with  $d$  spacing in Å.

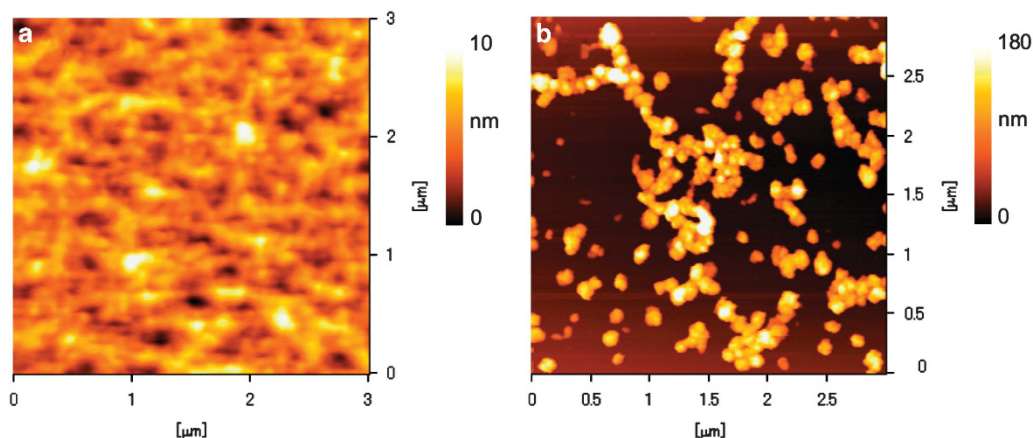
the fixation of the P3HT units by the xanthene-based polymer scaffold, as shown in the previous work.<sup>37</sup>

The absorption spectrum of **PF-BDAN** was red-shifted and broadened, and the emissions spectrum was also red-shifted in the film. These results suggest the presence of significant interchain interactions in these polymers, supported by the X-ray diffraction patterns indicative of their planar  $\beta$ -phase,<sup>49</sup> and highlighting the planarity and intermolecular stacking of the PF backbones (Supplementary Figure S18). The small shoulder absorption band in the ultraviolet spectrum and clear vibrational structure in the photoluminescence (PL) spectrum of **PF-BDAN** arose from the pyrene moieties. On the other hand, the absorption peak of **PF-P** in the film was slightly blue-shifted (by  $\sim 2$  nm) compared with the peak detected in solution without any peak-broadening. In addition, the emission peak of **PF-P** in the film was similar to the peak obtained in  $\text{CHCl}_3$  solution. The  $2\theta$ -value in the X-ray diffraction profile of **PF-P** is indicative of the  $\alpha$ -phase,<sup>49</sup> suggesting that the PF backbones in **PF-P** are twisted (Supplementary Figure S18), leading to the blue-shifted absorption spectrum. Thus, the PFs of **PF-P** were layered in a single polymer chain; however, planarization of the PF backbones was prevented by the alkyl chains of neighboring PFs, the large excluded volume of which, in turn, inhibited the intermolecular interactions between their  $\pi$ -systems.

The different intermolecular interactions displayed by the polymers in solution and in a film were further explored by examining their assembling behavior using transmission electron microscopy. Cast films were obtained from a  $\text{CHCl}_3/\text{EtOH}$  solution. As shown in Figure 5a, **P3HT-P** self-assembled into fibrous structures, whereas **P3HT-BDAN** formed small particles (Figure 5b). Fibers of various widths ranging from 20 nm to 100 nm were observed; 20 nm was approximately twice the value of the **P3HT-BDAN** chain length ( $n=20$ ,  $\sim 9$  nm), corresponding to the width of a single **P3HT-P**



**Figure 5** TEM images of (a) **P3HT-P**, (b) **P3HT-BDAN**, (c) **PF-P** and (d) **PF-BDAN**. All samples were prepared from  $\text{CHCl}_3/\text{EtOH}$  ( $v/v=3/1$ ) mixed solvent. TEM, transmission electron microscopy.



**Figure 6** (a) AFM image of **P3HT-P** and (b) AFM image of **PF-P**. Samples were prepared from  $\text{CHCl}_3/\text{EtOH}$  ( $v/v=3/1$ ) solution. AFM, atomic force microscopy.

molecule. The height of the fibers was 10 nm at most, as deduced from the atomic force microscopy image of **P3HT-P** shown in Figure 6a. Thus, **P3HT-P** assembled into the fibers through one-directional elongation along the stacking direction owing to the alignment of the P3HT units by the rigid polymer scaffold. On the other hand, **P3HT-BDAN** was not tightly pinned onto the scaffold, resulting in entanglement and particle formation instead of intermolecular  $\pi$ - $\pi$  stacking and elongation.

As shown in Figure 5c, **PF-P** self-assembled into submicrometer particles, whereas **PF-BDAN** formed aggregates of nanometer size (Figure 5d), similarly to **P3HT-BDAN**. A large number of aggregated particles by aggregation were also observed in the atomic force microscopy image of **PF-P** (Figure 6b), and their spherical shape was confirmed on the basis of their height information ( $\sim 170$  nm on average, Supplementary Figure S19). The average particle size of **PF-P** was estimated to be 184.6 nm (by transmission electron microscopy), 194.1 nm (by atomic force microscopy) and  $191.0 \pm 21.4$  nm (by dynamic light scattering, Supplementary Figure S20). Some of the particles shown in Figure 5c exhibited high contrast in the core region and low contrast at the edge where small fragments with high aspect ratio were observed. These particles were thought to be formed during the association. The small fragments were supposed to be single **PF-P** molecules, whose longer side length was estimated to be  $\sim 35$ – $40$  nm, approximately twice the value of the **PF-BDAN** chain length ( $n=18$ ,  $\sim 17$  nm). **PF-P** and **PF-BDAN** tended to form particles for the same reason discussed above for **P3HT-BDAN**; larger particles were formed in the case of **PF-P** owing to the larger size of the single **PF-P** molecule. On the basis of results of the optical measurements, and direct observations by transmission electron microscopy and atomic force microscopy, we can conclude that the grafting of  $\pi$ -conjugated polymers within a polymer scaffold facilitates the formation of higher-ordered structures with morphologies that depend essentially on the nature of the grafted  $\pi$ -conjugated polymers.

In summary, we prepared  $\pi$ -conjugated polymers end-capped with boronic acid (**P3HT-B(OH)<sub>2</sub>** and **PF-B(OH)<sub>2</sub>**) by chain-growth Suzuki–Miyaura polymerization. Condensation of the polymers with an aromatic ring-layered polymer scaffold yielded  $\pi$ -conjugated polymer-grafted polymers **P3HT-P** and **PF-P**. Despite their bulkiness, the conjugated polymers were efficiently introduced into the polymer scaffold. The polymer scaffold facilitated the formation of  $\pi$ -stacked P3HT structures with enhanced crystallinity. On the other hand, PFs were located close to each other in the scaffold; thus, their main chains

were twisted, suppressing the intermolecular interactions among the PF units. **P3HT-P** self-assembled into fibers by one-directional elongation along the  $\pi$ - $\pi$  stacking direction, whereas **PF-P** aggregated to form submicrometer particles. The present results show that the polymer scaffold can assist in the self-assembly process by pinning down the P3HT or PF units within a single polymer chain acting as a nucleus for the formation of higher-ordered structures. Dependence of the morphology on the molecular weights of the scaffold and grafting polymers, as well as the optoelectronic properties of the self-assemblies will be discussed in the future.

## CONFLICT OF INTEREST

The authors declare no conflict of interest.

## ACKNOWLEDGEMENTS

YT appreciates Research Fellowships (No. 11J00830) from the Japan Society for the Promotion of Science for Young Scientists.

- 1 Brunsveld, L., Folmer, J. B., Meijer, E. W. & Sijbesma, R. P. Supramolecular polymers. *Chem. Rev.* **101**, 4071–4097 (2001).
- 2 Hoeben, F. J. M., Jonkheijm, P., Meijer, E. W. & Schenning, A. P. H. J. About supramolecular assemblies of  $\pi$ -conjugated systems. *Chem. Rev.* **105**, 1491–1546 (2005).
- 3 Yamaguchi, T., Kimura, T., Matsuda, H. & Aida, T. Macroscopic spinning chirality memorized in spin-coated films of spatially designed dendritic zinc porphyrin J-aggregates. *Angew. Chem. Int. Ed.* **43**, 6350–6355 (2004).
- 4 Würthner, F., Chen, Z., Hoeben, F. J. M., Osswald, P., You, C. C., Jonkheijm, P., Herrikhuizen, J., Schenning, A. P. H. J., van der Schoot, P. P. A. M., Meijer, E. W., Beckers, E. H. A., Meskers, S. C. J. & Janssen, R. A. J. Supramolecular p-n-heterojunctions by co-self-organization of oligo(p-phenylene vinylene) and perylene bisimide dyes. *J. Am. Chem. Soc.* **126**, 10611–10618 (2004).
- 5 Das, A., Molla, M. R., Maity, B., Koley, D. & Ghosh, S. Hydrogen-bonding induced alternate stacking of donor (D) and acceptor (A) chromophores and their supramolecular switching to segregated states. *Chemistry* **18**, 9849–9859 (2012).
- 6 Lemaur, V., da Silva Filho, D. A., Coropceanu, V., Lehmann, M., Geerts, Y., Piris, J., Debije, M. G., van de Craats, A. M., Senthikumar, K., Siebbeles, L. D. A., Warman, J. M., Brédas, J. L. & Cornil, J. Charge transport properties in discotic liquid crystals: a quantum-chemical insight into structure-property relationships. *J. Am. Chem. Soc.* **126**, 3271–3279 (2004).
- 7 Debije, M. G., Piris, J., de Haas, M. P., Warman, J. M., Tomović, Z., Simpson, C. D. & Müllen, K. The optical and charge transport properties of discotic materials with large aromatic hydrocarbon cores. *J. Am. Chem. Soc.* **126**, 4641–4645 (2004).
- 8 Yasuda, T., Kishimoto, K. & Kato, T. Columnar liquid crystalline  $\pi$ -conjugated oligothiophenes. *Chem. Commun.* 3399–3401 (2006).
- 9 Feng, X., Marcon, V., Pisula, W., Hansen, M. R., Kirkpatrick, J., Grozema, F., Andrienko, D., Kremer, K. & Müllen, K. Towards high charge-carrier mobilities by rational design of the shape and periphery of discotics. *Nat. Mater.* **8**, 421–426 (2009).

- 10 Verilhac, J.-M., LeBlévenec, G., Djurado, D., Rieutord, F., Chouiki, M., Travers, J.-P. & Pron, A. Effect of macromolecular parameters and processing conditions on supramolecular organisation, morphology and electrical transport properties in thin layers of regioregular poly(3-hexylthiophene). *Synth. Met.* **156**, 815–823 (2006).
- 11 Noriega, R., Rivnay, J., Vandewal, K., Koch, F. P. V., Stingelin, N., Smith, P., Toney, M. F. & Salleo, A. A general relationship between disorder, aggregation and charge transport in conjugated polymers. *Nat. Mater.* **12**, 1038–1044 (2013).
- 12 Chen, Z., Lohr, A., Saha-Möller, C. R. & Würthner, F. Self-assembled  $\pi$ -stacks of functional dyes in solution: structural and thermodynamic features. *Chem. Soc. Rev.* **38**, 564–584 (2009).
- 13 De Greef, T. F. A., Smulders, M. M. J., Wolfs, M., Schenning, A. P. H. J., Sijbesma, R. P. & Meijer, E. W. Supramolecular polymerization. *Chem. Rev.* **109**, 5687–5754 (2009).
- 14 Schoonenbeek, F. S., van Esch, J. H., Wegewijs, B., Rep, D. B. A., de Haas, M. P., Klapwijk, T. M., Kellogg, R. M. & Feringam, B. L. Efficient intermolecular charge transport in self-assembled fibers of mono- and bithiophene bisurea compounds. *Angew. Chem. Int. Ed.* **38**, 1393–1397 (1999).
- 15 Ajayaghosh, A. & George, S. J. First phenylenevinylene based organogels: self-assembled nanostructures via cooperative hydrogen bonding and  $\pi$ -stacking. *J. Am. Chem. Soc.* **123**, 5148–5149 (2001).
- 16 Ajayaghosh, A. & Praveen, V. K.  $\pi$ -Organogels of self-assembled p-phenylenevinylenes: soft materials with distinct size, shape, and functions. *Acc. Chem. Res.* **40**, 644–656 (2007).
- 17 Lahieri, S., Thompson, J. L. & Moore, J. S. Solvophobic driven  $\pi$ -stacking of phenylene ethynylene macrocycles and oligomers. *J. Am. Chem. Soc.* **122**, 11315–11319 (2000).
- 18 van de Craats, A. M., Stutzmann, N., Nielsen, M. N., Watson, M., Müllen, K., Chanzy, H. D., Sirringhaus, H. & Friend, R. H. Meso-epitaxial solution-growth of self-organizing discotic liquid-crystalline semiconductors. *Adv. Mater.* **15**, 495–499 (2003).
- 19 Kastler, M., Pisula, W., Wasserfallen, D., Pakula, T. & Müllen, K. Influence of alkyl substituents on the solution- and surface-organization of hexa-peri-hexabenzocoronenes. *J. Am. Chem. Soc.* **127**, 4286–4296 (2005).
- 20 Cuccia, L. A., Lehn, J. M., Homo, J. C. & Schmutz, M. Encoded helical self-organization and self-assembly into helical fibers of an oligoheterocyclic pyridine - pyridazine molecular strand. *Angew. Chem. Int. Ed.* **39**, 233–237 (2000).
- 21 Azeroual, S., Surprenant, J., Lazzara, T. D., Kocun, M., Tao, Y., Cuccia, L. A. & Lehn, J. M. Mirror symmetry breaking and chiral amplification in foldamer-based supramolecular helical aggregates. *Chem. Commun.* **48**, 2292–2294 (2012).
- 22 Banno, M., Yamaguchi, T., Nagai, K., Kaiser, C., Hecht, S. & Yashima, E. Optically active, amphiphilic poly(meta-phenylene ethynylene)s: synthesis, hydrogen-bonding enforced helix stability, and direct AFM observation of their helical structures. *J. Am. Chem. Soc.* **134**, 8718–8728 (2012).
- 23 Zheng, Y., Zhou, H., Liu, D., Floudas, G., Wagner, M., Koynov, K., Mezger, M., Butt, H. J. & Ikeda, T. Supramolecular thiophene nanosheets. *Angew. Chem. Int. Ed.* **52**, 4845–4848 (2013).
- 24 Zen, A., Saphiannikova, M., Neher, D., Grenzer, J., Grigorian, S., Pietsch, U., Asawaprom, U., Janietz, S., Scherf, U., Lieberwirth, I. & Wegner, G. Effect of molecular weight on the structure and crystallinity of poly(3-hexylthiophene). *Macromolecules* **39**, 2162–2172 (2006).
- 25 Newbloom, G., Weigandt, K. M. & Pozzo, D. C. Structure and property development of poly(3-hexylthiophene) organogels probed with combined rheology, conductivity and small angle neutron scattering. *Soft Matter* **8**, 8854–8864 (2012).
- 26 Knoblock, K. M., Silvestri, C. J. & Collard, D. M. Stacked conjugated oligomers as molecular models to examine interchain interactions in conjugated materials. *J. Am. Chem. Soc.* **128**, 13680–13681 (2006).
- 27 Jagtap, S. P., Mukhopadhyay, S., Coropceanu, V., Brizius, G. L., Brédas, J. L. & Collard, D. M. Closely stacked oligo(phenylene ethynylene)s: effect of  $\pi$ -stacking on the electronic properties of conjugated chromophores. *J. Am. Chem. Soc.* **134**, 7176–7185 (2012).
- 28 Prabhakaran, P., Puranik, V. G., Chandran, J. N., Rajamohanam, P. R., Hofmann, H. & Sanjayan, G. J. Novel foldamer structural architecture from cofacial aromatic building blocks. *Chem. Commun.* 3446–3448 (2009).
- 29 Yoo, H., Yang, J., Yousef, A., Wasielewski, M. R. & Kim, D. Excimer formation dynamics of intramolecular  $\pi$ -stacked peryleneimides probed by single-molecule fluorescence spectroscopy. *J. Am. Chem. Soc.* **132**, 3939–3944 (2010).
- 30 Yoo, H., Bahng, H. W., Wasielewski, M. R. & Kim, D. Polymer matrix dependence of conformational dynamics within a  $\pi$ -stacked peryleneimide dimer and trimer revealed by single molecule fluorescence spectroscopy. *Phys. Chem. Chem. Phys.* **14**, 2001–2007 (2012).
- 31 Morisaki, Y., Murakami, T., Sawamura, T. & Chujo, Y. [2.2]Paracyclophane-layered polymers end-capped with fluorescence quenchers. *Macromolecules* **42**, 3656–3660 (2009).
- 32 Morisaki, Y., Fernandes, J. A. & Chujo, Y. Synthesis of anthracene-stacked oligomers and polymer. *Org. Lett.* **12**, 3188–3191 (2010).
- 33 Morisaki, Y., Fernandes, J. A. & Chujo, Y. Naphthalene-based oligothiophene-stacked polymers. *Polym. J.* **42**, 928–934 (2010).
- 34 Fernandes, J. A., Morisaki, Y. & Chujo, Y.  $\pi$ -Electron-system-layered polymers comprising thiophene/furan oligomers. *J. Polym. Sci. A Polym. Chem.* **49**, 3664–3670 (2011).
- 35 Morisaki, Y., Nakano, T. & Chujo, Y. Synthesis and photoluminescence behaviors of anthracene-layered polymers. *J. Polym. Sci. A Polym. Chem.* **52**, 2815–2821 (2014).
- 36 Nakano, T., Morisaki, Y. & Chujo, Y. Synthesis of hexabenzocoronene-layered compounds. *Tetrahedron Lett.* **56**, 2086–2090 (2015).
- 37 Tsuji, Y., Morisaki, Y. & Chujo, Y. Construction of aromatic-ring-layered structures using the terphenylene-layered polymer as the scaffold. *Polym. Chem.* **4**, 5361–5367 (2013).
- 38 Yokozawa, T. & Yokoyama, A. Chain-growth condensation polymerization for the synthesis of well-defined condensation polymers and  $\pi$ -conjugated polymers. *Chem. Rev.* **109**, 5595–5619 (2009).
- 39 Yokoyama, A., Miyakoshi, R. & Yokozawa, T. Chain-growth polymerization for poly(3-hexylthiophene) with a defined molecular weight and a low polydispersity. *Macromolecules* **37**, 1169–1171 (2004).
- 40 Miyakoshi, R., Yokoyama, A. & Yokozawa, T. Catalyst-transfer polycondensation. mechanism of Ni-catalyzed chain-growth polymerization leading to well-defined poly(3-hexylthiophene). *J. Am. Chem. Soc.* **127**, 17542–17547 (2005).
- 41 Miyakoshi, R., Shimon, K., Yokoyama, A. & Yokozawa, T. Catalyst-transfer polycondensation for the synthesis of poly(p-phenylene) with controlled molecular weight and low polydispersity. *J. Am. Chem. Soc.* **128**, 16012–16013 (2006).
- 42 Yokoyama, A., Suzuki, H., Kubota, Y., Ohuchi, K., Higashimura, H. & Yokozawa, T. Chain-growth polymerization for the synthesis of polyfluorene via suzuki–miyaura coupling reaction from an externally added initiator unit. *J. Am. Chem. Soc.* **129**, 7236–7237 (2007).
- 43 Yokozawa, T., Suzuki, R., Nojima, M., Ohta, Y. & Yokoyama, A. Precision synthesis of poly(3-hexylthiophene) from catalyst-transfer suzuki–miyaura coupling polymerization. *Macromol. Rapid Commun.* **32**, 801–806 (2011).
- 44 Noguchi, H., Hojo, K. & Sugimoto, M. Boron-masking strategy for the selective synthesis of oligoarenes via iterative Suzuki–Miyaura coupling. *J. Am. Chem. Soc.* **129**, 758–759 (2007).
- 45 Meier, H., Stalmach, U. & Kolshorn, H. Effective conjugation length and UV/vis spectra of oligomers. *Acta Polym.* **48**, 379–384 (1997).
- 46 Wang, Q., Qu, Y., Tian, H., Geng, Y. & Wang, F. Iterative binomial synthesis of monodisperse polyfluorenes up to 64-mers and their chain-length-dependent properties. *Macromolecules* **44**, 1256–1260 (2011).
- 47 Brown, P. J., Thomas, D. S., Kohler, A., Wilson, J. S., Kim, J. S., Ramsdale, C. M., Sirringhaus, H. & Friend, R. H. Effect of interchain interactions on the absorption and emission of poly(3-hexylthiophene). *Phys. Rev. B* **67**, 064203 (2003).
- 48 Dudenko, D., Kiersnowski, A., Shu, J., Pisula, W., Sebastiani, D., Spiess, H. W. & Hansen, M. R. A strategy for revealing the packing in semicrystalline  $\pi$ -conjugated polymers: crystal structure of bulk poly(3-hexylthiophene) (P3HT). *Angew. Chem. Int. Ed.* **51**, 11068–11072 (2012).
- 49 Chen, S. H., Su, A. G., Su, C. H. & Chen, S. A. Crystalline forms and emission behavior of poly(9,9-di-n-octyl-2,7-fluorene). *Macromolecules* **38**, 379–385 (2005).

Supplementary Information accompanies the paper on Polymer Journal website (<http://www.nature.com/pj>)

[2.2]Paracyclophanes

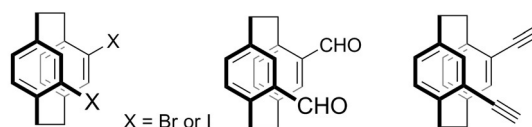
New Types of Planar Chiral [2.2]Paracyclophanes and Construction of One-Handed Double Helices

Yasuhiro Morisaki,\* Risa Sawada, Masayuki Gon, and Yoshiki Chujo\*<sup>[a]</sup>

**Abstract:** New types of planar chiral ( $R_p$ )- and ( $S_p$ )-4,7,12,15-tetrasubstituted [2.2]paracyclophanes were synthesized from racemic 4,12-dihydroxy[2.2]paracyclophane as the starting compound. Regioselective dibromination and transformation afforded a series of planar chiral ( $R_p$ )- and ( $S_p$ )-4,7,12,15-tetrasubstituted [2.2]paracyclophanes, which can be used as chiral building blocks. In this study, left- and right-handed double helical structures were constructed via chemoselective Sonogashira–Hagihara coupling. The double helical compounds were excellent circularly polarized luminescence (CPL) emitters with large molar extinction coefficients, good photoluminescence quantum efficiencies, and large CPL dissymmetry factors.

[2.2]Paracyclophane is a unique compound in which two phenylene groups face each other in proximity to form a stacked structure.<sup>[1,2]</sup> Due to the restricted rotary motion of the phenylenes, substituted [2.2]paracyclophane becomes a planar chiral compound depending on the position of the substituent(s).<sup>[1,3]</sup> Planar chiral [2.2]paracyclophane compounds have been utilized as chiral auxiliaries and ligands in organic and organometallic chemistry. We have focused on the planar chiral [2.2]paracyclophane compounds and recently developed a practical optical resolution method for 4,12-disubstituted [2.2]paracyclophane<sup>[4,5]</sup> and the first optical resolution method for 4,7,12,15-tetrasubstituted [2.2]paracyclophane.<sup>[6,7]</sup> In addition, we have employed enantiopure planar chiral [2.2]paracyclophanes as chiral building blocks (Figure 1) to construct optically active second-order structures, such as V-,<sup>[8]</sup> N-,<sup>[8]</sup> M-,<sup>[8]</sup> triangle-,<sup>[8,9]</sup> propeller-,<sup>[6,10]</sup> and X-shaped structures.<sup>[11]</sup> All compounds exhibited intense circularly polarized luminescence (CPL)<sup>[12]</sup> with

4,12-Disubstituted [2.2]paracyclophanes



4,7,12,15-Tetrasubstituted [2.2]paracyclophanes

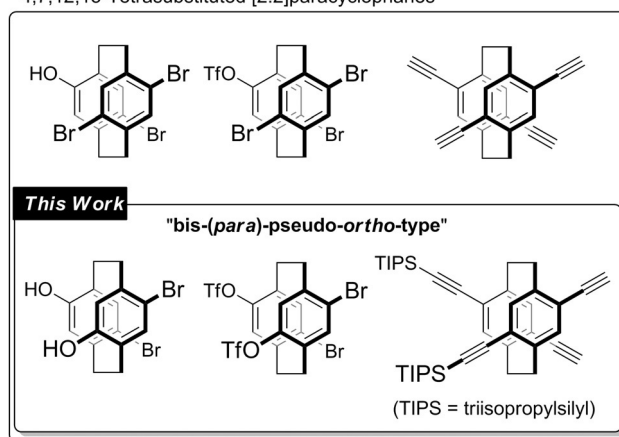


Figure 1. Structures of representative building blocks based on planar chiral [2.2]paracyclophane.

large molar extinction coefficients ( $\epsilon$ ), good photoluminescence (PL) quantum efficiencies ( $\Phi_{PL}$ ), and excellent CPL dissymmetry factors ( $g_{lum}$ ). Thus, we have developed the first CPL-emitting planar chiral compounds and applied planar chiral [2.2]paracyclophanes in the field of materials chemistry.

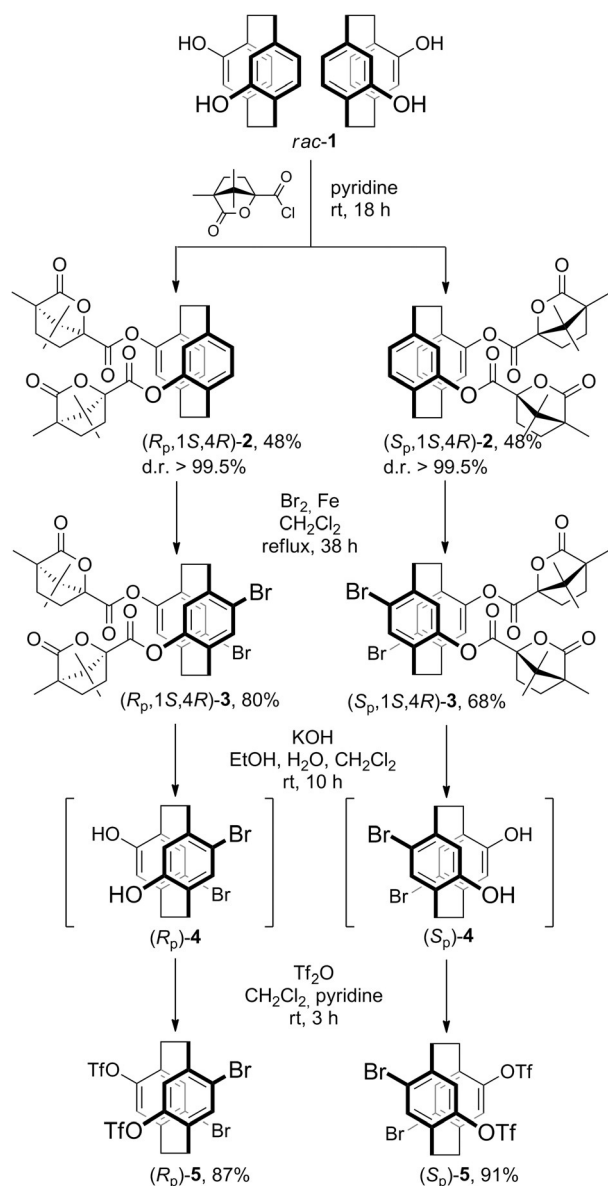
In this study, we prepared new types of 4,7,12,15-tetrasubstituted [2.2]paracyclophanes (bis-(para)-pseudo-ortho-type), as shown in Figure 1, in order to create a variety of planar chiral [2.2]paracyclophane-based compounds. By using chemoselective Sonogashira–Hagihara coupling, different  $\pi$ -conjugated substituents can be introduced at the 4,12- and 7,15-positions. We also constructed a one-handed double helix structure from the new type of 4,7,12,15-tetrasubstituted [2.2]paracyclophane chiral building blocks. Synthetic details and optical properties, including CPL profiles, are reported herein.

The synthetic route to the new type (bis-(para)-pseudo-ortho-type) of 4,7,12,15-tetrasubstituted [2.2]paracyclophanes ( $R_p$ )- and ( $S_p$ )-5 is shown in Scheme 1. Optical resolution of 4,12-disubstituted [2.2]paracyclophane from racemic 4,12-dihydroxy[2.2]paracyclophane (*rac*-1) was carried out by following Jiang's diastereomer method;<sup>[5d]</sup> our results are shown in

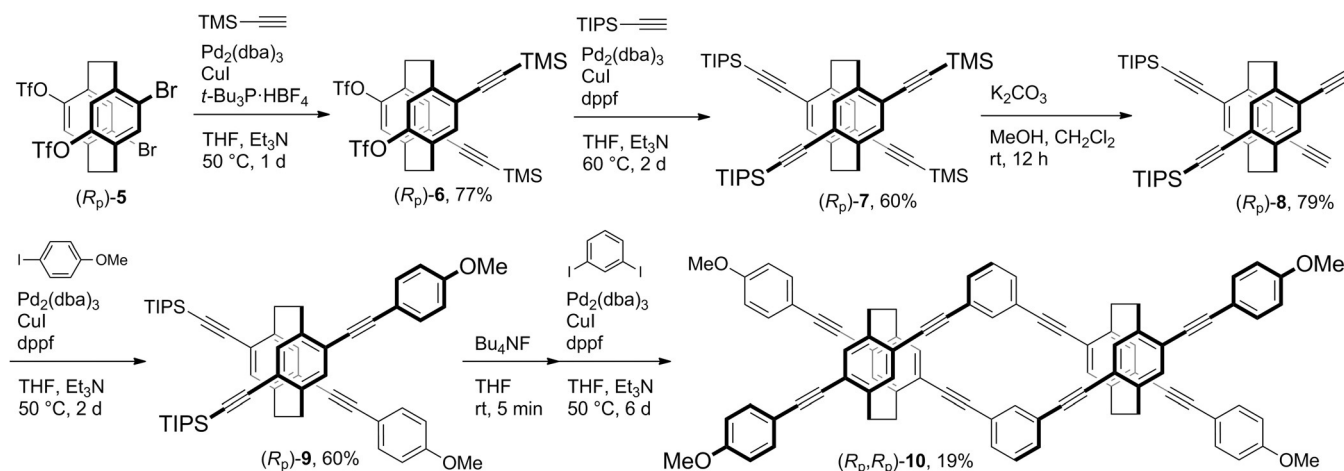
[a] Prof. Y. Morisaki,<sup>†</sup> R. Sawada, Dr. M. Gon, Prof. Y. Chujo  
Department of Polymer Chemistry  
Graduate School of Engineering  
Kyoto University  
Katsura, Nishikyo-ku, Kyoto 615-8510 (Japan)  
E-mail: ymo@kwansei.ac.jp  
chujo@chujo.synchem.kyoto-u.ac.jp

[†] Current address:  
Department of Applied Chemistry for Environment  
School of Science and Technology  
Kwansei Gakuin University  
2-1 Gakuen, Sanda, Hyogo 669-1337 (Japan)

Supporting information for this article can be found under <http://dx.doi.org/10.1002/asia.201601028>.



Scheme 1. Optical resolution and transformations.

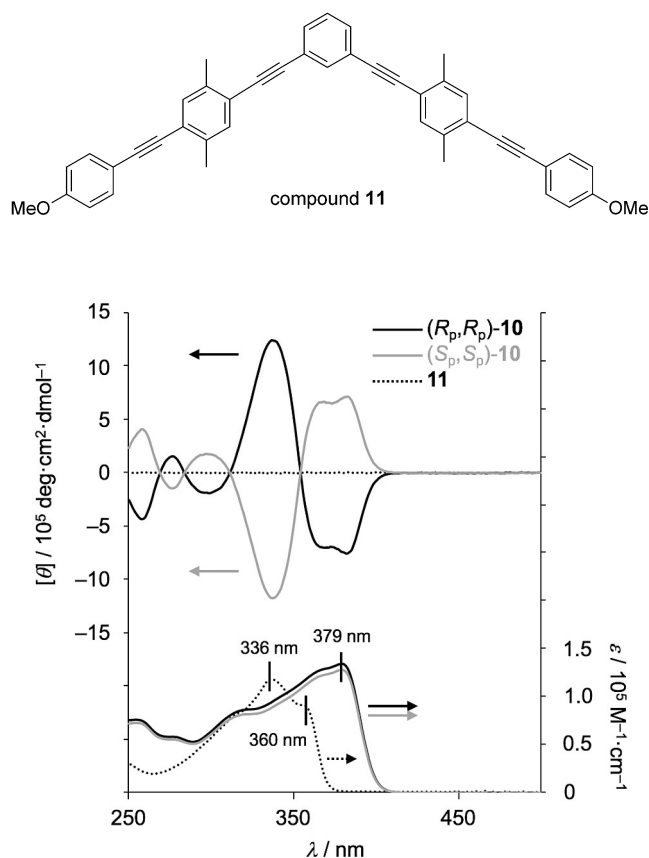


Scheme 2. Synthesis of  $(R_p,R_p)$ -10.

Scheme 1 (diastereomeric ratio = d.r.). The diastereomers could be separated by simple  $\text{SiO}_2$  column chromatography due to sufficient difference ( $> 0.10$ ) between the  $R_f$  values of the diastereomers. The separated diastereomers  $(R_p,1S,4R)$ -2 and  $(S_p,1S,4R)$ -2 were reacted with  $\text{Br}_2$  in the presence of a catalytic amount of Fe to obtain the corresponding dibrominated compounds. Only the *para* positions of the camphanoyloxy groups reacted regioselectively due to electronic and steric effects to afford 4,12-dibromo-7,15-biscamphanoyloxy[2.2]paracyclophanes  $(R_p,1S,4R)$ -3 and  $(S_p,1S,4R)$ -3. Camphanoyl groups were removed by hydrolysis using KOH and, without thorough purification, 4,12-dibromo-7,15-dihydroxy[2.2]paracyclophanes ( $(R_p)$ - and  $(S_p)$ -4) were reacted with  $\text{Tf}_2\text{O}$  to afford  $(R_p)$ - and  $(S_p)$ -4,12-dibromo-7,15-trifluoromethanesulfonyloxy[2.2]paracyclophanes ( $(R_p)$ - and  $(S_p)$ -5) in 87% and 91% isolated yields, respectively.

As shown in Scheme 2, Sonogashira–Hagihara coupling<sup>[13]</sup> of  $(R_p)$ -5 with trimethylsilylacetylene (TMS-acetylene) using a  $\text{Pd}_2(\text{dba})_3/\text{CuI}/t\text{Bu}_3\text{P}\cdot\text{HBF}_4$  (dba = dibenzylideneacetone) catalytic system afforded  $(R_p)$ -6 in 77% isolated yield; only bromide was chemoselectively reacted.<sup>[6]</sup> The OTf groups were converted into triisopropylsilylethynyl (TIPS-ethynyl) groups using a  $\text{Pd}_2(\text{dba})_3/\text{CuI}/\text{dppf}$  (dppf = 1,1'-bis(diphenylphosphino)ferrocene) catalytic system to obtain  $(R_p)$ -7 in 60% isolated yield. The TMS groups were chemoselectively removed by  $\text{K}_2\text{CO}_3/\text{MeOH}$  to obtain TIPS-protected compound  $(R_p)$ -8 in 79% yield, which was reacted with 4-iodanisole to obtain  $(R_p)$ -9 in 60% isolated yield. The TIPS groups in  $(R_p)$ -9 were removed by  $\text{Bu}_4\text{NF}$ , and the successive reaction with 1,3-diiodobenzene provided the target compound  $(R_p,R_p)$ -10 in 19% isolated yield. Enantiomer  $(S_p,S_p)$ -10 was also prepared from  $(S_p)$ -5 by the same procedure. Compounds  $(R_p,R_p)$ - and  $(S_p,S_p)$ -10 consist of two boomerang-shaped phenylene-ethynylenes 11 that are stacked at the second and fourth benzene rings to form left- and right-handed double helical structures,<sup>[14,15]</sup> respectively.

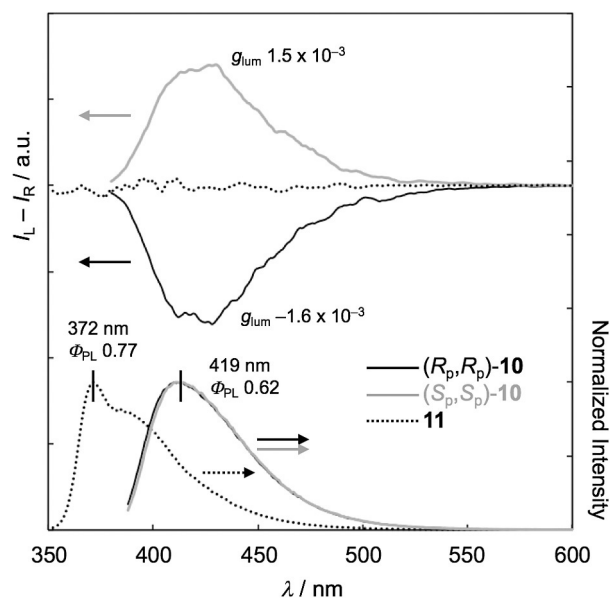
Figure 2 shows the UV/Vis absorption and circular dichroism (CD) spectra of  $\text{CHCl}_3$  solutions ( $1.0 \times 10^{-5} \text{ M}$ ) of  $(R_p,R_p)$ -10,  $(S_p,S_p)$ -10, and compound 11; the data are listed in Table S1 in



**Figure 2.** UV/Vis absorption and CD spectra of  $(R_p,R_p)$ - and  $(S_p,S_p)$ -**10** and **11** in  $\text{CHCl}_3$  ( $1.0 \times 10^{-5}$  M).

the Supporting Information. The absorption spectrum of **11** exhibited absorption peak maxima at 337 nm and 365 nm. Those of  $(R_p,R_p)$ - and  $(S_p,S_p)$ -**10** were apparently red-shifted compared to **11**, and the absorption maximum appeared at 378 nm. The boomerang-shaped  $\pi$ -electron systems of **11** were tightly fixed in proximity in  $(R_p,R_p)$ - and  $(S_p,S_p)$ -**10**, and strong  $\pi$ - $\pi$  interactions were observed. In the CD spectra, mirror image Cotton effects were exhibited. The absolute molar ellipticity  $[\theta]$  was in the order of  $10^6 \text{ deg cm}^2 \text{ dmol}^{-1}$ . The dissymmetry factor of absorbance ( $g_{\text{abs}}$ ) was slightly larger than that of the corresponding X-shaped compound<sup>[11b]</sup> we recently reported (Figure S21B and S22B for **10** and X-shaped compound, respectively), indicating that a high degree of chirality is induced in the ground state through the entire molecule of **10** due to the one-handed helical structure.

The PL and CPL spectra of  $(R_p,R_p)$ -**10**,  $(S_p,S_p)$ -**10**, and **11** in  $\text{CHCl}_3$  ( $1.0 \times 10^{-6}$  M for PL and  $1.0 \times 10^{-5}$  M for CPL) are shown in Figure 3; the data are shown in Table S2 in the Supporting Information. Compound **11** exhibited good PL properties; the peak maximum appeared at 372 nm with a vibrational structure, and the absolute  $\Phi_{\text{PL}}$  value was estimated to be 0.77. The PL decay curve was fitted with a single exponential curve, and the PL lifetime ( $\tau$ ) was 0.74 ns (Figure S25). The PL spectra of  $(R_p,R_p)$ - and  $(S_p,S_p)$ -**10** were featureless with peak tops at 412 nm, which were red-shifted by 40 nm compared to that of **11**. The  $\Phi_{\text{PL}}$  value of **10** was estimated to be 0.62 with a  $\tau$



**Figure 3.** PL and CPL spectra of  $(R_p,R_p)$ - and  $(S_p,S_p)$ -**10** and **11** in  $\text{CHCl}_3$  ( $1.0 \times 10^{-6}$  M for PL and  $1.0 \times 10^{-5}$  M for CPL) excited at each absorption maximum.

value of 1.8 ns (Figure S25). The PL profile of **10** was similar to that of the X-shaped compound, as shown in Figure S24.  $(R_p,R_p)$ - and  $(S_p,S_p)$ -**10** emitted intense CPL (Figure 3), and the absolute  $|g_{\text{lum}}|$  value was estimated to be approximately  $1.6 \times 10^{-3}$ . The  $g_{\text{lum}}$  value of **10** was almost identical to that of the X-shaped compound ( $|g_{\text{lum}}|$  of approximately  $1.5 \times 10^{-3}$ , Figure S24).

According to the absorption and PL spectra, the optical properties of **10** were similar to those of the X-shaped compounds; namely,  $\pi$ -conjugation is extended through the entire molecule (three-dimensional conjugation), which has been established experimentally and theoretically by Bazan, Mukamel, and coworkers.<sup>[16]</sup> The chiroptical behavior (CD and CPL spectra) of **10** and the X-shaped compounds were intrinsically identical. The double helical second-order structure of **10** provides the slightly larger dissymmetry factors.

In conclusion, new planar chiral bis-*(para)*-pseudo-*ortho*-type 4,7,12,15-tetrasubstituted [2.2]paracyclophanes were synthesized. Racemic 4,12-dihydroxy[2.2]paracyclophane was used as the precursor, and optical resolution was carried out by the diastereomer method. Regioselective dibromination and transformation afforded optically active bis-*(para)*-pseudo-*ortho*-type 4,7,12,15-tetrasubstituted [2.2]paracyclophanes, which can be used as chiral building blocks for a wide variety of second-order structures. To demonstrate this, left- and right-handed double helical structures were constructed via chemoselective Sonogashira-Hagihara coupling. The double helical compounds were highly emissive ( $\epsilon = 1.3 \times 10^6 \text{ M}^{-1} \text{ cm}^{-1}$  and  $\Phi_{\text{PL}} = 0.62$ ) with excellent chiroptical properties in the ground state ( $[\theta] > 10^6 \text{ deg cm}^2 \text{ dmol}^{-1}$ ) and, in particular, in the excited state ( $|g_{\text{lum}}| > 1.5 \times 10^{-3}$ ); namely, they are excellent organic CPL emitters. Planar chiral [2.2]paracyclophane building blocks can be used to create intriguing stacked  $\pi$ -electron systems and

further preparations of optically active [2.2]paracyclophane compounds are now in progress.

## Acknowledgements

The authors are grateful to Professor Kazuo Akagi and Dr. Kazuyoshi Watanabe (Department of Polymer Chemistry, Graduate School of Engineering, Kyoto University) for CPL data analysis.

**Keywords:** [2.2]paracyclophane · circularly polarized luminescence · double helices · planar chirality

- [1] a) *Cyclophane Chemistry: Synthesis Structures and Reactions* (Ed.: F. Vögtle), Wiley, Chichester, **1993**; b) *Modern Cyclophane Chemistry* (Eds.: R. Gleiter, H. Hopf), Wiley-VCH, Weinheim, **2004**; c) H. Hopf, *Angew. Chem. Int. Ed.* **2008**, *47*, 9808–9812; *Angew. Chem.* **2008**, *120*, 9954–9958.
- [2] a) C. J. Brown, A. C. Farthing, *Nature* **1949**, *164*, 915–916; b) D. J. Cram, H. Steinberg, *J. Am. Chem. Soc.* **1951**, *73*, 5691–5704.
- [3] a) D. J. Cram, N. L. Allinger, *J. Am. Chem. Soc.* **1955**, *77*, 6289–6294; b) V. Rozenberg, E. Sergeeva, H. Hopf in *Modern Cyclophane Chemistry* (Eds.: R. Gleiter, H. Hopf), Wiley-VCH, Weinheim, Germany, **2004**, pp. 435–462; c) G. J. Rowlands, *Org. Biomol. Chem.* **2008**, *6*, 1527–1534; d) S. E. Gibson, J. D. Knight, *Org. Biomol. Chem.* **2003**, *1*, 1256–1269; e) A. A. Aly, A. B. Brown, *Tetrahedron* **2009**, *65*, 8055–8089; f) J. Paradies, *Synthesis* **2011**, 3749–3766.
- [4] Y. Morisaki, R. Hifumi, L. Lin, K. Inoshita, Y. Chujo, *Chem. Lett.* **2012**, *41*, 990–992.
- [5] For optical resolution of 4,12-disubstituted [2.2]paracyclophane, see: a) P. J. Pye, K. Rossen, R. A. Reamer, N. N. Tsou, R. P. Volante, P. J. Reider, *J. Am. Chem. Soc.* **1997**, *119*, 6207–6208; b) K. Rossen, P. J. Pye, A. Maliaikal, R. P. Volante, *J. Org. Chem.* **1997**, *62*, 6462–6463; c) R. Zhuravsky, Z. Starikova, E. Vorontsov, V. Rozenberg, *Tetrahedron: Asymmetry* **2008**, *19*, 216–222; d) B. Jiang, X.-L. Zhao, *Tetrahedron: Asymmetry* **2004**, *15*, 1141–1143; e) P. G. Jones, J. Hillmer, H. Hopf, *Acta Crystallogr. Sect. E* **2003**, *59*, o24–o25; f) D. Pamperin, H. Hopf, C. Syladat, M. Pietzsch, *Tetrahedron: Asymmetry* **1997**, *8*, 319–325; g) D. Pamperin, B. Ohse, H. Hopf, M. Pietzsch, *J. Mol. Catal. B* **1998**, *5*, 317–319; h) D. C. Braddock, I. D. MacGilp, B. G. Perry, *J. Org. Chem.* **2002**, *67*, 8679–8681; i) G. Meyer-Eppler, E. Vogelsang, C. Benkhäuser, A. Schneider, G. Schnakenburg, A. Lützen, *Eur. J. Org. Chem.* **2013**, 4523–4532.
- [6] Y. Morisaki, M. Gon, T. Sasamori, N. Tokitoh, Y. Chujo, *J. Am. Chem. Soc.* **2014**, *136*, 3350–3353.
- [7] Optical resolution of *rac*-4,5,15,16-tetrasubstituted [2.2]paracyclophane was reported: N. V. Vorontsova, V. I. Rozenberg, E. V. Sergeeva, E. V. Vorontsov, Z. A. Starikova, K. A. Lyssenko, H. Hopf, *Chem. Eur. J.* **2008**, *14*, 4600–4617.
- [8] Y. Morisaki, K. Inoshita, Y. Chujo, *Chem. Eur. J.* **2014**, *20*, 8386–8390.
- [9] Y. Morisaki, R. Hifumi, L. Lin, K. Inoshita, Y. Chujo, *Polym. Chem.* **2012**, *3*, 2727–2730.
- [10] a) M. Gon, Y. Morisaki, Y. Chujo, *J. Mater. Chem. C* **2015**, *3*, 521–529; b) M. Gon, H. Kozuka, Y. Morisaki, Y. Chujo, *Asian J. Org. Chem.* **2016**, *5*, 353–359.
- [11] a) M. Gon, Y. Morisaki, Y. Chujo, *Eur. J. Org. Chem.* **2015**, 7756–7762; b) M. Gon, Y. Morisaki, R. Sawada, Y. Chujo, *Chem. Eur. J.* **2016**, *22*, 2291–2298.
- [12] a) J. P. Riehl, F. S. Richardson, *Chem. Rev.* **1986**, *86*, 1–16; b) J. P. Riehl, F. Muller, *Comprehensive Chiroptical Spectroscopy*, Wiley, New York, **2012**.
- [13] a) Y. Tohda, K. Sonogashira, N. Hagihara, *Tetrahedron Lett.* **1975**, *16*, 4467–4470; b) K. Sonogashira in *Handbook of Organopalladium Chemistry for Organic Synthesis* (Ed.: E. Negishi), Wiley, New York, **2002**, pp. 493–529.
- [14] For example, accounts and reviews on artificial double helices: a) E. C. Constable, *Tetrahedron* **1992**, *48*, 10013–10059; b) J.-M. Lehn, *Supramolecular Chemistry: Concepts and Perspectives*, VCH, Weinheim, Germany, **1995**; c) C. Piguet, G. Bernardinelli, G. Hopfgartner, *Chem. Rev.* **1997**, *97*, 2005–2062; d) M. Albrecht, *Chem. Rev.* **2001**, *101*, 3457–3497; e) D. J. Hill, M. J. Mio, R. B. Prince, T. S. Hughes, J. S. Moore, *Chem. Rev.* **2001**, *101*, 3893–4012; f) I. Huc, *Eur. J. Org. Chem.* **2004**, 17–29; g) Y. Furusho, E. Yashima, *Chem. Rec.* **2007**, *7*, 1–11; h) D. Halder, C. Schmuck, *Chem. Soc. Rev.* **2009**, *38*, 363–371; i) Y. Furusho, E. Yashima, *Macromol. Rapid Commun.* **2011**, *32*, 136–146; j) S. E. Howson, P. Scott, *Dalton Trans.* **2011**, *40*, 10268–10277; k) G. Guichard, I. Huc, *Chem. Commun.* **2011**, *47*, 5933–5941.
- [15] Examples on construction of one-handed double helical structures: a) A. Orita, T. Nakano, D. L. An, K. Tanikawa, K. Wakamatsu, J. Otera, *J. Am. Chem. Soc.* **2004**, *126*, 10389–10396; b) Y. Tanaka, H. Katagiri, Y. Furusho, E. Yashima, *Angew. Chem. Int. Ed.* **2005**, *44*, 3867–3870; *Angew. Chem.* **2005**, *117*, 3935–3938; c) H. Katagiri, T. Miyagawa, Y. Furusho, E. Yashima, *Angew. Chem. Int. Ed.* **2006**, *45*, 1741–1744; *Angew. Chem.* **2006**, *118*, 1773–1776; d) K. Miwa, Y. Furusho, E. Yashima, *Nat. Chem.* **2010**, *2*, 444–449.
- [16] a) G. C. Bazan, W. J. Oldham, Jr., R. J. Lachicotte, S. Tretiak, V. Chernyak, S. Mukamel, *J. Am. Chem. Soc.* **1998**, *120*, 9188–9204; b) S. Wang, G. C. Bazan, S. Tretiak, S. Mukamel, *J. Am. Chem. Soc.* **2000**, *122*, 1289–1297; c) J. Zyss, I. Ledoux, S. Volkov, V. Chernyak, S. Mukamel, G. P. Bartholomew, G. C. Bazan, *J. Am. Chem. Soc.* **2000**, *122*, 11956–11962; d) G. P. Bartholomew, G. C. Bazan, *Acc. Chem. Res.* **2001**, *34*, 30–39; e) G. P. Bartholomew, G. C. Bazan, *Synthesis* **2002**, 1245–1255; f) G. P. Bartholomew, G. C. Bazan, *J. Am. Chem. Soc.* **2002**, *124*, 5183–5196; g) D. S. Seferos, D. A. Banach, N. A. Alcantar, J. N. Israelachvili, G. C. Bazan, *J. Org. Chem.* **2004**, *69*, 1110–1119; h) G. P. Bartholomew, M. Rumi, S. J. K. Pond, J. W. Perry, S. Tretiak, G. C. Bazan, *J. Am. Chem. Soc.* **2004**, *126*, 11529–11542; i) J. W. Hong, H. Y. Woo, G. C. Bazan, *J. Am. Chem. Soc.* **2005**, *127*, 7435–7443; j) G. C. Bazan, *J. Org. Chem.* **2007**, *72*, 8615–8635.

Manuscript received: July 26, 2016

Accepted Article published: July 29, 2016

Final Article published: August 16, 2016



Contents lists available at ScienceDirect

Tetrahedron Letters

journal homepage: [www.elsevier.com/locate/tetlet](http://www.elsevier.com/locate/tetlet)

## Synthesis and properties of highly-rigid conjugation system based on bi(benzo[*b*]thiophene)-fused *o*-carborane

Kenta Nishino<sup>a</sup>, Kazushi Hashimoto<sup>a</sup>, Kazuo Tanaka<sup>a</sup>, Yasuhiro Morisaki<sup>b</sup>, Yoshiki Chujo<sup>a,\*</sup><sup>a</sup> Department of Polymer Chemistry, Graduate School of Engineering, Kyoto University, Katsura, Nishikyo-ku, Kyoto 615-8510, Japan<sup>b</sup> School of Science and Technology, Kwansei Gakuin University, 2-1 Gakuen, Sanda, Hyogo 669-1337, Japan

## ARTICLE INFO

## Article history:

Received 17 February 2016

Revised 16 March 2016

Accepted 22 March 2016

Available online 22 March 2016

## Keywords:

Carborane  
Fluorescence  
Conjugation

## ABSTRACT

To demonstrate the validity of *o*-carborane as an electronic anchoring unit for constructing robust conjugation system, bi(benzo[*b*]thiophene)-fused *o*-carborane was designed and synthesized. From the optical measurements, clear vibrational bands not only in the absorption but also in the emission spectra were observed. These data mean that the electronic delocalization should occur on the rigid template. In the cyclic voltammograms, the reversible reduction waves at  $-1.72$  eV and  $-2.37$  eV were detected that originated from the electron-accepting ability of *o*-carborane. It is suggested that *o*-carborane should be the versatile unit for constructing robust conjugation with electron-accepting ability.

© 2016 Elsevier Ltd. All rights reserved.

Conjugated compounds have attracted much attention as a platform for fabricating organic opto-electronic devices. In order to obtain highly-functional materials, the construction of the robust and expanded conjugation system is of significance in the molecular design because the rigid and planar structures are favorable not only for facilitating the electronic interaction through the extended conjugation but also for suppressing structural distortions or perturbations by the reinforced rigidity. The introduction of the fused-aromatic rings is one of feasible strategies for constructing robust conjugated systems. For example, various types of heteroatom-bridged bithiophenes have been synthesized,<sup>1</sup> and their unique optical properties have been reported.<sup>2</sup> In particular, by utilizing an ‘element-block’ which is defined as functional nano-building blocks composed of heteroatoms or inorganic elements, multiple functions that originated from the intrinsic properties of each element as well as the electronic conjugation can be expected.<sup>3</sup>

Carborane is the class of cluster compounds composed of boron and carbon atoms, and *o*-carborane which is composed of two carbon atoms and ten boron atoms (1,2-dicarba-*closo*-dodecaborane)<sup>4</sup> has been paid much attention as a versatile optically-functional ‘element-block’ according to the recent reports.<sup>5</sup> *o*-Carborane works as an electron-withdrawing group because of the electron-deficient characteristics of skeletal electrons delocalized via the 3-center-2-electron bonds. Therefore, by the combination with the electron-donating groups, strong emissions were obtained

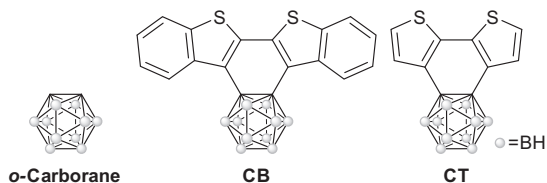
from the intramolecular charge transfer (CT) transition. Furthermore, it was found that *o*-carborane-containing main-chain-type conjugated polymers were aggregation-induced emission (AIE)-active compounds which can show the strong emission only in the solid state.<sup>6</sup> The vibration at the carbon–carbon bond in *o*-carborane can critically consume the excitation energy in the CT state, leading to the annihilation. On the other hand, in the aggregation state, the emission can be recovered by suppressing the decay process. These solid-state emissions are advantageous for fabricating efficient organic emissive devices.<sup>7</sup>

Recently, the series of biaryl-fused *o*-carboranes were synthesized, and the roles of *o*-carborane in the conjugation as an effective electron-acceptor were investigated.<sup>8</sup> Highly-planar structures were obtained, and it was observed that the energy levels of both highest occupied molecular orbitals (HOMOs) and lowest unoccupied molecular orbitals (LUMOs) were lowered compared to those of the corresponded biaryl compounds such as 2,2'-bithiophene (Fig. 1). These data represent that *o*-carborane works as the anchor and the electron-accepting unit. Herein, to show the applicability of the *o*-carborane anchor to the further expanded conjugated system, benzo[*b*]thiophene-fused *o*-carborane was prepared. From the series of optical and electrochemical measurements, the electronic structures were evaluated. The influence of *o*-carborane on the properties was investigated.

The synthesis of bi(benzo[*b*]thiophene)-fused *o*-carborane (CB) was performed according to Scheme 1.<sup>8a</sup> The precursor **3** for constructing *o*-carborane was prepared from 3-trimethylsilylethynylbenzo[*b*]thiophene **2** via the Sonogashira–Hagihara coupling in the presence of Pd(PPh<sub>3</sub>)<sub>2</sub>Cl<sub>2</sub> as a catalyst.

\* Corresponding author. Tel.: +81 75 383 2604; fax: +81 75 383 2605.

E-mail address: [chujo@chujo.synchem.kyoto-u.ac.jp](mailto:chujo@chujo.synchem.kyoto-u.ac.jp) (Y. Chujo).

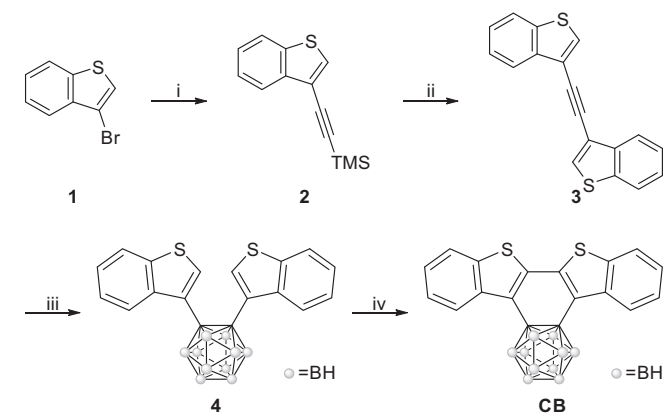


**Figure 1.** Chemical structures of *o*-carborane (left), bi(benzo[*b*]thiophene)-fused *o*-carborane (**CB**) and 2,2'-bithiophene-fused *o*-carborane (**CT**).

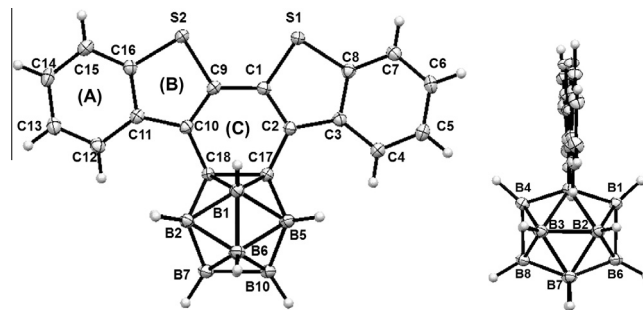
The di-substituted *o*-carborane **4** was obtained in the insertion reaction between decaborane and **3** in the presence of Lewis base (*N,N*-dimethylaniline) in a good yield (52%). 2-Position of the benzo[*b*]thiophene skeleton in **4** was lithiated by *n*-butyllithium, and then intramolecular-cyclization was induced by adding ZnBr<sub>2</sub> and CuCl<sub>2</sub>. Finally, **CB** was obtained in 10% isolated yield. All compounds were characterized by <sup>1</sup>H, <sup>11</sup>B, and <sup>13</sup>C NMR spectroscopies and mass measurements. From the recrystallization in CHCl<sub>3</sub> and MeOH, the single crystal for the X-ray structural analysis was obtained. The products showed good stability toward air and light under ambient conditions. From these data, we concluded that the product possessed the designed structure and high stability enough for the optical measurements.

**Figure 2** shows the ORTEP diagram of **CB** obtained from the X-ray single crystal analysis. The bond lengths in the center-ring (ring-C) except for the *o*-carborane-fused bond were observed in the region between 1.37 Å and 1.49 Å which are typical lengths as the sp<sup>3</sup>–sp<sup>3</sup> carbon bonds. Only in the carbon–carbon bond at *o*-carborane-fused moiety, the longer value (1.685 Å) was observed. This result corresponds to those of previous benzene-fused *o*-carboranes composed of three-center two-electron bonds. The dihedral angles between the benzo[*b*]thiophene moieties (C10–C9–C1–S1) and between the carbon–carbon bond at *o*-carborane-fused bond and the benzo[*b*]thiophene moiety (C18–C17–C2–C3) were 176.16° and 179.86°, respectively. These data represent that the conjugated moiety in **CB** should possess high planarity and parallel conformation of the *o*-carborane moiety to the carbon–carbon bond. These structural features are also identical to biaryl-fused *o*-carboranes.<sup>8</sup>

To gather information on the electronic state in the ground state, UV–vis absorption spectra of **CB** and 2,2'-bithiophene-fused *o*-carborane **CT**<sup>8a</sup> were measured in the THF solutions at room

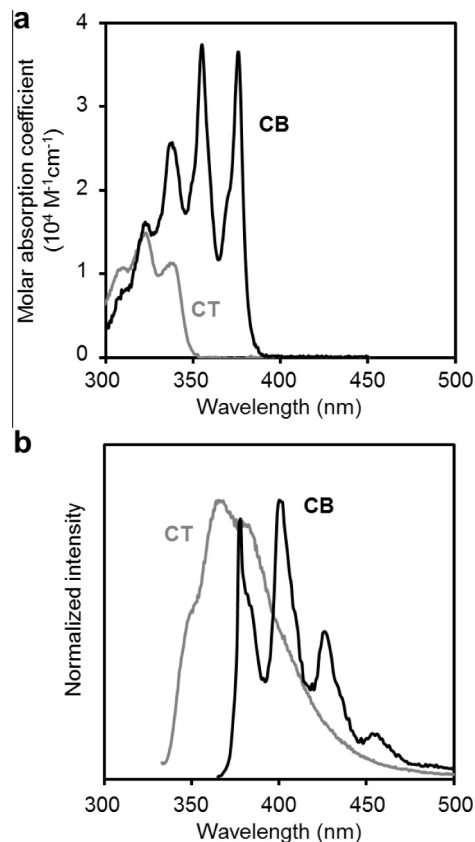


**Scheme 1.** Synthesis of **CB**. Reagents and conditions: (i) Trimethylsilylacetylene, PdCl<sub>2</sub>(PPh<sub>3</sub>)<sub>2</sub>, CuI, dppf, DMF, DIPA, 80 °C, 3 d, 71%. (ii) **1**, PdCl<sub>2</sub>(PPh<sub>3</sub>)<sub>2</sub>, CuI, Ruphos, NBu<sub>4</sub>F, DMF, DIPA, 80 °C, 1 d, 47%. (iii) Decaborane, *N,N*-dimethylaniline, toluene, reflux, 1 d, 52%. (iv) (1) *n*-Butyllithium in hexane (1.6 M), THF, –78 °C to 0 °C, 1 h, (2) ZnBr<sub>2</sub>, –78 °C, 1 h, (3) CuCl<sub>2</sub>, –78 °C to rt, 1 d, 10%.



**Figure 2.** ORTEP diagrams of **CB** from front (left) and side (right) views. Thermal ellipsoids are drawn at the 50% probability level. Selected bond lengths (Å) are C1C2 1.368(2); C2C17 1.484(2); C17C18 1.685(2); C18C10 1.486(2); C10C9 1.373(2); and C9C1 1.437(2).

temperature (**Fig. 3a**). The optical properties are listed in **Table 1**. The absorption bands were observed from **CT** with the peaks at 310, 323, and 337 nm. The highest molar absorption coefficient was approximately 15,000 M<sup>–1</sup> cm<sup>–1</sup>. In contrast, **CB** showed clear vibrational bands with the peaks at 324, 338, 355, and 376 nm. Moreover, a larger molar absorption coefficient was obtained (ca. 38,000 M<sup>–1</sup> cm<sup>–1</sup>). Band-gap energies were estimated from the absorption edge in the spectra. Accordingly, the smaller value (+3.25 eV) was obtained from **CB** than that from **CT** (+3.57 eV). These data indicate two significant issues: The robust conjugation should be constructed in **CB** in the ground state. Furthermore, the electron delocalization should be expanded through the robust conjugation system. It is likely that



**Figure 3.** (a) UV–vis absorption and (b) photoluminescence spectra of **CB** (black line) and **CT** (gray line). All samples were measured in THF (1.0 × 10<sup>–5</sup> M). The excitation wavelength was at λ<sub>ab,max</sub>.

**Table 1**  
Optical properties of **CB** and **CT**<sup>a</sup>

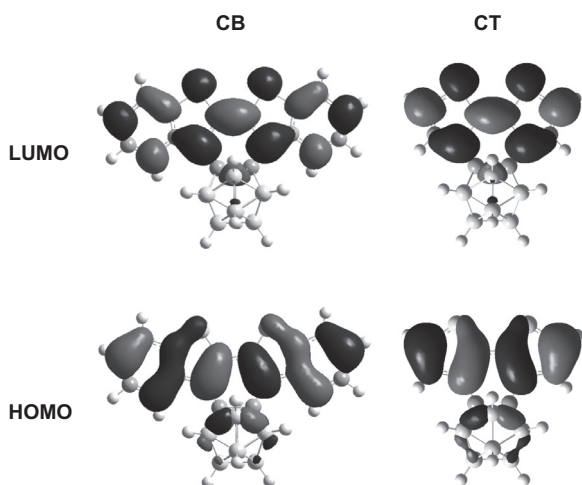
	$\lambda_{\text{abs}}$ (nm)	$\epsilon$ ( $10^4 \text{ M}^{-1} \text{ cm}^{-1}$ )	$\lambda_{\text{em}}$ <sup>b</sup> (nm)	$\Phi_{\text{PL}}$ <sup>c</sup>
<b>CB</b>	324, 338, 355, 376	1.7, 2.6, 3.8, 3.7	378, 400, 426, 453	0.007
<b>CT</b>	310, 323, 337	1.1, 1.5, 1.1	365	0.010

<sup>a</sup> In THF ( $1.0 \times 10^{-5} \text{ M}$ ).<sup>b</sup> Excited at the peak in the longest wavelength band.<sup>c</sup> Determined as an absolute value.

the planar skeleton owing to the anchoring effect of the *o*-carborane moiety should be favorable for realizing the efficient electron delocalization, resulting in the narrow band-gap energy.

To evaluate the electronic properties of *o*-carborane-fused conjugation systems in the excited state, the shapes of the photoluminescence (PL) spectra were compared with **CB** and **CT** in the THF solutions (Fig. 3b). The emission bands from the vibration were observed from **CB** more than those from **CT**. These data represent that the robust conjugation can be constructed in **CB** by the anchoring effect with *o*-carborane. Moreover, the red-shifted emission peaks in the spectrum of **CB** were observed compared to those of **CT**. This result means that the conjugation should be effectively expanded through the fused conjugation moiety even in the excited state. From the PL spectra in variable solvents, the peak shifts were hardly observed (Fig. S10). These data mean that the emission bands of **CB** should be originated not from the **CT** state but from the locally-excited state. It is proposed that the expansion of the conjugation and the anchoring effect by the *o*-carborane bridge could be responsible for the red-shifted vibrational spectrum from **CB**. The emission quantum efficiency ( $\Phi_{\text{PL}}$ ) of **CB** was 0.007. This value was smaller than that of bi(benzo[*b*]thiophene) ( $\Phi_{\text{PL}} = 0.128$ ). The intramolecular motion at the carbon–carbon bond in the *o*-carborane unit could induce the emission quenching according to the previous result.<sup>8b</sup> In addition, the emission quantum yield of **CB** was enhanced in the solid state ( $\Phi_{\text{PL}} = 0.043$ ). This result significantly supports the existence of the motion in the *o*-carborane unit. Furthermore, compared to the absorption and PL spectra of bi(benzo[*b*]thiophene), it was indicated that **CB** provided much narrower bands in the longer wavelength regions (Fig. S11). These data also clearly represent not only the suppression of the molecular motion but also the extension of the conjugated systems via the anchoring effect by the *o*-carborane unit.

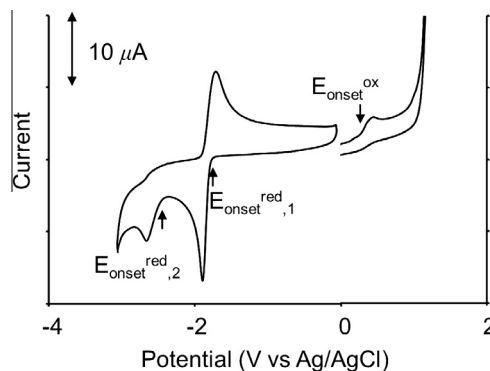
To deeply comprehend optical properties, we performed computational estimation with the *o*-carboranes using density

**Figure 4.** HOMOs and LUMOs of **CB** and **CT** (B3LYP/6-31G\*\*//B3LYP/6-31G\*\* level).

functional theory (DFT) with the B3LYP/6-31G\*\*//B3LYP/6-31G\*\* level. HOMOs and LUMOs of **CB** and **CT** are shown in Figure 4. The optimized structure of **CB** was almost identical to the result of X-ray single crystal analysis. The corresponded tendencies were obtained to those observed in their optical data. HOMO energy levels of **CB** and **CT** were  $-5.96 \text{ eV}$  and  $-6.13 \text{ eV}$ , and LUMO energy levels were  $-2.24 \text{ eV}$  and  $-1.99 \text{ eV}$ , respectively. It is suggested that the expansion of conjugation in the bi(benzo[*b*]thiophene) moiety could occur owing to the anchoring by the *o*-carborane unit. Indeed, it was proposed that both of their HOMO and LUMO were localized at the conjugated moiety. Nucleus-independent chemical shifts (NICS)<sup>9</sup> were also calculated with the B3LYP/6-31G\*\*//B3LYP/6-31G\*\* level (Fig. S9). It is known that the NICS(1) value under  $-5$  means the aromaticity of the target ring. Accordingly, the NICS(1) values of ring A, B, and C were  $-7.80$ ,  $-11.03$  and  $-1.41$ , respectively. These data mean that the rings A and B have aromaticity. In contrast, the ring C could have slight aromaticity. It is implied that the longer carbon–carbon bond at the *o*-carborane-fused bond might be unfavorable for the formation of an aromatic ring.

Electrochemical properties were investigated by cyclic voltammetry (Fig. 5). The reversible voltammogram was obtained, and the peaks at  $-1.72 \text{ eV}$  and  $-2.37 \text{ eV}$  were observed from **CB** in the reduction wave. These peaks should be originated from the *o*-carborane unit.<sup>5g</sup> In the irreversible oxidative wave, a peak appeared around  $+0.36 \text{ eV}$  that originated from the oxidation at the benzothiophene units. In particular, compared to the electrochemical properties of **CT**, the smaller absolute values were obtained.<sup>8a</sup> This fact also supports that the *o*-carborane unit plays a significant role in the stabilization of the energy levels via the enhancement of the electron delocalization on the rigid planar structure. Thus, it is suggested that **CB** could work as an electron-accepting anchoring unit in the conjugation materials. In summary, it is demonstrated that the *o*-carborane should be the facile building block for realizing the robust conjugation system just by introducing as a bridge.

This Letter describes the validity of the *o*-carborane unit for constructing robust conjugation system with aromatic rings. Because of the anchoring effect by the rigid *o*-carborane, both absorption and PL spectra presented the significant vibrational peaks. As a result, the electron delocalization was expanded through the planar conjugation system. The conjugated molecule showed durability during redox process and presented simultaneous electron-accepting and -donating units that originated from *o*-carborane and bithiophene, respectively. These *o*-carborane-based conjugated units could be versatile platforms not only for highly-efficient

**Figure 5.** Cyclic voltammogram of **CB** in  $\text{CH}_3\text{CN}$  ( $1.0 \text{ mM}$ ) containing  $\text{NBu}_4\text{PF}_6$  ( $0.1 \text{ M}$ ) for oxidation and in  $\text{DMF}$  ( $1.0 \text{ mM}$ ) containing  $\text{NBu}_4\text{PF}_6$  ( $0.1 \text{ M}$ ) for reduction using a Pt working electrode, a Pt wire counter electrode, a Ag/AgCl reference electrode, and a ferrocene/ferrocenium external standard at room temperature with a scan rate of  $0.1 \text{ V s}^{-1}$  under Ar.

carrier transport in the modern photovoltaic cells but also for clear and bright emissions in the deep-red or near infrared regions.

### Acknowledgments

This work was partially supported by a Grant-in-Aid for Scientific Research (B) (No. 15H03856) and a Grant-in-Aid for Scientific Research on Innovative Areas 'New Polymeric Materials Based on Element-Blocks (No. 2401)' (24102013) of The Ministry of Education, Culture, Sports, Science, and Technology, Japan.

### Supplementary data

Supplementary data associated with this article can be found, in the online version, at <http://dx.doi.org/10.1016/j.tetlet.2016.03.069>.

### References and notes

- (a) Mas-Torrent, M.; Rovira, C. *Chem. Rev.* **2011**, *111*, 4833–4856; (b) Mei, J.; Diao, Y.; Appleton, A. L.; Fang, L.; Bao, Z. *J. Am. Chem. Soc.* **2013**, *135*, 6724–6746; (c) Takimiya, K.; Shinamura, S.; Osaka, I.; Miyazaki, E. *Adv. Mater.* **2011**, *23*, 4347–4370; (d) Kim, Y.; Lim, E. *Polymers* **2014**, *6*, 382–407; (e) Baumgartner, T. *J. Inorg. Organomet. Polym.* **2005**, *15*, 389–409.
- (a) Zhang, S.; Guo, Y.; Fan, H.; Liu, Y.; Chen, H.-Y.; Yang, G.; Zhan, X.; Liu, Y.; Li, Y.; Yang, Y. *J. Polym. Sci., Part A: Polym. Chem.* **2009**, *47*, 5498–5508; (b) Zhan, X.; Tan, Z.; Zhou, E.; Li, Y.; Misra, R.; Grant, A.; Domercq, B.; Zhang, X.-H.; An, Z.; Zhang, X.; Barlow, S.; Kippelen, B.; Marder, S. R. *J. Mater. Chem.* **2009**, *19*, 5794–5803; (c) Nelson, T. L.; Young, T. M.; Liu, J.; Mishra, S. P.; Belot, J. A.; Balliet, C. L.; Javier, A. E.; Kowalewski, T.; McCullough, R. D. *Adv. Mater.* **2010**, *22*, 4617–4621; (d) Vanormelingen, W.; Van den Bergh, K.; Verbiest, T.; Koeckelberghs, G. *Macromolecules* **2008**, *41*, 5582–5589; (e) Baumgartner, T.; Neumann, T.; Wirges, B. *Angew. Chem., Int. Ed.* **2004**, *43*, 6197–6201; (f) Dienes, Y.; Durben, S.; Kárpáti, T.; Neumann, T.; Englert, U.; Nyulász, L.; Baumgartner, T. *Chem.-Eur. J.* **2007**, *13*, 7487–7500; (g) Romero-Nieto, C.; Merino, S.; Rodríguez-López, J.; Baumgartner, T. *Chem.-Eur. J.* **2009**, *15*, 4135–4145; (h) Ohshita, J.; Matsui, S.; Yamamoto, R.; Mizumo, T.; Ooyama, Y.; Harima, Y.; Murafuji, T.; Tao, K.; Kuramochi, Y.; Kaikoh, T.; Higashimura, H. *Organometallics* **2010**, *29*, 3239–3241; (i) Zhan, X.; Tan, Z.; Domercq, B.; An, Z.; Zhang, X.; Barlow, S.; Li, Y.; Zhu, D.; Kippelen, B.; Marder, S. R. *J. Am. Chem. Soc.* **2007**, *129*, 7246–7247; (j) Cicoira, F.; Santato, C.; Melucci, M.; Favaretto, L.; Gazzano, M.; Muccini, M.; Barbarella, G. *Adv. Mater.* **2006**, *18*, 169–174; (k) Ohshita, J. *Macromol. Chem. Phys.* **2009**, *210*, 1360–1370; (l) Liao, L.; Dai, L.; Smith, A.; Durstock, M.; Lu, J.; Ding, J.; Tao, Y. *Macromolecules* **2007**, *40*, 9406–9412; (m) Ohshita, J.; Kimura, K.; Lee, K.-H.; Kunai, A.; Kwak, Y.-W.; Son, E.-C.; Kunugi, Y. *J. Polym. Sci., Part A: Polym. Chem.* **2007**, *45*, 4588–4596; (n) Yau, C. P.; Fei, Z.; Ashraf, R. S.; Shahid, M.; Watkins, S. E.; Pattanasattayavong, P.; Anthopoulos, T. D.; Gregoriou, V. G.; Chochos, C. L.; Heeney, M. *Adv. Funct. Mater.* **2014**, *24*, 678–687; (o) Small, C. E.; Chen, S.; Subbiah, J.; Amb, C. M.; Tsang, S.-W.; Lai, T.-H.; Reynolds, J. R.; So, F. *Nat. Photon.* **2012**, *6*, 115–120; (p) Gendron, D.; Morin, P.-O.; Berrouard, P.; Allard, N.; Aich, B. R.; Garon, C. N.; Tao, Y.; Leclerc, M. *Macromolecules* **2011**, *44*, 7188–7193; (q) Ohshita, J.; Miyazaki, M.; Tanaka, D.; Morihara, Y.; Fujita, Y.; Kunugi, Y. *Polym. Chem.* **2013**, *4*, 3116–3122; (r) Tanaka, D.; Ohshita, J.; Ooyama, Y.; Kobayashi, N.; Higashimura, H.; Nakanishi, T.; Hasegawa, Y. *Organometallics* **2013**, *32*, 4136–4141; (s) Saito, M.; Shiratake, M.; Tajima, T.; Guo, J. D.; Nagase, S. *J. Organomet. Chem.* **2009**, *694*, 4056–4061; (t) Qi, T.; Guo, Y.; Liu, Y.; Xi, H.; Zhang, H.; Gao, X.; Liu, Y.; Lu, K.; Du, C.; Yu, G.; Zhu, D. *Chem. Commun.* **2008**, 6227–6229; (u) Ohshita, J.; Lee, K.-H.; Kimura, K.; Kunai, A. *Organometallics* **2004**, *23*, 5622–5625; (v) Matsumoto, T.; Tanaka, K.; Chujo, Y. *RSC Adv.* **2015**, *5*, 55406–55410.
- Chujo, Y.; Tanaka, K. *Bull. Chem. Soc. Jpn.* **2015**, *88*, 633–643.
- (a) Icosahedral carboranes: 1,2-C<sub>2</sub>B<sub>10</sub>H<sub>12</sub>: Grimes, R. N. In *Carboranes*, 2nd ed.; Academic Press: New York, 2011; pp 301–540. Chapter 9; (b) Dash, B. P.; Satapathy, R.; Maguire, J. A.; Hosmane, N. S. In *Boron Science: New Technologies and Applications*; Hosmane, N. S., Ed.; CRC: Boca Raton, FL, 2011; pp 675–699; (c) Nakamura, H.; Tazaki, L.; Kanoh, D.; Sato, S. *Pure Appl. Chem.* **2015**, *87*, 143–154; (d) Li, G. Z.; Azuma, S.; Sato, S.; Minegishi, H.; Nakamura, H. *Bioorg. Med. Chem. Lett.* **2015**, *25*, 2624–2628; (e) Nakamura, H.; Tasaki, L.; Kanoh, D.; Sato, S.; Ban, H. S. *Dalton Trans.* **2014**, *43*, 4941–4944.
- (a) Peterson, J. J.; Werre, M.; Simon, Y. C.; Coughlin, E. B.; Carter, K. R. *Macromolecules* **2009**, *42*, 8594–8598; (b) Lerouge, F.; Ferrer-Ugalde, A.; Viñas, C.; Teixidor, F.; Sillanpää, R.; Abreu, A.; Xochitiotzi, E.; Farfán, N.; Santillan, R.; Núñez, R. *Dalton Trans.* **2011**, *40*, 7541–7550; (c) Dash, B. P.; Satapathy, R.; Gaillard, E. R.; Norton, K. M.; Maguire, J. A.; Chug, N.; Hosmane, N. S. *Inorg. Chem.* **2011**, *50*, 5485–5493; (d) Wee, K.-R.; Han, W.-S.; Cho, D. W.; Kwon, S.; Pac, C.; Kang, S. O. *Angew. Chem., Int. Ed.* **2012**, *51*, 2677–2680; (e) Bae, H. J.; Kim, H.; Lee, K. M.; Kim, T.; Lee, Y. S.; Do, Y.; Lee, M. H. *Dalton Trans.* **2014**, *43*, 4978–4985; (f) Harder, R. A.; MacBride, J. A. H.; Rivers, G. P.; Yufit, D.; Goeta, A. E.; Howard, J. A. K.; Wade, K.; Fox, M. A. *Tetrahedron* **2014**, *70*, 5182–5189; (g) Kahert, J.; Stammer, H.-G.; Neumann, B.; Harder, R. A.; Weber, L.; Fox, M. A. *Angew. Chem., Int. Ed.* **2014**, *53*, 3702–3705.
- (a) Kokado, K.; Chujo, Y. *Macromolecules* **2009**, *42*, 1418–1420; (b) Kokado, K.; Chujo, Y. *J. Org. Chem.* **2011**, *76*, 316–319.
- (a) Davis, A. R.; Peterson, J. J.; Carter, K. R. *ACS Macro Lett.* **2012**, *1*, 469–472; (b) Wee, K. R.; Cho, Y. J.; Jeong, S.; Kwon, S.; Lee, J. D.; Suh, I. H.; Kang, S. O. *J. Am. Chem. Soc.* **2012**, *134*, 17982–17990.
- (a) Morisaki, Y.; Tominaga, M.; Chujo, Y. *Chem.-Eur. J.* **2012**, *18*, 11251–11257; (b) Morisaki, Y.; Tominaga, M.; Ochiai, T.; Chujo, Y. *Chem.-Asian J.* **2014**, *9*, 1247–1251.
- (a) Schleyer, P. v. R.; Maerker, C.; Dransfeld, A.; Jiao, H.; Hommes, N. J. R. v. E. *J. Am. Chem. Soc.* **1996**, *118*, 6317–6318; (b) Schleyer, P. v. R.; Manoharan, M.; Wang, Z. X.; Kiran, B.; Jiao, H.; Puchta, R.; Hommes, N. J. R. v. E. *Org. Lett.* **2001**, *3*, 2465–2468.

# Optically Active Cyclic Compounds Based on Planar Chiral [2.2]Paracyclophane with Naphthalene Units

Masayuki Gon,<sup>[a]</sup> Hiroto Kozuka,<sup>[a]</sup> Yasuhiro Morisaki,<sup>\*,[b]</sup> and Yoshiki Chujo<sup>\*,[a]</sup>

**Abstract:** Two optically active cyclic compounds based on a planar chiral [2.2]paracyclophane core and containing either benzene or naphthalene moieties at the four corners of the structures were synthesized. Their optical and chiroptical properties were investigated by UV/vis absorption, photoluminescence (PL), circular dichroism, and circularly polar-

ized luminescence (CPL) spectroscopy, as well as by density functional theory calculations. The circularly polarized luminescence (CPL) performance of the naphthalene-containing cyclic compound was high with a large molar extinction coefficient, good photoluminescence efficiency, and a good CPL dissymmetry factor.

## Introduction

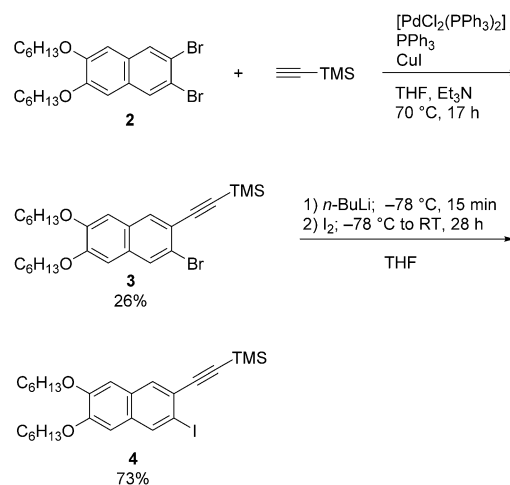
[2.2]Paracyclophane compounds have been extensively studied,<sup>[1]</sup> starting with the first reported synthesis of the parent compound by Brown and Farthing in 1949<sup>[2]</sup> and the development of the practical procedure by Cram and Steinberg in 1951.<sup>[3]</sup> Two benzene rings in [2.2]paracyclophane are closely stacked. We have focused on the stacked structure, having used it to synthesize through-space conjugated polymers and oligomers.<sup>[4]</sup> We have also been interested in the unique planar chirality of this moiety, a feature that is derived from suppressed rotary motion of the two fixed benzene rings.<sup>[5]</sup> This planar chirality can be observed in [2.2]paracyclophanes with one or more substituents, depending on the substituted position, and makes such compounds distinct from axially chiral compounds and those with chiral centers in that it conformationally fixes the orientation of the stacked  $\pi$ -electron system.

Recently, we developed optical resolution methods for 4,12-disubstituted<sup>[6]</sup> and 4,7,12,15-tetrasubstituted [2.2]paracyclophane derivatives.<sup>[7,8]</sup> In addition, we prepared chiral, conjugated compounds with optically active second-order structures, including V-shaped,<sup>[9a]</sup> X-shaped,<sup>[9b]</sup> and propeller-shaped systems.<sup>[7,9c]</sup> It was also reported that planar, chiral, [2.2]paracyclophane-based conjugated compounds are excellent circularly

polarized luminescence (CPL) emitters with large CPL dissymmetry factors ( $g_{lum}$ ). In this study, we modified the structure of the propeller-shaped compound to expand the substrate scope of the propeller-shaped cyclic compound by placing naphthalene units on the corners of the compound to extend the  $\pi$ -surface. After the structure was successfully synthesized, it was optically and chiroptically characterized. The obtained compound was highly emissive and exhibited intense CPL.

## Results and Discussion

Enantiopure 4,7,12,15-tetraethynyl[2.2]paracyclophanes, ( $S_p$ )- and ( $R_p$ )-**1**, were prepared by the method we developed previously.<sup>[7]</sup> The synthetic route to the dialkoxynaphthalene-containing cyclic compound is shown in Scheme 1 and 2. One bromide in dibromodihexyloxynaphthalene **2** was converted into a trimethylsilylethynyl group using a catalytic amount of



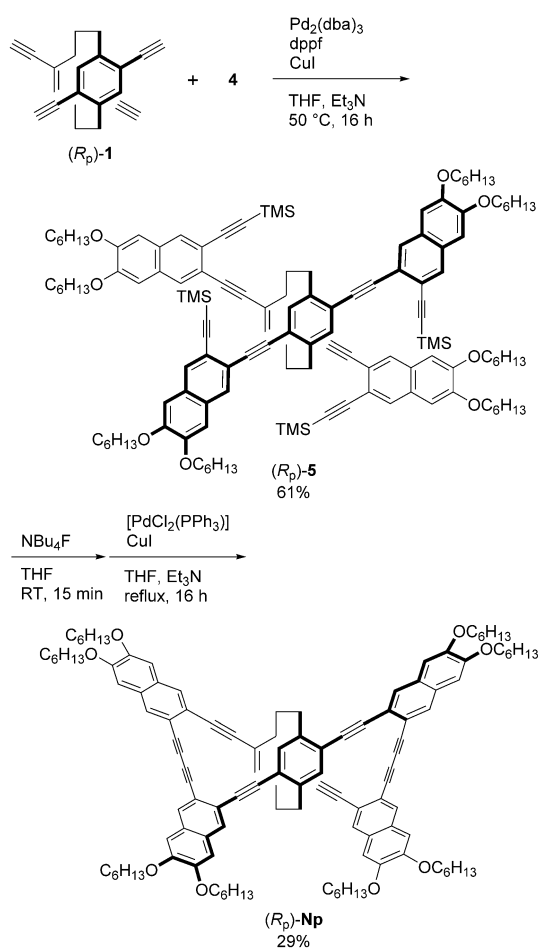
Scheme 1. Synthesis of compound **4**. TMS = trimethylsilyl.

[a] M. Gon, H. Kozuka, Prof. Dr. Y. Chujo  
Department of Polymer Chemistry, Graduate School of Engineering  
Kyoto University  
Katsura, Nishikyo-ku, Kyoto 615-8510 (Japan)  
E-mail: chujo@chujo.synchem.kyoto-u.ac.jp

[b] Prof. Dr. Y. Morisaki  
Department of Applied Chemistry for Environment  
School of Science and Technology  
Kwansei Gakuin University  
2-1 Gakuen, Sanda, Hyogo 669-1337 (Japan)  
E-mail: ymo@kwansai.ac.jp

Supporting information for this article is available on the WWW under <http://dx.doi.org/10.1002/ajoc.201500468>.

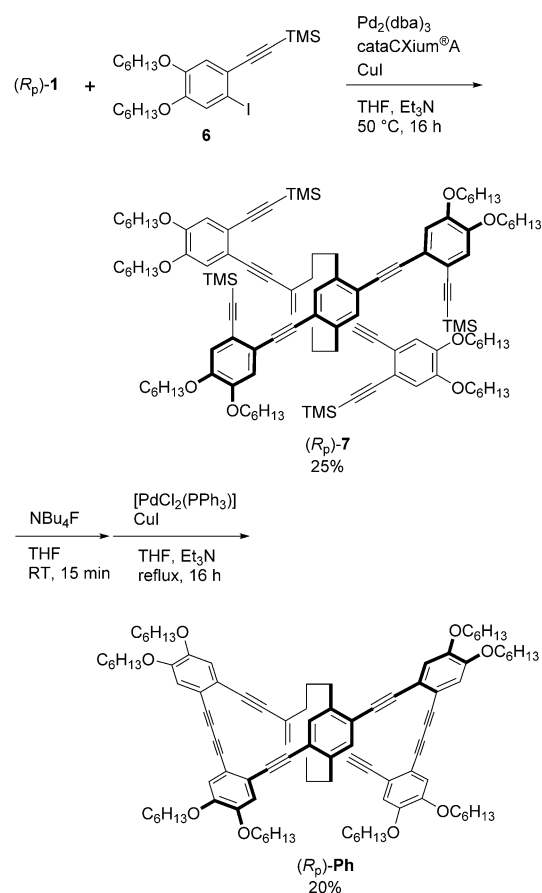
[PdCl<sub>2</sub>(PPh<sub>3</sub>)<sub>2</sub>], PPh<sub>3</sub>, and CuI (Scheme 1), giving 26% isolated yield of the monosubstituted product. Next, the reaction of **3** with *n*BuLi and the addition of I<sub>2</sub> afforded the iodinated compound **4** in 73% isolated yield. This reaction was followed by the Sonogashira-Hagihara coupling<sup>[10]</sup> of (*R<sub>p</sub>*)-**1** with **4** by using a Pd<sub>2</sub>(dba)<sub>3</sub>/dppf/CuI (dba = dibenzylideneacetone; dppf = 1,1'-bis(diphenylphosphino)ferrocene) catalytic system to obtain (*R<sub>p</sub>*)-**5** in 61% isolated yield (Scheme 2). Finally, (*R<sub>p</sub>*)-**5** was reacted with NBu<sub>4</sub>F to remove the trimethylsilyl groups, after which oxidative coupling was carried out catalyzed by [PdCl<sub>2</sub>(PPh<sub>3</sub>)<sub>2</sub>], CuI, and Et<sub>3</sub>N to obtain target compound (*R<sub>p</sub>*)-**Np** in 29% isolated yield. Enantiomer (*S<sub>p</sub>*)-**Np** was prepared by the same procedure with the opposite enantiomer.



Scheme 2. Synthesis of precursor (*R<sub>p</sub>*)-**5** and cyclic compound (*R<sub>p</sub>*)-**Np**.

A cyclic compound containing dialkoxybenzene was also synthesized, as shown in Scheme 3. The reaction of (*R<sub>p</sub>*)-**1** with **6** catalyzed by a Pd<sub>2</sub>(dba)<sub>3</sub>/cataCXiumA/CuI (cataCXiumA = di(1-adamantyl)-*n*-butylphosphine<sup>[11]</sup>) system afforded (*R<sub>p</sub>*)-**7** in 25% isolated yield. Removal of the trimethylsilyl groups with NBu<sub>4</sub>F and oxidative coupling with an excess amount of [PdCl<sub>2</sub>(PPh<sub>3</sub>)<sub>2</sub>] and CuI with Et<sub>3</sub>N under air gave the corresponding cyclic compound (*R<sub>p</sub>*)-**Ph** in 20% isolated yield.

In the cyclization step in Scheme 2 and 3, unidentified impurities were formed due to intermolecular reactions, including



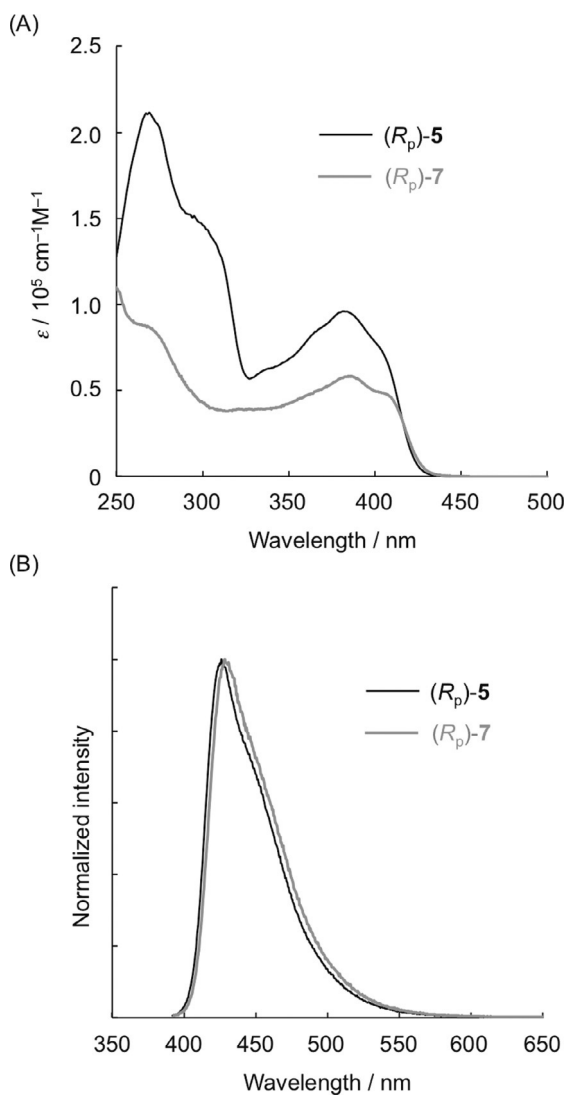
Scheme 3. Synthesis of precursor (*R<sub>p</sub>*)-**7** and cyclic compound (*R<sub>p</sub>*)-**Ph**.

oligomeric products as well as compounds with incomplete cyclic structures. They were removed by SiO<sub>2</sub> column chromatography, resulting in the low isolated yields (29% and 20% for (*R<sub>p</sub>*)-**Np** and (*R<sub>p</sub>*)-**Ph**, respectively). The structures of all the new compounds produced in this study were confirmed by <sup>1</sup>H and <sup>13</sup>C NMR spectroscopy, high-resolution mass spectrometry, and elemental analysis; the detailed synthetic procedures and NMR spectra are shown in the Supporting Information.

The optical data of the (*R<sub>p</sub>*)-isomers are summarized in Table 1, while Figure 1A and 1B show the UV/vis absorption spectra and PL spectra of the (*R<sub>p</sub>*) precursors in CHCl<sub>3</sub> (1.0 × 10<sup>-5</sup> and 1.0 × 10<sup>-6</sup> M, respectively). The absorption spectrum of (*R<sub>p</sub>*)-**5** was shifted hyperchromically compared with that of (*R<sub>p</sub>*)-

Table 1. Optical properties.				
Compound	$\lambda_{\text{abs}}^{\text{[a]}}$ [nm] ( $\epsilon/10^5 \text{ cm}^{-1} \text{ M}^{-1}$ )	$\lambda_{\text{lum}}^{\text{[b]}}$ [nm]	$\tau^{\text{[c]}}$ [ns] ( $\chi^2$ )	$\Phi_{\text{PL}}^{\text{[d]}}$
( <i>R<sub>p</sub></i> )- <b>5</b>	382 (0.96)	426	1.33 (1.01)	0.65
( <i>R<sub>p</sub></i> )- <b>7</b>	384 (0.58)	428	1.71 (1.07)	0.59
( <i>R<sub>p</sub></i> )- <b>Np</b>	353 (1.29)	446	1.83 (1.06)	0.51
( <i>R<sub>p</sub></i> )- <b>Ph</b>	325 (1.18)	482	4.67 (1.18)	0.44

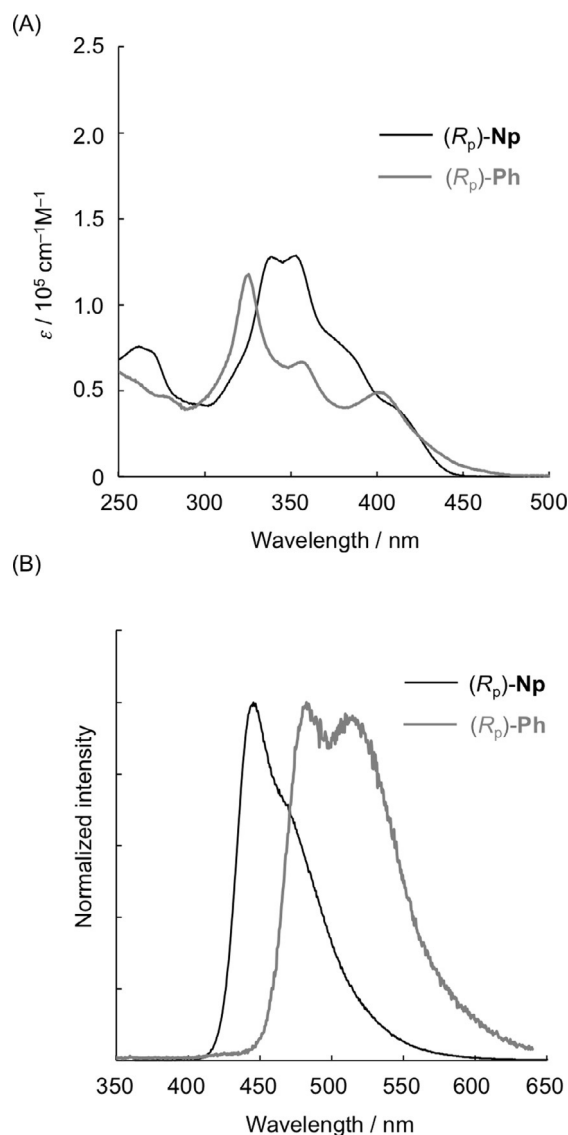
[a] In CHCl<sub>3</sub> (1.0 × 10<sup>-5</sup> M). [b] In CHCl<sub>3</sub> (1.0 × 10<sup>-6</sup> M), excited at each  $\lambda_{\text{abs}}$ . [c] PL lifetime at  $\lambda_{\text{lum}}$ . [d] Absolute PL quantum efficiency.



**Figure 1.** (A) UV/vis absorption spectra of precursors  $(R_p)$ -5 and  $(R_p)$ -7 in  $\text{CHCl}_3$  ( $1.0 \times 10^{-5}$  M). (B) PL spectra of precursors  $(R_p)$ -5 and  $(R_p)$ -7 in  $\text{CHCl}_3$  ( $1.0 \times 10^{-6}$  M), excited at absorption maxima.

7 due to the extension of the  $\pi$ -surface from a benzene to a naphthalene moiety. In Figure 1B, both species gave similar PL spectra, with absolute  $\Phi_{\text{PL}}$  values of 0.65 and 0.59 for  $(R_p)$ -5 and  $(R_p)$ -7, respectively.

Figure 2 shows the UV and PL spectra of the  $(R_p)$ -cyclic compounds in  $\text{CHCl}_3$  ( $1.0 \times 10^{-5}$  and  $1.0 \times 10^{-6}$  M, respectively). Hyperchromic and bathochromic effects were observed for the absorption band in  $(R_p)$ -Np, whereas the absorption edge of  $(R_p)$ -Np appeared at a shorter wavelength than that of  $(R_p)$ -Ph. This is consistent with density functional theory (DFT) calculations, which suggest a narrower band-gap energy for  $(R_p)$ -Ph (see below). Generally, through-space interactions in [2.2]paracyclophane derivatives depend on the stacked position of the  $\pi$ -electron systems. Because both of these molecules stack at the center phenylene rings, the  $\pi$ - $\pi$  interactions are strong and delocalization occurs throughout their structures.<sup>[12]</sup> The through-space interaction in  $(R_p)$ -Ph seems to be particularly effective, as can be seen in the tailing of the absorption edge.



**Figure 2.** (A) UV/vis absorption spectra of cyclic compounds  $(R_p)$ -Np and  $(R_p)$ -Ph in  $\text{CHCl}_3$  ( $1.0 \times 10^{-5}$  M). (B) PL spectra of precursors  $(R_p)$ -Np and  $(R_p)$ -Ph in  $\text{CHCl}_3$  ( $1.0 \times 10^{-6}$  M), excited at absorption maxima.

The excited states of  $(R_p)$ -Np and  $(R_p)$ -Ph were different. The PL spectrum of  $(R_p)$ -Np was relatively sharp, indicative of bright blue luminescence with a peak emission at 446 nm. The PL decay curve was fitted to a single exponential equation, leading to a calculated lifetime ( $\tau$ ) of 1.83 ns, as listed in Table 1. The difference in  $\tau$  values between precursor  $(R_p)$ -5 and cyclic compound  $(R_p)$ -Np was small, with a  $\tau$  value for  $(R_p)$ -5 of 1.33 ns. On the other hand, the spectrum of  $(R_p)$ -Ph was broad, indicative of greenish-blue emission and a  $\tau$  value of 4.67 ns. The  $\Phi_{\text{PL}}$  values of  $(R_p)$ -Np and  $(R_p)$ -Ph were 0.51 and 0.44, respectively. These results, coupled with a large  $\epsilon$  of  $1.29 \times 10^5 \text{ cm}^{-1} \text{ M}^{-1}$ , suggest that naphthalene-containing cyclic compound  $(R_p)$ -Np is a better emitter.

The chiroptical properties of the precursors and cyclic compounds were investigated by optical rotation analysis, circular dichroism (CD) spectroscopy, and CPL spectroscopy. Their specific rotation values ( $[\alpha]_D$ ) and CD dissymmetry factors ( $g_{\text{abs}}$ ),

Compound	$[\alpha]_D^{23[a]}$	$g_{abs}^{[b]}/10^{-3}$ at $\lambda_{abs}$	$g_{lum}^{[c]}/10^{-3}$ at $\lambda_{lum}$
( <i>R</i> <sub>p</sub> )- <b>5</b>	-41.2	-1.4	-1.4
( <i>R</i> <sub>p</sub> )- <b>7</b>	-17.9	-1.3	-1.5
( <i>R</i> <sub>p</sub> )- <b>Np</b>	+789.4	+3.3	+3.5
( <i>R</i> <sub>p</sub> )- <b>Ph</b>	+1086.4	+3.9	+8.4

[a] Specific rotation ( $c=0.1$ ,  $\text{CHCl}_3$  at  $23^\circ\text{C}$ ). The  $[\alpha]_D^{23}$  values of (*S*<sub>p</sub>)-isomers are described in the supporting information. [b]  $g_{abs}=2\Delta\epsilon/\epsilon$ , where  $\Delta\epsilon$  indicates differences of absorbance between left- and right-handed circularly polarized light, respectively. [c]  $g_{lum}=2(I_L-I_R)/(I_L+I_R)$ , where  $I_L$  and  $I_R$  indicate luminescence intensities of left- and right-handed CPL, respectively.

and  $g_{lum}$  values are shown in Table 2. Meanwhile, Figure 3A and 3B show the CD spectra of **5** and **7** in  $\text{CHCl}_3$  ( $1.0 \times 10^{-5}$  M), respectively. Both compounds exhibited intense and mirror-image Cotton effects in the absorption bands, while the difference between the left- and right-handed  $\epsilon$  values ( $\Delta\epsilon$ ) reached  $100 \text{ cm}^{-1} \text{ M}^{-1}$ .

The CD spectra of the **Np** and **Ph** isomers in  $\text{CHCl}_3$  ( $1.0 \times 10^{-5}$  M) are shown in Figure 4A and 4B, respectively. In both cases, mirror-image Cotton effects were observed along with higher absolute  $\Delta\epsilon$  values; in particular, (*R*<sub>p</sub>)- and (*S*<sub>p</sub>)-**Ph** reached values of  $500 \text{ cm}^{-1} \text{ M}^{-1}$ . The chirality was strongly induced by cyclization. This was also shown by optical rotation analysis; for example, the specific rotation value of (*R*<sub>p</sub>)-**7** was estimated to be  $-41.2$ , whereas that of (*R*<sub>p</sub>)-**Ph** was opposite and much larger, with a value of  $+1086.4$ . The second-order structures, that is, propeller-shaped structures, of cyclic compounds enhance the chirality in addition to the planar chirality of the [2.2]paracyclophane moiety.

Chirality in the excited state was evaluated by CPL spectroscopy. The corresponding spectra of the precursors and cyclic compounds are shown in Figure 5 and 6, respectively. Precursors **5** and **7** gave clear and mirror image CPL signals in the region of PL spectra, as shown in Figure 5A and 5B, respectively. The  $g_{lum}$  values ( $=2(I_L - I_R)/(I_L + I_R)$ , where  $I_L$  and  $I_R$  are left- and right-handed CPL signals, respectively) for (*R*<sub>p</sub>)-**5** and (*R*<sub>p</sub>)-**7** were sufficiently large, and they were estimated to be  $-1.4 \times 10^{-3}$  and  $-1.5 \times 10^{-3}$ , respectively. As can be expected, intense CPL signals were observed for cyclic compounds **Np** and **Ph**, as shown in Figure 6A and 6B, respectively. The  $g_{lum}$  values were enhanced by cyclization, with values of  $+3.5 \times 10^{-3}$  and  $+8.4 \times 10^{-3}$  for (*R*<sub>p</sub>)-**Np** and (*R*<sub>p</sub>)-**Ph**, respectively; these values are sufficiently high for optically active organic molecules.<sup>[13]</sup> On the other hand, the plus or minus signs of CPL signals in the cyclic compounds were different from the precursors, suggesting that cyclization changed the electronic and magnetic transition dipole moments in the excited states. Investigations on the relationship between the transition dipole moments and chiroptical profiles of the planar chiral [2.2]paracyclophane-based compounds are currently underway.

Figure 7 shows the highest occupied molecular orbitals (HOMOs) and the lowest unoccupied molecular orbitals (LUMOs) of cyclic compounds (*S*<sub>p</sub>)-**Np** and (*S*<sub>p</sub>)-**Ph**; for simplicity, the hexyl groups were replaced with methyl groups. The

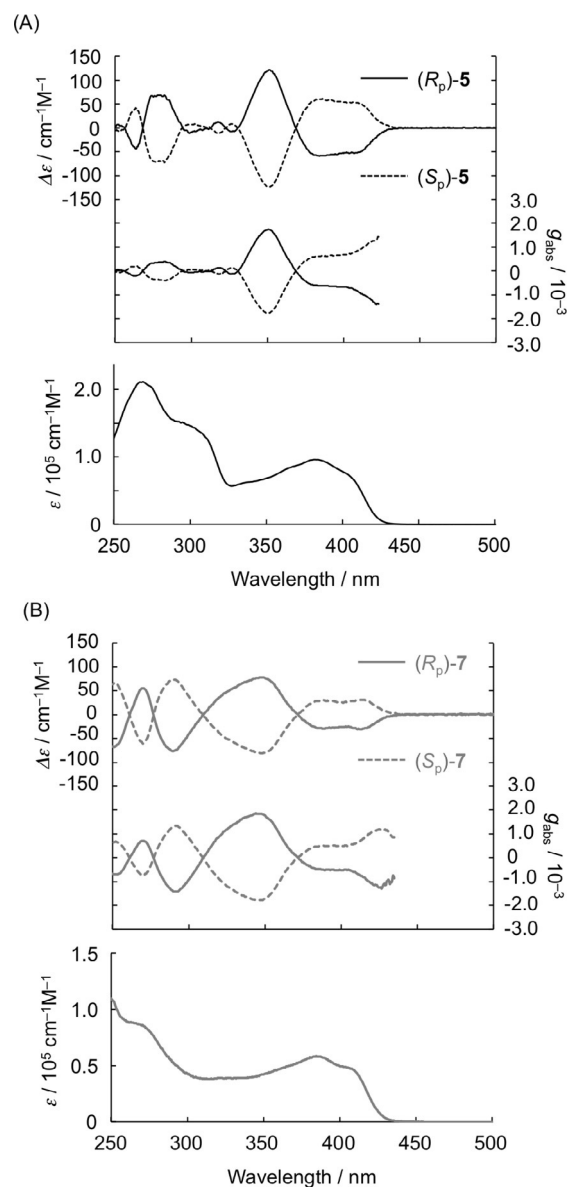
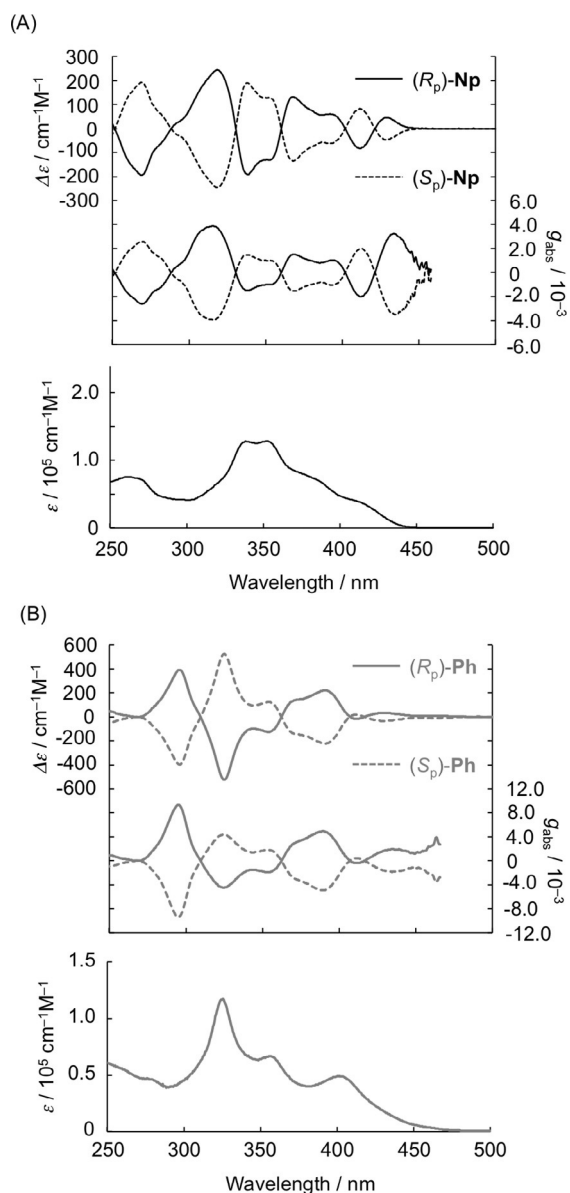


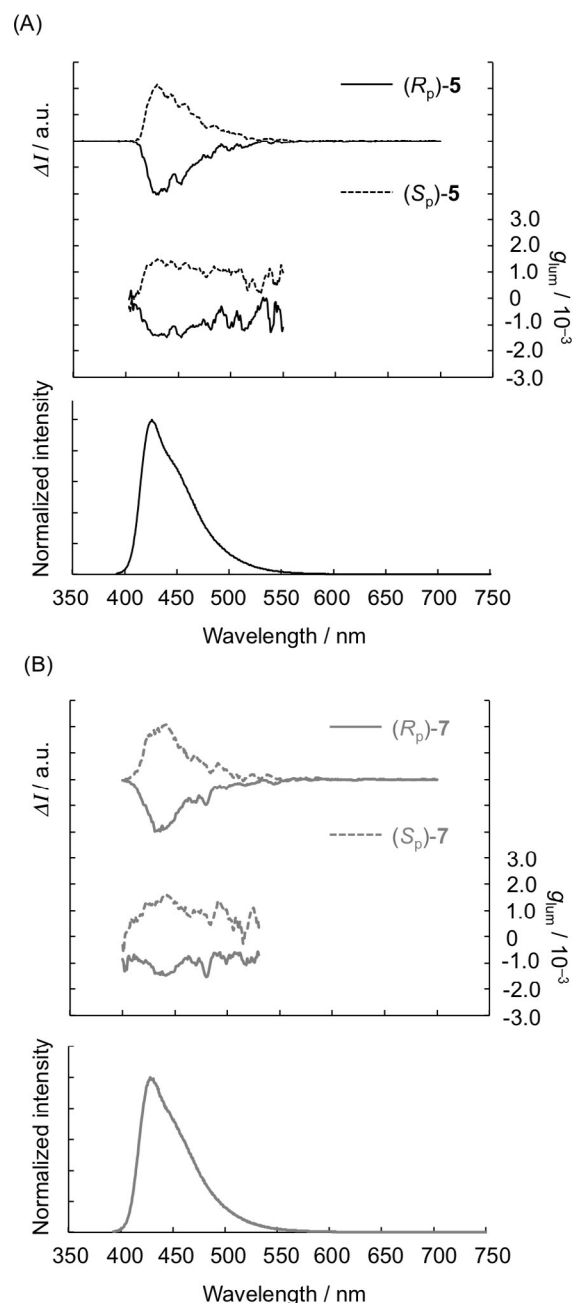
Figure 3. (A) CD and  $g_{abs}$  spectra of (*S*<sub>p</sub>)- and (*R*<sub>p</sub>)-**5** in  $\text{CHCl}_3$  ( $1.0 \times 10^{-5}$  M) including the absorption spectrum of (*R*<sub>p</sub>)-**5** in  $\text{CHCl}_3$  ( $1.0 \times 10^{-5}$  M). (B) CD and  $g_{abs}$  spectra of (*S*<sub>p</sub>)- and (*R*<sub>p</sub>)-**7** in  $\text{CHCl}_3$  ( $1.0 \times 10^{-5}$  M) including the absorption spectrum of (*R*<sub>p</sub>)-**7** in  $\text{CHCl}_3$  ( $1.0 \times 10^{-5}$  M).

molecular orbitals were obtained by DFT calculations at the TD-BH and HLYP/def2-TZVPP//BLYP/def2-TZVPP level; the data are summarized in Table 3. In both (*S*<sub>p</sub>)-**Np** and (*S*<sub>p</sub>)-**Ph**, the molecular orbitals extended through the entire molecules in the HOMO and LUMO. The HOMO level of (*S*<sub>p</sub>)-**Ph** was higher than that of (*S*<sub>p</sub>)-**Np**, and the LUMO level was lower, resulting in a narrower band gap. This supports the energy band-gaps in their UV/vis absorption spectra; the (*S*<sub>p</sub>)-**Np** and (*S*<sub>p</sub>)-**Ph** absorption edges at 430 and 465 nm, respectively, are in good agreement with the calculated values.

Torsion angles between the neighboring aromatic rings were estimated, as shown in Figure 8 and Table 3. The average torsion angle of (*S*<sub>p</sub>)-**Np** was  $23.7^\circ$ , which was larger than the  $23.1^\circ$  angle of (*S*<sub>p</sub>)-**Ph**, meaning that its  $\pi$ -conjugation was not



**Figure 4.** (A) CD and  $g_{\text{abs}}$  spectra of ( $S_p$ )- and ( $R_p$ )-**Np** in  $\text{CHCl}_3$  ( $1.0 \times 10^{-5}$  M) including the absorption spectrum of ( $R_p$ )-**Np** in  $\text{CHCl}_3$  ( $1.0 \times 10^{-5}$  M). (B) CD and  $g_{\text{abs}}$  spectra of ( $S_p$ )- and ( $R_p$ )-**Ph** in  $\text{CHCl}_3$  ( $1.0 \times 10^{-5}$  M) including the absorption spectrum of ( $R_p$ )-**Ph** in  $\text{CHCl}_3$  ( $1.0 \times 10^{-5}$  M).



**Figure 5.** (A) CPL and  $g_{\text{lum}}$  spectra of ( $S_p$ )- and ( $R_p$ )-**5** in  $\text{CHCl}_3$  ( $1.0 \times 10^{-5}$  M) including the PL spectrum of ( $R_p$ )-**5** in  $\text{CHCl}_3$  ( $1.0 \times 10^{-6}$  M); excitation wavelength: 300 nm. (B) CPL and  $g_{\text{lum}}$  spectra of ( $S_p$ )- and ( $R_p$ )-**7** in  $\text{CHCl}_3$  ( $1.0 \times 10^{-5}$  M) including the PL spectrum of ( $R_p$ )-**7** in  $\text{CHCl}_3$  ( $1.0 \times 10^{-6}$  M); excitation wavelength: 350 nm.

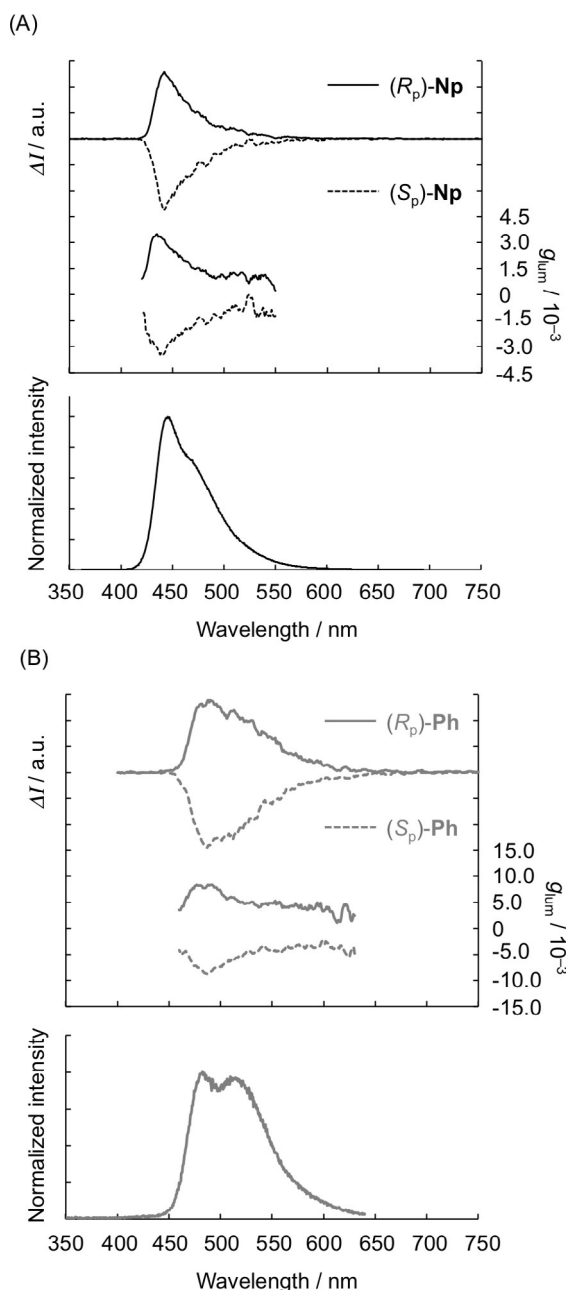
Table 3. Calculated and measured parameters.			
Compound	Band-gap energy	Measured	Average $\theta$ ( $\theta_1, \theta_2$ ) <sup>[d]</sup>
	Calculated $E^{[a,b]}$		
( $R_p$ )- <b>Np</b>	3.02 eV (411 nm)	430 nm	23.7 (24.6, 22.8)
( $R_p$ )- <b>Ph</b>	2.72 eV (456 nm)	465 nm	23.1 (23.0, 23.2)

[a] Calculated at the TD-BH and HLYP/def2-TZVPP//BLYP/def2-TZVPP level.  
 [b]  $\lambda = 1239.8/E$ . [c] Absorption edge of each UV/vis absorption spectrum.  
 [d] Calculated torsion angle between neighboring aromatic units (Figure 8).

extended as effectively. The average distances between bridge carbons of [2.2]paracyclophane for both compounds were estimated to be 2.80 Å. This suggests that the shorter conjugation length and weaker  $\pi$ - $\pi$  interactions in ( $R_p$ )-**Np** account for the wider band gap energy and superior  $\Phi_{\text{PL}}$ .

## Conclusions

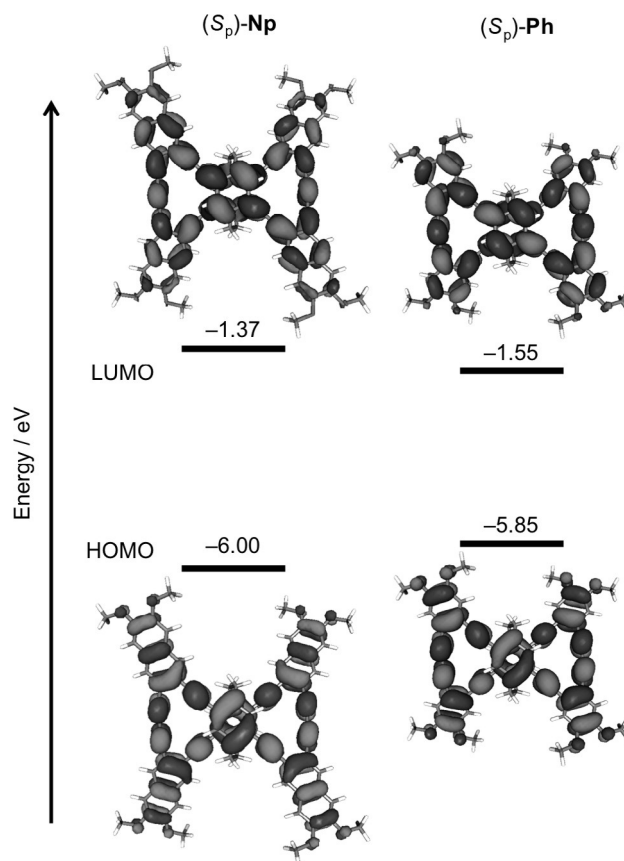
In summary, planar chiral [2.2]paracyclophane-based cyclic compounds with extended  $\pi$ -surfaces were synthesized. Cycli-



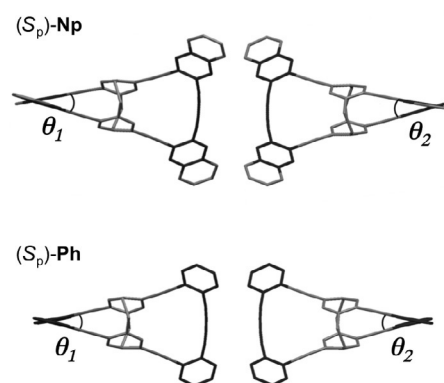
**Figure 6.** (A) CPL and  $g_{lum}$  spectra of  $(S_p)$ - and  $(R_p)$ -Np in  $CHCl_3$  ( $1.0 \times 10^{-5}$  M) including the PL spectrum of  $(R_p)$ -Np in  $CHCl_3$  ( $1.0 \times 10^{-6}$  M); excitation wavelength: 300 nm. (B) CPL and  $g_{lum}$  spectra of  $(S_p)$ - and  $(R_p)$ -Ph in  $CHCl_3$  ( $1.0 \times 10^{-5}$  M) including the PL spectrum of  $(R_p)$ -Ph in  $CHCl_3$  ( $1.0 \times 10^{-6}$  M); excitation wavelength: 350 nm.

zation enhanced slightly the optical and chiroptical properties because of the higher-order structure; thus, cyclic compounds were high-performance CPL emitters with excellent  $\epsilon$ ,  $\Phi_{PL}$ , and  $g_{lum}$ . Furthermore, the optical and chiroptical properties can be tuned by aromatic moieties in the cyclic skeleton.

Introduction of a naphthalene unit provided better  $\epsilon$  and absolute  $\Phi_{PL}$  values, whereas the benzene unit enhanced  $g_{lum}$  values. Such optically active higher-order structures provide a new means by which to obtain enhanced PL and CPL characteristics.



**Figure 7.** Frontier orbitals of  $(S_p)$ -Np and  $(S_p)$ -Ph (methyl groups were used in place of hexyl groups) obtained by density functional theory (DFT) at the TD-BH and HLYP/def2-TZVPP//BLYP/def2-TZVPP level.



**Figure 8.** Optimized structures and calculated torsion angles of  $(S_p)$ -Np and  $(S_p)$ -Ph by DFT.

## Acknowledgements

This work was supported by a Grant-in-Aid for Scientific Research on Innovative Areas (no. 15H00992) “ $\pi$ -Figuration” from the Ministry of Education, Culture, Sports, Science and Technology, Japan. M.G. appreciates a Research Fellowship (no. 14J02514) from the Japan Society for the Promotion of Science for Young Scientists. We are grateful to Professor Kazuo Akagi

and Dr. Kazuyoshi Watanabe (Department of Polymer Chemistry, Graduate School of Engineering, Kyoto University) for CPL data analysis.

**Keywords:** [2.2]paracyclophanes · circularly polarized luminescence · naphthalenes · planar chirality · photoluminescence

- [1] a) *Cyclophane Chemistry: Synthesis Structures and Reactions* (Ed.: F. Vögtle), Wiley, Chichester, **1993**; b) *Modern Cyclophane Chemistry* (Eds.: R. Gleiter, H. Hopf), Wiley-VCH, Weinheim, **2004**; c) H. Hopf, *Angew. Chem. Int. Ed.* **2008**, *47*, 9808–9812; *Angew. Chem.* **2008**, *120*, 9954–9958.
- [2] C. J. Brown, A. C. Farthing, *Nature* **1949**, *164*, 915–916.
- [3] D. J. Cram, H. Steinberg, *J. Am. Chem. Soc.* **1951**, *73*, 5691–5704.
- [4] a) Y. Morisaki, Y. Chujo, *Angew. Chem. Int. Ed.* **2006**, *45*, 6430–6437; *Angew. Chem.* **2006**, *118*, 6580–6587; b) Y. Morisaki, Y. Chujo, *Polym. Chem.* **2011**, *2*, 1249–1257; c) Y. Morisaki, Y. Chujo, *Chem. Lett.* **2012**, *41*, 840–846; d) Y. Morisaki, S. Ueno, A. Saeki, A. Asano, S. Seki, Y. Chujo, *Chem. Eur. J.* **2012**, *18*, 11251–11257.
- [5] a) D. J. Cram, N. L. Allinger, *J. Am. Chem. Soc.* **1955**, *77*, 6289–6294; b) V. Rozenberg, E. Sergeeva, H. Hopf, *Modern Cyclophane Chemistry* (Eds.: R. Gleiter, H. Hopf), Wiley-VCH, Weinheim, **2004**, pp. 435–462; c) G. J. Rowlands, *Org. Biomol. Chem.* **2008**, *6*, 1527–1534; d) S. E. Gibson, J. D. Knight, *Org. Biomol. Chem.* **2003**, *1*, 1256–1269; e) A. A. Aly, A. B. Brown, *Tetrahedron* **2009**, *65*, 8055–8089; f) J. Paradies, *Synthesis* **2011**, 3749–3766.
- [6] a) P. J. Pye, K. Rossen, R. A. Reamer, N. N. Tsou, R. P. Volante, P. J. Reider, *J. Am. Chem. Soc.* **1997**, *119*, 6207–6208; b) K. Rossen, P. J. Pye, A. Maliakal, R. P. Volante, *J. Org. Chem.* **1997**, *62*, 6462–6463; c) R. Zhuravsky, Z. Starikova, E. Vorontsov, V. Rozenberg, *Tetrahedron: Asymmetry* **2008**, *19*, 216–222; d) B. Jiang, X.-L. Zhao, *Tetrahedron: Asymmetry* **2004**, *15*, 1141–1143; e) P. G. Jones, J. Hillmer, H. Hopf, *Acta Crystallogr. Sect. E* **2003**, *59*, o24–o25; f) D. Pamperin, H. Hopf, C. Syltatk, M. Pietzsch, *Tetrahedron: Asymmetry* **1997**, *8*, 319–325; g) D. Pamperin, B. Ohse, H. Hopf, M. Pietzsch, *J. Mol. Catal. B* **1998**, *5*, 317–319; h) D. C. Braddock, I. D. MacGilp, B. G. Perry, *J. Org. Chem.* **2002**, *67*, 8679–8681; i) Y. Morisaki, R. Hifumi, L. Lin, K. Inoshita, Y. Chujo, *Chem. Lett.* **2012**, *41*, 990–992; j) Y. Morisaki, R. Hifumi, L. Lin, K. Inoshita, Y. Chujo, *Polym. Chem.* **2012**, *3*, 2727–2730; k) G. Meyer-Eppler, E. Vogelsang, C. Benkhäuser, A. Schneider, G. Schnakenburg, A. Lützen, *Eur. J. Org. Chem.* **2013**, 4523–4532.
- [7] Y. Morisaki, M. Gon, T. Sasamori, N. Tokitoh, Y. Chujo, *J. Am. Chem. Soc.* **2014**, *136*, 3350–3353.
- [8] Optical resolution of *rac*-4,5,15,16-tetrasubstituted [2.2]paracyclophane has already been reported: N. V. Vorontsova, V. I. Rozenberg, E. V. Sergeeva, E. V. Vorontsov, Z. A. Starikova, K. A. Lyssenko, H. Hopf, *Chem. Eur. J.* **2008**, *14*, 4600–4617.
- [9] a) Y. Morisaki, K. Inoshita, Y. Chujo, *Chem. Eur. J.* **2014**, *20*, 8386–8390; b) Gon, M.; Y. Morisaki, Y. Chujo, *Eur. J. Org. Chem.* **2015**, 7756–7762; c) M. Gon, Y. Morisaki, Y. Chujo, *J. Mater. Chem. C* **2015**, *3*, 521–529.
- [10] a) K. Sonogashira, Y. Tohda, N. Hagihara, *Tetrahedron Lett.* **1975**, *16*, 4467–4470; b) K. Sonogashira, *Handbook of Organopalladium Chemistry for Organic Synthesis* (Ed.: E. Negishi), Wiley-Interscience, New York, **2002**, pp. 493–529.
- [11] A. Zapf, A. Ehrentraut, M. Beller, *Angew. Chem. Int. Ed.* **2000**, *39*, 4153–4155; *Angew. Chem.* **2000**, *112*, 4315–4317.
- [12] a) S. Wang, G. C. Bazan, S. Tretiak, S. Mukamel, *J. Am. Chem. Soc.* **2000**, *122*, 1289–1297; b) G. P. Bartholomew, G. C. Bazan, *Acc. Chem. Res.* **2001**, *34*, 30–39; c) G. P. Bartholomew, G. C. Bazan, *Synthesis* **2002**, 1245–1255; d) G. P. Bartholomew, G. C. Bazan, *J. Am. Chem. Soc.* **2002**, *124*, 5183–5196; e) D. S. Seferos, D. A. Banach, N. A. Alcantar, J. N. Israelachvili, G. C. Bazan, *J. Org. Chem.* **2004**, *69*, 1110–1119; f) G. P. Bartholomew, M. Rumi, S. J. K. Pond, J. W. Perry, S. Tretiak, G. C. Bazan, *J. Am. Chem. Soc.* **2004**, *126*, 11529–11542; g) J. W. Hong, H. Y. Woo, G. C. Bazan, *J. Am. Chem. Soc.* **2005**, *127*, 7435–7443; h) G. C. Bazan, *J. Org. Chem.* **2007**, *72*, 8615–8635.
- [13] a) H. Maeda, Y. Bando, *Pure Appl. Chem.* **2013**, *85*, 1967–1978; b) E. M. Sánchez-Carnerero, A. R. Agarrabeitia, F. Moreno, B. L. Maroto, G. Muller, M. J. Ortiz, S. de La Moya, *Chem. Eur. J.* **2015**, *21*, 13488–13500.

Manuscript received: November 13, 2015

Revised: December 5, 2015

Accepted Article published: December 21, 2015

Final Article published: January 12, 2016

## Structure–Activity Relationships | Hot Paper |

 Synthesis of Optically Active, X-Shaped, Conjugated Compounds and Dendrimers Based on Planar Chiral [2.2]Paracyclophane, Leading to Highly Emissive Circularly Polarized LuminescenceMasayuki Gon,<sup>[a]</sup> Yasuhiro Morisaki,<sup>\*,[b]</sup> Risa Sawada,<sup>[a]</sup> and Yoshiki Chujo<sup>\*,[a]</sup>

**Abstract:** Optically active, Fréchet-type dendrimers containing an emissive X-shaped  $\pi$ -electron system as the core unit were synthesized. Gram-scale optical resolution and transformations of 4,7,12,15-tetrasubstituted [2.2]paracyclophanes were also carried out. The high-generation dendrons effectively absorbed UV light and transferred energy to the core, resulting in high photoluminescence (PL) from the core. In addition, the dendrons sufficiently isolated the emissive X-

shaped conjugated core and bright emission was observed from both thin films and solutions. Intense circularly polarized luminescence (CPL) was observed from the thin film. The dendrimer films exhibited excellent optical properties, such as large molar extinction coefficients, high fluorescence quantum efficiencies, intense PL and CPL, and large CPL dissymmetry factors.

## Introduction

Optically active, emissive, conjugated compounds exhibit a potential difference between their left- and right-handed circularly polarized luminescence (CPL<sup>[1]</sup>) intensities. Recently, the development of optically active CPL-emitting organic compounds<sup>[2–11]</sup> for applications in 3D organic light-emitting devices has received much attention. CPL characteristics are evaluated from the photoluminescence (PL) intensity and the luminescence dissymmetry factor ( $g_{\text{lum}}$ ), defined as  $2(I_{\text{left}} - I_{\text{right}}) / (I_{\text{left}} + I_{\text{right}})$ , in which  $I_{\text{left}}$  and  $I_{\text{right}}$  represent the left- and right-handed CPL intensities, respectively. The molar absorption coefficient ( $\epsilon$ ), PL quantum efficiency ( $\Phi_{\text{lum}}$ ), and large  $g_{\text{lum}}$  value are therefore important factors in CPL materials. However, it is generally difficult to achieve large PL intensities in combination with large  $g_{\text{lum}}$  values due to the existing challenges in obtaining large  $g_{\text{lum}}$  values in organic compounds.

We recently suggested that a second-ordered structure created from the rigid and conformationally stable [2.2]paracyclophane<sup>[12]</sup> structure was effective for achieving CPL.<sup>[9a,13]</sup> Despite the stacked structure of the  $\pi$ -electron systems, [2.2]paracyclophane-based conjugated compounds exhibit good  $\Phi_{\text{lum}}$  values in addition to a large  $\epsilon$ . Furthermore, the optically active,

second-ordered structures obtained from planar, chiral [2.2]paracyclophane, including V-shaped,<sup>[13b]</sup> helical,<sup>[13b]</sup> triangular,<sup>[9a,13b]</sup> and propeller-shaped structures<sup>[13a,c]</sup> in the excited state provided large  $g_{\text{lum}}$  values in the order of  $10^{-2}$  to  $10^{-3}$ . The CPL profiles of the optically active [2.2]paracyclophane compounds have been observed in dilute solutions, whereas the PL performance in the solid state, in particular, the PL intensity and  $\Phi_{\text{lum}}$ , decreased dramatically due to typical aggregation-caused quenching.

We report herein the synthesis of a simple X-shaped compound that contains two stacked  $\pi$ -electron systems. We focused on the dendritic structure<sup>[14]</sup> to investigate the optical and chiroptical properties of its thin film. In addition to the film-forming ability, the Fréchet-type dendrimer was selected to overcome aggregation-caused quenching, and to take advantage of its light-harvesting effect; dendrons protect the emissive core unit from aggregation and the benzene rings in the dendrons effectively absorb UV light. The dendrimers exhibited excellent CPL properties both in dilute solution and in the film state, which led to highly emissive CPL materials with large  $g_{\text{lum}}$  values. Gram-scale syntheses of enantiopure 4,7,12,15-tetrasubstituted [2.2]paracyclophanes are also disclosed.

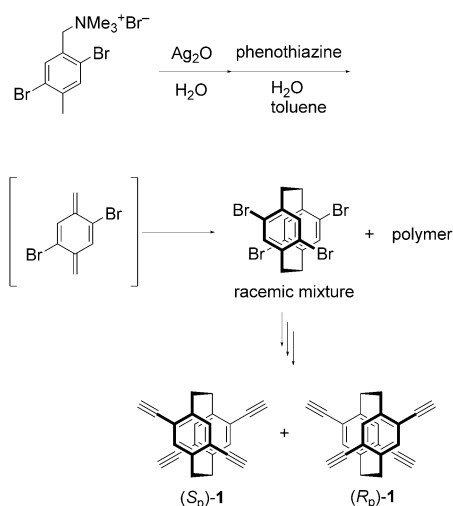
## Results and Discussion

The reported synthetic procedure to obtain *rac*-4,7,12,15-tetrabromo[2.2]paracyclophane was modified as outlined in the Supporting Information.<sup>[15]</sup> The method reported by Chow et al. selectively produces 4,7,12,15-tetrasubstituted [2.2]paracyclophane compounds,<sup>[15]</sup> as shown in Scheme 1; however, polymeric compounds are mainly obtained as byproducts. We successfully prepared *rac*-4,7,12,15-tetrabromo[2.2]paracyclophane in 68% yield under more dilute reaction conditions. The

[a] M. Gon, R. Sawada, Prof. Dr. Y. Chujo  
Department of Polymer Chemistry, Graduate School of Engineering  
Kyoto University, Katsura, Nishikyō-ku  
Kyoto 615-8510 (Japan)  
E-mail: chujo@chujo.synchem.kyoto-u.ac.jp

[b] Prof. Dr. Y. Morisaki  
Department of Applied Chemistry for Environment  
School of Science and Technology, Kwansei Gakuin University  
2-1 Gakuen, Sanda, Hyogo 669-1337 (Japan)  
E-mail: ymo@kwansei.ac.jp

Supporting information for this article is available on the WWW under <http://dx.doi.org/10.1002/chem.201504270>.

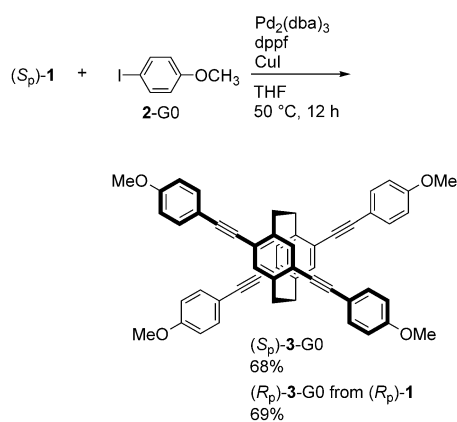


**Scheme 1.** Synthetic route to *rac*-4,7,12,15-tetrabromo[2.2]paracyclophane,<sup>[15]</sup> and structures of planar chiral 4,7,12,15-tetraethynyl[2.2]paracyclophanes (*S<sub>p</sub>*)- and (*R<sub>p</sub>*)-1.<sup>[13a]</sup>

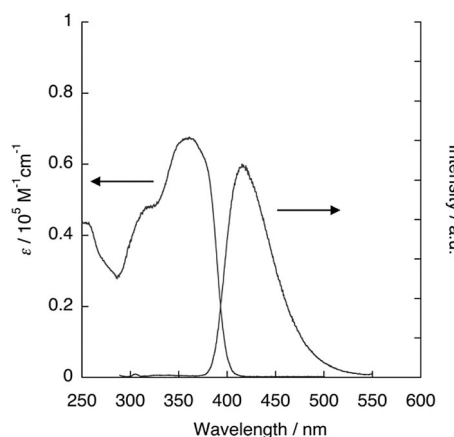
gram-scale optical resolution of planar chiral 4,7,12,15-tetra-substituted [2.2]paracyclophane,<sup>[16]</sup> and the successive transformations to enantiopure (*S<sub>p</sub>*)- and (*R<sub>p</sub>*)-1 (see Scheme 1) are also described in the Supporting Information.

The X-shaped conjugated compound (*S<sub>p</sub>*)-3-GO, in which two *p*-phenylene–ethynylenes were stacked at the central phenylene units,<sup>[17,18]</sup> was prepared from the reaction of (*S<sub>p</sub>*)-1 with commercially available *p*-iodoanisole (2-GO; Scheme 2). In addition, the enantiomer (*R<sub>p</sub>*)-3-GO was prepared from the corresponding (*R<sub>p</sub>*) isomer.

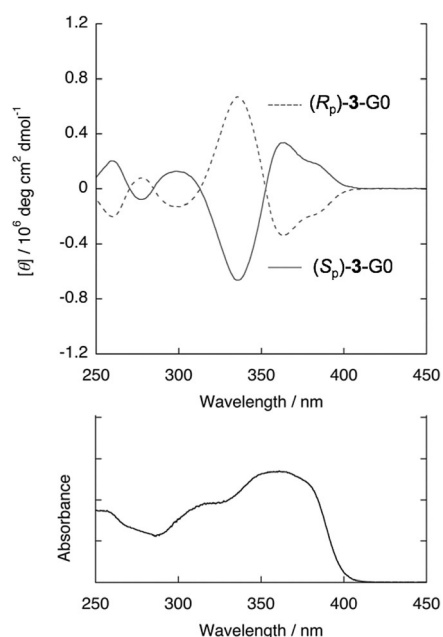
The UV/Vis absorption and PL spectra of dilute solutions of (*S<sub>p</sub>*)- and (*R<sub>p</sub>*)-3-GO in CHCl<sub>3</sub> ( $1.0 \times 10^{-5}$  M) were recorded.<sup>[18]</sup> Figure 1 shows the spectra for the (*S<sub>p</sub>*) isomer. The absorption bands derived from the  $\pi$ - $\pi^*$  transition of *p*-phenylene–ethynylene were observed with band maxima at  $\lambda = 361$  and around 315 nm. Photoexcitation of (*S<sub>p</sub>*)-3-GO at  $\lambda = 365$  nm gave an emission band at  $\lambda = 416$  nm with an absolute PL efficiency ( $\Phi_{lum}$ ) of 0.66. Figure 2 shows the circular dichroism



**Scheme 2.** Synthesis of (*S<sub>p</sub>*)-3-GO; dba = dibenzylideneacetone, dppf = 1,1'-bis(diphenylphosphino)ferrocene.

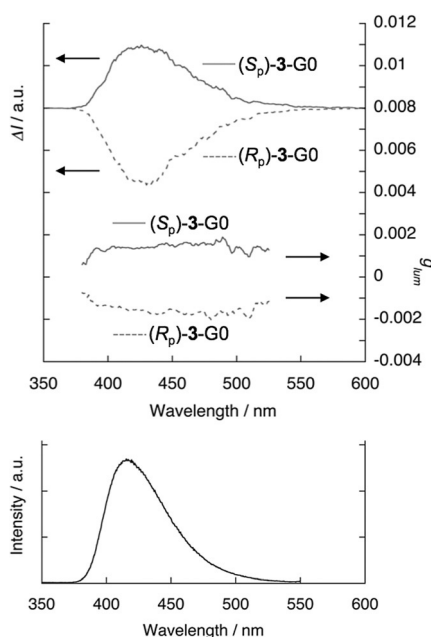


**Figure 1.** UV/Vis absorption and PL spectra of (*S<sub>p</sub>*)-3-GO in CHCl<sub>3</sub> ( $1.0 \times 10^{-5}$  M for UV and  $1.0 \times 10^{-7}$  M for PL). Excitation wavelength: 365 nm.



**Figure 2.** CD spectra of (*S<sub>p</sub>*)- and (*R<sub>p</sub>*)-3-GO in CHCl<sub>3</sub> ( $1.0 \times 10^{-5}$  M) and UV/Vis absorption spectrum of (*S<sub>p</sub>*)-3-GO in CHCl<sub>3</sub> ( $1.0 \times 10^{-5}$  M).

(CD) spectra of dilute solutions of (*S<sub>p</sub>*)- and (*R<sub>p</sub>*)-3-GO in CHCl<sub>3</sub> ( $1.0 \times 10^{-5}$  M). A clearly bisignate mirror-image Cotton effects was observed along with a relatively high  $[\theta]$  of  $6.7 \times 10^5$  deg cm<sup>2</sup> dmol<sup>-1</sup>, which suggested that the light-absorbing units involved were chirally perturbed by the planar chiral [2.2]paracyclophane. As expected, CPL was also observed. The CPL and  $g_{lum}$  spectra of a dilute solution of (*S<sub>p</sub>*)-3-GO in CHCl<sub>3</sub> ( $1.0 \times 10^{-5}$  M) are shown in Figure 3. Mirror-image CPL signals were observed in the PL region, and the absolute  $g_{lum}$  value was estimated to be  $1.4 \times 10^{-3}$ . The X-shaped compound of planar, chiral [2.2]paracyclophane is an excellent CPL emitter, that is, it has good  $\Phi_{lum}$ , intense CPL, and large  $g_{lum}$  properties. However, due to crystallization, thin films of (*S<sub>p</sub>*)- and (*R<sub>p</sub>*)-3-GO were not obtained, and the PL intensity and  $\Phi_{lum}$  observed in the solid state decreased due to typical aggregation-caused quenching.

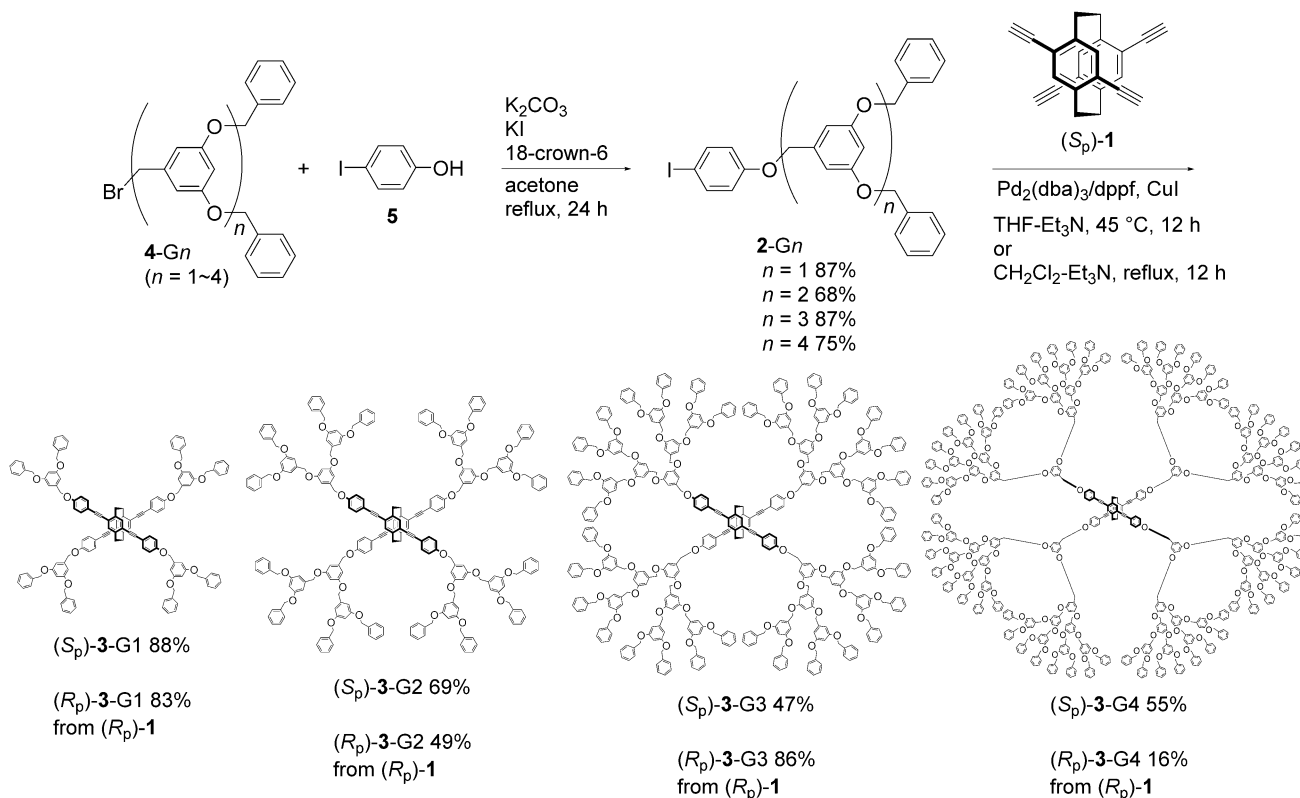


**Figure 3.** CPL and  $g_{lum}$  spectra of  $(S_p)$ - and  $(R_p)$ -3-G0 in  $CHCl_3$  ( $1.0 \times 10^{-5}$  M) and the PL spectrum of  $(S_p)$ -3-G0 in  $CHCl_3$  ( $1.0 \times 10^{-5}$  M). Excitation wavelength: 279 nm.

From the viewpoint of film formation for the X-shaped compound, we focused on the dendritic structure.<sup>[14,19,20]</sup> Fréchet-type<sup>[20]</sup> dendrons were introduced into the X-shaped compound to take advantage of the light-harvesting effect<sup>[21,22]</sup> of

the benzene rings on the dendrons to enhance the PL performance of the system. Fréchet-type bromo-substituted dendrons 4-Gn ( $n=1-4$ ) were prepared and treated with *p*-iodophenol (5) to obtain dendrons 2-Gn (Scheme 3). Sonogashira-Hagihara coupling<sup>[23]</sup> of  $(S_p)$ -1 with 2-Gn afforded the target dendrimers  $(S_p)$ -3-Gn ( $n=1-4$ ), which contained the X-shaped conjugated moiety as the core unit (Scheme 3). The yields of different enantiomers varied according to experimental error because of difficulties in handling as a result of increased hygroscopicity with increasing generations. The dendrimers were highly soluble in common organic solvents, including THF, toluene,  $CH_2Cl_2$ , and  $CHCl_3$ . In addition, they possessed film-forming abilities through spin coating of solutions in  $CHCl_3$  ( $2.0 \times 10^{-3}$  M).

The optical and chiroptical properties of  $(S_p)$ - and  $(R_p)$ -3-Gn ( $n=1-4$ ) were evaluated by means of UV/Vis absorption, PL, CD, and CPL spectroscopy. The optical and chiroptical data are summarized in Tables 1 and 2, respectively. Figures 4A and 4B show the UV/Vis absorption spectra of dilute solutions of all compounds in  $CHCl_3$  ( $1.0 \times 10^{-5}$  M) and spin-coated films, respectively. Absorption bands at  $\lambda \approx 275$  and 300–400 nm were assigned to the  $\pi-\pi^*$  bands of the benzene rings in the dendrons and *p*-phenylene-ethynylene moieties of the core unit, respectively. The absorption bands at  $\lambda \approx 275$  nm increased with increasing dendrimer generation (i.e., the number of benzene rings). As shown in Figure 4B, the absorption edges of the  $(S_p)$ -3-G1 and G2 films were redshifted relative to those of the G3 and G4 dendrimers because of core unit aggregation in the solid state.



**Scheme 3.** Synthesis of dendrimers  $(S_p)$ -3-Gn ( $n=1-4$ ).

**Table 1.** Spectroscopic data for the optical properties of the ( $S_p$ ) isomers.

	$\lambda_{\text{abs}}^{[a]}$ [nm] ( $\epsilon \times 10^{-5}$ [ $M^{-1} \text{cm}^{-1}$ ])	$\lambda_{\text{abs}}^{[b]}$ [nm]	$\lambda_{\text{lum}}^{[c]}$ [nm]	$\lambda_{\text{lum}}^{[d]}$ [nm]	$\Phi_{\text{lum}}^{[e]}$	$\Phi_{\text{lum}}^{[f]}$
( $S_p$ )-G0	361 (0.68)	–	416	–	0.66	–
( $S_p$ )-G1	279 (0.40), 363 (0.67)	368	415	425, 445	0.63	0.20
( $S_p$ )-G2	279 (0.61), 364 (0.69)	278, 367	416	423, 435	0.66	0.54
( $S_p$ )-G3	279 (1.00), 365 (0.68)	279, 369	417	421, 438	0.66	0.65
( $S_p$ )-G4	279 (1.76), 363 (0.68)	283, 368	416	420, 435	0.67	0.58

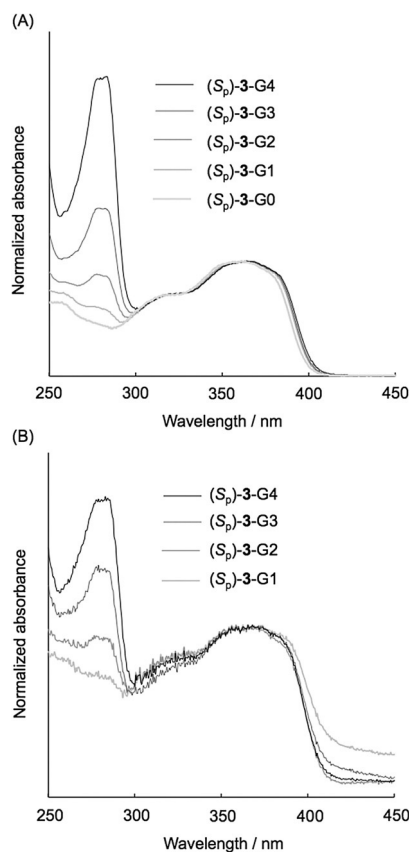
[a] In  $\text{CHCl}_3$  ( $1.0 \times 10^{-5}$  M). [b] Thin film prepared by the spin-coating method from solutions in  $\text{CHCl}_3$  ( $1.0 \times 10^{-3}$  M). [c] In  $\text{CHCl}_3$  ( $1.0 \times 10^{-7}$  M), excited at  $\lambda = 279$  nm. [d] Thin film, excited at  $\lambda = 279$  nm. [e] Absolute PL quantum efficiency in  $\text{CHCl}_3$  ( $1.0 \times 10^{-7}$  M) excited at the band maximum of the core unit ( $\lambda = 365$  nm). [f] Absolute PL quantum efficiency of the film prepared by the spin-coating method from solutions in  $\text{CHCl}_3$  ( $1.0 \times 10^{-3}$  M), excited at the band maximum of the core unit ( $\lambda = 370$  nm).

**Table 2.** Spectroscopic data for the chiroptical properties of the ( $S_p$ ) isomers.

	$g_{\text{abs}}^{[a]} \times 10^3$		$g_{\text{lum}}^{[d]} \times 10^3$	
	Solution <sup>[b]</sup>	Film <sup>[c]</sup>	Solution <sup>[b]</sup>	Film <sup>[c]</sup>
( $S_p$ )-G0	+ 1.3	–	+ 1.4	–
( $S_p$ )-G1	+ 1.3	+ 1.6	+ 1.4	+ 2.1
( $S_p$ )-G2	+ 1.3	+ 1.6	+ 1.4	+ 2.0
( $S_p$ )-G3	+ 1.6	+ 1.6	+ 1.4	+ 1.8
( $S_p$ )-G4	+ 1.3	+ 1.5	+ 1.4	+ 2.0

[a]  $g_{\text{abs}} = 2\Delta\epsilon/\epsilon$ , in which  $\Delta\epsilon$  indicates differences in absorbance between left- and right-handed circularly polarized light, respectively. The  $g_{\text{abs}}$  value of the band maximum at  $\lambda \approx 360$  nm was estimated. [b] In  $\text{CHCl}_3$  ( $1.0 \times 10^{-5}$  M). [c] Film prepared by the spin-coating method from solutions in  $\text{CHCl}_3$  ( $5.0 \times 10^{-3}$  M). [d]  $g_{\text{lum}} = 2(I_{\text{left}} - I_{\text{right}})/(I_{\text{left}} + I_{\text{right}})$ , in which  $I_{\text{left}}$  and  $I_{\text{right}}$  indicate the luminescence intensities of left- and right-handed CPL, respectively. The excitation wavelength was 279 nm in the CPL spectra. The  $g_{\text{lum}}$  value of the PL band maximum at  $\lambda \approx 415$  nm was estimated.

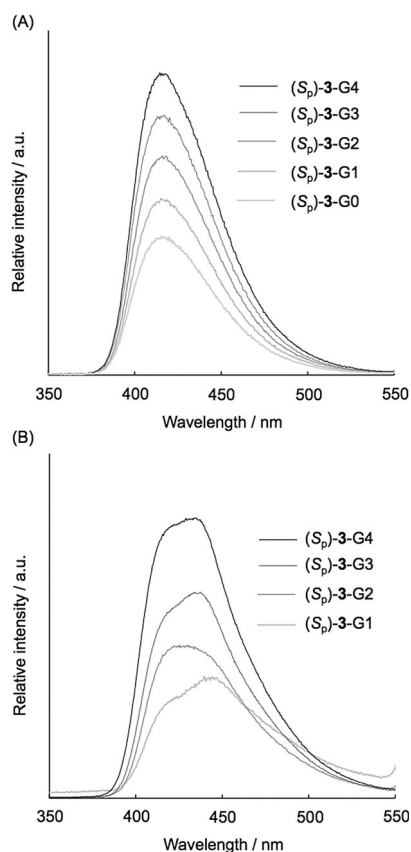
The PL spectra of dilute solutions of ( $S_p$ )-3-Gn in  $\text{CHCl}_3$  ( $1.0 \times 10^{-7}$  M) and the spin-coated films are shown in Figure 5A and B, respectively. Excitation was carried out at  $\lambda = 279$  nm to ensure excitation of the benzene rings in the dendrons. In Figure 5A, emission bands of the dendrimers ( $S_p$ )-3-Gn appeared at  $\lambda \approx 415$  nm, which was comparable to the spectrum of the dendron-free ( $S_p$ )-3-G0; thus indicating that emission occurred from the *p*-phenylene–ethynylene moieties in the core unit. Because the emitting species of ( $S_p$ )-3-Gn ( $n = 0-4$ ) were identical (i.e., the same core unit), their  $\Phi_{\text{lum}}$  values were also comparable and calculated to be approximately 0.65 (Table 1). The band intensity of the dendrimers increased with an increasing number of benzene rings in the dendrons because of the light-harvesting effect and energy transfer from the dendrimer surface to the core. The PL intensity of the films also increased with increasing dendrimer generation (Figure 5B). In contrast with the observations in solution, the  $\Phi_{\text{lum}}$  of the dendrimer film increased with increasing dendrimer generation. The  $\Phi_{\text{lum}}$  values of 3-G3 and -G4 were different, despite both cores being well protected by dendrons (see Figure 8, below). It is considered that, in the films, the conformations of the core units are slightly different in the excited states due to the restricted mobility of the cores by the congested dendrons. Aggregation of the core phenylene–ethynylene moieties is inhibited by the dendrons, and emission occurs from the isolated



**Figure 4.** A) UV/Vis absorption spectra of solutions ( $1.0 \times 10^{-5}$  M) of ( $S_p$ )-dendrimers in  $\text{CHCl}_3$ . B) UV/Vis absorption spectra of ( $S_p$ )-dendrimer thin films. The spectra were normalized at  $\lambda \approx 365$  nm.

phenylene–ethynylene moieties, despite their film state. As the result, the intense blue emission derived from large  $\epsilon$  and good  $\Phi_{\text{lum}}$  values was obtained from the higher generation dendrimers.

The CD spectra of dendrimers ( $S_p$ )- and ( $R_p$ )-3-Gn in  $\text{CHCl}_3$  ( $1.0 \times 10^{-5}$  M) and as films are shown in Figure 6A and B, respectively. In all cases, mirror-image Cotton effects with large  $\Delta\epsilon$  values were observed in the CD spectra. The dissymmetry factors of absorbance ( $g_{\text{abs}} = \Delta\epsilon/\epsilon$ ) are also plotted in Figure 6. The  $g_{\text{abs}}$  values of the  $\pi-\pi^*$  transition bands of the benzene rings at  $\lambda = 250-300$  nm decreased with increasing dendrimer generation (insets in Figure 6A and B). Because the Cotton



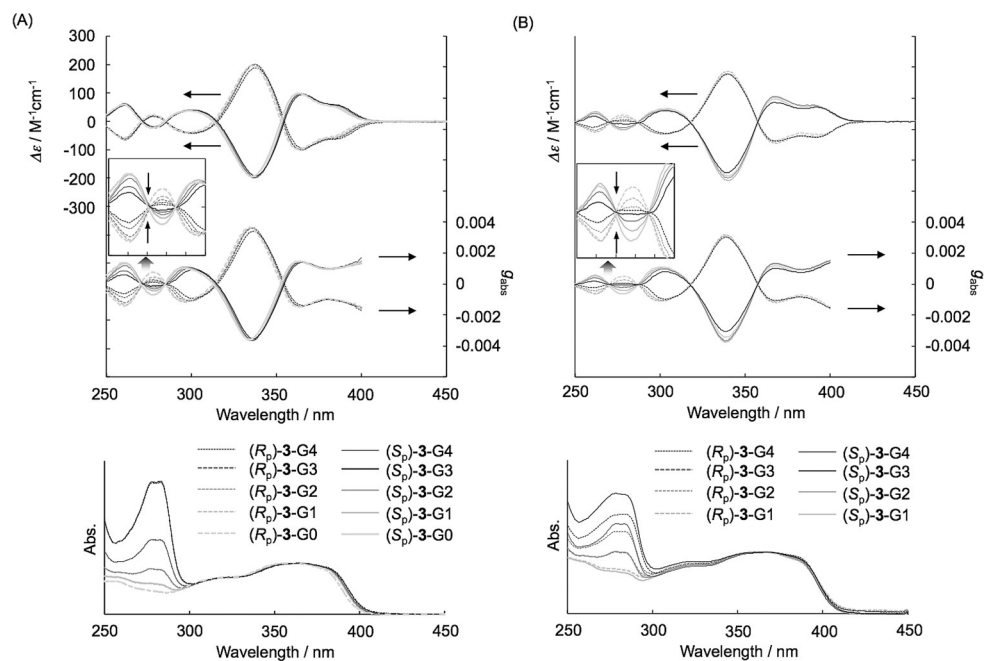
**Figure 5.** A) PL spectra of solutions ( $1.0 \times 10^{-7}$  M) of  $(S_p)$ -dendrimers in  $\text{CHCl}_3$ . B) PL spectra of  $(S_p)$ -dendrimer thin films. Excitation wavelength: 279 nm.

effect of the benzene rings is induced by the optically active [2.2]paracyclophane core, the planar chirality of the core is not effective for benzene rings on the dendron surface. In contrast,

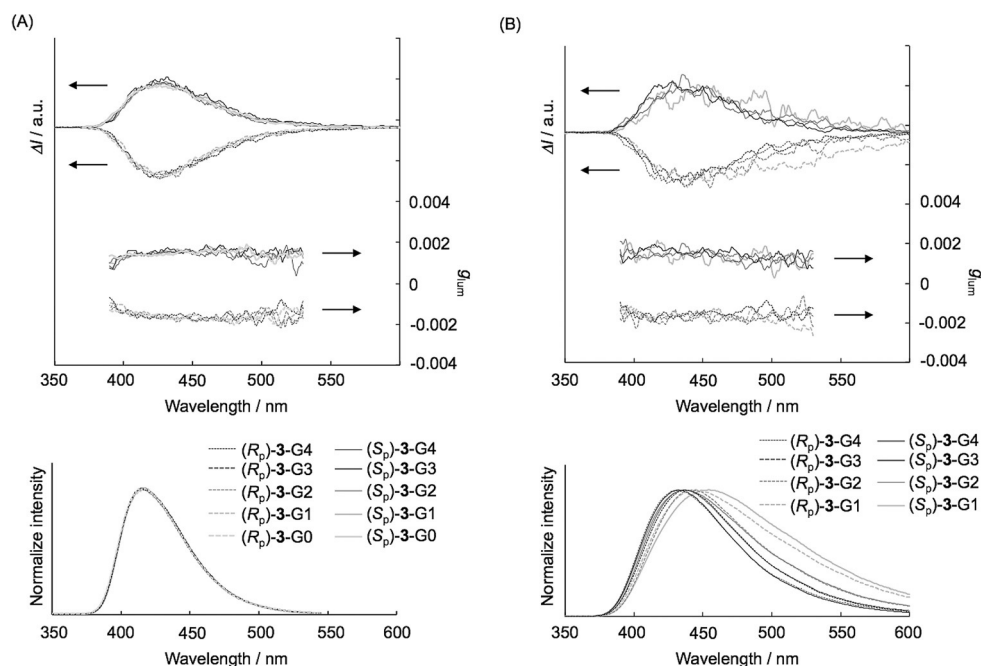
the  $g_{\text{abs}}$  values in the  $\pi$ - $\pi^*$  transition bands of the phenylene-ethynylene moieties were identical.

The X-shaped, second-order structure of the  $\pi$ -electron systems of planar chiral [2.2]paracyclophane was CPL active, as previously shown in Figure 3. Intense CPL signals were therefore observed for the dendrimers in  $\text{CHCl}_3$  ( $1.0 \times 10^{-5}$  M) and the spin-coated films (Figure 7 A and B, respectively). All dendrimers exhibited high  $g_{\text{lum}}$  values in the order of  $10^{-3}$ . Thus, the Fréchet-type dendron provided planar, chiral, [2.2]paracyclophane-based  $\pi$ -electron systems with unprecedented PL and CPL properties such as large  $\epsilon$ , good  $\Phi_{\text{lum}}$ , and excellent  $g_{\text{lum}}$  values both in solution and as films. Figure 8 shows the simulated structures of the dendrimers  $(S_p)$ -3-G $n$  ( $n=1-4$ ) obtained by using PM3<sup>[24]</sup> with MOPAC2012.<sup>[25]</sup> The dendrons of  $(S_p)$ -3-G1 and -G2 do not sufficiently protect the core unit, whereas those of  $(S_p)$ -3-G3 and -G4 isolate the core unit; thus inhibiting aggregation-caused quenching.

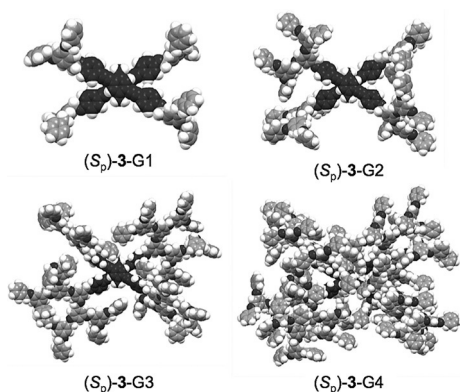
To investigate the dendritic effect on PL, X-shaped  $(S_p)$ -3-G0 was dispersed in a polystyrene (PS;  $M_n=8.1 \times 10^4$ ,  $M_w=2.1 \times 10^5$ ) matrix. The PL spectra of 5 and 10 wt%  $(S_p)$ -3-G0 in PS were compared with those of  $(S_p)$ -3-G3 and  $(S_p)$ -3-G4 spin-coated films (Figure 9 A). The PL intensities of 5 and 10 wt%  $(S_p)$ -3-G0 in PS were clearly lower than those of the dendrimer films, despite the benzene-rich environment. As shown in the excitation spectra (Figure 9 B), only weak bands derived from the PS phenylene moieties were observed at  $\lambda \approx 270$  nm, which implied that the benzene rings of PS did not participate significantly in emission from the core unit. On the other hand, as shown in Figure 9 B, bands appeared at  $\lambda \approx 275$  nm in the excitation spectra of the  $(S_p)$ -3-G3 and  $(S_p)$ -3-G4 dendrimer films. Figures S13A and S13B in the Supporting Information show the excitation spectra of  $(S_p)$ -3-G $n$  ( $n=1-4$ ) in  $\text{CHCl}_3$  and as spin-coated films, respectively. The band intensity derived



**Figure 6.** A) CD,  $g_{\text{abs}}$ , and UV/Vis absorption spectra of solutions ( $1.0 \times 10^{-5}$  M) of dendrimers in  $\text{CHCl}_3$ . B) CD,  $g_{\text{abs}}$ , and UV/Vis absorption spectra of the thin films. Expanded  $g_{\text{abs}}$  spectra (from  $\lambda = 250$  to 300 nm) are shown in the insets.



**Figure 7.** A) CPL,  $g_{lum}$ , and PL spectra of solutions ( $1.0 \times 10^{-5}$  M) of dendrimers in  $CHCl_3$ . B) CPL,  $g_{lum}$ , and PL spectra of dendrimer thin films. Excitation wavelength: 279 nm.

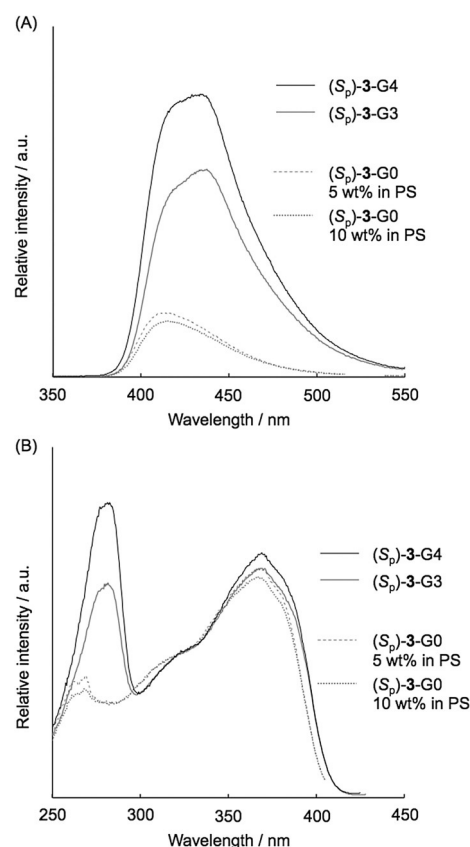


**Figure 8.** Space-filling model of the dendrimers simulated by means of PM3.<sup>[24]</sup> The conjugated core units are shown in dark gray.

from the benzene units in the dendrons increased as the dendrimer generation increased. These results clearly indicate the contribution of the benzene rings to emission from the core unit in the dendrimers through the light-harvesting effect.

## Conclusion

We achieved the gram-scale optical resolution and transformations of planar, chiral, 4,7,12,15-tetrasubstituted [2.2]paracyclophanes. Optically active Fréchet-type dendrimers containing an X-shaped conjugated core with the planar chiral [2.2]paracyclophane moiety were prepared. The dendrons effectively absorbed UV light and transferred energy to the core. In addition, the dendrons sufficiently isolated the emissive X-shaped conju-



**Figure 9.** A) PL spectra of  $(S_p)$ -3-G3 and -G4 films. PL spectra of PS films containing 5 and 10 wt%  $(S_p)$ -3-G0. B) Excitation spectra of  $(S_p)$ -3-G3 and -G4 films. Excitation spectra of PS films containing 5 and 10 wt%  $(S_p)$ -3-G0. Excitation spectra were obtained at the PL band maximum wavelength.

gated core, which resulted in high emission from the thin films. Intense CPL by the planar chiral [2.2]paracyclophane was observed with a high dissymmetry factor in the order of  $10^{-3}$ . The combination of Fréchet-type dendrons with planar chiral [2.2]paracyclophane provided emissive conjugated compounds with large  $\epsilon$  and  $\Delta\epsilon$  values, good  $\Phi_{lum}$  values, intense PL and CPL, and large  $g_{lum}$  factors. This strategy is promising for the design of organic CPL materials.

## Acknowledgements

This work was supported by a Grant-in-Aid for Scientific Research on Innovative Areas (no. 15H00992) "π-Figuration" from the Ministry of Education, Culture, Sports, Science and Technology, Japan. M.G. acknowledges Research Fellowships (no. 14J02514) from the Japan Society for the Promotion of Science for Young Scientists. We are grateful to Professor Kazuo Akagi and Dr. Kazuyoshi Watanabe (Department of Polymer Chemistry, Graduate School of Engineering, Kyoto University) for CPL data analysis.

**Keywords:** chirality · conjugation · dendrimers · luminescence · paracyclophanes

- [1] a) J. P. Riehl, F. S. Richardson, *Chem. Rev.* **1986**, *86*, 1–16; b) J. P. Riehl, F. Muller, *Comprehensive Chiroptical Spectroscopy*, Wiley, New York, **2012**.
- [2] a) H. Maeda, Y. Bando, *Pure Appl. Chem.* **2013**, *85*, 1967–1978; b) E. M. Sánchez-Carnerero, A. R. Agarrabeitia, F. Moreno, B. L. Maroto, G. Muller, M. J. Ortiz, S. de La Moya, *Chem. Eur. J.* **2015**, *21*, 13488–13500.
- [3] For compounds based on helical structures, see: a) J. E. Field, G. Muller, J. P. Riehl, D. Venkataraman, *J. Am. Chem. Soc.* **2003**, *125*, 11808–11809; b) T. Kaseyama, S. Furumi, X. Zhang, K. Tanaka, M. Takeuchi, *Angew. Chem. Int. Ed.* **2011**, *50*, 3684–3687; *Angew. Chem.* **2011**, *123*, 3768–3771; c) H. Maeda, Y. Bando, K. Shimomura, I. Yamada, M. Naito, K. Nobusawa, H. Tsumatori, T. Kawai, *J. Am. Chem. Soc.* **2011**, *133*, 9266–9269; d) Y. Haketa, Y. Bando, K. Takaishi, M. Uchiyama, A. Muranaka, M. Naito, H. Shibaguchi, T. Kawai, H. Maeda, *Angew. Chem. Int. Ed.* **2012**, *51*, 7967–7971; *Angew. Chem.* **2012**, *124*, 8091–8095; e) Y. Sawada, S. Furumi, A. Takai, M. Takeuchi, K. Noguchi, K. Tanaka, *J. Am. Chem. Soc.* **2012**, *134*, 4080–4083; f) H. Oyama, K. Nakano, T. Harada, R. Kuroda, M. Naito, K. Nobusawa, K. Nozaki, *Org. Lett.* **2013**, *15*, 2104–2107; g) H. Maeda, T. Shirai, Y. Bando, K. Takaishi, M. Uchiyama, A. Muranaka, T. Kawai, M. Naito, *Org. Lett.* **2013**, *15*, 6006–6009; h) K. Nakamura, S. Furumi, M. Takeuchi, T. Shibuya, K. Tanaka, *J. Am. Chem. Soc.* **2014**, *136*, 5555–5558; i) K. Murayama, Y. Oike, S. Furumi, M. Takeuchi, K. Noguchi, K. Tanaka, *Eur. J. Org. Chem.* **2015**, 1409; j) H. Sakai, S. Shinto, J. Kumar, Y. Araki, T. Sakanoue, T. Takenobu, T. Wada, T. Kawai, T. Hasobe, *J. Phys. Chem. C* **2015**, *119*, 13937–13947.
- [4] For compounds based on axially chiral scaffolds, see: a) T. Kawai, K. Kawamura, H. Tsumatori, M. Ishikawa, M. Naito, M. Fujiki, T. Nakashima, *ChemPhysChem* **2007**, *8*, 1465–1468; b) H. Tsumatori, T. Nakashima, T. Kawai, *Org. Lett.* **2010**, *12*, 2362–2365; c) T. Kimoto, N. Tajima, M. Fujiki, Y. Imai, *Chem. Asian J.* **2012**, *7*, 2836–2841; d) T. Amako, T. Kimoto, N. Tajima, M. Fujiki, Y. Imai, *RSC Adv.* **2013**, *3*, 6939–6944; e) T. Amako, T. Kimoto, N. Tajima, M. Fujiki, Y. Imai, *Tetrahedron* **2013**, *69*, 2753–2757; f) T. Kimoto, T. Amako, N. Tajima, R. Kuroda, M. Fujiki, Y. Imai, *Asian J. Org. Chem.* **2013**, *2*, 404–410; g) J. Kumar, T. Nakashima, H. Tsumatori, T. Kawai, *J. Phys. Chem. Lett.* **2014**, *5*, 316–321; h) Y. Kitayama, T. Amako, N. Suzuki, M. Fujiki, Y. Imai, *Org. Biomol. Chem.* **2014**, *12*, 4342–4346; i) N. Taniguchi, K. Nakabayashi, T. Harada, N. Tajima, M. Shizuma, M. Fujiki, Y. Imai, *Chem. Lett.* **2015**, *44*, 598–600.
- [5] For compounds based on central chirality, see: a) J. Kumar, T. Nakashima, H. Tsumatori, M. Mori, M. Naito, T. Kawai, *Chem. Eur. J.* **2013**, *19*, 14090–14097; b) for CPL from cryptochiral dioxolane-wired pyrenes, see: T. Amako, K. Nakabayashi, N. Suzuki, S. B. Guo, N. A. A. Rahim, T. Harada, M. Fujiki, Y. Imai, *Chem. Commun.* **2015**, *51*, 8237–8240; c) for aggregation-induced emission from L-leucine-containing tetraphenylethylene, see: H. K. Li, J. Cheng, H. Q. Deng, E. G. Zhao, B. Shen, J. W. Y. Lam, K. S. Wong, H. K. Wu, B. S. Li, B. Z. Tang, *J. Mater. Chem. C* **2015**, *3*, 2399–2404.
- [6] For reports on induced CPL from inherently achiral compounds by an axially chiral binaphthyl moiety, see: a) E. M. Sánchez-Carnerero, F. Moreno, B. L. Maroto, A. R. Agarrabeitia, M. J. Ortiz, B. G. Vo, G. Muller, S. de La Moya, *J. Am. Chem. Soc.* **2014**, *136*, 3346–3349; b) By cyclodextrins: M. Inouye, K. Hayashi, Y. Yonenaga, T. Itou, K. Fujimoto, T. Uchida, M. Iwamura, K. Nozaki, *Angew. Chem. Int. Ed.* **2014**, *53*, 14392–14396; *Angew. Chem.* **2014**, *126*, 14620–14624; c) for CPL from supramolecular gels of an achiral gelator, see: Z. C. Shen, T. Y. Wang, L. Shi, Z. Y. Tang, M. H. Liu, *Chem. Sci.* **2015**, *6*, 4267–4272.
- [7] For polymers emitting CPL in film or aggregated states, see: a) E. Peeters, M. P. T. Christiaans, R. A. J. Janssen, H. F. M. Schoo, H. P. J. M. Dekkers, E. W. Meijer, *J. Am. Chem. Soc.* **1997**, *119*, 9909–9910; b) A. Satrijo, S. C. J. Meskers, T. M. Swager, *J. Am. Chem. Soc.* **2006**, *128*, 9030–9031; c) J. N. Wilson, W. Steffen, T. G. McKenzie, G. Lieser, M. Oda, D. Neher, U. H. F. Bunz, *J. Am. Chem. Soc.* **2002**, *124*, 6830–6831; d) B. M. W. Langeveld-Voss, R. A. Janssen, M. P. T. Christiaans, S. C. J. Meskers, H. P. J. M. Dekkers, E. W. Meijer, *J. Am. Chem. Soc.* **1996**, *118*, 4908–4909; e) M. Oda, H.-G. Nothofer, G. Lieser, U. Scherf, S. C. J. Meskers, D. Neher, *Adv. Mater.* **2000**, *12*, 362–365; f) M. Oda, H.-G. Nothofer, U. Scherf, V. Šunjić, D. Richter, W. Regenstein, S. C. J. Meskers, D. Neher, *Macromolecules* **2002**, *35*, 6792–6798; g) H. Goto, K. Akagi, *Angew. Chem. Int. Ed.* **2005**, *44*, 4322–4328; *Angew. Chem.* **2005**, *117*, 4396–4402; h) H. Hayasaka, T. Miyashita, K. Tamura, K. Akagi, *Adv. Funct. Mater.* **2010**, *20*, 1243–1250; i) S. Fukao, M. Fujiki, *Macromolecules* **2009**, *42*, 8062–8067; j) J.-M. Yu, T. Sakamoto, K. Watanabe, S. Furumi, N. Tamaoki, Y. Chen, T. Nakano, *Chem. Commun.* **2011**, *47*, 3799–3801; k) K. Watanabe, T. Sakamoto, M. Taguchi, M. Fujiki, T. Nakano, *Chem. Commun.* **2011**, *47*, 10996–10998; l) T. Hirahara, M. Yoshizawa-Fujita, Y. Takeoka, M. Rikukawa, *Chem. Lett.* **2012**, *41*, 905–907; m) K. Watanabe, Y. Koyama, N. Suzuki, M. Fujiki, T. Nakano, *Polym. Chem.* **2014**, *5*, 712–717.
- [8] For polymer aggregates in optically active solvents, see: a) Y. Nakano, Y. Liu, M. Fujiki, *Polym. Chem.* **2010**, *1*, 460–469; b) Y. Kawagoe, M. Fujiki, Y. Nakano, *New J. Chem.* **2010**, *34*, 637–647.
- [9] For polymers emitting CPL in solution, see: a) Y. Morisaki, R. Hifumi, L. Lin, K. Inoshita, Y. Chujo, *Polym. Chem.* **2012**, *3*, 2727–2730; b) Y. Nagata, T. Nishikawa, M. Sugimoto, *Chem. Commun.* **2014**, *50*, 9951–9953; c) Y. Morisaki, K. Inoshita, S. Shibata, Y. Chujo, *Polym. J.* **2015**, *47*, 278–281.
- [10] For CPL by polymer–polymer complexation, see: T. Shiraki, Y. Tsuchiya, T. Noguchi, S. Tamaru, N. Suzuki, M. Taguchi, M. Fujiki, S. Shinkai, *Chem. Asian J.* **2014**, *9*, 218–222.
- [11] Optically active helicene can be used as a chiral dopant for a conjugated polymer film, resulting in induced circularly polarized electroluminescence, see: Y. Yang, R. C. da Costa, D.-M. Smilgies, A. J. Campbell, M. J. Fuchter, *Adv. Mater.* **2013**, *25*, 2624–2628.
- [12] a) F. Vögtle, *Cyclophane Chemistry: Synthesis Structures and Reactions*, Wiley, Chichester, **1993**; b) R. Gleiter, H. Hopf, *Modern Cyclophane Chemistry*, Wiley-VCH, Weinheim, **2004**; c) H. Hopf, *Angew. Chem. Int. Ed.* **2008**, *47*, 9808–9812; *Angew. Chem.* **2008**, *120*, 9954–9958.
- [13] a) Y. Morisaki, M. Gon, T. Sasamori, N. Tokitoh, Y. Chujo, *J. Am. Chem. Soc.* **2014**, *136*, 3350–3353; b) Y. Morisaki, K. Inoshita, Y. Chujo, *Chem. Eur. J.* **2014**, *20*, 8386–8390; c) M. Gon, Y. Morisaki, Y. Chujo, *J. Mater. Chem. C* **2015**, *3*, 521–529.
- [14] a) D. A. Tomalia, A. M. Naylor, W. A. Goddard III, *Angew. Chem. Int. Ed. Engl.* **1990**, *29*, 138–175; *Angew. Chem.* **1990**, *102*, 119–157; b) G. R. Newkome, C. N. Moorefield, F. Vögtle, *Dendritic Molecules: Concepts, Syntheses, Perspectives*, Wiley-VCH, Weinheim, **1996**; c) G. R. Newkome, C. N. Moorefield, F. Vögtle, *Dendrimers and Dendrons, Concepts, Syntheses, Applications*, Wiley-VCH, Weinheim, **2001**; d) J. M. J. Fréchet, D. A. Tomalia, *Dendrimers and Other Dendritic Polymers*, Wiley, Chichester, **2001**.
- [15] H.-F. Chow, K.-H. Low, K. Y. Wong, *Synlett* **2005**, 2130–2134.
- [16] Optical resolution of *rac*-4,5,15,16-tetrasubstituted [2.2]paracyclophane has already been reported, see: N. V. Vorontsova, V. I. Rozenberg, E. V.

- Sergeeva, E. V. Vorontsov, Z. A. Starikova, K. A. Lyssenko, H. Hopf, *Chem. Eur. J.* **2008**, *14*, 4600–4617.
- [17] B. König, B. Knieriem, A. de Meijere, *Chem. Ber.* **1993**, *126*, 1643–1650.
- [18] Photophysical properties of this class of X-shaped conjugated compounds with a racemic tetrasubstituted [2.2]paracyclophane skeleton have been disclosed, see: a) S. Wang, G. C. Bazan, S. Tretiak, S. Mukamel, *J. Am. Chem. Soc.* **2000**, *122*, 1289–1297; b) G. P. Bartholomew, G. C. Bazan, *Acc. Chem. Res.* **2001**, *34*, 30–39; c) G. P. Bartholomew, G. C. Bazan, *Synthesis* **2002**, 1245–1255; d) G. P. Bartholomew, G. C. Bazan, *J. Am. Chem. Soc.* **2002**, *124*, 5183–5196; e) D. S. Seferos, D. A. Banach, N. A. Alcantar, J. N. Israelachvili, G. C. Bazan, *J. Org. Chem.* **2004**, *69*, 1110–1119; f) G. P. Bartholomew, M. Rumi, S. J. K. Pond, J. W. Perry, S. Tretiak, G. C. Bazan, *J. Am. Chem. Soc.* **2004**, *126*, 11529–11542; g) J. W. Hong, H. Y. Woo, G. C. Bazan, *J. Am. Chem. Soc.* **2005**, *127*, 7435–7443; h) G. C. Bazan, *J. Org. Chem.* **2007**, *72*, 8615–8635.
- [19] a) D. A. Tomalia, H. Baker, J. Dewald, M. Hall, G. Kallos, S. Martin, J. Roeck, J. Ryder, P. Smith, *Polym. J.* **1985**, *17*, 117–132; b) G. R. Newkome, Z. Yao, G. R. Baker, V. K. Gupta, *J. Org. Chem.* **1985**, *50*, 2003–2004; c) E. Buhleier, W. Wehner, F. Vögtle, *Synthesis* **1978**, 155–158.
- [20] a) C. J. Hawker, J. M. J. Fréchet, *J. Am. Chem. Soc.* **1990**, *112*, 7638–7647; b) J. M. J. Fréchet, *Science* **1994**, *263*, 1710–1715; c) J. M. J. Fréchet, C. J. Hawker, in *Comprehensive Polymer Science Second Supplement* (Ed.: G. Allen), Pergamon, Elsevier Science, Oxford, **1996**, pp. 71–132.
- [21] a) A. Adronov, J. M. J. Fréchet, *Chem. Commun.* **2000**, 1701–1710; b) D. Liu, S. D. Feyter, M. Cotlet, A. Stefan, U.-M. Wiesler, A. Herrmann, D. Grebel-Koehler, J. Qu, K. Müllen, F. C. De Schryver, *Macromolecules* **2003**, *36*, 5918–5925; c) P. Ceroni, G. Bergamini, F. Marchioni, V. Balzani, *Prog. Polym. Sci.* **2005**, *30*, 453–473; d) Y. Zeng, Y.-Y. Li, J. Chen, G. Yang, Y. Li, *Chem. Asian J.* **2010**, *5*, 992–1005; e) A. Nantalaksakul, D. R. Reddy, C. J. Bardeen, S. Thayumanavan, *Photosynth. Res.* **2006**, *87*, 133–150; f) V. Balzani, G. Bergamini, P. Ceroni, E. Marchi, *New J. Chem.* **2011**, *35*, 1944–1954.
- [22] For examples, see: a) G. M. Stewart, M. A. Fox, *J. Am. Chem. Soc.* **1996**, *118*, 4354–4360; b) C. Devadoss, P. Bharathi, J. S. Moore, *J. Am. Chem. Soc.* **1996**, *118*, 9635–9644; c) D.-L. Jiang, T. Aida, *Nature* **1997**, *388*, 454–456; d) A. Bar-Haim, J. Klafiter, R. Kopelman, *J. Am. Chem. Soc.* **1997**, *119*, 6197–6198; e) M. R. Shortreed, S. F. Swallen, S.-Y. Shi, W. Tan, Z. Xu, C. Devadoss, J. S. Moore, R. Kopelman, *J. Phys. Chem. B* **1997**, *101*, 6318–6322; f) M. Kawa, J. M. J. Fréchet, *Chem. Mater.* **1998**, *10*, 286–296; g) D.-L. Jiang, T. Aida, *J. Am. Chem. Soc.* **1998**, *120*, 10895–10901; h) S. L. Gilat, A. Adronov, J. M. J. Fréchet, *Angew. Chem. Int. Ed.* **1999**, *38*, 1422–1427; *Angew. Chem.* **1999**, *111*, 1519–1524; i) T. Sato, D.-L. Jiang, T. Aida, *J. Am. Chem. Soc.* **1999**, *121*, 10658–10659; j) A. Adronov, S. L. Gilat, J. M. J. Fréchet, K. Ohta, F. V. R. Neuwahl, G. R. Fleming, *J. Am. Chem. Soc.* **2000**, *122*, 1175–1185; k) Z. Peng, Y. Pan, B. Xu, J. Zhang, *J. Am. Chem. Soc.* **2000**, *122*, 6619–6623; l) T. Weil, E. Reuther, K. Müllen, *Angew. Chem. Int. Ed.* **2002**, *41*, 1900–1904; *Angew. Chem.* **2002**, *114*, 1980–1984; m) J. S. Melinger, Y. Pan, V. D. Kleiman, Z. Peng, B. L. Davis, D. McMorrow, M. Lu, *J. Am. Chem. Soc.* **2002**, *124*, 12002–12012; n) M. Cotlet, T. Vosch, S. Habuchi, T. Weil, K. Müllen, J. Hofkens, F. De Schryver, *J. Am. Chem. Soc.* **2005**, *127*, 9760–9768; o) J.-L. Wang, J. Yan, Z.-M. Tang, Q. Xiao, Y. Ma, J. Pei, *J. Am. Chem. Soc.* **2008**, *130*, 9952–9962.
- [23] a) K. Sonogashira, Y. Tohda, N. Hagihara, *Tetrahedron Lett.* **1975**, *16*, 4467–4470; b) K. Sonogashira, in *Handbook of Organopalladium Chemistry for Organic Synthesis* (Ed.: E. Negishi), Wiley, New York, **2002**, pp. 493–529.
- [24] J. J. P. Stewart, *J. Comput. Chem.* **1989**, *10*, 209–220.
- [25] J. D. C. Maia, G. A. U. Carvalho, C. P. Manguera, S. R. Santana, L. A. F. Cabral, G. B. Rocha, *J. Chem. Theory Comput.* **2012**, *8*, 3072–3081.

Received: October 23, 2015

Published online on January 11, 2016



Contents lists available at ScienceDirect

Journal of Organometallic Chemistry

journal homepage: [www.elsevier.com/locate/jorganchem](http://www.elsevier.com/locate/jorganchem)

# Synthesis, characterization, and optoelectronic study of three biaryl-fused *closo-o*-carboranes and their *nido*-[C<sub>2</sub>B<sub>9</sub>]<sup>−</sup> species



Masato Tominaga, Kenta Nishino, Yasuhiro Morisaki\*, Yoshiki Chujo\*

Department of Polymer Chemistry, Graduate School of Engineering, Kyoto University, Katsura, Nishikyo-ku, Kyoto 615-8510, Japan

## ARTICLE INFO

## Article history:

Received 25 March 2015  
 Received in revised form  
 30 May 2015  
 Accepted 3 June 2015  
 Available online 20 June 2015

## Keywords:

Biaryl  
*o*-Carborane  
*nido*-Carborane  
 Charge transfer emission

## ABSTRACT

A biaryl-fused *closo-o*-carborane with a phenylthiophene moiety was synthesized and reacted with fluoride to obtain its *nido*-[C<sub>2</sub>B<sub>9</sub>]<sup>−</sup> species; the reaction with fluoride to obtain *nido*-[C<sub>2</sub>B<sub>9</sub>]<sup>−</sup> species was also performed for biphenyl- and bithiophene-fused *o*-carboranes, the synthesis of which we have previously reported. The structures and optoelectronic properties of the three carboranes and their *nido*-[C<sub>2</sub>B<sub>9</sub>]<sup>−</sup> species were experimentally and theoretically characterized. The *nido*-[C<sub>2</sub>B<sub>9</sub>]<sup>−</sup> species possessed high HOMO and LUMO energy levels because of the electron-rich anion species. They also displayed charge transfer (CT) transition bands, and efficient CT emissions were observed in the crystalline as well as solution state because of the shorter carbon–carbon bond length in the *nido*-carborane cage and suppression of the carbon–carbon bond vibration.

© 2015 Elsevier B.V. All rights reserved.

## 1. Introduction

Generally, carboranes are charge-neutral polyhedral boron–carbon cluster compounds that are thermally and chemically stabilized by delocalized three-center two-electron (3c,2e) bonds [1]. Representative carboranes are icosahedral dicarba-*closo*-dodecaboranes (*o*-, *m*-, and *p*-C<sub>2</sub>B<sub>10</sub>H<sub>12</sub>, Fig. 1A) consisting of two carbon and ten boron atoms [2]. Of these, *o*-carborane (*o*-C<sub>2</sub>B<sub>10</sub>H<sub>12</sub>), which contains a carbon–carbon bond in the cluster, has been extensively studied. Carboranes have been used in medical materials for boron neutron capture therapy (BNCT) [3], heat-resistant materials [4], and, more recently, solid-state emitting materials [5].

Our research has focused on the use of *o*-carborane as an electron-withdrawing building block for preparing various conjugated molecules and polymers. The electron-withdrawing effect of *o*-carborane depends on the dihedral angle between its carbon–carbon bond and the  $\pi$ -conjugated unit substituted at the carbon–carbon bond [6]. When the dihedral angle is approximately 90°, the molecular orbital of the  $\pi$ -conjugated plane interacts with the carbon–carbon bond in the excited states. As a result, photo-excited intramolecular charge transfer (CT) occurs from the  $\pi$ -conjugated moiety to the carborane cluster due to the resonance

electron-withdrawing effect [5g]. This is a key factor in the aggregation-induced emission (AIE) [7] observed with these materials. When the dihedral angle is close to 0°, *o*-carborane withdraws electrons inductively from the  $\pi$ -conjugated unit.

Recently, we prepared bithiophene- and biphenyl-fused *o*-carboranes (compounds **4c** [8a] and **4a** [8b], respectively), wherein the biaryl and carbon–carbon bond of the carborane cluster are fused. In these compounds, the dihedral angle between the biaryl unit and the carbon–carbon bond is 0°. Thus, the electron-deficiency and planarity of the biaryl unit are significantly improved. The highest occupied molecular orbital (HOMO) and lowest unoccupied molecular orbital (LUMO) energy levels of biaryls in **4c** and **4a** decrease by the inductive electron-withdrawing property of *o*-carborane.

Although it is chemically stable, *o*-carborane is attacked by strong nucleophiles such as fluoride and hydroxide, where one boron atom is selectively removed to form an anionic open-cage cluster termed 7,8-dicarba-*nido*-undecaborate (Fig. 1B), or, more simply, *nido*-carborane [9]. *nido*-Carborane is a known anionic cluster; however, there are only a few examples of investigations into the combination of *nido*-carborane species with  $\pi$ -conjugated moieties [5b,10] and luminescent *nido*-carborane-based compounds [11].

In this study, we prepared an asymmetric biaryl-fused *closo-o*-carborane containing phenylthiophene. This carborane **4b**, and **4a** and **4c** prepared previously, were reacted with fluoride to obtain their *nido*-[C<sub>2</sub>B<sub>9</sub>]<sup>−</sup> species. Their synthesis and optoelectronic properties are reported in detail.

\* Corresponding authors.

E-mail addresses: [yomo@chujo.synchem.kyoto-u.ac.jp](mailto:yomo@chujo.synchem.kyoto-u.ac.jp) (Y. Morisaki), [chujo@chujo.synchem.kyoto-u.ac.jp](mailto:chujo@chujo.synchem.kyoto-u.ac.jp) (Y. Chujo).

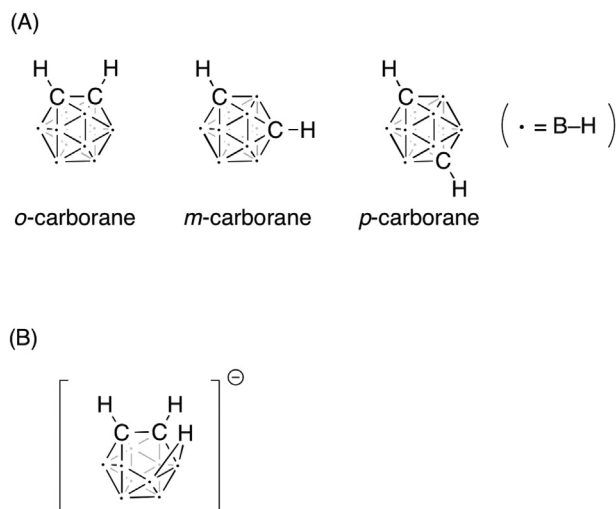


Fig. 1. Structures of (A) *o*-, *m*-, and *p*-carboranes, and (B) *nido-o*-carborane.

## 2. Results and discussion

Phenylthiophene-fused *o*-carborane **4b** was prepared, as shown in Scheme 1. Treatment of **1** with decaborane ( $B_{10}H_{14}$ , **2**) in the presence of  $AgNO_3/CH_3CN$  [12] afforded *o*-carborane **3** in 43% yield. Bromine–lithium exchange of **3** using *n*-BuLi proceeded to form a dilithiated species. Successive reactions with  $ZnBr_2$  and  $CuCl_2$  in situ afforded phenylthiophene-fused *o*-carborane **4b** in 22% isolated yield. The structure was confirmed by  $^1H$ ,  $^{13}C$ , and  $^{11}B$  NMR spectroscopy, high-resolution mass spectrometry, and X-ray crystallography. Although the phenyl and thiophene units are disordered, the crystal structure of **4b** revealed the high planarity of the phenylthiophene moiety, as shown in Figure S6 in the Supporting Information (SI).

The obtained compound **4b** and phenylthiophene as a model compound were characterized by density functional theory (DFT) calculations. The molecular orbitals of **4b** and phenylthiophene are shown in Fig. 2. The HOMO and LUMO of **4b** lie mainly on the phenylthiophene moiety, and are nearly identical to those of phenylthiophene. Intramolecular CT between the benzene and thiophene rings is not observed in either compound. The HOMO/LUMO energy band gaps in **4b** and phenylthiophene are also identical, and their values are estimated to be 4.46 and 4.43 eV, respectively. The HOMO/LUMO energy levels of **4b** are lower than those of phenylthiophene because of the electron-withdrawing character of *o*-

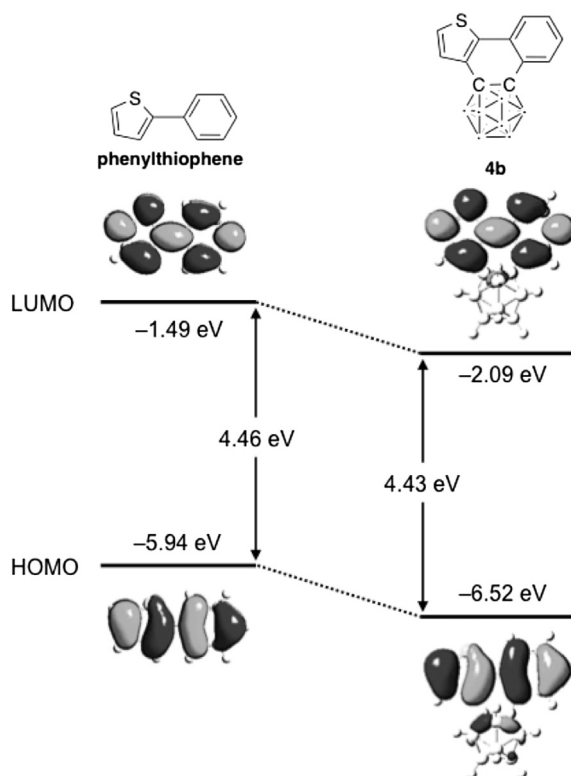
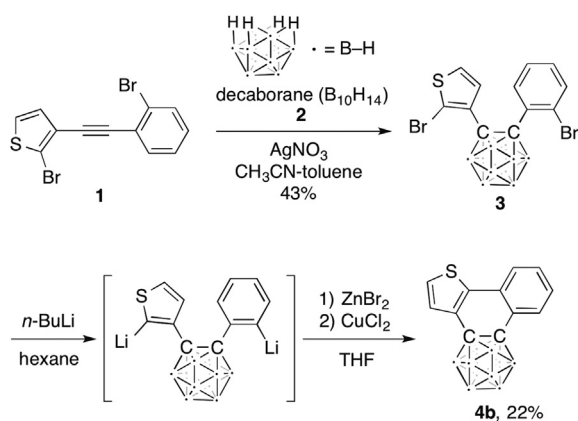


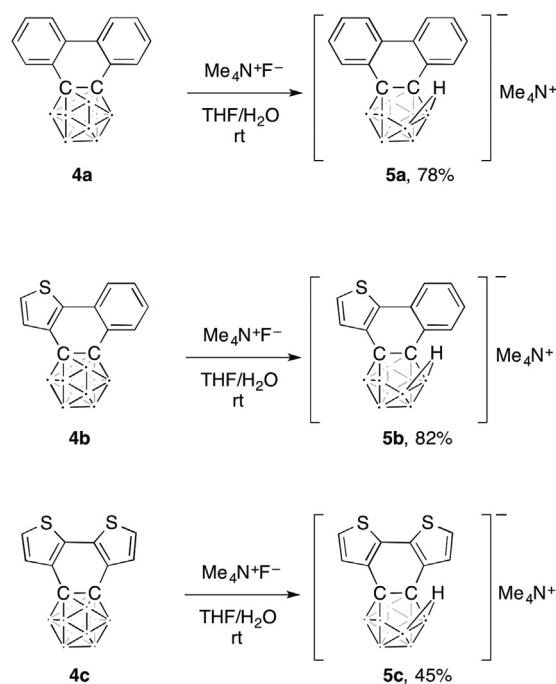
Fig. 2. Structures and molecular orbital diagrams for HOMO and LUMO of phenylthiophene and **4b** (B3LYP/6-31 + G(d,p)//B3LYP/6-31 + G(d,p)).

carborane. These phenomena were also observed in bithiophene- and biphenyl-fused *o*-carboranes, **4a** [8b] and **4c** [8a].

Biaryl-fused carboranes **4a–c** were reacted with fluoride using  $Me_4NF$ , as shown in Scheme 2. The reactions proceeded smoothly at room temperature, and the corresponding biaryl-fused *nido*-



Scheme 1. Synthesis of **4b**.



Scheme 2. Synthesis of **5a–c**.

carboranes **5a–c** were obtained in 78%, 82%, and 45% isolated yields, respectively. *nido*-Carboranes **5a–c** are air- and moisture-stable compounds and can be easily handled as solids and in solution.

All compounds were characterized by  $^1\text{H}$ ,  $^{13}\text{C}$ , and  $^{11}\text{B}$  NMR spectroscopy and high-resolution mass analysis. Suitable single crystals of the tetramethylammonium ( $\text{Me}_4\text{N}^+$ ) salts for X-ray crystallography could not be obtained; however, the tetrabutylammonium ( $\text{Bu}_4\text{N}^+$ ) salt of **5a**, which was prepared by the reaction of **4a** with  $\text{Bu}_4\text{NF}$  instead of  $\text{Me}_4\text{NF}$ , afforded suitable single crystals. Fig. 3 (and Figure S7 in the SI) show the molecular structure of **5a** ( $\text{Bu}_4\text{N}^+$  is omitted for clarity) and confirmed that the boron atom at the 3-position of *o*-carborane was removed to form the open-cage cluster. The dihedral angle between benzene rings was found to be  $179.5(2)^\circ$ ; thus, the planarity of the biphenyl skeleton is maintained. The carbon–carbon bond length of the *nido*-carborane cage is  $1.563(3)$  Å, which is shorter than the unusual carbon–carbon bond length of **4a** ( $1.643(2)$  Å) [8b]. One of the hydrogen atoms in the *nido*-carborane cage is bridged between two boron atoms. In the  $^1\text{H}$  NMR spectrum of **5a**, the bridged hydrogen signal appears around  $-2.7$  ppm as a very broad signal (Figure S3A in the SI). The bridged hydrogen signals of **5b** and **5c** are also observed around  $-3.0$  ppm (Figures S4A and S5A, respectively).

The simulated DFT molecular orbitals of **5a–c** are shown in Fig. 4. Their LUMOs are almost identical to those of **4a–c**, and are mainly located on the biaryl moieties. Conversely, the HOMOs of the *nido*- $[\text{C}_2\text{B}_9]^-$  species are quite different from those of **4a–c**, and are located on the entire molecule. Both the HOMO and LUMO energy levels of the *nido*- $[\text{C}_2\text{B}_9]^-$  species are higher than those of **4a–c** due

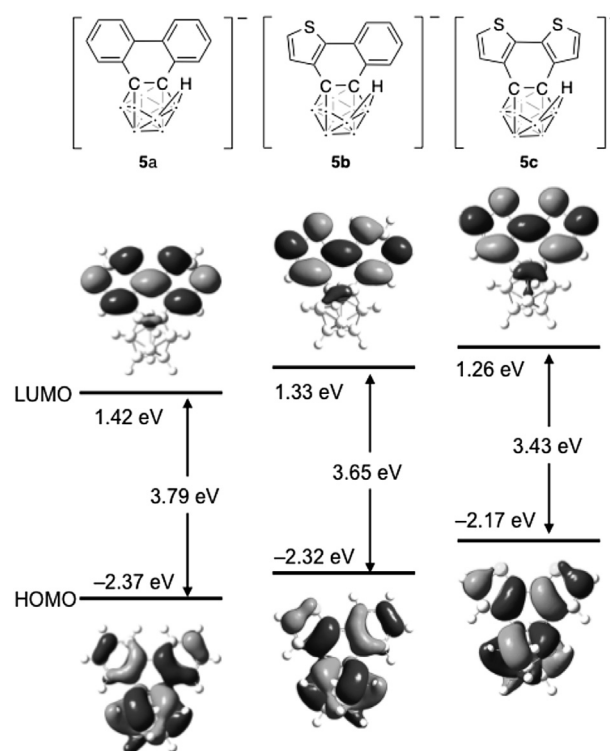
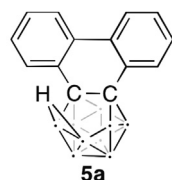


Fig. 4. Structures and molecular orbital diagrams for HOMO and LUMO of **5a–c** (B3LYP/6-31 + G(d,p)//B3LYP/6-31 + G(d,p)).



Front view

Side view

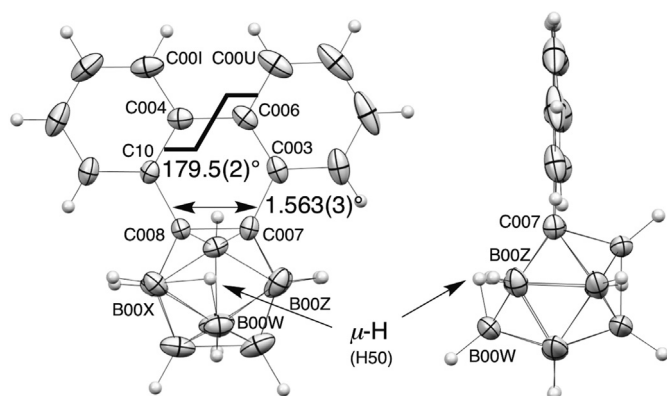


Fig. 3. X-ray crystal structure of **5a** with thermal ellipsoids drawn at the 50% probability level.  $\text{NBu}_4^+$  is omitted for clarity. Selected bond length (Å): C007–C008 =  $1.563(3)$ , C008–C10 =  $1.480(3)$ , C10–C004 =  $1.401(3)$ , C004–C006 =  $1.477(3)$ , C006–C003 =  $1.400(3)$ , C003–C007 =  $1.484(3)$ , C008–B00X =  $1.632(3)$ , C007–B00Z =  $1.623(3)$ , B00X–B00W =  $1.835(4)$ , B00W–B00Z =  $1.810(4)$ , H50–B00X =  $1.12(3)$ , and H50–B00W =  $1.13(4)$ . Selected bond angles ( $^\circ$ ): C007–C008–C10 =  $117.8(2)$ , C008–C10–C004 =  $121.8(2)$ , C10–C004–C006 =  $120.5(2)$ , C004–C006–C003 =  $121.1(2)$ , C006–C003–C007 =  $122.2(2)$ , C003–C007–C008 =  $116.4(2)$ , C007–C008–B00X =  $110.9(2)$ , C008–B00X–B00W =  $107.2(2)$ , B00X–B00W–B00Z =  $101.1(2)$ , B00W–B00Z–C007 =  $106.4(2)$ , and B00Z–C007–C008 =  $114.3(2)$ .

to the electron-rich anion species. The low HOMO/LUMO levels of biaryl-fused *o*-carboranes and the higher HOMO/LUMO levels of the *nido*- $[\text{C}_2\text{B}_9]^-$  species are supported by the experimental data. As a representative example, cyclic voltammetry of **4b** in solution exhibits a reduction peak with an onset value of  $-2.18$  V (vs. ferrocene/ferrocenium), while oxidation peaks are not observed (Figure S8 in the SI). On the other hand, **5b** is readily oxidized, and the peak onset is observed at  $0.22$  V (vs. ferrocene/ferrocenium), according to the cyclic voltammogram.

The optical properties of biaryls, biaryl-fused *o*-carboranes (**4a–c**), and the *nido*- $[\text{C}_2\text{B}_9]^-$  species (**5a–c**) were evaluated by UV–vis absorption spectroscopy and photoluminescence (PL) spectroscopy in dilute THF solutions ( $1.0 \times 10^{-5}$  M), and the optical data are summarized in Table 1. Fig. 5A shows the absorption (left) and PL spectra of biaryls, and Fig. 5B shows those of biaryl-fused *o*-carboranes (**4a–c**). The absorption spectra of biaryls are broad and featureless, while those of **4a–c** exhibit clear vibrational structures. In all cases, the absorption bands were assigned to the  $\pi$ - $\pi^*$  bands

Table 1  
Results of optical properties.<sup>a</sup>

	$\lambda_{\text{abs,max}}/\text{nm}$	$\epsilon/10^4 \text{ M}^{-1}\text{cm}^{-1}$	$E_g^b/\text{eV}$	$\lambda_{\text{PL,max}}/\text{nm}$	$\Phi_{\text{PL}}^c$
biphenyl	253	1.67	4.40	312	<0.01
<b>4a</b>	276	2.62	4.41	318	<0.01
<b>5a</b>	260, 346	2.72, 0.25	3.26	444	0.15
phenylthiophene	286	1.15	3.89	345	<0.01
<b>4b</b>	301	1.69	3.85	341	0.01
<b>5b</b>	269, 354	1.46, 0.34	3.18	450	0.25
bithiophene	305	1.14	3.60	366	0.11
<b>4c</b>	323	1.49	3.56	365	0.01
<b>5c</b>	283, 372	1.24, 0.46	3.01	459	0.12

<sup>a</sup> In THF solution ( $1.0 \times 10^{-5}$  M). PL spectra were obtained by excitation upon the  $\lambda_{\text{abs,max}}$ .

<sup>b</sup> Bandgap energy calculated from the absorption edge.

<sup>c</sup> Absolute PL quantum efficiency.

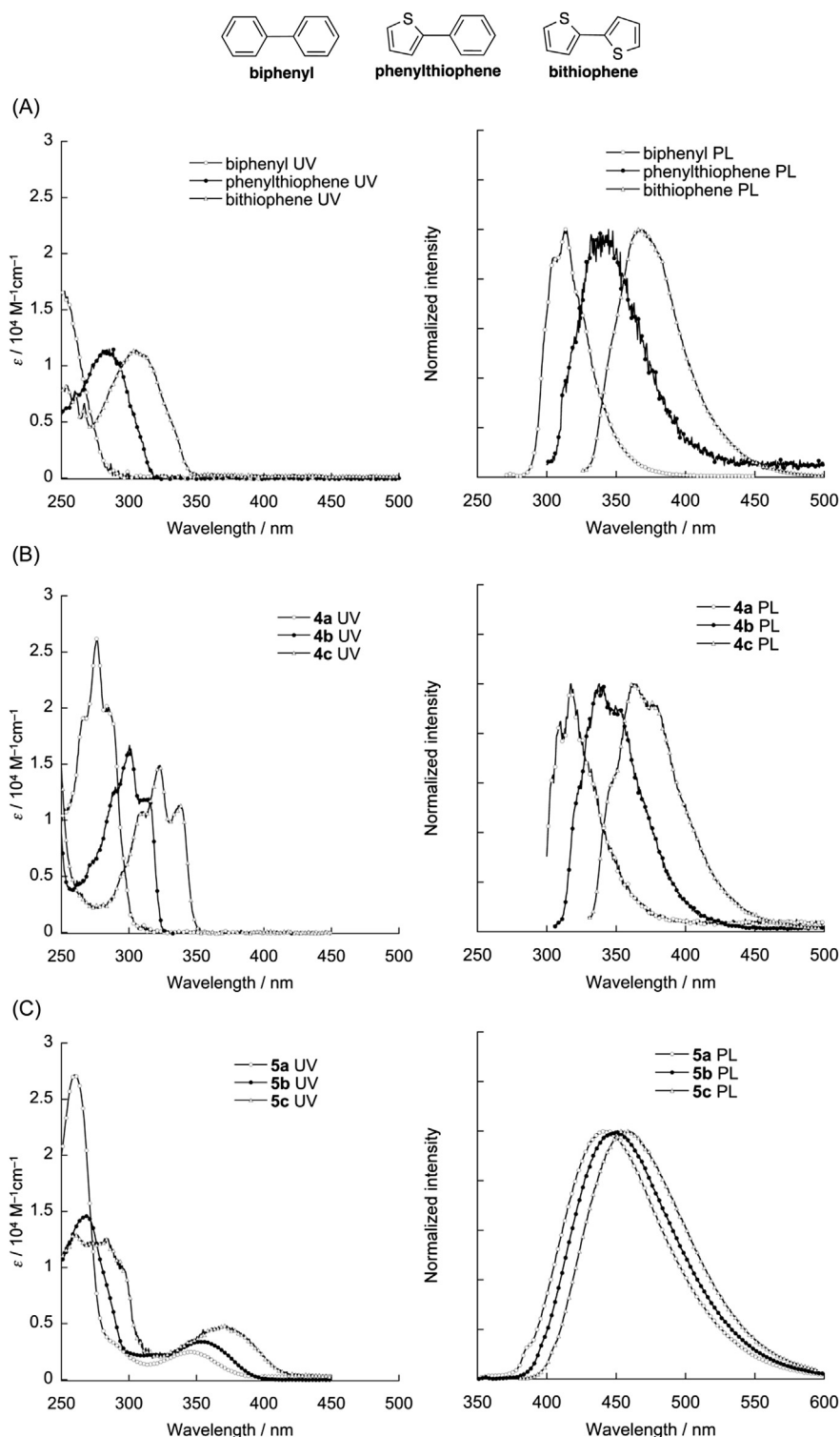


Fig. 5. UV-vis absorption and PL spectra of (A) biaryls, (B) 4a-c, and (C) 5a-c in dilute THF solutions ( $1.0 \times 10^{-5}$  M). Samples were excited at their  $\lambda_{\text{max}}$ .

of the biaryl moieties. Their peak tops and edges were bathochromically shifted. These results arise from the high planarity of the biaryl moiety by fixation with the *o*-carborane unit.

The PL spectra of biaryls and biaryl-fused *o*-carboranes (4a-c) are shown in Fig. 5A and B. Unlike the absorption spectrum, the PL spectrum of the biaryl is identical to that of the biaryl-fused *o*-carborane. In the ground state, two aryl units of the biaryl rotate

freely and are twisted, while they become coplanar in the excited state because of the contribution from the quinoidal structure, as illustrated in Figure S9 in the SI. Thus, the emitting species of the free biaryl and biaryl-fused *o*-carboranes are similar, leading to the identical PL spectra.

Fig. 5C shows the absorption and PL spectra of the *nido*-[C<sub>2</sub>B<sub>9</sub>]<sup>-</sup> species. In the absorption spectra, broad bands with small molar

absorption coefficients appear in the longer wavelength region. These bands correspond to the HOMO/LUMO CT transition bands, as shown in Fig. 4. In addition, the narrower band gaps of the *nido*-[C<sub>2</sub>B<sub>9</sub>]<sup>−</sup> species compared to those of the biaryl-fused *o*-carboranes are congruent with the DFT result.

The broad and featureless PL spectra of **5a–c** were obtained by excitation around broad absorption bands. Although no significant solvatochromic effect was observed (Figure S10 in the SI), the Stokes shift values in polar solvents were large. For example, in the case of **5b**, the Stokes shift value is 619 cm<sup>−1</sup> in THF, whereas it is 708 cm<sup>−1</sup> in CH<sub>3</sub>CN. Therefore, we assign the emission of the *nido*-[C<sub>2</sub>B<sub>9</sub>]<sup>−</sup> species to the CT emission. The absolute PL quantum efficiencies ( $\Phi_{\text{PL}}$ ) of **5a–c** were calculated to be 0.15, 0.25, and 0.12, respectively. The  $\Phi_{\text{PL}}$  values are higher than those of **4a–c** by around 0.01. In addition, the emissions of **5a–c** crystals are enhanced, with  $\Phi_{\text{PL}}$  values of 0.40, 0.63, and 0.21, respectively. Their PL spectra in the crystalline states are shown in Figure S11 in the SI. Generally, emission of the *o*-carborane compounds depends on the motion of the carbon–carbon bond in the *o*-carborane cluster, and freezing the carbon–carbon bond vibration causes efficient emission. According to X-ray crystallography, the carbon–carbon bond length of the *nido*-[C<sub>2</sub>B<sub>9</sub>]<sup>−</sup> species was much shorter than the unusual carbon–carbon bond length of typical *o*-carborane compounds, leading to the efficient emission behavior of *nido*-[C<sub>2</sub>B<sub>9</sub>]<sup>−</sup> species in both solution and crystalline states.

### 3. Conclusion

Phenylthiophene-fused *closo-o*-carborane was synthesized, and its electronic state was investigated by DFT calculations. The optical properties were discussed by comparison with those of biphenyl-fused and bithiophene-fused *o*-carboranes. These three kinds of biaryl-fused *o*-carboranes were reacted with fluoride to yield the *nido*-[C<sub>2</sub>B<sub>9</sub>]<sup>−</sup> species, the structures and optoelectronic properties of which were fully characterized. The *nido*-[C<sub>2</sub>B<sub>9</sub>]<sup>−</sup> species possess high HOMO and LUMO energy levels because of the electron-rich anion species. In the absorption spectra of the *nido*-[C<sub>2</sub>B<sub>9</sub>]<sup>−</sup> species, broad bands with small molar absorption coefficients were observed, and they were assigned by the CT transition. Efficient emissions were observed in the crystalline state as well as in the solutions due to the shorter carbon–carbon bond length in the *nido*-carborane cluster and suppression of the carbon–carbon bond vibration. Further investigation of the synthesis and properties of various *nido*-carborane-based conjugated molecules is currently underway.

## 4. Experimental section

### 4.1. General

<sup>1</sup>H, <sup>13</sup>C, and <sup>11</sup>B NMR spectra were recorded on a JEOL JNM-EX400 instrument at 400, 100, and 128 MHz, respectively. The <sup>1</sup>H and <sup>13</sup>C chemical shift values were expressed relative to Me<sub>4</sub>Si as an internal standard. The <sup>11</sup>B chemical shift values were expressed relative to BF<sub>3</sub>·Et<sub>2</sub>O as an external standard. High-resolution mass spectra (HRMS) were obtained on a Thermo Fisher Scientific EXACTIVE spectrometer for atmospheric pressure chemical ionization (APCI), JEOL JMS-MS700 spectrometer for electron impact ionization (EI), and JEOL JMS-T100CS spectrometer for electrospray ionization (ESI). Analytical thin-layer chromatography (TLC) was performed with silica gel 60 Merck F254 plates. Column chromatography was performed with Wakogel C-300 silica gel. UV–vis absorption spectra were obtained on a SHIMADZU UV3600 spectrophotometer. Photoluminescence (PL) spectra were obtained on a Horiba FluoroMax-4 luminescence spectrometer; absolute PL

quantum efficiencies ( $\Phi_{\text{PL}}$ ) were determined using a Horiba FL-3018 Integrating Sphere. Fluorescence lifetime measurement was performed on a Horiba FluoreCube spectrofluorometer system; excitation was carried out using a UV diode laser (NanoLED 375 nm). Cyclic voltammetry (CV) was carried out on a BAS CV-50W electrochemical analyzer in DMF containing 0.1 M of sample and 0.1 M of Bu<sub>4</sub>NClO<sub>4</sub> with a glassy carbon working electrode, a 4bouncer electrode, an Ag/AgCl (Ag/Ag<sup>+</sup>) reference electrode, and a ferrocene/ferrocenium (Fc/Fc<sup>+</sup>) external reference.

### 4.2. Materials

THF was purchased and purified by the GlassContour solvent purification system. CHCl<sub>3</sub>, toluene, and acetonitrile were obtained commercially and used without purification. Decaborane (**2**), AgNO<sub>3</sub>, *n*-BuLi (1.6 M hexane solution), CuCl<sub>2</sub>, ZnBr<sub>2</sub>, and Me<sub>4</sub>NF were obtained commercially, and used without further purification. 2-Bromo-3-(2-bromophenylethynyl)thiophene (**1**) [13], **4a** [8b], and **4c** [8a] were prepared as described in the literature. All reactions were performed under Ar atmosphere.

### 4.3. Synthesis of **3**

The mixture of **1** (2.86 g, 8.36 mmol), decaborane **2** (1.17 g, 9.53 mmol), and AgNO<sub>3</sub> (71.1 mg, 0.42 mmol) was dissolved in dry toluene (80 mL) at room temperature under Ar atmosphere. Acetonitrile (1.5 mL) was added, and the mixture was refluxed for 12 h. After cooling to room temperature, the solution was separated by decantation and evaporated. The crude residue was purified by silica gel column chromatography with hexane as an eluent. Recrystallization from CHCl<sub>3</sub> and MeOH afforded compound **3** as a colorless crystal (1.63 g, 3.53 mmol, 43%).

$R_f = 0.20$  (hexane). <sup>1</sup>H NMR (CDCl<sub>3</sub>, 400 MHz)  $\delta = 1.6$ – $4.9$  (m, 10H), 6.89 (d, 1H,  $J = 5.9$  Hz), 6.95 (d, 1H,  $J = 6.1$  Hz), 7.0–7.2 (m, 2H), 7.60 (dd, 1H,  $J = 7.7, 1.6$  Hz), 7.79 (dd, 1H,  $J = 8.1, 1.5$  Hz) ppm. <sup>13</sup>C NMR (CDCl<sub>3</sub>, 100 MHz)  $\delta = 83.7, 87.6, 116.7, 124.9, 125.8, 127.7, 127.9, 128.3, 131.4, 131.6, 135.4, 137.8$  ppm. <sup>11</sup>B NMR (CDCl<sub>3</sub>, 400 MHz)  $\delta = -10.56, -9.39, -2.74, -2.26, -1.67, -1.08$  ppm. HRMS (EI) calcd. for C<sub>12</sub>H<sub>16</sub>B<sub>10</sub>Br<sub>2</sub>S [M]<sup>+</sup>: 460.0270, found 461.0270. Anal. calcd. for C<sub>12</sub>H<sub>16</sub>B<sub>10</sub>Br<sub>2</sub>S: C 31.32H 3.50, found: C 31.08H 3.53.

### 4.4. Synthesis of **4b**

A solution of **3** (230 mg, 0.500 mmol) in THF (2.5 mL) was added slowly to a stirred solution of *n*-BuLi (1.60 M hexane solution 625  $\mu$ L) under Ar atmosphere at  $-78$  °C by a syringe, and the mixture was stirred at  $-78$  °C for 45 min. A solution of anhydrous ZnBr<sub>2</sub> (90.1 mg, 0.400 mmol) in THF (10.0 mL) was added dropwise to the stirred solution under Ar atmosphere at  $-78$  °C by a syringe, and the mixture was stirred at  $-78$  °C for 75 min. Anhydrous CuCl<sub>2</sub> (199 mg, 1.500 mmol) was added in one portion with vigorous stirring, and the mixture was stirred at  $-78$  °C for 2 h. Then, the reaction mixture was allowed to slowly warm to room temperature. After stirring at room temperature for 20 h, the reaction was quenched by the addition of 1 N HCl aq., and the product was extracted with CHCl<sub>3</sub>. The CHCl<sub>3</sub> solution was washed with aqueous HCl, and it was dried over MgSO<sub>4</sub>. MgSO<sub>4</sub> was removed, and the solvent was evaporated. The residue was purified by silica gel column chromatography with hexane as an eluent. Recrystallization from hexane provided **4b** (32.7 mg, 0.11 mmol, 22%) as a colorless crystal.

$R_f = 0.39$  (hexane). <sup>1</sup>H NMR (CDCl<sub>3</sub>, 400 MHz)  $\delta = 1.1$ – $3.6$  (m, 10H), 7.19 (dd, 2H,  $J = 5.4, 2.7$  Hz), 7.33 (dd, 1H,  $J = 5.1, 0.5$  Hz), 7.3–7.5 (m, 2H), 7.63 (d, 1H,  $J = 3.9$  Hz), 7.71 (d, 1H,  $J = 7.8$  Hz) ppm. <sup>13</sup>C NMR (CDCl<sub>3</sub>, 100 MHz)  $\delta = 71.1, 74.0, 124.2, 125.2, 125.4, 126.9,$

128.2, 128.3, 129.1, 129.5, 131.8, 133.2 ppm.  $^{11}\text{B}$  NMR ( $\text{CDCl}_3$ , 400 MHz)  $\delta$  –10.86, –9.88, –8.61, –7.53, –6.46, –5.48 ppm. HRMS (EI) calcd. for  $\text{C}_{12}\text{H}_{16}\text{B}_{10}\text{S}$   $[\text{M}]^+$ : 302.1903, found 300.1977. Anal. calcd. for  $\text{C}_{12}\text{H}_{16}\text{B}_{10}\text{S}$ : C 47.98H 5.37, found: C 47.01H 5.43.

#### 4.5. Synthesis of **5a-c**

Typical procedure is as follows. Aqueous  $\text{Me}_4\text{NF}$  was added to a THF solution of **4**. The mixture was stirred at room temperature for 7 h, and then the product was extracted with  $\text{CH}_2\text{Cl}_2$ . The  $\text{CH}_2\text{Cl}_2$  solution was dried over  $\text{MgSO}_4$ .  $\text{MgSO}_4$  was removed, and the solvent was evaporated. Compound **5** (13.9 mg, 0.039 mmol, 78%) was obtained by reprecipitation from THF and hexane.

**5a** (13.9 mg, 0.039 mmol, 78%) was obtained from aqueous  $\text{Me}_4\text{NF}$  (41.9 mg, 0.253 mmol) and THF (3 mL) solution of **4a** (14.7 mg, 0.050 mmol).

$^1\text{H}$  NMR ( $\text{DMSO}-d_6$ , 400 MHz)  $\delta$  = –3.2 to –2.2 (br, 1H), 0.5–3.80 (br, 9H), 3.09 (s, 12H), 7.10 (s, 4H), 7.27 (d, 2H,  $J$  = 6.3 Hz), 7.89 (d, 2H,  $J$  = 6.1 Hz) ppm.  $^{13}\text{C}$  NMR ( $\text{DMSO}-d_6$ , 100 MHz)  $\delta$  = 54.4, 121.8, 124.8, 127.0, 127.1, 127.3, 140.3 ppm.  $^{11}\text{B}$  NMR ( $\text{DMSO}-d_6$ , 400 MHz)  $\delta$  = –37.2, –36.3, –32.3, –31.7, –19.1, –18.0, –16.7, –7.3, –6.5 ppm. HRMS (ESI) calcd. for  $\text{C}_{12}\text{H}_{16}\text{B}_9$   $[\text{M}]^-$ : 285.2241, found 285.2249.

**5b** (15.0 mg, 0.041 mmol, 82%) was obtained from aqueous  $\text{Me}_4\text{NF}$  (41.8 mg, 0.253 mmol) and THF (3 mL) solution of **4b** (15.1 mg, 0.050 mmol).

$^1\text{H}$  NMR ( $\text{DMSO}-d_6$ , 400 MHz)  $\delta$  = –3.4 to –2.7 (br, 1H), 0.0–2.9 (br, 9H), 3.09 (s, 12H), 6.80 (d, 1H,  $J$  = 5.1 Hz), 7.02–7.08 (m, 2H), 7.20–7.27 (m, 3H) ppm.  $^{13}\text{C}$  NMR ( $\text{DMSO}-d_6$ , 100 MHz)  $\delta$  = 54.4, 122, 123.1, 123.2, 125.0, 126.4, 126.4, 127.3, 128.4, 139.3, 141.6 ppm.  $^{11}\text{B}$  NMR ( $\text{DMSO}-d_6$ , 400 MHz)  $\delta$  = –37.9, –36.9, –32.2, –31.5, –22.0, –20.9, –19.7, –18.6, –16.6, –15.8, –8.1, –7.4 ppm. HRMS (ESI) calcd. for  $\text{C}_{12}\text{H}_{16}\text{B}_9\text{S}$   $[\text{M}]^-$ : 291.1805, found 291.1818.

**5c** (4.2 mg, 0.011 mmol, 45%) was obtained from aqueous  $\text{Me}_4\text{NF}$  (20.2 mg, 0.122 mmol) and THF (1.5 mL) solution of **4c** (7.2 mg, 0.024 mmol).

$^1\text{H}$  NMR ( $\text{DMSO}-d_6$ , 400 MHz)  $\delta$  = –3.8 to –3.0 (br, 1H), –0.6–2.8 (br, 9H) 3.09 (s, 12H), 6.81 (d, 1H,  $J$  = 4.9 Hz), 7.19 (d, 2H,  $J$  = 5.1 Hz) ppm.  $^{13}\text{C}$  NMR ( $\text{DMSO}-d_6$ , 100 MHz)  $\delta$  = 54.4, 121.2, 124.0, 126.7, 140.6 ppm.  $^{11}\text{B}$  NMR ( $\text{DMSO}-d_6$ , 400 MHz)  $\delta$  = –38.9, –37.9, –32.2, –31.4, –19.6, –18.6, –17.2, –8.7, –7.8 ppm.

$^1\text{H}$  NMR chemical shift values of **5a-c** are summarized in Table S1 in Supporting Information.

#### 4.6. X-ray crystallographic studies of **4b** and **5a**

Intensity data were collected on a Rigaku RAXIS RAPID imaging plate area detector with graphite monochromated  $\text{MoK}\alpha$  radiation ( $\lambda$  = 0.71069 Å). The structures were solved by direct method (SIR97) [14] and refined by full-matrix least-squares procedures based on  $F^2$  (SHELX-97) [15]. CCDC deposit numbers of **4b** and **5a** are 1054985 and 1054939, respectively. Crystallographic data and ORTEP drawings are shown in Supporting Information.

#### Acknowledgments

This work was supported by a Grant-in-Aid for Scientific Research on Innovative Areas “New Polymeric Materials Based on Element-Blocks” (No. 24102013) from the Ministry of Education, Culture, Sports, Science and Technology, Japan.

#### Appendix A. Supplementary data

Supplementary data related to this article can be found at <http://dx.doi.org/10.1016/j.jorganchem.2015.06.002>.

#### References

- [1] (a) R.N. Grimes, *Carboranes*, second ed., Academic Press, New York, 2011; (b) B. Stibr, *Chem. Rev.* 92 (1992) 225; (c) J. Plešek, *Chem. Rev.* 92 (1992) 269.
- [2] (a) *Icosahedral carboranes: 1,2-C<sub>2</sub>B<sub>10</sub>H<sub>12</sub>* (Chapter 9), in: Russell N. Grimes (Ed.), *Carboranes*, Academic Press, New York, 2011, pp. 301–540; (b) B.P. Dash, R. Satapathy, J.A. Maguireb, N.S. Hosmane, in: N.S. Hosmane (Ed.), *Boron Science: New Technologies and Applications*, CRC Press, Boca Raton, 2011, pp. 675–699; (c) V.I. Bregadze, *Chem. Rev.* 92 (1992) 209; (d) A. González-Campo, E.J. Juárez-Pérez, C. Viñas, B. Boury, R. Sillanpää, R. Kivekäs, R. Núñez, *Macromolecules* 41 (2008) 8458; (e) F. Issa, M. Kassiou, L.M. Rendina, *Chem. Rev.* 111 (2011) 5701; (f) B.P. Dash, R. Satapathy, J.A. Maguireb, N.S. Hosmane, *New. J. Chem.* 35 (2011) 1955.
- [3] (a) *Carboranes in medicine* (Chapter 16), in: Russell N. Grimes (Ed.), *Carboranes*, Academic Press, New York, 2011, pp. 1053–1082; (b) M.F. Hawthorne, *Angew. Chem. Int. Ed.* 32 (1993) 950; (c) M.C. Parrott, E.B. Marchington, J.F. Valliant, A. Adronov, *J. Am. Chem. Soc.* 127 (2005) 127; (d) Y.C. Simon, C. Ohm, M.J. Zimny, E.B. Coughlin, *Macromolecules* 40 (2007) 5628.
- [4] (a) S.Y. Lu, I. Hamerton, *Prog. Polym. Sci.* 27 (2002) 1661; (b) H.M. Colquhoun, D.F. Lewis, J.A. Daniels, P.L. Herbertson, J.A.H. MacBride, I.R. Stephenson, K. Wade, *Polymer* 38 (1997) 2447; (c) R.A. Sundar, T.M. Keller, *J. Polym. Sci. Part A Polym. Chem.* 35 (1997) 2387; (d) D.Y. Son, T.M. Keller, *J. Polym. Sci. Part A Polym. Chem.* 33 (1995) 2969; (e) S. Papetti, B.B. Schaeffer, A.P. Gray, T.L. Heying, *J. Polym. Sci. Part A-1* 4 (1966) 1623.
- [5] (a) K. Kokado, Y. Chujo, *Macromolecules* 42 (2009) 1418; (b) J.J. Peterson, M. Werre, Y.C. Simon, E.B. Coughlin, K.R. Carter, *Macromolecules* 42 (2009) 8594; (c) K. Kokado, Y. Chujo, *J. Org. Chem.* 76 (2010) 316; (d) F. Lerouge, A. Ferrer-Ugalde, C. Viñas, F. Teixidor, A. Abreu, E. Xochitiotzi, N. Farfán, R. Santillan, R. Sillanpää, R. Núñez, *Dalton Trans.* 40 (2011) 7541; (e) B.P. Dash, R. Satapathy, E.R. Gaillard, K.M. Norton, J.A. Maguire, N. Chug, N.S. Hosmane, *Inorg. Chem.* 50 (2011) 5485; (f) A.R. Davis, J.J. Peterson, K.R. Carter, *ACS Macro Lett.* 1 (2012) 469; (g) K.-R. Wee, W.-S. Han, D.W. Cho, S. Kwon, C. Pac, S.O. Kang, *Angew. Chem. Int. Ed.* 51 (2012) 2677; (h) K.-R. Wee, Y.-J. Cho, S. Jeong, S. Kwon, J.-D. Lee, I.-H. Suh, S.O. Kang, *J. Am. Chem. Soc.* 134 (2012) 17982; (i) H.J. Bae, H. Kim, K.M. Lee, T. Kim, Y.S. Lee, Y. Do, M.H. Lee, *Dalton Trans.* 43 (2014) 4978; (j) M. Tominaga, H. Naito, Y. Morisaki, Y. Chujo, *Asian J. Org. Chem.* 3 (2014) 624; (k) M. Tominaga, H. Naito, Y. Morisaki, Y. Chujo, *New. J. Chem.* 38 (2014) 5686; (l) H. Naito, Y. Morisaki, Y. Chujo, *Angew. Chem. Int. Ed.* 54 (2015) 5084.
- [6] (a) L. Weber, J. Kahlert, R. Brockhinke, L. Böhling, A. Brockhinke, H.-G. Stammer, B. Neumann, R.A. Harder, M.A. Fox, *Chem. Eur. J.* 18 (2012) 8347; (b) L. Weber, J. Kahlert, L. Böhling, A. Brockhinke, H.-G. Stammer, B. Neumann, R.A. Harder, P.J. Low, M.A. Fox, *Dalton Trans.* 42 (2013) 2266.
- [7] (a) A. Qin, B.Z. Tang (Eds.), *Aggregation-induced Emission: Fundamentals*, Wiley, New York, 2013; (b) A. Qin, B.Z. Tang (Eds.), *Aggregation-induced Emission: Applications*, Wiley, New York, 2013; (c) J. Luo, Z. Xie, J.W.Y. Lam, L. Cheng, H. Chen, C. Qiu, H.S. Kwok, X. Zhan, Y. Liu, D. Zhu, B.Z. Tang, *Chem. Commun.* (2001) 1740.
- [8] (a) Y. Morisaki, M. Tominaga, Y. Chujo, *Chem.–Eur. J.* 18 (2012) 11251; (b) Y. Morisaki, M. Tominaga, T. Ochiai, Y. Chujo, *Chem.–Asian J.* 9 (2014) 1247.
- [9] (a) M.A. Fox, W.R. Gill, P.L. Herbertson, J.A.H. MacBride, K. Wade, *H.M. Colquhoun, Polyhedron* 15 (1996) 565; (b) *Eleven-vertex carboranes* (Chapter 7), in: Russell N. Grimes (Ed.), *Carboranes*, Academic Press, New York, 2011, pp. 187–266; (c) D. McKay, S.A. Macgregor, A.J. Welch, *Chem. Sci.* 6 (2015) 3117.
- [10] C. Shi, H. Sun, X. Tang, W. Lv, H. Yan, Q. Zhao, J. Wang, W. Huang, *Angew. Chem. Int. Ed.* 52 (2013) 13434.
- [11] (a) O. Crespo, M.C. Gimeno, P.G. Jones, A. Laguna, J.M. López-de-Luzuriaga, M. Monge, J.L. Pérez, M.A. Ramón, *Inorg. Chem.* 42 (2003) 2061; (b) F. Lerouge, C. Viñas, F. Teixidor, R. Núñez, A. Abreu, E. Xochitiotzi, R. Santillan, N. Farfán, *Dalton Trans.* (2007) 1898; (c) F. Teixidor, R. Sillanpää, A. Abreu, E. Xochitiotzi, N. Farfán, R. Santillan, R. Núñez, R. Santillan, *Dalton Trans.* 40 (2011) 7541; (d) P.A. Jelliss, *Photoluminescence from boron-based polyhedral clusters*, in: N.S. Hosmane (Ed.), *Boron Science – New Technologies and Applications*, Taylor & Francis, Boca Raton, 2012, pp. 355–384; (e) R. Visbal, I. Ospino, J.M. López-de-Luzuriaga, A. Laguna, M.C. Gimeno, *J. Am. Chem. Soc.* 135 (2013) 4712.
- [12] A. Toppino, A.R. Genady, M.E. El-Zaria, J. Reeve, F. Mostofian, J. Kent, J.F. Valliant, *Inorg. Chem.* 52 (2013) 8743.
- [13] S. Yasuike, F. Nakashima, J. Kurita, T. Tsuchiya, *Heterocycles* 45 (1997) 1899.
- [14] A. Altomare, M.C. Burla, M. Camalli, G.ascarano, C. Giacovazzo, A. Guagliardi, A.G. Molteni, G. Polidori, R. Spagna, *J. Appl. Cryst.* 32 (1999) 115.
- [15] G.M. Sheldrick, *SHELX-97 Programs for Crystal Structure Analysis*, University of Göttingen, Göttingen, Germany, 1997.

# *o*-Carborane-Based Anthracene: A Variety of Emission Behaviors\*\*

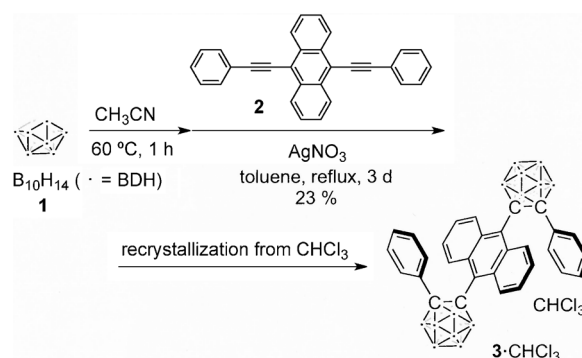
Hirofumi Naito, Yasuhiro Morisaki,\* and Yoshiki Chujo\*

**Abstract:** An *o*-carborane-based anthracene was synthesized, and single crystals, with incorporated solvent molecules, were obtained from the CHCl<sub>3</sub>, CH<sub>2</sub>Cl<sub>2</sub>, and C<sub>6</sub>H<sub>6</sub> solutions. The anthracene ring in the crystal is highly distorted by the formation of a  $\pi$ -stacked dimer between the anthracene units. The crystals exhibited a variety of emission behaviors such as aggregation-induced emission (AIE), crystallization-induced emission (CIE), aggregation-caused quenching (ACQ), and multichromism.

**O**-Carborane (C<sub>2</sub>B<sub>10</sub>H<sub>12</sub>) is a polyhedral boron cluster compound which includes two adjacent carbon atoms in the cluster cage.<sup>[1]</sup> The applications of carboranes for use in boron neutron capture therapy and for heat-resistant materials have been extensively studied because of their high boron content and thermal and chemical stability.<sup>[1,2]</sup> Recently, the construction of  $\pi$ -conjugated systems including the *o*-carborane moiety for applications as light-emitting materials has received significant attention.<sup>[3,4]</sup> Previously, we reported the syntheses of  $\pi$ -conjugated compounds in which  $\pi$ -electron systems were attached at the C1 and C2 positions of *o*-carborane, and found that they exhibited aggregation-induced emission (AIE).<sup>[4]</sup> The AIE properties<sup>[5]</sup> of *o*-carborane-based conjugated systems are caused by intramolecular charge transfer from the  $\pi$ -conjugated groups to *o*-carborane,<sup>[3e]</sup> and emission results from the restricted molecular motion of the *o*-carborane cage in the aggregated state or in frozen media at 77 K. To date, the synthesis and unique emission behaviors of AIE-active *o*-carborane derivatives have been reported. In addition to AIE properties, Tang and co-workers also reported a crystallization-induced emission (CIE) property.<sup>[6]</sup> Emission from the  $\pi$ -conjugated system in these molecules can be induced efficiently in the crystal state. Generally, luminescence properties of emissive molecules depend on the solid state and are influenced by various factors such as crystallinity, amorphous character, and solvent-molecule incorporation. Appropriate control of the compounds in the solid state leads to external stimuli-responsive luminescent materials.<sup>[7]</sup>

From this viewpoint, we attempted to synthesize an *o*-carborane-based stimuli-responsive compound. We selected anthracene as the  $\pi$ -electron system because of its prominent luminescent properties and facile functionalization.<sup>[8–10]</sup> Furthermore, the luminescent colors of anthracene derivatives in the solid state can be modified by varying their assemblies. Herein, we report the synthesis of *o*-carborane-based anthracene,<sup>[10]</sup> in which *o*-carboranes are substituted at the 9- and 10-positions of anthracene. The structures and their unprecedented emission behaviors such as AIE, CIE, aggregation-caused quenching (ACQ), thermochromism, vapochromism, and mechanochromism are discussed in detail.

As shown in Scheme 1, the compound **3** was synthesized from decaborane (B<sub>10</sub>H<sub>14</sub>; **1**), CH<sub>3</sub>CN,<sup>[11a]</sup> and 9,10-di(phenyl-



**Scheme 1.** Synthesis of *o*-carborane-based anthracene.

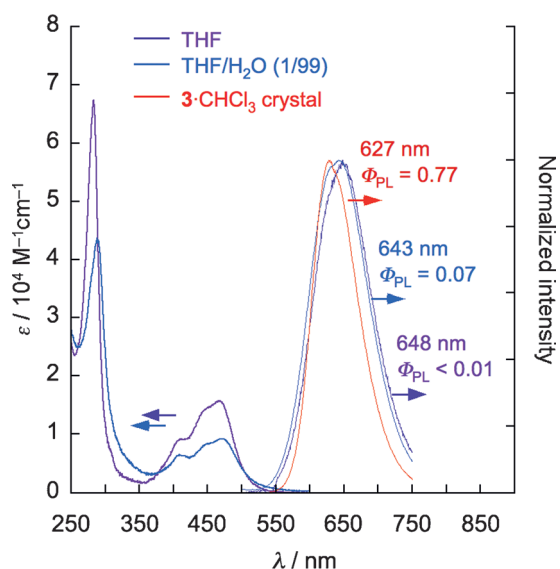
ethynyl)anthracene (**2**) using AgNO<sub>3</sub> as a Lewis acid.<sup>[11b]</sup> Recrystallization of **3** from CHCl<sub>3</sub> afforded the corresponding solvent cocrystal **3**·CHCl<sub>3</sub> in 23% yield. The compound **3**·CHCl<sub>3</sub> was stable to H<sub>2</sub>O, air, and heat in both solution and solid states. In addition, thermogravimetric analysis (TGA) of **3**·CHCl<sub>3</sub> showed that decomposition started at approximately 340 °C under N<sub>2</sub>, as shown in Figure S19 (see the Supporting Information). Furthermore, photoinduced dimerization of the anthracene units in **3**·CHCl<sub>3</sub> did not occur under UV irradiation in air. Thus, the anthracene ring is stabilized thermodynamically and kinetically by the electron-withdrawing character<sup>[12]</sup> of *o*-carborane and steric hindrance of the phenyl-substituted *o*-carborane, respectively.

Figure 1 shows the UV-vis absorption spectra of a dilute THF solution (1.0 × 10<sup>-5</sup> M) of **3** and the aggregates in a THF/H<sub>2</sub>O solution (v/v = 1/99, 1.0 × 10<sup>-5</sup> M). Both spectra exhibited the typical  $\pi$ - $\pi^*$  bands of the anthracene moiety at approximately  $\lambda$  = 280 and 450 nm, and that of the phenyl group at around  $\lambda$  = 280 nm. Figure 1 also shows the photoluminescence (PL) spectra of the THF solution, aggregates, and the crystal of **3**·CHCl<sub>3</sub>. The spectrum of the dilute THF solution exhibited a weak peak at  $\lambda$  = 650 nm which is derived from

[\*] H. Naito, Prof. Y. Morisaki, Prof. Y. Chujo  
Department of Polymer Chemistry  
Graduate School of Engineering, Kyoto University  
Katsura, Nishikyo-ku, Kyoto 615-8510 (Japan)  
E-mail: ymo@chujo.synchem.kyoto-u.ac.jp  
chujo@chujo.synchem.kyoto-u.ac.jp

[\*\*] This work was partially supported by Grant-in-Aid for Scientific Research on Innovative Areas "Element-Blocks" (No. 24102013) from the MEXT.

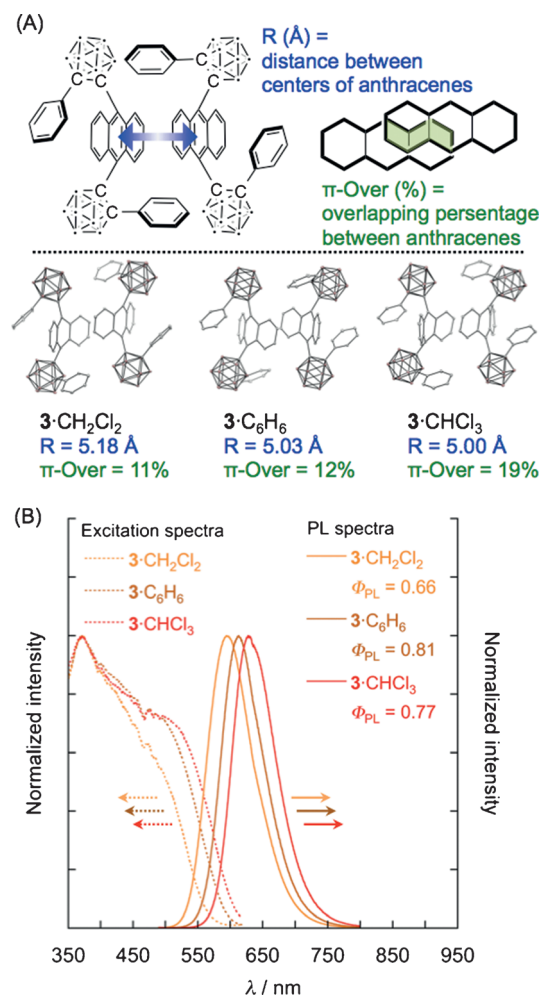
Supporting information for this article is available on the WWW under <http://dx.doi.org/10.1002/anie.201500129>.



**Figure 1.** Absorption spectra of **3** in THF ( $1.0 \times 10^{-5}$  M) and the aggregates (THF/H<sub>2</sub>O v/v = 1:99 solution,  $1.0 \times 10^{-5}$  M). Normalized PL spectra of **3** in THF ( $1.0 \times 10^{-5}$  M), the aggregates (THF/H<sub>2</sub>O = 1:99 solution,  $1.0 \times 10^{-5}$  M), and the **3**·CHCl<sub>3</sub> crystal (excited at  $\lambda = 470$  nm).

charge-transfer<sup>[3c]</sup> (CT) emission of the di(*o*-carboranyl)-anthracene moiety.<sup>[13]</sup> The absolute PL quantum efficiency ( $\Phi_{\text{PL}}$ ) of the dilute THF solution was less than 0.01 ( $\tau = 9.2$  ns,  $\chi^2 = 1.18$ ). From the aggregates, only CT emission was observed at  $\lambda = 643$  nm (Figure 1) with a slightly higher  $\Phi_{\text{PL}}$  value of 0.07 ( $\tau = 8.8$  ns,  $\chi^2 = 1.13$ ). The compound **3** exhibited a broad emission peak in the same region in frozen media (2-methyl-THF at 77 K,  $1.0 \times 10^{-5}$  M; see Figure S5 in the Supporting Information), thus indicating that the broad peak results from the AIE which arises because of the suppression of C–C bond vibration in the *o*-carborane and that emission from the aggregates in THF/H<sub>2</sub>O (v/v = 1:99) was bathochromically shifted because of the increase in the polarity by H<sub>2</sub>O. The most efficient emission (CIE) was observed from the crystal of **3**, with a calculated  $\Phi_{\text{PL}}$  value of 0.77.

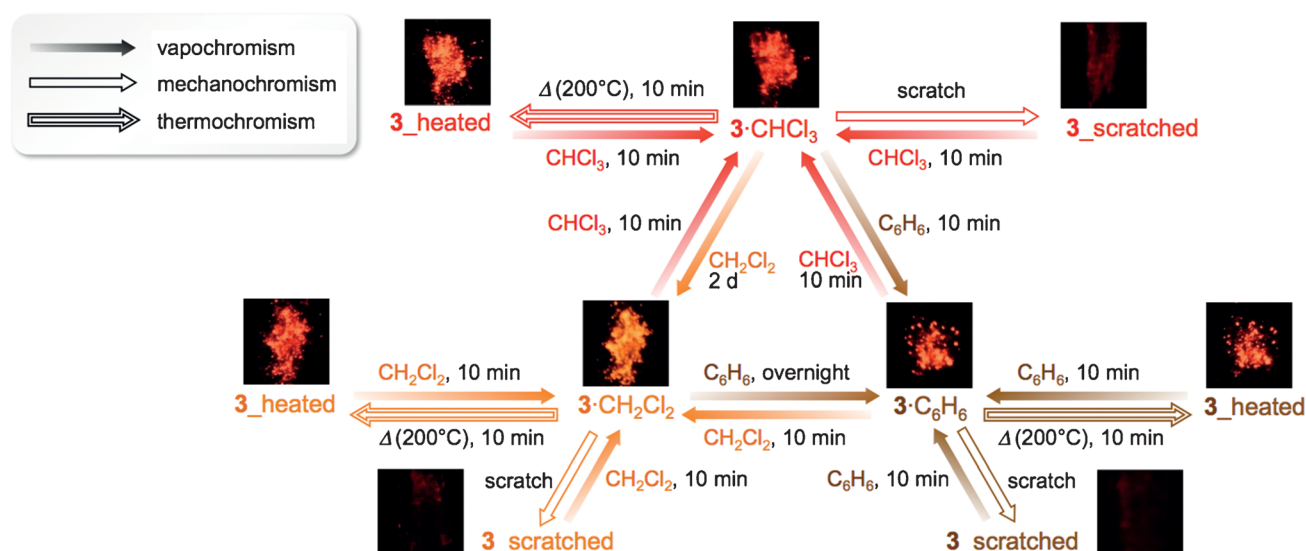
To better understand the CIE properties of **3**, its single crystals were obtained from CH<sub>2</sub>Cl<sub>2</sub> and C<sub>6</sub>H<sub>6</sub> solutions, in addition to a CHCl<sub>3</sub> solution, for X-ray crystallography. As shown in Figure 2A, the anthracene rings of two molecules of **3** form a  $\pi$ -stacked dimer and each solvent molecule is incorporated into each crystal lattice (see Figures S7–S9 in the Supporting Information). The overlapping area of two  $\pi$ -stacked anthracenes were estimated as 11, 12, and 19% for **3**·CH<sub>2</sub>Cl<sub>2</sub>, **3**·C<sub>6</sub>H<sub>6</sub>, and **3**·CHCl<sub>3</sub>, respectively (Figure 2A). The PL spectra of the crystals were then correlated to the difference in the overlapping percentages and distances between centers of anthracenes. The emission peak was observed at a longer wavelength for crystal structures which have a greater overlap and shorter distance between the two anthracenes in the stacked dimer (Figure 2B).<sup>[14,15]</sup> In contrast to emission from solution and aggregates, CIE consisted of two decay components (see Table S5 in the Supporting Information), that is, anthracene stacking influenced the CT emission, depending on the stacking distance and overlapping



**Figure 2.** A) Structure of  $\pi$ -stacked dimer and ORTEP drawings of **3**·CH<sub>2</sub>Cl<sub>2</sub>, **3**·C<sub>6</sub>H<sub>6</sub>, and **3**·CHCl<sub>3</sub>. B) Excitation and PL spectra of **3**·CH<sub>2</sub>Cl<sub>2</sub>, **3**·C<sub>6</sub>H<sub>6</sub>, and **3**·CHCl<sub>3</sub> crystals. Excitation spectra were monitored at 594 nm for **3**·CH<sub>2</sub>Cl<sub>2</sub>, 613 nm for **3**·C<sub>6</sub>H<sub>6</sub>, and 627 nm for **3**·CHCl<sub>3</sub>.

percentage rather than on the solvatochromic effect by the incorporated solvent molecules. Bathochromic shifts in the excitation spectra were also observed, and correspond to the overlapping percentage and distance between anthracenes (Figure 2B).

Interestingly, distortion of the anthracene ring was observed in the **3**-solvent crystals. The ring strain was evaluated with ring deformation angles  $\alpha$  and  $\beta$  for the central ring, as shown in Figure S10 in the Supporting Information. The  $\alpha$  and  $\beta$  values for the central rings of anthracene in **3**·CHCl<sub>3</sub> were 21.5° and 6.4°, respectively. For comparison, the deformation angles  $\alpha$  and  $\beta$  of [6,10]anthracenophane are 24.7° and 18.5°,<sup>[16a]</sup> respectively, and those of [1,1](9,10)anthracenophane are 16.3° and 5.8°,<sup>[16b]</sup> respectively.<sup>[17]</sup> Therefore, the anthracene ring in the **3**·CHCl<sub>3</sub> crystal is significantly distorted despite the fact that **3** is not a strained cyclophane compound. These large deformation angles are a result of  $\pi$ - $\pi$  interactions between the anthracene rings and steric hindrance of the phenyl-substituted *o*-carboranes in the  $\pi$ -stacked dimer. The aromaticity of the anthracene rings in the **3**-solvent crystals was studied by



**Figure 3.** Thermochromism, vapochromism, and mechanochromism of the **3**-solvent crystals.

nucleus-independent chemical shifts (NICS; see Table S4) and the results suggest that their aromaticity is maintained.

As shown in Figure 3, crystals of **3**-solvent exhibited reversible thermochromism, vapochromism, and mechanochromism, and PL spectra and X-ray diffraction (XRD) patterns were measured after each step (see Figures S23–S40 in the Supporting Information). Heating the crystals at 200 °C for 10 minutes under air resulted in the loss of solvent molecules from the crystals, and thus changes in their emission behavior. The loss of solvent molecules was confirmed by TGA, differential scanning calorimetry (DSC; see Figures S17–22 in the Supporting Information), and X-ray fluorescence (XRF)<sup>[18]</sup> analysis. For example, 86% of the CH<sub>2</sub>Cl<sub>2</sub> molecules in **3**-CH<sub>2</sub>Cl<sub>2</sub> were removed from the crystal by heating (see Figure S41 in the Supporting Information). Almost identical PL spectra (see Figure S12 in the Supporting Information) and excitation spectra (Figure S15) were observed after heating, and good  $\Phi_{\text{PL}}$  values were obtained (Table S5). When the heated solids were exposed to solvent vapor for 10 minutes in a Petri dish, the PL profile and XRD pattern of the crystal corresponding to each solvent was reversibly observed (see Figures S23, S24, S27, S28, S31, and S32).

Next, the response of the to a mechanical stimulus was monitored by PL. Scratching the crystals with a spatula or grinding with a mortar and a pestle dramatically decreases the  $\Phi_{\text{PL}}$  value (see Figure S13 and Table S5). For example, the  $\Phi_{\text{PL}}$  value of **3**-CH<sub>2</sub>Cl<sub>2</sub> changed from 0.66 to 0.08. In addition, the PL and excitation spectra for the scratched solid were bathochromically shifted (see Figure S13 and S16, respectively). The XRD pattern of **3**-CH<sub>2</sub>Cl<sub>2</sub> before scratching exhibited sharp peaks, whereas the scratched solid exhibited no clear signals (see Figure S26). Similar to the heated crystals, the XRF results show that approximately 97% of CH<sub>2</sub>Cl<sub>2</sub> was removed from **3**-CH<sub>2</sub>Cl<sub>2</sub> by scratching (see Figure S41). These results suggest that the crystals of **3**-CH<sub>2</sub>Cl<sub>2</sub> become amorphous after mechanical stress-induced loss of CH<sub>2</sub>Cl<sub>2</sub> molecules, thus leading to the ACQ. However,

annealing the scratched solids with CH<sub>2</sub>Cl<sub>2</sub> vapor resulted in the PL spectrum and XRD pattern (see Figure S25 and 26, respectively) identical to those of the original **3**-CH<sub>2</sub>Cl<sub>2</sub> crystals. This scratching and solvent annealing process could be repeatedly carried out at least ten times (see Figure S43), which demonstrates the robust reversible mechanochromism of the **3**-CH<sub>2</sub>Cl<sub>2</sub> crystals. It seems that access of solvent is relatively easy because there is sufficient space, and there are no interactions such as  $\pi$ - $\pi$  and CH— $\pi$  interactions between **3** and solvent molecules in the crystals, according to the X-ray crystallography.

Intrigued by the repeatability of the annealing process, we next tested substitution of the solvent in the crystals. Exposure of the crystals to a different solvent vapor in a Petri dish at room temperature afforded the desired substitution. Although the substitution time depended on the solvent and crystal, the PL and XRD changes were observed in all cases (see Figure S35–40).

In conclusion, *o*-carborane-substituted anthracene was successfully synthesized and characterized. Single crystals were obtained from CH<sub>2</sub>Cl<sub>2</sub>, CHCl<sub>3</sub>, and C<sub>6</sub>H<sub>6</sub> solutions, and each solvent molecule was incorporated into the crystals. In the crystal, the anthracene ring was highly distorted because of the formation of a  $\pi$ -stacked dimer between anthracene units. A wide variety of emission behaviors were observed for the crystals, including AIE, CIE, ACQ, thermochromism, vapochromism, and mechanochromism. Based on these results, bis(*o*-carborane)-substituted acenes are promising skeletons for solid stimuli-responsive emissive materials.

### Experimental Section

Decaborane (**1**; 1.51 g, 12.3 mmol) was dissolved in CH<sub>3</sub>CN (2.5 mL) at room temperature under Ar atmosphere.<sup>[1a]</sup> The mixture was stirred for 1 h at 60 °C, and then, 9,10-bis(phenylethynyl)anthracene (**2**; 1.40 g, 3.7 mmol), AgNO<sub>3</sub><sup>[1b]</sup> (54 mg, 0.32 mmol), and dry toluene (40 mL) were added. The mixture was refluxed for 3 days. After cooling to room temperature, solvent was evaporated, and the residue

was purified by column chromatography on silica gel (*n*-hexane/ $\text{CH}_2\text{Cl}_2$   $v/v = 3:2$ ). After evaporation of solvent, recrystallization from  $\text{CHCl}_3$  was carried out to afford **3**- $\text{CHCl}_3$  as a red single crystal (0.68 g, 1.10 mmol, 30% yield based on **1**).  $^1\text{H}$  NMR (400 MHz,  $\text{CD}_2\text{Cl}_2$ ):  $\delta = 8.60$  (4H, dd,  $J = 7.08$  Hz,  $J = 3.16$  Hz, Ar-H), 7.30–7.26 (10H, m, Ar-H), 7.06 (4H, t,  $J = 7.92$  Hz, Ar-H), 3.2–1.6 ppm (20H, br, B-H).  $^{13}\text{C}$  NMR (100 MHz,  $\text{CD}_2\text{Cl}_2$ ):  $\delta = 133.7, 132.4, 131.4, 129.9, 129.3, 126.4, 125.3, 125.1, 91.8, 88.5$  ppm.  $^{11}\text{B}$  NMR (128 MHz,  $\text{CD}_2\text{Cl}_2$ ):  $\delta = -1.2, -2.3, -4.5, -5.7, -10.4, -11.5$  ppm. HRMS (APCI): Calcd. for  $\text{C}_{30}\text{H}_{38}\text{B}_{20}$   $[\text{M}+\text{H}]^+$   $m/z$  619.4977, found  $m/z$  619.4969. Single crystals of **3**- $\text{CH}_2\text{Cl}_2$  and **3**- $\text{C}_6\text{H}_6$  were obtained as follows. Crystal of **3**- $\text{CHCl}_3$  (2 mg) was dissolved in  $\text{CH}_2\text{Cl}_2$  or  $\text{C}_6\text{H}_6$  (0.5 mL). Slow evaporation of the solution at room temperature afforded the corresponding single crystal **3**- $\text{CH}_2\text{Cl}_2$  or **3**- $\text{C}_6\text{H}_6$ .

**Keywords:** aggregation · carboranes · crystal growth · luminescence · solid-state structures

**How to cite:** *Angew. Chem. Int. Ed.* **2015**, *54*, 5084–5087  
*Angew. Chem.* **2015**, *127*, 5173–5176

- [1] a) “Icosahedral carboranes: 1,2- $\text{C}_2\text{B}_{10}\text{H}_{12}$ ”: R. N. Grimes in *Carboranes*, 2nd ed., Academic Press, New York, **2011**, chap. 9, pp. 301–540; b) B. P. Dash, R. Satapathy, J. A. Maguire, N. S. Hosmane in *Boron Science: New Technologies and Applications* (Ed.: N. S. Hosmane), CRC, Boca Raton, FL, **2011**, pp. 675–699.
- [2] a) V. I. Bregadze, *Chem. Rev.* **1992**, *92*, 209–223; b) A. González-Campo, E. J. Juárez-Pérez, C. Viñas, B. Boury, R. Sillanpää, R. Kivekäs, R. Núñez, *Macromolecules* **2008**, *41*, 8458–8466; c) F. Issa, M. Kassiou, L. M. Rendina, *Chem. Rev.* **2011**, *111*, 5701–5722; d) A. Ferrer-Ugalde, E. J. Juárez-Pérez, F. Teixidor, C. Viñas, R. Núñez, *Chem. Eur. J.* **2013**, *19*, 17021–17030.
- [3] a) J. J. Peterson, M. Werre, Y. C. Simon, E. B. Coughlin, K. R. Carter, *Macromolecules* **2009**, *42*, 8594–8598; b) F. Lerouge, A. Ferrer-Ugalde, C. Viñas, F. Teixidor, A. Abreu, E. Xochitlotzi, N. Farfán, R. Santillan, R. Sillanpää, R. Núñez, *Dalton Trans.* **2011**, *40*, 7541–7550; c) B. P. Dash, R. Satapathy, E. R. Gaillard, K. M. Norton, J. A. Maguire, N. Chug, N. S. Hosmane, *Inorg. Chem.* **2011**, *50*, 5485–5493; d) A. R. Davis, J. J. Peterson, K. R. Carter, *ACS Macro Lett.* **2012**, *1*, 469–472; e) K.-R. Wee, W.-S. Han, D. W. Cho, S. Kwon, C. Pac, S. O. Kang, *Angew. Chem. Int. Ed.* **2012**, *51*, 2677–2680; *Angew. Chem.* **2012**, *124*, 2731–2734; f) Y. Morisaki, M. Tominaga, Y. Chujo, *Chem. Eur. J.* **2012**, *18*, 11251–11257; g) K.-R. Wee, Y.-J. Cho, S. Jeong, S. Kwon, J.-D. Lee, I.-H. Suh, S. O. Kang, *J. Am. Chem. Soc.* **2012**, *134*, 17982–17990; h) H. J. Bae, H. Kim, K. M. Lee, T. Kim, Y. S. Lee, Y. Do, M. H. Lee, *Dalton Trans.* **2014**, *43*, 4978–4985.
- [4] a) K. Kokado, Y. Chujo, *Macromolecules* **2009**, *42*, 1418–1420; b) K. Kokado, Y. Chujo, *J. Org. Chem.* **2011**, *76*, 316–319.
- [5] a) *Aggregation-induced emission: Fundamentals* (Eds.: A. Qin, B. Z. Tang), Wiley, New York, **2013**; b) *Aggregation-induced emission: Applications* (Eds.: A. Qin, B. Z. Tang), Wiley, New York, **2013**; c) J. Luo, Z. Xie, J. W. Y. Lam, L. Cheng, H. Chen, C. Qiu, H. S. Kwok, X. Zhan, Y. Liu, D. Zhu, B. Z. Tang, *Chem. Commun.* **2001**, 1740–1741.
- [6] a) Y. Dong, J. W. Y. Lam, A. Qin, Z. Li, J. Sun, H. H.-Y. Sung, I. D. Williams, B. Z. Tang, *Chem. Commun.* **2007**, 40–42; b) Y. Dong, J. W. Y. Lam, A. Qin, J. Sun, J. Liu, Z. Li, J. Sun, H. H.-Y. Sung, I. D. Williams, H. S. Kwok, B. Z. Tang, *Chem. Commun.* **2007**, 3255–3257.
- [7] a) Y. Sagara, T. Kato, *Nat. Chem.* **2009**, *1*, 605–610; b) D. A. Davis, A. Hamilton, J. Yang, L. D. Cremer, D. Van Gough, S. L. Potisek, M. T. Ong, P. V. Braun, T. J. Martinez, S. R. White, J. S. Moore, N. R. Sottos, *Nature* **2009**, *459*, 68–72; c) X. Zhang, Z. Chi, Y. Zhang, S. Liu, J. Xu, *J. Mater. Chem. C* **2013**, *1*, 3376–3390.
- [8] a) X. Zhang, Z. Chi, B. Xu, L. Jiang, X. Zhou, Y. Zhang, S. Liu, J. Xu, *Chem. Commun.* **2012**, *48*, 10895–10897; b) M. R. Rao, C.-W. Liao, W.-L. Su, S.-S. Sun, *J. Mater. Chem. C* **2013**, *1*, 5491–5501; c) B. Chen, G. Yu, X. Li, Y. Ding, C. Wang, Z. Liu, Y. Xie, *J. Mater. Chem. C* **2013**, *1*, 7409–7417; d) Y. Dong, J. Zhang, X. Tan, L. Wang, J. Chen, B. Li, L. Ye, B. Xu, B. Zou, W. Tian, *J. Mater. Chem. C* **2013**, *1*, 7554–7559; e) X. Zhang, Z. Ma, Y. Yang, X. Zhang, Z. Chi, S. Liu, J. Xu, X. Jia, Y. Wei, *Tetrahedron* **2014**, *70*, 924–929.
- [9] a) Y. Mizobe, N. Tohnai, M. Miyata, Y. Hasegawa, *Chem. Commun.* **2005**, 1839–1841; b) Y. Mizobe, T. Hinoue, A. Yamamoto, I. Hisaki, M. Miyata, Y. Hasegawa, N. Tohnai, *Chem. Eur. J.* **2009**, *15*, 8175–8184; c) Z. Zhang, Y. Zhang, D. Yao, H. Bi, I. Javed, Y. Fan, H. Zhang, Y. Wang, *Cryst. Growth Des.* **2009**, *9*, 5069–5076; d) T. Hinoue, Y. Doi, Y. Mizobe, I. Hisaki, M. Miyata, N. Tohnai, *Chem. Eur. J.* **2012**, *18*, 4634–4643.
- [10] a) A. Sousa-Pedrares, C. Vinas, F. Teixidor, *Chem. Commun.* **2010**, *46*, 2998–3000; b) A. Ferrer-Ugalde, A. González-Campo, C. Viñas, J. Rodríguez-Romero, R. Santillan, N. Farfán, R. Sillanpää, A. Sousa-Pedrares, R. Núñez, F. Teixidor, *Chem. Eur. J.* **2014**, *20*, 9940–9951.
- [11] a) R. Schaeffer, *J. Am. Chem. Soc.* **1957**, *79*, 1006–1007; b) A. Toppino, A. R. Genady, M. E. El-Zaria, J. Reeve, F. Mostofian, J. Kent, J. F. Valliant, *Inorg. Chem.* **2013**, *52*, 8743–8749.
- [12] The reversible cyclic voltammogram of **3** is shown in Figure S6. The lowest unoccupied molecular orbital (LUMO) potential was calculated to be  $-4.16$  eV, which is similar to the value for  $\text{C}_{60}$  ( $-4.2$  eV). Electrochemical behaviors of *o*-carborane-based conjugated compounds (e.g., 2e reduction of a carborane unit) were reported by Weber, Fox, and co-workers. See: L. Weber, J. Kahlert, L. Böbling, A. Brockhinke, H.-G. Stammer, B. Neumann, R. A. Harder, P. J. Low, M. A. Fox, *Dalton Trans.* **2013**, *42*, 2266–2281.
- [13] Highest occupied molecular orbital (HOMO) and lowest unoccupied molecular orbital (LUMO) of pristine and distorted compounds **3** are shown in Figure S44 (see the Supporting Information). Both LUMOs were delocalized on anthracene and carborane moieties through the overlap between the  $\pi^*$ -orbital of anthracene and the antibonding orbital of the C1–C2 bond in the carborane cage, which caused CT. Solvatochromic effect of **3** was also investigated, and the result is shown in Figure S45 in the Supporting Information. The linear relationship was observed in the Lippert–Mataga plot, thus supporting the CT emission. For the Lippert–Mataga equation: a) E. Z. Lippert, *Electrochemistry* **1957**, *61*, 962–975; b) N. Mataga, Y. Kaifu, M. Koizumi, *Bull. Chem. Soc. Jpn.* **1956**, *29*, 465–470.
- [14] The PL decay study showed that the contribution of the long-lived ( $\tau_2$ ) component increased (Table S5).
- [15] Y. Dong, B. Xu, J. Zhang, X. Tan, L. Wang, J. Chen, H. Lv, S. Wen, B. Li, L. Ye, B. Zou, W. Tian, *Angew. Chem. Int. Ed.* **2012**, *51*, 10782–10785; *Angew. Chem.* **2012**, *124*, 10940–10943.
- [16] a) Y. Tobe, S. Saiki, N. Utsumi, T. Kusumoto, H. Ishii, K. Kakiuchi, K. Kobiro, K. Naemura, *J. Am. Chem. Soc.* **1996**, *118*, 9488–9497; b) E. Trzop, I. Turowska-Tyrk, *Acta Crystallogr. Sect. B* **2008**, *64*, 375–382.
- [17] To the best of our knowledge, the record for the largest deformation angle  $\alpha$  is  $24.3$ – $25.6^\circ$  with angle  $\beta$  of  $23.9$ – $26.8^\circ$  for a [1.1]paracyclophane derivative is found in: H. Kawai, T. Suzuki, M. Ohkita, T. Tsuji, *Chem. Eur. J.* **2000**, *6*, 4177–4187.
- [18] XRF analysis was carried out for **3**- $\text{CH}_2\text{Cl}_2$  and **3**- $\text{CHCl}_3$  by the detection of Cl, as shown in Figures S41 and 42, respectively, in the Supporting Information.

Received: January 7, 2015

Revised: February 6, 2015

Published online: February 27, 2015



Contents lists available at ScienceDirect

## Tetrahedron Letters

journal homepage: [www.elsevier.com/locate/tetlet](http://www.elsevier.com/locate/tetlet)

## Synthesis of hexabenzocoronene-layered compounds



Tatsuya Nakano, Yasuhiro Morisaki\*, Yoshiki Chujo\*

Department of Polymer Chemistry, Graduate School of Engineering, Kyoto University, Katsura, Nishikyo-ku, Kyoto 615-8510, Japan

## ARTICLE INFO

## Article history:

Received 8 January 2015

Revised 3 March 2015

Accepted 6 March 2015

Available online 12 March 2015

## Keywords:

Hexabenzocoronene

 $\pi$ - $\pi$  stacking

Xanthene

## ABSTRACT

We report herein the synthesis and properties of  $\pi$ -stacked dimeric and polymeric compounds that consisted of hexabenzocoronene (HBC) and xanthene as the stacked  $\pi$ -electron system and the scaffold, respectively; the compounds were obtained by Sonogashira–Hagihara coupling. The obtained polymer was separated into three fractions, and the through-space conjugation effect was estimated. HBC units were layered in proximity (approximately 3.4 Å), leading to  $\pi$ - $\pi$  stacking in the ground and excited states.

© 2015 Elsevier Ltd. All rights reserved.

Recently, the construction of  $\pi$ -stacked structures of aromatic rings and  $\pi$ -electron systems in single polymer chains has been the subject of focus.<sup>1</sup> Their face-to-face structures enable transannular communication between the layered  $\pi$ -electron systems. In addition, such a  $\pi$ -stacked orientation is an important factor for effective charge transport and exciton diffusion. In this context, several rigid scaffolds have been developed for aligning  $\pi$ -electron systems in proximity to each other, such as naphthalene,<sup>2</sup> anthracene,<sup>3</sup> [2.2]paracyclophane,<sup>4</sup> bicyclo[4.4.1]undecane,<sup>5</sup> 2-substituted trimethylene,<sup>6</sup> norbornane,<sup>7</sup> and so on. As an unique approach, Nakano et al. and coworkers reported the synthesis of poly(dibenzofulvene)s, wherein the side chain dibenzofulvene groups are tightly stacked, that is, the  $\pi$ -electron systems are fully overlapped, resulting in a large Stokes shift as well as efficient hole transport.<sup>8</sup>

We have also studied the construction of  $\pi$ -stacked structures using a xanthene skeleton as the rigid scaffold.<sup>9</sup> Some xanthene compounds are commercially available, and various xanthene derivatives can be easily prepared through facile functionalizations at the 4- and 5-positions; thus, a variety of aromatic groups and  $\pi$ -electron systems can be introduced at these positions. The rotary motion of the substituted  $\pi$ -electron systems is suppressed by steric hindrance, which leads to layered structures for these  $\pi$ -electron systems.

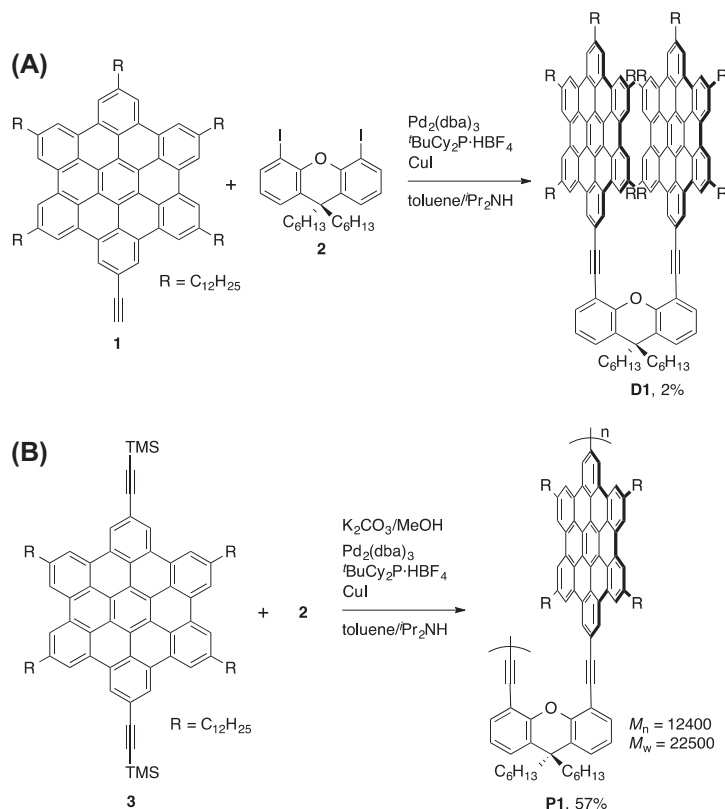
Further syntheses of novel aromatic-ring-layered compounds and investigations on the effect of the stacking on their properties are important for exploring their potential applications in opto-electronic devices. In this study, we selected

hexa-*peri*-hexabenzocoronene (HBC)<sup>10</sup> as the layered aromatic ring; HBC is chemically stable, and functionalized HBCs are readily obtained. The HBC-layered monomeric, dimeric, and polymeric compounds were synthesized using the xanthene skeleton as the scaffold, and their optical properties were investigated.

The HBC-layered dimeric compound **D1** and polymer **P1** with xanthene were synthesized by the Sonogashira–Hagihara coupling<sup>11</sup> using the Pd<sub>2</sub>(dba)<sub>3</sub> (dba = dibenzylideneacetone)/<sup>t</sup>ByCy<sub>2</sub>P·HBF<sub>4</sub>/CuI catalytic system (Scheme 1A and B, respectively). The reaction of HBC monoacetylene **1**<sup>12</sup> with xanthene compound **2**<sup>13</sup> afforded the corresponding crude compound **D1**, which was purified using a silica gel column and by recycling preparative high-performance liquid chromatography (HPLC) using gel permeation columns (GPC). Most of the products were lost during column chromatography, because of strong  $\pi$ - $\pi$  interactions among the molecules, and pure **D1** was obtained in 2% yield. As shown in Scheme 1B, polymerization was carried out by the treatment of trimethylsilyl-protected HBC diacetylene **3** with **2** in the presence of K<sub>2</sub>CO<sub>3</sub>, using the same catalytic system as Scheme 1A. The trimethylsilyl group of **3** was removed in situ because terminal alkynes are unstable towards oxidation. The obtained polymer **P1** was purified by reprecipitation from THF and MeOH (good and poor solvents, respectively). The number-average ( $M_n$ ) and weight-average ( $M_w$ ) molecular weights of **P1** were estimated, by GPC in CHCl<sub>3</sub> eluent using a calibration curve of polystyrene standard calibration curve, to be 12,400 and 22,500, respectively. Polymer **P1** was soluble in common organic solvents such as THF, CHCl<sub>3</sub>, CH<sub>2</sub>Cl<sub>2</sub> and toluene; it was separated by HPLC into three fractions (Fig. S9 in the Supporting information); **P1a** ( $M_n$  = 8700,  $M_w/M_n$  = 1.09, degree of polymerization (DP) = 5.5), **P1b** ( $M_n$  = 13,600,  $M_w/M_n$  = 1.11, DP = 8.6), and **P1c** ( $M_n$  = 17,500,  $M_w/M_n$  = 1.25, DP = 11). The structures of the

\* Corresponding authors. Fax: +81 75 383 2607.

E-mail addresses: [yimo@chujyo.synchem.kyoto-u.ac.jp](mailto:yimo@chujyo.synchem.kyoto-u.ac.jp) (Y. Morisaki), [chujyo@chujyo.synchem.kyoto-u.ac.jp](mailto:chujyo@chujyo.synchem.kyoto-u.ac.jp) (Y. Chujo).



**Scheme 1.** Synthesis of (A) dimeric compound **D1** and (B) polymer **P1**.

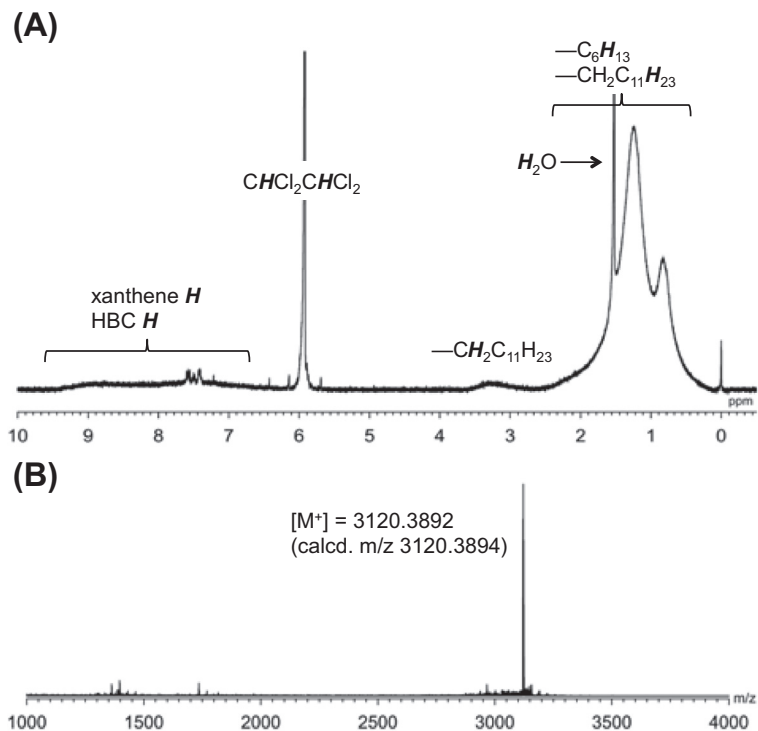
obtained compounds **D1** and **P1** were characterized by  $^1\text{H}$  NMR spectroscopy and/or matrix assisted laser desorption/ionization-time of flight (MALDI-TOF) mass spectrometry. In the  $^1\text{H}$  NMR spectra of **D1** and **P1**, all the signals were broadened because of the restricted mobility of the HBC moieties; for example, the  $^1\text{H}$  NMR spectrum of **D1** is shown in Figure 1. The MALDI-TOF mass spectrum of **D1** exhibited only one signal corresponding to the  $[\text{M}^+]$  ion of **D1** (Fig. 1B), supporting the formation of **D1**. It was difficult to obtain MALDI-TOF mass and  $^{13}\text{C}$  NMR spectra of **P1**. Although, thus, the existence of diyne units in **P1** by Sonogashira–Hagihara coupling could not be denied, stacked structure of the coronene moieties can be discussed in any cases.

To characterize the optical properties of **D1** and **P1**, model compounds **M1** and **M2** were synthesized for comparison, as shown in Scheme 2A and B, respectively. Figure 2A shows the UV–vis absorption and fluorescence spectra of **D1** and model compound **M1** in dilute  $\text{CHCl}_3$  solution ( $1.0 \times 10^{-5}$  and  $1.0 \times 10^{-6}$  M for the absorption and fluorescence spectra, respectively). In addition, the UV–vis absorption and fluorescence spectra of **D1**, **P1c** and the model compound **M2** are shown in Figure 2B. In the absorption spectra of **D1** and **M1** (Fig. 2A), the absorption edge of **D1** was red-shifted in comparison with that of **M1** because of  $\pi$ – $\pi$  interactions between two HBC units in the ground state of **D1**. The fluorescence spectrum of **M1** in dilute  $\text{CHCl}_3$  solution ( $1.0 \times 10^{-6}$  M) appeared at around 500 nm with a clear vibrational structure, while that of **D1** was observed at 515 nm as a broad and featureless signal. We confirmed that this concentration ( $1.0 \times 10^{-6}$  M) was sufficiently dilute; thus, each spectrum exhibits fluorescence from a single molecule. These results suggest that the stacked HBC units in **D1** exhibit  $\pi$ – $\pi$  interactions in the excited state, which leads to the excimer-like emission.

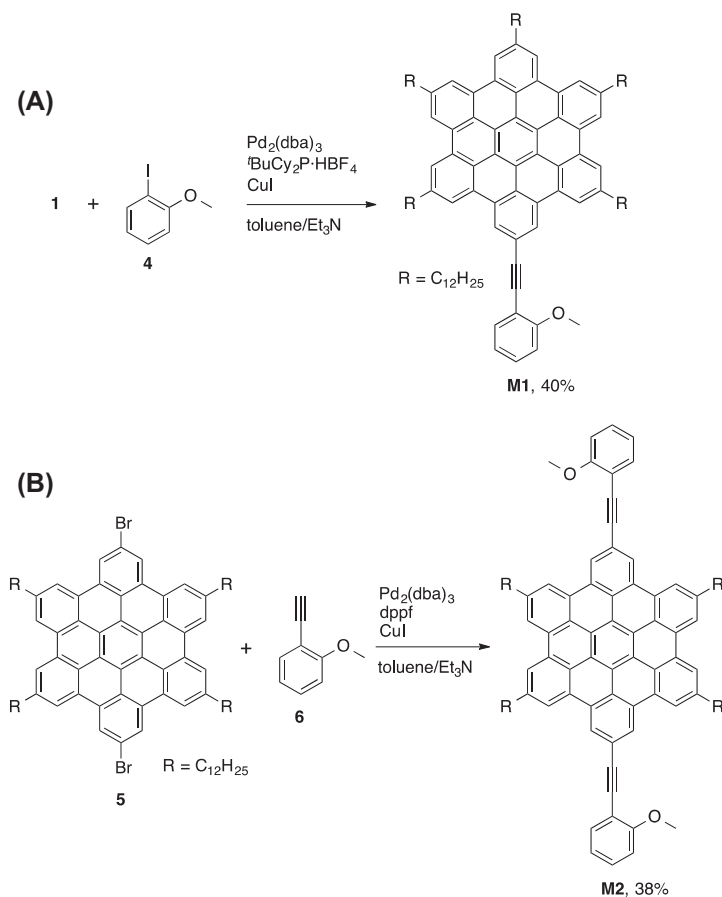
The peak tops of the absorption spectra of **D1** and **P1c** were identical and appeared at 367 nm, whereas that of **M2** was observed at 370 nm, which was slightly red-shifted in comparison

with those of **D1** and **P1c**. In **M2**, two anisoyl groups combine with an HBC unit to form a planar structure, because of which its  $\pi$ -conjugation length is expected to be well extended. Therefore, the absorption peak top appeared in a longer wavelength region than those of **D1** and **P1c**, wherein the twisting of the HBC rings suppresses the extension of the conjugation length. On the other hand, the absorption edges of **D1** and **P1c** were bathochromically shifted relative to that of **M2**, indicating  $\pi$ – $\pi$  interactions between HBC units in the ground state of **D1** and **P1c**. The energy band gaps of all compounds were calculated by the absorption edges, and the energy levels were estimated by cyclic voltammetry, as shown in Figure S10 and Table S1. The HOMO levels of all compounds were found to be approximately  $-5.0$  eV; thus, there were no noticeable differences by the stacked structure. Figure 2B shows their fluorescence spectra in dilute  $\text{CHCl}_3$  solution ( $1.0 \times 10^{-6}$  M). Despite the sufficiently dilute condition, the fluorescence spectra of **D1** and **P1c** were broad without any vibrational structures. Thus, in the excited state, the HBC rings in the polymer were interacting with one another even as single molecules. The molar extinction coefficient ( $\epsilon/\text{M}^{-1} \text{cm}^{-1}$ ) and photoluminescence quantum efficiency ( $\Phi_{\text{PL}}$ ) are listed in Table S1.

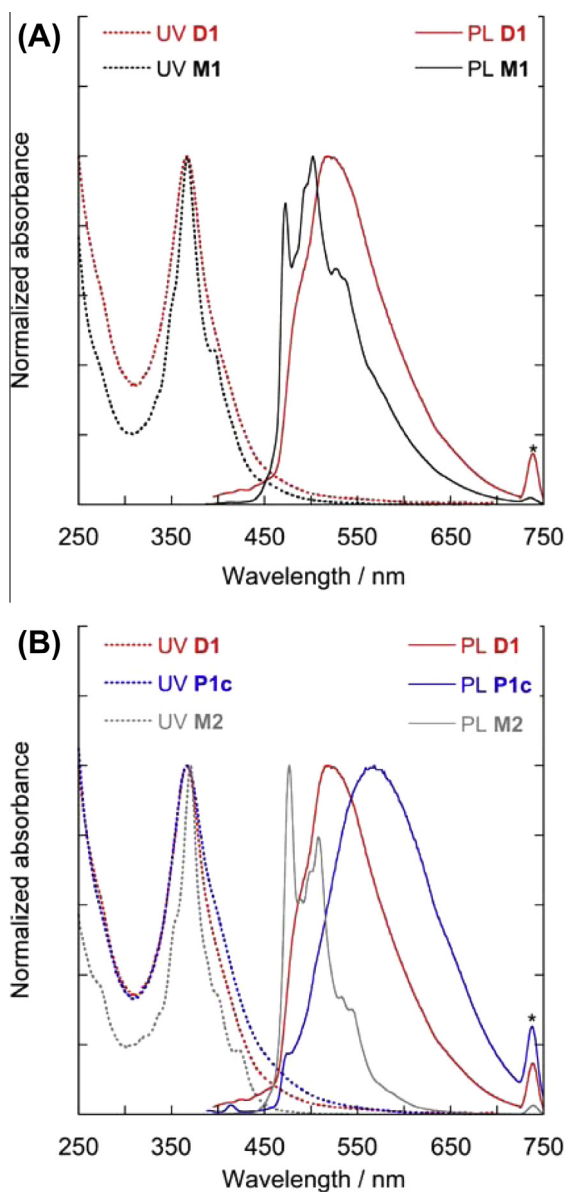
According to the absorption and fluorescence spectra of the polymers (Fig. 3), **P1b** ( $M_n = 13600$ ,  $M_w/M_n = 1.11$ ,  $\text{DP} = 8.6$ ) and **P1c** ( $M_n = 17,500$ ,  $M_w/M_n = 1.25$ ,  $\text{DP} = 11$ ) exhibited almost identical optical profiles. It is considered that, in both ground as well as excited states, the bathochromic shift of the HBC-stacked compound saturates upon reaching nine to eleven HBC units. The  $\pi$ – $\pi$  interactions of the stacked aromatic units in the  $\pi$ -stacked polymer have been studied. The electronic interactions of 7,7-diphenylnorbornane-based polymers<sup>7</sup> and poly(dibenzofulvene)<sup>8</sup> are effective through approximately five aromatic moieties in the ground state, whereas [2.2]paracyclophane-based through-space conjugated polymer exhibits the electronic interactions through at least ten  $\pi$ -electron systems due to the fixed  $\pi$ -stacked conformation.<sup>4h</sup>



**Figure 1.** (A)  $^1\text{H}$  NMR spectrum of **D1** in 1,1,2,2-tetrachloroethane- $d_2$  at 100 °C. (B) MALDI-TOF mass spectrum of **D1** (matrix: 2-[(*Z*E)-3-(4-*tert*-butylphenyl)-2-methylprop-2-enylidene]malononitrile).



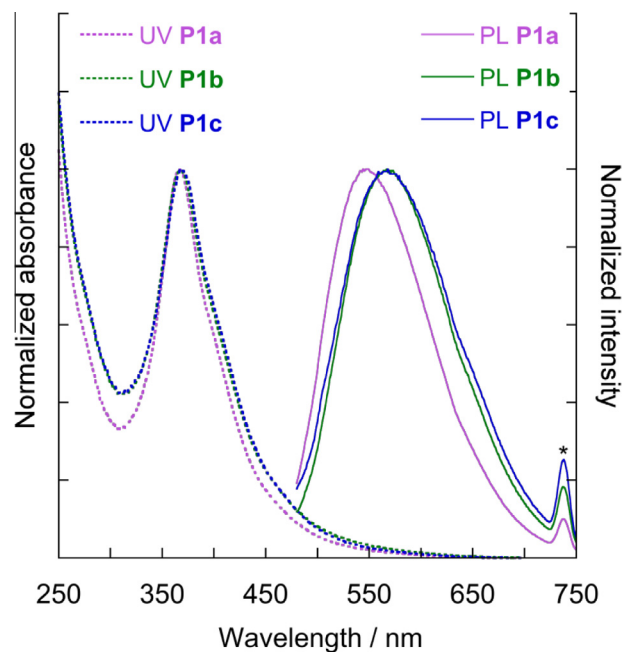
**Scheme 2.** Synthesis of model compounds (A) **M1** and (B) **M2**.



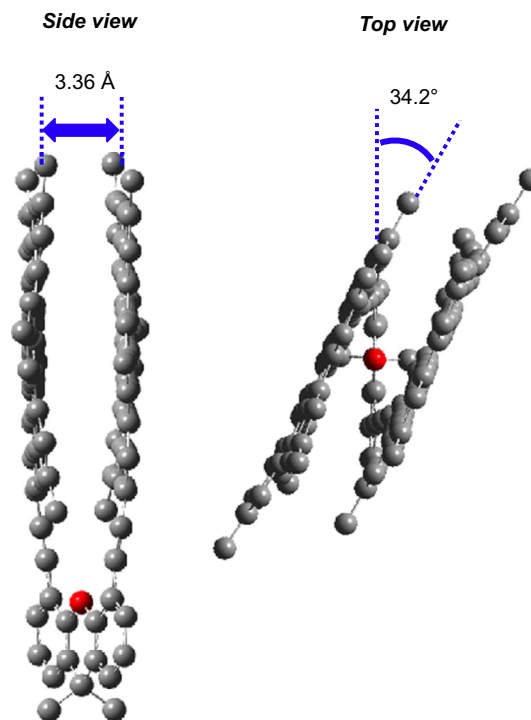
**Figure 2.** (A) UV-vis absorption and fluorescence spectra of **D1** and **M1** in dilute  $\text{CHCl}_3$  solution ( $1.0 \times 10^{-5}$  and  $1.0 \times 10^{-6}$  M for the absorption and fluorescence spectra, respectively). (B) UV-vis absorption and fluorescence spectra of **D1**, **P1c**, and **M2** in dilute  $\text{CHCl}_3$  solution ( $1.0 \times 10^{-5}$  and  $1.0 \times 10^{-6}$  M for the absorption and fluorescence spectra, respectively). All fluorescence spectra were obtained by excitation of their absorption peak tops. Asterisk denotes the overtone peaks of the excitation wavelength.

The  $\pi$ -stacked structure of the HBC-stacked polymer is conformationally stable; thus, the electronic interactions of the HBC-stacked compound reached to approximately ten HBC units.

As shown in Figure 4, the HBC-stacked structure was simulated by density functional theory (DFT; the M06-2X functional<sup>14</sup> and 6-31G\* basis sets<sup>15</sup>) using the HBC-stacked dimer as a model compound.<sup>16</sup> In this calculation, the dodecyl groups were replaced with methyl groups for simplicity. It was observed that two HBC rings rotate around carbon-carbon triple bonds and form a face-to-face structure in proximity. The dihedral angle between the HBC and xanthene units was estimated to be  $34.2^\circ$  and the shortest distance between HBC units was 3.36 Å. Since this distance is less than the sum of the van der Waals radii of  $\text{sp}^2$  carbons (3.4 Å), the  $\pi$ - $\pi$  stacking among HBC units in xanthene-based HBC-stacked compounds is considered to be effective.



**Figure 3.** UV-vis absorption and fluorescence spectra of **P1a-c** in dilute  $\text{CHCl}_3$  solution ( $1.0 \times 10^{-5}$  and  $1.0 \times 10^{-6}$  M for the absorption and fluorescence spectra, respectively). The fluorescence spectra were obtained by excitation of their absorption peak tops. Asterisk denotes the overtone peaks of the excitation wavelength.



**Figure 4.** Structure of **D1** by the DFT (M06-2X/6-31G\*). The  $\text{C}_{12}\text{H}_{25}$  group of **D1** was replaced with a methyl group.

In conclusion, HBC-stacked dimeric and polymeric compounds were synthesized using xanthene as a scaffold, and their structures and optical properties were characterized. UV-vis absorption spectroscopy and simulation by DFT proved the existence of  $\pi$ - $\pi$  interactions in the HBC layer in the ground state, while fluorescence spectroscopy proved the  $\pi$ - $\pi$  interactions in the excited state.

Therefore, this class of  $\pi$ -stacked oligomers and polymers are promising candidates for molecular wires that transport hole, electron, photo-excited electron and energy. Further studies will focus on the construction of a photo-excited energy transfer system using the HBC-stacked compounds with an end-capping group and evaluation of their performance.

### Supplementary data

Supplementary data (synthetic details, NMR spectra, GPC chromatograms, and cyclic voltammograms) associated with this article can be found, in the online version, at <http://dx.doi.org/10.1016/j.tetlet.2015.03.026>.

### References and notes

- $\pi$ -Stacked Polymers and Molecules: Synthesis, Properties, and Theory*; Nakano, T., Ed.; Springer: Berlin, 2014.
- (a) Arnold, R.; Matchett, S. A.; Rosenblum, M. *Organometallics* **1988**, *7*, 2261; (b) Nugent, H. M.; Rosenblum, M. *J. Am. Chem. Soc.* **1993**, *115*, 3848; (c) Rosenblum, M.; Nugent, H. M.; Jang, K.-S.; Labes, M. M.; Cahalane, W.; Klemarczyk, P.; Reiff, W. M. *Macromolecules* **1995**, *28*, 6330; (d) Hudson, R. D. A.; Foxman, B. M.; Rosenblum, M. *Organometallics* **1999**, *18*, 4098; (e) Kuroda, M.; Nakayama, J.; Hoshino, M.; Furusho, N.; Ohba, S. *Tetrahedron Lett.* **1994**, *35*, 3957; (f) Pina, J.; Seixas de Melo, J. S. *Phys. Chem. Chem. Phys.* **2009**, *11*, 8706; (g) Iyoda, M.; Nakao, K.; Kondo, T.; Kuwatani, Y.; Yoshida, M.; Matsuyama, H.; Fukami, K.; Nagase, S. *Tetrahedron Lett.* **2001**, *42*, 6869; (h) Nakao, K.; Nishiuchi, T.; Iyoda, M. *Heterocycles* **2008**, *6*, 727; (i) Morisaki, Y.; Fernandes, J. A.; Chujo, Y. *Polym. J.* **2010**, *42*, 928.
- (a) Nagata, T.; Osuka, A.; Maruyama, K. *J. Am. Chem. Soc.* **1990**, *112*, 3054; (b) Naruta, Y.; Sawada, N.; Tadokoro, M. *Chem. Lett.* **1994**, *23*, 1713; (c) Sangvikar, Y.; Fischer, K.; Schmidt, M.; Schlüter, A. D.; Sakamoto, J. *Org. Lett.* **2009**, *11*, 4112.
- For pseudo-*para*-linked [2.2]paracyclophane: (a) Guyard, L.; Audebert, P. *Electrochem. Commun.* **2001**, *3*, 164–167; (b) Morisaki, Y.; Chujo, Y. *Macromolecules* **2002**, *35*, 587; (c) Guyard, L.; Audebert, P.; Dolbier, W. R., Jr.; Duan, J.-X. *J. Electroanal. Chem.* **2002**, *537*, 189; (d) Salhi, F.; Lee, B.; Metz, C.; Bottomley, L. A.; Collard, D. M. *Org. Lett.* **2002**, *4*, 3195; (e) Salhi, F.; Collard, D. M. *Adv. Mater.* **2003**, *15*, 81; (f) Morisaki, Y.; Chujo, Y. *Angew. Chem., Int. Ed.* **2006**, *45*, 6430; (g) Morisaki, Y.; Chujo, Y. *Polym. Chem.* **2011**, *2*, 1249; (h) Morisaki, Y.; Ueno, S.; Saeki, A.; Asano, A.; Seki, S.; Chujo, Y. *Chem. Eur. J.* **2012**, *18*, 4216; (i) Morisaki, Y.; Chujo, Y. *Chem. Lett.* **2012**, *41*, 840; For pseudo-*ortho*-linked [2.2]paracyclophane: (j) Morisaki, Y.; Hifumi, R.; Lin, L.; Inoshita, K.; Chujo, Y. *Polym. Chem.* **2012**, *3*, 2727; (k) Morisaki, Y.; Inoshita, K.; Chujo, Y. *Chem. – Eur. J.* **2014**, *20*, 8386; For pseudo-geminal-linked [2.2]paracyclophane: (l) Jagtap, S. P.; Collard, D. M. *J. Am. Chem. Soc.* **2010**, *132*, 12208; (m) Jagtap, S. P.; Collard, D. M. *Polym. Chem.* **2012**, *3*, 463.
- (a) Knoblock, K. M.; Silvestri, C. J.; Collard, D. M. *J. Am. Chem. Soc.* **2006**, *128*, 13680; (b) Jagtap, S. P.; Mukhopadhyay, S.; Coropceanu, V.; Brizius, G. L.; Brédas, J.; Collard, D. M. *J. Am. Chem. Soc.* **2012**, *134*, 7176.
- (a) Watanabe, J.; Hoshino, T.; Nakamura, Y.; Sakai, E.; Okamoto, S. *Macromolecules* **2010**, *43*, 6562; (b) Nomura, R.; Moriai, R.; Kudo, M.; Hoshino, T.; Watanabe, J.; Funyu, S.; Ishitsuka, K.; Okamoto, S. *J. Polym. Sci., Part A: Polym. Chem.* **2013**, *51*, 3412; (c) Moriai, R.; Naito, Y.; Nomura, R.; Funyu, S.; Ishitsuka, K.; Asano, N.; Okamoto, S. *Tetrahedron Lett.* **2014**, *55*, 2649.
- (a) García Martínez, A.; Osío Barcina, J.; de Fresno Cerezo, A.; Schlüter, A.-D.; Frahn, J. *Adv. Mater.* **1999**, *11*, 27; (b) Caraballo-Martínez, N.; Colorado Heras, M. R.; Mba Blázquez, M.; Osío Barcina, J.; García Martínez, A.; Torres Salvador, M. R. *Org. Lett.* **2007**, *9*, 2943; (c) Osío Barcina, J.; Colorado Heras, M. R.; Mba, M.; Gómez Aspe, R.; Herrero-García, N. *J. Org. Chem.* **2009**, *74*, 7148.
- (a) Nakano, T. *Polym. J.* **2010**, *42*, 103; (b) Nakano, T.; Takewaki, K.; Yade, T.; Okamoto, Y. *J. Am. Chem. Soc.* **2001**, *123*, 9182; (c) Nakano, T.; Yade, T. *J. Am. Chem. Soc.* **2003**, *125*, 15474; (d) Nakano, T.; Yade, T.; Yokoyama, M.; Nagayama, N. *Chem. Lett.* **2004**, 296; (e) Nakano, T.; Yade, T.; Fukuda, Y.; Yamaguchi, T.; Okumura, S. *Macromolecules* **2005**, *38*, 8140; (f) Yade, T.; Nakano, T. *J. Polym. Sci., Part A: Polym. Chem.* **2006**, *44*, 561; (g) Nakano, T.; Tanikawa, M.; Nakagawa, O.; Yade, T.; Sakamoto, T. *J. Polym. Sci., Part A: Polym. Chem.* **2009**, *47*, 239.
- (a) Morisaki, Y.; Chujo, Y. *Tetrahedron Lett.* **2005**, *46*, 2533; (b) Morisaki, Y.; Murakami, T.; Chujo, Y. *Macromolecules* **2008**, *41*, 5960; (c) Morisaki, Y.; Murakami, T.; Sawamura, T.; Chujo, Y. *Macromolecules* **2009**, *42*, 3656; (d) Morisaki, Y.; Sawamura, S.; Murakami, T.; Chujo, Y. *Org. Lett.* **2010**, *12*, 3188; (e) Morisaki, Y.; Tsuji, Y.; Chujo, Y. *Tetrahedron Lett.* **2014**, *55*, 1631.
- For example, (a) Seyler, H.; Purushothaman, B.; Jones, D. J.; Holmes, A. B.; Wong, W. W. H. *Pure Appl. Chem.* **2012**, *84*, 1047; (b) Wu, J.; Pisula, W.; Müllen, K. *Chem. Rev.* **2007**, *107*, 718; (c) Hill, J. P.; Jin, W. S.; Kosaka, A.; Fukushima, T.; Ichihara, H.; Shimomura, T.; Ito, K.; Hashizume, T.; Ishii, N.; Aida, T. *Science* **2004**, *304*, 1481; (d) Watson, M. D.; Jäckel, F.; Severin, N.; Rabe, J. P.; Müllen, K. *J. Am. Chem. Soc.* **2004**, *126*, 766.
- (a) Sonogashira, K.; Tohda, Y.; Hagihara, N. *Tetrahedron Lett.* **1975**, *16*, 4467; (b) Sonogashira, K. In *Handbook of Organopalladium Chemistry for Organic Synthesis*; Negishi, E., Ed.; Wiley-Interscience: New York, 2002; p 493.
- Elmahdy, M. M.; Dou, X.; Mondeshki, M.; Floudas, G.; Butt, H.-J.; Spiess, H. W.; Müllen, K. *J. Am. Chem. Soc.* **2008**, *130*, 5311.
- Morisaki, Y.; Nakano, T.; Chujo, Y. *J. Polym. Sci., Part A: Polym. Chem.* **2014**, *52*, 2815.
- Zhao, Y.; Truhlar, D. G. *Theor. Chem. Acc.* **2008**, *120*, 215.
- (a) Ditchfield, R.; Hehre, W. J.; Pople, J. A. *J. Chem. Phys.* **1971**, *54*, 724; (b) Hehre, W. J.; Ditchfield, R.; Pople, J. A. *J. Chem. Phys.* **1972**, *56*, 2257; (c) Hariharan, P. C.; Pople, J. A. *Mol. Phys.* **1974**, *27*, 209; (d) Gordon, M. S. *Chem. Phys. Lett.* **1980**, *76*, 163; (e) Hariharan, P. C.; Pople, J. A. *Theo. Chim. Acta* **1973**, *28*, 213; (f) Blaudeau, J.-P.; McGrath, M. P.; Curtiss, L. A.; Radom, L. *J. Chem. Phys.* **1997**, *107*, 5016; (g) Francl, M. M.; Pietro, W. J.; Hehre, W. J.; Binkley, J. S.; DeFrees, D. J.; Pople, J. A.; Gordon, M. S. *J. Chem. Phys.* **1982**, *77*, 3654; (h) Binning, R. C., Jr.; Curtiss, L. A. *J. Comp. Chem.* **1990**, *11*, 1206; (i) Rassolov, V. A.; Pople, J. A.; Ratner, M. A.; Windus, T. L. *J. Chem. Phys.* **1998**, *109*, 1223; (j) Rassolov, V. A.; Ratner, M. A.; Pople, J. A.; Redfern, P. C.; Curtiss, L. A. *J. Comp. Chem.* **2001**, *22*, 976.
- Frisch, M. J.; Trucks, G. W.; Schlegel, H. B.; Scuseria, G. E.; Robb, M. A.; Cheeseman, J. R.; Scalmani, G.; Barone, V.; Mennucci, B.; Petersson, G. A.; Nakatsuji, H.; Caricato, M.; Li, X.; Hratchian, H. P.; Izmaylov, A. F.; Bloino, J.; Zheng, G.; Sonnenberg, J. L.; Hada, M.; Ehara, M.; Toyota, K.; Fukuda, R.; Hasegawa, J.; Ishida, M.; Nakajima, T.; Honda, Y.; Kitao, O.; Nakai, H.; Vreven, T.; Montgomery, J. A., Jr.; Peralta, J. E.; Ogliaro, F.; Bearpark, M.; Heyd, J. J.; Brothers, E.; Kudin, K. N.; Staroverov, V. N.; Kobayashi, R.; Normand, J.; Raghavachari, K.; Rendell, A.; Burant, J. C.; Iyengar, S. S.; Tomasi, J.; Cossi, M.; Rega, N.; Millam, M. J.; Klene, M.; Knox, J. E.; Cross, J. B.; Bakken, V.; Adamo, C.; Jaramillo, J.; Gomperts, R.; Stratmann, R. E.; Yazyev, O.; Austin, A. J.; Cammi, R.; Pomelli, C.; Ochterski, J. W.; Martin, R. L.; Morokuma, K.; Zakrzewski, V. G.; Voth, G. A.; Salvador, P.; Dannenberg, J. J.; Dapprich, S.; Daniels, A. D.; Farkas, Ö.; Foresman, J. B.; Ortiz, J. V.; Cioslowski, J.; Fox, D. J. *Computations were performed using the Gaussian 09 package of programs. Gaussian 09, Revision C.01*; Gaussian: Wallingford CT, 2009.

DOI: 10.1002/ejoc.201501181

# Highly Emissive Optically Active Conjugated Dimers Consisting of a Planar Chiral [2.2]Paracyclophane Showing Circularly Polarized Luminescence

Masayuki Gon,<sup>[a]</sup> Yasuhiro Morisaki,<sup>\*[b]</sup> and Yoshiki Chujo<sup>\*[a]</sup>**Keywords:** Luminescence / Cyclophanes / Chirality / Conjugation

Optically active X-shaped dimers based on the planar chiral [2.2]paracyclophane have been synthesized. The dimers consist of stacked *p*-arylene-ethynylenes with phenyl, naphthyl, and anthryl groups as terminal units. The optical and chiroptical properties of the dimers and the corresponding model compounds were investigated. The naphthalene-containing

dimer exhibits an intense circularly polarized luminescence (CPL) signal with a high dissymmetry factor ( $g_{lum}$ ) in the order of  $10^{-3}$  in addition to a high  $\epsilon$  and good photoluminescence quantum efficiency, which indicates that this compound is a highly emissive CPL material.

## Introduction

Conjugated compounds based on aromatic groups have attracted considerable attention owing to their application in various optoelectronic devices,<sup>[1]</sup> such as luminescent materials and organic thin film solar cells. [2.2]Paracyclophane is a unique aromatic compound consisting of two stacked benzene rings in close proximity.<sup>[2]</sup> Since the first synthesis by Brown and Farthing<sup>[3]</sup> in 1949 and the first directed synthesis by Cram and Steinberg<sup>[4]</sup> in 1951, a wide variety of [2.2]paracyclophane-based  $\pi$ -conjugated compounds have been prepared and their optoelectronic properties elucidated.<sup>[2]</sup> Bazan and co-workers revealed that the stacked arrangement of two phenylene-vinylene chromophores with a [2.2]paracyclophane skeleton structure affects the conjugated system in the ground and excited states.<sup>[5]</sup>  $\pi$ -Electron systems stacked at the center phenylenes in 4,7,12,15-tetra-linked [2.2]paracyclophane exhibit extensive delocalization throughout the entire molecule (i.e., 3D conjugation).<sup>[5b,5d,5e,5i,5j]</sup> Hopf and co-workers synthesized 3D cyclic compounds by taking advantage of the stacked structure of [2.2]paracyclophane and investigated their optical properties in detail.<sup>[6]</sup> We have focused on the planar chirality of [2.2]paracyclophane derivatives. Planar chirality, which arises from the proximally fixed benzene rings, is one of the interesting structural characteristics of the [2.2]para-

cyclophane skeleton.<sup>[2,7]</sup> Recently, we reported practical methods for the optical resolution of planar chiral 4,12-disubstituted<sup>[8a]</sup> and 4,7,12,15-tetrasubstituted [2.2]paracyclophanes.<sup>[9a]</sup> In addition, we have incorporated planar chirality into [2.2]paracyclophane-based 3D compounds and found that the obtained optically active compounds exhibited circularly polarized luminescence (CPL) with high dissymmetry factors ( $g_{lum}$ ).<sup>[8,9]</sup> However, achieving both brightness (namely, a high molar extinction coefficient and good photoluminescence quantum efficiency) and a high  $g_{lum}$  value by using organic molecules remains a challenge. Herein we report the design and synthesis of optically active X-shaped  $\pi$ -conjugated dimers based on the planar chiral 4,7,12,15-tetrasubstituted [2.2]paracyclophane. The obtained compounds consist of two stacked *p*-phenylene-ethynylenes functionalized by benzene, naphthalene, and anthracene. Their optical and chiroptical properties were investigated in detail. The naphthalene-containing dimer was highly emissive and showed strong CPL.

## Results and Discussion

### Synthesis

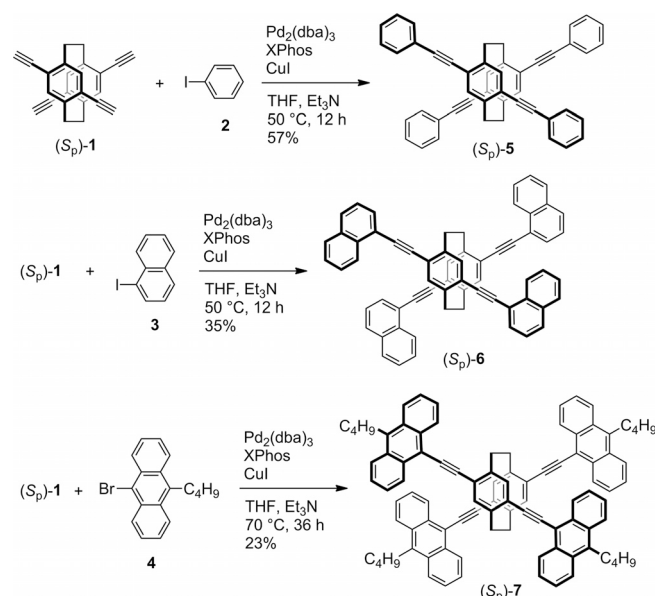
The optical resolution of planar chiral 4,7,12,15-tetra-substituted [2.2]paracyclophane was carried out by using the diastereomer method that we previously developed, and the obtained enantiopure compounds were converted into the corresponding ( $S_p$ )- and ( $R_p$ )-4,7,12,15-tetraethynyl-[2.2]paracyclophanes, ( $S_p$ )- and ( $R_p$ )-**1**.<sup>[9a]</sup> The synthetic routes to the target optically active X-shaped conjugated dimers ( $S_p$ )-**5**–**7** are shown in Scheme 1; the synthesis of the ( $S_p$ ) isomers are shown as representatives; the ( $R_p$ ) isomers were synthesized from ( $R_p$ )-**1** under the same conditions. The Sonogashira–Hagihara coupling<sup>[10]</sup> of ( $S_p$ )-**1** with iodobenzene (**2**) was carried out in the presence of the

[a] Department of Polymer Chemistry, Graduate School of Engineering, Kyoto University, Katsura, Nishikyo-ku Kyoto 615-8510, Japan  
E-mail: chujo@chujo.synchem.kyoto-u.ac.jp  
http://chujo.synchem.kyoto-u.ac.jp/en/

[b] Department of Applied Chemistry for the Environment, School of Science and Technology, Kwansei Gakuin University, 2-1 Gakuen, Sanda, Hyogo 669-1337, Japan  
E-mail: ymo@kwansei.ac.jp  
http://www.kg-applchem.jp/morisaki/en/

Supporting information for this article is available on the WWW under <http://dx.doi.org/10.1002/ejoc.201501181>.

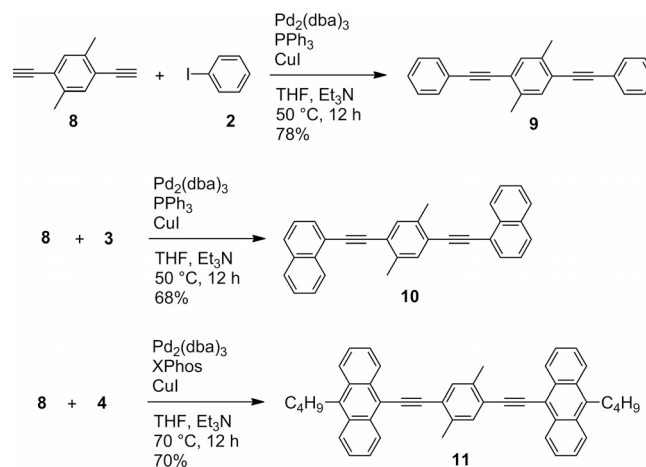
[Pd<sub>2</sub>(dba)<sub>3</sub>]/CuI catalytic system by using 2-dicyclohexylphosphino-2',4',6'-triisopropylbiphenyl (XPhos)<sup>[11]</sup> as phosphine ligand to obtain dimer (S<sub>p</sub>)-5 in an isolated yield of 57%. Dimers (S<sub>p</sub>)-6 and (S<sub>p</sub>)-7 were also obtained in isolated yields of 35 and 23%, respectively. In the synthesis of (S<sub>p</sub>)-7, the reaction temperature was higher than that used for the synthesis of (S<sub>p</sub>)-5 and (S<sub>p</sub>)-6 due to the lower reactivity of the brominated compound 4 as compared with the iodinated compounds 2 and 3. Thus, a variety of aromatic groups can be readily introduced to construct optically active X-shaped second-order structures by using (S<sub>p</sub>)- and (R<sub>p</sub>)-1 as the chiral scaffolds.



Scheme 1. Synthesis of the X-shaped conjugated dimers (S<sub>p</sub>)-5–7.

The X-shaped conjugated dimers (S<sub>p</sub>)-5–7 contain two stacked *p*-phenylene-ethynylenes. Therefore, compounds 9–11 were synthesized as monomeric model compounds (Scheme 2); the Sonogashira–Hagihara coupling of diethynylxylene 8 with 2–4 afforded the corresponding compounds 9–11 in isolated yields of 78, 68, and 70%, respectively. The

structures of all the new compounds in this study were confirmed by <sup>1</sup>H and <sup>13</sup>C NMR spectroscopy, HRMS, and elemental analysis.



Scheme 2. Synthesis of the monomeric model compounds 9–11.

### Optical Properties

The properties of (S<sub>p</sub>)- and (R<sub>p</sub>)-5–7 were evaluated by UV/Vis spectrophotometry, photoluminescence (PL), circular dichroism (CD), and CPL spectroscopy, and the results were compared with those of the monomeric model compounds 9–11. The optical and chiroptical data are summarized in Tables 1 and 2, respectively. Although the UV/Vis and PL properties of *rac*-5 and 9 were reported by Meijere and co-workers in 1993,<sup>[12]</sup> we measured them again and report our original results in this paper; the chiroptical data (CD and CPL) of (S<sub>p</sub>)- and (R<sub>p</sub>)-5 have not been reported previously. Figure 1 (A–C) show the UV/Vis absorption spectra and PL spectra of (S<sub>p</sub>)-5–7 and the model compounds 9–11 in dilute CHCl<sub>3</sub> (1.0 × 10<sup>−5</sup> M for UV and 1.0 × 10<sup>−6</sup> M for PL). As shown in Figure 1 (A), the absorption maximum (λ<sub>max</sub>) of (S<sub>p</sub>)-5 is 349 nm, which is bathochromically shifted in comparison with the λ<sub>max</sub> of 9 (λ<sub>max</sub> = 328 nm), thereby indicating the 3D extension of π

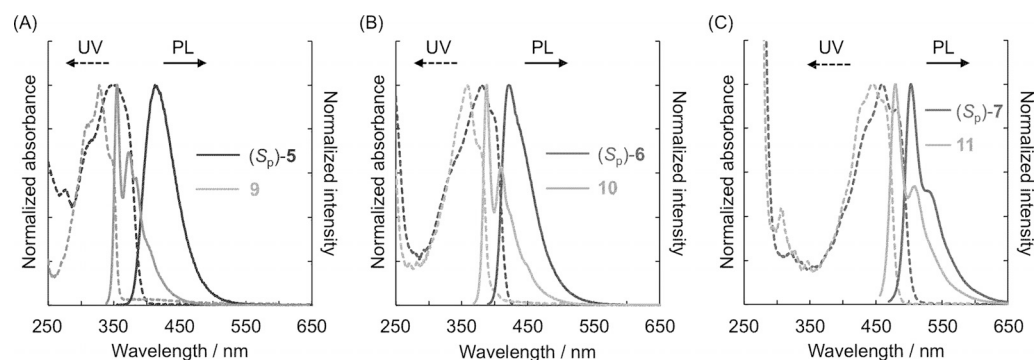


Figure 1. UV/Vis absorption spectra in dilute CHCl<sub>3</sub> (1.0 × 10<sup>−5</sup> M) and PL spectra in dilute CHCl<sub>3</sub> (1.0 × 10<sup>−6</sup> M, excited at each absorption maximum) for (A) (S<sub>p</sub>)-5 and 9, (B) (S<sub>p</sub>)-6 and 10, and (C) (S<sub>p</sub>)-7 and 11.

conjugation through the [2.2]paracyclophane in (*S<sub>p</sub>*)-**5**. The same 3D extension of  $\pi$  conjugation can be observed for naphthalene-containing (*S<sub>p</sub>*)-**6**; the  $\lambda_{\text{max}}$  values of (*S<sub>p</sub>*)-**6** and **10** are 380 and 358 nm, respectively. On the other hand, the differences between the UV/Vis absorption spectra of anthracene-containing (*S<sub>p</sub>*)-**7** and **11** are small, with the  $\lambda_{\text{max}}$  values of (*S<sub>p</sub>*)-**7** and **11** being 459 and 446 nm, respectively.

Table 1. Optical properties: Spectroscopic data of (*S<sub>p</sub>*)-**5–7** and the model compounds **9–11**.

	UV/Vis <sup>[a]</sup>		PL <sup>[b]</sup>		
	$\lambda_{\text{max}}$ [nm] ( $\epsilon$ [ $10^5 \text{ M}^{-1} \text{ cm}^{-1}$ ])	$\lambda_{\text{max}}$ [nm]	$\tau$ [ns]	$\chi^2$ [d]	$\Phi_{\text{lum}}$ [e]
( <i>S<sub>p</sub></i> )- <b>5</b>	349 (0.63)	412	3.67	1.12	0.60
( <i>S<sub>p</sub></i> )- <b>6</b>	380 (0.79)	421	1.89	1.16	0.78
( <i>S<sub>p</sub></i> )- <b>7</b>	268 (2.18), 459 (0.87)	503	2.09	1.03	0.42
<b>9</b>	328 (0.56)	355	0.78	1.11	0.52
<b>10</b>	358 (0.58)	388	0.99	1.18	0.57
<b>11</b>	270 (1.38), 446 (0.49)	479	1.80	1.13	0.48

[a] In  $\text{CHCl}_3$  ( $1.0 \times 10^{-5} \text{ M}$ ). [b] In  $\text{CHCl}_3$  ( $1.0 \times 10^{-6} \text{ M}$ ), excited at the absorption maxima. [c] Emission lifetime at PL  $\lambda_{\text{max}}$ . [d] All PL decay curves were fitted to a single-exponential equation. [e] Absolute PL quantum efficiency.

A broad peak can be observed in the PL spectrum of (*S<sub>p</sub>*)-**5** at 412 nm without vibronic structure (Figure 1, A), in contrast to the monomeric model compound **9**, which shows clear vibronic structure. As shown in Figure 1 (B), dimer (*S<sub>p</sub>*)-**6** shows similar PL behavior to (*S<sub>p</sub>*)-**5**; the PL spectrum is broad and differs from that of the monomeric model compound **10**. As shown in Figure S13 in the Supporting Information, the PL decay curves of all compounds could be fitted to a single-exponential equation, and their PL lifetimes ( $\tau$ ) were calculated (Table 1). The lifetimes of the dimers are longer than those of the monomers (Table 1); for example, the  $\tau$  of (*S<sub>p</sub>*)-**5** is 3.67 ns, whereas that of **9** was calculated to be 0.78 ns. When the energy levels of through-bond and through-space states are identical or close, the

excited state is delocalized throughout the whole molecule.<sup>[5b,5d,5e,5i,5j]</sup> Therefore, the emission from (*S<sub>p</sub>*)-**5** and **-6** occurs from the entire molecule. On the other hand, dimer (*S<sub>p</sub>*)-**7** and monomeric model **11** show similar emission behavior, as shown in Figure 1 (C). The emission maxima of (*S<sub>p</sub>*)-**7** and **11** are at 503 and 479 nm, respectively, and show vibronic structures. According to the PL decay studies on (*S<sub>p</sub>*)-**7** and **11**, their  $\tau$  values were calculated to be 2.09 and 1.80 ns, respectively, which implies that the emitting species are similar; specifically, emission occurs predominantly from the terminal anthryl moieties. The electronic state of (*S<sub>p</sub>*)-**7** resembles the corresponding monomeric chromophore in the same manner as the partly stacked dimer with pseudo-*p*-[2.2]paracyclophane, which results in emission from the monomer state (chromophore state) instead of emission from the entire molecule.<sup>[5,13]</sup>

### Chiroptical Properties

The chiroptical properties of compounds **5–7** in the ground and excited states were investigated by CD and CPL spectroscopy, respectively. The corresponding data are summarized in Table 2. Figure 2 (A–C) show the CD and absorption spectra of both enantiomers of **5–7** in dilute  $\text{CHCl}_3$  ( $1.0 \times 10^{-5} \text{ M}$ ). In all cases, mirror-image Cotton effects can be observed, and the absorbance dissymmetry factors ( $g_{\text{abs}}$ )<sup>[14]</sup> for the first Cotton effect in (*S<sub>p</sub>*)-**5–7** were estimated to be  $+1.6 \times 10^{-3}$ ,  $+1.7 \times 10^{-3}$ , and  $+0.9 \times 10^{-3}$ , respectively. The broad absorption peak at around 350 nm in the spectrum of (*S<sub>p</sub>*)-**5** is typical of the  $\pi$ - $\pi^*$  transition band of *p*-phenylene-ethynylenes, and the bands of (*S<sub>p</sub>*)-**6** are considered to be due to both the  $\pi$ - $\pi^*$  transition band of *p*-arylene-ethynylenes and the S0–S1 transition band of the naphthalene moiety. The vibrational absorption peaks of (*S<sub>p</sub>*)-**7** at around 450 nm are also assigned to the S0–S1 transition in the anthracene moiety. As shown in the CD

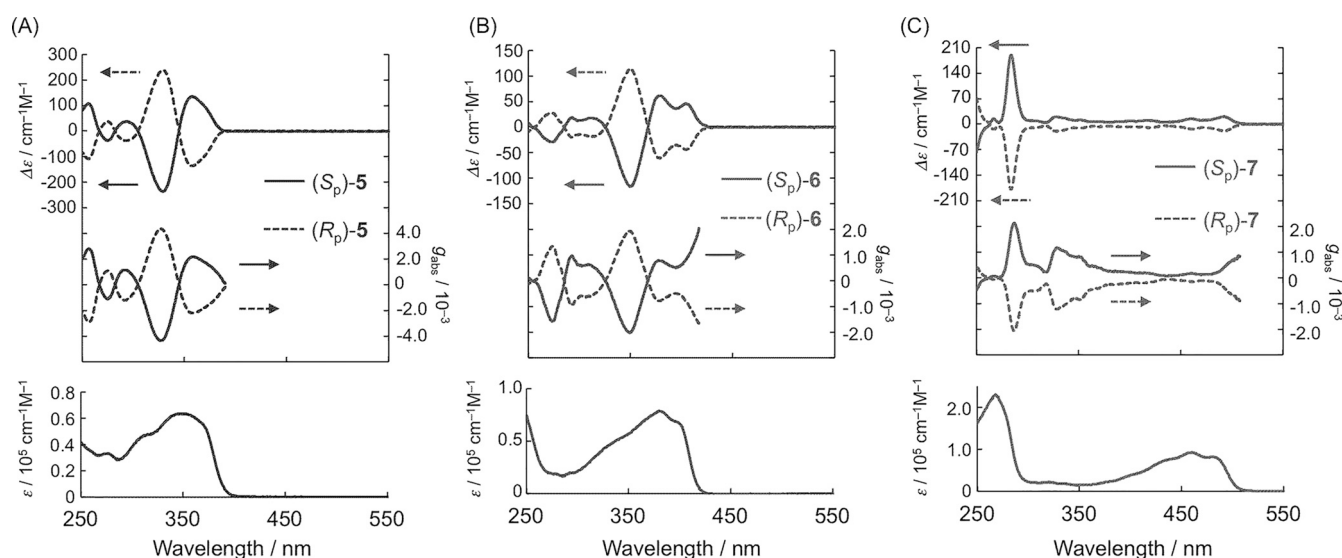


Figure 2. CD (top),  $g_{\text{abs}}$  (middle), and UV/Vis absorption (bottom) spectra of (A) (*S<sub>p</sub>*)-**5** and (*R<sub>p</sub>*)-**5**, (B) (*S<sub>p</sub>*)-**6** and (*R<sub>p</sub>*)-**6**, and (C) (*S<sub>p</sub>*)-**7** and (*R<sub>p</sub>*)-**7** in dilute  $\text{CHCl}_3$  ( $1.0 \times 10^{-5} \text{ M}$ ).

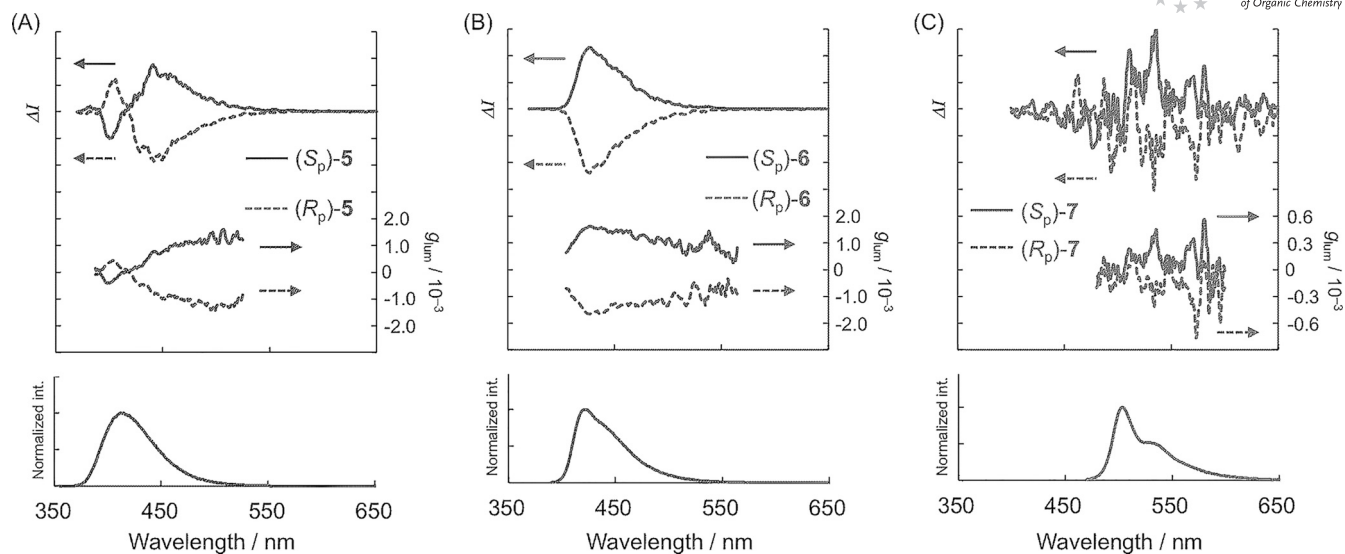


Figure 3. CPL (top),  $g_{lum}$  (middle), and PL (bottom) spectra of (A)  $(S_p)$ -**5** and  $(R_p)$ -**5**, (B)  $(S_p)$ -**6** and  $(R_p)$ -**6**, and (C)  $(S_p)$ -**7** and  $(R_p)$ -**7** in dilute  $CHCl_3$  ( $1.0 \times 10^{-5}$  M for CPL and  $1.0 \times 10^{-6}$  M for PL); excitation wavelengths were 300, 300, and 350 nm, respectively.

spectra of  $(S_p)$ -**5–7**, chirality was induced in the arylene-ethynylene moieties by the planar chiral [2.2]paracyclophane unit, but was not sufficiently induced in the terminal aromatic groups.

Table 2. Chiroptical properties: Spectroscopic data of  $(S_p)$ - and  $(R_p)$ -**5–7**.

	$g_{abs}^{[a]}$ [ $10^{-3}$ ] at UV $\lambda_{max}$	$g_{lum}^{[b]}$ [ $10^{-3}$ ] at PL $\lambda_{max}$
$(S_p)$ - <b>5</b>	+1.6	+1.1
$(S_p)$ - <b>6</b>	+1.7	+1.6
$(S_p)$ - <b>7</b>	+0.9	+0.5
$(R_p)$ - <b>5</b>	-1.7	-1.2
$(R_p)$ - <b>6</b>	-1.6	-1.7
$(R_p)$ - <b>7</b>	-0.9	-0.4

[a]  $g_{abs} = 2\Delta\epsilon/\epsilon$ , in which  $\Delta\epsilon$  indicates the difference in the absorbance between left- and right-handed circularly polarized light. [b]  $g_{lum} = 2(I_{left} - I_{right})/(I_{left} + I_{right})$ , in which  $I_{left}$  and  $I_{right}$  indicate the luminescence intensities of left- and right-handed CPL, respectively.

The CPL spectra of  $(S_p)$ - and  $(R_p)$ -**5–7** in dilute  $CHCl_3$  ( $1.0 \times 10^{-5}$  M) are shown in Figure 3. Mirror-image CPL signals can be observed in all cases. The CPL spectrum of  $(S_p)$ -**5** exhibits positive and negative signals. This implies that the PL consists of a few transitions. One or some of them exhibit opposite signs, and a split CPL signal is observed, depending on their oscillator strengths. At this stage, the types of transitions as well as their electric and magnetic transition dipole moments in the excited state are unclear. The systematic synthesis of planar chiral [2.2]paracyclophane-based compounds and their time-dependent density functional theory (TD-DFT) analyses in the excited state are underway. The absolute  $g_{lum}$  values<sup>[15]</sup> for  $(S_p)$ - and  $(R_p)$ -**5** were estimated to be approximately  $1.0 \times 10^{-3}$ . As shown in Figure 3 (B) the naphthalene-containing dimers  $(S_p)$ - and  $(R_p)$ -**6** give intense CPL signals with high  $g_{lum}$  values of +1.6 and  $-1.7 \times 10^{-3}$ , respectively. Judging from the high value of  $\epsilon$  of  $0.79 \times 10^5$  M<sup>-1</sup> cm<sup>-1</sup> and good  $\Phi_{lum}$  of

0.78 in addition to the high  $g_{lum}$  value, the dimers **6** are promising CPL materials. On the other hand, the anthracene-containing dimers  $(S_p)$ - and  $(R_p)$ -**7** did not show sufficient CPL performance. Their spectra show noisy CPL signals (Figure 3, C), and their  $g_{lum}$  values were estimated to be +0.5 and  $-0.4 \times 10^{-3}$ , respectively, which indicates that the anthracenes in **7** do not interact in the excited state.

## Conclusions

Optically active X-shaped  $\pi$ -conjugated dimers based on planar chiral [2.2]paracyclophane have been synthesized. The dimers comprise two *p*-arylene-ethynylenes stacked at the center phenylenes. The terminal aryl unit controls the PL behavior of the  $\pi$ -conjugated dimers. The phenyl- and naphthyl-containing dimers emit mainly from the whole molecule, whereas the anthryl-containing dimer emits predominantly from the unstacked terminal anthryl moieties. CD spectroscopy revealed that the planar chirality of the [2.2]paracyclophane unit is induced in the X-shaped arylene-ethynylene moieties, but that chirality was not sufficiently induced in the terminal aromatic groups. The phenyl- and naphthyl-containing dimers emit intense CPL, whereas a weak CPL signal was observed in the case of the anthracene-containing dimer. In particular, the naphthyl-containing dimer is an excellent CPL emitter, achieving a high  $g_{lum}$  in the order of  $10^{-3}$ , a high  $\epsilon$  of  $0.79 \times 10^5$  M<sup>-1</sup> cm<sup>-1</sup>, and a good  $\Phi_{lum}$  of 0.78. These results indicate the importance of the relationship between the planar chiral [2.2]paracyclophane and the attached chromophore. 4,7,12,15-Tetraethynyl[2.2]paracyclophane can be modified by various aromatic groups to construct X-shaped second-order structures. The design of new planar chiral [2.2]paracyclophane-based  $\pi$ -conjugated systems as CPL emitters and elucidation of the CPL mechanism will be investigated in our future work.

## Experimental Section

**General:**  $^1\text{H}$  and  $^{13}\text{C}$  NMR spectra were recorded with JEOL EX400 and AL400 spectrometers at 400 and 100 MHz, respectively. Samples were analyzed in  $\text{CDCl}_3$  and  $\text{CD}_2\text{Cl}_2$ . Analytical TLC was performed with silica gel 60 Merck F254 plates. Column chromatography was performed with Wakogel C-300 silica gel. HRMS was performed at the Technical Support Office (Department of Synthetic Chemistry and Biological Chemistry, Graduate School of Engineering, Kyoto University) by using a Thermo Fisher Scientific orbitrapXL spectrometer for matrix-assisted laser desorption/ionization (MALDI). UV/Vis spectra were recorded with a Shimadzu UV-3600 spectrophotometer, and samples were analyzed in  $\text{CHCl}_3$  at room temperature. Fluorescence emission spectra were recorded with a HORIBA JOBIN YVON Fluoromax-4 spectrofluorimeter, and samples were analyzed in  $\text{CHCl}_3$  at room temperature. The PL lifetimes were measured with a Horiba FluoreoCube spectrofluorimeter; excitation was carried out by using a UV diode laser (NanoLED 292 nm). Specific rotations ( $[\alpha]_D^{25}$ ) were measured with a HORIBA SEPA-500 polarimeter. Circular dichroism (CD) spectra were recorded with a JASCO J-820 spectropolarimeter with  $\text{CHCl}_3$  as solvent at room temperature. Circularly polarized luminescence (CPL) spectra were recorded with a JASCO CPL-200S instrument with  $\text{CHCl}_3$  as solvent at room temperature. Elemental analyses were performed at the Organic Elemental Microanalysis Laboratory of Kyoto University.

The following compounds are commercially available and were used without purification: Iodobenzene (**2**), 1-iodonaphthalene (**3**), and  $[\text{Pd}_2(\text{dba})_3]$  (dba = dibenzylideneacetone) all from Tokyo Chemical Industry Co, Ltd., 2-dicyclohexylphosphino-2',4',6'-triisopropylbiphenyl (XPhos) from Sigma-Aldrich Co. LLC., and  $\text{PPh}_3$  and CuI from Wako Pure Chemical Industries, Ltd.

THF (Wako Pure Chemical Industries, Ltd.) and  $\text{Et}_3\text{N}$  (Kanto Chemical Co., Inc.) are commercially available and were purified by the GlassContour solvent purification system.<sup>[16]</sup>

$(R_p)$ - and  $(S_p)$ -4,7,12,15-tetraethynyl[2.2]paracyclophane [ $(R_p)$ - and  $(S_p)$ -**1**],<sup>[9a]</sup> 9-bromo-10-butylanthracene (**4**),<sup>[17]</sup> and 2,5-diethynyl-*p*-xylene (**8**)<sup>[18]</sup> were prepared as described in the literature.

**Synthesis of  $(S_p)$ -5:** A mixture of  $(S_p)$ -**1** (50 mg, 0.164 mmol), **2** (80.4  $\mu\text{L}$ , 0.722 mmol),  $[\text{Pd}_2(\text{dba})_3]$  (30.1 mg, 0.0329 mmol), XPhos (62.5 mg, 0.131 mmol), CuI (12.5 mg, 0.0657 mmol), THF (5 mL), and  $\text{Et}_3\text{N}$  (5 mL) was placed in a round-bottomed flask equipped with a magnetic stirring bar. After degassing the reaction mixture several times, the reaction was carried out at 50 °C for 12 h. After cooling the reaction mixture to room temperature, the precipitate was removed by filtration and the solvent removed on a rotary evaporator. The residue was purified by column chromatography on  $\text{SiO}_2$  ( $\text{CHCl}_3/\text{hexane} = 1:2$ , v/v, as eluent) and recrystallization from hexane to afford  $(S_p)$ -**5** (56.7 mg, 0.0931 mmol, 57%) as colorless needle crystals.  $R_f = 0.16$  ( $\text{CHCl}_3/\text{hexane} = 1:4$ , v/v).  $^1\text{H}$  NMR ( $\text{CDCl}_3$ , 400 MHz):  $\delta = 3.07$ – $3.15$  (m, 4 H),  $3.54$ – $3.61$  (m, 4 H),  $7.17$  (s, 4 H),  $7.35$ – $7.43$  (m, 12 H),  $7.58$ – $7.61$  (m, 8 H) ppm.  $^{13}\text{C}$  NMR ( $\text{CDCl}_3$ , 100 MHz):  $\delta = 32.7$ , 89.2, 94.5, 123.7, 125.2, 128.3, 128.5, 131.6, 134.7, 141.9 ppm. HRMS (MALDI): calcd. for  $\text{C}_{48}\text{H}_{32} [\text{M}]^+$  608.24985; found 608.25171.  $\text{C}_{48}\text{H}_{32}$  (608.78): calcd. C 94.70, H 5.30; found C 94.82, H 5.17.  $(R_p)$ -**5** was obtained by the same procedure in an isolated yield of 42%.

$(S_p)$ -**5**:  $[\alpha]_D^{25} = -77.4$  ( $c = 0.1$ ,  $\text{CHCl}_3$ ).  $(R_p)$ -**5**:  $[\alpha]_D^{25} = +72.9$  ( $c = 0.1$ ,  $\text{CHCl}_3$ ).

**Synthesis of  $(S_p)$ -6:** A mixture of  $(S_p)$ -**1** (30 mg, 0.0986 mmol), **3** (63.4  $\mu\text{L}$ , 0.434 mmol),  $[\text{Pd}_2(\text{dba})_3]$  (18.0 mg, 0.0197 mmol), XPhos

(37.6 mg, 0.0789 mmol), CuI (7.5 mg, 0.0394 mmol), THF (5 mL), and  $\text{Et}_3\text{N}$  (5 mL) was placed in a round-bottomed flask equipped with a magnetic stirring bar. After degassing the reaction mixture several times, the reaction was carried out at 50 °C for 12 h. After cooling the reaction mixture to room temperature, the precipitate was removed by filtration and the solvent removed on a rotary evaporator. The residue was purified by column chromatography on  $\text{SiO}_2$  ( $\text{CHCl}_3/\text{hexane} = 1:2$ , v/v, as eluent) and recrystallization from hexane and  $\text{CHCl}_3$  (poor and good solvents, respectively) to afford  $(S_p)$ -**6** (27.9 mg, 0.0345 mmol, 35%) as yellow plate crystals.  $R_f = 0.46$  ( $\text{CHCl}_3/\text{hexane} = 1:2$ , v/v).  $^1\text{H}$  NMR ( $\text{CDCl}_3$ , 400 MHz):  $\delta = 3.29$ – $3.37$  (m, 4 H),  $3.78$ – $3.86$  (m, 4 H),  $7.34$  (dt,  $J = 0.96$ , 6.8 Hz, 4 H),  $7.44$  (s, 4 H),  $7.47$ – $7.51$  (m, 8 H),  $7.84$  (dd,  $J = 0.96$ , 7.1 Hz, 8 H),  $7.90$  (d,  $J = 8.3$  Hz, 4 H),  $8.53$  (d,  $J = 8.3$  Hz, 4 H) ppm.  $^{13}\text{C}$  NMR ( $\text{CDCl}_3$ , 100 MHz):  $\delta = 33.0$ , 93.0, 94.1, 121.2, 125.4, 125.5, 126.2, 126.5, 127.1, 128.3, 128.9, 130.7, 133.3, 133.3, 135.0, 142.1 ppm. HRMS (MALDI): calcd. for  $\text{C}_{64}\text{H}_{40} [\text{M}]^+$  808.31245; found 808.31519.  $\text{C}_{64}\text{H}_{40}$  (809.02): calcd. C 95.02, H 4.98; found C 94.81, H 4.85.  $(R_p)$ -**6** was obtained by the same procedure in an isolated yield of 64%.

$(S_p)$ -**6**:  $[\alpha]_D^{25} = +209.1$  ( $c = 0.1$ ,  $\text{CHCl}_3$ ).  $(R_p)$ -**6**:  $[\alpha]_D^{25} = -203.8$  ( $c = 0.1$ ,  $\text{CHCl}_3$ ).

**Synthesis of  $(S_p)$ -7:** A mixture of  $(S_p)$ -**1** (40 mg, 0.131 mmol), **4** (180.5 mg, 0.576 mmol),  $[\text{Pd}_2(\text{dba})_3]$  (24.0 mg, 0.0262 mmol), XPhos (50.0 mg, 0.105 mmol), CuI (10.0 mg, 0.0524 mmol), THF (5 mL), and  $\text{Et}_3\text{N}$  (5 mL) was placed in a round-bottomed flask equipped with a magnetic stirring bar. After degassing the reaction mixture several times, the reaction was carried out at 70 °C for 36 h. After cooling the reaction mixture to room temperature, the precipitate was removed by filtration and the solvent removed on a rotary evaporator. The residue was purified by column chromatography on  $\text{SiO}_2$  ( $\text{CHCl}_3/\text{hexane} = 1:2$ , v/v, as eluent) and recrystallization from  $\text{CHCl}_3$  (good solvent) with hexane and MeOH (poor solvents) to afford  $(S_p)$ -**7** (37.4 mg, 0.0303 mmol, 23%) as light-brown crystals.  $R_f = 0.58$  ( $\text{CHCl}_3/\text{hexane} = 1:2$ , v/v).  $^1\text{H}$  NMR ( $\text{CD}_2\text{Cl}_2$ , 400 MHz):  $\delta = 1.10$  (t,  $J = 7.4$  Hz, 12 H), 1.67 (sext,  $J = 7.6$  Hz, 8 H), 1.84–1.92 (m, 8 H), 3.60–3.71 (m, 12 H), 4.08–4.16 (m, 4 H), 7.06–7.10 (m, 8 H), 7.38–7.42 (m, 8 H), 7.71 (s, 4 H), 8.32 (d,  $J = 8.8$  Hz, 8 H), 8.73 (d,  $J = 8.3$  Hz, 8 H) ppm.  $^{13}\text{C}$  NMR ( $\text{CD}_2\text{Cl}_2$ , 100 MHz):  $\delta = 14.3$ , 23.8, 28.5, 33.7, 34.1, 92.9, 101.0, 116.5, 125.2, 126.1, 126.3, 126.7, 127.7, 129.7, 133.0, 135.5, 138.1, 142.3 ppm. HRMS (MALDI): calcd. for  $\text{C}_{96}\text{H}_{80} [\text{M}]^+$  1232.62545; found 1232.62964.  $\text{C}_{96}\text{H}_{80}$  (1233.69): calcd. C 93.46, H 6.54; found C 93.25, H 6.38.  $(R_p)$ -**7** was obtained by the same procedure in an isolated yield of 20%.

$(S_p)$ -**7**:  $[\alpha]_D^{25} = +875.4$  ( $c = 0.1$ ,  $\text{CHCl}_3$ ).  $(R_p)$ -**7**:  $[\alpha]_D^{25} = -873.3$  ( $c = 0.1$ ,  $\text{CHCl}_3$ ).

**Synthesis of 9:** A mixture of **2** (0.18 mL, 1.62 mmol), **8** (100 mg, 0.648 mmol),  $[\text{Pd}_2(\text{dba})_3]$  (29.7 mg, 0.0324 mmol),  $\text{PPh}_3$  (34.0 mg, 0.130 mmol), CuI (12.4 mg, 0.0648 mmol), THF (5 mL), and  $\text{Et}_3\text{N}$  (5 mL) was placed in a round-bottomed flask equipped with a magnetic stirring bar. After degassing the reaction mixture several times, the reaction was carried out at 50 °C for 12 h. After cooling the reaction mixture to room temperature, the precipitate was removed by filtration and the solvent removed on a rotary evaporator. The residue was purified by column chromatography on  $\text{SiO}_2$  (hexane as eluent) and recrystallization from hexane to afford **9** (154.4 mg, 0.504 mmol, 78%) as colorless plate crystals.  $R_f = 0.16$  (hexane).  $^1\text{H}$  NMR ( $\text{CDCl}_3$ , 400 MHz):  $\delta = 2.47$  (s, 6 H), 7.33–7.37 (m, 8 H), 7.52–7.54 (m, 4 H) ppm.  $^{13}\text{C}$  NMR ( $\text{CDCl}_3$ , 100 MHz):  $\delta = 20.0$ , 88.3, 94.5, 123.0, 123.4, 128.3, 128.4, 131.5, 132.6, 137.3 ppm. HRMS (MALDI): calcd. for  $\text{C}_{24}\text{H}_{18} [\text{M}]^+$  306.14030;

found 304.14056. C<sub>24</sub>H<sub>18</sub> (306.41): calcd. C 94.08, H 5.92; found C 94.03, H 5.86.

**Synthesis of 10:** A mixture of **3** (2.37 mL, 1.62 mmol), **8** (100 mg, 0.648 mmol), [Pd<sub>2</sub>(dba)<sub>3</sub>] (29.7 mg, 0.0324 mmol), PPh<sub>3</sub> (34.0 mg, 0.130 mmol), CuI (12.4 mg, 0.0648 mmol), THF (5 mL), and Et<sub>3</sub>N (5 mL) was placed in a round-bottomed flask equipped with a magnetic stirring bar. After degassing the reaction mixture several times, the reaction was carried out at 50 °C for 12 h. After cooling the reaction mixture to room temperature, the precipitate was removed by filtration and the solvent removed on a rotary evaporator. The residue was purified by column chromatography on SiO<sub>2</sub> (CHCl<sub>3</sub>/hexane = 1:9, v/v, as eluent) and recrystallization from hexane and toluene (poor and good solvents, respectively) to afford **10** (179.6 mg, 0.442 mmol, 68%) as light-yellow crystals. R<sub>f</sub> = 0.20 (CHCl<sub>3</sub>/hexane = 1:9, v/v). <sup>1</sup>H NMR (CDCl<sub>3</sub>, 400 MHz): δ = 2.63 (s, 6 H), 7.46–7.50 (m, 2 H), 7.53–7.57 (m, 4 H), 7.60–7.64 (m, 2 H), 7.79 (dd, J = 1.4, 7.1 Hz, 2 H), 7.85–7.89 (m, 4 H), 8.47 (d, J = 8.3 Hz, 2 H) ppm. <sup>13</sup>C NMR (CDCl<sub>3</sub>, 100 MHz): δ = 20.4, 92.9, 93.3, 121.2, 123.4, 125.3, 126.3, 126.5, 126.9, 128.4, 128.8, 130.5, 133.0, 133.3, 133.4, 137.3 ppm. HRMS (MALDI): calcd. for C<sub>32</sub>H<sub>22</sub> [M]<sup>+</sup> 406.17160; found 406.17014. C<sub>32</sub>H<sub>22</sub> (406.53): C 94.55 H 5.45; found C 94.56 H 5.47.

**Synthesis of 11:** A mixture of **4** (213 mg, 0.681 mmol), **8** (50 mg, 0.324 mmol), [Pd<sub>2</sub>(dba)<sub>3</sub>] (14.8 mg, 0.0162 mmol), XPhos (30.9 mg, 0.648 mmol), CuI (6.2 mg, 0.0324 mmol), THF (5 mL), and Et<sub>3</sub>N (5 mL) was placed in a round-bottomed flask equipped with a magnetic stirring bar. After degassing the reaction mixture several times, the reaction was carried out at 70 °C for 12 h. After cooling the reaction mixture to room temperature, the precipitate was removed by filtration and the solvent removed on a rotary evaporator. The residue was purified by column chromatography on SiO<sub>2</sub> (CHCl<sub>3</sub>/hexane = 1:4, v/v, as eluent) and recrystallization from hexane and toluene (poor and good solvents, respectively) to afford **11** (140.8 mg, 0.228 mmol, 70%) as yellow crystals. R<sub>f</sub> = 0.38 (CHCl<sub>3</sub>/hexane = 1:4, v/v). <sup>1</sup>H NMR (CDCl<sub>3</sub>, 400 MHz): δ = 1.05 (t, J = 7.6 Hz, 6 H), 1.62 (sext, J = 7.3 Hz, 4 H), 1.79–1.87 (m, 4 H), 2.77 (s, 6 H), 3.62–3.66 (m, 4 H), 7.55–7.65 (m, 8 H), 7.70 (s, 2 H), 8.32 (d, J = 8.6 Hz, 4 H), 8.76–8.78 (m, 4 H) ppm. <sup>13</sup>C NMR (CDCl<sub>3</sub>, 100 MHz): δ = 14.1, 20.9, 23.5, 28.2, 33.7, 92.1, 99.7, 116.3, 123.6, 124.9, 125.6, 126.1, 127.6, 129.2, 132.4, 132.9, 137.1, 137.4 ppm. HRMS (MALDI): calcd. for C<sub>48</sub>H<sub>42</sub> [M]<sup>+</sup> 618.32810; found 618.32677. C<sub>48</sub>H<sub>42</sub> (618.86): C 93.16 H 6.84; found C 93.13 H 6.86.

## Acknowledgments

This work was supported by the Ministry of Education, Culture, Sports, Science and Technology (MEXT), Japan for a Grant-in-Aid for Scientific Research on Innovative Areas (grant number 15H00992) “π-Figuration”. M. G. thanks the Japan Society for the Promotion of Science for Young Scientists for a research fellowship (grant number 14J02514). The authors are grateful to Professor Kazuo Akagi and Dr. Kazuyoshi Watanabe (Department of Polymer Chemistry, Graduate School of Engineering, Kyoto University) for CPL data analysis.

[1] See, for example: a) T. A. Skotheim, R. L. Elsenbaumer, J. R. Reynolds (Eds.), *Handbook of Conducting Polymers*, 3rd ed., Marcel Dekker, New York, **2006**; b) K. Müellen, U. Scherf (Eds.), *Organic Light Emitting Devices: Synthesis Properties and Application*, Wiley-VCH, Weinheim, Germany, **2006**; c) J. R. Groza, J. J. Locklin (Eds.), *Organic Field-Effect Transistors*, CRC Press, Taylor & Francis Group, New York, **2007**; d)

C. Brabec, V. Dyakonov, U. Scherf (Eds.), *Organic Photovoltaics: Materials, Device Physics, and Manufacturing Technologies*, Wiley-VCH, Weinheim, Germany, **2008**.

- [2] a) F. Vögtle (Ed.), *Cyclophane Chemistry: Synthesis Structures and Reactions*, Wiley, Chichester, UK, **1993**; b) R. Gleiter, H. Hopf (Eds.), *Modern Cyclophane Chemistry*, Wiley-VCH, Weinheim, Germany, **2004**; c) H. Hopf, *Angew. Chem. Int. Ed.* **2008**, *47*, 9808–9812; *Angew. Chem.* **2008**, *120*, 9954.
- [3] C. J. Brown, A. C. Farthing, *Nature* **1949**, *164*, 915–916.
- [4] D. J. Cram, H. Steinberg, *J. Am. Chem. Soc.* **1951**, *73*, 5691–5704.
- [5] a) G. C. Bazan, W. J. Oldham Jr., R. J. Lachicotte, S. Tretiak, V. Chernyak, S. Mukamel, *J. Am. Chem. Soc.* **1998**, *120*, 9188–9204; b) S. Wang, G. C. Bazan, S. Tretiak, S. Mukamel, *J. Am. Chem. Soc.* **2000**, *122*, 1289–1297; c) J. Zyss, I. Ledoux, S. Volkov, V. Chernyak, S. Mukamel, G. P. Bartholomew, G. C. Bazan, *J. Am. Chem. Soc.* **2000**, *122*, 11956–11962; d) G. P. Bartholomew, G. C. Bazan, *Acc. Chem. Res.* **2001**, *34*, 30–39; e) G. P. Bartholomew, G. C. Bazan, *Synthesis* **2002**, 1245–1255; f) G. P. Bartholomew, G. C. Bazan, *J. Am. Chem. Soc.* **2002**, *124*, 5183–5196; g) D. S. Seferos, D. A. Banach, N. A. Alcantar, J. N. Israelachvili, G. C. Bazan, *J. Org. Chem.* **2004**, *69*, 1110–1119; h) G. P. Bartholomew, M. Rumi, S. J. K. Pond, J. W. Perry, S. Tretiak, G. C. Bazan, *J. Am. Chem. Soc.* **2004**, *126*, 11529–11542; i) J. W. Hong, H. Y. Woo, G. C. Bazan, *J. Am. Chem. Soc.* **2005**, *127*, 7435–7443; j) G. C. Bazan, *J. Org. Chem.* **2007**, *72*, 8615–8635.
- [6] a) L. Bondarenko, I. Dix, H. Hinrichs, H. Hopf, *Synthesis* **2004**, *16*, 2751–2759; b) H. A. Hinrichs, J. Boydston, P. G. Jones, K. Hess, R. Herges, M. M. Haley, H. Hopf, *Chem. Eur. J.* **2006**, *12*, 7103–7115.
- [7] a) D. J. Cram, N. L. Allinger, *J. Am. Chem. Soc.* **1955**, *77*, 6289–6294; b) V. Rozenberg, E. Sergeeva, H. Hopf, in: *Modern Cyclophane Chemistry* (Eds.: R. Gleiter, H. Hopf), Wiley-VCH, Weinheim, Germany, **2004**, p. 435–462; c) G. J. Rowlands, *Org. Biomol. Chem.* **2008**, *6*, 1527–1534; d) S. E. Gibson, J. D. Knight, *Org. Biomol. Chem.* **2003**, *1*, 1256–1269; e) A. A. Aly, A. B. Brown, *Tetrahedron* **2009**, *65*, 8055–8089; f) J. Paradies, *Synthesis* **2011**, 3749–3766.
- [8] a) Y. Morisaki, R. Hifumi, L. Lin, K. Inoshita, Y. Chujo, *Chem. Lett.* **2012**, *41*, 990–992; b) Y. Morisaki, R. Hifumi, L. Lin, K. Inoshita, Y. Chujo, *Polym. Chem.* **2012**, *3*, 2727–2730; c) Y. Morisaki, K. Inoshita, Y. Chujo, *Chem. Eur. J.* **2014**, *20*, 8386–8390; d) Y. Morisaki, K. Inoshita, S. Shibata, Y. Chujo, *Polym. J.* **2015**, *47*, 278–281.
- [9] a) Y. Morisaki, M. Gon, T. Sasamori, N. Tokitoh, Y. Chujo, *J. Am. Chem. Soc.* **2014**, *136*, 3350–3353; b) M. Gon, Y. Morisaki, Y. Chujo, *J. Mater. Chem. C* **2015**, *3*, 521–529.
- [10] a) Y. Tohda, K. Sonogashira, N. Hagihara, *Tetrahedron Lett.* **1975**, *16*, 4467–4470; b) K. Sonogashira, in: *Handbook of Organopalladium Chemistry for Organic Synthesis* (Ed.: E. Negishi), Wiley-Interscience, New York, **2002**, p. 493–529.
- [11] K. Billingsley, S. L. Buchwald, *J. Am. Chem. Soc.* **2007**, *129*, 3358–3366.
- [12] B. König, B. Knieriem, A. Meijere, *Chem. Ber.* **1993**, *126*, 1643–1650.
- [13] a) Y. Morisaki, Y. Chujo, *Angew. Chem. Int. Ed.* **2006**, *45*, 6430–6437; *Angew. Chem.* **2006**, *118*, 6580; b) Y. Morisaki, Y. Chujo, *Polym. Chem.* **2011**, *2*, 1249–1257; c) Y. Morisaki, Y. Chujo, *Chem. Lett.* **2012**, *41*, 840–846; d) Y. Morisaki, S. Ueno, A. Saeki, A. Asano, S. Seki, Y. Chujo, *Chem. Eur. J.* **2012**, *18*, 4216–4224.
- [14] The absorption dissymmetry factor ( $g_{\text{abs}}$ ) is defined as  $g_{\text{abs}} = 2\Delta\epsilon/\epsilon$ , in which  $\Delta\epsilon$  indicates the difference in the molar extinction coefficients of left- and right-handed circularly polarized light.
- [15] CPL dissymmetry factor ( $g_{\text{lum}}$ ) is defined as  $g_{\text{lum}} = 2(I_{\text{left}} - I_{\text{right}})/(I_{\text{left}} + I_{\text{right}})$ , in which  $I_{\text{left}}$  and  $I_{\text{right}}$  indicate the luminescence intensities of left- and right-handed CPL, respectively.

- [16] A. B. Pangborn, M. A. Giardello, R. H. Grubbs, R. K. Rosen, F. J. Timmers, *Organometallics* **1996**, *15*, 1518–1520.
- [17] P. Keg, A. Dell'Aquila, F. Marinelli, O. L. Kapitanchuk, D. Fichou, P. Mastroilli, G. Romanazzi, G. P. Suranna, L. Torsi, Y. M. Lam, S. G. Mhaisalkar, *J. Mater. Chem.* **2010**, *20*, 2448–2456.
- [18] S. Takahashi, Y. Kuroyama, K. Sonogashira, N. Hagihara, *Synthesis* **1980**, *8*, 627–630.

Received: September 10, 2015  
Published Online: November 10, 2015

# Direct $\alpha$ -Arylation of Alcohols with Aryl Halides through a Radical Chain Mechanism

Kohei Aoki,<sup>a</sup> Kyohei Yonekura,<sup>a</sup> Yuko Ikeda,<sup>a</sup> Ryota Ueno,<sup>b</sup> and Eiji Shirakawa<sup>a,\*</sup>

<sup>a</sup> Department of Applied Chemistry for Environment, School of Science and Technology, Kwansei Gakuin University, Sanda, Hyogo, 669-1337 (Japan)

E-mail: eshirakawa@kwansei.ac.jp

<sup>b</sup> Department of Chemistry, Graduate School of Science, Kyoto University, Sakyo, Kyoto, 606-8502 (Japan)

Manuscript received: February 16, 2020; Revised manuscript received: April 7, 2020;

Version of record online: ■■, ■■



Supporting information for this article is available on the WWW under <https://doi.org/10.1002/adsc.202000216>

**Abstract:** Alcohols were found to be arylated directly at their  $\alpha$ -C–H bond with aryl halides in the presence of a base and a substoichiometric amount of *t*-BuOO*t*-Bu through a homolytic aromatic substitution mechanism.

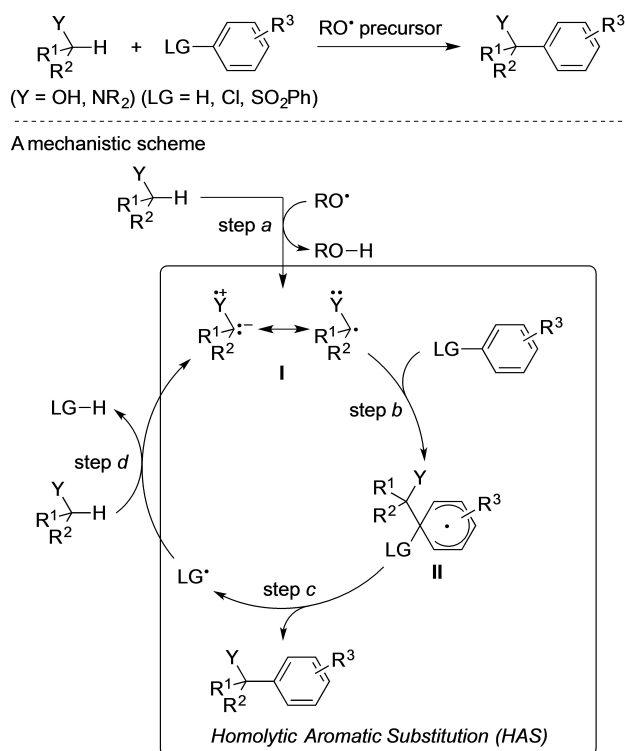
**Keywords:** Alcohols; Aromatic substitution; Radical reactions; Synthetic methods

Direct  $\alpha$ -C–H arylation of alcohols is one of the most straightforward methods to prepare  $\alpha$ -aryl alcohols (equation at top of Scheme 1: Y = OH).<sup>[1]</sup>  $\alpha$ -Hydroxyalkyl radicals, stabilized by resonance with the lone pairs on the oxygen atom as shown in **I** in Scheme 1, are easily and regioselectively prepared from alcohols through hydrogen-abstraction (H-abstraction) by an oxyradical (RO<sup>•</sup>) as step *a* in Scheme 1. Therefore, the method involving homolytic aromatic substitution (HAS), consisting of addition of an  $\alpha$ -hydroxyalkyl radical to an aromatic ring (step *b*) and formal elimination of a radical leaving group (LG<sup>•</sup>) (step *c*), is one of the most straightforward methods for the  $\alpha$ -arylation of alcohols. However, the dearomatizing addition (step *b*) of such stable radical species as  $\alpha$ -hydroxyalkyl radicals is unfavored. This drawback was overcome in the Minisci reaction to obtain  $\alpha$ -aryl alcohols through dehydrogenative coupling between alcohols and pyridine derivatives (LG<sup>•</sup> = H<sup>•</sup>) in the presence of a Brønsted acid.<sup>[2]</sup> Here  $\alpha$ -hydroxyalkyl radicals, showing nucleophilicity due to the resonance as shown as **I**, effectively react with electrophilic arenes such as protonated pyridine derivatives. The scope of arenes was later widened to heteroarenes other than pyridine derivatives,<sup>[3]</sup> but it is intrinsically difficult with the Minisci-type reaction that an optional

proton on the aromatic ring is regioselectively substituted. In addition, in the Minisci-type reactions thus far mentioned, a stoichiometric amount of a radical precursor is required because no radical regenerating step such as step *d* in Scheme 1 is available. In 2016, Opatz reported the light-induced  $\alpha$ -arylation of alcohols with 2-chlorobenzoxazole using benzophenone as a photosensitizer (Scheme 2a).<sup>[4]</sup> In 2018, MacMillan disclosed the  $\alpha$ -arylation of alcohols with aryl bromides using a clever system consisting of hydrogen atom transfer (HAT), photoredox and nickel catalysis (Scheme 2b).<sup>[5]</sup> Here we report the direct  $\alpha$ -arylation of alcohols with aryl halides using just a base (and a solvent) in addition to a substoichiometric amount of *t*-BuOO*t*-Bu (Scheme 2c).

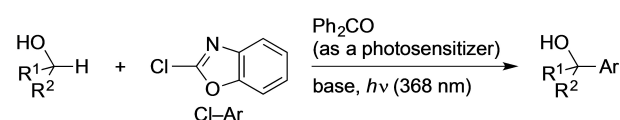
We have recently reported the direct  $\alpha$ -arylation of alkylamines with benzenesulfonylarenes (PhSO<sub>2</sub>–Ar) using a substoichiometric amount of a *t*-BuO<sup>•</sup> precursor (Scheme 2d).<sup>[6]</sup> The reaction proceeds through a HAS mechanism consisting of addition of an  $\alpha$ -aminoalkyl radical (step *b* in Scheme 1) and elimination of PhSO<sub>2</sub><sup>•</sup> (step *c*). An  $\alpha$ -aminoalkyl radical is generated through H-abstraction primarily by *t*-BuO<sup>•</sup> (step *a*) then by PhSO<sub>2</sub><sup>•</sup> (step *d*), and thus a radical chain is operative to save the amount of the *t*-BuO<sup>•</sup> precursor to be substoichiometric. Upon use of alcohols instead of alkylamines, step *d* would not proceed with benzenesulfonylarenes as PhSO<sub>2</sub><sup>•</sup> is more stable than  $\alpha$ -hydroxyalkyl radicals. We anticipated that step *d* is possible with aryl chlorides (Cl–Ar), which are much more readily available than benzenesulfonylarenes, as Cl<sup>•</sup> has a stability comparable to  $\alpha$ -hydroxyalkyl radicals.<sup>[7]</sup>

The reaction of 2-chlorobenzothiazole (**2a**) with 2-propanol (**1a**: 30 equiv.) as a substrate and a solvent in the presence of *t*-BuOO*t*-Bu (0.2 equiv.) at 120 °C for 24 h gave 2-(2-benzothiazolyl)-2-propanol (**3aa**) in

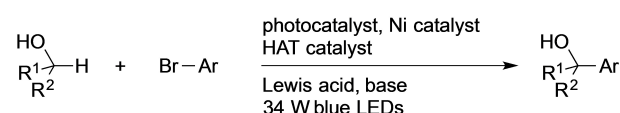


**Scheme 1.**  $\alpha$ -Arylation of heteroatom-containing aliphatic compounds through homolytic aromatic substitution.

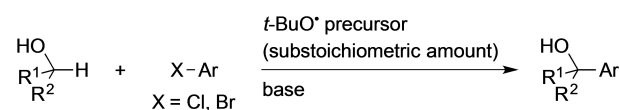
(a) Opatz's work



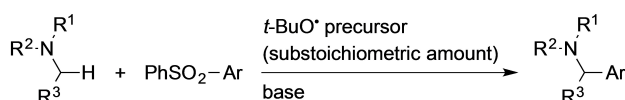
(b) MacMillan's work



(c) This work



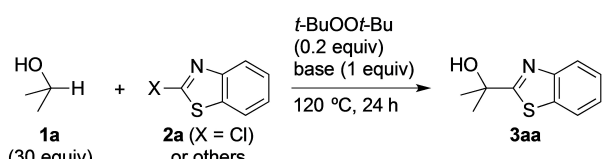
(d) Our previous work



**Scheme 2.** Previous works and this work.

25% yield with 38% conversion of **2a** (Table 1, entry 1). Use of NaOAc as a base for the purpose of neutralizing co-produced HCl increased the yield

**Table 1.**  $\alpha$ -Arylation of 2-Propanol (**1a**) with 2-Halobenzothiazole Using *t*-BuOO*t*-Bu.<sup>[a]</sup>



Entry	X	Base	Conv. <sup>[b]</sup> (%)	Yield <sup>[b]</sup> (%)
1	Cl	None	38	25
2	Cl	NaOAc	99	84
3	Cl	NaHCO <sub>3</sub>	98	98 (98) <sup>[c]</sup>
4	Cl	KHCO <sub>3</sub>	96	95
5	Cl	Li <sub>2</sub> CO <sub>3</sub>	92	90
6	Cl	Na <sub>2</sub> CO <sub>3</sub>	90	91
7	Cl	K <sub>2</sub> CO <sub>3</sub>	74	33 <sup>[d]</sup>
8	Cl	Cs <sub>2</sub> CO <sub>3</sub>	> 99	< 1 <sup>[e]</sup>
9	Cl	MgCO <sub>3</sub>	62	55
10	Cl	CaCO <sub>3</sub>	63	61
11	Cl	BaCO <sub>3</sub>	94	91
12	Br	NaHCO <sub>3</sub>	99	95
13	F	NaHCO <sub>3</sub>	49	41
14	SO <sub>2</sub> Ph	NaHCO <sub>3</sub>	24	18

<sup>[a]</sup> The reaction was carried out under a nitrogen atmosphere at 120 °C for 24 h using a 2-halo- or 2-(benzenesulfonyl) benzothiazole (0.50 mmol), 2-propanol (**1a**: 15 mmol), *t*-BuOO*t*-Bu (0.10 mmol) and a base (0.50 mmol).

<sup>[b]</sup> Determined by GC.

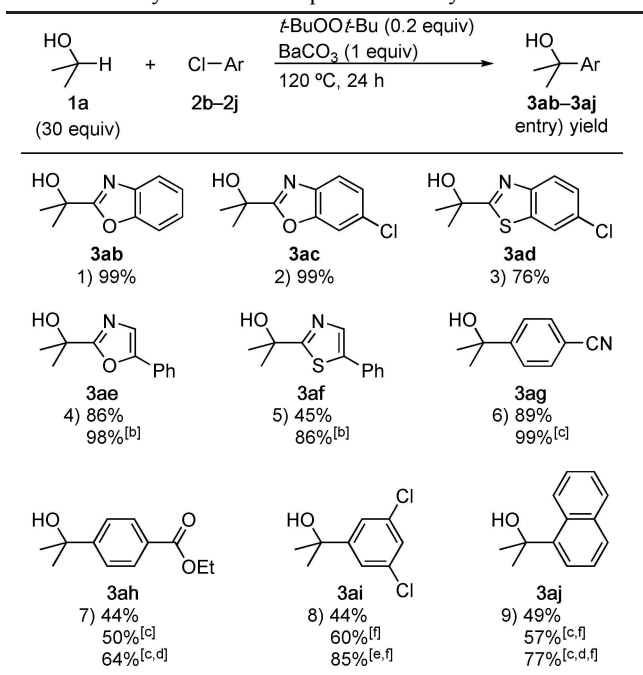
<sup>[c]</sup> The yield of the isolated product.

<sup>[d]</sup> 2-Isopropoxybenzothiazole (8%) and benzothiazole (19%) were obtained.

<sup>[e]</sup> 2-Isopropoxybenzothiazole (68%) and benzothiazole (22%) were obtained.

(entry 2). The result that the yield exceeded the maximum amount (40%) of *t*-BuO• generation indicates operation of a radical chain. Use of an alkali metal bicarbonate or carbonate as a more strong base generally improved the yield (entries 3–8), though K<sub>2</sub>CO<sub>3</sub> and Cs<sub>2</sub>CO<sub>3</sub> were found to be too strong to induce nucleophilic aromatic substitution with an isopropoxy group and reduction into benzothiazole, probably due to formation of a metal isopropoxide (entries 7 and 8).<sup>[8]</sup> Among the alkaline earth metal carbonates examined, BaCO<sub>3</sub> was most effective (entries 9–11). The reaction using 2-bromobenzothiazole instead of chloro derivative **2a** scored a comparable yield, whereas a much lower yield with a low conversion was observed with the fluoro or benzenesulfonyl derivative (entries 12–14). It is likely that F• is too unstable to be eliminated in step *c* and PhSO<sub>2</sub>• is too stable to undergo H-abstraction in step *d*.

The procedure of Table 1 was applied to  $\alpha$ -arylation of 2-propanol using diverse (hetero)aryl chlorides, where BaCO<sub>3</sub> works as a base slightly better than NaHCO<sub>3</sub> as a whole (Table 2). Monocyclic and

**Table 2.**  $\alpha$ -Arylation of 2-Propanol with Aryl Chlorides.<sup>[a]</sup>

<sup>[a]</sup> The reaction was carried out under a nitrogen atmosphere at 120 °C for 24 h using an aryl chloride (0.50 mmol), 2-propanol (**1a**: 15 mmol), *t*-BuOO*t*-Bu (0.10 mmol) and BaCO<sub>3</sub> (0.50 mmol). The yield of the isolated product is given.

<sup>[b]</sup> *t*-BuOO*t*-Bu (0.25 mmol) was used.

<sup>[c]</sup> The corresponding aryl bromide was used instead of the chloride.

<sup>[d]</sup> *t*-BuOO*t*-Bu (0.20 mmol) was used.

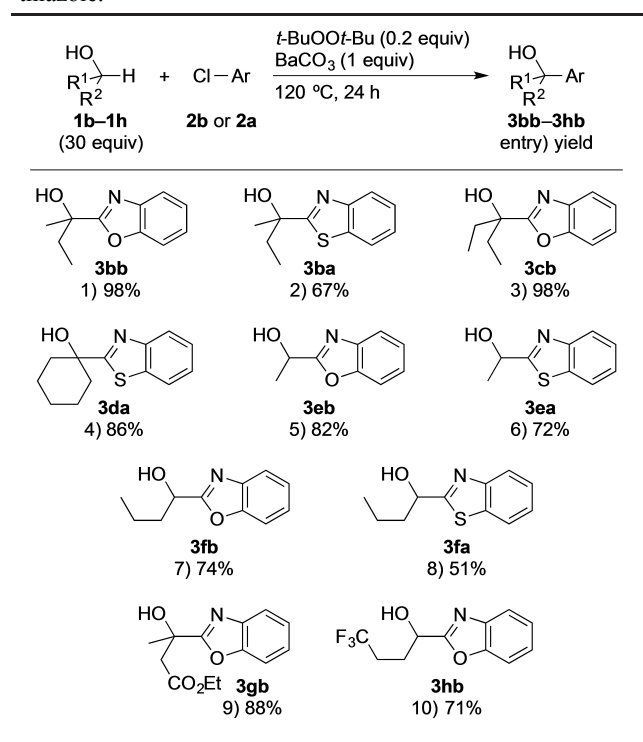
<sup>[e]</sup> *t*-BuOO*t*-Bu (0.50 mmol) was used.

<sup>[f]</sup> NaHCO<sub>3</sub> was used instead of BaCO<sub>3</sub>.

bicyclic 2-chlorooxazoles and -thiazoles underwent the reaction with 2-propanol (entries 1–5). HAS took place also on benzene rings having an electron-withdrawing group, where aryl bromides worked better than the chlorides (entries 6 and 7). Just one Cl of 1,3,5-trichlorobenzene was replaced even with an increased amount (1 equiv.) of *t*-BuOO*t*-Bu (entry 8). No electron-withdrawing groups were required for 1-bromonaphthalene (entry 9).

The  $\alpha$ -arylation was applied to various secondary and primary alcohols (Table 3). Unfunctionalized secondary alcohols other than 2-propanol reacted with 2-chlorobenzoxazole (**2b**) or -thiazole (**2a**) to give the  $\alpha$ -arylated products (entries 1–4). Primary alcohols also underwent the  $\alpha$ -arylation, though the yields were slightly low (entries 5–8). Functional groups such as ester and trifluoromethyl on alcohols are tolerated (entries 9 and 10).

Reduction of the amount of alcohols from 30 equiv. to 3 equiv. is possible by use of acetonitrile as a solvent, though an increased amount (0.4 equiv.) of *t*-

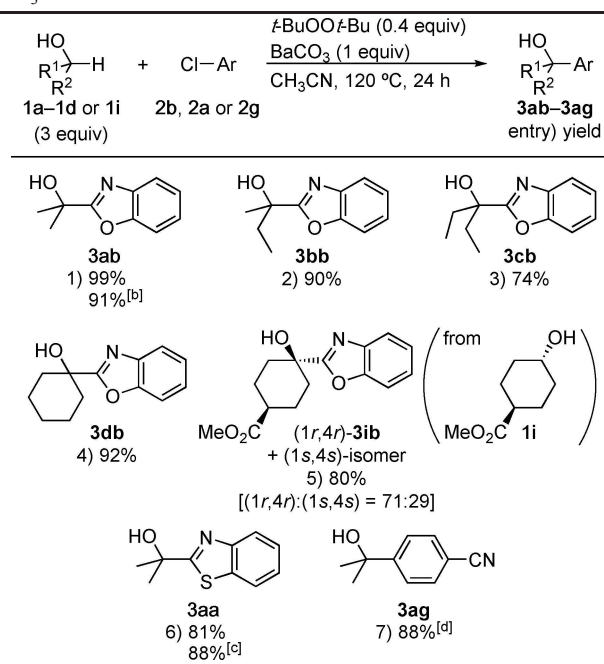
**Table 3.**  $\alpha$ -Arylation of Alcohols with 2-Chlorobenzoxazole or -thiazole.<sup>[a]</sup>

<sup>[a]</sup> The reaction was carried out under a nitrogen atmosphere at 120 °C for 24 h using an aryl chloride (0.50 mmol), an alcohol (15 mmol), *t*-BuOO*t*-Bu (0.10 mmol) and BaCO<sub>3</sub> (0.50 mmol). The yield of the isolated product is given.

BuOO*t*-Bu is required for high yields (Table 4). The  $\alpha$ -arylation of 2-propanol (3 equiv.) with 2-chlorobenzoxazole (**2b**) in the presence of *t*-BuOO*t*-Bu (0.4 equiv.) in CH<sub>3</sub>CN gave **3ab** in 99% yield (entry 1). Other secondary alcohols were  $\alpha$ -arylated with **2b** in moderate to high yields (entries 2–5). The stereochemistry of cyclohexanol **1i** was not retained, supporting the involvement of the  $\alpha$ -hydroxyalkyl radical intermediate (entry 5). 2-Chlorobenzothiazole and 4-bromobenzonitrile participated in the  $\alpha$ -arylation (entries 6 and 7).

On the basis of the above experimental results and the previous findings reported by us, a plausible mechanism is drawn in Scheme 3, exemplified by the reaction of a chlorobenzene derivative (**2**). H-abstraction from alcohol **1** by *t*-BuO•, generated by homolysis of *t*-BuOO*t*-Bu, gives  $\alpha$ -hydroxyalkyl radical **I** (step *a*), which adds to the aromatic ring of chloroarene **2** (step *b*). Cl• departs from the resulting cyclohexadienyl radical (**II**) to give  $\alpha$ -arylation product **3** (step *c*). The eliminated Cl• undergoes H-abstraction to regenerate  $\alpha$ -hydroxyalkyl radical **I** (step *d*). From the results that even a weak base such as KOAc is sufficiently effective (*cf.* Table 1, entries 1 and 2) and that strong bases such as K<sub>2</sub>CO<sub>3</sub> and Cs<sub>2</sub>CO<sub>3</sub>, which can form the corresponding metal alkoxides, induce side reactions

**Table 4.**  $\alpha$ -Arylation of Alcohols with Aryl Chlorides in  $\text{CH}_3\text{CN}$ .<sup>[a]</sup>



<sup>[a]</sup> The reaction was carried out under a nitrogen atmosphere at 120 °C for 24 h using an aryl chloride (0.50 mmol), an alcohol (1.5 mmol), *t*-BuOO*t*-Bu (0.20 mmol), BaCO<sub>3</sub> (0.50 mmol) and CH<sub>3</sub>CN (0.5 mL). The yield of the isolated product is given.

<sup>[b]</sup> *t*-BuOO*t*-Bu (0.10 mmol) was used.

<sup>[c]</sup> NaHCO<sub>3</sub> was used instead of BaCO<sub>3</sub>.

<sup>[d]</sup> The corresponding aryl bromide was used instead of the chloride.

works to neutralize HCl generated in step *d* as the type of bases sensitively affects the efficiency.

In conclusion, we have developed a simple protocol for the direct  $\alpha$ -arylation of alcohols using aryl chlorides and a substoichiometric amount of *t*-BuOO*t*-Bu respectively as arylation reagents and a radical initiator, where a radical chain involving a homolytic aromatic substitution mechanism is operative.

## Experimental Section

### $\alpha$ -Arylation of Alcohols with Aryl Chlorides (Tables 1, 2 and 3): Representative Procedure (Table 1, Entry 3)<sup>[9]</sup>

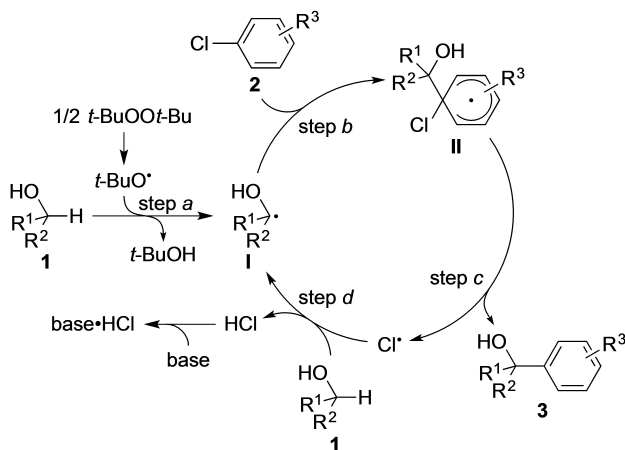
To a 4 mL vial equipped with a stir bar in a glove box were added successively 2-propanol (**1a**: 902 mg, 15.0 mmol), 2-chlorobenzothiazole (**2a**: 84.8 mg, 0.500 mmol), *t*-BuOO*t*-Bu (14.6 mg, 0.100 mmol) and NaHCO<sub>3</sub> (42.0 mg, 0.500 mmol). The vial was taken out of the glove box and the mixture was stirred for 24 h at 120 °C. The resulting mixture was poured into water (10 mL), extracted with ethyl acetate (15 mL  $\times$  3), washed with brine (5 mL), and dried over Na<sub>2</sub>SO<sub>4</sub>. After filtration and concentration, the crude mixture was subjected to silica gel chromatography (CHCl<sub>3</sub>/MeOH = 15/1) to give the corresponding product (**3aa**: 94.7 mg, 98% yield).

## Acknowledgements

This work has been supported financially in part by Grant-in-Aids for Scientific Research (B) (16H04151 to E.S.) and Scientific Research (B) (19H02728 to E.S.). We thank Professor Manabu Abe (Hiroshima University) for assistance in DFT calculations.

## References

- [1] For examples of the transition metal-mediated reaction: a) C. A. Correia, L. Yang, C.-J. Li, *Org. Lett.* **2011**, *13*, 4581–4583; b) C. Berini, O. Navarro, *Chem. Commun.* **2012**, *48*, 1538–1540; c) S. Wang, S. Xing, Y. Zhang, Y. Fan, H. Zhao, J. Wang, S. Zhang, W. Wang, *RSC Adv.* **2019**, *9*, 41847–41850. For the photoredox-catalyzed reaction: d) C. A. Huff, R. D. Cohen, K. D. Dykstra, E. Streckfuss, D. A. DiRocco, S. W. Krska, *J. Org. Chem.* **2016**, *81*, 6980–6987. For the light-induced reaction: e) L. Niu, J. Liu, X.-A. Liang, S. Wang, A. Lei, *Nat. Commun.* **2019**, *10*, 467. For a review: f) S.-R. Guo, P. S. Kumar, M. Yang, *Adv. Synth. Catal.* **2017**, *359*, 2–25.
- [2] For early examples, see: a) M. H. Palmer, P. S. McIntyre, *Tetrahedron Lett.* **1968**, *9*, 2147–2150; b) W. Buratti, G. P. Gardini, F. Minisci, F. Bertini, R. Galli, M. Perchinunno, *Tetrahedron* **1971**, *27*, 3655–3668. For reviews, see: c) F. Minisci, *Synthesis* **1973**, 1–24; d) F. Minisci, E. Vismara, F. Fontana, *Heterocycles* **1989**, *28*, 489–519. For recent advances in the Minisci-type reaction, see refs 1d and 1e as well as the following review: e) R. S. J. Proctor, R. J.



**Scheme 3.** A Plausible Mechanism.

(cf. Table 1, entries 7 and 8), the role of a base is not likely to form a metal alkoxide to facilitate abstraction of  $\alpha$ -hydrogen. It is also unlikely that a base simply

- Phipps, *Angew. Chem. Int. Ed.* **2019**, *58*, 13666–13699; *Angew. Chem.* **2019**, *131*, 13802–13837.
- [3] For examples of benzothiazoles: a) T. He, L. Yu, L. Zhang, L. Wang, M. Wang, *Org. Lett.* **2011**, *13*, 5016–5019; b) W.-X. Xu, X.-Q. Dai, J.-Q. Weng, *ACS Omega* **2019**, *4*, 11285–11292. For thiophenes having an electron-withdrawing group: c) E. Kianmehr, M. Fardpour, K. M. Khan, *Eur. J. Org. Chem.* **2017**, 2661–2668.
- [4] a) A. Lipp, G. Lahm, T. Opatz, *J. Org. Chem.* **2016**, *81*, 4890–4897; b) A. M. Nauth, A. Lipp, B. Lipp, T. Opatz, *Eur. J. Org. Chem.* **2017**, 2099–2103.
- [5] J. Twilton, M. Christensen, D. A. DiRocco, R. T. Ruck, I. W. Davies, D. W. C. MacMillan, *Angew. Chem. Int. Ed.* **2018**, *57*, 5369–5373; *Angew. Chem.* **2018**, *130*, 5467–5471.
- [6] a) Y. Ikeda, R. Ueno, Y. Akai, E. Shirakawa, *Chem. Commun.* **2018**, *54*, 10471–10474. For the  $\alpha$ -arylation of alkylamines with aryl halides using a stoichiometric amount of a *tert*-butoxy radical precursor, see: b) R. Ueno, Y. Ikeda, E. Shirakawa, *Eur. J. Org. Chem.* **2017**, 4188–4193.
- [7] The stability of radical species is evaluated by bond dissociation energy (BDE). According to DFT calculations using B3LYP/6-31+G (dp), BDE values (kcal/mol) of the O–H bond in PhS(=O)O–H, the  $\alpha$ -C–H bond in ethanol and H–Cl are 81, 93 and 100, respectively, showing that benzenesulfonyl radical is much more stable than  $\alpha$ -hydroxyethyl radical and Cl $\cdot$ . The experimental BDE values of the latter two are available (96 and 103, respectively) in the literature and are almost the same as the calculated values. For the experimental BDE values, see: Y.-R. Luo, *Comprehensive Handbook of Chemical Bond Energies*, CRC Press, Boca Raton, **2007**.
- [8] We have reported the reduction of aryl halides into arenes using 2-propanol (80 equiv.) and Cs<sub>2</sub>CO<sub>3</sub> (1.2 equiv.) in the presence of *t*-BuOO*t*-Bu (0.2 equiv.), where formation of cesium isopropoxide is considered to be crucial for the high efficiency. In this reduction, K<sub>2</sub>CO<sub>3</sub> or Na<sub>2</sub>CO<sub>3</sub> as a base respectively is less or much less effective than Cs<sub>2</sub>CO<sub>3</sub>. R. Ueno, T. Shimizu, E. Shirakawa, *Synlett* **2016**, *27*, 741–744.
- [9] A glove box is used for ease of experimental procedure but it is not essential. In addition, the reaction can be conducted in a larger scale. For example, the reaction of 2-chlorobenzothiazole (**2a**: 1.5 mmol) with 2-propanol (**1a**: 30 equiv.), corresponding to that in entry 3 of Table 1, but with no use of a glove box gave 2-(2-benzothiazolyl)-2-propanol (**3aa**) in 96% yield with 97% conversion of **2a**, which are comparable to the reaction using a glove box (*cf.* entry 3 in Table 1: 98% yield with 98% conversion). See the Supporting Information for details.

## COMMUNICATIONS

Direct  $\alpha$ -Arylation of Alcohols with Aryl Halides through a Radical Chain Mechanism

*Adv. Synth. Catal.* **2020**, *362*, 1–6

 K. Aoki, K. Yonekura, Y. Ikeda, R. Ueno, E. Shirakawa\*



# Electron-Catalyzed Cross-Coupling of Arylboron Compounds with Aryl Iodides

Keisho Okura, Tsuyoshi Teranishi, Yuto Yoshida, and Eiji Shirakawa\*

**Abstract:** Arylboroxines in combination with zinc chloride and potassium *tert*-butoxide were found to undergo the electron-catalyzed cross-coupling with aryl iodides to give the corresponding biaryls without the aid of transition-metal catalysis.

Transition-metal-catalyzed cross-coupling of arylmetals with aryl halides is one of the most useful and powerful methods for biaryl synthesis.<sup>[1]</sup> Among these, Suzuki–Miyaura coupling, which employs arylboron compounds as arylmetals, is one of the most widely used due to the high stability and high availability of the reagents and the high functional-group tolerance of the reaction.<sup>[2]</sup> On the other hand, since our group reported the first electron-catalyzed cross-coupling, where aryl Grignard reagents are employed and an electron derived from them instead of a transition metal acts as a catalyst,<sup>[3]</sup> we and other groups have reported transition-metal-free cross-coupling of arylmetals (Zn<sup>[4]</sup>/Al<sup>[5]</sup>/Sn<sup>[6]</sup>) as well as alkyl<sup>[7]</sup> and alkynylzinc<sup>[8]</sup> reagents.<sup>[9,10]</sup> Herein, we report for the first time that arylboron compounds can be utilized as aryl nucleophiles in the electron-catalyzed cross-coupling with the aid of a zinc reagent such as diethylzinc or zinc chloride/potassium *tert*-butoxide.<sup>[11]</sup>

Many reports are available on the preparation of arylzinc reagents from arylboronic acids through treatment with an excess of diethylzinc.<sup>[12,13]</sup> We anticipated that the thus prepared arylzinc reagents would undergo the electron-catalyzed cross-coupling. However, treatment of phenylboronic acid (**1a**, 2 equiv) with Et<sub>2</sub>Zn (6 equiv) in THF at 23 °C for 1 h followed by reaction with 4-iodoanisole (**2a**) in toluene/THF (1:3) at 110 °C for 24 h failed to give the corresponding coupling product, 4-methoxybiphenyl (**3aa**), at all, with a low conversion of **2a** (Table 1, entry 1). In contrast, rather surprisingly, use of a much reduced amount (1.5 equiv) of Et<sub>2</sub>Zn promoted the coupling to some extent (19% yield of **3aa** with 22% conv. of **2a**; Table 1, entry 2). Addition of LiCl (1.5 equiv), an effective accelerator in the previous electron-catalyzed cross-coupling reactions,<sup>[3c,4b,6]</sup> led to full conversion

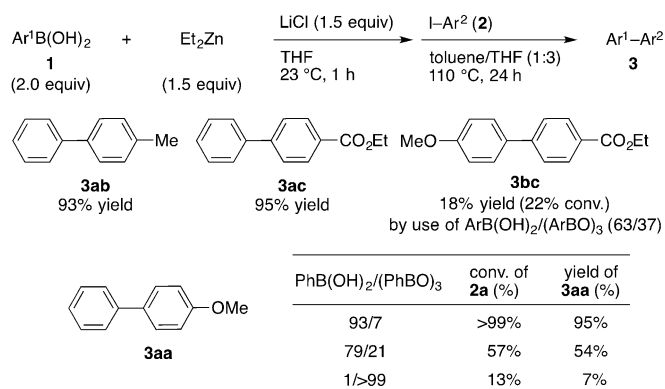
**Table 1:** Effect of the amounts of diethylzinc and lithium chloride in the coupling of phenylboronic acid (**1a**) with 4-iodoanisole (**2a**).<sup>[a]</sup>

Entry	Et <sub>2</sub> Zn (equiv)	LiCl (equiv)	Conv. of <b>2a</b> [%] <sup>[b]</sup>	Yield of <b>3aa</b> [%] <sup>[b]</sup>
1	6	0	9	< 1
2	1.5	0	22	19
3	1.5	1.5	> 99	95 (93) <sup>[c]</sup>
4	0	1.5	3	< 1

[a] A toluene solution of diethylzinc (1.2 mmol for entry 1; 0.30 mmol for entries 2 and 3) was added to phenylboronic acid (**1a**, 0.40 mmol) in THF in the presence or absence of lithium chloride (0.30 mmol) under a nitrogen atmosphere. After stirring the resulting mixture at 23 °C for 1 h, addition of 4-iodoanisole (**2a**, 0.20 mmol, 0.22 M) was followed by stirring at 110 °C for 24 h. [b] Determined by GC based on **2a**. [c] Yield of the isolated product based on **2a**.

of **2a** to give **3aa** in a high yield (Table 1, entry 3). No reaction took place in the absence of diethylzinc (Table 1, entry 4).

The electron-catalyzed cross-coupling of phenylboronic acid (**1a**) in the presence of Et<sub>2</sub>Zn (1.5 equiv) was found to be applicable to iodobenzene with an alkyl or ester substituent (Scheme 1, top). However, the coupling reaction was found to show a low reproducibility, depending on the arylboronic acids used. For example, the reaction of 4-methoxyphenylboronic acid (**1b**) with ethyl 4-iodobenzoate (**2c**) resulted in a low yield with a low conversion (Scheme 1, top). Analysis of the purity of **1b** used here showed that it contains a certain amount of the corresponding boroxine (boronic acid/boroxine = 63:37),<sup>[14]</sup> thus prompting us to consider that arylborox-



**Scheme 1.** Coupling of arylboronic acids with aryl iodides using diethylzinc as an activator.

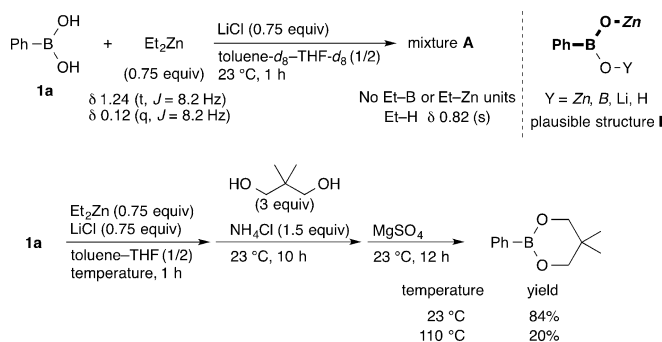
[\*] K. Okura, Y. Yoshida  
Department of Chemistry, Graduate School of Science  
Kyoto University, Sakyo-ku, Kyoto 606-8502 (Japan)

T. Teranishi, Prof. Dr. E. Shirakawa  
Department of Applied Chemistry for Environment  
School of Science and Technology, Kwansai Gakuin University  
Sanda, Hyogo 669-1337 (Japan)  
E-mail: eshirakawa@kwansai.ac.jp

Supporting information and the ORCID identification number(s) for the author(s) of this article can be found under:  
<https://doi.org/10.1002/anie.201802813>.

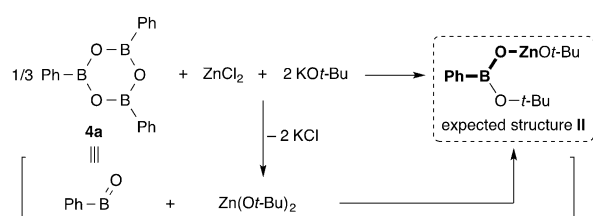
ines are unreactive in this coupling. Actually, the boronic acid/boroxine ratio with a phenylboron system was found to affect the conversion and the yield, whereas genuine phenylboroxine has an extremely low reactivity (Scheme 1, bottom). The tendency of arylboronic acids to be transformed into the corresponding arylboroxines by spontaneous dehydration potentially damages the reproducibility of this method.

In order to develop a more reliable cross-coupling system using arylboron compounds, we investigated what kind of species is generated at the starting point of the cross-coupling reaction by analyzing the mixture (**A** in Scheme 2) after



**Scheme 2.** Elucidation of the species generated upon mixing an arylboronic acid and diethylzinc.

treatment of phenylboronic acid (**1a**) with  $\text{Et}_2\text{Zn}$  (0.75 equiv) in the presence of lithium chloride (0.75 equiv) in  $[\text{D}_8]\text{toluene}/[\text{D}_8]\text{THF}$  (1:2) at  $23^\circ\text{C}$  for 1 h (see Table 1, entry 3). In the  $^1\text{H}$  NMR spectrum of mixture **A**, no peaks for Et-B and Et-Zn were observed but an Et-H peak derived from the ethyl group of  $\text{Et}_2\text{Zn}$  was observed (Scheme 2, top), thus indicating that no Zn-B transmetalation takes place at this point, and each Et-Zn unit of  $\text{Et}_2\text{Zn}$  works as a base to abstract protons from the hydroxyl groups of  $\text{PhB}(\text{OH})_2$  to give arylboron species **I** with a Ph-B-O-Zn sequence (Scheme 2, top right). The observation that the C-B bond of **1a** is not cleaved at this stage was further confirmed by the outcome that the phenylboron unit was trapped as the corresponding boronate in 84% yield upon treatment of a mixture, prepared in the same way as above (mixture **A**) but in non-deuterated solvents, with 2,2-dimethyl-1,3-propanediol (3 equiv) and ammonium chloride (1.5 equiv) followed by  $\text{MgSO}_4$  (Scheme 2, bottom). However, after treatment of **1a** with  $\text{Et}_2\text{Zn}$  and LiCl for 1 h at  $110^\circ\text{C}$  instead of  $23^\circ\text{C}$ , the phenylboron unit remained in only 20%, thus showing that, under the cross-coupling conditions at a high temperature, the phenylboron species is converted into some other species, which are likely to be the real active species for the cross-coupling reaction. We anticipated that if we prepare a species of type **I** with a Ph-B-O-Zn sequence, it should be converted at a high temperature into some active species that can undergo the coupling with aryl iodides. We expected that treatment of arylboroxines with  $\text{ZnCl}_2$  and  $\text{KO}t\text{-Bu}$  as shown in Scheme 3 would give species **II**, which is suitable for this purpose. This method will be advantageous over the previous one because no organometallic reagents such as  $\text{Et}_2\text{Zn}$  are

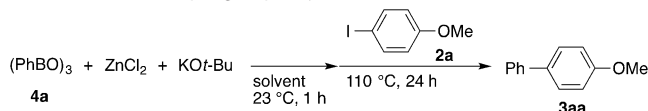


**Scheme 3.** Working hypothesis for the generation of arylboron species for the cross-coupling.

required and the boronic acid/boroxine equilibrium does not matter under anhydrous conditions.

As we expected, arylboroxine-derived species underwent the coupling reaction, although some modification was required. After stirring a mixture of phenylboroxine (**4a**, 1.5 equiv),  $\text{ZnCl}_2$  (1.5 equiv) and  $\text{KO}t\text{-Bu}$  (3.0 equiv) in THF at  $23^\circ\text{C}$  for 1 h, the resulting mixture was treated with 4-iodoanisole (**2a**) at  $110^\circ\text{C}$  for 24 h to give 4-methoxybiphenyl (**3aa**) in 15% yield with 19% conversion of **2a** (Table 2,

**Table 2:** Effect of the amounts of zinc chloride and potassium *tert*-butoxide on the coupling of phenylboroxine with 4-iodoanisole.<sup>[a]</sup>



Entry	<b>4a</b> [equiv]	$\text{ZnCl}_2$ [equiv]	Base (equiv)	Solvent	Conv. of <b>2a</b> [%] <sup>[b]</sup>	Yield of <b>3aa</b> [%] <sup>[b]</sup>
1	1.5	1.5	$\text{KO}t\text{-Bu}$ (3.0)	THF	19	15
2	1.5	2.4	$\text{KO}t\text{-Bu}$ (3.0)	THF	46	38
3	1.5	2.4	$\text{KO}t\text{-Bu}$ (1.8)	THF	42	40
4	1.5	2.4	$\text{KO}t\text{-Bu}$ (1.8)	NMP	> 99	99
5	1.2	2.1	$\text{KO}t\text{-Bu}$ (1.5)	NMP	> 99	98
6	1.2	2.1	$\text{K}_3\text{PO}_4$ (1.5)	NMP	3	1
7	1.2	2.1	$\text{K}_2\text{CO}_3$ (1.5)	NMP	8	2
8	1.2	0	$\text{KO}t\text{-Bu}$ (1.5)	NMP	98	< 1

[a] To a mixture of phenylboroxine (**4a**), zinc chloride, and potassium *tert*-butoxide was added THF (1.0 mL for entries 1–3) or NMP (1.0 mL for entries 4–8). After stirring the resulting mixture at  $23^\circ\text{C}$  for 1 h, addition of 4-iodoanisole (**2a**, 0.50 mmol, 0.50 M) was followed by stirring at  $110^\circ\text{C}$  for 24 h. [b] Determined by GC.

entry 1). An increased amount (2.4 equiv) of  $\text{ZnCl}_2$  enhanced the reactivity, whereas reduction of the amount (1.8 equiv) of  $\text{KO}t\text{-Bu}$  did not affect the yield (Table 2, entries 2 and 3). Use of *N*-methylpyrrolidone (NMP) as a solvent instead of THF drastically improved the conversion and the yield (Table 2, entry 4), and reduction of the amounts of the reagents while keeping the ratio among these ( $\text{4a}/\text{ZnCl}_2/\text{KO}t\text{-Bu} = 1.2:2.1:1.5$ ) the same also worked (Table 2, entry 5). Use of a weaker base was ineffective (Table 2, entries 6 and 7).<sup>[15]</sup> No coupling product was obtained in the absence of  $\text{ZnCl}_2$ , and anisole was the major product (60% yield) (Table 2, entry 8).<sup>[16]</sup>

The coupling of arylboroxines with aryl iodides using the combination of  $\text{ZnCl}_2$  and  $\text{KO}t\text{-Bu}$  showed a wide substrate scope (Table 3). Phenyl iodides with an electron-donating or electron-withdrawing group at the *para* or *meta* position



## Acknowledgements

This work has been supported financially in part by Grant-in-Aid for Scientific Research (B) (25288046 to E.S.) from JSPS and Nagase Science and Technology Foundation (E.S.).

## Conflict of interest

The authors declare no conflict of interest.

**Keywords:** arylboron compounds · biaryl compounds · cross-coupling · electron catalysis · radical reactions

**How to cite:** *Angew. Chem. Int. Ed.* **2018**, *57*, 7186–7190  
*Angew. Chem.* **2018**, *130*, 7304–7308

- [1] Reviews: a) *Metal-Catalyzed Cross-Coupling Reactions and more*, Vol. 1–2, 2nd ed. (Eds.: A. de Mijere, S. Bräse, M. Oestreich), Wiley-VCH, Weinheim, **2014**; b) J.-P. Corbet, G. Mignani, *Chem. Rev.* **2006**, *106*, 2651–2710.
- [2] Reviews: a) N. Miyaoura, A. Suzuki, *Chem. Rev.* **1995**, *95*, 2457–2483; b) F.-S. Han, *Chem. Soc. Rev.* **2013**, *42*, 5270–5298.
- [3] a) E. Shirakawa, Y. Hayashi, K. Itoh, R. Watabe, N. Uchiyama, W. Konagaya, S. Masui, T. Hayashi, *Angew. Chem. Int. Ed.* **2012**, *51*, 218–221; *Angew. Chem.* **2012**, *124*, 222–225; b) N. Uchiyama, E. Shirakawa, T. Hayashi, *Chem. Commun.* **2013**, *49*, 364–366; c) E. Shirakawa, K. Okura, N. Uchiyama, T. Murakami, T. Hayashi, *Chem. Lett.* **2014**, *43*, 922–924; For the coupling with alkenyl halides, see: d) E. Shirakawa, R. Watabe, T. Murakami, T. Hayashi, *Chem. Commun.* **2013**, *49*, 5219–5221.
- [4] a) H. Minami, X. Wang, C. Wang, M. Uchiyama, *Eur. J. Org. Chem.* **2013**, 7891–7894; b) E. Shirakawa, F. Tamakuni, E. Kusano, N. Uchiyama, W. Konagaya, R. Watabe, T. Hayashi, *Angew. Chem. Int. Ed.* **2014**, *53*, 521–525; *Angew. Chem.* **2014**, *126*, 531–535.
- [5] H. Minami, T. Saito, C. Wang, M. Uchiyama, *Angew. Chem. Int. Ed.* **2015**, *54*, 4665–4668; *Angew. Chem.* **2015**, *127*, 4748–4751.
- [6] Q. He, L. Wang, Y. Liang, Z. Zhang, S. F. Wnuk, *J. Org. Chem.* **2016**, *81*, 9422–9427.
- [7] K. Okura, E. Shirakawa, *Eur. J. Org. Chem.* **2016**, 3043–3046.
- [8] K. Okura, H. Kawashima, F. Tamakuni, N. Nishida, E. Shirakawa, *Chem. Commun.* **2016**, *52*, 14019–14022.
- [9] Borylation of aromatic compounds including aryl halides with diborons or silyboranes is reported to proceed with no aid from transition-metal catalysis. a) F. Mo, Y. Jiang, D. Qiu, Y. Zhang, J. Wang, *Angew. Chem. Int. Ed.* **2010**, *49*, 1846–1849; *Angew. Chem.* **2010**, *122*, 1890–1893; b) E. Yamamoto, K. Izumi, Y. Horita, H. Ito, *J. Am. Chem. Soc.* **2012**, *134*, 19997–20000; c) J. Yu, L. Zhang, G. Yan, *Adv. Synth. Catal.* **2012**, *354*, 2625–2628; d) D. Qiu, L. Jin, Z. Zheng, H. Meng, F. Mo, X. Wang, Y. Zhang, J. Wang, *J. Org. Chem.* **2013**, *78*, 1923–1933; e) J. Zhang, H.-H. Wu, J. Zhang, *Eur. J. Org. Chem.* **2013**, 6263–6266; f) W. Erb, A. Hellal, M. Albin, J. Rouden, J. Blanchet, *Chem. Eur. J.* **2014**, *20*, 6608–6612; g) E. Yamamoto, S. Ukigai, H. Ito, *Chem. Sci.* **2015**, *6*, 2943–2951; h) R. Uematsu, E. Yamamoto, S. Maeda, H. Ito, T. Taketsugu, *J. Am. Chem. Soc.* **2015**, *137*, 4090–4099; i) K. Chan, M. S. Cheung, Z. Lin, P. Li, *Org. Chem. Front.* **2016**, *3*, 875–879; j) A. M. Mfuh, J. D. Doyle, B. Chhetri, H. D. Arman, O. V. Larionov, *J. Am. Chem. Soc.* **2016**, *138*, 2985–2988; k) K. Chen, S. Zhang, P. He, P. Li, *Chem. Sci.* **2016**, *7*, 3676–3680; l) M. Jiang, H. Yang, H. Fu, *Org. Lett.* **2016**, *18*, 5248–5251; m) A. M. Mfuh, V. T. Nguyen, B. Chhetri, J. E. Burch, J. D. Doyle, V. N. Nesterov, H. D. Arman, O. V. Larionov, *J. Am. Chem. Soc.* **2016**, *138*, 8408–8411; n) L. Zhang, L. Jiao, *J. Am. Chem. Soc.* **2017**, *139*, 607–610; o) L. Zhang, L. Jiao, *Chem. Sci.* **2018**, *9*, 2711–2722.
- [10] Reviews on “electron catalysis”: a) A. Studer, D. P. Curran, *Nat. Chem.* **2014**, *6*, 765–773; b) A. Studer, D. P. Curran, *Angew. Chem. Int. Ed.* **2016**, *55*, 58–102; *Angew. Chem.* **2016**, *128*, 58–106.
- [11] The transition-metal-free coupling of arylboronic acids with allylic, propargylic, and benzylic halides has been reported, where a non-radical mechanism is proposed: a) A. Scriveranti, V. Beghetto, M. Bertoldini, U. Matteoli, *Eur. J. Org. Chem.* **2012**, 264–268; b) M. Ueda, K. Nishimura, R. Kashima, I. Ryu, *Synlett* **2012**, *23*, 1085–1089; c) M. Ueda, K. Nishimura, I. Ryu, *Synlett* **2013**, *24*, 1683–1686; d) M. Ueda, D. Nakakoji, Y. Kuwahara, K. Nishimura, I. Ryu, *Tetrahedron Lett.* **2016**, *57*, 4142–4144.
- [12] Aryl(ethyl)zinc reagents, prepared from arylboronic acids and diethylzinc, have often been used for the asymmetric arylation of aldehydes. The first example: a) C. Bolm, J. Rudolph, *J. Am. Chem. Soc.* **2002**, *124*, 14850–14851; For reviews, see: b) F. Schmidt, R. T. Stemmler, J. Rudolph, C. Bolm, *Chem. Soc. Rev.* **2006**, *35*, 454–470; c) M. W. Paixão, A. L. Braga, D. S. Lüdtkke, *J. Braz. Chem. Soc.* **2008**, *19*, 813–830.
- [13] A mechanistic study on transmetalation between boron and zinc: a) C. Jimeno, S. Sayalero, T. Fjermestad, G. Colet, F. Maseras, M. A. Pericàs, *Angew. Chem. Int. Ed.* **2008**, *47*, 1098–1101; *Angew. Chem.* **2008**, *120*, 1114–1117; Transmetalation between arylboronic acids and diethylzinc is reported to give not only aryl(ethyl)zinc species but also aryl<sub>n</sub>(ethyl)<sub>4–n</sub>borates ( $n = 0–4$ ). b) R. B. Bedford, N. J. Gower, M. F. Haddow, J. N. Harvey, J. Nunn, R. A. Okopie, R. F. Sankey, *Angew. Chem. Int. Ed.* **2012**, *51*, 5435–5438; *Angew. Chem.* **2012**, *124*, 5531–5534.
- [14] Electron-rich arylboronic acids such as **1b** are reported to have high tendency to form the corresponding boroxines: Y. Tokunaga, H. Ueno, Y. Shimomura, T. Seo, *Heterocycles* **2002**, *57*, 787–790.
- [15] ZnCl<sub>2</sub> (99.999% trace metals basis, Sigma–Aldrich Co., product number 229997) and KO<sup>t</sup>-Bu (99.99% trace metals basis, Sigma–Aldrich Co., product number 659878) were used in all entries in Table 2. The reaction using ZnCl<sub>2</sub> and KO<sup>t</sup>-Bu purchased from a different supplier (Wako Pure Chemical Industries) under the conditions of entry 5 produced a comparable yield (96%) of **3aa** with a full conversion of **2a**. For the details, see the Supporting Information. In addition to this result, the outcome that no coupling took place when using K<sub>3</sub>PO<sub>4</sub> or K<sub>2</sub>CO<sub>3</sub> instead of KO<sup>t</sup>-Bu (entries 6 and 7 of Table 2) excludes the possibility that the present cross-coupling is catalyzed by a trace amount of a transition metal such as palladium contained in the reagents since K<sub>3</sub>PO<sub>4</sub> and K<sub>2</sub>CO<sub>3</sub> are known to be effective bases for the palladium-catalyzed Suzuki–Miyaura coupling. For a recent example of a Suzuki–Miyaura coupling that was initially considered to be transition-metal-free but later was revealed to be catalyzed by a trace amount of palladium contained in the reagents, see: a) K. Inamoto, C. Hasegawa, K. Hiroya, Y. Kondo, T. Osaka, Y. Uozumi, T. Doi, *Chem. Commun.* **2012**, *48*, 2912–2914; b) K. Inamoto, L. D. Campbell, T. Doi, K. Koide, *Tetrahedron Lett.* **2012**, *53*, 3147–3148.
- [16] An enolate derived from NMP and KO<sup>t</sup>-Bu is known to work as a single-electron donor toward aryl halides in the reduction of aryl halides into arenes: S. Zhou, E. Doni, G. M. Anderson, R. G. Kane, S. W. MacDougall, V. M. Ironmonger, T. Tuttle, J. A. Murphy, *J. Am. Chem. Soc.* **2014**, *136*, 17818–17826.
- [17] No involvement of aryl radical species is supported by a radical clock experiment using 2-(3-butenyl)phenyl iodide (**2h**), which is often used for a radical clock reaction, the radical derived from which is known to readily cyclize ( $k_c = 5 \times 10^{-8} \text{ s}^{-1}$  at 50 °C). The coupling of **2h** did not give any cyclization product but the coupling product in a high yield (Table 3, entry 8). Radical clock reactions using **2h**: a) A. L. J. Beckwith, W. B. Gara, *J. Am.*

- Chem. Soc.* **1969**, *91*, 5691–5692; b) H.-X. Zheng, X.-H. Shan, J.-P. Qu, Y.-B. Kang, *Org. Lett.* **2017**, *19*, 5114–5117; See also Refs. [3b] and [4b].
- [18] A DFT calculation study on the coupling of aryl Grignard reagents with aryl iodides (see Ref. [3a]) is reported to show that the coupling proceeds through an aryl radical intermediate derived from an aryl iodide in a unique situation, where the aryl radical does not behave as a usual  $\sigma$ -radical species: B. E. Haines, O. Wiest, *J. Org. Chem.* **2014**, *79*, 2771–2774.
- [19] Cation radical  $[\text{Ar}^1\text{-Y}]^{+\cdot}$ , which is generated by SET in the initiation step, reacts with another  $\text{Ar}^1\text{-Y}$  to give  $[\text{Ar}^1\text{-Ar}^1]^-$ , from which SET to  $\text{I-Ar}^2$  takes place to give  $\text{Ar}^1\text{-Ar}^1$  and  $[\text{I-Ar}^2]^-$ . Actually, a small amount of  $\text{Ar}^1\text{-Ar}^1$  derived from an arylboroxine (**4**) is observed in each reaction. For example, the coupling reaction of phenylboroxine (**4a**) with 4-iodoanisole (**2a**) gave biphenyl in 1.1 % yield based on **2a** (Table 2, entry 5). See also Refs. [3b] and [4b].
- [20] Bromo- or chloro-substituted iodobenzenes are often used to probe the involvement of radical anion intermediates in  $\text{S}_{\text{RN}}1$  reactions, where bissubstitution predominantly takes place: a) J. F. Bunnett, X. Creary, *J. Org. Chem.* **1974**, *39*, 3611–3612; b) J. F. Bunnett, X. Creary, *J. Org. Chem.* **1974**, *39*, 3612–3614; For an effective utilization of this system, see: c) B. Janhsen, C. G. Daniliuc, A. Studer, *Chem. Sci.* **2017**, *8*, 3547–3553.

Manuscript received: March 7, 2018  
Revised manuscript received: April 10, 2018  
Accepted manuscript online: April 25, 2018  
Version of record online: May 16, 2018

## Cross Coupling

## Electron-Catalyzed Coupling of Magnesium Amides with Aryl Iodides

Kazuya Kiriyama,<sup>[a]</sup> Keisho Okura,<sup>[a]</sup> Fumiko Tamakuni,<sup>[a]</sup> and Eiji Shirakawa\*<sup>[b]</sup>

**Abstract:** An electron was found to catalyze the coupling of magnesium diarylamides with aryl iodides giving triarylamines through a radical-anion intermediate. The transformation requires no transition metal catalysts or additives, and a wide array of products are formed in good-to-excellent yields.

Triarylamines are important structures in the fields of organic electronics and pharmacy. For synthesis of triarylamines, the transition-metal-catalyzed coupling of aryl halides with diarylamines is widely used, whereby aryl halides are activated by two-electron reduction.<sup>[1,2]</sup> Activation by single-electron reduction is another method to induce substitution reactions of aryl halides with heteroatom nucleophiles. This is termed the S<sub>RN</sub>1 reaction, which does not require transition-metal catalysis.<sup>[3]</sup> For example, the reaction of iodobenzene (Ph-I) with potassium anilide (KNHPh) in liquid ammonia in the presence of potassium metal gives diphenylamine, the N-arylation product, but C-arylation at *ortho*- and *para*-positions also takes place.<sup>[4]</sup> The reaction is initiated by single electron transfer (SET) from K to Ph-I, giving radical-anion K<sup>+</sup>[Ph-I]<sup>-•</sup>, which decomposes to Ph<sup>•</sup> and KI. Ph<sup>•</sup> radicals react with the nitrogen and carbon atoms of KNHPh, leading to the N- and C-arylation products, respectively, with regeneration of K<sup>+</sup>[Ph-I]<sup>-•</sup>. The transition-metal-free cross-coupling reaction of aryl halides (Ar-X) with organometallic reagents has recently been reported.<sup>[5]</sup> The reaction follows essentially the same mechanism as the S<sub>RN</sub>1 reaction, but radical-anions ([Ar-X]<sup>-•</sup>) of aryl halides directly react with organometallic reagents instead of decomposing to aryl radicals (Ar<sup>•</sup>), where an electron acts as a catalyst instead of a transition metal.<sup>[6]</sup> An absence of Ar<sup>•</sup> intermediates removes the possibility of side reactions derived from highly reactive Ar<sup>•</sup> species. We anticipated that this electron-catalyzed cross-coupling reaction is also applicable to the Buchwald-Hartwig-type C-N coupling reaction. Herein we report the electron-catalyzed

coupling of aryl halides with magnesium diarylamides free from transition-metal catalysts.<sup>[7]</sup>

The reaction of 2-iodonaphthalene (**1a**) with Ph<sub>2</sub>NMgCl (3 equiv), prepared from diphenylamine (**2a**: 3.3 equiv) and a THF solution of ethylmagnesium chloride (3 equiv), in mesitylene at 185 °C for 72 h gave 2-(diphenylamino)naphthalene (**3aa**) in 72% yield (Table 1, entry 1). As expected, no C-arylation at the *ortho*- or *para*-positions of **2a** takes place. However, 4-(diphenylamino)-1-butanol, which is likely to be produced by nucleophilic attack of Ph<sub>2</sub>NMgCl on the 2-position of THF, was also obtained in 57% yield (based on the amount of **1a**). To suppress this side reaction, the solvent of the Grignard reagent was changed from THF to 2-methyltetrahydrofuran (2-Me-THF), which is more bulky and thus less susceptible to nucleophilic attack,<sup>[8]</sup> and accordingly EtMgCl was replaced by BuMgCl (Table 1, entry 2).<sup>[9]</sup> As a result, the production of the aminoalcohol was completely suppressed and the yield of **3aa** was improved to 91%. Use of NaH as a base was much less effective, giving **3aa** in only 21% yield, where considerable amounts of naphthalene (14%) as well as 4- and 2-(2-naphthyl)-*N*-phenylanilines (**3'aa**/**3''aa**: 1.2%/0.8%) were produced (Table 1, entry 3). These byproducts are considered to be derived from 2-naphthyl radical, generated from the radical anion of 2-iodo-

**Table 1.** Effect of bases in the coupling of diphenylamine with 2-iodonaphthalene.<sup>[a]</sup>

Entry	Base	Solvent	Conv. of <b>1a</b> [%] <sup>[b]</sup>	Yield of <b>3aa</b> [%] <sup>[c]</sup>
1	EtMgCl in THF	mesitylene	76 <sup>[d]</sup>	72
2	BuMgCl in 2-Me-THF	mesitylene	93	91
3	NaH in 2-Me-THF	mesitylene	49 <sup>[e]</sup>	21
4 <sup>[f]</sup>	BuMgCl in 2-Me-THF	mesitylene	56	50
5 <sup>[g]</sup>	BuMgCl in 2-Me-THF	mesitylene	72	71
6 <sup>[h]</sup>	BuMgCl in 2-Me-THF	mesitylene	45	40
7	BuMgCl in 2-Me-THF	toluene	55	53

[a] The reaction was carried out under nitrogen atmosphere at 185 °C for 72 h using 2-iodonaphthalene (**1a**: 0.20 mmol), diphenylamine (**2a**: 0.66 mmol), and a base (0.60 mmol in THF or 2-Me-THF) in a solvent (1.20 mL). [b] Determined by <sup>1</sup>H NMR spectroscopy. [c] Determined by GC. [d] 4-(Diphenylamino)-1-butanol was obtained in 57% yield (<sup>1</sup>H NMR). [e] 4- and 2-(2-naphthyl)-*N*-phenylanilines (**3'aa** and **3''aa**) were obtained in 1.2% and 0.8% yields, respectively, in addition to naphthalene in 14% yield. [f] At 140 °C. [g] At 200 °C. [h] Diphenylamine (**2a**: 0.33 mmol) and BuMgCl (0.30 mmol) were used.

[a] K. Kiriyama, K. Okura, F. Tamakuni  
Department of Chemistry, Graduate School of Science  
Kyoto University, Sakyo, Kyoto 606-8502 (Japan)

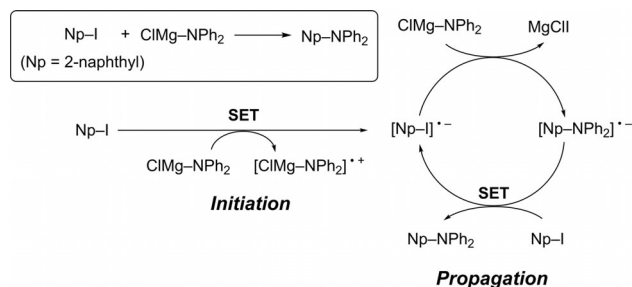
[b] Prof. E. Shirakawa  
Department of Applied Chemistry for Environment  
School of Science and Technology, Kwansai Gakuin University  
2-1 Gakuen, Sanda, Hyogo 669-1337 (Japan)  
E-mail: eshirakawa@kwansai.ac.jp

Supporting information and the ORCID identification number for the author of this article can be found under <https://doi.org/10.1002/chem.201800011>.

naphthalene through decomposition instead of reacting with  $\text{NaNPh}_2$ .<sup>[10]</sup> The coupling reaction at a temperature lower or higher than 185 °C resulted in a lower yield (Table 1, entries 4 and 5). Use of a reduced amount (1.5 equiv) of  $\text{Ph}_2\text{NMgCl}$  or changing the solvent to toluene severely affected the efficiency of the reaction (Table 1, entries 6 and 7).

The coupling reaction is applicable to various aryl iodides and diarylamines (Table 2). In addition to 2-iodonaphthalene (**1a**), iodobenzene (**1b**) and 4-iodobiphenyl (**1c**) underwent coupling with diphenylamine (**2a**) to give coupling products in good yields (Table 2, entries 1–3). Although the reaction is rather slow using a relatively hindered aryl iodide such as 1-iodonaphthalene (**1d**) and 2-iodotoluene (**1e**), the corresponding coupling products were obtained in moderate to high yields (Table 2, entries 4 and 5). Substitution took place solely at the iodide in the reaction of 4-chloriodobenzene (**1f**; Table 2, entry 6). A heteroaryl iodide also participated in the coupling (Table 2, entry 7). Diphenylamines bearing chloro or methyl substituents at *para*-positions and dissymmetrical diarylamines also underwent coupling with **1a** (Table 2, entries 8–11). The reaction is slow with an *ortho*-substituted diphenylamine (Table 2, entry 12). Bisamination products were obtained from diiodoarenes (Table 2, entries 13–15).

Considering that the present reaction follows the course of the electron-catalyzed cross-coupling reaction of aryl Grignard reagents with aryl halides,<sup>[5c]</sup> the mechanism shown in Scheme 1, exemplified by the reaction of 2-iodo-



**Scheme 1.** A plausible mechanism for the coupling of aryl iodides with secondary amines.

naphthalene (**1a**) with  $\text{CIMgNPh}_2$  (derived from **2a**), can be proposed.<sup>[11]</sup> Thus, the reaction is initiated by SET from  $\text{CIMgNPh}_2$  to  $\text{Np-I}$  to give  $[\text{Np-I}]^{\bullet-}$ ,<sup>[12]</sup> which reacts with  $\text{CIMgNPh}_2$ . SET from the resulting radical anion ( $[\text{Np-NPh}_2]^{\bullet-}$ ) to  $\text{Np-I}$  gives the coupling product (**3aa**) and regenerates  $[\text{Np-I}]^{\bullet-}$ .

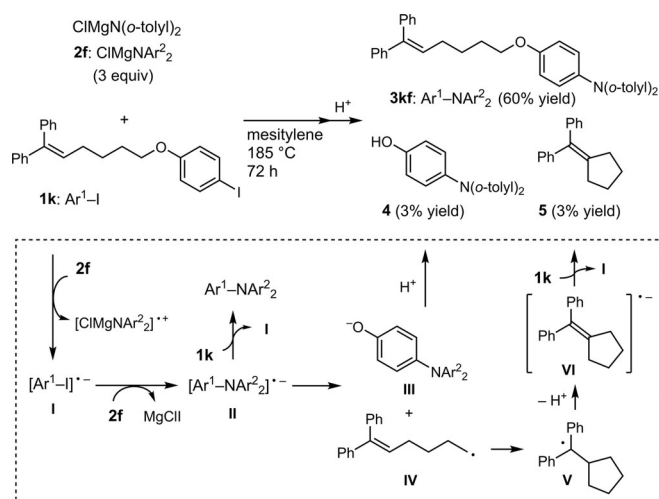
The involvement of radical-anion intermediates was supported by a radical clock experiment shown in Scheme 2. Thus, the reaction of 4-(6,6-diphenyl-5-hexenyloxy)iodobenzene (**1k**) with  $\text{CIMgN}(o\text{-tolyl})_2$  under the standard conditions gave not only the normal coupling product (**3kf**) but also, albeit in low yields, the dealkylated coupling product (**4**) and (diphenylmethylidene)cyclopentane (**5**). Production of **4** and **5** is rationally

**Table 2.** Coupling of magnesium diarylamides with aryl iodides.<sup>[a]</sup>

Entry	1	2	3	Yield [%] <sup>[b]</sup>	Prod.
1				92	<b>3aa</b>
2				75	<b>3ba</b>
3				88	<b>3ca</b>
4 <sup>[c]</sup>				65	<b>3da</b>
5				78	<b>3ea</b>
6				75	<b>3fa</b>
7				74	<b>3ga</b>
8				71	<b>3ab</b>
9				71	<b>3ac</b>
10				71	<b>3ad</b>
11 <sup>[c]</sup>				76	<b>3ae</b>
12 <sup>[c]</sup>				65	<b>3af</b>
13 <sup>[c]</sup>				89 <sup>[d]</sup>	<b>3ha</b>
14				89 <sup>[e]</sup>	<b>3ia</b>
15				71 <sup>[f]</sup>	<b>3ja</b>

[a] The reaction was carried out under a nitrogen atmosphere at 185 °C for 72 h using an aryl iodide (**1**: 0.20 mmol), a diarylamine (0.66 mmol), a 1.5 M 2-Me-THF solution of butylmagnesium chloride (0.40 mL, 0.60 mL) in mesitylene (1.2 mL). [b] Yield of the isolated product based on **1**. [c] At 200 °C. [d] Yield of 1,4-bis(diphenylamino)benzene. [e] Yield of 4,4'-bis(diphenylamino)biphenyl. [f] Yield of 9,9-dimethyl-2,7-bis(diphenylamino)fluorene.

understood as follows (Scheme 2, bottom). SET from  $\text{CIMgN}(o\text{-tolyl})_2$  converts **1k** into radical anion (**I**), which reacts with  $\text{CIMgN}(o\text{-tolyl})_2$  to give radical anion (**II**) of **3kf**. Most of **II** is converted into **3kf** upon SET to **1k** but a small part of **II** undergoes decomposition into 4-[di(*o*-tolyl)amino]phenolate (**III**) and 6,6-diphenyl-5-hexenyl radical (**IV**),<sup>[13]</sup> the latter of which readily cyclizes to cyclopentyl(dimethyl)methyl radical (**V**).<sup>[14]</sup>



Scheme 2. Proof of the involvement of radical-anion intermediates.

Deprotonation from **V** gives radical anion **V**, from which SET to **1k** takes place to give **5** and regenerate radical anion **I**.<sup>[15]</sup>

In conclusion, we have developed the electron-catalyzed coupling reaction of magnesium diarylamides with aryl iodides to give triaryl amines, proceeding through a single-electron-transfer mechanism without the aid of transition-metal catalysis.

## Acknowledgement

This work has been supported financially in part by Grant-in-Aid for Scientific Research (B) (25288046 to E.S.) from JSPS.

## Conflict of interest

The authors declare no conflict of interest.

**Keywords:** radical-anions • C–N coupling • organic transformations • single-electron transfer • triaryl amines

- [1] For recent reviews of the transition metal-catalyzed amination of aryl halides, see: a) P. Ruiz-Castillo, S. L. Buchwald, *Chem. Rev.* **2016**, *116*, 12564–12649; b) I. P. Beletskaya, A. V. Cheprakov, *Organometallics* **2012**, *31*, 7753–7808.
- [2] For transition-metal-catalyzed coupling reactions of aryl halides with magnesium diarylamides, see: a) C. Chen, L.-M. Yang, *Org. Lett.* **2005**, *7*, 2209–2211; b) T. Hatakeyama, R. Imayoshi, Y. Yoshimoto, S. K. Ghorai, M. Jin, H. Takaya, K. Norisuye, Y. Sohrin, M. Nakamura, *J. Am. Chem. Soc.* **2012**, *134*, 20262–20265; c) X.-L. Li, W. Wu, X.-H. Fan, L.-M. Yang, *Org. Biomol. Chem.* **2014**, *12*, 1232–1236.
- [3] For reviews of the  $S_{RN}1$  reaction, see: a) J. F. Bunnett, *Acc. Chem. Res.* **1978**, *11*, 413–420; b) R. A. Rossi, A. B. Pierini, A. B. Peñeñory, *Chem. Rev.* **2003**, *103*, 71–167.
- [4] J. F. Bunnett, J. K. Kim, *J. Am. Chem. Soc.* **1970**, *92*, 7464–7466.
- [5] For the coupling of aryl Grignard reagents: a) E. Shirakawa, Y. Hayashi, K. Itoh, R. Watabe, N. Uchiyama, W. Konagaya, S. Masui, T. Hayashi, *Angew. Chem. Int. Ed.* **2012**, *51*, 218–221; *Angew. Chem.* **2012**, *124*, 222–225; b) E. Shirakawa, K. Okura, N. Uchiyama, T. Murakami, T. Hayashi, *Chem. Lett.* **2014**, *43*, 922–924. c) For a mechanistic study on the coupling of aryl Grignard reagents: N. Uchiyama, E. Shirakawa, T. Hayashi, *Chem. Commun.* **2013**, *49*, 364–366. d) For the coupling of aryl zinc reagents: H. Minami, X. Wang, C. Wang, M. Uchiyama, *Eur. J. Org. Chem.* **2013**, 7891–7894; e) E. Shirakawa, F. Tamakuni, E. Kusano, N. Uchiyama, W. Konagaya, R. Watabe, T. Hayashi, *Angew. Chem. Int. Ed.* **2014**, *53*, 521–525; *Angew. Chem.* **2014**, *126*, 531–535. f) For the coupling of arylaluminum reagents: H. Minami, T. Saito, C. Wang, M. Uchiyama, *Angew. Chem. Int. Ed.* **2015**, *54*, 4665–4668; *Angew. Chem.* **2015**, *127*, 4748–4751. g) For the coupling of alkyl zinc reagents: K. Okura, E. Shirakawa, *Eur. J. Org. Chem.* **2016**, 3043–3046. h) For the coupling of tetraaryl-stannanes: Q. He, L. Wang, Y. Liang, Z. Zhang, S. F. Wnuk, *J. Org. Chem.* **2016**, *81*, 9422–9427. i) For the coupling of alkynyl zinc reagents: K. Okura, H. Kawashima, F. Tamakuni, N. Nishida, E. Shirakawa, *Chem. Commun.* **2016**, *52*, 14019–14022.
- [6] For reviews on “electron catalysis”, see: a) A. Studer, D. P. Curran, *Nat. Chem.* **2014**, *6*, 765–773; b) A. Studer, D. P. Curran, *Angew. Chem. Int. Ed.* **2016**, *55*, 58–102; *Angew. Chem.* **2016**, *128*, 58–106.
- [7] Aryl-nitrogen bond-forming products are known to be obtained from aryl halides without transition metal catalysis. Through a  $S_NAr$  mechanism, see: a) R. Cano, D. J. Ramón, M. Yus, *J. Org. Chem.* **2011**, *76*, 654–660; b) D. Dehe, I. Munstein, A. Reis, W. R. Thiel, *J. Org. Chem.* **2011**, *76*, 1151–1154; c) A. Kaga, H. Hayashi, H. Hakamata, M. Oi, M. Uchiyama, R. Takita, S. Chiba, *Angew. Chem. Int. Ed.* **2017**, *56*, 11807–11811; *Angew. Chem.* **2017**, *129*, 11969–11973. d) Through aryne intermediates, see: J. L. Bolliger, C. M. Frech, *Tetrahedron* **2009**, *65*, 1180–1187; e) Y. Fang, Y. Zheng, Z. Wang, *Eur. J. Org. Chem.* **2012**, 1495–1498.
- [8] 2-Me-THF is reported to be much less susceptible to ring-opening attack by benzylmagnesium chloride compared to THF, see: S. H. Christensen, T. Holm, R. Madsen, *Tetrahedron* **2014**, *70*, 4942–4946.
- [9] We used a THF solution of ethylmagnesium chloride purchased from Sigma-Aldrich Co. Upon changing the solvent from THF to 2-Me-THF, we changed the alkyl moiety of the alkylmagnesium chloride from ethyl to butyl as butyl chloride is much more convenient as a Grignard reagent starting material than ethyl chloride, which has a low boiling point (12.3 °C).
- [10] A similar difference between alkali metals and alkaline earth metals is also observed in the electron-catalyzed cross-coupling reaction of aryl halides with organometallic reagents. As mentioned in the Introduction section, free aryl radicals are not involved in the reaction of arylmagnesium bromides. In contrast, the products derived from aryl radical intermediates were observed in the reaction of aryllithiums. For example, the reaction of phenyllithium, prepared from bromobenzene (1.5 equiv) and *tert*-butyllithium (3.0 equiv), with 4-iodoanisole (**11**) in the presence of THF (6 equiv) in toluene at 110 °C for 24 h gave 4-methoxybiphenyl only in 3% yield, with a full conversion of **11**, where anisole (60%) and 1,2-diphenylethane (39%) were the main products. These are likely to be produced through a hydrogen abstraction of 4-methoxyphenyl radicals from toluene and radical-radical homocoupling of the resulting benzyl radicals. For details of the reaction of phenyllithium with **11**, see the Supporting Information.
- [11] The possibility that the reaction proceeds through aryne intermediates is excluded on grounds of the regioselective production of triaryl amines from all the aryl iodides used herein.
- [12] There is some possibility that SET from a magnesium amide to an aryl iodide takes place indirectly, for example, through an aryne intermediate, generated upon deprotonation from the aryl iodide by the magnesium amide, and the successive generation of an efficient single electron donor as reported by Tuttle, Murphy and co-workers: J. P. Barham, G. Coulthard, K. J. Emery, E. Doni, F. Cumine, G. Nocera, M. P. John, L. E. A. Berlouis, T. McGuire, T. Tuttle, J. A. Murphy, *J. Am. Chem. Soc.* **2016**, *138*, 7402–7410. For more discussion on whether SET from a base to an aryl halide takes place directly or indirectly, see the above work and references cited therein.
- [13] Radical-anions of alkyl aryl ethers are known to be converted into the corresponding phenolate and the alkyl radical: a) U. Azzena, T. Denurra, G. Melloni, *J. Org. Chem.* **1992**, *57*, 1444–1448; b) U. Azzena, F. Dessanti, G. Melloni, L. Pisano, *ARKIVOC* **2002**, *v*, 181–188. c) The fragmentation of this type is also studied in the photostimulated  $S_{RN}1$  reaction of  $RS^-$  (R=alkyl) with Ar–X, where the radical-anion  $[RSAr]^-$  decompose to  $R^\cdot$  and  $^-SAr$ . R. A. Rossi, S. M. Palacios, *J. Org. Chem.* **1981**, *46*, 5300–5304.

- [14] The cyclization rate of 6,6-diphenyl-5-hexenoxy radical at 20 °C is estimated as  $k_c = 5.0 \times 10^7 \text{ s}^{-1}$ . C. Ha, J. H. Horner, M. Newcomb, T. R. Varick, *J. Org. Chem.* **1993**, *58*, 1194–1198.
- [15] The involvement of radical-anion intermediates was supported also by the following experiment. The reaction of 1,4-diodobenzene (**1h**) with magnesium diphenylamide (6 equiv) in mesitylene at 200 °C in a short reaction period (4 h instead of 72 h as in entry 13 of Table 2) gave the bisaminated product (**3ha**) and the monoaminated product (**3'ha**) in 31% and 26% yields, respectively, with 64% conversion of **1h**. Predominated production of **3ha** even in the presence of a considerable amount of the remaining **1h** is rationally understood as follows. A radical-anion of **3'ha**, generated upon the C–N bond formation in the propagation step, undergoes another C–N bond formation to be converted to a radical-anion of **3ha** leading to **3ha**, rather than passes an

electron to **1h** to be converted to **3'ha**. The possibility that predominated production of **3ha** is ascribed to an exceptionally high reactivity of **3'ha** is excluded by the outcome that the reaction of **3'ha** with  $\text{Ph}_2\text{NMgCl}$  (6 equiv) at 200 °C for 4 h resulted in just 14% conversion (10% yield of **3ha**). For the detail, see Supporting Information. Use of this type of observation as a proof of the involvement of radical-anion intermediates, see: a) J. F. Bunnett, X. Creary, *J. Org. Chem.* **1974**, *39*, 3611–3612; b) B. Janhsen, C. G. Daniliuc, A. Studer, *Chem. Sci.* **2017**, *8*, 3547–3553.

---

Manuscript received: January 2, 2018

Accepted manuscript online: February 15, 2018

Version of record online: March 6, 2018

## 電子触媒クロスカップリング反応

白川英二 Eiji SHIRAKAWA 関西学院大学理工学部環境・応用化学科教授

### 1 はじめに

遷移金属触媒を用いる、有機金属化合物とハロゲン化アリのルのクロスカップリング反応は、入手容易なアリル求電子剤であるハロゲン化アリルを原料に、そのハロゲン部位を様々な炭素置換基に変換できる汎用性の高い反応である。中でもアリル金属を用いるクロスカップリング反応は、ビアリルを合成する他の直截的な手法に乏しいため、特に重要である。様々な遷移金属が触媒として働くが、パラジウムやニッケルなどの第10族遷移金属が使やすい。特に「パラジウム触媒によるクロスカップリング反応」として、「鈴木-宮浦カップリング」、「根岸カップリング」、「溝呂木-Heck 反応」(この反応は通常狭義ではクロスカップリング反応には含まれない)が2010年ノーベル化学賞授与の対象となったのは、これらの合成化学的有用性が認められた結果と言える。しかしながら、遷移金属を触媒として利用することには、以下の問題がある。パラジウムをはじめとする多くの遷移金属は存在量に限りがあり高価であるという点と、通常用いられる均一触媒条件では、反応混合物から遷移金属触媒を取り除くことが容易ではないという点である。医薬品製造においては、遷移金属による毒性の影響がより大きいので、後者の問題が重要になる。遷移金属触媒を用いなければ遷移金属の残存量を調べる必要さえないので都合がよいが、我々が2012年にアリル Grignard 反応剤とハロゲン化アリルの電子触媒クロスカップリング反応を報告するまでは、遷移金属触媒の利用が必要不可欠とされてきた。

本稿では、電子触媒クロスカップリング反応を見つけるに至った経緯から、現在までの展開について

概説する。

### 2 ハロゲン化アリルの置換反応

$sp^2$ -炭素上で起こるハロゲン化アリル(Ar-X)の置換反応では、 $S_N2$  反応も  $S_N1$  反応も起こせない。ハロゲン化アリルの置換反応において遷移金属触媒の必要度が非常に高いのは、低原子価遷移金属が2電子還元することでハロゲン化アリルを容易に活性化し、置換反応に至らしめるからである。例えば、パラジウム触媒を用いる有機金属化合物(R-m)とのクロスカップリング反応では、低原子価錯体であるパラジウム(0)錯体( $Pd^0$ )がAr-Xを2電子還元することで炭素-ハロゲン結合を切断し(酸化的付加)、生じた酸化的付加体(Ar- $Pd^{II}$ -X:パラジウムから見ると2電子酸化されている)がR-mと反応しAr- $Pd^{II}$ -Rとなる(トランスメタル化)。ここからの還元的脱離によってカップリング体(Ar-R)が得られると同時に、パラジウムは還元されて $Pd(0)$ が再生される。

このようにハロゲン化アリルは、低原子価遷移金属によって2電子還元されることで置換反応を起こすが、1電子還元による活性化も置換反応に利用できる。これは、 $S_N1$  反応になぞらえて  $S_{RN}1$  (Substitution Radical Nucleophilic Unimolecular) 反応と呼ばれ、実は約50年の歴史がある(図1)。<sup>1,2)</sup> まず、アルカリ金属などの1電子供与体(D)からハロゲン化アリル(Ar-X)に1電子移動(Single Electron Transfer: SET)が起こり、Ar-Xがアニオンラジカル( $[Ar-X]^{\cdot-}$ )として活性化される(ステップa)。これに続くハロゲン化物イオン( $X^-$ )の脱離によってアリルラジカル(Ar $^{\cdot}$ )が生じる(ステップb)。これに、脱プロトン化(ステップc)に

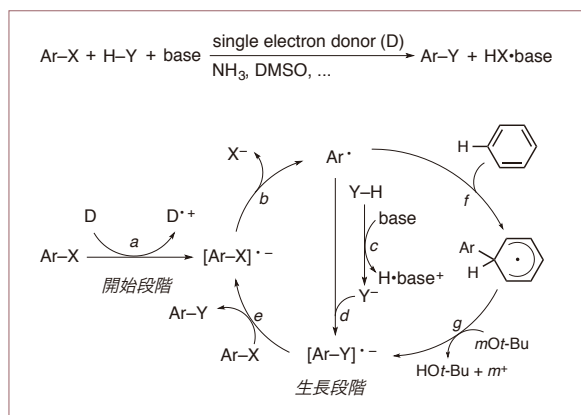


図1

よって系中で生成したアニオン性求核剤(Y<sup>-</sup>)が付加反応を起こし、置換生成物のアニオンラジカル([Ar-Y]<sup>•-</sup>)に変換される(ステップd)。最後に、このアニオンラジカルからAr-XにSETが起こることで置換生成物が得られると同時に[Ar-X]<sup>•-</sup>が再生される(ステップe)。反応を開始するステップaの1電子還元が重要であるのは言うまでもないが、このラジカル連鎖機構で最も秀逸なのはステップeである。ここでは、置換反応を起こすのに必要なハロゲン化アリの1電子還元と酸化還元の収支を合わせるのに必要な1電子酸化が同時に起こっており、SETで授受される電子が触媒として働いていると見なせる。このように電子という極めて小さなもの(質量でパラジウムの約20万分の1)が触媒となるという特異な機構を持ちながら、不思議なことに、我々以前にこの種の反応を「電子触媒反応」と呼ぶことはなかった。このような秀逸な機構を持つSRN1反応が有機合成上幅広く用いられなかったのは、以下の問題があるからである。まず基本的には、系中での脱プロトン化(ステップc)によって求核剤を生じることができる基質しか用いられない。言い換えると、ある程度高い酸性度を持つプロ求核剤しか出発原料にはならないということで、炭素-炭素結合形成反応への応用はケトンやポリエンなどのsp<sup>3</sup>-炭素プロ求核剤に限られ、ビアリール合成に必要なsp<sup>2</sup>-炭素同士の結合を作ることにはできなかった。2番目の問題は、反応性の高すぎるアリールラジカルを中間体とすることである。アリールラジカルは、多くの溶媒から水素を引き抜い

てアレンとなるほか、様々な副反応を起こしてしまうが、一般にそれらを完全に抑えるのは難しい。

このような背景のもと、我々のグループを含む3グループが、化学量論量のtert-ブトキシドと少量の窒素二座配位子存在下ハロゲン化アールをベンゼンと反応させるとビアリールが得られることを、ほぼ同時期(2010年後半)に報告した(図2)<sup>3-5)</sup>。当初からラジカルが関与していることは示唆されていたが、図1右部分に示す変則SRN1反応と言える機構で反応が進行していることが明らかにされたのはしばらく経ってからのことである。<sup>6,7)</sup> ステップbまでは従来のSRN1反応と同様に進行し、ここでは金属tert-ブトキシドと窒素二座配位子の混合物が1電子供与体として働く。ここからAr•がベンゼンに付加したのち(ステップf)、生じたシクロヘキサジエニルラジカルからtert-ブトキシドがプロトンを引き抜くことでビアリールのアニオンラジカル([Ar-Ph]<sup>•-</sup>)となる(ステップg)ところが従来と異なる。すなわち、本法では付加と脱離の順序が逆になっていることによって、ベンゼンのような容易には脱プロトン化できないものでもSRN1反応に用いることができるようになってきている。本来必要であった求核性(電子豊富さ)は、付加ののちの強塩基による脱プロトン化によって導入されている。こうしてsp<sup>2</sup>-炭素(プロ)求核剤がSRN1反応で使えるようになったわけである。この基質の組み合わせによるカップリング反応では遷移金属触媒が必須というわけではないが、遷移金属が得意とするタイプの反応である。このカップリング反応が、tert-ブトキシドと少量の窒素二座配位子(その後、窒素二座配位子以外の様々な添加剤を用いる例が報告されている)を加え

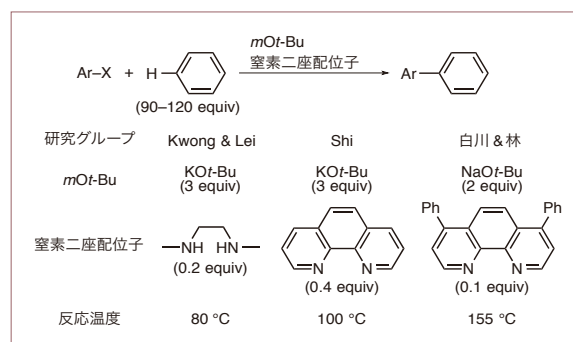


図2

るだけで進行することは有機合成上極めて有用であるが、ベンゼン以外の芳香族化合物を用いる場合には、その合成的価値はあまり高くない。大過剰の芳香族化合物を用いる必要があるうえにアリールラジカルの付加が位置選択的ではないため、対称性の低いアレーン(一置換ベンゼンなど)の反応では生成物は異性体の混合物になるからである。

### 3 Grignard クロスカップリング反応

従来の  $S_{RN}1$  反応では、開始段階における SET を起こしやすい条件が採用されることが多い。例えば、液体アンモニア中でアルカリ金属を 1 電子供与体として用いる Birch 還元条件などが代表例であるが、有機金属化合物との相性は良くない。また、アリールラジカル中間体は反応性が高く、多くの溶媒から水素を引き抜いてしまうので、有機金属化合物と相性の良いエーテル系溶媒の使用は避けられてきた。このような背景のもと我々は、先のハロゲン化アリールとベンゼンのカップリング反応の系で用いていたベンゼン誘導体を溶媒とし、アリール Grignard 反応剤のような電子豊富なものを用いれば、これがアリールラジカルと反応する求核剤および開始段階における 1 電子供与体として働き、ハロゲン化アリールとのクロスカップリング反応が進行すると考えた(図 3)。検討を始めて間もなく、THF 中で調製した臭化フェニルマグネシウム(PhMgBr)からほとんどの THF を留去したのち、2-ヨードナフタレンとトルエン中 110°C で 24 時間反応させると、カップリング体である 2-フェニルナフタレンが収率よく得られることを見つけた。<sup>8)</sup> ジエチルエーテル中で調製した Grignard 反応剤を同様にして用いても反応は全く進行せず、そこに THF を 6 当量加えると反応性を回復したことから、少量の

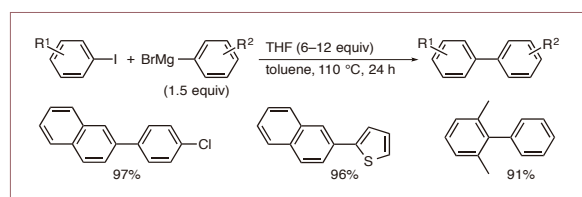


図 3

THF の存在が重要であることが判ったが、THF を溶媒として用いるとハロゲン-マグネシウム交換が優先しカップリング体はほとんど得られない。ハロゲン化アリールの適用範囲はヨウ化アリールにほぼ限られるものの、この Grignard クロスカップリング反応によって様々なビアリールが概ね 90% 以上の高収率で得られる。

ここでは反応機構の解明を目的とした検討の詳細を示さないが、電子が触媒として働いていることを端的に表す実験結果を 1 例だけ紹介する。臭化アリールの反応性は低く、2-ブromoナフタレン(Np-Br)を 80°C で 12 時間臭化フェニルマグネシウム(PhMgBr)と反応させても Np-Br はほとんど消費されないのに対して、リチウムジ *tert*-ブチルピフェニリド(LDBB: ビアリールのアニオンラジカル)を 0.2 当量加えると、カップリング体が収率 80% で得られた(図 4)。1 電子等価体と言える LDBB を加えることで反応が大幅に加速されたということは、電子が触媒として働き、開始段階のアリール Grignard 反応剤からハロゲン化アリールへの SET の段階が全過程の中で最も遅いということを示している。その他の検討により、当初想定していたアリールラジカル中間体は経由しない、以下に示す機構で反応が進行していることが判った。<sup>9)</sup> その機構を臭化フェニルマグネシウム(PhMgBr)と 2-ヨードナフタレン(Np-I)の反応を例に図 5 に示す。まず、PhMgBr からの SET で Np-I がアニオンラジカルとして活性化される(ステップ a)。生じた  $[Np-I]^{\cdot-}$  が PhMgBr と反応することでカップリング体のアニオンラジカル( $[Ph-Np]^{\cdot-}$ )に変換され

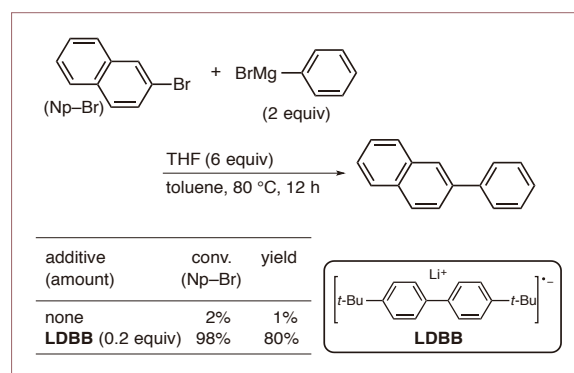


図 4

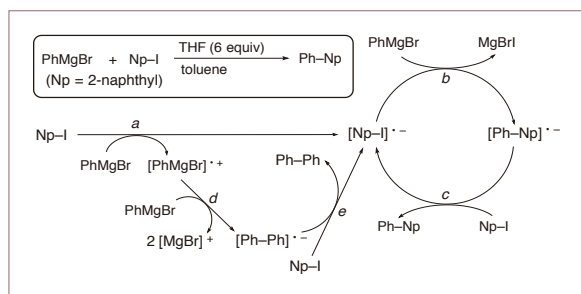


図 5

たのち(ステップ *b*), ここから  $\text{Np-I}$  への SET によってカップリング体 ( $\text{Ph-Np}$ ) が得られると同時に  $[\text{Np-I}]^{\cdot-}$  が再生される(ステップ *c*). 一方, 開始段階で 1 電子を  $\text{Np-I}$  に渡した  $\text{PhMgBr}$  はカチオンラジカル ( $[\text{PhMgBr}]^{\cdot+}$ ) に変換されたのち(ステップ *a*), もう 1 分子の  $\text{PhMgBr}$  と反応し(ステップ *d*), 生じたビフェニルのアニオンラジカルからの SET によってもう 1 分子の  $\text{Np-I}$  が活性化される(ステップ *e*). ここでの 4 個の中間体は全てイオンラジカルであり, ラジカル機構でありながら, 反応性が高く副反応を起こしやすいアリールラジカルを中間体としないことが高収率に貢献していると考えられる.

Grignard クロスカップリング反応は, ヨウ化アルケニルにも適用可能である(図 6).<sup>10)</sup> シス-トランスの異性化を速やかに起こしてしまうアルケニルラジカル中間体を經由しないので, アルケニル基の立体化学は保たれる. ヨウ化アリールやヨウ化アルケニルに比べて臭化物の反応性が低いのは, LUMO のエネルギー準位がより高く, 開始段階においてアリール Grignard 反応剤 ( $\text{ArMgBr}$ ) から 1 電子を受け取りにくいからである. そこで,  $\text{ArMgBr}$  の電子密度を上げてやればハロゲン化アリールやハロゲン化アルケニルへの SET が容易になると考え, 塩化物イオンがマグネシウムに配位することで  $\text{ArMgBr}$  とアート錯体 ( $\text{Li}[\text{ArMgBrCl}]$ ) を形成する塩化リチウムを加えたところ, 期待通り臭化物でもクロスカップリング反応が進行することが判った(図 7).<sup>11)</sup> 図 3 に記した条件では,  $\text{ArMgBr}$  を THF 中で調製したのち THF 溶媒を留去して反応に用いていたが, ヨウ化アリールの反応ではトルエン/THF = 3/1 の溶媒系(反応温度は 80°C)で, ま

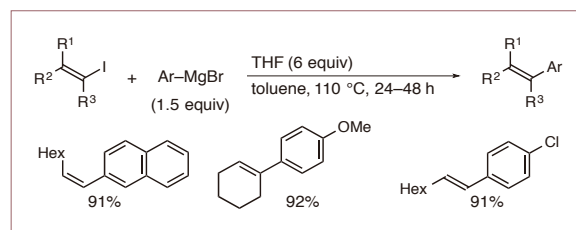


図 6

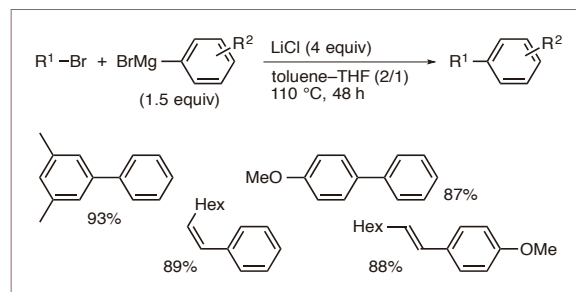


図 7

た, 臭化アリールの反応では塩化リチウム 4 当量を加えトルエン/THF = 2/1 の溶媒系で各々反応させれば, THF を留去する必要もなく高収率でカップリング体を得られることも判った.

## 4 有機亜鉛反応剤を用いるクロスカップリング反応

Grignard クロスカップリング反応は, 調製が容易なアリール Grignard 反応剤を用いる点で求電子性官能基を持たない基質の反応には好都合であるが, エステルやニトリルなどを持つ基質には適用できない. そこで, 官能基許容度が高いアリール亜鉛反応剤を用いるクロスカップリング反応の開発に取り組んだ. Grignard 反応剤と同様に, ハロゲン化アリール(ここではヨウ化物)に亜鉛粉末を作用させ

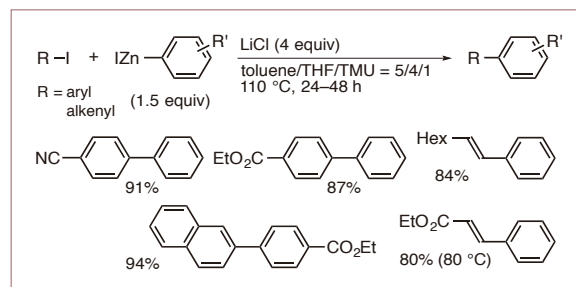


図 8

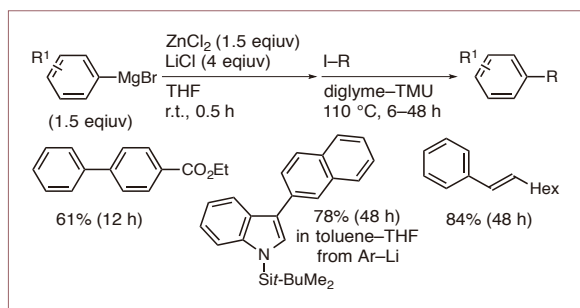


図 9

て調製したヨウ化アリール亜鉛は、種々のヨウ化アリールとカップリングを起こし、塩化リチウムを添加することで反応性が向上した(図8).<sup>12)</sup> エステルやニトリルなどの求電子基を持つアリール亜鉛反応剤やヨウ化アリールにも適用可能である。臭化アリールマグネシウムと塩化亜鉛の間のトランスメタル化で調製したアリール亜鉛反応剤も用いることができる(図9)。なお、ほぼ同時期に内山らのグループもアリール亜鉛反応剤としてジアリール亜鉛を用いる電子触媒クロスカップリング反応を報告している。<sup>13)</sup>

有機亜鉛化合物を用いる電子触媒クロスカップリング反応は、アルキル亜鉛やアルキニル亜鉛にも適用できることが明らかになった。アルキルリチウムとヨウ化亜鉛のトランスメタル化によって得られるアルキル亜鉛反応剤に、ヨウ化リチウムを加えてヨウ化アリールと反応させると、カップリング体であるアルキルアレーンが得られた(図10).<sup>14)</sup> アリール亜鉛反応剤の場合と異なり、塩化物イオンは反応を阻害する。ハロゲン化物イオンの違いが有機亜鉛反応剤の会合度に影響し、その影響が有機亜鉛反応剤の種類によって異なるためと考えている。ヨウ化アルキルを出発原料に、ハロゲン-リチウム交換とト

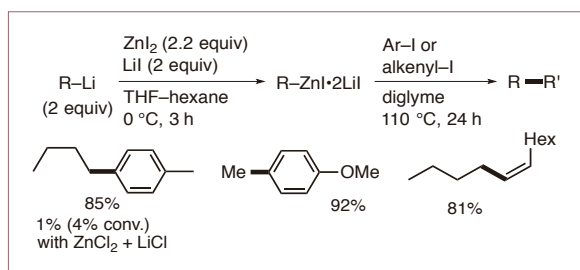


図 10

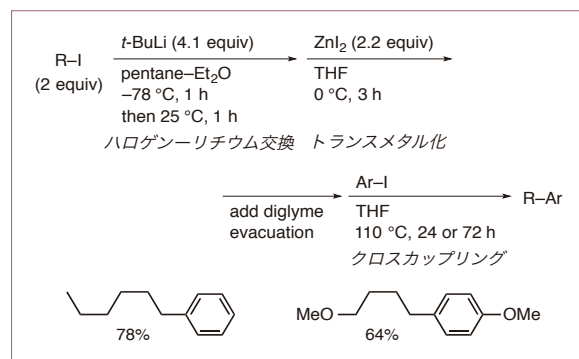


図 11

ランスメタル化を経て調製したアルキル亜鉛反応剤も用いることができる(図11)。

アルキニル亜鉛反応剤は末端アルキンにジエチル亜鉛を作用させることで調製できるが、これらを2:1の比で、ヨウ化アリールとトリス(4-トリフルオロメチルフェニル)ホスフィン(0.1当量)と一緒に混合し加熱かく拌すると、収率よくカップリング体が得られた(図12).<sup>15)</sup> ホスフィンを加えないとカップリングは全く進行せず、ホスフィンをより電

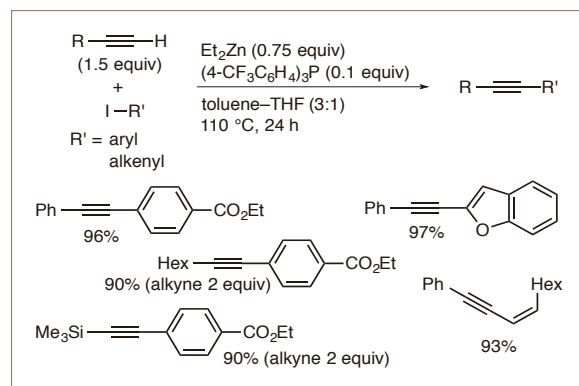


図 12

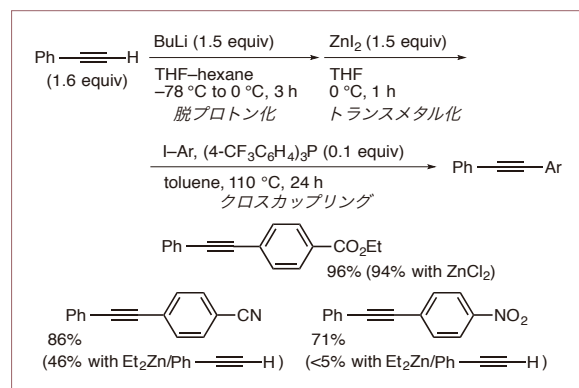


図 13

子豊富なものやより電子不足なものに代えると反応性が低下する。遷移金属との相性がよいホスフィンが、典型金属反応剤の反応性を高めたという興味深い現象で、今後のこの分野の発展が期待される。末端アルキンからブチルリチウムでプロトンを引き抜いたのち、ヨウ化亜鉛とトランスメタル化することで調製したヨウ化アルキニル亜鉛もカップリング反応に用いることが可能で、強い求電子基を持つヨウ化アリールとの反応では、ジエチル亜鉛に由来するアルキニル亜鉛反応剤よりも高収率で反応が進行した(図 13)。

## 5 おわりに

以上、電子が触媒として働いていると見なせるハロゲン化アリーの  $S_{RN}1$  反応に  $sp^2$ -炭素求核剤を持ち込むという、電子触媒クロスカップリング反応における我々のグループによる展開を紹介した。他のグループによる同様の反応の報告例として、先に触れたジアリール亜鉛を用いる反応のほか、<sup>13)</sup> アリールアルミニウム<sup>16)</sup>やテトラアリースズ<sup>17)</sup>のクロスカップリング反応も報告されてきている。電子触媒クロスカップリング反応には、基質の適用範囲がまだまだ狭い、あるいは反応の進行に高温を要するといった、解決しなければならない課題も残され

ている。しかし本法が、普遍に存在し、かつサイズの小さな電子を触媒に用いるという効率の良さを活かした有機合成上真に有用な反応になることを期待している。

## 引用文献

- 1) Bunnett J. F., *Acc. Chem. Res.*, 11, 413-420(1978).
- 2) Rossi R. A. *et al.*, *Chem. Rev.*, 103, 71-167(2003).
- 3) Shirakawa E. *et al.*, *J. Am. Chem. Soc.*, 132, 15537-15539(2010).
- 4) Lei A. *et al.*, *J. Am. Chem. Soc.*, 132, 16737-16740(2010).
- 5) Shi Z. -J. *et al.*, *Nat. Chem.*, 2, 1044-1049(2010).
- 6) Studer A., Curran D. P., *Angew. Chem., Int. Ed.*, 50, 5018-5022(2011).
- 7) Shirakawa E., Hayashi T., *Chem. Lett.*, 41, 130-134(2012).
- 8) Shirakawa E. *et al.*, *Angew. Chem., Int. Ed.*, 51, 218-221(2012).
- 9) Shirakawa E. *et al.*, *Chem. Commun.*, 49, 364-366(2013).
- 10) Shirakawa E. *et al.*, *Chem. Commun.*, 49, 5219-5221(2013).
- 11) Shirakawa E. *et al.*, *Chem. Lett.*, 43, 922-924(2014).
- 12) Shirakawa E. *et al.*, *Angew. Chem., Int. Ed.*, 53, 521-525(2014).
- 13) Uchiyama M. *et al.*, *Eur. J. Org. Chem.*, 7891-7894(2013).
- 14) Okura, K., Shirakawa E., *Eur. J. Org. Chem.*, 3043-3046(2016).
- 15) Shirakawa E. *et al.*, *Chem. Commun.*, 52, 14019-14022(2016).
- 16) Uchiyama M. *et al.*, *Angew. Chem., Int. Ed.*, 54, 4665-4668(2015).
- 17) Wnuk S. F. *et al.*, *J. Org. Chem.*, 81, 9422-9427(2016).

## キーワード

ラジカル、連鎖機構、ビアリール、ハロゲン化アリール、カップリング

***tert*-Butoxide-promoted Coupling of Aryl Iodides with Arenes  
Using Di-*tert*-butyl Hyponitrite as an Initiator**

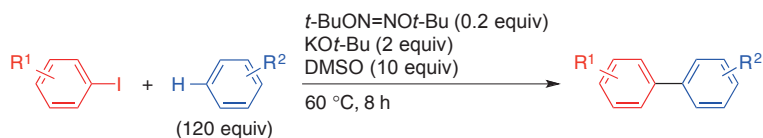
Kazuya Kiriya<sup>1</sup> and Eiji Shirakawa<sup>\*2</sup>

<sup>1</sup>*Department of Chemistry, Graduate School of Science, Kyoto University, Sakyo, Kyoto 606-8502*

<sup>2</sup>*Department of Applied Chemistry for Environment, School of Science and Technology,  
Kwansei Gakuin University, 2-1 Gakuen, Sanda, Hyogo 669-1337*

(E-mail: eshirakawa@kwansei.ac.jp)

The coupling reaction of aryl iodides with arenes was found to proceed to give biaryls under mild conditions through a homolytic aromatic substitution mechanism, using potassium *tert*-butoxide and di-*tert*-butyl hyponitrite as a stoichiometric promoter and a radical initiator, respectively.



REPRINTED FROM

**Chemistry  
Letters**

Vol.46 No.12 2017 p.1757–1759

CMLTAG  
December 5, 2017

The Chemical Society of Japan

## *tert*-Butoxide-promoted Coupling of Aryl Iodides with Arenes Using Di-*tert*-butyl Hyponitrite as an Initiator

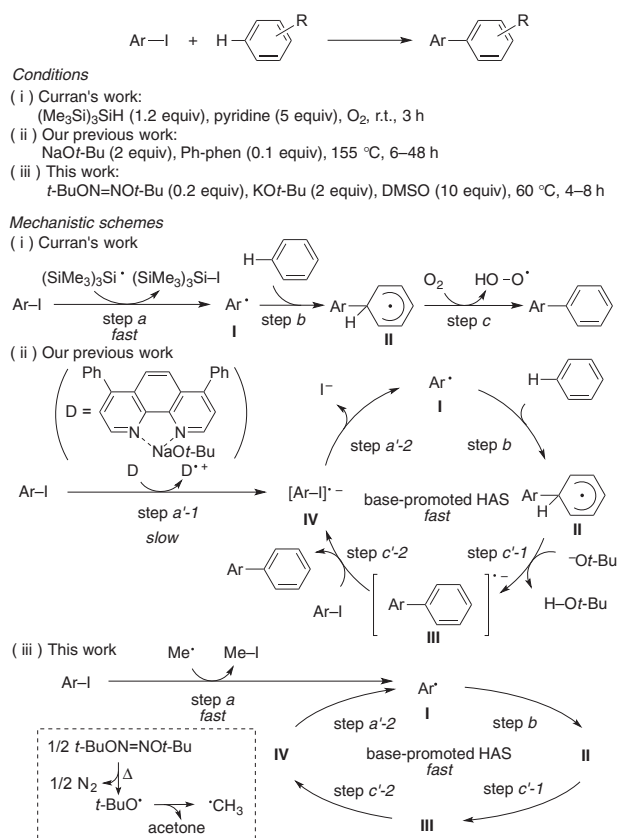
Kazuya Kiriya<sup>1</sup> and Eiji Shirakawa\*<sup>2</sup><sup>1</sup>Department of Chemistry, Graduate School of Science, Kyoto University, Sakyo, Kyoto 606-8502<sup>2</sup>Department of Applied Chemistry for Environment, School of Science and Technology, Kwansai Gakuin University, 2-1 Gakuen, Sanda, Hyogo 669-1337

(E-mail: eshirakawa@kwansai.ac.jp)

The coupling reaction of aryl iodides with arenes was found to proceed under mild conditions to give biaryls through a homolytic aromatic substitution mechanism, using potassium *tert*-butoxide and di-*tert*-butyl hyponitrite as a stoichiometric promoter and a radical initiator, respectively.

**Keywords:** Coupling reaction | Biaryl framework | Iodine abstractor

The transition-metal-catalyzed coupling of aryl halides with arenes is one of the most straightforward methods to obtain biaryl frameworks, where heteroarenes, electron-deficient arenes, and arenes with a directing group are representative substrates.<sup>1</sup> Iodine abstraction from an aryl iodide (Ar-I), followed by homolytic aromatic substitution (HAS) consisting of addition of the resulting aryl radical (Ar<sup>•</sup>) to an arene and elimination of “H” (or H<sup>+</sup> + e<sup>-</sup>) from the cyclohexadienyl radical intermediate, also has a high potential for this purpose.<sup>2</sup> However, it is difficult to settle the conflict between single electron (1e<sup>-</sup>) reduction in the iodine abstraction step and 1e<sup>-</sup> oxidation in the “H” elimination step.<sup>3</sup> Curran and co-workers solved the intrinsic conflict by use of (Me<sub>3</sub>Si)<sub>3</sub>SiH and molecular oxygen as a reductant and an oxidant, respectively (Scheme 1-i).<sup>3c</sup> (Me<sub>3</sub>Si)<sub>3</sub>Si<sup>•</sup> readily abstracts I<sup>•</sup> from Ar-I (step *a*) to give Ar<sup>•</sup> (I),<sup>4</sup> which adds to benzene (step *b*). The cyclohexadienyl radical (II) is oxidized by molecular oxygen, which is a mild oxidant compatible with the 1e<sup>-</sup> reduction process, giving Ar-Ph and HOO<sup>•</sup> (step *c*). The use of a stoichiometric amount of the expensive (Me<sub>3</sub>Si)<sub>3</sub>SiH is a major drawback here. On the other hand, we have recently reported a method using NaOt-Bu and 4,7-diphenyl-1,10-phenanthroline (Ph-phen) as stoichiometric and substoichiometric promoters, respectively.<sup>5</sup> As shown in Scheme 1-ii, upon coordination by Ph-phen, NaOt-Bu passes an electron to Ar-I, giving anion radical [Ar-I]<sup>-•</sup> (step *a*'-1), which undergoes decomposition into Ar<sup>•</sup> and I<sup>-</sup> (step *a*'-2). After the addition of Ar<sup>•</sup> to benzene (step *b*), deprotonation from II gives anion radical [Ar-Ph]<sup>-•</sup> (III) (step *c*'-1). Single electron transfer (SET) from [Ar-Ph]<sup>-•</sup> to Ar-I gives Ar-Ph and regenerates [Ar-I]<sup>-•</sup> (step *c*'-2), where the 1e<sup>-</sup> reduction and the 1e<sup>-</sup> oxidation indispensable for the reaction to be completed take place simultaneously. Although the intrinsic conflict is effectively solved, a high temperature (155 °C) is required, probably due to the reluctant initiation (step *a*'-1). On the other hand, Rossi and co-workers reported that KOt-Bu-promoted reaction of aryl halides with arenes proceeds at room temperature with the aid of photo-irradiation, which is considered to accelerate the SET process in the initiation step but does not largely affect the propagation step.<sup>6</sup> This observation shows that the propagation step is fast enough to proceed even at room temperature, prompting us to



**Scheme 1.** Biaryl synthesis from aryl iodides through homolytic aromatic substitution.

improve our previous method by changing the way to get into the propagation cycle (Scheme 1-iii). Thus, we planned to employ the I-abstraction (step *a*) instead of SET to Ar-I (step *a*'-1) as an entrance to the propagation cycle, where even a substoichiometric amount of an I-abtractor will work. We have chosen Me<sup>•</sup> as an I-abtractor for the following reasons: 1) Me<sup>•</sup> is readily generated at a relatively low temperature through two successive homolysis from di-*tert*-butyl hyponitrite (*t*-BuON=NOt-Bu),<sup>7,8</sup> which is advantageous over common I-abtractor precursors such as (Me<sub>3</sub>Si)<sub>3</sub>SiH and Bu<sub>3</sub>SnH from economic and environmental points of view; 2) Me<sup>•</sup> is likely to have sufficient I-abstraction ability, considering the report that cyclohexyl radical, which is more stable than Me<sup>•</sup>, undergoes I-abstraction from iodobenzenes having a bulky substituent at the *ortho*-position.<sup>9</sup> Here we report the arylation of arenes through the KOt-Bu-promoted HAS mechanism initiated by Me<sup>•</sup> derived from *t*-BuON=NOt-Bu.

**Table 1.** Effect of additives in the coupling of 4-iodoanisole with benzene<sup>a</sup>

Entry	Additive	Temp. /°C	Time /h	Conv. of <b>1a</b> /% <sup>b</sup>	Yield /% <sup>b</sup>
1 <sup>c</sup>	<i>t</i> -BuON=NO <i>t</i> -Bu	60	8	48	34
2	<i>t</i> -BuON=NO <i>t</i> -Bu	60	8	>99	81
3	None	60	8	19	7
4	<i>t</i> -BuOO <i>t</i> -Bu	60	24	25	9
5	<i>t</i> -BuOO <i>t</i> -Bu	120	24	>99	52
6	(Me <sub>3</sub> Si) <sub>3</sub> SiH, V-70 <sup>d</sup>	60	8	90	47

<sup>a</sup>The reaction was carried out under a nitrogen atmosphere using 4-iodoanisole (**1a**: 0.20 mmol), benzene (**2a**: 2.1 mL, 24 mmol), an additive (0.040 mmol), KO*t*-Bu (0.40 mmol), and dimethyl sulfoxide (0.14 mL, 2.0 mmol). <sup>b</sup>Determined by GC. <sup>c</sup>Na*t*-Bu was used instead of KO*t*-Bu. <sup>d</sup>(Me<sub>3</sub>Si)<sub>3</sub>SiH (0.040 mmol) and 2,2'-azobis(4-methoxy-2,4-dimethyl)valeronitrile (V-70: 0.040 mmol) were used.

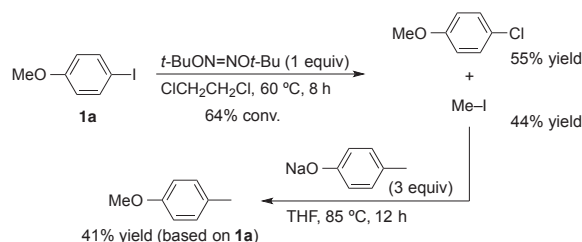
Treatment of 4-iodoanisole (**1a**: 1 equiv) with Na*t*-Bu (2 equiv) and *t*-BuON=NO*t*-Bu (0.2 equiv) in benzene (**2a**: 120 equiv) in the presence of dimethyl sulfoxide (10 equiv) at 60 °C for 8 h gave 4-methoxybiphenyl (**3aa**) in 34% yield (Table 1, Entry 1). By the use of the more basic KO*t*-Bu, **1a** was fully consumed to give **3aa** in 81% yield (Entry 2).<sup>10</sup> A drastic decrease in the yield was observed in the reaction in the absence of *t*-BuON=NO*t*-Bu (Entry 3). *t*-BuOO*t*-Bu also worked as a promoter at a temperature high enough to undergo homolysis, giving *t*-BuO<sup>•</sup>, albeit in a lower yield (Entries 4 and 5). Although the reaction using (Me<sub>3</sub>Si)<sub>3</sub>SiH and V-70 [2,2'-azobis(4-methoxy-2,4-dimethyl)valeronitrile], which produce an effective I-abstractor, (Me<sub>3</sub>Si)<sub>3</sub>Si<sup>•</sup>, resulted in a moderate yield (Entry 6),<sup>11,12</sup> the result shows that the combination of the base-promoted HAS with a conventional I-abstraction system is valid.

The arylation of arenes by the use of KO*t*-Bu and *t*-BuON=NO*t*-Bu as a stoichiometric promoter and a radical initiator, respectively, is applicable to various aryl iodides and arenes (Table 2). In addition to *p*-iodoanisole (**1a**), the *meta*- and *ortho*-isomers (**1b** and **1c**) underwent coupling with benzene (**2a**) in high yields (Entries 1–3). The use of KO*t*-Bu as a base was also effective for the coupling of iodobenzene (**1d**) and that having a methyl or fluoro substituent, but not for that having a cyano group, which was transformed to –C(=O)NH<sub>2</sub> (Entries 4–7).<sup>13</sup> The use of the less basic Na*t*-Bu instead of KO*t*-Bu overcame the problem, giving 4-cyanobiphenyl in a high yield (Entry 8), where the electron-withdrawing character of the cyano group increased the acidity of the cyclohexadienyl intermediate **II** to relax the requirement for basicity in step *c'*-I of Scheme 1 (cf. Table 1, Entries 1 vs. 2). For the coupling of methyl 4-iodobenzoate (**1h**), NaOMe was used in order to avoid the ester exchange, giving the coupling product (**3ha**) in 72% yield (Table 2, Entry 9). Heteroaryl iodides also participated in the coupling reaction (Entries 10 and 11). A bisphenylation product was obtained from *p*-diiodobenzene (**1k**) (Entry 12). Arenes other than benzene also accepted arylation with **1a**, giving regioisomeric mixtures in ratios characteristic of the HAS mechanism (Entries 13–16).<sup>2</sup>

**Table 2.** Coupling of aryl iodides with arenes<sup>a</sup>

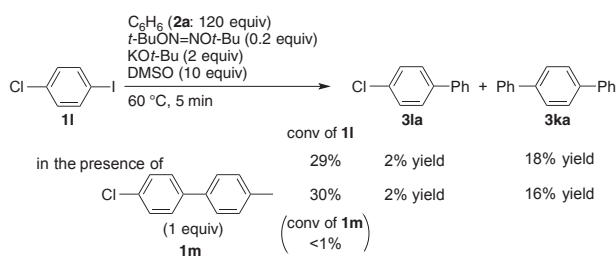
Entry	Ar <sup>1</sup> -I ( <b>1</b> )	Ar <sup>2</sup> -H ( <b>2</b> )	Yield/% <sup>b</sup>	Prod.
1	4-MeOC <sub>6</sub> H <sub>4</sub> -I ( <b>1a</b> )	benzene ( <b>2a</b> )	81	<b>3aa</b>
2	3-MeOC <sub>6</sub> H <sub>4</sub> -I ( <b>1b</b> )	benzene ( <b>2a</b> )	85	<b>3ba</b>
3	2-MeOC <sub>6</sub> H <sub>4</sub> -I ( <b>1c</b> )	benzene ( <b>2a</b> )	76	<b>3ca</b>
4	Ph-I ( <b>1d</b> )	benzene ( <b>2a</b> )	85	<b>3da</b>
5	4-MeC <sub>6</sub> H <sub>4</sub> -I ( <b>1e</b> )	benzene ( <b>2a</b> )	75	<b>3ea</b>
6	4-FC <sub>6</sub> H <sub>4</sub> -I ( <b>1f</b> )	benzene ( <b>2a</b> )	79	<b>3fa</b>
7	4-NCC <sub>6</sub> H <sub>4</sub> -I ( <b>1g</b> )	benzene ( <b>2a</b> )	21	<b>3ga</b>
8 <sup>c,d</sup>	4-NCC <sub>6</sub> H <sub>4</sub> -I ( <b>1g</b> )	benzene ( <b>2a</b> )	81	<b>3ga</b>
9 <sup>d,e</sup>	4-MeO <sub>2</sub> CC <sub>6</sub> H <sub>4</sub> -I ( <b>1h</b> )	benzene ( <b>2a</b> )	72	<b>3ha</b>
10	2-pyridyl-I ( <b>1i</b> )	benzene ( <b>2a</b> )	73	<b>3ia</b>
11	3-thienyl-I ( <b>1j</b> )	benzene ( <b>2a</b> )	81	<b>3ja</b>
12 <sup>f</sup>	4-IC <sub>6</sub> H <sub>4</sub> -I ( <b>1k</b> )	benzene ( <b>2a</b> )	86 <sup>g</sup>	<b>3ka</b>
13	4-MeOC <sub>6</sub> H <sub>4</sub> -I ( <b>1a</b> )	pyridine ( <b>2b</b> )	90 <sup>h</sup>	<b>3ab</b>
14	4-MeOC <sub>6</sub> H <sub>4</sub> -I ( <b>1a</b> )	thiophene ( <b>2c</b> )	70 <sup>i</sup>	<b>3ac</b>
15	4-MeOC <sub>6</sub> H <sub>4</sub> -I ( <b>1a</b> )	fluorobenzene ( <b>2d</b> )	79 <sup>j</sup>	<b>3ad</b>
16	4-MeOC <sub>6</sub> H <sub>4</sub> -I ( <b>1a</b> )	1,4-difluorobenzene ( <b>2e</b> )	88	<b>3ae</b>

<sup>a</sup>The reaction was carried out under a nitrogen atmosphere at 60 °C using an aryl iodide (**1**: 0.20 mmol), an arene (**2**: 24 mmol), KO*t*-Bu (0.40 mmol), and dimethyl sulfoxide (0.14 mL, 2.0 mmol) in the presence of di-*tert*-butyl hyponitrite (7.0 mg, 0.040 mmol). <sup>b</sup>Isolated yield based on **1**. <sup>c</sup>Na*t*-Bu was used instead of KO*t*-Bu. <sup>d</sup>Reaction time: 4 h. <sup>e</sup>NaOMe was used instead of KO*t*-Bu. <sup>f</sup>**1k** (0.10 mmol) was used. <sup>g</sup>The yield of *p*-terphenyl. <sup>h</sup>A 41:29:30 mixture of 2-, 3-, and 4-(4-methoxyphenyl)pyridines was obtained. <sup>i</sup>A 79:21 mixture of 2- and 3-(4-methoxyphenyl)thiophenes was obtained. <sup>j</sup>A 47:20:33 mixture of *o*-, *m*-, and *p*-(4-methoxyphenyl)fluorobenzene was obtained.

**Scheme 2.** Verification of I-abstraction from an aryl iodide by Me<sup>•</sup> derived from *t*-BuON=NO*t*-Bu.

In order to verify our hypothesis that Me<sup>•</sup> derived from *t*-BuON=NO*t*-Bu undergoes I-abstraction from an aryl iodide to initiate the coupling, we examined what happens between these two (Scheme 2). GC analysis showed that treatment of 4-iodoanisole (**1a**) with *t*-BuON=NO*t*-Bu (1 equiv) in 1,2-dichloroethane at 60 °C for 8 h gave 4-chloroanisole (55% yield) and iodomethane (44% yield). Generation of iodomethane was further confirmed by trapping it with sodium *p*-cresolate as 4-methylanisole (41% yield). 4-Chloroanisole is most likely to be produced through the reaction of the aryl radical intermediate with 1,2-dichloroethane, though it is unclear at present what was the rest of 1,2-dichloroethane transformed into.

In S<sub>RN</sub>1 type reactions,<sup>14</sup> the high preference for double substitution over single substitution in the reaction of a dihalobenzene (X–C<sub>6</sub>H<sub>4</sub>–X) with a nucleophile (Nu<sup>–</sup>) is used to prove the involvement of an anion radical intermediate



**Scheme 3.** Proof of anion radical intermediacy.

corresponding to **III** in Scheme 1.<sup>5c,14,15</sup> Anion radical intermediate  $[\text{Nu}-\text{C}_6\text{H}_4-\text{X}]^{\cdot-}$  should undergo decomposition into  $\text{Nu}-\text{C}_6\text{H}_4^\cdot$  and  $\text{X}^-$  rather than pass an electron to  $\text{X}-\text{C}_6\text{H}_4-\text{X}$ . Thus, the predominant production of  $\text{Nu}-\text{C}_6\text{H}_4-\text{Nu}$  over  $\text{Nu}-\text{C}_6\text{H}_4-\text{X}$  is a proof of the anion radical intermediacy, and this was found to hold true for the present reaction as follows. The reaction of 4-chloroiodobenzene (**11**) with benzene (**2a**) for a short period (5 min, 29% conv.) gave *p*-terphenyl (**3ka**) and 4-chlorobiphenyl (**3la**) in 18% and 2% yields, respectively (Scheme 3). A possibility that **3la** has exceptional reactivity to be converted immediately into **3ka** was ruled out by the result that 4-chloro-4'-methylbiphenyl (**1m**), which undoubtedly has reactivity similar to **3la**, did not react at all under the conditions where the coupling of **11** with **2a** proceeds in 30% conversion of **11** (Scheme 3).

In conclusion, we have introduced  $t\text{-BuON}=\text{NO}t\text{-Bu}$  as a radical initiator into the *tert*-butoxide-promoted coupling of aryl iodides with arenes to conduct the reaction at a low temperature.  $t\text{-BuON}=\text{NO}t\text{-Bu}$ , after decomposition into  $\text{Me}^\cdot$ , is considered to act as an I-abstractor from aryl iodides to give aryl radicals required for the base-promoted homolytic aromatic substitution process.

This work has been supported financially in part by Grant-in-Aid for Scientific Research (B) (No. 25288046 to E.S.) from JSPS.

Supporting Information is available on <http://dx.doi.org/10.1246/cl.170814>.

Dedicated to the late Professor Yoshihiko Ito on the occasion of the 10th anniversary of his sudden death.

## References and Notes

- For recent reviews, see: a) L. Ackermann, R. Vicente, A. R. Kapdi, *Angew. Chem., Int. Ed.* **2009**, *48*, 9792. b) G. P. McGlacken, L. M. Bateman, *Chem. Soc. Rev.* **2009**, *38*, 2447.
- For reviews, see: a) R. Bolton, G. H. Williams, *Chem. Soc. Rev.* **1986**, *15*, 261. b) W. R. Bowman, J. M. D. Storey, *Chem. Soc. Rev.* **2007**, *36*, 1803.
- a) V. Martínez-Barrasa, A. G. de Viedma, C. Burgos, J. Alvarez-Builla, *Org. Lett.* **2000**, *2*, 3933. b) P. T. F. McLoughlin, M. A. Clyne, F. Aldabbagh, *Tetrahedron* **2004**, *60*, 8065. c) A. Núñez, A. Sánchez, C. Burgos, J. Alvarez-Builla, *Tetrahedron* **2004**, *60*, 6217. d) D. Crich, M. Patel, *Tetrahedron* **2006**, *62*, 7824. e) D. P. Curran, A. I. Keller, *J. Am. Chem. Soc.* **2006**, *128*, 13706.
- C. Chatgililoglu, *Chem. Rev.* **1995**, *95*, 1229.
- For our previous work, see: a) E. Shirakawa, K. Itoh, T. Higashino, T. Hayashi, *J. Am. Chem. Soc.* **2010**, *132*, 15537. b) E. Shirakawa, T. Hayashi, *Chem. Lett.* **2012**, *41*, 130. For similar examples reported coincidentally as independent studies: c) W. Liu, H. Cao, H. Zhang, H. Zhang, K. H. Chung, C. He, H. Wang, F. Y. Kwong, A. Lei, *J. Am. Chem. Soc.* **2010**, *132*, 16737. d) C.-L. Sun, H. Li, D.-G. Yu, M. Yu, X. Zhou, X.-Y. Lu, K. Huang, S.-F. Zheng, B.-J. Li, Z.-J. Shi, *Nat. Chem.* **2010**, *2*, 1044. For the coupling with pyrazine and pyridine derivatives reported earlier, see: e) S. Yanagisawa, K. Ueda, T. Taniguchi, K. Itami, *Org. Lett.* **2008**, *10*, 4673. For a stimulating essay leading to proper appreciation of the reaction mechanism, see: f) A. Studer, D. P. Curran, *Angew. Chem., Int. Ed.* **2011**, *50*, 5018. For a review, see: g) C.-L. Sun, Z.-J. Shi, *Chem. Rev.* **2014**, *114*, 9219.
- For photoinduced direct C–H arylation using  $\text{KO}t\text{-Bu}$  as a promoter, see: a) M. E. Budén, J. F. Guastavino, R. A. Rossi, *Org. Lett.* **2013**, *15*, 1174. b) Y. Cheng, X. Gu, P. Li, *Org. Lett.* **2013**, *15*, 2664.
- Di-*tert*-butyl hyponitrite is reported to undergo clean decomposition into  $t\text{-BuO}^\cdot$  and  $\text{N}_2$  with  $t_{1/2}$  of 29 min at  $65^\circ\text{C}$ . The rate constant is estimated to be  $4.00 \times 10^4 \text{ s}^{-1}$  in isooctane at  $65^\circ\text{C}$ . H. Kiefer, T. G. Traylor, *Tetrahedron Lett.* **1966**, *7*, 6163.
- The rate constant of decomposition of  $t\text{-BuO}^\cdot$  into  $\text{Me}^\cdot$  and acetone is estimated to be  $1.1 \times 10^5 \text{ s}^{-1}$  in cumene at  $60^\circ\text{C}$ . T. Nakamura, W. K. Busfield, I. D. Jenkins, E. Rizzardo, S. H. Thang, S. Suyama, *J. Org. Chem.* **2000**, *65*, 16.
- a) D. Dolenc, B. Plesničar, *J. Am. Chem. Soc.* **1997**, *119*, 2628. b) D. Dolenc, B. Plesničar, *J. Org. Chem.* **2006**, *71*, 8028.
- The reaction under the conditions of Entry 2 of Table 1 but in the absence of DMSO scored a lower yield (54%) with a lower conversion (67%) of **1a**. The effect of DMSO is unclear at present but it possibly affects  $\text{KO}t\text{-Bu}$  to enhance its basicity. As a slightly lower yield (75% with a full conversion of **1a**) was observed with an increased amount (20 equiv) of DMSO, we used 10 equiv of DMSO as in Entry 2 of Table 1 for further investigation.
- The half-life of V-70 is reported to be 0.1 h at  $60^\circ\text{C}$ . A. D. Smith, E. Lester, K. J. Thurecht, J. E. Harfi, G. Dimitrakis, S. W. Kingman, J. P. Robinson, D. J. Irvine, *Ind. Eng. Chem. Res.* **2010**, *49*, 1703.
- For examples of generation of  $(\text{Me}_3\text{Si})_3\text{Si}^\cdot$  from  $(\text{Me}_3\text{Si})_3\text{SiH}$  and V-70, see: a) S. Kim, C. J. Lim, *Angew. Chem., Int. Ed.* **2004**, *43*, 5378. b) J. Demarteau, A. Kermagoret, I. German, D. Cordella, K. Robeyns, J. De Winter, P. Gerbaux, C. Jérôme, A. Debuigne, C. Detrembleur, *Chem. Commun.* **2015**, *51*, 14334.
- $\text{KO}t\text{-Bu}$  is reported to promote hydration of nitriles into the corresponding amides under anhydrous conditions, whereas no hydration takes place with  $\text{NaO}t\text{-Bu}$  under the same conditions. G. C. Midya, A. Kapat, S. Maiti, J. Dash, *J. Org. Chem.* **2015**, *80*, 4148.
- $\text{SRN1}$  reaction is an effective reaction to achieve substitution of aryl halides with anionic nucleophiles, proceeding through anion radical intermediates. Its reaction mechanism shares key features with that of the base-promoted homolytic aromatic substitution shown in Scheme 1-ii (steps  $a'-1$ ,  $a'-2$ , and  $c'-2$ ) as follows. Single electron reduction of an aryl halide ( $\text{Ar}-\text{X}$ ) gives its anion radical ( $[\text{Ar}-\text{X}]^{\cdot-}$ ), which undergoes decomposition to give the corresponding aryl radical ( $\text{Ar}^\cdot$ ) with elimination of  $\text{X}^-$ . The reaction of  $\text{Ar}^\cdot$  with an anionic nucleophile ( $\text{Nu}^-$ ) gives anion radical  $[\text{Ar}-\text{Nu}]^{\cdot-}$ , which passes an electron to  $\text{Ar}-\text{X}$  to give the substitution product ( $\text{Ar}-\text{Nu}$ ) and regenerate  $[\text{Ar}-\text{X}]^{\cdot-}$ . For reviews, see: a) J. F. Bunnett, *Acc. Chem. Res.* **1978**, *11*, 413. b) R. A. Rossi, A. B. Pierini, A. B. Peñéñory, *Chem. Rev.* **2003**, *103*, 71.
- J. F. Bunnett, X. Creary, *J. Org. Chem.* **1974**, *39*, 3611.

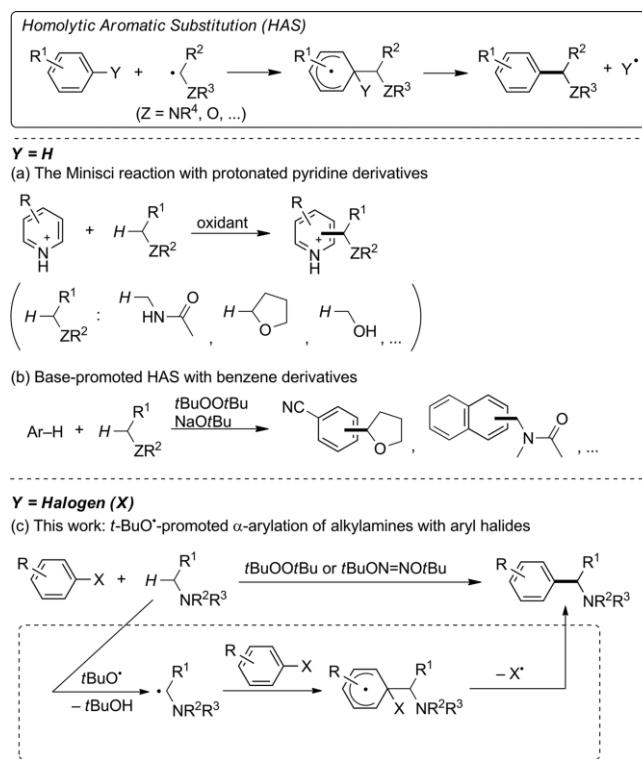
## α-Arylation of Alkylamines

**tert**-Butoxy-Radical-Promoted α-Arylation of Alkylamines with Aryl HalidesRyota Ueno,<sup>[a]</sup> Yuko Ikeda,<sup>[b]</sup> and Eiji Shirakawa<sup>\*,[b]</sup>**Abstract:** In the presence of a *tert*-butoxy radical precursor, the reaction of alkylamines with aryl halides was found to give α-

arylated alkylamines through homolytic aromatic substitution of the halogen atoms.

## Introduction

Homolytic aromatic substitution (HAS), consisting of the addition of an aliphatic *sp*<sup>3</sup>-carbon radical adjacent to a heteroatom on an aromatic compound (Ar–Y) followed by the elimination of radical Y<sup>•</sup>, has high potential to achieve α-arylation of heteroatom-containing aliphatic compounds (Scheme 1, top).<sup>[1]</sup> The most successful example is the Minisci reaction, which employs *sp*<sup>3</sup>-carbon radicals with an adjacent heteroatom in combination with protonated pyridine derivatives to give α-pyridination products of amides, ethers and alcohols. H<sup>•</sup> presents the leaving group Y<sup>•</sup> in this case (Scheme 1, a).<sup>[2]</sup> The Minisci reaction utilizes readily available *sp*<sup>3</sup>-carbon radicals generated through hydrogen abstraction from heteroatom-containing aliphatic compounds such as amides and ethers. However, the unfavorable aromaticity-breaking radical addition step requires highly electrophilic aromatic compounds to facilitate the reaction with the nucleophilic *sp*<sup>3</sup>-carbon radicals having a heteroatom at α-position. This requirement limits its scope essentially to protonated pyridine derivatives. In this context, we have recently reported that the use of a strong base such as NaOtBu as a promoter reduces this limitation and allows to expand the scope to benzene derivatives with electron-withdrawing groups and to polycyclic aromatics (Scheme 1, b).<sup>[3]</sup> Both methods employ H<sup>•</sup> as leaving group Y<sup>•</sup> and suffer from the production of a mixture of regioisomers because selectivity towards a particular C–H bond is intrinsically difficult. The regioselectivity problem can be solved by use of aryl halides [Y = halogen (X)], making the halogen atom to leave as radical X<sup>•</sup>.<sup>[4,5]</sup> Here we report α-arylation of alkylamines with aryl halides substituted by an electron-withdrawing group and with polycyclic aryl halides in the presence of a *tert*-butoxy radical precursor, through an HAS mechanism with X<sup>•</sup> as a leaving group.<sup>[6,7]</sup>



Scheme 1. α-Arylation of heteroatom-containing aliphatic compounds through homolytic aromatic substitution (HAS).

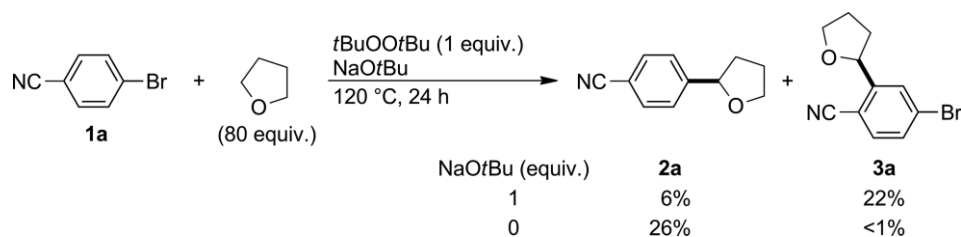
## Results and Discussion

During the course of the investigation on the α-arylation of ethers with arenes through dehydrogenative coupling (Scheme 1, b),<sup>[3]</sup> we found that the reaction of 4-bromobenzonitrile (**1a**) with tetrahydrofuran (THF: 80 equiv.) in the presence of *t*BuOOtBu (1 equiv.) and NaOtBu (1 equiv.) at 120 °C for 24 h gave a dehydrobrominative coupling product, 4-(2-tetrahydrofuranyl)benzotrile (**2a**: 6%), in addition to a dehydrogenative coupling product, 4-bromo-2-(2-tetrahydrofuranyl)benzotrile (**3a**: 22%) (Scheme 2). The reaction in the absence of NaOtBu, which had been shown to be indispensable for the effective dehydrogenative coupling, gave **2a** exclusively but only in a low yield (26%). The eliminated bromine atom (Br<sup>•</sup>)

[a] Department of Chemistry, Graduate School of Science, Kyoto University, Sakyo-ku, Kyoto 606-8502, Japan

[b] Department of Applied Chemistry for Environment, School of Science and Technology, Kwansei Gakuin University, Sanda, Hyogo 669-1337, Japan  
E-mail: eshirakawa@kwansei.ac.jp  
<http://sci-tech.ksc.kwansei.ac.jp/en/>

Supporting information and ORCID(s) from the author(s) for this article are available on the WWW under <https://doi.org/10.1002/ejoc.201700548>.



Scheme 2. The reaction of tetrahydrofuran with 4-bromobenzonitrile by using *t*BuOO*t*Bu in the presence or absence of NaOtBu.

is likely to be reduced to Br<sup>-</sup> by THF. We anticipated that alkylamines, which are more electron-rich than alkyl ethers, readily reduce Br<sup>+</sup>, or successively generated Br<sub>2</sub>, to Br<sup>-</sup>, and therefore examined the α-arylation of alkylamines with aryl halides with the aid of *t*BuOO*t*Bu.

Treatment of 4-bromobenzonitrile (**1a**) with *N*-methylpyrrolidine (**4a**; 10 equiv.) and *t*BuOO*t*Bu (1 equiv.) at 120 °C for 24 h gave *N*-methyl-2-(4-cyanophenyl)pyrrolidine (**5aa**) and *N*-(4-cyanophenylmethyl)pyrrolidine (**5'aa**) (85:15) in 79 % combined yield; no dehydrogenative coupling products were observed (Table 1, entry 1).<sup>[8]</sup> The conversion and the yield were significantly lowered by using a decreased amount (0.2 equiv.) of *t*BuOO*t*Bu (Table 1, entry 2), which shows that only a short radical chain is operative. No reaction took place in the absence of *t*BuOO*t*Bu or at a low temperature (60 °C) of which homolysis of *t*BuOO*t*Bu is negligible (Table 1, entries 3 and 4). The reaction using *t*BuON=NO*t*Bu, which undergoes much more facile homolysis than *t*BuOO*t*Bu to give *t*BuO<sup>•</sup>,<sup>[9]</sup> at 60 °C gave a high yield with a high regioselectivity (Table 1, entry 5). These results show that the reaction proceeds at 60 °C when *t*BuO<sup>•</sup> is available. In the following investigation, we used the reaction conditions shown in Table 1 (entry 1 or 5) according to the combination of substrates.

Table 1. α-Arylation of *N*-methylpyrrolidine with 4-bromobenzonitrile using a *t*BuO<sup>•</sup> source.<sup>[a]</sup>

Entry	<i>t</i> BuO <sup>•</sup> source (equiv.)	<i>T</i> (°C)	Conv. of <b>1a</b> (%) <sup>[b]</sup>	Yield of <b>5aa</b> + <b>5'</b> (%) <sup>[b]</sup>	<b>5aa/5'</b> <b>aa'</b> <sup>[c]</sup>
1	<i>t</i> BuOO <i>t</i> Bu (1)	120	100	79	85:15
2	<i>t</i> BuOO <i>t</i> Bu (0.2)	120	37	35	79:21
3	none	120	< 1	< 1	–
4	<i>t</i> BuOO <i>t</i> Bu (1)	60	< 1	< 1	–
5	<i>t</i> BuON=NO <i>t</i> Bu (1)	60	99	98 (95) <sup>[d]</sup>	94:6

[a] The reaction was carried out under a nitrogen atmosphere for 24 h by using 4-bromobenzonitrile (**1a**: 0.25 mmol), *N*-methylpyrrolidine (**4a**: 2.5 mmol), and *t*BuO<sup>•</sup> source. [b] Determined by <sup>1</sup>H NMR spectroscopy. [c] Determined by GC and confirmed by <sup>1</sup>H NMR spectroscopy. [d] Yield of the isolated product.

The α-arylation of *N*-methylpyrrolidine (**4a**) by using *t*BuON=NO*t*Bu at 60 °C for 24 h was applied to various aryl bromides (Table 2). Bromobenzenes with a conjugating electron-withdrawing group such as cyano and methoxycarbonyl in *para* or *ortho* position underwent the reaction in high yields, whereas

Table 2. α-Arylation of *N*-methylpyrrolidine with aryl halides.<sup>[a]</sup>

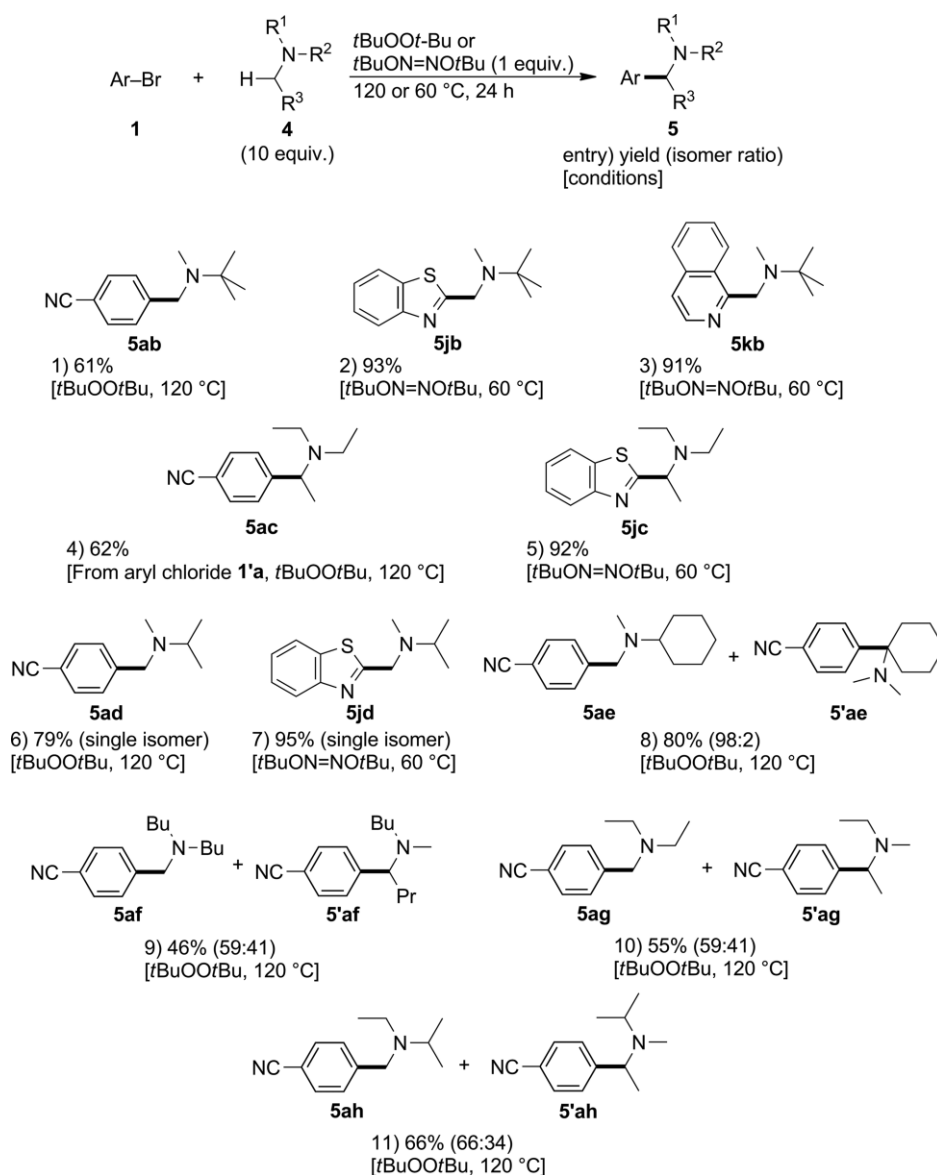
Entry	<b>1</b>	Yield of <b>5</b> + <b>5'</b> [%] <sup>[b]</sup>	<b>5:5'</b> <sup>[c]</sup>
1		78	93:7
2		83	79:21
3		16 <sup>[d]</sup>	77:23
4		3 <sup>[d]</sup>	78:22
5		<1 <sup>[d]</sup>	–
6		88	90:10
7		81	88:12
8		22 <sup>[d]</sup>	88:12
9		95	82:18
10		85	83:17
11		57	94:6
12 <sup>[e]</sup>		88	85:15
13 <sup>[e]</sup>		70	90:10
14 <sup>[e]</sup>		80	85:15
15 <sup>[e,f]</sup>		53	95:5

[a] The reaction was carried out under a nitrogen atmosphere for 24 h using an aryl halide (**1** or **1'**: 0.25 mmol), *N*-methylpyrrolidine (**4a**: 2.5 mmol), and *t*BuON=NO*t*Bu (0.25 mmol). [b] The yield of the isolated products. [c] Determined by GC and confirmed by <sup>1</sup>H NMR spectroscopy. [d] Determined by <sup>1</sup>H NMR spectroscopy. [e] *t*BuOO*t*Bu was used instead of *t*BuON=NO*t*Bu at 120 °C. [f] *t*BuOO*t*Bu (2 equiv.) was used.

a cyano group in *meta* position or an inductively electron-withdrawing trifluoromethyl group in *para* position did not promote the reaction effectively (Table 2, entries 1–4; Table 1, entry 5). These results show that the radical addition to monocyclic aryl halides has the character of a nucleophilic conjugate addition.<sup>[10]</sup> Besides this type, another mode to accept addition of an  $\alpha$ -aminoalkyl radical is available when the aryl halides have a polycyclic structure. Nonsubstituted bromobenzene (**1f**) was unreactive toward **4a**, whereas 1-naphthyl and 9-anthryl bromides participated in the coupling without the aid of a conjugating electron-withdrawing group (Table 2, entries 5–7). The radical addition step proceeds easier with these polycyclic aromatics compared with their corresponding monocyclic derivatives because the loss of aromaticity upon addition is less severe. However, the yield was much lower with 2-bromonaphthalene than with 1-bromonaphthalene (Table 2, entries 6 and 8), due to the difference in the stability of the intermediates after the

radical addition: just a benzylic radical resonance structure for the former in comparison to a benzylic as well as an allylic radical resonance structure for the latter. Heteroaryl bromides also participated in the  $\alpha$ -arylation (Table 2, entries 9 and 10). The reaction is applicable also to aryl chlorides, though a high temperature is required. For example, the yield in the reaction of 4-chlorobenzonitrile (**1'a**) was improved from 57 % to 88 % by raising the temperature from 60 °C to 120 °C in the presence of *t*BuOO*t*Bu instead of *t*BuON=NO*t*Bu (Table 2, entries 11 and 12).<sup>[11]</sup> Other aryl chlorides underwent the  $\alpha$ -arylation with **4a** under these conditions (Table 2, entries 13–15).

Acyclic trialkylamines were also employed (Scheme 3). *tert*-Butyl(dimethyl)amine (**4b**) and triethylamine (**4c**) underwent the  $\alpha$ -arylation with aryl and heteroaryl halides in moderate to high yields (Scheme 3, entries 1–5). Dimethyl(*sec*-alkyl)amines (**4d** and **4e**) were arylated at a methyl group in high preference to the secondary alkyl group (Scheme 3, entries 6–8). Preference

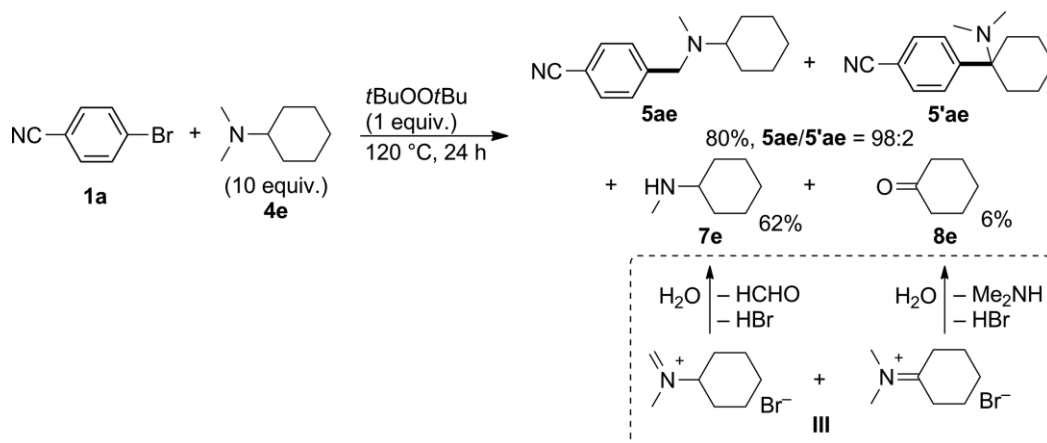


Scheme 3.  $\alpha$ -Arylation of acyclic tertiary alkylamines.

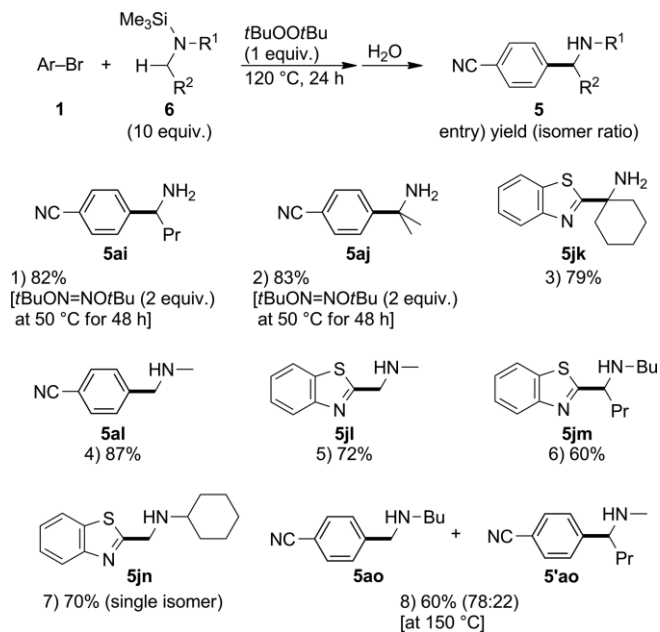
for methyl over primary alkyl groups was observed but with low selectivity (Scheme 3, entries 9–11). The regioselectivity in the  $\alpha$ -arylation of dissymmetric alkylamines is well-understood, considering the regioselectivity of the hydrogen abstraction as well as the rates in which the resulting radicals add to an aryl halide. In the hydrogen abstraction step, the steric factor, which favors the reaction order of methyl > primary >> secondary, seems to slightly surpass the electronic factor, which depends on the stability of the resulting radicals in order of secondary > primary > methyl. The same tendencies of the steric and electronic factors are likely to be operative in the addition step, where the electronic factor seems to slightly surpass the steric factor. As a consequence, the steric factor in both steps makes secondary alkyl groups less reactive, whereas methyl and primary alkyl groups show similar reactivities due to the conflicting reaction orders based on steric and electronic factors. This does not hold true for *N*-methylpyrrolidine (**4a** in Table 1 and Table 2), the five-membered primary alkyl group of which gives an exceptionally stable alkyl radical,<sup>[12]</sup> which makes it electronically favored in both the hydrogen abstraction and the addition steps.

Although no  $\alpha$ -arylation took place with primary and secondary alkylamines,<sup>[13]</sup> trimethylsilylated ones reacted with aryl bromides (**1**) to give the corresponding desilylated  $\alpha$ -arylation products after aqueous work up (Scheme 4). The resonance effect by the  $\beta$ -silyl group is likely to facilitate formation of the radical intermediates and enhance the reactivities toward aryl bromides with increased nucleophilicities.<sup>[14]</sup> Primary amines such as butyl, isopropyl, and cyclohexylamines were subjected to the silyl protection– $\alpha$ -arylation–deprotection protocol to give the corresponding  $\alpha$ -arylated primary alkylamines (Scheme 4, entries 1–3). The protocol is applicable also to secondary alkylamines (Scheme 4, entries 4–8). The arylation of cyclohexyl(methyl)(trimethylsilyl)amine (**6n**) took place exclusively at the methyl group (Scheme 4, entry 7). The selectivity of methyl over a primary alkyl was high in the reaction of butyl(methyl)(trimethylsilyl)amine (**6o**) compared with the reaction of dibutyl(methyl)amine (**4f**) (Scheme 4, entry 8; cf. Scheme 3, entry 9).

In order to elucidate the stoichiometry of the  $\alpha$ -arylation, we pursued the products derived from an alkylamine (Scheme 5).



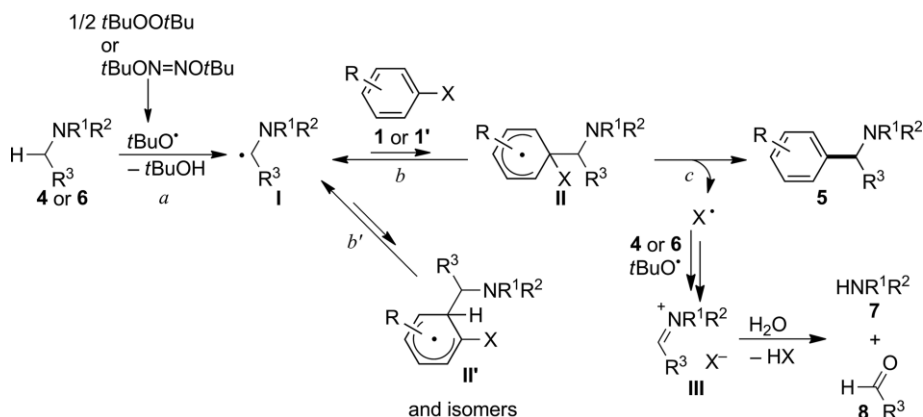
Scheme 5. Elucidation of the stoichiometry of the  $\alpha$ -arylation of alkylamines.



Scheme 4.  $\alpha$ -Arylation of trimethylsilylamines to give  $\alpha$ -arylated primary and secondary alkylamines.

In the reaction of 4-bromobenzonitrile (**1a**) with cyclohexyl(dimethyl)amine (**4e**) (cf. Scheme 3, entry 8), cyclohexyl(methyl)amine (**7e**) and cyclohexanone (**8e**) were obtained in 62 % and 6 % yields, respectively. Products **7e** and **8e** are most likely to be obtained through hydrolysis of methylenedene- and cyclohexylidene-containing iminium bromides (Scheme 5, **III**), respectively, showing that an extra equivalent of the alkylamine is consumed to reduce X<sup>+</sup> into X<sup>-</sup>.

On the basis of these results, the  $\alpha$ -arylation of alkylamines with aryl halides is likely to proceed through the mechanism we initially expected (Scheme 6). Homolysis of *t*BuOO*t*Bu or *t*BuON=NOtBu gives *t*BuO<sup>•</sup>, which abstracts a hydrogen atom from a carbon–hydrogen bond adjacent to the nitrogen atom of an alkylamine (**4** or **6**) (Scheme 6, step *a*). The resulting  $\alpha$ -aminoalkyl radical (**I**) adds to an aryl halide (**1** or **1'**) to give cyclohexadienyl radical intermediate **II** (Scheme 6, step *b*). Although attack of **I** toward **1/1'** takes place also on carbon atoms



Scheme 6. A plausible mechanism.

substituted with a hydrogen atom (Scheme 6, step  $b'$ ), addition products such as **II'** do not react further but instead go back to give **I** and **1/1'** because the radical addition step is reversible and its equilibrium lies far on the side of **I**. Elimination of the halogen radical ( $X^\bullet$ ) gives  $\alpha$ -arylation product **5** (Scheme 6, step  $c$ ). Although it is unclear how the eliminated  $X^\bullet$ , or the successively generated  $X_2$ , is reduced to  $X^-$ , alkylamine **4/6** accept two electron oxidations directly or indirectly by  $X^\bullet$  and  $t\text{BuO}^\bullet$  to give iminium halides **III**, which are converted into the corresponding dealkylated amine (**7**) and aldehyde/ketone (**8**) by aqueous workup.<sup>[15]</sup>

## Conclusion

We have disclosed  $\alpha$ -arylation of tertiary alkylamines or silylated primary and secondary alkylamines with aryl halides utilizing a  $t\text{BuO}^\bullet$  source. The reaction proceeds through chemoselective homolytic aromatic substitution, in which halogen atoms (Br and Cl) act as leaving groups.

## Acknowledgments

This work has been supported financially in part by the Japan Society for the Promotion of Science in form of a Grand-in-Aid for Challenging Exploratory Research (26620082 to E. S.), a Grand-in-Aid for Scientific Research (B) (16H04151 to E. S.), and a Research Fellowship for Young Scientists (awarded to R. U.).

**Keywords:** Synthetic methods · Amines · Reaction mechanisms · Radical reactions · Aromatic substitution

- [1] For reviews, see: a) *Free Radicals in Organic Chemistry* (Eds.: J. Fossey, D. Lefort, J. Sorba), John Wiley and Sons, Chichester, **1995**, chap. 14, pp. 166–180; b) R. Bolton, G. H. Williams, *Chem. Soc. Rev.* **1986**, *15*, 261–289; c) W. R. Bowman, J. M. D. Storey, *Chem. Soc. Rev.* **2007**, *36*, 1803–1822.
- [2] For selected examples, see: a) G. P. Gardini, F. Minisci, G. Palla, A. Arnone, R. Galli, *Tetrahedron Lett.* **1971**, *12*, 59–62; b) A. Arnone, M. Cecere, R. Galli, F. Minisci, M. Perchinunno, O. Porta, G. Gardini, *Gazz. Chim. Ital.* **1973**, *103*, 13–29. For reviews, see: c) F. Minisci, *Synthesis* **1973**, 1–24; d) F. Minisci, E. Vismara, F. Fontana, *Heterocycles* **1989**, *28*, 489–519.
- [3] R. Ueno, E. Shirakawa, *Org. Biomol. Chem.* **2014**, *12*, 7469–7473.

- [4] For reviews on HAS with a halogen leaving group, see: a) J. G. Traynham, *Chem. Rev.* **1979**, *79*, 323–330; b) M. Tiecco, *Acc. Chem. Res.* **1980**, *13*, 51–57; c) M. Tiecco, *Pure Appl. Chem.* **1981**, *53*, 239–258.
- [5] For example, the reaction of bromobenzene (6.2 equiv.) with cyclohexane (5 equiv.) in the presence of  $t\text{BuOOtBu}$  (1 equiv.) gives a mixture of cyclohexylbenzene and bromo(cyclohexyl)benzenes (1:5). J. R. Shelton, C. W. Uzelmeier, *J. Am. Chem. Soc.* **1966**, *88*, 5222–5228.
- [6] Several research groups have recently reported the  $\alpha$ -arylation of heteroatom-containing aliphatic compounds with heteroaryl halides under photoredox catalysis. Although an HAS mechanism is considered to be operative, it is not clarified how the elimination of the halogen atom proceeds. The reaction requires a rather complicated photoredox system and the scope of aryl halides is limited to heteroaryl chlorides containing more than two heteroatoms on the aromatic ring; a) A. Singh, A. Arora, J. D. Weaver, *Org. Lett.* **2013**, *15*, 5390–5393; b) C. K. Prier, D. W. C. MacMillan, *Chem. Sci.* **2014**, *5*, 4173–4178; c) A. Lipp, G. Lahm, T. Opatz, *J. Org. Chem.* **2016**, *81*, 4890–4897. As a similar example under photoredox catalysis,  $\alpha$ -arylation of alkylamines with benzonitriles substituted with electron-withdrawing groups has been reported, where the proposed mechanism includes single-electron reduction of a benzonitrile to give the corresponding anion radical, which undergoes coupling with an  $\alpha$ -aminoalkyl radical, and the following elimination of cyanide ( $\text{CN}^-$ ) gives the  $\alpha$ -arylation product; d) A. McNally, C. K. Prier, D. W. C. MacMillan, *Science* **2011**, *334*, 1114–1117. Recently,  $\alpha$ -arylation of alkylamines with aryl halides by using a photoredox catalyst and a nickel catalyst has been reported, in which an  $\alpha$ -aminoalkyl radical was transformed into an  $\alpha$ -aminoalkyl nickel species to undergo the cross-coupling reaction with an aryl halide e) D. T. Ahneman, A. G. Doyle, *Chem. Sci.* **2016**, *7*, 7002–7006. For a related example, see: f) D. R. Heitz, J. C. Tellis, G. A. Molander, *J. Am. Chem. Soc.* **2016**, *138*, 12715–12718.
- [7]  $\alpha$ -Arylation of secondary alkylamines is achieved e.g., through acylation of a secondary amine, deprotonation by butyllithium, transmetalation of the resulting  $\alpha$ -(acylamino)alkyllithium with  $\text{ZnCl}_2$ , the Negishi coupling with a heteroaryl halide, and deacylation; a) K. R. Campos, A. Klapars, J. H. Waldman, P. G. Dormer, C.-Y. Chen, *J. Am. Chem. Soc.* **2006**, *128*, 3538–3539. For a review, see: b) E. A. Mitchell, A. Poeschiulli, N. Lefevre, L. Meerpoel, B. U. W. Maes, *Chem. Eur. J.* **2012**, *18*, 10092–10142.
- [8] The reaction of **1a** with a reduced amount (2 equiv.) of **4a** resulted in a much lower yield (19 %, **5aa:5'aa** = 84:16) with a low conversion (28 %) of **1a** under the conditions of entry 1 of Table 1.
- [9] H. Kiefer, T. G. Traylor, *Tetrahedron Lett.* **1966**, *7*, 6163–6168.
- [10] Aryl halides substituted with an electron-donating group such as 4-bromoanisole did not participate in the  $\alpha$ -arylation at all.
- [11] The use of  $t\text{BuON}=\text{NOtBu}$  (1 equiv.) at 120 °C in the reaction of 4-chlorobenzonitrile (**1'a**) with *N*-methylpyrrolidine (**4a**; 10 equiv.) scored a lower yield of **5aa** and **5'aa** (64 %, 88:12), probably because supply of  $t\text{BuO}^\bullet$  through homolysis is too fast and thus mismatches with other steps.
- [12] Facility in generating the corresponding radical from pyrrolidine compared with structurally similar compounds is discussed on the basis of stereoelectronic effects of the lone pair on the nitrogen atom; a) D.

- Griller, J. A. Howard, P. R. Marriott, J. C. Scaiano, *J. Am. Chem. Soc.* **1981**, *103*, 619–623. For discussion on the radical structures and stabilization energies of alkylamines including pyrrolidine, see: b) D. D. M. Wayner, K. B. Clark, A. Rauk, D. Yu, D. A. Armstrong, *J. Am. Chem. Soc.* **1997**, *119*, 8925–8932.
- [13] The reaction of butylamine or diethylamine (10 equiv.) with 4-bromobenzonitrile (**1a**: 1 equiv.) in the presence of *t*BuON=NO*t*Bu (1 equiv.) at 60 °C for 24 h gave no  $\alpha$ -arylated products with no consumption of **1a**.
- [14] N. Auner, R. Walsh, J. Westrup, *J. Chem. Soc., Chem. Commun.* **1986**, 207–208.
- [15] The possibility that the halogen atom (X) undergoes elimination in a form of  $X^-$  after single-electron reduction of cyclohexadienyl radical **II** by  $\alpha$ -aminoalkyl radical **I**, giving  $\alpha$ -arylation products **5** and iminium salts **III**, cannot be excluded. A similar mechanism has been proposed in the reduction of alkyl halides into alkanes by using  $\alpha$ -aminoalkyl radicals; a) J. Lalevée, J. P. Fouassier, N. Blanchard, K. U. Ingold, *Chem. Phys. Lett.* **2011**, *511*, 156–158. In the reaction of dihalobenzenes ( $X-C_6H_4-X'$ ) with dibenzylmercury giving  $PhCH_2-C_6H_4-X'$  through an HAS mechanism, benzyl radical, which is generated in situ and acts as the radical attacking  $X-C_6H_4-X'$ , is considered to work also as a single-electron reductant toward X-substituted cyclohexadienyl radicals to give  $PhCH_2-C_6H_4-X'$  and  $PhCH_2X$ ; b) R. Henriquez, D. C. Nonhebel, *Tetrahedron* **1993**, *49*, 6497–6500.

---

 Received: April 20, 2017

## トピックス

## 遷移金属触媒を用いないハロゲン化アリのルのカップリング反応

関西学院大学理工学部環境・応用化学科 白川 英二

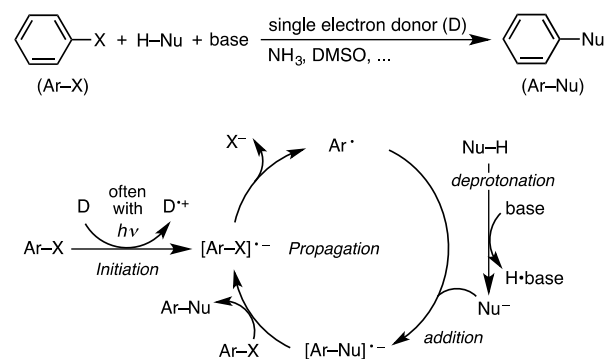
## はじめに

種々の求核剤 (Nu-Y: Y = 金属、水素、...) によりハロゲン化アリール (Ar-X) のハロゲンを置換しカップリング生成物 (Nu-Ar) を得る反応は、通常反応の収支としては酸化も還元も伴わないが、S<sub>N</sub>1 反応も S<sub>N</sub>2 反応も起こせないハロゲン化アリールを活性化するには、これを一旦還元する必要がある。それを得意とするのが低原子価後周期遷移金属錯体で、例えばパラジウム(0)錯体による Ar-X の 2 電子還元では Ar-Pd(II)-X が生じる。この錯体 (遷移金属の分野では、Ar-X の Pd(0) に対する酸化的付加体と呼ばれる) は、様々な求核剤 (Nu-Y) と反応し Ar-Pd(II)-Nu を経てカップリング体 Ar-Nu を与える汎用性の高い中間体である。求核剤として有機ホウ素化合物・有機亜鉛化合物・アルケンを用いるパラジウム触媒反応は、それぞれ鈴木-宮浦カップリング・根岸カップリング・溝呂木-Heck 反応と呼ばれ、その何れにも 2010 年ノーベル化学賞が授与された有用な反応である。

一方、ハロゲン化アリのルの 1 電子還元による活性化を置換反応に利用する例も知られている。S<sub>RN</sub>1 (Substitution Radical Nucleophilic Unimolecular) 反応と呼ばれるこの反応は、先述の遷移金属触媒を用いるカップリング反応と同様に 40 年以上の歴史を持つ<sup>1)</sup>。S<sub>RN</sub>1 反応の基本的な機構をスキーム 1 に示す。まず 1 電子供与体 (D) からハロゲン化アリール (Ar-X) への 1 電子移動によって、後者がアニオンラジカル ([Ar-X]<sup>•-</sup>) として活性化される。続くハロゲン化物イオン (X<sup>-</sup>) の解離によって、反応性の非常に高いアリールラジカル (Ar<sup>•</sup>) となり、これが系中での求核剤前駆体 (Nu-H) からの脱プロトン化によって生じるアニオン性求核剤 (Nu<sup>-</sup>) と付加反応を起こすことで、置換生成物のアニオンラジカル

([Ar-Nu]<sup>•-</sup>) に変換され、最後にここから Ar-X に 1 電子が移動することで、置換生成物 (Ar-Nu) が得られると同時に [Ar-X]<sup>•-</sup> が再生される。ここでは、電子一つが触媒として働いていると見なすことができる。分子レベルの有機反応に対する触媒として、この上なく小さなものが働いているという点で極めて効率が良いと言えるが、Birch 還元に使われるような、液体アンモニア中アルカリ金属を作用させるといった反応条件や光照射条件が必要とされ実験操作が煩雑になることが多い。また、入手容易なものから、アリールラジカルという極めて反応性の高い種が得られるということは強力な特長となる反面、一般的に用いられる多くの溶媒とも反応してしまうため、反応相手が限られるという問題点があった。

Scheme 1



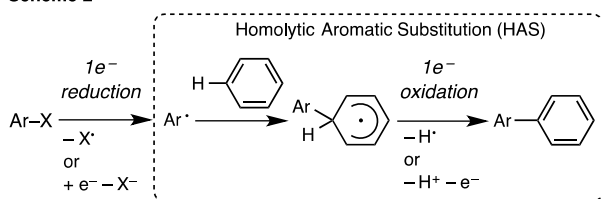
本トピックスでは、電子一つが触媒として働くという S<sub>RN</sub>1 反応の効率の良さを活かしつつ、上記の問題点の解消に向けた最近 5 年ほどのこの分野の進展を解説する。

## 1. ベンゼンやアルケンとのカップリング反応

高い反応性をもつアリールラジカルにとって、ベンゼンは数少ない好ましい反応相手の一つである。不安定なアリールラジカルは、芳香族性を崩してまでもベンゼン環に付加し、生じ

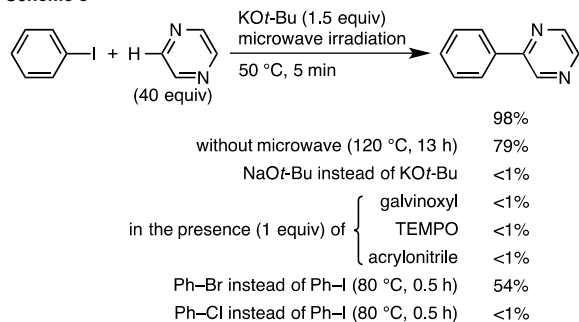
たシクロヘキサジエニルラジカルから水素ラジカル ( $H^\bullet = H^+ + e^-$ ) を取り除けばビアリアルとなる (スキーム 2)。この芳香環に対するラジカル種の付加とそれに続く別のラジカル種の脱離からなる過程は、Homolytic Aromatic Substitution (HAS: 芳香族ラジカル置換反応) と呼ばれるが、2 段階目が芳香族性の回復という強力な原動力をもつため、アリールラジカルの高い反応性を収めるのに都合がよい過程と言える<sup>2)</sup>。しかしながら、入手容易なハロゲン化アリールをアリールラジカル源として用いる場合は、アリールラジカル発生段階および水素ラジカル引き抜き段階に、それぞれ 1 電子還元および 1 電子酸化が求められるので、これら相反する要求を両立させるのが必ずしも容易ではない<sup>3)</sup>。これから紹介する改良型  $S_{RN}1$  反応は、この問題を巧妙に解決する。

Scheme 2



つい最近までハロゲン化アリールとアレーンの間の置換反応でビアリアルを得るには、光照射などの特殊な手法を用いない限り、遷移金属触媒の利用が不可欠であると考えられていた。2008 年に伊丹らは、ピラジンやピリジンなどの  $\pi$  電子不足  $N$ -ヘテロアレーンとヨウ化アリールの置換反応が遷移金属触媒を用いなくても進行することを報告した (スキーム 3)<sup>4)</sup>。

Scheme 3

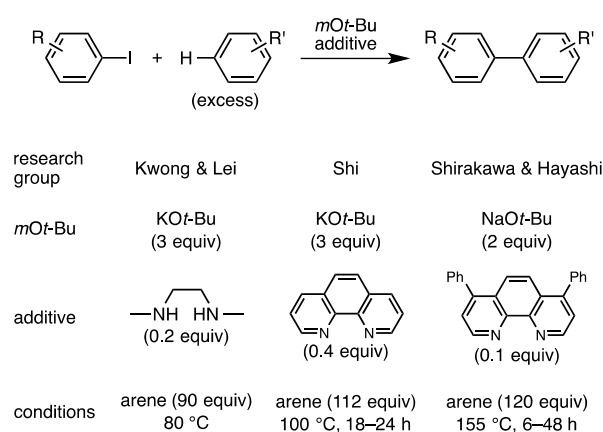


$KOt-Bu$  のような強塩基の利用が必要不可欠で、

マイクロウェーブの照射によって反応が加速される。ラジカル捕捉剤によって反応が阻害されることから、ラジカルの関与が示唆されたが、機構の詳細は解っていなかった。

2010 年になって、我々を含む三つのグループが、ほぼ同時期に、ハロゲン化アリールとベンゼンの間の置換反応を報告した (スキーム 4)<sup>5)</sup>。tert-ブトキシドと窒素二座配位子を用いるという共通点がある。 $\pi$  電子不足  $N$ -ヘテロアレーンからベンゼン誘導体へと一般性が高まったことで、「遷移金属触媒を用いないカップリング反応」として大いに注目を集めた。2010 年以降、そのタイトルに “transition metal free” という枕詞を冠した論文が飛躍的に増加した<sup>6)</sup>。

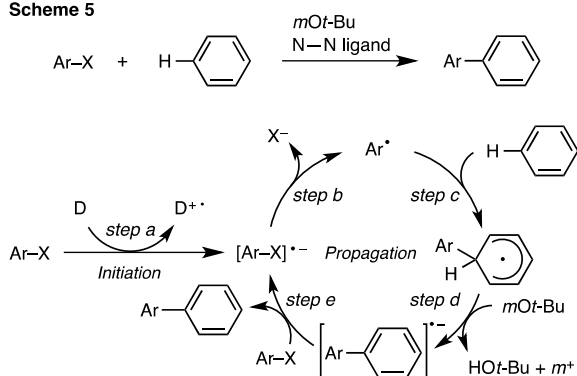
Scheme 4



発表当初、我々は現在想定しているのとは異なる機構を提唱していたが<sup>5a)</sup>、 $NaOt-Bu$ -1,10-フェナントロリン錯体からハロゲン化アリール ( $Ar-X$ ) への 1 電子移動によって生じたアニオンラジカル ( $[Ar-X]^\bullet$ ) からハロゲン化物イオン ( $X^-$ ) が脱離することによって生じたアリールラジカル ( $Ar^\bullet$ ) が関与していることを明らかにしていた。一方、Kwong・Lei らは、反応がカップリング体のアニオンラジカルを経由して進行することを示していた<sup>5b)</sup>。これらの現象と “base-promoted HAS” という Russell らが過去に報告していた概念<sup>7)</sup> を組み合わせた機構が Studer と Curran によって提唱され<sup>8)</sup>、現在ではこの機構が受け入れられている (スキーム 5)<sup>9)</sup>。まず、開始段階 (step a) において  $Ar-X$

が 1 電子を受け取り、 $[\text{Ar-X}]^{\bullet-}$  として生長段階に入る。続いて、 $\text{X}^-$  の脱離 (*step b*) により生じた  $\text{Ar}^\bullet$  がベンゼンに付加し (*step c*)、シクロヘキサジエニルラジカル中間体からプロトンを引き抜くことでカップリング体のアニオンラジカル ( $[\text{Ar-Ph}]^{\bullet-}$ ) となる (*step d*)。最後に  $[\text{Ar-Ph}]^{\bullet-}$  から  $\text{Ar-X}$  への 1 電子移動によって  $[\text{Ar-X}]^{\bullet-}$  が再生されると同時にカップリング体 ( $\text{Ar-Ph}$ ) が得られる (*step e*)。ベンゼン環に対するラジカル種の付加 (*step c*) とそれに続く別のラジカル種の脱離 (*step d*) からなる HAS の過程が含まれているが、ハロゲン化アリールをアリールラジカル源とする HAS の先述した課題である 1 電子還元と 1 電子酸化の両立が、 $\text{S}_{\text{RN}}1$  反応の肝である *step e* において巧妙に実現されている。スキーム 1 に示した従来の  $\text{S}_{\text{RN}}1$  反応との相違点は、脱プロトン化とベンゼン環へのラジカル種の付加の順序が逆になっていることであるが、芳香族性の回復を原動力としつつ強塩基を用いることで *step d* を可能にし、ベンゼンのような反応性の低いものをハロゲン化アリールに対する求核剤として反応させることに成功している。ここでベンゼンは、*tert*-ブトキシドによって求核性を付与されていると見なすことができるが、*tert*-ブトキシドは開始段階における 1 電子供与体としても働いている。先に述べた通り、我々は  $\text{NaOt-Bu}$ -1,10-フェナントロリン錯体からハロゲン化アリールへの 1 電子移動が起こることを実験で明らかにしているが、1,10-フェナントロリン以外の促進剤を用いる場合も含めて、加えたものがそのままの形で 1 電子供与体として

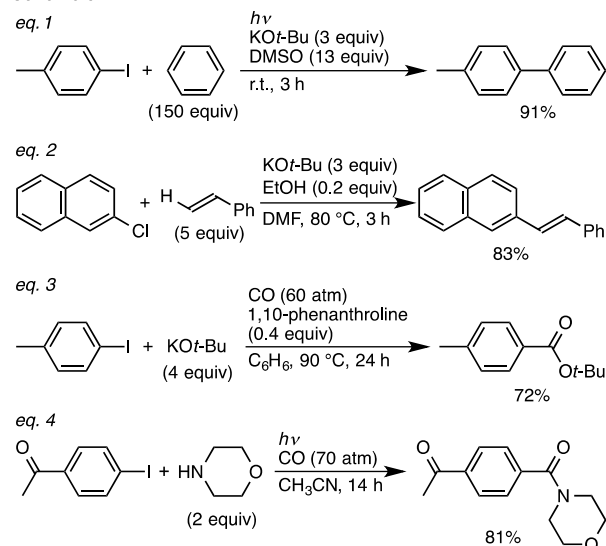
Scheme 5



働くのではなく、化学変化を起こした後に働くという考えも提唱されている<sup>10)</sup>。そうであった場合にも、ハロゲン化アリールに 1 電子をもたらす電子豊富さの源は *tert*-ブトキシドにあると考えるべきであり、やはり強塩基の利用が鍵となっていると言える。

このカップリング反応に関連する反応をスキーム 6 に挙げる。Rossi らは、窒素二座配位子を用いる代わりに光照射することで、開始段階の 1 電子移動が促進され、ハロゲン化アリールとベンゼンのカップリング反応が室温で進行するようになることを報告している (スキーム 6・式 1)<sup>11)</sup>。 $\text{KOt-Bu}$  の代わりに、より塩基性の低い  $\text{NaOt-Bu}$  を用いると反応がほとんど進行しなくなることから、スキーム 5 の *step d* において強い塩基性が求められることが判る。一方我々は、ベンゼンの代わりにアルケンを用いる溝呂木-Heck 型反応も可能であることを報告した (スキーム 6・式 2)<sup>12)</sup>。アルケンの適用範囲は、アリールラジカルが付加体が安定なベンジルラジカルになるスチレン誘導体に限られる。一酸化炭素もアリールラジカル付加の効果的な受容体となるが、これはアリールラジカルがより安定なアシルラジカルに変換されるためである。これを利用したカルボニル化反応を Lei ら (スキーム 6・式 3)<sup>13)</sup> および柳ら (スキーム 6・式 4)<sup>14)</sup> が報告している。

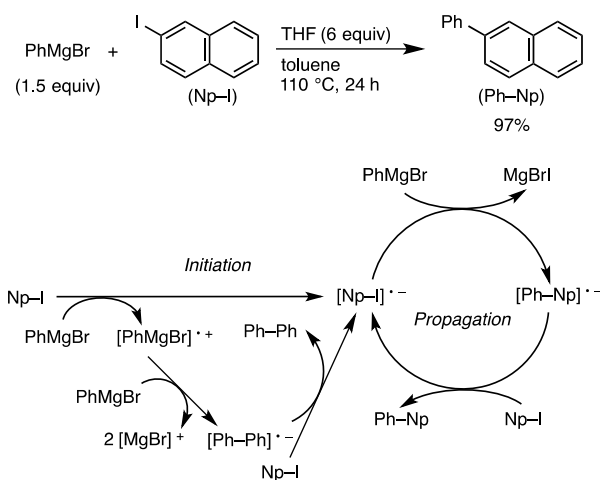
Scheme 6



## 2. 有機金属化合物とのクロスカップリング反応

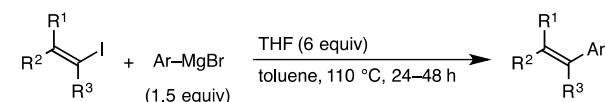
*tert*-ブトキシドの代わりにアリール Grignard 反応剤 ( $\text{Ar}'\text{-MgBr}$ ) を用いれば、ハロゲン化アリール ( $\text{Ar-X}$ ) に対する 1 電子供与体として働くだけでなく、生じたアニオンラジカル ( $[\text{Ar-X}]^{\cdot-}$ ) からの  $\text{X}^-$  の解離によって生成するアリールラジカル ( $\text{Ar}^{\cdot}$ ) に対する求核剤として反応し、カップリング体のアニオンラジカル ( $[\text{Ar}'\text{-Ar}]^{\cdot-}$ ) に至ると考えた。種々検討した結果、溶媒としてテトラヒドロフラン (THF) を用いるとハロゲン-マグネシウム交換が優先してしまうが、トルエン溶媒に THF を少量加えるという反応系で期待したクロスカップリングが高収率で進行することを明らかにした (スキーム 7)<sup>15)</sup>。ラジカルクロックなどを用いたその後の検討で、 $\text{Ar}^{\cdot}$  を経由することなく  $[\text{Ar-X}]^{\cdot-}$  が直接  $\text{Ar}'\text{-MgBr}$  と反応していることが判った<sup>16,17)</sup>。ここでは詳細は述べないが、スキーム 7 に示すように、全ての間体がイオンラジカルである機構で反応が進行すると考えている。ラジカル反応でありながら、反応性が高く副反応を起こしやすい  $\sigma$  ラジカルを経由しないことが、高収率に貢献していると考えられる。

Scheme 7



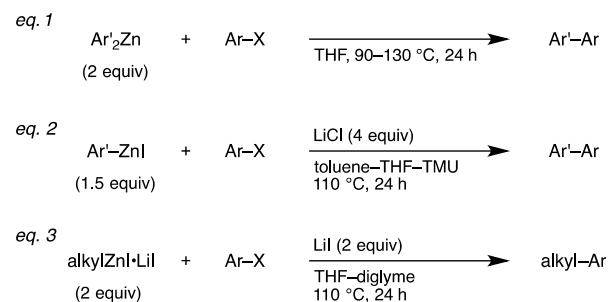
ハロゲン化アルケニルがアリール Grignard 反応剤とクロスカップリングを起こすことも明らかにした (スキーム 8)<sup>18)</sup>。アルケン部位の立体化学が保たれることから、ここでも  $\sigma$  ラジカル中間体を経由していないことが判る。

Scheme 8



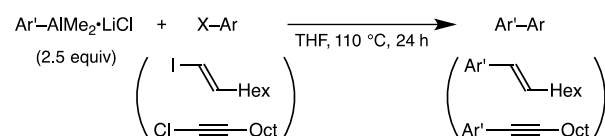
内山ら<sup>19)</sup> および我々<sup>20)</sup> は、それぞれジアリール亜鉛 (スキーム 9・式 1) およびヨウ化アリール亜鉛 (スキーム 9・式 2) がハロゲン化アリールとカップリングを起こすことを報告した。有機亜鉛化合物の利用は、Grignard 反応剤の系と比べて官能基選択性の点で有利で、エステルやニトリルのような求電子的な官能基をもつ基質も用いることができる。式 2 の系では、塩化リチウムの添加が反応の促進に有効であることが明らかにされている。塩化リチウムの添加効果は、アリール Grignard 反応剤のカップリング反応においても見られた<sup>21)</sup>。我々は、アルキルリチウムとハロゲン化亜鉛の間のトランスメタル化で調製したアルキル亜鉛でもハロゲン化アリールとのクロスカップリング反応が進行することを明らかにしているが、ここでは塩化リチウムには反応の促進効果はなく、ヨウ化亜鉛とヨウ化リチウムを用いる必要がある (スキーム 9・式 3)<sup>22)</sup>。

Scheme 9



内山らはアリールアルミニウム化合物もクロスカップリング反応に利用できることを明らかにするなど (スキーム 10)<sup>23)</sup>、遷移金属触媒を用いない有機金属化合物のクロスカップリング反応は、その幅をさらに広げつつある。

Scheme 10



## おわりに

以上、ここ数年の間に発展してきた変則  $S_{RN}1$  反応について紹介した。これらは、これまで遷移金属触媒の利用が必要不可欠とされてきたハロゲン化アリールのカップリング反応を、特別なものを用いずに進行させる、有機合成上重要な手法となりつつある。本稿の「1」では、ハロゲン化アリールのように入手容易なものから簡便にアリールラジカルを発生させ、その高い反応性を利用し強塩基の力も借りてベンゼンのような反応性の低いものとの間で  $C(sp^2)-C(sp^2)$  結合を作っている。「2」では、アリールラジカルに分解する前に、ハロゲン化アリールのアニオンラジカルを有機金属化合物がうまく捉えて、やはり炭素-炭素結合形成に結び付けている。この分野をさらに発展させる鍵は、以下の三つを如何に広げていくかにある：(1) 二つのタイプに共通することとして、穏和な条件で簡便に触媒となる 1 電子をハロゲン化アリールに渡すシステム、(2) 「1」における、アリールラジカルの高い反応性をうまく収める反応相手、(3) 「2」における、ハロゲン化アリールのアニオンラジカルをうまく捉える反応相手。新たなアイデアに基づくこの分野の発展に期待したい。

## 謝辞

本稿で紹介した研究のうち、筆者らによる成果については、筆者が京都大学大学院理学研究科化学専攻在籍時に林民生教授（現 Nanyang Technological University、シンガポール）のもとで始めたものであり、林教授に深く感謝いたします。また、実験結果は、共同研究者であり、原著論文に共著者として名を記された学生諸氏らによって得られたものであり、その努力と創意に対して厚く感謝いたします。

## 参考文献

- (a) J. K. Kim, J. F. Bunnet, *J. Am. Chem. Soc.*, **92**, 7463 (1970); (b) R. A. Rossi, A. B. Pierini, A. B. Peñéñory, *Chem. Rev.*, **103**, 71 (2003).
- R. Bolton, G. H. Williams, *Chem. Soc. Rev.*, **15**, 261 (1986).
- この問題をうまく回避した例: D. P. Curran, A. I. Keller, *J. Am. Chem. Soc.*, **128**, 13706 (2006).
- Y. Yanagisawa, K. Ueda, T. Taniguchi, K. Itami, *Org. Lett.*, **10**, 4673 (2008).
- (a) E. Shirakawa, K. Itoh, T. Higashino, T. Hayashi, *J. Am. Chem. Soc.*, **132**, 15537 (2010); (b) W. Liu, H. Cao, H. Zhang, H. Zhang, K. H. Chung, C. He, H. Wang, F. Y. Kwong, A. Lei, *J. Am. Chem. Soc.*, **132**, 16737 (2010); (c) C.-L. Sun, H. Li, D.-G. Yu, M. Yu, X. Zhou, X.-Y. Lu, K. Huang, S.-F. Zheng, B.-J. Li, Z.-J. Shi, *Nat. Chem.*, **2**, 1044 (2010).
- SciFinder における “transition metal free” のキーワード検索の年度ごとのヒット件数は、以下の通りである: 31 (2009), 49 (2010), 66 (2011), 145 (2012), 167 (2013), 250 (2014), 340 (2015).
- (a) G. A. Russell, P. Chen, B. H. Kim, R. Rajaratnam, *J. Am. Chem. Soc.*, **119**, 8795 (1997); (b) C. Wang, G. A. Russell, W. S. Trahanovsky, *J. Org. Chem.*, **63**, 9956 (1998).
- A. Studer, D. P. Curran, *Angew. Chem., Int. Ed.*, **50**, 5018 (2011).
- E. Shirakawa, T. Hayashi, *Chem. Lett.*, **41**, 130 (2012).
- ここでは関連する論文を数報挙げるに留める: (a) H. Yi, A. Jutand, A. Lei, *Chem. Commun.*, **51**, 545 (2015); (b) S. Zhou, G. M. Anderson, B. Mondal, E. Doni, V. Ironmonger, M. Kranz, T. Tuttle, J. A. Murphy, *Chem. Sci.*, **5**, 476 (2014); (c) S. Zhou, E. Doni, G. M. Anderson, R. G. Kane, S. W. MacDougall, V. M. Ironmonger, T. Tuttle, J. A. Murphy, *J. Am. Chem. Soc.*, **136**, 17818 (2014); (d) J. Cuthbertson, V. J. Gray, J. D. Wilden, *Chem. Commun.*, **50**, 2575 (2014); (e) M. Patil, *J. Org. Chem.*, **81**, 632 (2016).
- M. E. Budén, J. F. Guastavino, R. A. Rossi, *Org. Lett.*, **15**, 1174 (2013).
- E. Shirakawa, X. Zhang, T. Hayashi, *Angew. Chem., Int. Ed.*, **50**, 4671 (2011).
- H. Zhang, R. Shi, A. Ding, L. Lu, B. Chen, A. Lei, *Angew. Chem., Int. Ed.*, **51**, 12542 (2012).
- T. Kawamoto, A. Sato, I. Ryu, *Chem. Eur. J.*, **21**,

14764 (2015).

- 15) E. Shirakawa, Y. Hayashi, K. Itoh, R. Watabe, N. Uchiyama, W. Konagaya, S. Masui, T. Hayashi, *Angew. Chem., Int. Ed.*, **51**, 218 (2012).
- 16) N. Uchiyama, E. Shirakawa, T. Hayashi, *Chem. Commun.*, **49**, 364 (2013).
- 17) DFT 計算に基づきアリアルラジカルを経る機構を提唱する報告があるが、その活性種は、ある特殊な環境にある、フリーラジカルとしての性質を示さないものとされている: B. E. Haines, O. Wiest, *J. Org. Chem.*, **79**, 2771 (2014).
- 18) E. Shirakawa, R. Watabe, T. Murakami, T. Hayashi, *Chem. Commun.*, **49**, 5219 (2013).
- 19) H. Minami, X. Wang, C. Wang, M. Uchiyama, *Eur. J. Org. Chem.*, 7891 (2013).
- 20) E. Shirakawa, F. Tamakuni, E. Kusano, N. Uchiyama, W. Konagaya, R. Watabe, T. Hayashi, *Angew. Chem., Int. Ed.*, **53**, 521 (2014).
- 21) E. Shirakawa, K. Okura, N. Uchiyama, T. Murakami, T. Hayashi, *Chem. Lett.*, **43**, 922 (2014).
- 22) K. Okura, E. Shirakawa, *Eur. J. Org. Chem.*, 3043 (2016).
- 23) H. Minami, T. Sato, C. Wang, M. Uchiyama, *Angew. Chem., Int. Ed.*, **54**, 4665 (2015).

(2016 年 7 月 27 日受理)

## COMMUNICATION



Cite this: *Chem. Commun.*, 2016, 52, 14019

Received 5th October 2016,  
Accepted 10th November 2016

DOI: 10.1039/c6cc08038c

www.rsc.org/chemcomm

# Single electron transfer-induced coupling of alkynylzinc reagents with aryl and alkenyl iodides†‡

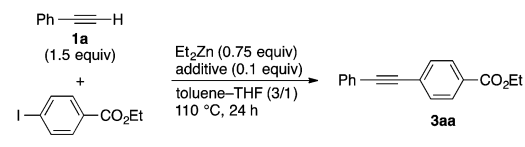
Keisho Okura,<sup>a</sup> Hitomi Kawashima,<sup>a</sup> Fumiko Tamakuni,<sup>a</sup> Naoyo Nishida<sup>a</sup> and Eiji Shirakawa<sup>\*b</sup>

**Alkynylzinc reagents were found to undergo coupling with aryl and alkenyl iodides to give arylalkynes and alkenylalkynes without the aid of transition metals. The coupling reaction proceeds through a single electron transfer mechanism, where a substoichiometric amount of a phosphine works as an indispensable activator.**

Transition metal-catalyzed cross-coupling reactions of organometallic reagents with aryl halides are widely used for the introduction of carbon-based substituents into aromatic rings.<sup>1</sup> However, we have reported a series of transition metal-free coupling reactions of aryl/alkylmetals (Mg/Zn) with aryl/alkenyl halides where a single electron brought by single electron transfer (SET) from the organometals to the organic halides works as a catalyst.<sup>2,3</sup> Here we report that the SET-induced coupling is also applicable to alkynylzincs, even though they are less electron-rich than aryl/alkylzincs and thus are considered to be less efficient single electron donors in the SET process. Alkynylzinc reagents undergo coupling with aryl iodides with the aid of a triarylphosphine (0.1 equiv.),<sup>4</sup> by mixing and heating all the materials including terminal alkynes and Et<sub>2</sub>Zn (in a 2 : 1 ratio), which are converted into alkynylzincs *in situ*.<sup>5</sup>

The treatment of ethyl 4-iodobenzoate (**2a**) with phenylacetylene (**1a**: 1.5 equiv.) and Et<sub>2</sub>Zn (0.75 equiv.) in toluene–THF (3/1) at 110 °C for 24 h did not give the coupling product, ethyl 4-(phenylethynyl)benzoate (**3aa**), at all (Table 1, entry 1). In contrast, the addition of a substoichiometric amount (0.1 equiv.) of triphenylphosphine promoted the coupling to some extent (entry 2). The reaction was further promoted by the use of tris[4-(trifluoromethyl)phenyl]phosphine (**L**), giving 98% yield of **3aa** with a full conversion of **2a**, whereas more or less electron-rich triarylphosphines showed lower efficiencies (entries 3–5).

Table 1 Coupling of phenylacetylene with ethyl 4-iodobenzoate with the aid of diethylzinc<sup>a</sup>



Entry	Additive	Conv. <sup>b</sup> ( <b>2a</b> , %)	Yield <sup>b</sup> ( <b>3aa</b> , %)
1	None	<1	<1
2	Ph <sub>3</sub> P	31	31
3	(4-CF <sub>3</sub> C <sub>6</sub> H <sub>4</sub> ) <sub>3</sub> P ( <b>L</b> )	>99	98
4	(4-MeOC <sub>6</sub> H <sub>4</sub> ) <sub>3</sub> P	51	48
5	[3,5-(CF <sub>3</sub> ) <sub>2</sub> C <sub>6</sub> H <sub>3</sub> ] <sub>3</sub> P	13	11

<sup>a</sup> The reaction was carried out under a nitrogen atmosphere at 110 °C for 24 h using phenylacetylene (**1a**: 0.30 mmol), ethyl 4-iodobenzoate (**2a**: 0.20 mmol), and a toluene solution of Et<sub>2</sub>Zn (1.3 M, 0.12 mL, 0.15 mmol) in toluene–THF (0.63 mL/0.25 mL) in the presence (0.020 mmol) or absence of an additive. <sup>b</sup> Determined by GC.

The alkynyl–aryl coupling with the aid of Et<sub>2</sub>Zn and phosphine **L** is applicable to various terminal alkynes and aryl iodides (Table 2). The alkynylzinc reagent prepared *in situ* from phenylacetylene (**1a**) underwent coupling with iodobenzene derivatives of diverse electronic characters (entries 1–10). Heteroaryl iodides containing an oxygen, sulfur or nitrogen atom coupled with the phenylethynylzinc reagent (entries 11–14). Phenylacetylenes having an electron-withdrawing or -donating substituent and heteroarylacetylenes also participated in the coupling with ethyl 4-iodobenzoate (**2a**) in high yields (entries 15–19). The reaction using 1-octyne (**1g**) resulted in a moderate yield (80%) due to competitive ethylation (7%) of **2a** (entry 20). The side reaction is likely to be derived from Et<sub>2</sub>Zn remaining unreacted due to low acidity of **1g** (*vide infra*, Table 3). In order to facilitate the formation of alkynylzinc species, the reaction was conducted by using an increased amount (2 equiv.) of **1g** to give the coupling product **3ga** in a higher yield (90%), suppressing the formation of the ethylation product (entry 21). A trimethylsilyl-ethynylarene was also obtained in high yield by the use of

<sup>a</sup> Department of Chemistry, Graduate School of Science, Kyoto University, Sakyo, Kyoto 606-8502, Japan

<sup>b</sup> Department of Applied Chemistry for Environment, School of Science and Technology, Kwansei Gakuin University, Sanda, Hyogo 669-1337, Japan.  
E-mail: eshirakawa@kwansei.ac.jp

† Dedicated to Prof. Tamejiro Hiyama on the occasion of his 70th birthday.

‡ Electronic supplementary information (ESI) available. See DOI: 10.1039/c6cc08038c

**Table 2** Coupling of terminal alkynes with aryl iodides with the aid of diethylzinc<sup>a</sup>

Entry	R in 1	Ar in 2	Yield <sup>b</sup> (%)	Prod.
1	Ph ( <b>1a</b> )	2-Naphthyl ( <b>2b</b> )	97	<b>3ab</b>
2	Ph ( <b>1a</b> )	Ph ( <b>2c</b> )	93	<b>3ac</b>
3	Ph ( <b>1a</b> )	4-EtO <sub>2</sub> CC <sub>6</sub> H <sub>4</sub> ( <b>2a</b> )	96	<b>3aa</b>
4	Ph ( <b>1a</b> )	4-CF <sub>3</sub> C <sub>6</sub> H <sub>4</sub> ( <b>2d</b> )	97	<b>3ad</b>
5	Ph ( <b>1a</b> )	4-ClC <sub>6</sub> H <sub>4</sub> ( <b>2e</b> )	90	<b>3ae</b>
6 <sup>c</sup>	Ph ( <b>1a</b> )	4-MeOC <sub>6</sub> H <sub>4</sub> ( <b>2f</b> )	91	<b>3af</b>
7	Ph ( <b>1a</b> )	4-MeC <sub>6</sub> H <sub>4</sub> ( <b>2g</b> )	93	<b>3ag</b>
8	Ph ( <b>1a</b> )	3,5-Me <sub>2</sub> C <sub>6</sub> H <sub>3</sub> ( <b>2h</b> )	96	<b>3ah</b>
9	Ph ( <b>1a</b> )	3-EtO <sub>2</sub> CC <sub>6</sub> H <sub>4</sub> ( <b>2i</b> )	95	<b>3ai</b>
10	Ph ( <b>1a</b> )	2-(3-Butenyl)C <sub>6</sub> H <sub>4</sub> ( <b>2j</b> )	87	<b>3aj</b>
11	Ph ( <b>1a</b> )	2-Benzofuranyl ( <b>2k</b> )	97	<b>3ak</b>
12	Ph ( <b>1a</b> )	2-Benzothienyl ( <b>2l</b> )	87	<b>3al</b>
13	Ph ( <b>1a</b> )	3-Pyridyl ( <b>2m</b> )	98	<b>3am</b>
14	Ph ( <b>1a</b> )	3-Thienyl ( <b>2n</b> )	89	<b>3an</b>
15	4-CF <sub>3</sub> C <sub>6</sub> H <sub>4</sub> ( <b>1b</b> )	4-EtO <sub>2</sub> CC <sub>6</sub> H <sub>4</sub> ( <b>2a</b> )	94	<b>3ba</b>
16	4-MeOC <sub>6</sub> H <sub>4</sub> ( <b>1c</b> )	4-EtO <sub>2</sub> CC <sub>6</sub> H <sub>4</sub> ( <b>2a</b> )	97	<b>3ca</b>
17	2-MeOC <sub>6</sub> H <sub>4</sub> ( <b>1d</b> )	4-EtO <sub>2</sub> CC <sub>6</sub> H <sub>4</sub> ( <b>2a</b> )	95	<b>3da</b>
18	2-Thienyl ( <b>1e</b> )	4-EtO <sub>2</sub> CC <sub>6</sub> H <sub>4</sub> ( <b>2a</b> )	79	<b>3ea</b>
19	3-Thienyl ( <b>1f</b> )	4-EtO <sub>2</sub> CC <sub>6</sub> H <sub>4</sub> ( <b>2a</b> )	95	<b>3fa</b>
20	Hex ( <b>1g</b> )	4-EtO <sub>2</sub> CC <sub>6</sub> H <sub>4</sub> ( <b>2a</b> )	80 <sup>d</sup>	<b>3ga</b>
21 <sup>e</sup>	Hex ( <b>1g</b> )	4-EtO <sub>2</sub> CC <sub>6</sub> H <sub>4</sub> ( <b>2a</b> )	90	<b>3ga</b>
22 <sup>e</sup>	Me <sub>3</sub> Si ( <b>1h</b> )	4-EtO <sub>2</sub> CC <sub>6</sub> H <sub>4</sub> ( <b>2a</b> )	90	<b>3ha</b>

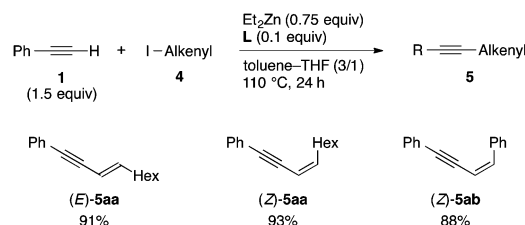
<sup>a</sup> The reaction was carried out under a nitrogen atmosphere at 110 °C for 24 h using a toluene-THF (3:1) solution of an alkyne (**1**: 0.30 mmol) and an aryl iodide (**2**: 0.20 mmol) in the presence of Et<sub>2</sub>Zn in toluene (1.3 M, 0.12 mL, 0.15 mmol) and tris[4-(trifluoromethyl)phenyl]phosphine (**L**: 0.020 mmol). <sup>b</sup> Isolated yield based on **2**. <sup>c</sup> Reaction time = 48 h. <sup>d</sup> Determined by GC. <sup>e</sup> Alkyne **1** (0.40 mmol) was used.

**Table 3** Behavior of organozinc species toward aryl iodides<sup>a</sup>

Entry	<b>1a</b> (equiv.)	Et <sub>2</sub> Zn (equiv.)	Zn Species	Conv. <sup>b</sup> ( <b>2a</b> , %)	Yield <sup>b</sup> (%)			
					<b>3aa</b>	<b>6a</b>	<b>7a</b>	<b>8a</b>
1	0	0.75	<b>A</b>	>99	—	65	3	11
2	1.5	1.5	<b>B</b>	98	92	0.1	0.4	<0.1
3	1.5	0.75	<b>C</b>	>99	90	<0.1	0.1	<0.1

<sup>a</sup> After treatment of phenylacetylene (**1a**: 0.30 mmol) with Et<sub>2</sub>Zn (0.30 mmol for entry 2; 0.15 mmol for entry 3) under a nitrogen atmosphere at 110 °C for 10 h in toluene-THF (3:1), the resulting mixture was treated with tris[4-(trifluoromethyl)phenyl]phosphine (**L**: 0.020 mmol) and ethyl 4-iodobenzoate (**2a**: 0.20 mmol) at 110 °C for 24 h. For entry 1, Et<sub>2</sub>Zn (0.15 mmol) was used for the reaction with **2a** without treatment with **1a**. <sup>b</sup> Determined by GC.

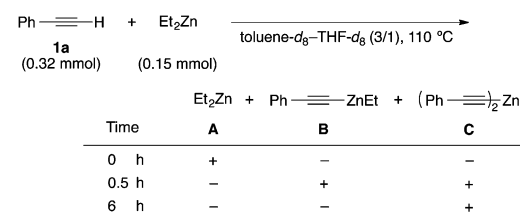
2 equiv. of trimethylsilylacetylene (**1h**) (entry 22). Aryl bromides such as ethyl 4-bromobenzoate and 2-bromonaphthalene did not undergo coupling with the phenylethynylzinc reagent at all. In addition to aryl iodides, alkenyl iodides underwent the

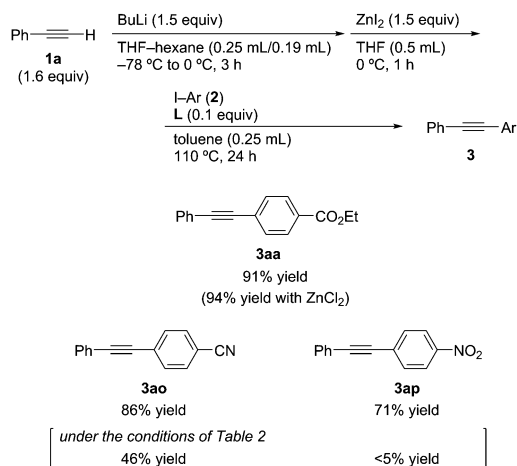
**Scheme 1** Coupling of terminal alkynes with alkenyl iodides with the aid of diethylzinc.

coupling, where the complete retention of the stereochemistries was observed (Scheme 1).<sup>6</sup>

The procedure of just mixing a terminal alkyne (**1**: 1.5 equiv.) and Et<sub>2</sub>Zn (0.75 equiv.) in toluene-THF in the presence of an aryl iodide (**2**) and the phosphine (**L**: 0.1 equiv.), instead of preparing alkynylzinc species in advance, is convenient from a practical point of view. However, the procedure could cause side reactions derived from the Et-Zn moieties, which inevitably remain, at least, in the early stage of the reaction. As shown in entry 1 of Table 3, the Et-Zn moiety of Et<sub>2</sub>Zn (**A**) was found to undergo coupling with ethyl 4-iodobenzoate (**2a**) to give the ethylation product (**6a**) of **2a**, being accompanied by the reduction and homocoupling products (**7a** and **8a**). On the other hand, the Et-Zn moiety of PhC≡CZnEt (**B**) does not undergo coupling with **2a**, whereas the PhC≡C-Zn moiety of **B** undergoes the coupling to give **3aa** similar to the PhC≡C-Zn moieties of (PhC≡C)<sub>2</sub>Zn (**C**) (entries 2 and 3).<sup>7</sup> An NMR experiment (Scheme 2) pursuing the transformation of the Et-Zn moieties to PhC≡C-Zn moieties shows that one of the Et-Zn moieties of **A** is immediately transformed to give **B**, but a certain reaction period (0.5 h < time < 6 h) is required for the transformation of the second Et-Zn moiety to give **C**. The observation that Et<sub>2</sub>Zn (**A**), which is the original organozinc reagent and induces side reactions, is immediately transformed to alkynylzinc species (**B** and **C**), which selectively give the alkynyl-aryl coupling product, fully explains why the simple procedure to mix and heat all the starting materials works properly.

Another feature of the procedure employed here is that less than 1 equivalent (0.75 equiv.) of Et<sub>2</sub>Zn is required to complete the coupling reaction, implying that the corresponding alkynylzinc iodide, which must be the predominant organozinc species in a late stage, should also participate in the coupling with aryl iodides. Actually, phenylethynylzinc iodide, prepared from phenylacetylene

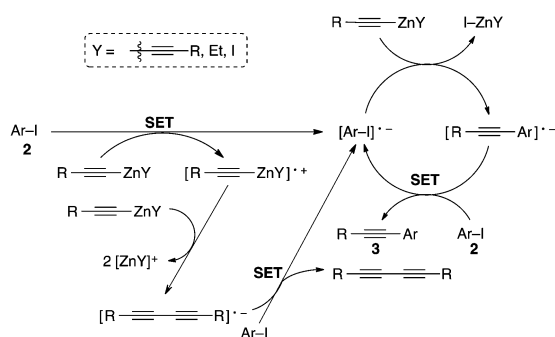
**Scheme 2** NMR experiment pursuing transformation of Et-Zn moieties to PhC≡C-Zn moieties.



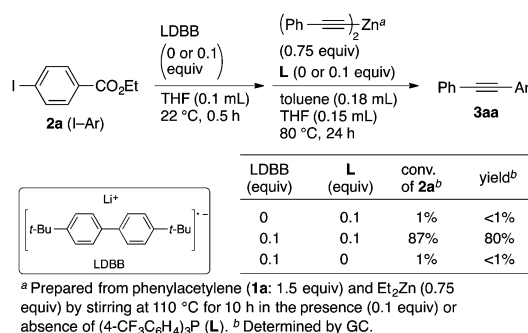
**Scheme 3** Coupling of alkynylzinc halides, prepared by transmetalation between an alkynyllithium and a zinc halide, with aryl iodides.

(**1a**: 1.6 equiv.) through deprotonation with butyllithium (1.5 equiv.) followed by transmetalation with  $\text{ZnI}_2$  (1.5 equiv.), underwent coupling with ethyl 4-iodobenzoate (**2a**) at 110 °C for 24 h to give **3aa** in 91% yield (Scheme 3). This protocol is effective also with  $\text{ZnCl}_2$ .<sup>8</sup> The use of alkynylzinc halides, the nucleophilicity of which is weakened by electron-withdrawing halogens, was found to be beneficial for the reaction of aryl iodide having a highly electrophilic substituent. For example, *p*-cyano- or nitro-substituted iodobenzenes (**2o** and **2p**), the reaction of which under the conditions of Table 2 scored low yields, underwent coupling with the phenylethynylzinc iodide in moderate to high yields (Scheme 3).

We consider that the present coupling reaction is likely to follow the mechanism of the coupling reaction of organo-magnesium and -zinc reagents as shown in Scheme 4.<sup>2</sup> SET from an alkynylzinc species ( $\text{R-C}\equiv\text{C-ZnY}$ ;  $\text{Y} = \text{R-C}\equiv\text{C}$ , Et, I) to an aryl iodide ( $\text{Ar-I}$ ) gives  $[\text{Ar-I}]^{\bullet-}$ , which reacts with  $\text{R-C}\equiv\text{C-ZnY}$  to give an anion radical of the coupling product (**3**). Finally, SET from  $[\text{R-C}\equiv\text{C-Ar}]^{\bullet-}$  to  $\text{Ar-I}$  gives  $\text{R-C}\equiv\text{C-Ar}$  and regenerates  $[\text{Ar-I}]^{\bullet-}$ . On the other hand, upon SET in the initiation step,  $\text{R-C}\equiv\text{C-ZnY}$  is converted into its cation radical, which reacts with  $\text{R-C}\equiv\text{C-ZnY}$  to give an anion radical of  $\text{R-C}\equiv\text{C-C}\equiv\text{C-R}$ .  $[\text{R-C}\equiv\text{C-C}\equiv\text{C-R}]^{\bullet-}$  acts as a single electron donor toward  $\text{Ar-I}$  to give  $[\text{Ar-I}]^{\bullet-}$  and  $\text{R-C}\equiv\text{C-C}\equiv\text{C-R}$ . Actually, a small amount of the corresponding



**Scheme 4** A plausible mechanism.



**Scheme 5** Acceleration of the reaction by the addition of a single electron donor.

diyne is inevitably observed in the coupling reaction. In order to prove the operation of the SET mechanism in the coupling reaction of arylmagnesium and -zinc reagents with aryl halides, we have shown that the coupling reaction is accelerated by the addition of lithium 4,4'-di-*tert*-butylbiphenylide (LDBB), which is a better single electron donor than arylmagnesium and -zinc reagents.<sup>2a,e</sup> A similar acceleration effect was observed also in the present coupling reaction. Ethyl 4-iodobenzoate (**2a**) was not consumed at all in the reaction with bis(phenylethynyl)zinc, prepared in advance in the same manner as given in entry 3 of Table 3, in the presence of phosphine **L** (0.1 equiv.) at 80 °C for 24 h (Scheme 5). In contrast, the reaction in the presence of LDBB (0.1 equiv.) gave the coupling product in a high yield. It is noteworthy that this drastic acceleration effect has disappeared in the absence of phosphine **L**, showing that **L** is likely to play a significant role in the carbon-carbon bond forming step rather than in SET processes, though it is unclear how it affects.<sup>9</sup> No involvement of aryl radical species was confirmed by a radical clock reaction using 2-(3-butenyl)phenyl iodide (**2j**), the corresponding aryl radical of which is known to readily cyclize ( $k_c = 5 \times 10^8 \text{ s}^{-1}$  at 50 °C).<sup>10</sup> The reaction of **2j** with a phenylethynylzinc reagent did not give any cyclization product but gave the normal coupling product in a high yield (entry 10 of Table 2).

In conclusion, we have developed a coupling reaction of alkynylzinc reagents with aryl and alkenyl iodides without the aid of transition metal catalysis. A substoichiometric amount of a triarylphosphine works here as an indispensable activator to promote the coupling reaction, though how it works is unclear at present and has to be clarified for the further development of the single electron transfer-induced cross-coupling reactions.

This work has been supported financially in part by Grant-in-Aid for Scientific Research (B) (25288046 to E. S.) from JSPS and Nagase Science and Technology Foundation (E. S.).

## Notes and references

- For reviews, see: *Metal-Catalyzed Cross-Coupling Reactions*, ed. A. de Meijere and F. Diederich, Wiley-VCH, Weinheim, 2nd edn, 2004, vol. 1–2; J.-P. Corbet and G. Mignani, *Chem. Rev.*, 2006, **106**, 2651–2710.
- For the coupling of aryl Grignard reagents with aryl or alkenyl halides, see: (a) E. Shirakawa, Y. Hayashi, K. Itoh, R. Watabe, N. Uchiyama, W. Konagaya, S. Masui and T. Hayashi, *Angew. Chem., Int. Ed.*, 2012, **51**, 218–221; (b) N. Uchiyama, E. Shirakawa and T. Hayashi, *Chem. Commun.*, 2013, **49**, 364–366; (c) E. Shirakawa,

- R. Watabe, T. Murakami and T. Hayashi, *Chem. Commun.*, 2013, **49**, 5219–5221; (d) E. Shirakawa, K. Okura, N. Uchiyama, T. Murakami and T. Hayashi, *Chem. Lett.*, 2014, **43**, 922–924. For the coupling of arylzinc reagents with aryl or alkenyl halides, see: (e) E. Shirakawa, F. Tamakuni, E. Kusano, N. Uchiyama, W. Konagaya, R. Watabe and T. Hayashi, *Angew. Chem., Int. Ed.*, 2014, **53**, 521–525. For the coupling of alkylzinc reagents with aryl or alkenyl iodides, see: (f) K. Okura and E. Shirakawa, *Eur. J. Org. Chem.*, 2016, 3043–3046.
- Uchiyama and coworkers have reported the transition metal-free coupling of arylmetals with aryl halides. For the coupling of diarylzinc reagents, see: H. Minami, X. Wang, C. Wang and M. Uchiyama, *Eur. J. Org. Chem.*, 2013, 7891–7894. For the coupling of arylaluminum reagents, see: H. Minami, T. Saito, C. Wang and M. Uchiyama, *Angew. Chem., Int. Ed.*, 2015, **54**, 4665–4668. Very recently, Zhang, Wnuk and coworkers have reported the transition metal-free coupling of tetra-arylstannanes with aryl halides, see: Q. He, L. Wang, Y. Liang, Z. Zhang and S. F. Wnuk, *J. Org. Chem.*, 2016, **81**, 9422–9427.
  - Triarylphosphines are used as indispensable additives to obtain  $\alpha$ -arylpropargyl alcohols through iodine–zinc exchange between an alkynyl iodide and diethylzinc followed by the addition of the resulting alkynylzinc species to an aromatic aldehyde. Phosphines are considered to have acceleration effects both on the former iodine–zinc exchange step and the latter addition step, though how they work is not clearly understood. E. E. Wilson, A. G. Oliver, R. P. Hughes and B. L. Ashfeld, *Organometallics*, 2011, **30**, 5214–5221.
  - For preparation of bisalkynylzincs *via* the treatment of terminal alkynes with diethylzinc, see: O. Yu. Okhlobystin and L. I. Zakharkin, *J. Organomet. Chem.*, 1965, **3**, 257S–258S. This method to prepare bisalkynylzincs is often used for the asymmetric addition of alkynylzinc reagents to aldehydes. For an early example, see: S. Niwa and K. Soai, *J. Chem. Soc., Perkin Trans. 1*, 1990, 937–943.
  - The complete retention of the stereochemistries has been observed also in the previous SET-induced coupling reactions of alkenyl halides, supporting no involvement of alkenyl radical intermediates, see ref. 2c–f.
  - From the result shown in Scheme 2, the treatment of phenylacetylene (**1a**) with  $\text{Et}_2\text{Zn}$  for 10 h at 110 °C is considered to be sufficient to convert the acetylenic proton to zinc to give **B** and **C** (entries 2 and 3 in Table 3), respectively.
  - The reaction using **1a** (1.6 equiv.), BuLi (1.5 equiv.),  $\text{ZnCl}_2$  (1.5 equiv.) and **2a** (1 equiv.) in the absence of phosphine **L** did not proceed at all, showing that acceleration of the transformation of Et–Zn moieties to  $\text{RC}\equiv\text{C–Zn}$  is not, at least, the main role of **L** in the standard procedure. On the other hand, the reaction using **1a** (1.6 equiv.), BuLi (1.5 equiv.),  $\text{ZnCl}_2$  (0.75 equiv.) and **2a** (1 equiv.) in the presence of phosphine **L** (0.1 equiv.) gave 86% of **3aa**, showing that  $(\text{PhC}\equiv\text{C})_2\text{Zn}$  undergoes coupling with aryl iodides regardless of the method of preparation.
  - In ref. 4,  $\text{PhC}\equiv\text{C–Zn–Et}$  coordinated by  $\text{PPh}_3$  is shown to form a cyclic dimer, where the alkyne moiety of  $\text{PhC}\equiv\text{C–Zn–Et}$  coordinates with zinc of the other  $\text{PhC}\equiv\text{C–Zn–Et}$ . This type of phosphine-induced interaction possibly is concerned with the role of the phosphine in the coupling reaction.
  - A. N. Abeywickrema and A. L. J. Beckwith, *J. Chem. Soc., Chem. Commun.*, 1986, 464–465; H. Yasuda, Y. Uenoyama, O. Nobuta, S. Kobayashi and I. Ryu, *Tetrahedron Lett.*, 2008, **49**, 367–370. See also ref. 2b.

## Cross-Coupling

## Single-Electron-Transfer-Induced Coupling of Alkylzinc Reagents with Aryl Iodides

Keisho Okura<sup>[a]</sup> and Eiji Shirakawa\*<sup>[b]</sup>

**Abstract:** Alkylzinc reagents prepared from an alkyllithium and zinc iodide were found to undergo coupling with aryl and alk- enyl iodides in the presence of Lil in a mixed solvent consisting

of THF and diglyme (1:1). Alkylzinc reagents, prepared by halogen- lithium exchange between an alkyl iodide and *tert*-butyllithium, are also converted to alkylarenes through alkylzinc reagents.

## Introduction

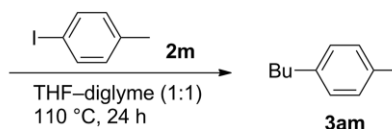
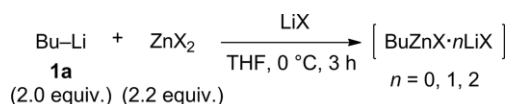
The transition-metal-catalyzed cross-coupling reaction of organometals with aryl halides is widely used to introduce substituents into benzene rings.<sup>[1]</sup> On the other hand, we reported a transition-metal-free version of the cross-coupling reaction of aryl Grignard reagents with aryl iodides, for which a single electron, produced by single-electron transfer (SET) from an aryl Grignard reagent to an aryl iodide, acts as the catalyst.<sup>[2–4]</sup> We also reported that arylzinc reagents undergo coupling with aryl halides through the SET mechanism with the aid of LiCl,<sup>[5]</sup> which acts as an accelerator in the Grignard cross-coupling, and this led to expansion of the scope of the aryl halides from iodides to bromides.<sup>[6]</sup> However, transition-metal-free cross-coupling has only been applied to arylmetals.<sup>[7,8]</sup> Herein, we report that the SET-induced coupling of alkylzinc reagents with aryl iodides takes place with the aid of Lil; LiCl does not work at all in this reaction, in contrast to the aryl–aryl coupling case.

## Results and Discussion

Treatment of 4-iodotoluene (**2m**) with BuZnCl·LiCl (2 equiv.), prepared by transmetalation between BuLi (**1a**: 2 equiv.) and ZnCl<sub>2</sub> (2.2 equiv.), in THF/diglyme/hexane (1.2:1.2:1) at 110 °C for 24 h gave 4-butyltoluene (**3am**), but only in 1 % yield with 6 % conversion of **2m** (Table 1, entry 1). The addition of LiCl (2 equiv.) did not enhance the reactivity (Table 1, entry 2). In contrast, the addition of Lil drastically increased the conversion and the yield and gave **3am** in 69 % yield, but toluene and 4,4'-bitolyl were also produced in considerable amounts (9 and 5 %, respectively; Table 1, entry 3).<sup>[9]</sup> BuZnI·Lil prepared from ZnI<sub>2</sub> instead of ZnCl<sub>2</sub> was also effective, and an additional amount

of Lil (2 equiv.) further improved the conversion and the yield (Table 1, entries 4 and 5).<sup>[10]</sup> No coupling took place with salt-free BuZnI prepared from 1-iodobutane and zinc powder (Table 1, entry 6), but an additional amount of Lil (4 equiv.) promoted the coupling to some extent (Table 1, entry 7). These results show that the reactivity of an alkylzinc reagent is largely dependent on the type of halogen existing in the reaction mixture. Considering the effect of the halogen atom, the reactivity is possibly governed by higher order structures such as BuZnX·*n*LiX. BuZnX·LiX is known to form a butylzincate Li<sup>+</sup>[BuZnX<sub>2</sub>]<sup>-</sup>, and Li<sup>+</sup>[BuZnCl<sub>2</sub>]<sup>-</sup> and Li<sup>+</sup>[BuZnI<sub>2</sub>]<sup>-</sup> tend to form oligomeric and monomeric complexes, respectively.<sup>[11,12]</sup> Al-

Table 1. Effect of constituents of butylzinc reagents in the coupling with 4-iodotoluene.<sup>[a]</sup>



Entry	ZnX <sub>2</sub>	LiX	Constituent of BuZnX· <i>n</i> LiX	Conversion [%] <sup>[b]</sup>	Yield [%] <sup>[b]</sup>
1	ZnCl <sub>2</sub>	none	BuZnCl·LiCl	6	1
2	ZnCl <sub>2</sub>	LiCl	BuZnCl·2LiCl	4	1
3	ZnCl <sub>2</sub>	Lil	BuZnCl·LiCl·Lil	85	69
4	ZnI <sub>2</sub>	none	BuZnI·Lil	86	68
5	ZnI <sub>2</sub>	Lil	BuZnI·2Lil	98	86
6 <sup>[d]</sup>	–	none	BuZnI	1	<1
7 <sup>[d,e]</sup>	–	Lil	BuZnI·2Lil	36	28

[a] Department of Chemistry, Graduate School of Science, Kyoto University, Kyoto, Kyoto 606-8502, Japan

[b] Department of Applied Chemistry for Environment, School of Science and Technology, Kwansei Gakuin University, Sanda, Hyogo 669-1337, Japan  
E-mail: eshirakawa@kwansei.ac.jp  
<http://sci-tech.ksc.kwansei.ac.jp/en/>

Supporting information and ORCID(s) from the author(s) for this article are available on the WWW under <http://dx.doi.org/10.1002/ejoc.201600367>.

[a] The reaction was performed at 110 °C for 24 h in THF/diglyme/hexane (1.2:1.2:1, 0.85 mL) under a nitrogen atmosphere by using 4-iodotoluene (**2m**) (0.20 mmol) and a butylzinc reagent prepared from a zinc halide (0.44 mmol) and butyllithium (**1a**) (1.6 M in hexane, 0.25 mL, 0.40 mmol) in the presence or absence of a lithium halide (0.40 mmol). [b] Determined by GC. [c] Yield of isolated product based on **2m**. [d] A lithium halide free butylzinc iodide (1.4 M in THF, 0.28 mL, 0.40 mmol) prepared from 1-iodobutane and zinc dust (1.5 equiv.) was used. [e] Lil (0.80 mmol) was used.

though we are not certain what effect the structural difference exerts, a mononuclear complex of an alkylzincate is likely to be effective for the coupling reaction with aryl halides.

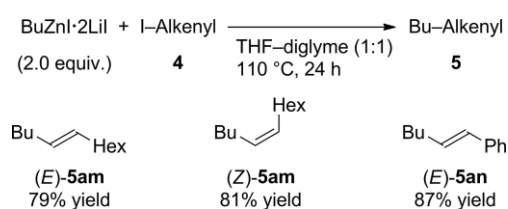
The alkyl–aryl coupling was found to be applicable to various aryl iodides and alkylzinc reagents (Table 2). Iodobenzene derivatives having no substituents underwent the coupling with butylzinc iodide (Table 2, entries 1 and 2). Substituted phenyl iodides also participated in the coupling, and the electronic character of the substituents did not largely affect the reactivity and the yield (Table 2, entries 3–8). The coupling of the butylzinc reagent with phenyl iodide **2s** having an ester moiety gave ethyl 4-butylbenzoate (**3as**) in 53 % yield but also the corresponding butyl ester and carboxylic acid in yields of 13 and 10 %, respectively. Simple treatment of the crude product transformed the carbon–carbon bond-forming products into methyl 4-butylbenzoate (**3as'**) (Table 2, entry 7).<sup>[13]</sup> High yields were attained in the reaction of the corresponding methylzinc reagent (Table 2, entries 9–11).

Table 2. Coupling of alkylzinc reagents with aryl iodides.<sup>[a]</sup>

Entry	R	Ar	Yield [%] <sup>[b]</sup>	Product
1	Bu ( <b>1a</b> )	2-naphthyl ( <b>2n</b> )	85	<b>3an</b>
2	Bu ( <b>1a</b> )	Ph ( <b>2o</b> )	75	<b>3ao</b>
3	Bu ( <b>1a</b> )	4-MeC <sub>6</sub> H <sub>4</sub> ( <b>2m</b> )	85	<b>3am</b>
4	Bu ( <b>1a</b> )	4-F <sub>3</sub> CC <sub>6</sub> H <sub>4</sub> ( <b>2p</b> )	72	<b>3ap</b>
5	Bu ( <b>1a</b> )	4-MeOC <sub>6</sub> H <sub>4</sub> ( <b>2q</b> )	72	<b>3aq</b>
6	Bu ( <b>1a</b> )	4-PhC <sub>6</sub> H <sub>4</sub> ( <b>2r</b> )	81	<b>3ar</b>
7	Bu ( <b>1a</b> )	4-ETOC <sub>6</sub> H <sub>4</sub> ( <b>2s</b> )	75 <sup>[c]</sup>	<b>3as'</b>
8	Bu ( <b>1a</b> )	2-EtC <sub>6</sub> H <sub>4</sub> ( <b>2t</b> )	72	<b>3at</b>
9	Me ( <b>1b</b> )	2-naphthyl ( <b>2n</b> )	97	<b>3bn</b>
10	Me ( <b>1b</b> )	4-MeOC <sub>6</sub> H <sub>4</sub> ( <b>2q</b> )	92	<b>3bq</b>
11	Me ( <b>1b</b> )	4-PhC <sub>6</sub> H <sub>4</sub> ( <b>2r</b> )	95	<b>3br</b>

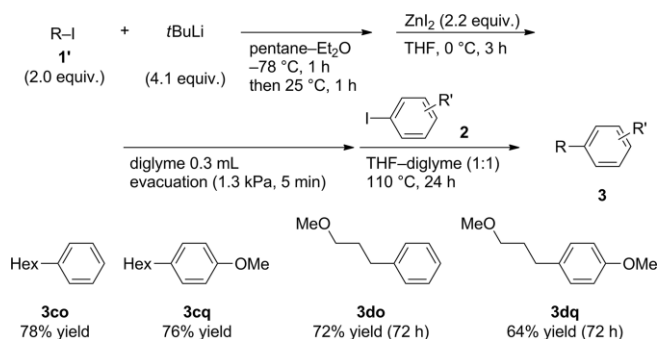
[a] The reaction was performed at 110 °C for 24 h in THF/diglyme/hexane (1.2:1.2:1, 0.85 mL) or THF/diglyme/Et<sub>2</sub>O (1:1:1, 0.85 mL) under a nitrogen atmosphere by using an alkylzinc reagent, prepared from zinc iodide (0.44 mmol) and an alkyllithium (**1a**: a hexane solution, 0.25 mL; **1b**: a Et<sub>2</sub>O solution, 0.30 mL), and aryl iodide **2** (0.20 mmol) in the presence of Lil (0.40 mmol). [b] Yield of isolated product based on **2**. [c] The yield of methyl 4-butylbenzoate (**3as'**) obtained by treatment of the crude product with NaOMe in MeOH at 25 °C for 6 h and then with MeOH/HCl at 25 °C for 36 h.

In addition to aryl iodides, alkenyl iodides underwent the coupling (Scheme 1). The stereochemistry was retained in the reaction of the butylzinc reagent with 1-octenyl and styryl iodides, as in cross-coupling reactions with the use of arylmagnesium and arylzinc reagents.



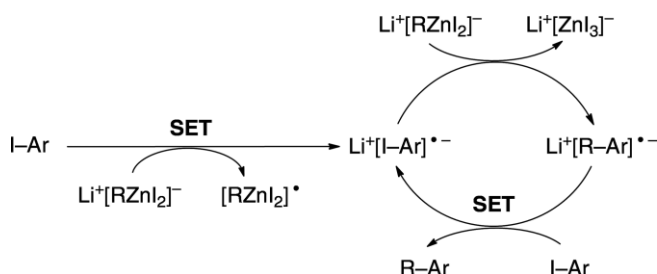
Scheme 1. Coupling of the butylzinc reagent with alkenyl iodides.

Alkylolithiums prepared through halogen–lithium exchange were also converted into alkylarenes through alkylzinc reagents (Scheme 2). A pentane solution of *t*BuLi was added to alkyl iodide **1'** in pentane/Et<sub>2</sub>O. Stirring at –78 °C for 1 h and then at 25 °C for 1 h was followed by treatment with a THF solution of ZnI<sub>2</sub> at 0 °C for 3 h. After the addition of diglyme and evacuation at 1.30 kPa for 10 min to remove the low-boiling solvents, the resulting alkylzinc reagent was subjected to the reaction with aryl iodide **2** by using THF as an additional solvent at 110 °C for 24–72 h to give the corresponding coupling product.



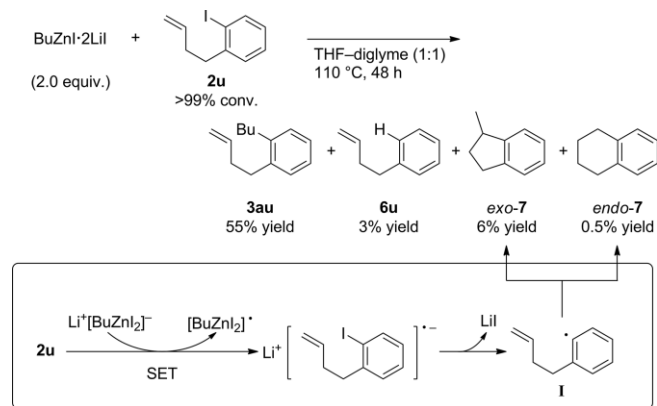
Scheme 2. Coupling of alkylzinc reagents, prepared through halogen–lithium exchange, with aryl iodides.

If we consider that the present alkyl–aryl coupling follows the SET mechanism operative in the aryl–aryl coupling,<sup>[2,3,5,6]</sup> the pathway shown in Scheme 3 can be drawn. Considering the striking effect of I<sup>–</sup>, alkylzinc species are described as Li<sup>+</sup>[RZnI<sub>2</sub>]<sup>–</sup> in all cases, though it is unclear what kind of alkylzinc species exists in each step. Initiation by SET from Li<sup>+</sup>[RZnI<sub>2</sub>]<sup>–</sup> to Ar–I gives [Ar–I]<sup>•–</sup>, which reacts with Li<sup>+</sup>[RZnI<sub>2</sub>]<sup>–</sup>.<sup>[14]</sup> SET from the resulting anion radical, [R–Ar]<sup>•–</sup>, to I–Ar gives R–Ar and regenerates [I–Ar]<sup>•–</sup>. The involvement of the [I–Ar]<sup>•–</sup> intermediate is strongly supported by the fact that the reaction of 2-(3-butenyl)phenyl iodide (**2u**) with BuZnI·2Lil under the standard conditions gives certain amounts of reductive cyclization products (i.e., compounds *exo*-**7** and *endo*-**7**) in addition to coupling product **3au** (Scheme 4).<sup>[15]</sup> Considering that *o*-homoallylphenyl radical **I** is known to cyclize readily, the reductive cyclization products are most likely produced from aryl radical **I**, which is undoubtedly formed through elimination of Lil from Li<sup>+</sup>[**2u**]<sup>•–</sup>. We already showed that aryl radicals derived from aryl halides are not intermediates in coupling reactions with aryl Grignard reagents.<sup>[3,16]</sup> Then, we examined whether this also holds true for the present alkyl–aryl coupling by conducting a similar experiment. Thus, treatment of BuZnI·2Lil with phenylazo(tri-

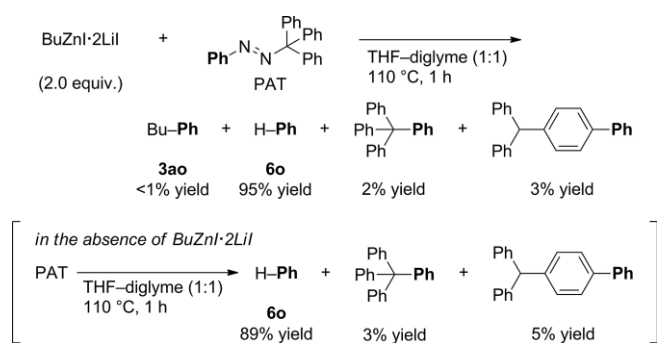


Scheme 3. Plausible mechanism.

phenyl)methane (PAT) as a Ph<sup>•</sup> precursor<sup>[17]</sup> did not give butylbenzene (**3ao**) at all (Scheme 5). This result shows that, under the standard conditions, BuZnI<sub>2</sub>Lil shows no reactivity towards Ph<sup>•</sup>, which rather reacts with the solvents to give benzene (**6o**) as the major product (Scheme 5). No involvement of  $\sigma$ -radical intermediates is supported by retention of the stereochemistry in the coupling of alkenyl iodides shown in Scheme 1.<sup>[18–20]</sup>



Scheme 4. Coupling of the butylzinc reagent with 2-(3-butenyl)phenyl iodide.



Scheme 5. Treatment of the butylzinc reagent with phenylazo(triphenyl)methane as a phenyl radical precursor.

## Conclusion

In conclusion, we developed the first example of the alkylmetal version of the single-electron-transfer-induced cross-coupling reaction of organometals with aryl and alkenyl iodides, in which Lil plays a critical role.

## Acknowledgments

This work was financially supported in part by the Japan Society for the Promotion of Science (JSPS) through a Grant-in-Aid for Scientific Research (B) (25288046, grant to E. S.) and by the Nagase Science and Technology Foundation (grant to E. S.).

**Keywords:** Alkylation · Arenes · C–C coupling · Cross-coupling · Electron transfer · Radical reactions

- [1] For reviews, see: a) A. de Meijere, F. Diederich (Eds.), *Metal-Catalyzed Cross-Coupling Reactions*, Wiley-VCH, Weinheim, Germany, **2004**, vol. 1 and 2; b) J.-P. Corbet, G. Mignani, *Chem. Rev.* **2006**, *106*, 2651–2710.
- [2] For coupling with aryl iodides, see: E. Shirakawa, Y. Hayashi, K. Itoh, R. Watabe, N. Uchiyama, W. Konagaya, S. Masui, T. Hayashi, *Angew. Chem. Int. Ed.* **2012**, *51*, 218–221; *Angew. Chem.* **2012**, *124*, 222–225.
- [3] For mechanistic studies on coupling with aryl halides, see: N. Uchiyama, E. Shirakawa, T. Hayashi, *Chem. Commun.* **2013**, *49*, 364–366.
- [4] We also reported the coupling of aryl Grignard reagents with alkenyl halides, see: E. Shirakawa, R. Watabe, T. Murakami, T. Hayashi, *Chem. Commun.* **2013**, *49*, 5219–5221.
- [5] E. Shirakawa, F. Tamakuni, E. Kusano, N. Uchiyama, W. Konagaya, R. Watabe, T. Hayashi, *Angew. Chem. Int. Ed.* **2014**, *53*, 521–525; *Angew. Chem.* **2014**, *126*, 531–535.
- [6] E. Shirakawa, K. Okura, N. Uchiyama, T. Murakami, T. Hayashi, *Chem. Lett.* **2014**, *43*, 922–924.
- [7] Uchiyama and co-workers reported the transition-metal-free coupling of arylmetals with aryl halides. For diarylzinc reagents, see: a) H. Minami, X. Wang, C. Wang, M. Uchiyama, *Eur. J. Org. Chem.* **2013**, 7891–7894; for arylaluminum reagents, see: b) H. Minami, T. Saito, C. Wang, M. Uchiyama, *Angew. Chem. Int. Ed.* **2015**, *54*, 4665–4668; *Angew. Chem.* **2015**, *127*, 4748–4751.
- [8] In the report on the copper-catalyzed coupling of perfluoroalkyl iodides with aryl iodides by use of a stoichiometric amount of Et<sub>2</sub>Zn to give perfluoroarylarenes, the coupling is reported to take place even in the absence of CuI, albeit to a much lower extent. H. Kato, K. Hirano, D. Kurauchi, N. Toriumi, M. Uchiyama, *Chem. Eur. J.* **2015**, *21*, 3895–3900.
- [9] Iodine–zinc exchange between 4-iodotoluene (**2m**) and the butylzinc reagent is likely to take place to give a *p*-tolylzinc reagent, which is converted into toluene and 4,4'-bitolyl through hydrolysis and cross-coupling, respectively.
- [10] Use of THF/diglyme as a mixed solvent is critical. The reaction in THF alone gave **3am** only in 56 % yield (73 % conversion) under the conditions of Table 1, entry 5. On the other hand, the reaction in diglyme alone showed poor reproducibility, and the conversion of **2m** ranged from 80 to >99 %. The use of toluene, DME, or DMF as a co-solvent with THF was much less effective than diglyme; the yields of **3am** (conversions of **2m**) were 68 (99), 54 (70), or 43 % (50 %), respectively.
- [11] a) K. Koszinowski, P. Böhler, *Organometallics* **2009**, *28*, 100–110; b) K. Koszinowski, P. Böhler, *Organometallics* **2009**, *28*, 771–779.
- [12] Although we are not certain why butylzinc reagents (BuZnI<sub>2</sub>Lil) prepared by transmetalation (Table 1, entry 5) and a redox process followed by addition of Lil (Table 1, entry 7) show different reactivities, the latter reagent, relative to the former reagent, possibly cannot attain sufficient affinity between BuZnI and Lil to promote the coupling efficiently.
- [13] Treatment of the crude product with NaOMe in MeOH at 25 °C for 6 h and then with MeOH/HCl at 25 °C for 36 h gave methyl 4-butylbenzoate (**3as'**).
- [14] In the carbon–carbon bond-forming step, Li<sup>+</sup> possibly works as a Lewis acid toward the iodine of the [I–Ar]<sup>•–</sup> anion radical to promote its elimination as I<sup>•</sup>. In the monoethylation of tetrafluoroethene with diethylzinc, Lil is used as an effective additive in which Li<sup>+</sup> is considered to work as a Lewis acid toward fluorine to promote its elimination as F<sup>•</sup>: a) M. Ohashi, R. Kamura, R. Doi, S. Ogoshi, *Chem. Lett.* **2013**, *42*, 933–935; for a review of effects of lithium salts, see: b) D. Seebach, A. K. Beck, A. Studer, in: *Modern Synthetic Methods* (Eds.: B. Ernst, C. Leumann), Helvetica Chimica Acta/VCH, Basel/Weinheim, Germany, **1995**, vol. 7, p. 1–178.
- [15] a) A. N. Abeywickrema, A. L. J. Beckwith, *J. Chem. Soc., Chem. Commun.* **1986**, 464–465; b) H. Yasuda, Y. Uenoyama, O. Nobuta, S. Kobayashi, I. Ryu, *Tetrahedron Lett.* **2008**, *49*, 367–370.
- [16] DFT calculation on the Grignard aryl–aryl cross-coupling (ref.<sup>[2]</sup>) implies that the coupling proceeds through an aryl radical intermediate in a unique situation. B. E. Haines, O. Wiest, *J. Org. Chem.* **2014**, *79*, 2771–2774.
- [17] PAT is known to decompose into Ph<sup>•</sup>, N<sub>2</sub>, and Ph<sub>3</sub>C<sup>•</sup> in chlorobenzene at 45 °C (t<sub>1/2</sub> = 2.6 h): a) G. A. Russell, R. F. Bridger, *Tetrahedron Lett.* **1963**, *4*, 737–740; b) R. G. Kryger, J. P. Lorand, N. R. Stevens, N. R. Herron, *J. Am. Chem. Soc.* **1977**, *99*, 7589–7600; c) T. Suehiro, A. Suzuki, Y. Tsuchida, J. Yamazaki, *Bull. Chem. Soc. Jpn.* **1977**, *50*, 3324–3328.

- [18] Alkenyl radicals are known to isomerize readily to give a stereoisomeric mixture, see: a) C. Galli, P. Gentili, A. Guarnieri, Z. Rappoport, *J. Org. Chem.* **1996**, *61*, 8878–8884; b) C. Galli, A. Guarnieri, H. Koch, P. Men-carelli, Z. Rappoport, *J. Org. Chem.* **1997**, *62*, 4072–4077; see also ref.<sup>[4]</sup>
- [19] The possibility that alkylarenes are obtained through iodine–zinc exchange followed by nucleophilic substitution between the resulting aryl-zincs and alkyl iodides is excluded by the following experiment. Treatment of 1-iododecane with PhZnI·2LiI (1.0 equiv.) in THF/diglyme/Bu<sub>2</sub>O (2.4:2.4:1) at 110 °C for 24 h hardly gave decylbenzene, whereas 1-iododecane was converted (37 % conversion) into decane and 1-decene in yields of 14 and 6 %, respectively. For the production of alkylarenes from alkyllithiums and aryl bromides through bromine–lithium exchange followed by nucleophilic substitution, see: R. E. Merrill, E. Negishi, *J. Org. Chem.* **1974**, *39*, 3452–3453.
- [20] Additional experiments show that aryl and alkyl radicals, which would be generated from aryl iodides and alkylzinc reagents, respectively, are not intermediates leading to the coupling products. For details, see the Supporting Information.

---

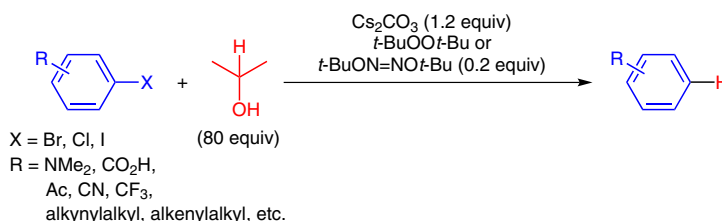
Received: March 24, 2016  
Published Online: June 10, 2016

# Reduction of Aryl Halides into Arenes with 2-Propanol Promoted by a Substoichiometric Amount of a *tert*-Butoxy Radical Source

Ryota Ueno<sup>a</sup>  
Takashi Shimizu<sup>a</sup>  
Eiji Shirakawa<sup>a,b</sup>

<sup>a</sup> Department of Chemistry, Graduate School of Science, Kyoto University, Kyoto, Kyoto 606-8502, Japan

<sup>b</sup> Department of Applied Chemistry for Environment, School of Science and Technology, Kwansei Gakuin University, Sanda, Hyogo 669-1337, Japan  
eshirakawa@kwansei.ac.jp



Received: 01.12.2015

Accepted after revision: 11.01.2016

Published online: 27.01.2016

DOI: 10.1055/s-0035-1561342; Art ID: st-2015-r0932-c

**Abstract** Aryl halides are reduced into the corresponding arenes in high yields, using 2-propanol, cesium carbonate, and di-*tert*-butyl peroxide (or di-*tert*-butyl hyponitrite) as a reductant/solvent, a base, and a radical initiator, respectively. This simple system reduces a wide variety of aryl bromides, chlorides, and iodides through single-electron-transfer mechanism with high functional-group tolerance.

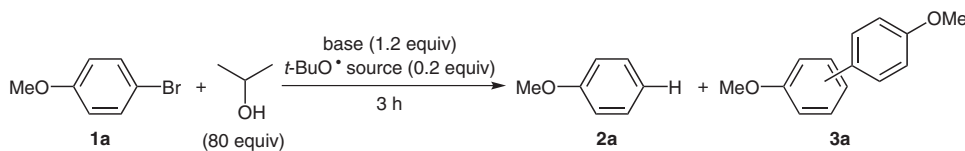
**Key words** reduction, radical chain mechanism, anion radical, ketyl, *tert*-butoxy radical

Reduction of aryl halides (ArX) into arenes (ArH) is an important transformation not only in organic synthesis but also in environmental protection since several harmful halogen-containing compounds (e.g., dioxins, polychlorobiphenyls) can be detoxified.<sup>1,2</sup> Reduction using a combination of a hydride source and a transition-metal catalyst such as palladium is one of the most typical methods for the reduction.<sup>3</sup> Although the transition-metal-catalyzed reductions achieve high tolerance towards various functional groups, it suffers from high cost of transition-metal catalysts and incompatibility with carbon–carbon unsaturated bonds. On the other hand, single-electron reduction is also effective for activation of ArX, in particular for those having a relatively low-lying LUMO. The successive elimination of X<sup>−</sup> from the resulting anion radical, [ArX]<sup>•−</sup>, gives Ar<sup>•</sup>, which is readily reduced into ArH by a hydrogen donor. Bunnett and co-workers reported such a method using NaOMe and K<sub>2</sub>S<sub>2</sub>O<sub>8</sub>, where formaldehyde ketyl generated through hydrogen abstraction from NaOMe by SO<sub>4</sub><sup>•−</sup> is considered to act as a single-electron reductant toward ArX and to be regenerated through hydrogen abstraction from NaOMe by Ar<sup>•</sup>.<sup>4</sup> However, the method employs a large excess amount of NaOMe and is applied merely to aryl iodides but not to

bromides and chlorides. Here we report a simple reduction system consisting of 2-propanol, Cs<sub>2</sub>CO<sub>3</sub>, and a *t*-BuO<sup>•</sup> source,<sup>5</sup> where aryl halides including bromides and chlorides are converted into the corresponding arenes with high functional-group tolerance.

One of the most effective protocols thus far examined is shown in entry 1 of Table 1. Treatment of 4-bromoanisole (**1a**) with Cs<sub>2</sub>CO<sub>3</sub> (1.2 equiv) and *t*-BuOO*t*-Bu (0.2 equiv) in 2-propanol (80 equiv) at 120 °C for three hours gave anisole (**2a**) in 97% yield, where (*p*-methoxyphenyl)anisoles (**3a**) were produced as a regioisomeric mixture (*o*/*m*/*p* = 60:40:<1) in 0.4% yield. Bisanisoles **3a** are most likely to be produced through homolytic aromatic substitution on **1a** by *p*-methoxyphenyl radical with H<sup>•</sup> followed by reduction of the bromoarene moieties.<sup>6</sup> No reduction took place at 50 °C, at which temperature there is little homolysis of *t*-BuOO*t*-Bu, or in the absence of *t*-BuOO*t*-Bu.<sup>7</sup> In contrast, even at 50 °C, the reduction took place by use of *t*-BuON=NO*t*-Bu, which readily undergoes thermal homolysis at this temperature to give *t*-BuO<sup>•</sup> and N<sub>2</sub> (Table 1, entry 4).<sup>8</sup> All these results show that *t*-BuO<sup>•</sup> plays a crucial role in the reduction. The reaction in a decreased amount (30 equiv) of 2-propanol retarded the reduction and increased generation of **3a** to 0.4% (Table 1, entry 5), whereas use of an increased amount (2.4 equiv) of Cs<sub>2</sub>CO<sub>3</sub> considerably suppress formation of **3a** to 0.2% (Table 1, entry 6). Use of other alkali metal carbonates was much less effective (Table 1, entries 7 and 8). Although the conditions in entry 4 (Table 1) scored a yield comparable to those in entry 1, we chose entry 1 as standard conditions because *t*-BuOO*t*-Bu is more readily available than *t*-BuON=NO*t*-Bu.

The protocol shown in entry 1 of Table 1 is applicable to reduction of various aryl bromides, chlorides, and iodides into the corresponding arenes.<sup>9</sup> Phenyl bromides having no or alkyl substituents are reduced in high yields by treatment of Cs<sub>2</sub>CO<sub>3</sub> (1.2 equiv) and *t*-BuOO*t*-Bu (0.2 equiv) in 2-

**Table 1** Reduction of 4-Bromoanisole<sup>a</sup>

Entry	Base (equiv)	<i>t</i> -BuO <sup>•</sup> source	Temp (°C)	Conv. of <b>1a</b> (%) <sup>b</sup>	Yield of <b>2a</b> (%) <sup>b</sup>
1	Cs <sub>2</sub> CO <sub>3</sub> (1.2)	<i>t</i> -BuOOT-Bu	120	>99.9	97
2	Cs <sub>2</sub> CO <sub>3</sub> (1.2)	<i>t</i> -BuOOT-Bu	50	<0.1	<0.1
3	Cs <sub>2</sub> CO <sub>3</sub> (1.2)	none	120	<0.1	<0.1
4	Cs <sub>2</sub> CO <sub>3</sub> (1.2)	<i>t</i> -BuON=NO <i>t</i> -Bu	50	>99.9	96
5 <sup>c</sup>	Cs <sub>2</sub> CO <sub>3</sub> (1.2)	<i>t</i> -BuOOT-Bu	120	90	82
6	Cs <sub>2</sub> CO <sub>3</sub> (2.4)	<i>t</i> -BuOOT-Bu	120	>99.9	99
7	K <sub>2</sub> CO <sub>3</sub> (1.2)	<i>t</i> -BuOOT-Bu	120	20	19
8	Na <sub>2</sub> CO <sub>3</sub> (1.2)	<i>t</i> -BuOOT-Bu	120	2	0.5

<sup>a</sup> The reaction was carried out under a nitrogen atmosphere for 3 h using 4-bromoanisole (**1a**, 82 mg, 0.25 mmol), 2-PrOH (1.5 mL, 0.020 mol), a base (0.30 mmol), and *t*-BuO<sup>•</sup> source (0.050 mmol).

<sup>b</sup> Determined by GC using decane as an internal standard.

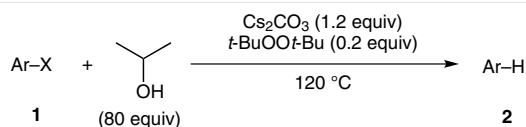
<sup>c</sup> A reduced amount (7.5 mmol) of 2-PrOH was used.

propanol (80 equiv) at 120 °C for 3 or 24 hours (Scheme 1, entries 1–3). Reduction of 2-bromonaphthalene (**1e**) under the standard conditions suffered from a relatively large amount (6%) of formation of 1,2'- and 2,2'-binaphthyls (**3e**), giving reduction product **2e** only in 85% yield (Scheme 1, entry 4). This must be due to high reactivities of **1e** and **2e** towards radicals, accepting addition of 2-naphthyl radical more readily than monocyclic benzene derivatives. Use of an increased amount (240 equiv) of 2-propanol suppressed the side reaction to an acceptable level (1%) and raised the yield of **2e** to 93% (Scheme 1, entry 5). In the reaction of 4-bromo-*N,N*-dimethylaniline (**1f**) under the standard conditions (24 h), a large amount (8%) of a dimer of **1f**, *N,N'*-dimethyl-*N,N'*-diphenylethylenediamine, was produced, probably through homocoupling of *N*-methyl-*N*-phenylaminomethyl radical. The side reaction was suppressed again by use of 240 equivalents of 2-propanol (Scheme 1, entry 6). The reduction is tolerant towards carboxylic acids and alkynes (Scheme 1, entries 7 and 8). Worthy of note is the stability of alkynes in this reaction as they are frequently incompatible with transition-metal-catalyzed reductions. Heteroaryl bromides are also reduced, though a larger amount (0.4 equiv) of *t*-BuOOT-Bu was required (Scheme 1, entries 9 and 10). As for hexabromobenzene (**1k**), all the bromine atoms are converted into hydrogen atoms, using appropriate amounts of the reagents (Scheme 1, entry 11). The reduction is applicable also to iodobenzene but is reluctant for chlorobenzene (8% yield with 13% conversion) (Scheme 1, entries 12 and 13), and thus selective reduction of aryl bromides over chlorides is possible (Scheme 1, entry 14). However, aryl chlorides are reduced when they have a low-lying LUMO as in the case with 3-chloropyridine (**1'm**)

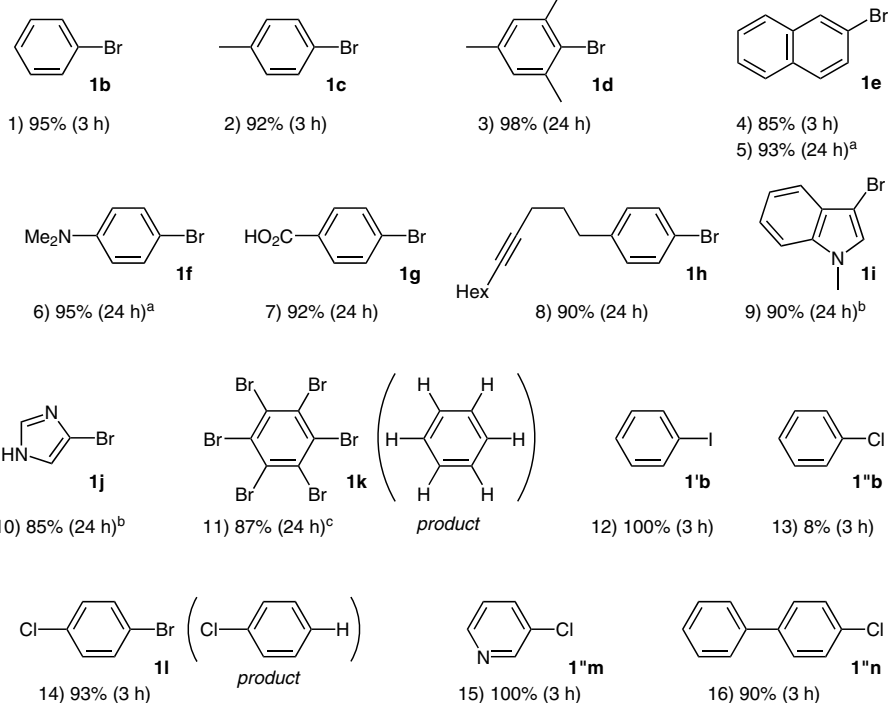
and 4-chlorobiphenyl (**1'n**), the LUMOs of which are lowered, respectively, by the electron-deficient character of the pyridine ring and a conjugating substituent (Scheme 1, entries 15 and 16). The result that a chlorine atom on biphenyl is removed shows that the reduction is a promising method to detoxify polychlorobiphenyls (PCB).<sup>1</sup>

The reduction of the aryl bromides shown in Scheme 2 under the standard conditions induced side reactions other than the biaryl formation. Thus, ketone (**1o**), trifluoromethyl (**1p**), cyano (**1q**), alkene (**1r**), and thiazole (**1s**) moieties suffered, respectively, from reduction into alcohol (**1o**), hydrodefluorination (**1p**), conversion into amide (**1q**), hydroxymethylation (**1r**), and nucleophilic aromatic substitution at 2-position (**1s**). All these side reactions are suppressed by lowering the reaction temperature from 120 °C to 50 °C by use of *t*-BuON=NO*t*-Bu as a *t*-BuO<sup>•</sup> source (cf. Table 1, entry 4), leading to high yields of the reduction products.

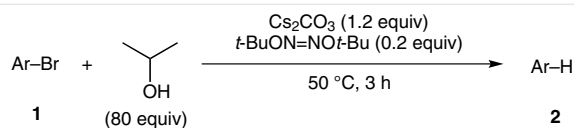
The reduction is considered to proceed through a mechanism similar to that proposed by Bunnett and co-workers.<sup>4</sup> As shown in Scheme 3, thermal homolysis of *t*-BuOOT-Bu gives *t*-BuO<sup>•</sup>, which abstracts H<sup>•</sup> from cesium isopropoxide (steps *a* and *b*). Single-electron transfer (SET) from the resulting acetone ketyl **I** to ArX **1** gives anion radical, Cs<sup>+</sup>[ArX]<sup>-</sup> **II**, which undergoes homolysis to give Ar<sup>•</sup> **III** and CsX (step *c* and *d*). Ar<sup>•</sup> **III** abstracts H<sup>•</sup> from cesium isopropoxide to be converted into reduction product **2** and regenerate ketyl **I** (step *e*). Otherwise, Ar<sup>•</sup> **III** reacts with ArX **1**, and in some cases also with ArH **2**, to give ArAr **3**. Thus, the selectivity for **2** over **3** should depend on reaction rates of step *e* and addition of Ar<sup>•</sup> to the aromatic rings. Actually, the selectivity is higher when concentration of cesium iso-



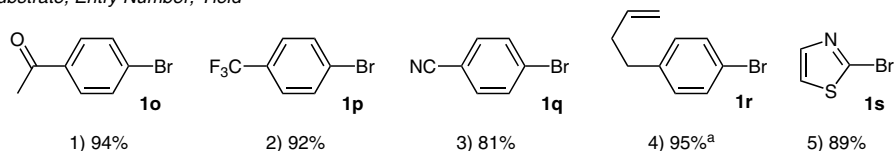
Substrate (Product), Entry Number, Yield, Time



**Scheme 1** Reduction of aryl halides using *t*-BuOOT-Bu as a radical initiator. *Reagents and conditions:* The reaction was carried out under a nitrogen atmosphere at 120 °C for 3 or 24 h using an aryl halide **1** (0.25 mmol), 2-PrOH (1.5 mL, 0.020 mol), Cs<sub>2</sub>CO<sub>3</sub> (0.30 mmol), and *t*-BuOOT-Bu (0.050 mmol). The yields were determined by GC using decane as an internal standard. For products having a relatively high boiling point, the yields of the isolated products are given (entries 7, 8, 10, and 16). <sup>a</sup> 2-PrOH (4.6 mL, 60 mmol) was used. <sup>b</sup> *t*-BuOOT-Bu (0.10 mmol) was used. <sup>c</sup> *t*-BuOOT-Bu (0.20 mmol) and Cs<sub>2</sub>CO<sub>3</sub> (1.8 mmol) were used.



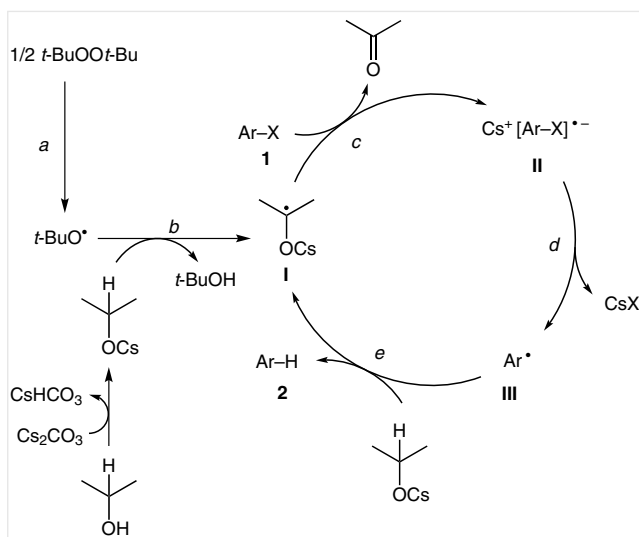
Substrate, Entry Number, Yield



**Scheme 2** Reduction of aryl halides using *t*-BuON=NOt-Bu as a radical initiator. *Reagents and conditions:* The reaction was carried out under a nitrogen atmosphere at 50 °C for 3 h using an aryl bromide **1** (0.25 mmol), 2-PrOH (1.5 mL, 0.020 mmol), Cs<sub>2</sub>CO<sub>3</sub> (0.30 mmol), and *t*-BuON=NOt-Bu (0.050 mmol). The yields were determined by GC using decane as an internal standard. <sup>a</sup> 2-PrOH (4.6 mL, 60 mmol) was used.

proxide is higher (cf. Table 1, entries 1 vs. 5 and 6 vs. 1). The reactivity order of aryl halides is fairly consistent with SET mechanism (step c): aryl iodides and bromides are more re-

active than aryl chlorides, which are reduced only when their LUMO energy levels are lowered (cf. Scheme 1, entries 13, 15, and 16).



**Scheme 3** A plausible reaction mechanism

In conclusion, we have developed a simple method to reduce aryl halides into arenes with high functional-group tolerance, where a radical chain mechanism initiated by  $t\text{-BuO}^\bullet$  is operative, employing 2-propanol and  $\text{Cs}_2\text{CO}_3$  as a reductant/solvent and a base, respectively. This method is expected to be utilized for detoxification of harmful halogen-containing compounds such as PCB.

## Acknowledgment

This work has been supported financially in part by Grant-in-Aid for Challenging Exploratory Research (26620082 to E.S.). R.U. thanks the JSPS for a Research Fellowship for Young Scientists.

## Supporting Information

Supporting information for this article is available online at <http://dx.doi.org/10.1055/s-0035-1561342>.

## References and Notes

- (1) (a) Harrad, S.; Robson, M.; Hazrati, S.; Baxter-Plant, V. S.; Deplanche, K.; Redwood, M. D.; Macaskie, L. E. *J. Environ. Monit.* **2007**, *9*, 314. (b) Safe, S. H. *Crit. Rev. Toxicol.* **1994**, *85*, 131.
- (2) For overview on the methods to reduce aryl halides into arenes, see: Smith, M. B. *March's Advanced Organic Chemistry*; Wiley: Hoboken, **2013**, 7th ed., 647–648.
- (3) For a recent example, see: Bhattacharjya, A.; Klumphu, P.; Lipshutz, B. H. *Org. Lett.* **2015**, *17*, 1122; and references cited therein.
- (4) (a) Bunnett, J. F.; Wamser, C. C. *J. Am. Chem. Soc.* **1967**, *89*, 6712. (b) Tomaselli, G. A.; Cui, J.-J.; Chen, Q.-F.; Bunnett, J. F. *J. Chem. Soc., Perkin Trans. 2* **1992**, *9*. (c) Tomaselli, G. A.; Bunnett, J. F. *J. Org. Chem.* **1992**, *57*, 2710. (d) Bunnett, J. F. *Acc. Chem. Res.* **1992**, *25*, 2.
- (5) A combination of  $\text{LiAlH}_4$  as a reductant with  $t\text{-BuOO}t\text{-Bu}$  as a radical initiator is used for reduction of aryl halides under photoirradiation, see: (a) Beckwith, A. L. J.; Goh, S. H. *J. Chem. Soc., Chem. Commun.* **1983**, 905. (b) Beckwith, A. L. J.; Goh, S. H. *J. Chem. Soc., Chem. Commun.* **1983**, 907.
- (6) *p*-Methoxyphenyl radical possibly reacts also with anisole (**2a**). However, it would give *p*-(*p*-methoxyphenyl)anisole in addition to *ortho* and *meta* isomers. No generation of the *para* isomer shows that such a reaction hardly took place under the reaction conditions.
- (7) The half-life of  $t\text{-BuOO}t\text{-Bu}$  is reported to be more than 1000 h even at 80 °C. See: Walling, C. *Tetrahedron* **1985**, *41*, 3887.
- (8)  $t\text{-BuON}=\text{NO}t\text{-Bu}$  is reported to undergo decomposition into  $t\text{-BuO}^\bullet$  and  $\text{N}_2$  with  $t_{1/2} = 29$  min at 65 °C. See: Kiefer, H.; Traylor, T. G. *Tetrahedron Lett.* **1966**, *7*, 6163.
- (9) **General Procedure**  
To a 3 mL vial equipped with a stir bar in a glove box were added successively an aryl halide **1** (0.25 mmol), 2-PrOH (1.5 mL, 0.020 mol),  $\text{Cs}_2\text{CO}_3$  (97.7 mg, 0.30 mmol), and  $t\text{-BuOO}t\text{-Bu}$  (8.8 mg, 0.050 mmol). The vial was taken out of the glove box and stirred at 120 °C for 3 or 24 h. Decane was added to the reaction mixture as an internal standard for GC analysis. After dilution with EtOAc (1.0 mL), an aliquot was subjected to GC analysis. For products having a boiling point that is high enough not to be lost in evacuation process, addition of  $\text{H}_2\text{O}$  (20 mL) was followed by extraction with EtOAc ( $3 \times 20$  mL). The combined organic layer was dried over  $\text{MgSO}_4$ , filtered, and concentrated in vacuo. The residue was subjected to silica gel chromatography (PTLC) to give the corresponding arene **2**.

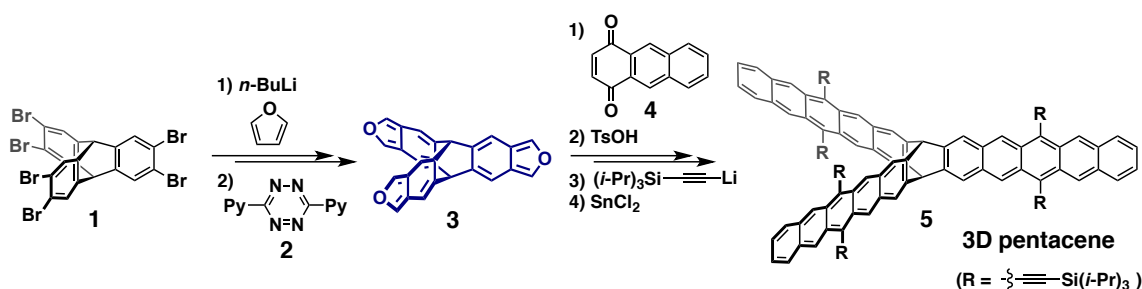
## Syntheses of High-Ordered Iptycene Derivatives

Sunna Jung, Toshiyuki Hamura

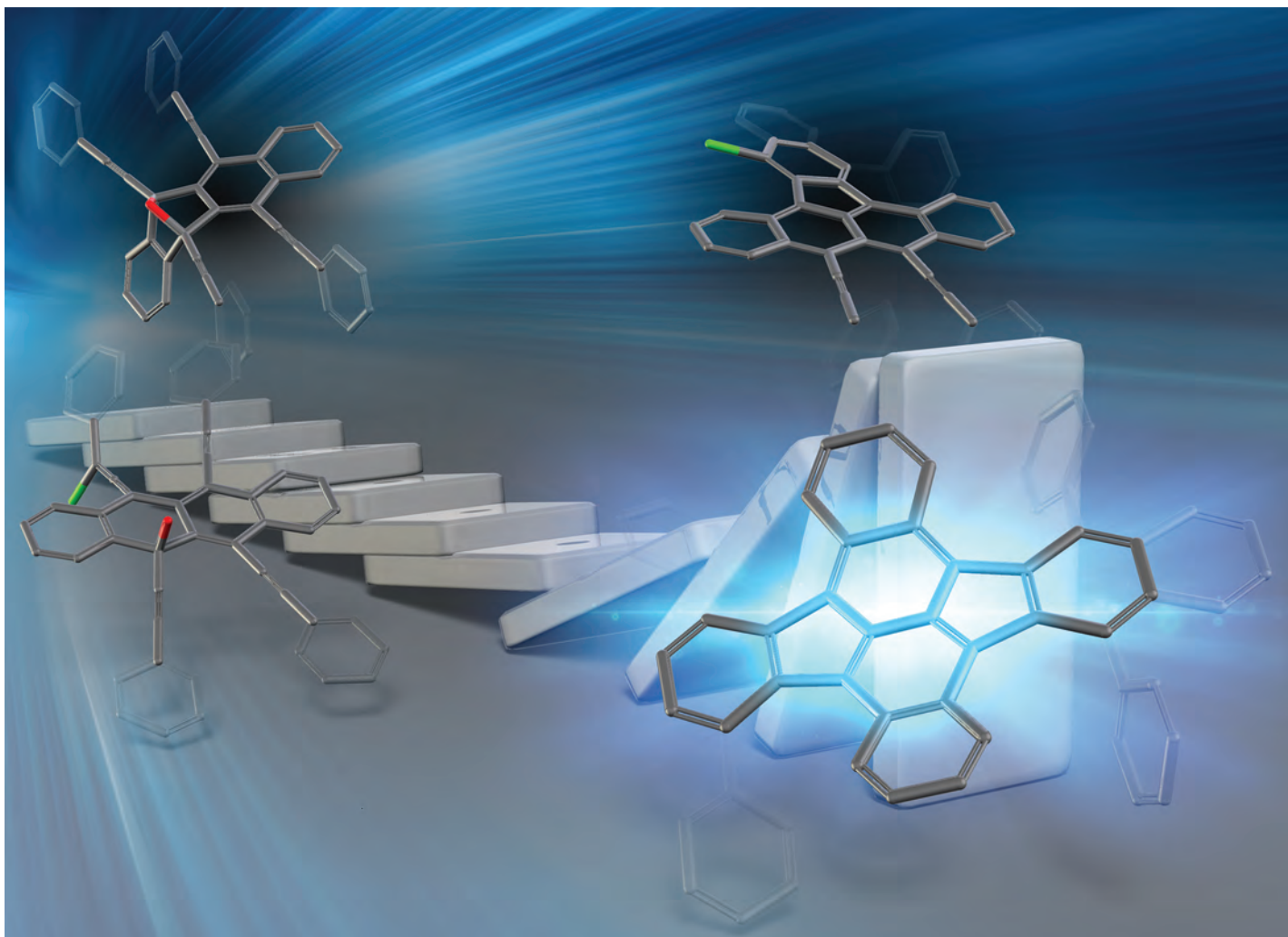
School of Science and Technology, Kwansai Gakuin University  
2-1 Gakuen, Sanda, Hyogo, 669-1337, Japan  
(thamura@kwansai.ac.jp)

Iptycenes are highly condensed aromatic compounds, in which several aromatic rings are fused to bicyclo[2.2.2]octatriene core in three directions, and therefore they have potential utilities as organic materials derived from their unique structure. In spite of these attractive features, syntheses of high-ordered iptycene derivatives are quite limited due to the lack of appropriate building blocks and/or annulation method to construct 3D polycyclic structures. In this context, we previously developed a synthetic access to functionalized polyacene derivatives by using isobenzofurans as a reactive platform.<sup>1-4</sup> Along these lines, we now report efficient syntheses of high-ordered iptycene derivatives including 3D pentacene **5** via three-fold cycloadditions of propeller-shaped isobenzofuran **3**.

Starting from hexabromotriptycene **1**, tris-isobenzofuran **3** was easily prepared by three-fold [4+2] cycloadditions of tris-aryne, and subsequent treatment of the cycloadduct with tetrazine **2**. This highly reactive species **3**, thus obtained, underwent three-fold [4+2] cycloadditions with anthraquinone **4** to give the cycloadduct, which was converted to 3D pentacene **5** by nucleophilic additions of silylethynyl lithium, and the reductive aromatization of the resulting hexa-alcohol. Several interesting properties including singlet fission of this new class of iptycene derivatives will be also described in the presentation.



1. Hamura, T. *et al. Org. Lett.* **2014**, *16*, 286–289.
2. Hamura, T. *et al. Org. Lett.* **2015**, *17*, 3094–3097.
3. Hamura, T. *et al. Chem. Eur. J.* **2018**, *24*, 14034–14038.
4. Hamura, T. *et al. Chem. Eur. J.* **2018**, *24*, 18886–18889.

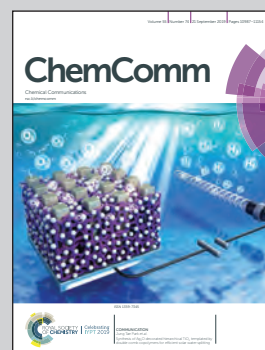


Showcasing research from Professor Hamura's laboratory,  
Department of Applied Chemistry for Environment,  
Graduate School of Science and Technology,  
Kwansei Gakuin University, Sanda, Japan.

Intramolecular benzoallene–alkyne cycloaddition initiated  
by site-selective  $S_N2'$  reaction of epoxytetracene en route  
to  $\pi$ -extended pyracylene

A hydrogen halide promoted cascade reaction of epoxytetracene  
to halo-benzoindenotetracene including a benzoallene  
intermediate was developed. The remaining two alkynyl groups  
in benzoindenotetracene were further reacted with  
norboreadiene or arylamine through transition metal-catalyzed  
cyclization to give  $\pi$ -extended pyracylene derivatives.

As featured in:



See Toshiyuki Hamura et al.,  
*Chem. Commun.*, 2019, 55, 11021.

# CHEMISTRY

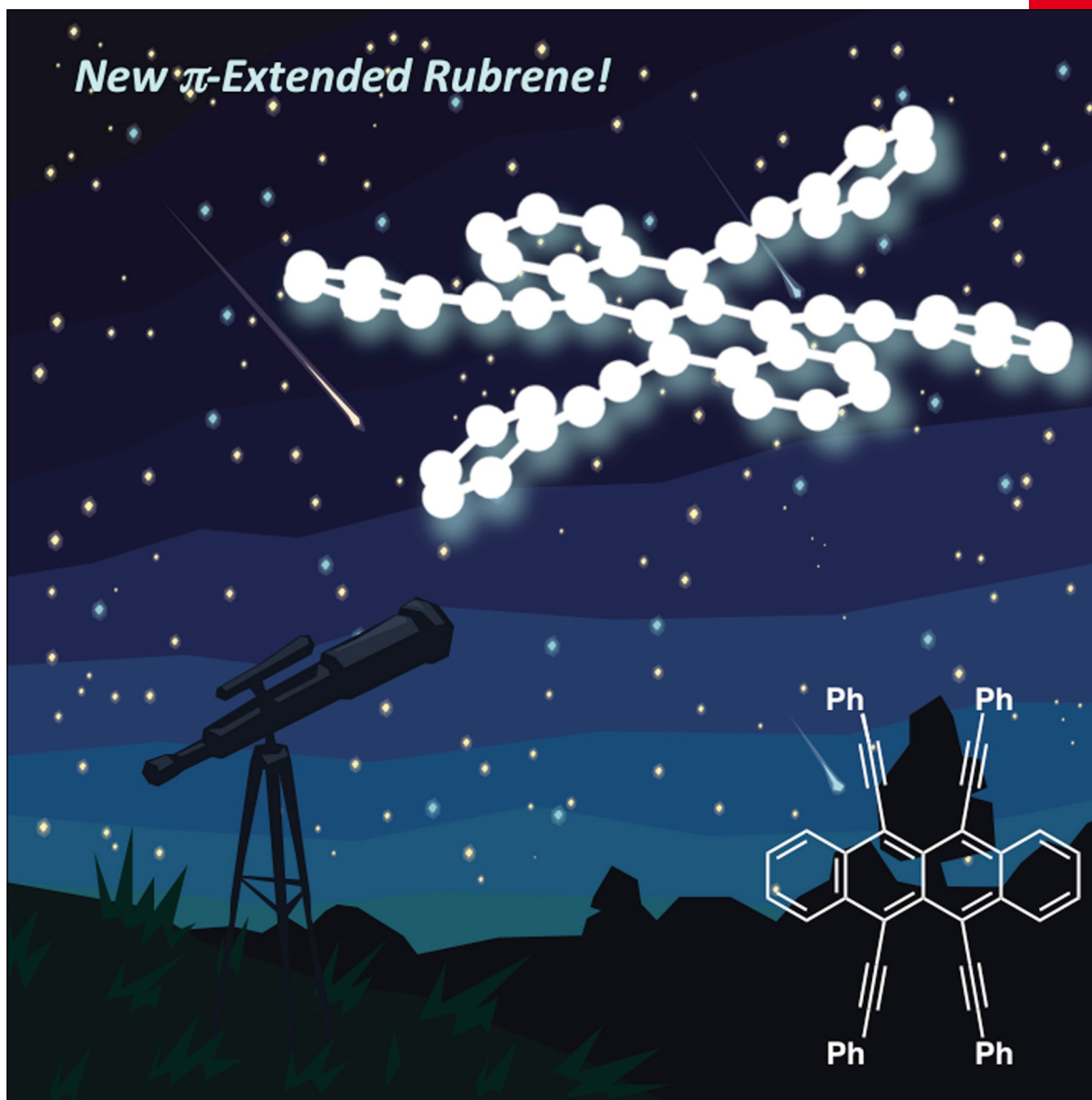
## A **European** Journal

www.chemeurj.org

A Journal of



2018-24/53



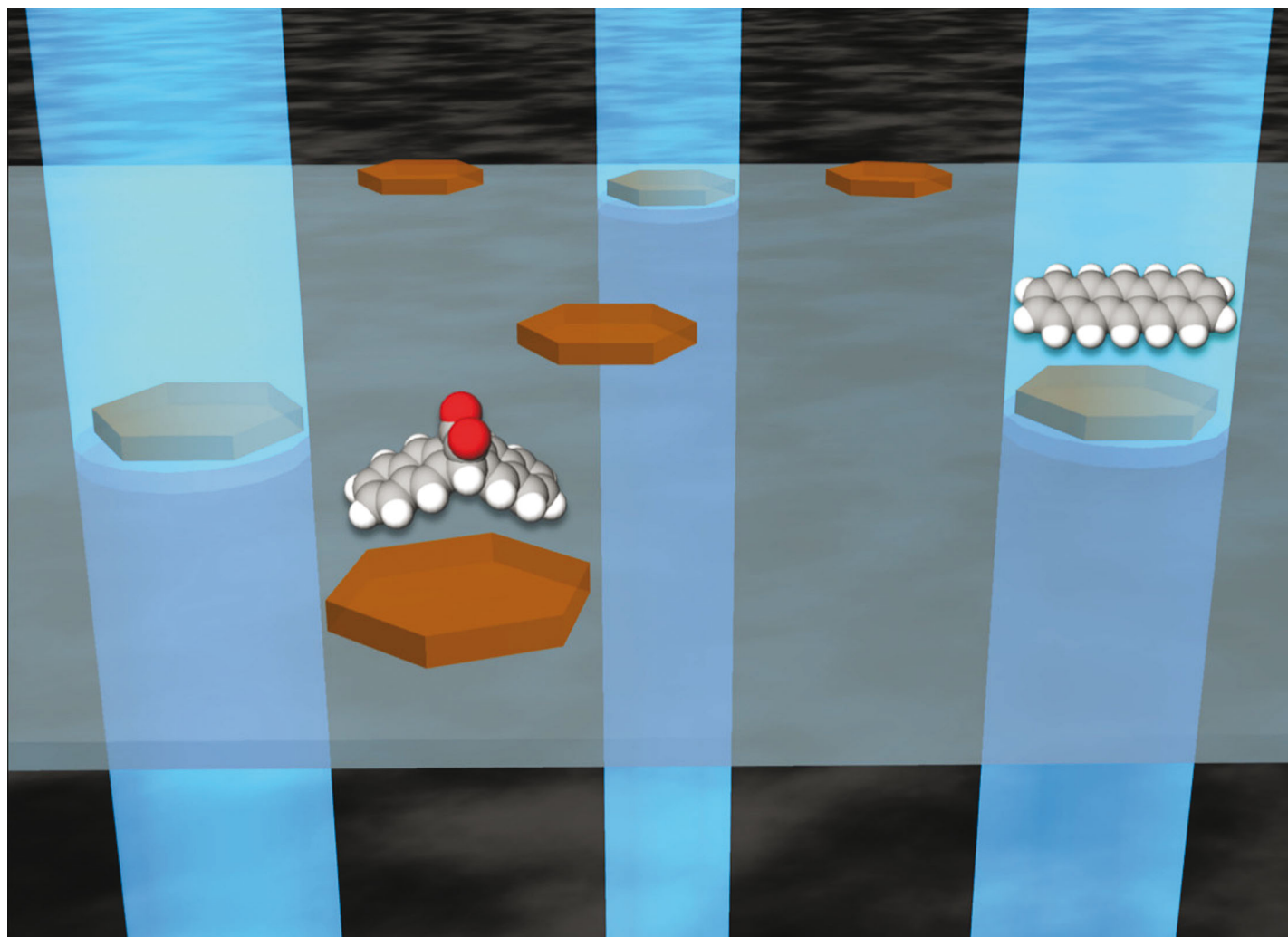
**Cover Feature:**

*T. Hamura et al.*

Tetrakis(phenylethynyl)tetracene: A New  $\pi$ -Extended Rubrene Derivative

Supported by





**Showcasing research from the group of Prof. Sadahiro Masuo at Kwasei Gakuin University, Japan**

**Photoconversion of 6,13- $\alpha$ -diketopentacene single crystals exhibiting light intensity-dependent morphological change**

Micrometre-sized single crystals of 6,13- $\alpha$ -diketopentacene exhibit a laser intensity-dependent morphological change with photoconversion into pentacene. Photoirradiation with a strong intensity resulted in hole formation in the crystal. Upon photoirradiation with a very low intensity, protruding pillar objects were observed on the crystal surface as visualized by atomic force microscopy. When a medium intensity was irradiated, destruction including separation and jumping of the crystal occurred. Our work provides important insights into stimuli-responsive crystal materials and could contribute to the construction of remotely controllable smart materials.

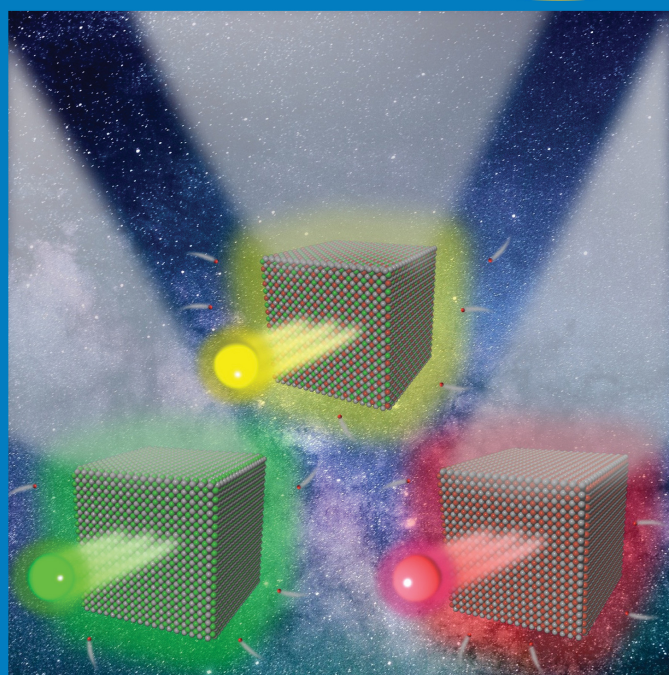
**As featured in:**



See Sadahiro Masuo *et al.*,  
*Phys. Chem. Chem. Phys.*,  
2019, **21**, 6348.

THE JOURNAL OF  
PHYSICAL CHEMISTRY  
*Letters*

January 16, 2020 | Volume 11, Number 2



 ACS Publications  
Most Trusted. Most Cited. Most Read.

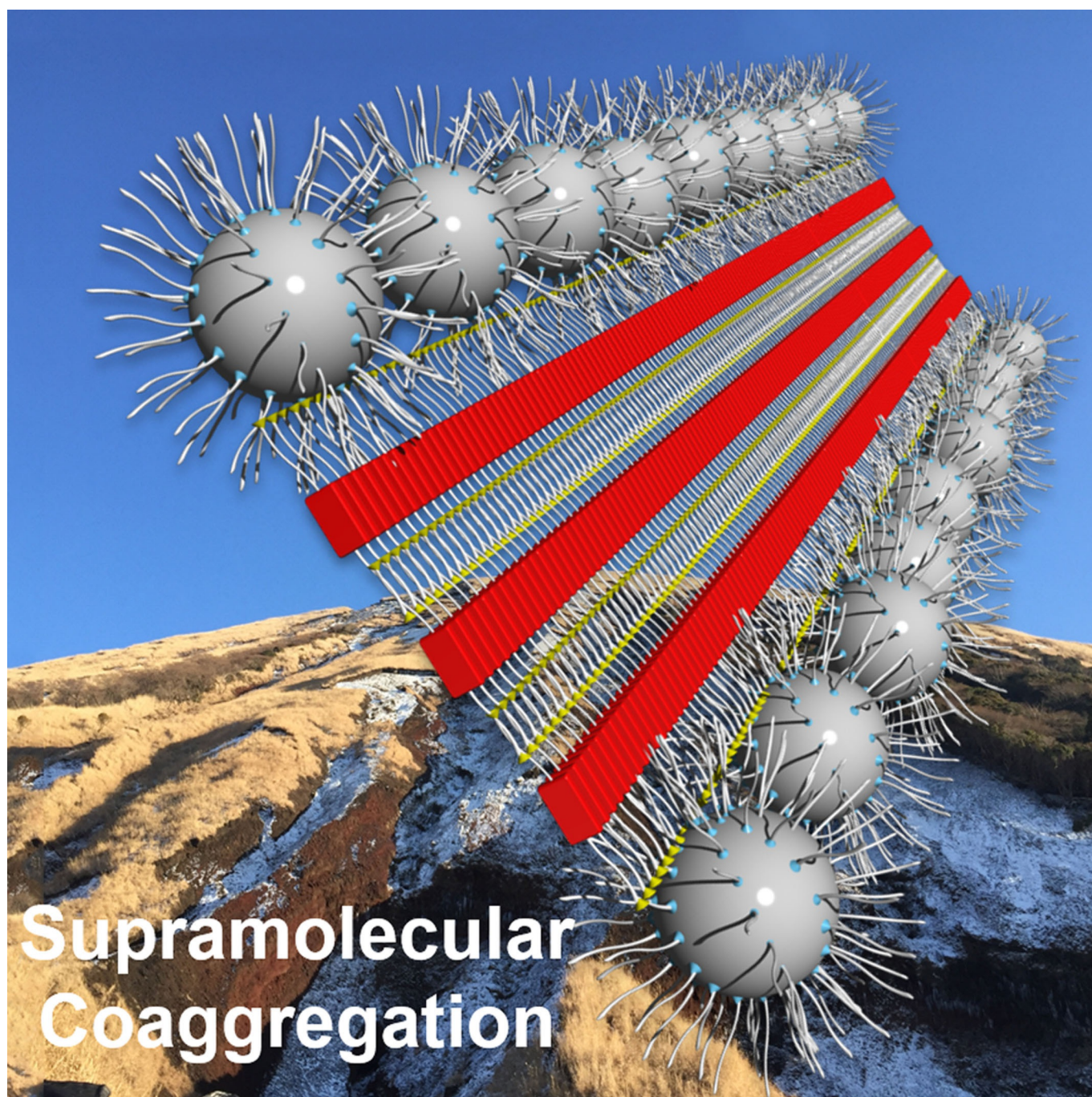
[www.acs.org](http://www.acs.org)

雜誌論文 1 8 Cover

■ Supramolecular Chemistry | *Hot Paper* |

## Colloidal Quantum Dot Arrangement Assisted by Perylene Bisimide Self-Assembly

Mitsuaki Yamauchi\* and Sadahiro Masuo\*[a]

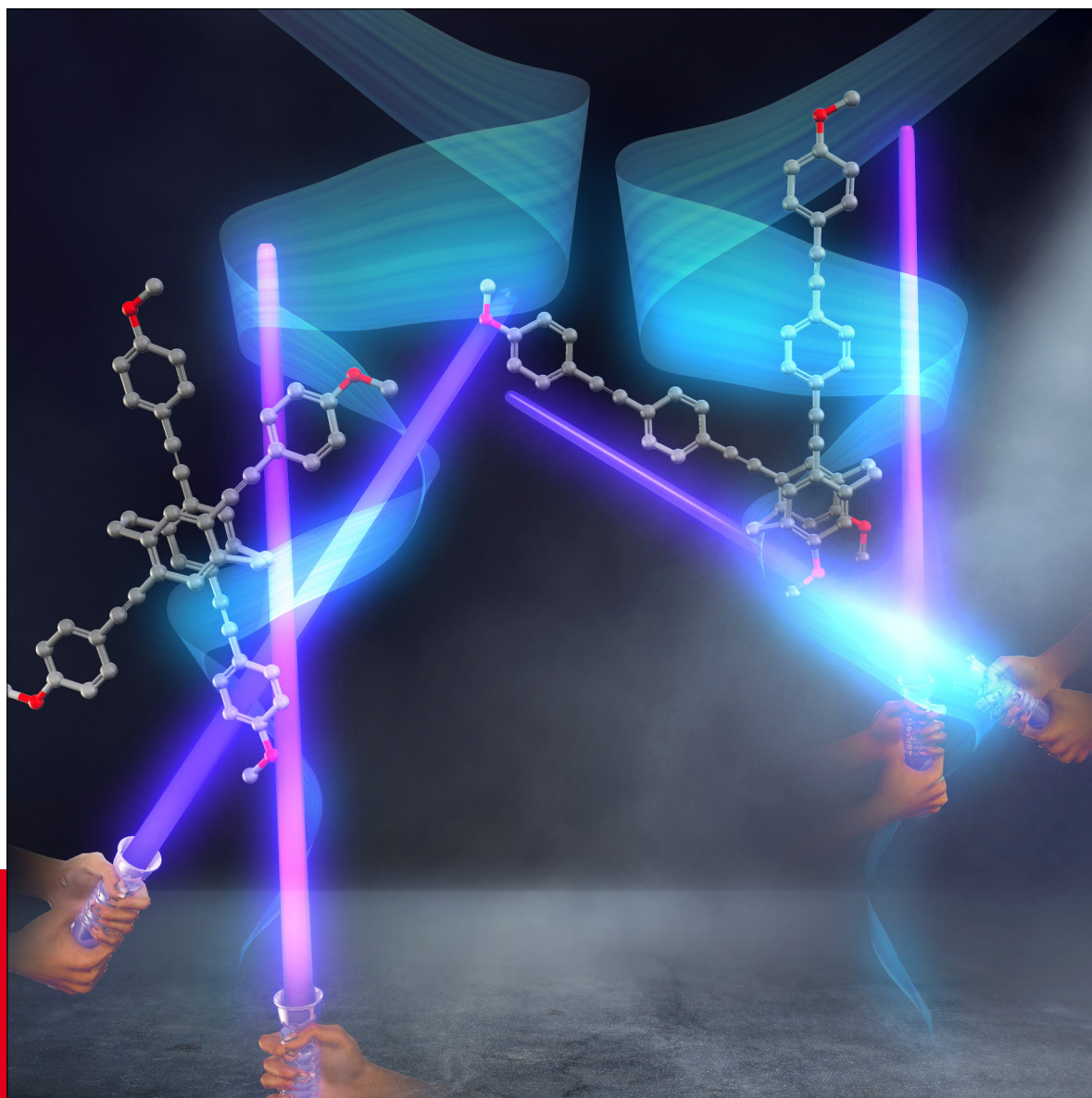


# CHEMISTRY

---

## AN **ASIAN** JOURNAL

[www.chemasianj.org](http://www.chemasianj.org)



**14/10**  
**2019**

A Journal of

**ACES**

Asian Chemical  
Editorial Society

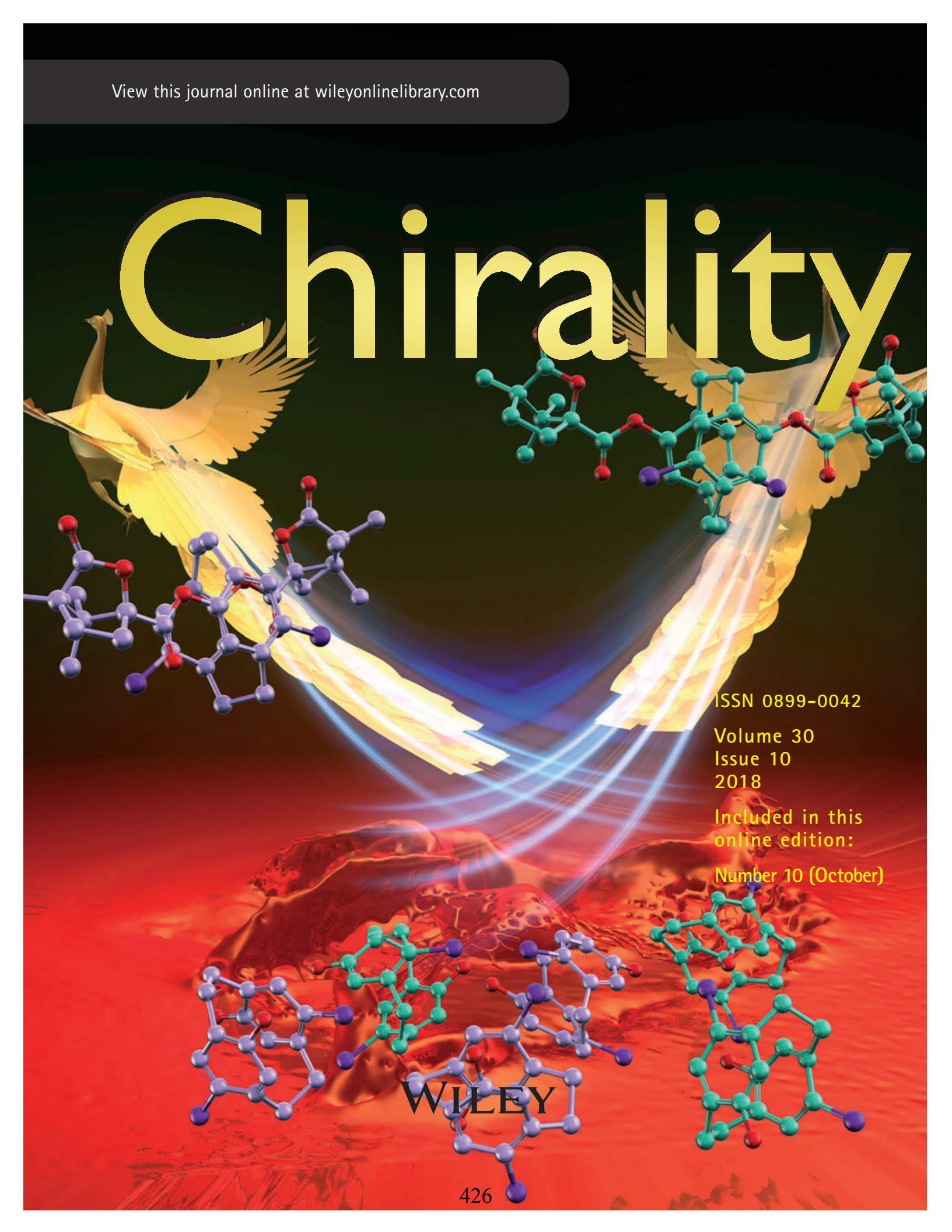
A sister journal of *Angewandte Chemie*  
and *Chemistry – A European Journal*

**Cover Feature:**

*Yasuhiro Morisaki et al.*  
Control of Circularly Polarized Luminescence by  
Orientation of Stacked  $\pi$ -Electron Systems

View this journal online at [wileyonlinelibrary.com](http://wileyonlinelibrary.com)

# Chirality



ISSN 0899-0042

Volume 30

Issue 10

2018

Included in this  
online edition:

Number 10 (October)

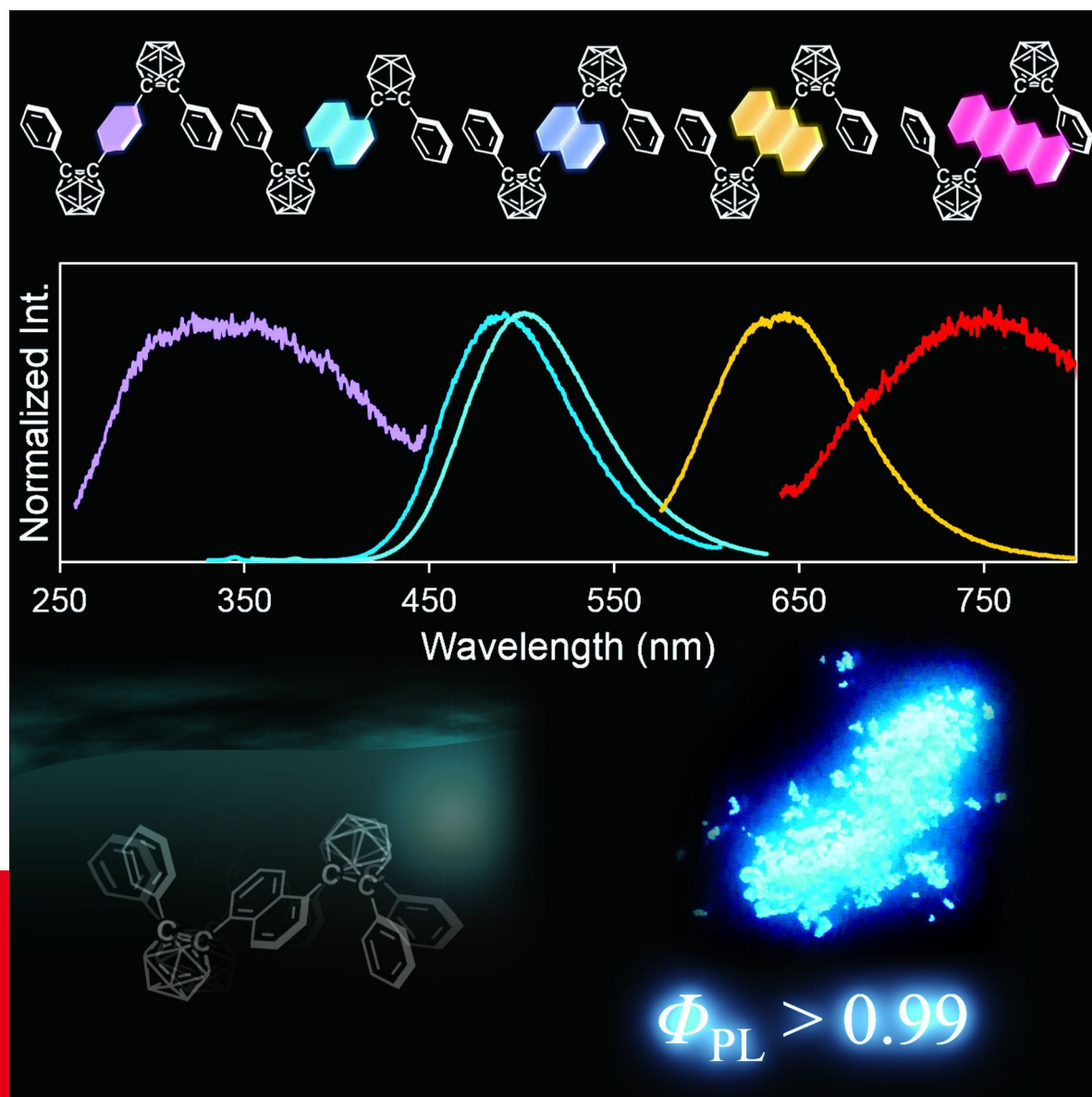
WILEY

# CHEMISTRY

---

## AN **ASIAN** JOURNAL

www.chemasianj.org



12/16  
2017

A Journal of

**ACES**

Asian Chemical  
Editorial Society

A sister journal of *Angewandte Chemie*  
and *Chemistry – A European Journal*

**Cover Picture:**

*Yoshiki Chujo et al.*

Luminescent Solid Materials Based  
on Bis-*o*-Carborane-Substituted Oligoacenes

# CHEMISTRY

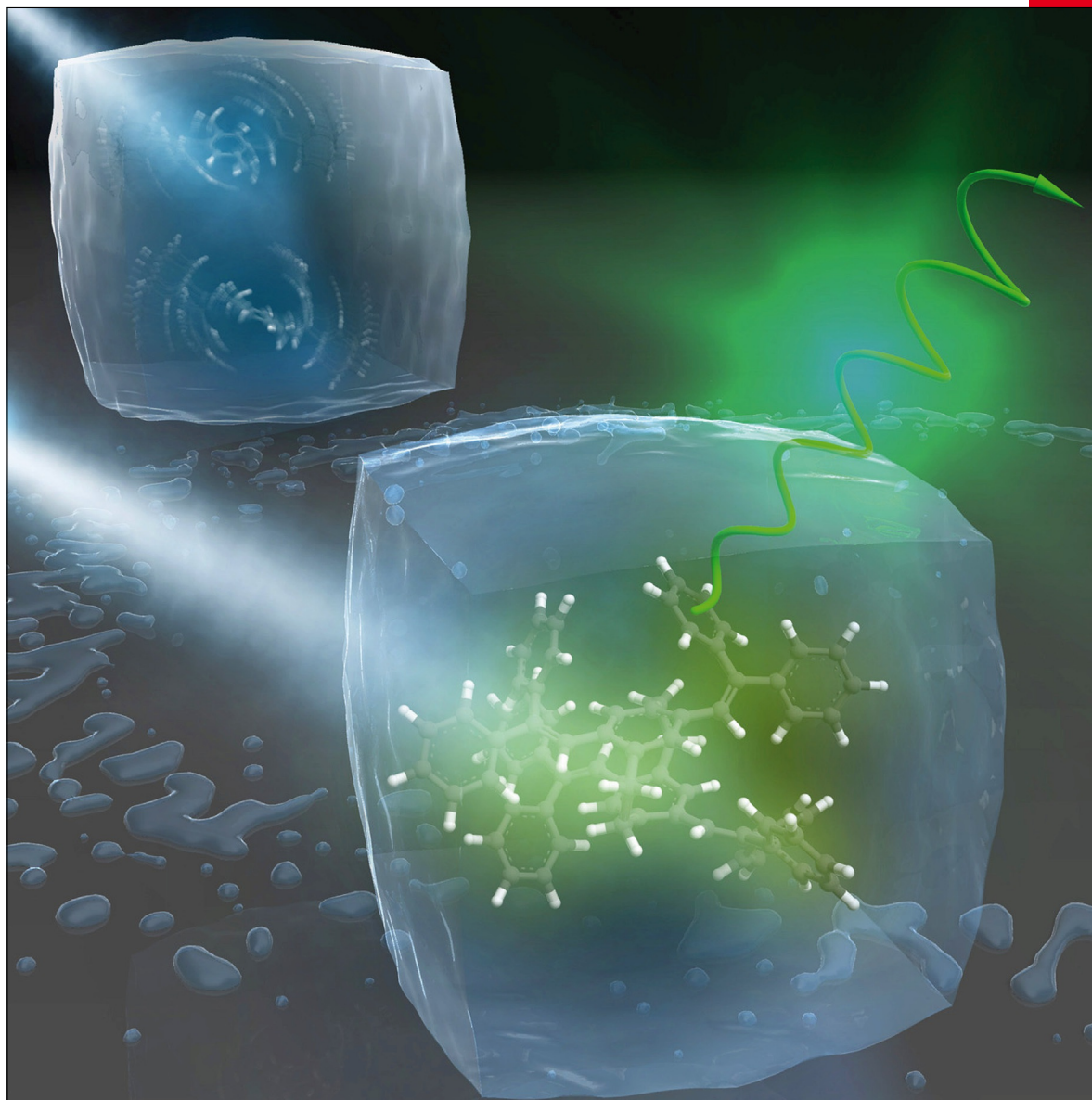
## A **European** Journal

www.chemeurj.org

A Journal of



2017-23/26



**Cover Picture:**

*Y. Morisaki, Y. Chujo et al.*

Optically Active Phenylethene Dimers Based on Planar Chiral Tetrasubstituted [2.2]Paracyclophane

Supported by

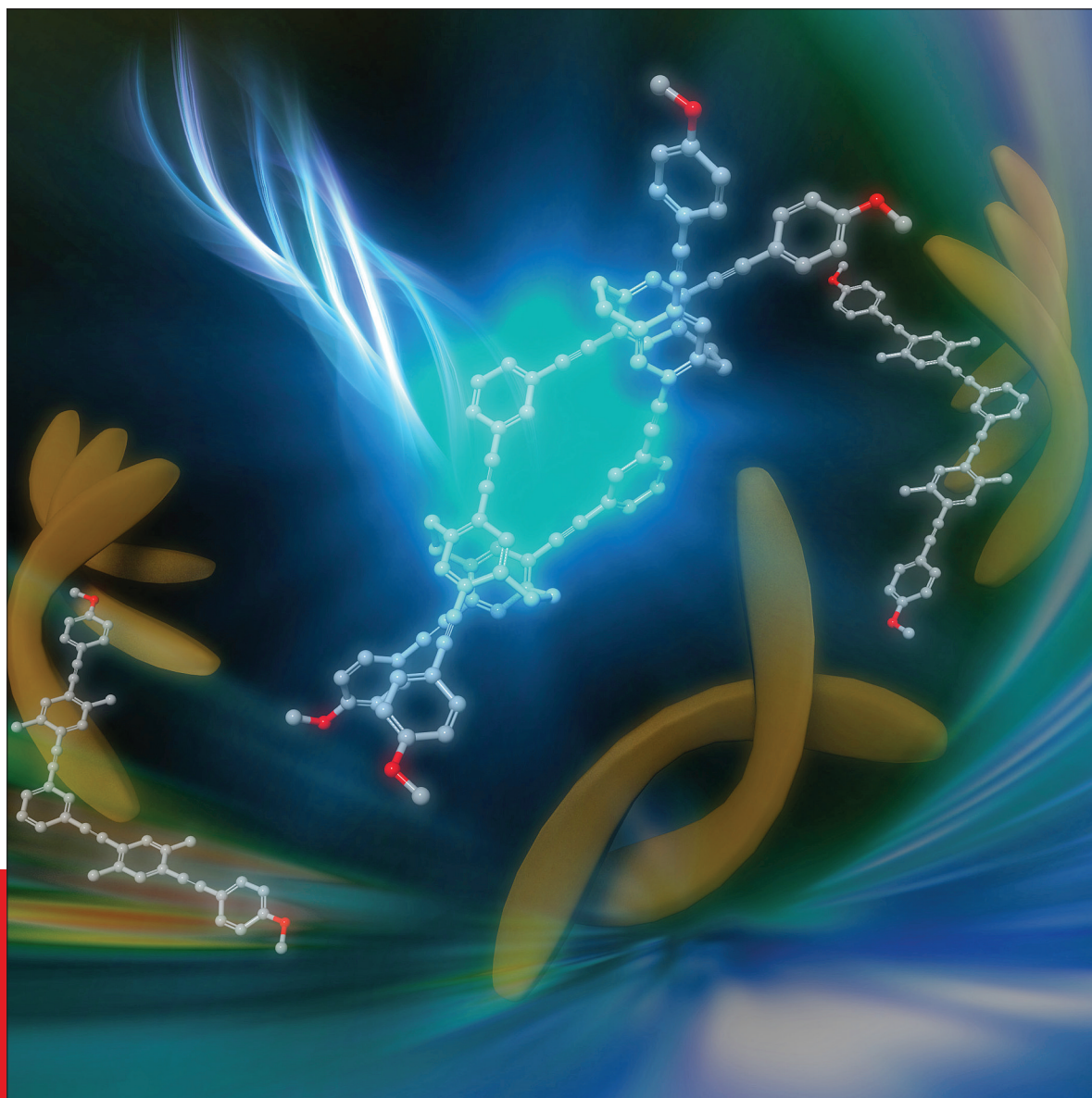


# CHEMISTRY

---

## AN **ASIAN** JOURNAL

[www.chemasianj.org](http://www.chemasianj.org)



**11/18**  
**2016**

**A Journal of**

**ACES**

Asian Chemical  
Editorial Society

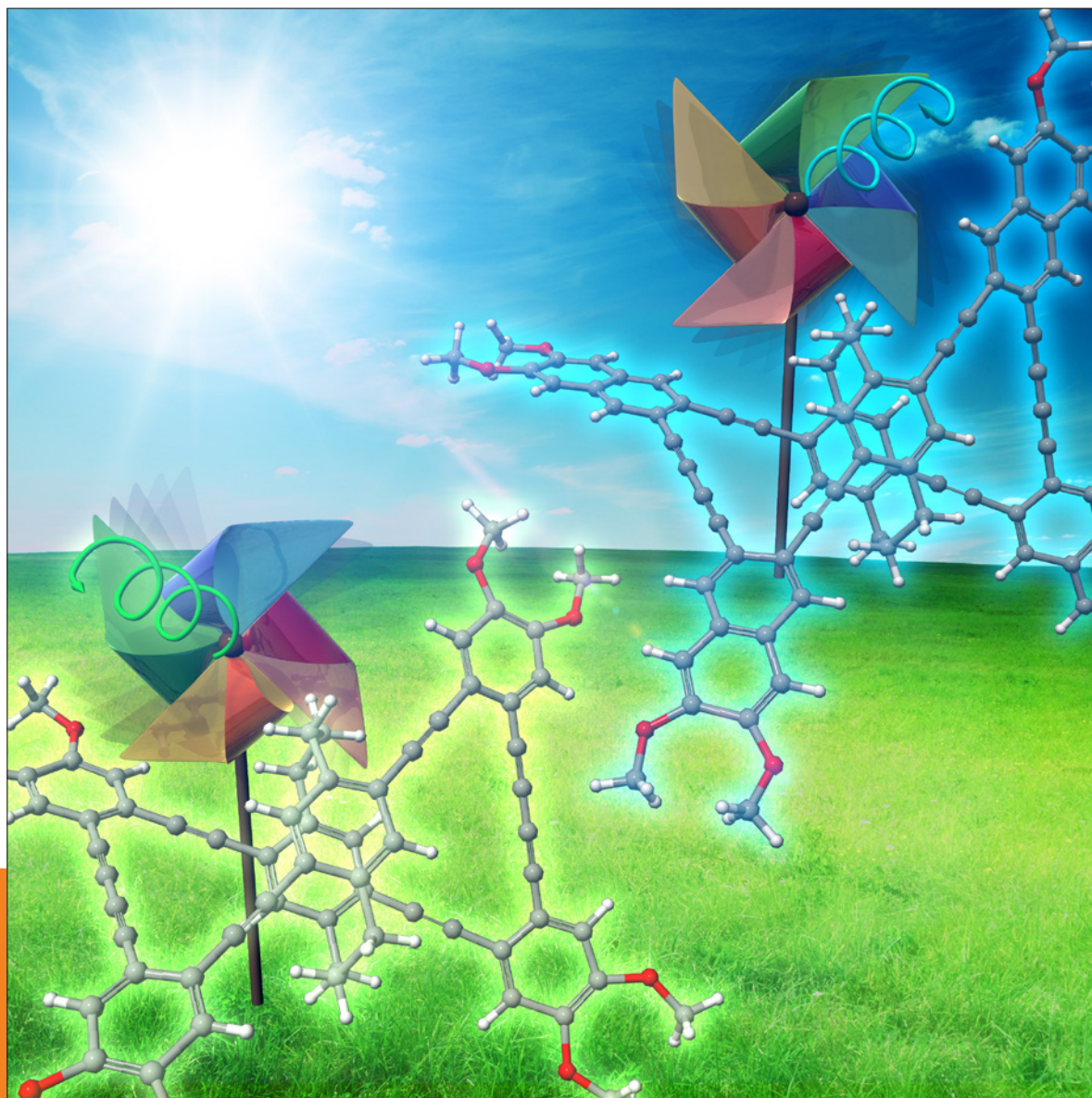
A sister journal of *Angewandte Chemie*  
and *Chemistry – A European Journal*

**Inside Cover:**

*Yasuhiro Morisaki, Yoshiki Chujo et al.*  
New Types of Planar Chiral [2.2]Paracyclophanes  
and Construction of One-Handed Double Helices

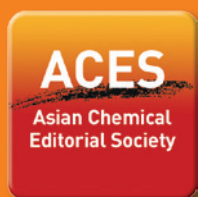
# ASIAN JOURNAL OF ORGANIC CHEMISTRY

www.AsianJOC.org



3/05  
2016

A Journal of



A sister journal of Chemistry – An Asian Journal  
and European Journal of Organic Chemistry

**Front Cover:**

*Y. Morisaki and Y. Chujo et al.*

Optically Active Cyclic Compounds Based  
on Planar Chiral [2.2]Paracyclophane with Naphthalene Units

# CHEMISTRY

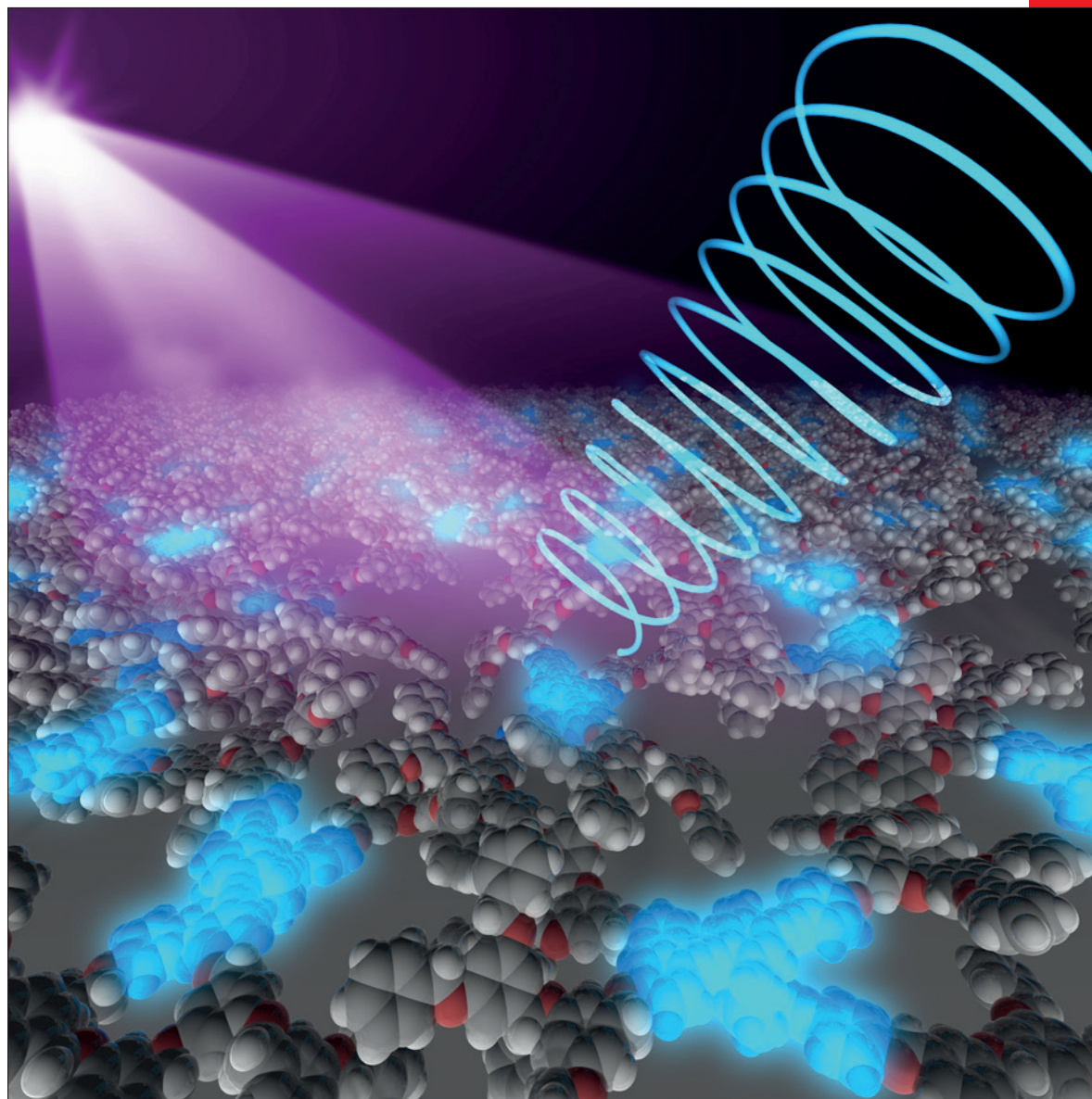
## A European Journal

A Journal of



www.chemeurj.org

2016-22/7



**Front Cover Picture:**

*Y. Morisaki, Y. Chujo et al.*

Synthesis of Optically Active, X-Shaped, Conjugated Compounds and Dendrimers Based on Planar Chiral [2.2]Paracyclophane, Leading to Highly Emissive Circularly Polarized Luminescence

Supported by

**ACES** Asian Chemical Editorial Society



関西学院大学大学院理工学研究科

パイスター分子制御による未来型物質変換研究拠点

## 第1回若手シンポジウム

日時: 2015年12月12日(土)13時～

場所: 関西学院大学 神戸三田学キャンパス 7号館104号教室

### プログラム

13:00-13:10 開会の辞

13:10-13:40 関西学院大学理工学部 赤井勇斗 助教

「キラルスイッチングを特徴とするらせん高分子配位子を用いた触媒的不斉合成」

13:40-14:40 京都大学大学院工学研究科 櫻井庸明 助教

「有機半導体のバルク・界面における非接触電荷輸送特性評価」

14:40-14:50 休憩

14:50-15:20 関西学院大学理工学部 北村圭 助教

「パラジウム(0)触媒を用いる不斉ナザロフ型反応の開発」

15:20-16:20 東京工業大学大学院理工学研究科 鷹谷絢 准教授

「高周期14族元素含有ピンサー型錯体の化学 一触媒設計に基づく合成反応開発の面白さ」

16:20-16:30 休憩

16:30-17:30 分子科学研究所 東林修平 助教

「ヒドラジンユニットを有する新規三次元 $\pi$ 電子系分子」

17:30-17:40 閉会の辞

無料、一般の参加可。申し込み不要

問合せ先: 関西学院大学理工学研究科 兵庫県三田市学園2-1

パイスター分子制御研究センター (研究代表: 羽村) TEL: 079-565-7591



# 関西学院大学大学院理工学研究科

機能性ナノ単一サイズ有機分子創製研究

パイスター分子制御による未来型物質変換研究拠点

## 2016年度 合同シンポジウム

日時: 2016年12月16日(金)13時～

場所: 関西学院大学 神戸三田学キャンパス 4号館202号教室

### プログラム

13:00-13:05 開会の辞

13:05-13:30 関西学院大学理工学部 池内 和忠 助教

「*p*-メチルベンジル基を起点とした独自の研究開拓」

13:30-14:25 東京大学大学院理学研究科 宮村 浩之 助教

「不均一系金属ナノ粒子触媒を用いる有機合成反応の開発  
—反応集積化と不斉合成への展開—」

14:25-14:35 休憩

14:35-15:00 関西学院大学理工学部 仲辻 秀文 助教

「多置換オレフィンのパラレル合成とその応用展開」

15:00-15:55 広島大学大学院理学研究科 安部 学 教授

「 $\pi$  単結合は可能か」

15:55-16:05 休憩

16:05-16:30 関西学院大学理工学部 北村 圭 助教

「 $\pi$ 拡張ルブレンを基盤とする高次縮環芳香族化合物の合成」

16:30-17:25 鳥取大学大学院工学研究科 野上 敏材 准教授

「糖鎖の液相自動合成を目指して」

17:25-17:35 休憩

17:35-18:30 岐阜大学工学部 村井 利昭 教授

「チオアミドを基軸とする新反応、新規機能性分子の開発」

18:30-18:35 閉会の辞

無料、一般の参加可。申し込み不要

問合せ先: 関西学院大学理工学研究科 兵庫県三田市学園2-1

機能性ナノ単一サイズ有機分子創製センター (研究代表: 山田) TEL: 079-565-8342

パイスター分子制御研究センター (研究代表: 羽村) TEL: 079-565-7591



関西学院大学大学院理工学研究科  
パイスター分子制御による未来型物質変換研究拠点  
2017年度 公開シンポジウム

日時: 2017年12月16日(土)13時～

場所: 関西学院大学 神戸三田学キャンパス 7号館104号教室

プログラム

13:00-13:05 開会の辞

13:05-14:00 大阪大学理学研究科 久保 孝史 教授

「 $\pi$ 電子系有機ラジカルの不對電子間相互作用に関する最近の研究」

14:00-14:20 関西学院大学工学部 山内 光陽 助教

「超分子マクロサイクルの協働的超分子重合」

14:20-14:40 関西学院大学工学部 Jung Sunna 博士

「高反応性分子イソベンゾフランを活用した高次イプチセン類の合成研究」

14:40-14:50 休憩

14:50-15:10 京都大学大学院理学研究科(白川研究室) 大倉 圭翔 (D3)

「電子触媒クロスカップリング反応の新展開」

15:10-15:30 関西学院大学工学部 森崎 泰弘 教授

「面性不斉を基盤とする円偏光発光性分子の合成」

15:30-16:25 東京工業大学大学院化学系 福原 学 准教授

「アロステリズム機構が発現する分析化学センサーの創成」

16:25-16:35 休憩

16:35-17:30 京都府立大学大学院生命環境科学研究科 沼田 宗典 准教授

「マイクロ空間が拓く超分子化学の新展開」

17:30-18:25 京都大学大学院工学研究科 中尾 佳亮 教授

「協働金属触媒による有機合成反応」

18:25-18:30 閉会の辞

無料、一般の参加可。申し込み不要

問合せ先: 関西学院大学理工学研究科 兵庫県三田市学園2-1

パイスター分子制御研究センター(研究代表:羽村) TEL: 079-565-7591



関西学院大学大学院理工学研究科  
パイスター分子制御による未来型物質変換研究拠点  
2018年度 公開シンポジウム

日時: 2018年12月15日(土)12時45分～

場所: 関西学院大学 神戸三田学キャンパス 7号館104号教室

プログラム

12:45-12:50 開会の辞

12:50-13:30 大阪大学大学院工学研究科 小西 彬仁 助教  
「縮環制御に基づいた非交互炭化水素類の合成と物性」

13:30-13:45 関西学院大学理工学部(羽村研究室) 池島 諒 (M2)  
「ビフェニレン骨格を有した新規 $\pi$ 共役系分子の創製」

13:45-14:00 関西学院大学理工学部(森崎研究室) 笹井 優作 (M2)  
「異種 $\pi$ 電子系の積層による光学活性分子の合成」

14:00-14:40 東京工業大学科学技術創成研究院 小池 隆司 助教  
「芳香環フォトドックス触媒系の開拓」

14:40-14:50 休憩

14:50-15:05 関西学院大学理工学部(増尾研究室) 吉村 宏之 (M2)  
「ペロブスカイトナノ結晶のハロゲン置換反応における発光挙動観測」

15:05-15:20 関西学院大学理工学部(白川研究室) 池田 佑子 (D1)  
「ラジカル連鎖機構による含ヘテロ原子脂肪族の直接 $\alpha$ -アリール化反応」

15:20-16:15 岡山大学大学院自然科学研究科 仁科 勇太 教授  
「炭素触媒を用いる有機合成」

16:15-16:25 休憩

16:25-17:20 東京大学大学院工学研究科 山東 信介 教授  
「論理的分子設計が実現する高感度生体分子イメージング」

17:20-18:15 九州大学先端物質化学研究所 友岡 克彦 教授  
「珍奇なキラル分子」

18:15-18:20 閉会の辞

無料、一般の参加可。申し込み不要

問合せ先: 関西学院大学理工学研究科 兵庫県三田市学園2-1

パイスター分子制御研究センター(研究代表: 羽村) TEL: 079-565-7591



関西学院大学大学院理工学研究科  
パイスター分子制御による未来型物質変換研究拠点  
2019年度 公開シンポジウム

日時：2020年1月29日（水）13時00分～

場所：関西学院大学 神戸三田学キャンパス 7号館104号教室

プログラム

13:00-13:05 開会の辞

13:05-13:25 関西学院大学理工学部 米倉 恭平 博士  
「インジウム触媒によるアミン類を用いたアルコキシヘテロアレーン上での芳香族求核置換反応」

13:25-13:45 関西学院大学理工学部 足立 和彦 助教  
「安定型オルトキノジメタンの合成・構造・反応」

13:45-14:35 九州大学大学院工学研究院 楊井 伸浩 准教授  
「励起三重項の機能化学：アップコンバージョンと超核偏極」

14:35-14:45 休憩

14:45-15:05 関西学院大学理工学部 井上 僚 助教  
「渡環型白金錯体が示す結晶発光の理論解析と非対称性白金錯体の精密合成法の開発」

15:05-15:55 京都大学化学研究所 若宮 淳志 教授  
「高性能ペロブスカイト太陽電池のための材料化学」

15:55-16:05 休憩

16:05-16:55 大阪大学産業科学研究所 家 裕隆 教授  
「エレクトロニクス応用に向けた新規 $\pi$ 電子系分子の開発と構造物性相関の解明」

16:55-17:45 東京工業大学物質理工学院 田中 健 教授  
「ロジウム触媒を用いた付加環化反応による高歪み $\pi$ 共役分子の合成」

17:45-17:50 閉会の辞

無料、一般の参加可。申し込み不要

問合せ先：関西学院大学理工学研究科 兵庫県三田市学園2-1

パイスター分子制御研究センター（研究代表：羽村） TEL: 079-565-7591

**【問合せ先】**

〒658-0016

兵庫県西宮市上ヶ原一番町1-155

研究推進社会連携機構事務部

電 話：0798-54-6104

F A X：0798-54-6905